

Technical Document 2938
December 1996

Proceedings of the 1996 Battlespace Atmospherics Conference 3–5 December 1996

Editors: J. H. Richter K. D. Anderson

Naval Command, Control and
Ocean Surveillance Center
RDT&E Division

San Diego, CA
92152–5001

19970327 070

Approved for public release; distribution is unlimited.

Technical Document 2938
December 1996

Proceedings of the 1996 Battlespace Atmospherics Conference 3–5 December 1996

Editors: J. H. Richter K. D. Anderson

Naval Command, Control and
Ocean Surveillance Center
RDT&E Division

San Diego, CA
92152–5001





DTIC QUALITY INSPECTED 3

Approved for public release; distribution is unlimited.

NAVAL COMMAND, CONTROL AND OCEAN SURVEILLANCE CENTER
RDT&E DIVISION
San Diego, California 92152–5001

H. A. WILLIAMS, CAPT, USN
Commanding Officer

R. C. KOLB
Executive Director

ADMINISTRATIVE INFORMATION

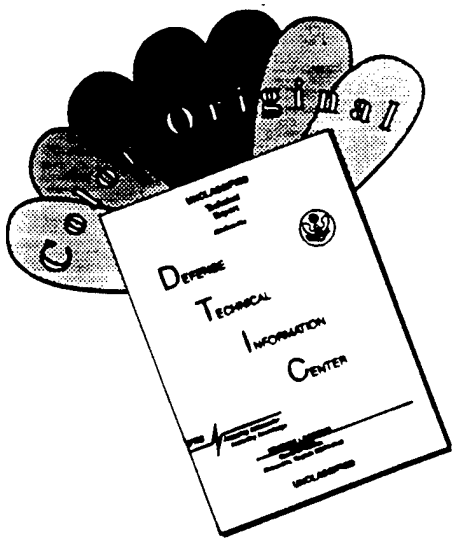
The work detailed in the Proceedings of the 1996 Battlespace Atmospherics Conference was compiled for the Office of Naval Research 322 (MM) by the Naval Command, Control and Ocean Surveillance Center RDT&E Division, Tropospheric Branch, Code D883.

Released by
R. A. Paulus, Head
Troposperic Branch

Under authority of
J. H. Richter, Head
Propagation Division

SB

DISCLAIMER NOTICE



THIS DOCUMENT IS BEST QUALITY AVAILABLE. THE COPY FURNISHED TO DTIC CONTAINED A SIGNIFICANT NUMBER OF COLOR PAGES WHICH DO NOT REPRODUCE LEGIBLY ON BLACK AND WHITE MICROFICHE.

Proceedings of the 1996 Battlespace Atmospherics Conference
3-5 December 1996

Conference Chairs
Dr. Juergen H. Richter and Kenneth D. Anderson

Technical Committee
K.D. Anderson, Dr. W. Bach, Dr. D. Brown, G.D. Dockery, Dr. A. Goroch, CDR D. Markham, Dr. J.H. Richter, Dr. R. Shirkey, P. Tattleman and LCDR R. Dees

Executive Committee
K.D. Anderson, S. Campbell, L. MacPherson, Dr. J.H. Richter, and N. Vorce

Until 1995, Battlefield Atmospherics Conferences were hosted annually by the Army's Atmospheric Sciences Laboratory (ASL) at White Sands, NM. These conferences, while primarily addressing Army concerns, had Navy, Air Force, and international participation. With the incorporation and move of ASL into the Army Research Laboratory, this widely recognized conference could not be hosted by the Army in 1996. DDR&E recommended that it become a tri-service event and be hosted by each of the three U.S. services in succession whereby each service would be responsible for the conference two years in a row. The Navy was selected for 1996 and 1997. The conference name was changed to *Battlespace* Atmospherics Conference to reflect the broader concerns of all service branches. The 1996 Battlespace Atmospherics Conference (BAC '96) was held in San Diego, California from 3-5 December 1996. The conference covered modeling, measurement, and prediction of atmospheric effects on electromagnetic, electrooptical, and acoustic systems. A total of 67 papers and 5 poster sessions were presented. These proceedings contain the written versions for most of the presentations and posters.

The Battlespace Atmospherics Conferences are unclassified. All DoD agencies and their contractors are welcome; attendance by foreign nationals is encouraged. The next conference (BAC '97) is scheduled for 2-4 December 1997 in San Diego. The web site http://www.sunspot.nosc.mil/bac97 has up-to-date information on BAC '97 developments.

Juergen Richter and Kenn Anderson
Chairmen, BAC '96 and BAC '97

Table of Contents

Plenary Session, Chair: Kenn Anderson

		Page
COL R.P. Price	Reorganization and Relocation of the Battlefield Environment Division of the U.S. Army Research Laboratory	1
J.H. Richter and K.D. Anderson	Cooperative Efforts in Atmospheric Effects Assessment	5
CDR T.F. Sheridan, C.R. Miller, III, and E.J. Harrison, Jr.	The U.S. Navy Meteorological and Oceanographic Systems Program	13
C.W. Christensen and J.D. Turton	Co-operation on Meteorological Tactical Decision Aids within NATO	23
D.D. Grantham, S. Brand, A. Wetmore, T.M. Piwowar, J.C. Burgeson, and P.D. Try	Overview of DoD Requirements and Capabilities for Natural Environmental Effects in Military Models and Simulations	37
A. Wetmore, P. Gillespie, A. McCann, and J. Schroeder	EOSAEL and PcEosael	47

Decision Aids, Chair: Paul Tattelman

		Page
P. Tattelman	Progress Update on Decision Aids for EO Weapons Sensors	51
R.J. Szymber and M. Corbett	The Integrated Meteorological System (IMETS) Weather Supporting Concept	57
R.J. Szymber and L. Page III	Owning the Weather for Information Operations	67
D.P. Sauter	The Integrated Weather Effects Decision Aid (IWEDA): Status and Future Plans	75
R.J. Farrell, Jr.	METOC Support Within Command & Control Systems: Context-Sensitive METOC Decision Support Tools	83
S.B. Dreksler and A.K. Goroch	Paper Not Available	
R.E. Turner and A.K. Goroch	Solar-Reflected Radiation From the Sea Surface	93

Radio Propagation, Chair: COL Al Shaffer

		Page
H. Hitney, A. Barrios, and W. Patterson	Radio Propagation Over Terrain	103
E. Mandine and M.C. Pelissier	Direct Stochastic Treatment of Electromagnetic Propagation Problems in a Random Range-Dependent Medium, Using a PE Model	113
V.J. Procopio, A. Vigants, W.T. Barnett, and M. Lambert	Atmospheric Multipath Effects Prediction for Army Communications Links	123
L. Phegley, D.W. Merdes, B. Daly, and J.W. Chu	Atmospheric Analysis Capability to Support Electromagnetic Applications	133
G.C. Konstanzer, J.R. Rowland, G.D. Dockery, J.J. Sylvester, M.R. Neves, and D.R. Davis	SEAWASP: A Prototype System for Shipboard Assessment Based on in situ Environmental Measurements	143
J.R. Rowland, G.C. Konstanzer, M.R. Neves, R.E. Miller, J.H. Meyer, and J.R. Rottier	SEAWASP: Refractivity Characterization Using Shipboard Sensors	155
S. Kang and J. Stapleton	Microwave Propagation Measurements in the Low Altitude Region Using Single Frequency and Wideband Systems	165

Measurements and Modeling of EO Parameters, I, Chair: Dr. Andy Goroch

		Page
H.E. Snell, G.P. Anderson, J.H. Chetwynd, and S. Miller	FASCODE for the Environment (FASE)	175
D.H. Höhn, W. Jessen, and D. Clement	Atmospheric IR Transmittance Statistics in Arid Climates Based Upon Synoptic Data from Selected Middle East Weather Stations	183
G. de Leeuw, A.M.J. van Eijk, and D.R. Jensen	Marine Aerosol Properties and Thermal Imager Performance (MAPTIP): Synopsis	193
C.R. Zeisse, D.R. Jensen, and K.M. Littfin	EOPACE (Electrooptical Propagation Assessment in Coastal Environments) Overview and Initial Accomplishments	203
A.K. Goroch	Slant Path Extinction in a Stratified Atmosphere	211

Measurements and Modeling of EO Parameters, I, Chair: Dr. Andy Goroch

		Page
K.L. Davidson, C.H. Wash, and M.S. Jordan	Remote Sensing of Coastal Atmosphere EM/EO Conditions	217
B. Ben-Dor, A.D. Devir, and A. Ben-Shalom	Atmospheric Scattering Effect on Spatial Resolution of Imaging Systems	223

Battlespace Sensing, Chair: CDR David Markham

		Page
G. Frederick, R. Foster, J. Daniels, and M. Smith	Essential Atmospheric & Oceanographic Measurements in Hard to Reach Areas of the Battlespace	235
D.K. Wilson	On the Degradation of Acoustic Angle-of-Arrival Estimates Due to Atmospheric Turbulence	243
R.M. Cionco, G. Steele, and G. Moran	Paper Not Available	
R.M. Cionco and J.H. Byers	Influence of Airfield Structures and Complex Terrain Upon Simulated Local Wind Fields	253
J.R. Roadcap, R.A. Swirbalus, M.H. Laird, P.J. McNicholl, and D.L.A. Rall	Wind Velocity and Aerosol Backscatter measured by CO_2 Doppler Lidar	263
L.T. Rogers and R.A. Paulus	Measured Performance of Evaporation Duct Models	273
L.T. Rogers, R.A. Paulus, and J. Cook	Fusing Data from the Mesoscale Model and Radio Remote Sensing	283

Measurements and Modeling of EO Parameters, II, Chair: Prof. Dieter Höhn

		Page
W.S. Andrews, S.D. Roney, and G. Roy	An Examination of Modelling Approaches for Predicting the Dispersion of Aerosols from Obscurant Grenades	293
R. Knapp, K. Eis, T. Vonder Haar, and K. Fuller	Detection of Battlefield Visibility from Satellite	303
T. J. Hall, D.L.einke, and T. Vonder Haar	Forecasting Applications of High Resolution Diurnal Satellite Cloud Composite Climatologies over former Yugoslavia and the Adriatic Sea	313

Measurements and Modeling of EO Parameters, II, Chair: Prof. Dieter Höhn

		Page
R.E. Davis and A.C. Rishel	Modeling the Effects of Screening Aerosols on Pulsed Designator Systems	323
J.M. Forsythe, D.L. Reinke, D.L. Randel, K.E. Eis, and C.L. Combs	CLVL: A Global High-Resolution Layered Cloud Database	333
J.B. Mozer and T.R. Caudill	The Lattice Boltzmann Method: A New Approach to Radiative Transfer Through Clouds	343
D.W. Hoock Jr., J.C. Giever, and S.G. O'Brien	A Practical Model for Contrast Under Nighttime, Artificial Illumination	349

Simulation and Visualization, Chair: LCDR R. Dees

		Page
G. McWilliams	DoD Air and Space Natural Environment Modeling and Simulation	359
R. Shirkey, J. Turner, and R. Schaffer	Atmospheric Modeling in the Synthetic Theater of War (STOW 97)	367
D.W. Hoock, D.H. Tofsted, and J.C. Giever	Tactical Battlefield Visualization of Forecast Weather and Effects	377
E. Nunez, J. Medeiros, B. Burns, and G. McWilliams	Development of an Atmospheric and Space Environmental Models and Simulations Directory	387
D.H. Tofsted and S.G. O'Brien	Application of the WAVES Modeling Suite to the Visualization of Natural Cloud Fields	393
C. Lamar, W. Cook, and W. Gebhart	FASTPROP Environmental Effects for Constructive Simulations	403
A.R. Boehm	Wargaming Ultra-Fast Propagation Algorithms for FASTPROP	413
M.C. Sola, M.W Orletsky, Q.B. Vuong, and C.R. Kohler	Proposal for Validation of a Multi-Spectral Synthetic Scene Generator	423

Meteorological Modeling and Data Assimilation, Chair: Dr. Walter Bach

		Page
R.M. Hodur	Paper Not Available	
S. Khanna and J.C. Wyngaard	Local Refractive Index Structure-function Parameter and its Application to Wave Propagation	433
M.J. Otte, N.L. Seaman, D.R. Stauffer, and J.C. Wyngaard	A Mesoscale Model for EM Ducting in the Marine Boundary Layer	441
K.E. Eis, J. Foresythe, and D. Reinke	The Fractal Behavior of Cloud Systems	447
T. Henmi	Forecasting of Fog/Cloud and Precipitation by the Battlescale Forecast Model (BFM)	455
F.H. Ruggiero, K.D. Sashegyi, and R.V. Madala	Assimilation of Remotely Sensed Data in a Portable Forecast and Analysis System	465
D. Bustamante, J. Cogan, W. Gutman, E. Measure, and G. Vaucher	Results and Implications of Neural Network Retrievals of Satellite Temperature Soundings	473

Environmental EM Modeling System (EEMS), Chair: Dan Dockery

		Page
D. Lewis and P. Beattie	The Environmental Electromagnetic Modelling System (EEMS) Project Overview	483
S.J. Moss and A.C. Steele	Meteorological Support for UK Navy Operations	489
M.F. Levy and K.H. Craig	TERPEM Propagation Package for Operational Forecasting with EEMS	497
M. Williams and A. Ayoola	Blue Water EEMS - TDRSS	507
M.R. Moore and A.K. Shukla	High Frequency Coverage Prediction for EEMS	513
A. Shukla, P. Cannon, and M. Moore	A HF Tactical Decision Aid for Conventional and Automated Radio Control Systems	521

Radar Sensing, Chair: Dr. Richard Shirkey

		Page
N.J. Bucci, H.S. Owen, J.V. Melody, and J.F. Heimmer	Tactical Weather Radars for Theater Meteorological Data Collection and Assimilation	531
Owen, H. Urkowitz, N. Bucci, J. Melody, and R. McLean	Tactical Weather Radar Experiment for a Shipborne Radar	541
J. Cogan, E. Measure, and D. Wolfe	Atmospheric Soundings in Near Real Time from Combined Satellite and Ground-Based Remotely Sensed Data	551
M.J. Post and K.P. Moran	New Cloud Profiling Radar for Air Operations	561
M.J. Post, C.W. Fairall, A.B. White, J.R. Jordan, and K.S. Gage	Shipboard Wind Profiling by Radar: Problems and Possible Solutions	567
M.J. Post, E.E. Gossard, B.B. Stankov, D.E. Wolfe, and K.P. Moran	Evaluation of the Continuous Profiling of Refractive Index Gradients and Humidity Using Radar Signals	573

Posters

		Page
W.T. Matthew, W.R. Santee, R.W. Hoyt, P. Tikuisis, E.S. Barnes, G.B. McWilliams, H.D. Pfeiffer, and J. Furlong	Automated Thermal Injury Risk Assessment in the Dismounted Infantry Battlespace	579
J.A. Penn, H.M. Nguyen, C.R. Kohler, and M.C. Sola	The CREATION Scene-Generation Program Applied To Battlespace Flight Scenarios	587
C.R. Philbrick and D.B. Lysak, Jr.	Lidar Measurements of Meteorological Properties and Profiles of RF Refractivity	595
J. Rosenthal, M. McGovern, and R. Helvey	Battle Space Weather Conditions for Joint Strike Support	611
S. Lowe, N. Alper, C. Stein, and R. Siquig	Paper Not Available	

Reorganization and Relocation of the Battlefield Environment Division of the U S Army Research Laboratory

COL Richard P. Price
US Army Research Laboratory
Information Science and Technology Directorate
Director, Battlefield Environment Division, AMSRL-IS-E,
2800 Powder Mill Road
Adelphi, MD 20783-1197
Phone: 301-394-2286, FAX: 301-394-4797
e-mail: rprice@arl.mil

Abstract

Current organization, strength, and technology thrusts are presented for the US Army Research Laboratory (ARL) Battlefield Environment Division (BED). Near-term tactical weather deliverables for the Army's artillery and intelligence customers are discussed. Generalized funding and long-range research goals are discussed. 1991 Base Realignment and Closure (BRAC) requirements for relocating portions of the former Atmospherics Sciences Laboratory at White Sands, NM, are reviewed. Subsequent restructuring of ARL and current alignment of atmospheric sciences research continues at the US Army Research Lab, Adelphi, MD, and White Sands Missile Range, NM.

1. Introduction

Over the last year, two efforts have been completed which resulted in the reorganization and relocation of the Battlefield Environment Division, which was formerly the independent Atmospheric Sciences Laboratory located in White Sands Missile Range, New Mexico, and then the Battlefield Environment Directorate of the Army Research Laboratory. The first of these was the movement of the atmospherics effects mission from White Sands to Adelphi, Maryland, as a result of the Base Realignment and Closure Act of 1991. This move coincided with the construction of new facilities to receive the 56 research positions transferred to Adelphi. A new $2.3 million High Bay building was completed in October, 1996, to house the electro-optics and adaptive intelligent optics laboratories, and a new site for atmospherics/acoustics propagation studies is currently being constructed at Blossom Point, Maryland. The second effort was the internal reorganization of the Army Research Laboratory from 11 original directorates to 5 new directorates. One of these directorates, Information Science and Technology, was formed consolidating all or part of three directorates with nine division and ended in a structure of three divisions, of which the Battlefield Environment Division is the largest.

2. Division Mission

The United States Army Research Laboratory (ARL) Battlefield Environment Division (BE) of the Information Sciences and Technology Directorate is the lead Department of Defense organization for research and development in the portion of the atmosphere unique to the Army warfighter's battlespace--the planetary boundary layer. BE's mission is to "Own the Weather" (OTW) by providing atmospheric effects information to decision makers on the battlefield in planning and executing operations. The joint Army/Air Force OTW initiative will provide knowledge of current and forecast battlefield environment conditions, along with their effects on systems, soldiers, operations, and tactics, to provide a decisive advantage over opponents. Succinctly stated, the mission is to own the weather by advancing our understanding of the atmosphere and its critical relationship to performance of Army systems operations. To do this, BE acts to develop, acquire and integrate new atmospheric science technologies that enable Land Force Dominance. Annual mission funding for this mission is on the order of $11 million excluding customer funding from outside agency sources.

Under the DOD Project Reliance taxonomy, BE is the lead agency for multi-service programs in transport and diffusion modeling and mobile atmospheric profiling, with the latter technology transferring out of BE to advanced engineering development in FY 99. In addition, BE contributes to tri-service goals in the areas of theater data fusion

and predictions, boundary layer processes, and atmospheric effects. The branches remaining at White Sands are the Weather Exploitation and Artillery Meteorology Branches. The branches at Adelphi are the Atmospheric Effects and Synthetic Environments Branches.

The BE program is driven by the Army's need for boundary layer meteorological information at scales smaller than those used by either the Air Force, Navy, or civilian community, and over data sparse geographic regions. The requirement to host this capability on Army tactical hardware further impacts the research and development programs.

3. Specific Division Functions

Listed below are the specific functions provided by the Battlefield Environment Division:

(1) Direct atmospheric sciences programs consistent with priority Army requirements; and manage the division's research, development, and applications plans.

(2) Provide executive management, advice, and assistance for the division and manage division resources.

(3) Recommend the establishment of appropriate technical plans, policies, and procedures; serve as the point of contact (POC) on matters related to technical plans and programs.

(4) Analyze potential customer requirements and foster effective customer relationships.

(5) Prepare the division's portion of planning and marketing documents, and coordinate technical planning and marketing with ARL to ensure technical plans agree with ARL strategy and business plan.

(6) Coordinate and consolidate the technical program, monitor implementation, and review and analyze accomplishment of directorate objectives, including the WEATHER XXI Campaign Plan and the Army After Next initiatives.

(7) Recommend the establishment of appropriate atmospheric research and development programs based on documented Army requirements.

(8) Develop and coordinate long-range planning and programming for the division mission with ARL and publish the Directorate Strategic Long Range Plan.

(9) Formulate organizational budget requests for the Budget Year (subsequent fiscal year) for all program elements.

(10) Manage the financial resources during the execution and Five Year Defense Plan (FYDP) for the current and prior year.

4. Atmospheric Effects Branch

The mission of the Atmospheric Effects Branch is to improve the understanding of boundary layer processes of the battlefield and provide a means of implementation of these Army-scale processes for use by the Commander. This includes developing a capability for the Army to effectively detect and identify the presence of biological agents, both in situ, and remotely. It also includes research on first principal acoustic propagation models for use as battlefield decision aids. The branch provides enhanced knowledge of NBC hazard zones and the effects of local meteorology on various types of military operations. They perform theoretical and experimental investigations into nonlinear optical dynamics designed to develop systems capable of correcting severe phase distortion and improving image quality.

The Atmospheric Effects Branch was entirely relocated to Adelphi. These are the principal basic researchers in atmospheric physics. The Atmospheric Effects efforts address: (1) acoustic propagation and background models for predicting environmental effects on acoustic signatures and sources; (2) micrometeorology of urban and vegetative canopies, (3) optics and beam propagation in the boundary layer; (4) transport and diffusion of chemical/biological agents and other aerosols released into the atmosphere; and (5) in-situ and remote detection of chemical/biological agents and pollution aerosols. ARL BE performs associated boundary layer profiling research, with the FM-CW radar and Sodars, and acoustic field work, including the 56 foot long Mobile Acoustic Source, at Blossom Point, Maryland, upon completion of the site preparation and equipment refurbishment in FY98.

There are five teams within this branch. Their missions and functions follow:

(1) Atmospheric Transport & Diffusion Modeling Team

(a) Develop techniques and parameterization methodologies for improving Large Eddy Simulation and micro meteorological models.

(b) Developments are being directed so that results can have a more direct application to command post tools such as Tactical Decision Aids.

(2) Atmospheric Acoustics Team

(a) Develop validated acoustic propagation and background models for assessing and predicting environmental effects of the atmosphere.

(b) Develop validated acoustic propagation models for assessing and predicting atmospheric turbulence, and land-sea interfaces on acoustic signatures as propagated from source to receiver.

(3) Chemical/Biological Research Team

(a) Provides atmospheric effects on stand off detection through both a laboratory research effort and a modeling effort.

(b) Simulate the effects of natural background interferrents such as bacteria spores, pollens, molds, and clay minerals using ultraviolet detection of agents.

(c) Investigate the potential for using circular polarization as an alternative to fluorescence detection. Explore new technologies for detection of bioagents such as Acoustic-Optical Tunable Filters (AOTF) and Optical Parametric Oscillator (OPO).

(4) Boundary Layer Processes Team

(a) Establish a boundary layer field measurement facility

(b)Develop an inventory of Army relevant boundary layer and micro meteorological models/codes.

(5) Adaptive Optics

(a) Develop new techniques to mitigate optical turbulence effects

(b) Transition understanding of atmospheric effects to imaging and sensor technologies

(c) Develop capability using adaptive optics to permit target recognition in a cluttered environment.

5. Synthetic Environments Branch

The Synthetic Environments effort addresses: models and simulations of environmental effects on electro-optical systems and visualization of models and synthetic environments using realistic battlefield conditions. This branch develops and investigates research methods by which to model and depict the battlefield environment and to develop scientific methods by which to evaluate these models. Using a combination of models and both laboratory and field experiments, this branch scientifically describes both natural and battlefield environments. The branch consists of the following teams.

(1) Atmospheric Electro-Optics Team

(a) Develop a complete suite of models to be used for characterizing and simulating the battlespace atmospheric environment.

(b)Continue to develop experimental capabilities to determine the effects on electro-optical propogation.

(2) Virtual Proving Ground/Virtual Sand Table Team

(a) Develop tools to simulate dynamic terrain and dynamic cultural features to provide realism.

(b) Develop multi-level of detail at variable resolution

(c) Develop efficient algorithms and employ high performance and distributed computing techniques to increase the speed of physical rendering of models

(d) Develop a methodology for providing for interoperability between models based on model description language.

6. Weather Exploitation Branch

The Weather Exploitation efforts address: (1) battlescale forecasts of tactical weather, (2) tactical weather data assimilation and distribution, (3) advanced tactical decision aids integrated with tactical weather data products; and (4) transitioning advanced weather technology to Battlefield Automated Systems and Battle Laboratories. The mission of this branch is to develop and market Owning the Weather technologies to the warfighter

through Advanced Warfighting Experiments (AWEs), Advanced Technology Demonstrations (ATDs) and other technical demonstrations for both Army and Air Force users. Develop automated capabilities to acquire weather data from all available sources on the battlefield and distribute information to Battlefield Automated Systems (BASs). The three teams and their functions are:

(1) Weather Intelligence Team

(a) Develop the capability for battlefield commanders to exploit weather as a combat multiplier to gain advantage over the enemy

(b) Enhance battle command effectiveness through the use of automated weather decision aids.

(2) Weather Effects Integration Team

(a) Develop, implement, and demonstrate client/server IMETS applications based upon Battlescale Forecast Model (BFM) forecasts of the battlefield environment.

(b) Integrate BFM and weather effects models for unified weather effects for operations, mission rehearsal, training and combat simulations

(3) Technology Transition Team

(a) Adapt the IMETS client/server approach to interface with environmental effects visualization models and combat simulation tools to provide a common, unified weather effects environment.

(b) Support Task Force XXI through deployment of battle command systems and on-site support of hardware and software tools.

7. Artillery Meteorology Branch

The Artillery Meteorology efforts include: (1) integration of tactical weather data and forecasts into artillery indirect fire and precision strike operations, and (2) remote sensing Profiler technology for artillery upper air soundings, which will transition in FY99 to the engineering developer for advanced engineering and fielding with the Army. The mission of this branch is to use Own the Weather technologies to enhance the warfighter's ability to exploit weather as a combat multiplier and execute precision strikes. This includes developing technologies to accurately predict battlescale and target area weather for use in automated weather effects decision aids that transform weather data into weather intelligence for Army Battle Command System (ABCS) Battlefield Automated Systems (BASs). The two teams and their functions are:

(1) Met Systems and Fusion Team

(a) Develop a prototype mobile atmospheric profiler system, which when coupled with meteorological satellite and other battlefield met sources, eliminates the requirement for logistically burdensome artillery balloon borne sensor and hydrogen generators.

(b) Develop and demonstrate techniques to fuse atmospheric data from battlefield met data sources such as artillery met systems, wind radar profilers and radiometers, met satellites, UAV dropsondes and onboard met sensors, and automated in-situ surface sensors for a more coherent and timely measurement of battlefield met conditions.

(2) Computer Assisted Artillery Met Team

(a) Develop Computer Assisted Artillery Meteorology (CAAM) software that uses fused data and mesoscale meteorological modeling to more accurately predict trajectory and target area meteorology.

(b) Horizontally integrate CAAM data into artillery C4I systems to minimize met effects on indirect fire systems, and as a combat multiplier for deep attack planning and execution.

8. Conclusion

The reorganization and relocation of the Battlefield Environment Division has not changed any of the missions and functions of the organization. In fact, there are considerable advantages of synergy with the merging of atmospheric effects and synthetic environment with the Information Science and Technology Directorate which focuses on battlefield situation awareness through visualization, advanced telecommunications, software and intelligent systems research. As can be seen by the number of papers presented at this Battlespace Atmospherics Conference and in the past, the research continues to be excellent and the organization continues to achieve its mission of advancing our understanding of the atmosphere and its critical relationship to the performance of Army specific requirements, enabling land force dominance.

COOPERATIVE EFFORTS IN ATMOSPHERIC EFFECTS ASSESSMENT

Juergen H. Richter and Kenneth D. Anderson
Propagation Division

NCCOSC RDTE DIV CODE D88
53570 Silvergate Ave
SAN DIEGO, CA, 92152-5230
Ph: 619-553-3053
Fax: 619-553-3058
E-mail: richter@nosc.mil; kenn@nosc.mil

ABSTRACT

This first Battlespace Atmospherics Conference reflects the increasing emphasis on joint operations, not only among the different branches of the military services but also with allies, such as NATO countries. Atmospheric effects assessment for military operations or hardware design would not be at the state it is today were it not for joint R&D programs in the past. A few of such programs are reviewed and highlights of their accomplishments presented. They include the tri-service Atmospheric Transmission Plan and joint programs performed by Research Study Group 8 of Panel 4 of the Defense Research Group (DRG) of NATO; evaporation ducting assessment addressed by Research Study Group 6 of Panel 3 of DRG/NATO; measurement of variability of coastal atmospheric refractivity and EO parameters conducted under sponsorship by the Office of Naval Research involving many participants. It is concluded that cooperative programs not only leverage increasingly scarce resources they also provide much broader perspectives resulting in more generally applicable solutions.

INTRODUCTION

Research and development (R&D) efforts, especially those that require data from different geographic regions, are most efficiently carried out cooperatively. This is especially true for military R&D in the post-cold war environment where defense budgets are significantly reduced. Since this is a conference sponsored by the joint services in the U.S. and has broad international participation, it seems appropriate to review some examples of highly successful cooperative efforts. Three examples are presented: the Department of Defense Plan for Atmospheric Transmission Research and Development; evaporation ducting assessment by the DRG of NATO; and a series of coastal propagation programs for electromagnetic and electrooptical propagation assessment.

ATMOSPHERIC TRANSMISSION PLAN

In the late 1970s, the Director, Defense Research and Engineering (DDR&E) issued guidance for cooperation between the U.S. Army, Navy and Air Force in the area of transmission of optical, infrared, and millimeter wave propagation through the atmosphere (Perry, 1978). This guidance identified technical issues and assigned responsibilities to the services for their solution. The Air Force was assigned responsibility for development and maintenance of atmospheric transmission codes (such as LOWTRAN, HITRAN, MODTRAN). The Army was assigned responsibility for measurement and modeling of atmospheric propagation for battlefield conditions. The Navy was assigned responsibility for predicting propagation conditions in marine environments. For the Navy, the most pressing issue was the development of suitable marine aerosol models. The development of the first in a series of marine aerosol models is an example of using cooperatively obtained data from complex field experiments. Until that time, marine aerosol models considered by the U.S. Navy were based on a two component distribution (Wells et al., 1977). Gathman (1983) examined a large body of previously obtained aerosol data. Among them were measurements by various groups in the Atlantic, the Pacific, and the Baltic. The platforms used were U.S. and Dutch research vessels, British, German, and U.S. research towers, shore stations, and aircraft. A careful statistical analysis of the data revealed three peaks within in the aerosol size distributions suggesting a three-component aerosol model for the marine environment.

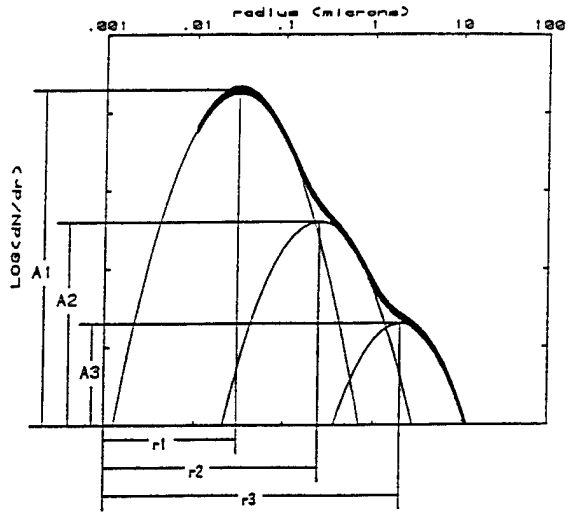


Figure 1. The Navy Marine Aerosol Model (NAM).

Consequently, a Navy Aerosol Model (NAM) was defined by a linear combination of three log-normal distributions. Figure 1 shows the three component NAM with each component characterized by a mode radius r and an amplitude A. The distribution with the smallest mode radius is the background aerosol related to the air mass characteristics and independent of the local wind parameters. The second component represents marine aerosols that can statistically be related to the 24-hour wind average. The third component with the largest mode radius is related to the current wind. NAM was incorporated into LOWTRAN 6 (Kneizys et al., 1983) and subsequently extended to include vertical dependencies in a model

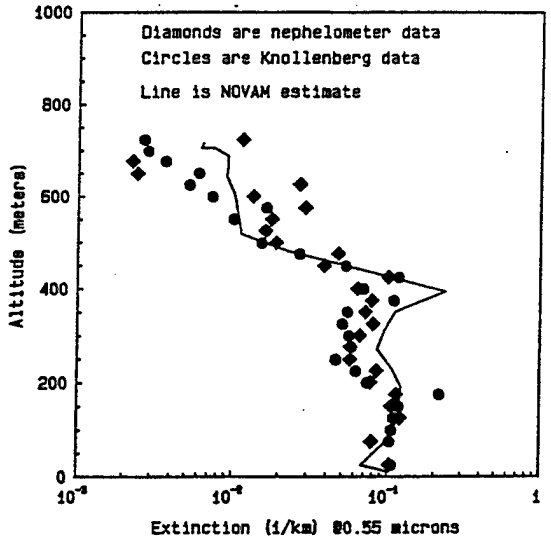


Figure 2. Extinction profiles from aerosol model NOVAM, nephelometer, and drop size distribution (Knollenberg spectrometer) measurements.

called the Navy Oceanic Vertical Aerosol Model (NOVAM) (Gathman et al., 1990). Figure 2 is an example of an extinction profile at 0.55 μm wavelength calculated using NOVAM (solid line). NOVAM-derived extinction profiles compare favorably with those calculated from nephelometer (diamonds) and drop-size distribution measurements (circles). The threat to ships by sea skimming missiles and the need to detect such threats with electrooptical devices, prompted a careful investigation of near-surface drop size distributions. It was found necessary to add a fourth aerosol component to account for very large, near-surface aerosols generated by high winds under white-capping conditions. Measurement of such aerosol distributions is very difficult and was one of the objectives of a multi-national experiment conducted by Research Study Group 8 of Panel 4 (Optics and Infrared) of NATO's DRG. The experiment was called Marine Aerosol Properties and Thermal Imager Performance (MAPTIP) and conducted on the Netherland's Meetpost Noordwijk, an oceanographic platform 9 km off the Dutch coast (Jensen et al.,1993). Gathman (1996) added a fourth component to the aerosol model that is now called the Advanced Navy Aerosol Model (ANAM). This fourth component has a mode radius that is independent of wind speed and the amplitude of the distribution looses its vertical height dependence for high wind speeds. The carefully planned multi-national experiment for obtaining the data necessary to describe this fourth component is an excellent example of the need for and the success of cooperative programs.

MICROWAVE DUCTING

Atmospheric refractive layers may channel or duct electromagnetic (EM) energy very effectively. One persistent ducting mechanism found over oceans is the so-called evaporation duct. It is caused by the rapid decrease of humidity directly at the water surface to an ambient value above as shown in the left panel of Figure 3. The center panel shows radio refractivity N and the right panel modified refractivity M. The inflection point in the M-profile defines "duct height", the commonly used parameter to describe the strength of the evaporation duct. Figure 4 illustrates effects of evaporation ducting on signal strength (expressed as propagation loss) for different duct heights. Propagation loss increase (signal decrease) within the radio horizon with increasing duct height (between 7-20 km in figure 4) can be detrimental when trying to detect an incoming missile while propagation loss decrease (signal enhancement) at longer ranges aids detecting such missiles. Depending on frequency,

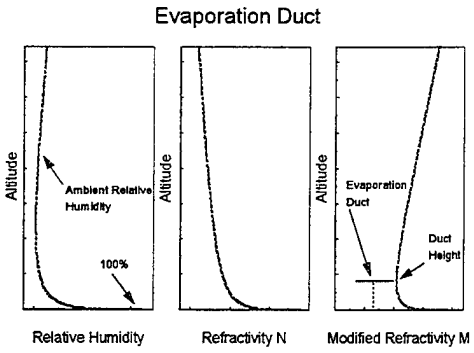


Figure 3. Humidity and refractivity profiles for evaporation ducting.

evaporation ducting can produce many orders of magnitude in signal enhancement for over-the-horizon propagation. Figure 5 is an example of radar measurements under evaporation ducting conditions (Anderson, 1993). A shore-based radar at a height of 23.5 m above mean sea level and a frequency of 9.4 GHz tracked a target at height of 4.9 m between 4 - 18 km. Propagation loss is shown by the solid line for a standard atmosphere and by the triangles for the prevailing ducting condition (duct height 10 m). The radar data clearly show both the theoretically predicted initial decrease (between 8 -12 km) and a subsequent increase (>16 km) of signal levels due to evaporation ducting.

Timely and reliable assessments of evaporation ducting effects are crucial for ship surveillance and point-defense purposes. Profiles of vertical humidity

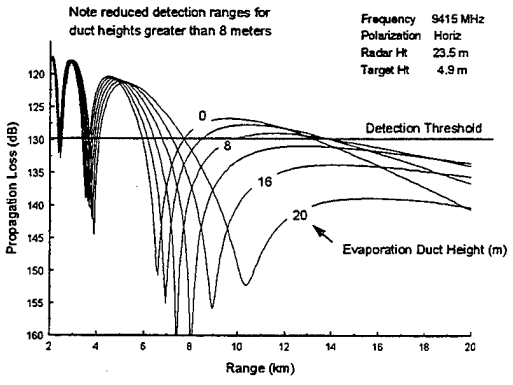


Figure 4. Propagation loss for different evaporation duct heights.

(and thereby refractivity) are not readily measurable because the most rapid profile changes occur within the first few cm above the water surface. Apart from the fact that it would be very difficult to make measurements that close to the surface, the height of the surface is only constant when averaged over several minutes. In surface layer meteorology, semi-empirical relationships between fluxes of meteorological quantities and their profiles have been developed and so-called bulk measurements (i.e., point measurements at a reference height) are used to infer the meteorological profiles. The need for developing, improving, and validating evaporation ducting assessment prompted several NATO cooperative efforts.

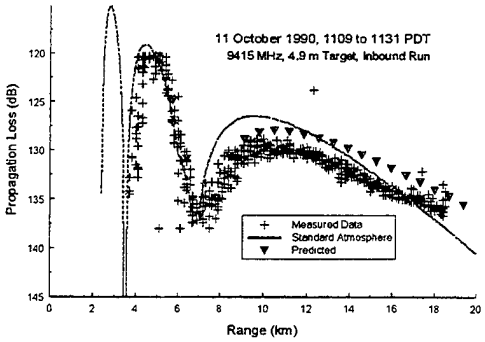


Figure 5. Measured propagation loss under evaporation ducting conditions.

One effort was a joint U.S. - Greek measurement program in the strategically important eastern Mediterranean. With support from the University of Athens, the U.S. Navy established a propagation link between the islands of Mykonos and Naxos in the Aegean Sea (Richter and Hitney, 1988). The shore station at Mykonos used vertically spaced antennas for receiving signals in the 1 - 40 GHz range radiated from the island of Naxos 35 km away. The link was operated during four measurement periods in different seasons, each lasting approximately two weeks. The objectives of these measurements were to gather statistical evaporation ducting data in this important geographic area, validate ducting models, and provide information on choosing optimal shipboard antenna heights for maximum detection ranges. An example of a two week measurement period is shown in figure 6 where the dots represent measured path loss values at 9.6 GHz for a receiving antenna at 4.9 m and the transmitter antenna at 4.8 m above mean sea level. Most striking is the persistent signal enhancement of

up to 60 dB over what would be expected under standard atmospheric conditions (the upper dashed line indicates free space path loss values and the lower diffraction path loss values).

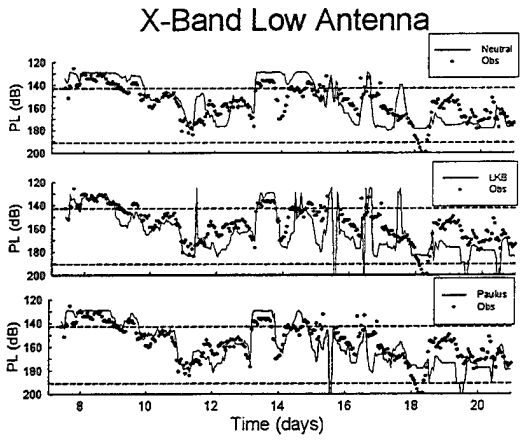


Figure 6. Path loss values under evaporation ducting conditions (dots) and evaporation duct models.

In addition to the propagation measurements in Greece, another important cooperative initiative was the establishment of NATO DRG (Panel 3) Research Study Group 6 (RSG 6). This group was chartered to "*investigate the low level maritime duct and its influence on microwave propagation.*" RSG 6 was chaired by Professor Jeske of the University of Hamburg, Germany. At the time, he and his institution had performed the most comprehensive analyses and measurements with respect to evaporation ducting (Jeske, 1965; 1971). Participating nations in RSG 6 were Canada, Denmark, Germany, Italy, Netherlands, Norway, U.K., and U.S. The group conducted meetings, measurement campaigns, and analyses and concluded its work in 1977. The final report states that "*for the evaporation duct well understood models are at hand*" (Jeske, 1977). The conclusion, that evaporation ducting effects can be reliably assessed under operational conditions, has been proven by two decades of experience even though the understanding of the physical processes governing flux-profile relationships in the surface layer have been and probably will be further improved (Liu et al., 1979; Fairall et al., 1996). The prediction accuracy for evaporation ducting effects is not limited by an incomplete understanding of surface layer physics but by horizontal variability. Evaporation ducting is operationally significant primarily for propagation paths over tens to hundreds of kilometers. Over such distances, surface water temperature and surface layer properties will change thereby causing horizontally varying duct heights. This is the reason that newer evaporation duct models have not shown improved assessment accuracies. Rogers and Paulus (1996) have compared several models with different measurements. In figure 6, they compare three different evaporation duct models (shown by the solid lines) with the previously described measurements in the Aegean Sea. The meteorological data used as input to the different models are based on shore measurements taken at the receiving site. In the top panel, Jeske's (1971) formulation is used with the assumption of neutral stability in the surface layer. The solid line in the center panel shows calculated path loss based on the formulation of Liu et al. (1979) and the bottom panel a modification of Jeske's (1971) model by Paulus (1985). All three models do a credible job in predicting evaporation duct enhancements with none of them showing a clear superiority over the others. The conclusion reached by RSG 6 almost two decades ago still holds today and data obtained in cooperative efforts under NATO auspices remain an invaluable source of information. NATO-sponsored ducting investigations have continued, the most recent being a microwave/millimeter wave effort under NATO DRG (Panel 3) RSG 8 sponsorship (Christophe et al., 1995).

The finding that evaporation ducting effects could be reliably assessed under operational conditions was one of the foundations that made the development of the first military microwave propagation assessment system possible. The Integrated Refractive Effects Prediction System (IREPS) (Hitney and Richter, 1976) was first operationally implemented in the late 1970s aboard U.S. aircraft carriers and is now used as part of the U.S. Navy's Tactical Environmental Support System (TESS) (Sheridan et al., 1996).

The above evaporation ducting findings could not have been obtained without the cooperative effort with leading experts in the field and access to locations in other nations. Today's propagation assessment capability available to the U.S. fleet owes much to highly successful cooperative efforts performed under NATO auspices.

PROPAGATION ASSESSMENT IN COASTAL ENVIRONMENTS

The shifting military emphasis from global to regional conflicts and the experience that the latter often involve coastal areas, prompted an intensified research effort into often highly variable coastal EM and EO propagation conditions. The Navy's Office of Naval Research has supported a program aimed at

understanding and predicting microwave, millimeter, and electrooptical propagation in coastal environments.

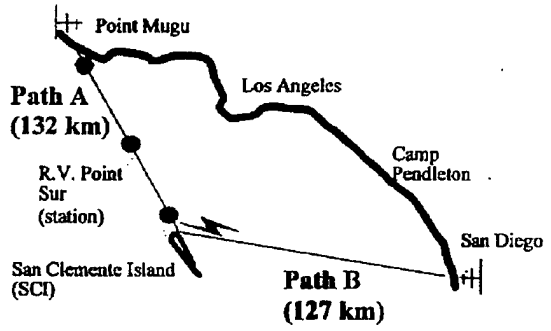


Figure 7. Propagation paths during VOCAR

The first measurement program was the Variability of Coastal Atmospheric Refractivity (VOCAR) conducted in 1993 in the southern California off-shore region (Paulus, 1995). Participants included the Naval Command, Control and Ocean Surveillance Center, the Naval Air Warfare Center, the Naval Research Laboratory, the Naval Postgraduate School, the Environmental Technology Laboratory of the National Oceanic and Atmospheric Administration, and the Pennsylvania State University. One of the objectives of VOCAR was to provide long-term radio propagation data in conjunction with meteorological measurements for the development and validation of mesoscale models capable of predicting vertical refractivity structure. Another objective was to use reception of radio signals from known emitters to infer refractivity. A third objective was the development and use of satellite and ground-based remote sensors for either measuring or inferring refractivity conditions. Figure 7 shows the geometry for two propagation paths in the southern California bight. Signals were radiated from the northern tip of San Clemente Island and received simultaneously in Point Mugu (path A) and in San Diego (path B). Paths A and B are nearly identical in length but traverse different areas in the southern California bight where complex mesoscale circulations (such as the Catalina eddy) and an irregular coast line with varying

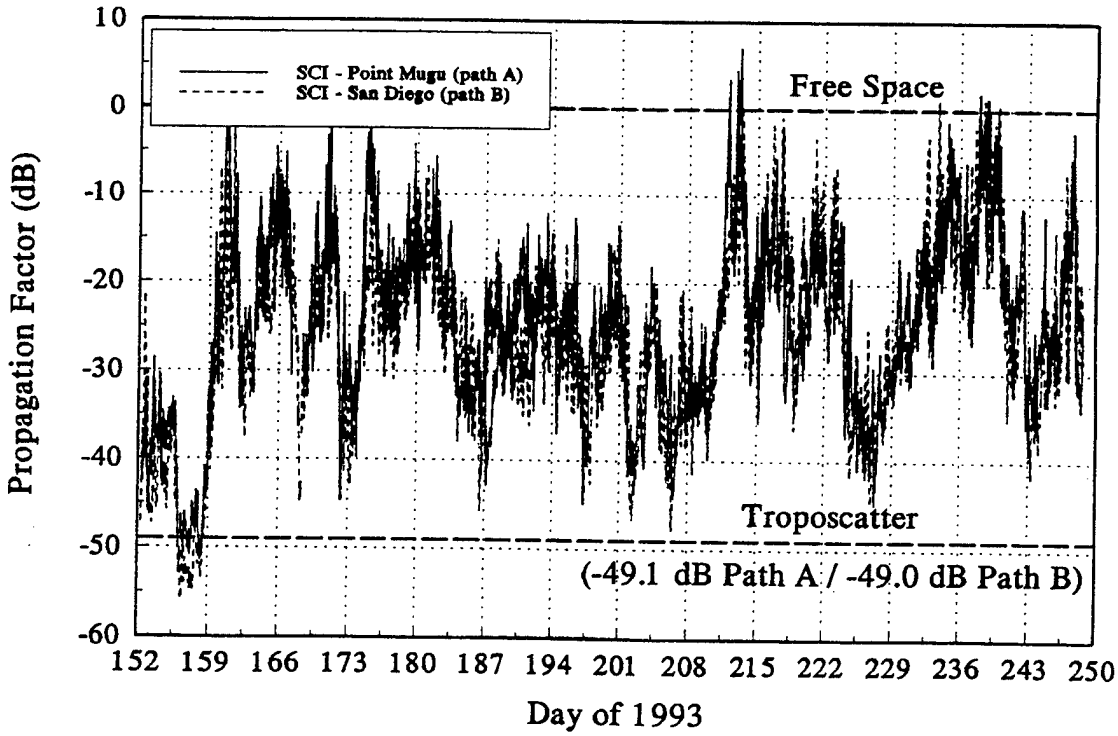


Figure 8. Long-term propagation measurements during VOCAR.

topography might cause horizontally inhomogeneous refractivity fields. Figure 8 shows a 99-day time series of signal strength (expressed here as propagation factor) for a frequency of 262.85 MHz for the two paths (Rogers, 1995). In the absence of any ducting, a propagation factor of -49 dB would be expected and in free space, it would be 0 dB. Over the time period

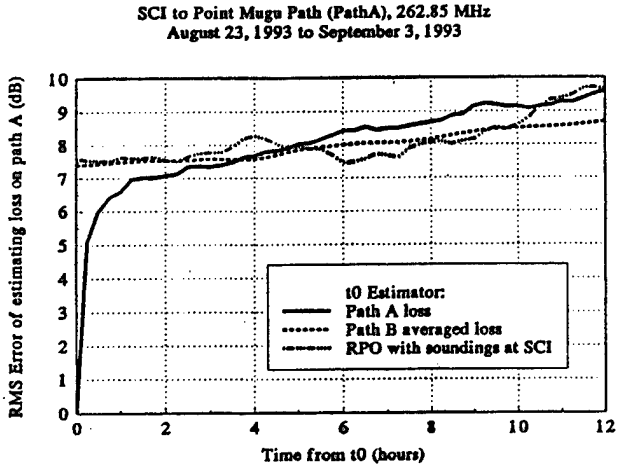


Figure 9. Propagation estimates.

displayed, the signals vary between those limits (spanning five orders of magnitude) illustrating significant ducting enhancements most of the time. The signals for the two different propagation paths follow the same trend even though there are instantaneous differences. Following the same trend indicates sufficient horizontal extent of gross refractivity structures giving confidence to the expectation that high-resolution mesoscale models eventually will be able to describe the refractive environment for propagation assessment purposes (Hodur, 1996). A subset of the data shown in figure 8 was used for statistical analyses and to provide quantitative answers to where and how often the environment should be sampled. In figure 9, the root mean square (rms) error is plotted as a function of lag time (Rogers, 1995). The solid curve is the rms error based on the actual measurement over this path. At time zero, there is, of course, no error. One would expect the same zero error result at time zero if the refractivity field along path A were known precisely and a perfect propagation model applied. If the path loss value measured (or calculated based on perfect information) at time zero is used to estimate future path loss values, the error increases to approximately 6 dB within 30 minutes and to 10 dB in the next 12 hours. This information may be used to specify the frequency for updating environmental measurements. The other two curves in figure 9 show the rms error if either the path loss measured over the other path (B) is used to estimate path loss values for path A or if radiosonde-inferred refractivity profiles at San Clemente Island (SCI) in conjunction with the Radio Physical Optics (RPO) model (Hitney, 1992) are used to calculate path loss for path A. All three curves converge to the same range of rms errors which is a good indication of the prediction accuracy that is feasible for the conditions and geometries involved.

Under the objective of VOCAR to investigate the feasibility of using received signal levels either by themselves or in conjunction with other techniques for inferring refractivity conditions, Rogers et al. (1996) demonstrated a simple bias-correction method for fusing radio reception data with mesoscale models. In the refractivity sensing effort, a multi-wavelength Raman lidar produced excellent vertical humidity profiles (Philbrick and Blood, 1995) and satellite sensing techniques were developed for incorporation into automated knowledge-based predictive and assessment systems (Helvey et al., 1995).

The second measurement program specifically designed for coastal environments is called EO Propagation Assessment in Coastal Environments (EOPACE) (Littfin and Jensen, 1996; Zeisse et al., 1996). EOPACE started in 1996 and has three primary objectives. The first addresses measurement, modeling, and prediction of large, surf-generated aerosols that are important for sea skimmer missile detection; the second is to provide comprehensive data for the development of mesoscale models that are capable of predicting EO propagation conditions, and the third is to provide a testbed for infrared surveillance systems. Participants in EOPACE include the Naval Command, Control and Ocean Surveillance Center, the Naval Air Warfare Center, the Naval Research Laboratory, the Naval Postgraduate School, the Pennsylvania State University, and researchers from Australia, the Netherlands, and the United Kingdom. Initial results include dramatic visualizations of aerosol plume generation in the surf zone and important effects of both large aerosols and refraction on near-surface infrared propagation.

CONCLUSIONS

Atmospheric effects assessment for military operations is far too costly and too complex to be carried out in isolation. Within the U.S. military service branches, DDR&E has a long and successful record of facilitating such coordination. Various research organizations within NATO have provided superb

opportunities for fruitful joint research and possess a proud record of significant accomplishments. In today's competitive environment, it is mandatory to produce quantifiable results in joint R&D efforts in short order. There are, however, also long-term pay-offs that may even be difficult to trace and important intangible benefits like getting to know different research facilities, approaches to solving problems, work environments, and cultures. These aspects should also be considered when planning cooperative arrangements rather than relying solely on *quid pro quo* arguments.

ACKNOWLEDGEMENT
This work was supported by the Office of Naval Research.

REFERENCES

Anderson, K.D., Radar detection of low-altitude targets in a maritime environment, NCCOSC RDTE DIV (NRaD) TR 1630, Vol 1 and 2, 1993

Christophe, F., N. Douchin, Y. Hurtaud, D. Dion, R. Makaruschka, H. Heemskerk, and K.D. Anderson, Overview of NATO/AC243/Panel 3 activities concerning radiowave propagation in coastal environments, AGARD CP 567, pp. 27.1-27.9, 1995

Fairall, C., E.F. Bradley, D.P. Rogers, J.B. Edson, and G.S. Young, Bulk parameterization of air-sea fluxes for Tropical Ocean-Global Atmosphere Coupled-Ocean Atmosphere Response Experiment, J. Geoph. Res., 101 (C2), pp. 3747-3764, 1996

Gathman, S.G., Optical Properties of the marine aerosol as predicted by the Navy aerosol model, Opt. Eng., Vol 22 (1), pp. 57-62, 1983

Gathman, S.G., G. de Leeuw, and K.L. Davidson, The Naval Oceanic Vertical Aerosol Model: Progress Report, AGARD CP 454, pp. 17.1-17.11, 1990

Gathman, S.G., MAPTIP observations of large aerosol in the lowest 10 m above waves, SPIE Proc., Vol. 2828, pp. 15-23, 1996

Helvey, R., J. Rosenthal, L. Eddington, P. Greiman, and C. Fisk, Use of satellite imagery and other indicators to assess variability and climatology of oceanic elevated ducts, AGARD CP 567, pp. 33.1-33.14, 1995

Hitney, H.V., Hybrid ray optics and parabolic equation methods for radar propagation modeling, Radar 92, IEE Conf. Pub. 365, pp. 58-61, 1992

Hitney, H.V. and J.H. Richter, The Integrated Refractive Effects Prediction System (IREPS), Naval Engineers Journal, Vol. 88, No. 2, pp. 257-262, 1976

Hodur, R.M., Forecast capability of the Coupled Ocean/Atmosphere Mesoscale Prediction System (COAMPS) in the Arabian Gulf and the Gulf of Oman, Proc. Battlespace Atmosph. Conf., 3-5 Dec. 1996, NRaD TD 2938, 1996

Jensen, D.R., G. de Leeuw, and A.M.J. van Eijk, Work plan for the Marine Aerosol Properties and Thermal Imager Performance (MAPTIP), NCCOSC RDTE DIV (NRaD) TD 2573, 1993

Jeske, H., *Die Ausbreitung elektromagnetischer Wellen im cm- bis m - Band über dem Meer unter besonderer Berücksichtigung der meteorologischen Bedingungen in der maritimen Grenzschicht*, Hamburger Geophysikalische Einzelschriften, Heft 6, Cram, de Gruyter u. Co., Hamburg, 1965

Jeske, H., The state of radar-range prediction over sea, AGARD CP 70, paper 50, 1971

Jeske, H., Final Report to DRG Panel on Physics and Electronics, NATO AC/243, Panel III/RSG 6, Dec. 1977

Kneizys, F.X., E.P. Shettle, W.O. Gallery, J.H. Chetwynd, Jr., L.W. Abreu, J.E.A. Selby, S.A. Clough, and R.W. Fenn, Atmospheric Transmittance/ Radiance: Computer Code LOWTRAN 6, AFGL-TR-83-0187 environmental research papers, #846, 1983

Littfin, K.M. and D.R. Jensen, An overview of EOPACE (Electrooptical Propagation Assessment in Coastal Environments), including in-situ and remote sensing techniques, AGARD CP 582, pp. 10.1-10.8, 1996

Liu, W.T., K.B. Katsaros, and J.A. Businger, Bulk parameterization of air-sea exchanges of heat and water vapor including the molecular constraints at the interface, J. Atmos. Sci, 36, pp. 1722-1735, 1979

Paulus, R.A., Practical application of an evaporation duct model, Radio Sci., Vol. 20, No. 4, pp. 887-896, 1985

Paulus, R.A., An overview of an intensive observation period on variability of coastal atmospheric refractivity, AGARD CP 567, pp. 30.1-30.6, 1995

Perry, W.J., DoD Plan for Atmospheric Transmission Research and Development, DDR&E memorandum of 16 March 1978

Philbrick, C.R. and D.W. Blood, Lidar measurements of refractive propagation effects, AGARD CP 567, pp. 3.1-3.13, 1995

Richter, J.H. and H.V. Hitney, Antenna heights for the optimum utilization of the oceanic evaporation duct, Part III: Results from the Mediterranean Measurements, Naval Ocean Systems Center TD 1209, Vol 2, 1988

Rogers, L.T., Effects of spatial and temporal variability of atmospheric refractivity on the accuracy of propagation assessments, AGARD CP 567, pp. 31.1-31.9, 1995

Rogers, L.T. and R.A. Paulus, Measured performance of evaporation duct models, Proc. Battlespace Atmosph. Conf., 3-5 Dec. 1996, NRaD TD 2938, 1996

Rogers, L.T., R.A. Paulus, and J. Cook, Fusing data from the mesoscale model and radio remote sensing, Proc. Battlespace Atmosph. Conf., 3-5 Dec. 1996, NRaD TD 2938, 1996

Sheridan, T.F., C.R. Miller III, and E.J. Harrison, The U.S. Navy METOC systems program, Proc. Battlespace Atmosph. Conf., 3-5 Dec. 1996, NRaD TD 2938, 1996

Wells, W.C., G. Gal, and M.W. Munn, Aerosol distributions in maritime air and predicted scattering coefficients in the infrared, Appl. Optics, 16, pp. 654-659, 1977

Zeisse, C.R., D.R. Jensen, and K.M. Littfin, EOPACE (Electrooptical Propagation Assessment in Coastal Environments) Overview and initial accomplishments, Proc. Battlespace Atmosph. Conf., 3-5 Dec. 1996, NRaD TD 2938, 1996

The U. S. Navy Meteorological and Oceanographic Systems Program

Commander Timothy F. Sheridan, USN, SPAWARSYSCOM,
Charles R. Miller III and Edward J. Harrison, Jr., Computer Sciences Corporation

INTRODUCTION

The Oceanographer of the Navy is responsible to the Chief of Naval Operations for managing the Navy's Meteorology and Oceanography (METOC) programs. Under the policy guidance and resource sponsorship of the Oceanographer, the METOC Systems Program Office (PMW 185) of the Space and Naval Warfare Systems Command (SPAWAR), oversees the development, acquisition and life cycle support of all METOC systems and associated applications software, and also serves as his METOC systems architect. The METOC systems under the purview of PMW 185 directly support the Commander, Naval METOC Command concept of operations. This paper will examine how METOC support is developed and managed within the Navy, describe the major METOC systems that are in development and/or procurement and the associated RDT&E that supports them.

All through the cold war and into the early 1990s, the U. S. Navy focused on operations in the "blue waters" of the world - that is in the open oceans - against a strategic threat posed by a bloc of communist nations led by the Soviet Union. For the Navy, countering the particular threat represented by the Soviet nuclear powered ballistic missile submarines was foremost. With the demise of the political regime in Eastern Europe, the Navy shifted its focus towards the littoral and hinterland regions of the world, where the threat evolved into one of a major regional conflict or smaller scale "brushfires" - scenarios involving one or more third world countries. The challenge for the METOC community, given this new Navy focus, is incalculably more complex. Figure 1 provides a comparison between the deep ocean where, in the past, acoustics was the principal concern, and the coastal regime which is complicated by many interactive factors.

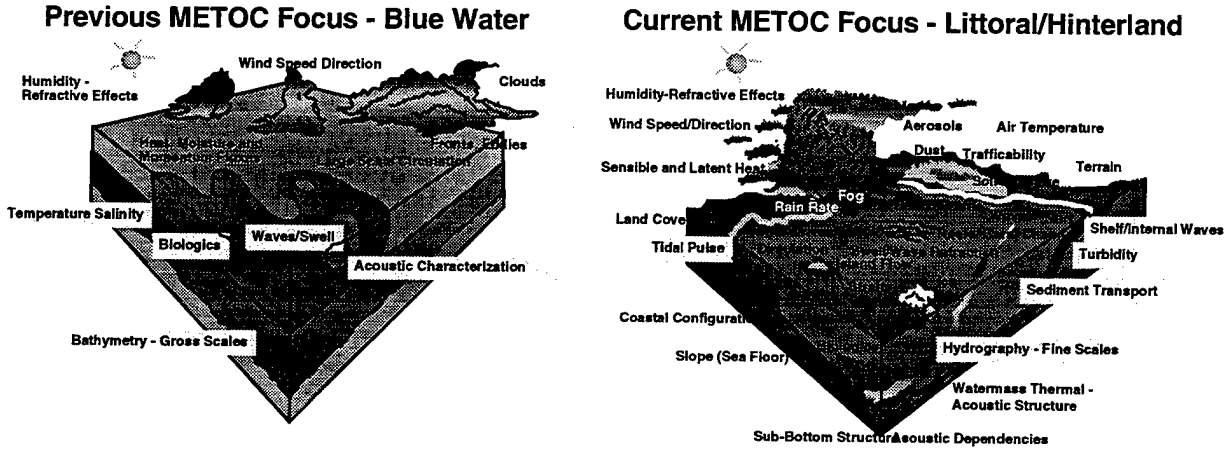


Figure 1. Side by side comparison of METOC features of "Blue Water" and coastal areas.

In order to respond to the requirements that this new focus presents, the Navy METOC Systems Program Office has developed a concept for, and is working toward achieving, a seamless architecture. This architecture, schematically depicted in Figure 2, is based on developing global numerical model products and data at central site computing facilities and transmitting them through the theater METOC centers to the Tactical Environmental Support System (TESS) afloat. Finally, individual fleet and Marine Corps units are provided highly specialized METOC information which assists them in decision making. Locally acquired data can be infused anywhere along the process to add value to the final products.

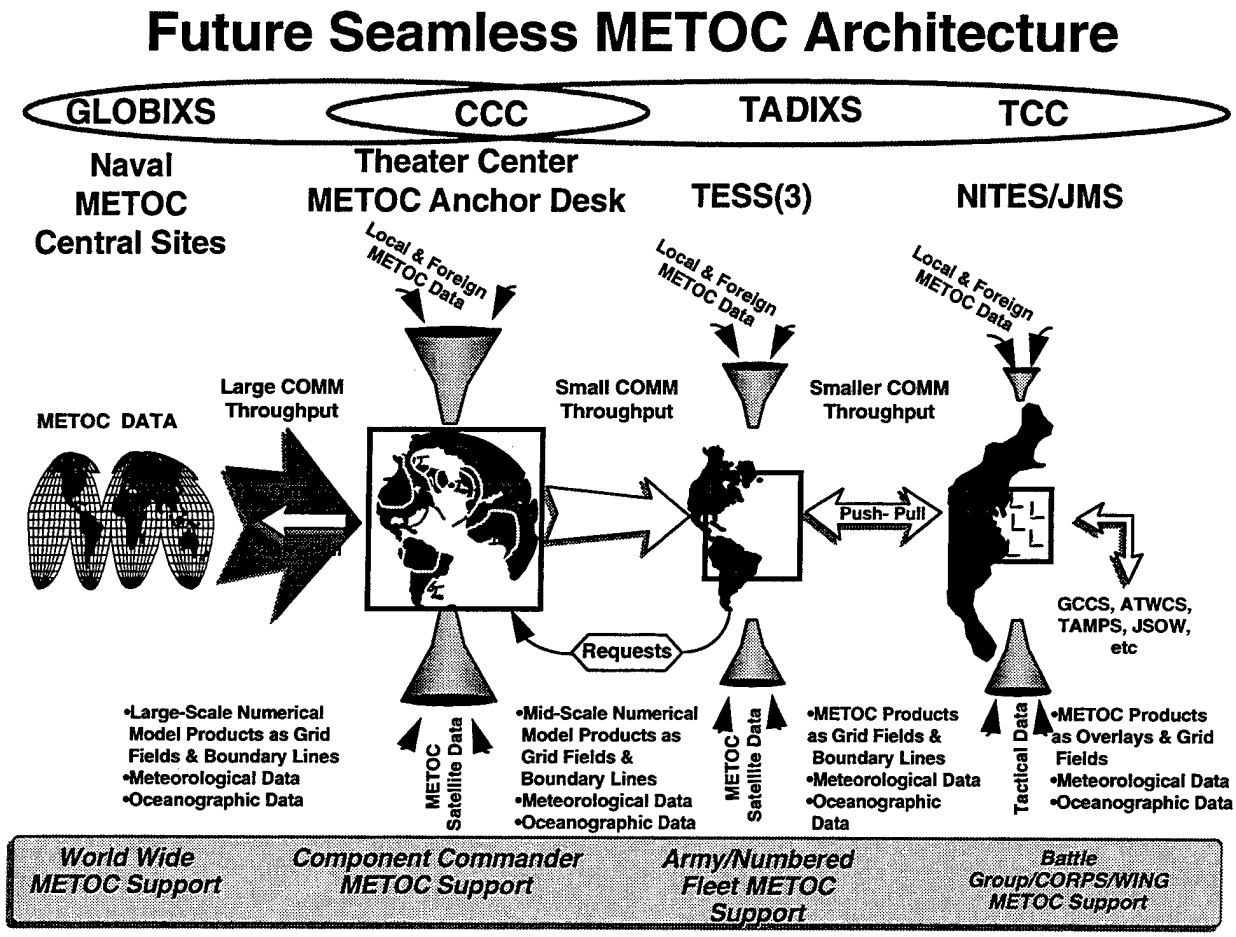


Figure 2. Schematic of Future Seamless METOC Architecture.

TESS

The system that will serve as the cornerstone of METOC support for the future is the TESS (Next Century) - TESS(NC). TESS(NC) will be a computer-based, interactive environmental data receiving, storing, processing and display system to be installed on major Navy ships and shore stations. TESS(NC) will dramatically upgrade and expand current capabilities and will be fully compliant with evolving Joint Command, Control, Communications and Computers and Intelligence, Surveillance and Reconnaissance (C4ISR) architectures.

TESS(NC) will feature a number of cornerstone applications that will allow on-scene METOC data assimilation and analysis, as well as a real time characterization of the electromagnetic, electro-optical and acoustic properties of the battlespace. TESS(NC) will exploit emerging PC technology and use commercially developed, off-the-shelf software, wherever possible. Figure 3 depicts some of these TESS(NC) features.

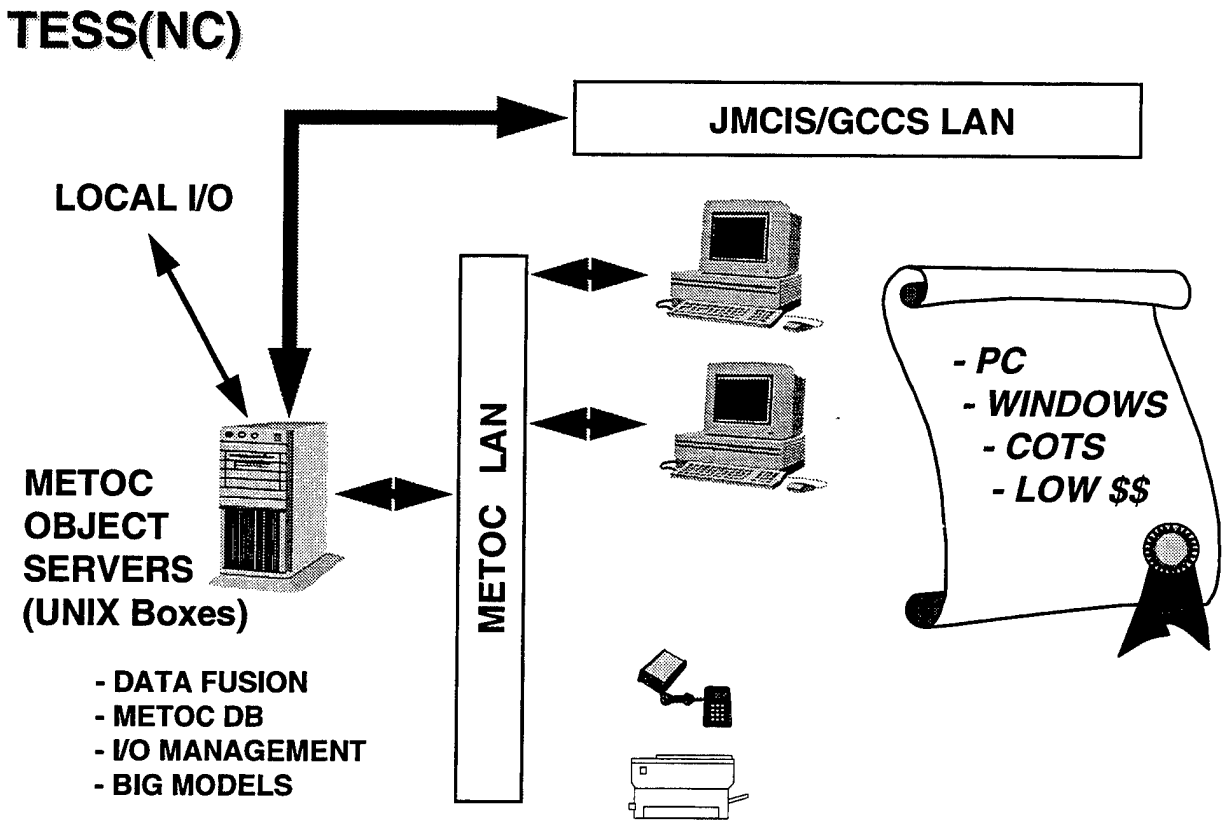


Figure 3. Schematic depicting TESS(NC) features. Locally acquired METOC data is fused with model output data in powerful workstations. User interfaces will be high end PCs. METOC data and products will then be distributed via the ship's LAN.

As TESS becomes fully integrated into the Joint Maritime Command Information System (JMCIS)/Global Command and Control System (GCCS), the METOC data and products provided will then more fully permit assessments and predictions of the effects of the environment on Battle Group, friendly, and enemy units, sensors, weapons, and communications.

SMOOS

The Shipboard Meteorological and Oceanographic Observing System (SMOOS) is a suite of sensors designed to provide automatic and continuous readouts of local air/ocean observations. This data is sent directly to the TESS database. The suite has been installed aboard all TESS-capable ships and automatically provides METOC data via digital interfaces. The baseline consists of five sensors that measure: 1) air temperature and dewpoint; 2) sea

surface temperature; 3) cloud height; 4) atmospheric pressure and; 5) visibility and precipitation. In addition, TESS is connected to the shipboard anemometer to provide wind speed and direction. A program to provide replacement sensors for SMOOS - SMOOS(R) will facilitate the introduction of new sensors in an evolutionary manner, as they become available. Commercially available, highly automated sensor packages for surface combatant ships have been extensively tested at sea aboard the RV Pt. Sur and the USNS SUMNER. It is anticipated that SMOOS(R) will be fielded in the FY98-99 timeframe.

AN/SMQ-11

The AN/SMQ-11 is the environmental satellite receiver-recorder for use aboard selected Navy ships and METOC activities ashore. The antenna has recently been significantly reduced in weight and size by the Naval Air Warfare Center, Aircraft Division, Indianapolis. The AN/SMQ-11 is capable of receiving data from the Defense Meteorological Satellite Program (DMSP) satellites, the NOAA TIROS-N (High Resolution) satellites and the geostationary (GOES), METEOSAT and GMS satellites (WEFAX only). In addition, the system can provide black and white hard copy prints of the imagery transmitted by these satellites within three minutes of the conclusion of the transmission. Data retention on magnetic tape permits automatic archiving of 14 consecutive satellite passes for subsequent enlargement and/or enhancement without operator intervention. The AN/SMQ-11 digitally interfaces with other systems such as TESS. It is currently being modified to copy the GFO datastream (Satellite Data Record) and convert it to an Environmental Data Record of sea surface topography. Procurement of 75 AN/SMQ-11 units was completed last year, with 32 slated for ships, and 43 for shore activities. A significant computer upgrade to the AN/SMQ-11 is underway whereby the processing units within the two cabinets will be replaced by state-of-the-art computers, providing a new color monitor capability. This upgrade will allow the system to be merged with TESS and NITES over the next couple of years. Figure 4 highlights the features of the AN/SMQ-11 hardware upgrade.

NITES

The Navy Integrated Tactical Environmental subsystem (NITES), being fielded as a JMCIS segment, is designed to meet current and all known future METOC support requirements of Navy Command nodes afloat and ashore and on non-TESS equipped ships. The current version includes grid fields and overlays, maintains a METOC observational database and features limited Integrated Refractive Effects functionality to produce EM coverage and threat diagrams. In the near future, NITES software will include additional products such as wind and high seas warnings and horizontal weather depictions, as well as management of frequently updated METOC digital data, to use as inputs to mission planning systems and decision aids.

ASOS

The Automated Surface Observing System (ASOS) is an interagency program of the National Weather Service, Federal Aviation Administration and the Navy. It consists of a state-

of-the-art suite of eight electronic sensors which are connected to a high speed processor. The system measures, processes and creates surface observations of:

- precipitation
- wind speed and direction
- temperature and dew point
- air pressure
- visibility (fog and haze)
- cloud height

Of the total procurement of 76 Navy systems, 45 have been installed and are operational at Naval and Marine Corps facilities. Installations should be completed by the end of FY 97. Figure 5 depicts a typical ASOS sensor installation at an air station.

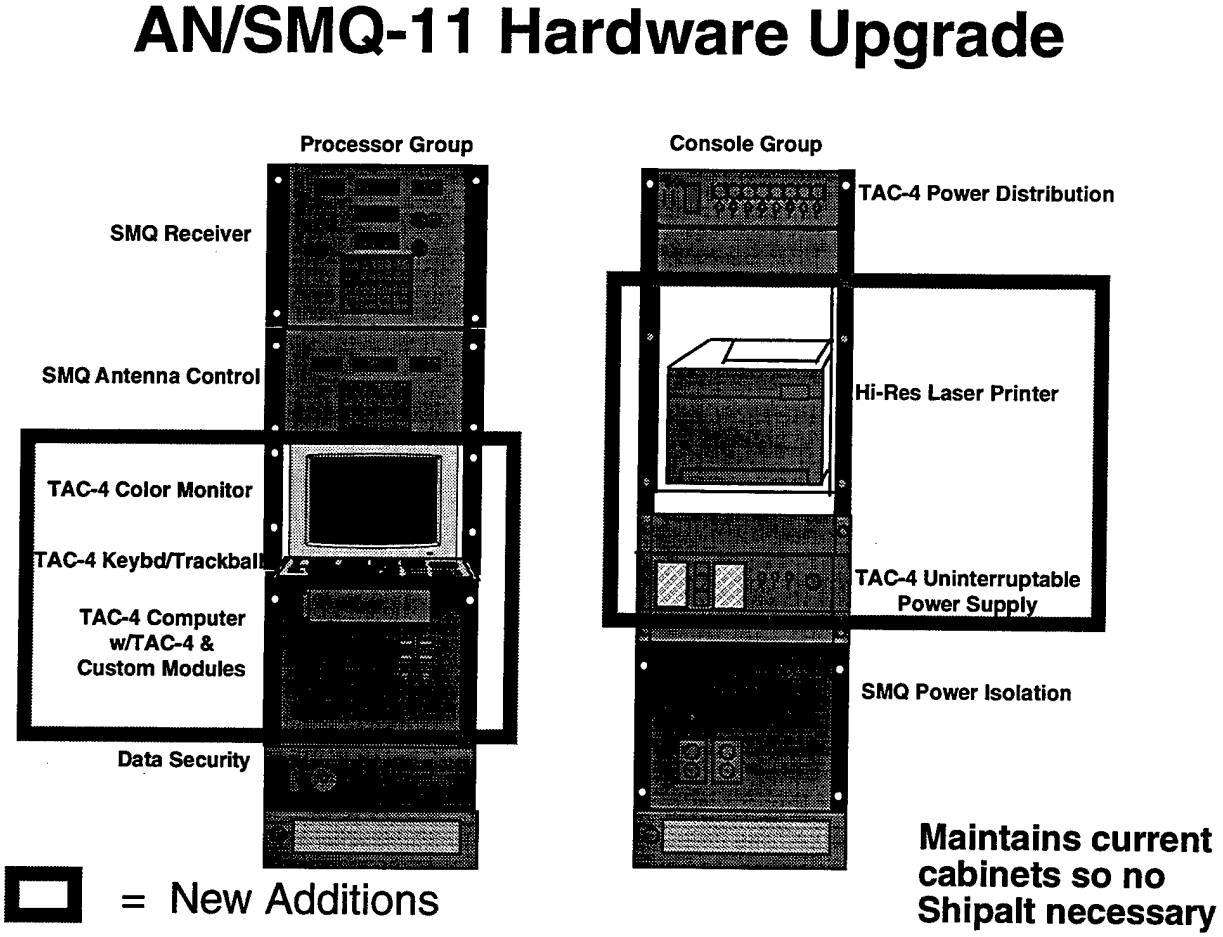


Figure 4. AN/SMQ-11 hardware upgrade, featuring the TAC4 and laser printer additions.

NEXRAD PUPs

The joint inter-agency Next Generation Weather Radar program is fielding systems that exploit Doppler radar technology for continuous wide area surveillance of potentially hazardous weather conditions. Navy and Marine Corps forecasters on watch at some 44 air facilities within the United States are now able to select products for display and printing on their principal user processors (PUP). Installation of the last few systems was completed last year. These products, along with data derived from local meteorological sensors and communications links, enable forecasters to prepare and disseminate more accurate and timely local weather forecasts and warnings, especially those where potentially hazardous weather is involved. Figure 6 depicts a NEXRAD radar tower and a typical PUP installation.

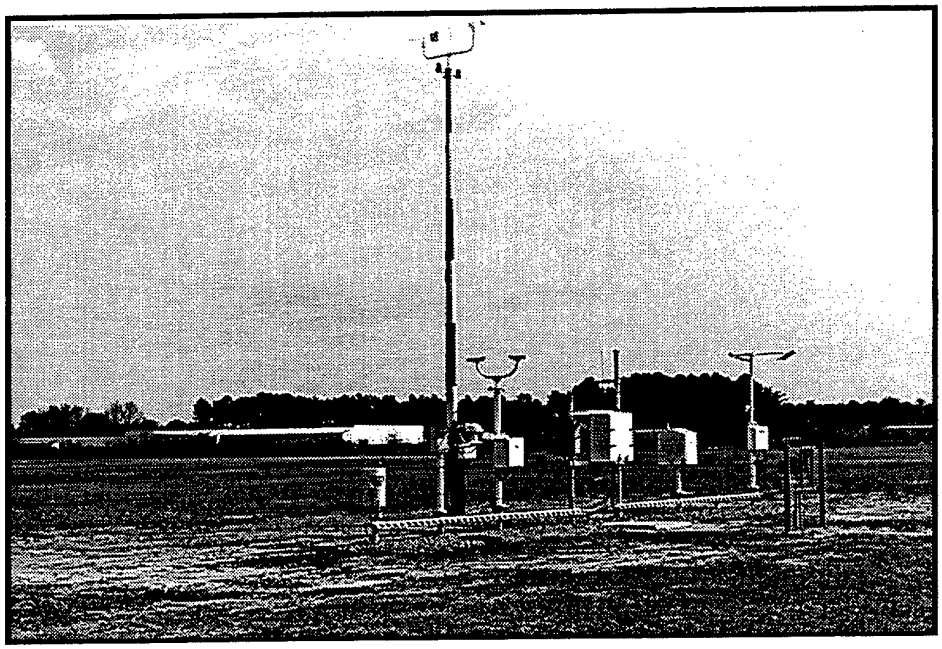


Figure 5. Typical ASOS installation at a Naval Air Station in CONUS. A total of 75 units are to be procured by the Navy.

Supplemental Weather Radar

As discussed above, NEXRAD PUPs have been procured to meet Navy needs for improved detection and surveillance of hazardous weather. However, a number of Navy and Marine Corps Air Stations lie outside the NEXRAD network. These activities currently have either inadequate radar surveillance capabilities or none at all. However, commercially available weather radars could provide sufficient coverage for these activities. Based on this need, an Operational Requirements Document for procurement of the Supplemental Weather Radar was approved in April and the Request for Proposals was released earlier this summer. Contract award is expected to be made by the end of this fiscal year with deliveries commencing shortly thereafter. The first two systems will be installed at NAS Fallon, NV and Guantanamo Bay, Cuba in the March 1997 time frame, for design test and evaluation. The remainder of the

systems will be installed at NAVSTA Rota, NAVSTA Diego Garcia, NAS Souda Bay, NAS Sigonella, NAVBASE Yokosuka, MCAS Iwakuni and NTTU Keesler AFB by June 1998.

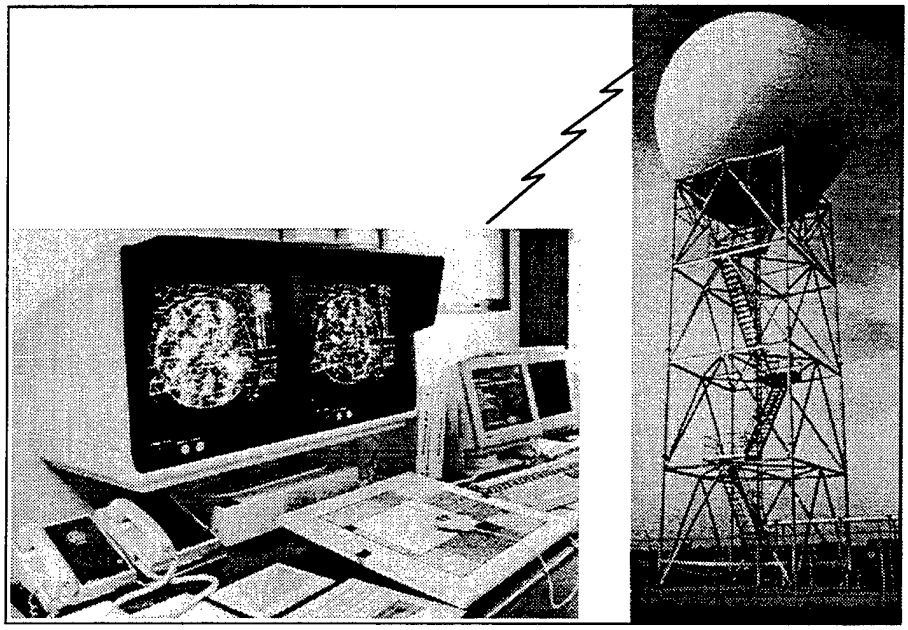


Figure 6. NEXRAD Principal User Process on left and antenna installation on right. The Navy has completed installation of the PUPs it has procured.

METMF Replacement

The Meteorological Mobile Facility Replacement program will provide a full range of weather support for Marine Air Ground Task Force (MAGTF) Expeditionary Operations. Government and commercial off-the-shelf (GOTS/COTS) technology enhancements are expected to allow miniaturization of all components into a single van versus the four vans that are now required for METMF. It will be deployable worldwide via C-130 sized airlift. The current schedule calls for 14 fully capable vans to be delivered beginning in FY 97. A fully integrated system, METMF(R) will consist of a TAC4 version of TESS (described in an earlier section); communication equipment for HF, VHF, UHF (line-of-sight), UHF/SATCOM communications, as well as SHF connectivity to a supporting communication unit; an AN/TMQ-43 satellite receiver, also known as the U.S. Air Force's Small Tactical Terminal (STT); an AN/UMQ-12; one local and two remote sensor systems; Supplemental Weather Radar; and two MOSS (3) units, all housed within an environmentally controlled single shelter. Figure 7 is an artist's conception of METMF Replacement.

Initial Operating Capability is planned for the first quarter of FY 97 with the fielding of a single shelter equipped with each of the subsystems operating in stand-alone mode, and a TESS Remote Workstation (TRWS) for MAGTF C^4I/GCCS connectivity. Phase 2 of development will leverage fielding of the TAC4-based TESS, beginning in the first quarter of FY 98, and serve as

the data fusion center for the METMF(R) . Full Operational Capability is planned for FY 01 with the fielding of the last two of 14 shelters.

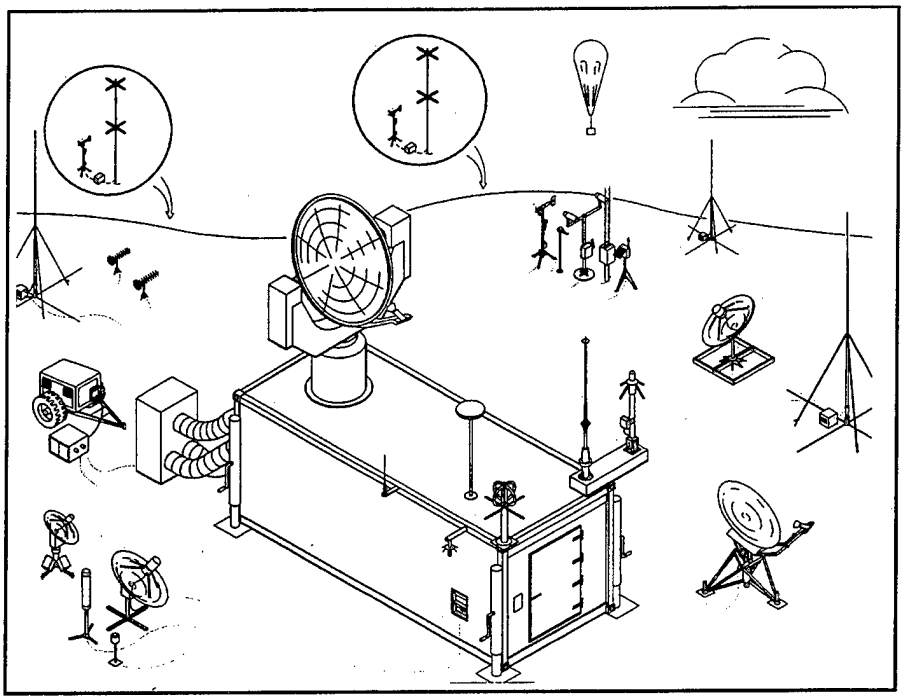


Figure 7. Artist's conception of the typical USMC METMF Replacement layout.

MRS

The AN/UMQ-12, Mini-Rawin System employs 100 gram balloons to launch radiosondes which provide atmospheric elements such as temperature, dewpoint, pressure and winds to the receiver which automatically analyzes and codes the atmospheric data. These units represent one of the first efforts by the Navy to procure a system from commercially off-the-shelf hardware. MRS units have been successfully deployed aboard ship and at shore activities worldwide for over 10 years and have proven to be very accurate, reliable and cost effective. In 1995, PMW 185 procured two MRS systems with GPS capability for testing. The GPS capable sondes will provide more accurate data. Testing, which began in December 1995, continues aboard ship, but has been completed at shore sites. Preliminary results are promising, and it is anticipated that a contract will have been awarded by the time this article is published for procurement of 128 MRS conversion kits to be installed at all activities that have GPS capability. It is foreseen that these installations will be completed by October 1997.

GFO

Between 1985 and 1990, the Navy GEOSAT Mission demonstrated the capability of a satellite radar altimeter to provide global measurements of the absolute dynamic topography of mesoscale ocean features (fronts, eddies, and ice edge) to high precision. The GEOSAT Follow-on (GFO) program is designed to apply this experience to the benefit of the Navy until an operational altimeter is flown on NPOESS. Now scheduled for launch in 1997, GFO will

provide and maintain an operational source of altimetry data with high measurement precision and downlink data directly to the AN/SMQ-11 receiver/recorders aboard many Navy ships and CNMOC shore activities. Algorithms are being developed for use by the Altimetry Data Fusion Center in NAVOCEANO at the Stennis Space Center, MS and TESS/AN/SMQ-11 equipped ships to process the data to derive oceanographic features, such as currents, warm and cold eddies and sea heights.

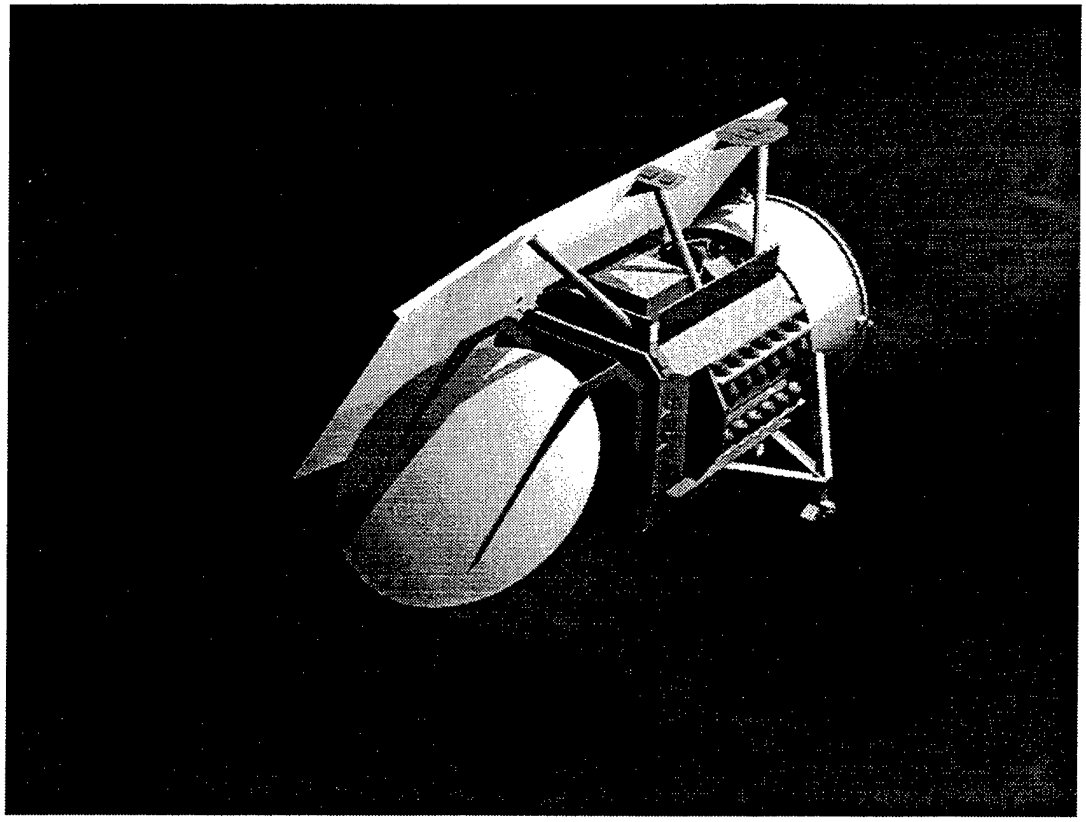


Figure 8. Artist's conception of the GFO spacecraft general layout.

DMSP

The Defense Meteorological Satellite Program (DMSP) helps ensure that Navy-unique sensor requirements are addressed both within DMSP and the National Polar-orbiting Operational Environmental Satellite System (NPOESS) program which have been presidentially directed to consolidate. At this point, new spacecraft is planned to be launched in 2006. Developments within the current program include the calibration and validation of each Special Sensor Microwave Imager (SSM/I) that has been launched. Potential new sensors will likely include a new microwave imager, radar altimeter and scatterometer.

Precise Timing and Astrometry

The DoD assigns the Navy responsibility for coordinating precise time and time interval (PTTI) requirements and maintaining a PTTI reference standard. This responsibility is carried

out at the U. S. Naval Observatory in Washington, DC, where the master clock for the United States is maintained. In this thrust area, dem/val of new techniques for increasing master clock reliability and stability; improved time transfer by exploitation of satellites, fiber optics, etc.; upgraded earth orientation determination using GPS; new EO/IR telescope technology for improved reference frame determination and use of interferometry for precise astrometric positions are performed.

Atmospheric/Oceanographic Research Programs

PMW 185 oversees an expansive METOC R&D program that includes modeling, tactical systems development, satellite applications, and tactical decision aids. The Program Office also manages the Navy's METOC Satellite Programs under the resource sponsorship of the Director, Space and Electronic Warfare. In the area of METOC modeling, the Navy Operational Global Atmospheric Prediction System (NOGAPS) has been delivered and is operational at the Fleet METOC Numerical Center in Monterey, CA. In addition, the relocatable high resolution Navy Operational Regional Atmospheric Prediction System (NORAPS) is being developed to provide more accurate predictions over limited areas. The Coupled Ocean/Atmospheric Mesoscale Prediction System (COAMPS) and a family of thermodynamic ocean circulation models, as well as data assimilation and quality control efforts are also currently under development.

Within the area of tactical systems development, demonstration, validation and engineering of METOC sensors (e.g., SMOOS Replacement), communication interfaces and processing and display equipment such as the AN/SMQ-11 are being performed along with TESS hardware and software engineering. Important thrust areas in the satellite applications arena are tropical cyclone position and intensity algorithms and automated image analysis techniques. Other focuses include GFO processing and development of littoral zone analysis capabilities, as well as SAR exploitation within littoral regions. A family of tactical decision aids that capitalize on all of the above include EM/EO and Chem/Bio models, relocatable tide and surf models and a stand-alone tactical atmospheric and oceanographic forecasting capability. These latter efforts will eventually enable the organic METOC teams to develop their own limited forecasts even in the absence of data and products from the central computing sites.

SUMMARY

The METOC Systems Program Office, PMW 185, has responsibility for a wide variety of both operational and developmental efforts. Each of these has been conceived, developed and fielded with the intent of providing the METOC community with up-to-date tools of the trade so that they in turn may provide the best support possible to the tactical commanders afloat. Among other things, this requires close monitoring and testing of new technologies that might be exploited to improve existing capabilities. In this era of shrinking fiscal and personnel resources, the program office is also committed to seeking the most cost effective ways to deliver the best METOC products and data available.

Paper prepared for the 1996 Battlespace Atmospherics Conference
3-5 December 1996, Naval Command, Control and Ocean Surveillance Center
RDT&E Division, San Diego, California, USA.

CO-OPERATION ON METEOROLOGICAL TACTICAL DECISION AIDS WITHIN NATO

Charlotte Wiin Christensen
Staff Meteorological Officer, HQ Chief of Defence, 2960 Vedbaek, Denmark
and
Jonathan David Turton
Meteorological Support Group, Ministry of Defence, Whitehall, London, SW1A 2HB, UK

ABSTRACT

The Military Committee Meteorological Group (MCMG) is responsible for advising the North Atlantic Treaty Organisation (NATO) Military Committee (MC) on meteorological matters affecting NATO. It also acts as the co-ordinating agency of the MC for all meteorological policies, procedures and techniques within NATO. The MCMG is supported by two working groups: WG-OPC (Operations, Plans and Communications) and WG-BMSS (Battle-area Meteorological Systems and Support). The mission of the WG-BMSS is to support the MCMG in carrying out its functions of encouraging co-operative effort and interoperability in the area of meteorological research, development, and transition of new equipment, techniques and software to operational capability in the field of maritime operations, air operations and specifically land operations.

In particular the WG-BMSS has a programme of work on the development, exchange and interoperability of land, air and maritime Tactical Decision Aids (TDAs) having battle-area environmental and/or meteorological parameters as an input. This includes TDAs for a wide range of applications including acoustic propagation, atmospheric dispersion, electro-optical and electromagnetic systems, icing (airframes, runways and ships) predictions, trafficability and topographic/geographical analyses. This paper outlines the background to this work programme, which has the objective of producing a fully documented NATO library of meteorological TDAs, and discusses some of those TDAs that have been offered by individual nations together with verification and validation results where available.

1. BACKGROUND

The Military Committee Meteorological Group (MCMG) advises the North Atlantic Treaty Organisation (NATO) Military Committee (MC) on meteorological matters affecting NATO. It also acts as the co-ordinating agency of the MC for all meteorological policies, procedures and techniques within NATO. The history of the MCMG dates back to 1950 when it first met as the Standing Group Ad Hoc Meteorological Information Committee. Almost immediately it became the Standing Group Meteorological Committee (SGMC). In 1968 the group became known as the MCMG and since 1954 it has been supported by one or more working groups. Currently the

MCMG is supported by two working groups: WG-OPC (Operations, Plans and Communications) and WG-BMSS (Battle-area Meteorological Systems and Support).

The mission of the WG-OPC is to support the MCMG by identifying and correcting deficiencies in NATO's operational meteorological organisation, plans and communications. WG-OPC is responsible for maintaining the AWP (Allied Weather Publication) series of documents. These are AWP-1(B) the NATO Maritime Meteorological Procedures and Services Manual, AWP-2 the NATO Meteorological Support Manual, AWP-3(A) the NATO Meteorological Communications Manual and AWP-4 the NATO Meteorological Codes Manual. In particular AWP-2 describes the level of meteorological support required for NATO maritime, air and land operations. This includes providing basic meteorological data and forecasts, together with more specialised products for mission-specific and tactical planning. For the latter, basic weather forecasts are not sufficient and more detailed predictions prepared using Tactical Decision Aids (TDAs) are needed. These incorporate weather and environmental information, together with information on the mission and the equipment being used (e.g. platforms and sensors). Thus TDAs are tools that allow the meteorologist, or the operator, to predict the effect that meteorological and environmental conditions have on military systems and equipment, and the impact that this might have on a specific operation.

The mission of the WG-BMSS is to support the MCMG by encouraging co-operative effort and interoperability in the area of meteorological research and development. The working group follows the transition of equipment, techniques and software from the developmental stage to operational status within the military meteorological community. An important aspect of this task is in encouraging the development, exchange and interoperability of TDAs for land, air and maritime applications. This work started a number of years ago when the group existed as ISWG.3 (Independent Special Working Group No. 3 on Meteorology) within the NAAG (NATO Army Armaments Group). As ISWG.3 under the NAAG the focus of the group was on the development of TDAs specifically for supporting Army operations. This effort was in addition to the groups responsibility in artillery meteorology, maintaining a series of artillery meteorology STANAGS, and providing support to other NAAG Panels. With the transfer of the group in 1995, from the NAAG to the MCMG, there is now an increased emphasis towards the work on meteorological TDAs, and the scope of this work has been extended to cover TDAs for air and maritime applications.

Over the years a significant number of TDAs have been developed by different nations within NATO and there is a growing need to harmonise, or standardise, on the TDAs or the models being used. This is likely to be particularly important in the context of multi-national operations, where the provision of consistent tactical advice is essential. Furthermore, the various models used to support air, land and maritime operations should produce consistent results. The objective of the WG-BMSS work is to develop a fully documented NATO library of meteorological TDAs which can then be made available for use by all NATO nations. It is envisaged that this will comprise a library of ready-to-use (i.e. executable) TDAs suitable for use on a standard PC or low-end workstation. In addition to this, it is also hoped to provide a library of TDA/TDA sub-model source codes so that individual nations, if they prefer, can build their own TDA packages, but still maintain consistency. It is planned that this library of TDAs/TDA

sub-models will be documented by a new AWP manual (AWP-5). Through this work on TDAs, the WG-BMSS is promoting interoperability and, by the collective nature of the work, assisting the different nations in improving their meteorological support capabilities; thus helping to offset the effects of budget cuts, to which no nation is immune. The first stage of this work is to develop a catalogue of TDAs as described below.

2. CATALOGUE OF TDAs AND SUPPLEMENTARY INFORMATION

The group is currently in the process of developing an inventory of TDAs comprising several matrices; the first part is a summary matrix simply listing TDAs by name and application for each nation. Table 1 shows a subset of some of the summary information, which is as yet incomplete.

However, not all those TDAs that have been identified/notified are likely to be available for release within NATO. This may be due to national interests and/or commercial considerations, and this information also needs to be compiled. Therefore the second part of the inventory contains further information regarding the TDA application, owner (or developer), status (e.g. under development or in operational use) and its availability for release. Recently compiled information has resulted in a list identifying national priorities with respect to the importance and relevance of each TDA application. Whilst this list is not complete, inputs received so far suggest that the areas of IR (infrared), visible/near IR, electromagnetic (RF/μ-wave) propagation, airframe icing, personnel factors (i.e. heat stress/wind chill), NBC/smoke and runway icing are of wider interest.

In addition to this catalogue of TDAs, various other supplementary matrices are being compiled by WG-OPC on the availability of weather data for running TDAs and on the weather support capabilities. The first of these identifies the various types of weather data (observational data, NWP products and gridded data, satellite data etc.) that are available at different echelons (military forecast centre, airfield, at sea, mobile met unit etc.). The second focuses on the support capabilities (e.g. processing equipment, communications, personnel) available at these echelons. Thus, these two supplementary matrices provide valuable information on identifying where, or how far down the echelon structure, the various TDAs could be used.

The next stage in this work is to review the various TDAs, by application, in order to make recommendations towards a NATO approved TDA or TDA models. Individual nations have accepted the task of reviewing TDAs, on behalf of the group, for different application areas, as shown in Table 2. In this way the workload is being shared amongst the nations.

The various TDAs, for each of the specific applications shown, have been provided (where available) to the designated nation to review in detail. These reviews should include an assessment of the physics contained in the models, and validation and verification of the results where such data is available. In some cases, where there are a number of nations with expertise in the subject it is expected that ad-hoc working groups may be established to assist the lead nation in the review process and in formulating recommendations. These recommendations would then be presented to the WG-BMSS to collectively discuss candidate TDAs before making

any decisions on which TDAs, or TDA sub-models, should be adopted. In some cases the preferred approach may well be a hybrid of different TDA sub-models originating from different nations.

TDAs for	**CA**	**FR**	**GE**	**UK**	**US**
IR (8-12 μm)	✓		NAVFLIR	EOTDA v2 IRVIS	TARGAC EOTDA 3.1 EOMDA *ACT/EOS*
IR (3-5 μm)			NAVFLIR		*EOMDA ACT/EOS*
Visible/Near IR (.7-.9 μm)	ANVIS		BIVPROG	ILLUMW	NVG TARGAC NITELITE *NOWS*
Visible (.4-.7 μm)	ANVIS		BIVPROG	ILLUMW	NVG TARGAC NITELITE *NOWS*
EM (RF/μ-wave Propagation)	IREPS *TEMDA*	RADAR	IR-RADAR IREPS EREPS	IREPS EVDUCTW *EEMS (TERPEM)*	IREPS *RPOT*
EM (HF Propagation)	✓		MINIFTZ	*EEMS (JIVE)*	PROPHET IREPS
Acoustic Propagation	✓		SNDCAL	LARKW APP	Acoustic TDA
NBC/Smoke	✓		HEARTS AUTAG	BRACIS *CHEBDA*	KWIK VLSTRACK
Airframe Icing	Tephi IFW AIFC		POTICE STANDICE	NWP products	ICING
Airfield Runway Icing			RIME	RSTW	
Ship Icing					Topside Icing Model
Heat Stress/ Wind Chill	HUMID WINDCHILL			HUMPARS	MERCURY
Trafficability	✓		CACTUS	SOILM	DTSS
Parachute Operations		High Altitude Opening		DZ WIND	
Weather Effects			FOGMIN GUST JETLIGHT		IWEDA TESS

Table 1. Allied Tactical Decision Aids. Adapted from the WG-BMSS Inventory of Existing or Planned TDAs. Planned TDAs are denoted by italics and applications where there is a national requirement but no available TDA are indicated with a ✓.

TDA Application	Lead Nation
Infrared	US
Visible/Near IR	GE
EM (RF/μ-wave) Propagation	UK
Acoustic Propagation	US
NBC/Smoke	GE
Airframe Icing	CA
Wind Chill/Heat Stress	NL

Table 2. Lead nations for reviewing different TDA applications.

Where presentational aspects are concerned, it is likely that different nations, or perhaps even different services within a nation, will wish to have customised output, so it is probably not appropriate to standardise on this. Another factor to be considered is that different nations have already invested in developing certain TDAs and will not wish to withdraw these from use and replace them with another, particularly if the alternative looks very different. However, it may be that different TDA sub-models could be used if this is considered to be of benefit. Thus, one of the aims of this work is to standardise on the actual models/sub-models being used.

3. REVIEW OF TDA APPLICATIONS

A summary of the current status and progress made in some of the different application areas is given below, space precludes a description of all the subject areas. The details given here are largely based upon the results of a recent Technical Review held at the German Military Geophysical Office (GMGO) during May 1996 and described in RECORD MCMG/WG-BMSS-2[1] with an update following the recent November 1996 WG-BMSS-3 meeting. Those applications discussed are introduced in alphabetical order.

3.1 Airframe Icing

In certain conditions ice will form on, and adhere to, parts of the airframe and engine. Whilst various preventative measures, plus the performance and capability of modern aircraft, have reduced the frequency of this hazard, it is still an important factor to be considered in aircraft operations. Potentially dangerous effects are: (i) ice may alter the wing profile, reducing the available lift, (ii) engine intakes may become blocked, causing loss of power, (iii) the weight of ice may overload the aircraft, and (iv) forward facing windows may become opaque. For helicopters there are additional risks, (v) uneven ice accretion on the rotor blades, causing severe vibration and (vi) cyclic pitch controls may become jammed, causing loss of control. Clearly, icing forecasts are important to aircraft, particularly helicopter, operations and these predictions are usually expressed in terms of the intensity of expected ice accretion: i.e. trace, light, moderate or severe, and there are a variety of icing forecasting techniques currently used in the US and Europe.

A recent study by the US Air Force (Comell et al[2]), suggested that the Air Weather Service (AWS) decision-tree method (which is based on empirical aircraft icing forecasting rules) performed best out of three (1 US Air Force, 2 US Navy) techniques investigated and concluded that more rigorous techniques, based on cloud liquid water content (LWC) and dropsize distribution were needed to improve the quality of icing forecasts. Within the WG-BMSS forum there are a number of other methods that have been discussed. These vary in sophistication from a modified version of the AWS decision-tree approach as used by the NL, and a similar technique used by GE, through to the computer-based Ice For Windows (IFW) TDA developed by CA. The IFW TDA is based on a program to forecast icing on fixed and rotor winged aircraft developed for the US Army Atmospheric Sciences Laboratory in the late 80's. Given information on cloud layers and an atmospheric vertical profile, the model forecasts the severity of the icing conditions.

From an initial comparison of the NL and GE decision-tree methods and the IFW TDA against some 40 reported cases of icing in CA, Yip[1] found that the NL method appeared to give the most reliable results, with 34 correct predictions of icing category with the GE method being correct for 27 of the cases. The lower performance of the GE method was due in part to the absence of a "100 nautical miles ahead of a warm front" category which is included in the NL method. Rather surprisingly the IFW TDA, despite being more sophisticated, proved to be less reliable with a tendency to under-forecast the severity of the icing category. In the interim CA have developed an automated (windows-based) modified Aircraft Icing Flow Chart (AIFC) code that combines the strengths of the NL and GE methods, and this has been made available to NATO nations. However, in the longer term, it is considered that the (updated) Smith-Feddes cloud physics model, which forms the basis of the IFW TDA, needs to be properly examined as some of the assumptions made may not be valid and could partly explain the poorer performance of the IFW TDA. Given the availability of an improved cloud physics model, it is considered that the more rigorous approach ought to produce more reliable results.

As the currently available validation data is rather limited, CA plans to collect more icing reports over the coming winter to further assess the different methods. Given this, and an improved cloud physics model for the IFW TDA, it is expected that it should be possible to make a more definitive recommendation on which method should be adopted for the NATO TDA library during 1997. With a reliable description of the cloud environment (i.e. LWC, temperature, dropsize distribution) it is then possible, using an ice accretion model, to predict the extent of ice accretion on aircraft surfaces. Such a model has been developed by GMGO, Brueggemann[1], and it is intended that this model will eventually be linked to a cloud physics prediction model to provide a complete system for determining the extent of ice accretion on specific aircraft and helicopters.

3.2 Atmospheric Acoustic Propagation

The propagation of sound near the ground is a complex problem involving a number of different mechanisms. In addition to spherical spreading and atmospheric absorption, (which are straightforward) the effects of refraction (by wind and temperature gradients), scattering (by atmospheric turbulence), and reflection and diffraction from the surface are important. There are

two main applications for atmospheric acoustic propagation models, (i) predicting the performance of acoustic sensor systems for detecting guns, helicopters and ground vehicles, and (ii) for noise assessment and mitigation at military and test ranges. Over the years considerable effort has been made with regard to the latter problem and several nations have made noise predictions operationally for many years. Whilst many simple acoustic propagation models exist, these often fail to take proper account of the meteorological conditions which can have a significant effect on long-range sound propagation, giving rise to areas of sound enhancement, shadows and focusing.

An example of an early prediction method, which includes meteorology, is the semi-empirical Larkhill model (Turton et al[3]). This model has been used operationally in the UK (LARKW) since the early 80's and is also used in the NL and GE (SNDCAL), where it has been assessed and shown to give good results (Kießling and aufm Kampe[1]). However, recently both the UK (West et al[4]) and US (Olsen and Noble[5]) have introduced more sophisticated hybrid ray/parametric models into use, these being the APP (Acoustic Prediction Package) and the NAPS (Noise Assessment and Prediction System) respectively. A validation of the APP[4] has shown that it is an improvement on the Larkhill model used previously, whilst an evaluation of the NAPS has been reported by Okrasinski and Dennis[6]. These models are candidates for adoption as a NATO library model for predicting blast noise from ranges. This is a problem which is affecting more countries throughout Europe as noise pollution increasingly becomes a politically sensitive issue.

Whilst the latest models (APP, NAPS) offer improved prediction accuracy compared to the older methods, they are still unable to account for the effects of terrain (e.g. water surfaces), topography (hills and valleys) and turbulence (which scatters sound energy into shadow zones). Parabolic Equation (PE) based techniques are now being applied and these are capable of representing these effects. In the longer term it is expected that PE based models will replace the ray based models used in the APP and NAPS. These effects are particularly significant when predicting the performance of acoustic sensor systems, e.g. sound scattering by turbulence can aid sensor systems in locating targets which are downwind. Reliable prediction systems for acoustic sensor systems must await the availability of mature, fully validated, PE models which incorporate all of the factors noted above.

3.3 EM (RF/μ-wave) Propagation

Environmental conditions affect the propagation of RF signals in four different ways: (i) refraction, (ii) attenuation, (iii) ground/terrain effects, and (iv) troposcatter. Refractive effects affect the performance of radar, giving rise to extended ranges in ducting conditions and reduced ranges in sub-refracting conditions and can affect the performance of radars used for target acquisition, range-finding, tracking and communications.

Current operational propagation assessment TDAs such as the US Navy IREPS (Integrated Refractive Effects Prediction System) are based on ray tracing. However, in recent years there has been considerable effort in developing PE methods for making field strength calculations.

One of the benefits of the PE approach is that it can give more quantitative information on the propagation, in particular it is able to predict 'skip' zones.

In recent years, the military emphasis has shifted very strongly from operations over the open ocean to operating in coastal waters (the littoral environment) where the atmospheric environment is much more complex and variable, and it is essential that range-dependent conditions are available for propagation modelling since conditions vary significantly along the path. Range-dependent PE models, that can also include terrain, have been developed which enables both land/sea and coastal applications. However, PE models are more computationally demanding and much slower to run. Due to the computation required to run PE models, faster hybrid models have been developed for operational use. These include the US Navy RPO (Radio Physical Optics) model and the TERPEM (TERrain Parabolic Equation Model) developed for the RN EEMS (Environmental Electromagnetic Modelling System) as noted at the July 1995 ISWG.3 meeting[7]. More recently, the US Navy have combined the RPO model and their TPEM (Terrain Parabolic Equation Model) to form the RPOT (Radio Propagation Over Terrain) propagation assessment system.

As noted above, the emphasis is now on predicting radar performance in the littoral environment, which demands the use of range-dependent schemes able to account for the effects of topography/terrain, and appropriate models (RPOT, TERPEM) have been developed for operational use in the US and the UK. Whether or not, these models can be made available to WG-BMSS for inclusion in a NATO TDA-library has yet to be established.

3.4 Infrared

Atmospheric propagation of infrared radiation is of importance for many military EO systems. Infrared systems are not all-weather systems and are affected by weather and other environmental effects. Consequently, a number of TDAs for infrared systems have been developed. The simplest of these is the UK infrared "visibility" calculator (IRVIS), although more sophisticated TDAs have been developed in the US and GE. In the US there are three different TDAs for each of the three services: the Air Force EOTDA 3.1, the Navy EOMDA and the Army TARGAC (although all of these are derived from the EOTDA). The TARGAC model has been developed to account for the effects of smoke and dust, which can be important in army operations, whilst the EOMDA has been modified to better represent the maritime environment for US Navy use. However, only an earlier version of the US Air Force EOTDA (v2) has previously been made available to NATO nations and there is general consensus that this version is insufficiently reliable. However, the version EOTDA 3.1 is reported to be much improved. Indeed, the US Air Force consider that the basic models in EOTDA 3.1 have reached a plateau and are now applying these models in the ACT/EOS (Air Combat Targeting/EO Simulation) programme for generating scene visualisation capabilities (Alleca[8]).

Similar capabilities have also been developed by GMGO in their NAVFLIR TDA, as described by von Ruesten[1]. This TDA is designed to support the use of airborne FLIR used for navigation rather than targeting and provides predictions of temperature contrasts and FLIR "ranges" for a variety of natural backgrounds, as well as some simple visualisation products. Results from the

NAVFLIR TDA are currently being verified by GMGO and will be reported on through WG-BMSS. The NAVFLIR model has also been linked directly to the GMGO BLM (Boundary Layer Model) prediction model to produce forecast charts of infra-red range for selected background combinations. Such charts show the spatial and temporal variation in the infra-red "visibility" and have potential for use in the advance planning of air sorties.

Considerable work on compiling verification and validation results is likely before WG-BMSS can recommend any of the above models for inclusion in the NATO TDA library. However, at this time only the GE NAVFLIR TDA and the simpler UK IRVIS calculator have been confirmed as being available for consideration. The availability of the latest US models to NATO has still to be established, but it is possible that commercial considerations may preclude some of these being released.

3.5 NBC/Smoke

Current NATO NBC doctrine is in accordance with ATP-45 (STANAG 2103). Whilst this is largely based on manual techniques, these are being replaced by computer-based implementations, although the methods used remain relatively simple. Within the civil sector most regulatory models used are based on Gaussian diffusion and these models make a number of assumptions which are not normally met (e.g. on the homogeneity of meteorological conditions). However, they are still used because of their low computational requirements. More sophisticated particle models are available, which overcome the shortcomings of the Gaussian model, but these are much more computationally demanding and so are not suitable for warning purposes. A compromise between these two extremes are the Gaussian puff models, which simulate a release of gases or aerosols by a series of single puffs, which themselves behave in a Gaussian manner, but are independent of each other. In this way inhomogeneous meteorological fields can be handled, whilst the computational requirements remain within acceptable limits.

All Gaussian models require a set of parameters which depend upon the local environment and weather conditions. These cannot be derived theoretically but must be determined from field measurements. As a consequence, parameter sets have been described for different scenarios by various authors and these show considerable differences. Important factors, amongst others, influencing these parameters are the atmospheric stability, the emission height and the exposure time. Therefore a model used for warning purposes should be able to choose a parameter set which is most appropriate to the situation at hand. An examination of these "sigma parameters" has been made by aufm Kampe and Weber[9], who concluded that there is no reason to change the ATP-45 parameters since they show excellent agreement with available experimental data. However at distances greater than 10 km there is substantial disagreement with the data, and there is a need for longer range diffusion experiments, especially under very stable conditions.

More sophisticated dispersion models are being developed by GE (HEARTS - Hazard Estimation after Accidental Release of Toxic Substances, aufm Kampe and Weber[1]), the US (ABCSIM - Atmospheric, Biological and Chemical SIMulator, Brown[1]) and various models are also being assessed in the UK (e.g. ADMS - Atmospheric Dispersion Modelling System, Carruthers et al[10]). For military applications, such dispersion models need to be able to handle episodic, localised,

small sources where the release is often near the surface. Therefore it is necessary to represent the effects of turbulence and terrain (e.g. the influence of hills, woodland and urban areas). It is also important to be able to consider the effects of short term and fluctuating exposures to toxic materials. Transport over complex terrain can be split into two main contributing factors: wind flow and dispersion effects. At present the simpler flow over terrain models, which can be integrated into dispersion TDAs, cannot account for all situations (e.g. they often break down in severe terrain or very stable conditions) and these limitations need to be addressed.

In the longer term the adoption of more sophisticated dispersion models for NBC purposes within NATO must be co-ordinated with the relevant NATO groups (NAAG Land Group 7 and the MAS NBC WP) with the improved techniques being documented within ATP-45. Whilst the adoption of improved models will bring a benefit in terms of the more accurate prediction of BC hazard areas, the penalty of adopting more sophisticated dispersion models is that they require more reliable and detailed meteorological data than the current ATP-45 "broad-brush" methods. Nevertheless, this is an area where current NATO practices could be brought more up to date, and WG-BMSS are well placed to make appropriate recommendations on models to be used to the other NATO groups mentioned above.

3.6 Visible/Near IR

Within the NATO community a number of different TDAs for supporting the use of Night Vision Goggles (NVG) have been developed. These include the ANVIS (CA), ILLUMW (UK), NITELITE (US) and NVG (US) astronomical models, together with the BIVPROG (GE) and EOTDA TV module (US) which also predict NVG "visual range". Also, in the US, the Night Vision Goggles Operations Weather Software (NOWS) is being developed (Alleca[8]) and this will provide, in addition to predictions of illumination levels, target detection ranges and cloud free line of sight probabilities. Future versions of NOWS are expected to include NVG scene visualisation.

As many of these TDAs are relatively mature some verifications have been reported. These include an evaluation of the accuracy of some of the US astronomical models (Keith[11]) and comparison of the predicted illumination levels from some of the available models against measurements made in Canada and Germany (Gross[1]) which have highlighted some consistent differences between the models. It was found that the US NVG model tends to predict the lowest illumination levels whilst the UK ILLUMW tended to give the highest values. Cultural lighting effects were present in the data and this was believed to be a cause of some of the discrepancy between the model predictions and the measurements. As yet, the models have only been assessed against a limited dataset; however, there is a much larger database of illumination measurements available at GMGO and it is planned to use this for a more complete verification

One of the characteristics of the various models is that they predict the photometric (0.4-0.7 μm) illumination whilst Gen III NVG are sensitive into the near infrared (0.6-0.9 μm) and there is the question of whether this is a significant limitation of the models. However, theoretical considerations and comparisons of photometric/radiometric measurements suggest that there is a linear relationship between the photometric illumination and the near infrared irradiance so this

can be accounted for relatively simply. The BIVPROG TDA also provides predictions of NVG visual range (as a function of illumination and the meteorological visibility) which are based on a multi-linear regression of data from pilot debriefings, whilst the US TVTDA computes detection ranges based on the sensor characteristics. Further data are required to verify these range predictions.

Given the availability of a number of different TDAs for NVG systems and verification/validation results, it is expected that WG-BMSS should be able to make recommendations in 1997 on which TDA, or TDA sub-models, for supporting the use of NVG, should be adopted for the NATO TDA library.

3.7 Other Applications

Other applications for which TDAs are being developed include: models for predicting runway icing conditions (as developed by GE and the UK), the US Navy Topside Ship Icing model, new contrail prediction techniques, models for trafficability, parachute operations (in particular a new technique developed by FR to support long range parachute insertions) and HF propagation. Another area which is of interest to many nations is in personnel factors (heat stress/wind chill etc.). This is an area which is being led by the Royal NL Air Force who are commissioning an "expert system" for predicting personnel factors which considers both meteorological and physiological effects. In addition to the previously mentioned TDAs for individual applications, there is also the possibility of providing advice on how weather impacts an entire mission, by looking at the weather effects on all the systems likely to be used. This is the rationale behind the US Army Research Laboratory Integrated Weather Effects Decision Aid (IWEDA), Sauter[12], which is a knowledge-based expert system designed to provide weather effects information at all organisational levels, with the ability to examine weather impacts on specific systems.

4. DISCUSSION AND FUTURE DEVELOPMENTS

Current meteorological support, as provided by the various NATO Weather Analysis Centres (WACs) and Military Forecast Centres (MFCs) is based on Numerical Weather Prediction (NWP) products for the theatre of operations. This in turn, demands the availability of high resolution relocateable (i.e. can be configured for different regions) models for the areas of operations. Such models are available to GE, the UK and the US. In addition to these there are many other high resolution models, which are centred over national territories, run at various WACs. However, there is a real need to improve on the quality of the predictions of moisture parameters (e.g. humidity, cloud, precipitation) from these models, since these are critical inputs to many TDAs, and at present generally require manual forecaster input.

In general, mission-specific and tactical forecasts (using TDAs) require more detailed meteorological data on the battle-area scale than can be produced at WACs and this is being addressed by the development of very high resolution battle-area scale models. The need for these battle-area predictions is in the theatre of operations, and it is considered that the ability of such models to produce more accurate meteorological forecasts will largely depend upon their

ability to assimilate more up to date in-theatre data. This suggests that these models would probably have to be run in-theatre since they would need to be able to assimilate, in short time, various sources of meteorological data from the operational area. Such models are currently being developed, these include the US Army Battlescale Forecast Model (BFM), Lee et al[13], the US Navy Coupled Ocean Atmosphere Mesoscale Prediction System (COAMPS), Hodur[14] and for the British Army the Computerised METeorological System (CMETS), Turton[15].

The availability of such models, together with the development of new systems to collect meteorological data from the battle-area (surface sensors, military radiosonde systems, remote profilers, sensors on air vehicles, satellites etc.), should lead to improved predictions of local effects such as those caused by topography/terrain/coasts. This in turn should lead to improved tactical forecasts made using TDAs. At present many of the TDAs that have been developed are stand-alone and run on a variety of disparate platforms. In the longer term it is envisaged that such battle-area scale models and the various meteorological TDAs will be integrated together such that TDAs for various applications would all be run using data from a single, consistent, very high resolution, 4 dimensional meteorological database.

It is expected that the NATO library of TDAs would be made available for nations to use on national Command, Control and Information Systems (CCIS) as well as on NATO CCIS, e.g. the SACLANT Allied Environmental Support System (AESS), and the planned SACEUR Automated CCIS (ACE ACCIS). Currently, AESS includes TDAs for electromagnetic/electro-optic systems and there are requirements for TDAs for NBC defence, mine warfare and amphibious warfare. Similarly, there are national plans to include the various TDAs within integrated systems such as the GE GEophysical DIsplay System (GEDIS), the NL METeorological Information System (METIS), the UK CMETS and the US Integrated METeorological System (IMETS).

The provision of 4 dimensional gridded meteorological data fields into NATO CCIS, and within the context of the "digitised battlefield", is likely to be an issue that will need to be addressed by WG-OPC, as it will be necessary to ensure that the NATO CCIS are capable of handling the appropriate meteorological message formats. In the longer term there may be a need to transmit meteorological data between different national (and NATO) systems and this is an area currently being investigated by WG-OPC.

To conclude, it is envisioned that the NATO library of TDAs will help to ensure the consistency of TDAs on various national and NATO systems, thus improving the consistency of tactical meteorological advice and supporting interoperability within NATO.

REFERENCES

1. Summary Record of the 2nd Meeting of the Military Committee Meteorological Group Working Group on Battle-area Meteorological Systems and Support. RECORD MCMG/WG-BMSS-2 dated 19 August 1996.

2. Comell Capt D, Donahue Capt C A and Keith Capt C. A Comparison of Aircraft Icing Forecast Models. USAF Combat Climatology Centre, Report No. AFCC/TN-95-004 (1995).

3. Turton J D, Bennetts D A and Nazer D J W. The Larkhill Noise Assessment Model. Part I: Theory and Formulation. Met Mag, 117 (1989), 145-154.

4. West M, Turton J D and Kerry G. A New Package for Blast Noise Prediction at UK Artillery and Testing Ranges. Applied Acoustics, 48 (1996), 133-154.

5. Olsen R O and Noble J M. A Noise Assessment and Prediction System. In Proceedings of the 11th Annual EOSAEL/TWI Conference, 27-30 November 1990, Las Cruces, New Mexico, US.

6. Okrasinski R and Dennis S. Evaluation of the Noise Assessment and Prediction System used at Aberdeen Proving Ground. US ARL report ARL-CR-204 (Sept 1995).

7. Decision Sheet of the NATO Armies Armaments Group Independent Special Working Group No. 3 on Meteorology. AC/225 (ISWG.3) DS/40 dated 17 August 1995. (Annex I. A Review of Tactical Decision Aids to Predict the Effects of the Atmosphere on Radiowave/Microwave Propagation.)

8. Alleca J P. Weather Impact Decision Aids for Electro-Optical (E-O) Weapons Support. In Proceedings of the 1995 Battlefield Atmospherics Conference, White Sands Missile Range, New Mexico, US.

9. aufm Kampe W and Weber H. A Discussion of "Sigma Parameters" for Diffusion Calculations. Report prepared for NATO NAAG AC/225 Land Group 7.

10. Carruthers D J, Holroyd R J, Hunt J C R, Weng W S, Robins A G, Apsley D D, Thomson D J and Smith F B. UK-ADMS: A New Approach to Modelling Dispersion in the Earth's Atmospheric Boundary Layer. J Wind Eng and Ind Aerodynamics, 52(1994), 139-153.

11. Capt Keith C W. Astronomical Models Accuracy Study. In Proceedings of the 1994 Battlefield Atmospherics Conference, White Sands Missile Range, New Mexico, US.

12. Sauter D P, Chesley C H and Spillane A R. The Integrated Weather Effects Decision Aid Threat Module. In Proceedings of the 1994 Battlefield Atmospherics Conference, White Sands Missile Range, New Mexico, US.

13. Lee M E, Harris J E, Endlich R W, Henmi T, Dumais R E, Knapp Maj D I and Weems, D C. U.S. Army Battlescale Forecast Model. In Proceedings of the 1994 Battlefield Atmospherics Conference, White Sands Missile Range, New Mexico, US.

14. Hodur R M. Pre-Operational Tests of the NRL Coupled Ocean Atmosphere Prediction System (COAMPS). In Proceedings of the 1995 Battlefield Atmospherics Conference, White Sands Missile Range, New Mexico, US.

15. Turton J D. Future Applications of Meteorological Modelling for Artillery Ballistics. To appear in the Journal of the Royal Artillery.

OVERVIEW OF DoD REQUIREMENTS AND CAPABILITIES FOR NATURAL ENVIRONMENTAL EFFECTS IN MILITARY MODELS AND SIMULATIONS

Donald D. Grantham, AF Phillips Laboratory
PL/GPA, 29 Randolph Rd Hanscom AFB MA 01731-3010
Ph: 617-377-2982 Fax: 617-377-2984 E-mail: grantham@plh.af.mil

Sam Brand, Naval Research Laboratory.
Alan Wetmore, Army Research Laboratory
Thomas M. Piwowar, John C. Burgeson, and Paul D. Try, Science and Technology Corp

1. INTRODUCTION

The Defense Modeling and Simulation Office (DMSO) sponsored surveys to be taken to establish the DoD requirements and capabilities for the natural environment and environmental effects in military models and simulations. The survey was conducted as a task within the DMSO Project, Environmental Effects for Distributed Interactive Simulation, E^2DIS (Heckathorn, 1994). A tri-service survey team was established and the Science Technology Corporation (STC) was selected to conduct a survey of DoD requirements for environmental effects in military M&S and a second survey to catalog the current and eminent models and data bases relevant to satisfying those requirements. STC also conducted an analysis of the shortfalls between stated requirements and current capabilities. This paper describes the results of the surveys and the analyses of needed new capabilities.

2. REQUIREMENTS AND CAPABILITIES SURVEY QUESTIONNAIRES

Because the results of both the requirements and capabilities surveys would be compared and assessed, the two questionnaires were structured as similarly as possible. Both questionnaires were divided into two parts: administrative information and technical information.

The administrative information section requested information on the simulation or model title, a brief general description, the Service office of responsibility and a technical expert for the simulation or model.

The technical information section of the questionnaires is the essence of the surveys. It has seven subsections and three attachments. The seven subsections were:

-- Critical Environmental Factors
-- Status of the Simulation, Model or Database
-- Application of the Simulation, Model or Database
-- Simulation or Model's Spatial and Temporal Domain
-- Current Requirements
-- Future Requirements
-- E2DIS and/or Environmental Capabilities Briefing

Attachment 1 requested information for atmospheric data and effects (surface to 300 km altitude) for each simulation or model:

-- Atmospheric Data Type
-- Fidelity Requirements
-- Sensor, Communications and Weapon System Description(s)

Attachment 2 requested similar information for near space (300 km to 70,000 km) data and effects. (Only the atmospheric applications were briefed at the BAC.) Attachment 3 addressed other requirements, such as, scalability of the simulation domain, computer software and hardware issues, security, VV&A, data currency (i.e., model, real-world or real-time data)

The requirements and capabilities survey questionnaires are provided in the respective, complementary documents (Piwowar et al., 1996 and Burgeson et al., 1996a).

3. RESULTS OF THE REQUIREMENTS SURVEY

The Requirements Survey was initiated as a "top-down" project, that is, to initiate the survey from the highest office in each Service that had direct responsibility for modeling and simulation. As Figure 1 shows, 170 service organizations were polled and 208 major M&S efforts were identified. The 208 major efforts are listed in Piwowar et al., 1996. The Army identified 107 M&S efforts which is more than the other Services combined. Of the 208 major programs, 74 were thoroughly documented through the survey questionnaire process.

The models and simulations were categorized by DMSO functional area and hierarchical level. The functional areas are: Research and Development; Test and Evaluation; Analysis; Production and Logistics; and, Military operations, Education and Training. Hierarchical levels of simulations or models are: Campaign; Mission; Many-0n-Many or Few-on-Few; One-on-One; and, Engineering Level. Figure 2 shows the functional area versus hierarchical level distribution of the 74 survey models /simulations. With the exception of the production and logistics category, there is a fairly even distribution across these areas/levels. Because of this even distribution across functional areas and hierarchical levels, the sample size of 74 well-documented questionnaires was considered to be sufficient to draw broad conclusions to benchmark current status and to develop new requirements and plans.

Also shown in Figure 2 are those models/simulations that were identified by the returned questionnaires as having critical environmental factors. These are displayed in parenthesis in the lower right of each cell. It is noteworthy that only 55% (5 of 9) of the Campaign-level M&S, only 60% of the Military Operations M&S, and only 68% of the Analysis M&S were identified as having critical environmental factors. These statistics are somewhat perplexing since these are the models and simulations that warfighters, who are the ultimate customers for M&S efforts and who are reasonably familiar with real-world environmental factors, would be expected to use routinely.

Sixty percent of the models and simulations were operational at the time the requirements survey was taken and ninety percent were expected to be operational by FY97. Figure 3 shows the number of models/simulations identified by military object families (i.e., forces, platforms, weapon systems, communication systems and sensors) and the number that identified atmospheric effects by family type. The lack of atmospheric effects in so many of these families indicate the environmental support groups, perhaps through the DMSO Executive Agent for Air and Space, need to work more closely with these modelers/simulators to bring to their recognition the potential atmospheric impacts and the current capabilities that are available.

Figure 4 shows the distribution of simulation types surveyed: live, virtual and constructive. Virtual simulations have by far the greatest usage. Distributed Interactive Simulations (DIS) were reported to be used currently by 19 % of the models/simulations. By FY97 this number was projected to grow to 57%. Thirty six percent of the responses that had no plan to be involved with DIS.

The requirements survey listed 26 atmospheric data types and 23 near-space environment data types for the respondents to select as requirements for their models/simulation. (Only the atmospheric applications were briefed at the BAC.) Respondents were requested to indicate the current usage and the potential for future usage of the data types. The results are shown in Figure 5. Those most commonly identified parameters were wind, precipitation, clouds, aerosols, fog, temperature and visibility. Each parameter was identified in 60% or more of the model/simulation requirements.

The spatial and temporal domains of atmospheric data requirements are shown in Figures 6 through 8. It is interesting to note that for most atmospheric data types, the requirements for spatial and temporal resolution spans 7 or more orders of magnitude.

Other topics that are addressed in the requirements survey results are model scalability, computer operating systems, host computer hardware, programming language, database management systems, transportability, data media, security and VV&A.

4. RESULTS OF THE CAPABILITIES SURVEY

Figure 9 shows that 41 service organizations were polled and 156 major M&S models or databases were identified. The 156 major efforts are listed in Burgeson et al., 1996a. The Air Force and Navy, respectively, identified 65 and 60 M&S efforts. Of the 156 major models or databases, 152 were thoroughly documented through the capabilities survey questionnaire process.

Figure 10 shows the functional area versus hierarchical level distribution of the 152 environmental databases and models. The data in this figure indicate that there are three dominant functional areas for the databases and models surveyed: Research and Development, Analysis, and Military Operations. Only one model supported Campaign-level models and simulations.

Figure 11 shows that the environmental capabilities database was comprised of 26 environmental databases, 57 environmental models, and 59 environmental effects models.

Figure 12 depicts the number of capabilities that provide each atmospheric data type. Note that transmissivity and clouds dominate the list of current capabilities, being provided by 25 and 26 models or databases, respectively. Temperature, wind and radiative features account for secondary peaks.

An appendix in Burgeson et al., 1996a presents a brief description of each model and database, along with the technical point of contact and critical environmental factors.

5. ANALYSIS OF REQUIREMENTS VERSUS CAPABILITIES

This section discusses the comparison between the environmental fidelity requirements identified from the 74 DoD simulation models in the Requirements Survey and the 152 environmental model and database capabilities in the Capabilities Survey. Burgeson, et al., 1996b compares fidelity requirements and capabilities for the eight atmospheric data types identified as those needed the most in the Requirements Survey. Those atmospheric data types are: aerosols, clouds, fog, humidity, precipitation, temperature, visibility and wind. The analysis compares the surveyed environmental fidelity requirements with capabilities in terms of their horizontal, vertical and temporal scales. The comparative analysis identifies deficiencies of current environmental simulation tools and environmental databases, and points out critically needed new environmental models, codes, and databases.

As an example analysis, the following shows the fidelity requirements and capabilities for cloud data. Comparisons are depicted in bargraphs that display the fidelity requirements and capabilities in the horizontal, vertical and temporal scales (Figures 13, 14 and 15 respectively). Each white vertical bar represents a unique environmental M&S requirement whose fidelity has been specified; each black vertical bar represents a unique environmental capability at its available fidelity. The requirements and capabilities are arranged along the horizontal axis in order of decreasing fidelity from left to right, an ordering that readily shows the match between requirements and capabilities. Figure 13 shows that there were 5 simulation models that required horizontal fidelity of cloud data at 100 meters or less and that there is one environmental model that can provide 100 meter fidelity.

A primary purpose of the E^2DIS Survey Task was to assess current capabilities for specifying the atmospheric environment for modeling and simulation at the fidelity needed by the military services M&S communities. The assessment was made by: (1) comparing the spatial and temporal environmental fidelity requirements and capabilities; (2) identifying the extent of defined deficiencies; and, (3) recommending the development of new models and/or databases with suggested fidelity capabilities.

Figure 16 shows the resulting deficiencies determined from these analyses. A deficiency (d) was defined as a condition in which 25 percent or more of the total requirements cannot be

matched by current capabilities. A major deficiency (D) was defined when more than 50 percent of the total fidelity requirements cannot be matched. Note that in Figure 16, all horizontal fidelity capabilities are deficient (eight of eight) and that half are major deficiencies. Additionally, more than half the vertical capabilities are deficient.

Analogous to the requirements report, the capabilities report also addresses model scalability, computer operating systems, host computer hardware, programming language, database management systems, transportability, data media, security and VV&A.

6. DATABASE AVAILABILITY

The complete database for the Requirements and Capabilities Surveys are available in the form of tables, queries and reports in *PARADOX for Windows*-Version 5.0. It can be obtained through the first author of this report.

7. ACKNOWLEDGMENTS

The E^2DIS Survey Team extends their thanks to the following personnel who assisted tin the Requirements and Capabilities Survey effort: Dr. Harry Heckathorn, Program Manager, E^2DIS; Lt Col J. Borger, USAF, Directorate of Weather; Capt. B Shapiro, USAF, Combat Climatology Center; Mr. L. Page, Department on the Army; CDR T. Tielking, USN; and Mr. E. Khedouri and Ms. E. Schroeder, Naval Oceanographic Office.

REFERENCES

Burgeson J.C., T.M. Piwowar, P.D. Try, D.D. Grantham, S. Brand, A.E. Wetmore, 1996a: *Natural Environmental Effects in Military Models and Simulations: Part II - A Survey of Capabilities.* Technical Report No. PL-TR-96-2040, U.S. Air Force Phillips Laboratory, Hanscom Air Force Base, Massachusetts.

Burgeson J.C., T.M. Piwowar, P.D. Try, D.D. Grantham, S. Brand, A.E. Wetmore, 1996b: *Natural Environmental Effects in Military Models and Simulations: Part III - An Analysis of Requirements Versus Capabilities.* Technical Report No. PL-TR-96-2039, U.S. Air Force Phillips Laboratory, Hanscom Air Force Base, Massachusetts.

Heckathorn, H., 1994: Environmental Effects for Distributed Interactive Simulation (E^2DIS). *Proceedings, 1994 Meeting of the IRIS Specialty Group on Targets, Backgrounds and Discrimination*, Infrared Imagery Society, Monterey California, February 1994.

Piwowar, T.M., J.C. Burgeson, P.D. Try, D.D. Grantham, S. Brand, A.E. Wetmore, 1996: *Natural Environmental Effects in Military Models and Simulations: Part I - A Survey of Requirements.* Technical Report No. PL-TR-96-2029, U.S. Air Force Phillips Laboratory, Hanscom Air Force Base, Massachusetts.

Service / Agency	Requirements Survey Results			
	No. of Organizations Polled	No. of Organizations Responding	No. of Major M&S Efforts	No. of Questionnaires Completed
Army	98	40	107	17
Navy	28	16	51	28
Marine Corps	5	5	8	5
Air Force	37	17	39	21
ARPA	2	1	1	1
Coast Guard	0	1	2	2
Totals	170	80	208	74

Figure 1. Requirements Survey Results

	Requirements Survey DMSO Function Areas (Critical Environmental Factors)						
Model/ Simulation Hierarchical Level	Research and Development	Test and Evaluation	Analysis	Production and Logistics	Military Operations	Education and Training	Totals
Campaign			4 (2)		2 (1)	3 (2)	9 (5)
Mission	4 (3)		3 (3)	2 (2)	3 (1)	4 (3)	16 (12)
Many-on-Many / Few-on-Few	3 (2)	2 (2)	6 (3)		8 (5)	3 (2)	22 (14)
One-on-One	1 (1)	8 (6)	4 (3)		1 (1)	6 (6)	20 (17)
Engineering	5 (4)		2 (2)				7 (6)
Totals	13 (10)	10 (8)	19 (13)	2 (2)	14 (8)	16 (13)	74 (54)

Figure 2. Models and Simulations Categorized by DMSO Functional Area and Hierarchical Level

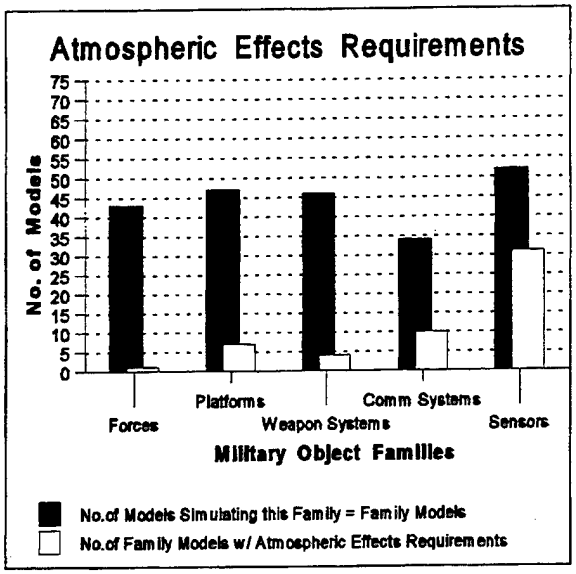


Figure 3. The number of models and simulations incorporating specific military object families and having atmospheric effects requirements for each military object family.

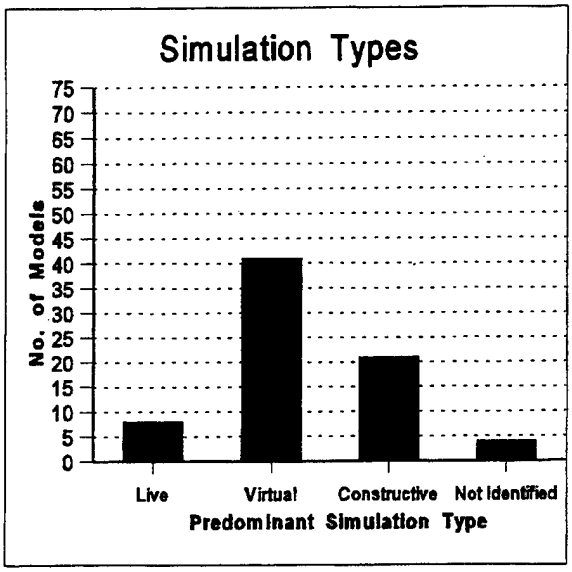


Figure 4. The number of models and simulations identified to be predominantly either live, virtual, or constructive.

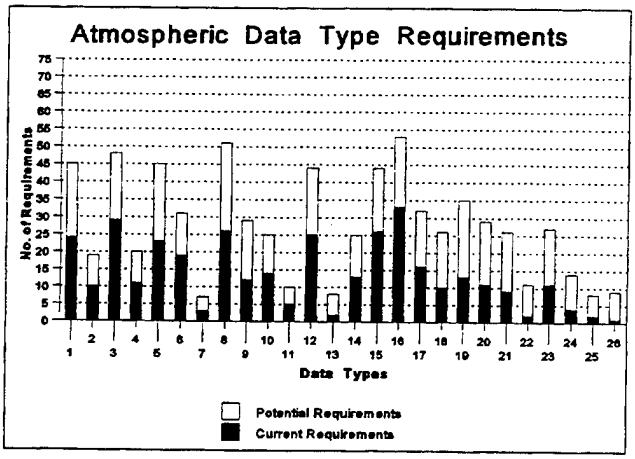


Figure 5. The number of requirements for each of the 26 atmospheric data types (see List).

Atmospheric Data Types

1. Aerosols
2. Atmospheric Electricity
3. Clouds
4. Dew Point
5. Fog
6. Humidity
7. Mixing Ratio
8. Precipitation
9. Refractivity
10. Sea Level Pressure
11. Static Stability
12. Temperature
13. Trace Gases
14. Transmissivity
15. Visibility
16. Wind
17. Wind Features (e.g., hurricanes)
18. Radiative Features (e.g., sky brightness)
19. Smoke
20. Chaff Dispersion
21. Combat-Generated Dust
22. Contrail Formation and Dispersion
23. Biological and Chemical Agent Dispersion
24. Nonnuclear Munitions Effects
25. Nuclear Detonation Effects
26. Ship Exhaust Tracks

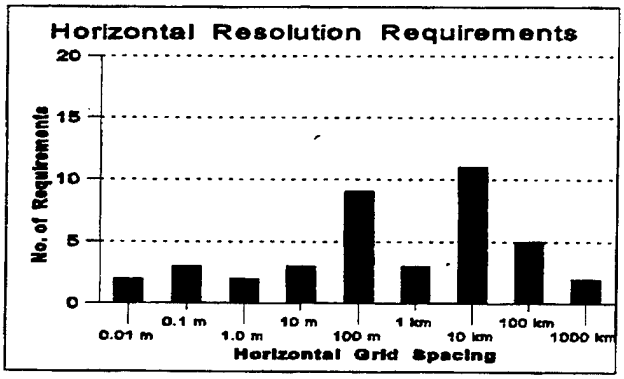


Figure 6. The number of horizontal resolution requirements for specific grid spacings.

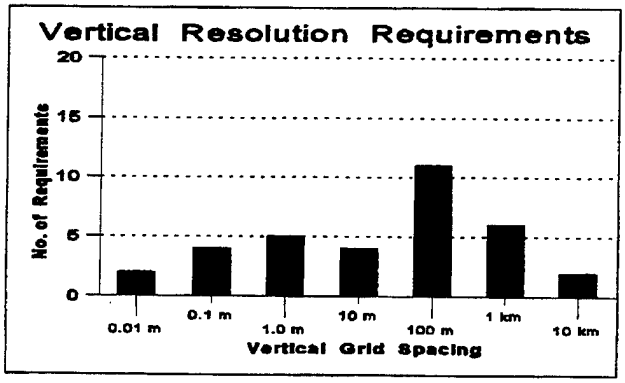


Figure 7. The number of vertical resolution requirements for specific grid spacings

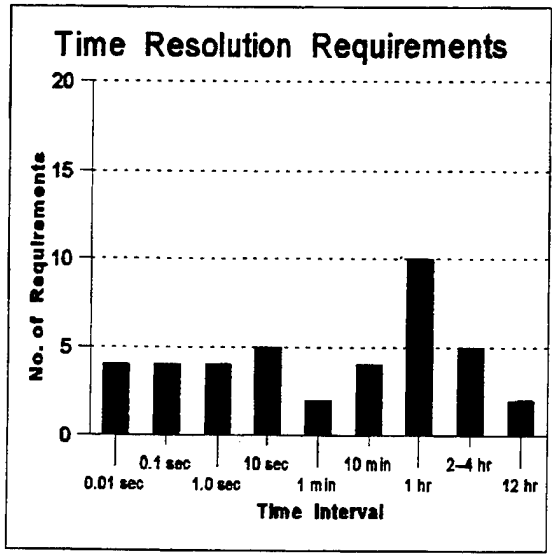


Figure 8. The number of time resolution requirements for specific time intervals.

US Military Service	Capabilities Survey Results			
	No. of Organizations Polled	No. of Organizations Responding	No. of Major M&S Efforts	No. of Questionnaires Completed
Army	6	5	31	31
Navy	26	14	60	58
Marine Corps	1	0	0	0
Air Force	7	3	65	63
Coast Guard	1	1	0	0
Totals	41	23	156	152

Figure 9. Capabilities Survey Results

Model or Simulation Hierarchical Level	DMSO Functional Areas						Totals
	Research and Develop-ment	Test and Evalua-tion	Analysis	Production and Logistics	Military Operations	Education and Training	
Campaign					1		1
Mission	2		12		5		19
Many-on-Many / Few-on-Few		1	10		1		12
1-on-1	33		21		25		79
Engineering	13	1	4		3		21
Not Indicated	6		4		8	2	20
Totals	54	2	51	0	43	2	152

Figure 10. Environmental Databases and Models Categorized by DMSO Functional Area and Hierarchical Level.

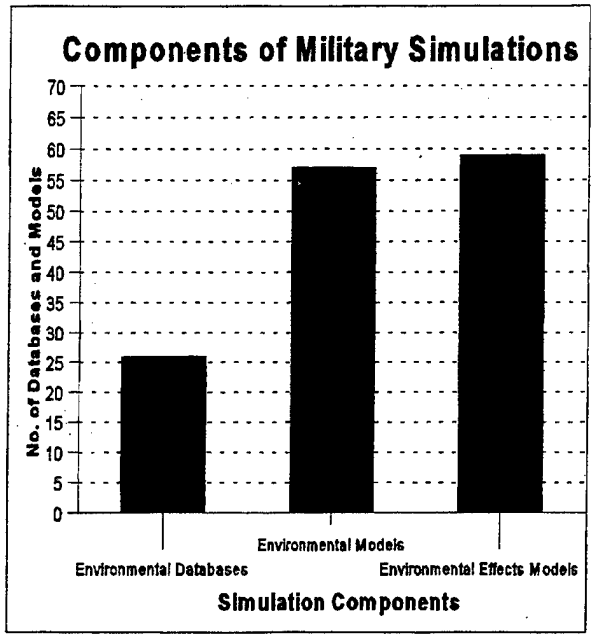


Figure 11. Surveyed environmental databases and models grouped as components of military simulations.

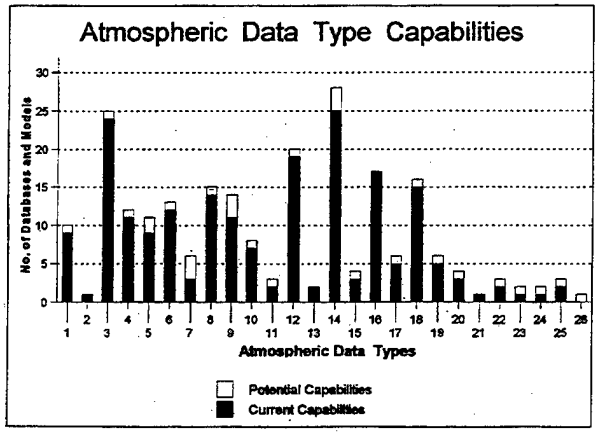


Figure 12. The number of environmental databases and models surveyed having a capability to provide a specific atmosphere data type. The 26 atmospheric data types are listed next to figure 5.

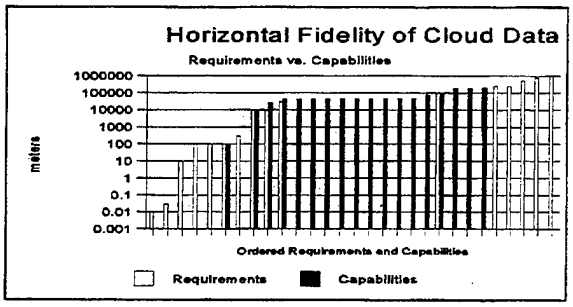


Figure 13. Comparison between environmental capabilities and M&S requirements for data on the horizontal structure of clouds.

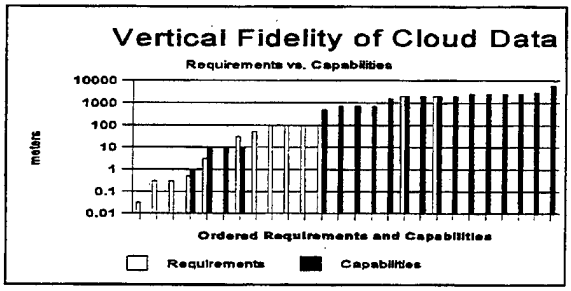


Figure 14. Comparison between environmental capabilities and M&S requirements for data on the vertical structure of clouds.

Primary Type of Atmospheric Data Required	Deficiency of Fidelity Capability (d) (D => Major Deficiency)		
	Horizontal	Vertical	Temporal
Aerosols	D	d	d
Clouds	d	d	
Fog	D	D	
Humidity	D	D	d
Precipitation	d		d
Temperature	d		
Visibility	D	D	d
Wind	d		d
Summary	4D/4d	3D/2d	5d

Figure 16. Overall Deficiencies of Current Environmental Models and Databases.

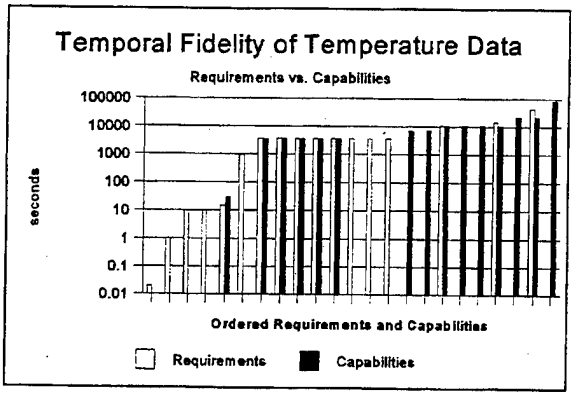


Figure 15. Comparison between environmental capabilities and M&S requirements for temporal data on temperature.

Primary Type of Atmospheric Data Required	Needed Fidelity of Capability		
	Horizontal	Vertical	Temporal
Aerosols	1000 m	100 m	
Clouds		100 m	
Fog	100 m	100 m	
Humidity	100 m	100 m	15 min
Precipitation	500 m		
Temperature	100 m		
Visibility	100 m; 10 km	100 m	10 s
Wind	100 m		5 s

Figure 17. Required New Environmental Models or Databases

EOSAEL and PcEosael©

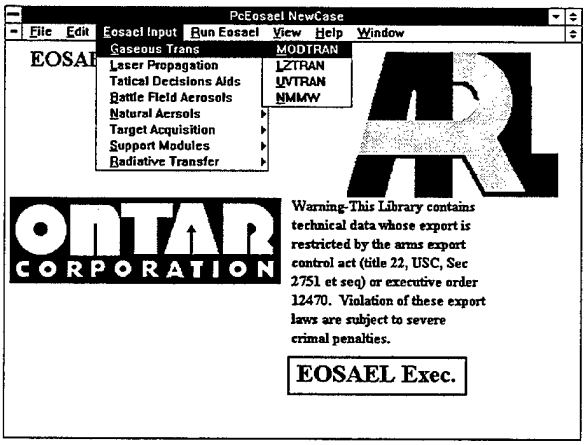
Dr. Alan Wetmore, Dr. Patti Gillespie, Army Research Laboratory, Adelphi MD

Mr. Andrew McCann, Dr. John Schroeder, Ontar Corporation

This work is implementing a Microsoft Windows™ interface for the Army Research Laboratory's family of EOSAEL modules under a Phase II SBIR Contract (DAAL01-96-C-2007). The work is sponsored by the Army Research Laboratory, Adelphi, MD and is being directed by Dr. Alan Wetmore of ARL. He can be contacted via e-mail at Awetmore@arl.mil, or via the World Wide Web at www.EOSAEL.com. This paper briefly described EOSAEL, PcEosael, current and future software development directions, and distribution of EOSAEL products. User can keep up to data on EOSAEL development through the web page www.EOSAEL.com.

The **EOSAEL** is a state-of-the-art computer library comprised of fast-running, theoretical, semiempirical, and empirical computer programs that mathematically describe aspects of electromagnetic propagation in a battlefield environments. The 25 modules are connected through an executive routine, but often are exercised individually. They may be categorized into eight generic atmospheric effects areas: atmospheric gases, laser propagation, tactical decision aids, battlefield aerosols, natural aerosols, target acquisition, support modules, and radiative transfer.

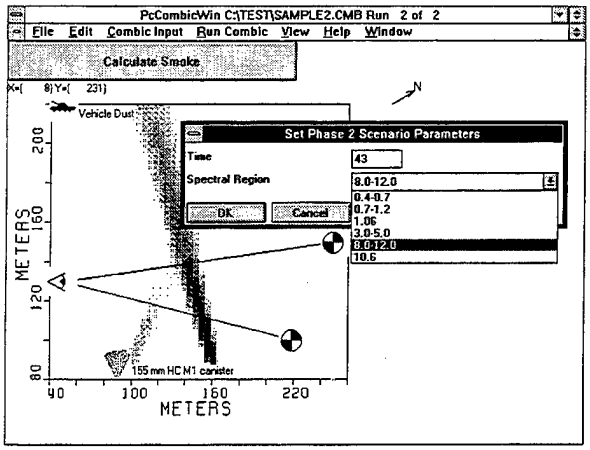
The EOSAEL modules and documentation are currently distributed to approved users through TECNET. Approval to access the system is obtained by contacting Dr. Wetmore at the addresses given above. The user may obtain, upon approval: The FORTRAN source code of the module, PC executable code for the module, the module manual in a PostScript™ format, and several test cases to insure the proper compiling and running of the module. Data input is accomplished by using a text editor to produce the appropriately formatted ASCII file, and output are given in ASCII tables. Several of the modules have limited graphical output files in an ASCII format.



PcEosael is Ontar's implementation of a user-friendly, Microsoft Windows based interface for the for each of the EOSAEL modules together with and overall executive to link them into a unified package as shown by the figure to the left. The work will be completed by the Spring of 1998.

The interface allows the user to set parameters by an intuitive, visual point

and click method, output plots of computed results, and generate images that are easily viewed. The interface is independent of the internal workings of the individual EOSAEL modules, and has on-line documentation for each of the modules and its suite of input parameters. It significantly simplifies setting scenario parameters common to all the modules (e.g. spectral band, range, etc.), and provides tools to easily compare the results from the different EOSAEL modules.



An example of the GUI is shown in the figure to the left which is produced by the COMBIC module. COMBIC compute the transmission through dust clouds, smoke, fire and other man made obstructions. The figure shows an observer (the eyeball), two paths (the end point are designated by the circles), and two obscurant sources. The first is the dust generated by a moving vehicle which is designated by the tank symbol in the upper left corner of the screen. The second source is a smoke canister designated by the symbol at the bottom of the plot toward the left hand side. This visual representation is used to two purposes.

First, it allows the user to specify the location of the sources, and the end points of the paths for the calculation. The user can either click on the object, e.g. the eyeball, and bring up an input screen were he can input the numeric x-y values for the location, or he can click and drag the object on the screen to the desired location. Similarly he can add (or subtract) sources and other paths.

The second use of this GUI is to view the output from the COMBIC calculation. In this case we are showing the dissipation of the smoke cloud from the 155 mm canister at 43 seconds after the beginning of the scenario. The user does this by clicking on the horizontal bar near the top of the screen labeled "**Calculate Smoke**" which brings up the dialog box shown at the right of the figure. The user first specifies the time from the beginning of the scenario at which he wishes to view the cloud and the spectral band in which he wishes to see the results (in this example the 8 to 12 μm band). The result are shown, in this case, by the vertical strip running from the smoke canister at the bottom of the display area (near the 160 meter grid point) to the top of the screen. The dust from the moving vehicle has moved out of the viewing screen by 43 seconds. At an earlier both the smoke and dust clouds will be in the field of view.

The strip is a visual representation, projected onto a 2d plane, of the spatial extent and transmission of the smoke cloud at the time and in the spectral band specified by the user. In this case the display is at 43 seconds after the release for the . 8 to 12 μm spectral region. The spatial extent is indicated by the x-y spread in the data. The transmission is

depicted as a gray scale going from black (0% transmission) to white (100% transmission). A second display, not shown, allows the user to generate a transmission plot (0 to 100%) as a function of time along each of the paths shown in the display.

Similar GUI are available for the other EOSAEL module where it is appropriate to display the inputs and outputs in a graphical format.

The software is designed for cross platform use, and the Windows software will be followed by corresponding UNIX versions. All documentation, including the ARL/ASL scientific reports, ARL technical manual for each module, associated software manuals, and on-line help is in the Adobe Acrobat Portable Document Format™ (PDF). The documentation is used as either a stand along product to be read at your leisure, or in conjunction with operation the software via hyperlinks.



A second major objective of the work is to better keep user informed EOSAEL developments. The is being accomplished via the URL site www.EOSAEL.com. Requests for the access to TECNET can be sent via the web site which also contains a descriptions of each module and the interactions between the modules.

The complete PcEosael interface will be completed by the Spring of 1998. In the interim, beta versions of selected modules are available for testing. These can be obtained by contacting Dr. Wetmore.

PROGRESS UPDATE ON DECISION AIDS FOR EO WEAPON SENSORS

Paul Tattelman
Phillips Laboratory
Geophysics Directorate
Hanscom AFB, MA 01731
DSN: 478-5956
tattelman@plh.af.mil

The Geophysics Directorate of the USAF Phillips Laboratory manages a Weather Impact Decision Aids (WIDA) program that develops software to predict the influence of the weather and other environmental parameters on the operational performance of Electro-Optical (EO) sensors (infrared, laser, visible) used in air-to-ground munitions, navigation systems, and Night Vision Goggles (NVGs).

The WIDA program has established unique measurement facilities to evaluate EO target and background signature models in the infrared (3-5 and 8-12 micron) and near-infrared (.7-.9 micron). EO data and imagery along with supporting meteorological and geophysical data are collected for systematic model validation. Experiments have been conducted at a fixed site at Hanscom AFB for nearly two years. A mobile van is also being equipped to conduct infrared and NVG experiments at several sites on Otis ANGB, Cape Cod, MA. Infrared experiments began in Jun 96 with NVG experiments to follow in 1997.

WIDA experiment data are being used to evaluate and develop the physics models used to predict the environmental impacts on EO sensors. These models drive WIDA applications software that determines target acquisition data for mission planning/execution activities and produce realistic target-area scenes for use by aircrews on automated mission planning systems during mission rehearsals.

An overview of the WIDA program was presented at the Dec 95 BAC. This presentation will report on progress made over the past year and provide an update on anticipated WIDA end-products and completion dates.

1. Introduction

The Weather Impact Decision Aid (WIDA) program is developing new products that provide performance predictions for EO Systems. Current focus is on IR and night vision systems. WIDA efforts translate conventional weather data into information needed by the warfighter to exploit the battlespace environment. WIDA products provide warfighters with predictions and visualizations of the influence of weather and other environmental parameters on Electro-Optical (EO) Sensors (infrared, laser, visible) used in air-to-ground munitions, navigation systems, and night vision goggles (NVGs). These products allow mission planners to factor weather into key decisions such as mission time, target approach heading, tactics, and weapons selection. They provide combat aircrews with detection/lock-on range predictions and/or target scene predictions, facilitating target location and positive identification.

The current WIDA program is divided into three components:

a. Air Combat Targeting/Electro-Optical Simulation (ACT/EOS) - Develops and upgrades models for predicting and visualizing weather impacts on air-to-ground IR targeting and navigation.

b. Night Vision Goggle (NVG) Operations Weather Software (NOWS) - Develops and integrates models for determining the influence of weather and illumination on the performance of NVGs.

c. Weather Automated Mission Planning Software (WAMPS) - Integrates new IR and NVG weather impact models developed in ACT/EOS and NOWS with existing laser and TV weather impact models into a product that will automate the generation of EO weather impacts in force-level automated mission planning systems.

The above components are discussed in more detail in the following sections. The validation effort is also described.

2. Air Combat Targeting/Electro-Optical Simulation (ACT/EOS)

The ACT/EOS effort was organized when the final version of the EO Tactical Decision Aid (EOTDA) was being completed. EOTDA Version 3.1 was delivered in 1994, and is currently being used operationally by the AF and Navy. This product was developed during a period of relatively primitive PC and workstation capabilities, limiting its utility. Furthermore, the EOTDA had only limited validation, is tedious to run, and often requires subjective manipulation by forecasters to adjust for discrepancies or bias in the core physics models.

The ACT/EOS objectives are to model weather effects on air-to-ground IR targeting systems and develop tools to enhance mission planning and execution. The models fall into the following three categories:

a. Thermal Contrast - Physics models are used to calculate IR radiances of elements of the targets and surrounding terrain. The current EOTDA uses TCM2. ACT/EOS is upgrading TCM2 for targets, and evaluating radiance models developed by the Smart Weapons Operability Enhancement Program (SWOE) for backgrounds. The upgrade to TCM2 is being based on TCM2 assessment measurements made using a FLIR 2000 IR sensor to observe simple test targets along with a comprehensive suite of meteorological observation equipment including a TPQ-11 cloud profiling radar. Data are being used to identify weather sensitivities causing differences between observed and predicted radiances. Current modeling is for 8-12 μm; a 3-5 μm model will be added in the future.

b. Atmospheric Transmission - Atmospheric transmission is calculated using MODTRAN, but calculation time is minimized using a spatial interpolation scheme developed for ACT/EOS.

c. Sensor Performance - Sensor performance modeling characterizes the ability of specific IR sensors to distinguish targets and backgrounds. ACT/EOS is developing an improved sensor performance model to overcome limitations in the models currently used in the EOTDA.

In addition, ACT/EOS is developing automated data management techniques to drive the above models. Geographic data sets are generated using ARC/INFO, a commercial Geographic Information System (GIS). Geographic data sets are generated from a variety of sources, including National Imagery and Mapping Agency (NIMA, formerly DMA), USGS, commercial satellites, and national imagery, and can support large areas (e.g. 40 km x 40 km at 10m resolution). The GIS is being programmed to fully automate this process. ACT/EOS models are also driven using real-time weather derived from the AF Automated Weather Distribution System (AWDS).

The models described above support the development of the following two software packages.

a. IR Target-scene Simulation Software (IRTSS) - This product provides an IR visualization of the target scene (currently 8-12 μm, but 3-5 μm will be added). The visualization capability includes terrain shadowing, realistic vegetation graphics and animated fly-throughs that allow for 3-dimensional positioning of the sensor to view the scene from any angle. IRTSS is primarily being developed for incorporation into the AF Mission Support System (AFMSS) that will support aircrew mission planning and execution. It is being evaluated by the 46th Test Wing and 46th Weather Squadron at Eglin AFB, FL. Pilots are briefed using IRTSS, and cockpit video and meteorological validation data are returned for analysis and product upgrade.

b. Target Acquisition Weather Software (TAWS) - TAWS is currently planned as a replacement for the EOTDA. ACT/EOS will provide the IR portion of TAWS. Requirements for TAWS are being discussed with AF Weather and the Naval Research Lab, Monterey. As a minimum, TAWS would provide more accurate acquisition and lock-on ranges, improved guidance on tactics, far superior visualizations, probability outputs, ability to support multiple taskings, and guidance on weather sensitivities.

3. Night Vision Goggle (NVG) Operations Weather Software (NOWS) - The NOWS effort began with a deficiency in AFSOC weather support to covert night-time helicopter air refueling using NVGs. After meeting with pilots of the 9th Special Operations Squadron and AFSOC weather personnel in March 91, Phillips Lab (PL) Geophysics Directorate initiated an R&D effort to predict weather impacts on the performance of NVGs. A contractual effort began in FY92. The prototype NOWS was delivered in FY94 and demonstrated to AF Weather. This led to a greatly expanded list of requirements for NOWS from AFSOC and ACC to support differing scenarios, targets, backgrounds and hazards for NVG operations. NOWS Version 1.0 was delivered in FY95 for evaluation by AFSOC weather (16th OSS). The NOWS Graphical User Interface (GUI) and products were developed in close coordination with AFSOC.

NOWS Version 3.0 was delivered in Dec 96 to ACC and AFSOC for evaluation at more than 30 operational weather units including those in PACAF and USAFE. The current version offers distinct advantages over other NVG support products including:

a. Physics-based models incorporating relevant weather for target/background detection range,
b. Upward and downward lines-of-sight,
c. Atmospheric attenuation and path radiance effects, and
d. NVG sensor modeling

NOWS provides worldwide map backgrounds for displaying, choosing, and tracking missions. It provides alerts to NVG operations hazards such as loss of horizon and towers, and provides NVG ranges as a function of user-selected probabilities. It also depicts optimum azimuth to approach a target or background. Weather-data input is automated with manual override capability.

The recently delivered NOWS 3.0 provides terrain elevation and features, full sensor bandpass spectral computations, an urban illumination model, and map-based color-coded output products. Future plans call for modeling individual light sources, terrain shadowing and masking effects, and incorporation of additional customer requirements.

4. Weather Automated Mission Planning Software (WAMPS) - Currently, weather impacts on systems and operations are not included in force-level automated mission planning systems. In order to support the appropriate selection of weapon and navigation sensors for hundreds, or even thousands of sorties, it is imperative that mission planners have WIDAs that automatically assess weather impacts for specific sensors against selected targets and backgrounds.

A survey of EO requirements was conducted for the WIDA program. This study acknowledged the importance of understanding and exploiting weather effects on EO systems. The survey of planners and pilots pointed out numerous WIDA requirements including the need for simultaneous guidance for multiple targets, guidance for weapon selection, target-area visualization, and more wavelengths than the current EOTDA.

Whereas TAWS is primarily a tool to support mission execution, WAMPS is envisioned as a force-level (24-72 hrs) stoplight weather impact mission planning capability. By providing red/yellow/green (unfavorable/marginal/favorable) guidance for each weapon/target combination, planners can better select weapons or alternatives or modify times-over-target. WAMPS will integrate new technologies developed in the PL WIDA program with other decision aids available in the EOTDA and elsewhere. The goal here is to demonstrate how weather decision aids can greatly enhance mission planning by exploiting both offensive and defensive weather sensitivities.

5. WIDA Model Validation

An integral part of the PL WIDA program is product validation. Two separate facilities are used to make comprehensive meteorological and sensor measurements. A fixed site at the Geophysics Directorate at Hanscom AFB, MA., (about 15 miles north of Boston) is used to collect all meteorological and EO data required by the ACT/EOS thermal models. Hiett (1995) provides a complete description of this facility. In addition to comprehensive meteorological and EO-related measurements, imagery is collected using a FLIR 2000 (8-12 μm), a FLIR PRISM (3-5 μm), and a TV camera (visible) observing two simple test targets. Currently, only the 8-12 μm data are being used for thermal-model validation and improvement.

A mobile platform has also been instrumented for ACT/EOS and NOWS validation measurements. Data collection using the mobile (trailer) facility will be primarily at the Camp Edwards range at Otis ANGB, Cape Cod, MA. For NOWS, the mobile facility includes measurements utilizing three laboratory-grade radiometers, NVGs, and tailored bar targets.

The fixed and mobile facilities are referred to as WIDA Lab, and data collected ensure that WIDA products will be thoroughly evaluated during their development.

6. Closing Remarks and Summary

The Department of Defense has spent considerable sums of money trying to engineer "all-weather" systems that are not impacted by the environment. A recent study by the GAO found that smart weapons were overrated. The study found that "all-weather" effectiveness was overstated by DoD, that precision guided munitions functioned effectively only in optimum conditions, and that IR, EO, and laser systems were seriously degraded by weather. Considerable improvement could be obtained by tailoring weapon choice, time of attack, and tactics to the weather. The use of validated environmental decision aids in mission execution and the automated mission planning process would bring current "smart systems" closer to the desired "all-weather" capability than trying to engineer-out the weather, and at a small fraction of the cost.

The WIDA program is developing products that translate conventional weather data into information that the warfighter needs to exploit the battlespace environment. This article presented an overview and progress report on projects that support air-to-ground IR targeting and operations using NVGs. Future efforts will incorporate weather sensitivities of other EO sensors into decision aids that will enhance all levels mission planning and execution.

Reference

1. Hiett, T. (1995) A User's Guide to the ACT/EOS Validation Experiment Level-2 Data Set, PL-TR-95-2136, Environmental Research Papers No. 1181, October 1995.

THE INTEGRATED METEOROLOGICAL SYSTEM (IMETS) WEATHER SUPPORTING CONCEPT

Richard J. Szymber
US Army Research Laboratory
Fort Huachuca, AZ 85613

MAJ Mike Corbett
US Army Intelligence Center & Ft Huachuca
Fort Huachuca, AZ 85613

ABSTRACT

This paper describes objective IMETS capabilities envisioned in the 2005 timeframe to include: a) battlespace observing systems and data sources ingested by IMETS; b) IMETS connectivity and interoperability with the Air Force Tactical Forecast System (TFS) and Defense Meteorological Satellite Program (DMSP) Small Tactical Terminal (STT); c) weather support products and data provided to Army battlefield functional areas and operating systems, and other "warrior C4I" systems; and d) IMETS communications connectivity and dependencies within the tactical weather support structure, and interaction with the Army Battle Command System (ABCS). We will overview the weather architecture and key concepts essential to fully exploit the capabilities of IMETS and enable warfighters to ultimately "own the weather."

1. INTRODUCTION

The most significant improvement in Army weather equipment over the next few years is the fielding of IMETS, and it's reception of real-time DMSP data. This will down-size and automate collection/ingest, processing, product preparation, and dissemination of weather information to all echelons of command in wartime and stability/support operations. Combined weather observations over the entire battlespace will be built into a three dimensional data base and stored in IMETS. IMETS will use the current observation data base and synoptic forecasts prepared by Air Force Global Weather Center (AFGWC) to generate detailed, tailored mesoscale forecasts, that will serve as the source of input for Tactical Decision Aids (TDAs) and automated Intelligence Preparation of the Battlefield (IPB) weather analysis products. Weather effects TDAs, like the Integrated Weather Effects Decision Aid (IWEDA), will run on IMETS, Digital Topographic Support System (DTSS), All Source Analysis System (ASAS), Maneuver Control System (MCS), and other nodes of the ABCS. The TDAs run by users outside IMETS will have electronic linkage to IMETS through area communication networks to receive the weather information required. Users will be able to receive electronically tailored weather data and products made to meet their mission, software, and operational requirements.

The IMETS is an Intelligence and Electronic Warfare (IEW) system of the ABCS. IMETS is Army furnished equipment that is manned and operated by US Air Force Weather Teams (WETM) at echelons above corps, corps, division, aviation brigade, separate brigade, armored calvary regiment, and ranger regiment/special forces. It is a heavy High Mobility Multi-Purpose Wheeled Vehicle (HMMWV) mounted tactical system deployable with supported high speed forces. IMETS is a mobile, automated weather information processing and communications system that will carry Army weather support into the 21st century. The target date for the weather supporting concept outlined here is 2005.

2. ARMY TACTICAL WEATHER SUPPORT PROCESS

The focus of all weather support to the Army will be upon the production and dissemination of information and decision aids - mainly TDAs - needed to conduct battlefield operations. Three sequential processes are used to provide Army tactical weather support. The first step is the collection of meteorological observation and forecast data. The next phase is the automated ingest, collation, validation, processing, analysis, and application of data and forecasts to predict effects. The final process involves the automatic, electronic dissemination of weather effects products to the user, primarily in the form of tactical decision aids.

With respect to the tactical Army weather support process as it relates to the IMETS, this paper will focus on the four stages that lead to Owning the Weather (OTW). The four components in order are: 1) "know the weather" - observations/collection; 2) "predict and apply the weather" - processing, analysis, forecasting, data/product generation, and dissemination; 3) "understand and exploit the weather" - TDAs, battlefield visualization, and information operations; and 4) "own the weather" - combat force multiplier. OTW provides the capability to anticipate the differential impacts of weather conditions on friendly and threat capabilities, allowing commanders to exploit windows of opportunity created by the weather.

3. KNOWING THE WEATHER

Weather observations are the foundation for weather forecasts, advisories/warnings, and weather effects information and TDAs. More frequent observations taken in a smaller area are a necessary part of improving mesoscale and microscale forecasts. IMETS will collect environmental observations and data from all available sources. Current and forecast synoptic and regional scale meteorological data and products are received in a timely manner from central facilities and centers. This information is supplemented by real-time, local battlefield weather observations received from sensing systems and observers. The goal is to build the most complete, detailed and accurate weather database for running atmospheric models, TDAs, and other applications.

3.1 Central Facilities/Centers

Strategic and theater weather data sources for IMETS are AFGWC, Fleet Numerical Meteorology and Oceanography Center (FNMOC), Air Force Combat Climatology Center (AFCCC), Air Force Space Forecast Center (AFSFC), National Oceanographic and Atmospheric Administration (NOAA), World Meteorological Organization (WMO), and Joint Meteorological Forecasting Units (JMFU) and Theater Forecasting Centers (TFC). The primary data source is AFGWC, with data and products from all other sources, except JMFU/TFC, available through AFGWC.

Vital battlefield surface, upper-air, and airborne observations must be relayed back to higher echelons and central forecasting facilities by IMETS via terrestrial lines such as Secret Internet Protocol Router Network (SIPRNET) or Global Command and Control System (GCCS). Since Army units are mobile and location must be included as part of the weather observation report, these reports are classified and must be transmitted over secure communications.

3.2 Real-time Battlespace Observations

IMETS will acquire local observational data from a variety of complementary space based, airborne, and ground based automatic remote and in-situ sensing systems, and human observers. In particular, the Army requires local area observations forward of division command posts and in target areas deep into enemy territory.

Observations from meteorological satellites (METSAT) provide the best area coverage, globally, and in theater. IMETS will directly receive low and high resolution imagery (visible, infrared, and microwave) and atmospheric soundings from polar orbiting DMSP and NOAA/TIROS satellites (to be replaced by the converged National Polar-Orbiting Operational Environmental Satellite System (NPOESS) around 2006), and Russian METEOR and Chinese FENG-YUN satellites. High temporal resolution observations from the geostationary METSAT, GOES (United States), METEOSAT (Europe) and GMS (Japan), will also be directly received by IMETS.

Airborne observations in crucial forward and deep areas will eventually be provided by an automatic meteorological sensor onboard unmanned aerial vehicles (UAV) and dropsondes ejected by UAV over critical target areas. These atmospheric profiles from dropsondes released at maximum flight altitude and flight path measurements from the meteorological sensor will come from a family of UAV flying at different altitudes and ranges/depths in the battlespace. The UAV-Tactical (i.e., Outrider) will have a maximum range past the forward line of own troops (FLOT) of 50 km and maximum flight altitude of 3 km above ground level (AGL) at 7 hour time endurance. At 4.5 hour endurance, it's maximum range past the FLOT is 200 km and maximum altitude is 6 km AGL. The UAV-Short Range (Hunter) will have a maximum range of 200 km and altitude of 4.5 km AGL. The UAV-Endurance (Predator) will fly out to a range of

500 km at a maximum altitude of 7.5 km. And the UAV-Medium Range will have a maximum range of 650 km and altitude of 12 km. Present weather information (e.g., clouds, precipitation, visibility) can also be obtained from UAV visible and infrared video camera imagery. Other airborne observations that can be received by IMETS include Air Force and Army aviation pilot reports (PIREPS) and target weather information (TARWI).

Upper air observations, up to an altitude of 30 km AGL, are taken near artillery units by Artillery Meteorological (ARTYMET) sections with the Meteorological Measuring System (MMS), using the Computer Assisted Artillery Meteorology (CAAM) models and software. Eventually, after the year 2005, tactical atmospheric profilers (i.e., the Profiler) will provide vertical profiles with extremely rapid refresh rates. IMETS will also receive upper air profiles from Air Force WETM taken at fixed airfields.

Several automatic, remote surface sensing systems will provide IMETS with surface weather observations taken at different areas on the extended battlefield. These unattended sensing systems will be selectively deployed throughout the depth of the battlefield and tied into an automated communication system. Brigade and battalion S2 sections will provide surface weather data taken at key terrain points forward of division command posts with hand emplaced and vehicle mounted Automatic Meteorological Sensor Systems (AMSS). Also, the S2 section's Improved Remotely Monitored Battlefield Sensor System (IREMBASS) with AMSS (IRAMSS) will provide surface observations in forward close battle areas and flanking areas along likely enemy avenues of approach. The IRAMSS can be hand emplaced or air delivered from the FLOT to deep behind enemy lines. ARTYMET sections will provide surface observations near artillery batteries taken by the MMS's automated surface meteorological sensor. Surface observations for deep areas will be received by IMETS from the Remote Miniature Weather Sensor (RMWS) deployed by Special Operations Forces (SOF). Finally, rear area surface observations will be taken by the Air Force WETM at IMETS locations.

Human manual surface weather observations taken all over the battlefield will also be obtained by IMETS. Long range ground reconnaissance and surveillance elements/units will provide surface observations for close battle and deep areas. Observations for areas forward of divisional command posts will be provided by the S2 Forward Area Limited Observing Program (FALOP), the ARTYMET section Artillery Limited Surface Observation Program (ALSOP), and Engineer units. Rear area weather observations will be taken by Air Force WETM observers at airfields and IMETS locations, Air Traffic Control (ATC) units, and Army aviation brigades/squadrons.

Other potential sources of observational data for IMETS may include Air Force Tactical Weather Radar (TWR) and tactical lightning detection/location systems, DoD/INTEL satellite imagery interpretation elements, Artillery Global Positioning System (GPS) rocketsondes (for deep operations support), and other theater Air Force, Navy, Marines, and indigenous sources.

4. PREDICTING AND APPLYING THE WEATHER

The four main areas of IMETS functions and capabilities to be discussed here are data ingest, processing/forecasting, product preparation, and dissemination. The most critical element of tactical weather support is weather communications. It is also the most difficult aspect to consider for establishing a future objective architecture. Tactical weather communication systems must provide dependable, wireless, two-way communications. The primary method of communication will be satellite based, with high frequency (HF) radio providing a secondary means of communication. The objective concept is to have a "single data stream" which travels over an open systems, common-user network, using satellite based system like Global Broadcast Service (GBS) and common-user networks such as SIPRNET.

Original IMETS organic communications equipment include Mobile Subscriber Equipment (MSE), Combat Net Radio (CNR) Single Channel Ground and Airborne Radio System (SINCGARS), HF radio, and Systems West METSAT receiver. Eventually, IMETS will be supplemented with the STT and satellite communications (SATCOM) equipment, and MSE will be replaced by Warfighter Information Network (WIN) and SINCGARS will be replaced by Future Digital Radio (FDR).

4.1 Communications for Acquisition/Ingest

IMETS will receive data and products from AFGWC primarily through GBS and SIPRNET. The AFGWC personal computer based dial-in access system, Air Force Dial-In Subsystem (AFDIS), can also be used through the IMETS' forecaster workstation TFS software. A variety of networks and systems can be accessed through SIPRNET to provide IMETS connectivity to AFGWC. A few such hosts include: GCCS; Joint Worldwide Intelligence Communications System (JWICS); Joint Deployable Intelligence Support System (JDISS); WIN; the integrated Intelligence information service INTELLINK; and the AFGWC homepage, Air Force Weather Information Network (AFWIN). The AFGWC primary uplink peak data rate for GBS is expected to be about 64 Kbps to support IMETS with GBS ground receiving terminals. Data and products from JMFU, TFC, and indigenous sources will be received by IMETS mainly through Theater Deployable Communications (TDC), High Frequency Regional Broadcast (HFRB) system, WIN, and GCCS.

Real-time battlefield observational data will be acquired by IMETS through various means, depending on the particular observing system. Automated sensor systems will be linked electronically to IMETS through self-contained communications, standard Army communications systems, or up-linked via satellites. IMETS will have a direct readout capability to receive all available METSAT transmissions. IMETS' Systems West will receive polar-orbiting METSAT Automatic Picture Transmission (APT) imagery and geostationary METSAT Weather Facsimile (WEFAX) imagery and other products. The STT will directly receive DMSP Realtime Data Smooth (RDS) and Real Time Data (RTD) transmissions, NOAA/TIROS High Resolution Picture Transmission (HRPT) data, and geostationary

METSAT low and high resolution imagery. All data received by the STT, and products it generates, will be ingested into the IMETS TFS on the forecaster workstation through an internal Local Area Network (LAN) line. All UAV meteorological data will be received by IMETS through the UAV tactical ground control station via MSE/WIN. ARTYMET upper air profiles and other data will be transmitted to IMETS through MSE/WIN. SOF RMWS observations will be received by IMETS through SATCOM link. AMSS data will be relayed to the S2's AMSS monitor/programmer unit by line-of-sight radio link. The S2 can store, display, and print the weather data on the monitor station and forward the data to the nearest IMETS and ASAS. IRAMSS data will be relayed to the S2's IREMBASS monitor/programmer station by 599-channel synthesized radio frequency (RF) data link, with a 25 ms burst transmission and 15 km line-of-sight range for sensors and repeaters. The IREMBASS monitor station stores, displays, prints, and forwards the weather data to IMETS and ASAS. The S2's AMSS and IRAMSS data will be transmitted to IMETS via area communications (i.e., IMETS will receive the data by hard wire line or through SINCGARS/FDR).

4.2 Processing, Analysis, Forecasting, and User Product Generation

The key to IMETS producing tailored weather effects forecasts is the timely, automated processing of current battlefield weather data/observations, together with central or networked weather facility products and forecasts. Unique IMETS processing and forecasting capabilities focus on the production of high resolution, local area forecast gridded data and graphic displays that will feed directly to IMETS and other user system client software applications. IMETS ingest, processing, analysis, forecasting, product preparation, and dissemination functions reside on the forecaster and weather effects workstations.

The forecaster workstation hosts the Air Force TFS software which ingests and processes alphanumeric, graphic, and gridded data from AFGWC and JMFU/TFC. The TFS provides theater weather forecasts out to 72 hours or more, and other standard TFS products. TFS also ingests, displays, and provides all STT METSAT imagery/data and products. The forecaster workstation passes data/products to the weather effects workstation (WEW) for further processing and generation of tailored products and TDAs.

WEW models and software applications include: the Battlescale Forecast Model (BFM); Atmospheric Sounding Program (ASP); IWEDA; Weather Maker program; Air Force Electro-Optical TDA; Night Vision Goggles TDA; Army Electro-Optical System Performance - Target Acquisition Ranges TDA, Thermal Reversals/Crossover TDA, and Weapons Zones TDA; Nitelite and EOCLIMO TDAs; Terrain Evaluation Module (TEM) with Digital Terrain Elevation (DTED) Level 1; Joint Mapping Tool Kit; and communications management functions. The WEW ingests AFGWC data and current battlefield meteorological observations to initialize the BFM, and can contour, streamline, and overlay BFM output on terrain map backgrounds of the area of operations.

Detailed weather forecasts tailored to the specific operational and tactical environment will be provided by IMETS using the BFM. This battle-scale or mesoscale meteorological model produces forecasts of weather conditions for a more limited region than the usual large-scale forecasts and includes the effects of complex terrain on atmospheric conditions. Currently, the BFM is initialized by the Navy Operational Global Atmospheric Prediction System (NOGAPS) every 12 hours via AFGWC. Eventually, AFGWC will acquire a high resolution mesoscale numerical weather prediction model that will be used for BFM initialization. Initializing the BFM with higher resolution gridded fields improves it's mesoscale forecasts. BFM has a 24 hour forecast period with forecasts at 0, 3, 6, 9, 12, 18, and 24 hr. It has 3 modes of area coverage and horizontal resolution: 500 x 500 km area (grid size) at 10 km resolution (grid point spacing); 250 x 250 km area at 5 km resolution; and 100 x 100 km area at 2.5 km resolution. The BFM has high vertical resolution in the lower atmosphere, i.e., 16 vertical levels from the surface to 7 km AGL, with greatest distribution of levels near surface. The weather parameters it forecasts are wind speed/direction and gusts, moisture (dew point, relative humidity, etc.), temperature, pressure, cloud cover (cloud liquid water), non-convective precipitation, precipitation type, and snow amount.

The ASP is an automated weather hazards and Skew T/Log P program that is coupled to the BFM. Combining current data and BFM output, ASP predicts atmospheric moisture, convection, and other parameters anywhere over the BFM's coverage area. Specifically, it forecasts the following weather parameters at all BFM grid points: visibility, cloud coverage and ceiling, fog, turbulence, wind shear, icing, thunderstorm probability, precipitation, atmospheric stability, and inversion layers.

The IWEDA is a sophisticated expert system based on hundreds of identified weather sensitivities of Army, Air Force, and threat weapon systems and operations. It automatically identifies and provides favorable, marginal, and unfavorable weather-effects impacts based on operating limitations of both friendly and threat weapons systems, their subsystems and components, personnel, and missions with respect to time and area of operation. IWEDA is tailored to specific tactical operations and missions, and provides detailed weather impacts information in terms of what operations and equipment are effected, as well as when, where, and why they are effected. Real map backgrounds are used to overlay geographic weather impacts for particular weapon systems, subsystems, or components. The user can query the program to display detailed textual weather impact statements for a specific location on the battlefield. Output is in readily understood color coded matrices (red = unfavorable, amber = marginal, and green = favorable conditions), map overlays, and succinct text statements. A "what-if" wargaming feature allows the user to quickly look at alternative mission/system setups and weather conditions. The BFM and ASP, together with additional forecaster inputs, automatically drive IWEDA. IWEDA will also be used on other Army command and

control (C2) systems to allow tactical customers to obtain weather effects information at all organizational levels.

IMETS will automate product generation as much as possible by providing the WETM the tools to build, automate, store, and recall products, and enable client pull of data and products. The WETM will build product templates, which will automatically draw on the IMETS database to fill in template fields, and which can be stored and recalled for later use. The forecaster workstation and WEW produces and disseminates processed data and products such as observations, forecasts, advisories/warnings, messages, graphics, imagery, tailored weather effects information, and automated weather effects TDAs. Data and products can be pushed to users or pulled from the IMETS server by client customers. The main Army functional areas supported are IEW, fire support, maneuver, aviation, IEW, air defense, engineer, and combat service support.

4.3 Communications for Dissemination

IMETS connectivity to all Army customers/users is accomplished through the ABCS. IMETS will operate in the same common operating environment as the Battlefield Operating Systems (BOS) and C2 systems it serves. IMETS data and products can be sent to or retrieved by any BOS and C2 system with access to the ABCS. These products are available on the LAN through a client server architecture. IMETS at highest echelon builds the weather database and exchanges products/data with lower echelons. IMETS connectivity to users within each echelon is by LAN and its connectivity between echelons is through a Wide Area Network (WAN) via SIPRNET, WIN, and CNR.

IMETS ABCS communications systems will be primarily the Army Common-User System (ACUS) MSE/WIN and secondarily the CNR SINCGARS/FDR. ABCS components vary by echelon. At echelon above corps, IMETS will be directly connected to the Battlefield Functional Area (BFA) C2 systems by the Army Global Command and Control System (AGCCS). At corps and division, IMETS will be directly connected to BFA C2 systems and BOS by the Army Tactical Command and Control System (ATCCS). IMETS will be indirectly connected to brigade and battalion BOS and C2 systems by the Force XXI Battle Command-Brigade and Below (FBCB2). The AGCCS is the Army component of the GCCS and provides the primary link to joint and combined systems.

A "smart push" will be used to send routine data and products to systems with formal user interface requirements (UIR) with IMETS. The IMETS server will send gridded data (and other information) to client applications on BOS and C2 systems directly from IMETS or through the MCS (the tactical forces information system), as specified in UIR. Additionally, a client-server "direct pull" will be used for data/products which are not routinely pushed and are made available to access as they are needed. One form of direct pull will be via an IMETS homepage/menu system.

GBS is a multicast system, allowing simultaneous broadcast of a variety of data/products. The system can provide these products to all users, a small subset of users, or a single user, depending on how the information is addressed and/or routed. The GBS allows two types of uplink: primary site and mobile inject. From tactical injection points, IMETS can use GBS to smartly push data/products to Army users with GBS ground receiving terminals, particularly those at brigade and battalion. IMETS mobile inject uplink peak data rate for GBS will be approximately 64 kbps.

IMETS will host a homepage server and browser accessible via the SIPRNET to get weather information and products especially to users without access to a C4I interface and to provide enhanced interoperability with joint meteorological systems. All WEW, STT, and forecaster workstation user products can be saved to the IMETS homepage. The homepage/menu will be organized in two broad categories by echelon and mission/BOS.

5. UNDERSTANDING AND EXPLOITING THE WEATHER

The ABCS, battlefield visualization, TDAs, and information operations provide the understanding and means to exploit the weather and it's battlefield effects.

5.1 ABCS BOS and C2 Systems

IMETS enables the warfighter to understand and exploit the weather by providing their ABCS BFA systems with products in the form of weather data fields, preprocessed TDAs, specially tailored output fields for other specific TDAs, and - in the far term - automated virtual reality displays of weather conditions linked to terrain displays. These products will be utilized in maneuver, targeting, and fire support; mission planning and rehearsal systems, and wargamming tools; models and simulations; TDAs; and other weather-related system applications. Systems with IMETS supported software applications, tools, and TDAs will include: AGCCS, ASAS, DTSS, MCS, Advanced Field Artillery Tactical Data System (AFATDS) and MMS, Forward Area Air Defense C3I (FAADC3I) system, Combat Service Support Control System (CSSCS), Automated Nuclear Biological and Chemical Information System (ANBACIS), Aviation Mission Planning System (AMPS), and UAV Mission Planning and Control Station.

5.2 Weather IEW Information Operations (IO)

The objective of weather IO is to guarantee and maximize our capability to anticipate and exploit the weather to our advantage while simultaneously denying the enemy the ability to use or manipulate the weather to their advantage. This is accomplished by protecting our access to, integrity of, and use of our weather information systems (INFOSYS), and to exploit and attack the enemy's weather INFOSYS.

The three components of weather IO are weather intelligence, INFOSYS, and C2 warfare (C2W). Weather intelligence concerns

automated IPB weather analysis, battlefield visualization of the environment/effects, and automated weather effects TDAs. Weather INFOSYS is comprised of IMETS and other weather support systems and infrastructure. Weather C2W involves weather information warfare consisting of weather C2W-protect and C2W-attack. Weather C2W-protect entails plans and actions to protect and secure our weather support INFOSYS (systems, databases, computers, communications, and personnel). Weather C2W-attack includes physical destruction or disruption of the enemy's weather INFOSYS to deny them weather information, understanding the enemy's weather INFOSYS to intercept and utilize their information and/or to influence/modify their weather picture, and limited tactical weather modification.

6. OWNING THE WEATHER (OTW)

OTW is the use of advance knowledge of environmental conditions, and their effects on friendly and enemy soldiers, systems, operations, and tactics, to gain a decisive advantage over opponents. It involves improving and exploiting the weather-related technological advantages for our battlefield systems over threat systems, making adverse weather a combat force multiplier. For decisive victory, the force exchange ratio can be increased to approximately 20-to-1 as a result of both Owning the Night and OTW.

IMETS is the centerpiece of OTW. The key ingredients for OTW are seamless communications, accurate and detailed weather forecasts, and a complete database of environmental sensitivities (i.e critical threshold values) of friendly and threat equipment, weapons systems and operations. The ABCS and IMETS' communications equipment, BFM, and IWEDA provide these essential capabilities necessary to anticipate and exploit the weather for tactical advantage.

7. CONCLUSION

The commander who can best measure and take advantage of weather conditions has a decided advantage over his opponent. By understanding the effects of weather, seeing the opportunities it offers, and anticipating when they will come into play, the commander can set the terms for battle to maximize his performance and take advantage of limits on enemy forces. An effective "all weather" mission capability can be achieved through the selection of the appropriate mix of sensors, weapons systems, and tactics that give friendly forces the ability to see, maneuver, fight and win in all types of weather.

IMETS satisfies the Army's requirement for an automated method of ingesting, processing, preparing and disseminating weather information and effects for the warfighter. IMETS provides commanders and their staffs with known and predicted conditions in the air and on the ground. This enables them to plan for conditions and their effects before a battle, helping the commander to choose the best time, manner, and place of engagement.

OWNING THE WEATHER FOR INFORMATION OPERATIONS

Richard J. Szymber
Army Research Laboratory
Fort Huachuca, AZ 85635

Leander Page III
Office of the Deputy Chief of Staff for Intelligence
Washington, DC 20310

ABSTRACT

Situational awareness and the relevant common picture enable commanders to perceive changes in the environment and then act upon those changes to produce a desirable end state. Battlefield visualization of weather, and its effects, is an essential element of battle command, and is necessary for out-thinking the enemy and gaining information dominance. Owning the Weather (OTW) is the use of advance knowledge of the environment, and its effects on friendly and enemy personnel, systems, operations and tactics, to gain a decisive advantage over opponents. OTW technology and information systems (INFOSYS) can serve as a force multiplier by providing commanders and their staffs with known and predicted conditions and effects, enabling them to choose the time, manner, and place of engagement. OTW involves a four step process for knowing, applying, and integrating the weather: 1) battlespace sensing and data collection; 2) processing, forecasting, analysis, and dissemination; 3) battlefield visualization and decision aids; and 4) combat weather exploitation and information operations (IO). The objective of OTW IO is to guarantee and maximize our ability to exploit the weather to our advantage while simultaneously denying the enemy the ability to use or manipulate the weather to their advantage. This is accomplished by protecting our weather INFOSYS and attacking the enemy's INFOSYS, through weather C2W-protect and C2W-deny/influence operations, respectively. By the command and control warfare (C2W) methodology of data denial, we can limit threat force ability to know and forecast the weather conditions in the joint task force area of operations, thereby increasing our ability to win the information war and out-maneuver and out-fight the enemy. It is crucial to deny the enemy access to meteorological satellite information in order to maximize our advantage. Additionally, the enemy can be put at a disadvantage at a critical time and place if we could covertly modify their picture of the weather, thereby influencing them to take detrimental courses of action. And, possibilities exist for intercepting enemy weather data bases and transmissions without their knowing. OTW provides the capability to anticipate the differential impacts of weather on friendly and threat capabilities allowing commanders to exploit windows of opportunity created by the weather. Improved weather information and IO, combined with knowledge of the limitations of weather on warfighting capabilities, is a powerful information warfare weapon.

1.0 INTRODUCTION

Situational awareness and the relevant common picture give commanders the opportunity to understand adverse weather conditions exist or are forecast on a battlescale. In the era of Information Operations (IO), commanders can act on this advanced knowledge of environmental conditions and to use this knowledge for tactical advantage over threat forces. Battlefield visualization of weather, and its effects, is an essential element of battle command, and is necessary for out-thinking the enemy and gaining information dominance. Owning the Weather (OTW) is the use of advance knowledge of the environment, and its effects on friendly and enemy personnel, systems, operations and tactics, to gain a decisive advantage over opponents. OTW technology and information systems (INFOSYS) can serve as a force multiplier by providing commanders and their staffs with known and predicted conditions and effects, enabling them to choose the time, manner, and place to fight. The OTW vision describes a four step process for integrating weather into IO: 1) battlespace sensing and data collection; 2) processing, forecasting, analysis, and dissemination; 3) battlefield visualization and decision aids; and 4) combat weather exploitation through application to IO. OTW provides the capability to anticipate the differential impacts of weather on friendly and threat capabilities allowing commanders to integrate weather information into the decision process at targeting cells and therefore plan and exploit windows of opportunity created by adverse weather.

The objective of OTW IO has three parts. First, to guarantee commanders have high technology capabilities to receive and use surface and space based weather observations, battlescale weather forecasts, and weather effects on tactical operations. Second, to provide the comparative means to know when friendly forces will have advantage in adverse weather conditions before battles are fought. Third, to deny the threat forces the basic space based, high resolution information and high resolution forecast technology so they must fight without advance knowledge of the effects of adverse weather on their systems and personnel. This objective is accomplished by protecting our weather INFOSYS and attacking the enemy's INFOSYS, through weather C2W-protect and C2W-deny/influence operations, respectively. By the command and control warfare (C2W) methodology of data denial, we can limit threat force ability to know observed and forecast weather conditions in the joint task force area of operations, thereby increasing our ability to win the information war and out-maneuver and out-fight the enemy. It is crucial to deny the enemy access to meteorological satellite information in order to maximize our advantage. Additionally, the enemy can be put at a disadvantage at a critical time and place if we could covertly modify their picture of the weather, thereby influencing them to take detrimental courses of action. And, possibilities exist for intercepting enemy weather data bases and transmissions without their knowing.

2.0 INFORMATION OPERATIONS AND WARFARE

The force multipliers that are embodied within the Information War can be defined as see the enemy, hear and locate the enemy's command and control (C2) structure, disrupt the C2 structure by physical destruction, deny hostile C2 by jamming, and communicate and out think the enemy using a robust C2 system and assured seamless communications. These battlefield functions are supported by capabilities that include those listed in figure 1.

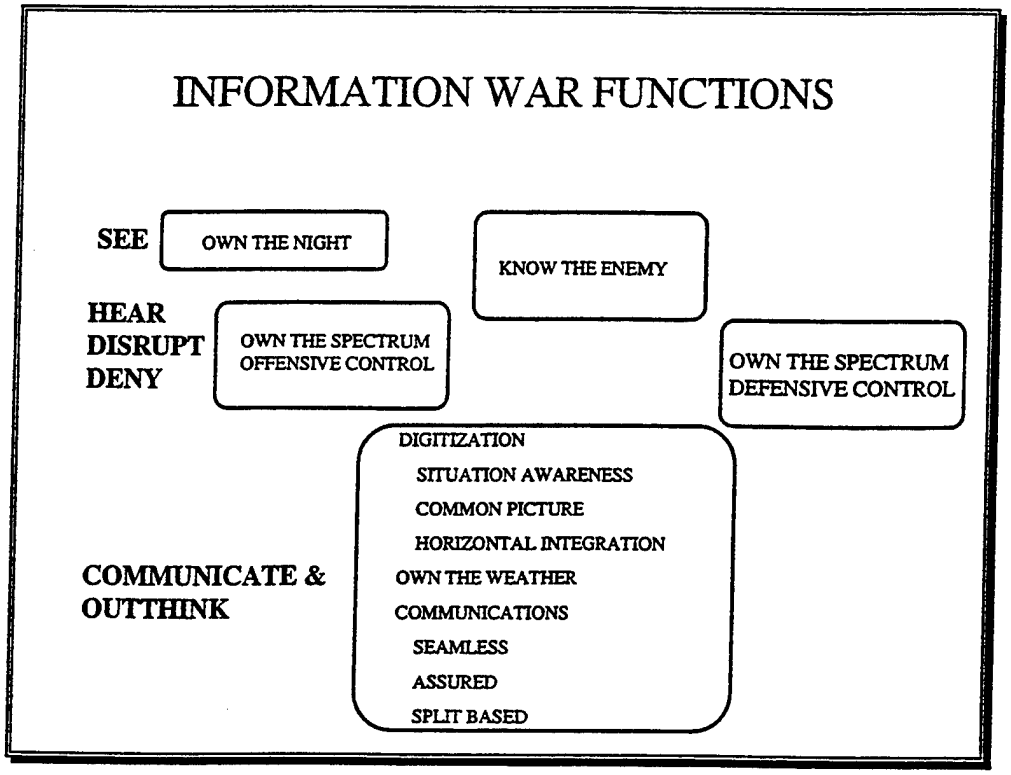


Figure 1. Information war functions.

Seamless Communications – User transparent communications from National Command Authority (NCA) to the individual soldier. Assured communications for split based operations and asset control from contractor to foxhole.

Own the Spectrum –The most critical resource required to win the information war is the electromagnetic spectrum. Sensors, information transport and smart weapons-smart munitions all require assured use of the spectrum. At the same time the enemy must be exploited and denied the use of the spectrum.

Digitized Battlefield – Common picture and situation awareness implemented horizontally across battlefield functional areas.

Own the Night – See and engage the enemy beyond his range day/night/all weather.

Own the Weather – Operate smart weapons, smart munitions under all weather conditions and provide the commander decision aids to plan/conduct all weather operations.

According to FM 100-6 Information Operations (1996), IO are military operations, supporting battle command, that enable, enhance and protect the commander's decision cycle and mission execution, while denying and exploiting the adversary's, to achieve an information advantage across the full range of operations. Information warfare (IW) is actions taken to preserve the integrity of one's INFOSYS from exploitation, corruption, or destruction while at the same time exploiting, corrupting, or destroying an adversary' INFOSYS and in the process achieving information dominance. Information dominance is that level of awareness where we know more about our battlespace and operations than an adversary.

3.0 WEATHER INFORMATION OPERATIONS

The objective of OTW IO is to guarantee and maximize our capability to anticipate and exploit the weather to our advantage while simultaneously denying the enemy the ability to use or manipulate the weather to their advantage. In general, this is accomplished by protecting our access to, integrity of, and use of our weather INFOSYS, and to exploit and attack the enemy's weather INFOSYS. There are three main components to weather information operations: weather intelligence, INFOSYS, and C2W. The remainder of this paper will focus on the military weather aspects of C2W. The thrust of OTW IO weather C2W has three parts, as summarized in figure 2.

WEATHER (WX) COMMAND AND CONTROL WARFARE (C2W) COMPONENTS	
WX C2W PROTECT	* Protect and secure our weather support INFOSYS (systems, databases, computers and communications, and personnel)
WX C2W EXPLOIT	* Understand enemy weather INFOSYS * Steal and utilize enemy weather data
WX C2W ATTACK	* Deny enemy weather information * Modify enemy weather data * Influence enemy weather picture

Figure 2. Weather Information Warfare

3.1 Weather C2W-Protect

With threats to our INFOSYS steadily increasing, priority of effort in the near term should be on implementing a C2W weather protect plan. Our ability to observe and know the weather conditions in the battlespace is of critical importance, since the rest of the

weather supporting process hinges on this. Tactically, it is necessary to protect our capability to take forward weather observations, and to automate the relay of observations via secure Army systems. Key satellite controlled remote sensors must be camouflaged, and the use of tactical weather radar should be limited. Weather observing systems and communications can be especially vulnerable to enemy electronic jamming countermeasures. Weather data bases can also be easily corrupted.

At the strategic level, plans and procedures must be established to protect our weather INFOSYS and it's support structure. Some preventative actions include: a) identification of potential vulnerabilities in our weather INFOSYS and potential threat capabilities and intentions to attack our INFOSYS; b) use of secure communication paths, e.g., SIPRnet; c) defending meteorological satellite downlink sites, major communication paths/nodes and transmission sites, and centralized facilities and regional sites; and d) evaluating threat jamming capabilities and providing for alternate means when jammed.

3.2 Weather C2W-Exploit

In order to exploit the enemy one must first know and understand the enemy. Threat weather force structure and concept of operations can be deduced from their doctrine and exercises. Threat weather technology and capabilities can be determined through information gathered from the National Ground Intelligence Center and Air Intelligence Agency, and included in the commander's intelligence estimate and essential elements of information. With this information, key threat weather capabilities (e.g., weather radar) can be identified and targeted for exploitation.

"Weather" considerations should be included in overall intelligence exploitation procedures. Knowledge of the enemy's weather communications architecture can provide opportunities for interception of in clear and coded broadcasts. Other intelligence sources should be considered for the potential of extracting additional weather information. Finally, we must provide the means to relay threat weather data to friendly weather teams in a timely manner once it is acquired.

3.3 Weather C2W-Attack

A key aspect of IO and IW involves the trade-off between attacking and exploiting an opponent's INFOSYS, with respect to the need to affect information versus denying information. The most basic way of attacking information is to go after the communication channels. However, direct destruction of your enemy's communications channels also denies your access to these channels.

Similar to exploiting the enemy, in order to plan for attack one must fist know how the adversary uses weather information and what role it plays in their decision making process. It is also necessary to identify how the threat receives weather information

and what type of information. C2W-attack weather involves not only physical destruction and denial, but also deceiving the enemy. The three main aspects of weather C2W-attack considered here are deny, influence, and change the weather.

3.3.1 Weather C2W-Attack: Deny

This involves denying the enemy the full picture of the battlespace weather situation by destroying their weather observing capability through physical destruction during a major regional conflict. Key threat weather observing sites such as weather radars, satellite ground stations, and satellite communications relay nodes should be included in the joint task force (JTF) target sets. Another means of denial is through disruption by electronic warfare. This can be accomplished by jamming threat weather system communication paths (e.g., high frequency transmissions of weather broadcasts in the area of operations).

The enemy can also be denied weather information through the encryption of friendly sources. The encryption capabilities to use would be in mutual agreement with our allies. The Defense Meteorological Satellite Program (DMSP) provides secure data transmissions, and SIPRnet and the Joint Worldwide Intelligence Communication System (JWICS) classified systems should be used to carry routine weather data.

3.3.2 Weather C2W-Attack: Influence

The enemy can be deceived by hiding the real picture of the weather and in its place paint and insert a false weather picture. Weather deception considerations would be integrated into the major deception plans of the JTF commander and used only occasionally with key JTF deception actions. Options include transmitting false weather observations for enemy interception and the store/forward and transmission of modified weather satellite imagery with false timing (i.e., modified valid times).

For example, lets consider a role for meteorological satellites in potential deception plans. Prior to the deception action, threat forces would be allowed to directly receive in clear satellite transmissions. Then at a critical time, the threat's reception would be changed to acquire false imagery while friendly forces continue to receive the true imagery by encrypted link. Modification of the satellite image and/or header (i.e., valid date/time) could result in the delay of enemy planning of attack or defense strategy, throwing threat timing off enough for fast friendly strikes and delay of threat defensive actions. A scenario of altered imagery showing a weather front and heavy clouds moving into an area early could enable a movement of enemy forces expecting to be hidden from detection by the cloud cover to be caught out in the open.

3.3.3 Weather C2W-Attack: Change

It would be of great value to the Army to acquire even a modest capability to modify the weather, such as clearing fog or initiating precipitation over a selected but limited region. Currently, little progress is being made in this area, but in the future, improved knowledge and understanding of the physical processes affecting the weather may eventually provide a limited capability to modify weather effectively, if only locally. However, the military must follow International agreements not to modify weather in threat territory.

Some examples of the use of a limited capability to modify/clear adverse weather conditions include: a) fog dissipation at our launch sites and landing zones when it would delay or stop operations; b) inducing precipitation over key areas to raise ceilings/visibility and enable launches; and c) eliminating ice fog in arctic artillery operations.

3.4 Summary of Weather C2W-Attack/Exploit Options and Objectives

3.4.1 Deny the Enemy

Leave the enemy with no weather picture or an incomplete picture through denial/disruption from electronic warfare or destruction of their weather INFOSYS. With no weather data, the enemy is denied information needed to take effective action and adjust his course of action.

3.4.2 Influence the Enemy

Trick the enemy with a skewed weather picture through deception and manipulation. Furthermore, once the deception is discovered by the enemy, he is left with an unreliable picture of the weather that he does not know if he can trust and will come to distrust his weather INFOSYS. With skewed weather information, the enemy can be influenced not to take action or to take the wrong action, or to take action at the wrong time and/or place.

3.4.3 Exploit the Enemy

Leave the enemy weather picture and INFOSYS undisturbed so we can steal and exploit their weather information, and so we can know what they know about the weather to help us predict expected enemy course of actions based on the weather. With in-tact, undisturbed weather information, the enemy can take their usual, expected actions based on the weather that we know about and can anticipate.

4.0 CONCLUSION

Weather IO guarantees and maximizes our ability to anticipate and exploit the weather to our advantage, and enables friendly forces to indeed "own the weather." The enemy must be denied access to meteorological satellite data in order to maximize our advantage

and attain information dominance. Above all, we must protect our own weather INFOSYS and support capabilities. With threats to our INFOSYS increasing daily, the top priority of our weather C2W methodology is weather C2W-protect.

"Critical Army thrusts such as Digitize the Battlefield, Own the Night and Own the Weather are vital to winning the information war... Owning the Weather is one of the force multipliers that will ensure Land Force Dominance by giving the warfighter the information he needs to fight under all weather conditions... We will Own the Night and the Weather so we can support day, night, all weather operations." -(General Jimmy D. Ross, 1994)

The Integrated Weather Effects Decision Aid (IWEDA): Status and Future Plans

By David P. Sauter

U.S. Army Research Laboratory
White Sands Missile Range, NM 88012
Ph: (505) 678-2078 Fax: (505) 678-3385 <dsauter@arl.mil>

The Integrated Weather Effects Decision Aid (IWEDA) is automated software that transforms raw weather data into weather intelligence for the battle space commander. IWEDA provides detailed information on the effect weather has on weapon systems, subsystems and components, and operations. This information is tailored to the end user and can provide detailed text explanations and geographic map overlays of what and where the impacts are, or simplified colored matrices that provide information about them. Over the past year, the Army Research Laboratory (ARL) has made significant enhancements to the software and ported it from the personal computer to a Sun Sparc 20 Workstation under XWindows. These efforts primarily relate to the initialization of IWEDA with output from ARL Battlescale Forecast Model (BFM) and Atmospheric Sounding Program (ASP) and the inclusion of a realistic map background at various scales. Efforts have also been made to include Navy and Air Force weapon systems in the expansion. Future plans include the integration of output from additional Army decision aids to be used as input in the IWEDA decision-making process as well as a rule editor that allows users to tailor weather impact rules for their operations.

Introduction

In 1991, the Science and Technology Corporation (STC) proposed a work effort to the then Atmospheric Sciences Laboratory to integrate portions of three existing automated weather effects tactical decision aids (TDA) and create a new IWEDA. In the subsequent five years, BED of ARL, along with their contractors STC and the Physical Science Laboratory of New Mexico State University, have developed IWEDA into a powerful tool that allows battlefield commanders to query specific information regarding the effects weather has on weapon systems and operations.

Because papers on IWEDA have been published in previous Battlespace Atmospheric Conferences (BAC) proceedings, an exhaustive overview of the software is not be presented here. Instead, the remainder of the paper focuses on the current status of the software and planned enhancements.

Current Status

Personal Computer Version

The work that began in 1991 on the Army IWEDA, was completed in early 1995 and contains 71 weapon systems (along with additional subsystems and components), and over 500 weather effects rules. Because this version of IWEDA contains systems also of interest to the Air Force and Marines, the software has been requested and distributed to numerous tri-service units throughout the Department of Defense.

In 1996, the Air Force expressed an interest in having the BED modify IWEDA to be more applicable for Air Force weapon systems. As a result, the Air Force funded an effort to develop a prototype IWEDA to include 13 Air Force systems (primarily fixed-wing aircraft). BED collected the pertinent rules for these systems and included the threat anti-air systems from the Army IWEDA. In addition to the data collection effort, the IWEDA database had to be modified to include several new environmental parameters that were not a part of the existing IWEDA. These parameters are flight level visibility, thunderstorm severity, and time of day. The software was delivered, installed, and Air Force personnel were trained at the Air Force Combat Weather Center at Hurlburt Field, Florida, in July of 1996. Testing and evaluation of the software is nearly complete.

UNIX/XWindows Version

Because the Army's common hardware/software platform for tactical field operations at most echelons is a UNIX-based platform, efforts were initiated in early 1995 to port and enhance the PC version to a Hewlett Packard 700 series workstation. The fact that the Army's Integrated Meteorological System (IMETS) is a UNIX-based system also weighed heavily in the decision to rehost IWEDA.

Although the PC version of IWEDA provided an opportunity to solicit feedback on the functionality of the software, it became apparent early in the software development effort that there would be at least two significant deficiencies. These

were primarily a function of the computing power and display limitations of the PC several years ago and included:

Manual weather data entry of all of the required IWEDA input parameters (approximately 30). While this provided flexibility for the user in not having to rely on being connected to a weather data source, it proved to be almost overwhelming to expect users to enter values for all of the parameters for all forecast periods and regions. Due to the time required for users to enter this data and the limitations of the PC to process hundreds of forecast regions, IWEDA limited the user to a maximum of eight forecast regions and six forecast periods. In turn, this resulted in poor resolution of weather impacts due to the limited number of forecast regions.

Crude map graphics. Primitive MS-Windows tools were provided to the user to draw geographic features on a blank map background. The tools were limited to lines, ellipses, polygons, and text. Because of memory constraints, only 15 to 20 of the geographic features could be added to any given map. Although this did provide a frame of reference for the user to determine the general geographic distribution of the weather impacts, it was at best adequate for the interim. As a result, all efforts shifted to the development of the UNIX/XWindows version in 1995 (with the exception of the Air Force funded PC effort in 1996). This effort proved to be challenging, and was compounded by a mandated switch from the Hewlett Packard platform to a Sun Sparc 20 Workstation in early 1996, and resulted in an initial version of IWEDA on the new hardware/software platform in June of 1996. The significant features of this software are:

Use of a commercial relational database management system (RDBMS) - INFORMIX - for all database tables and queries. Raw meteorological data is stored in a gridded meteorological database (GMDB) from which embedded structured query language (ESQL) calls are made to create an impacts table to store the grid locations and times for all IWEDA thresholds that have been exceeded. The GMDB is an INFORMIX binary large object created from meteorological data, output from BED's BFM, ASP, and WeatherMaker (a separately developed software application to allow a user friendly method of supplementing the GMDB with the required IWEDA inputs). ESQL within C programs allows the user to query the database tables through a user friendly graphical user interface to determine what systems are impacted, and when. Additional program functionality allows the user to determine why there are impacts, and where the impacts are occurring or are forecast to occur.

Replace the crude PC map graphics with a realistic digital map background. The maps are Arc Digitized Raster Graphics based and allow the user to choose from

a variety of scales (including 1:5,000,000, which is ideal for displaying mesoscale weather information from the BFM). Software was written to allow the user to click the mouse button on any portion of the map to query why the system is impacted at that location.

Incorporate an automated weather data ingest capability to preclude the user from having to manually enter all weather inputs. IWEDA currently runs for the same location and time as the BFM/ASP. After every BFM/ASP run (typically twice a day), the users are prompted to update the IWEDA impacts table. They are also asked whether or not they would like to run the WeatherMaker application to modify any of the four weather parameters (total snow depth, blowing snow, blowing sand, and precipitation) that are currently not predicted by the BFM or ASP. This allows for a much more detailed resolution of the weather impacts as the BFM is typically run on a 51 by 51 grid (yielding 2601 unique points as opposed to the maximum eight regions on the PC). The BFM/ASP currently runs to 24 h.

Support of a client/server architecture. IWEDA can provide the impacts table to other Battlefield Functional Area (BFA) nodes upon request, in support of the Army's Brigade Task Force XXI. The IWEDA binary is located on the individual BFA, which allows for fast response once the required INFORMIX tables have been loaded onto the client. It takes only minutes to transfer the required tables, both over a local area network and surrogate data radios.

To expand the tri-service applicability of IWEDA, a proposal was made to the Office of Naval Research (ONR) in late 1995 to develop a prototype Navy version of the software. This IWEDA would have Navy-specific weapon systems, platforms, and rules. ONR subsequently approved this proposal and funded BED (early 1996) to develop a UNIX/XWindows version for them. Efforts to date have focused on porting/enhancing the PC version to the Sun Sparc 20 and collecting rules for the Navy platforms/systems. At the time that this paper was written, neither the commercial RDBMS to use (INFORMIX, Oracle, or Sybase), the map server, or the location for the software to be delivered and installed, had yet been identified. IWEDA will also be an integral part of the next major software upgrade for the IMETS (Block II). Testing and evaluation of the IMETS Block II software and hardware begins in early 1997.

Future Status

PC Version

There are no plans to modify the PC IWEDA software. Based on limited BED resources, all efforts will focus on the UNIX/X Windows version. Any additional work on the PC version would have to be supported by external resources.

UNIX/XWindows Version

Although a tremendous amount of progress has been made over the last year and a half in terms of the porting and enhancing of the PC IWEDA to the Hewlett Packard and Sun Sparc 20 workstation environment, several critical tasks remain to be completed.

Design and implementation of a dynamic rule editor. As IWEDA currently exists, there is only one set of critical environmental threshold rules for all users. Although these values serve their purpose as defaults, it became apparent early in the IWEDA development that users require a method for tailoring these values for their unit's application. Several issues must be resolved before a complete design can be attempted:

1. Are all users allowed to edit the IWEDA rules or only a subset of users? For example, can every BFA within a unit edit the rules, or only a designated BFA who is then responsible for creating and maintaining the common database for the unit?
2. Is the current client server architecture with the INFORMIX tables (or Oracle for the All Source Analysis System BFA) maintained on all BFA, or do we change to an architecture where all database tables reside on the server (that is, IMETS)? If the current architecture is maintained, then the rules table modified via the dynamic rule editor must reside on the individual BFA hardware. If not, IMETS must have some way of maintaining and keeping track of multiple rules tables. A change in architecture is considered because software maintenance and distribution for the BFA becomes simpler in certain aspects with all tables only on the server. However, a drawback is that all SQL IWEDA calls are made on the server. The issue of connectivity also becomes more critical (if the network or radio communications go down, the BFA will be unable to run IWEDA).
3. Are user-modified impacts flagged for display to the user? That is, any IWEDA systems that contained one or more edited rules would appear in a different font color or style for a quick visual indicator that this system's weather effects are not based on the default values. An initial dynamic rule

editor is anticipated for IWEDA in FY98. A follow on effort will focus on allowing users to add new systems to the database in addition to editing rules for existing systems.

Incorporate quantitative tactical decision aid output as IWEDA input. IWEDA currently contains numerous rules that are general indicators of weapon system performance. For example, if visibility is less than 1000 m, night vision goggle (NVG) use is flagged as marginal. In reality, the NVG performance is a more complex function of ambient illumination. BED has an illumination module that predicts ambient illumination as a function of cloud amount, cloud type, precipitation, etc. This module would be run at all IWEDA grids (51 by 51) and then compared to a new NVG rule that relates performance to illumination. Likewise, existing electro-optics tactical decision aids could be used to compute target recognition and detection ranges at every gridpoint and used in IWEDA rules for target acquisition devices. The illumination module incorporation is anticipated in FY98, the EOTDA incorporation in FY99.

Incorporate the IWEDA map overlays into the common map display used by the individual BFA. Because of initial time constraints, IWEDA was coded to use its own map display, which is separate from the BFA map display window. As a result, IWEDA cannot insert any map overlays into the stack of overlays shared by other applications. Whether this is done via the current map display software (the Army's Terrain Evaluation Module) or the Joint Mapping Tool Kit (JMTK) will be determined by the availability of the JMTK, and the decision made by the Army on whether or not to use JMTK for the BFA. This functionality will be available in either FY97 or FY98.

Complete ONR IWEDA. This is slated for FY97 and will include the collection of rules specifically for Navy and/or Marine systems and platforms. Tasks related to the rewrite of the ESQL code for Oracle or Sybase and the map display are also likely.

Continue support for Brigade Task Force XXI. Although the actual exercise is not until March of 1997, BED personnel have been heavily involved in the software integration, testing, training, and support since May of 1996.

Division XXI Support. This will be a follow-up to the Brigade Task Force XXI and is scheduled for the fall of 1997. Early indications are that there will be no time off (in terms of BED support) between the Brigade and Division exercises. Division XXI support is expected to continue into early FY98.

Summary

A software application has been developed to transform raw weather data into weather intelligence for the battlespace commander. IWEDA has proven itself to be an extremely valuable tool for users, as indicated by their feedback and demand for the application. Although IWEDA has primarily Army weapon systems in its database, the ONR work and addition of a dynamic rule editor should allow for expanded applicability within the tri-service community. A number of other new capabilities will provide an even more powerful tool for the planning and analysis of weapon systems on the battlefield.

METOC SUPPORT WITHIN COMMAND & CONTROL SYSTEMS: CONTEXT-SENSITIVE METOC DECISION SUPPORT TOOLS

Robert J. Farrell, Jr.
USAF Rome Laboratory
Acquisition Meteorology Office
RL/WE, 26 Electronic Parkway, Rome NY 13441-4514

ABSTRACT:

The concept of context-sensitive METOC decision support tools is described using a specific scenario and a notional mission planning system as a vehicle for demonstration. To better understand the challenges of integrating METOC support into the decision-making process, a simple conceptual framework is first presented. This framework is proving beneficial for hammering out integration details. It categorizes integration into situational awareness, constraint-checking, and context-sensitive decision support tools.

As planners build battle plans, their C^2 systems continually check constraints on what they are trying to accomplish. As the knowledgebase detects problems, the application alerts the planners. Once alerted, they work around the problems using decision support tools at their disposal. Prototypes of possible METOC Decision Support Tools are presented within the flow of the planning process to demonstrate how planners would solve environmental problems.

1. INTRODUCTION:

The goal of Meteorological/ Oceanographic (METOC) support is to inform all levels of command how the natural environment, from the depths of the ocean to the surface of the sun, will impact operations; both ours and our adversaries. Our commanders want the opportunity to exploit the natural environment wherever and whenever they can.

Toward that end, much work is being done in the weather community to enhance anticipation skills and to figure out automated ways of determining impact. The command and control (C^2) community is also working hard to automate the decision-making process, and is making great strides; speed and volume are increasing at an ever accelerating pace. Because of C^2 successes, without true, complete integration, weather support will end up being completely squeezed out of the process. Therefore, the difficult chore of integrating these two efforts lies before us.

The question then, is, "How do we infuse METOC support into the decision-making process?" What products does the METOC support community need to make available and where will these products reside? To be of any value, they MUST be available within the flow of the decision-making process. Hence, the logical step would be to look at the process and determine were in that process METOC support could add value. It is from this analysis that product, modeling, and data requirements should be determined.

This paper presents a METOC integration conceptual framework that has been proving beneficial for getting a handle around the integration details. A mission scenario suggested by USAF Checkmate, the famed Pentagon think-tank, is introduced and a prototype mission planning system is used to demonstrate how METOC support could be part of the decision-making process. This paper does not present an ultimate solution, but suggests a framework for discussion and future development directions.

2. A METOC Integration Conceptual Framework

Incorporating METOC support into C^2 systems has proved to be an overwhelming task. To more easily manage the task, METOC integration requirements can be divided into the following three categories: situational awareness, constraint-checking, and context-sensitive decision support tools. All three are necessary for effective support, but each can be worked on separately.

The most active category, and hence closest to realization, is situational awareness. As it stands currently, the main way commanders and planners are kept apprised of the weather is via stand-up briefings. On a cyclic basis, weather duty officers use weather applications to create slides and then present these slides to explain how the anticipated weather may impact strategies and plans.

Very soon, command centers will have battlefield situational displays that show the situation in real-time, on a continuous basis. It will display terrain, location of friendly and enemy assets, threats, and the weather up on big screens visible to all. Duty officers will be able to look up at a screen to evaluate the current situation as they need it.

Most C^2 systems under development have requirements to overlay weather information directly on their map displays. However, there has not been much progress making this happen. The main obstacle has been the incompatibility of weather products with the Common Mapping Program standards. The next generation mapping standard, the Joint Mapping Toolkit, has substantial requirements to provide functions that will enable C^2 systems to overlay weather information. Duty officers will eventually be able to toggle overlays of "weather" on their situational maps.

Situational awareness is a necessity, but depending only on map representations has a limitation. Decision-makers at the force level are making hundreds to thousands of decisions in short succession. There is just too much going on, too quickly for a human brain to maintain the connection between what is being planned, the hundreds of applicable weather-thresholds, and the anticipated weather. Even if a person could keep up, continually comparing map overlays with intentions is simply too time consuming. Hence, the application will have to maintain the links for them.

As planners define events, the application, in the background, would compare the weather at the time and location of the event with thresholds specific to the event. Thresholds must be a function of things like mission, tactics, aircraft, and weapon system. If the weather is beyond a specific threshold, the application generates an alert and displays it on the planner's screen. As with any other threshold violation like running out of fuel or tasking a sortie to fly faster than capabilities, the duty officer will click on the alert flag to

see what the problem is. When the flag is clicked, a dialogue box will pop up to display the reason or reasons for the alert. They will have the opportunity to either ignore the alert or solve the problem. It is at this point that duty officers need tools available to help get around the problem.

One problem that C^2 system developers must contend with is information overload. It is imperative that users get only the information necessary to solve the specific problem. Hence, it is important that the tools available be sensitive to the context in which they are called upon. All of the information presented must be tailored to the problem at hand. This is the place for true, real-time, on-the-fly METOC support tailoring.

Another important concept to keep in mind is that METOC support is only one of the parameters mission planners have to contend with. Hence, it is necessary to think of METOC support as only part of the decision support toolkit. Consequently, it is better to talk about context-sensitive decision support tools with integrated METOC information.

3. DEMONSTRATION

The best way to describe this concept of context-sensitive decision support tools with integrated METOC information is to propose a scenario, plan a mission to meet the objective, and describe the tools as they pop up. The scenario presented was inspired by a briefing Col Bob Plebanek gave while he was at HQ USAF Checkmate Division (Plebanek, 1996). His strategy-to-task guidelines provided the framework for creating a realistic objective with constraints that would require four of the five components (Air Force, Army, Navy, and Special Forces) and a Combined Force asset (United Kingdom) to work together.

The objective is to supply 10 tanks, 6 helicopters, and a water storage capability to a site prepared by a Special Operation Forces (SOF) unit at a coastal location near the Forward Edge of Battle Area (FEBA). As part of the mission planning challenge, the force-level planners must locate the SOF site, the supplies, and a means to transport them. A constraint levied on the plan is that the supplies must be collected at a naval port and delivered to the SOF unit via cargo ship. A C-130 must bring the water storage system and tanks must transport themselves to the port. The cargo ship will have to be protected from an en route threat with an available U.K. destroyer and attack submarine. Finally, one of the six Apache helicopters must eliminate a shore threat along the way.

Rome Laboratory has been developing a mission planning mockup to describe complicated concepts without having to be bogged down with complicated systems. As with all C^2 systems currently being developed, this mockup is graphics based with pull-down menus, pop-up lists, and hot-buttons to accomplish tasks. The mockup demonstrates how a planner at the force level (Joint Task Force Level) would go about tasking assets to meet objectives and ultimately strategies.

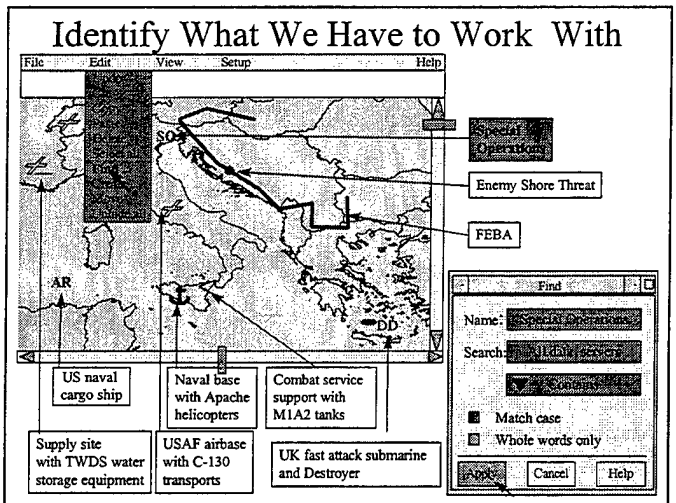


Figure 1: Mission Planning System

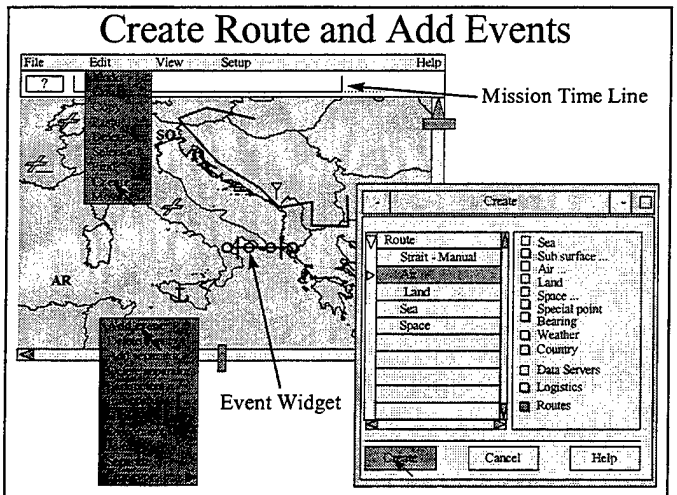


Figure 2: Drag, Drop, and Fill in

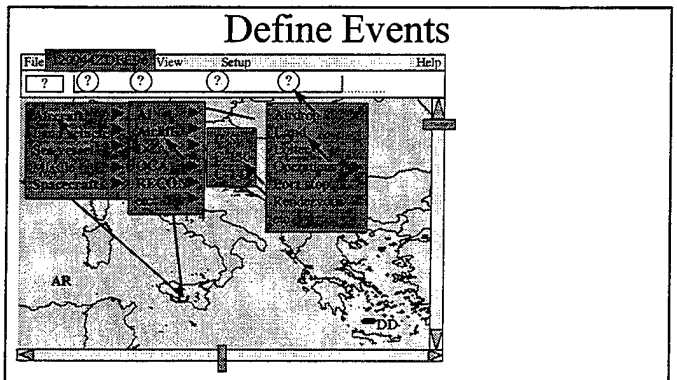


Figure 3: Airlift TWDS

The first step toward building a plan that would meet the defined objective is to search for resources. Clicking on *Edit* then *Find* would bring up tools to search pertinent data servers for the items needed. The results of the searches would be displayed on the map as the items are found (Figure 1).

Clicking on *Create* then *Add Event* would bring up two features: an Event Widget used to graphically anchor event hooks (circles) to map features, and a mission time line used to define the events (Figure 2). A planner would click on the event widget and drag the circles on to the appropriate glyph on the map. For this particular scenario, dragging the widget on to the airlift base glyph would anchor the first circle there. The next step would be to drag the widget to the airfield with the TWDS. The second circle would latch onto that airfield glyph. Continuing, the widget would be anchored to the naval port and then back to the original airfield to complete the circuit.

Clicking on the event place-keepers in the mission timeline would display pop-up menus. Choices offered in these menus would only be those that are available to the planner at the time. For example, in Figure 3, C-5s, C-130s, and C-141s are stationed at the launch airfield but only "C-130" is highlighted as a possible choice. This is because all of the C-141s are tasked and the application knowledgebase determined that C-5s can not land at one of the airfields that was anchored.

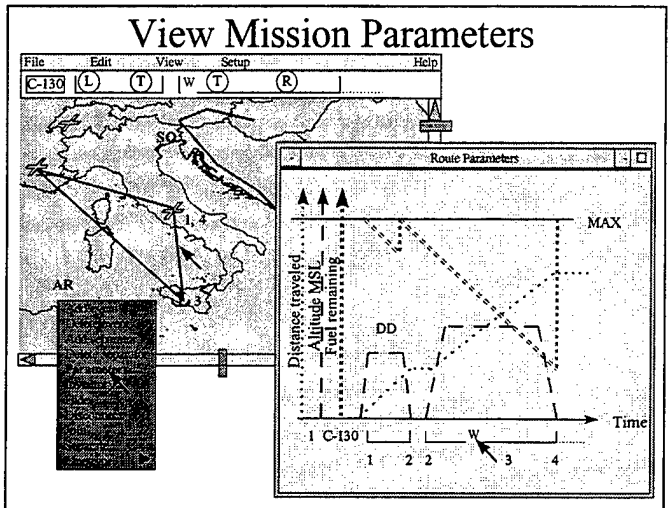


Figure 4: Click Alert Flag

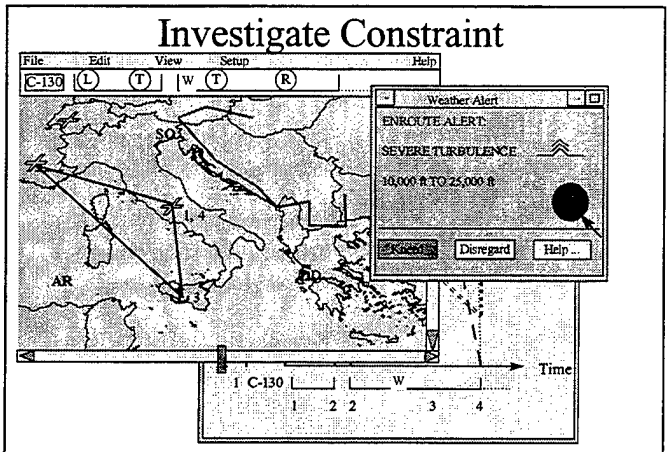


Figure 5: Toggle Weather Overlay

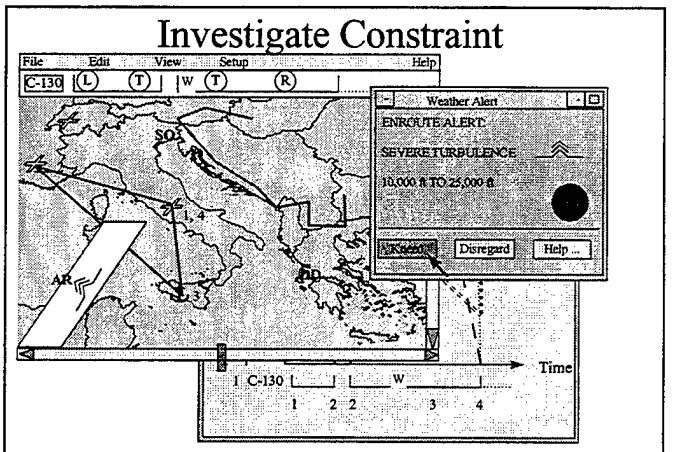


Figure 6: Pull Up Help

Once a mission is defined, clicking on *Parameters...* would bring up a timeline chart showing how important mission-parameters are resolving (Figure 4). Note that as this mission was defined, an alert flag appeared on the mission timeline (and subsequent parameter timeline). In this case, a "W" signifies that weather at the time and location of a critical event is beyond a threshold of that event (as specified in the system's knowledgebase). The application is constantly checking the constraints on what is being accomplished.

Also note, however, that the system doesn't directly intervene and keep the planner from continuing on without the problem being resolved. This feature is a result of user requirements and feedback. Applications must allow planners to ignore warnings and constraint violations. This reasoning is also why the alert is registered as a flag and does not go immediately to an intrusive dialogue box.

In this demonstration, the planner chooses not to ignore the weather problem and clicks on the alert flag. Only then does a dialogue box pop up to explain that there is severe turbulence somewhere en route (Figure 5). Clicking on the map toggle would overlay the area of offending weather on the map (Figure 6). Realize that the turbulence forecast displayed is specifically for a C-130 airframe.

One can argue that having the weather on the map at the beginning of this process would provide situa-

tional awareness and save this step. However there are two barriers to doing it that way. First, users insist that displayed information be kept to a minimum to mitigate clutter. The second, and more poignant, barrier is that until the planner defines the event, weather impact is indeterminable. This is a key consideration when discussing tailoring METOC support for the warfighter; especially outside of the decision-making process. Until the event is defined, there is no way to specify impact.

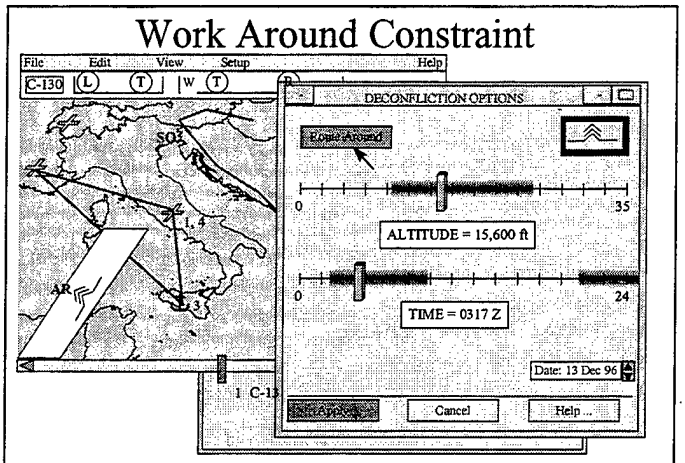


Figure 7: 1-D Tool Example

But once a planner defines a mission and the computer sounds the alert, how do they get around the problem? Clicking on *Kneed* would pull up a tool that would help make a decision to do just that. One important aspect that must be dealt with is that weather is four dimensional (with time the fourth dimension). A map shows two dimensions, but some of the simpler decisions could use a 1-D tool like that shown in Figure 7. The constraints would be highlighted on the scroll line (darker shading) and a planner would move the scroll bars until the flight path is outside of the hazardous space. As shown here, the planner could change altitude, time, or route to solve the problem. Clicking *Apply* would enter the changes into the system and display the results on the map and mission timeline.

Since we have a 2-D screen, perhaps we should strive for 2-D tools as much as possible. An altitude by time chart, as shown in Figure 8, would allow the planner to solve the problem with one click and drag of the cross-hair. A time scroll on either the tool window or the map window would allow the planner to manually animate the hazards to see when the hazard would be out of the way. The two windows would be dynamically linked so that a change made in one would be reflected in the other. For example, moving the cross-hair in the vertical cross-section along the time axis would alter the shape of the area represented on the map.

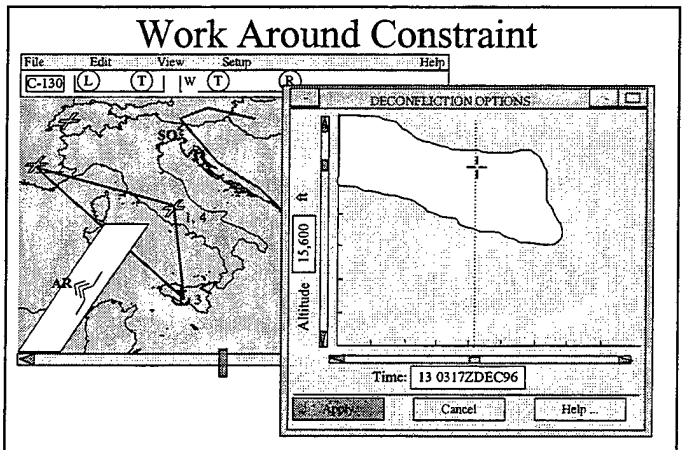


Figure 8: 2-D Tool Example

Perhaps a more expedient, more practical tool would be a 3-D representation of the hazards and a time scroll. NOAA, Environmental Research Laboratories, Forecast Sys-

tems Laboratory, Aviation Division, Aviation Gridded Forecast System Branch is working on 3-D visualizations of aviation hazards. They are using AVS®, from Advanced Visual Systems Inc., as a user-interface for their Aviation Impact Variable (AIV) Editor (AIV, 1996). AIV views hazards in 1, 2 and 3 dimensions.

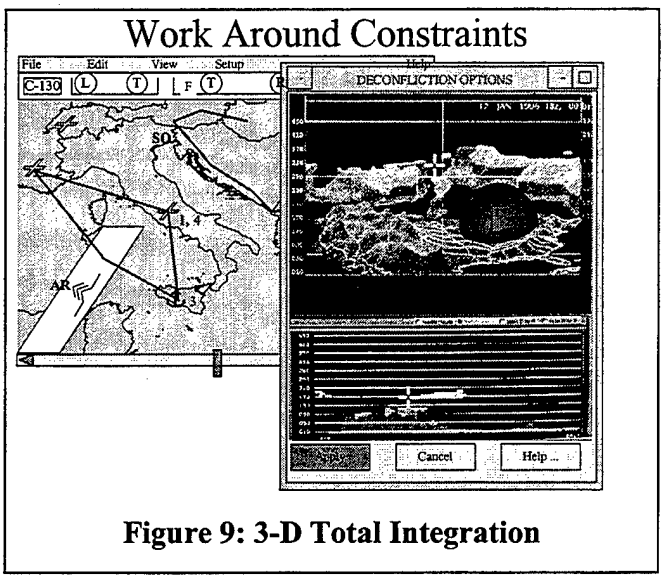


Figure 9: 3-D Total Integration

What must be done to make this product useful to the decision-maker is to incorporate it within the C^2 system (Figure 9). As described previously, all threats must be included in the view; the weather "threats" would be just part of the overall threat environment. As depicted in Figure 9, the planner would see weather hazards along side enemy air defense hazards (bubble). In this window, the planner would click and drag the crosshair to an open area. If necessary, the planner would manipulate orientation toggles to get the best view (Pitch, Yaw, Zoom, and Time). Clicking on *Apply* would change the event widget and mission timeline accordingly.

Note that when the route got longer, a fuel alert appeared. Clicking on this flag would pop up an options list or a decision support tool that would help plan around this problem. Some of the obvious choices are to add extra fuel at the first or second airfield or via an air re-fueling. A not-so-obvious choice would be to find an altitude (and/or time) with more favorable winds. Critical wind factors represented in Figure 9 would then be necessary. Having the application constraint-check altitudes for the most favorable winds on a consistent basis and then prompt for change (or automatically adjust) would be a tremendous force multiplier! Over the course of an operation, fuel savings, both financially and logistically, would be significant. Potentially, one small operation could pay for the total weather integration effort.

Fast forward through the planning process to the next to last scenario task: destroying the shore threat. As with the airlift process, a planner would click on *Create* then *Add Event* to bring up an Event Widget and a Mission Timeline, and then

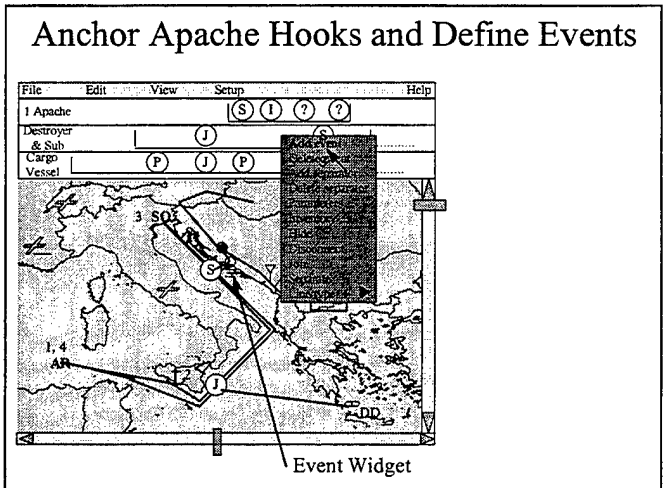


Figure 10: Drag, Drop, and Fill In

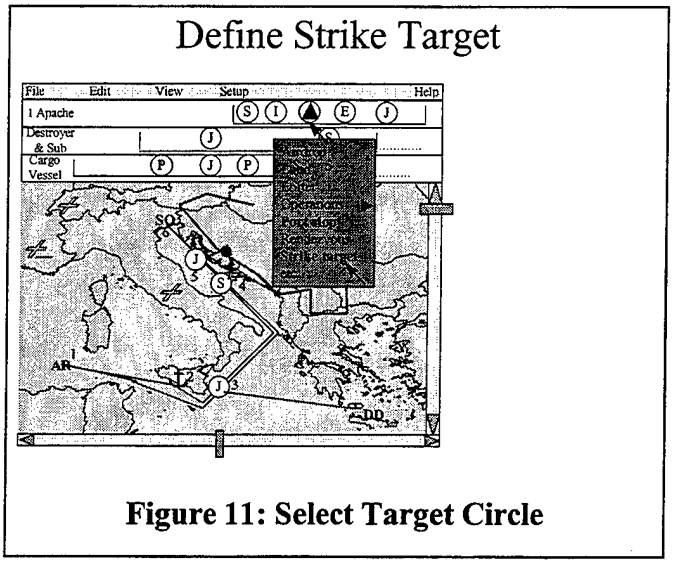


Figure 11: Select Target Circle

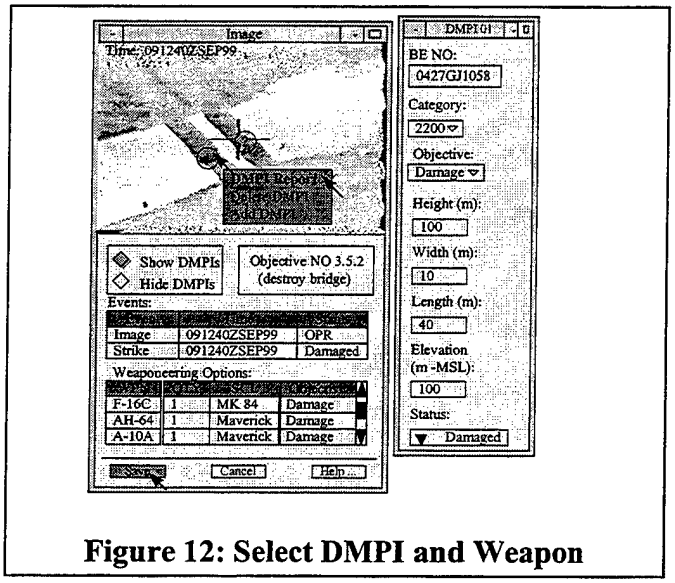


Figure 12: Select DMPI and Weapon

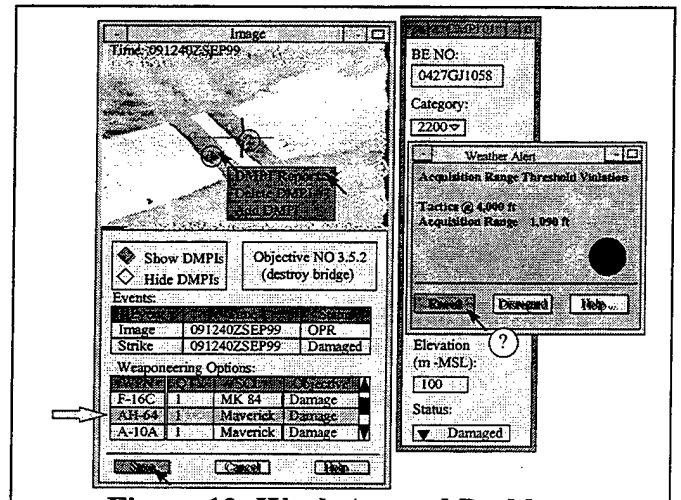


Figure 13: Work Around Problem

drag, drop, and fill to build an Apache mission (Figure 10).

The planner must also build the details of the strike against the target. Simply by clicking on the event circle and selecting *Strike Target* from the pop-up menu (Figure 11), the planner can pull up a target/ weaponeering tool (Figure 12).

The tool represented in Figure 12 integrates target intelligence into the decision-making process. Notice that the planner has target imagery, target details, and weaponeering information only a click away. The tool would allow planners to query the target database to garner the information they need to optimize the plan. Ultimately, they are looking for optimum attack directions, time over target, air deconfliction with other missions, weapon choice, and threat mitigation or elimination requirements.

When a planner enters enough detail (e.g., times, locations, weapon type, etc.) for the application to determine constraints, alert-flags and highlighted-options would appear. Eventually the planner will run into problems that require resolution. This, again, is where context-sensitive decision support tools come into play.

As depicted in Figure 13, selecting target points, weapon, and time over target triggers a threshold violation. When a planner clicks on *Kneed,* a window with an appropriate decision support tool would pop up. What will it look like?

4. The Future

Answering questions like this one will help the weather community determine productive research paths to follow and help the C^2 community integrate METOC support in places and ways that enhance the decision-making process. These answers will also, collectively, answer the bigger question, "How do we infuse METOC support into the decision-making process?" The overall strategy is to break the effort into three categories of integration: situational awareness, constraint-checking, and context-sensitive decision support tools.

First, warfighters need to be aware of the situation. Situational awareness displays are an important feature of all command centers. Once the planning process starts, planners need help making sure that what they are building is doable. Hence, computer constraint-checking, in the background, on a non-interference basis, alerting by exception, is a necessity. Indeed, constraint-checking is an integral part of modern C^2 strategies. However, what the warfighter does once the application sounds an alert that a threshold has been violated has not been adequately addressed.

The obvious step is to provide the warfighter with interactive windows displaying all of the necessary information tailored to the problem at hand; all integrated within the planning process. In other words, they need context-sensitive decision support tools. To be of any use, these tools must contain information fused from ALL functions (e.g., intelligence, weather, logistics, tactics, and command guidance).

The USAF C^2 development program, Theater Battle Management Core Systems (TBMCS) and specifically the Force Level Execution System (FLEX), are looking to incorporate these ideas. The requirements have been established. However, priorities for the System Program Office are such that there are currently minimal, if any, resources available to tackle METOC support integration problems.

It would be extremely helpful if Rome Laboratory could provide the contractors with a collection of functions, models, datasets, etc. that they could quickly incorporate into their systems. The Acquisition Meteorology Office envisions a METOC Toolkit not unlike the Joint Mapping Toolkit currently under development. Like Rome Laboratory's Common Mapping Program, the Joint Mapping Toolkit will be a library of compatible functions that a programmer can simply match parameters and drop into the code. The Electro-Optical Systems Atmospheric Effects Library (EOSAEL), the Master Environmental Library (MEL), and other cataloguing efforts currently underway will help considerably, but none of them yet provide the plug-and-play capability that contractors require and a toolkit would provide.

As of the publishing of this paper, contractors are not being given the resources to figure out METOC support integration on their own. If METOC support is to remain a viable contributor to the ever accelerating decision-making process, we must, as a community, either find the funds to beef up contractor resources, or develop the answers ourselves and provide them with standardized plug-and-play functions.

Acknowledgments. I am indebted to 1Lt Gregory M. Smith, USAF Rome Laboratory, Command & Control Directorate, Advanced Concepts Branch (RL/C3AA) for letting me help him develop his notional mission-planning system and allowing me to use it for this paper. I also wish to thank Captain Robert J. Carroll, Jr. (ACC/DOWR) for his insightful advice and review of this paper.

5. REFERENCES

AIV: Aviation Impact Variable Editor User's Guide, NOAA, Environmental Research Laboratories, Forecast Systems Laboratory, Aviation Division, Boulder CO, and National Weather Service, National Centers for Environmental Prediction, Aviation Weather Center, Kansas City, MO, Version 3.0, February 14, 1996.

Christensen, Charlotte W., and Jonathan D. Turton: "Co-Operation On Meteorological Tactical Decision Aids Within NATO," In *Proceedings Battlespace Atmospheric Conference 96*, NRaD, San Diego, CA 92152, (in press), 1997.

EOSAEL: Electro-Optical Systems Atmospheric Effects Library, www.eosael.com, as of 10 January 1997.

MEL: Master Environmental Library, www-mel.nrlmry.navy.mil, as of 10 January 1997.

Piwowar, Thomas M., John Burgeson, Paul Try, Donald Grantham, Sam Brand, and Alan Wetmore: *Natural Environmental Effects In Military Models and Simulations: Part I - A Survey of Requirements*, PL-TR-96-2029, Phillips Laboratory, Directorate of Geophysics, AFMC, Hanscom AFB MA, 01731-3010, 259 pp., 1996.

Plebanek, Robert, Col USAF: "JFACC Planning Process to Support Integrated Airpower Employment", *Defensive Planning Module Technical Interchange Meeting*, Alphatech Inc., Burlington, MA, 29 May 1996.

SOLAR-REFLECTED RADIATION FROM THE SEA SURFACE

Dr. Robert E. Turner
Science Applications International Corporation
550 Camino El Estero, Suite 205
Monterey, CA 93940

Dr. Andreas K. Goroch
Naval Research Laboratory Monterey
7 Grace Hopper Avenue
Monterey, CA 93943-5506

ABSTRACT

For investigations in aircraft remote sensing and in the description of tactical decision aids for military operations it is usually assumed that solar radiation is of little significance in the thermal infrared portion of the electromagnetic spectrum. For many situations in atmospheric radiation models this is true because the Earth's surface consists of materials with diffuse or nearly diffuse reflectance properties. This is certainly not true, however, for water bodies as the surface is then specular or nearly specular, depending upon wind conditions. As a result, the ocean can reflect a large amount of radiation into an infrared sensor, thereby greatly reducing the effectiveness of that system. In this paper we present the results of computations of the directly-reflected solar radiation from a smooth ocean surface in terms of sun angle, atmospheric optical thickness, and wavelength. The importance of the solar effect is clearly indicated in various plots. As a result of this work it is clear that one can no longer neglect the effect of direct solar radiation in the thermal infrared part of the spectrum, especially for atmospheric radiation models which use infrared sensors in ocean operations.

1. INTRODUCTION

The extraterrestrial solar irradiance has a peak value in the visible part of the spectrum between 0.46 and 0.48 μm wavelength with only about 0.4 % of the solar radiation lying in the region beyond 5 μm. On the other hand, a 20° C blackbody has a peak near 10 μm. It is interesting to compare the solar irradiance at the Earth's surface (with no atmospheric attenuation) and the irradiance of the blackbody at this wavelength. Thus,

Solar irradiance (5770 K) = 0.2858 Watts m^{-2} μm^{-1}
Blackbody irradiance (20° C) = 28 Watts m^{-2} μm^{-1}

It is apparent that the irradiance from the blackbody is about 100 times the solar value for a thermal infrared wavelength of 10 μm. The radiances (~ irradiances/solid angle), however, are totally different, i.e.,

Solar radiance = 4205 Watts m^{-2} sr^{-1} μm^{-1}
Blackbody radiance = 9 Watts m^{-2} sr^{-1} μm^{-1}

with a very large solar value as a result of the small solid angle of the Sun. It is primarily for this reason that the radiation reflected from a nearly specular surface such as the ocean is so important in the thermal infrared part of the spectrum.

2. RADIOMETRIC QUANTITIES

The radiance reflected from a surface with bistatic reflectivity $r(\hat{\Omega},\hat{\Omega}')$ is given by

$$L(\hat{\Omega}) = \int_{2\pi} r(\hat{\Omega},\hat{\Omega}') L_{in}(\hat{\Omega}') d\hat{\Omega}' \tag{1}$$

for any arbitrary input radiation field integrated over the upper hemisphere. The "total" radiance from a general surface with a unidirectional solar input is given by

$$L(\hat{\Omega}) = E_0 r(\hat{\Omega},\hat{\Omega}_0) T + \int_{2\pi} r(\hat{\Omega},\hat{\Omega}') L_{sky}(\hat{\Omega}') d\hat{\Omega}' + \varepsilon_{eff}(\hat{\Omega}) B \tag{2}$$

where E_0 is the extraterrestrial solar irradiance at the top of Earth's atmosphere, T is the transmittance through the atmosphere and B is the thermal radiance from a surface with an effective emissivity $\varepsilon_{eff}(\hat{\Omega})$. The second term in equation (2) is the contribution due to the integrated sky radiation. The corresponding radiance from a specular surface with a finite solid angle for the Sun is

$$L(\hat{\Omega}) = \frac{E_0 T \rho_F(\hat{\Omega}_0)}{\Omega_0} + \rho_F(\hat{\Omega}_0) L_{sky}(\hat{\Omega}_0) + \varepsilon(\hat{\Omega}_0) B \tag{3}$$

in the direction of the Sun with a Fresnel reflectance of $\rho_F(\hat{\Omega})$. Thus, in the limit, as a rough surface approaches a smooth surface the bistatic reflectivity becomes the Fresnel reflectance multiplied by the Dirac delta function for a unidirectional source. In this equation the emissivity is equal to one minus the Fresnel reflectance, whereas the effective emissivity in equation 2 is <u>not</u> equal to the one minus the bistatic reflectivity. Therefore, the solar radiances for a "point" Sun and for the actual Sun with a finite solid angle are given by

$$L_{Sun}(\hat{\Omega}) = E_0 \delta(\hat{\Omega} - \hat{\Omega}_0) \qquad \text{Infinite for a "point" Sun} \tag{4}$$

$$L_{Sun}(\hat{\Omega}) = \frac{E_0}{\Omega_{eff}} = 4205 \text{ Watts } m^{-2} \text{ } sr^{-1} \text{ } \mu m^{-1} \qquad \text{Actual Sun} \tag{5}$$

where the numerical value for the finite Sun is for a wavelength of 10 μm with an effective photospheric temperature of 5770 K.

3. BISTATIC REFLECTANCE MODEL

The model for the sea surface that will be used is one developed by Yoshimori et al. [1,2,3,4] in a series of papers produced in recent years to characterize the wave structure of a wind-roughened water surface. A critical parameter in their model is the slope variance of the water waves, defined as

$$\gamma^2 = \int_0^\infty \Psi(\omega)[k(\omega)]^2 d\omega \tag{6}$$

where $\Psi(\omega)$ is the so-called Joint North Sea Wave Project (JONSWAP) spectrum for water waves as described by Hasselmann et al. [5]. The quantity $k(\omega)$ is the wave propagation constant which is related to the angular frequency by the dispersion relation

$$\omega(k) = \left[\left(\frac{g}{k} + \frac{\Gamma k}{\rho}\right)\tanh(hk)\right]^{1/2} k \tag{7}$$

where g(= 9.80665 m s^{-2}) is the acceleration due to gravity, Γ (=0.07353 N m^{-1}) is the surface tension, ρ(= 1024.75 kg m^{-3}) is the water density, and h(= 100 m) is the water depth. In addition, we will assume a water salinity of 35 parts per thousand and a surface water temperature of 20° Celsius. The JONSWAP spectrum is depicted in Fig.1 for three wind speeds

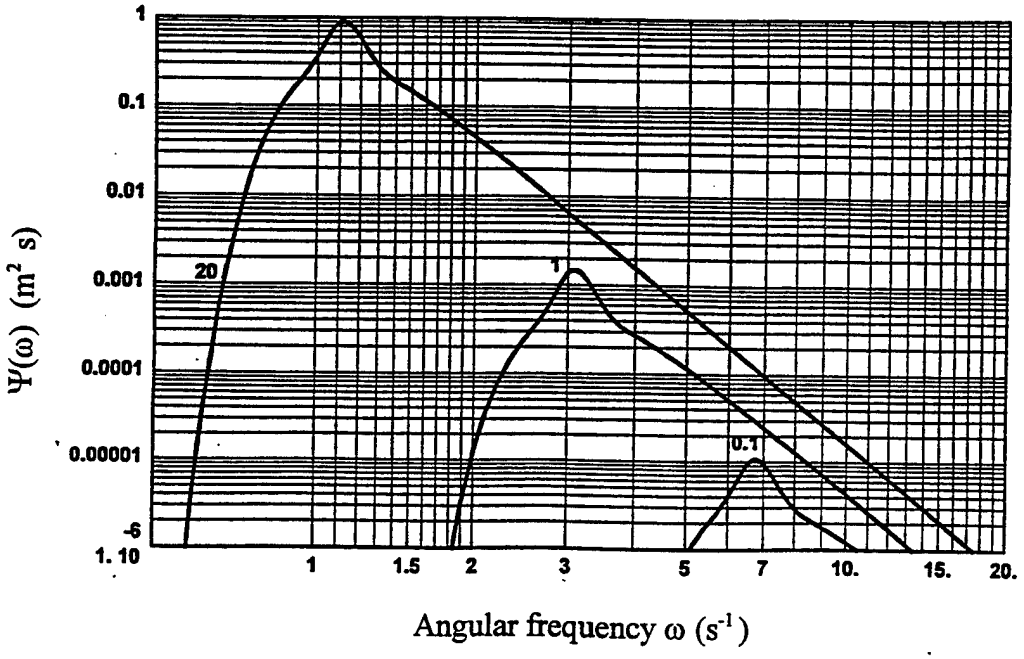


Fig. 1. JONSWAP spectrum for various wave speeds (m s^{-1}) for a fetch of 40 km.

and for a fetch (range for which the wind blows uniformly over the surface) of 40 kilometers. Likewise, Fig. 2 illustrates the dependence of the square root of the slope variance (γ) on the wind speed. It should be noted that this quantity is very sensitive to the wind speed for low values between zero and ~ 1 meter per second.

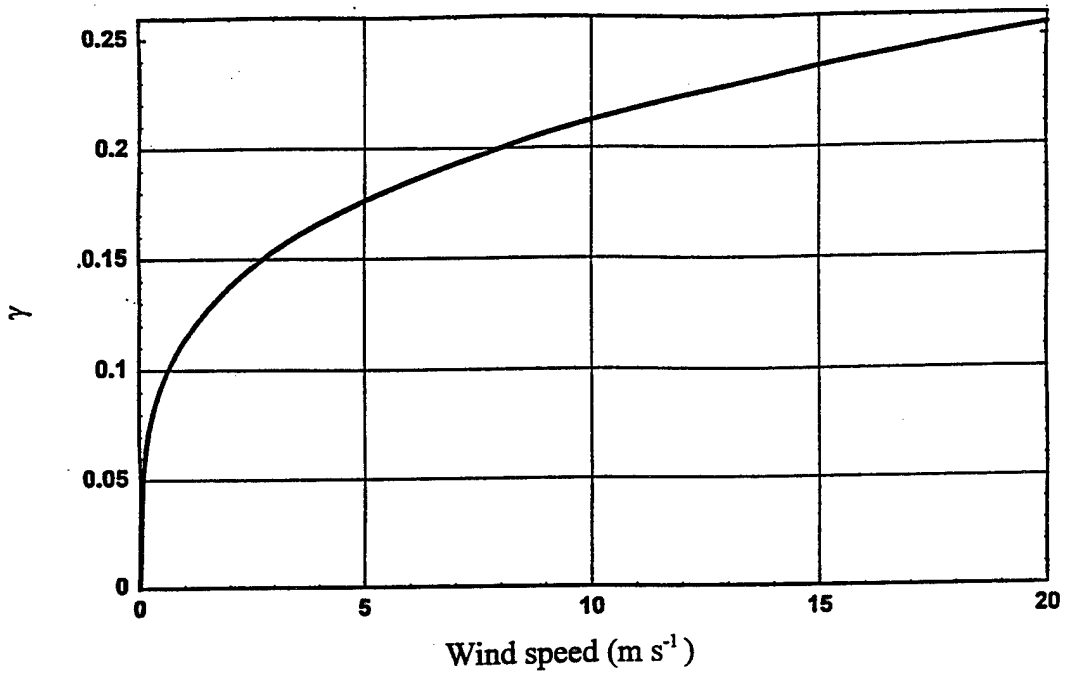


Fig. 2. Square root of the wave slope variance vs. wind speed (m s^{-1}).

Using Gaussian distributions for the wave slopes in both the x and y directions on a horizontal surface, Yoshimori et al. [4] developed a closed-form expression for the bistatic reflectivity of the water surface for a point source of radiation. On the other hand, Zeisse [6] developed a formulation to account for a finite solid angle source. We have used these formulas to compute the bistatic reflectivity for water at a wavelength of 10 μm with a complex index of refraction of 1.210 - 0.055 i for the particular case when the solar zenith angle is equal to the nadir view angle of 85 degrees. The results are illustrated in Fig. 3. The agreement is excellent for wind speeds from 20 m s^{-1} down to about 0.1 m s^{-1} but as the wind speed decreases to zero there is a discrepancy as the "delta-function" approximation increases without bound. The exact value for a wind speed of zero is known for the "finite Sun" case however, since it is the Fresnel reflectance divided by the solid angle of the Sun, i.e.,

$$r(\hat{\Omega},\hat{\Omega}_0) = \rho_F(\hat{\Omega}_0)/\Omega_0 \;=\; 7707 \text{ sr}^{-1} \qquad \text{Finite Sun} \qquad (8)$$

The exact calculation was performed down to a wind speed of 0.01 m s^{-1} but computations for lower wind speeds were discontinued because of the excessive computer time required. Nevertheless, the plot does clearly show that the delta-function, closed-form method of Yoshimori et al. [4] is valid throughout a broad range of wind speeds.

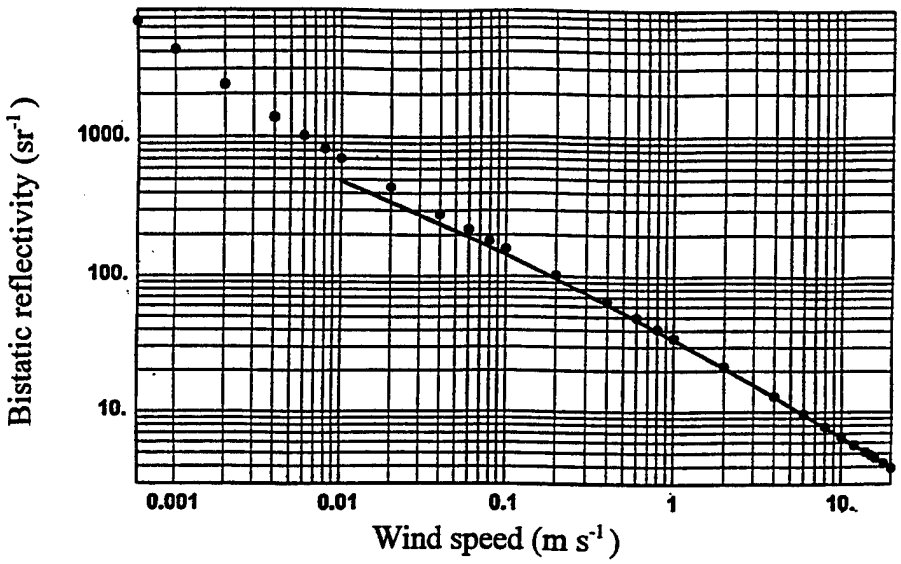


Fig. 3. Comparison between the delta-function method of Yoshimori et al. (points) and the exact formula (solid line) for the bistatic reflectivity. Solar zenith angle is equal to the nadir view angle = 85°.

4. RADIATION COMPUTATIONS

In a manner similar to that for the bistatic reflectivity, Yoshimori et al. [4] also developed a formulation for the effective emissivity of a water surface by integrating the Fresnel reflectance over the distribution of wave slopes. Because emissivity only depends upon the outgoing direction the formulation is not as complicated as for the bistatic reflectivity. Multiplying the effective emissivity by the Planck radiance for a blackbody at a temperature of 20° C allows us to compute the thermal radiance from the water surface. It is depicted in Fig. 4 as a function of the wind speed for the large nadir view angle region from 70° to 90°. As the viewer looks straight down at the surface the radiance is about 8 Watts m^{-2} sr^{-1} μm^{-1} but for large nadir angles there is significant departure in terms of the wind speed. It should be noted that the viewer is assumed to be at or near the surface so that atmospheric attenuation can be neglected.

The more interesting situation is for the bistatic reflectivity as a function of the incident Sun angle and the wind speed, U expressed in m s^{-1}. Figure 5 illustrates the variation of the sum of the reflected radiance and the emitted radiance in terms of wind speed for a large nadir view angle of 89°. In all cases the extraterrestrial solar irradiance is 0.2858 Watts m^{-2} μm^{-1} and the attenuation of the incoming solar radiation has been computed using the computer program MODTRAN 3 [7]. We have chosen the U. S. Standard atmosphere with the Navy maritime model and an air-mass parameter of 5 which means that the observer is somewhere between the coast and the open sea. One can see that the radiance is not much greater than the "background" value of the emitted radiance for these wind speeds, but if we use lower wind speeds such as those in Fig. 6, the total radiance is considerable greater than the emitted radiance. We can also examine the radiance as a function of the nadir view angle and wind speed. Calculations were made for various Sun angles and the largest effect seems to be for a solar zenith angle of 83°.

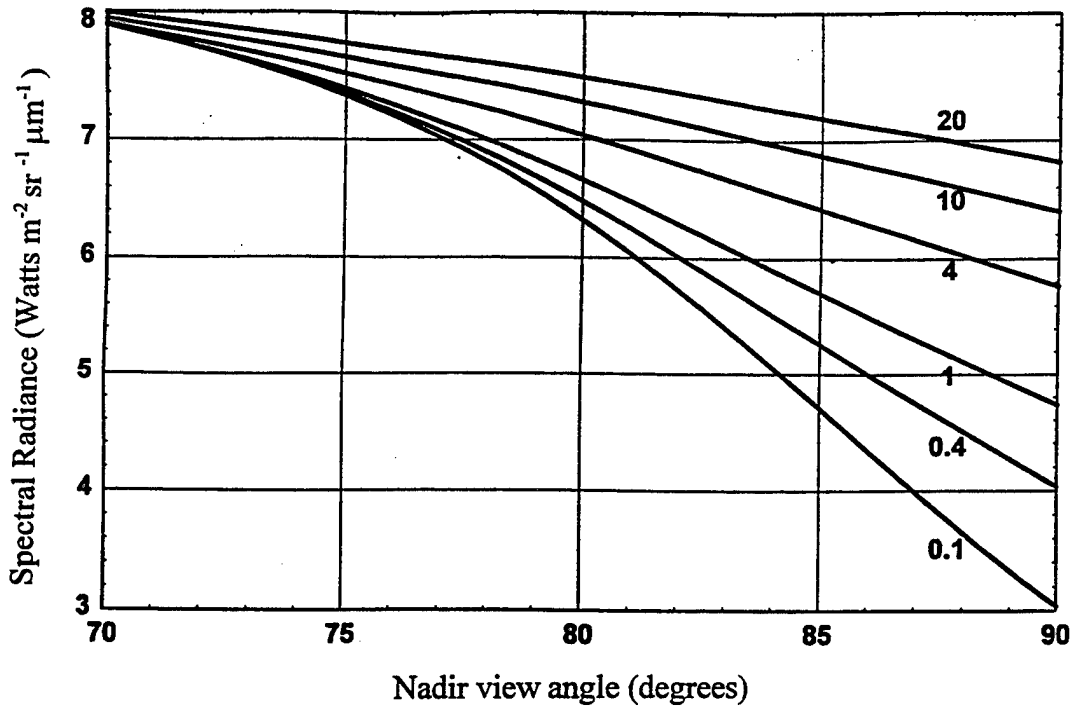


Fig. 4. Thermal spectral radiance vs. nadir view angle for water waves with various wind speeds (m s^{-1}).

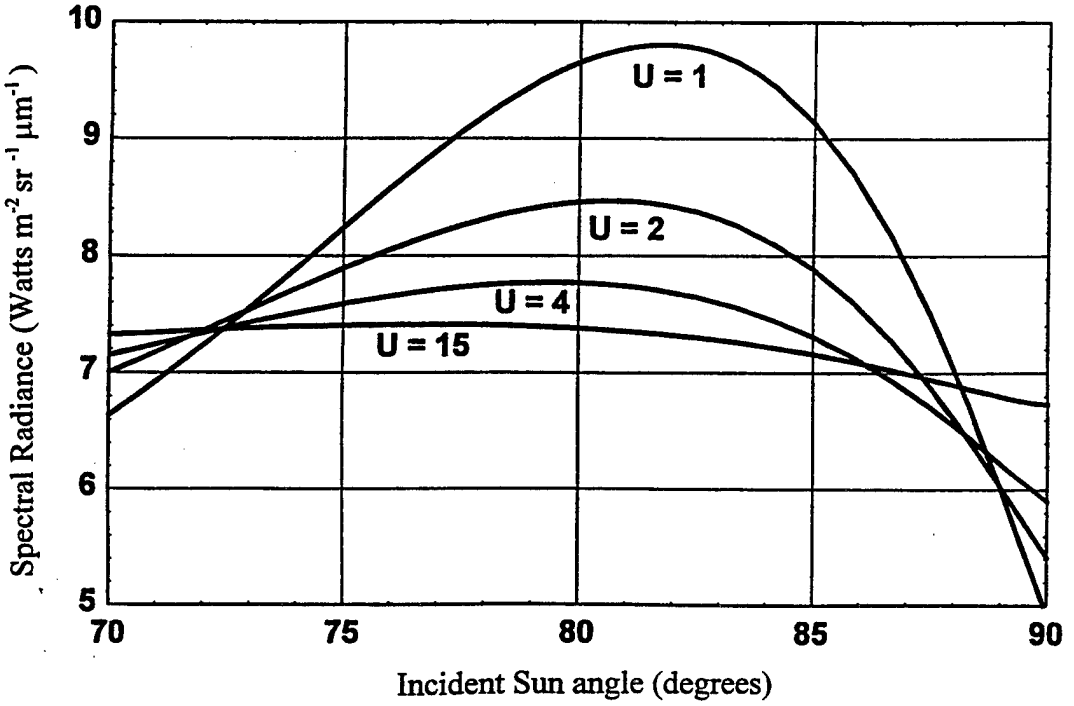


Fig. 5. Total spectral radiance vs. solar zenith angle for water waves with various high wind speeds (m s^{-1}) and a nadir view angle of 89° with the atmospheric attenuation computed according to the program MODTRAN 3.

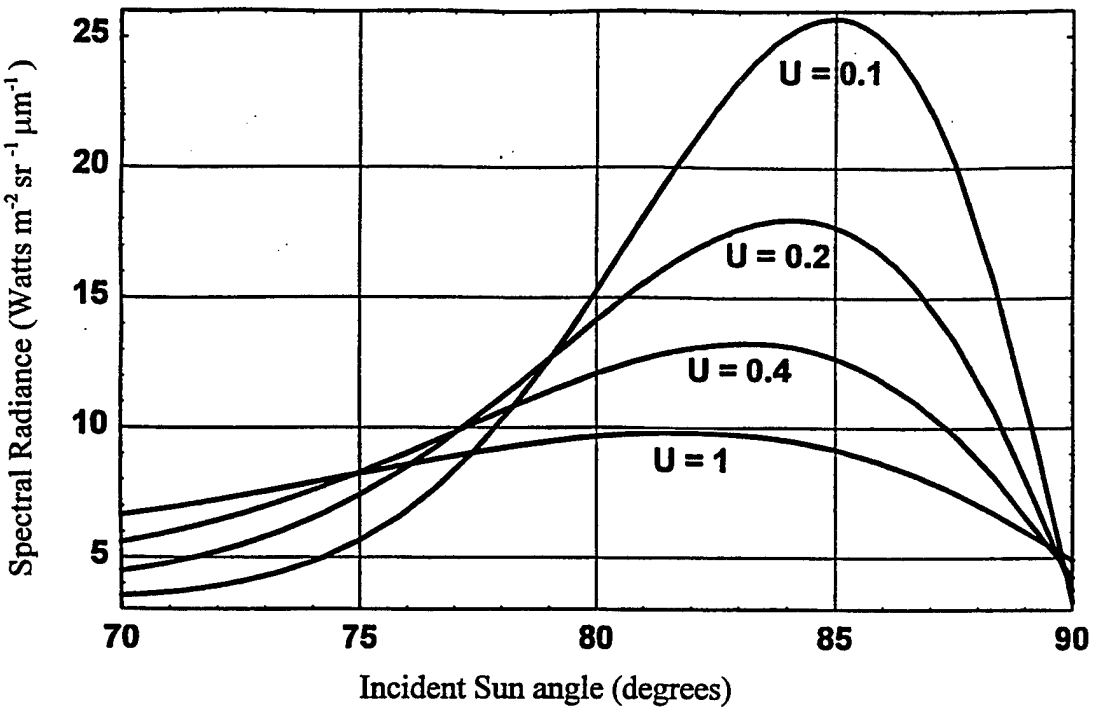


Fig. 6. Total spectral radiance vs. solar zenith angle for water waves with various low wind speeds (m s^{-1}) and a nadir view angle of 89° with the atmospheric attenuation computed according to the program MODTRAN 3.

The variation is illustrated in Fig. 7 for four wind speeds where it is important to realize that the total radiance here is much greater than the thermal background for wind speeds below about 0.2 m s^{-1}. The most important feature to be noticed, however, is the variation in the radiance from the surface facets in terms of the nadir view angle. Figure 8 depicts this interesting result of the total radiance for four facet slopes. The curves here are those for the reflected and emitted radiance for Fresnel reflectors taking into consideration the atmospheric attenuation, which accounts for the sharp decrease on the right side of each curve. The radiance values can be at least forty times greater than the thermal background values, a fact that is not always understood for the infrared part of the spectrum.

The radiation components can also be calculated explicitly in terms of the wind speed for various nadir view angles and solar zenith angles. Fig. 9 illustrates the variability in the thermal radiance with wind speed for three nadir view angles. For these large angles the thermal radiation is quite small for low wind speeds because the surface is nearly specular whereas this is not true for the rough surface generated by the high wind speeds. In Fig. 10 the total radiance is illustrated as a function of the wind speed from 1 m s^{-1} to 20 m s^{-1} for the same three angles. Below one m s^{-1} all radiances increase up to the Fresnel limit for zero wind speed but as the wind speed increases the radiance decreases to a minimum value because of the increasing surface roughness. Eventually, however, the total radiance increases again because of the thermal background.

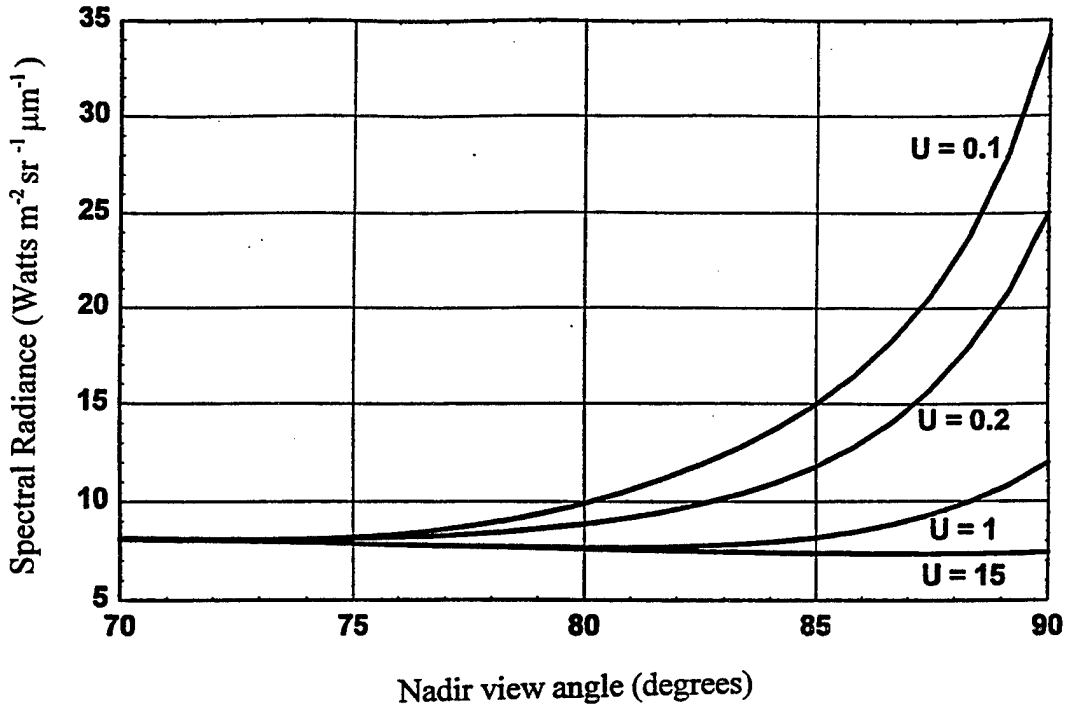


Fig. 7. Spectral radiance vs. nadir view angle for water waves with various wind speeds (m s^{-1}) and a solar zenith angle of 83°.

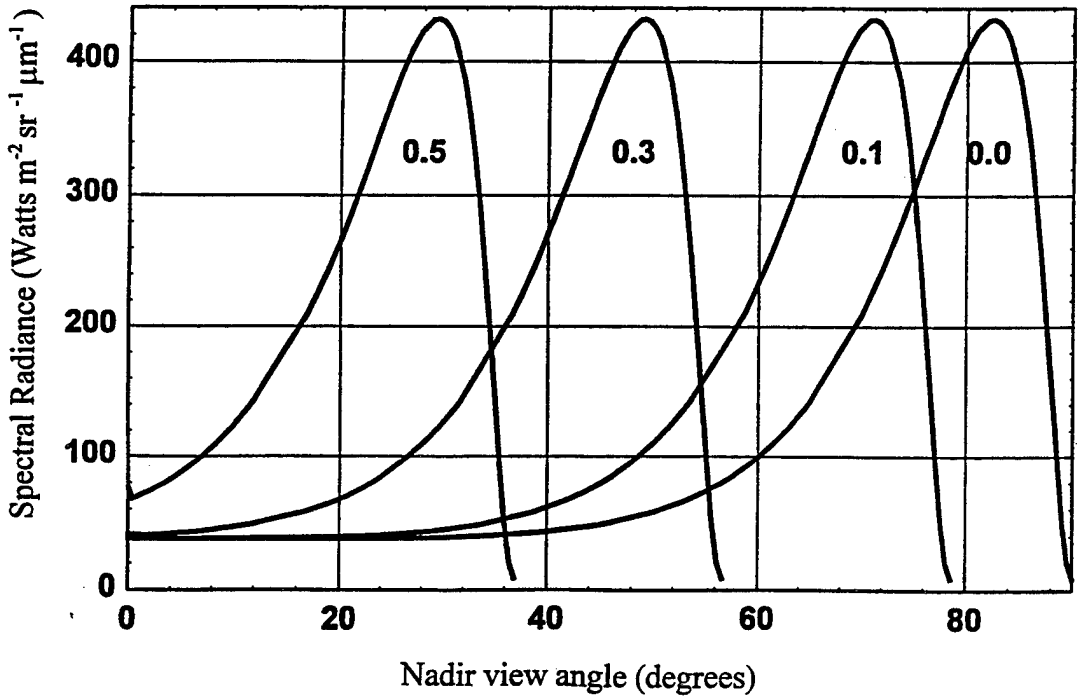


Fig. 8. Spectral radiance vs. nadir view angle for water waves with various instantaneous slopes.

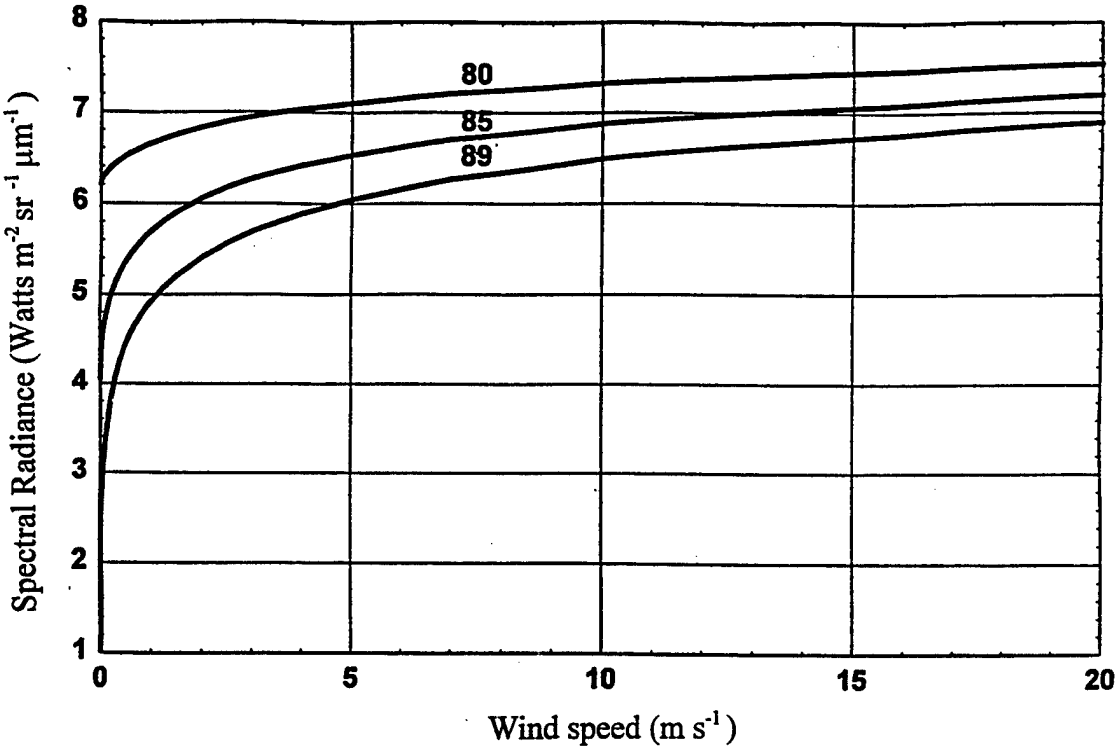


Fig. 9. Thermal spectral radiance vs. wind speed for water waves for three nadir view angles (degrees).

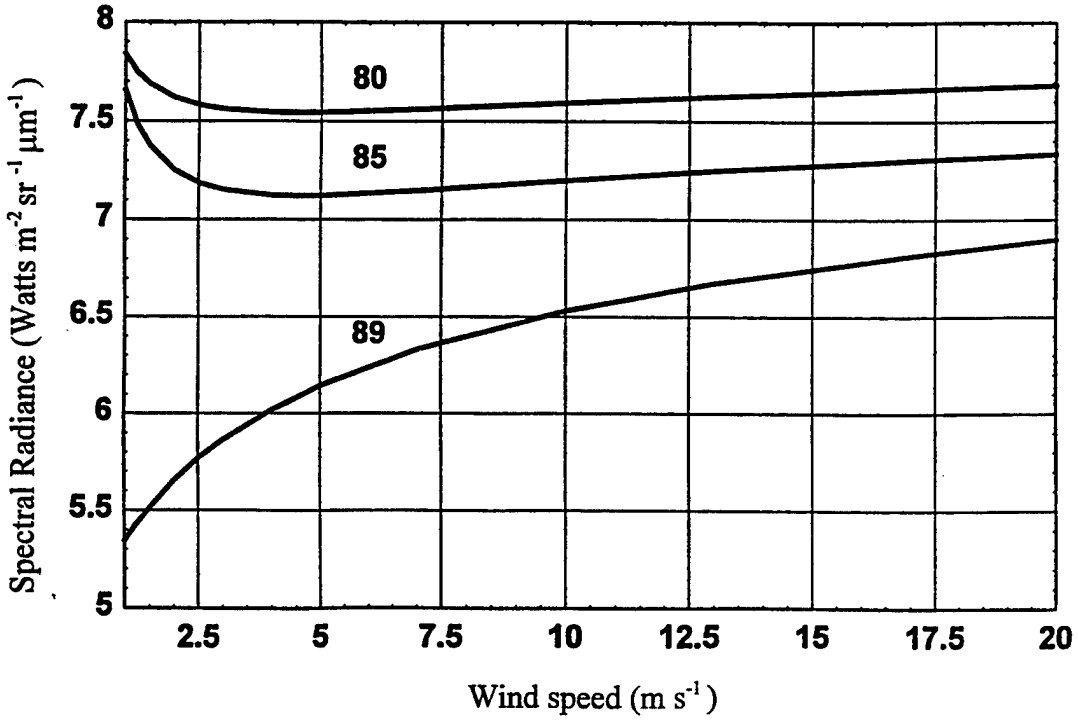


Fig. 10. Total spectral radiance vs. wind speed for water waves for three solar zenith angles (= nadir view angles) with the atmospheric attenuation computed according to the program MODTRAN 3.

5. CONCLUSIONS

It has clearly been demonstrated that the average solar-reflected radiance from a water surface in the thermal infrared part of the spectrum (~ 10 μm) can, under certain circumstances, be quite large, in a manner not unlike the similar well-known result in the visible part of the spectrum. The effect is especially significant for low wind speeds and for large nadir view angles. In addition, the infrared speckle pattern should be quite noticeable as can be seen from the large instantaneous reflected radiances from the individual facets with slopes from zero to 0.5. The hemispherical sky radiance has not been included in the present calculations but it has been estimated to be relatively small. Nevertheless, for completeness it should be included in the calculations although it is dependent upon the particular atmospheric model. Also, it would be instructive to calculate these effects for other wavelengths, fetch lengths, and atmospheres.

REFERENCES

1. K. Yoshimori, K. Itoh, and Y. Ichioka, "Statistical formulation for an inhomogeneous random water surface: a basis for optical remote sensing of oceans," J. Opt. Soc. Am. A, Vol. 11, No. 2, 723-730 (1994).

2. K. Yoshimori, K. Itoh, and Y. Ichioka, " Thermal radiative and reflective characteristics of a wind-roughened water surface," J. Opt. Soc. Am. A, Vol. 11, No. 6, 1886-1893 (1994).

3. K. Yoshimori, K. Itoh, and Y. Ichioka, "Statistically corrected ocean thermography," Applied Optics, Vol. 33, No. 30, 7078-7087, (1994).

4. K. Yoshimori, K. Itoh, and Y. Ichioka, "Optical characteristics of a wind-roughened water surface: a two-dimensional theory," Applied Optics, Vol. 34, No. 27, 6236-6247, (1995).

5. K. Hasselmann, T. P. Barnett, E. Bouws, H. Carlson, D. E. Cartwright, K. Enke, J. A. Ewing, H. Gienapp, D. E. Hasselmann, P. Kruseman, A. Meerburg, P. Muller, D. J. Olbers, K. Richter, W. Sell, and H. Walden, *Measurements of Wind-Wave Growth and Swell Decay during the Joint North Sea Wave Project (JONSWAP),* (Deutsches Hydrographisches Institut, Hamburg, Germany, 1973).

6. C. R. Zeisse, "Radiance of the ocean horizon," J. Opt. Soc. Am. A, Vol. 12, No. 9, 2022-2030, (1995).

7. MODTRAN 3, A Moderate Resolution Model of LOWTRAN 7, A. Berk, L. S. Bernstein, and D. C. Robertson, Spectral Sciences, Inc., Burlington, Final Report, GL-TR-889-0122, 30 April 1989.

RADIO PROPAGATION OVER TERRAIN

Herbert Hitney*, Amalia Barrios, Wayne Patterson
NCCOSC RDTE DIV D883
49170 PROPAGATION PATH
SAN DIEGO CA 92152-7385
Ph: 619-553-1428
Fax: 619-553-1417
E-mail: herb@nosc.mil

ABSTRACT

A completely new propagation assessment system called Radio Propagation Over Terrain (RPOT) is presented. This system is designed for PC platforms using the Windows 95 operating system. The internal propagation model is a combination of the Terrain Parabolic Equation Model (TPEM) and the Radio Physical Optics (RPO) model, which allows for range-dependent refractivity variations over terrain or sea paths.

RPOT computes and displays radar probability of detection and/or Electronic Support Measure (ESM) vulnerability or communications capability versus range, height, and bearing from the source. Refractivity data can be entered using several methods, including a fully automated decoding of common World Meteorological Organization (WMO) codes already available on many local area networks. For each bearing, terrain elevation data are automatically extracted from the National Imaging and Mapping Agency (NIMA, formerly the Defense Mapping Agency, DMA) Digital Terrain Elevation Data (DTED), supplied on CD-ROMs. Coverage diagrams are computed and stored as graphics files for each bearing desired, and then displayed in rapid sequence as either full 360 degree rotations or as sector scans.

Both RPO and TPEM have been developed in parallel at NCCOSC RDTE DIV (NRaD) and until recently have remained as two completely separate models. RPO is an efficient ray-optics and parabolic equation (PE) hybrid model for all over-water paths. TPEM began as a pure PE model for terrain paths, but recent versions also employ hybrid models. An effort to consolidate RPO and TPEM into one single model that includes the capabilities of both will be described. The combined model computes propagation loss versus height and range for range-dependent refractivity over smooth and variable terrain, also accounting for variable antenna patterns and range-varying dielectric properties of the ground.

The power of RPOT derives from its user interface as well as the modern high-fidelity propagation models. RPOT is a Windows 95 application, making full use of drop-down menus, on-line help, and other standard Windows features to make a fully integrated and user friendly propagation assessment system.

BACKGROUND

The Office of Naval Research maintains a book titled "Technologies for Rapid Response" that lists technologies under current development that could be accelerated into operational

capabilities in 6 to 12 months, provided there was a strong operational need for them. In 1995 our group submitted one such technology description to this book with the title "Radar Propagation Over Terrain" (RPOT) based on the Terrain Parabolic Equation Model (TPEM) that was under development at NRaD. The following is an excerpt from that description. "This capability provides the ability to assess shipboard radar coverage over water, across coastlines, and over varying terrain in range-dependent refractive environments. Required inputs include digital terrain elevation data, refractive structure, and radar parameters. Output would be radar detection probability contours in a vertical cross-section versus azimuth, taking first-order effects of terrain into account." In late 1995 the Commander, Sixth Fleet staff expressed a serious interest in developing the RPOT capability to support Sixth Fleet ships and aircraft operating in the Adriatic in support of the Bosnia peace mission. At the same time a new ONR program called the Naval Technology Insertion Program (NTIP) was preparing to fund some of the technologies listed in the book. In early FY96 the final decision was made to fund the RPOT effort under the NTIP program with the goal of providing the final system to Sixth Fleet forces by June 1996.

In early FY96 TPEM was already developed to the point that radar coverage diagrams could be produced based on terrain data read from the DTED Level 1 CD-ROMs (horizontal resolution of 3 arc seconds, about 100 m), and EM system and refractivity data read from special format ASCII files. TPEM at this time was a 32-bit DOS application developed with Microsoft Fortran Powerstation Version 1.0. Several other DOS programs had also been developed to support TPEM, for example to rapidly display a series of coverage diagrams versus bearing angle. Using these programs directly for operational support was deemed too impractical because of the time and training required for the operators to edit ASCII input files and use the programs in the proper sequence. A more user-friendly windows based user interface was required, and Microsoft Windows-95 and Fortran Powerstation 4.0 were selected as the host operating system and program development environment. The goal was to repackage TPEM into a user-friendly system that would use normal pull down menus and other Windows features, and to provide an easy interface to user-defined radar parameter libraries, DTED CD-ROMs, and existing meteorological data.

The Windows-95 RPOT assessment system was developed on schedule and delivered to the Sixth Fleet Flagship USS La Salle in June 1996. By this time, the Commander, Naval Meteorology and Oceanography Command (CNMOC) had asked the Space and Naval Warfare Systems Command (PMW-185) to make RPOT available fleet wide by August 1996. By August, a capability to assess radio communications coverage had been added to RPOT, and the name was changed slightly to Radio Propagation Over Terrain to better describe this addition. RPOT is now available fleet wide.

ASSESSMENT SYSTEM

This paper describes RPOT version 3.01. The minimum hardware requirements for RPOT are Windows-95 and a CD-ROM drive. In addition, we recommend a 100 MHz Pentium processor or better, at least 16 MB of RAM, a hard disk drive with at least one GB of free space, and an 800 by 600 resolution monitor. The RPOT software is distributed on either one CD-ROM, five high density 3.5 inch floppy disks, or via the internet. RPOT and all of its support files require

about 8 MB of space on the PC's hard drive. Additional disk space is required to store the DTED files and graphics format files generated by RPOT for each bearing desired, plus other files generated for each project.

The user interface to RPOT is via pull-down menus and dialogue boxes that are similar to most Windows-95 applications. A project is defined as one or more vertical coverage diagrams for a radar or communications transmitter located at one geographic location. To generate a project, the user first fills in a project window to specify the radar, platform (such as a ship class), target, environment, latitude, longitude, initial bearing, bearing increment, and number of bearings desired, plus a few options to select the type of display, type of terrain area map, and propagation model desired. After entering all the required data in the project window, the user clicks on the "compute" button to begin all computations. The DTED manager first checks to see if all the required DTED files are already stored on the hard disk. If not, the user is provided with a list of required DTED CD-ROMs and is prompted to insert each one. After all of these files are loaded, the DTED manager will generate the terrain height profile along each bearing desired and TPEM or RPO will generate the corresponding coverage diagram. On a 100 MHz Pentium, TPEM will require about 15 seconds to a few minutes to compute a single coverage diagram, depending on frequency.

By default the propagation model automatically selects between RPO and TPEM. RPO is used for paths that are entirely over water if the transmitter or radar height is less than 100 m. TPEM is used for all other cases. However, the use of either TPEM or RPO exclusively may also be selected.

The DTED files are normally transferred from one or more CD-ROMs to the hard drive prior to their use by TPEM for two reasons. First, a hard disk drive has a much faster data transfer rate than the typical CD-ROM drive. Since most projects require multiple runs by TPEM from the same fixed location for multiple bearings, the same DTED files are typically accessed many times, and therefore the total file access time is reduced compared to reading the files always from a CD-ROM. Second, for projects that require 2, 3, or 4 DTED CD-ROMs due to the project's location near one or more boundaries between CD-ROMs, there is no need to load the same CD-ROMs over and over as RPOT generates the various coverage diagrams. However, for projects where all of the required terrain data are stored on one CD-ROM and the user does not have sufficient hard disk space, there is a provision where the terrain data can be read directly from the CD-ROM.

ENVIRONMENTAL INPUTS

RPOT provides several options for entering refractivity data. For many applications, the most useful method is to input the WMO significant level upper air radiosonde code (part UUBB or UUTT), which is widely available on many local area networks and in some cases available on the internet. RPOT can read an ASCII text file containing this code or use the windows clipboard feature to cut and paste the ASCII text from another windows application. RPOT can then automatically decode this text and create an environment file containing the modified refractivity versus height profile which is ready for use by the RPOT propagation models. If the sounding

comes from a ship station, then by default an evaporation duct profile is appended to the radiosonde profile based on the assumption of a thermally neutral atmosphere, where the sea water temperature is assumed to be equal to the air temperature at the lowest measurement height. If this option is not desired by the user, it may be turned off.

The user may also enter the refractivity profile, either as M or N units versus height in feet or meters, or in the form of pressure, temperature, and humidity. All commonly used units are provided for in this case.

RPOT also has a limited capability to accept range-dependent refractivity profiles. The propagation models are completely capable of using range-dependent refractivity, but RPOT has no method to change the environment from one azimuth to the next. Hence, one range-dependent environment can be defined that may be representative over a limited number of bearings, such as in a particular threat direction. This range-dependent environment must be created by the user with a text editor following a number of rules in combining profiles at different ranges. These rules are contained in the on-line RPOT help file.

PROPAGATION MODELS

The RPO propagation model is version 1.15 which is a fully accredited model in the Oceanographic and Atmospheric Master Library (OAML) maintained by CNMOC. RPO is a true hybrid method that uses the complimentary strengths of both Ray Optics (RO) and Parabolic Equation (PE) techniques to account for range-dependent vertical refractivity profiles. The RO techniques include full amplitude and integrated optical path length effects from refraction. The PE technique follows the method described by Dockery [1]. A brief description of the RPO models, and some comparisons to other models, are given by Hitney [2] and a complete description of the RPO model is given by Patterson and Hitney [3]. Two features of the PE model are real-valued sine Fast Fourier Transforms (FFTs) and variable transform sizes up to a maximum of only 1024 points. In comparisons of RPO to pure split-step PE models for stressful cases that are typical of those required for the Tactical Environmental Support System (TESS), RPO has proven to be from 25 to 100 times faster than the PE model alone, with overall accuracy at least as good as the pure PE models. In addition, RPO can solve problems for very high elevation angles, that PE methods alone cannot solve. RPO version 1.15 also includes models to account for tropospheric scatter and oxygen and water vapor absorption, but these parts of the model are not used in RPOT.

The TPEM propagation model is version 1.5, which is a pure split-step PE propagation model capable of accounting for terrain and range-dependent refractivity effects. This model is not yet accredited in OAML, but it is in the process of being included. The model and its use are described by Barrios [4-6]. This model uses the discrete mixed Fourier transform method developed by Dockery and Kuttler [7] which allows for rigorous modeling of vertical polarization and finite conductivity. The model uses a numerical shortcut known as the "boundary shift" method to substantially reduce computation times. Although the model allows conductivity to vary with range, RPOT has no way to provide this information to the model. Since TPEM is a pure PE model, there is no limitation on source height, except as determined by the maximum transform size, which allows for assessments of airborne systems up to the maximum altitude permitted by the frequency and transform size. For UHF Airborne

Early Warning (AEW) radars, such as used on the E-2 aircraft, TPEM will typically allow assessments to be made at operational altitudes. For X-band radars, there will be significant height restrictions. TPEM only performs calculations below a predetermined maximum elevation angle that depends on source height and maximum output height and range. TPEM version 1.5 does not include either a troposcatter or an absorption model for oxygen and water vapor, but these capabilities are considered second or third order effects for most applications.

SAMPLE PRODUCTS

This section presents a selection of sample RPOT products to illustrate the various display options. These samples are all located in the Adriatic Sea and focus on paths toward and over Bosnia. In operation, RPOT displays coverage diagrams for a series of azimuths in a rapid sequence to form either sector scans or full rotational displays, which give very effective three dimensional assessments of coverage, but in this paper we can show only one azimuth at a time.

Figure 1 is a coverage diagram for a typical two-dimensional shipboard radar versus a small jet aircraft target. The colors (shades of gray in the figure) represent radar single-scan probability of detection (Pd) of the target. In this case, a strong surface based duct was assumed, which is evident in the diagram from the downward deflection of the region of high Pd just beyond the first several terrain features. Masking by the higher terrain features just beyond 50 nmi is clearly shown, as are the interference effects from the direct and sea-reflected paths. The white region at high angles is the region beyond the maximum elevation angle cut off for TPEM. The circular area map in the lower right corner is included to give the user a visual reference to the particular azimuth being displayed, which is indicated in the area map as a white line. Figure 2 is a coverage diagram for the same radar as figure 1, but here both radar detection and Electronic Support Measure (ESM) receiver counter detection are displayed together. Note the penetration by diffraction into the shadow region beyond the highest terrain features that allows an ESM receiver to detect the radar. Figure 3 illustrates the use of RPOT in assessing airborne radar coverage for a typical UHF AEW radar stationed at 18 thousand feet. This example assumed a strong elevated duct at 15 thousand feet, and the radar "hole" formed by this duct for ranges beyond 60 nmi is obvious in the figure. Figure 4 is a coverage diagram of ship-to-air UHF communications, and is displayed with just two colors representing the regions where communications is and is not possible. The conditions are the same as those for figure 1. Figure 5 is a refractive conditions summary that shows refractivity and modified refractivity in N and M units plotted versus height, and also indicates the heights corresponding to ducts. This display also indicates by color (not evident in the figure) what the refractive gradient is in each segment of the profile, and lists a numerical summary of the height of any ducts. This display is most useful to the operator in getting a quick look at the refractive conditions before generating any coverage diagrams.

COMBINED PROPAGATION MODEL

In developing RPOT it became clear that a new propagation model that combines the features of RPO and TPEM is needed. Such a model would eliminate the need to test for and switch between the two existing models, and also would fill in the high elevation angle region that

is currently beyond the capability of TPEM. We intend to call this new model the Advanced Propagation Model (APM) as a logical extension of the Standard Propagation Model that has long been included in OAML and was the propagation model used by the Integrated Refractive Effects Prediction System (IREPS). APM will be a hybrid RO and PE model similar to RPO in overall structure. It will account for terrain effects and range-dependent refractivity using the discrete Fourier transform split-step PE model from TPEM. Unlike RPO, it will not be restricted to source heights below 100 m and when fully developed it will include a tropospheric scatter model and oxygen and water vapor absorption model. We expect APM to be the propagation model used in the Advanced Refractive Effects Prediction System (AREPS), an application being developed for the Tactical Environmental Support System (Next Century) - TESS(NC).

SUMMARY

RPOT is a quick response development effort to support a Sixth Fleet specific requirement. In addition it provides a framework for the development of follow on assessment systems and propagation models. It provides a fleet wide assessment capability using modern high-fidelity propagation models that include terrain and refractive effects in a user friendly windows based environment.

REFERENCES

[1] G. Daniel Dockery in "Modeling Electromagnetic Wave Propagation in the Troposphere Using the Parabolic Equation," IEEE Trans. on Antennas & Propagation, vol. 36, no. 10, October 1988.

[2] H.V. Hitney, "Hybrid Ray Optics and Parabolic Equation Methods for Radar Propagation Modeling," IEE Conference Publication 365, Brighton, UK, 12-13 October 1992.

[3] W.L. Patterson and H.V. Hitney, "Radio Physical Optics CSCI Software Documents," NCCOSC RDTE DIV Technical Document 2403, December 1992.

[4] A.E. Barrios, "A Terrain Parabolic Equation Model for Propagation in the Troposphere," IEEE Trans. On Antennas & Propagation, vol. 42, no. 1, January 1994.

[5] A.E. Barrios, "Terrain and Refractivity Effects on Non-Optical Paths," *AGARD Conference Proceedings 543, Multiple Mechanism Propagation Paths (MMPPs): Their Characterization and Influence on System Design (pp. 10-1 to 10-9),* October 1993.

[6] Barrios, "Terrain Parabolic Equation Model (TPEM) Version 1.5 User's Manual," NCCOSC RDTE Div. Technical Document 2898, February 1996.

[7] G.D. Dockery and J.R. Kuttler, "An Improved Impedance Boundary Algorithm for Fourier Split-Step Solutions of the Parabolic Wave Equation," IEEE Trans. On Antennas & Propagation, vol. 44, no. 12, December 1996.

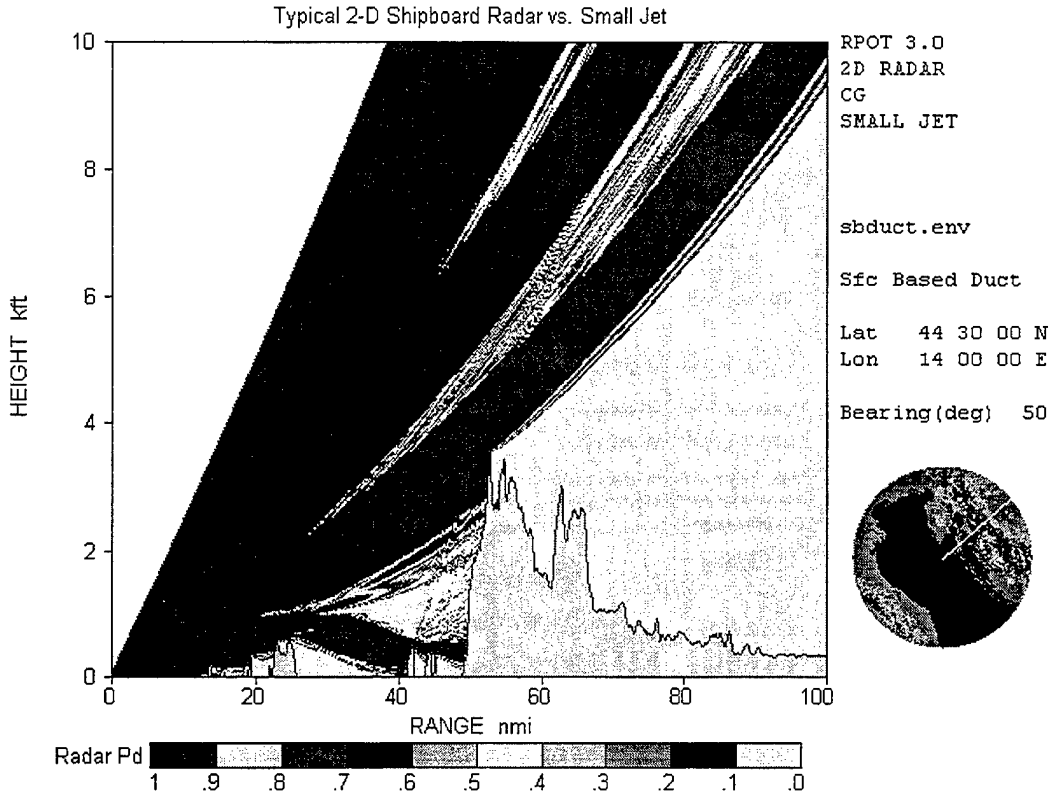


Figure 1. Coverage diagram for a shipboard radar versus a small jet aircraft.

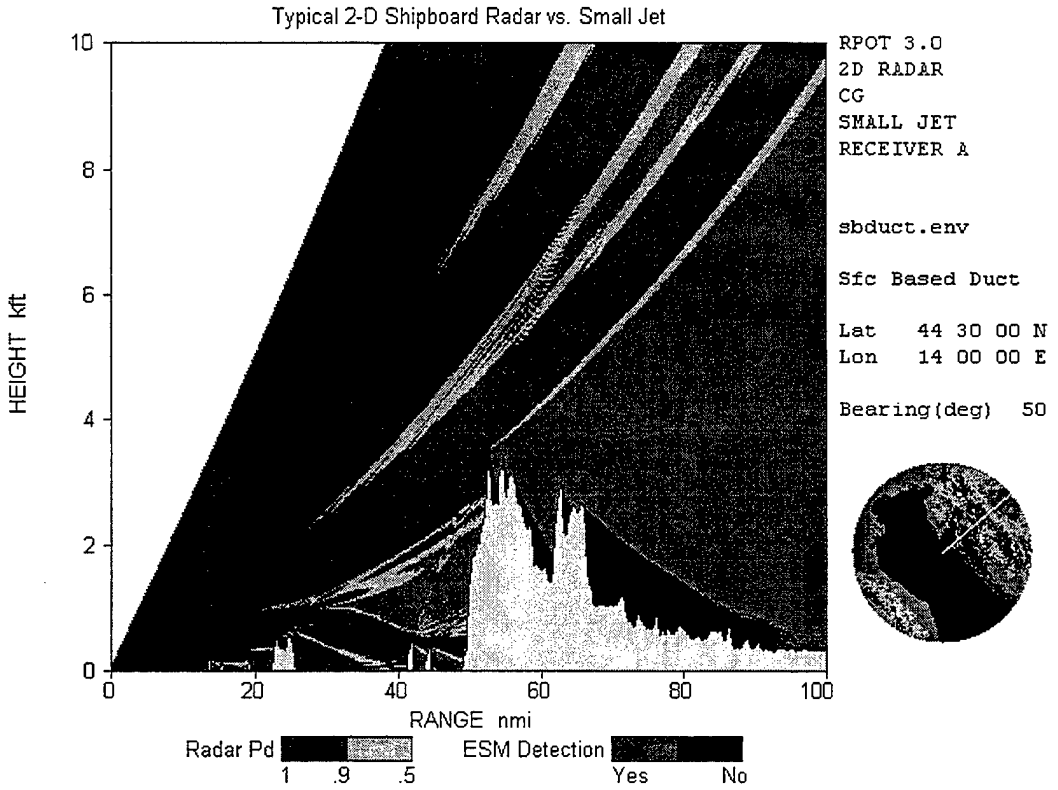


Figure 2. Coverage diagram showing both radar detection and ESM vulnerability.

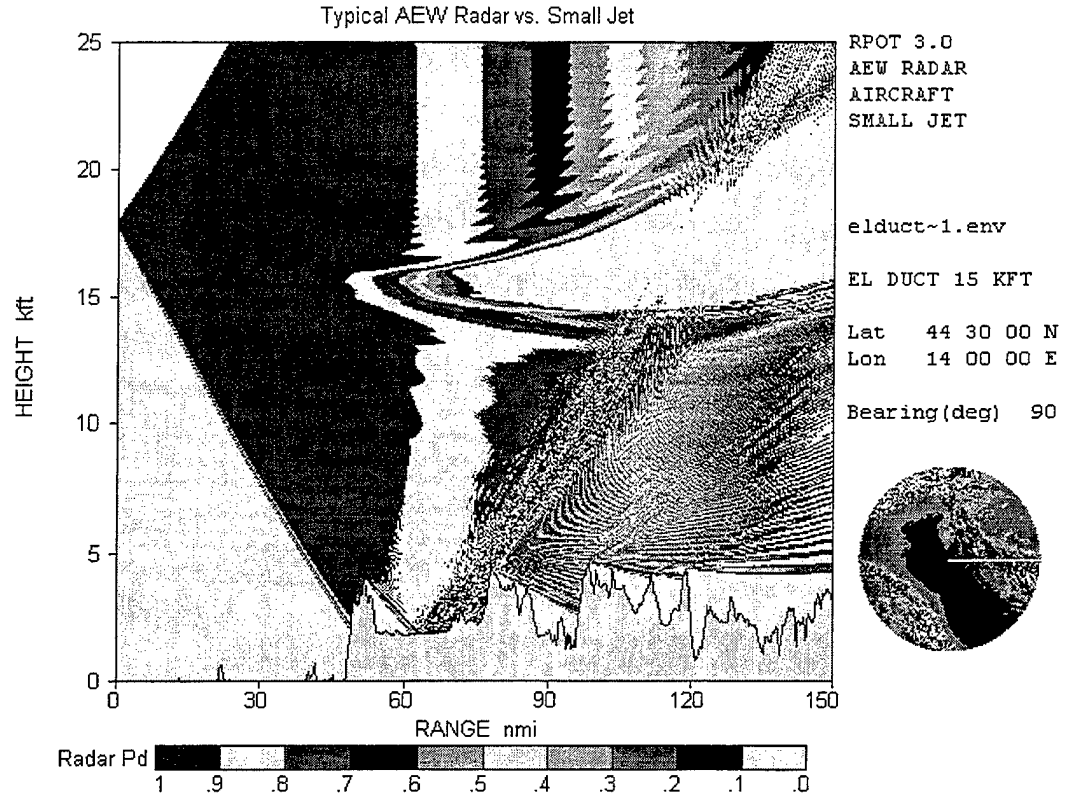


Figure 3. Coverage diagram for an airborne radar.

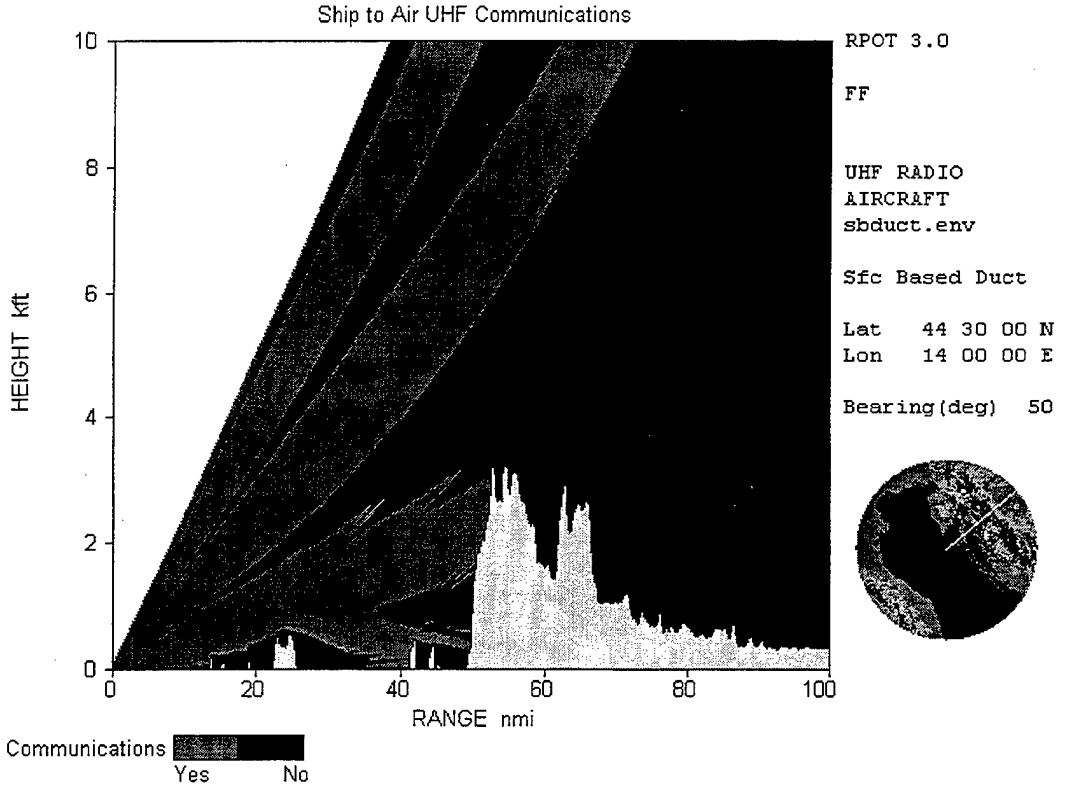


Figure 4. Coverage diagram for UHF communications.

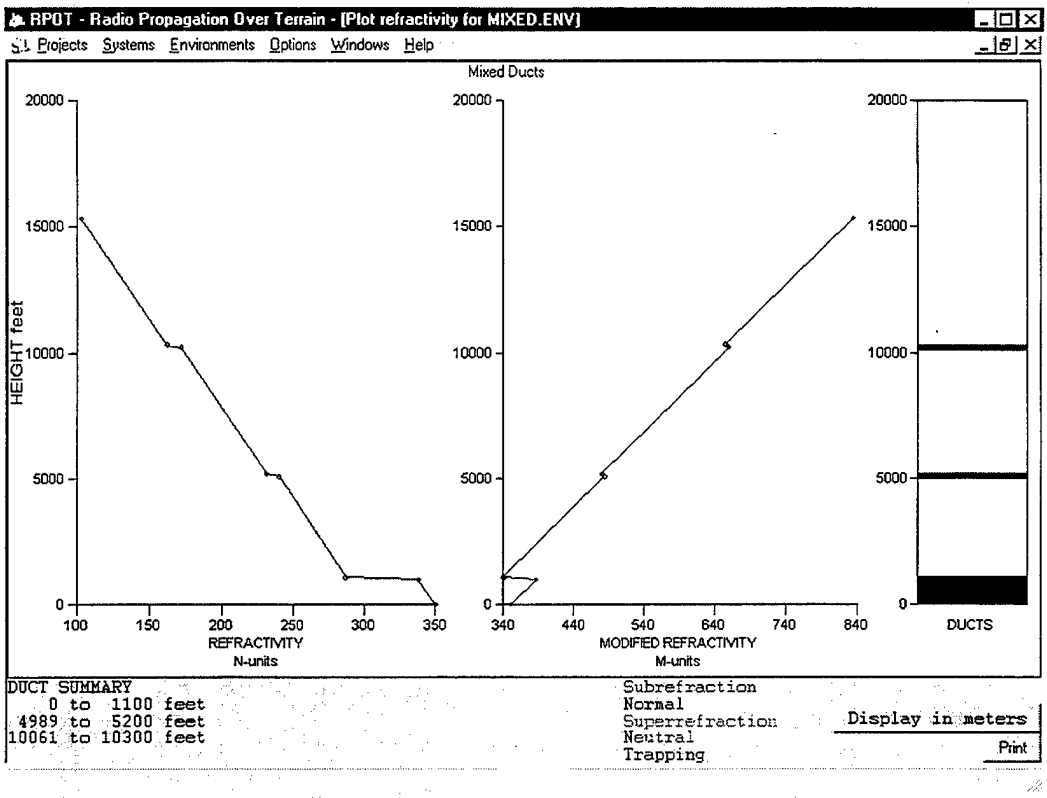


Figure 5. Refractive summary display.

DIRECT STOCHASTIC TREATMENT OF ELECTROMAGNETIC PROPAGATION PROBLEMS IN A RANDOM RANGE-DEPENDENT MEDIUM, USING A PE MODEL

E. MANDINE (1) (2), M.C. PELISSIER (2)

(1) : DCN CTSN/LSA - BP 28 - 83800 TOULON NAVAL (FRANCE)
email : mandine@isitv.univ-tln.fr

(2) : Universite de Toulon - Laboratoire Modelisation et Signal/ETMA/MNC
BP 56 - 83162 La Valette du Var Cedex (FRANCE)
email : mcpel@isitv.univ-tln.fr

1. Introduction

The atmospheric turbulence is known to have significant effects on radiowave propagation ; they are mainly characterized by scintillations in the wavefront. It is particularly true for frequencies over 10 GHz, inside the boundary layer where the turbulence intensity is stronger than in free atmosphere, and in the presence of a duct, at observation points where destructive interference from multipaths can yield a null in the coherent field.

A standard way to describe the refractive index fluctuations due to turbulent eddies consists in adding to the mean refractive profile a random component n_1, assumed to depend upon the sole vertical coordinate :

$$n(r,s) = \langle n_0(r) \rangle + n_1(r,s) \ , \quad s : \text{range}, \quad r : \text{altitude} \tag{1}$$

Since the turbulent motions of the atmospheric cells are highly chaotic, and eddy size can range from 1 mm to one hundred meters, a deterministic description of n_1 is not possible. So we classically characterize the turbulent medium through its statistical properties, for instance the correlation function or the density power spectrum. The electromagnetic field in a turbulent medium is consequently known by its statistics too : mainly, first and second order moment or mean electromagnetic field and mean intensity.

In this work, we present a direct computation of the statistics of the electromagnetic field in presence of turbulent refractive fluctuations, using a standard parabolic equation (PE) model. This new approach is based on stochastic calculus and more precisely on the Itô formalism which will allow us to generate all the response statistics equations. In addition, the last paragraph will show how to characterize the turbulent medium in connexion with this study and examine some results.

2. Study framework

The starting point of this approach is a standard P.E. model, CORAFIN, developped at DCN, associated with a finite difference method using a Crank-Nicolson scheme. The propagation equation takes the parabolic form :

$$\frac{\partial U}{\partial s} = -\frac{j}{2k_0}\frac{\partial^2 U}{\partial r^2} - j\frac{k_0}{2}\left(m^2 - 1\right)U \tag{2-a}$$

with associated boundary conditions : $\begin{cases} \dfrac{\partial U}{\partial r} - jk_0 q_{H,V} U = 0 \\ \lim\limits_{r\to\infty}\left(\dfrac{\partial U}{\partial r} + jk_0 U\right) = 0 \end{cases}$ (2-b)

m is the modified refractive index and $q_{H,V}$ depends upon the polarisation.

Introduction of the random componant n_1, under the form : $n^2 = \langle n_0 \rangle^2 + 2n_1$ leads to a Stochastic Partial Differential Equation (SPDE) :

$$\frac{\partial U}{\partial s} = -\frac{j}{2k_0}\frac{\partial^2 U}{\partial r^2} - j\frac{k_0}{2}\left(m^2 - 1\right)U - jk_0 n_1 U \tag{3}$$

in which the last coefficient is a physical random process. The solutions of this equation will be determined by computing their statistic moments.

A classical way to solve this kind of equation and obtain some of the moments is to use a statistical approach like a Monte Carlo method, which means first generating numerical random fluctuations n_1, generally from the turbulence spectrum, then solving the deterministic parabolic equation for each realization of n_1, and last averaging on the whole set of independent simulations.

This method has become very popular, due to increasing computer power. The first order moment is easily generated, as is a particular value of the second order moment : its value at origine. A wide choice of turbulence spectra allows an accurate description of the physical phenomenum. But on the other side, it requires a huge computational time, because the error on the result behaves like the inverse of the square root of the number of simulations. Moreover, it is quite difficult to determine rigorous convergence criterions : the choice of a "right" simulation number, for which the method converges, remains empirical, and in all cases, this number seems to be greater than one hundred trials.

The interest of a direct stochastic treatment of the SPDE is then obvious : if we can derive from the stochastic equation deterministic partial differential equations for all the moments, we shall then obtain each response statistics by solving single equation. The treatment of stochastic differential equations has been discuted extensively in the literature. The main difficulty is a closure problem : for instance, getting the first order moment, implies averaging equation (3) :

$$\frac{\partial \langle U \rangle}{\partial s} = -\frac{j}{2k_0}\frac{\partial^2 \langle U \rangle}{\partial r^2} - j\frac{k_0}{2}\left(m^2 - 1\right)\langle U \rangle - jk_0 \langle n_1 U \rangle \tag{4}$$

(4) contains the first moment $\langle U \rangle$as expected, but also the crossed moment $\langle n_1 U \rangle$, for which no statistics are known. To deal with this problem, we thus need closure assumptions ; they will

be obtained from hypothesis on the turbulent process. We propose here an approach based on the stochastic calculus rules. This formalism permits us to derive the first and second order moment equations, but also the higher order moment equations.

3. Stochastic treatment of the SPDE

Using the properties of some random processes, and particularly the Brownian motion, mathematicians have established a number of theorems which define the rules of stochastic calculus. As we will see, these rules slightly differ from ordinary calculus operations. It is particularly the case for the integration operations we will have to treat. But before introducing the stochastic equation formalism, we prefer to transform the SPDE into a stochastic ordinary differential equation. This is easily achieved by semi-discretization in r, and makes things easier. We thus use :

$$\left.\frac{\partial^2 U(r,s)}{\partial r^2}\right|_{r=ih} = \frac{1}{h^2}\left(U_{i+1}(s) - 2U_i(s) + U_{i-1}(s)\right) + \mathrm{O}\left(h^2\right) \quad i=0,\ldots,\mathrm{M} \tag{5}$$

where h is the vertical step, to obtain the ordinary stochastic differential system :

$$\frac{dU_i(s)}{ds} = bU_{i+1}(s) - d_i U_i(s) + bU_{i-1}(s) + \sigma_i(s)U_i(s) \tag{6}$$

where $U_i(s)$ is an O(h^2)-approximation of $U(ih,s)$, i=0,...,M

$$\begin{cases} b = -j/2k_0h^2 \\ d_i = -2b - j\dfrac{k_0}{2}\left(m_i^2 - 1\right), \qquad i = 1,\cdots,M-1 \\ \sigma_i = -jk_0n_1(ih), \qquad i = 0,\cdots,M \end{cases}$$

$$U_{-1} = U_{M+1} = 0$$

$$d_0 = -2b - j\frac{k_0}{2}\left(m_0^2 - 1\right) - 2jbhk_0\, q_{H,P}$$

$$d_M = -2b - j\frac{k_0}{2}\left(m_M^2 - 1\right) - 2jbhk_0$$

This set of M equations can be written under the following matricial form :

$$\frac{d}{ds}\underline{U}(s) = \underline{\underline{f}}\left(\underline{U}(s)\right) + \underline{\underline{G}}\left(\underline{U}(s)\right).\underline{\sigma}(s) \tag{7}$$

where the M-vectors U, σ, and MxM-matrixes f, G are defined by :

$$\underline{U} = \left(U_0,\cdots,U_M\right)^T, \qquad \underline{\sigma} = \left(\sigma_0,\cdots,\sigma_M\right)^T, \qquad \underline{\underline{f}}\left(\underline{U}(s)\right) = \underline{\underline{f}}.\underline{U}(s)$$

$$\underline{\underline{f}} = \begin{bmatrix} d_0 & 2b & 0 & \cdots & 0 \\ & \ddots & & & \vdots \\ & b & d_i & b & \\ & & & \ddots & \\ 0 & \cdots & 0 & 2b & d_M \end{bmatrix}, \qquad \underline{\underline{G}} = \mathrm{diag}(\underline{U}) = \begin{bmatrix} U_0 & 0 & \cdots & & 0 \\ \vdots & \ddots & & & \vdots \\ & 0 & U_i & 0 & \\ & & & \ddots & \\ 0 & \cdots & & 0 & U_M \end{bmatrix}$$

At this point, we have transformed the initial SPDE under a more suitable form. Matricial system (7) describes the response U of a structural system under a wide band random parametric excitation σ. To apply standard results on stochastic differential equation, the main assumption is now that the physical random process σ is close to a gaussian white noise, defined as the formal derivative of a Brownian motion B :

$$\underline{\sigma}(s) \approx \frac{d\underline{B}(s)}{ds} \tag{8}$$

Going back to the physics, the underlying assumptions on the turbulent process are then :

(H1) the random process is Gaussian, i.e.completely described by its first and second moments,

(H2) the random fluctuations are zero-mean $\langle n_1(r,s) \rangle = 0$

(H3) the random medium is delta-correlated in the propagation direction. The correlation function takes the form : $\langle n_1(r,s)\, n_1(r',s') \rangle = \delta(s-s') A(r,r')$

Two additionnal hypothesis are made for the sake of simplicity :

(H4) the medium is homogeneous, with correlation function :

$A(r,r') = A\big(r-r', (r+r')/2\big)$, where the second argument is the mean height.

(H5) the medium is isotropic :

$A(r,r') = A\big(|r-r'|, (r+r')/2\big)$

Under *(H1)* to *(H5)* , σ can be replaced by dB and system (7) becomes :

$$d\underline{U}(s) = \underline{\underline{f}}(\underline{U}(s))ds + \underline{\underline{G}}(\underline{U}(s)).d\underline{B}(s) \tag{9}$$

By integration, we obtain :

$$\underline{U}(s) - \underline{U}(0) = \int_0^s \underline{\underline{f}}(\underline{U}(s))ds + \int_0^s \underline{\underline{G}}(\underline{U}(s)).d\underline{B}(s) \tag{10}$$

In the right handside of (10), the first term is an ordinary Riemann integral because the matrix f has "deterministic" elements. But the last integral is a stochastic integral and can not be treated with ordinary rules, since the brownian motion process B is continuous with unbounded variations. The main problem of this approach is thus the definition of this stochastic integral.

For physical reasons, we chose the Stratonovich stochastic integral, and obtain the following final form of (9) :

$$d\underline{U}(s) = \underline{F}(\underline{U}(s))ds + \underline{\underline{G}}(\underline{U}(s))\cdot d\underline{B}(s), \quad F_i(\underline{U}(s)) = f_i(\underline{U}(s)) + \frac{1}{2}k_0^2 A_{ii} U_i(s) \qquad (11)$$

We have thus obtained a general stochastic equation for the full stochastic field. From this equation, we can derive deterministic (it means ordinary) partial differential equations for all the moments of the stochastic process U. Numerical treatments can then be applied.

4. First and second order moments

It is now easy to derive the partial differential equations for the first and second moments.

We obtain the following ordinary partial equation for the first moment :

$$\frac{d}{ds}E[U_i] = E[\{F_i(\underline{U})\}] = E[f_i(\underline{U})] - \frac{k_0^2}{2}A(0,ih)E[U_i] \qquad (12)$$

which appears to be the semi-discretized form of :

$$\frac{\partial}{\partial s}E[U(r,s)] = \left(-\frac{j}{2k_0}\frac{\partial^2}{\partial r^2} - j\frac{k_0}{2}(m^2-1) - \frac{k_0^2}{2}A(0,r)\right)E[U(r,s)] \qquad (13)$$

It is very interesting to note that in this case of the first order moment, we still obtain a parabolic equation. The numerical implementation thus implies only a slight change in the existing code.

In the same way, to obtain for the second moment the following equation :

$$\frac{\partial}{\partial s}E[U(r_k,s)U(r_l,s)] = \left[-\frac{j}{2k_0}\left(\frac{\partial^2}{\partial r_k^2} - \frac{\partial^2}{\partial r_l^2}\right) - j\frac{k_0}{2}\left(m^2(r_k,s) - m^2(r_l,s)\right) - \frac{k_0^2}{2}\left(A\left(0,\frac{r_k+r_l}{2}\right) - A\left(|r_k-r_l|,\frac{r_k+r_l}{2}\right)\right)\right]E[U(r_k,s)U(r_l,s)] \qquad (14)$$

This higher order moment equation is of course more complicated and its numerical treatment is specific.

Remark : Our results are a generalisation of those obtained by Tatarski using an other formalism (Novikov-Furutsu formulae) [4]. In our case, the assumptions on the medium are less restrictive, giving the possibility to take into account a non homogeneous turbulence in altitude, through the expression of the correlation function A.

5. First order moment coverage : results

According to paragraph 4, we can compute the mean loss coverage of the field in a turbulent medium by a slight change of the existing parabolic code. A simple validation of this method consists then in comparing its numerical results with those obtained by a statistical approach (Monte-Carlo method), using a random profile generator [2][3].

Notice that the cost of a Monte Carlo method is approximatively a hundred times (in fact, the number of trials times) the cost of our direct method.

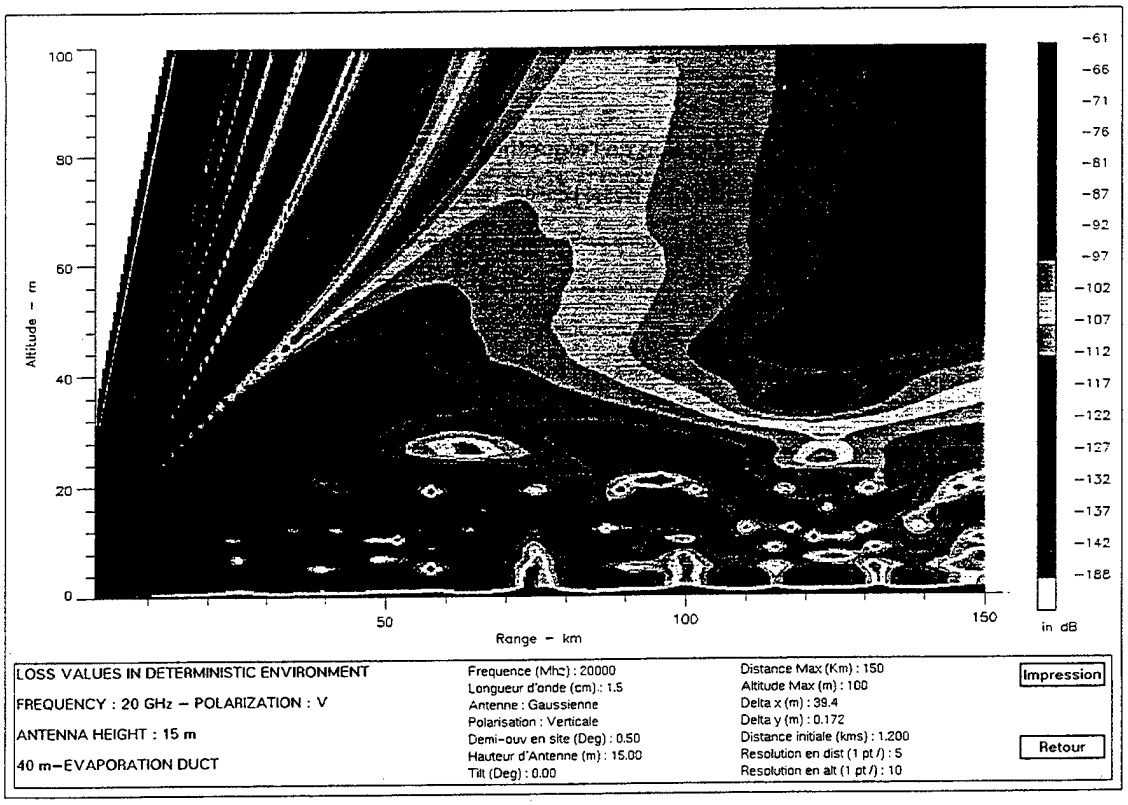
In the following example, the turbulence is described by a Kolmogorov model. As in Kolmogorov theory no correlation function is defined, the difficulty was to derive from the structure function the correlation function term which appears in our equation. This was done using relationship [4] :

$$A(0,r) = \langle n_1^2 \rangle = \frac{C_n^2(r)}{1.91 L_0^{-2/3}}$$

where the constant structure C_n^2 is given by the Gossard model, well suited to the evaporation duct case, L_0 being the external length of the turbulence.

A radar frequency of 20 GHz frequency propagates, in presence of a strong 40m evaporation duct (Battaglia model). The electromagnetic loss coverage is computed up to 100 meters versus 150 kilometers range. The antenna height is 15 meters. Figure 1 below shows the "deterministic" radar coverage.

fig. 1



Figures 2-a,b present the difference in dB beetwen the results in deterministic medium and in turbulent medium : 2-a for the stochastic approach, 2-b for the statistical approach using 120 simulations. In both cases, this difference can reach 14 dB, but this strong value appears at points where we observe destructive interference from multipaths. We can see the very good agreement between the two methods. We remind that the second case is 120 times more expansive than the first one.

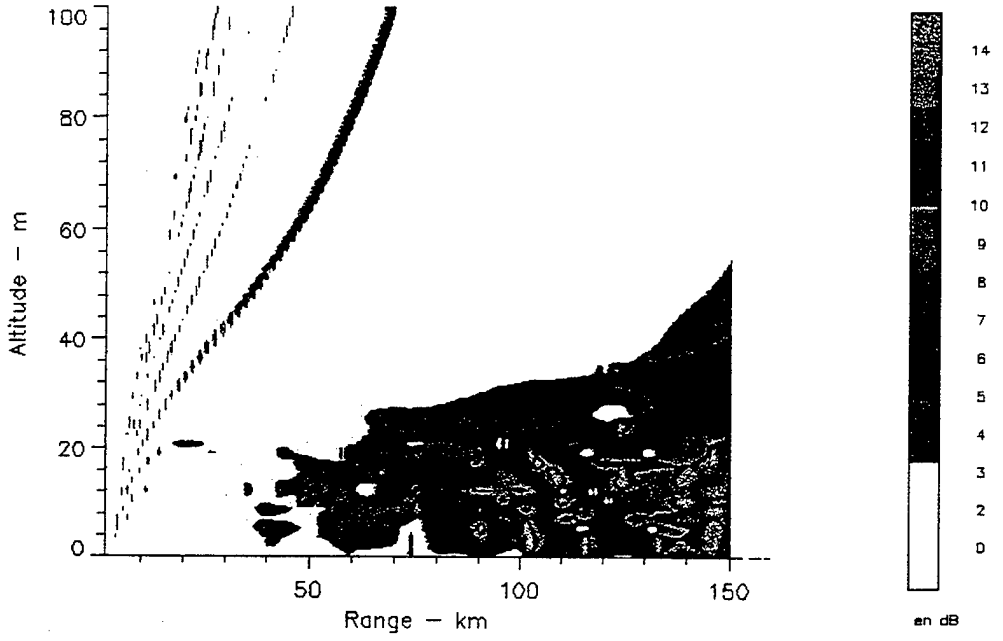


Fig 2-a

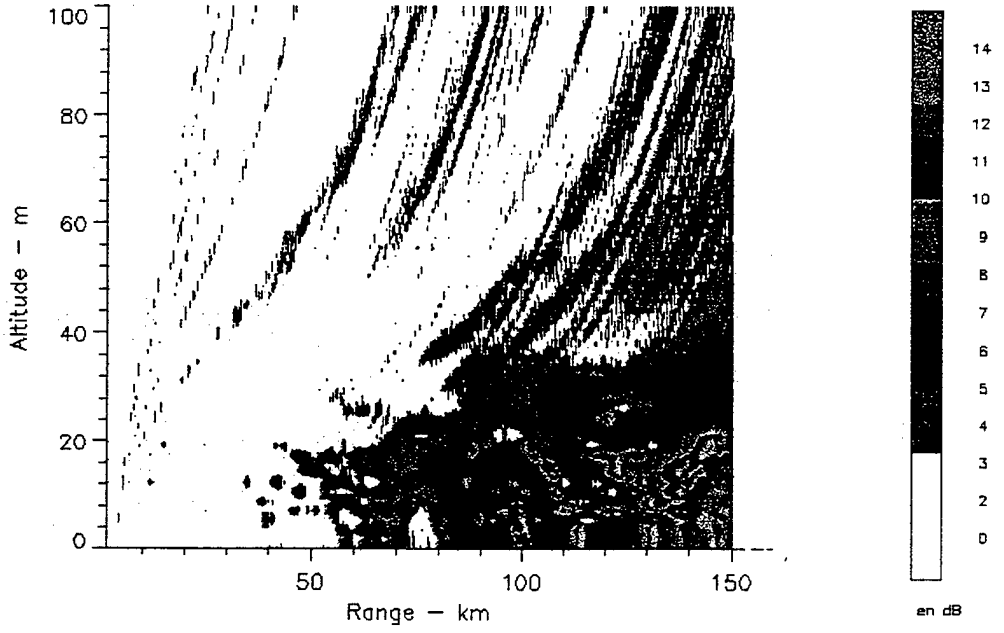


Fig 2-b

The same agreement can also be observed on the following range loss diagrams at altitudes 10 m. (fig. 3), 20m. (fig. 4) and 60 m. (fig. 5). Each fig. (-a) contains the "non-turbulent" result (continuous curve) followed by the stochastic and statistical turbulent results (dashed curves). The second boxes (-b) give the difference beetwen turbulent and non-turbulent cases.

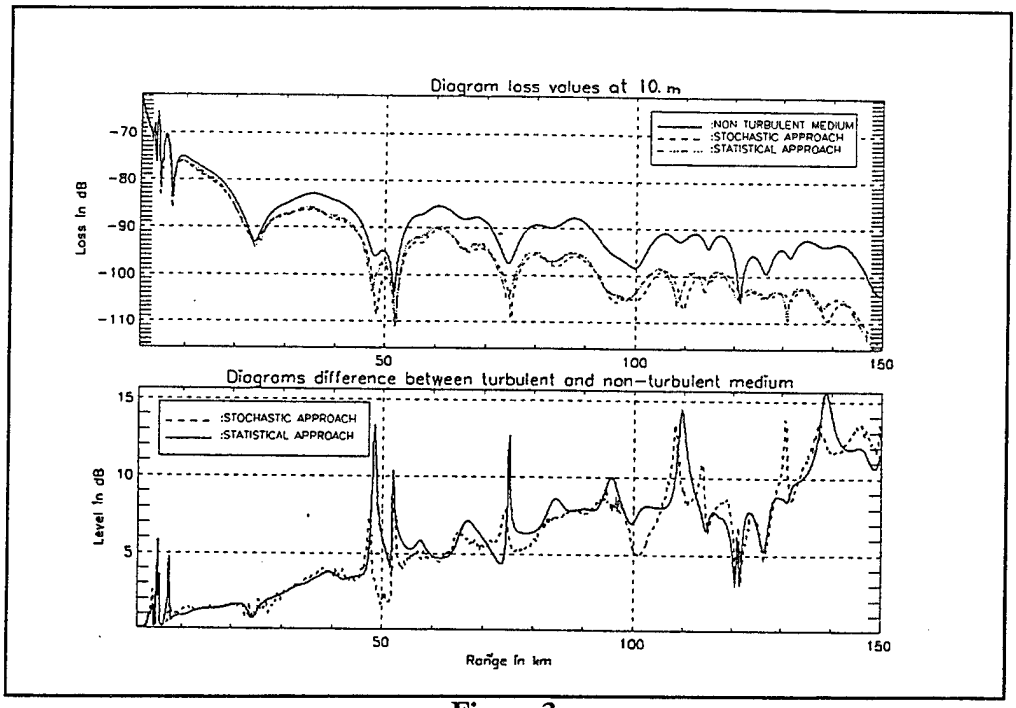


Figure 3

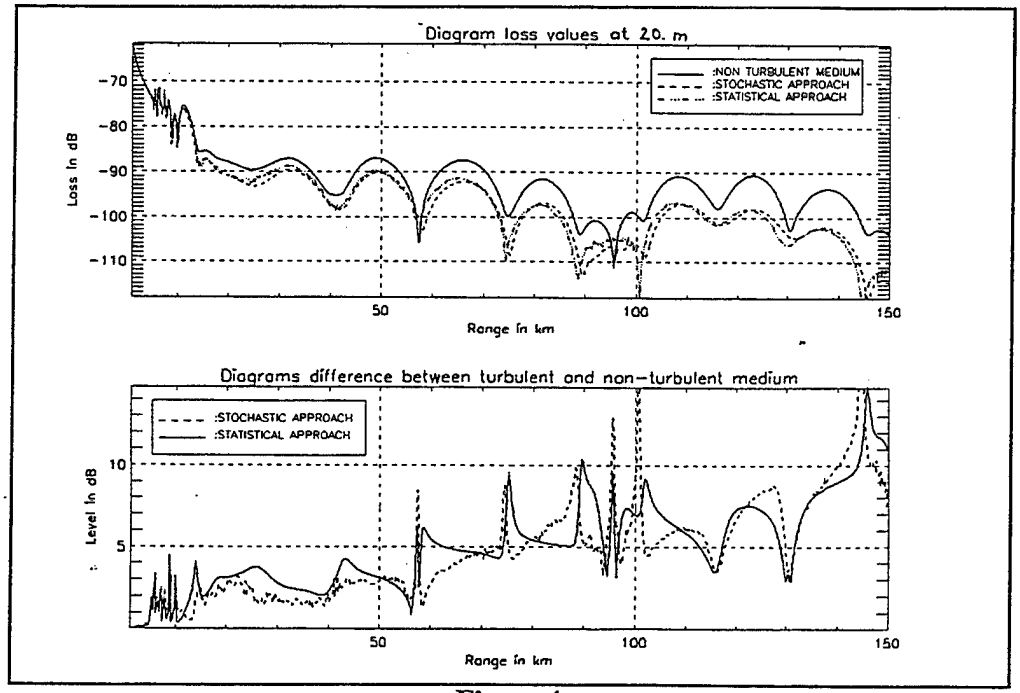


Figure 4

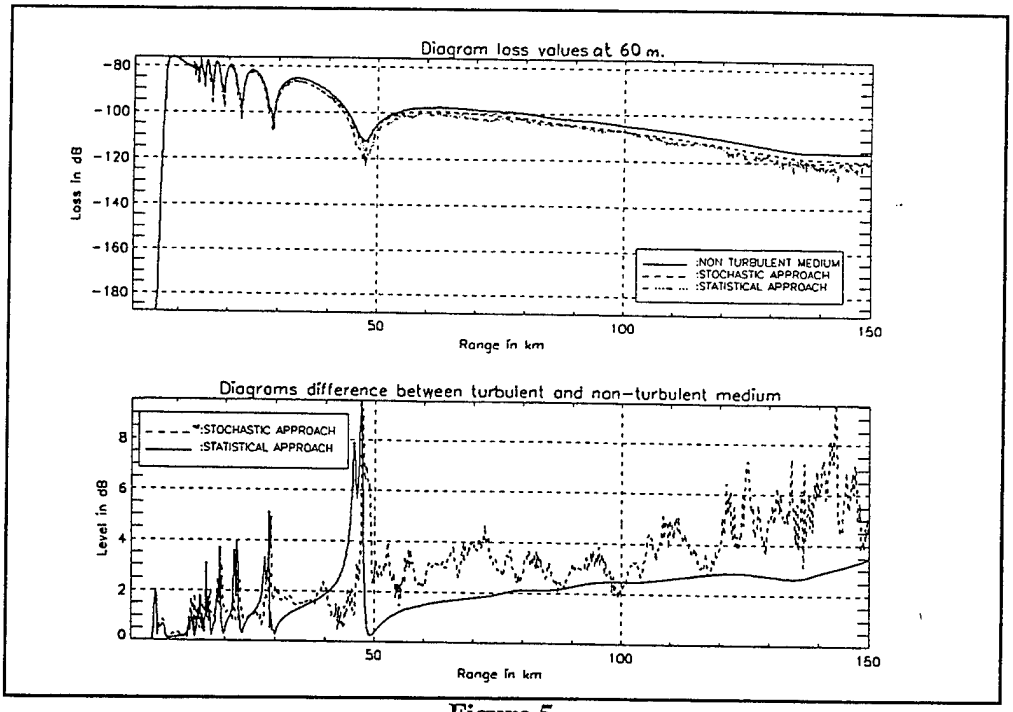


Figure 5

6. Conclusion

We propose a direct stochastic treatment to solve the problem of radar wave propagation in a random turbulent medium. The Stochastic Differential Equations formalism allows us to compute the mean electromagnetic field (first moment) coverage in a turbulent medium by solving only ONE parabolic equation, while a statistical approach needs more than 100 independant simulations. The numerical results are shown to be in very good agreement for the two methods.

Moreover, we generalize Tatarski results, our formalism allowing us to relaxe some of the assumptions on the turbulent medium and to take into account vertically non-homogeneous correlation functions.

References :

[1] R.A.IBRAHIM, "*Parametric Random Vibration*"
Research studies press ltd. - John Wiley & Sons inc.

[2] E.Mandine, M.C. Pelissier, C.Giannilevigne: " *Radar propagation in a turbulent atmosphere : a random profiles generator* "
Electromagnetic Propagation Workshop, Maryland, July 1995.

[3] E.Mandine, M.C. Pelissier : " *Construction d'un generateur de profils aleatoires - application a la propagation radar en milieu turbulent*",
15eme colloque GRETSI, Juan Les Pins , sept. 1995.

[4] A. ISHIMARU : "*Wave propagation and scattering in random media*"
1978, Academic Press

Atmospheric Multipath Effects Prediction for Army Communications Links

Victor J. Procopio
U. S. Army Communications-Electronics Command
Research, Development and Engineering Center
Space and Terrestrial Communications Directorate
Fort Monmouth, New Jersey

Arvids Vigants
Monmouth University
West Long Branch, New Jersey

William T. Barnett
Telos Corporation
Shrewsbury, New Jersey

Mark Lambert
Atlantic Consulting Services, Inc.
Eatontown, New Jersey

Introduction

Army tactical communications at echelons brigade and above are dependent on line-of-sight (LOS) radio links. As current military doctrine stresses the requirement to rapidly deploy to meet a range of threats at locations worldwide, the Army cannot utilize a fixed infrastructure consisting of coaxial or fiber cable as is used in the commercial sector. Given the requirement to deploy worldwide, the propagation environment and resulting link reliability is an issue of serious concern to Army communications-systems planners. This concern becomes even greater in light of current initiatives to gain additional system capacity through modification of legacy systems and insertion of evolving communications system technology. In response to serious fading problems encountered during Operation Desert Storm [1], the U.S. Army Communications-Electronics Command (CECOM), in cooperation with the Project Manager, Joint Tactical Area Communications Systems (PM JTACS), initiated several efforts that addressed the subject of LOS propagation reliability. These efforts resulted in enhanced network planning and management tools that accounted for the impacts of climate-induced fading and improved operational procedures for establishing LOS links [2, 3, 4].

The link propagation reliability associated with microwave line-of-sight fading, caused by atmospheric layering, changes from month to month as temperature, humidity, and wind patterns change. Commercial practice has been to design links using the propagation reliability for the worst month of the year. The assumption there is that the links will be in service for many years and will operate on a year-round basis. This assumption is not valid for tactical links that have a transient existence. This paper extends the previous CECOM work and describes propagation reliability for links that must be highly reliable and may be in service for as short a time as an hour. This is accomplished by providing a bad-hour probability of fading for a calendar month. A bad hour is defined as the hour with the largest concentration of fading in a calendar month. The predicted concentration is to be viewed as an average over many years for a calendar month. The purpose of this paper is to describe these new reliability concepts and a model for predicting bad-hour reliability. The model can be used for narrowband radio channels and in some cases for wideband digital-radio channels when the dispersive fade margin is much larger than the thermal-noise fade margin [5].

Army Tactical Communications

Legacy Systems. The Army's Area Common User System (ACUS) consists of the Mobile Subscriber Equipment (MSE) at echelons corps and below (ECB) and the Tri-Service Tactical Communications System (TRI-TAC) at echelons above corps (EAC). The MSE system is a fully automated area-common-user system providing voice and data communications within the corps structure and interoperability with adjacent corps and EAC forces, North Atlantic Treaty Organization (NATO) forces, and commercial networks. TRI-TAC is an automated switching service that provides both voice and data communications for theater tactical corps and above forces. It is a digital, secure, common-user network, which provides subscribers with connectivity to strategic systems, the MSE system, commercial networks, other services' systems, and allied networks.

Both MSE and TRI-TAC consist of digital switches that use time-division multiplexing operating at 16 or 32 kilobits per second (kbps). MSE switches are supported by transmission systems that range from 8 to 64 channels, while EAC is deployed with transmission systems that range from 4 to 144 channels. It is expected that information-transport requirements for the digitized battlefield will exceed the capacity of these legacy transmission systems. The future infrastructure must support anticipated requirements that will range from 1.544 megabits per second (Mbps) for extension nodes to 10 Mbps or greater for interswitch links. In anticipation of future needs for higher capacity, there is a CECOM Research, Development and Engineering Center (RDEC) effort for 45- and 156-Mbps systems.

PM JTACS is executing an ACUS modernization plan (MP) that will support the migration of the Army's ACUS to the Warfighter Information Network (WIN). WIN is a coherent information systems architecture needed to support the requirements of the 21st-century force (Force XXI). As part of the ACUS MP, existing GRC-226 and GRC-222 radios used for internodal connectivity will be replaced by a High-Capacity LOS (HCLOS) radio system providing additional throughput to support emerging requirements for the high levels of voice, data, video and imagery traffic and the introduction of asynchronous transfer mode (ATM) switching, also planned as part of the MP.

Battlefield Information Transmission System. The Battlefield Information Transmission System (BITS) is an umbrella program comprising the Digital Battlefield Communications (DBC) Advanced Technology Demonstration (ATD), SPEAKEASY, Commercial Communications Technology Laboratory (C2TL), Advanced Concepts and Technology (ACT II), and related programs. BITS will provide enabling technologies for ACUS and WIN.

A major thrust of BITS and the DBC ATD is a series of High-Capacity Trunk Radios (HCTRs) designed to provide greater capacities for the ACUS and to support requirements for a mobile Radio Access Point (RAP). The RAP, using the HCTR and advanced phased-array antenna technology, will provide on-the-move connectivity between highly mobile forces at brigade and the fixed ATM infrastructure. The HCTR research and development efforts will also help to define appropriate technology for the next-generation ACUS LOS radio.

The HCTR(-), with a performance goal of 45 Mbps and a range of 25 kilometers (km), will be demonstrated during the Division XXI Advanced Warfighting Experiment (AWE) to show the potential of ATM technology with MSE. The HCTR(-) is a commercially available product selected as the result of a market survey sponsored by the DBC ATD. The objective HCTR is a developmental effort and will provide a minimum throughput of 45 Mbps, in both stationary and mobile operation. The objective HCTR will be demonstrated in conjunction with the RAP during the Corps XXI AWE and Joint Warfighter Interoperability Demonstration (JWID) '99.

CECOM Propagation Reliability Background

An LOS propagation-reliability working group, convened by CECOM has developed a propagation-reliability model of clear-air multipath fading suitable for link engineering of LOS Army tactical radio [6]. This program was stimulated by reports from LOS operators indicating that path reliability on many of their radio links was a daily problem during operations in Southwest Asia (SWA). The climate in SWA and elsewhere is known to be difficult for LOS radio propagation because of the high incidence of clear-air refractive effects causing large and frequent reductions in received signal strength (RSS), referred to as multipath fading.

The ability of an LOS radio installation to withstand decreases in RSS is represented by its fade margin, i.e., the amount of power in dB by which the average RSS exceeds the receiver's threshold for a permissible bit-error-rate, say 10^{-5}. The propagation-reliability model for multipath fading relates fade

margin to path reliability with site-specific parameters of path length, frequency, and calendar-month climate factors [6, 7]. Link engineering is executed by calculating the fade margin required to obtain an objective path reliability for given parameter values. The link is satisfactorily engineered if its fade margin equals or exceeds the required fade margin. This propagation reliability model has been incorporated in a battlefield automated system, the JTACS Network Planning Terminal (NPT) [2, 3] for MSE. The propagation reliability is the complement of the probability of fading. For example, a probability of fading of 0.01 (one percent) corresponds to a propagation reliability of 0.99. All probabilities in this paper are expressed as fractions (not as percentages).

Climate Factors. The propagation reliability model describes the transmission effects of the atmosphere on LOS links at tactical radio frequencies. Horizontal layers of differing humidity and temperature provide the mechanism for multiple rays from the transmitter to reach the receiving antenna. The received power during such multipath propagation varies rapidly in time (fades) because of the interference between the multiple rays. Superimposed on this fast fading is a slower variation associated with ducting.

The effects of geophysical and meteorological variables are consolidated into an empirical coefficient, the climate factor, because analytical description of these effects is intractable. Values for the climate factor range from 0 to about 100. The climate factors pertain to the existence of horizontal atmospheric layers of differing humidity and temperature. Fading can vary from insignificant at freezing temperatures to substantial at warm temperatures. There is monthly variation in the amount of fading even in climates where fading is present year-round. Monthly climate factors have been developed for the NPT [7]. There can also be significant hourly concentration in a fading month [8]. A model of the hourly concentration effect is introduced and applied in this paper.

Deep-Fade Region

Historically, parameters in the probability of fading have been defined in terms of equations for the deep-fade region where the received signal has a value that is much smaller than the value of the signal in the absence of fading. This has come about because much of the development of the probability of fading has been associated with commercial radio systems that can operate reliably in the presence of large reductions of RSS (deep fades). The signal strength in the equations in this paper is described in terms of a fade depth (A)

$$A = -10 \log (\text{normalized power}) \qquad (1)$$

where normalized power describes the received signal as a fraction of the received power in the absence of fading. For example, a normalized power of 0.01 corresponds to a fade depth of 20 dB. The calendar-month probability-of-fading equations developed by CECOM classify fades as deep when A is 25 dB or greater.

The mathematical expression for the calendar-month probability of fading in the deep fade region is [6]

$$P_m(A) = C_m K_{link} 10^{-A/10}, A \geq 25 \qquad (2)$$

This is the probability that the received signal has faded to depth A or more. The link parameter K_{link} contains the path length (D, in km) and the radio frequency (F, in GHz)

$$K_{link} = 10^{-7.12} D^{3.6} F^{0.89} \qquad (3)$$

The calendar-month climate factor C_m is obtained from charts or computer databases [7]. Descriptive categories of climate in terms of C_m are 1 (average), 10 (difficult), and 100 (very difficult).

Shallow-Fade Region

Tactical wireless communications links are designed for parameter values different from those for commercial links. The probability of fading in the shallow-fade region, A < 25 dB, is important for the design and operation of tactical links. The shallow-fade calendar-month probability of fading developed by CECOM [6, 9], based on international information, is

$$P_m(A) = 1 - \exp(-10^{-A\, q(A)/20}), A < 25 \qquad (4)$$

where

$$q(A) = 2 + K(A)(q_t + R(A)) \qquad (5)$$

$$K(A) = 10^{-0.016\, A} (1 + 0.3\, 10^{-A/20}) \qquad (6)$$

$$R(A) = 4.3\, (10^{-A/20} + (A/800)) \qquad (7)$$

$$q_t = ((r - 2)/K(25)) - R(25), qt > -2 \qquad (8)$$

$$r = -0.8 \log [-\ln(1 - P_m(25))] \qquad (9)$$

where $P_m(25)$ is obtained from the deep-fade probability of fading.

Defocusing Region

It is common knowledge that during periods of heavy fading the average value of the received signal can become smaller than the value of the received signal in the absence of fading. This depression of the received signal is associated with strong atmospheric layering (ducting). To allow representation of possible defocusing during the bad hour, the description in this paper of the probability of fading is split into three regions. Fading more severe than that described by the Rayleigh distribution is in the defocusing region (see Figure 1). The expressions for the fading probabilities in the deep-fade and shallow-fade regions in Figure 1 remain as in the previous sections. Mathematically, the shallow-fade equation applies when $r < 2$. The shallow-fade equation becomes the Rayleigh distribution when $r = 2$.

The working hypothesis in this paper is that the fading probability in the defocusing region can be represented by a Rayleigh distribution with a smaller (depressed) root-mean-square (rms) value. This is a physically reasonable approach that permits more realistic modeling of fading in the defocusing region than was previously possible. It would be desirable to perform analysis of fading data to test or modify the hypothesis.

The bad-hour probability of fading in the defocusing region, expressed a Rayleigh distribution with a depressed rms value, is

$$P_h(A) = 1 - \exp(-10^{-(A - DL)/10}), \text{ any } A \qquad (10)$$

where DL is the defocusing loss in positive dB. The deep-fade expression corresponding to this is

$$P_h(A) = 10^{-(A-DL)/10}, (A-DL) > 25 \qquad (11)$$

In terms of the calendar-month probability of fading, from Equation 2,

$$P_h(A) = 730\, K_{mh}\, C_m\, K_{link}\, 10^{-A/10}, \text{ large } A \qquad (12)$$

where K_{mh} is the fraction of the calendar-month fading contained in the bad hour. The factor 730 comes from the renormalization of probability (there are 730 hours in an average month, 365 x 24/12). The expression for DL, obtained by combining the above two equations, is

$$DL = 10 \log(730\, K_{mh}\, C_m\, K_{link}), DL \geq 0 \qquad (13)$$

The probability of fading is in the defocusing region when DL is positive. If DL is negative, then equations for the deep or shallow fading region must be used.

Parameter Values

The bad-hour fading fraction K_{mh} is certainly a function of meteorological variables. It has a relatively large value when the climate is average [8]. Conversely, it can be expected to have a relatively small value when many hours in a month contain severe fading. A meteorological description of K_{mh} requires a separate investigation, but we can use the above two statements to construct a representative equation for K_{mh} for use in illustrative application in this paper. The function that we construct has a value of b for an average climate ($C_m = 1$) and decreases to a value of a when C_m becomes large

$$K_{mh} = a + (b - a)/C_m, C_m > 0.1 \qquad (14)$$

Measurements in the United States suggest that [8]

$$b = 0.2 \qquad (15)$$

To obtain a value for a, we consider a hypothetical climate with a very large C_m, where fading is severe and approximately equal for four hours every day. Then all the fading in the month is contained in 121.7 hours of equal-intensity fading (from 1/6 of 730 hours in an average month). The fraction of fading in one hour is therefore (from 1/121.7)

$$a = 0.0082 \qquad (16)$$

The behavior of our illustrative bad-hour fading fraction as a function of C_m for these coefficients is shown in Figure 2.

The value of $P_h(A)$ is much larger than the value of $P_m(A)$ for the same large value of A because of the concentration of fading in the bad hour and the renormalization of probability (the denominator in the probability becomes smaller by a factor of 730). This increase can be illustrated by considering an equivalent bad-hour climate factor (from Equation 12)

$$C_h = 730\, K_{mh}\, C_m \qquad (17)$$

Values of C_h as a function C_m, for K_{mh}, as described in Equations 14 to 16, are shown in Figure 3. The large values of C_h substantiate the need for a new description of the fading probability in the defocusing region. Furthermore, the implied large values of $P_h(A)$ suggest reconsideration of link engineering and the requirements for link performance.

Examples

We present fading probabilities for path lengths of 25 kilometers (maximum MSE link length) and 40 kilometers (maximum length of links for EAC use) to illustrate prediction and application of the probability of fading for a bad hour. The radio frequency in the examples is 5.0 GHz, in recognition of the suitability of frequencies in that neighborhood for high-capacity radio channels. The probabilities are presented for average climate (C_m = 1, Figure 4), difficult climate (C_m = 10, Figure 5), and very difficult climate (C_m = 100, Figure 6). The bad-hour fading fraction K_{mh} is obtained from Equation (14). Each figure shows calendar-month fading probability P_m and the corresponding bad-hour fading probability P_h for the two path lengths. The numbers on the probability curves identify path length. The letter *m* identifies curves of P_m, and the letter *h* identifies curves of P_h. The curve for the Rayleigh probability distribution (rms value equal to zero fade level), identified by the letter *R*, is included for comparison.

It is intuitively obvious that the probability of fading for a bad hour is larger than the probability of fading for a month because the latter can be viewed as the average over the hours in the month. The examples in Figures 4 through 6 allow numerical comparison. Suppose the links are designed such that P_m is 0.001 (propagation reliability of 0.999). Let the fade margin for this design be denoted by $A_{0.001m}$. The quantity of interest is the ratio P_h/P_m at $A_{0.001m}$. These ratios are listed in Table 1. The largest ratio is 156 for a 25-kilometer path in an average climate. Ratios for the other climates are smaller because the concentration of fading in a bad hour decreases as the climate becomes more severe.

Link-design issues for bad-hour performance are highlighted when the fade margin to achieve a certain transmission performance is plotted as a function of the desired value of P_h in Figure 7. The probability scale covers P_h values from 0.001 to 0.1, corresponding to propagation reliabilities of 0.999 to 0.9. The number on the left on each curve is the path length in kilometers. The number on the right is the value of C_m. A fade margin of over 50 dB is needed to achieve a bad-hour propagation reliability of 0.999 on a 40-kilometer link in a very difficult climate. Equipment may not support such large fade margins, and 0.999 reliability for a bad hour may be an unrealistic requirement.

Outage time instead of propagation reliability in a bad hour may be a way to address bad-hour transmission performance. Fade margins as a function of allowed bad-hour outage time are shown in Figure 8. Curves for 15-kilometer links have been added in acknowledgment of the fact that link design for a bad hour may require shorter paths. The required fade margin for a 40-kilometer link in a very difficult climate is smaller than 40 dB when an outage of 100 seconds is allowed (propagation reliability of 0.972). The suitability of such a design depends on the composition of fade events (number and duration) contained in the 100 seconds, the type of communications traffic, and the network protocol. Criteria for transmission performance during a bad hour is an area for future work.

Table 1. Comparison of Calendar-Month and Bad-Hour Fading

C_m	D, km	$A_{0.001m}$, dB	P_h/P_m
1	25	14.7	156
1	40	22.4	145
10	25	25.3	20
10	40	32.7	20
100	25	35.3	7
100	40	42.7	7

Conclusions and Recommendations

This paper has continued the evolution of CECOM propagation-reliability work by describing new reliability concepts and developing a new propagation-reliability model for links that may be in service in a bad hour. Examples show that links engineered for a monthly propagation outage may have a propagation outage from 7 to 156 times worse in the bad hour of the month, depending on the fading climate. This suggests reconsideration of link engineering to include link reliability for any hour in the month. For example, the nominal monthly link propagation-reliability objective of 0.999 may not be appropriate for every hour in the month.

Further research of the hourly propagation-reliability model and criteria for transmission performance during a bad hour are areas for future work. However, immediate application of the simple hourly link propagation-reliability model to existing and planned Army LOS radio systems is recommended.

References

[1] Brockel, K. H. and A. Vigants, "Line-of-Sight Radio Fading Prompts Remedial Program," *SIGNAL*, pp. 63-65, November 1992.

[2] Brockel, K. H., T. Cheng, and M. P. Mitchum, "NPT - A Success Story Evolving From Teamwork and Innovation," Conference Record, IEEE MILCOM '93.

[3] Mostow, J. R., M. J. Harrigan, J. C. Powell, L. R. Kennedy, and W. T. Barnett, "NPT, The Tool for Planning MSE Networks," Conference Record, IEEE MILCOM '94.

[4] Chaney, K. D., K. H. Brockel, W. T. Barnett, J. R. Inserra, R. J. Locher, F. G. Loso, V. J. Procopio, and A. Vigants, "Tactical Line-of-Sight Path Reliability: Improved MSE System Procedures," Research and Development Technical Report CECOM-TR-92-1, April 1992.

[5] Procopio, V. J., K. H. Brockel, J. R. Inserra, F. G. Loso, P. A. Major, K. D. Chaney, R. J. Locher, W. T. Barnett, and A. Vigants, "High-Capacity Trunk Radio for Tactical Communication on the Digitized Battlefield," Conference Record, IEEE MILCOM '94.

[6] Procopio, V. J., K. H. Brockel, J. R. Inserra, F. G. Loso, P. A. Major, K. D. Chaney, R. J. Locher, A. Vigants, M. Riehl, and W. T. Barnett, "Tactical Line-of-Sight Radio Propagation Reliability Modeling," Conference Record, IEEE MILCOM '93.

[7] Brockel, K. H., J. R. Inserra, F. G. Loso, P. A. Major, V. J. Procopio, K. D. Chaney, R. J. Locher, A. Vigants, W. T. Barnett, and M. Riehl, "Tactical Line-of-Sight Path Reliability: Propagation Climate Factors," Conference Record, IEEE MILCOM '93.

[8] Barnett, W. T., "Multipath Propagation at 4, 6, and 11 GHz," Bell System Technical Journal, Vol. 51, No. 2, pp. 321-361, February 1972.

[9] Brockel, K. H., W. T. Barnett, K. D. Chaney, J. R. Inserra, R. J. Locher, F. G. Loso, V. J. Procopio, and A. Vigants ,"Tactical Line-of-Sight Radio Propagation Reliability," Research and Development Technical Report CECOM-TR-91-3, October 1991.

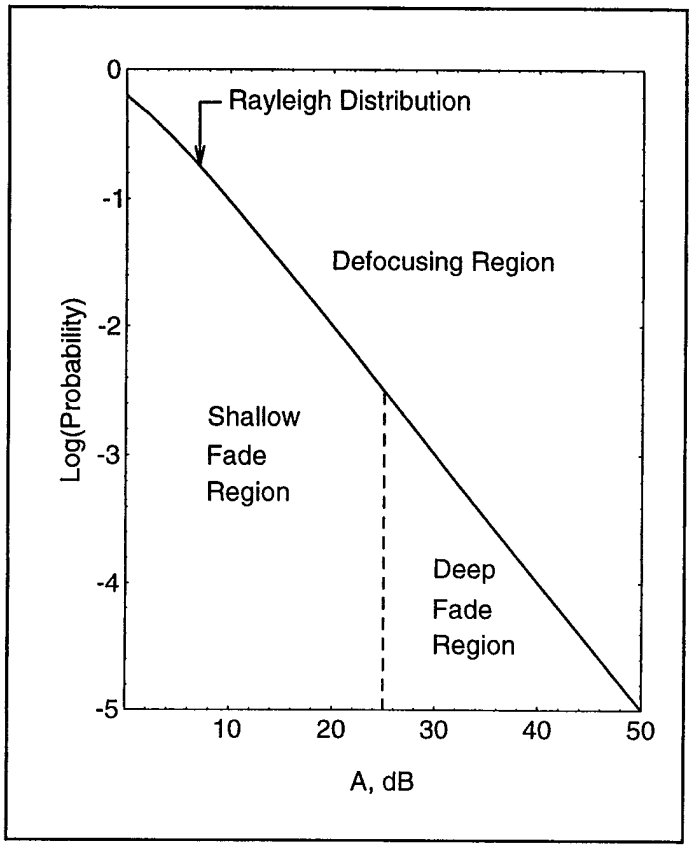


Figure 1

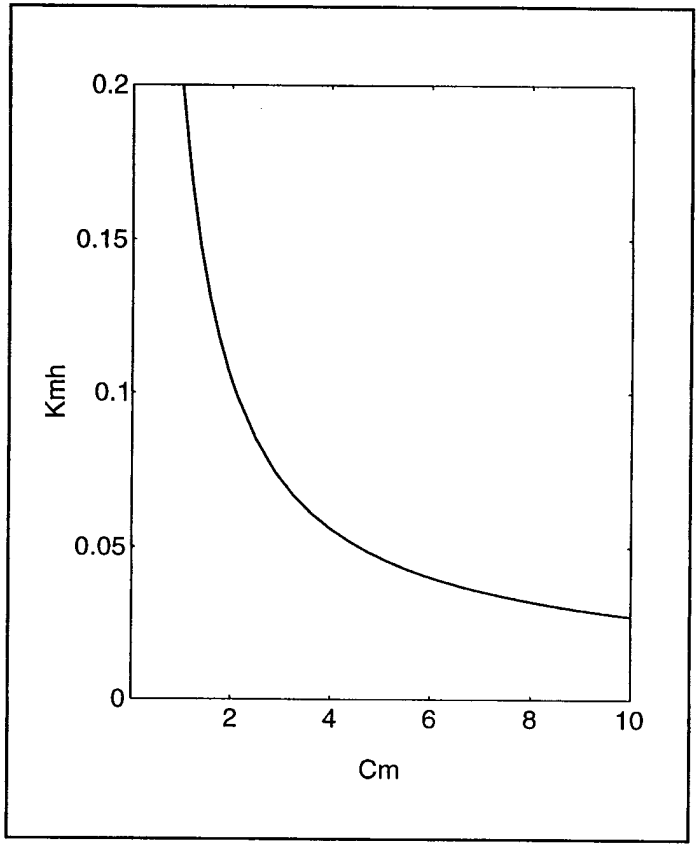


Figure 2

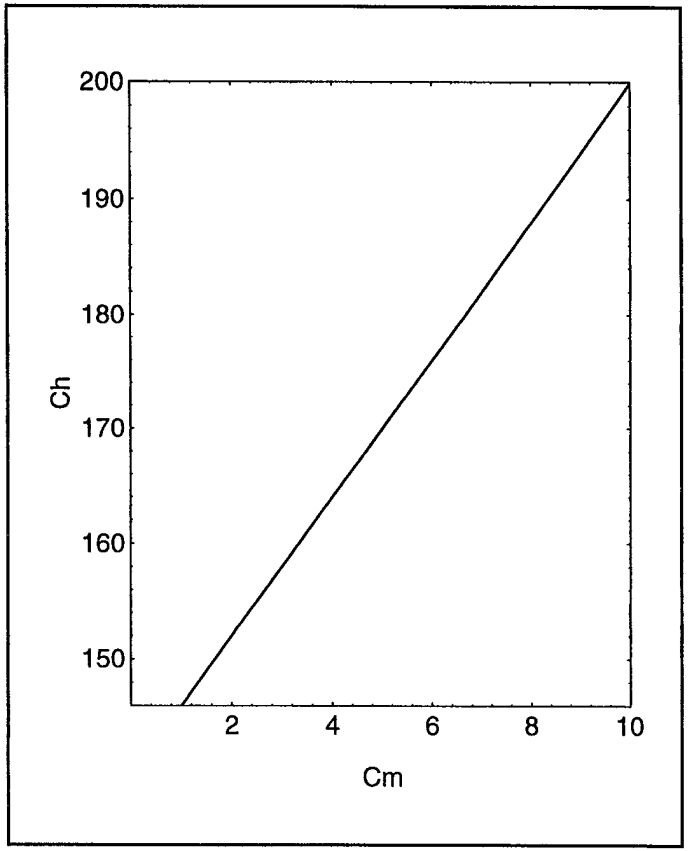


Figure 3

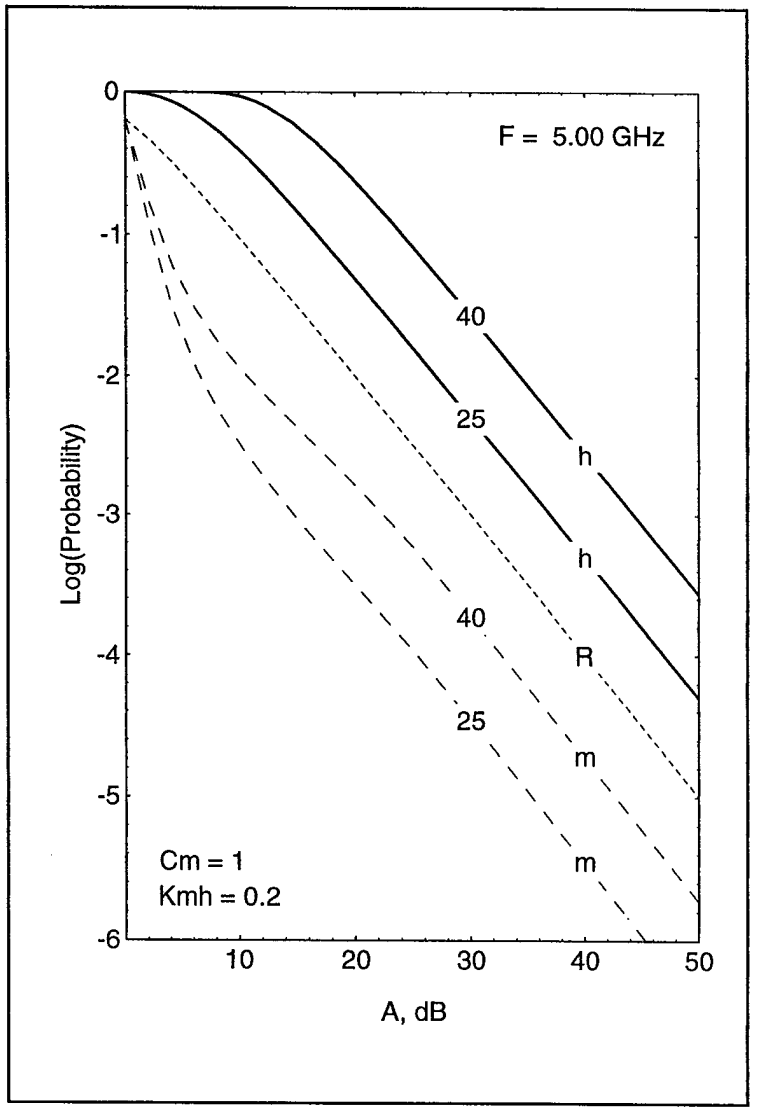


Figure 4

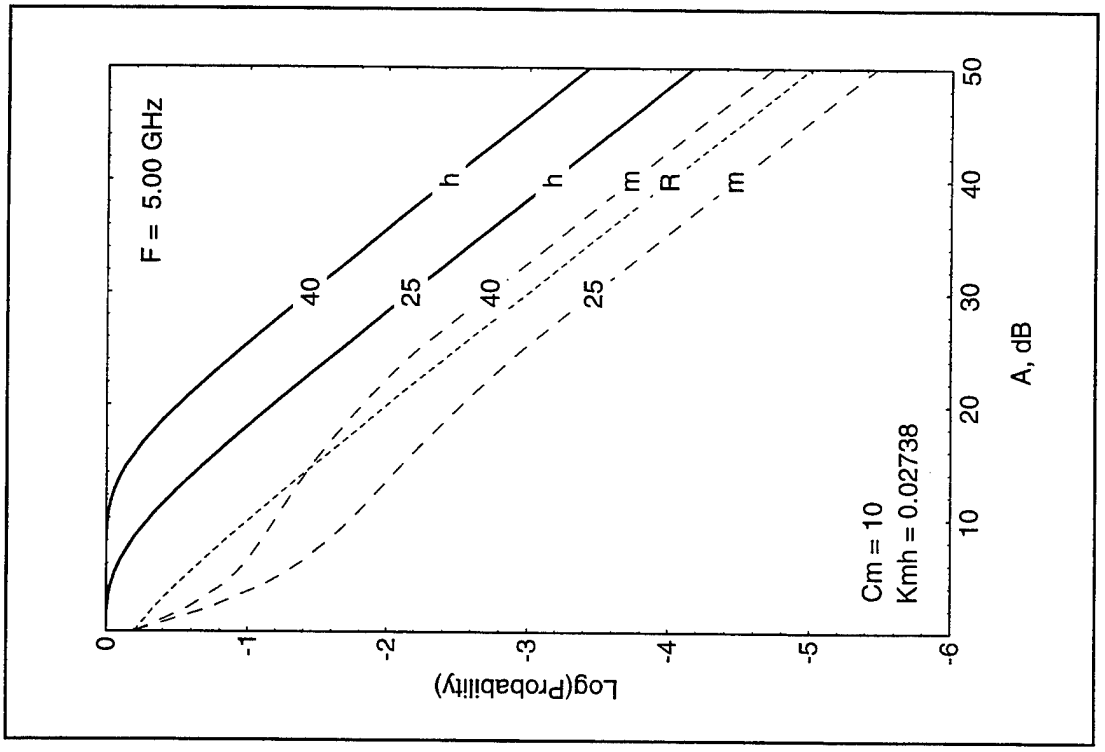


Figure 5

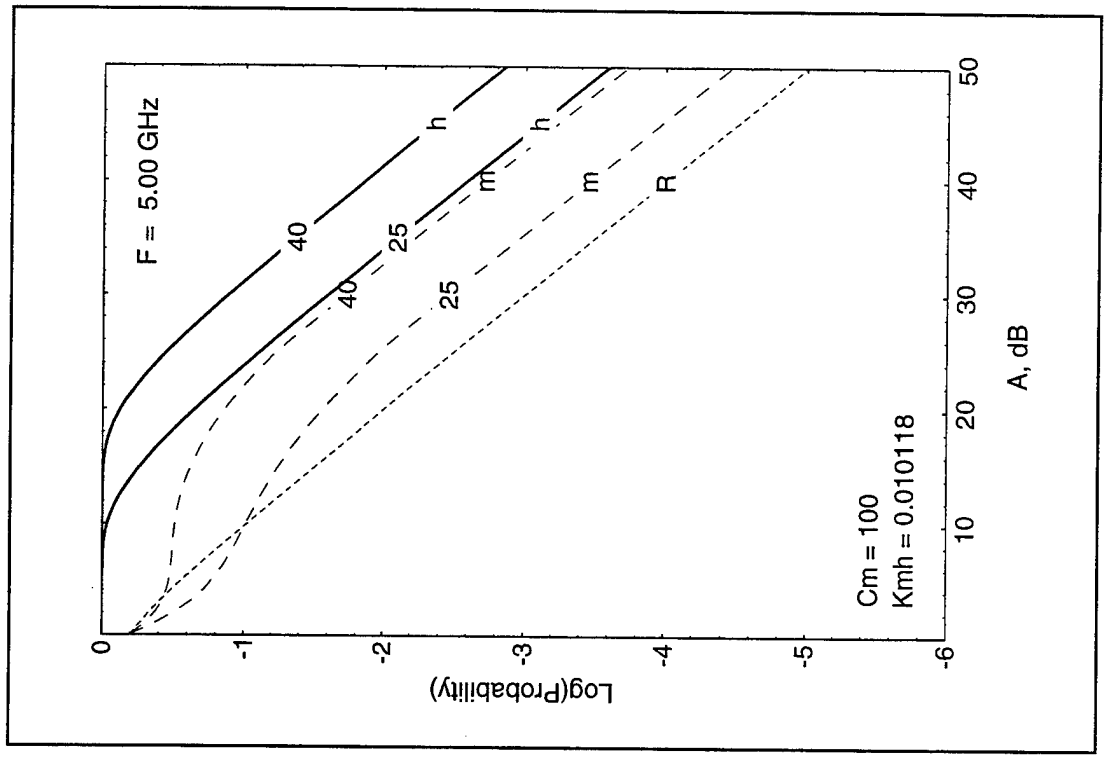


Figure 6

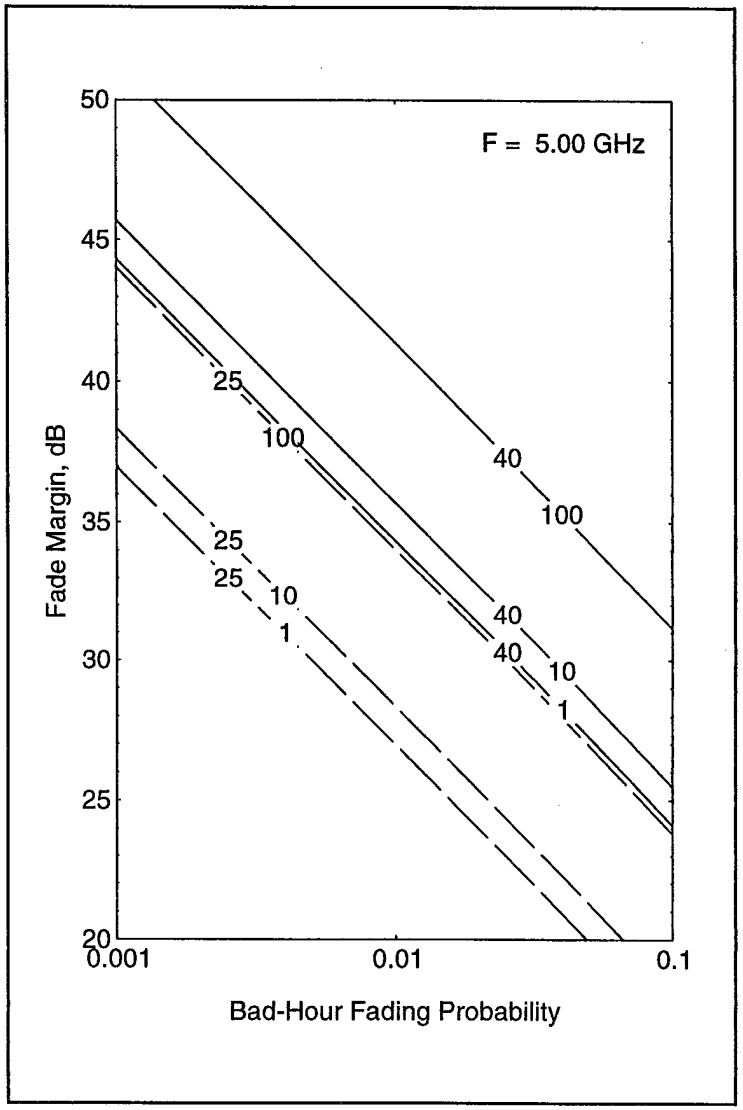


Figure 7

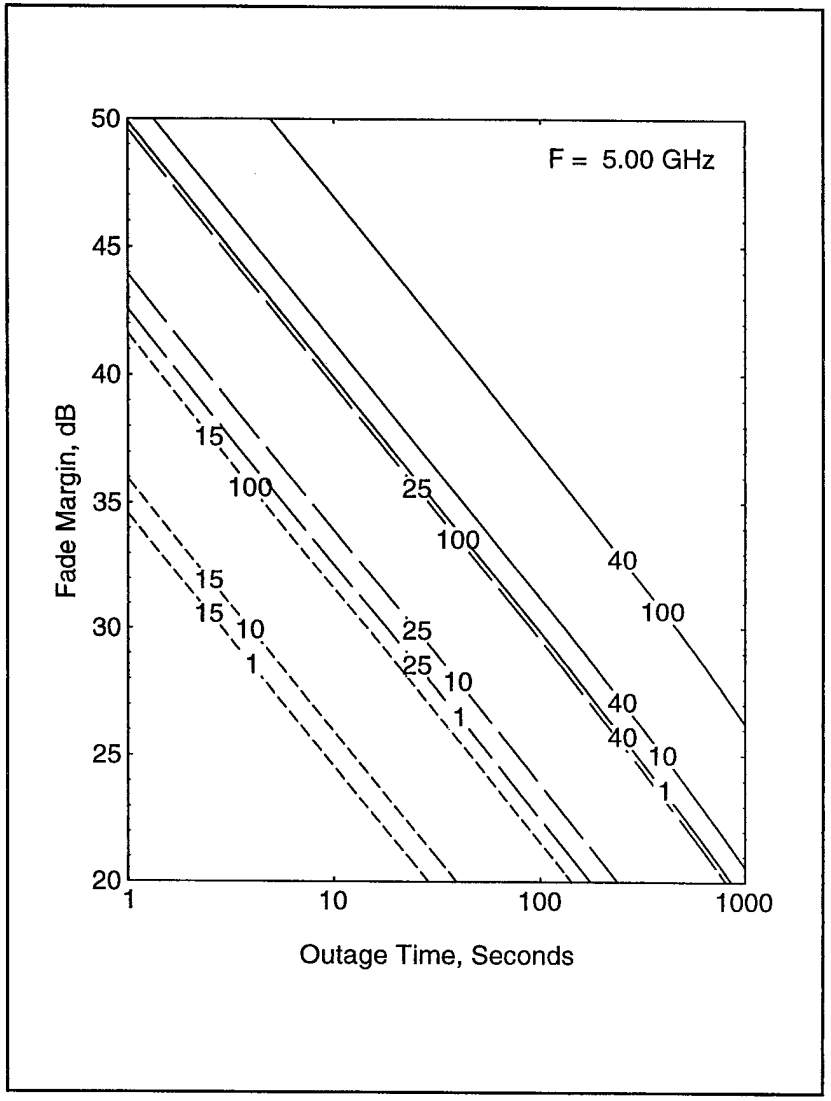


Figure 8

ATMOSPHERIC ANALYSIS CAPABILITY TO SUPPORT ELECTROMAGNETIC APPLICATIONS

Larry Phegley, Naval Research Laboratory,
7 Grace Hopper Ave.
Box 2
Monterey, CA 93943-5502

CAPT Daniel W. Merdes, USNR
Office of Naval Research
Reserve Unit: NR ONR SCI&TECH HQ 106
Civ Address: Applied Research Laboratory
The Pennsylvania State University
P O Box 30
State College PA 16804-0030

LCDR Brian Daly, USNR
Office of Naval Research
Reserve Unit: NR ONR SCI&TECH 510
Civ Address: National Weather Service Training Center
617 Hardesty
Building 9
Kansas City, Mo 64124-3097

Dr J W Chu, Naval Research Laboratory,
7 Grace Hopper Ave
Box 2
Monterey, CA 93943-5502

Introduction

As tactical applications and users have become more sophisticated, a need for a consistent four dimensional volume of environmental information has become evident. This paper discusses the Naval Research Laboratory's first effort to provide a three dimensional consistent volume of atmospheric data to support an electromagnetic propagation application, the Radio Physics Optics (RPO) model. From this experience, and as computer workstations become more powerful the Laboratory hopes to be able to forecast as well as analyze the atmospheric volume adding the fourth dimension, time. This work was funded by the Office of Naval Research and the Oceanographer of the Navy through the Space and Naval Warfare Systems Command.

The Ship Anti-submarine warfare Readiness Effectiveness Measurement (SHAREM) 110A exercise in the Arabian Gulf was chosen as the first opportunity to test such an analysis scheme in an operational setting. SHAREM exercises are coordinated by the Surface Warfare Development Group (SWDG) in Little Creek, Virginia. They are Naval Exercises that have a scientific bent to them allowing for the investigation of a particular phenomenon.

One of the areas that SHAREM 110A was designed to examine was the radar ducting environment of the Arabian Gulf. The participating vessels were an Aegis Cruiser USS Lake Erie, a destroyer USS David R Ray, a frigate USS Vandegift and a research vessel from the Naval Oceanographic Office USNS Silas Bent. To provide observation data for the analysis, the USNS Silas Bent, USS David R Ray, and USS Lake Erie all had a balloon sounding capability. A rocketsonde was also installed aboard USS Lake Erie and a helicopter with a dropsonde capability was embarked aboard USS Vandegrift. Special surface meteorological sensing instruments were installed aboard USS Lake Erie. Five fights by an instrumented C-130 provided by the Met Research Flight of the UK provided data which will be used to verify the analysis.

Operational Concept of SHAREM 110A

Figure 1 shows the communications links which were utilized during the exercise. The data flow starts with the running of a regional forecast model at the Fleet Numerical Meteorology and Oceanography Center (FNMOC). This model, the Naval Operational Regional Atmospheric Prediction System (NORAPS) is a 36 level model that was run at a 20 km horizontal resolution. Meteorologists are accustomed to using model data which has been interpolated on constant pressure levels such as the 500 mb surface. In this case as much vertical structure as possible was required. The model data was provided to the site in Bahrain (Naval Pacific Meteorology and Oceanography Detachment, NPMOD, colocated with the U S Naval Central Command, NAVCENT) in Sigma-P coordinates. Sigma-P is the ratio of the grid pressure to the surface pressure. The lower 18 levels (up to approximately 10,000ft) of wind (U and V components), temperature, and mixing ratio and the terrain pressure and surface temperature were sent to NPMOD. This model data was provided at forecast intervals of 3 hours from 9 hours past the model analysis time (0Z or 12Z) out to 24 hours.

The observations from the participating ships were sent back to NPMOD on a circuit known as the Officer in Tactical Command Information Exchange System (OTCIXS). This is a satellite communications link for ships operating together. The World Meteorological Organization (WMO) codes were used to encode the observations using the standard definitions of significant data points (Federal Meteorological Handbook No 4). The analyses were later redone in Monterey using radiosonde, dropsonde, and rocketsonde data which were reprocessed from data taken every 2 seconds in an attempt to capture more detail than required by the standard definition (except for the USS David R Ray's soundings where only the encoded message was available).

At NPMOD the model data was fuzed with the observation data (both land and ship observations) using the analysis techniques to be discussed in the next section and 3-D volumes of modified refractivity index (M-Units) were calculated. A small subset of M-Units plus the parameters used to calculate the evaporative duct height were packaged for transfer to USS Lake Erie via OTCIXS for use with RPO.

Techniques utilized for data fusion at NPMOD

The Multivariate Optimum Interpolation (MVOI)(Barker 1992) is the central component of the data fusion process. The MVOI is the analysis scheme used at FNMOC to analyze the atmosphere in preparation for forecast model initialization. As implemented at FNMOC, MVOI is a geostrophically constrained analysis of heights and winds on standard meteorological pressure surfaces (1000 - 10 mb). The application has controls for not using the geostrophic constraint during the analysis. The MVOI is capable of analyzing a wide array of different atmospheric observation types including standard surface observations, radiosonde observations, aircraft observations, Special Sensor Microwave Imagery (SSMI), satellite soundings, and cloud track winds.

During SHAREM 110A the goal was to support the RPO application with vertical profiles of refractivity derived from moisture and temperature along with the surface wind speed. These profiles would need to capture as accurately as possible the vertical atmospheric structures. In order to attempt to capture the vertical features desired, the sigma-P definitions from the supporting NORAPS model were used. The lowest 18 sigma-P ratios were multiplied by a surface pressure from one of the participating units to define 18 analysis levels between the surface and approximately 10,000 ft. Table 1 shows the sigma-P ratios used.

To provide data for each analysis level the profile data (radiosondes, dropsondes, and rocketsondes) were interpolated to the level using log- P as the vertical coordinate.

0.999	0.969	0.91
0.9965	0.96	0.895
0.993	0.95	0.87
0.989	0.94	0.83
0.984	0.93	0.77
0.977	0.92	0.6925

Table 1: Sigma-P Ratios used during SHAREM 110A

Since MVOI does not provide any information about the moisture distribution, a Cressman dewpoint depression analysis was provided by Dr James Goerss of NRL. The Cressman analysis only uses radiosonde data in the analysis. The Cressman analysis is performed in three passes with the initial radius of influence set to eight grid points.

During the exercise the temperatures were computed from the layer thicknesses. Figure 2 shows one of the resulting analyzed profiles. The noise in the profile was recognized as temperature buckling (Barker 1980). This is caused by small errors in the height analysis which result in large temperature deviations for thin layers. To correct the temperature buckling problem a Cressman temperature analysis was also implemented. The heights from the MVOI and the temperatures from the Cressman analysis were then placed into hydrostatic balance (Barker 1980). Figures 3 through 6 show results after these changes.

Figure 3 is the temperature and moisture profiles from a single sounding from the USS Lake Erie. The figure shows that the analysis forced the profile closer to the observed profile demonstrating some ability to reflect some of the structure in the sounding. However, the higher in the volume the smoother the analyzed profile becomes due to the reduced density of analysis levels.

Figures 4 through 6 are from a time when three simultaneous soundings were taken. Here a low level inversion is analyzed based on the feature from the USNS Silas Bent sounding. In this case the USS Lake Erie is on the northwest side of the other ships. The USNS Silas Bent is about one grid point south and USS David R Ray is about one grid point to the east.

In digitized (gridded) atmospheric data it is generally understood that the value at the grid point represents the average value of that parameter in the volume surrounding that grid point. The Cressman analysis techniques not only averages within the grid volume but allows data from, in this case, 8 grids points away to have an effect on the value at a specific grid point. Here the interplay of the 3 radiosondes has produced a shallow inversion over the three depicted locations. The soundings would seem to show that the inversion only existed at the location of the USS Silas Bent. Atmospheric features that are smaller than the horizontal spacing of the grid will be miss represented as in this example.

Summary

The analysis software developed to support the SHAREM exercises has shown skill in improving forecast fields of temperature and moisture by using real time observations. This improvement includes modifying the values of the points closer to those observed and more accurately depicting the vertical structure. These volumes of data will next be checked against an independent data set provided by the Met Research Flight instrumented C-130 to quantify the accuracy.

References

Barker, E. H., 1980: Solving for Temperature Using Unnaturally Latticed Hydrostatic Equations. Monthly Weather Review Vol 108 No 8 1260-1268

Barker, E. H. 1992: Design of the Navy's Multivariate Optimum Interpolation Analysis System. Weather and Forecasting, Vol 7 No 2 220-231

Federal Meteorological Handbook No 4, Radiosonde Code (Standards and Procedure for the Coding of Radiosonde Reports), Revised January 1,1976, Second Edition, U S Department of Commerce, U S Department of Defense, U S Department of Transportation

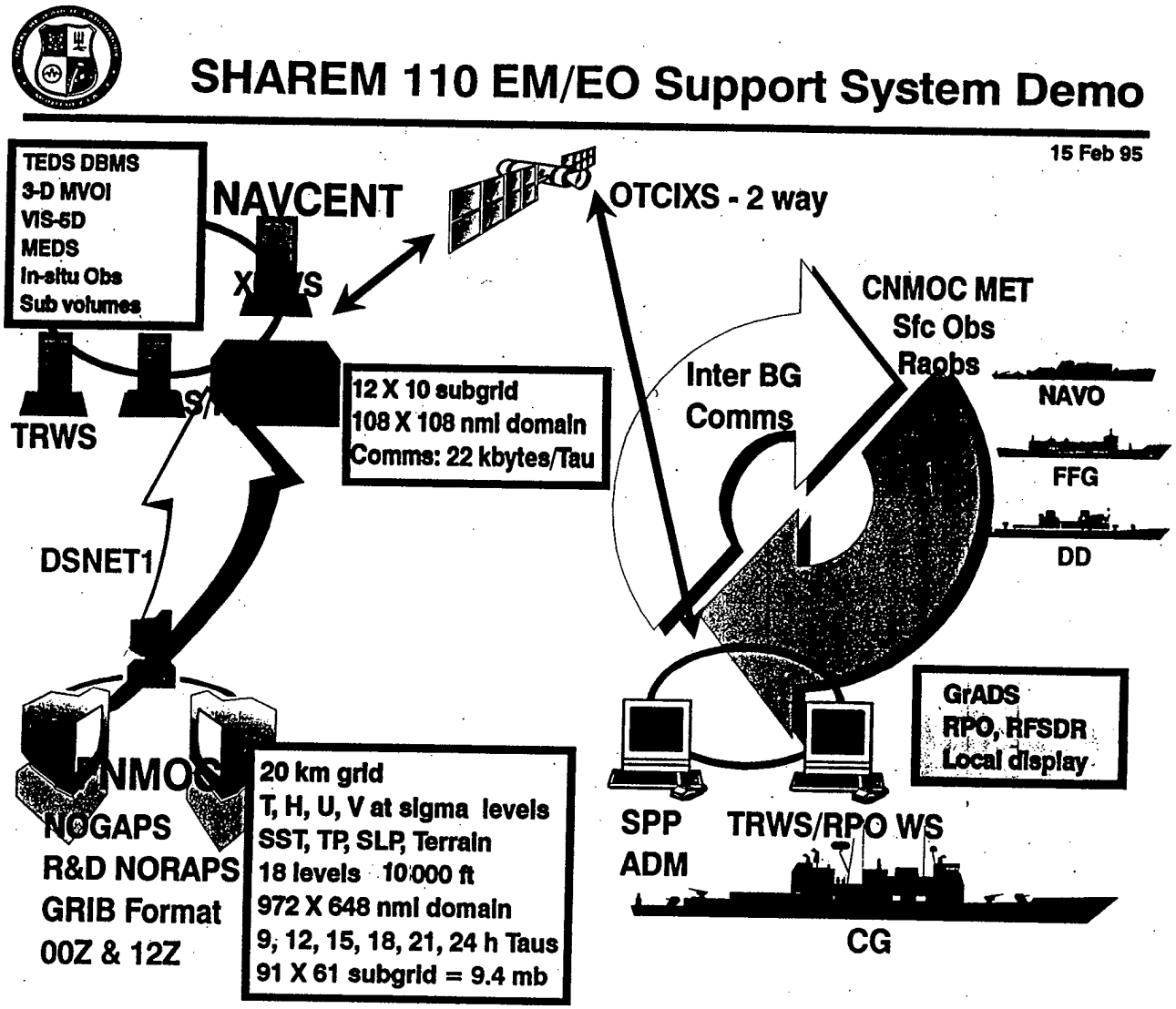


Figure 1: Data Transfers During SHAREM 110A

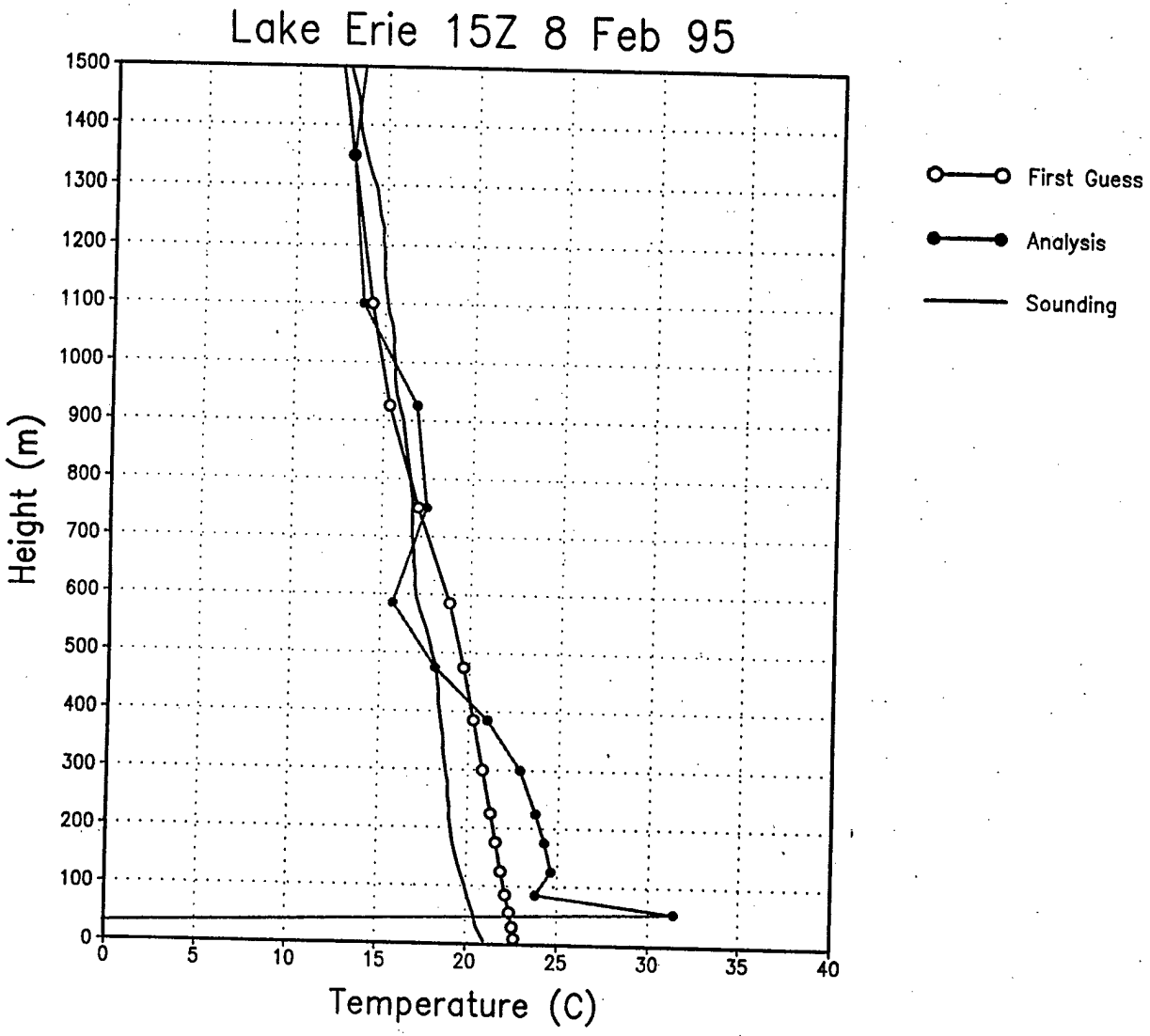


Figure 2: Temperature Buckling

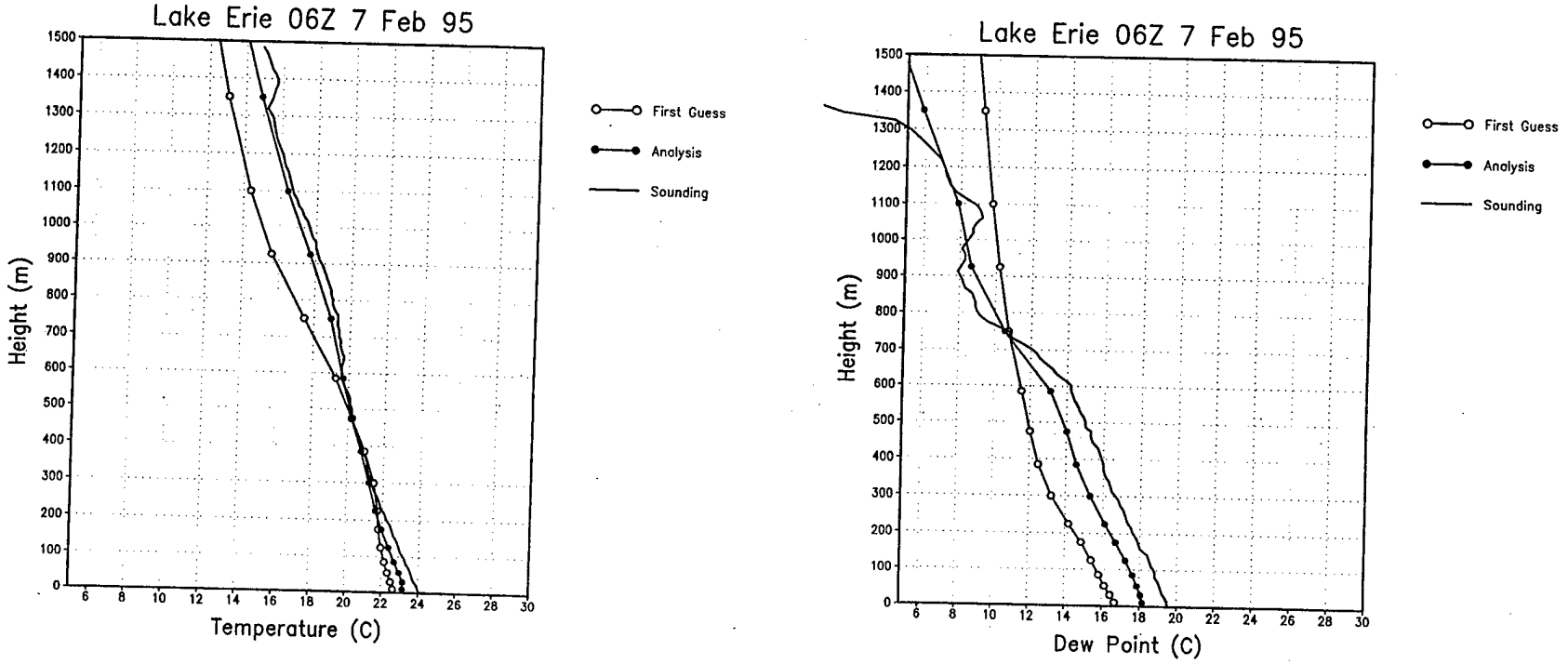


Figure 3: Temperature and Moisture Profiles for Single Sounding Case

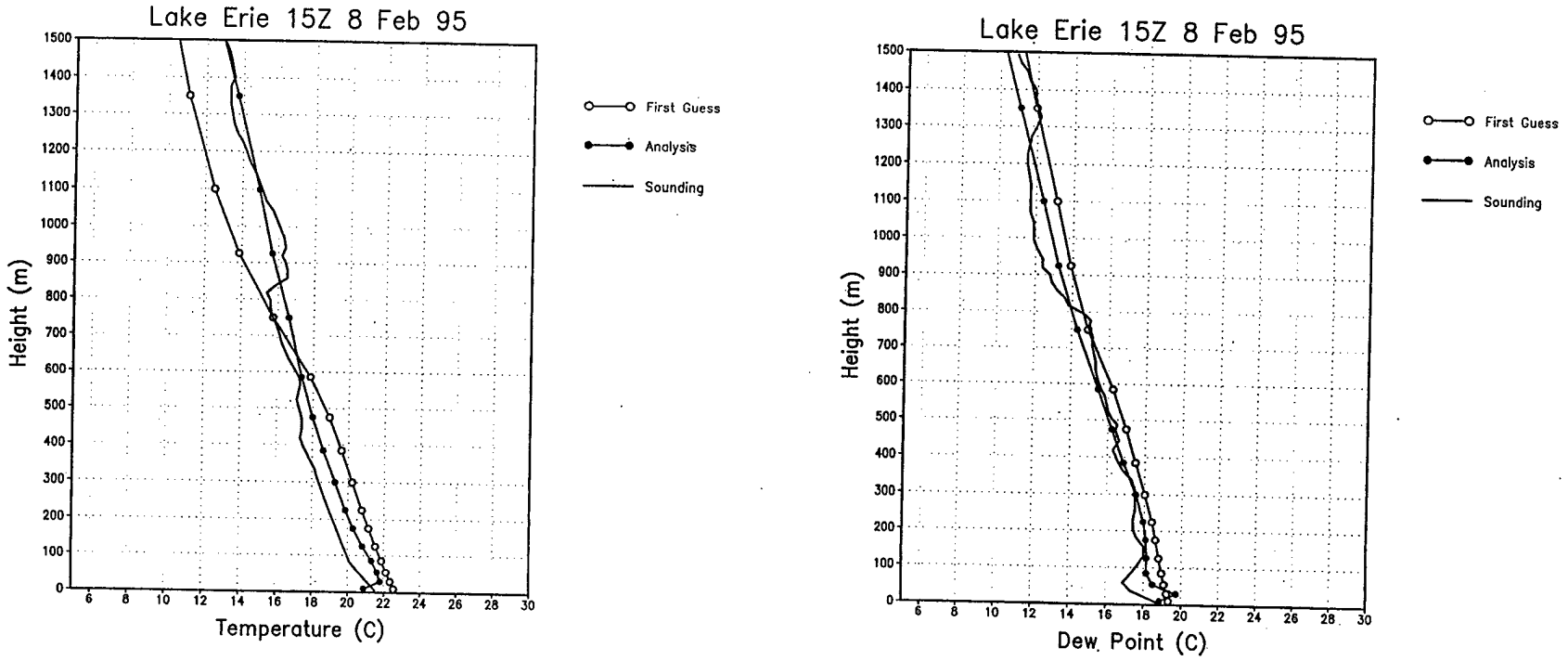


Figure 4: Temperature and Moisture Profiles from USS Lake Erie

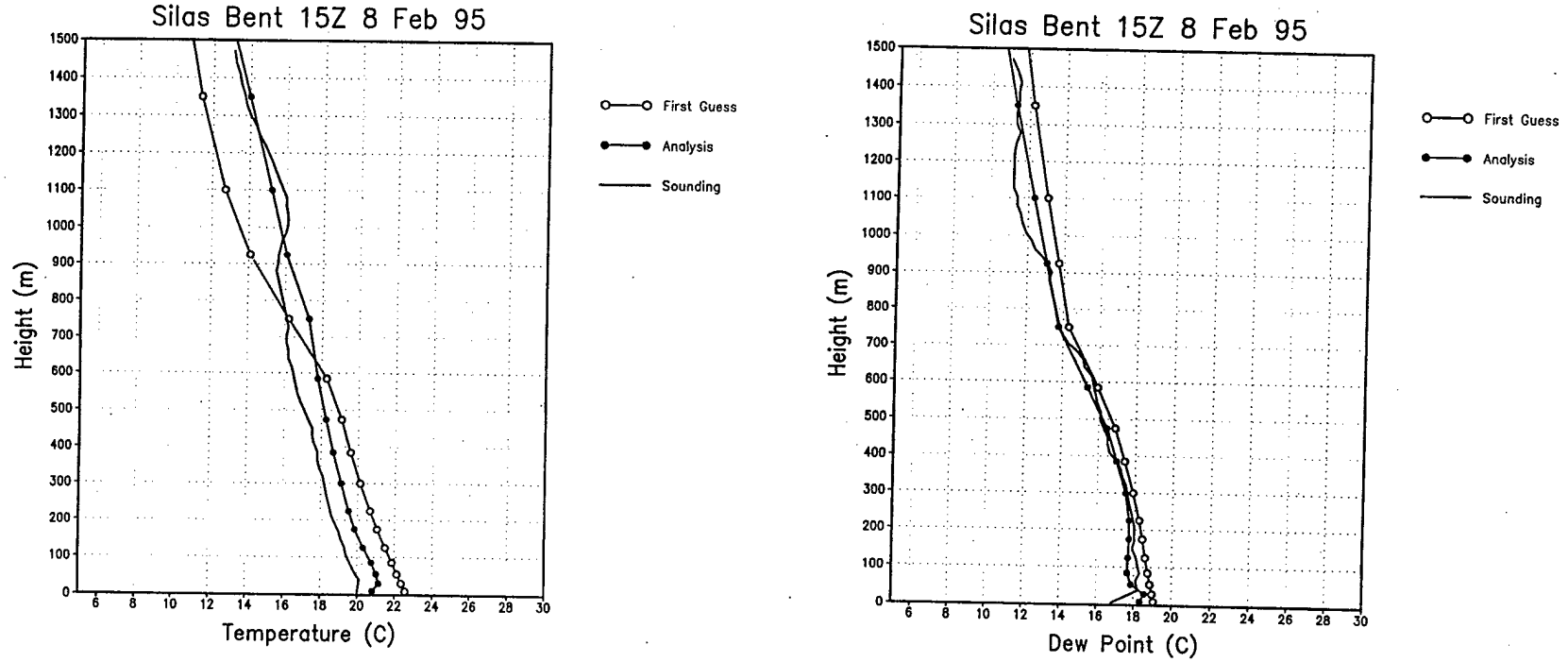
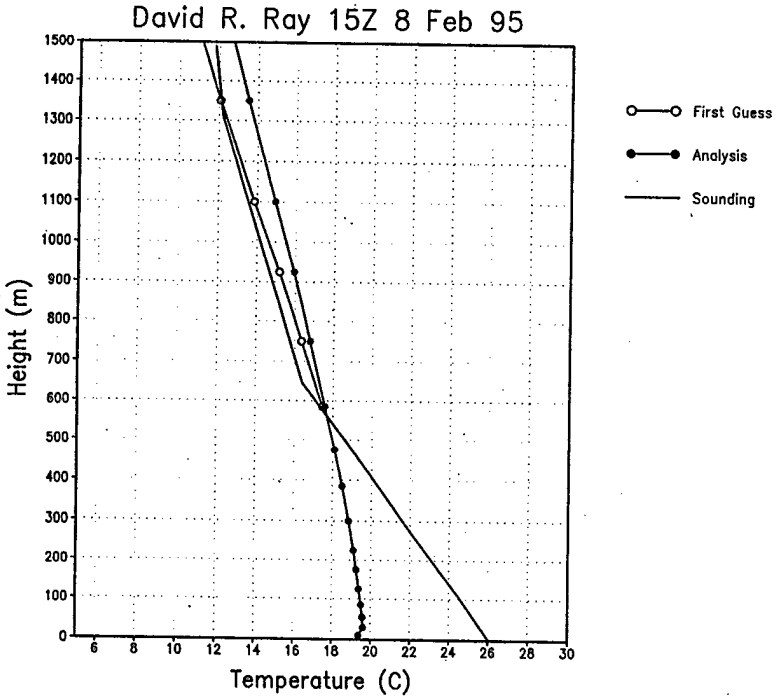


Figure 5: Temperature and Moisture Profiles from USNS Silas Bent



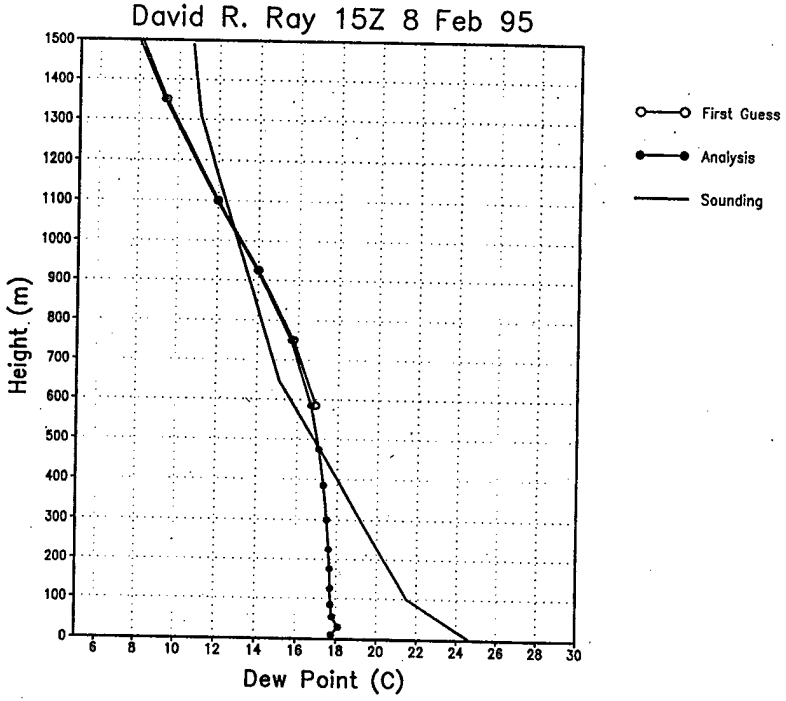


Figure 6: Temperature and Moisture Profiles from USS David R Ray

SEAWASP: A PROTOTYPE SYSTEM FOR SHIPBOARD ASSESSMENT BASED ON IN SITU ENVIRONMENTAL MEASUREMENTS

G. C. Konstanzer, J. R. Rowland, G. D. Dockery
J. J. Sylvester, M. R. Neves, D. R. Davis
The Johns Hopkins University Applied Physics Laboratory
Johns Hopkins Road
Laurel MD 20723-6099
Phone: (301)953-6000 ext.7518 Fax: (301)953-5458
E-mail: gerald.konstanzer@jhuapl.edu

Introduction

This paper describes a prototype tactical decision aid called SEAWASP (Shipboard Environmental Assessment/WeApon System Performance), developed by the AEGIS Shipbuilding Program to demonstrate the feasibility of in situ estimation of radar and weapon system performance. The need for this capability has been made clear by the wide range of radar performance experienced by AEGIS ships in operational exercises and confirmed in post-test analyses during the past 12 years. AN/SPY-1 track initiation ranges have been observed to vary by factors of two or more for the same target due to atmospheric conditions; surface clutter conditions have also been seen to vary enormously. Both of these effects are most severe in particular littoral environments where strong refractive inhomogeneities are prevalent due to land influences and land backgrounds result in large clutter returns. Furthermore, the importance of accounting for these effects is heightened as anti-ship missile threats develop toward increasing speeds and decreasing radar cross sections and altitudes.

The initial goal of SEAWASP is to aid in the selection of AN/SPY-1 radar configuration parameters for the variety of environments encountered by AEGIS ships. Specifically, radar operators frequently reduce sensitivity to remove unwanted clutter tracks without being able to assess the associated impact on target detection and track capability. Large or extended surface clutter is often due to surface ducting conditions. In these situations, reducing radar sensitivity may be justifiable since the ducting also increases the power on low-altitude targets. However, in other cases this is not true and sensitivity could be reduced to a point where tracking performance is significantly degraded. SEAWASP makes radar operators aware of impacts on performance of radar configuration changes in the prevailing environment. In addition to aiding AN/SPY-1 configuration, SEAWASP can also aid in depth-of-fire assessments for weapons doctrine selections and in decisions regarding ship placement.

The development of SEAWASP was a natural outgrowth of earlier environmental characterization and system performance modeling efforts at JHU/APL associated with quantitative post-test analysis of AEGIS exercises. During these efforts a high-fidelity propagation model (References 1 through 4), environmental measurement techniques (References 5 through 7), and an AN/SPY-1 simulation were developed and exercised extensively. In the course of this work, an ability to reconstruct signal levels within nominally 5 dB, and firm track ranges to within 10%, in the low-altitude region was demonstrated (Reference 2). These successes depended, however, on the acquisition of timely, high-resolution atmospheric data. Work is underway to quantify the resolution required for accurate propagation and radar performance predictions (References 8 and 9).

The approach to performance assessment used in SEAWASP was first demonstrated on an AEGIS cruiser, the USS LEYTE GULF (CG 55), in 1988. This work was reported during an NATO AGARD (Advisory Group for Aerospace Research & Development) meeting devoted to discussion of operational decision aids for dealing with propagation effects (Reference 10). The

present SEAWASP program was initiated in 1992, and shipboard testing of the environmental data acquisition portion of SEAWASP began in 1993. Periodic testing aboard AEGIS cruisers, including the USS PORT ROYAL (CG 73) and USS LAKE ERIE (CG 70), has continued up to the present. The two SEAWASP systems currently installed on the USS ANZIO (CG 68) and USS CAPE ST GEORGE (CG 71) are the first fully autonomous versions of SEAWASP, and will undergo at-sea evaluation for 9 to 12 months.

General System Description

A high-level depiction of SEAWASP as installed on CGs 68 and 71 is illustrated in Figure 1. SEAWASP is comprised of two primary subsystems: the Environmental Characterization and Radar Performance Assessment Subsystems. The former is described only briefly here since it is the subject of a companion paper in this conference. A description of Environmental Data Processing functions is shared between the two papers. The primary focus of this paper is the Radar Performance Assessment Subsystem.

The basic components of the Environmental Subsystem are two meteorological masts (met masts), rocketsondes, floatsondes, and a data acquisition/processing system. Each met mast contains a microprocessor controlled instrument package that measures air temperature, relative humidity, and wind speed/direction at a nominal height of 9 meters above the sea surface. The starboard met mast also includes a GPS antenna/receiver, a compass, and IR temperature sensors. The sonde receive antenna, used for both the rocketsondes and floatsondes, is mounted on the port met mast.

Acquisition, processing, management, and communication of environmental data are coordinated by the Control Manager program which runs on a RADISYS 486 processor board under the OS/2 operating system. This processor board complies with the VME 6U standard adopted by the Navy and is installed in the NGP AN/UYQ-70 (Next Generation Peripheral) console in the ships' computer rooms (Computer Central). This subsystem produces refractivity profiles that characterize propagation conditions in the ship's vicinity. The processing algorithms include surface layer (evaporation duct) models, data smoothing/assimilation/quality control algorithms, and expert-system procedures which monitor changing conditions and are planned to make automatic recommendations regarding rocketsonde and floatsonde deployment. Processed data from met masts and floatsondes are used primarily for evaporation duct estimation, while temperature/pressure/humidity profiles from the rocketsonde system characterize refractive structures above the evaporation duct. These data are "blended" to form a complete characterization of the refractivity profile in the ship's vicinity. The remainder of the Environmental Subsystem processing functions are described in the companion paper.

As seen in Figure 2, the Radar Performance Assessment Subsystem is comprised of a propagation model (TEMPER), an AN/SPY-1 radar performance model (FIRMTRAK), server programs which control data flow and model execution, and a Human-Machine Interface (HMI). Functionally, this part of SEAWASP accepts refractivity profiles from the Environmental Subsystem and computes and displays AN/SPY-1 performance estimates for the prevailing local environment, based on 'live' radar settings and selected target options. Some of these radar settings are chosen automatically by the combat system, not by an operator. SEAWASP also provides the capability for an operator to enter trial radar doctrine and manually initiate performance assessments. Results are automatically displayed along side the performance assessments based on the 'live' radar settings.

Most of the development effort for the Performance Assessment subsystem focused on designing and implementing the HMI and client-server processes, integrating tactical AN/SPY-1 radar settings via existing ship systems, and configuring hardware and software for robust, autonomous shipboard operation. Propagation and AN/SPY-1 radar models were taken from

proven versions used for in-house analysis with no substantial modification.

The Radar Performance Assessment portion of the system runs on three HP 743i processors, each with a dedicated 2-gigabyte hard disk, and an X-station. The processors are in the VME 6U form factor, are mounted in the NGP AN/UYQ-70 console, and run under the HP-UX operating system. The X-station and trackball are mounted above the SPY-1 RSC (Radar System Controller) console in CIC (Combat Information Center) as shown in Figure 3. The X-station in CIC is needed since the RSC console in Baseline 5 Phase 1 is not MOTIF/X-Windows compatible. The processors and X-station communicate via a SEAWASP ethernet LAN (Local Area Network).

The two AEGIS ships currently hosting SEAWASP also have an experimental tactical display system called the Command Display & Control System (CDCS), prototype to the AEGIS Display System MK 6 presently under development. CDCS can drive two of the four large-screen displays in CIC. The CDCS experiment also includes installation and operation of the Navy's new MOTIF/X-Windows capable AN/UYQ-70 consoles in CIC. SEAWASP's access to the 'live' radar settings is via a router connection to the CDCS display LAN. In addition to making combat system data available, this connection opens the potential for the MOTIF-compatible SEAWASP displays to be available to all of the AN/UYQ-70 consoles in CIC.

Propagation Model (TEMPER)

SEAWASP presently relies on the Tropospheric ElectroMagnetic Parabolic Equation Routine (TEMPER) to calculate RF propagation factor (References 1 through 4). TEMPER calculates propagation factor based on refractivity profiles supplied by the Environmental Characterization Subsystem. An input file specifies antenna and frequency parameters corresponding to the lowest beam position of the AN/SPY-1 radar. TEMPER calculations are performed for the lowest 1500 feet of the atmosphere and out to 128 nautical miles in range. These parameters are chosen to support the current SEAWASP implementation which estimates AN/SPY-1 performance for low-elevation targets.

The intention is to eventually replace TEMPER with the Navy Standard propagation model, RPO (Radio Physical Optics) when it is upgraded to achieve TEMPER's fidelity for the low elevation region. With the speed of a hybrid program like RPO, SEAWASP could address the full AN/SPY-1 coverage space. Also, as propagation over land is introduced, models such as the Advanced Propagation Model (APM), currently under development by the Navy, will be implemented.

AN/SPY-1 Firm Track Model (FIRMTRAK)

The FIRMTRAK program uses an event-driven, Monte Carlo simulation to represent track initiation, track maintenance, and drop track processes of AN/SPY-1. FIRMTRAK randomly varies several parameters, such as target altitude, on each Monte Carlo iteration to accumulate probabilities of tracking a target. System noise and target RCS parameters are represented by multiple draws from a random number generator. Other relevant parameters in FIRMTRAK include transmit power, transmit gain, beam-shape loss, search frame time (SFT), waveform mode, baseline sensitivity, sensitivity time control (STC), pulse compression, and TEMPER-generated propagation factors. The elevation beam shape, antenna height, pointing direction, and of course, environmental effects, enter via the TEMPER propagation factor.

SEAWASP calls FIRMTRAK from a main program designed to represent the AEGIS Baseline program currently on CGs 68 and 71, Baseline 5 Phase 1. This main program accepts AN/SPY-1 parameters for baseline, sector, and subsector regions and creates the appropriate number of input sets for FIRMTRAK to represent performance for 360 degrees around own-ship. Results are displayed as ranges from own-ship corresponding to 10%, 50%, and 90% probability

of firm track. Differences in the 10%, 50%, and 90% ranges are an indicator of the sensitivity of the calculation. Track drops and re-acquisitions are represented to indicate track continuity.

Human-Machine Interface (HMI)

SEAWASP's HMI designed leveraged off of concepts and layouts already familiar to SPY operators while maintaining compatibility with developing AEGIS combat system display conventions and allowing for future growth into planned assessment capabilities. Lessons learned from at-sea evaluations of a previous SEAWASP display design were also incorporated into this version of the HMI.

The SEAWASP HMI indicates embedded hardware and software status information, permits configuration of radar and threat parameters, provides for initiation and display of performance assessments, and allows communications with rocketsonde and floatsonde launch systems. It is comprised of the following five panels: 1. 'Status Message' Panel, 2. 'System' Performance Assessment' Panel, and 3. 'Operator' Performance Assessment Panel, 4. 'Rocketsonde Launch' Panel, 5. 'Floatsonde Launch' Panel. The default display includes the first three panels (Figure 4). The following paragraphs provide a high-level description of the primary functions and options of the default panels.

'Status Message' Panel

The 'Status Message' panel (left-most panel) has three modes: Environmental, System and Operator. The Environmental mode indicates the health and activity of hardware and software in SEAWASP's Environmental Characterization Subsystem. Hardware messages are indicated as "OK" or "Not Responding" for the compass, GPS, IR surface and cloud sensors, and the port and starboard met mast microprocessors, temperature and humidity sensors, and anemometers. The need to change the desiccants in the port or starboard met mast instrumentation packages is also indicated. Environmental Software Status Messages indicate when the data acquisition programs for met masts (MAST), rocketsonde (ROCKET), floatsonde (FLOAT), and the processing programs for evaporation duct modeling (EVAP DUCT), and Rocketsonde/Evaporation Duct merging (RED) are "Active" or "Inactive".

Several Alert Messages can appear automatically in the lower part of the 'Status Message' panel. These alerts can indicate rocketsonde or floatsonde launch requests ore a variety of error conditions. Requests to launch rocketsondes or floatsondes are entered via a small, hand-held I/O terminal from the aft VLS deck. This I/O terminal consists of an integrated display and key pad and plugs into the starboard met mast instrumentation package during rocketsonde and floatsonde launches. Because rocketsondes and floatsondes use the same receiver, they cannot be operated simultaneously. An attempt to do this triggers alert error messages.

The purpose of the System and Operator modes of the 'Status Message' panel is to indicate, sector by sector, warnings for performance displays in the corresponding Performance Assessment Panels. Because the functionality and layout of the 'System' and'Operator' Performance Assessment panels are very similar, their associated 'Status Message' panel modes are functionally identical.

'System' and 'Operator' Performance Assessment Panels

The 'System' and 'Operator' Performance Assessment panels are similar in function and appearance but are intended for different purposes. The purpose of the 'System' panel is to react automatically to updates in radar parameters and environmental data to maintain a near real-time assessment of current radar capability. In contrast, the 'Operator' panel allows entry of hypothetical radar and threat data and manually initiated FIRMTRAK calculations. The resulting performance plot in the 'Operator' panel can be compared directly to the plot of current capability in

the 'System' window.

The 'System' and 'Operator' Performance Assessment panels have "Control" pulldown menus that allow manual initiation of FIRMTRAK runs from either panel. The 'System' panel's "Control" menu additionally allows the operator to open 'Rocketsonde' or 'Floatsonde Launch' Panels, or to shutdown or reset the SEAWASP system.

Both 'System' and 'Operator' panels have "Radar," "Target," and "Environment" modes. The "Radar" mode contains a Radar Doctrine Window with a layout similar to that of the RSC console in CIC. There are Global and Baseline pages, and eight Sector and Subsector pages. The "Radar" mode also contains a Radar Performance Window containing plots of radar capability based on FIRMTRAK results. These plots are "tied to" the doctrine window such that, as an operator pages through doctrine, the corresponding region in the Radar Performance Window is indicated. A PPI view is shown by default; a range-altitude plot for each sector is available.

Trial doctrine can be entered in the 'Operator' Panel by clicking the cursor on a parameter in the Radar Doctrine Window. This opens a secondary window which presents options for that parameter, selectable using radio buttons or sliders. After manually altered parameters are saved, they are identified as "Manual" instead of "AN/SPY-1" in the Doctrine Window. Modified parameters can be reset to the values active in the cmobat system individually or globally, throughout the 'Operator' Radar Doctrine window. Manual configuration of trial radar doctrine is not allowed in the 'System' panel since its radar performance plots are intended to always represent current, actual SPY-1 performance.

The "Threat" mode of both Performance Panels allows the operator to select from a library of threats or define his own constant altitude threat by choosing a radar cross section, altitude, and speed. The "Environment" mode of both Performance Panels presents a plot of the RF propagation factor used in the performance assessment of that panel.

Server Processes of the Radar Performance Assessment Subsystem

A substantial amount of software has been developed to support integrating and controlling SEAWASP's models, data interfaces, and displays for embedded operation. Primary among these is the Model Server (MS) program. This program handles interprocess communications with the Environmental Data Processor, the HMI, Task Server (TS) programs, and the two server programs that receive 'live' radar doctrine: CDCS_Interface Server (CDCSIS), and CEP_Interface Server (CEPIS). The TS programs are responsible for starting and monitoring TEMPER and FIRMTRAK in response to requests by MS. There is one TS process for each processor. CDCSIS is responsible for receiving, processing, and forwarding to MS all SPY-1 doctrine, except for SPY-1 Sensitivity Time Control (STC) Fence parameters. These data are not passed from SPY to the C&D computer and, therefore, are not available to the CDCS LAN or SEAWASP. The Cooperative Engagement Capability's (CEC) Cooperative Engagement Processor (CEP) does, however, have access to STC Fence parameters from the SPY computer and broadcasts the data to the CDCS LAN for SEAWASP. CEPIS is responsible for receiving and processing STC Fence messages from the CEP for MS.

MS makes requests of TS for model runs due to three types of events: 1. Receipt of new environmental data from the Environmental Subsystem, 2. receipt of new radar doctrine data from either CDCSIS or CEPIS, and 3. operator requests from the HMI. When new environmental data is received, MS determines which processors is least busy and requests a TEMPER runs from the corresponding TS process. Upon TEMPER 's completion, TS starts FIRMTRAK based on the resultant propagation factor table, using 'live' radar doctrine from CDCSIS and CEPIS and selected target parameters from the HMI. Upon FIRMTRAK's completion, MS passes results to the HMI for display. Likewise, for new radar doctrine data, if CDCSIS or CEPIS indicate that

there is a "significant" change in at least one SPY parameter, MS selects a TS to start a FIRMTRAK run based on the new radar parameters and the most recent TEMPER propagation results. Results are again used to create new performance plots.

Operator-initiated performance assessment requests from the HMI result in MS selecting a TS, TS starting a FIRMTRAK run based on either 'live' or trial radar doctrine, and the HMI displaying results of the FIRMTRAK run.

Additional capabilities being implemented into SEAWASP provide for robust embedded operation. These capabilities include monitoring the health of processes, restarting failed processes, gracefully shutting down the system when power is switched off or is lost, and displaying additional fault messages on the HMI.

Field Test Experience

The following summarizes the test periods to date:

September 1993	Puerto Rico & Mid-Atlantic Coast	CG 71	13 Days
April 1994	Mid-Atlantic Coast	CG 68	10 Days
June 1994	Puerto Rico	CG 68	9 Days
October 1994	Kauai, HI	CG 73	19 Days
February 1995	Arabian Gulf & Gulf of Oman	CG 70	14 Days
Current	Mid-Atlantic Coast	CG 68 & 71	Ongoing

The first three periods focused on automated environmental characterization. The tested system automatically collected and processed environmental data and computed propagation factors for SPY-1 radar parameters. Testing the Radar Performance Assessment Subsystem began during the October 1994 period. The latest SEAWASP version, presently installed on CG 68 and CG 71, will remain on board these cruisers until at least Fall 1997.

Figure 5 presents raw rocketsonde and processed composite refractivity profiles form 19 October 1994; these data were collected and processed aboard CG 73 while on the Pacific Missile Range Facility (PMRF), Kauai, Hawaii. The smoothing/filtering performed by the Environmental Data Processor is clearly evident. This processor also merged a 22-meter evaporation duct profile with the smoothed rocketsonde profile. As it happens, however, the atmosphere was marginally stable and the rocketsonde profile partially captured the evaporation duct profile shape. For this reason, the merging process is not obvious in Figure 5. Figure 6 focuses on the first 200 feet of the profile, and the impact of the merger is more visible. For this case, the algorithm discards the lowest three points of the rocketsonde data, then gradually transitions from the modeled evaporation duct profile to the rocketsonde profile. This transition occurs between the duct height (22 ft) and twice the duct height (44 ft). Note that the nominal 10-to-12 foot resolution of the rocketsonde only permits 2 or 3 samples in an evaporation duct of this size. However, the good agreement between the modeled and measured profiles for the evaporation duct is encouraging.

For this particular condition, the small features in the rocketsonde profile, such as the small elevated layer at approximately 80 feet, significantly impacted the AN/SPY-1 firm track range predictions. Our experience has been that this is generally the case in all areas where we routinely conduct tests, with the exception of Puerto Rico, where knowledge of the evaporation duct alone often provides a good performance estimate.

Another type of verification test of the shipboard sensors was performed in June 1994 on the Atlantic Fleet Weapon Test Facility (AFWTF) near Puerto Rico. During this time, SEAWASP was on CG 68 and JHU/APL also had a fully instrumented civilian boat as close to the AEGIS cruiser as safety would permit. The instrument environment on board the civilian

boat was more advantageous than that of CG 68, and the civilian boat also had additional sensors at various heights. Throughout the tests, the evaporation duct estimates from the two systems agreed to within 1 meter of each other. This agreement suggested that, at least for the environments and ship behavior experienced during this period, the SEAWASP sensors were avoiding contamination from the ship environment.

The true tests of SEAWASP's effectiveness from the end-user's point-of-view occur when well-characterized, controlled, low-altitude targets are presented to SEAWASP-equipped ship. During the test events listed above, four low-altitude drone events and eight controlled manned aircraft events took place. In each case, SEAWASP firm track range estimates agreed with the observed performance with an error of less than 10%. These events included instances when the firm track range was doubled due to ducting. The authors recognize that these events still represent a statistically small sample, but every effort will be made to take advantage of future controlled target opportunities.

Finally, throughout the various shipboard tests, feedback has been solicited from the SPY-1 operators and other ship's personnel regarding the user-friendliness of SEAWASP and the various HMI features. The SEAWASP system was also presented to the AEGIS Training Center (ATC) at the Naval Surface Warfare Center/Dahlgren Division (NSWCDD). These exposures to the Navy's operational and training communities produced both strong support for the SEAWASP approach and excellent suggestions for improvements. When feasible, the suggestions have been incorporated in subsequent versions of SEAWASP. As previously mentioned, the current version is aboard CG 68 and CG 71, and it will deploy for the first time with these ships without engineering support. This deployment will test the robustness of the environmental instrumentation and computer hardware, the reliability of autonomous software, and long-term ease of use by ship operators.

Future Work

The following is a partial list areas where SEAWASP and other shipboard assessment systems would need development to support a variety of extended performance assessment capabilities including area defense and littoral operation:

1. Incorporation of high-fidelity land and sea clutter models - This will also require some clutter model development and validation. Integration of rudimentary sea clutter models and land blockage algorithms into SEAWASP are planned for late 1997.

2. Implementation of interfaces to the Naval Integrated Tactical Environmental System (NITES) via the Joint Maritime Combat Information System (JMCIS) - The purpose is for SEAWASP to have access to, and to contribute to, environmental data being distributed through the fleet, and NITES/JMCIS is the Naval Oceanographer's method for doing so. This work will be completed for SEAWASP in the next 1-to-2 years.

3. Assimilation of data from other sources (particularly data that may be available from NITES/JMCIS) - This problem is particularly challenging due to the variety of potential data sources which use different environmental quantities, and have different levels of accuracy, timeliness, and resolution. The Naval Research Laboratory in Monterey is presently working in this area. A simpler sub-problem is to accommodate range- and azimuth-varying environmental information of the same type. Such algorithms would be employed, for example, if SEAWASP data were passed to other SEAWASP-equipped ships via the Cooperative Engagement Capability Data Distribution System (CEC DDS).

4. Automation of AN/SPY-1 doctrine recommendations - The current version of SEAWASP requires the operator to employ trial-and-error in determining the best radar settings (using the Operator Performance Assessment Panel). This feature performs an intelligent search over the appropriate radar parameters and develops a recommended radar setup. An initial capability is

planned for 1997 with follow-ons over the next 2 years.

5. Development and integration of new remote sensing and environmental modeling approaches - A particularly important goal of such advances is to reduce, or eliminate, the requirement for expendables; for SEAWASP these include rocketsondes and floatsondes. The Navy, other US services, and the civilian remote sensing community are working in this area, but significant progress is likely to be long-term. However, approaches using lidars for atmospheric profiling hold considerable promise.

Acknowledgement

This work has been sponsored by the Navy's AEGIS Shipbuilding Program, PMS-400B. The authors would also like to thank the following people for their valuable participation in the development of SEAWASP: Pete Econ, Dodd Huffaker, Eric Thews, Robert Miller, Mike McCullough, Jim Darling, Paul McMullin.

References

1. J. R. Kuttler and G. D. Dockery, "Theoretical description of the parabolic approximation /Fourier split-step method of representing electromagnetic propagation in the troposphere," Rad. Sci., Vol. 26, No. 2, pp. 381-393, 1991.

2. G. D. Dockery and G. C. Konstanzer, "Recent Advances in Prediction of Tropospheric Propagation Using the Parabolic Equation," Johns Hopkins APL Tech. Dig., Vol. 8, No. 4, pp. 404-412, 1987.

3. G. D. Dockery and J. R. Kuttler, "An Improved Impedance Boundary Algorithm for Fourier Split-Step Solutions of the Parabolic Wave Equation," IEEE Trans. Ant. Prop., Vol. 44, No. 12, 1996, In Press.

4. G. C. Konstanzer and G. D. Dockery, "Progress in Modeling Tropospheric Propagation Using the Parabolic Equation," Proceedings: Conference on Microwave Propagation in the Marine Boundary Layer, 21-22 September 1988, NRL/Monterey, Monterey, CA, pages 3-3 to 3-13.

5. J. R. Rowland and S. M. Babin, "Fine-Scale Measurements of Microwave Refractivity Profiles with Helicopter and Low-Cost Rocket Probes," Johns Hopkins APL Tech. Dig., Vol. 8, No. 4, 1987, pp. 413-417.

6. J. H. Meyer and J. R. Rowland, "Instrumentation for Probing the Air-Water Interface," Oceans 91 Conference, 1-3 October 1991, Honolulu, HA. (Reprints available)

7. J. H. Meyer and J. R. Rowland, "An Instrumentation SLED for Measurement of Near-Ocean Surface Temperature, Humidity, and Water Temperature," MTS90 Conference Proceedings: Science and Technology for a New Oceans Decade, Vol. 2, pp. 489-494, 26-28 September 1990, Washington, DC.

8. G. D. Dockery and J. Goldhirsh, "Atmospheric Data Resolution Requirements for Propagation Assessment: Case Studies of Range-Dependent Coastal Environments," AGARD Conference Proceedings 567: Propagation Assessment in Coastal Environments, 19-22 September 1994, Bremerhaven, Germany, pp. 7-1 to 7-13.

9. J. Goldhirsh and G. D. Dockery, "Measurement Resolution Criteria for Assessment of Coastal Ducting," Conference Publication No. 407: ICAP'95, Vol. 2, 4-7 April 1995, Eindhoven, The Netherlands.

10. G. D. Dockery and E. R. Thews, "The Parabolic Equation Approach to Predicting Tropospheric Propagation Effects in Operational Environments," AGARD Conference Proceedings No. 453: Operational Decision Aids for Exploiting or Mitigating Electromagnetic Propagation Effects, AGARD-CP-453, pp. 18-1 to 18-9, conference held 15-19 May 1989, San Diego, CA.

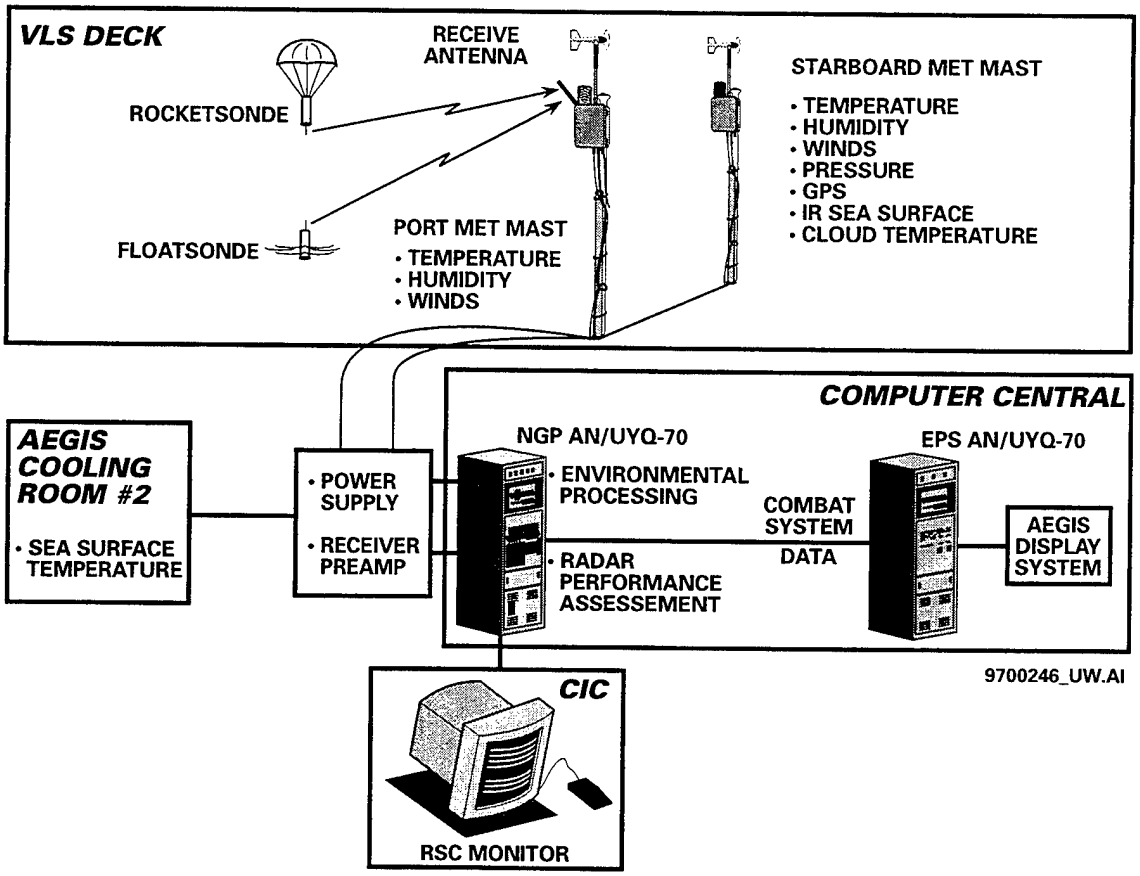


Figure 1. Overview of SEAWASP System Layout

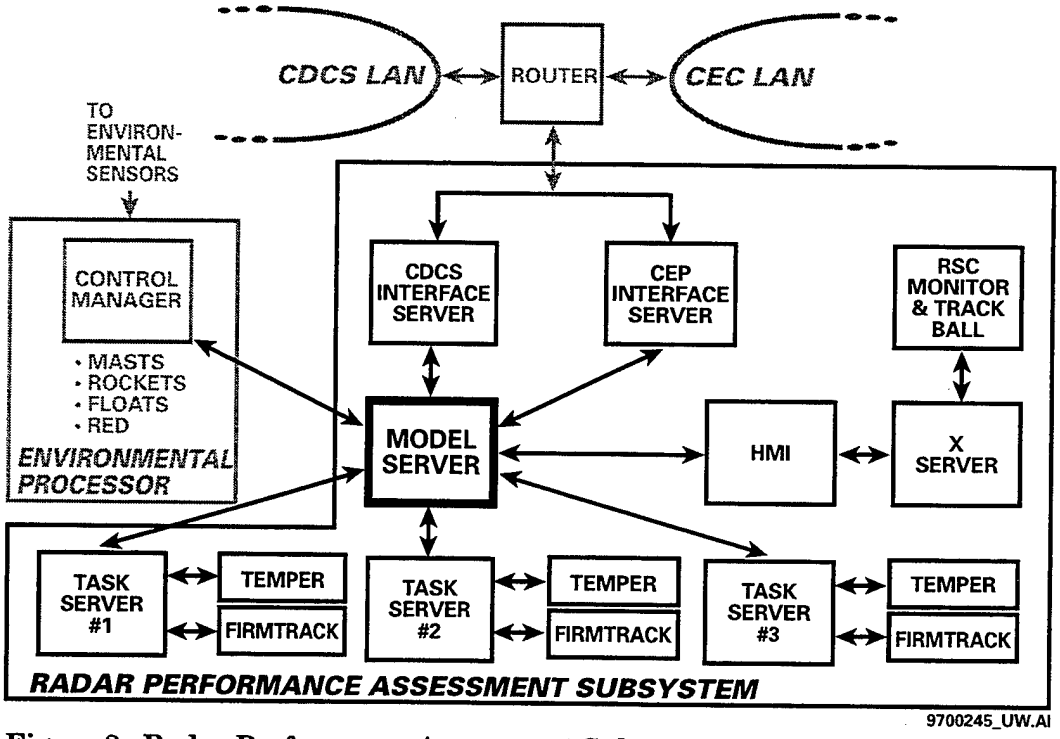


Figure 2. Radar Performance Assessment Subsystem Software Architecture

Figure 3. SEAWASP X-Station Near SPY RSC Console in CIC of CG68

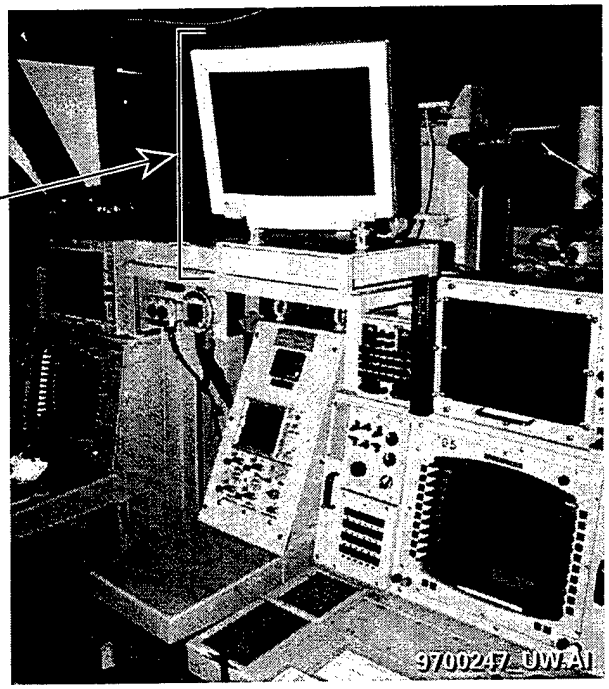
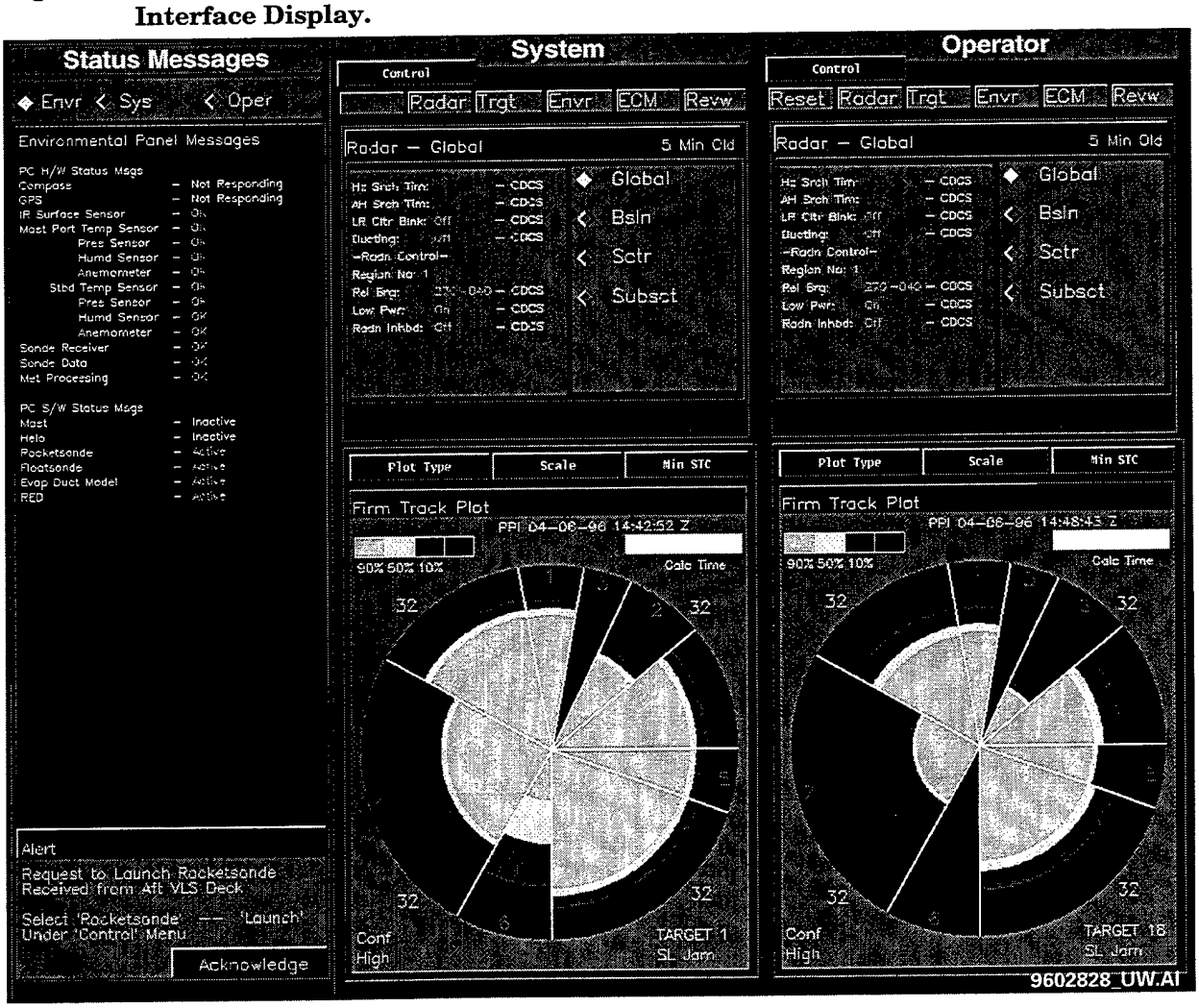


Figure 4. SEAWASP Human-Machine Interface Display.



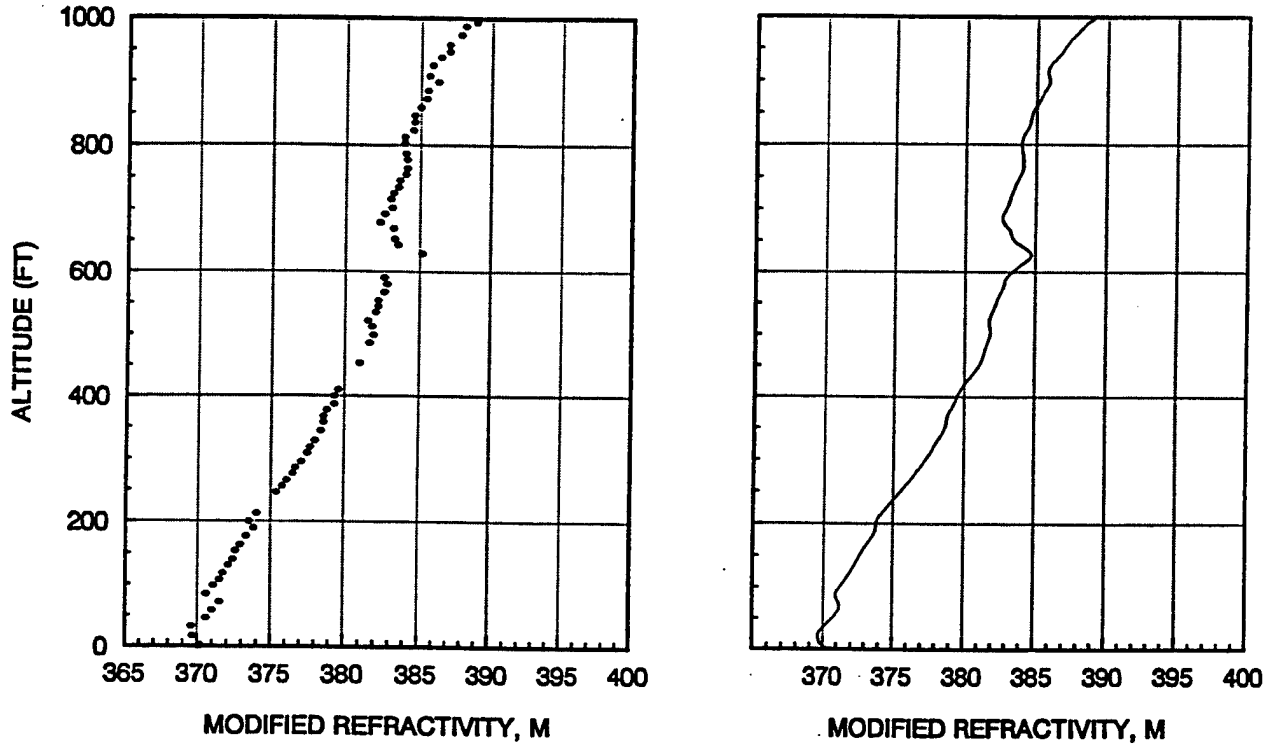


Figure 5: Raw rocketsonde and composite refractivity profiles from CG 73,19 October 1994

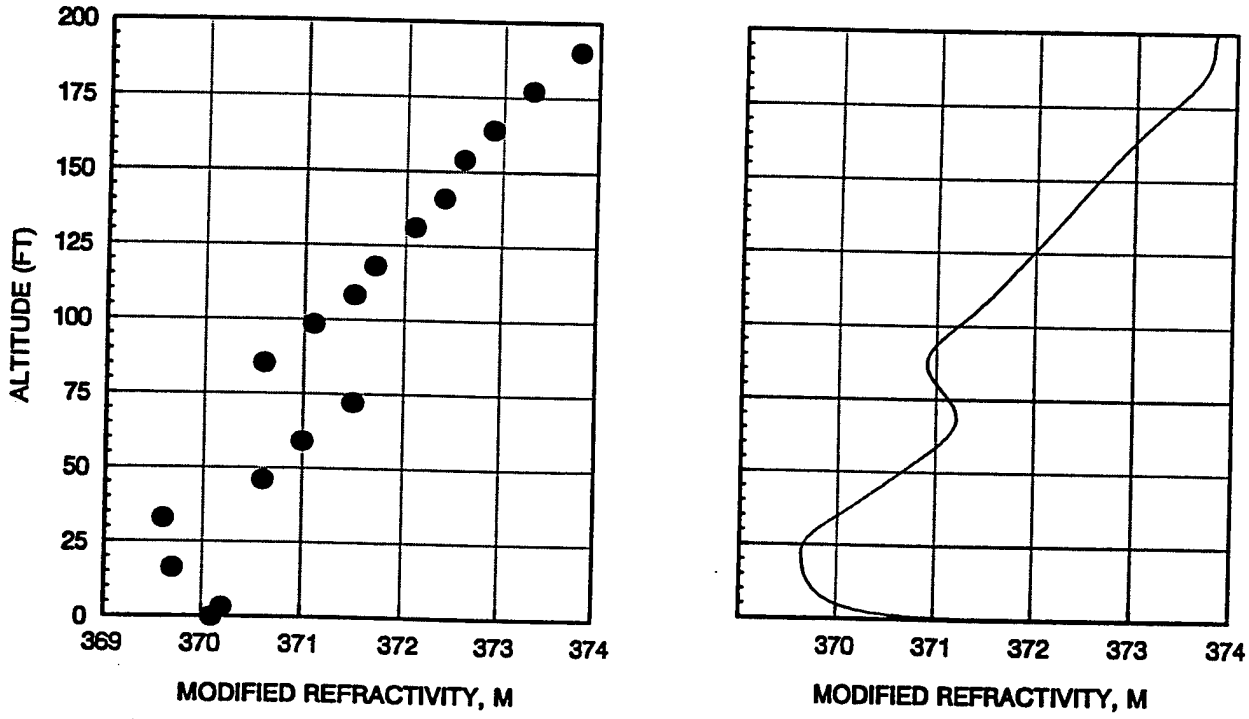


Figure 6: Expanded view of refractivity profile from CG 73, 19 October 1994

SEAWASP: REFRACTIVITY CHARACTERIZATION USING SHIPBOARD SENSORS

J. R. ROWLAND, G. C. KONSTANZER, M. R. NEVES
R. E. MILLER, J. H. MEYER, J. R. ROTTIER
The Johns Hopkins University Applied Physics Laboratory
Johns Hopkins Road
Laurel, MD 20723-6099
Phone: (301)953-6000 ext.8660 Fax: (301)953-5458
E-mail: john.rowland@jhuapl.edu

Introduction

A companion paper (Reference 1) contains an overall description of the SEAWASP (Shipboard Environmental Assessment/WeApon System Performance) system. The initial goal of the system is to characterize, in real time, the effect of the environment on AN/SPY-1 radar performance. The system consists of two primary parts, a radar performance component and an environmental characterization component. The purpose of this paper is to describe the environmental characterization component.

Overall System Description

The major purpose of the environmental measurement system is to produce a profile of modified refractivity from the surface to a 350 m altitude and automatically output this profile to the radar performance assessment portion of SEAWASP. To produce these refractivity profiles, the environmental portion of the system must make detailed measurements of meteorological parameters. Although the system was designed for the purpose of generating refractive index profiles, it has proven to be a general purpose tool for gathering detailed meteorological measurements aboard ships.

In order to accurately describe the profile of modified refractivity from the surface to a 350 m altitude, two different techniques are required. The lower region extending from the surface to an altitude of some tens of meters, frequently contains an evaporation duct and must, in general, be modelled utilizing time-averaged bulk meteorlogical measurements, (Reference 2). The upper region, extending from the top of the evaporation duct region to 350 m must, in general, be measured (Reference 3). The two separate profiles must then be merged with great care to avoid generating false artifacts that would cause unrealistic radar propagation calculations.

In the case of the SEAWASP system mounted on AEGIS class cruisers, the bulk measurements are made with fixed sensors mounted on the ship at a height of 9 m to measure atmospheric pressure, temperature, relative humidity, relative wind speed and direction, and infrared surface temperature. In addition, accurate measurements of air temperature and relative humidity at a height of 2 cm and surface water temperature at a depth of 1cm are made with a disposable telemetering float periodically thrown overboard (Reference 4). The upper region is directly measured with a rocketsonde. The rocketsonde is periodically fired from the ship, ascends to an altitude of roughly 800 m and telemeters temperature, relative humidity and pressure back to the ship as it descends to the surface. Figure 1 shows an overall block diagram of the environmental measurement system.

Sensor Location Considerations

Airflow over the ship can cause serious contamination of the meteorological measurements. In addition, the location of the meteorological sensors must not have a negative impact on existing weapons systems or ship operations. Also, bulk measurements used for evaporation duct modeling (Reference 2) must be made at a relatively low altitude. These constraints have limited the locations available for

mounting SEAWASP sensors. In our case the superstructure is too high. The fantail and bow have guns that do not allow fixed sensors to be used on these decks. The flight deck is not suitable because of a hazzard during flight operations. The optimum location for meteorological sensors on AEGIS class cruisers is the aft VLS (Vertical Launch System) deck. This deck has few obstructions that interfere with airflow across the sensors.

The wake from the ships superstructure, which is dependent on wind speed, wind direction, ship speed and ship heading, may cause serious measurement contaminiation for sensors located on the aft VLS deck. It has been found that uncontaminated measurements are obtained when the relative wind speed across the sensors is above 2 knots and the wind direction relative to the ships longitudinal axis is between 15 and 170 degrees for sensors mounted on the starboard side and 190 and 345 degrees for sensors mounted on the port side. For this location dual sensors have been found to supply satisfactory data for 75% of the time on average. A quick analysis shows that if the ship were dead in the water and the wind were blowing at a speed above 2 knots, we would expect good data for 86% of the time. If the ship were underway at a speed of 10 knots with a 10 knot wind we would expect good data for 77% of the time.

Detailed System Description

A detailed block diagram of the system is shown in Figure 2. The system has three fixed sensor locations. A sensor suite located on the starboard side of the VLS deck is used to measure air temperature, relative humidity, pressure, relative wind speed and direction, ship compass heading and ship position using GPS (Global Positioning System). Water temperature is measured with a downward pointing pointing IR (infrared) thermometer. A small handheld launch control terminal is connected by a short cable to the starboard sensor box and serves to give the operator launching rocketsondes or floats necessary inputs to and feedback from the computer controlling the telemetry receiver. A second sensor suite located on the port side of the VLS deck is used to measure air temperature, relative humidity and relative wind speed and direction. The antenna used to receive telemetry signals from the rocketsonde and floatsonde is also at this location. The third sensor location is in the AN/SPY-1 radar aft cooling water pump room where we measure sea water temperature at the inlet to the radar cooling water supply.

Analog signals in the port sensor box are digitized and multiplexed into a single RS-422 data stream. This port signal is routed through a junction box to the starboard side where a microcontroller digitizes analog signals from sensors in that box, multiplexes them with the outputs of digital sensors and the launch control terminal. The output of the starboard sensor box thus contains, in one RS-422 data stream, the mutiplexed outputs of the port and starboard boxes and launch control terminal. This data stream is routed through the junction box to an IBM-compatible notebook computer which communicates via an ethernet link to the radar performance assessment portion of the SEAWASP system. Communication from the computer back to the starboard box is also possible and is used to change configuration of the starboard microcontroller, and do such tasks as calibrating the compass and communicating with the launch control terminal. The water temperature sensor in the radar cooling room is digitized and routed through the junction box to the computer along an RS-485 line. RS-485 was chosen for this purpose since it allows multiple low data rate sensors, that may be located some distance from each other, to be connected in parallel along one data line and separately interrogated by the central computer. Future expansion of the system will probably be done using this RS-485 line.

A power supply in the junction box supplies the low current 12Vdc to the sensors and contains a preamp for the telemetry antenna. The signals and 12Vdc power are run to all sensor locations and the computer along a 6 shielded pair cable. This cable has a bus structure so that any signal is available at any location. Photographs of the interior of the port and starboard sensor boxes are presented in Figures 3 and 4, respectively. Figure 5 is a photograph of the sensors mounted on the AEGIS cruiser USS Anzio (CG-68).

Two types of disposible sensors are used in the SEAWASP system. The first of these is the floatsonde (Reference 4). This sensor is a small 1.25 inch diameter x 12 inch long device which is thrown overboard and telemeters measurements of surface air temperature, relative humidity and water temperature back to the ship for use in evaporation duct calculations. A photograph of the sensor is shown in Figure 6. The second disposable sensor, a rocketsonde, is periodically launched from the ship to an altitude of 800 m and telemeters back to the ship measurements of temperature, relative humidity and pressure as it descends from apogee to the surface. Measurements with the 2.5 inch diameter x 28 inch long cardboard rocketsonde are made at 1 second intervals which corresponds to a vertical resolution of 2.5 m. A photograph of the rocketsonde components is shown in Figure 7. A photograph of the rocketsonde in its launcher with the ignition box and handheld launch control terminal is shown in Figure 8.

Software Features

The SEAWASP data acquisition program is run in a multitasking environment on an IBM-compatible notebook computer under the OS-2 operating system. The software is designed to run at system power up with no operator assistance with all applications running. Initial setup including calibration and tailoring the system to individual ship configurations is menu driven with intervention of an operator. Thereafter, all operation can be automatic with operator intervention only required to fix hardware trouble reports displayed on the workstation or to answer questions regarding rocketsonde and floatsonde launches displayed at the handheld launch control terminal.

-Measured Parameters

The computer makes a determination in realtime if the relative wind speed at the sensors is above 2 knots and the wind direction is in the range of 15-170 degrees for the starboard sensors or 190-345 degrees for the port sensors. If these conditions are met for the majority of a 5 minute period, data is considered valid and uncontaminated by the ships wake. Air temperature and humidity from the appropriate sensor suite, sampled at a 2 second rate, is averaged for a 5 minute period. At times, however, the ships course and the true wind vector will not be suitable, and no average will be calculated. IR water temperature, compass heading, ship GPS course, ship position and relative wind vector are also averaged for the 5 minute period. For the rocketsonde case, air temperature, relative humidity and pressure are measured and recorded at a 1 second rate as the instrument package descends from apogee to the surface. Air temperature, relative humidity and water temperature are measured and recorded at 1 second intervals by the floatsonde. Time used by the system is GMT time synchronized to the GPS receiver.

-Calculated Parameters

Ship compass heading is automatically corrected for local magnetic declination at the current ship position by the computer. The compass is also corrected for changing magnetic anomolies caused by the steel-hulled ship based on an algorithm using the GPS receiver. The corrected compass data along with ship heading from the GPS receiver and average relative wind vector is used to calculate the true wind vector. The averaged ship data, by itself, or at times in conjunction with surface air temperature, relative humidity and water temperature from the floatsonde, is used in a calculation of the modified refractivity profile in the evaporation duct. The rocketsonde pressure data is used to calculate altitude, while temperature, pressure and relative humidity data are used with the altitude calculation to calculate the profile of modified refractivity to an altitude of 350 m. These two profiles are carefully spliced to produce a single profile for the radar performance assessment component of SEAWASP running on HP 743I processors.

-Engineering Realtime Display and Playback Capability

Realtime and post processing data analysis features have been built into the software for research and engineering purposes. All measured and calculated data may be recorded on the hard drive of the notebook computer. Plots or tabulations of all data, including the results of model calculations, rocketsonde refractivity profiles, and location of all data samples acquired plotted on a detailed world map

are available in realtime or by playing back data taken previously. Realtime display of all sensor outputs is available in table form or time history plots. A compass rose with simultaneous display of corrected compass heading, ship course, relative wind direction from both starboard and port sensors, along with results of the most recent true wind direction is available. All displays may be viewed individually or windowed with other displays. Viewing of current data or analysis of previous data does not interrupt realtime data acquisition or calculation capability. Further, these data are potentially available to the SEAWASP display in CIC (Combat Information Center) if they are found to present insight into phenomena that impact combat system performance.

Evaporation Duct Models

Most existing models tend to overestimate the height of the evaporation duct, on the average. This can be serious problem when they are used to predict weapon system performance. Overestimation of the evaporation duct height usually produces an unrealistically large detection range for low altitude targets. Reference 2 describes the model on which our work was based. In general, evaporation duct models use time averaged inputs of temperature, humidity, and wind speed at some reference height near the top of the evaporation duct along with an estimation of temperature and humidity at the surface boundary. Most models use water temperature as a measure of surface air temperature and assume a value of 100% relative humidity for the surface value. Reference 2 also does not account for the effect of humidity on air density although this is often not a large effect. All models should use virtual temperature in their calculations. Virtual temperature is defined as the temperature that a parcel dry air would need to have to be of the same density as a parcel of moist air at the same pressure. At times most models exhibit a large sensitivity to input measurements and and their calculations tend to become unstable when the atmosphere is stable ie when the surface virtual temperature is cooler than the virtual temperature at the reference height especially in the presence of low winds. Most of the time the air over the ocean surface is slightly unstable. When the atmosphere is unstable large variability in the measurements is observed. No technique is available for making a direct measurement of the refractivity profile in the evaporation duct region under these conditions. When the atmosphere is stable, however, the atmosphere tends to be non-turbulent and a direct measure with high resolution instruments such as the rocketsonde is possible. This characteristic is fortunate, for when the models break down under stable conditions, direct measurements work best. Unfortunately, it is easy to make continuous calculations of the evaporation duct with fixed sensors in unstable conditions, but in stable conditions the evaporation duct must be directly measured with disposable sensors and continuous measurements are impossible.

Two evaporation duct models are currently being used for calculation of the modified refractivity profile in the evaporation duct. Both models are based on work described in Reference 2 with the incorporation of several modifications. Both models use virtual temperature in all calculations. The first model assumes that the atmosphere is neutrally stable with a constant virtual temperature profile within the evaporation duct. A controversial empirical method is used in this model to calculate the surface humidity from the humidity measured at the reference height so that only inputs of temperature and relative humidity at the reference height are required to model the evaporation duct. Since the model only works in neutral or slightly unstable conditions, a rough measurement of water temperature is required to insure that region is not very stable; ie water temperature is not much cooler than temperature at the reference height. This model is very robust and not subject to calculation instability or overestimation of the duct height. It does, however, tend to underestimate duct height and can be thought of as supporting conservative radar performance assessments. This model can run continuously with only fixed sensor inputs. The second model uses true windspeed, temperature, and relative humidity measured at the reference height with fixed sensors, as well as surface air temperature and relative humidity measured at the surface with the disposable floatsonde. While this approach is controversial, it has been found to better characterize the evaporation duct. Unfortunately continuous measurements at the surface are impossible since they require

expendable sensors. Use of the floatsonde does, however, provide a non controversial sanity check on the presence of an evaporation duct. If the measured refractivity at the surface is less than the refractivity at the reference height, subrefractive conditions exist regardless of model calculations. Present operation of the SEAWASP system automatically picks the best model based on the availability of timely data.

Practical Considerations

The shipboard environment is particularly hard on meteorological sensors. A number of engineering problems have been overcome in order to meet the system design lifetime of 1 year without operator-assisted calibration or routine maintenance other than a weekly fresh water washdown. A few of the problems encountered and their solutions are described: 1. Corrosion is a serious problem. All SEAWASP topside components are made of plastic, fiberglass, titanium or in a few areas, stainless steel. No surfaces are painted. 2. High RF power densities are often present. All topside electronic components are RF shielded and analog sensors are digitized at the sensor to avoid noise pickup. 3. Shipboard cable runs are often complicated so sensor signals are multiplexed where possible. 4. IR sensor aperatures must be protected from salt spray. We use a thin polyethelene window material for our 8-14 micron sensors commonly available as Glad Cling Wrap. This is treated with Rain-X to shed water droplets that would otherwise contaminate the sensor readings. 5. R. M. Young Corp. manufactures the most widely used radiation shield that is required to reduce temperature and humidity sensor heating from direct sunlight. This shield has an unnecessarily restricted airflow that causes errors at low winds. This unit must have spacers installed between shield plates. 6. In damp situations (common aboard ship) the aforementioned shield becomes wet and causes the humidity sensor to overestimate relative humidity. The shield plates are sprayed with a hydrophobic coating to eliminate this problem. We use a material made by the Vellox Corp. for this purpose. 7. Magnetic anomolies associated with steel hulled ships change with time. Automatic correction of the compass calibration is periodically done in the SEAWASP system using selected data from the GPS receiver. 8. One of the most important characteristics of any commercial temperature/humidity sensor is the manufacturer supplied filter which protects the delicate sensor elements from the environment and mechanical damage but lets air and water vapor pass freely through it. Rotronic Instrument Corp. has the best sensor/filter combination and the only unit that can maintain a +/- 2% calibration over a 1 year period in our application. 9. Electronics generally used to measure humidity are very susceptible to high humidities and are of a nature that is difficult to encapsulate. We have decided to place a dessicant within all electronics boxes topside. The humidity within these boxes is monitored with a dedicated humidity sensor and an alert message requesting that an operator replace the dessicant is displayed on the SEAWASP monitor in CIC.

Acknowledgement

This work has been sponsored by the Navy's shipbuilding program, PMS-400B.

References

1. G. C. Konstanzer, J. R. Rowland, G. D. Dockery, J. J. Sylvester, M. R. Neves and D. R. Davis, "SEAWASP: A Prototype System for Shipboard Assessment Based on In Situ Environmental Measurements," Proceedings: Battlespace Atmospheric Conference, 3-5 Dec. 1996, San Diego, CA.
2. R. A. Paulus, "Specification for Environmental Measurements to Assess Radar Sensors," Technical Document 1685, Nov. 1989, Naval Ocean Systems Center, San Diego, CA., 92152-5000.
3. J. R. Rowland an S. M. Babin, "Fine-Scale Measurements of Microwave Refractivity Profiles with Helicopter and Low-Cost Rocket Probes," Johns Hopkins APL Tech. Dig., Vol. 8, No. 4, 1987, pp. 413-417.
4. J. H. Meyer and J. R. Rowland, "Instrumentation for Probing the Air-Water Interface," Oceans 91 Conference, 1-3 October 1991, Honolulu, HA.

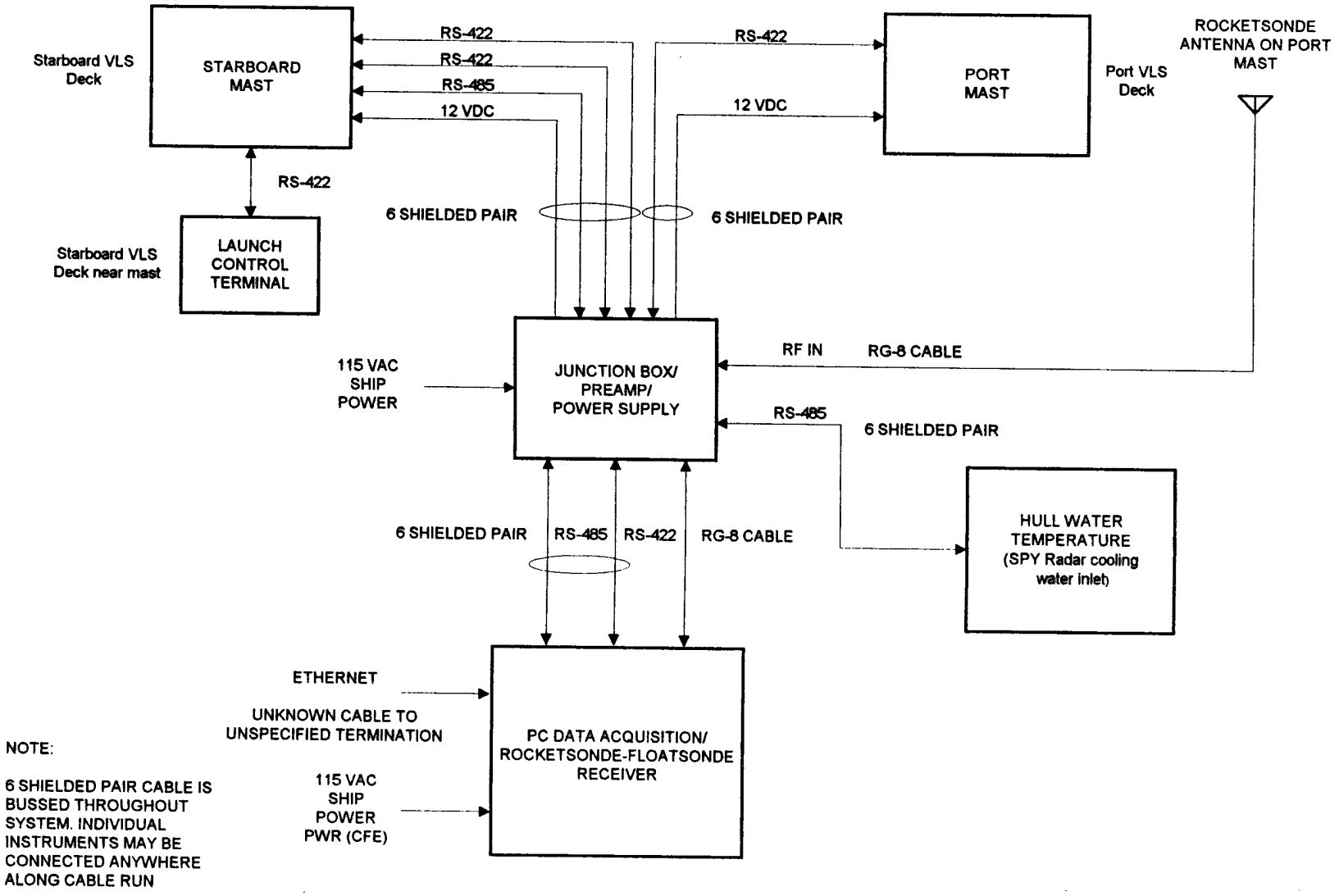


Figure 1: SEAWASP environmental system overview block diagram (USS Anzio CG-68)

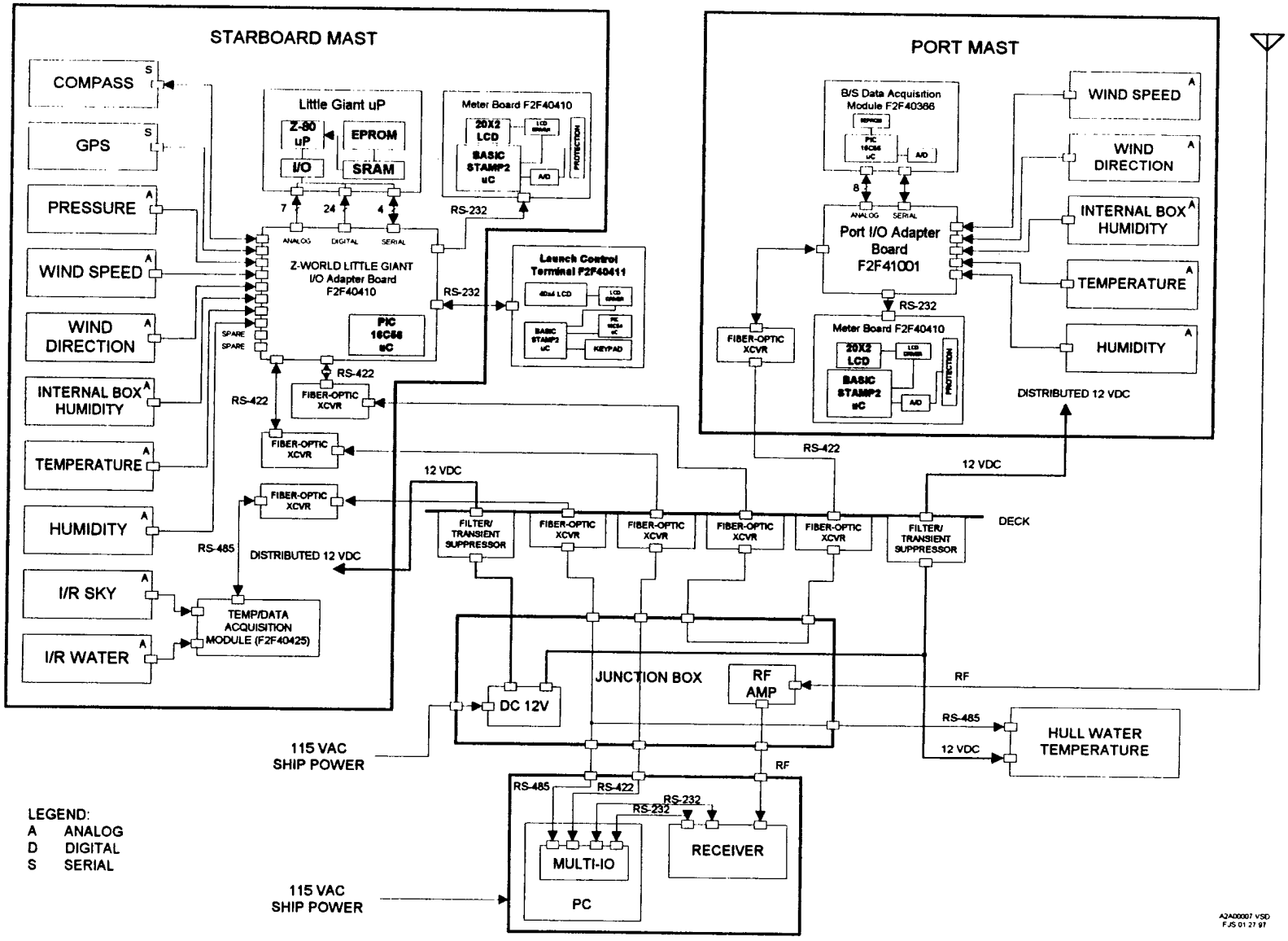


Figure 2: SEAWASP environmental system detailed block diagram (USS Anzio CG-68)

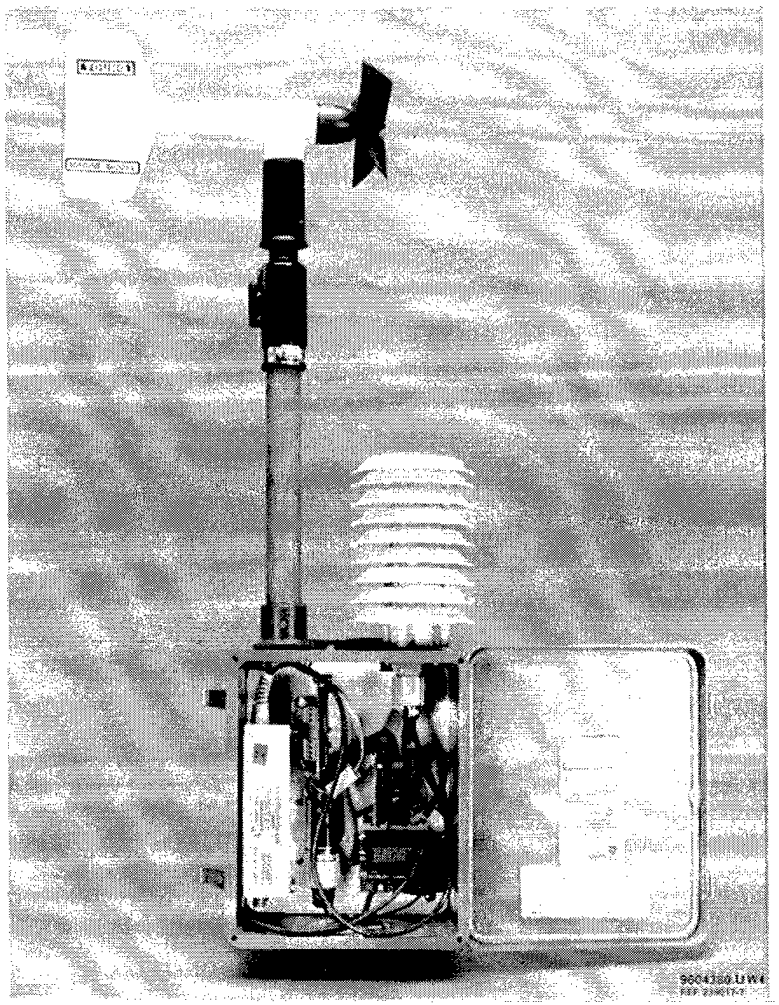


Figure 3: Port sensor mast electronics

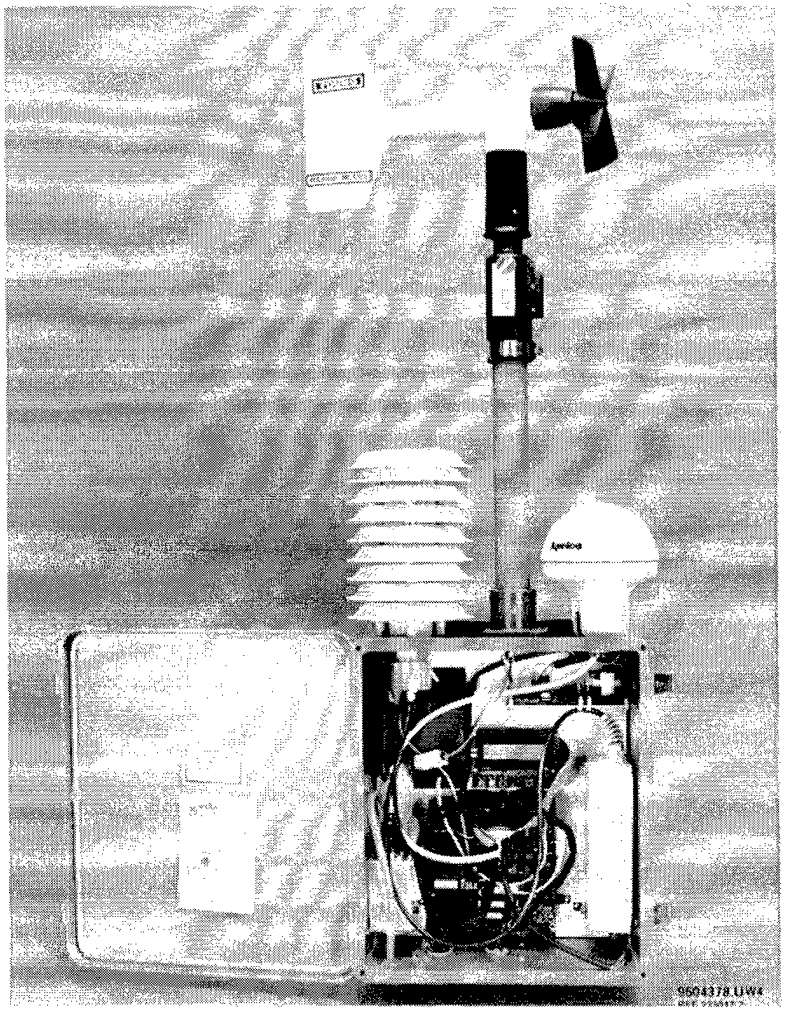


Figure 4: Starboard sensor mast electronics

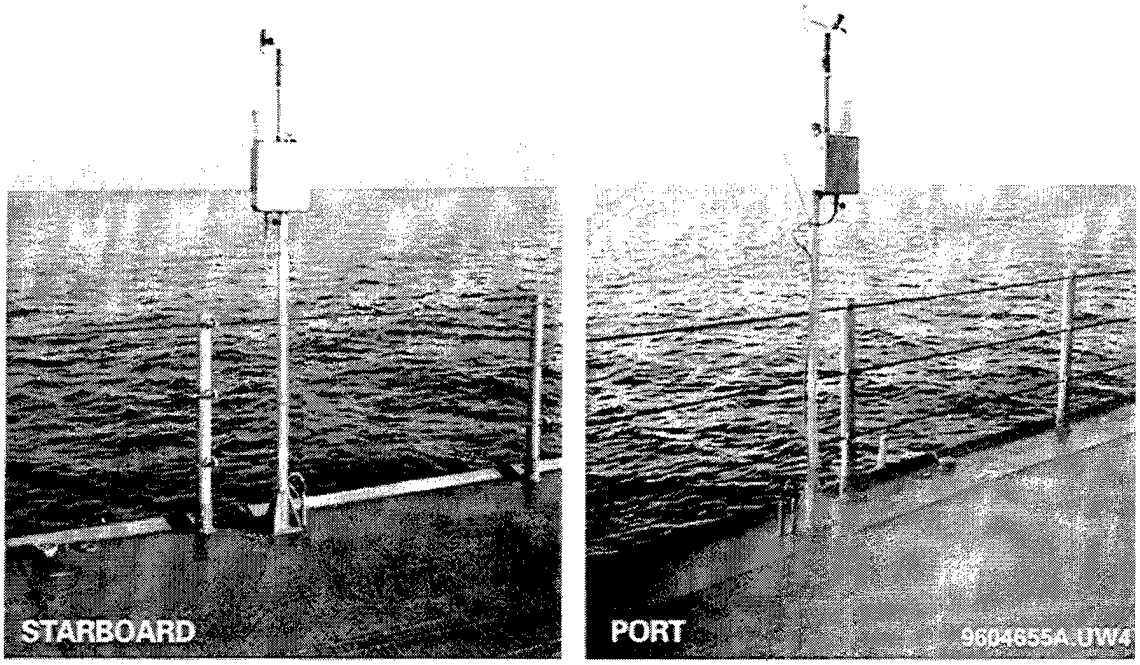
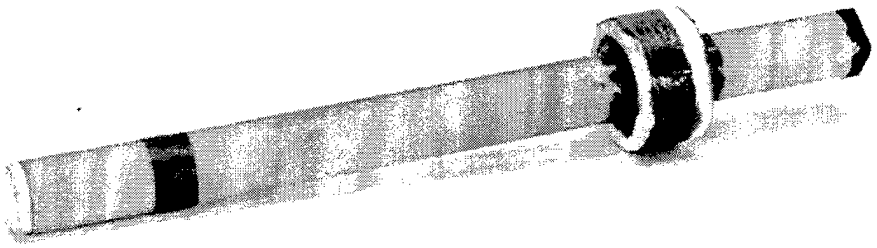


Figure 5: Port and starboard sensor masts installed on ship



9604708.UW4

Figure 6: Floatsonde

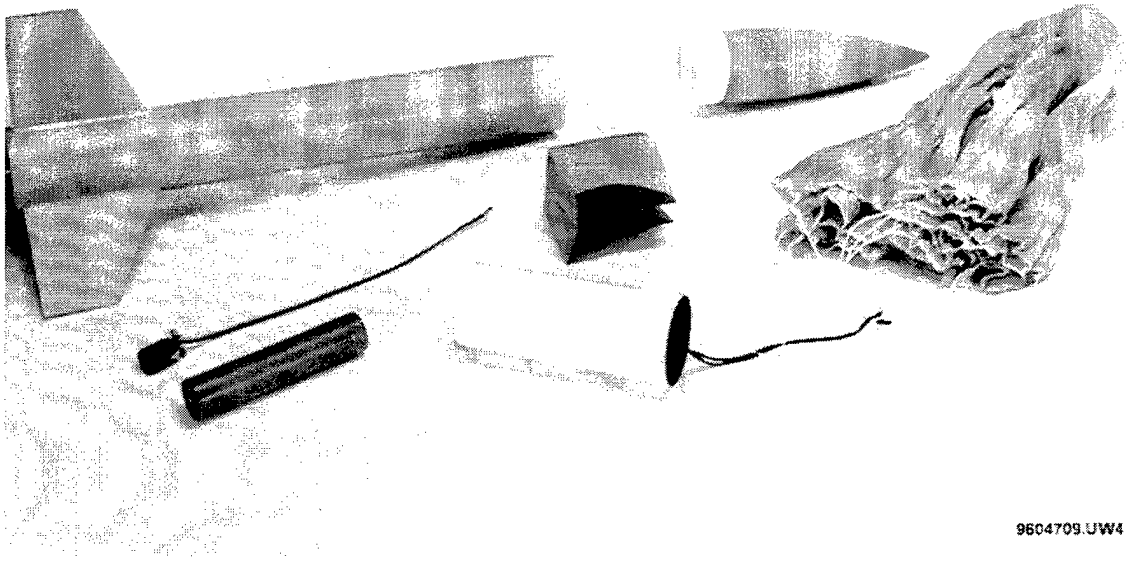


Figure 7: Rocketsonde component parts including instrument package, parachute, rocket motor and ignitor

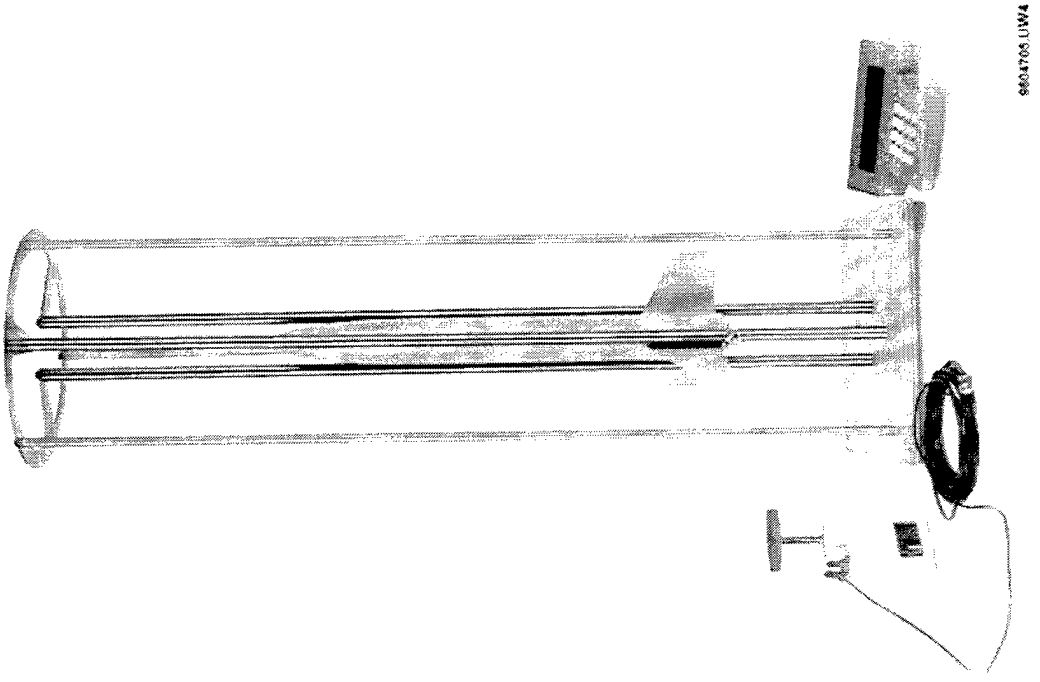


Figure 8: Rocketsonde in launcher with ignition box and launch control terminal

MICROWAVE PROPAGATION MEASUREMENTS IN THE LOW ALTITUDE REGION USING SINGLE FREQUENCY AND WIDEBAND SYSTEMS

Steven Kang
Janet Stapleton
Naval Surface Warfare Center
Dahlgren Division
Code T42
17320 Dahlgren Road
Dahlgren, VA 22448

1. ABSTRACT

Low altitude microwave propagation is a dominant factor in the detection and tracking of low flying cruise missiles by shipboard naval radars. Significant temporal and spatial fluctuations in microwave propagation loss have been observed in the lower ten meters above the sea surface. In order to better understand these fluctuations and to support the design and test of future naval radars, two systems were developed which allowed the direct measurement of microwave propagation loss. One system measured propagation pathloss versus range at a single frequency either at Ku or X band, while the other system measured propagation pathloss versus time at a fixed range for frequencies in the 2-18 GHz band. The receivers were located at fixed heights commensurate with shipboard radar heights and the transmitters simulated low flying target heights of 3 to 39 feet.

A selected set of the data collected both on the Potomac River near the Naval Surface Warfare Center in Dahlgren, VA and at the NSWC Detachment in Wallops Island, VA is shown to illustrate some of the unique insight gained through these measurements. The information obtained from the collected data has been and continues to be used in sensor design and specification, and can be directly applied to the acquisition of sensors. Installation of a 2-18 GHz measurement system on a boat further enables a study of propagation effects versus range over a wide frequency band at a high temporal update rate. The measurement capability and the resulting database can serve the Navy with great value in areas such as supporting Combat Ship System Qualification Trials (CSSQT), land based testing of developmental sensor systems, radar design and development, and operational testing.

2. INTRODUCTION

Microwave propagation at low altitudes is strongly affected by the structure of the refractive index of the lower atmosphere. Microwave propagation in this region, especially down at 10 meters above the sea surface, has long been known to vary with altitude, range, time and frequency. Under subrefractive conditions, the radar horizon may be significantly reduced. Under enhanced propagation conditions (ducting), deep nulls have been both predicted and observed with widths less than 3 feet in altitude, and having varying, and inadequately defined, temporal and spatial characteristics. A number of threats have been designed to take advantage of this low altitude region. Testing of developmental sensor systems in this complicated low altitude propagation region is confronted by the difficulty of achieving enough test runs over broad environmental conditions to adequately quantify system performance. The performance of the radar can vary significantly on a given day. These propagation induced variations often overshadow other important parameters such as target radar cross section.

The parabolic equation-based microwave propagation models using the refractive index profiles as input are relatively accurate when adequate profiles are available along the propagation path. However, adequate sampling of these refractive profiles can be difficult to obtain. Thus, to accurately assess the performance of a sensor system, it is necessary to make a direct microwave propagation measurement. In order to provide key input to future sensor requirements and design, and to support performance testing and evaluation of existing systems, two direct microwave measurement systems were developed. One system operated at a single frequency in Ku or X band, and the other system covered 2 to 18 GHz frequency range at a high temporal update rate. Analysis performed during the NATO AAW program indicated that unique propagation effects such as the horizontal fade were most evident in the X to Ku frequency bands (Ref. 1). Therefore, the initial single frequency measurements were made at Ku band to enhance the likelihood that these propagation effects would be detected. The single frequency measurements focused on X band in the summer of 1995 in support of joint testing with the Naval Research Laboratory's Naval Engagement Radar.

This work was sponsored internally at the Naval Surface Warfare Center Dahlgren Division (NSWCDD).

3. MEASUREMENT SYSTEMS

3.1 Single Frequency System (SFS)

The single frequency system consisted of a transmitter receiver pair, which operated at 13.95 GHz. It was designed to probe propagation profiles versus range. A single receiver was mounted on a tower to simulate various test radar heights. A single transmitter emitting 0.1 watt of continuous wave microwave signal was placed on a moving shuttle on a tower that was mounted on the stern of the boat, *Sea Lion*. The transmitter was moved up and down the tower by a computer controlled motor, covering target heights from 3 to 33 ft. The receiver measured the received signal level and calculated the one way propagation loss using the calibrated transmitter output power level. During the measurement, the boat was brought into position with a stern aspect at approximately six nautical miles from the receiver. Then the boat made an outbound run from the receiver on a given radial covering a typical range of 6 to 20 nautical miles in approximately 40 minutes. Global Positioning System (GPS) data and compass data showing the coordinate and the heading of the boat were also recorded.

3.2 Microwave Propagation Measurement System (MPMS) - Wideband

The Microwave Propagation Measurement System (MPMS) covered the 2 to 18 GHz frequency band in 16 discrete frequency steps during an 8 second cycle. The system consisted of ten transmitters mounted on a 30-foot tower with 3 feet of spacing between each and four receivers mounted on a 100-foot tower. This configuration gave 40 simultaneous propagation paths. These ten transmitters simulated target heights, and the four receivers at various heights simulated test radar heights. The original measurements were made with the ten transmitters mounted on shore 16 nautical miles from the four receivers which were mounted on an opposing shoreline.

The output signals from the transmitters were separated by predetermined audio-frequency offsets from a common carrier frequency. Each receiver channel performed Fast Fourier Transforms (FFT) on incoming sampled data allowing discrimination between the individual transmitters and transmitter heights using the position of each received signal in the output frequency spectrum. A computer controlled telemetry link between the transmit and receive terminals allowed automated data collection around-the-clock unattended.

3.3 Meteorological and Environment Data

Meteorological data, such as temperature, relative humidity and pressure, were needed to calculate refractive profiles used as input to the microwave propagation models for comparison with the directly measured RF propagation factor. These data were collected using an array of ten meteorological sensors mounted on the 100-ft tower where the microwave propagation receivers were also mounted. Nine sensors were mounted at fixed heights and one was mounted on a moving shuttle that traveled between fixed sensors acting as an offset and calibration measurement. Johns Hopkins University/Applied Physics Laboratory (JHU/APL) also participated in the tests, collecting meteorological data using several sensor systems mounted on their research boat, *Chessie*, and meteorological sensors mounted on a helicopter. Although the refractive profiles collected by the helicopter were considered the best source of meteorological data to be used with the microwave propagation models, the times and radials were often inconsistent with the microwave propagation measurement data. The primary reason for this problem was that the collection of the helicopter refractive profiles was often coordinated with air targets and other sensor radials with higher priorities during the tests.

A van near the receiver test site collected local meteorological data as well as serving as base collection site for several remote sensors that included a waverider buoy and tide gauge. Along with temperature and relative humidity, wind speed and direction, pressure, and rain rate were also collected.

4. TEST LOCATIONS AND TIME PERIODS

The microwave propagation data was collected during two different test periods and locations. First, as a part of the Multi-Sensor Integration Tests, data was collected on the Potomac River near Dahlgren, Virginia during June through August of 1993. During this test period, only the SFS was available. The MPMS was delivered to NSWCDD in September of the same year. The SFS along with the MPMS were moved to Wallops Island, Virginia in December. The MPMS propagation data was collected along a 16 nautical mile coastal path during January through April of 1994. The data collection paths for SFS varied depending on the day and the condition of the test. In all cases, one-way propagation profiles were measured. The X band SFS measurements made during the summer of 1995 are not included in this report.

5. MEASUREMENTS

5.1 Single Frequency System (SFS)

5.1.1 Horizontal Fade

A phenomenon called *"horizontal fade"* has been both predicted and measured experimentally (Ref. 1). From the data collected at the NSWCDD Potomac River test location, this effect is clearly shown. Figure 1 illustrates the data in a coverage diagram format with propagation factor relative to freespace shown using a gray scale. The horizontal axis shows the range as determined by GPS, and the vertical axis represents the height of the target.

The propagation profile plot of Figure 1 shows a fade region where the propagation factor is 20 to 25 dB below freespace which persists at a constant altitude versus range. Just above and below this horizontal fade, there is an enhancement in propagation of 5dB better than freespace. So for a target crossing these regions, a two-way system sensor would experience 50 to 60 dB of signal fluctuation from propagation alone. The enhancement of propagation just above the surface will increase the surface clutter, further reducing the ability to detect and track the target.

The lower subplot in Figure 1 shows propagation model output for a 92 ft duct which was consistent over the range covered. The Personal Computer Parabolic Equation Model (PCPEM) (Ref. 2) was used for all modeled data in this report. The refractive profile used to model this duct is shown in Figure 2. The modeled data also indicates the horizontal fade at the same approximate location and shows relatively good agreement with the measured data. The horizontal fade was observed on several occasions.

5.1.2 Multi-Modal Propagation

Evidence of a surface-based duct is depicted by the data shown in Figure 3. This data was collected at the Wallops Island test location. In the upper subplot of Figure 3, a definite change in the propagation structure at approximately 15 nmi can be seen. Smooth transitions between different propagation factors in the nearer ranges show a standard atmosphere or low evaporation duct characteristic. The multi-modal interference characteristics are evident beyond 15 nmi. The lower subplot in Figure 3 shows the model output for the refractive profiles collected by the helicopter. The time and radial coincidence of the refractive profile data and the measured propagation factor data was quite good. Although the nature of the propagation characteristic agrees, the range of the transition is approximately 18 nmi versus the 15 nmi in the upper subplot. The model output also indicates larger propagation factors overall and shows the bending downward of the destructive interference region at closer range and lower height than the measured propagation data. The reason for this discrepancy is not known, but it does point out that even with good temporal and spatial correlation between meteorological data collection and microwave measurements, there can be significant differences in the propagation factors generated from each.

Figure 4 shows the refractive profiles that were used as input to the propagation model which generated the data shown in the lower subplot of Figure 3. These refractive profiles were preprocessed using a program called LARRI (Large-Scale Atmospheric Refractivity Range Interpolator) which smoothes and prepares measured meteorological data for use by propagation models. LARRI was developed by the Johns-Hopkins University Applied Physics Laboratory for use with their helicopter-based meteorological measurements (Ref. 3).

5.1.3 Subrefraction

On several occasions the SFS data collected at the Wallops Island location indicated a subrefractive environment. One example of a subrefractive case is shown in Figure 5. The black regions in the upper subplot represent data points that were discarded when the boat was unable to maintain proper alignment with the receiver. If more than 1 dB of antenna gain loss could have been incurred, the data was not used in the resulting plot. Since the boat's heading was recorded using a digital compass, and the bearing was available from GPS, a filter could be used to reject these measurements. The modeled and measured data match reasonably well in this case. The refractive profile used in the model is shown in Figure 6. The refractive data was collected as a function of range on nearly the same radial the boat traveled and at nearly the same time.

5.1.4 Data Summary

Considering only the 13.95 GHz SFS data (no examples of the 9.5 GHz data are shown in this report), the horizontal fade was measured on two days at NSWCDD Potomac River and perhaps once to a lesser degree at Wallops Island. Three other days at NSWCDD Potomac River also showed some evidence of the *horizontal fade*. Several other characteristics of multimode propagation were also sensed by the system during periods of ducting that were dominated by surfaced-based ducts rather than the evaporation duct. During these periods, a high degree of variability in the propagation factor versus range and altitude (and most likely also time) was

sensed by the system. Seventeen test days were covered at two locations during two seasons of the year (6 at NSWCDD and 11 at Wallops Island). Some degree of ducting or enhanced propagation was exhibited during all but three of the days. On the three days that did not exhibit ducting, a subrefractive environment was indicated. All of the subrefractive days were measured at Wallops Island. The data set is not large enough to draw statistical conclusions about the percentage occurrence of ducting or subrefraction. However, the fact that such a range of conditions was sensed over a relatively short period of time indicates that the propagation environment is quite dynamic and can easily dominate sensor performance. Many of the ducting environments exhibited spatial variations in one-way propagation factor as large as 30 dB. That would significantly effect sensor performance, depending on the location of the target in height and range.

In general, the model predictions made using the best refractive profile data with respect to time and radial coincidence with the microwave measurements, yielded reasonable agreement at least with regard to trends. Most notable were the good comparisons between measured and predicted *horizontal fade* situations. In the case of some of the more complicated refractive environments, exact matches seem out of reach, perhaps due to the temporal variability present in the refractive environment.

5.2 Microwave Propagation Measurement System

5.2.1 Temporal Variability

Both long and short term temporal variability were observed during the data collection period. The long term variability was marked primarily by a transition from ducting to subrefraction and vice versa. Figure 7 shows an example of such a transition from ducting to subrefraction. The propagation factors are plotted for four different frequencies for the receiver at 54 feet. In Figure 7 the four horizontal bands depict the measured propagation factors at four frequencies. The horizontal axis shows the time span of approximately 12 hours. The vertical axes for each of the four frequencies represent target heights. The propagation factors relative to freespace are plotted in gray scale. Two-minute periods where the data was not taken are shown as gray vertical stripes. At 0600 hours, a wide stripe of gray is shown when the system was off-line.

The earlier part of the time period covered in Figure 7 indicates enhanced propagation factors better than 10 dB above the freespace. At higher frequencies strong null structures can be seen versus target altitude. A helicopter sounding taken about 30 km off the coast of Wallops Island showed a surface duct up to about 50 meters about five hours (2002 UTC, Mar 23) prior to the beginning of the time period covered in Figure 7. On March 23 at 1800 UTC, a surface pressure chart showed that the Wallops Island area was within a warm maritime tropical air mass associated with a high pressure center located near Bermuda. There were no fronts within 300km of Wallops Island (Ref. 4).

Around 0600 UTC on March 24, the transition from strong ducting to subrefraction occurred. The transition took approximately 2 hours, and subrefractive conditions lasted for over twenty hours. During the subrefractive period, the highest sensor showed least loss of the four, but all frequencies performed poorly. Weather data shows at 1200 UTC on March 24, a warm front lying just north of the Wallops Island area. A helicopter sounding, taken on March 24 at 1508 UTC about 18km off the coast of Wallops Island, showed subrefractive conditions below 90 meters (Ref. 4). Unfortunately, during the time of transition, no local weather data were available and no helicopter or boat meteorological data were available because of the time of the day. However, the timing of this fade transition was compared to the data from a C-band link operated by APL along a similar path (Ref. 5) and showed a good agreement.

The line plot in Figure 8 shows an example of a highly variable propagation which occurred over a short period of time. This short term variability occurred primarily during periods when a ducting environment was present. In Figure 8 the propagation profiles are shown for four different frequencies for the receiver height of 84 feet. The horizontal axes show the one-way propagation factor relative to the freespace in dB, and the vertical axes show the target heights. The overlapped traces represent eight minutes of collected data and display a large degree of variability in propagation factor. Since each frequency was revisited every 8 seconds, sixty samples are displayed. Significant changes in the null height and depths, 20 to 30 dB, can be seen. This rapid and large variability (as much as 60 dB for a two-way radar system) could have a significant impact on the performance of a radar depending on its threshold and track filter characteristics.

5.2.2 Frequency Effects On Null Filling

Much of the data collected are useful in analyzing the percentage bandwidth necessary to reduce or "fill in" the null structures in the pathloss profiles created by multimode propagation in ducting environments. The data in Figure 9 shows four different frequencies, 5.9, 8.475, 13.57, and 17.35

GHz, for the receiver at 54 feet. It shows a shift in null heights with a change in frequency as well as a change in the number of nulls. The lowest frequency shown in Figure 9 appears to have the best overall loss performance and no large null structures. These effects or null structures also occur with range changes which could not be measured during this test because the transmit and receive arrays were at fixed locations.

5.2.3 Data Summary

In general, the mid frequency range of 5.9 to 12.3 GHz showed the least loss over all conditions and least variability with time and transmitter height. Best performance versus sensor height depended on the environment type. Under some strong ducting conditions, the lower sensors showed the least loss. In other situations, higher sensors showed less loss.

Considering all the data collected over the test period, propagation worse than the 4/3 earth (subrefraction) occurred between 20 to 60 % of the time depending on geometry and frequency. Figure 10 shows the histogram of propagation factor values over the entire test period for 3.6 GHz (receiver at 54 feet and target at 15 feet). The data indicate that 42% of the propagation data was worse than 4/3 earth, or subrefractive. This shows that, at least for the period of the four months covered by these tests, subrefraction occurred a significant portion of the total test time.

6. SYSTEM UPGRADE

There is a current effort to install both the SFS and the MPMS on the boat, *Sea Lion,* to further our ability to characterize propagation effects by covering a wide frequency band vs. range. This would allow a capability to measure propagation across 2 to 18 GHz versus range with a very rapid temporal update rate.

7. CONCLUSION

The measurements of RF propagation in this report have shown that the propagation environment varies significantly with altitude, range, time and frequency in the low altitude region. Over 15 dB of variation in one-way propagation loss was observed for target height differences of 3 feet, or time periods of less than 20 seconds. This variation would be doubled for a two-way system like a radar. Longer term variations from ducting to subrefractive environments that resulted in a 40 dB change in one-way loss were also observed. These subrefractive environments lasted over thirty hours in some cases, and the loss values were essentially frequency-independent over the 2 to 18 GHz band. Only increasing the height of the radar receiver showed any decrease in pathloss during these subrefractive environments. The data indicate that under many of the extreme environments, the performance of the conventional narrowband radars will vary significantly against sea-skimming threats. The data also show that having a sensor with a wideband capability could improve propagation related performance by 20 to 30 dB. Subrefractive conditions occurred a significant percentage of the total test period.

The information obtained from the collected data should be useful for sensor design and specification. With the development of two direct microwave propagation systems, the Single Frequency System and the Microwave Propagation Measurement System, it is possible to validate many of the propagation models and make ground truth measurements for radar test observations. The data discussed could be used for remote sensing in terms of the development of refractivity inversion techniques (Ref. 6).

These two systems, could and should be used to support the operational and engineering testing of ship combat systems. In events such as Combat Ship System Qualification Trials (CSSQT) where assessment of true performance of sensor systems is critical, the SFS and MPMS could play a vital role. Utilization of the unique capability of the MPMS to measure propagation for low elevation targets with fine height and frequency resolution covering most of the shipboard radar frequency band, provides invaluable input to the design of future Navy radars.

8. REFERENCES

[1] Dockery, G. D., "Propagation Fade Characteristics in Low-Altitude Surface Ducts," The Johns Hopkins University Applied Physics Laboratory, Technical Report, NATO AAW Task 3-1-19, Radar Performance Analysis, October 20, 1988.

[2] PCPEM [Personal Computer Parabolic Equation Model] © 1989, 1990 of Signal Science Limited.

[3] Dockery, G. D., and G. C. Konstanzer, "Recent Advances in Prediction of Tropospheric Propagation Using the Parabolic Equation", Johns Hopkins APL Tech. Dig., Vol. 8, No. 4, 1987, pp. 404-412.

[4] Babin, S. M., "A Case Study of Subrefractive conditions at Wallops Island, Virginia," Journal of Applied Meteorology, Volume 34, Number 5, May 1995.

[5] Goldhirsh, J., and G. D. Dockery, "Propagation Measurements and Modeling at C band for Over-the-Water, Line-of-Sight Propagation Links in the Mid-Atlantic Coast," Radio Science, Vol. 26, Number 3, May-June 1991.

[6] Boyer, D. et al, "Using Remote Refractivity Sensing to Predict Tropospheric Refractivity from Measurements of Microwave Propagation," AGARD Conference Proceedings 582, October 1996.

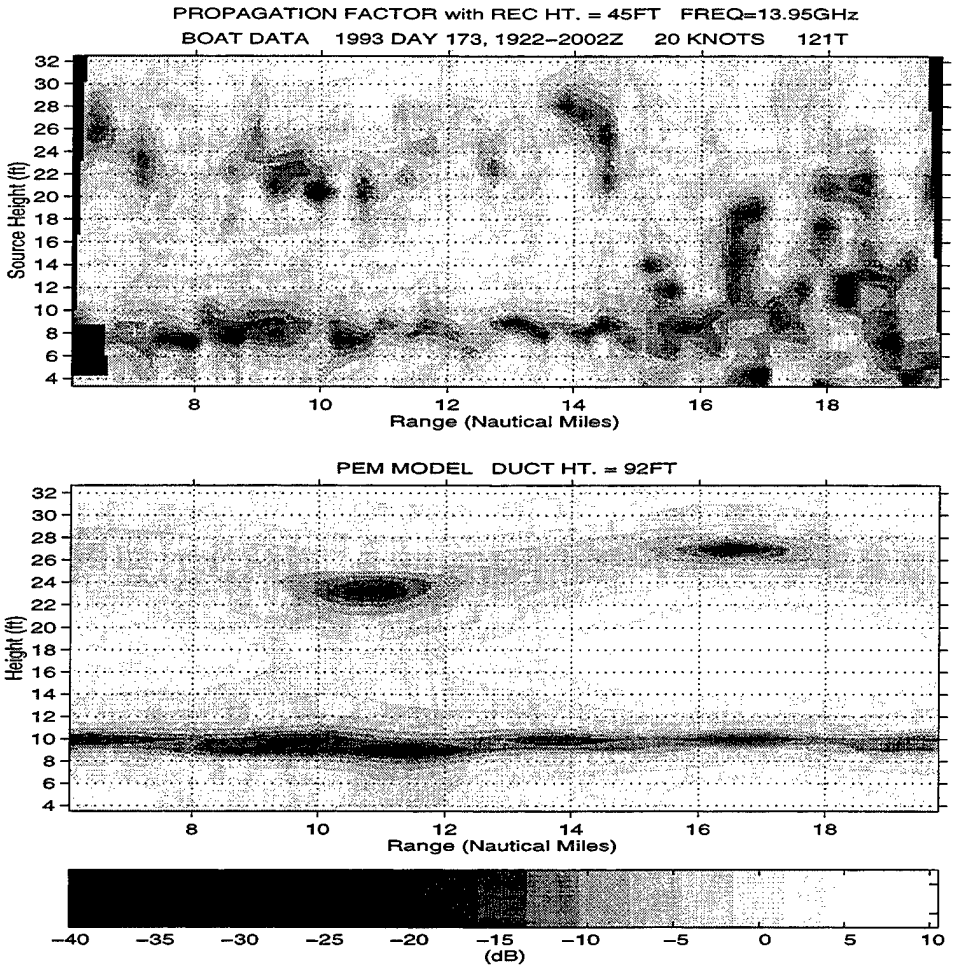


Figure 1. Horizontal Fade

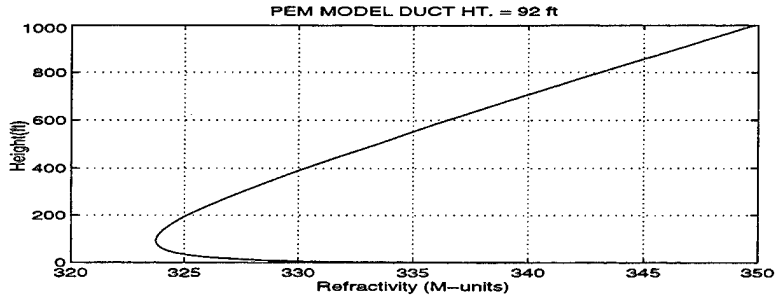


Figure 2. Refractive Profile for a 92 ft. Evaporation Duct

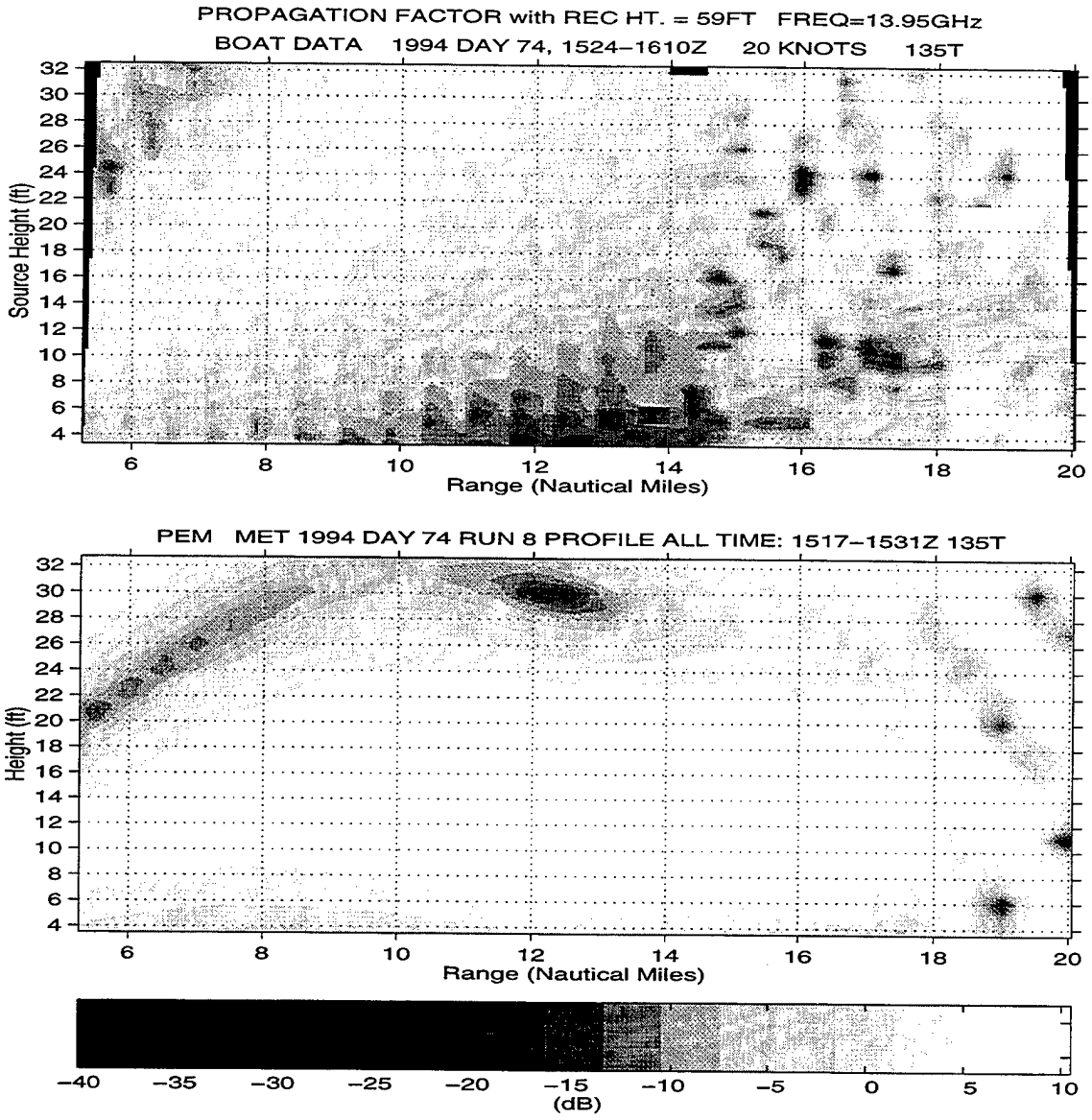


Figure 3. Propagation Due to a Surface Based Duct

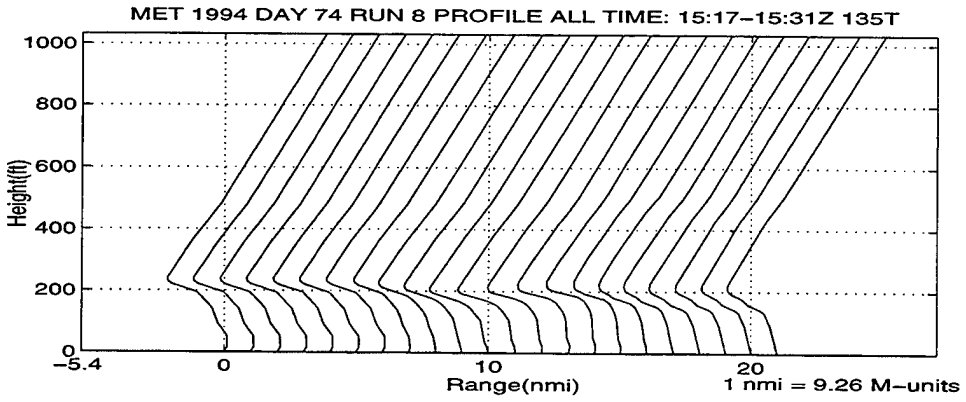


Figure 4. Measured Refractive Profile Versus Range

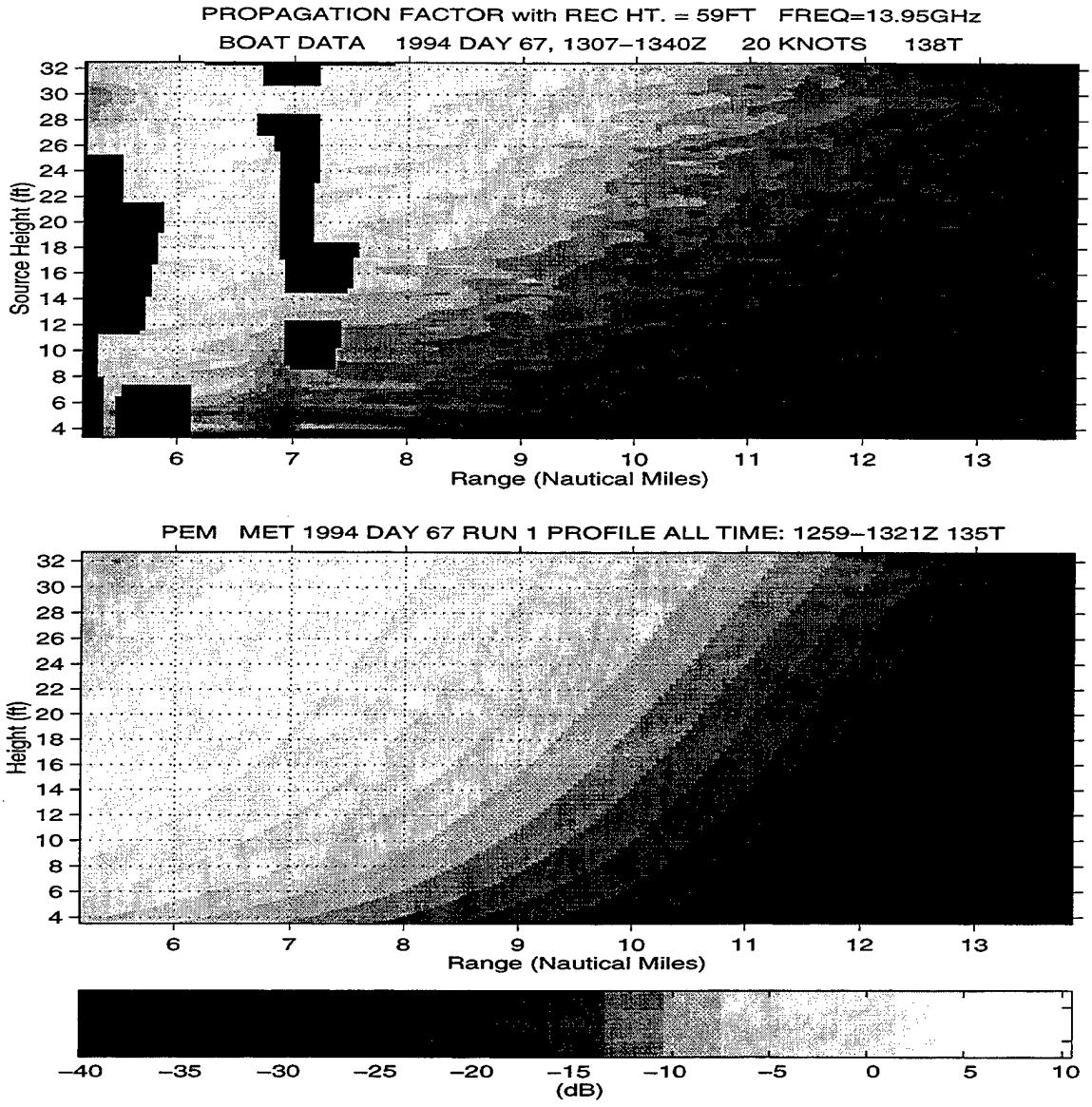


Figure 5. Subrefraction

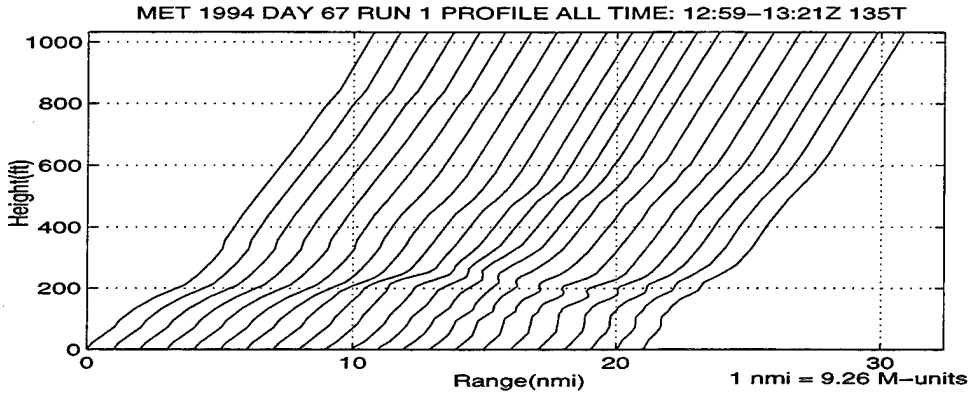


Figure 6. Measured Refractive Profile Versus Range for a Subrefractive Environment

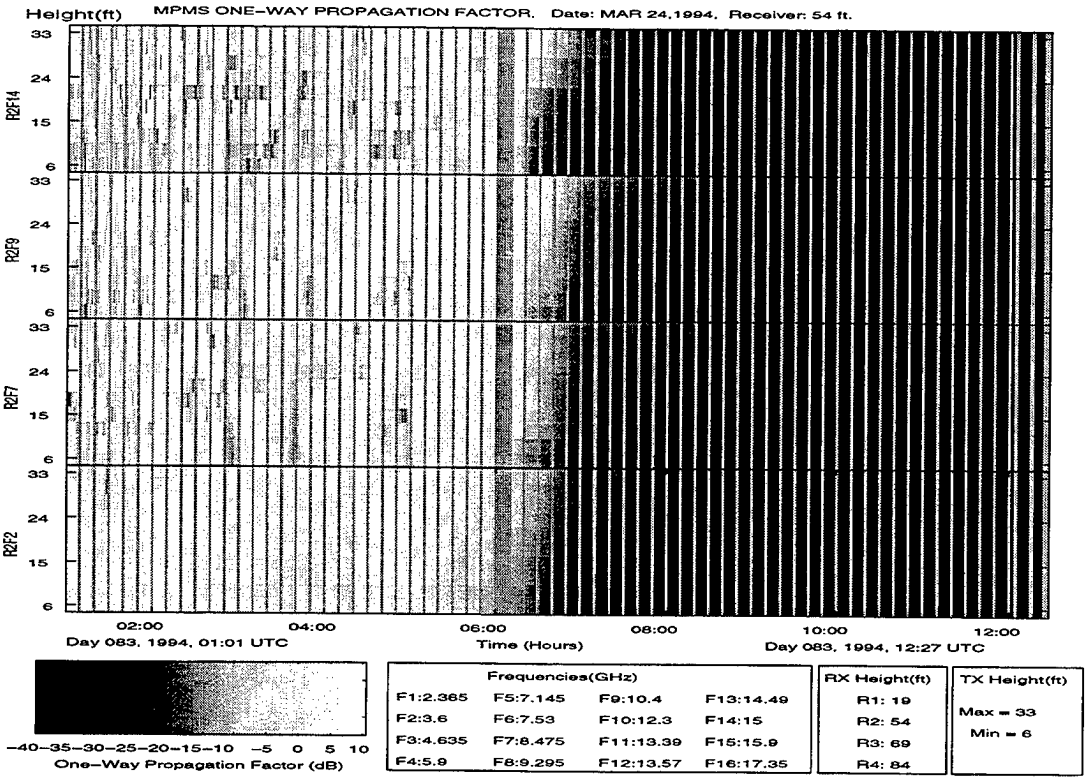


Figure 7. MPMS Measured Long Term Variability

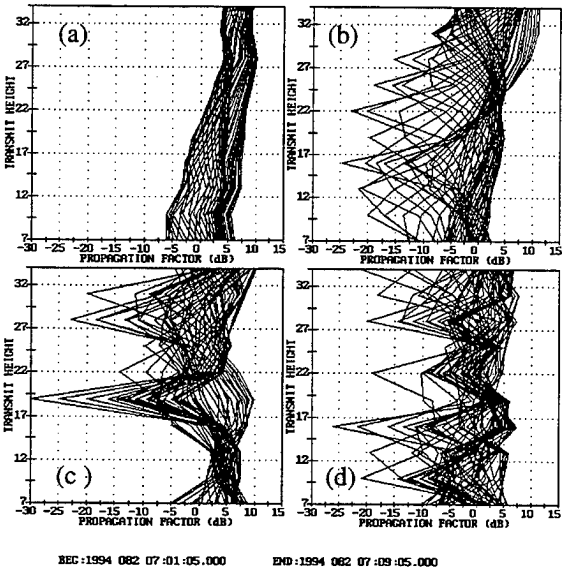


Figure 8. MPMS Measured Short Term Variability for Receiver at 84 ft: (a) 3.6 GHz (b) 5.9 GHz (c) 10.4 GHz (d) 15.0 GHz

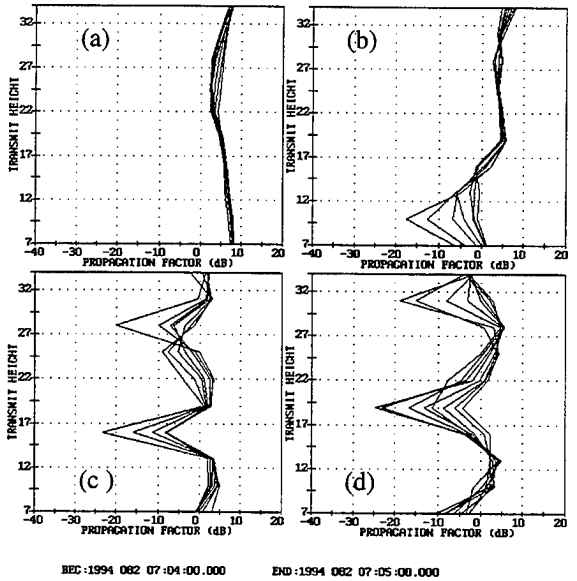


Figure 9. Frequency Effects On Null Filling Receiver at 54 ft: (a) 5.9 GHz (b) 8.475 GHz (c) 13.57 GHz (d) 17.35 GHz

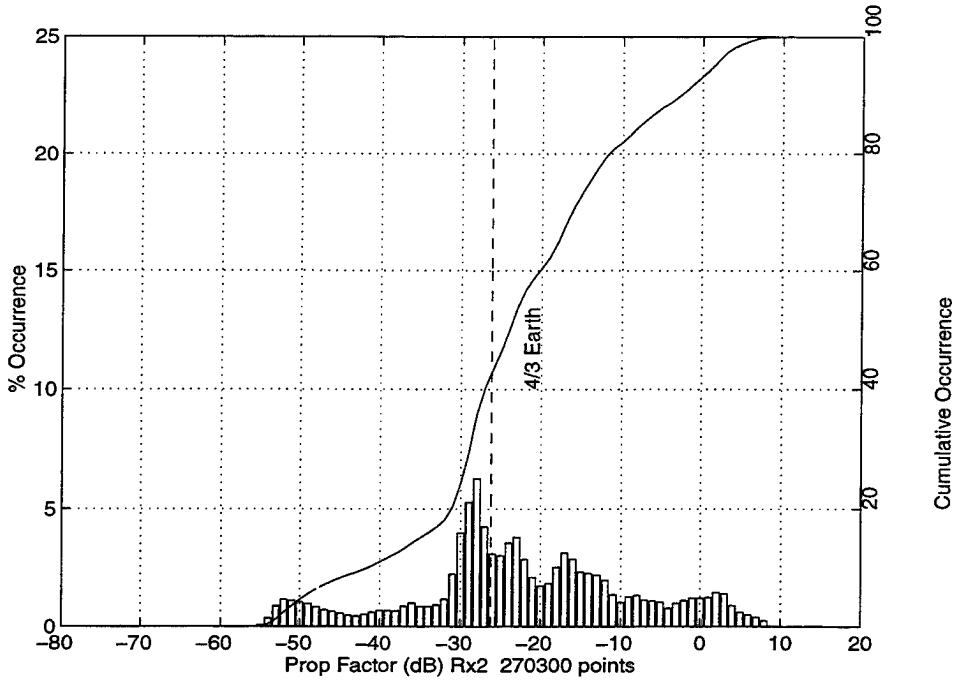


Figure 10. Propagation Statistic for the Receiver at 54 ft., Frequency 3.6 GHz, Target Height 15ft.

FASCODE for the Environment (FASE)

H.E. Snell
Atmospheric and Environmental Research, Inc.
840 Memorial Dr.
Cambridge, MA 02139
(617)-547-6207

G.P. Anderson, J.H. Chetwynd, and S. Miller
Geophysics Directorate, Phillips Laboratory
Hanscom AFB, MA 01731

The Optical Physics Division of the Air Force Phillips Laboratory with support from the Department of Energy (DOE) Atmospheric Radiation Measurement (ARM) Program is developing a state-of-the-art line-by-line atmospheric radiative transfer model as the successor to FASCODE (Fast Atmospheric Transmittance Code). The goal of this project is to create a computationally efficient model which contains the most up-to-date physics. The new model, known as FASCODE for the Environment, or "FASE", combines the best features of FASCODE and LBLRTM (Line-by-Line Radiative Transfer Model), the DOE's standard radiative transfer model. Upgrades to FASE include the addition of a solar spectrum module to compute the attenuated, line-of-sight solar radiance, improvement of the cloud and aerosol descriptors, based on changes made to MODTRAN (Moderate Resolution Transmittance Model), and the ability to incorporate the new heavy molecule absorption cross-section data found on the HITRAN96 database, which is of slightly different format from the previous HITRAN cross-section data. This paper addresses changes which have been made to FASCODE and LBLRTM to create FASE, and gives an overview of the new capabilities and recent model validations.

The ability to accurately model radiation propagating through the atmosphere requires the continual development of existing models, especially as measurement techniques and instrumentation become more sophisticated. The joint US Air Force (USAF) and Department of Energy Atmospheric Radiation Measurement program (DOE-ARM) line-by-line radiative transfer model "FASE" is the latest in the FASCODE[1] series of line-by-line models. FASE is grounded in FASCOD3[2], with important contributions from FASCOD3P, the USAF band model MODTRAN[3], and the standard DOE line-by-line model LBLRTM[4]. Once the initial development and beta-testing of FASE are complete, the code will be re-named FASCOD4. This manuscript gives an overview of FASE and addresses future development issues.

The core of FASE consists of the FASCODE lineshape algorithm[5]. After FASCOD3, parallel development funded by DoD and DOE resulted in the creation of FASCOD3P and LBLRTM. These codes, separately, made a number of advances over FASCOD3. As it became clear that DoD would benefit from specific advances in LBLRTM, the FASE effort was initiated to merge FASCOD3P and LBLRTM. Since a number of FASCOD3 features were not required for the DOE-ARM community (e.g. the non-local thermodynamic equilibrium routines), they were eliminated. However, the advances for LBLRTM resulted in significant changes to the core modules which compute the layer optical depth, as well as vectorization and parameterization of the entire code. Thus a thorough evaluation of the two codes was necessary to determine the best way to create FASE: by transferring the changes directly to FASCOD3P, or by starting with LBLRTM and adding the routines that were dropped. It was found that the most expedient method would be to start with LBLRTM and add the features from FASCOD3P[6]. This effort was undertaken only after it was established that the optical depth calculations of both codes gave results that differed by less than 1% for a set of standard test cases[7].

The most significant changes to FASCOD3 found in LBLRTM are vectorization of the code to significantly decrease the run-time of the model, modifications to increase the accuracy of the Voigt lineshape function, and parameterization of array dimensions. The vectorization and parameterization changes involved both the re-writing of portions of the code to eliminate "if-then" tests from within "do-loops", as well as a general cleaning of the code to improve user accessibility. The change in the sampling of the Voigt lineshape was made to increase the mathematical accuracy of the optical depth calculations to less than 0.5%. This change was prompted by advances in sensor technology which enable measurements to be made with very high spectral resolution[8]. Table 1 lists the changes to FASE which originated in LBLRTM.

Table 1: FASE Features from LBLRTM

•vectorization and parameterization of the code	•improved accuracy of the Voigt lineshape
•2020 cm-1 calculation spectral range	•embedded FFT scanning functions
•alternate O2 line coupling in microwave scaled to agree with data	•alternate CO2 line coupling in thermal infrared scaled to attain agreement with data
•option: fixed wavenumber grid output for all layers driven by the smallest sample value	•option: layer optical depth in separate files for compatibility with external multiple scattering codes

NEW FEATURES

In addition to upgrades of existing features, several new features were added to FASE. These are listed in Table 2. Of particular significance are the addition of the solar spectrum module and upgrades to the aerosol, cloud and rain routines. Also, FASE has been updated to accept all of the molecular and atomic species on the HITRAN96[9] database.

Table 2: Partial List of New FASE Features

•solar spectrum module	•updated aerosol, cloud, and rain module
•fully compatible with HITRAN96	•external file for emissivity and reflectivity coefficients
•Schumann-Runge bands and continuum	•updated coefficients for Hartley-Huggins band
•corrections to the spherical geometry algorithm	•corrections to the NLTE routines
•option: layer input in 'atm-cm'	•check for required line coupling coefficients

The solar spectrum module allows the user to compute the attenuated solar irradiance. This can be either along a direct line-of-sight, or a line-of-sight that involves surface reflection. The default solar spectrum has two components[10,11], one from 50 - 50000 cm^{-1}, and the other from 50000 - 57500 cm^{-1}. The spectra are stored in unformatted data files which allows the user to use an alternative spectrum with minimal effort. As a time saving measure, FASE has an option to write the attenuated radiance to a separate file. This enables the user to do a number of calculations with, for example, different surface reflection properties, without having to re-compute the attenuated solar radiance.

The routines to compute the spectral properties of aerosols and hydrometeors (including clouds and rain) are part of a module adopted from LOWTRAN[12] prior to FASCOD3. The changes to the module in FASE reflect changes that were made for MODTRAN (version 3.5)[13]. In particular, these routines are now able to simulate mixed phase cloud types as well as multiple cloud decks. Further, with the new routines it is much easier for the user to specify and simulate the spectral and microphysical properties of a particular type of cloud.

The latest version of the HITRAN spectroscopic database, HITRAN96, has been expanded to include a total of 36 molecular species. The FASE array sizes and atmospheric input specifications have been updated to accommodate all of these species. HITRAN96 also contains new values for the absorption cross-sections of heavy-molecules (e.g. CFCs) based on the work of Varanasi[14]. Since these cross-sections are given as a function of pressure and temperature, they must be used in a different fashion than the previous cross-section files, which were only a function of temperature. Rather than interpolating or extrapolating the tabulated values to the pressure/temperature combination required for a calculation, Toon and Sen[15] created a set of 'pseudo-lines' for these species, allowing the calculations to be done in the same manner as the

line-by-line calculation. The pseudo-lines were created by fitting a set of equally-spaced spectral lines to the cross-sectional data to create a line file similar to the HITRAN format. The least-squares fit was done for the line strength, halfwidth, and lower state energy, and the resulting series of lines can be merged directly with lines selected from the HITRAN database. The pseudo-line fits from Toon and Sen cover also some measurements not on the HITRAN96 database. The pseudo-line file is part of the FASE databases, and can easily be changed as new species or alternative fits become available.

An example of a calculation with the heavy-molecule cross-sections is given in Figure 1. The lower curve shows the spectrum without CFCs, while the upper curves show the spectrum with current levels of CFCs, and with the CFC levels that can be expected by 2002. It is clear that accurate simulation of these species is required if the 8 -12 μm widow region is to be utilized for the quantitative information required for the sensing of boundary and cloud properties, as well as for surveillance applications. It should be noted that the calculation without CFCs represents that which would be calculated by LOWTRAN, which does not have any CFC species in its band model.

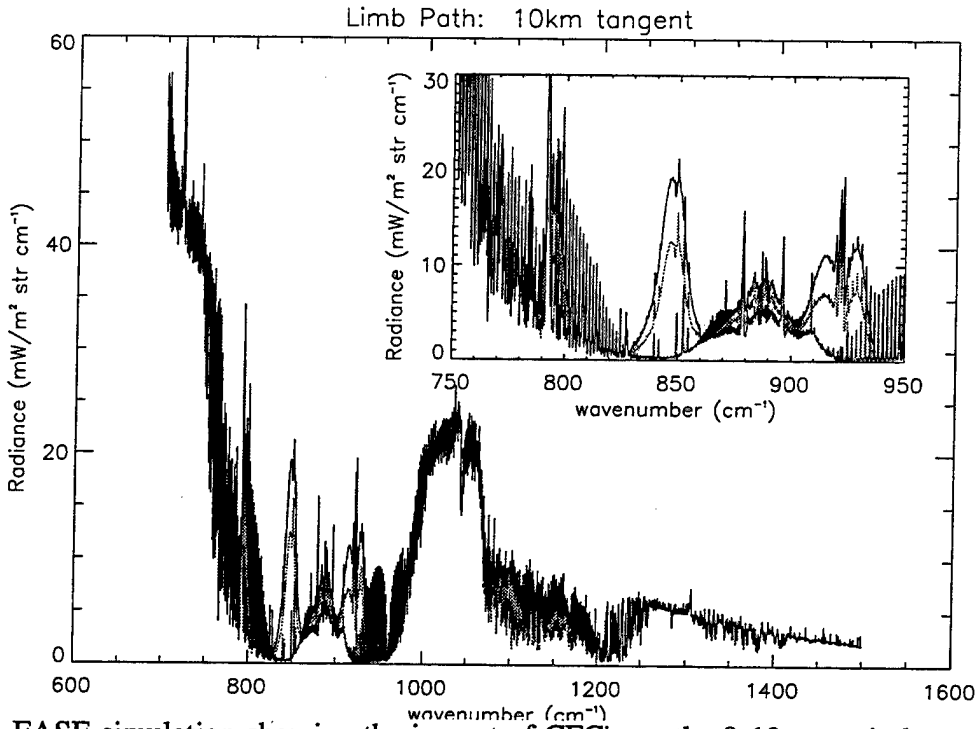


Figure 1: FASE simulation showing the impact of CFC's on the 8-12 μm window region. The lower curve is without CFC's (and is comparable to a LOWTRAN calculation), the middle curve is with current CFC levels, and the upper curve is with the CFC levels anticipated for the year 2002. Note that the levels of H_2O (e.g. 700 - 800 cm^{-1}), HNO_3 (870 - 900 cm^{-1}), and O_3 (1000 - 1050 cm^{-1}) were kept constant for this simulation.

CURRENT AND FUTURE FASE/FASCODE DEVELOPMENT

Current work on FASE involves the addition of the FASCODE multiple scattering routines. FASE has an input option whereby the layer optical depth information necessary for a stand-alone multiple-scattering program will be written to a series of data files. Currently the output file format is that required for input to the multiple-scattering programs CHARTS[16] and DISORT[17]. The FASCODE routines contain a 2-stream approximation to the scattering[18] and are useful for low-scattering atmospheres, or relatively fast, preliminary calculations in a given spectral band. Once the 2-stream multiple-scattering has been implemented in FASE, the code will have all of the original capabilities of FASCOD3P. At that point is will be re-named FASCOD4 and will be made available from the Air Force with DOE consent.

It is anticipated that future upgrades to FASCOD4 will include (1) the ability to compute the single-scattered solar radiance, and (2) the addition of the Herzberg bands in the 240 - 280 nm region of the UV. The single-scattered solar radiation is an important component to the radiance in the near infrared. The fact that this is not included in the current state-of-the-art LBL model could lead to serious errors in near-infrared calculations under sunlit conditions. The inclusion of the Herzberg bands is important in the solar blind region, which is often used for UV communications and sensors. As with single-scattering, the lack of this information in LBL models could have serious consequences.

"Hyperspectral sensing" is a relatively new descriptor for nadir-viewing measurement techniques historically used by the atmospheric remote sensing communities. As opposed to "multi-spectral" sensing, which includes any instrument with a finite number of specific channels, filters, or bands, hyperspectral implies employing enough channels, usually contiguous, to provide information sufficient to de-correlate the spectral characteristics of the surface and the atmosphere. This definition[19] can be contrasted with others, such as "any instrument with better than 4 cm^{-1} resolution used for surveillance."[20] The latter definition can be entirely inadequate in the thermal infrared (TIR) because overlapping molecular systems will not be sufficiently discriminated at such low spectral resolution. However, in the visible and near-infrared regions of the spectrum, a typical wavelength resolution of 10 nm at 600 nm, e.g., that employed by the AVIRIS instrument for the airborne sensing of surface properties[21], corresponds to a wavenumber resolution of over 200 cm^{-1}, and the 4 cm^{-1} "hyperspectral resolution" is more than sufficient to separate the atmospheric and surface contributions to the radiance.

While the definition of hyperspectral sensing typically refers only to nadir-viewing instruments, the concept can be expanded to limb- and zenith-viewing instruments as well. In these cases, high spectral resolution in the infrared is required to achieve high vertical resolution and to aid in de-correlating contributions from the atmosphere and clouds. Because FASCODE calculations are at monochromatic spectral resolution, FASCODE can be used for TIR

hyperspectral sensing. In fact, the FASCODE algorithm has been used extensively to compute the atmospheric compensation for interferometer data taken from ground, aircraft and satellite platforms[22,23]. One drawback of line-by-line models is the amount of time required for computation, and the use of FASCODE for operational hyperspectral sensing will require time-saving modifications to the code. A number of approaches to this problem are being tested and evaluated[24].

MODEL VALIDATIONS

Validation of FASCODE is an on-going process involving the comparison of calculations with measured spectra. This exercise requires accurate knowledge of the atmospheric profile in order to separate differences due to the atmospheric path from differences due to the algorithm itself. Recently, validation of data from the High-resolution Interferometer Sounder (HIS)[25] showed that FASCOD3P is capable of fitting the measurements within a few percent, given accurate sonde data. This work also showed that, independent of sonde information, the high resolution measurements were able to reveal the state of the atmosphere and allow the determination of sea surface albedo and temperature. When applied to hyperspectral imaging this process is termed 'atmospheric compensation'.

CONCLUSIONS

The Air Force Phillips Laboratory development of high spectral resolution radiative transfer models continues with the merger between FASCOD3P and LBLRTM to create FASE, which will ultimately become FASCOD4. A number of new features have been added to FASE, the most notable of which are the ability to compute the attenuated solar radiance, the ability to use all the species on the HITRAN96 database, and major improvements to the cloud/rain routines. These features greatly expand the capabilities of the model and allow for realistic simulations of the atmospheric radiation environment.

While they are often thought of as slow and cumbersome, line-by-line models such as FASCODE play an important role in the development of faster radiative transfer models. The ability of these codes to compute the fundamental physics is an important link between the fundamental radiative transfer and the fast model approximations. Because of its breadth, covering the microwave to the ultraviolet under LTE and NLTE conditions with a spherical path geometry algorithm, FASCODE will play a key role in the development and validation of fast algorithms applicable to real-time hyperspectral sensing and imaging.

ACKNOWLEDGMENTS

Support from this project was obtained from the Air Force Phillips Laboratory under contract #F19628-93-C-0040 with partial funding from DOE/PNL ARM subcontract #218101-A. The authors would also like to thank Lex Berk (Spectral Sciences, Inc.), Geoff Toon and Bhaswar Sen (JPL), Prasad Varanasi (SUNY-Stony Brook), Jinxue Wang (NCAR), and Pat Brown and Tony Clough (AER, Inc.).

REFERENCES

[1]Smith, H.J.P., D.J. Dube, M.E. Gardner, S.A. Clough, F.X. Kneizys, and L.S. Rothman, FASCODE - Fast Atmospheric Signature Code (Spectral Transmittance and Radiance), Air Force Geophysics Laboratory Tech. Report AFGL-TR-78-0081, 1978.

[2]Clough, S.A., F.X. Kneizys, G.P. Anderson, E.P. Shettle, J.H. Chetwynd, L.W. Abreu, L.A. Hall, and R.D. Worsham, FASCOD3: Spectral Simulation, in *IRS '88: Current Problems in Atmospheric Radiation*, p. 372-375, A. Deepak Publishing, 1989.

[3]Berk, A., L.S. Bernstein, and D.C. Robertson, MODTRAN: A Moderate Resolution Model for LOWTRAN 7, Air Force Geophysics Laboratory Tech. Report GL-TR-89-0122, 1989.

[4]Clough, S.A., Radiative Transfer Model Development in Support of the Atmospheric Radiation Measurement Program, in *Proceedings of the 3rd Atmospheric Radiation Measurement (ARM) Science Team Meeting*, CONF-9303112, Norman, OK, 1993.

[5]Clough, S.A., and F.X. Kneizys, Convolution Algorithm for the Lorentz Function, *Applied Optics, 18*, 2329, 1979.

[6]Snell, H.E., J.-L. Moncet, G.P. Anderson, J.H. Chetwynd, S. Miller, and J. Wang, FASCODE for the Environment (FASE), in *Atmospheric Propagation and Remote Sensing IV*, J.C. Dainty, Editor, Proc. SPIE 2471, 88-95, 1995.

[7]Snell, H.E., G.P. Anderson, J. Wang, J.-L. Moncet, J.H. Chetwynd, and S.J. English, Validation of FASE (FASCODE for the Environment) and MODTRAN3: updates and comparisons with clear-sky measurements, in *Passive Infrared Remote Sensing of Clouds and the Atmosphere III*, D.K. Lynch and E.P. Shettle, Editors, Proc. SPIE 2578, 194-204, 1995.

[8]Clough, S.A., C.P. Rinsland, and P.D. Brown, Retrieval of Tropospheric Ozone from Simulations of Nadir Spectral Radiances as Observed from Space, *J. Geophys. Res., 100*, 16579-16593, 1995.

[9]Rothman, L.S., and A. McCann, HITRAN 1996, Phillips Laboratory Geophysics Directorate, Hanscom AFB, MA, released on CD-ROM, June 1996.

[10]Kurucz, R.L., The Solar Irradiance by Computation, in *Proceedings of the 17th Annual Review Conference on Atmospheric Transmission Models, June 1994*, Phillips Laboratory Geophysics Directorate, Hanscom AFB, MA, 1995.

[11]Hall, L.A., and G.P. Anderson, High-Resolution Solar Spectrum between 2000 and 3100 Å, *J. Geophys. Res.*, *96*, 12927-12931, 1991.

[12]Shettle, E.P., Models of Aerosols, Clouds, and Precipitation for Atmospheric Propagation Studies, in *Atmospheric Propagation in the UV, Visible, IR, and MM-Wave Region and Related Systems Aspects*, AGARD-CP-454, 1990.

[13]Berk, A., L.S. Bernstein, P.K. Acharya, D.C. Robertson, G.P. Anderson, JH.H. Chetwynd, and J.J. Vail, MODTRAN3.5 and Cloud Applications, in *Proceedings of the 19th Annual Review Conference on Atmospheric Transmission Models, June 1996*, Phillips Laboratory Geophysics Directorate, Hanscom AFB, MA, 1996.

[14]for example, Varanasi, P., and V. Nemtchinov, Thermal Infrared Absorption Coefficients of CFC-12 at Atmospheric Conditions, *J.Q.S.R.T.*, *51*, 679-687, 1994.

[15]G.C. Toon and B. Sen, Jet Propulsion Laboratory, private communication, 1996.

[16]Moncet, J.-L., and S.A. Clough, Accelerated Monochromatic Radiative Transfer for Cloudy Atmospheres: A New Model, submitted to *J. Geophys. Research*, September 1996.

[17]Stamnes, K., S.-C. Tsay, W.J. Wiscombe, and K. Jayaweera, Numerically Stable Algorithm for Discrete-Ordinate-Method Radiative Transfer in Multiple Scattering and Emitting Layered Media, *Applied Optics*, *27*, 2502-2509, 1988.

[18]Isaacs, R.G., W.-C. Wang, R.D. Worsham, and S. Goldenberg, Multiple Scattering LOWTRAN and FASCODE Models, *Applied Optics*, *26*, 1272-1281, 1987.

[19]Alex Goetz, University of Colorado, private communication, 1996.

[20]G.P. Anderson, Air Force Phillips Laboratory, private communication, 1996.

[21]Green, R.O., J.E. Conel, C.J. Bruegge, J.S. Margolis, V. Carrere, G. Vane, G. Hoover, In-Flight Calibration and Validation of the Spectral and Radiometric Characteristics of the Airborne Visible/Infrared Imaging Spectrometer (AVIRIS), *Remote Sensing of the Environment*, 1992.

[22]Ellingson, R.G., and Y. Fouquart, The Intercomparison of Radiation Codes in Climate Models: An Overview, *J. Geophys. Res.*, *96*, 8925-8927, 1991.

[23]Wang, J., and G.P. Anderson, Validation of FASCOD3: Comparison of Model Calculations with Interferometer Observations from SPECTRE and ITRA, in *Passive Infrared Remote Sensing of Clouds and the Atmosphere III, Rome, Italy*, Proc. SPIE, 1994.

[24]J.-L. Moncet and H.E. Snell, work in progress, 1996.

[25]Wang, J., G.P. Anderson, H.E. Revercomb, and R.O. Knuteson, Validation of FASCOD3 and MODTRAN3: comparison of model calculations with ground-based and airborne interferometer observations under clear-sky conditions, *Applied Optics*, *35*, 6028-6040, 1996.

Atmospheric IR Transmittance Statistics in Arid Climates Based upon Synoptic Data from Selected Middle East Weather Stations

D. H. Höhn, W. Jessen, D. Clement

Forschungsgesellschaft für Angewandte Naturwissenschaften
Forschungsinstitut für Optik (FGAN-FfO)
Dok. Nr. 1996/57
Schloss Kressbach
D-72072 Tübingen, Germany

1. General

Operations in desert environments may be influenced by effects not found under climatic conditions of middle latitudes. Apart from the different general climatic situations also other effects typical for desert regions will affect systems operation, e. g. through blowing dust and sand by reducing atmospheric transmittance of electro-magnetic radiation. This can cause severe problems in system operation and even prevent it.

This study analyzes synoptic weather data from nine Middle East meteorological stations. Furthermore, to characterize ir propagation conditions the atmospheric transmittance was derived from the meteorological data. The resulting statistics are presented and analyzed.

The stations cover a wide geographical range from the northern Middle East states to the southern part of the Saudi-Arabian peninsula. It is assumed that this choice will describe typical climatic areas of interest.

2. Origin and Scope of Source Data

Synoptic weather data from the Middle East desert regions formed the basis for the following climatological survey. They are available to FGAN-FfO through the Global Telecommunication Service (GTS) of the World Meteorological Organization (WMO). The national data bank of GTS data is held by the German Weather Service, Seewetteramt Hamburg (SWA), which distributes the data.

The data covers the complete set of meteorological parameters as collected world-wide at fixed synoptic hours of observation. A total period of one year of observations has been evaluated for nine meteorological stations as listed below in Table 1.

block-nr.	station-nr.	period	longitude degr. E	latitude degr. N	name	(country)
40	072	1985	40.9	34.4	Abu-Kamal	(S)
40	250	1985	38.2	32.5	H4	(J)
40	310	1985	35.8	30.2	Ma'an	(J)
40	340	1985	35.0	29.6	Aqaba	(J)
40	356	1985	38.7	31.7	Al-Turayf	(A)
40	394	1985	41.7	27.4	Hail	(A)
41	024	1985	39.2	21.7	Jiddah	(A)
41	062	1985	45.6	20.5	Sulayel	(A)
41	136	1985	47.2	17.5	Sharurah	(A)

Table 1: Nine selected Middle East meteorological stations with geographical location and time period covered. The first two columns indicate the international block number and the station number for identification.
(S: Syria, J: Jordan, A: Saudi-Arabia)

Fig. 1 presents a map to illustrate the geographical positions of each station. Obviously seven of these stations are lying in desert or desert-like territory, whereas two of them (Aqaba and Jiddah) have a coastal environment. Note that the desert stations partly have a considerable large altitude above sea level.

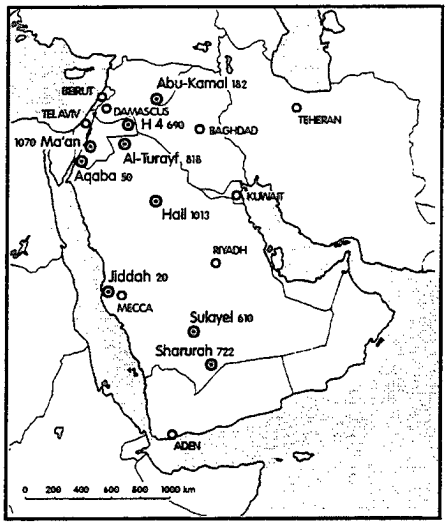


Fig. 1: Geographical location of nine selected Middle East meteorological stations. Numbers indicate altitude in m above sea level.

The data from the GTS through the SWA is distributed in a coded form (SWASYNOP) similar to the international weather code of the WMO. It has to be decoded before use. Furthermore it is generally uncorrected and therefore requires a thorough inspection and validation. Both procedures have been applied in the FGAN-FfO to the data set described above. The Saudi-Arabian observations are nearly complete. The other stations (Syria and Jordan) show larger gaps, preferably during night hours. Therefore for detailed studies only the Saudi-Arabian stations were considered.

3. Data Structure and Evaluation

All available data were stored on one file for each station in chronological order. The parameters contained in each file are listed in Table 2.

General Data and File Identification
Julian date, block-nr., station-nr., altitude a.s.l., longitude, latitude, date, time (UTC)
Observed Parameters
Present weather, incl. cloud cover
Pressure at station, pressure reduced to sea level
Visual range, wind speed and wind direction
Temperature, dew point temperature
Amount of precipitation since last observation
Derived Quantities
Relative humidity
Absolute humidity
IR transmittance (3 - 5 µm, 8 - 13 µm) over 1 km range: molecular, aerosol, total

Table 2: Quantities contained in each record of the data file.

As mentioned above one file for each meteorological station was created. They can serve as a data base for further analyses. To complement the original data some derived quantities have been added as listed in Table 2.

The transmittances were calculated (for 1 km horizontal range) after SYTRAN [1] which is a short version of LOWTRAN 7 [2], assuming a transmissometer source temperature of 650 °C and standardized system response functions for both atmospheric window regions (3 - 5 µm and 8 - 13 µm).

The molecular contribution to atmospheric transmittance is fairly well known from LOWTRAN. The calculation of the transmittance contribution due to atmospheric aerosols requires the assumption of an aerosol model as long as no further information - for example transmission measurements - is available. The following study makes use of the LOWTRAN 7 Desert Aerosol Model throughout. For the coastal stations, which have been included for comparisons, this assumption may not be justified. Therefore the aerosol transmittances at these locations must be considered with care. This Desert Aerosol Model is described in detail in [3]. In its original form it describes the atmospheric aerosol mass loading as a function of wind speed only. It represents an average of many findings and is not more than a generic rather than a specific model. Other than in [3] it is possible to enter in LOWTRAN 7 an observed visual range as an input parameter for scaling the resulting aerosol transmittance according to visibility.

The data evaluation has been performed in several steps. In a first step time series of a number of meteorological parameters were plotted to get an overview of occurring annual and diurnal variations. Also for the derived quantities time series plots are available. Examples will be shown below. In a second step statistical evaluations were performed in the form of cumulative frequency distributions of meteorological and other, derived parameters over the whole year. The third step dealt with the annual variability of the cumulative frequency distribution of trans-

mittance. Some selected results also on this topic are given below. An estimate of thermal imagers ranges statistics is given in the last section.

4. Data Presentation and Statistical Results

Selected examples of the data evaluation and general statistical results are summarized in the following chapter.

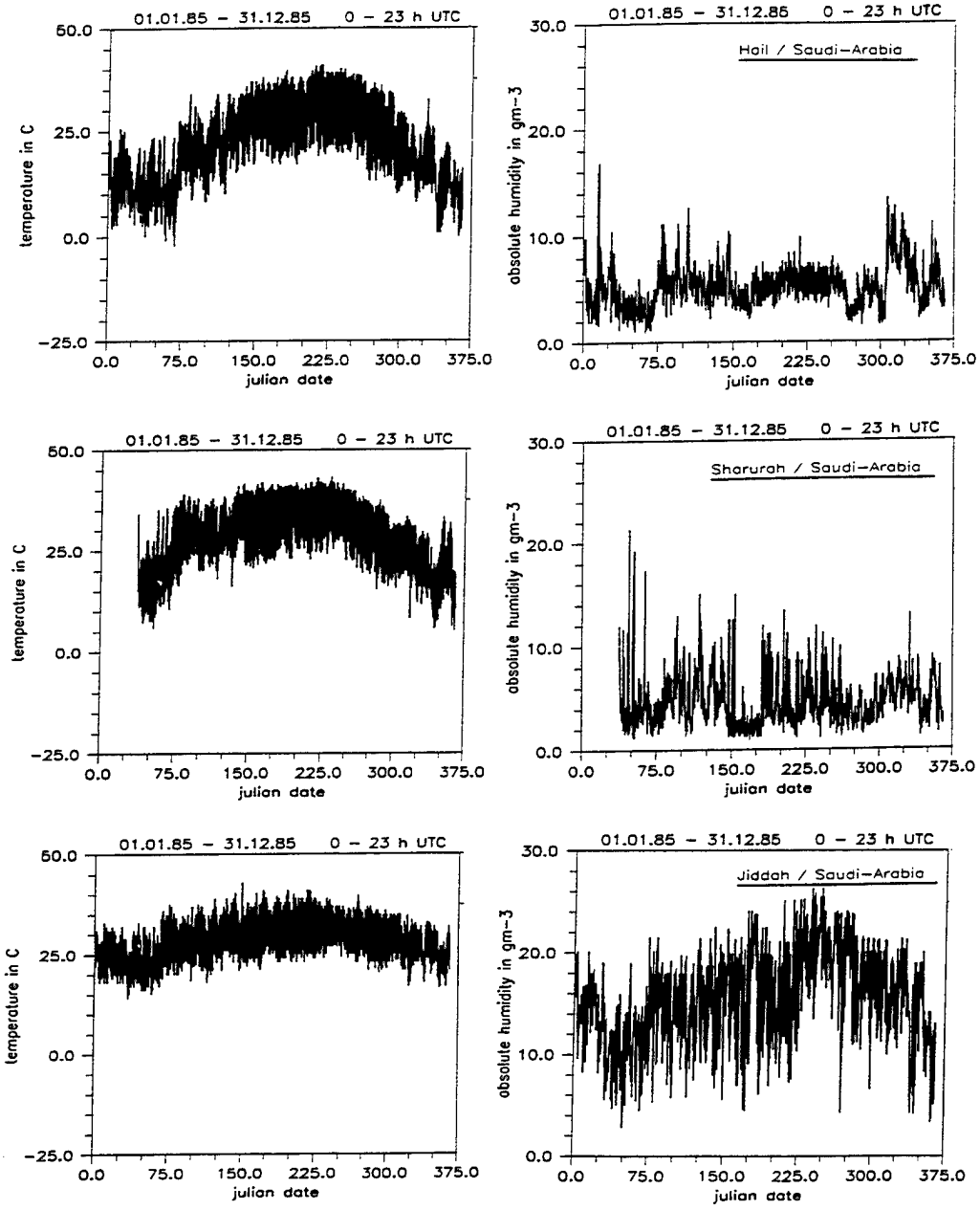


Fig. 2: Temperature (left) and absolute humidity (right) as a function of the Julian date at stations Hail, Sharurah, and Jiddah (Saudia-Arabia).

4.1 Selected Time Series of General Meteorological Data

In Fig. 2 time series over one year of atmospheric temperature and absolute humidity at three of the Middle East stations are presented.

The annual variation of temperature can reach an amplitude of nearly 40 °C at least in typical desert locations as shown in Fig. 2. In contrast the station Jiddah shows a more moderate amplitude of less than 20 °C due to its coastal environment. However, in both cases considerable diurnal variations of nearly 20 °C are observed. It should be mentioned that temperature in the desert even can reach the freezing point during nights of extreme radiative cooling. This is especially the case at higher altitudes, e. g. at Hail (see Figs. 1 and 2).

The absolute humidity can also vary extremely rapidly and reaches maximum values in Jiddah with extreme humidities in late summer of 20 - 25 gm^{-3}. All other stations examined in this study never reach these extreme absolute humidities, which obviously is related to the coastal position. Only Aqaba as a station near coast has comparable humidities. Cumulative probabilities of visual range V_N are shown in Fig. 3. At the stations considered, V_N rarely exceeds 15 km. This is a clear contradiction to the prediction contained in the original Desert Aerosol Model [3]. There a value $V_N \approx 80$ km is quoted for calm conditions. Therefore simultaneous measurements of meteorological, ir and aerosol conditions at desert locations seem extremely necessary. They are currently under preparation by the FGAN-FfO. Furthermore, the results seem to indicate a need for more sophisticated desert type aerosol models. The discrepancy may result from visibility estimation conventions or even from observational errors or inadequate positioning of visibility marks near the observation site.

4.2 Cumulative Probabilities of IR Transmittances

The calculated transmittances at the nine Middle East meteorological stations have been evaluated in the form of cumulative transmittance curves. In Fig. 4 some exemplary results are presented for the Middle East desert region (stations Hail, Sulayel and Sharurah) and the coastal station Jiddah. As stated earlier, the LOWTRAN 7 Desert Aerosol Model was applied throughout. Fig. 4 shows the molecular, aerosol, and total transmittance, respectively, for both atmospheric window regions (3 - 5 µm left, and 8 - 13 µm right). The molecular contribution is strongly related to the atmospheric water content, which assumes excessive values at the coastal station of Jiddah. Consequently the cumulative curve of Jiddah deviates strongly from those of all other stations. (The water content at Jiddah has already been shown in Fig. 2). In general the transmittance (over 1 km range as shown here) at 8 - 13 µm is approximately 10 - 15 % larger in comparison with the 3 - 5 µm region. For Jiddah, a strong broadening of the molecular transmittance distribution is observed when changing from the 3 - 5 µm region to 8 - 13 µm. This effect must be attributed to the weaker water vapor dependence of absorption in the 3 - 5 µm region in comparison to the 8 - 13 µm region, which becomes even more effective at extreme high water contents (above 15 gm^{-3}) as occurring at Jiddah.

The aerosol transmittances are quite similar at all stations and for both regions as can to be seen from Fig. 4 (middle). The partly stepped curves reflect the wind and mainly the visibility statistics, which are often given by rough step functions due to human eye observations or instrumental readings. Fig. 4 (bottom) shows the total transmittance statistics. As aerosol transmittance usually is relatively high mainly the molecular contribution determines the total trans-

mittance and the form of the cumulative curves. But still further analyses based on relevant measurements will have to take into account visibilities exceeding 15 km and should be based on experimentally proven aerosol models.

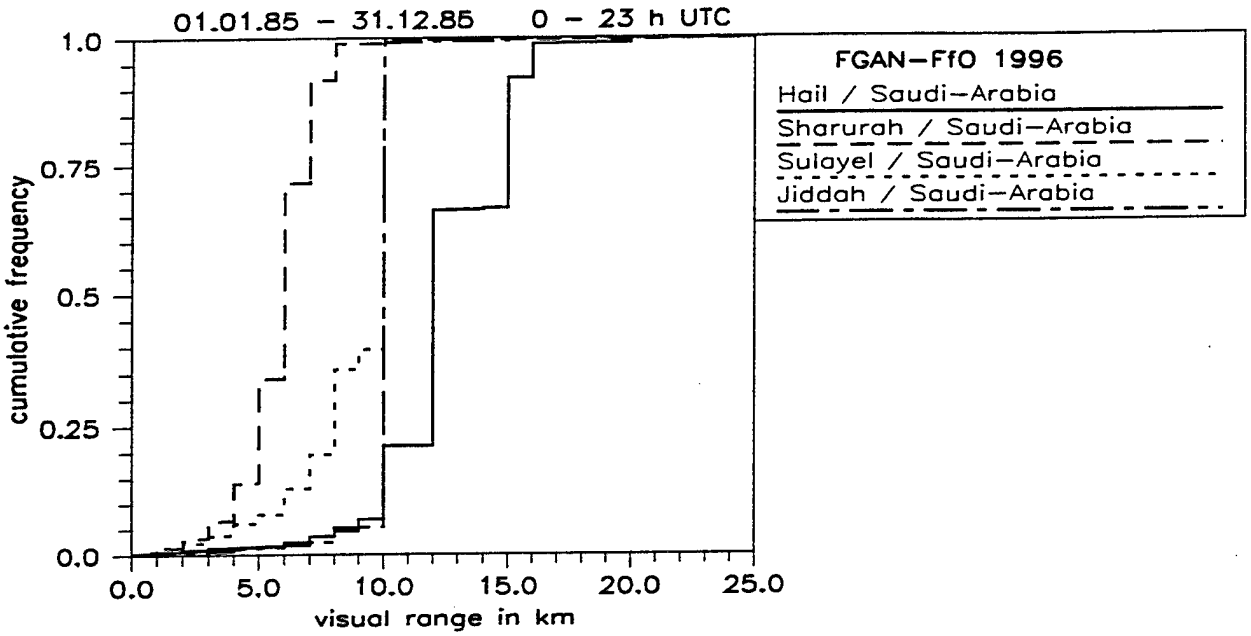


Fig. 3: Cumulative probabilities of visual range based on 1 year of observations (1985) at the desert stations Hail, Sulayel, and Sharurah, and the coastal station Jiddah.

(Values exceeding 15 km seem not to occur due to observation / documentation conventions used)

4.3 Annual Variability of IR Propagation Conditions

So far only annual statistics data have been presented. Fig. 5 illustrates the seasonal variability of seven n-percentiles (n = 5, 10, 25, 50, 75, 90, 95) of the total transmittances (3 - 5 µm and 8 -13 µm) for the stations Jiddah and Sulayel which seem to be representative for a coastal and a central desert station, respectively.

A relatively broad distribution in the 8 - 13 µm region can be observed in Jiddah, which shrinks to a nearly constant value over the whole year in the 3 - 5 µm region, caused by the weaker dependence against water content variations mentioned under 4.2. The annual variations are comparatively small, also in the 8 - 13 µm region, and probably also influenced by local circulation systems which cannot be analyzed in detail without further information about the different locations of the meteorological stations involved in this study.

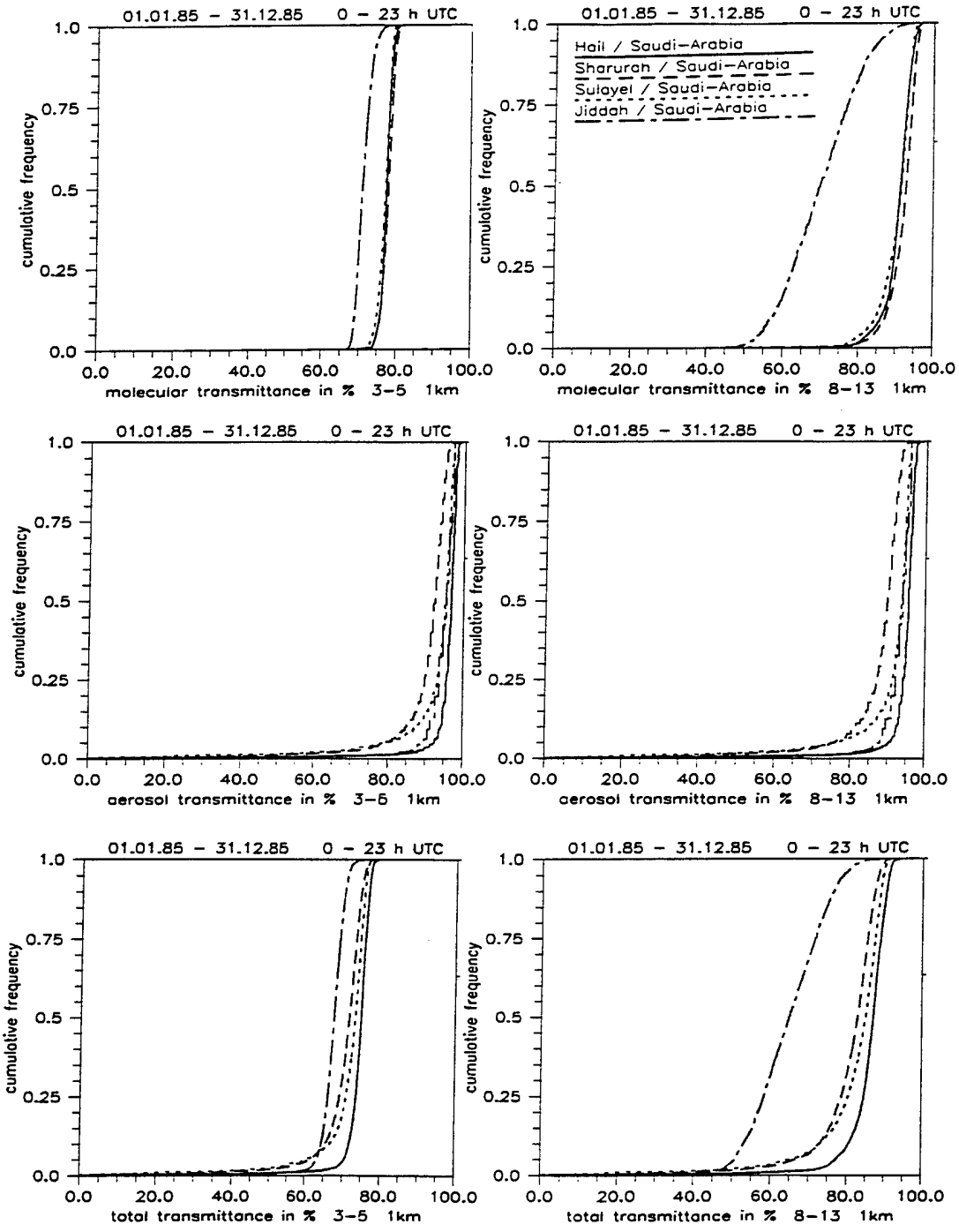


Fig. 4: Cumulative frequencies of molecular (top), aerosol (middle) and total (bottom) ir transmittances over 1 km range for stations Hail, Sharurah, Sulayel and Jiddah: wavelength regions 3 - 5 µm (left) and 8 - 13 µm (right).

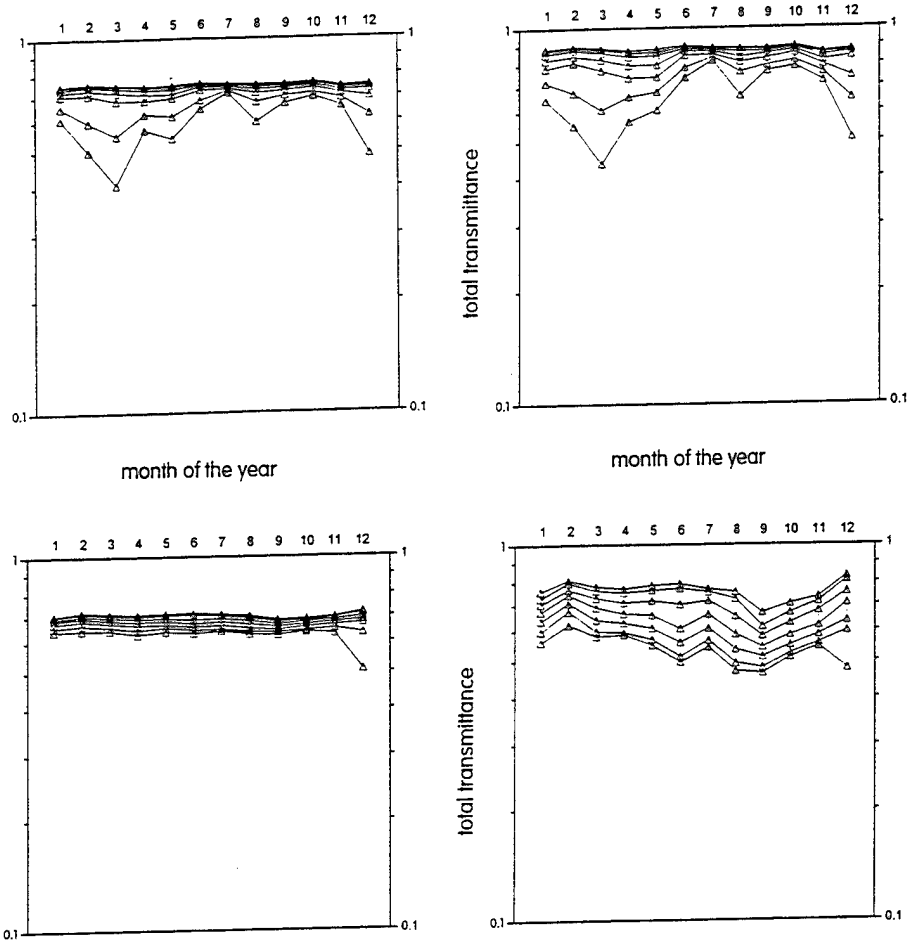


Fig. 5: Cumulative seasonal variation of total transmittance over 1 km in the 3 - 5 µm region (left) and the 8 - 13 µm region (right) at the station Sulayel (top) and Jiddah (bottom). The seven curves represent various n-percentiles with n = 5, 10, 25, 50, 75, 90 and 95, counted from bottom to top.

The conditions in Sulayel are different from those in Jiddah but seem nevertheless more characteristic for desert regions. The 8 - 13 µm region (for 1 km) is generally 10 - 15 % "better" than the 3 - 5 µm region. During the months December to May also larger transmittance reductions can occur. The general form of the curves is mainly determined by the molecular contribution, whereas the aerosol contribution is generally very small. It turned out that only for comparatively short periods the aerosol extinction becomes the dominating factor. This holds for all desert stations, where these events are mainly attributed to sand / dust storms.

4.4 Estimation of Thermal Ranges Statistics

The knowledge of range statistics for modern thermal imagers operating under arid climatic conditions is extremely important. On the basis of the meteorological data set described above an estimate of such statistics was performed.

Mathematically the range R of a thermal imager is determined by the intersection point of its *MNTD* (Minimum Necessary Temperature Difference) and the Effective Temperature Difference (*ETD*) [4]. Both functions are - besides others - a function of range R. The *ETD* is scaled by the absolute value of the initial target-to-background temperature difference, ΔT_0. Thus the following equation has to be solved to calculate a thermal range R of a certain imager and for a certain observation task:

$$ETD = \Delta T_0 \cdot \tau_{eff}(R) = N \cdot MNTD(R), \tag{1}$$

where $\tau_{eff}(R)$ is the effective, i. e. systems weighted, atmospheric transmittance. N is a normalizing factor converting the *MNTD* measured under laboratory conditions to real meteorological conditions. The calculations were performed for the following conditions:

thermal imager:	generic system 8 - 13 µm,
observation task:	50 % recognition probability,
target size:	2.3 m x 2.3 m.

The *MNTD* was taken from the FGAN-FfO Thermal Range Model (TRM) [4]. The effective atmospheric transmittance was calculated via the SYTRAN-Code [1]. The initial temperature difference was estimated from a simple zero order model assuming a sinusoidal diurnal variation of ΔT_0, with a maximum around early afternoon and a minimum during night or early morning hours, both extremes depending on season and cloud cover. Extreme values of ΔT_0 range from 3.5 K (summer, afternoon) to 0.4 K (winter, night and early morning hours).

Equation (1) was solved numerically to obtain the thermal range R for a given meteorological condition. A statistical evaluation is given in Fig. 6, where cumulative frequencies of thermal ranges are plotted for the nine Middle East weather stations and the conditions listed above.

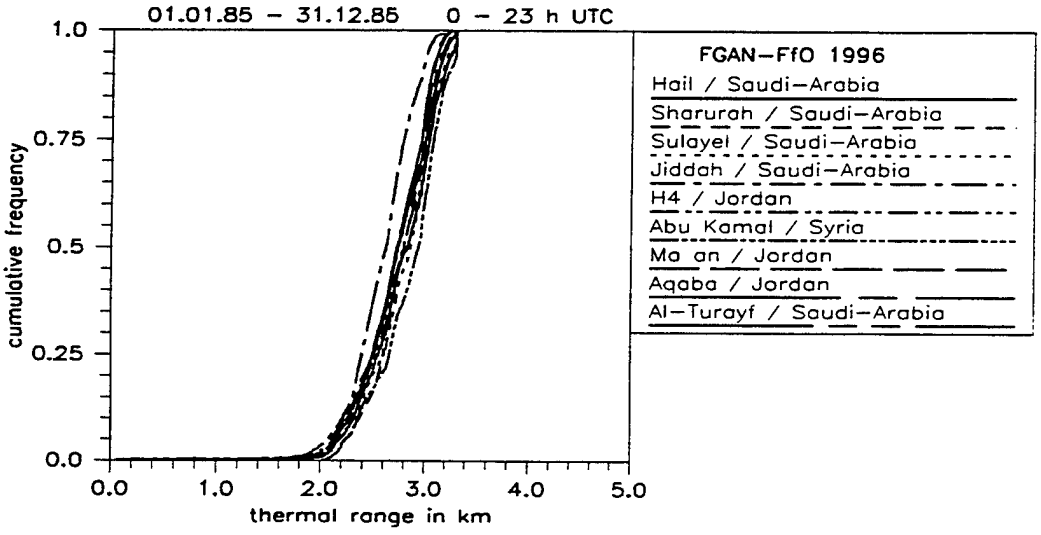


Fig. 6: Cumulative frequencies of tank recognition ranges for a generic thermal imager in the 8-13 µm region at nine Middle East weather stations.

5. Conclusions

Synoptic weather data from nine Middle East meteorological stations have been analyzed with respect to ir propagation conditions. Apart from coastal stations the ir transmittances behave quite similar at all stations. The conditions at the coastal stations are mainly influenced by high atmospheric water vapor amounts which drastically influences the molecular transmittance contribution.

Statistics of visual ranges cannot be explained by the LOWTRAN 7 Desert Aerosol Model. Therefore comprehensive field measurements on a regular basis performed under desert conditions including aerosol measurements seem extremely necessary to derive well established statistics and a more sophisticated desert type aerosol model.

The individual characteristics of ir propagation conditions at each station will certainly be influenced also by local climatological and orographic effects. A detailed interpretation of the results will, however, only be possible, when related information will be available.

To derive realistic thermal imager performance ranges, additional relevant target-background models have to be established and the influence of clutter to be included, which can be quite excessive under desert conditions.

References

[1] Halavee, U., W. Jessen, A. Hirneth, A. Kohnle: Systems-Weighted Infrared Broad-Band Atmospheric HorizontalTransmittance: The Computer Code SYTRAN, Report FGAN-FfO 1981/ 78

[2] Kneizys, F.X., E.P. Shettle, L.W. Abreu, J.H. Chetwynd, G.P. Anderson, W.O. Gallery, J.E.A. Selby, S.A. Clough: Users Guide to LOWTRAN7, AFGL-TR-88-0177, ERP No. 1010, August 1988

[3] Longtin, D.R., E.P. Shettle, J.R. Hummel, J. D. Price: A Wind Dependent Desert Aerosol Model: Radiative Properties, AFGL-TR-88-0112, April 1988

[4] Büchtemann, W., D. H. Höhn, W. Wittenstein: Thermisches Reichweitenmodell des FGAN-FfO, Report FGAN-FfO 1977/23

Acknowledgements

The authors are grateful to the German Weather Service, Seewetteramt Hamburg, for providing the basic data set.

Our thanks are also due to Hans-Jörg Neu, who helped us analyzing the data and preparing the graphical presentations.

MARINE AEROSOL PROPERTIES AND THERMAL IMAGER PERFORMANCE (MAPTIP): SYNOPSIS

Gerrit de Leeuw and Alexander M.J. van Eijk

TNO Physics and Electronics Laboratory
P.O. Box 96864, 2509 JG The Hague, The Netherlands
phone +31 70 3740462, FAX +31 70 3280961
email: deleeuw@fel.tno.nl, amjn1@fel.tno.nl

Douglas R. Jensen

Propagation Division
NCCOSC RDTE DIV D883
49170 Propagation Path
San Diego CA 92152-7385, USA
Phone: +1 619 553 1415, FAX: +1 619 553 1417
email: djensen@nosc.mil

ABSTRACT

The MAPTIP (Marine Aerosol Properties and Thermal Imager Performance) experiment was organised as part of a project to assess atmospheric effects on the performance of electro-optical sensor systems in coastal areas. The main issue was the detection and identification of targets. The experiment took place at the North Sea from 11 October to 5 November, 1993, and was centred around Meetpost Noordwijk, a research tower 9 km from the Dutch coast. Platforms included a beach station, ship, research airplane, P3 Orion, helicopter and three buoys. The aim was to characterise the atmosphere (aerosols, extinction, turbulence, refractivity, and the vertical and horizontal variations of relevant meteorological parameters) in combination with detailed measurements of optical and IR effects using thermal imagers, visual cameras, transmissometers and visibility meters, as well as a variety of point sources and ship, aircraft and helicopter serving as targets. Detection and identification ranges were determined and, for the interpretation of IR signature measurements, IR properties of extended targets were continuously monitored with radiometers. Extensive studies were made on polarisation effects, backgrounds and effects of sun glint. An overview of the experimental efforts and the ensuing analysis and modeling studies is presented. MAPTIP was the first validation of some recently developed atmospheric propagation models, including aerosol models, in a coastal environment. MAPTIP has yielded a wealth of data for the development of advanced aerosol models, description of horizontal variability, improvement of point target detection algorithms, validation of detection range models, and EOTDA validation.

1 INTRODUCTION

The development and assessment of the performance of electro-optical (EO) detection systems requires validated models describing the sensor and target characteristics, the background and the propagation medium. The propagation medium, i.e. the intervening atmosphere, introduces extinction, refraction and turbulence, leading to degradation of the radiance contrast between a target and its natural background, as viewed by the sensor. Atmospheric constituents absorb and scatter radiation. Therefore, atmospheric models used in the propagation prediction codes, in particular for aerosols but also for gaseous constituents, need to be accurate. Turbulence and refraction, due to temperature fluctuations and temperature gradients, respectively, cause blurring, scintillation, beam wander, mirages, etc. In thermal imagers, these effects may result in image distortion, contrast reduction and other detection problems. In this contribution we focus on atmospheric models and their validation.

Presently, the Atmospheric Transmission/Radiance computer code, LOWTRAN,[44,45] or its more recent version MODTRAN, is the primary tool used for the assessment of atmospheric effects on systems performance. With the inclusion of the Navy Aerosol Model, NAM, [46-53] into LOWTRAN6 and an upgraded version of NAM into

LOWTRAN7,[46] users are now able to determine the effects of aerosols on EO propagation in a maritime environment. This model has proven to be a useful tool in predicting transmission in the marine atmosphere along horizontal paths at shipboard levels (around 10 m). In coastal areas the influence of continental aerosol renders the NAM predictions less reliable. The Navy Oceanic Vertical Aerosol Model (NOVAM)[54-64] has been developed to predict the vertical profiles of extinction, from shipboard heights upward, throughout the marine boundary layer and above, up to 5000 feet. NOVAM uses NAM as its kernel and the model accounts for the generation, dispersal and removal of the marine aerosols. However, to date, the NAM and NOVAM validation has been restricted to a limited range of meteorological situations and geographical locations and must be extended to include coastal regions which are often governed by substantial concentrations of continental aerosol.[53] Also, recent studies have shown that NAM/NOVAM in their present forms should not be extrapolated into the region very near the surface of the ocean (below 10 m) for predicting atmospheric properties.[53, 65]

The propagation properties in the lower few meters above the mean surface are important for the assessment of atmospheric effects on EO propagation over long ranges, along paths skimming the wave tops. Examples are Long-Range IR Search and Track (LR-IRST) applications for detection of sea-skimming missiles, periscope detection, etc. The only available model for extinction near the ocean surface is an empirical formulation based on very few measurements over the open ocean.[58] In coastal areas this model has not been validated. However, based on comparisons of aerosol profile data, measured in different regions and under different meteorological conditions,[53] this simple empirical formulation is not expected to be generally applicable.

Other effects that are important for long-range propagation close to the sea surface are turbulence and refraction. Turbulence increases significantly close to the surface, because of generation due to the friction between wind and waves. Refractivity is caused by refractive index structure due to temperature gradients. Turbulence and refraction are not taken into account in MODTRAN. Until recently these effects were not considered important over sea, because of low turbulence intensities and short propagation ranges. However, now that technological progress will allow for much longer detection ranges, the effects of turbulence and refraction may be significant factors. Models are being developed and validated based on experimental data. An example is IRTOOL, that includes extinction, turbulence, refraction, as well as other features required to assess IR sensor performance. Models describing effects of refraction and turbulence are still being developed (e.g., refs. 30, 34, 35, 36) and experimental data are required for their validation.

It is therefore important to obtain more detailed information on atmospheric characteristics for the 3-5 and 8-12 μm wavelength bands in the first few meters above the sea surface, and to use this information in an effort to model this region (from the ocean surface to about 10 m). Simultaneous characterisation of the atmosphere, and application of sensor systems for the detection of a variety of well-defined targets are required. In particular point targets within a few meters of the ocean surface are important, but also targets at higher elevations and extended targets.

2 MAPTIP

The MAPTIP (Marine Aerosol Properties and Thermal Imager Performance) experiment was the first effort to determine atmospheric effects on electro-optical propagation at low levels in coastal areas. The NATO AC/243 (Panel 4/RSG.8), a study group on atmospheric effects on EO propagation, planned and conducted MAPTIP with participation of NATO AC/243 (Panel 4/RSG.5) (IR targets and backgrounds). This cooperation brought together the unique combination of expertise required to obtain the necessary experimental data and for the subsequent interpretation.

MAPTIP thus had two main goals. The first was the development and validation of models describing atmospheric effects on electro-optical propagation properties (aerosol extinction, refraction and turbulence), in particular for (slant) long-range propagation paths. This required a comprehensive study of relevant atmospheric processes, both from the experimental and modeling points of view, at levels from the sea surface to the top of the boundary layer. Simultaneous application of IR-sensor systems was used to provide data for testing of the models in simulated operational conditions. The result, i.e. the validated models, are intended to be included in tactical decision aids for naval defence.

The second aim of MAPTIP was the assessment of thermal imager performance in a maritime environment. This requires, apart from atmospheric effects, ship signatures and other target characteristics, models for backgrounds and clutter, etc., in a variety of atmospheric conditions. This topic will not be discussed in this contribution. More information and references can be found in ref. 26.

The MAPTIP experiment was conducted in the North Sea, October 11 - November 5, 1993. The focal point was Meetpost Noordwijk (MPN), position 45° 16' 25.9" N; 04° 17' 45.8" E. MPN is a research tower 9 km from the Dutch coast, owned and maintained by the Dutch Ministry of Public Works. This coastal location is subjected to strong anthropogenic influences. Surrounding land masses of continental Europe and the UK include industrial areas, large cities and agricultural and rural areas. North-westerly wind directions, however, bring clean polar air masses that are representative of open-ocean conditions,[67] in combination with large fetches. In addition to MPN, MAPTIP platforms included a beach station in Katwijk, a ship, the NRaD airborne platform, the oceanographic research vessel Hr.Ms.Tydeman, a P3 Orion, a Lynx helicopter and three buoys.

Aerosol and meteorological instruments, thermal imagers and calibrated targets, were utilised on the MAPTIP platforms, cf. refs. 4, 6, or 12 for extensive descriptions of the MAPTIP experiment. This network of instrumentation was used for obtaining a comprehensive data base of aerosol size distributions, including surface layer profiles of the aerosol and (size segregated) chemical composition and relevant meteorological variables. Profiles of aerosol particle size distributions and meteorological parameters in the marine atmospheric boundary layer were measured with radiosondes and with the NRaD airborne platform.

Information was also required for the development of the next generation aerosol model ANAM (Advanced Navy Aerosol Model). Emphasis was placed on observations close to the ocean surface (below 10 m). Thermal imagery was also included to provide ground truth for assessing the ANAM model development for low-level propagation. For characterisation of spatial variation effects on electro-optical propagation in this coastal area, measurements on the horizontal distribution of the aerosol and the meteorological variables were made using the Hr. MS. Tydeman and the NRaD airborne platform.

Further, measurements of atmospheric turbulence and refractivity effects in the visible and IR bands were made to assess marine boundary layer effects on the degradation of thermal images that were recorded from the various platforms.

MAPTIP was organised by the TNO Physics and Electronics Laboratory (The Hague, The Netherlands), and supervised by a scientific committee chaired by Dr. Jensen from NCCOSC, with participation of about 50 scientific and engineering personnel from 16 scientific institutes located in 9 countries.[1]

3 THE MAPTIP DATA

A large data set was collected during MAPTIP, including thermal images, video recordings of refractive effects, 3-D lidar maps showing boundary layer dynamical behaviour, etc. Support data include the meteorological data, aerosol data and the calculated extinction coefficients that are needed for the analysis and interpretation of the results.

Aerosols and meteorological parameters were measured by different groups, on different platforms, and with different instrumentation. For instance, some of the meteorological parameters were measured during MAPTIP by as many as nine different instruments. For an unambiguous interpretation of the MAPTIP results, it is of crucial importance that the support data are reliable and single-valued. Therefore, a strong effort has been made to deliver consensus data sets both for the meteorological parameters[21] and for the aerosol size distributions, cq. extinction coefficients.[23] See ref. 26 for a brief summary.

4 MODELS AND VALIDATION

4.1 Development and validation of aerosol models

One of the principal objectives of MAPTIP was to collect data for the development of a model that describes the aerosol concentrations in the lowest few meters above the sea surface (ANAM). To accomplish this, NRaD deployed an instrument package with optical particle counters, rotorods and meteorological equipment[14, 27] that was lowered from MPN to just above the wave tops. Data were collected at a range of levels, thus providing aerosol and meteorological 'profiles'. Due to the wind direction relative to MPN, that was generally encountered during MAPTIP but is not common for the area in the fall, few data were collected for which the samplers had optimum exposure to air masses advected from open sea. Nevertheless, enough data were collected to allow for the determination of the variation of the extinction values with height. The analysis of the aerosol size distributions led to the formulation of a preliminary version of ANAM.[27] The large-particle mode that had earlier been suggested[60] (NAM mode 4) is presented as a log-normal distribution with a mode radius that is independent of wind speed, and a mode amplitude that increases exponentially with wind speed.[27] At wind speeds above 5-6 m/s the evidence of a gradient in the concentrations of large aerosols disappears. The turbulence produced by the high wind speed also mixes the large aerosol in the lowest 10 m of the atmosphere. As a result, any vertical structure in the aerosol spectrum disappears while the net amount of large aerosol increases non-linearly with the wind speed.

The analysis[19] of the rotorod data measured by TNO from the north side of the platform, using a mast extending 10 m out (cf. ref. 73 for a description), shows that the gradients can be described by existing surface layer formulations. However, in many other cases, positive gradients were observed, a situation that cannot be handled by the model. Physically, positive gradients, i.e. concentrations at elevated levels that are larger than close the source, are not likely. However, in off-shore winds, particles advected form land need to be considered as well as the balance between these continental particles and freshly produced aerosol. The situation is complicated by the relatively short fetches, developing wave fields and developing boundary layers, all resulting in different transport regimes. This is a very complicated situation that cannot be described by current aerosol transport models.

Existing empirical aerosol models are not always reliable in coastal areas. An evaluation of NAM with the HEXOS aerosol data collected at MPN in 1986 has clearly indicated the large discrepancies in continentally influenced air masses.[53] In purely marine air masses, on the other hand, NAM predictions for the MPN area compare favourably with experimental data. The HEXOS aerosol data set has been analysed to identify the most important parameters affecting the aerosol concentrations, and an empirical model has been formulated.[67] This HEXOS model has been validated with the MAPTIP data collected at the MPN.[13] The model has been extended for wind directions that were not available in the HEXOS data set.[67, 13] During MAPTIP the wind was mainly from easterly directions, as opposed to the westerly winds that usually prevail in the fall in this area.

Using the aerosol particle size distributions measured during MAPTIP on Hr.Ms. Tydeman, the HEXOS model was evaluated for North Sea areas other than MPN. The analysis clearly shows that the model performance degrades rapidly with the distance to the area for which it was developed.[13]

The spatial variability was investigated using the MPN/Tydeman aerosol and meteorological data sets.[28] Horizontal variations of both the aerosol and the meteorological parameters were clearly demonstrated. Concentrations of large aerosol particles (typically 5 μm) increased with fetch. On the other hand, the expected decrease in the concentrations of the small aerosol particles (0.5 μm as a typical example) was not significant. The time lags between variations occurring at MPN, and downwind from MPN at the Tydeman, are in good agreement with the time required to transport the air mass.

Further evidence for the horizontal variation of the aerosol concentrations was provided by the aerosol maps produced from the data collected with the NRaD airborne platform. In contrast to the analysis of the data from Hr.Ms. Tydeman, the aircraft data did indicate considerable structure in the smallest sizes. Strong gradients were observed and plumes were clearly identified.[15] The aircraft measured in a relatively small area (on the order of 25 km) during a short time in which aerosol plumes may have had little time to disperse. The aircraft data therefore

may be representative of local plumes. The ship, on the other hand, measured over larger distances (200 km) during long times and used the MPN data as reference.

In analogy with the above discussion on the vertical gradients, a detailed description of the horizontal variations is complicated by the vicinity of land-based sources and the fetch-dependent generation of fresh marine aerosol. The wave field is not fully developed at short fetches. A small-scale coastal aerosol model is needed to adequately take into account complex structures of the coastal environment. An effort to get better insight into coastal phenomena is underway in the framework of EOPACE (Electro-Optical Propagation Assessment in Coastal Environments).[71]

Chemical analyses of the aerosol composition were made using data collected on MPN and Hr. Ms. Tydeman. The MPN data include volatility samples that give insight in the composition of the aerosol.[16] The ship data were impactor samples that were analysed on the elemental composition of the size fractionated aerosol. Results were used in the studies on the horizontal variability of the aerosol[13] and gave a clear indication of the influence of anthropogenic aerosol. These results were further used in a study on aerosol deposition into the North Sea.[42]

4.2 Extinction

Direct measurements of extinction coefficients were made with visibility meters operated by DREV.[37] These data were used in the formulation of the consensus aerosol data set as discussed in section 2.

In addition, extinction coefficients were determined from the variation of the intensity of the source suspended under the Lynx helicopter, as observed with thermal imagers at MPN, when the helicopter moved away from the tower. These data compare favourably with extinction coefficients derived from the measured aerosol particle size distributions and MODTRAN calculated molecular extinction. When, instead of the 'experimental' aerosol extinction, extinction values were used that were calculated with MODTRAN, using either the maritime model or the urban model, large discrepancies were observed. This result indicates that the use of existing models in this coastal environment may lead to wrong conclusions. The effect of continental aerosol must be taken into account, but it is not clear, *a priori*, how this must be done. Obviously, this requires the application of an aerosol transport model with the appropriate length scales.

Extinction coefficients at a wavelength of 1.064 μm were deduced from measurements with the IFU lidar.[29] Over the surf zone the extinctions are clearly enhanced and are in the range 0.05-0.3 km^{-1} . These values are in agreement with low-level extinction values calculated from the aerosol measured from MPN.[28] Since IFU lidars were used at four wavelengths, the wavelength dependence of the extinction coefficients could be determined.[29]

4.3 Marine boundary layer and surf zone characterisation by lidar and horizontal variability

Lidar provides a unique remote sensing tool for the characterisation of atmospheric properties such as boundary layer structures, turbulence, convective cells and the variation of extinction in both the horizontal and the vertical dimension. During MAPTIP, lidars were used at MPN and at the beach station.[8, 29] Convective and turbulent mixing were clearly demonstrated, in many occasions, with the TNO lidar on MPN. The influence of waves on the surface layer structures (below 10 m) were revealed and ship plumes could be detected. The IFU lidar at the beach station clearly demonstrated larger scale structures at somewhat higher elevations, with periods of 300-400 m. The effect of the surf on the extinction was also clearly visible.

MAPTIP was one of the first experiments where the IFU eye-safe lidar was used (after VAST92, another NATO AC/243 (Panel 4/RSG.8) trial).[8] The extinction in fog is much lower at the eye-safe wavelength (1.56 μm) then at the wavelength of 0.532 μm (factor 7). See also section 3.2 for extinctions measured with the lidar.

4.4 Refraction

Refractivity effects during MAPTIP were studied by three groups.[18, 30, 40] MAPTIP was the first validation of the French model PIRAM.[72] For the WKD model from DREV it was the second test at open sea. The results are in satisfactory agreement with model predictions in both the mid-infrared and the visible. Differences are ascribed to

inhomogeneities in the MBL due to coastal influences.[18] A comparison between the PIRAM and WKD models is presented in ref. 30. The Maximum Inter-Visibility Range (MIVR) was often well within 1 km of the measured values, and always within 2 km. The minimum mirage range and maximum and minimum mirage height predictions are also reasonably good.

4.5 Effects of turbulence on long-range measurements

Several models describing effects of turbulence on EO propagation are available in the MAPTIP community. Direct measurements were made for the evaluation of these models,[35] and for comparison with bulk formulations.[19, 34] The bulk turbulence model was compared with direct measurements of the friction velocity u_* from the NPS buoy to test its predictive value.[19] This is extremely valuable for those occasions when direct measurements are not available. The comparison led to the conclusion that the bulk values are sufficient for characterisation when no data are available. The inertial-dissipation derived u_* is larger than the bulk derived values, probably due to the bulk formulation at short fetches. Values for the temperature structure function parameter C_T^2 were derived from the bulk formulation and from the inertial dissipation method. The results are in good agreement for $C_T^2 > 10^{-2}$, i.e. in strongly unstable conditions.[34] In the lower C_T^2 regime the turbulent fluctuations of temperature are not important for optical propagation.

The TNO-FEL bulk meteorological model has been validated with measurements of optical turbulence.[35] This was done in an extension of the MAPTIP work. The measurements were made along a 19 km propagation path that was completely over water. The model predicts the scintillation and refractive index structure function parameter (C_N^2) well in on-shore winds. In off-shore winds, a non-equilibrium situation is created in which the theory does not strictly apply. The comparison between the model predictions and the experimental data confirms that large discrepancies may occur.

5 CONCLUSION

An overview has been presented of the accomplishments and achievements from the MAPTIP experiment in the field of modeling and model validation. Other important topics are detection ranges, polarisation, ship signatures and background and clutter models. Details have been presented in, thus far, 40 publications.[1-40] The MAPTIP data are also being used for other studies.[41-43] MAPTIP has served as a testbed for the first validation of atmospheric propagation models,[18, 36, 40, 72] and aerosol models.[13, 19, 28] This has resulted in the preliminary formulation of ANAM.[27] Surf zone effects were reported.[29] Horizontal variability of aerosol concentrations, and thus aerosol extinction, was indicated on various scales, ranging from hundreds of meters[29] to some tens of km[15] and also to hundreds of km.[28] Turbulence models were tested with regard to their predictive value.[34] Detection range models and EOTDA were validated[9, 32] and the application of polarisation filters has resulted in a wealth of knowledge that can be used, e.g., to improve the contrast between target and background. Point target detection algorithms were significantly improved.[17, 31, 39] The use of lidar to reveal structures in the marine boundary layer, as well as in the surface layer, has been demonstrated.[29] Extinction coefficients were measured with lidar[29] and with visibility meters[37] for model validation. The results also demonstrate the use of lidar as a tool for remote sensing of the propagation environment. An assessment has been made on the use of MODTRAN in coastal regimes.[31]

Studies on electro-optical propagation effects in the coastal environments are continued in EOPACE.[71] EOPACE experiments are taking place in Southern California, centred around San Diego and Monterey, during 1996-1997. Among the objectives of EOPACE are:
- characterise aerosol production in the surf zone and its effects on transmission in the visible and IR wavelengths,
- characterise the air mass in an off-shore flow and the inherent changes in aerosol content and optical properties,
- long-range transmission (7, 15, 22 km) and scintillation measurements.

The wide variety of instrumentation used in the EOPACE experiments includes aerosol counters, meteorological instruments, radiometers, lidar, satellite remote sensing, polarisation measurements, thermal imaging and IRST performance. EOPACE intensive observational periods (IOPs) took place in April and November 1996, both centered around San Diego Bay. During the April IOP, an air mass characterisation experiment was also conducted in the Los Angeles basin. The aerosol plume was sampled from a ship providing ground truth aerosol particle size

distributions and chemical composition, meteorological data, and radiosonde and lidar profiles, while aerosol optical depth was retrieved from satellite data (AVHRR). The first surf zone experiments were conducted in San Diego, off Scripps Pier, in January/February 1996, and in Monterey Bay off the Moss Landing Marine Institutes Pier in March 1996. Long-range transmission was measured across Monterey Bay over a 22 km path.

6 ACKNOWLEDGEMENTS

MAPTIP was supported by NATO AC/243 (Panel 4) (Grants 6056 and 6092) and by the US Office of Naval Research ONR (Grant N00014-91-J-1948). The remaining logistics costs were shared by the individual participants listed in Table 2. The Netherlands Royal Navy made available the oceanic research vessel Hr.Ms. Tydeman, a Lynx helicopter, a P3 Orion and the Naval Air Station Valkenburg, and provided logistics support for these platforms. The efforts of the crews and personnel of these platforms made MAPTIP a success. The activities of the TNO Physics and Electronics Laboratory were supported by the Netherlands Ministry of Defence (assignments A91KM614, A91KM615 and A92KM776). The NCCOSC participation was funded under program element 62435N, RL3C Project RO35E82/01, Marine EO Effects. We wish to express our thanks to Direktie Noordzee of the Dutch Ministry of Public Works for the cooperation, advice and the use of MPN, the Scheveningen harbour facility, the ships Albatros and Smal Agt, and the dedication of the respective crews, in particular the crew of MPN. KNMI made available the boom at MPN. The MAPTIP experiment was organised by the TNO Physics and Electronics Laboratory. We thank our colleagues at TNO-FEL for their dedication. The authors also wish to acknowledge the fine cooperation with other colleagues in the MAPTIP project. The present compilation of results is only a small sample, reflecting the huge amount of work that has been done in MAPTIP.

7 REFERENCES

1. Jensen, D.R., G. de Leeuw and A.M.J. van Eijk (1993). Work plan for the Marine Aerosol Properties and Thermal Imager Performance trial (MAPTIP). Naval Command, Control and Ocean Surveillance Center, San Diego, CA, USA, Technical Document 2573 (September 1993).
2. Taczak, W., (Ed.) (1993). MAPTIP quick-look report. Prepared by Office of Naval Research, Arlington, VA, USA.
3. Chan, Padres M. (1993). Experimental Investigation of Infrared Polarization Effects in Target and Background Discrimination, MS Thesis, NPS, December 1993.
4. De Leeuw, G., A.M.J. van Eijk and D.R. Jensen (1994). MAPTIP experiment, Marine Aerosol Properties and Thermal Imager Performance: An overview. TNO Physics and Electronics Laboratory, report FEL-94-A140.
5. Jensen, D.R., G. de Leeuw and A.M.J. van Eijk (1994). Summary of the Marine Aerosol Properties and Thermal Imager Performance Trial (MAPTIP). Presented at the meeting of the International Union of Radio Science (URSI), 6-8 January 1994, Univ. Colorado, Boulder (CO), USA.
6. Van Eijk, A.M.J., D.R. Jensen and G. de Leeuw (1994). MAPTIP experiment, Marine Aerosol Properties and Thermal Imager Performance. In Atmospheric Propagation and Remote Sensing III, W.A. Flood and W.B. Miller (Eds.), SPIE Proceedings 2222, 299-315.
7. Cooper, A.W., W.J. Lentz, P.L. Walker and P.M. Chan (1994). Infrared Polarization Measurements of Ship Signatures and Background Contrast, In Characterization and Propagation of Sources and Backgrounds, Wendell W. Watkins and Dieter Clement, Eds, Proceedings SPIE Vol. 2223, pp. 300 - 309.
8. Carnuth, W. and T. Trickl (1994). A powerful eyesafe aerosol lidar: application of stimulated Raman backscattering of 1.06 μm radiation. Rev. Sci. Instrum.. 65, 3324-3331.
9. De Jong, A.N. (1994). NL ship-IR imagery at MAPTIP, TNO Physics and Electronics Laboratory, Report FEL-94-A143.
10. Moretz, D.G. (1994). Analysis of Target Contrast Improvement using Polarization Filtering in the Infrared Region; MS Thesis, Naval Postgraduate School, December 1994.
11. Walker, P.L., W.J. Lentz, and A.W. Cooper "Atmospheric and Sea State Dependence of Polarized Infrared Contrast", SPIE Proceedings Vol 2469, 393-399, (1995).
12. Jensen, D.R., G. de Leeuw and A.M.J. van Eijk (1995). Summary of the Marine Properties and Thermal Imager Performance Trial (MAPTIP). AGARD electromagnetic wave propagation panel 55th specialists' meeting on

"Propagation assessment in coastal environments", Bremerhaven, Germany, 19-23 September, 1994. AGARD CP 567, pp. 18-1 to 18-10.
13. Van Eijk, A.M.J., F.H. Bastin, F.P. Neele, G. de Leeuw and J. Injuk (1995). Characterisation of atmospheric properties during MAPTIP. AGARD electromagnetic wave propagation panel 55th specialists' meeting on "Propagation assessment in coastal environments", Bremerhaven, Germany, 19-23 September, 1994. AGARD CP 567, pp. 19-1 to 19-8.
14. Gathman, S.G. (1995). Aerosol profiles near the sea surface during MAPTIP. AGARD electromagnetic wave propagation panel 55th specialists' meeting on "Propagation assessment in coastal environments", Bremerhaven, Germany, 19-23 September, 1994. AGARD CP 567,pp. 20-1 to 20-11.
15. Gathman, S.G. and D.R. Jensen (1995). Aerosol maps made during MAPTIP. AGARD electromagnetic wave propagation panel 55th specialists' meeting on "Propagation assessment in coastal environments", Bremerhaven, Germany, 19-23 September, 1994. AGARD CP 567, pp. 21-1 to 21-7.
16. Smith, M.H. (1995). UMIST observations of accumulation mode aerosol concentrations and composition during MAPTIP. AGARD electromagnetic wave propagation panel 55th specialists' meeting on "Propagation assessment in coastal environments", Bremerhaven, Germany, 19-23 September, 1994. AGARD CP 567, pp. 22-1 to 22-8.
17. Stein, K., A. Kohnle, W. Schuberth and R. Jantzen (1996). Impact of coastal environment on point target detection. AGARD electromagnetic wave propagation panel 55th specialists' meeting on "Propagation assessment in coastal environments", Bremerhaven, Germany, 19-23 September, 1994. AGARD CP 567, pp. 23-1 to 23-10.
18. Forand, J.L., D. Dion and J. Beaulieu (1995). MAPTIP: Canada's measurements of refraction effects. AGARD electromagnetic wave propagation panel 55th specialists' meeting on "Propagation assessment in coastal environments", Bremerhaven, Germany, 19-23 September, 1994. AGARD CP 567, pp. 24-1 to 24-7.
19. Davidson, K.L., P.A. Frederickson and G. de Leeuw (1995). Surface layer turbulence and aerosol profiles during MAPTIP. AGARD electromagnetic wave propagation panel 55th specialists' meeting on "Propagation assessment in coastal environments", Bremerhaven, Germany, 19-23 September, 1994. AGARD CP 567, pp. 25-1 to 25-9.
20. Cooper, A.W., W.J. Lentz, P.L. Walker and P.M. Chan (1995). Polarization enhancement of contrast in infrared ship/background imaging. AGARD electromagnetic wave propagation panel 55th specialists' meeting on "Propagation assessment in coastal environments", Bremerhaven, Germany, 19-23 September, 1994. AGARD CP 567, pp. 26-1 to 26-10.
21. De Leeuw, G., A.M.J. van Eijk and D.R. Jensen (1996). MAPTIP Analysis Workshop, Quebec, May 24-25, 1995. In preparation.
22. De Leeuw, G., A.M.J. van Eijk and D.R. Jensen (1995). MAPTIP - Marine aerosol properties and thermal imager performance: summary and initial results. In 9th Meeting on Optical Engineering in Israel, I. Shladov, Y. Weissman, N. Kopeika (Eds.), SPIE Proceedings 2426, 67-78.
23. Smith, M.H. (1995). Aerosol measurements on the MPN during MAPTIP: is there an aerosol consensus? Report, University of Manchester Institute of Science and Technology, Manchester, UK.
24. De Jong, A.N. (1996). Proceedings NATO IRIS meeting, London, UK, 25-28 June, 1996.
25. Dainty, J.C., and L.R. Bissonnette, Editors (1996). Image Propagation Through the Atmosphere, Proc. SPIE 2828.
26. De Leeuw, G., A.M.J. van Eijk and D.R. Jensen (1996). Marine Aerosol Properties and Thermal Imager Performance (MAPTIP): an overview. In: Image Propagation Through the Atmosphere, J.C. Dainty and L.R. Bissonnette, Editors, Proc. SPIE 2828, 2-14.
27. Gathman, S.G. (1996). MAPTIP observations of large aerosol in the lowest 10 m above waves. In: Image Propagation Through the Atmosphere, J.C. Dainty and L.R. Bissonnette, Editors, Proc. SPIE 2828, 15-23.
28. Van Eijk, A.M.J., G. de Leeuw and M.M. Moerman (1996). Lateral variations of meteorological properties and aerosols in off-shore winds. In: Image Propagation Through the Atmosphere, J.C. Dainty and L.R. Bissonnette, Editors, Proc. SPIE 2828, 24-30.
29. Kunz, G.J. and T. Trickl (1996). Lidar measurements of atmospheric extinction during the MAPTIP trial. In: Image Propagation Through the Atmosphere, J.C. Dainty and L.R. Bissonnette, Editors, Proc. SPIE 2828, 31-38.
30. Forand, J.L. (1996). MAPTIP: refractive effects in the visible and IR. In: Image Propagation Through the Atmosphere, J.C. Dainty and L.R. Bissonnette, Editors, Proc. SPIE 2828, 39-49.

31. Schwering, P.B.W., G. de Leeuw and A.M.J. van Eijk (1996). Transmission of 10 micron radiation over coastal waters: comparison of point source image intensities with aerosol extinction and MODTRAN calculations. In: Image Propagation Through the Atmosphere, J.C. Dainty and L.R. Bissonnette, Editors, Proc. SPIE 2828, 64-75.
32. McGrath, C.P., P.B.W. Schwering and P.J. Fritz (1996). A comparison of MAPTIP FLIR detection ranges to the EOTDA prediction model. In: Image Propagation Through the Atmosphere, J.C. Dainty and L.R. Bissonnette, Editors, Proc. SPIE 2828, 76-84.
33. Cooper, A.W., W.J. Lentz and P.L. Walker (1996). Infrared polarization ship images and contrast in the MAPTIP experiment. In: Image Propagation Through the Atmosphere, J.C. Dainty and L.R. Bissonnette, Editors, Proc. SPIE 2828, 85-96.
34. Davidson, K.L., and P.A. Frederickson (1996). Small-scale turbulence measurements from a buoy during MAPTIP. In: Image Propagation Through the Atmosphere, J.C. Dainty and L.R. Bissonnette, Editors, Proc. SPIE 2828, 97-107.
35. Kunz, G.J., M.M. Moerman, P.J. Fritz and G. de Leeuw (1996). Validation of a bulk turbulence model with thermal images of a point source. In: Image Propagation Through the Atmosphere, J.C. Dainty and L.R. Bissonnette, Editors, Proc. SPIE 2828, 108-116.
36. Forand, J.L., and D. Dion (1996). Predictive comparisons of marine boundary layer models. In: Image Propagation Through the Atmosphere, J.C. Dainty and L.R. Bissonnette, Editors, Proc. SPIE 2828, 129-140.
37. Hutt, D. L. (1996). Estimate of effective aerosol droplet radius from visible and infrared extinction measurements. In: Image Propagation Through the Atmosphere, J.C. Dainty and L.R. Bissonnette, Editors, Proc. SPIE 2828, 503-514.
38. De Leeuw, G., A.M.J. van Eijk and M.M. Moerman (1996). Aerosol dynamics over the North Sea in off-shore winds. J. Aerosol Sci. 27, Suppl. 1, S63-S64.
39. Schwering, P.B.W., and H.A. Lensen (1996). Infrared point source behaviour during the MAPTIP trials. TNO Physics and Electronics Laboratory, Report FEL-94-A326.
40. Forand, J.L., Y. Hurtaud and K. Stein (1996). MAPTIP work group report: Refractive effects in the visible and the Infrared. Defence Research Establishment Valcartier, Québec, Canada, Report DREV-MM-NNNN (in preparation).
41. Piazzola, J. (1996). Etude de la repartition verticale des particules d'aerosols au voisinage de l'interface mer-air en zone cotiere Mediterraneene. PhD Thesis, L'Universite de Toulon et du Var.
42. Injuk, J., R. van Grieken and G. de Leeuw (1996). Deposition of atmospheric trace elements into the North Sea: coastal, ship, platform measurements and model predictions. Submitted for publication in Atm. Env. (June 1996).
43. Flossmann, A.I., W. Wobrock, P.J.H. Builtjes, M. Roemer, G. de Leeuw, A.M.J. van Eijk, P.G. Mestayer, B. Tranchant, S.E. Larsen, L.-L.S. Geernaert, E. Ljungström and R. Karlson (1996). Vertical fluxes in the marine boundary layer. In preparation.
44. Kneizys, F.X., E.P. Shettle, W.O. Gallery, J.H. Chetwynd, Jr., J.H. Abreu, J.E.A. Selby, S.A. Clough and R.W. Fenn (1983). Atmospheric Transmittance/Radiance: Computer Code LOWTRAN 6, Air Force Geophysical Laboratory Technical Report No. 83-0187, August 1983.
45. Kneizys, F.X., E.P. Shettle, L.W. Abreu, J.H. Chetwynd, G.P. Anderson, W.O. Gallery, J.E.A. Selby, and S.A. Clough (1988). Users Guide to LOWTRAN 7, Air Force Geophysical Laboratory Technical Report No. 88-0177, Aug 1988.
46. Gathman, S.G. (1983a). Optical Properties of the Marine Aerosol as Predicted by the Navy Aerosol Model, Opt. Eng. 22, 57-62.
47. Gathman, S.G. (1983b). Optical Properties of the Marine Aerosol as Predicted by a BASIC Version of the Navy Aerosol Model, NRL Memo Report #5157.
48. Gathman, S.G. (1984). Navy Hygroscopic Aerosol Model. In: Hygroscopic Aerosol, L.H. Ruhnke & A. Deepak, editors, A. Deepak publisher, Hampton, VA., p93.
49. Hughes, H.G. (1987). Evaluation of the LOWTRAN 6 Navy Maritime Aerosol Model Using 8 to 12 micron Sky Radiances. Opt. Eng., Vol. 26, #11, 1155-1160.
50. Battalino, T.E., and R.A. Helvey (1985). Air Mass Parameterization in the Navy Aerosol Model. Geophysical Sciences Technical Note # 103, PMTC, Point Mugu, CA.
51. Gerber, H.E. (1985). Relative-Humidity Parameterization of the Navy Aerosol Model (NAM). NRL Report #8956, December 1985.

52. Hughes, H.G., and M.R. Paulson (1989). Lidar Technique for Adjusting Aerosol Model Number Densities to Existing Conditions. NOSC TD #1637, September 1989.
53. De Leeuw, G. (1993a). Aerosol effects on electro-optical propagation over sea. In: 8th meeting on Optical Engineering in Israel: Optical Engineering and Remote Sensing, M. Oron, I. Shladov and Y. Weissman (Eds.) Proc. SPIE 1971, 2-15.
54. Gathman, S.G. (1989). A Preliminary Description of NOVAM, the Navy Oceanic Vertical Aerosol Model. NRL Report #9200.
55. Gathman, S.G. (1992). Ocean Aerosol Measurements and Models in the Straits of Florida (The Key-90 Experiment). Atmospheric Propagation and Remote Sensing, A. Kohnle and W.B. Miller, editors, SPIE proceedings Vol. 1688, 2-13.
56. Gathman, S.G., G. de Leeuw, K.L. Davidson and D.R. Jensen (1989). The Navy Oceanic Vertical Aerosol Model: Progress Report. In: Atmospheric propagation in the UV, visible, IR and mm-wave region and related systems aspects, AGARD-CP-454 17-1 to 17-11.
57. Gathman, S.G., S.G., D.R. Jensen, W.P. Hooper, J.E. James, H.E. Gerber, K.L. Davidson, M.H. Smith, I.E. Consterdine, G. de Leeuw, G.J. Kunz and M.M. Moerman (1993). NOVAM evaluation utilizing electro-optics and meteorological data from KEY-90. Naval Command, Control and Ocean Surveillance Center, San Diego, CA, USA, Technical Report 1608 (September 1993).
58. De Leeuw, G. (1991). Aerosol models for optical and IR propagation in the marine atmospheric boundary layer. Propagation Engineering: Fourth in a series, L.R. Bissonnette and W.B. Miller (Eds.), Proc. SPIE 1487, 130-159.
59. De Leeuw, G., K.L. Davidson, S.G. Gathman, R.V. Noonkester (1989a). Modeling of Aerosols in the Marine Mixed-Layer. In: Propagation Engineering, SPIE proceedings, vol 1115, , p 287-294.
60. De Leeuw, G., K.L. Davidson, S.G. Gathman and R.V. Noonkester (1989b). Physical Models for Aerosol in the Marine Mixed-Layer. In: Operational decision aids for exploiting or mitigating electromagnetic propagation effects, AGARD-CP 453, pp. 40-1 to 40-8.
61. Davidson, K.L., G. de Leeuw, S.G. Gathman and D.R. Jensen (1990). Verification of the Naval Oceanic Vertical Aerosol Model During FIRE. In: FIRE Science Results 1989, D.S. McDougal, editor, NASA Conference Report #3079, pp. 191-196.
62. Gerber, H., S.G. Gathman, J. James, M.H. Smith, I. Consterdine and S. Brandeki (1990). NRL Tethered Balloon Measurements at San Nicolas Island during FIRE IFO 1987. In: FIRE Science Results 1988, D.S. McDougal and H.S. Wagner, editors, NASA conference publication #3079, 191-196.
63. Cecere, T.H. (1991). An Evaluation of the Naval Oceanic Vertical Aerosol Model during Key-90. Thesis. Naval Postgraduate School, Monterey, CA, USA.
64. De Leeuw, G. and G.J. Kunz (1992). NOVAM Evaluation from Aerosol and Lidar Measurements in a Tropical Marine Environment, In: Atmospheric Propagation and Remote Sensing, A. Kohnle and W.B. Miller (Eds.), Proc. SPIE 1688, 14-27.
65. Paulson, M.R., and H.G. Hughes (1990). A lidar technique for adjusting aerosol model number densities close to the ocean surface. Naval Ocean Systems Center Technical Report 1388, December 1990.
66. De Leeuw, G. (1993b). Aerosols near the air-sea interface. Trends in Geophys. Res. 2, 55-70.
67. Van Eijk, A.M.J., and G. de Leeuw (1992). Modeling aerosol particle size distributions over the North Sea. J. Geophys. Res. 97, (Vol. C9), 14417-14429.
68. Monin, A.S., and A.M. Obhukov (1954). Basic turbulent mixing laws in the atmospheric surface layer, Trudy, Geofys. Inst. AN SSSR, No 24 (151), 163-187.
69. Liu, W.T., K.B. Katsaros, and J.A. Businger (1979). Bulk Parameterizations of Air-Sea Exchanges of Heat and Water Vapor Including the Molecular Constraints at the Interface. J. Atm. Sci. 36, 1722-1735.
70. Jensen, D.R., R. Jeck, G. Trusty and G. Schacher (1983). Intercomparison of Particle Measuring Systems, Inc's particle-size spectrometers. Opt. Eng. 22, 746-752.
71. Jensen, D.R. (1995). EOPACE workplan. NRaD, San Diego, USA
72. Hurtaud, Y. (1996). Private communication.
73. De Leeuw, G. (1990). Profiling of aerosol concentrations, particle size distributions and relative humidity in the atmospheric surface layer over the North Sea. Tellus 42B, 342-354, 1990.

EOPACE (Electrooptical Propagation Assessment in Coastal Environments) Overview and Initial Accomplishments

C. R. Zeisse, D. R. Jensen, and K. M. Littfin
Propagation Division
NCCOSC RDTE DIV D883
49170 Propagation Path
San Diego, CA 92152-7385

SUMMARY

EOPACE is a five year international experiment to improve performance assessment for electrooptical systems operating in coastal environments. Initial results concern coastal aerosols. Aerosol optical depths in the marine atmospheric boundary layer derived from satellite images compare well with those measured directly inside the layer. Analysis of mid wave infrared transmission at low altitude above San Diego Bay shows a constant (30%) attenuation due to molecules and a variable (0% to 70%) attenuation due to aerosols and refractive focusing effects. Extinction coefficients derived from aerosol particle size distributions measured in the air above breaking surf show that aerosol extinction increases by an order of magnitude as the ocean surface is approached from a height of 8 meters.

LIST OF SYMBOLS

L Range (km).
m Subscript referring to molecules.
N Particles per unit volume (cm^{-3}).
p Subscript referring to particles.
Q Mie efficiency factor.
r Particle radius (microns).
x Position or distance (km).
T Optical depth.

β_p Aerosol extinction coefficient (km^{-1}).
λ Wavelength (microns).
τ Measured transmission (%).
τ_m Molecular transmission (%).
τ_p Aerosol transmission (%).

1. EOPACE OVERVIEW

EOPACE is a measurement and analysis program to improve performance assessment for electrooptic weapon and sensor systems operating in coastal environments [1]. The measurement campaign, which began in January, 1996, is being conducted in the California coastal region by participants from NATO countries. Coastal conditions may differ significantly from those in the open ocean and have not yet been fully characterized. The climate of the California region is similar to that of other interesting regions, such as the Mediterranean Sea, and represents an excellent example of a littoral environment.

The specific objectives of EOPACE are: (1) to assist in the development of mesoscale and data assimilation models, (2) to evaluate the performance of EO systems in coastal regions, and (3) to investigate coastal aerosols.

The key feature of EOPACE[1] is its long observation period, one to two years, interspersed with several intensive operational periods lasting two to three weeks each. Long term observations increase the chance of encountering a full range of atmospheric conditions. EOPACE will provide the database for mesoscale model development and evaluation. The performance of EO systems will be evaluated from measurements and studies of targets and backgrounds, polarization effects, IRST and FLIR performance, and tactical decision aids. For the coastal aerosol study, measurements will support the investigation of surf production of aerosols, characterization of coastal air masses, and characterization of near ocean surface transmission.

2. COASTAL AIR MASSES.

The goals of the air mass characterization effort are: (1) to provide a database for initializing and testing the mesoscale coastal aerosol models currently under development, (2) to determine if the air mass parameters in various coastal locations can be derived from remotely sensed satellite imagery, (3) to evaluate the optimum satellite-derived air mass parameters for Navy real-time assessment and dynamic aerosols models, and (4) to establish the variability of aerosol concentration and composition for coastal air masses.

[1] Further information is available on the internet at http://sunspot.nosc.mil//543/eopace/eomain.html.

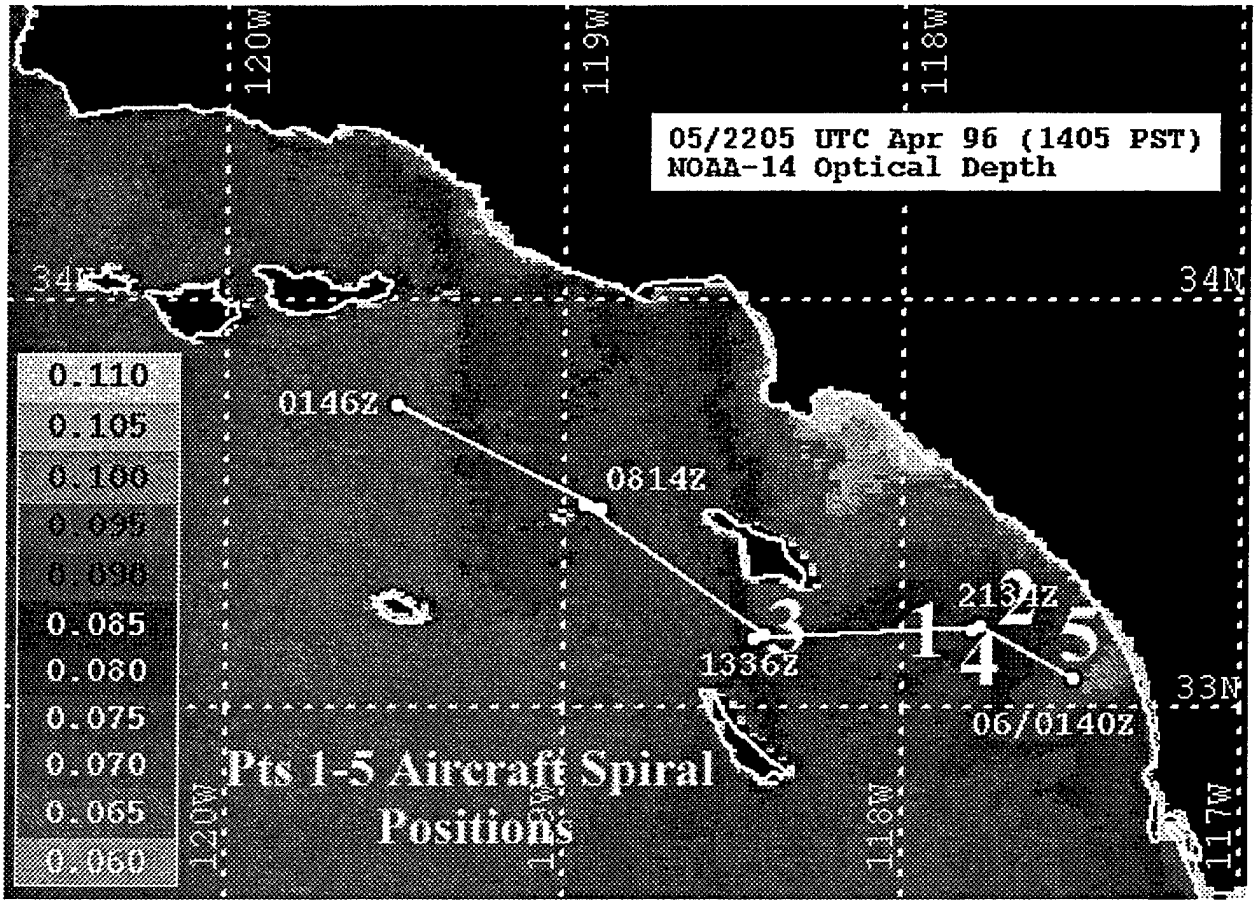


Figure1. Aerosol optical depth in the marine atmospheric boundary layer off the coast of Southern California inferred from visible and near infrared data provided by the NOAA AVHRR satellite. The large numerals, 1 thorugh 5, refer to the location of a Piper Navajo aircraft which carried equipment capable of directly measuring the aerosol size distribution within the boundary layer. The white line is the track of the research vessel Point Sur which carried similar instruments. The Point Sur measurements are not discussed in this paper.

Figure 1 shows the coast of California, stretching from San Diego in the lower right hand corner through the Los Angeles basin to Santa Barbara in the upper left hand corner. Land regions are blacked out. Also shown in black are islands off the California coast. The shading superimposed on the water of the California bight represents the aerosol optical depth

$$T_\lambda(L) = \int_0^L \beta_p(x,\lambda)\,dx \qquad (1)$$

whose values are given in the inset on the left hand side of the figure. The aerosol optical depth was derived from radiometric measurements transmitted by the NOAA AVHRR satellite on 5 April, 1996, at 2205 GMT. The analysis follows the Durkee retrieval technique [2, 3] applied to satellite channels 1 (visible) and 3 (mid wave infrared). The technique rests [4] on three assumptions: (1) that the boundary layer is well mixed, (2) that optical depth is completely determined by aerosol extinction, and (3) that the amount of water vapor in the boundary layer is known by other techniques. The optical depths shown in figure 1 do not include molecular absorption, but they do include aerosol scattering in the troposphere and the marine atmospheric boundary layer. It is assumed that aerosols in the marine boundary layer provide the major contribution to these data.

On the same day, a twin engine Piper Navajo aircraft carrying a forward scattering spectrometer probe [5] executed vertical spiral patterns at locations given by the large numerals in figure 1. The probe measures the aerosol particle size distribution, *dN/dr*. From

Table 1
Aerosol Optical Depth

Location	Aircraft	Satellite
1	0.073	0.075
2	0.052	0.085
3	0.063	0.085
4	0.056	0.075
5	0.072	0.090

these data the extinction was calculated from Mie theory [6] using

$$\beta_p(x,\lambda) = \int_0^\infty \pi r^2 Q_p(x,\lambda) \frac{dN}{dr} dr \qquad (2)$$

along with equation (1).

Table 1 compares satellite depths with aircraft depths. In all cases the aerosol depth measured by the aircraft inside the boundary layer is close to, but slightly less than, the satellite derived optical depth. This is to be expected if tropospheric aerosols represent the small excess of satellite over aircraft optical depths.

3. LOW ALTITUDE TRANSMISSION.

The goal of the near ocean surface transmission characterization is to quantify infrared propagation characteristics for the mid wave (3-5 micron) and long wave (8-12 micron) bands for transmission close to the surface of the ocean, and to determine the measurable meteorological parameters near the ocean surface by which IR transmission may be estimated.

Continuous mid wave infrared transmission has been measured close to (several meters above) the ocean surface over a two week period. The transmission range [1] extended 6998 m from a transmitter located at Coronado, California, to a receiver located at Point Loma, California, on a bearing of 255.9° true. The transmitter consisted of a 1000 K glower placed in the focal plane of a 20 cm diameter F/6 paraboloidal mirror coated with aluminum. The source was chopped at 960 Hz. The transmitter was mounted 3.41 m above mean sea level on the stable platform shown in figure 2. The receiver consisted of a 3 mm square InSb detector placed in the focal plane of an identical mirror at an altitude of 3.04 m above mean sea level. A room temperature optical filter with a pass band of 3.4 to 4.0 microns was placed in front of the detector. The mid wave signal was detected by a lock-in amplifier which received a reference signal transmitted from the source by a radio operating at 160.1 MHz.

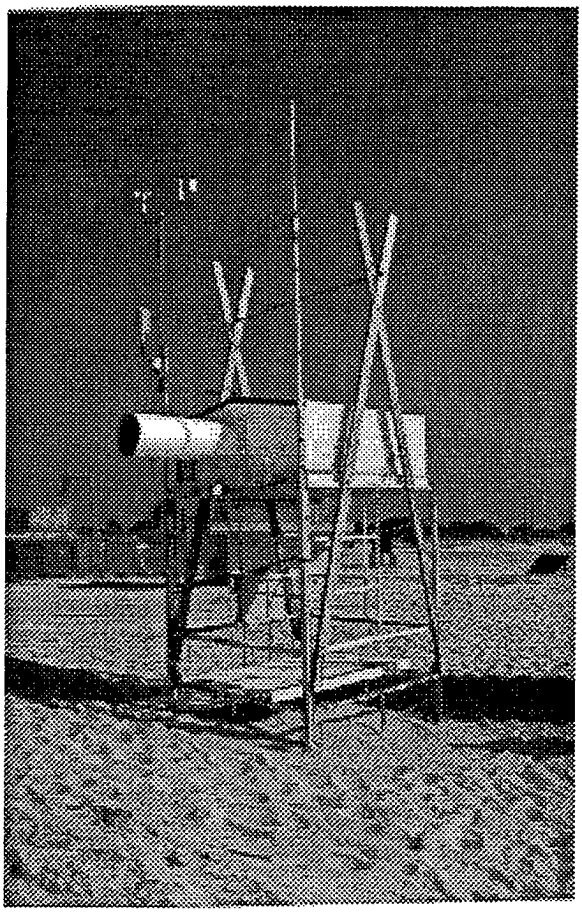


Figure 2. The transmitter located at the Naval Amphibious Base at Coronado.

Prior to field deployment, the equipment was calibrated in the laboratory with the same settings as those used in the field. By correcting the laboratory signal for inverse square law fall-off, a full range free space[2] signal of 6.32 ± 1.90 mV was obtained. In the field the time constant of the lock-in was 1 s with a roll-off of 12 dB/octave and the average of 6 consecutive readings, each separated by 10 s, was recorded every minute in a computer. With these

[2] By "free space" we mean what would loosely be thought of as "100% transmission". The correction assumes a source underfilling the detector field of view at full range, no atmospheric absorption, no refractive ray bending, and no refractive focusing.

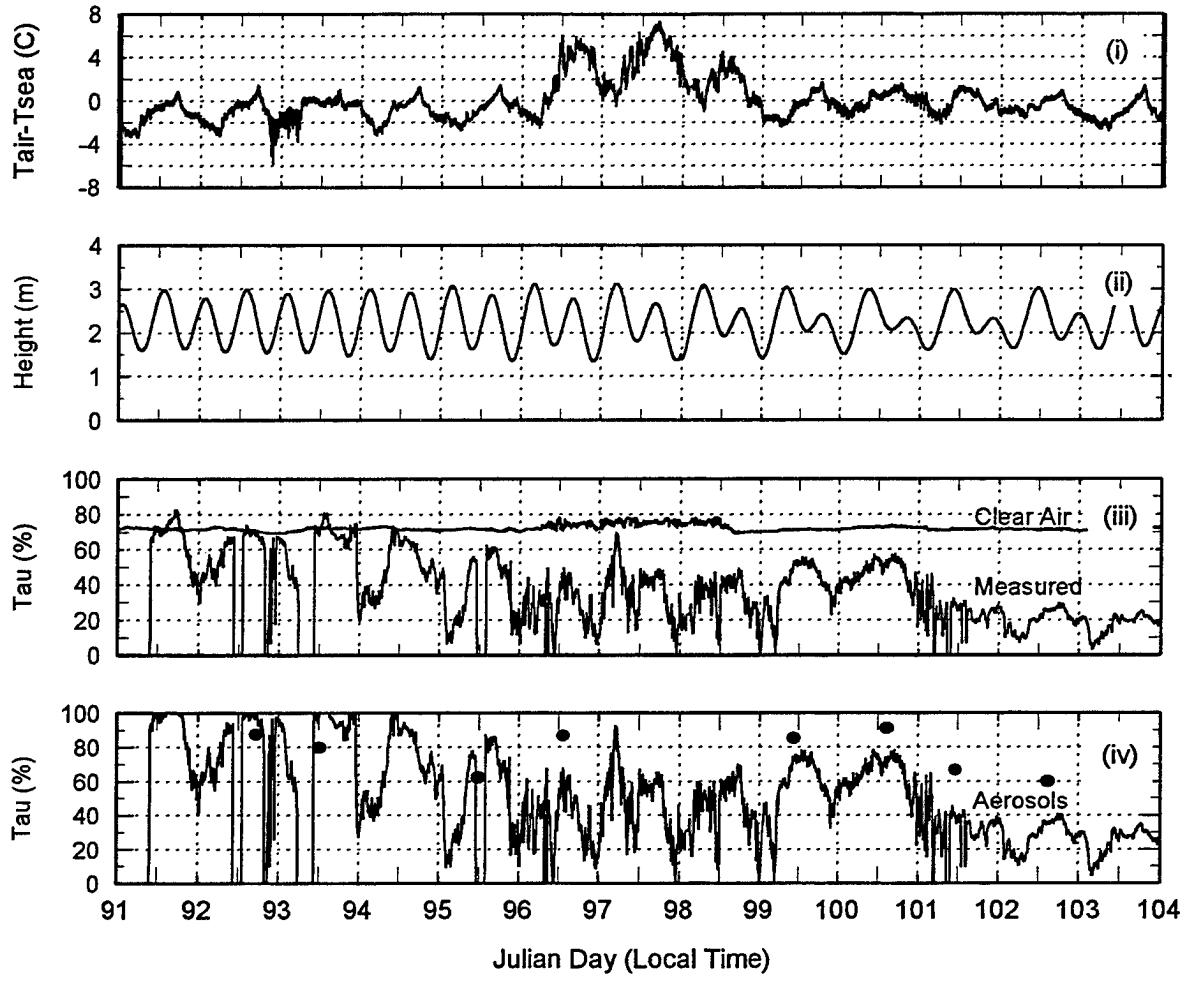


Figure 3. Meteorological and transmission data measured along a 7 km path across San Diego Bay during 13 days in April 1996. (i) Difference between air and sea temperatures measured at the mid path buoy. (ii) Altitude of optical path above the ocean surface at the mid path buoy assuming no refraction (i. e., a straight line path between transmitter and receiver). (iii) Lower curve: measured mid wave infrared transmission. Upper curve: clear air (molecular) transmission predicted by MODTRAN2 from the temperature and relative humidity at the mid path buoy. (iv) Curve: ratio of results in figure (iii). Solid circles: aerosol transmission inferred from particle size distribution measured from a small boat traversing the 7 km path.

settings, the detector noise was 3 μV (0.05 % of free space). The sensitivity of the system in the field was limited by turbulent fluctuations of the signal which were observed to be on the order of 0.6 mV (10% of free space).

Transmission and meteorological data from this experiment are shown in figure 3 for a 13 day period in April 1996. The uppermost curve is the difference between air and sea temperatures at a buoy located in San Diego Bay at the middle of the transmission path. The sea temperature remained almost constant, so this curve reflects normal diurnal temperature variations in a coastal region. The increased amplitude in the middle of this curve resulted from a Santa Ana weather condition which took place on days 96, 97, and 98. The next curve, figure 3 (ii), is the height of the optical signal above the ocean at mid path assuming free space conditions, i.e., a straight line path between transmitter and receiver. The height variation is due to the tide. Transmission measurements for the mid wave infrared band are shown by the lower curve[3] in part (iii) of figure 3.

[3] Sections of the this curve which change abruptly to zero, for example at day 92.5, are artifacts due to the detector running out of liquid nitrogen.

The upper curve in part (iii) is the clear air[4] transmission that would be expected under the conditions of pressure, temperature, and relative humidity observed each minute at the mid path buoy. Those times when the measurements exceed the clear air result can be explained either by the absolute accuracy of the measurement (± 30%) or the presence of refractive focusing effects. Molecular effects were removed by applying the left hand equality of

$$\tau_p = \frac{\tau}{\tau_m} \approx \exp\{-\beta_p(\lambda) \cdot L\} \qquad (3)$$

to the measured data, resulting in the curve shown in part (iv) of figure 3.

The solid circles in figure 3 (iv) represent the transmission that would be expected on the basis of aerosol effects alone. These data were measured by transporting a forward scattering spectrometer probe [5] in a small boat inbound (that is, from the transmitter to the receiver) along the over-water portion of the 7 km range. The inbound trip took about 30 minutes, and the aerosol size distribution was integrated for the entire inbound path[5]. A representative inbound spectrum is shown in figure 4. Applying equations (2) and (1) to data[6] such as those shown in figure 4 for a wavelength of 3.5 microns resulted in the solid circles shown in figure 3 (iv).

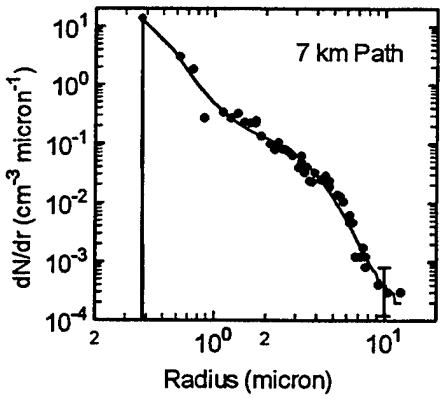


Figure 4. Aerosol size distribution measured inbound on the 7 km transmission path on April 8, 1996. The solid line is a fifth order polynomial fit to the data from which the mid wave extinction coefficient was derived using Mie theory.

The transmission data shown in figure 3 deserve two comments. First, the molecular transmission remained remarkably constant: the mean value was 72% and the standard deviation was 1.6% during the entire 13 day period. This is no doubt due to the fact that the molecular transmission depends on the specific humidity, the number grams of water vapor per unit volume of the atmosphere, and the specific humidity remains relatively constant in spite of wide variations in air temperature and relative humidity from one day to the next. Second, the measured transmission can be successfully explained by molecular and aerosol effects because of the agreement (within the experimental error) between the solid circles and the curve in figure 3 (iv). Nevertheless, we must warn that refractive focusing and mirages will contribute substantially to any signal such as this one, observed at low altitudes over land or sea, and such contributions have yet to be analyzed for these data.

We close this section by noting that, in comparing the aerosol data from the boat with the transmission data, we have made use of Beer's Law, the right hand equality of equation (3). Beer's Law holds for aerosols because of their smooth spectral behavior, but it does not hold either for the measured transmission, the numerator of equation (3), or the molecular transmission, the denominator of equation (3), because of their rapidly varying spectral

---

[4] By "clear air" is meant the transmission due solely to molecular absorption and scattering with no aerosol or refractive focusing effects taken into account. This curve was calculated using MODTRAN2 without the subroutine "Fudge", a procedure whose result, for a single typical value of temperature and relative humidity, was within 2% of the MODTRAN3 calculation.

[5] Outbound data were taken but not used because they were compromised by the prevailing wind, which tended to blow aerosols from the diesel exhaust toward the bow of the boat where the aerosol spectrometer was mounted.

[6] The integral in equation (2) was truncated at a radius of 0.4 μm, the smallest radius for which data were available. The neglected particles of smaller radius, while undoubtedly present to some degree given the observed visibility of 15 km, are not so numerous as to substantially alter the extinction at 3.5 μm because of their small size with respect to that wavelength.

behavior[7]. Hence, of the transmission results shown here, only the aerosol data can be extrapolated to other ranges; the clear air and measured data cannot.

4. SURF PRODUCTION OF AEROSOLS

The goals of the aerosol surf production effort are (1) to determine the impact of surf-generated aerosols on visual and infrared extinction in coastal environments, and (2) to evaluate the measurable meteorological and physical oceanographic parameters of a surf zone by which surf aerosol production may be estimated.

The role of surf generated aerosols has been investigated by measuring aerosol size distributions in the atmosphere close (several meters) above breaking waves. A forward scattering spectrometer probe [5] was again used to measure the aerosol size distribution, this time by being placed in a box which was suspended from the pier at the Scripps Institute

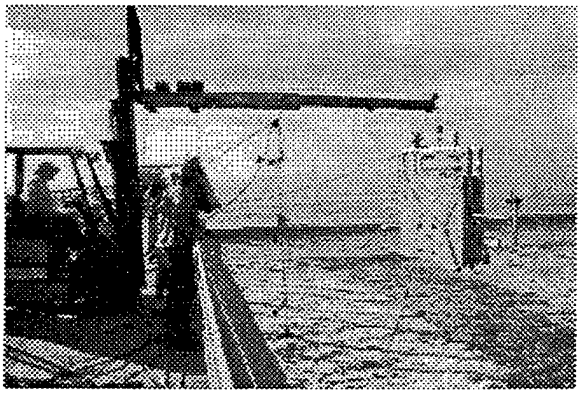


Figure 5. The instrumented box could be suspended at varying heights above the surf for aerosol and supporting meteorological measurements.

of Oceanography at fixed heights above the ocean surface. Figure 5 is a photograph of the box, which also contained aerosol rotorods and standard meteorological instruments for measuring temperature, wind speed, and relative humidity. Typical integration times spent at each height were 30 minutes, resulting in particle size distributions similar to that shown in figure 4. Following the procedure involving equations (1) and (2) which has already been described, the extinction coefficient at four[8] different optical wavelengths shown in figure 6 were derived. The spectral dependence of these curves, which always show a maximum at 3.5 μm, is consistent with supplemental data, not included here, showing that the concentration of surf aerosols reached a peak for radii between 1 and 10 μm and so would be most influential near 3.5 μm. The height dependence of these curves show that, as the breaking waves on the surface of the ocean are approached from the initial altitude of 8 m, the visible and infrared extinction increase by almost an order of magnitude. Since aerosol transmission follows Beer's Law and thus depends exponentially on extinction, these data demonstrate a large influence of surf aerosols on electrooptic systems in

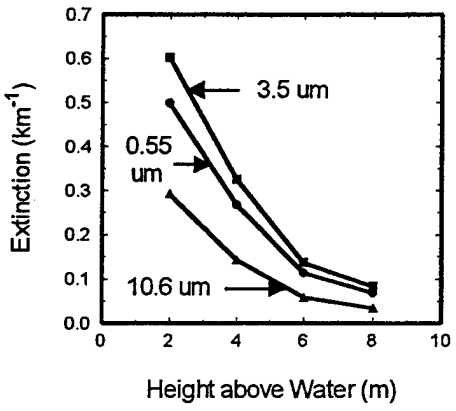


Figure 6. Extinction coefficient at three optical wavelengths as a function of altitude above the ocean surface.

coastal environments.

5. CONCLUSION

Electrooptical systems operating in coastal environments are subject to varied and complex atmospheric conditions which can change rapidly. EOPOACE is a five year field experiment designed to gather information about the coastal environment in the Southern California bight. Initial results concern coastal aerosols. Satellite data on aerosol optical depth in the marine atmospheric boundary layer have been correlated with airborne aerosol size

[7] The spectral integral of a rapidly varying spectrum does not obey Beer's Law, even though it might be obeyed at each wavelength in that spectrum, for the same reason that the sum of two different exponentials is not equivalent to a single exponential.

[8] The data at 1.06 μm overlapped the data at 0.55 μm to within the experimental error and have been removed from the figure for clarity.

distributions measured at the same time directly within the boundary layer. Mid wave infrared transmission measurements made along a 7 km path several meters above the surface of San Diego Bay are consistent with the hypothesis that aerosols and molecules determine the transmission behavior. Aerosol size distributions at fixed altitudes close above breaking surf predict an order of magnitude increase in optical extinction as the ocean surface is approached.

EOPACE PARTICIPANTS

From the United States, participating organizations include the Office of Naval Research (ONR) in Washington, D.C.; the Naval Command, Control and Ocean Surveillance Center, RDT&E Division (NRaD) in San Diego, California; the Naval Research Laboratories in Monterey, California and in Washington, D.C.; the Naval Air Warfare Center at Pt. Mugu, California; the Applied Research Laboratory at Pennsylvania State University; California State University at Long Beach; the Naval Postgraduate School in Monterey, California; the Naval Surface Warfare Center in Silver Springs, Maryland; and the California Air Resources Board.

Foreign participants include the Physics and Electronics Laboratory TNO from The Netherlands; the University of Manchester Institute of Science and Technology (UMIST) in the United Kingdom; the Defense Research Establishment Valcartier in Quebec, Canada; and the Australian Defence Science and Technology Organization, Adelaide/University of Western Australia in Perth, Australia.

ACKNOWLEDGEMENTS

We thank K. L. Davidson of the Naval Postgraduate School for supplying the satellite data and the meteorological data used in our transmission analysis. We also thank E. P. Shettle of the Naval Research Laboratory for being the first to educate us about Beer's Law. This work was supported by the Office of Naval Research.

REFERENCES

1. Littfin, K. M. and Jensen, D. R. "An Overview of EOPACE (Electrooptical Propagation Assessment in Coastal Environments), Including In Situ and Remote Sensing Techniques," paper 10 in Proceedings CP-582 of the AGARD SPP Symposium on "Remote Sensing: A valuable Source of Information," Toulouse, France, 22-25 April, 1996.

2. Rouault, M. and Durkee, P. A., "Characterization of Aerosols from Satellite Remote Sensing," Nucleation and Atmospheric Aerosols, N. Fukuta and P. E. Wagner, eds., 1992, p. 357.

3. Davidson, K. L., Wash, C. H., and Jordan, M. S., "Remote Sensing of Coastal Atmospheric EM/EO Conditions," these proceedings.

4. Wash, C. H. Davidson, K. L., Jordan, M. S. "Multispectral Remote Sensing of the Coastal Atmospheric Boundary Layer," paper 45 in Proceedings CP-582 of the AGARD SPP Symposium on "Remote Sensing: A valuable Source of Information," Toulouse, France, 22-25 April, 1996.

5. Model FSSP-100, Particle Measuring Systems Incorporated, 5475 Airport Boulevard, Boulder, CO 80301-2339.

6. McCartney, E. J., *"Optics of the Atmosphere"*, John Wiley & Sons, London, 1976, p. 134 and p. 264.

Slant path extinction in a stratified atmosphere

Andreas K. Goroch

Marine Meteorology Branch
Naval Research Laboratory
Monterey, CA 93943

Introduction

Helicopter FLIR systems are used for detection and observation of ship targets in support of a variety of coastal naval operations. The coastal environment is complex with large scale conditions strongly modified by local variations of topographic and sea surface conditions. The ambient atmosphere is often stratified with different atmospheric layers characterized by substantially different moisture and signal propagation conditions. These conditions can strongly affect tactical operations.

This report describes the detection of a destroyer target by a standard helicopter FLIR during operational exercises in the Arabian Gulf. The observations show the detection range to be dependent on approach altitude, first increasing , then decreasing as altitude increases. This results suggests that the tactical user may have an optimal altitude for maximum detection range during FLIR operations. The altitude is potentially dependent on the characteristics of the target, the sensor, and the intervening atmosphere. We have developed a closed form model of detection range in a stratified atmosphere. This model is used to describe the sensitivity of FLIR extinction to stratification and extinction characteristics of the atmosphere.

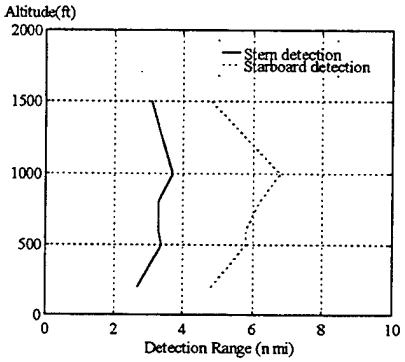


Figure 1. Detection range of destroyer using FLIR imager.

Observations

Structured FLIR detection runs were conducted during the SHAREM 115 exercise in the central Arabian Gulf on 23 and 24 April, 1996. A UH 60B helicopter was deployed with a standard FLIR imager during the exercise. FLIR performance was evaluated with a Spruance class destroyer, USS Caron, as a detection target. The destroyer moved at a steady speed of 5 knots to the northwest. The helicopter approached the destroyer first from starboard and then from the stern at different altitudes, ranging from 200 to 1500 ft. At each altitude, the helicopter would move away from the ship until the ship could no longer be seen on the video screen. The helicopter would the approach the ship until the target could be recognized as a warship. Detection was determined when the yardarms of the ship were distinguishable. Range was found from the ship radar, which provided ground range, the distance on the surface between the ship and the spot on the ocean directly under the helicopter. This procedure was completed for altitudes with first a starboard approach, followed by a stern approach.

The resulting ranges are shown in Figure 1 for the starboard and stern approaches. In general, the starboard approach had a longer detection range than the stern approach. This is obviously expected since the perceived cross section of the ship is greater in a beam approach. Both approaches showed a consistently longer detection range at an altitude of 1000 ft with a significantly reduced range at 1500 ft. The observation of longer ranges at 1000 ft was substantiated by the helicopter pilots in debriefs after each flight. The reason for this observation was not clear. It was conjectured that this could simply be due to the geometry of the approach, to the structure of the intervening atmosphere, or to the characteristics of the target or the sensor. To evaluate these possibilities a model was built which included these effects.

Extinction Model

The effect of atmospheric stratification on the extinction was modeled with a simple profile of atmospheric extinction . The atmosphere is assumed to consist of two layers; a lower layer of high extinction, and an upper layer of less extinction. This corresponds to the mixed layer models (Deardorff 1976, Roll, 1965, Hsu, 1988). The vertical behaviour is described using a parametrization of Moore(1991), originally applied to horizontal variation of sea surface temperature, but found to be reasonably useful for this application. This parametrization has the advantage of not only describing the vertical profile reasonably well, but also of being integrable. The vertical profile of the extinction coefficient , *k(z)*, is ,

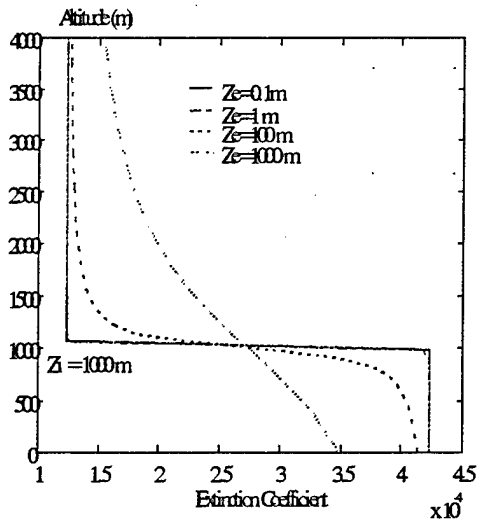


Figure 2. Extinction coefficient model for different parameter values.

$$k(z) = k_{sfc} + \left(k_{aloft} - k_{sfc}\right)\left[1 + \frac{2}{\pi}\left(\arctan\left\{\frac{z - z_i}{z_e}\right\}\right)\right] / 2$$
$$= \frac{k_{sfc} + k_{aloft}}{2} + \frac{k_{aloft} - k_{sfc}}{\pi}\arctan\left\{\frac{z - z_i}{z_e}\right\}, \quad (1)$$

where k_{sfc}, k_{aloft} are the surface and aloft volume extinction coefficients respectively, z is altitude, z_i is the altitude of center of the transition, and z_e is the depth of the transition zone. An example of the dependence of the volume extinction coefficient for different parameter values is shown in Figure 2.

The total extinction over a slant path S, from the surface to a given altitude Z is

$$\sigma = \int_0^S k(z)ds$$
$$= \frac{1}{\mu}\int_0^Z k(z)dz, \quad (2)$$

where μ is the depression angle from the horizontal at the sensor. For a given altitude and depression angle, the total optical extinction can be evaluated in closed form as,

$$\sigma = \frac{k_{sfc} + k_{alft}}{2}\sqrt{R^2 + Z^2} + \frac{k_{alft} - k_{sfc}}{\pi}\frac{\sqrt{R^2 + Z^2}}{Z} *$$

$$\left[(Z - z_i)\arctan(\frac{(Z - z_i)}{z_e}) - z_i \arctan(\frac{z_i}{z_e}) + \frac{z_e}{2}\log\left(\frac{1 + \left(\frac{(Z - z_i)}{z_e}\right)^2}{1 + (\frac{z_i}{z_e})^2} \right) \right]. \quad (3)$$

The detection range is defined for our purposes as that range where the total optical depth exceeds a given threshold. A common criterion is the 5% contrast threshold (Lloyd, 1975), where the detection range is defined as the separation where total loss of signal is 5%, or,

$$R = \frac{3.912}{\sigma}. \quad (4)$$

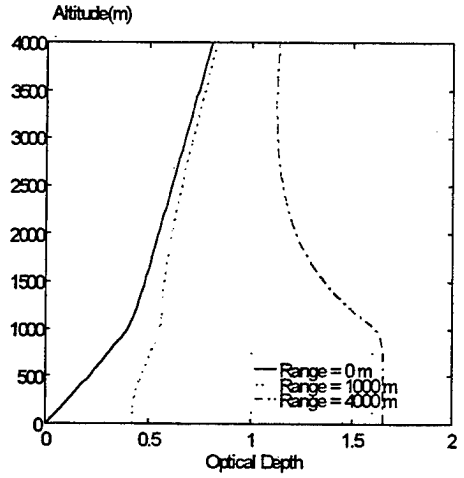


Figure 3. Optical depth as function of range for several surface range values.

Using the range model defined by equations (1) and (2), the calculated optical depth for a given range, R, is obtained as a function of altitude for different horizontal ranges between target and detector. For a detector directly overhead (R=0), the extinction increases most rapidly in the lower layer, and then decreases more slowly in the upper layer. At any value of range, the extinction increases as a function of altitude in the lower layer, but then decreases in the lowest part of the upper layer. This occurs because a part of the slant path in the lower layer is replaced by part of the path being in the upper layer, decreasing the total extinction. The altitude dependence of the optical depth is shown for several values of ground range in Figure 3.

The detection range also depends on the cross sectional area of the target presented to the detector. For a target of significant width, the presented area thus increases with altitude to a maximum, and then decreases. In this model, the optical depth required for detection is scaled by the ratio of presented area at a particular depression angle to the presented area at the surface. For a target of width W, length L, and height H, the effective cross section at a depression angle θ is given by

$$\sigma = \sigma_0 \frac{H\cos\theta + W\sin\theta}{H}. \quad (5)$$

Sensitivity

The model of equations (3) and (4) is used to describe the sensitivity of the detection range to the details of atmospheric structure and to the characteristics of the sensor. The most general characteristic of the detection range behaviour with altitude is that as altitude increases, range increases because of the increased presented area. As the altitude increases farther, the range starts to decrease because of the increase in total optical depth from the increased altitude. This general behaviour is modified by the stratification, the difference between surface and aloft extinction, and the sensitivity of the detector.

The dependence on kind of stratification is seen from the change in z_e, the depth of the transition zone. The gradual stratification is accompanied by a more abrupt increase in range at the transition zone. The range also exhibits a maximum with height, but the abrupt stratification exhibits a slightly longer detection range. This is due to the shorter path in the high extinction zone for the abrupt stratification by comparison to the smoother profile. The dependence on stratification is shown in Figure 4.

The dependence on surface extinction is shown in Figure 5. With higher surface extinction, the detection range shows a pronounced maximum in the range. With a lower extinction, the profile is more diffuse, without a clear maximum in range with altitude.

The dependence on receiver sensitivity can be shown by varying the optical depth necessary for detection. Figure 6 shows the changes as this optical depth is changed by 30%. The less sensitive receiver has a more pronounced maximum in range with altitude. The more sensitive receiver has less altitude dependence, with a range of altitudes where the range is not changing significantly.

Conclusions

The optimal choice of altitude for using a FLIR sensor depends on the environment, as well as operational and equipment conditions. The geometry of the detection, determined by the size of target, separation of target and sensor, and the sensitivity of the sensor are generally modified by the specifics of the intervening atmosphere. Operational observations and theoretical modeling indicate that atmospheric stratification, strength of extinction, and the sensitivity of the sensor modify the optimal altitude for best system performance. The model shows that the stratification of the atmosphere modifies the optimal altitude by increasing the best altitude, but resulting in a longer altitude range than an unstratified profile. The relative volume extinction at the surface and aloft affect the shape of the detection range profile. With a higher surface extinction, the optimal detection range is restricted to a smaller range of altitudes by comparison to the lower surface extinction. Sensor sensitivity exhibits similar results, in that

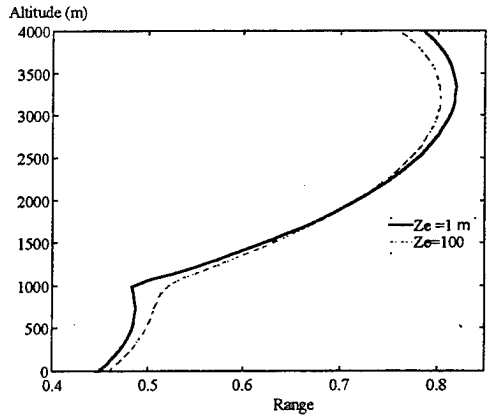


Figure 4. Vertical detection range profile for slight and strong stratification. Range scale is in non-dimensional units.

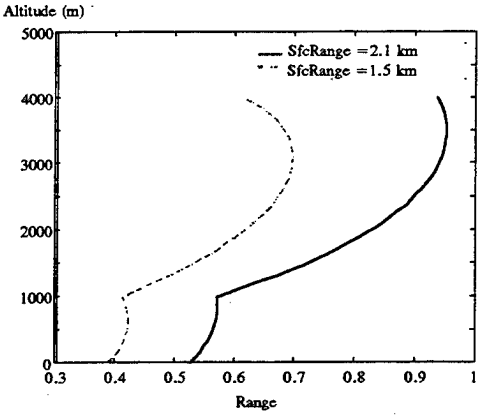


Figure 5. Detection range dependence on surface extinction (expressed as range).

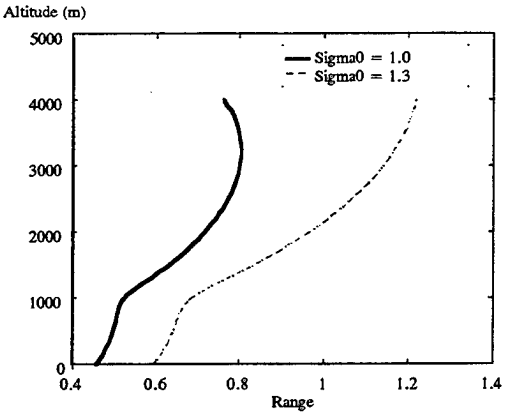


Figure 6. Detection range profiles for different receiver sensitivities.

the more sensitive system, has a less well defined optimal altitude than the less sensitive system.

Acknowledgments

This work has been sponsored by the Oceanographer of the Navy (OP-096) through the supported by the Space and Naval Warfare Systems Command PMW-185, program element 0603207N. The author would like to thank CDR Tim Sheridan for support of the work and Mr. Patrick Jackson and LCDR Gene Nissen for cooperation and support during the SHAREM exercise.

References

Deardorff, J.W., 1976: "On the entrainment rate of a stratocumulus-topped mixed layer," Quart J. R. Met. Soc., **102**, 563-582.

Hsu, S. A., 1988: "Coastal Meteorology," Academic Press, New York. 260 pp.

Lloyd, J. M., 1975:"Thermal Imaging Systems," Plenum Press, New York, 456 pp.

Moore, G. W. Kent, 1991:"Frontogenesis in the presence of surface heating," J. Atmos. Sci. **48**, 63-75.

Roll, H. U. , 1965: "Physics of the Marine Atmosphere," Academic Press, New York, 276 pp.

Remote Sensing of Coastal Atmosphere EM/EO Conditions

Kenneth L. Davidson, Carlyle H. Wash and Mary S. Jordan
Department of Meteorology
Naval Postgraduate School
589 Dyer Rd., Room 254
Monterey, CA 93943-5114, USA
Phone: 408-656-2309 Fax: 408-656-3061
davidson@nps.navy.mil

SUMMARY

Coastal region Marine Atmospheric Boundary Layer (MABL) EM/EO properties vary dramatically over short distances, 10-30 km. The properties are affected by the vertical gradients of temperature and humidity from the surface to the top of a capping inversion. They are also affected by locally produced and advected aerosol. Remote sensing offers a desirable approach to estimate variations of the MABL, such as its depth and moisture content, which affect these properties. A multispectral approach using visible and infrared data is tested to indirectly estimate the depth of the MABL, aerosol optical depth, surface moisture, and sea-surface temperature. Remote data describe high resolution horizontal and temporal variations, important in the coastal regions, but not described by point measured data. The technique has been tested with data from recent exercises and field experiments. The technique was applied to cases off the southern California coast in August 1993 (VOCAR) and in the Arabian Gulf and Gulf of Oman in February 1995 (SHAREM 110), and compared to in situ measurements of the coastal MABL from aircraft, ship and shoreline stations. Limitations of the approach due to sun glint, continental aerosols and more complex MABL structures are also discussed.

1. INTRODUCTION

Knowledge of the characteristics of the marine atmospheric boundary layer (MABL) is critical to large scale investigations of air-sea interactions as well to coastal analysis and prediction. Coastal region MABL structures vary dramatically over short distances, 10-30 km. The height of the MABL is a feature of interest in several applications. For example, it is the location of elevated trapping layers affecting radio/radar waves. It is also the upper limit for mixing volume of pollution arising from shoreline activities. The depth of the MABL may be quite variable in coastal regions because it is influenced by both synoptic scales meteorological and local coastal circulations. In either case, horizontal variations occur in both the height of the MABL and strength of the capping inversion.

Conventional means of in situ measurement are necessarily limited due to the lack of vertical profile measurements over the coastal ocean. Methods using satellite atmospheric soundings are limited by the broad weighting functions resulting in poor resolution of the sharp temperature and moisture gradients at the top of the MABL. Therefore, the further development of satellite-based MABL characterization methods to estimate variations of the MABL, such as its depth and relative moisture content, are valuable both for regional and global scale studies.

This paper describes an indirect method to obtain MABL descriptions for clear regions by balancing the estimates of aerosol optical depth and the total water vapor with a relationship between relative humidity and radiative extinction. This method is referred to as the multispectral approach. The method estimates MABL height and moisture variables in the well-mixed boundary layer. First, the technique is presented followed by an evaluation during the Variability of Coastal Atmospheric Refraction (VOCAR) experiment during August/September 1993. Then results from other cases from the Persian Gulf and coastal Central California are discussed.

2. MULTISPECTRAL METHOD

The method described here relies on previously developed techniques for estimating aerosol optical depth and total column water vapor. Aerosol optical depth techniques have been developed by Refs 1, 2 and others. This study uses the red-visible radiance measurements of the NOAA AVHRR (channel 1 & 2) and their direct relation to aerosol optical depth (Ref 2). Also, several techniques have been developed to detect atmospheric water vapor variations from satellite measurements (Refs 3 and 4). The method used here follows Ref 4 that relates total column water vapor to the difference between the split window brightness temperatures from the NOAA AVHRR sensor (channel 4 and 5). Since both estimates are derived from the same sensor, the boundary layer estimates described below can be derived from a single data source.

Three assumptions about the marine boundary layer and vertical profile of extinction and water vapor are needed to relate optical depth and column water vapor to MABL depth and relative humidity. First is that the MABL is well-mixed. Second, the only significant contribution to aerosol optical depth results from extinction by aerosols in the MABL. Finally, the percentage of water vapor in the MABL can be estimated from in situ data or other satellite measurements.

Within the clear, well-mixed MABL, potential temperature and specific humidity/mixing ratio tend to be constant with height. Adiabatic mixing due to buoyancy and wind shear effects, described by Ref 5 and others, is responsible for maintaining these well-mixed profiles. Fig. 1 illustrates the evolution of a well-mixed boundary layer using a time series of ship-measured rawinsonde soundings off the Southern California coast. Note that potential temperature is nearly constant with height in the boundary layer. Mixing ratio (not shown) is also nearly constant with height in the MABL. The multispectral technique takes advantage of these simple distributions and is also based on the well-known relationships between temperature, saturation vapor density and relative humidity.

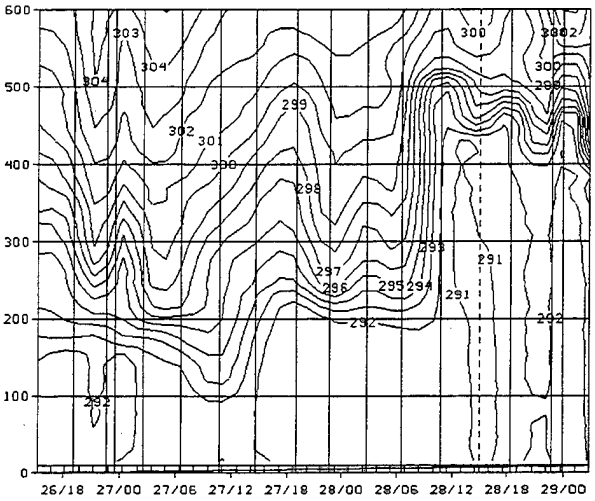


Fig. 1. Time series of MABL evolution using 17 rawinsondes off the Southern California coast, 26-29 August 1993. Contours of virtual potential temperature (K) illustrate the height (m) of the MABL.

The technique further assumes that aerosol optical depth at the red-visible and near-infrared wavelengths results from particles that are confined primarily within the MABL. If this assumption is true, then the optical depth in the red-visible would be due to the integrated effects of extinction due to these aerosols in the MABL. Ref 6 describes atmosphere aerosol distributions and concludes that for marine particles, absorption is small and the extinction is due to scattering. This extinction coefficient is a function of the cross sectional area for a given particle radius, the extinction efficiency (dependent on the complex refraction index and particle radius), and the distribution of particles by radius. Variations in each of these three factors produce corresponding changes in extinction. Ref 7 showed that the dominant term affecting extinction is particle size. Ref (2) developed a relationship between extinction and relative humidity consistent with Ref 7. This relationship is based on aircraft measurements of extinction within the MABL off the southern California coast in 1982.

Satellite estimates of optical depth and column water vapor are both related to the MABL height and moisture. An iteration method was devised to solve for the MABL height and surface relative humidity for clear regions in a satellite pass using the AVHRR data, Refs 8 and 9. Sensitivity estimates using a model atmosphere indicated the method is reliable when the MABL satisfies the assumptions of the technique, Ref 9.

3. VOCAR RESULTS

The multispectral approach has been successfully applied to MABL analyses over coastal regions of Northern California and Southern California (Ref 10 & 11) and the Persian Gulf (Ref 12). In this paper we present a validation of the technique using two cases during the Variability of Coastal Atmospheric Refractivity (VOCAR) experiment, off the southern California coast, in August-September 1993, using rawinsondes and newly available aircraft data from Naval Weapons Test Center, Point Mugu, CA. The initial VOCAR results are contained in the thesis, Ref 10, and conference presentations at the 1994 AGARD meeting, Ref 11.

To use the VOCAR period to test the technique, an estimate of the percentage of the water vapor in the MABL was used. This is an important improvement to the technique for climatological regions where significant water vapor is found above the marine inversion.

The VOCAR cases presented here were chosen because each was a clear day in the VOCAR region and rawinsondes were launched within 30 minutes of the satellite pass time at seven locations (one ship, two island, 4 coastal locations). In addition, aircraft data are

now available providing low-level temperature and moisture profiles between the coast and San Nicolas (NSI) and San Clemente (NUC) islands within two hours of the satellite overpass. The aircraft flew saw-tooth vertical profiles between 75 m and 825 m, penetrating the mixed layer.

The two cases use AVHRR afternoon satellite passes on consecutive days, 26-27 August 1993. In each case, there is significant mid-tropospheric water vapor. We computed the percentage of water vapor density in the MABL, compared with the total from the surface to 400 mb, for all rawinsonde locations. The percentage, which is representative of the MABL throughout the region, is 14% for each case. These cases indicate that the multispectral technique will work when significant amount of mid-tropospheric water vapor is present.

Fig. 2 shows the multispectral MABL depth analysis for the 23:47 UT 26 August 1993 (4:47 pm local) NOAA AVHRR satellite pass. The dark areas indicate that the pixels were over land, are clouds, or the iterative method did not converge at that point. The rawinsonde observations are indicated by yellow dots on the image while aircraft profiles are denoted by white dots.

Fig. 2 also shows the slope of the MABL, from shallow values to the West (75 m) to deeper values along the eastern portion of the coastal region (225 to 275 m). The thicker MABL region is associated with warmer sea surface temperatures (SST) along the California coast from Point Vincente (PVN) to North Island (NZY) near San Diego. The range of SST is from 23 to 24 C in the warmer area to 16 to 18 C south of Point Arguello (PDR) along the eastern edge of the California Current.

Rawinsonde and aircraft data confirm the coastal MABL and SST structure indicated by the mulispectral technique. The only overwater rawinsondes are from the R/V Point Sur (PSUR). Data from one rawinsonde launched during the aircraft flight, 26/2242 UT (3:42 pm), and another launched at 2332 UT (4:32 pm), near the AVHRR satellite overpass time, are used to compare with the multispectral estimates of MABL depth. The rawinsonde measured MABL depths of 152 m and 148 m compare favorably with the shallow 127 m satellite estimate.

Fig. 3 shows the multispectral MABL depth analysis for the 23:34 UT 27 August 1993 (4:34 pm local) NOAA AVHRR satellite pass. Thin stratus clouds developed to the west of San Nicholas Island (NSI), with cloud patches north and east, which reduced the clear area for the multispectral technique. In this case, the MABL depth is significantly deeper (30-65 meters) than the previous afternoon, again with a west-to-east slope of the MABL. Two Point Sur rawinsondes and the aircraft data confirmed a 25-65 meter deeper MABL at points along nearly coincident aircraft tracks as flown the previous day.

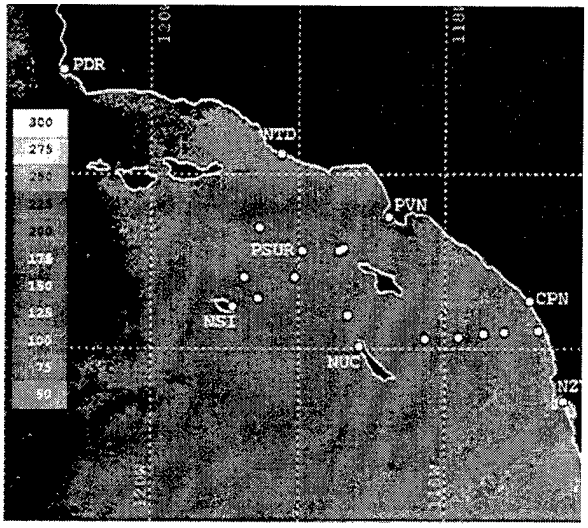


Fig. 2. Multispectral MABL depth (m) for 23:47 UT 26 August 1993 NOAA AVHRR satellite pass. VOCAR rawinsonde observations are devoted by yellow dots and aircraft profiles are given by white dots. The dark areas indicate the pixels were over land, are clouds, or the iterative method did not converge at that point.

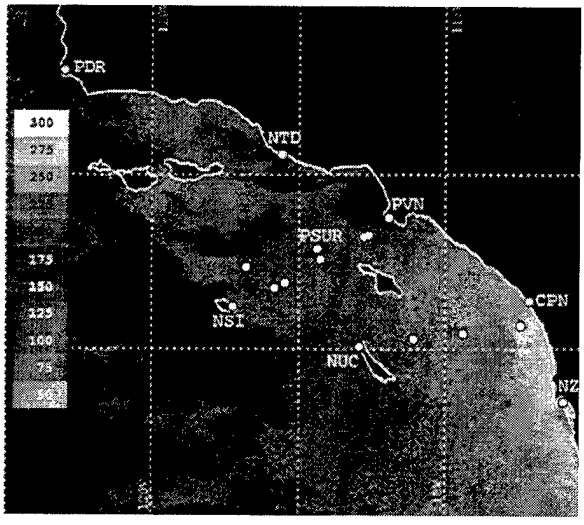


Fig. 3. As in Fig. 2, Multispectral MABL depth (m) for 23:34 UT 27 August 1993 NOAA AVHRR satellite pass. The dark areas of nonconvergence are due to the thin stratus clouds over the area west of NSI, with cloud patches to the north and east.

For statistical analysis, we compared the Point Sur rawinsondes and aircraft measurements of MABL height and virtual potential temperature at the locations indicated in Figs. 2 and 3 with the corresponding multispectral MABL height and SST estimates for each case. Combining the cases, we have 24 data points for analysis. Fig. 4 is a scatterplot of measured MABL height versus satellite estimates of MABL height. Similarly, Fig. 5 compares the virtual potential temperature from rawinsonde and aircraft data with satellite-derived SST. The statistical information is presented in Tables 1 and 2.

Two 26 August aircraft soundings in the lee of San Nicolas Island (NSI) were excluded from the analysis because the MABL appears influenced by local island effects. Aircraft soundings on 27 August were excluded if there was evidence of thin stratus clouds in the vicinity of the sounding.

For both cases, the aircraft soundings confirm the distinct gradient in MABL height and SST between San Clemente Island (NUC) and San Diego (NZY). The satellite data underestimates the depth by 40 m, but the RMS differences are less than 46 m. The aircraft virtual potential temperatures of the mixed layer fall within 1.3C of the satellite-derived SST.

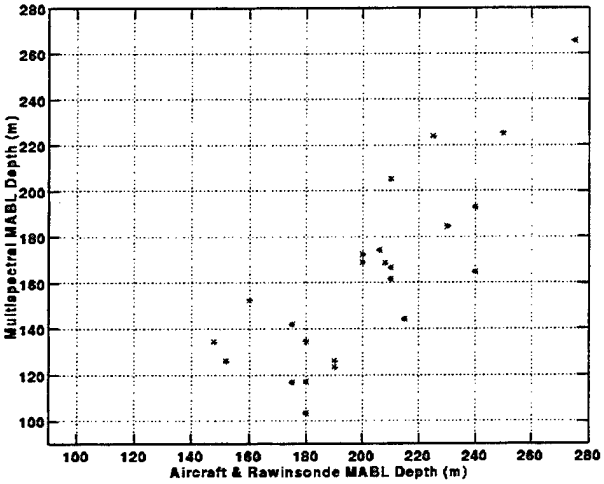


Fig. 4. Scatterplot of aircraft and rawinsonde measured and multispectral satellite estimates of MABL depths (m).

Table 1.
Comparison of Aircraft versus Multispectral MABL Height

BIAS	39.7 m
RMS differences	45.6 m
Correlation Coefficient	.816

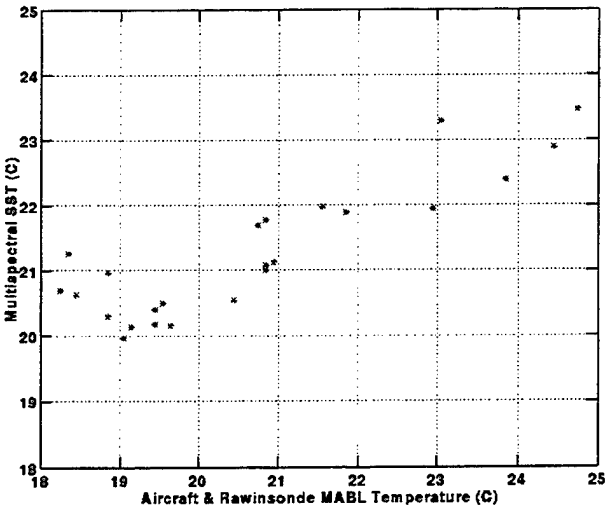


Fig. 5. Scatterplot of aircraft and rawinsonde MABL virtual potential temperature (C) and satellite estimates of SST (C).

Table 2.
Comparison of Aircraft MABL Temperature versus Satellite SST

BIAS	-0.59 C
RMS differences	1.29 C
Correlation Coefficient	0.877

4. OTHER VALIDATION CASES AND METHOD LIMITATIONS

The multispectral technique has been applied to several other coastal data sets (Ref 12). The results from these cases are summarized here and presented in more detail at the conference.

The SHAREM 110 exercise was held in the Persian Gulf and Gulf of Oman during the period of 6 to 18 February 1995. Rawinsondes were available from three ships during the entire period while aircraft data were available on five days. Due to the geography of the Persian Gulf, the atmosphere is never completely free from land influences. However, a Shamel occurred during the experiment with a period of moderate northwest winds from the Northwest along the axis of the Gulf. This flow with a long overwater fetch satisfied the conditions of the technique. A deep well-mixed MABL developed during this period (10 February). The MABL depth was measured to be approximately 1000 meters with most (83%) of the column water vapor in the MABL.

Table 3 presents an evaluation for this case from soundings from the USS David R. Ray and USNS Silas Bent. The difference between the sounding and satellite

estimate was near 50 meters and the boundary layer slope was correctly determined by the satellite analysis. The satellite MABL analyses also was consistent with the cloud top temperature of some boundary layer cumulus over the western part of the Gulf. The multispectral technique proved to be very successful in this case even with considerably thicker MABLs than observed in VOCAR.

Table 3
MABL Height Comparisons for the Persian Gulf
10 February 1995

	D.R. Ray	Silas Bent
Multispectral	1005 m	1042 m
Rawinsonde	1055 m	1090 m
Difference	50 m	48 m

Other SHAREM and coastal California cases illustrate limitations to the approach. These limitations are sun glint, continental aerosols and more complex MABL structures. With polar-orbiting sun synchronous satellites, sun glint can be a major difficulty. In conducting these validation studies, approximately 30% of the clear (otherwise usable) passes can not be analyzed because of the solar reflection from the sea surface. This problem may occur less frequently when using data from the new US NOAA geostationary satellites, GOES-8 and 9.

In one of the SHAREM cases, strong off-shore continental flow with significant dust caused plumes of elevated optical depth. The multispectral technique did converge in this case and produced MABL analyses. However, the MABL depth was hundreds of the meters in error due to the continental influences present. This case illustrates that situations with significant off-shore transport of aerosols need to examined closely. The plume-type structure of the optical depth and MABL height analyses give strong indications of the impact of the continental aerosols.

Finally, cases with multiple mixed layer structure and elevated trapping layers have been found. This is particularly common over regions undergoing cold upwelling events along the west coast of continents. Here a new mixed layer is formed over the cold water, distinctly colder than the mixed layer above it. In these situations, the multispectral approach does successful map the lower mixed layer, but does not provide any information about the inversion structure above the lowest mixed layer. In these cases, the technique can not provide any information about elevated inversions or refractive layers that are not associated with the surface but may be tactically relevant to electromagnetic-electro-optical propagation and other applications.

5. CONCLUSIONS

We have described the evaluation of remotely sensed estimates of mixed layer structure at and above the ocean surface in coastal regions using aircraft data during VOCAR and from other field experiments. Both successful and unsuccessful cases have been studied. The multispectral approach has accurately mapped the topography of the MABL, SST and optical depth conditions for cases from coastal Southern California, Persian Gulf and Central California coast. The comparisons with aircraft and rawinsondes show the satellite data to correctly describe the MABL topography and agree to within 20% with in situ observations. The method can be applied to all cases of clear skies. However, sun glint, continental aerosols and situations with complex MABL structures can not be analyzed with this approach using polar-orbiting satellite data. The sun glint problem should occur less frequently with the new US geostationary satellites. Future studies will evaluate this source of multispectral data for MABL studies.

6. ACKNOWLEDGMENTS

We thanks the NPS staff who contributed to the in situ VOCAR data collection and analyses (K. Jones, P. Frederickson, T. Neta). Special thanks goes to C. Skupniewicz, NPS, for his assistance in using the multispectral process code. Roger Helvey of Pacific Missile Test Center, Point Mugu provided the aircraft data and was of great assistance in its interpretation and use.

7. REFERENCES

1. Griggs, M., "Satellite Measurements of Tropospheric Aerosols," *Adv. Space. Res.*, vol. 2, pp. 109-118, 1983.

2. Durkee, P.A., D.R. Jensen, E.E. Hindman and T.H. VonderHaar, "The Relationship Between Marine Aerosol Particles and Satellite-Detected Radiance," *J. Geophys. Res.*, vol. 91, pp. 4063-4072, 1986.

3. Prabhakara, C.G., G. Dalu, R. Lo and N. Nath, "Remote Sensing of Seasonal Distributions of Precipitable Water Vapor over the Oceans and the Inference of Boundary Layer Structure," *Mon Wea Rev.*, 107, 1388-1401, 1979.

4. Dalu, G., "Satellite Remote Sensing of Atmospheric Water Vapor," *Intl. J. Remote Sensing*, vol. 7, 1089-1097, 1986.

5. Rogers, R.R., "A Short Course in Cloud Physics," Pergamon Press, New York, NY, 235 pp., 1979.

6. Shettle, E.P. and R.W. Fenn, "Models are the Aerosols of the Lower Atmosphere and the Effects of Humidity Variations on their Optical Properties," AFGL TR-79-0214, Air Force Geophysics Laboratories, Hanscom AFB, MA, 94 pp., 1979.

7. Fitzgerald, J.W., W.A. Hoppel and M.A. Vietti, "The Size and Scattering Coefficient of Urban Aerosol Particles at Washington, DC as a function of Relative Humidity," *J. Atmos Sci*, 39, 1838-1852, 1982

8. Kren, R.J., "Estimation of Marine Boundary Layer Depth and Relative Humidity with Multispectral Satellite Measurements," Masters Thesis, Naval Postgraduate School, Monterey, CA, 73 pp., June 1987.

9. Smolinski, S.P., "Marine boundary layer depth and relative humidity estimates using multispectral satellite measurements," Masters Thesis, Naval Postgraduate School, Monterey, CA, 70 pp., March 1988.

10. Walsh, D.J., "Multispectral NOAA Marine Atmospheric Boundary Layer (MABL) Estimates During VOCAR," Masters Thesis, Naval Postgraduate School, Monterey, CA, 106 pp., June 1994.

11. Davidson, K.D. and C. H. Wash, "Remote Measurement of Atmospheric Refraction Conditions in the Coastal Region," AGARD-94, Propagation Assessment in Coastal Environments, Bremerhaven, Germany, Sept 1994.

12. Teadt, T.L., "Studies in Satellite Multispectral Analyses of MABL Depth," Masters Thesis, Naval Postgraduate School, Monterey, CA, 55 pp., March 1996.

Atmospheric Scattering Effect on Spatial Resolution of Imaging Systems

B. Ben Dor, A. D. Devir and A. Ben-Shalom

Electro-Optics R&D Division (EORD)
Technion - Israel Institute of Technology, 32000 Haifa, Israel.

ABSTRACT

In this paper a physical model that describes the relationship between the optical properties of the atmosphere and the characteristics of an imaging system is suggested. The model describes how different components of the light reaching the imaging system, after passing through the atmosphere, are detected by it. The model includes the effects of the final size of the detector elements of the imaging system and the dynamic range and the final field of view limits of the imager. It is found that for common imaging systems (with resolution of 8bit or 12bit) working in general atmospheric conditions (VIS≥5km), the processes of atmospheric scattering and absorption hardly contribute to spatial blurring of the recorded images. A field experiment was carried out in order to verify the predictions of the suggested model. The measurements were performed using a scanning point radiometer, while a local meteorological station and a visibility meter measured the properties of the atmosphere. Theoretical predictions, which were accomplished by using a Monte-Carlo simulation of atmospheric scattering effects, are compared with the experimental data acquired in the field tests. A good agreement was obtained between the measured data and the theoretical predictions.

1. INTRODUCTION

Light emanating from a radiation source is scattered and absorbed by molecules and aerosols in the atmosphere. It is also deflected from it's original path by atmospheric turbulence. Some of the above phenomena give rise to reduction of the source intensity and some give rise to spatial blurring of the source radiation. The contribution of the atmospheric turbulence to spatial blurring is well known and have been characterized by many authors (see e.g. [1,2,3,4,5,6]). Since the problem of light propagation in a scattering and absorbing atmosphere has no general analytical solution, various analytical approximations have been suggested. The Small Angle Approximation (SAA), the Diffuse Approximation (DA) and the Small Angle Diffuse Approximation (SADA) [7,8,9] are some of the known analytical approximations, each having it's own range of validity. Another approximation, implemented for vertical viewing from satellites, is the two stream approximation [10,11]. For certain simple geometries it is possible to solve the equation of radiation transfer either numerically [12,13] or analytically [14,15,16] and to get an analytical expression for the atmospheric contribution to spatial blurring (laser beams [17]). The most general numerical technique used to calculate the effects of an arbitrary turbid atmosphere on optical systems is the Monte Carlo method [18,19,20,21,22,23]. All the above mentioned methods pertain to the blurring effects of the scattering atmosphere at the focal plane of the optics but do not consider other properties of the imaging systems. Sadot and Kopeika suggested a "practical" model [24] that describes how the properties of an imaging system affect the detected radiation by considering the Modulation Transfer Function (MTF) at the image plane. The image plane (not to be confused with the focal plane) is a virtual plane that includes also the effects of the detector and the electronics of an imaging system. A comment on that model by Bissonnette [25] and the response to it by Sadot and Kopeika [26] showed that though there is a common agreement on the blurring effects of the scattering atmosphere at the focal plane, there exist a disagreement in the issue of how the scattered radiation

is detected by an imaging system. The aim of this paper is to present a physical model of the detection process of the incident radiation by an imaging system. This model allows to calculate the distribution of the detected radiation (the Point Spread Function - PSF) in the image plane. A field experiment was performed in which atmospheric scattering effect on the PSF of a scanning point radiometer was measured. Theoretical predictions of the suggested model agree well with our experimental results and the experimental results of Bissonnette.

2. THEORY

The radiation that is detected by the detector of an imaging system is composed of 3 main constituents: A) direct radiation from the source blurred by three different mechanisms, B) radiation scattered by the atmosphere and C) radiation scattered within the optical system. Here we follow the common approach to the solution of imaging problems in the atmosphere [8,17] by treating the light, that is propagating in the atmosphere, as composed of the unscattered (direct) and the scattered components. The radiation that is scattered within the optical system originates in reflections from mechanical elements and non perfect optical components and coatings. Baffles and glare stops are few of the methods to reduce this stray light, but most of the commercially available imaging systems do not have these elements in their optical design. Stray light is usually several orders of magnitude weaker than the direct radiation, therefore it is noticeable only when a strong source of light is introduced into or near the field of view of the system or in case that the imaging system has a wide dynamic range.

2.1 The Point Spread Function

The basic physical function that describes the spatial response of an optical system is the Point Spread Function - PSF. If several conditions are met in the imaging process then it possible also to describe the spatial response of the optical system in terms of its Modulation Transfer Function - MTF, the amplitude of the bi-dimensional Fourier transform of the PSF:

$$MTF(\nu_x, \nu_y) = \left| \int_{-\infty}^{\infty} \int_{-\infty}^{\infty} PSF(x,y) e^{-2\pi i(x\nu_x + y\nu_y)} dxdy \right| \quad (1)$$

where x and y are spatial coordinates and ν_x and ν_y are spatial frequency coordinates in the focal plane. The conditions for the validity of the representation of the spatial response by the MTF are given by the linear filter theory [27]:

1. All the steps in the process of image formation should be linear.
2. All those steps should be isoplanatic (stationary in time and space).
3. The imaging process should be one-to-one mapping of the input plane to the output plane.

In the spatial domain the cumulative effect of two successive optical elements in the imaging process is given by a convolution between their PSF. In the spatial frequency domain the cumulative effect is given by a regular multiplication between their MTF (a property of the Fourier transform). This decomposition of the response of two successive optical elements into multiplication between their MTF is valid only if their spatial responses are uncorrelated. The above property, which makes system analysis much simpler in the spatial frequency domain rather than in the spatial domain, is the main reason that MTF became so popular in representing the spatial response of imaging systems.

The major drawback of using MTF in representing the spatial response of imaging systems is that some of the above mentioned conditions are not valid for those systems. For example some of the light detection processes are not linear (non linearity of the detection process) and some are not isoplanatic (spatial sampling

effects). There exist a dependence between various stages in the imaging process which makes the MTF decomposition into multiplicative terms invalid (atmospheric effects on imaging systems are a function of the imaging system properties). Though there are some attempts to overcome these drawbacks [28,29] of the MTF formalism, we will consider in the following model only the basic physical function that describes the spatial response of an optical system, the PSF.

2.2 The direct radiation

The direct radiation from a distant point source arrives at an imaging system as a plane wave (paraxial approximation). If the optics of the imaging system was unlimited in size and no system effects were present, then this plane wave would be focused to a point (spatial delta function) in the focal plane. This spatial delta function transforms to a blurred wider distribution function when the direct radiation is passing through the optical components of the imaging system and especially when it is detected by the system's detector. There are three main blurring processes in imaging systems: optical (diffraction) blurring, blurring due to the finite size of the detector elements and the display (electronic) spatial blurring. The blurring due to electronic effects varyies from system to system and is dependent on its specific signal processing. In this paper we will describe an imaging system that has the most simple signal processing that does not add to the spatial blurring. The optical blur is due to a diffraction by a size limited optics of the system. The optical blur of a light source with a unit intensity is described by an Airy disk pattern [8]:

$$I_{OPT}(r) = \frac{D^2}{4r^2} J_1^2\left(\frac{\pi D r}{\lambda f_0}\right) \tag{2}$$

Where $I_{OPT}(r)$ is radial distribution of the radiation flux in the focal plane. λ is the wavelength of the incident radiation, D and f_0 are the diameter and the focal length of the optical system, respectively, and J_1 is the Bessel function of the first order. The first zero of the Airy disk pattern occurs at a distance r_{Airy} from the axis of the system:

$$r_{Airy} = 1.22\frac{\lambda f_0}{D} \tag{3}$$

After passing through the optics the radiation is incident on the detection system that has detection elements with finite size. The detection elements can be either elements of a focal plane array or a single/vector of scanning detectors. The distribution of the detected radiation of a unit intensity light source between those detector elements is not an ideal rectangular function with dimension of the detection element, as can be assumed if we neglect the diffraction effect. This distribution is commonly described [28,29] by a Gaussian function that depends on σ - the size of the detection element. This distribution is not the actual distribution of the radiation (which is assumed here as a spatial delta function) but an effective radiation distribution as sensed by the detection elements of the imaging system.

$$I_{DIR}(r) = \frac{1}{2\pi\sigma^2}\cdot e^{\left(-\frac{r^2}{2\sigma^2}\right)} \tag{4}$$

Where $I_{DIR}(r)$ is an effective radial distribution of the radiation flux in the focal plane. σ is the typical size of the detection element and is related to the IFOV - Instantaneous Field Of View of the system and to its focal length f_0 - by:

$$IFOV = \arctan\left(\frac{\sigma}{f_0}\right) \cong \frac{\sigma}{f_0} \tag{5}$$

This approximation is valid here since the IFOV is usually a very small angle. The above radiation distributions are integrated over the detector element area, and hence they should be multiplied by σ^2 to yield the detected signal by the system. Since the atmosphere absorbs the radiation and scatters it out of the line of sight, then the measured signal will be obtained by multiplying the above distributions of a unit intensity light source by $T = e^{-\tau}$, where T is the atmospheric transmittance and τ is the optical depth of the atmosphere. For most of the imaging systems the spatial resolution is limited by the final size of the detection elements ("detector limited" case where $r_{Airy} << \sigma$) and not by the diffraction limit of the optics ("diffraction limited" case where $r_{Airy} >> \sigma$). Analysis of a diffraction limited imaging system operating in a turbid medium is given by Ishimaru [30]. In this paper the spread of the direct radiation as detected by an imaging system will be modeled by considering a detector limited system (and the diffraction effect will be neglected). Hence the detected signal of a unit intensity light source will be described by the product of the terms of Eq. 4, atmospheric transmittance and the area of the detector element:

$$PSF_{DIR}(r) = I_{DIR}(r) \cdot e^{-\tau} \cdot \sigma^2 = \frac{e^{-\tau}}{2\pi} \cdot e^{\left(-\frac{r^2}{2\sigma^2}\right)} \tag{6}$$

In a general case neither of the blurring effects is neglected and the PSF relative to the direct radiation is given by a convolution between the terms in Eq. 2 and 4. It is important to note here that the above described direct radiation distribution is what is usually referred to as the imaging system PSF. Depending on the system properties, this imaging system PSF may also include the contribution of the radiation which is scattered within the imaging system.

2.3 The radiation scattered by the atmosphere

The light emanating from the radiation source is scattered and absorbed by molecules and aerosols in the atmosphere. Various analytical and numerical solutions exist for the problem of radiation transfer in the atmosphere. In the present work a modified version [31] of the SEMIM [21,22,23] Monte Carlo code is used to evaluate the contribution of atmospheric turbidity to the augmentation of the Point Spread Function. SEMIM code output was successfully compared [21] with published data from controlled laboratory measurements by Donelli et al. [32] and by Kuga and Ishimaru [33,34]. The scattered radiation reaching the imaging system is a function of the view angle in the lens plane, θ (see Fig. 1):

$$\tan(\theta) = \frac{r}{f_0} \tag{7}$$

However in order to obtain the detector signal PSF_{SCA} this radiation should be integrated over the solid angle subtended by the detector element of the imager, and hence it should be multiplied by $IFOV^2$ (or by $(\sigma/f_0)^2$ - see Eq. 5):

$$PSF_{SCA}(r) = I_{SCA}(r/f_0) \cdot (\sigma/f_0)^2 \tag{8}$$

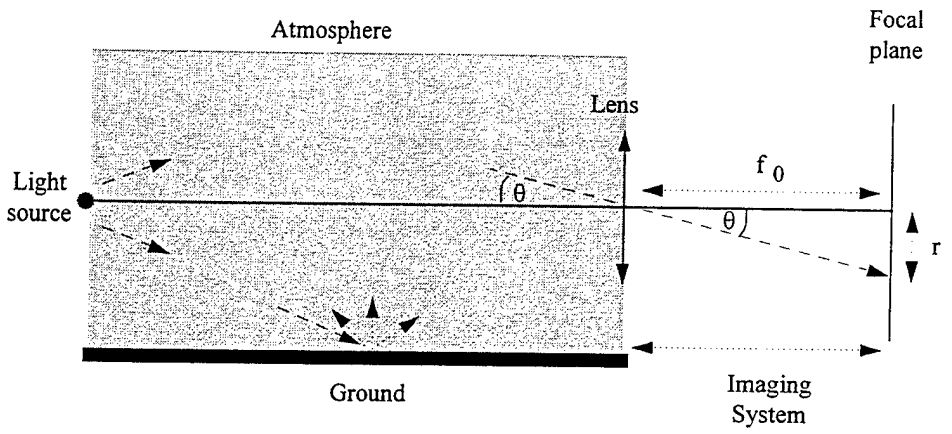


Figure 1: Geometry of an imaging system looking at a point source through the intervening atmosphere.

where $I_{SCA}(r/f_0)$ is the angular distribution of the scattered radiation (in Watt/str) that is obtained through the Monte-Carlo method as will be described later. This equation is based on the assumption of a constant IFOV for all detector elements (based on the paraxial approximation of $r << f_0$). For imaging systems with short focal length this assumption may not be valid and a $\cos^3(\theta)$ correction factor for the projected IFOV should be applied:

$$PSF_{SCA}(r) = I_{SCA}(r/f_0)\cdot\frac{\sigma\cdot\sigma\cos(\theta)}{\left[f_0/\cos(\theta)\right]^2} = I_{SCA}(r/f_0)\cdot\frac{\sigma^2}{f_0^{\,2}}\cdot\left(\frac{f_0}{\sqrt{r^2+f_0^{\,2}}}\right)^3 \qquad (9)$$

2.4 The model for the detected light

In the theoretical model presented herein we try to quantify the relative contributions of the scattered and the direct radiation components to the spatial distribution of radiation from a point source as detected by an imaging system. We assume a linear imaging system and the input radiation to the system is the sum of two independent components (scattered and unscattered radiations). Hence the detected signal is the sum of the two detected components:

$$PSF_{DET}(r) = I_{SCA}(r/f_0)\cdot\frac{\sigma^2}{f_0^2}\cdot\left(\frac{f_0}{\sqrt{r^2+f_0^{\,2}}}\right)^3 + \frac{e^{-\tau}}{2\pi}\cdot e^{\left(-\frac{r^2}{2\sigma^2}\right)} \qquad (10)$$

Using the angular presentation, the above distribution is given by:

$$PSF_{DET}(\theta) = I_{SCA}(\theta)\cdot IFOV^2\cdot\cos^3(\theta) + \frac{e^{-\tau}}{2\pi}\cdot e^{\left(-\frac{\theta^2}{2\cdot IFOV^2}\right)} \qquad (11)$$

The internal system scattered radiation is a third term that is usually present in Eq. 10 and 11. However, this term is very dependent on the specific properties of the imaging system and it is quite hard to model it properly.

2.5 Theoretical calculations

A modified version of the SEMIM Monte Carlo code is used in the present work to evaluate the contribution of atmospheric turbidity to the augmentation of the Point Spread Function. The effect of atmospheric turbidity is evaluated in the SEMIM code as due to the presence of scatterers (the secondary sources) whose defocused images are distributed on the image plane of the primary source. The positions of the scatterers are determined by a Monte Carlo procedure, while the contribution of each secondary source to the irradiance on the image plane is evaluated by means of Geometrical Optics.

Several simulations were performed in order to investigate the effects of atmospheric scattering and absorption on the spatial resolution of imaging systems. The calculations were done for a CCD camera operating in the visible spectral region (0.55 μm). The size of a detector element was chosen to be 15 μm and a number of detectors in the array is 512 detectors (these numbers are typical for a commercial available CCD cameras). The diameter of the lens was kept constant at 4 cm and the focal length of the optics varied between 1 cm (a system with a wide field of view ~ 38 deg) to 100 cm (a system with a narrow field of view ~ 0.44 deg). Figures 2a and 2b presents the calculated normalized PSF (using Eq. 10 and dividing by PSF(0)) of this imaging system for a point lambertian source located 1 km horizontally from the system for the rural and radiation fog aerosol models, respectively. The atmospheric parameters used in the above simulation were calculated [31] using the data of the size distributions and the refractive indices of atmospheric aerosols, tabulated in the report by Shettle and Fenn [35], and by using the LOWTRAN7 code [36].

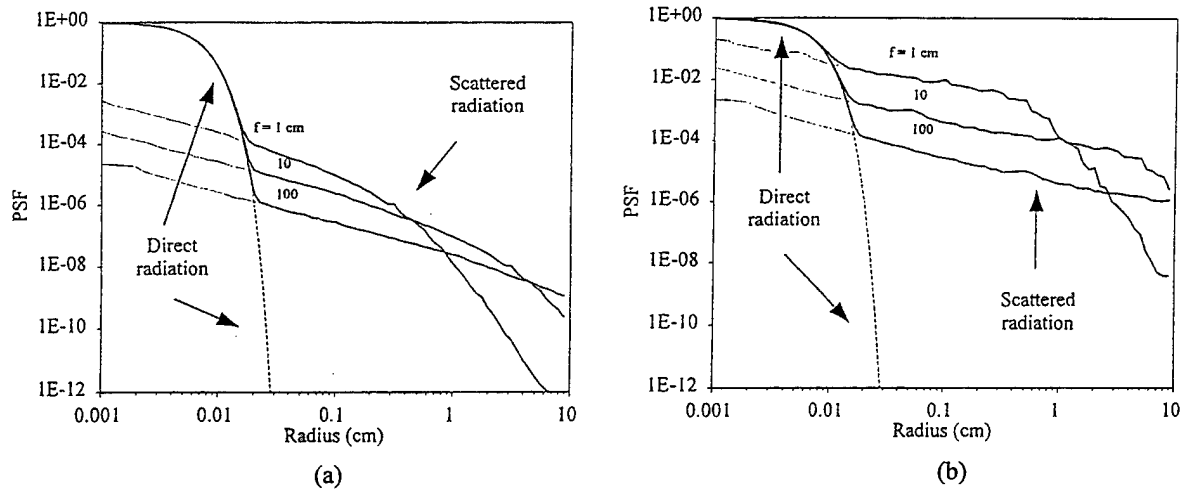


Figure 2: Simulated normalized PSF of an imaging system operating in the visible wavelength for 3 different focal length's = 1, 10 and 100 cm. The aerosol models used are: (a) Rural aerosol (VIS = 5 km); (b) Radiation fog (VIS = 0.5 km).

As one can see, the common feature in figure 2 is the increase in the contribution of the scattered radiation to the PSF when the field of view becomes wider (smaller focal length). Common imaging systems have a dynamic range with about 2-4 orders of magnitude (8 bits = 1:256 to 12 bits = 1:4096). Due to this technical limitation the curves in figure 2a shows that for most common viewing conditions in the atmosphere and for most common types of imaging systems, the atmospheric scattering will not have any effect on spatial blurring of the images. Only at very extreme atmospheric conditions (such as dense fog, rain or sand storm) imaging systems with wide FOV will produce somewhat blurred images due to atmospheric scattering. At this point it is important to note that atmospheric scattering and absorption have a strong influence on the reduction of the contrast of the objects seen through the atmosphere in most of atmospheric conditions (see

Fig. 3). This contrast reduction must not be confused with spatial blurring, which, as was shown here, is not influenced usually by atmospheric scattering and absorption.

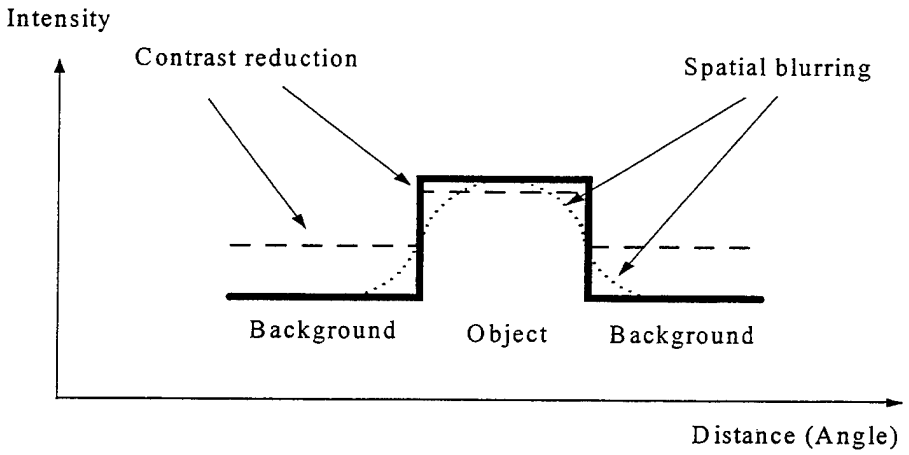


Figure 3: Visualization of the differences between two different atmospheric effects : Contrast reduction and Spatial blurring. The thick line represents a spatial (angular) scan over the object in the object plane, and the dashed/dotted lines are the scans over the object in the optics plane, which includes the atmospheric effects.

3. EXPERIMENTAL SETUP

The basic instrument that we used in the field tests that we performed was a scanning point radiometer. This instrument was chosen since it does not suffer from most of the drawbacks of regular imaging cameras: It has a large dynamic range and almost an unlimited angular region. Figure 4 describes the general geometry of the field test: Two radiometers together with the meterological station and the visibility meter were placed on a roof of one building, and a strong quartz halogen lamp was placed on the roof of another building 650 meters away. The PSF was measured by using that lamp as a point source. The effects of turbulance were minimized by choosing the optical path to be about 50m above the ground.

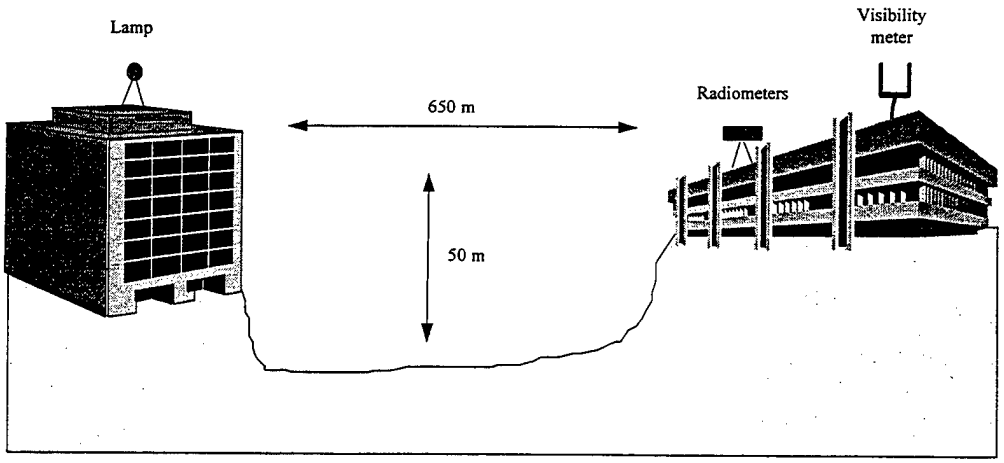


Figure 4: General geometry of the field experiments.

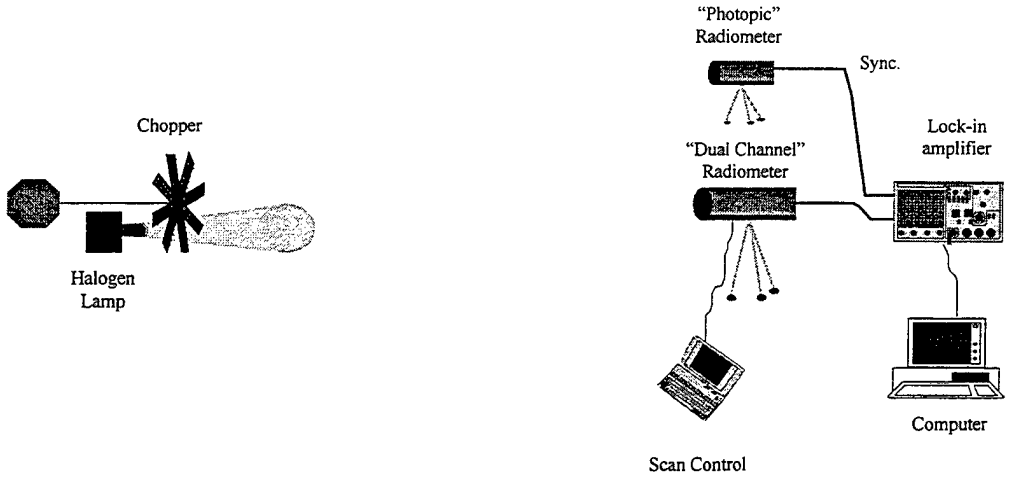


Figure 5: The experimental setup.

Figure 5 shows the experimental setup that was used in the measurement of the PSF: As a light source a 250W quartz halogen lamp was used with a divergence of about ±30°. The radiation from the lamp was chopped by a mechanical chopper at 280 Hz. In order to detect only the chopped radiation three SR-850 lock-in amplifiers were used. The reference signal to the lock-in amplifier was obtained from a second fixed "Photopic" point radiometer that monitored the frequency of the chopper. The main instrument that we used was a "Dual Channel" point radiometer (FOV = 2 mrad, $\lambda = 0.87 \pm 0.17$ μm with low-noise Si detector) that was placed on a precise scanning mechanism (1.5 deg in 5 minutes). Three SR-850 Lock-in amplifiers measured (at different amplifications) the output of the Si detector and their amplified signals were sampled by a computer. Since each one of the lock-ins has a dynamic range of 2.5 a total dynamic range of 6 orders of magnitude was covered by them. The meteorological station measured the temperature of the air, pressure, relative humidity. The scattering coefficient of the aerosols ($k_e^t \approx 3.0/VIS$) was measured by the visibility meter (model HSS-500).

4. RESULTS

A series of field measurements were performed in April-May 1996 in Haifa, Israel. Since we did not had an aerosol PMS (particle measurement system), a rough estimation of the aerosol type and size distribution was carried out. Usually an urban aerosol model was used (with the modifications of the local relative humidity), except on several days, when an eastern wind brought aerosols from the inland: On those days the rural aerosol model seemed to be a more suitable model. The details of aerosol models in the report by Shettle and Fenn [35] were used for the simulation of the predicted signal. The contribution of the radiation that is scattered inside the radiometer (system scattered radiation) was measured by placing the lamp a distance of 70 meter from the radiometer. The contribution of atmospheric turbulence, for the hottest day in the experiment, was estimated by the IMTURB model [37] to be about 0.015 mrad. Since the field of view of the radiometer was 2 mrad, the effects of atmospheric turbulence could be neglected.

Figures 6a, 6b, 6c and 6d presents a comparison between the PSF as measured by the "Dual Channel" radiometer and the predicted PSF according to model described in section 2.4. In each figure the measured data (●) appears together with 3 theoretical curves: A) the predicted direct ($PSF_{DIR}(\theta)$ with a square field of view was used in the model) combined with the system scattered radiation (.....), B) the predicted direct and atmospheric scattered radiation (___) and C) the predicted signal which is composed of the sum of the direct, system and atmosphere scattered radiations (━━━).

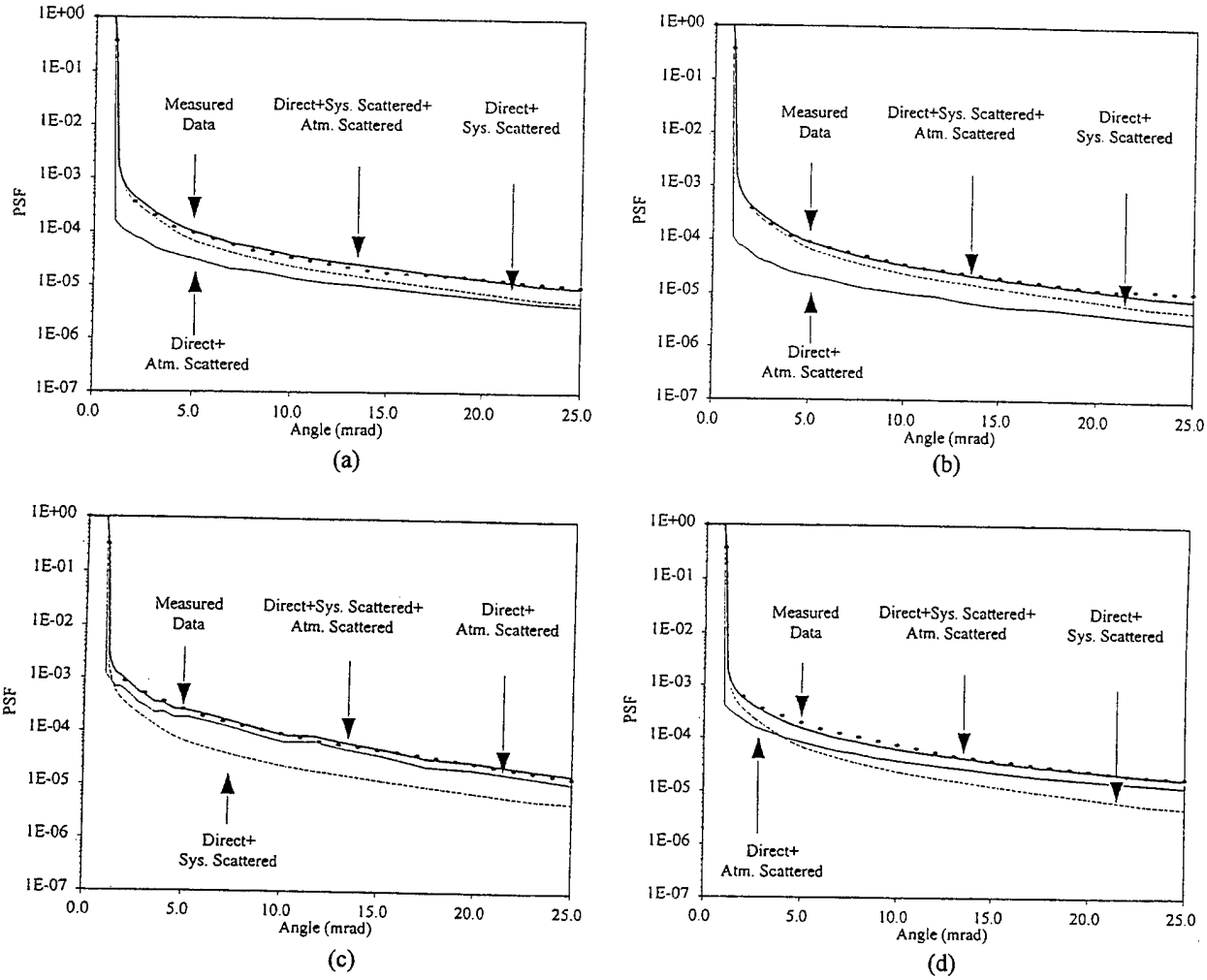


Figure 6: Comparison of the measured PSF by the "Dual Channel" radiometer with the predicted PSF according to the presented model. The comparisons are for measurements made at an urban aerosol loading of (a) $k_e^t \approx 0.1$ km^{-1}; (b) $k_e^t \approx 0.2$ km^{-1}; and at rural aerosol loading of (c) $k_e^t \approx 0.4$ km^{-1}; (d) $k_e^t \approx 0.6$ km^{-1}.

5. CONCLUSION

A physical model, which describes the effect of the radiation scattered by the aerosols and molecules in the atmosphere on an imaging system, is presented. This model explains how the field of view, the dynamic range and other characteristics of the imaging system as well as the turbidity of the atmosphere affect the measured PSF of a distant point source. It is found that for common imaging systems in general atmospheric conditions, the processes of atmospheric scattering and absorption do not contribute to spatial blurring of the recorded images. Only at extreme conditions of atmospheric turbidity (such as dense fog, rain or sand storm) and for imaging systems with wide FOV, the atmospheric scattering will blur the images as seen by them.

The agreement of theoretical predictions with the measured data in our field measurements is very good. Figures 6 demonstrate the ability of the proposed model to predict quantitatively the relative contributions of the direct, atmospheric scattered and system scattered components.

REFERENCES

[1] R.E. Hufnagel and N.R. Stanley, "Modulation Transfer Function associated with image transmission through turbulent media", *J. Opt. Soc. Am.* **54**, 52-61 (1964).

[2] D.L. Fried, "Optical resolution through a randomly inhomogeneous medium for very long and very short exposures", *J. Opt. Soc. Am.* **56**, 1372-1379 (1966).

[3] V.I. Tatarski, *The effect of the turbulent atmosphere on wave propagation*, Israel Program for Scientific Translations, Jerusalem (1971).

[4] R.L. Fante, "Electromagnetic beam propagation in a turbulent media", *Proc. IEEE* **63**, 1669-1692 (1975).

[5] M.I. Charnotskii, "Anisoplanatic short-exposure imaging in turbulence", *J. Opt. Soc. Am. A* **10**, 492-501 (1993).

[6] F. Roddier, "The effects of atmospheric turbulence in optical astronomy", in *Progress in Optics*, E. Wolf ed., vol. 19, 281-376 (North-Holland, Amsterdam, 1981).

[7] R.F. Lutomirski, "Atmospheric degradation of electro-optical system performance" *Appl. Opt.* **17**, 3915-3921 (1978).

[8] A. Ishimaru, *Wave propagation and scattering in random media*, Academic press, New-York (1978).

[9] E.P. Zege, A.P. Ivanov and I.L. Katsev, *Image transfer through a scattering medium*, Springer-Verlag, Berlin (1991).

[10] Y. Mekler and Y.J. Kaufman, "The effect of Earth's atmosphere on contrast reduction for a nonuniform surface albedo and 'two-halves' field", *J. Geophys. Res.* **85**, 4067-4083 (1980).

[11] Y.J. Kaufman, "Atmospheric effect on spatial resolution of surface imagery: errata", *Appl. Opt.* **23**, 4164-4172 (1984).

[12] A. Zardecki, S.A.W. Gerstl and F. Embury, "Multiple scattering effects in spatial frequency filtering", *Appl. Opt.* **23**, 4124-4130 (1984).

[13] Y. Kuga, A. Ishimaru, H.W. Chang and L. Tsang, "Comparisons between the small-angle approximation and the numerical solution for radiative transfer theory", *Appl. Opt.* **25**, 3803-3805 (1986).

[14] Y.J. Kaufman, "Solution of the equation of radiative transfer for remote sensing over nonuniform surface reflectivity", *J. Geophys. Res.* **87**, 4137-4147 (1982).

[15] D.J. Diner and J.V. Martonchik, "Influence of aerosol scattering on atmospheric blurring of surface features", *IEEE Trans. Geophys. Remote Sens.* **GE-23**, 618-624 (1985).

[16] D.J. Diner and J.V. Martonchik, "Atmospheric transfer of radiation above an inhomogeneous non-lambertian reflective ground - I. Theory", *J. Quant. Specrosc. Transfer* **31**, 97-125 (1984).

[17] L.R. Bissonnette, "Multiscattering model for propagation of narrow light beams in aerosol media", *Appl. Opt.* **27**, 2478-2484 (1988).

[18] W.A. Pearce, *A study of the effects of the atmosphere on Thematic Mapper observations*, Report 004-77 (EG&G/Washington Analytical Service Center, Riverdale, Md., 1977).

[19] G.I. Marchuk, G.A. Mikhailov, M.A. Nazaraliev, R.A. Darbinyan, B.A. Karagin and B.S. Elepov, *Monte-Carlo methods in atmospheric optics*, Springer-Verlag, Berlin (1980).

[20] M.T. Valley, "Evaluation of equivalent spheres for use in modeling nonspherical aerosol modulation transfer function", *Proc. SPIE* **1968**, 130-141 (1993).

[21] P. Bruscaglioni, P. Donelli, A. Ismaelli and G. Zaccanti, "A numerical procedure for calculating the effect of a turbid medium on the MTF of an optical system", *J. mod. Optics* **38**, 129-142 (1991).

[22] P. Bruscaglioni, P. Donelli, A. Ismaelli and G. Zaccanti, "Inhomogenety of turbid medium and its effect on the MTF of an optical system", *Nuovo Cimento* **15D**, 775-783 (1993).

[23] P. Bruscaglioni, P. Donelli, A. Ismaelli and G. Zaccanti, "Monte Carlo calculations of the modulation transfer function of an optical system operating in a turbid medium", *Appl. Opt.* **32**, 2813-2824 (1993).

[24] D. Sadot and N.S. Kopeika, "Imaging through the atmosphere: practical instrumentation-based theory and verification of atmospheric modulation transfer function", *J. Opt. Soc. Am.* **A 10**, 172-179 (1993).

[25] L.R. Bissonnette, "Imaging through the atmosphere: practical instrumentation-based theory and verification of atmospheric modulation transfer function: comment", *J. Opt. Soc. Am.* **A 11**, 1175-1179 (1994).
[26] N.S. Kopeika and D. Sadot, "Author's reply to: Imaging through the atmosphere: practical instrumentation-based theory and verification of atmospheric modulation transfer function: comment", *J. Opt. Soc. Am.* **A 12**, 1017-1023 (1995).
[27] J.W. Goodman, *Introduction to Fourier Optics*, McGraw-Hill, New-York (1968).
[28] A.H. Lettington and Q.H. Hong, "A discrete modulation transfer function for focal plane arrays", *Infrared Phys.* **34**, 109-114 (1993).
[29] L. de Luca and G. Cardone, "Modulation transfer function cascade model for a sampled IR imaging system", *Appl. Opt.* **30**, 1659-1664 (1991).
[30] A. Ishimaru, "Limitation on image resolution imposed by a random medium", *Appl. Opt.* **17**, 348-352 (1978).
[31] B. Ben Dor, P. Bruscaglioni, A. Devir, P. Donelli and A. Ismaelli, "Cloud, fog and aerosol effect on the MTF of optical systems", *Proc. SPIE* **2580**, 106-114 (1995).
[32] P. Donelli, P. Bruscaglioni, A. Ismaelli and G. Zaccanti, "Experimental validation of a Monte Carlo procedure for the evaluation of the effect of a turbid medium on the point spread function of an optical system", *J. mod. Optics* **38**, 2189-2201 (1991).
[33] Y. Kuga and A. Ishimaru, "Modulation transfer function and image transmission through randomly distributed spherical particles", *J. Opt. Soc. Am.* **A 2**, 2330-2335 (1985).
[34] Y. Kuga and A. Ishimaru, "Modulation transfer function of layered inhomogeneous random media using the small-angle approximation", *Appl. Opt.* **25**, 4382-4385 (1986).
[35] E.P. Shettle and R.W. Fenn, *Models for the aerosols of the lower atmosphere and the effects of humidity variations on their optical properties*, **AFGL-TR-79-0214**, Air Force Geophysics Laboratory, U.S. Air Force Systems Command, Hanscom Air Force Base, Bedford, MA (1979).
[36] F.X. Kneizis et al., *Atmospheric Transmittance/Radiance: computer code LOWTRAN 7*, **AFGL-TR-88-0177**, Air Force Geophysics Laboratory, U.S. Air Force Systems Command, Hanscom Air Force Base, Bedford, MA (1988).
[37] J. Ricklin and W. Miller, *IMTURB - A model for imaging through optical turbulence,* U. S. Army, Atmospheric Sciences Laboratory, White Sands Missile Range, NM (1991).

Essential Atmospheric & Oceanographic Measurements in Hard to Reach Areas of the Battlespace

by

G. Frederick[1], R. Foster[2], J. Daniels[2], & M. Smith[1]

Abstract

Understanding the environmental effects on weapons systems in all dimensions of the battlespace is essential to effective employment of those weapons. Understanding is based on data -- data which may not be available when really needed. Weather satellites provide an important overall view of the atmosphere and ocean and make may of the measurements used in numerical models which analyze and predict future status. Surface based in-situ and remote sensing devices help fill in many of the voids in the data base. But, there are large regions of the world which do not have adequate coverage and during combat there are many areas where data are denied or impractical to measure with conventional instruments. The US Navy's Naval Research Laboratory has embarked on a campaign to refine our capability to fill the data gaps in the Battlespace, particularly in fulfilling the need for mesoscale measurements near the ocean-atmosphere interface. One such effort has been support for the demonstration of a new miniaturized GPS-based sensor platform which promises to provide a broad range of applications. This paper describes the development and testing of the first versions of this device which measures temperature, pressure, humidity and winds from a package that is 1.5" in diameter and 8.1" long for deployment from standard countermeasures dispensing systems. Initial demonstrations were conducted using an EA-6B and a P-3 aircraft. Follow-on demonstrations are scheduled on the SH-60 helicopter, the Predator UAV, and other aircraft. Results of these demonstrations are presented along with future plans for oceanographic, rocket propelled, and surface implant deployments and integration of additional sensor types. The significance of this development is that these instruments can be launched from almost any military and many civilian aircraft equipped with standard countermeasures dispensing systems without any modification to the aircraft. Data can be received on board the aircraft, via satellite links, or by surface based receivers and input to fine scale and large scale models for various applications. Some of these applications are presented in the paper.

1. Overview

Meteorological satellites provide excellent broad scale coverage of weather patterns and deliver very good estimates of some of the meteorological data elements needed to predict the future state of the atmosphere. The worldwide upper air observing system supplements satellite observations with data from radiosondes and other instruments. Data collected from this network of satellite and surface based systems feed the numerical weather forecast models of the world's meteorological centers. Unfortunately there are gaps in the data base caused by several factors. In the case of the satellites, they lack the spatial and temporal resolution required for some forecasts and for others they are inhibited from making required measurements by intervening atmospheric phenomena or deficient technological capability. The surface based systems are limited in filling the

[1]*Radian International Electronics Division, 15508 Bratton Ln, Austin TX 78728*

[2]*Tracor Aerospace, 6500 Tracor Lane, Austin TX 78725*

void because large areas of the earth are covered by water or are sparsely inhabited and thus not ideal for radiosonde or other types of observing systems. Finally, when political or combatant conflicts occur, conventional weather data -- both satellite and surface based -- are often denied or otherwise not readily available. Thus, there is a valid need for further supplementing the data base with other sources. The US Navy's Naval Research Laboratory is sponsoring a tactical dropsonde program to demonstrate a method for obtaining essential atmospheric measurements in hard to reach areas of the combat zone -- otherwise known as "the battlespace". This paper describes a unique Global Positioning System (GPS) based instrument which has been initially designed to be employed as a dropsonde but which has many other potential applications.

2. Dropsonde History

Current dropsondes which use Omega or Loran navigation systems for winds evolved from earlier versions which measured pressure, temperature and humidity (PTH) only. The US Air Force Hurricane Hunters employ a National Center for Atmospheric Research (NCAR) designed dropsonde which uses the Omega system for winds. It measures 16 inches in length, has a circular cross-section which is 3.5 inches in diameter and it weighs about one pound. It is deployed from WC-130 aircraft by means of a specially designed tube mounted in the floor of the aircraft cargo compartment. The Navy's objective in sponsoring a tactical dropsonde program was to employ a design which could be deployed from many different aircraft without significant aircraft modification. Their approach was to demonstrate a "tactical dropsonde" deployed from standard countermeasures dispensing systems (CDMS), normally used for chaff and flare dispensing.

3. Tactical Dropsonde Development

The Naval Research Laboratory (NRL) Center for Tactical Oceanographic Warfare Support (TOWS) Program Office contracted with Neptune Sciences, Inc. (NSI) and its two subcontractors, Tracor Aerospace and Radian International Electronics Division to demonstrate this capability. The contractor team embarked on internally financed independent research and development (IRAD) design and development activity to come up with a completely new miniaturized, ruggedized dropsonde capable of deployment from standard CDMS, able to survive the harsh operating environment, and able to measure critical atmospheric elements. Phase 1 of the effort resulted in the successful demonstration of a PTH-Only dropsonde such as the one depicted in Figure 1.

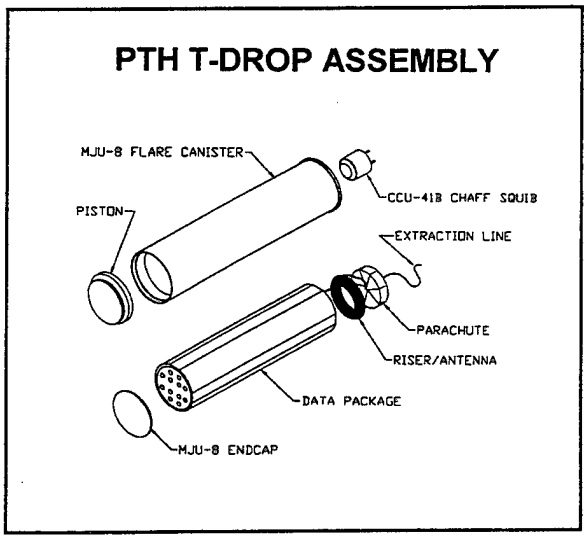


Figure 1.

On 29 Feb 1996 an operational EA-6B from VAQ-139, Whidbey Island NAS, WA, successfully deployed several PTH TDrop™ (for tactical dropsonde) units off the coast of Washington near Ocean Shores.

Figure 2 depicts the ejection sequence.

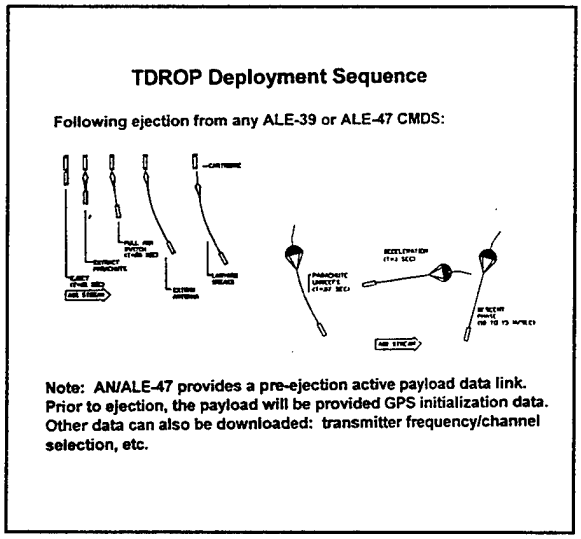


Figure 2.

Data were received by a ground based receiver stationed on the shoreline some 5-10 miles from the drop point. While this was an uncalibrated demonstration, data from the upper air site at Quillayute (UIL) are shown in figure 3 along with data from one of the TDrop™ deployments. UIL is a land based site 70 miles north of the drop point and the data were observed some 3 hours prior to the drop. The temperature inversion evident at UIL was most likely not present over the water at the drop site, thus making for a relatively good comparison between the radiosonde and the dropsonde data. The most important aspect of the demonstration was that the sonde survived ejection from the CDMS after experiencing extreme temperatures and vibrations while captive in the EA-6B's CDMS prior to launch. Following this initial success, the contractor

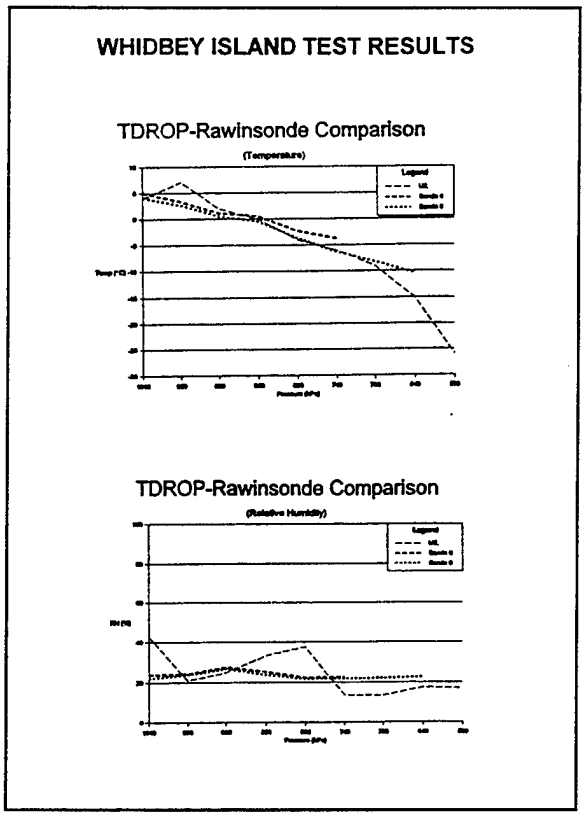


Figure 3.

team embarked on further internally financed IRAD design and development of a GPS based TDrop™.

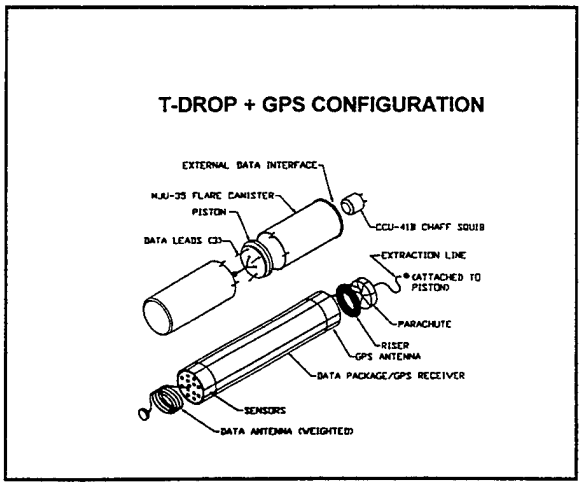


Figure 4.

This has resulted in initial prototypes similar to the one depicted in Figure 4. As this paper was being written, the prototypes had successfully completed ground testing, had survived ejection and vibration tests, and were about to experience first flight tests. GPS TDrop™ is 8.1 inches long, has a circular cross-section of 1.5 inches in diameter and weighs less than a pound. It employs a full GPS engine which is capable of geographic navigation, time capture, and Doppler velocity determination. In addition to geo-location, the other advantage of this approach over the alternative "codeless" technique is maximum potential signal-to-noise ratio for resolving signals from the GPS constellation.

4. Applications

Potential applications for TDrop™ technology are wide and varied. The Navy initially plans to use it for determining the temperature and humidity structure in the lowest layers of the atmosphere.

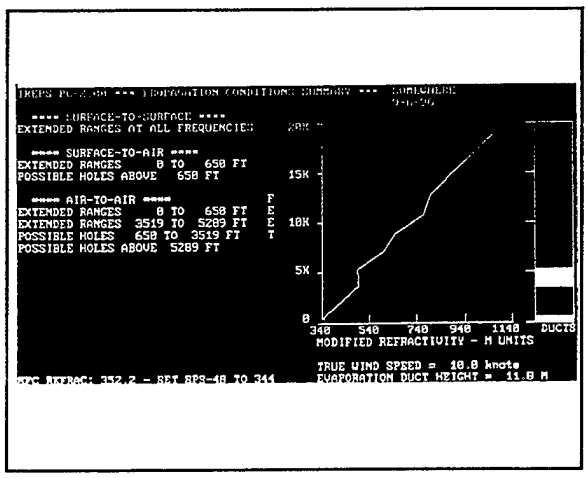


Figure 5.

This will allow them to input high resolution data to mesoscale models and tactical decision aids such as the Integrated Refractive Effects Prediction System (IREPS) as depicted in Figure 5 (Patterson 1990). Other applications include wind profiles for input to computed air release point calculations for precision airdrop operations and atmospheric profiles for input to a number of tactical decision aids and mesoscale models.

An example of the utility of observations such as those obtained from a flexible observing system like the dropsonde, came out of a winter storm reconnaissance effort conducted in the northeast Pacific Ocean during the winters of 1994 and 1995 (Peterman et al 1996). At that time the National Centers for Environmental Prediction (NCEP) (formerly the National Meteorological Center - NMC) cooperated with the US Air Force Hurricane Hunters, the National Weather Service Forecast Office in Seattle, several NOAA Laboratories and Radian to deploy NCAR-designed dropsondes in data sparse areas in the northeast Pacific Basin. WC-130 aircraft staged out of McChord AFB WA near Tacoma to areas designated by forecasters in Seattle and NCEP. Areas were agreed upon during teleconference calls between the forecasters and were based on suspected voids in the data base which could adversely affect the numerical model runs. The 1994 deployments identified procedural and technical problems with ingesting asynoptic data such as the dropsondes into the data base. The 1995 deployments provided sufficient data and realized significant procedural changes that detailed post analyses of the value of the dropsonde data could be performed. Spearheaded by scientists at NCEP (Lord et al, 1996), ensemble forecasts were assembled with and without dropsonde data. In some cases the dropsonde data had little or no impact on the resulting forecast, but in other cases the data had a significant impact. Figure 6 shows standard deviation of forecast error for the 2-11 Feb 95 period. Dropsonde data had a significant impact on

the forecasts valid on 8 Feb.

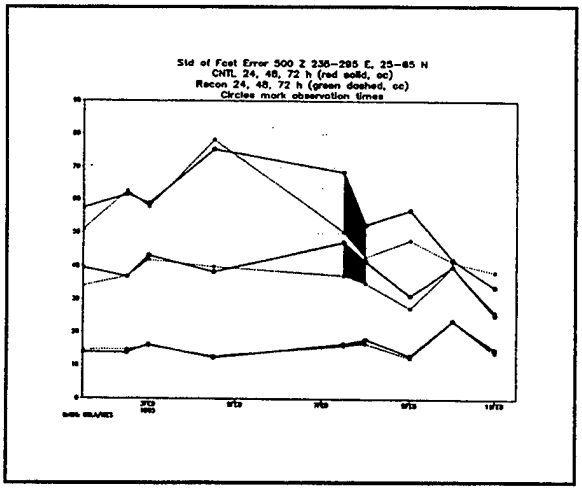


Figure 6.

The analogy for potential TDrop™ operations is that a strategy for when and where tactical dropsondes are employed could be based on similar ensemble techniques. Lord, et al has suggested that the ensembles could be analyzed for suspect areas where accurate data would have the most impact on the forecast some 12-18 hours ahead of when the data are needed. The results of this analysis would then dictate where one would deploy flexible observing assets.

5. Future Plans

Following initial flight testing of the GPS TDrop™, a series of demonstrations are planned. One such demonstration anticipates deployment from an SH-60 where several methods for communicating the data are anticipated. Figure 7 illustrates the data flow which allows for transmission of coded data to several locations where they can be decoded and applied in various support scenarios. The key is that the TDrop™ signal is a simple frequency modulation on a selected carrier wave. PTH and GPS information are packed in frames which when demodulated and decoded provide the observed values. Standard sonobuoy frequencies are used for this demonstration but other frequencies in the standard meteorological bands are planned.

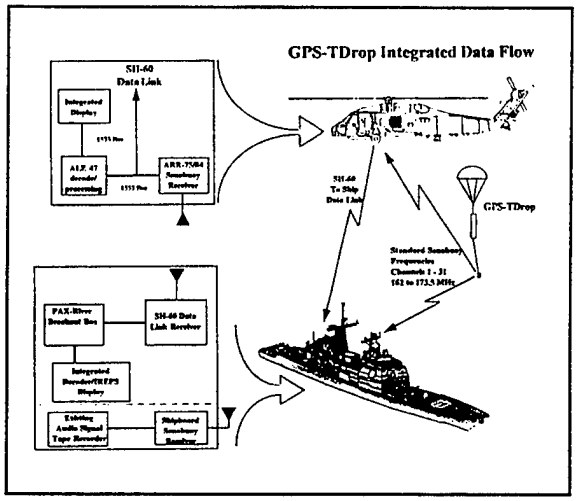


Figure 7.

Another demonstration is planned on the Predator UAV. In this case a special pod is being developed which will house the CMDS as well as the data receiver and GPS initialization unit. Flight tests will demonstrate the ability to warm start the GPS chip in TDrop™ prior to launch. Successful deployment, data reception and relay for operational use will also be demonstrated. Concepts are being developed for operational employment on the Predator UAV while Predator is performing other required tasks without interfering with those tasks.

Since TDrop™ is basically an instrumentation package centered on the GPS engine and its controlling microprocessor, TDrop™ can be the backbone for many other sensor requirements. Figures 8 and 9 depict two such future roles: use as an unattended ground based sensor and as a rocketsonde, respectively. Other concepts on the drawing boards see modified TDrop™ packages as

chemical sensors, oceanographic monitors, etc. The key to TDrop™'s utility is its ability to geo-locate itself, determine its own velocity, interrogate multiple on-board sensors, and communicate all of that information over an RF link to a nearby ground or airborne receiver.

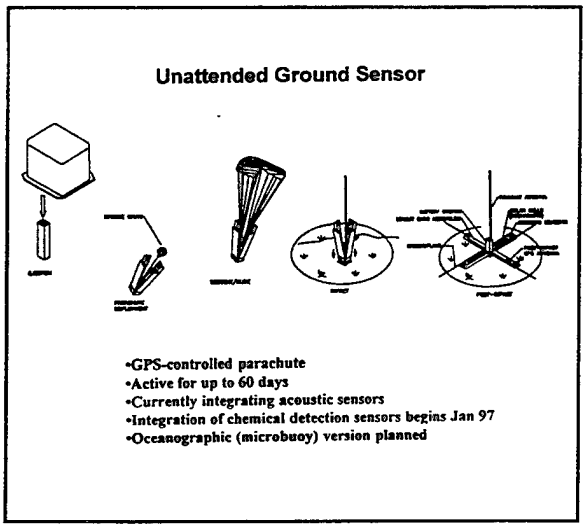


Figure 8.

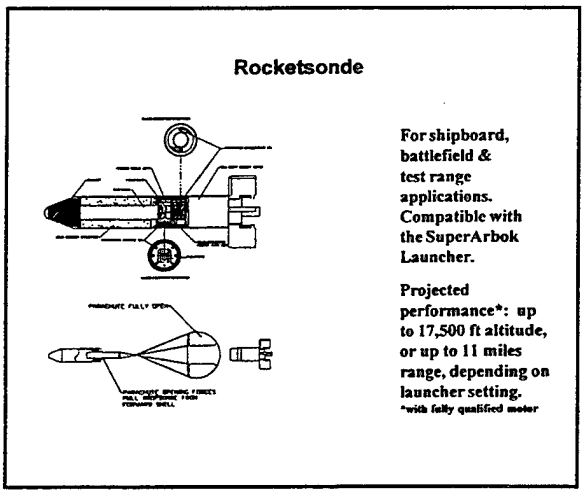


Figure 9.

6. Summary

The US Navy has sponsored a forward looking demonstration of essential atmospheric measurements using GPS technology and standard aircraft CDMS. Operational concepts are being developed which take advantage of the flexibility inherent in a deployable observing system such as TDrop™. Initial prototypes have been successful with future deployments scheduled from SH-60, Predator UAV and other aircraft. Data can be received on board the dispensing aircraft, can be relayed to other sites, or can be monitored by other receivers within line of site of the instrument. The flexibility of the GPS/microprocessor based platform promises a variety of other sensor and employment applications for this technology.

Acknowledgements. The authors wish to thank Mr. Ken Ferer, NRL/TOWS office and his staff for leadership and guidance on this project. TDrop™ team members from NSI, Tracor, and Radian have committed long hard hours to the success of this project and we are grateful for their significant contributions.

REFERENCES

Dumont RJ, Nelson, CA, Caviness DG, Thormeyer CD, Martin DL, & Pereira JJ, 1996: Cooperation and Collaboration among the Nation's Meteorology, Oceanography, and Satellite Operational Processing Centers: An Evolving Era in US Civilian-Military Partnerships, *BAMS*, **77**, 2067-2076.

Frederick GL & Weiher L, 1995: The Use of Dropwindsondes in the Northeast Pacific Basin, *Preprint of Pacific Northwest Weather Workshop*, NWS, Seattle WA.

Lord SJ, 1995: Research Reconnaissance Flights in NE Pacific, *Personal Communication, Memo dated 11 Jan 95.*

Lord, SJ, Tracton, S, Katz, B, 1996: The Impact on Synoptic-Scale Forecasts Over the United States of Dropwindsonde Observations Taken in the Northeast Pacific Ocean, *Personal Communication, Briefing Slides, Fall 1996.*

National Center for Atmospheric Research. 1994: *SSSF Observing Facilities: Description and Specifications, Version 1.0*, Boulder CO, 62 pp.

Patterson WL, 1990: *Integrated Refractive Effects Prediction System (IREPS) Users Manual*, Rev PC-2.0, NRaD Technical Document 1874, San Diego CA, 42 pp..

Peterman KR, Frederick GL, Lord SJ, Weiher L, & Smith MV, 1996: WC-130 Research Reconnaissance Flights in the Northeast Pacific and Gulf of Alaska, *Preprints, AMS Conference on Coastal Oceanic and Atmospheric Prediction*, 252-254.

Tracton SM & Kalnay E, 1993: Operational Ensemble Prediction at the National Meteorological Center: Practical Aspects, *Weather Forecasting*, **8**, 379-398.

Working Group Summary, 1996: Sensors and Weapon Systems, *Proceedings of the Symposium on Tactical Meteorology and Oceanography Support for Strike Warfare and Ship Self-Defense* , Ocean Studies Board, NRC, Washington DC..

ON THE DEGRADATION OF ACOUSTIC ANGLE-OF-ARRIVAL ESTIMATES DUE TO ATMOSPHERIC TURBULENCE

D. Keith Wilson
Acoustics Team, Battlefield Environment Division, U. S. Army Research Laboratory
ATTN: AMSRL-IS-EE, 2800 Powder Mill Road, Adelphi, MD 20783-1197

Abstract

The ability of an acoustic array to accurately track sources is limited primarily by background noise and by atmospheric turbulence. Modeling of the latter effect is the main topic of this paper. The turbulence degrades angle-of-arrival (AOA) estimates by creating uncorrelated phase and amplitude fluctuations at the individual array elements. Theoretically optimal array performance can be determined by calculating Cramer-Rao lower bounds (CRLB's) on the AOA estimates. CRLB calculations are presented in this paper for several different turbulence models and propagation environments. It is shown that the turbulent degradation becomes quite important in low signal-to-noise scenarios, particularly for propagation distances greater than several hundred meters and acoustic frequencies above 50 Hz. The reduction in array coherence is found to be caused almost exclusively by along-path wind velocity fluctuations generated by near-ground wind-shear instabilities. Large turbulence structures, such as boundary-layer thermals characteristic of a sunny day, may play an indirect role by creating regions of locally high shear near the ground. A theory for propagation through such intermittent turbulence is used to show that accuracy of AOA estimates can fluctuate by several degrees, depending on whether the propagation is through a locally active region of turbulence or not.

1. Introduction

Acoustic sensor arrays have long been used to detect, locate, and identify objects in the ocean. In the atmosphere, however, these roles are more often performed by radar and optical systems than by acoustical ones. The primary reason for this state of affairs is simple: sound waves are minimally attenuated when they propagate through water, but strongly so through air; the situation is essentially reversed for electromagnetic (EM) waves.

Given such a fundamental physical constraint, it may seem surprising that there has been renewed interest and activity during recent years in the development of acoustical systems for atmospheric battlespaces. Systems under development by the U.S. Army that incorporate acoustical arrays include the Brilliant Antitank Munition (BAT), the Remote Sentry, the Wide Area Mine (WAM), and the Intelligent Minefield (IMF). There are several reasons why acoustical systems have overcome their inherent limitations to achieve this new popularity. For one, they are relatively inexpensive and simple to design, a benefit attributable in no small part to modern capabilities in digital signal processing. This makes it feasible to deploy them in large numbers. Acoustical systems also are unaffected by smoke and other obscurants that hamper optical systems. They furthermore do not necessarily require a line-of-sight propagation path, since sound energy often readily penetrates into shadow regions by diffraction and turbulent scattering. Although acoustical systems never will completely supplant the dominant EM technologies, it does appear that they can beneficially supplement existing EM systems, in many cases providing additional, useful information on the battlefield.

One important characteristic of acoustic arrays deployed in the atmosphere is that their performance depends strongly upon atmospheric conditions. Performance is normally enhanced by still, nighttime conditions, and degraded by atmospheric turbulence occurring during windy conditions or on a sunny day. This is because array beamforming relies on good mutual coherence between the signals received by the individual sensors; turbulence causes a loss of such coherence. Effective deployment of acoustic arrays requires understanding and quantification of this turbulent degradation.

This paper describes a theoretical framework for analyzing turbulence effects on acoustic arrays that are used to determine source bearings. Some example calculations of array performance are given for typical atmospheric conditions.

2. General Procedure and Assumptions

As shown in Fig. 1, the analysis of turbulence effects on sensor arrays involves many sub-problems: it requires adequate characterization of atmospheric conditions, a realistic turbulence model, a realistic background noise model, a suitable theory for acoustic propagation through turbulence, and statistical methods from estimation theory. Because of the complex nature of the problem, it is impossible to explore all of the important issues here. I will focus on the turbulence modeling, and simplify many other aspects of the problem.

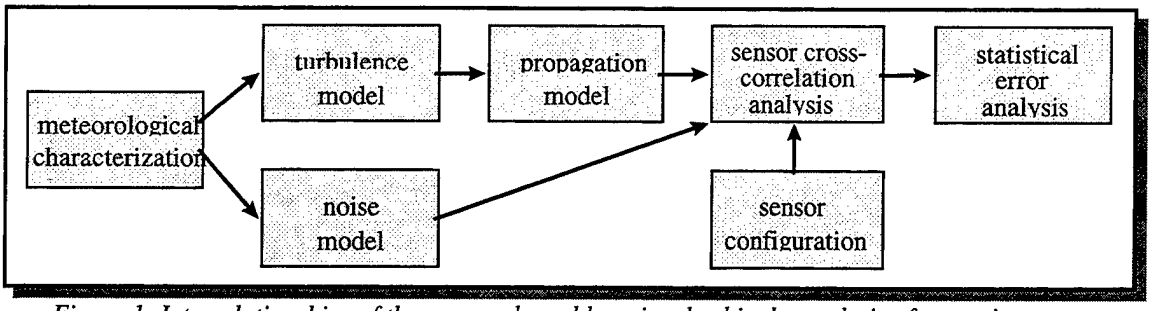


Figure 1: Interrelationships of the many sub-problems involved in the analysis of acoustic sensor array performance in the atmosphere.

One simplifying assumption I make is that the noise at the individual sensors is uncorrelated and equal in variance. This is probably not a good assumption, in general: the sources of noise that are usually most significant, such as other battlefield participants and wind-induced pressure fluctuations, undoubtedly produce correlated noise. Much remains to be learned regarding the realistic modeling of these noise sources.

I will also assume that the acoustic propagation may be approximated by plane waves. This is quite reasonable if the size of the array is small compared to its distance from the source.

In this paper I make the distinction between *angle-of-bearing* and *angle-of-arrival. Angle-of-bearing (AOB)*, of course, refers to the actual direction of the source. *Angle-of-arrival (AOA)* refers to the orientation of the wavefront normal when the sound reaches the array. For horizontal arrays the two angles are usually nearly the same. The situation is quite different for vertical arrays, however, as shown in Fig. 2. In this case refraction of the sound normally causes the AOA and AOB to be different. For downwind propagation, there are typically multiple ray paths and hence a distribution of AOA's. For upwind propagation, the AOA is normally determined by the location of the "scattering volume," i.e., the region from which the sound energy reaching the source was scattered by turbulence.

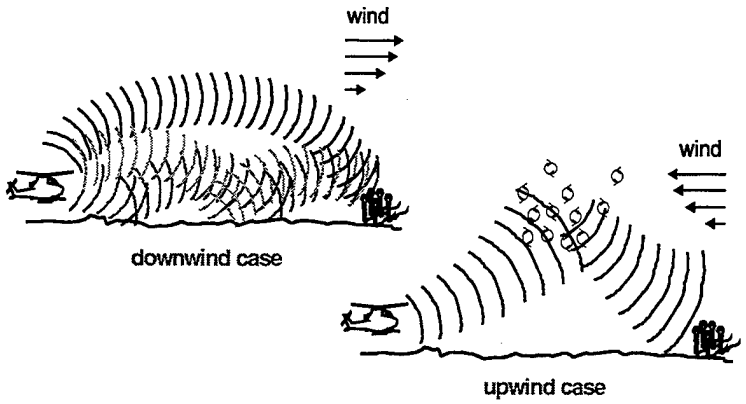


Figure 2. The effect of refraction on the acoustic wavefront angle-of-arrival. In the downwind (or in the temperature inversion) case, multiple arrivals are created. In the upwind (or in the temperature lapse) case, the sound reaching the receiver is normally scattered there by turbulence.

Because of the refraction effects, most of the existing acoustic systems only attempt to determine horizontal source bearings. It is possible that reasonable vertical bearings could be obtained if a refraction model were incorporated into the analysis. In this paper I circumvent the refraction issue by explicitly considering the accuracy of AOA estimates; the reader should keep in mind that if vertical bearings are the concern, the AOA estimate may not be useful without additional information.

3. Sensor Cross Correlation Analysis

It is perhaps easier to discuss the steps shown in Fig. 1 in essentially reverse order. We will start with the sensor cross correlation analysis, and the ensuing statistical analysis of AOA errors. The derivation in this section is similar to one given recently by Song and Ritcey (1996), for the case of ocean acoustic arrays.

The received signal at each sensor has contributions from the source of interest, whose sound arrives at the angle ψ, as well as from all other sources (the "noise"). Hence the total signal $\mathbf{p}(\psi,t)$ consists of additive contributions from the source $\mathbf{s}(\psi,t)$ and the noise $\mathbf{n}(t)$:

$$\mathbf{p}(\psi,t) = \mathbf{s}(\psi,t) + \mathbf{n}(t),$$

where t is time, and the bolding indicates an $N \times 1$ column vector, N being the number of array elements. Assuming that the source signals have been normalized to unit variance, that the signal and noise are mutually uncorrelated, and that the noise at each of the sensors is equal in variance, we have

$$\mathbf{R}_{\mathbf{pp}}(\psi) = \langle \mathbf{p}(\psi,t)\mathbf{p}^*(\psi,t) \rangle = \mathbf{R}_{\mathbf{ss}}(\psi) + \sigma_n^2 \mathbf{I},$$

where σ_n^2 is the noise variance, and $\mathbf{I}$ is the identity matrix. The signal-to-noise ratio is by definition

$$\mathrm{SNR} = -10 \log \sigma_n^2.$$

The source signal cross correlation matrix $\mathbf{R}_{\mathbf{ss}}(\psi)$ is approximately equal to the element-by-element product of an array steering matrix $\mathbf{S}(\psi)$ and a mutual coherence matrix $\mathbf{T}$. The elements of these two matrices are, respectively,

$$S_{mn}(\psi) = \exp\left[-ikd_{mn}\cos(\psi - \alpha_{mn})\right]$$

$$T_{mn} = \Gamma(d_{mn})$$

in which k is the acoustic wavenumber, d_{mn} is the distance between sensors m and n and α_{mn} the angle between them (see Fig. 3). The function Γ is called the mutual coherence function (MCF), and will be discussed in the next section.

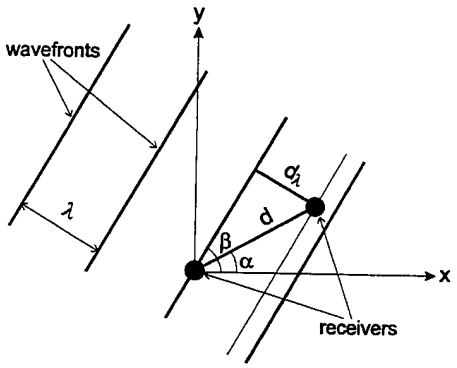


Figure 3. Planar wavefronts incident on a pair of receivers. The distance between the sensors is d and the angle is α.

According to the Cramer-Rao theorem, the mean-square error in an angle of arrival estimate $\hat{\psi}$ is always greater than or equal to the inverse of the Fisher information matrix $\mathbf{J}(\psi)$:

$$\left\langle (\psi - \hat{\psi})^2 \right\rangle \geq \mathbf{J}^{-1}(\psi),$$

In our case the Fisher matrix is given by the following matrix product (Song and Ritcey, 1996):

$$\mathbf{J}(\psi) = M\mathrm{tr}\left(\mathbf{R}_{pp}^{-1} \frac{\partial \mathbf{R}_{pp}}{\partial \psi} \mathbf{R}_{pp}^{-1} \frac{\partial \mathbf{R}_{pp}}{\partial \psi} \right),$$

where M is the number of statistically independent samples used to estimate the sensor cross correlations (i.e., the number of applications of the beamformer prior to averaging).

The inverse of the Fisher matrix is called the *Cramer-Rao Lower Bound* (CRLB). The CRLB gives the lowest mean-square error that is theoretically obtainable. That is, if we had the best possible algorithm for converting the sensor phase information to AOA estimates, the mean-square error of our estimates would equal the CRLB. Fortunately it appears that practical methods yield performance comparable to the CRLB (Song and Ritcey, 1996). Actually, in the rest of this paper, when I mention the CRLB I will actually mean its square root. This quantity corresponds to the best obtainable root-mean-square error, and is more natural to deal with since its dimensions are linear rather than squared.

4. Propagation Model

The MCF needed for the sensor cross correlation analysis is equal to the coherence between the signals at two receivers. In the case of plane-wave propagation, the MCF is approximately (Rytov *et al.*, 1989)

$$\Gamma(\rho) \equiv \exp\left\{-\frac{\pi k^2 X}{2}\left[b(0)-b(\rho)\right]\right\},$$

where X is the propagation distance, ρ is the separation between the receivers, and $b(\rho)$ is the two-dimensional (2D) correlation function (sometimes called the transverse correlation function). The 2D correlation can be found from the 3D correlation R using the equation

$$b(r_2,r_3)=\frac{1}{2\pi}\int_{-\infty}^{\infty} R(r_1,r_2,r_3)\,dr_1,$$

in which r_1 is in the direction of propagation, and r_2 and r_3 are the two transverse directions. For isotropic turbulence $\rho^2 = r_2^2 + r_3^2$, and $b(r_2,r_3)=b(\rho)$. If the turbulence is anisotropic, the MCF generally becomes a function of r_2 and r_3 instead of just ρ.

In order to better compare the behavior of the MCF corresponding to various turbulence models, it is worthwhile to define a *two-dimensional structure function (TSF)* $d(\rho)$ such that

$$d(\rho)=2\left[b(0)-b(\rho)\right].$$

The TSF is the 2D counterpart of the usual 3D structure function. A quantity that is also closely related to the 2D correlation and useful when comparing turbulence models is the *integral length scale*, $\mathcal{L}$:

$$\mathcal{L}=\frac{1}{\sigma^2}\int_0^{\infty} R(r)\,dr=\frac{\pi}{\sigma^2}b(0).$$

If the source of the coherence loss is fluctuations in the sound speed, then the MCF should be computed using the 2D correlation function for the index of refraction N, where

$$N \approx -2c'/c_0 \approx -T'/T_0,$$

T being the temperature. (Primes indicate fluctuations, and the subscript "0" indicates the mean value.) For acoustic propagation in the atmosphere, however, it is most frequently the situation that the coherence loss is caused by fluctuations in the along-path wind speed v_1. In this case the correlation function of

$$u_1 = -2v_1/c_0$$

is to be used (Ostashev, 1994). The situation for wind speed fluctuations is further complicated by the fact that correlation functions for an isotropic, homogeneous, solenoidal vector field are *not* interchangeable with those for a scalar field. For example, the functional form of $b(\rho)$ for the scalar Gaussian model differs from the vector Gaussian model. These issues are beyond the scope of this paper, however; the reader is referred to Batchelor (1953) and Wilson (1996) for details.

5. Turbulence Models

The turbulence model plays a critical role in determining the MCF. A fully 3D turbulence model is required for the computation. Unfortunately, most existing correlation and spectral equations for atmospheric turbulence are 1D in nature, since they are based on measurements made from stationary towers.[1] As a result we are forced to consider highly idealized turbulence models that, although they may lack realism, are at least 3D.

The simplest model is the isotropic *Gaussian* model. It is quite easy to handle analytically, and is not completely unreasonable for the large, energetic eddies in the turbulence, called the *energy subrange*. The disadvantage of the Gaussian model is that it does not realistically describe the turbulent *inertial subrange* (the eddies participating in the cascade of energy from large to very small scales). This is a serious problem with regard to array performance evaluation, since the inertial scales are usually comparable to the spacing between the microphones.

A much better model than the Gaussian is the *von Kármán*. Like the Gaussian model, the von Kármán model is reasonable for the energy subrange. The main benefit of the von Kármán model is that it also works very well in the inertial subrange. Although it is more analytically difficult to handle the Gaussian model, closed-form results can still be obtained using the von Kármán model.

Like the von Kármán model, the *Kolmogorov* model is valid in the inertial subrange. It has the additional advantage of simplicity. The disadvantage is that it is based on scaling laws that are *only* valid in the inertial subrange, being inapplicable to the energy subrange. We will see that the energy subrange structure of atmospheric turbulence does affect acoustic arrays in significant ways.

The final model we will consider is the Wilson and Thomson (1993), anisotropic, Gaussian model. Due to its Gaussian nature the Wilson and Thomson model is poor for the inertial subrange. However, it attempts to capture realistic anisotropic features characteristic of atmospheric turbulence. It is interesting to compare the Wilson and Thomson model to the isotropic Gaussian model, in order to learn about the significance of the anisotropy.

Basic equations for the different models are listed in Fig. 4. The Gaussian, von Kármán, and Kolmogorov models are plotted for comparison in Fig. 5.

6. Example Calculations

All of the example calculations we will consider are for five element uniform-line arrays. The wavefront incidence is assumed to be broadside ($\beta = \alpha$ in Fig. 3).[2] Furthermore, in the CRLB calculations there are assumed to be M=5 independent samples.

Figure 6 shows the compares the CRLB from the scalar Gaussian and von Kármán models, as a function of the spacing between the array elements and the total index-of-refraction variance. The SNR in both cases was 20 dB, and the integral length scale was chosen such that $\mathcal{L}=5\lambda$, where λ is the acoustic wavelength. The length of the propagation path was $50\,\mathcal{L}$.

One can conclude from the Fig. 6 that, at least for this propagation distance, the effect of turbulence becomes important only when $\sigma^2 \geq 10^{-4}$. There is a general tendency for performance to diminish with decreasing array spacing. The reason is that small arrays have small phase differences between the elements, and these small differences are more difficult to detect above the noise.

Another very noticeable feature for both models is a peak in the CRLB (i.e., poor array performance) when $2d/\lambda \approx 10$ ($d \approx \mathcal{L}$). This peak results from the fact that most of the turbulent energy occurs around the scale $\mathcal{L}$. When the spacing is much larger than $\mathcal{L}$, the phase differences between the sensors are large enough that turbulence has little effect. When the array spacing is much less than $\mathcal{L}$, the phase fluctuations tend to be uniform across the array, and hence do not diminish performance. The von Kármán model suggests a greater sensitivity to turbulence at small spacings than the Gaussian model, because it (more realistically) contains more small-scale turbulent energy (see Fig. 5).

---

[1] The direction of tower-based spectral measurement is effectively the along-wind direction. The time series for the turbulent fluctuations is converted to a spatial series by setting $\Delta x = U\Delta t$, where U is the wind speed.

[2] Array performance is best at broadside incidence. When the wavefronts are perpendicular to the array axis, the CRLB becomes infinite.

Gaussian scalar model

The scalar Gaussian model is defined by the following correlation function:

$$R(r)=\sigma^2\exp\left(-\frac{r^2}{L^2}\right),$$

where σ^2 is the variance, and L is the Gaussian length scale. The corresponding energy spectrum is

$$E(\kappa)=\frac{\sigma^2\kappa^2L^3}{4\sqrt{\pi}}\exp\left(-\frac{\kappa^2L^2}{4}\right),$$

and the two-dimensional correlation function is

$$b(\rho)=\frac{\sigma^2L}{2\sqrt{\pi}}\exp\left(-\frac{\rho^2}{L^2}\right).$$

The Gaussian length scale and integral length scale $\mathcal{L}$ are related by

$$\mathcal{L}=\frac{\sqrt{\pi}}{2}L\equiv 0.886L.$$

von Kármán scalar model

The scalar von Karman model is defined by the following energy spectrum:

$$E(\kappa)=\frac{4\Gamma(17/6)}{3\sqrt{\pi}\Gamma(1/3)}\frac{\sigma^2\kappa^4\ell^5}{\left(1+\kappa^2\ell^2\right)^{17/6}},$$

where σ^2 is the variance, and ℓ is the von Karman length scale. The corresponding correlation function is

$$R(r)=\frac{2\sigma^2}{\Gamma(1/3)}\left(\frac{r}{2\ell}\right)^{1/3}\left[K_{1/3}\left(\frac{r}{\ell}\right)-\left(\frac{r}{3\ell}\right)K_{2/3}\left(\frac{r}{\ell}\right)\right],$$

where K_ν is the modified Bessel function. The two-dimensional correlation function is

$$b(\rho)=\frac{4\sigma^2\ell}{3\sqrt{\pi}\Gamma(1/3)}\left(\frac{\rho}{2\ell}\right)^{5/6}\left[K_{5/6}\left(\frac{\rho}{\ell}\right)-\left(\frac{\rho}{2\ell}\right)K_{1/6}\left(\frac{\rho}{\ell}\right)\right].$$

The von Karman length scale and integral length scale $\mathcal{L}$ are related by

$$\mathcal{L}=\frac{2\sqrt{\pi}\Gamma(5/6)}{3\Gamma(1/3)}\ell\equiv 0.498\ell.$$

Kolmogorov scalar model

Define the structure function for the scalar N as

$$D(r)=\left\langle\left[N(r)-N(0)\right]^2\right\rangle.$$

The structure-function parameter is

$$C_N^2=\lim_{r\to 0}D(r)/r^{2/3}.$$

The approximate energy spectrum (valid for $k\mathcal{L}\gg 1$) is

$$E(\kappa)=\frac{2^{5/3}}{11\sqrt{\pi}}\frac{\Gamma(17/6)}{\Gamma(2/3)}C_N^2\kappa^{-5/3}\equiv 0.207C_N^2\kappa^{-5/3}.$$

The approximate two-dimensional structure function (valid for $r/\mathcal{L}\ll 1$) is

$$d(\rho)=\frac{\Gamma(1/6)}{5\sqrt{\pi}\Gamma(2/3)}C_N^2\rho^{5/3}\equiv 0.464C_N^2\rho^{5/3}.$$

Wilson and Thomson model

The Wilson and Thomson semi-empirical model (*J. Acoust. Soc. Am.* 96, 1080) is the sum of six Gaussian correlation functions, representing:

1. small-scale temperature fluctuations
2. small-scale velocity fluctuations (along wind)
3. small-scale velocity fluctuations (cross wind)
4. temperature / velocity covariance
5. large-scale velocity fluctuations (along wind)
6. large-scale velocity fluctuations (cross wind)

The model incorporates some observed features of anisotropy characteristic of atmospheric turbulence.

For most common daytime conditions the small-scale velocity fluctuations dominate. For propagation downwind, the two-dimensional correlation is then

$$b(\rho)=\frac{6.3\sigma^2L}{2\sqrt{\pi}}\left(1-\frac{\rho^2}{L^2}\right)\exp\left(-\frac{\rho^2}{L^2}\right),$$

where $L=z$, and $\sigma^2=22u_*^2/c_0^2$. The 6.3 is an anisotropy factor, resulting from vortex stretching due to wind shear.

Figure 4. Basic results for several turbulence models. More complete derivations, including the vector forms of the models, can be found in Wilson (1997a).

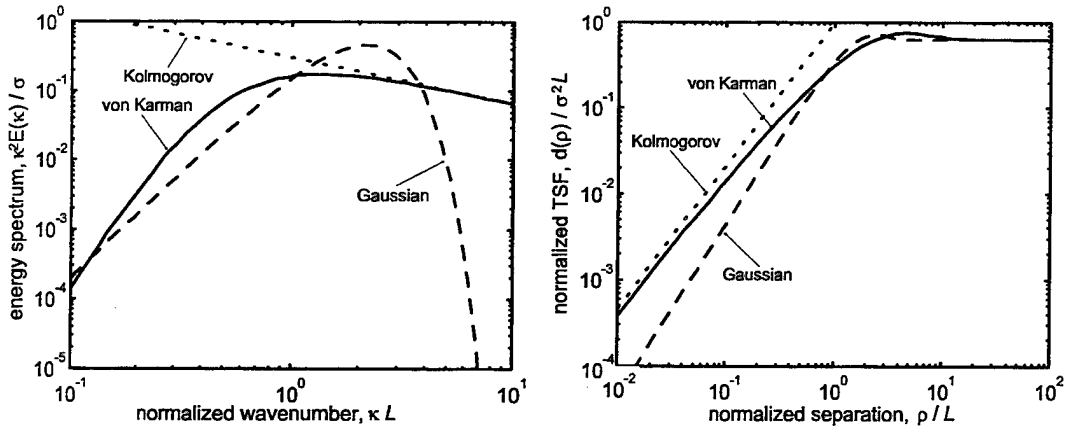


Figure 5. Comparison of the scalar Gaussian, von Kármán, and Kolmogorov models. On the left are the energy spectra, and on the right are the 2D correlation functions (TSF's). The energy subrange corresponds to $\kappa\mathcal{L}\ll 1$ and $\rho/\mathcal{L}\gg 1$, and the inertial subrange to $\kappa\mathcal{L}\gg 1$ and $\rho/\mathcal{L}\ll 1$.

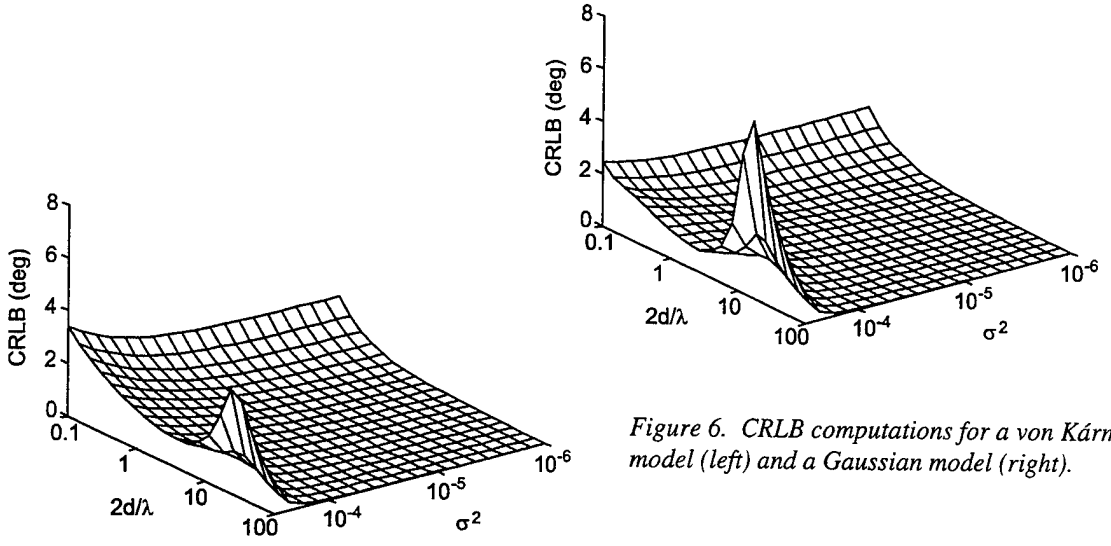


Figure 6. CRLB computations for a von Kármán model (left) and a Gaussian model (right).

The four turbulence models are compared in Fig. 7. The variance was set to $22u_*^2 / c_0^2$, where u_* is the friction velocity, and the Gaussian length scale was set to z (Wilson and Thomson, 1993). The length scale needed for the von Kármán model can be determined from the integral length scale, which is known from the Gaussian scale (Fig. 4). The Kolmogorov model parameters can be determined from the inertial subrange asymptote of the von Kármán model.

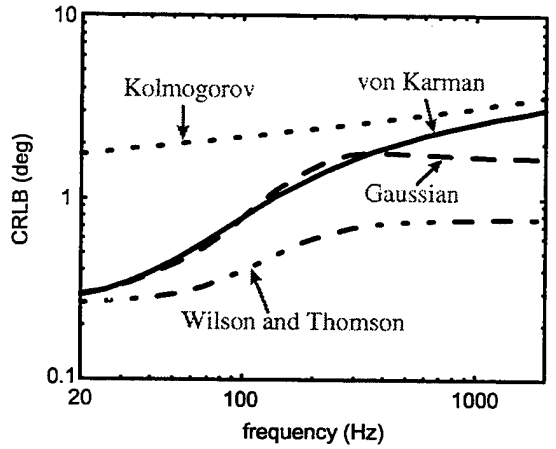


Figure 7. Comparison of the four turbulence models for windy atmospheric conditions.

The meteorological parameters used in the creation of Fig. 7 were typical of a windy, neutral atmosphere: $u_* = 0.5$ m/s, $T_* = -0.01$ K, and z_i (the inversion height) = 1000 m. The interelement array spacing was one-half wavelength, the propagation distance was 500 m, the array height was 2 m, and SNR was 20 dB.

All of the models except for the Kolmogorov one lead to similar results at very low frequency. The Kolmogorov model performs well only above 1000 Hz or so. The Gaussian and von Kármán models agree well up to several hundred Hz. At this point they diverge, because the Gaussian model does not have a realistic inertial subrange. The reason why the isotropic Gaussian and Wilson and Thomson models diverge above 20 Hz or so is due to the anisotropy factor present in the latter. The Wilson and Thomson model contains a factor of 6.3 representing the stretching of eddies in the direction of the wind. Overall we see that the von Kármán model is the only one that behaves reasonably well for all frequencies, although it does not capture anisotropic effects that are evidently important.

Figure 8 shows MCF and CRLB predictions for the Wilson and Thomson model as a function of the meteorological conditions. The computations use the same parameters as in Fig. 7, although the frequency has been fixed at 200 Hz, and u_* and T_* were varied. It is evident that the turbulence effect depends more strongly on u_* than

on T_*, implying wind shear-generated turbulence plays a more important role than thermal structure. Hence it is often justifiable to neglect the effect of temperature fluctuations.

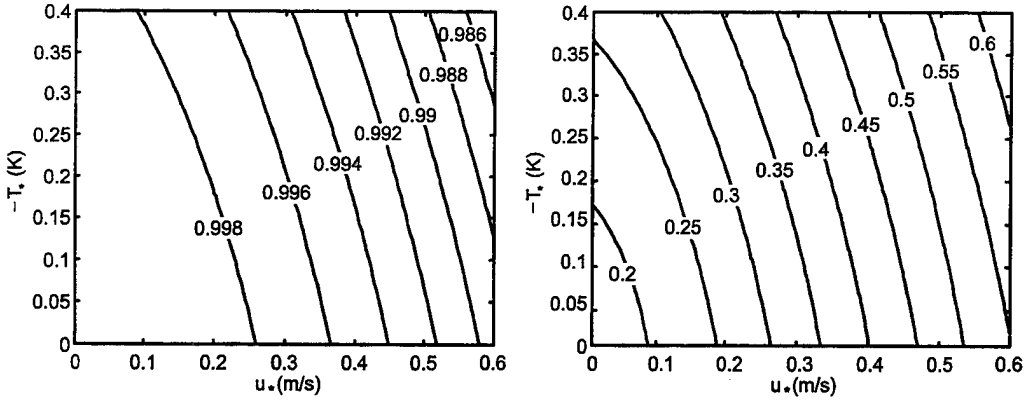


Figure 8. Dependence of the MCF (left) and the CRLB (right) on the turbulence scaling parameters u_* and T_*.

7. Turbulent Intermittency

The analysis in the previous section implicitly assumed that the strength of the turbulence (e.g., the variance or the structure-function parameter), averaged over the length of the propagation path, was constant. Although this is a standard assumption, it is probably not a good one. In actuality the statistical properties of a turbulent flow, even when the flow may be considered homogeneous and stationary, are a local property of the averaging region *unless* the region is large compared to the external scales associated with the flow. In the atmosphere, the relevant external scale is the boundary-layer inversion height, which is on the order of 1 km. Hence, unless an acoustical system operates over scales of many kilometers, the variation in local turbulence properties could be significant.

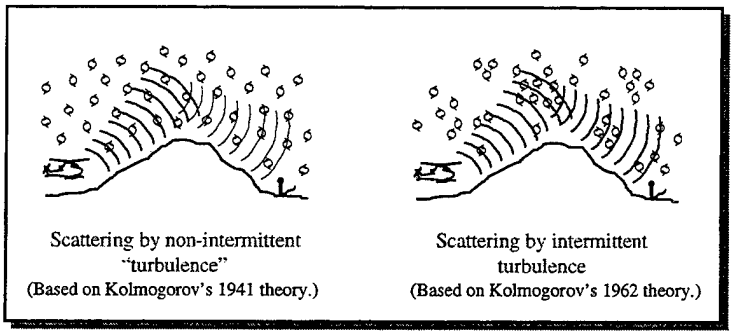


Figure 9. Scattering from both the non-intermittent and intermittent viewpoints. The strength of the turbulence is depicted (non-rigorously) by the concentration of eddies.

This characteristic of turbulence statistics, called *intermittency*, was first described systematically by Kolmogorov (1962). An illustration of the effect is given in Fig. 9. So far very little research has been done on incorporating intermittency effects into theoretical treatments for propagation through turbulence. This is a significant oversight from the standpoint battlefield acoustics, and probably also for many EM scenarios. Among the few authors who have consider intermittency effects on wave propagation are Gurvich and Kukharets (1986) and Tatarskii and Zavorotnyi (1985).

We can account for intermittency in the Kolmogorov model simply by using a structure function parameter $\tilde{C}_V^2$ that is *local* (average) to the propagation path, in place of its ensemble mean $C_V^2 = \langle \tilde{C}_V^2 \rangle$ (Tatarskii and Zavorotnyi, 1985). (Tildes are used here to indicate local parameters.) The resulting local MCF is

$$\tilde{\Gamma}\left(\rho, \tilde{C}_V^2\right) \equiv \exp\left\{-0.21\pi k^2 X \tilde{C}_V^2 \rho^{5/3}\right\}.$$

The local structure function parameter has an approximately log-normal distribution (Kolmogorov, 1962). That is, $\ln \tilde{C}_V^2$ is approximately normal. It can be shown (Wilson, 1997b) that $\tilde{C}_V^2$ is less than $\exp\left(\ln\left\langle \tilde{C}_V^2 \right\rangle - 2.15\sigma_V^2\right)$ 5% of the time, and greater than $\exp\left(\ln\left\langle \tilde{C}_V^2 \right\rangle + 1.15\sigma_V^2\right)$ 95% of the time, where σ_V^2 is the variance of $\ln \tilde{C}_V^2$. These particular values for $\tilde{C}_V^2$ are called the 5% lower and 95% upper confidence bounds, respectively. The log-mean and log-variance parameters can be estimated from the following formulas (Wilson, 1997b):

$$\left\langle \tilde{C}_V^2 \right\rangle \approx 2\left\langle \frac{u_*^3}{0.4z} \right\rangle^{2/3}, \quad \sigma_V^2 \approx 0.16 \ln\left(\frac{0.3z_i}{X}\right),$$

where z is the height. (These parameterizations assume a neutral atmosphere.)

An example calculation of the MCF and its confidence bounds is shown in Fig. 10. The non-intermittent MCF curve corresponds to $\tilde{\Gamma}\left(\rho, \left\langle \tilde{C}_V^2 \right\rangle\right)$. The lower 5% confidence bound for the MCF is just $\tilde{\Gamma}$ evaluated at the lower 5% bound for $\tilde{C}_V^2$ given above, and likewise for the upper 95% bound. The actual mean MCF is $\left\langle \tilde{\Gamma}\left(\rho, \tilde{C}_V^2\right) \right\rangle$. The computations are for a frequency of 100 Hz, propagation distance 100 m, and inversion height 1000 m. The index-of-refraction variance was 2 x 10^{-5}. The figure shows that the actual mean MCF is not all that different from the MCF calculated using the non-intermittent theory. However, the non-intermittent theory does neglect substantial variability in the MCF. At $\rho/\mathcal{L}$=0.02, for example, coherence varies between approximately 0.2 and 0.95. When the wind is momentarily weak, and hence the wind-shear generated turbulence is momentarily weak, excellent coherence is obtained; a strong gust nearly wipes out the coherence.

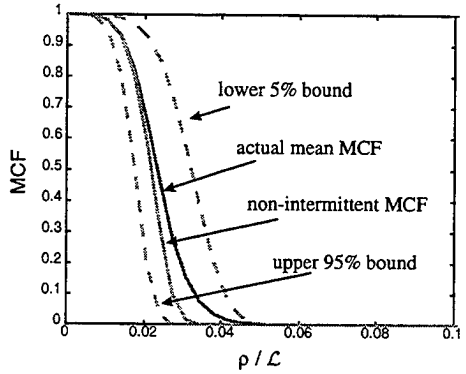


Figure 10. Example calculations of the MCF in intermittent turbulence using the Kolmogorov model.

CRLB calculations, as a function of frequency and propagation distance, are shown in Fig. 11. For these calculations, u_*=0.5 m/s and z=2 m. The SNR was 20 dB and the interelement spacing was 1 m. When the CRLB is plotted in this manner, it is nearly independent of propagation distance near to the source and at low frequency. This is the region where array performance depends mostly on the noise environment. As the frequency and distance are increased, however, the CRLB increases sharply. This is the turbulence effect. The turbulence effect is only minimally significant for momentarily weak winds (the 5% lower bound), but becomes dominant in most cases during a strong gust (the 95% upper bound). At 80 Hz and 1000 m, for example, the CRLB fluctuates between 0.6 and 2 deg. Tracking schemes should be designed to take advantage of this effect, by locking onto the source during the episodes of weak turbulence, and maintaining the track during temporary dropouts due to strong turbulence.

8. Conclusions

When an acoustic array is positioned near to a source, its ability to produce accurate AOA estimates and hence track the source is limited primarily by the noise present. As the distance is increased, however, turbulence takes over as the limiting factor in AOA accuracy. The transition typically occurs at about 100 m for a frequency 100 Hz and SNR 20 dB.

A lack of good, 3D turbulence models hinders accurate predictions of the performance of acoustic arrays. The main modeling difficulty is the anisotropy occurring at large scales. Although imperfect, the von Kármán model

appears to be the best overall choice for now. Gaussian and Kolmogorov models can both be very misleading, since they work well for only certain subranges of the turbulence.

Wind velocity fluctuations caused by near-ground wind shear are almost always the most important source of turbulent degradation in AOA estimates. Significant variation in the intensity of these wind fluctuations occurs as the wind intermittently weakens and gusts. This intermittency can cause the accuracy of the AOA estimates to fluctuate dramatically.

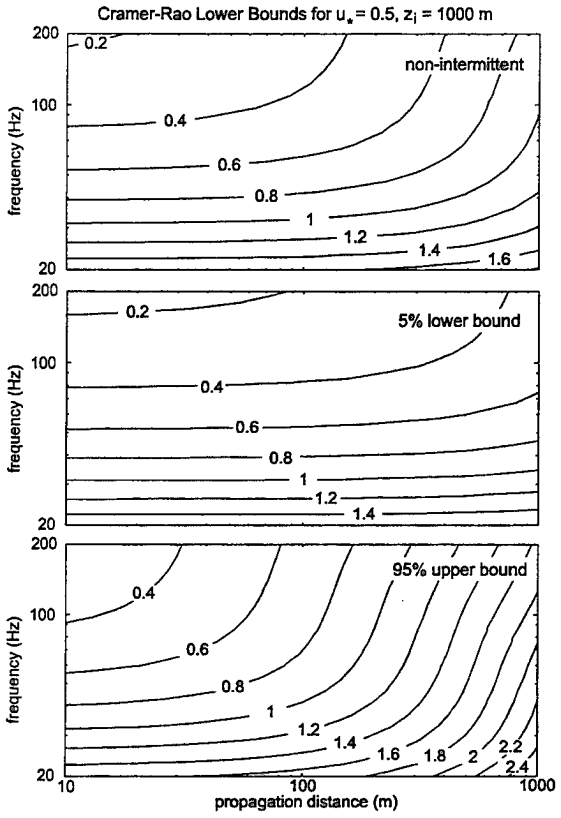


Figure 11. CRLB calculations (in deg) showing the effect of turbulent intermittency. The calculation in the top box is for the non-intermittent case. The middle and bottom boxes are the 5% lower and 95% upper confidence bounds, respectively (i.e., the CRLB fluctuates so that it is between the two bounds 90% of the time).

References

Batchelor, G. K. (1953): *The Theory of Homogeneous Turbulence.* Cambridge University Press, Cambridge, Great Britain.

Gurvich, A. S., and V. P. Kukharets (1986): The influence of intermittence of atmospheric turbulence on the scattering of radio waves. *Sov. J. Comun. Technol. Electron.* **30**, 52–58.

Kolmogorov, A. N. (1962): A refinement of previous hypotheses concerning the local structure of turbulence in a viscous incompressible fluid at high Reynolds number. *J. Fluid Mech.* **13**, 82–85 (1962).

Ostashev, V. E. (1994): Sound propagation and scattering in media with random inhomogeneities of sound speed, density, and medium velocity. *Waves Rand. Med.* **4**, 403–428.

Rytov, S. M., Y. A. Kravtzov, V. I. Tatarskii (1989): *Principles of Statistical Radio Physics, Part 4: Wave Propagation through Random Media.* Springer, Berlin.

Song, B. G., and J. A. Ritcey (1996): Angle of arrival estimation of plane waves propagating in random media. *J. Acoust. Soc. Am.* **99**, 1370–1379.

Tatarskii, V. I., and V. U. Zavorotnyi (1985): Wave propagation in random media with fluctuating turbulence parameters. *J. Opt. Soc. Am. A* **2**, 2069–2076.

Wilson, D. K., and D. W. Thomson (1993): Acoustic propagation through anisotropic, surface-layer turbulence. *J. Acoust. Soc. Am.* **96**, 1080–1095.

Wilson, D. K. (1997a): Turbulence models for wave propagation and scattering calculations. Technical report, U.S. Army Research Laboratory, 2800 Powder Mill Road, Adelphi, MD 20783. (In preparation.)

Wilson, D. K. (1997b): Performance bounds for acoustic angle-of-arrival arrays operating in atmospheric turbulence. Submitted to *J. Acoust. Soc. Am.*

INFLUENCE OF AIRFIELD STRUCTURES AND COMPLEX TERRAIN UPON SIMULATED LOCAL WIND FIELDS

Ronald M. Cionco and John H. Byers
US Army Research Laboratory
Adelphi, Maryland 20783-1155 USA

ABSTRACT

The High Resolution Wind model, HRW, is used to simulate the influence and effects that complex terrain and land morphology features such as airfield structures have on wind fields. Fort Hunter-Liggett airfield is the site selected for this study and the high resolution, terrain elevation data base, PEGASUS, for Fort Hunter-Liggett is used as the digitized terrain input for the model. Structures such as three airfield buildings prescribed for other aspects of the study are defined for model input. Two contrasting sets of meteorological conditions are identified from Fort Hunter-Liggett's data archives. Meteorological fields of wind vectors and wind streamlines are produced by HRW. Both scenarios exhibit a changing wind field over the variable mountainous terrain flanking each side of the valley. Wind fields in the valley's smoother terrain are relatively uniform except in and about the airfield's buildings. An additional analysis is also applied to further quantify and interpret the influence and effects of terrain and structures upon the localized wind fields as well as for applications such as the release of smoke and obscurants for a battlespace environment. Results show that wind fields are readily influenced by structures to cause accelerations and decelerations or change of direction within a few hundred meters downwind. The HRW model clearly detects and responds to the presence of structures on terrain that is also variable in nature.

1. INTRODUCTION

US Army Research Laboratory's (ARL) High Resolution Wind model (Cionco 1985), HRW, is used to simulate the interactions and effects that complex terrain and land morphology features, such as buildings, have on wind fields over an airfield. Fort Hunter-Liggett's airfield in California is the site selected for this study. The high resolution terrain elevation data base, PEGASUS, for Fort Hunter-Liggett is used as the digitized terrain input for the model. Three airfield buildings prescribed for other aspects of the study are defined also for model input. Two contrasting sets of meteorological conditions are identified from Fort Hunter-Liggett's data archives. Meteorological fields of wind vectors and wind streamlines are numerically simulated by HRW. An additional analysis (Cionco and Byers, 1993) is also applied to further quantify

the influence and effects of terrain and structures upon the localized wind fields as well as for numerous applications such as the release of smoke and obscurants. Examples of the simulated wind fields are shown for the full domain and also for the limited area focused and magnified at the airfield site.

2. APPROACH

Several simulation tools are identified and two differing scenarios for analysis are established. The tools to be used are a high-resolution wind flow model/code, digitized terrain elevation, building structure data sets, and meteorological data for model initialization. ARL's HRW code is selected to simulate the desired meteorological fields. Fort Hunter-Liggett airfield is the site selected for this simulation study. The PEGASUS high-resolution, terrain elevation data base is used as the digitized terrain elevation input for the code. Figure 1 shows the terrain as contoured values ranging from 280 m to 420 m. The airfield runway and buildings are also plotted in this figure. The three airfield buildings are shown enlarged in figure 2 where the two hangers and control tower are located northwest of the apron for Scenario A. Note that for Scenario B, the buildings are relocated to the southeast of the apron.



Figure 1. Contoured topography of the 5Km x 5Km Ft. Hunter-Liggett domain including the airfield runway, apron, and buildings.

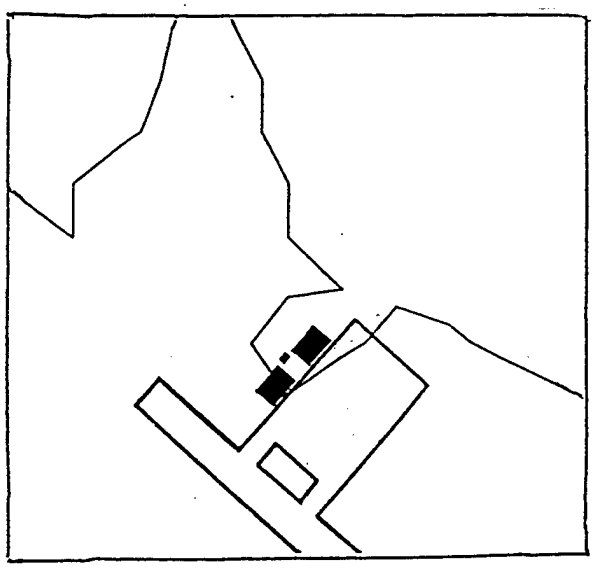


Figure 2. An enlarged image of the airfield apron and buildings for Scenario A. Note that for Scenario B the buildings are located along the southeast edge of the apron.

Two contrasting sets of meteorological conditions are identified from the Fort Hunter-Liggett Meteorological Team's data archives and presented in Table 1.

TABLE 1. METEOROLOGICAL CONDITIONS

VARIABLES:	SCENARIO A	SCENARIO B
WIND SPEED	5.0 M/S	2.7 M/S
DIRECTION	137.5^0	311.5^0
TURBULENCE	MODERATE	LOW
STABILITY	UNSTABLE	STABLE
SUN ANGLE	HIGH	LOW

Scenario A is a late morning condition with a high sun angle and slightly unstable atmosphere with a wind speed of 5.0 m/s from the southeast (up valley) and higher turbulence levels. Scenario B is prescribed to be for a stable atmosphere just at sunrise with a low sun angle and a wind speed of 2.7 m/s from the northwest (down valley) and lower turbulence levels. Both scenarios are for the same day.

3. THE SIMULATION MODEL

Two models are available at the US ARL, to analyze flow fields over complex terrain and land morphology features. They are (1) the High-Resolution Wind Model, HRW, and (2) the Canopy-Coupled to the Surface Layer Model, C-CSL (Cionco, 1985). The High Resolution Wind Model, HRW, is chosen to simulate the influence and effects complex terrain and morphology features (buildings) have on wind fields. These simulations are also used for the terrain effects analysis described herein.

3.1 The wind model

HRW is a two-dimensional, diagnostic, time independent model that simulates the wind flow over a grided area of 5 km by 5 km with a preferred spacial resolution of 100 meters. The computational domain size can range from 2 km by 2 km to 20 km by 20 km with grid resolutions of 40 meters to 400 meters respectively. The thickness of the computational layer is defined as 1/10th the magnitude of the grid size.

Beginning with initial uniform wind and temperature fields, the simulation results are obtained by a direct variational relaxation of the wind and temperature fields in the surface layer. The solution is reached when the internal constraint forces imposed by the warped terrain surface, thermal structure and the requirement for flow continuity are minimized. The procedure makes use of Gauss' Principle of Least Constraints (Lanczos, 1962) which requires these forces to be minimized in order to satisfy the equations of motion. When applied to the surface layer, this

procedure also requires the use of empirical wind and temperature profiles.

3.1.1 Input data

For the application described herein, an area of 5 km by 5 km with a grid size of 100 meters is used for the two simulation cases. Terrain elevation is required at 100 meter intervals in x and y coordinates for the entire area of interest. Land morphology feature information such as building structures can also be used as input in a digital format. The initialization of the model requires, as a minimum: wind speed and direction, temperature, and pressure from one local surface station at the 10 m level and one upper air sounding of temperature and pressure-height profiles to estimate the atmospheric stability (buoyancy) of the domain. Note that data from only one site are used to start the simulation. Similar data from additional soundings and surface stations can also be used for initialization.

3.1.2 Simulated data fields

The resulting output is in the form of listings and binary random access archive files containing simulated values for the wind and other meteorological parameters. Simulated x,y fields of the u and v wind components and their vector field, streamline flow, potential temperature, friction velocity, the power law exponent, and Richardson's Number are computed. Scenario A's simulated vector field and streamline flow field are shown in figures 3 and 4. For the full domain, vector magnitudes, in general, range from 4.5 to 5.5 m/s except in the mountainous areas and immediately over the airfield structures noted as white areas (i.e., no vector is plotted) where speeds are accelerating 110 to 150% of the input velocity (5.0 m/s) in figure 3. Directionally, the streamlines show changes in figure 4 throughout the domain, but most notably in the mountainous areas and a slow sweeping change upvalley. The simulated vector field and streamline flow field for Scenario B are presented in figures 5 and 6. In general, more areas of accelerating speeds are occurring noted again by the 'white' areas over the mountainous areas, along the terrain contours, and above the buildings in figure 5. Locations of greatest acceleration are generated in the midst of the heavily-contoured terrain northeast and southwest of the valley. Streamline patterns show changes everywhere in figure 6 with areas of convergence and divergence and a distinct directional response to the presence of the airfield structures.

3.2 Adverse impact analysis

Our terrain effects analysis method (Cionc and Byers, 1993) provides a means to interpret the meteorological output from HRW for a customized usage and assessment. The method uses the microscale wind flow model output and a visualization technique. The method provides a simple means for quick and easy quantification of the wind effects and identifying those areas that may be adversely or favorably affected by or impacted upon during your field activities. An appropriate set of criteria for the activity being analyzed is applied to these simulated fields such as wind to determine the degree that these terrain effects may or may not impact on your field operations. Each type of operation, study, or experiment has its own particular criteria that you, the user, must establish.

The method involves analyzing the newly simulated field in comparison to the initialized field:

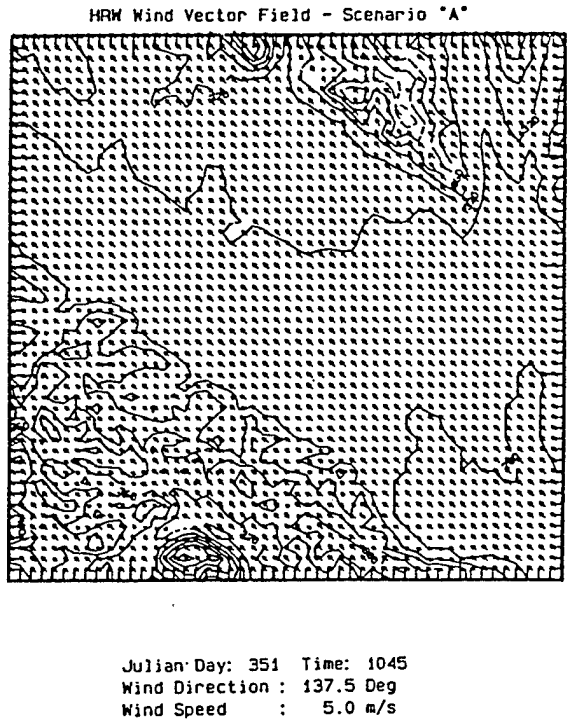


Figure 3. The simulated field of wind vectors for Scenario A (upslope flow)

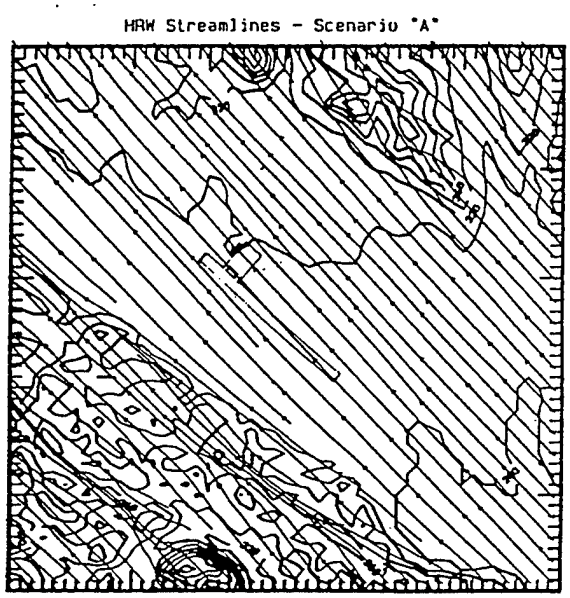


Figure 4. Streamline field of wind flow for Scenario A.

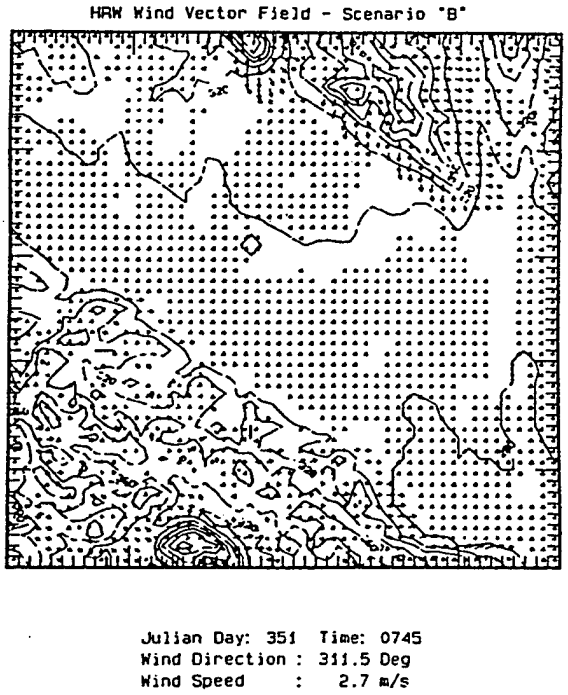


Figure 5. The simulated field of wind vectors for Scenario B (downslope flow)

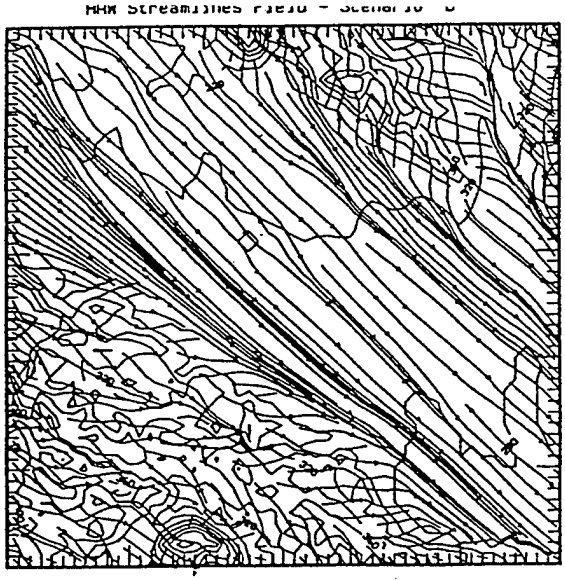


Figure 6. Streamline field of the simulated wind flow for Scenario B.

EFFECT = FINAL SIMULATED FIELD - INITIAL FIELD

More specifically, the wind speed effect and the wind direction effect are determined separately, first. The Wind speed Effect (E_{ws}) is the difference between the values for the final simulated wind speed field (S_s) and the initial wind speed field (S_i):

$$E_{ws} = S_s - S_i$$

The Wind Direction Effect (E_{wd}) is the difference between the values for the final simulated wind direction field (D_s) and the initial wind direction field (D_i):

$$E_{wd} = D_s - S_i$$

A qualitative assessment of the Total EFFECT can be made, first, by combining the effects of the two difference fields. To quantify these effects, a set of appropriate operational criteria is established for the phenomena under study or test. Three levels of EFFECT are defined for aerosol diffusion studies and field experiments: Light, Moderate, and Severe.

The results can be visualized by next constructing color-coded maps (not provided herein) showing the degree of the wind effects. The effect/ impact can then be quickly and easily assessed when the terrain features, vector or streamline field of the domain are added to these maps. Examples of terrain and structures effects analyses are given for Scenario A in figure 7 and Scenario B in figure 8 as derived from simulated high-resolution wind fields. Both speed and directional effects are shown here. Although the gray scale rendition of the original color-coded figures is marginal, one can discern the areas of light, moderate, and severe impacts for speed and direction as dark, white, and heavy black boxes and no hatching (no symbol), hatching, and cross-hatching areas respectively. For Scenario A in Figure 7, the analysis field generally exhibits a light impact whereas the white areas indicate a moderate impact and the heavy black boxes within the white areas are severe impact locations. The hatch patterns denote areas of moderate directional impact. For Scenario B in figure 8, the valley is now a light to moderate impact area and the mountainous slopes are producing moderate to severe adverse terrain effects upon both speed and direction.

4. RESULTS

Zooming in to a 1 Km by 1 Km area to inspect the building's effects upon the flow, we note that HRW is capable of detecting and responding to the presence of structures positioned on the smoother valley floor. In the vicinity of the buildings, Scenario A shows changes in wind speed with only minor directional changes in figure 9 and Scenario B exhibits both wind speed acceleration and direction changes in figure 10. Recall that the white areas are for vectors depicting notable accelerations. The adverse impact analysis readily depicts increased interactions and building effects in figures 11 and 12. The impact of the buildings for Scenario A (figure 11) is moderate (white areas) for wind speed accelerations, but only light (no hatching pattern) for directional changes. For Scenario B in figure 12, the impact of the buildings is notably moderate for both wind speed (white areas) and direction (hatching pattern).

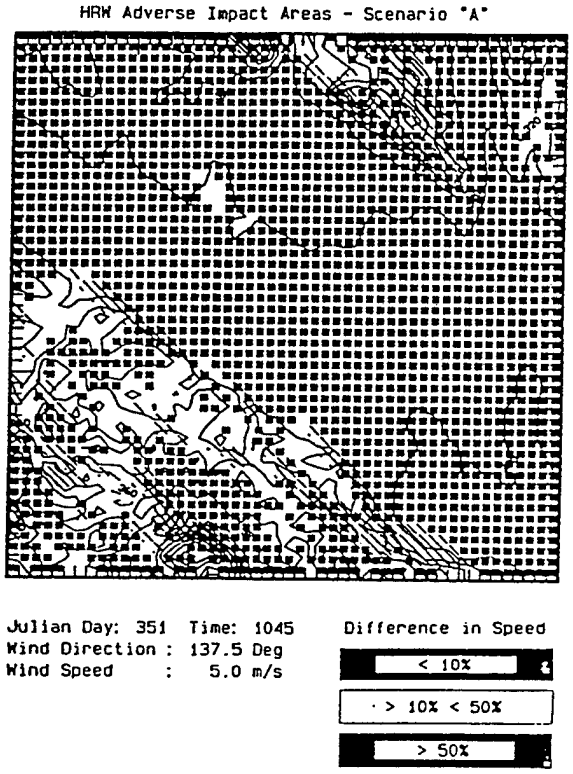


Figure 7. Terrain effects analysis depicting areas of adverse impact for Scenario A.

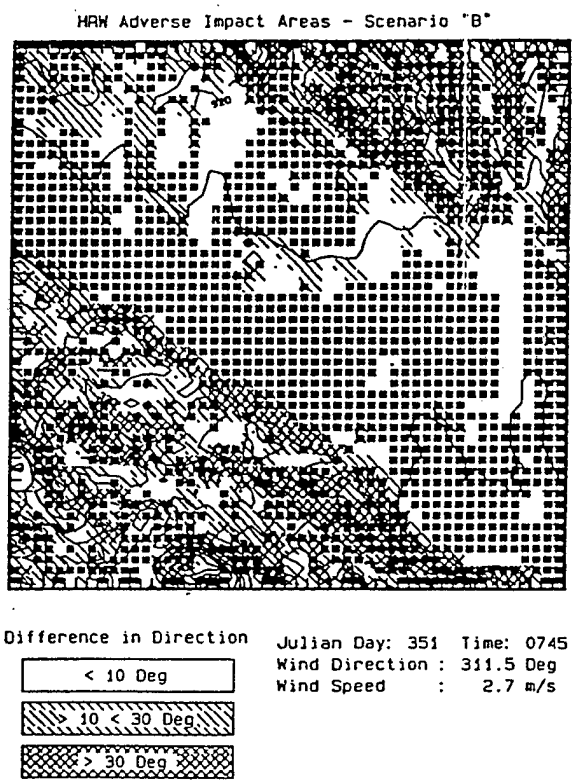


Figure 8. Terrain effects analysis depicting areas of adverse impact for Scenario B.

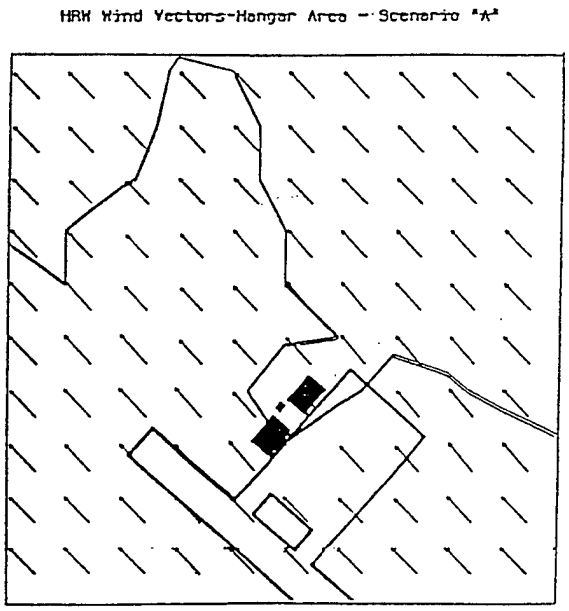


Figure 9. Close-up, localized view of the simulated vector field in and about the airfield for Scenario A.

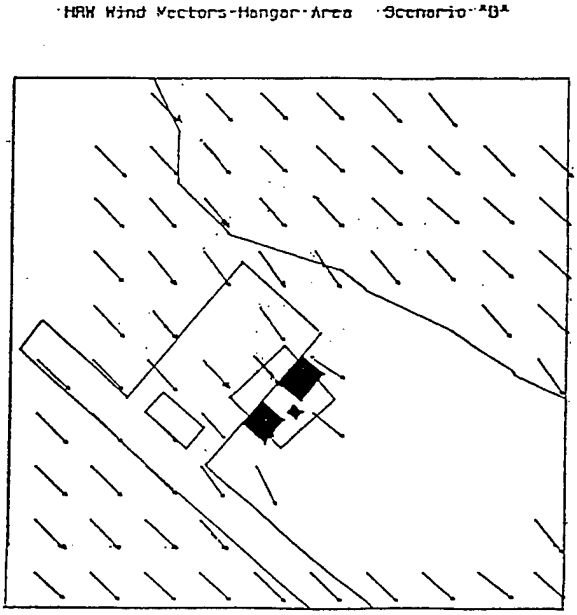


Figure 10. Close-up, localized view of the simulated vector field in and about the airfield for Scenario B.

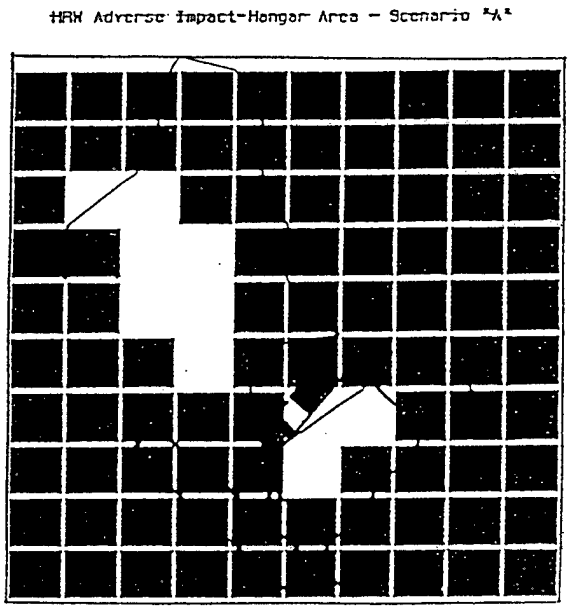


Figure 11. Close-up, localized view of the building effects for Scenario A.

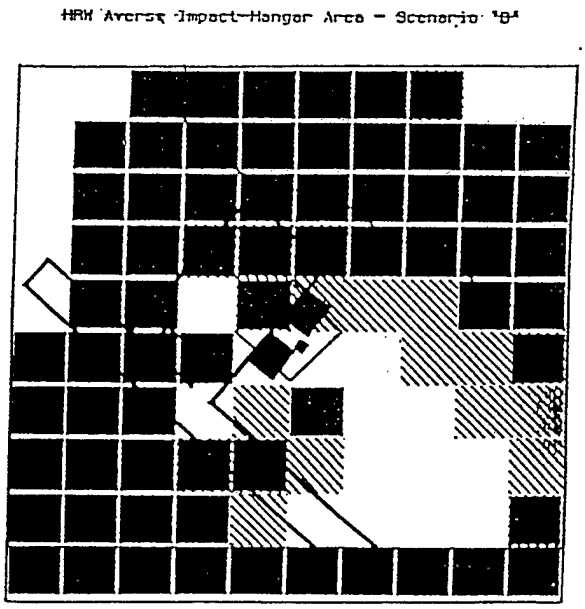


Figure 12. Close-up, localized view of the building effects for Scenario B.

5. CONCLUSIONS

The HRW model clearly detects and responds to the presence of structures in a terrain domain that is also variable in nature. For the full domain, both scenarios exhibit a changing wind field over the variable mountainous terrain flanking each side of the valley. Wind fields in the valley's smoother terrain are relatively uniform except in and about the airfield's buildings. A closer look at Scenario A shows that simulations produce both terrain and building influences and effects on wind speed and direction. Scenario B with the lower speed regime shows a greater degree of influence and effect particularly in and about the buildings than did the Scenario A simulations.

An additional analysis is also applied to further quantify the influence and effects of terrain and structures upon the localized wind fields for applications such as the release of smoke and obscurants. Results of the adverse impact analysis also show that both adverse and favorable impact areas are readily identified as speed or direction changes within a few hundred meters downwind of structures and terrain features. A release of smoke and obscurants in these two contrasting scenarios clearly will be influenced and affected by the interaction with both variable terrain and airfield structures.

ACKNOWLEDGEMENT

This research and participation in a showcase study was partially funded by the Joint Program Office for Special Technology Countermeasures at the Naval Surface Warfare Center, Dahlgren, VA.

REFERENCES

1. Cionco, R. M., (1985): Modeling Wind Fields and Surface Layer Profile over Complex Terrain and Within Vegetative Canopies, The Forest-Atmosphere Interaction, Editors: B. A. Hutchison and B. B. Hicks, D. Reidel Publishing Co., Holland.

2. Lanczos, C., 1962: The Variational Principles of Mechanics. (2nd edition), The University of Toronto Press, Toronto, Canada.

3. Cionco, R. M. and J. H. Byers, 1993: On Analyzing Wind Effects That May Impact Adversely Upon CB/Obscuration Activities. Proceedings of the 1993 CB Modeling and Simulation Conference, US Army Edgewood Research, Development, and Engineering Center, MD.

WIND VELOCITY AND AEROSOL BACKSCATTER MEASURED BY CO_2 DOPPLER LIDAR

John R. Roadcap*, Robert A. Swirbalus, and Mitchell H. Laird
Phillips Laboratory, Geophysics Directorate Hanscom AFB, Massachusetts

Patrick J. McNicholl and David L. A. Rall
PhotoMetrics, Inc. Woburn, Massachusetts

1. INTRODUCTION

The real-time detailed vertical structure of wind velocity is of great interest to Air Force operations such as precision cargo drops and high altitude bomb delivery. Aerosols, clouds, and precipitation can also greatly affect the performance of optical sensors and weapons systems -- both passive and active -- from the visual through the long-wave infrared region.

To better understand the factors involved in real-time measurement of range-resolved wind velocity and aerosol backscatter under various atmospheric conditions, the Phillips Laboratory's Geophysics Directorate developed and fielded a ground-based eye-safe CO_2 Doppler lidar. The lidar has provided wind and aerosol backscatter profiles in support of several Department of Defense field programs including ballistic wind determination, high altitude cargo drops, post-detonation cloud tracking and diffusion, and high resolution ground-to-space imaging.

2. LIDAR DESCRIPTION

The Geophysics CO_2 Doppler lidar is a transportable pulsed heterodyne lidar system operating at a wavelength of approximately 10.6 μm. The laser lines are generated by Transverse Excited Atmospheric (TEA) CO_2 electric discharge lasers using an 80% mixture of buffer gases (He and N_2) with the CO_2. The laser output energy is about 60 mJ (60 x 10^{-3} Joules) with a pulse repetition frequency of 60 Hz. The laser scanning mirror possesses a hemispherical field-of-view. The range gates along the laser line-of-sight are approximately 150 meters. Characteristics of the CO_2 Doppler lidar are listed in Table I. In addition to measurement of the range-resolved

Phillips Laboratory CO_2 Doppler Lidar	
Wavelength	10.6 μm
Pulse Energy	60-100 x 10^{-3} Joules (mJ)
Pulse Rep. Frequency	10-100 s^{-1} (Hz)
Pulse Length	~ 1 x 10^{-6} s (μsec)
Range Gate Length	150 m
Laser	TEA Electric Discharge
Gas	CO_2 with 80% mixture of N_2 and He Buffer Gases
Telescope	30 cm Mersenne
Scanner	Hemispherical
Processor	Programmable DSP Array

Table 1. CO_2 Doppler lidar characteristics

radial wind component, the lidar also measures relative aerosol backscatter which can be used to determine the location of aerosols and clouds. As an example, a time-height cross-section of relative backscatter measured at

* *Corresponding author address*: Lt Col John R. Roadcap, USAF, PL/GPOL, 29 Randolph Road, Hanscom AFB, Massachusetts 01731-3010 DSN 478-3016 fax: DSN 478-3661 e-mail: roadcap@plh.af.mil

Hanscom AFB by CO_2 Doppler lidar is shown in Figure 1. Regions of enhanced backscatter for this particular period were found near the atmospheric boundary layer below 1.5 km (AGL), within a relatively thick cirrus layer between 6 and 7 km, and in a thinner cirrus layer between 10 and 12 km.

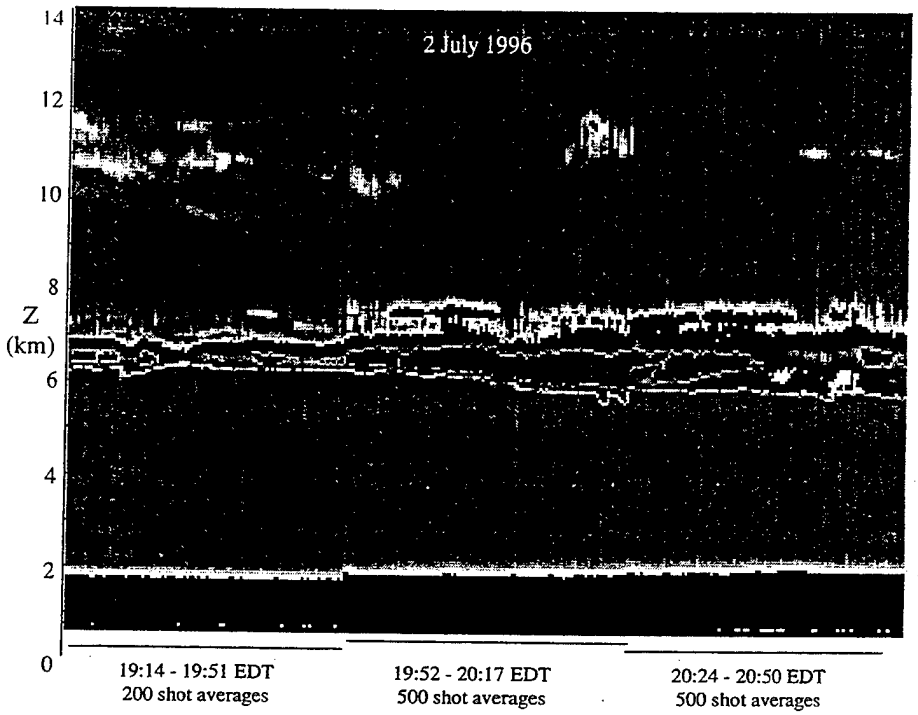


Figure 1. Time-height cross-section of relative backscatter measured by CO_2 heterodyne lidar at Hanscom AFB, Massachusetts on 2 July 1996

3. WIND VELOCITY DETERMINATION

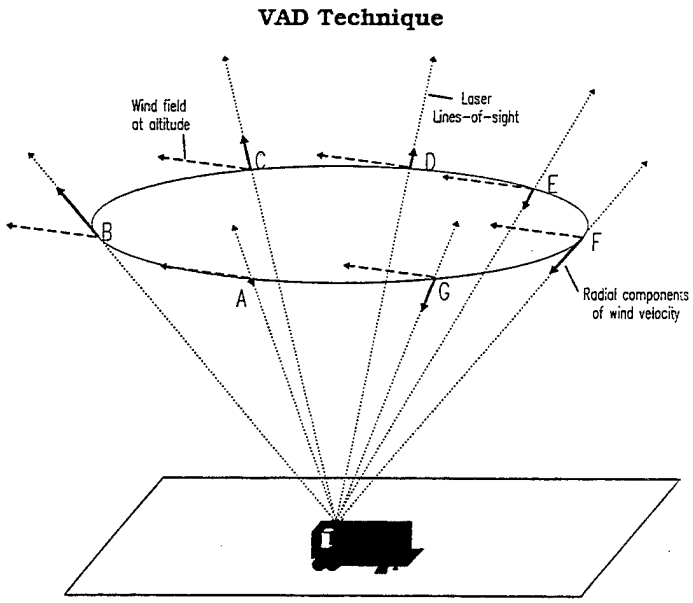


Figure 2. The Velocity-Azimuth Display (VAD) technique uses harmonic analysis of radial velocity as a function of azimuth angle to determine horizontal wind velocity

Because the Doppler lidar scanner possesses a hemispherical field-of-view and relies on ambient background aerosols for backscatter, the kinematic properties of the wind field in clear air (given sufficient backscatter) above the lidar can readily be determined under conditions where the wind field is homogeneous. The method used is the Velocity-Azimuth Display (VAD) technique (see Figure 2) which involves scanning the lidar about a vertical axis at a fixed elevation angle (Browning and Wexler, 1968). VAD curves of radial velocity as a function of azimuth angle are then constructed for each range gate. From the VAD curve coefficients, the horizontal wind vector and its kinematic properties can be computed at each range bin, and thus for a non-zero elevation angle scan, each altitude level.

Normally, at least 16 points or directions are used to construct each VAD scan consisting usually of 1000 laser shots per direction. The use of 16 points to construct the VAD curve is necessary to adequately represent the VAD curve such that measurement error is minimized consistent with the available backscatter. Figure 3 illustrates both the azimuthal and range distribution of radial velocity (part a.) and the construction of VAD curves for several range gates (part b) using 16 points. Alternating low (≤ 5 deg.) and high (~ 30 deg.) elevation angle scans are used to determine low level (near surface to 500 m) and higher level (200 m to 4 km) profiles of horizontal wind. A period of approximately five minutes is required to complete each scan.

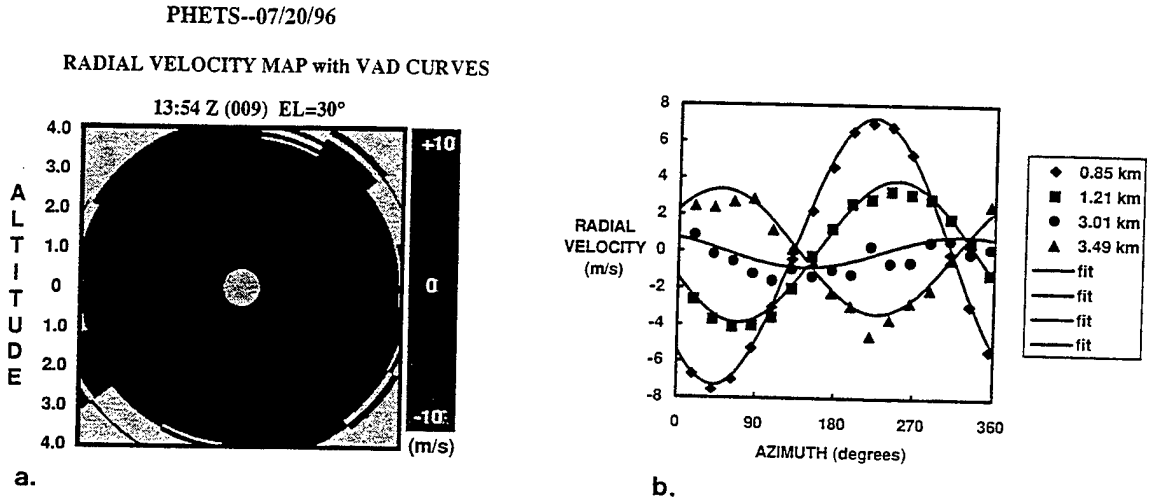


Figure 3. Construction of VAD curves for different range gates at 30 degree elevation angle. New Mexico, 20 July 1996

4. MEASUREMENT ACCURACY

The algorithm used to extract radial velocity from the Power Spectral Density (PSD) -- the square of the Fast Fourier Transform of the lidar pulse returns -- consists of two parts. The first is a search algorithm used to identify and locate the signal spectral feature in the PSD. Then, a centroid algorithm finds the central moment of the feature in some interval about this location. For example, the simplest and most often-used process seeks a maximum in the PSD and then calculates the centroid over a specified number of frequency intervals about this maximum.

In this two-step algorithm, there are two easily distinguishable Signal-to-Noise ratio (SNR) regimes. The SNR is defined here as the ratio of the sum of the signal over the centroid interval to the expected RMS variation of the corresponding sum of the noise power baseline. At sufficiently high SNR, the extraction accuracy is limited by the centroid analysis -- i.e., by the ability to determine the center frequency of a well-defined but noisy feature. As the SNR decreases, a point is reached where the search algorithm identification of the signal spectral feature becomes increasingly suspect. Below this SNR, the velocity measurement error can drastically increase. A typical velocity measurement error for sufficiently high SNR is ≤ 1 m/s.

Yuma, Arizona (Times MST)	Top (km-AGL)	Starfire Range, N.M. (Times MDT)	Top (km-AGL)
6 March 1034	5.8	15 October 2315	2.5
7 March 1529	7.3	16 October 1950	4.5
8 March 1444	5.2	17 October 2138	2.5
8 March 1450	5.5	18 October 1928	2.5
9 March 1111	4.9	22 October 1420	1.5
9 March 1136	5.8	24 October 0120	2.5
9 March 1152	5.8	25 October 0053	3.0

Table 2. Apparent aerosol wind layer tops determined from CO_2 Doppler lidar during 1996

The RMS VAD deviation has two components: (1) a SNR-dependent part indicative of velocity extraction errors as discussed above, and (2) a SNR-independent part indicative of the atmospheric wind field deviations in the sampled volume from the homogeneous and horizontal model. With typical 16 azimuth point VAD scans and using prior knowledge gained from preceding VAD scans, we have found that reliable velocity extraction can be extended down to SNRs on the order of 4. Using this SNR threshold, in the absence of clouds, the upper height for wind velocity retrieval can vary widely depending on location and weather conditions. Table 2 illustrates examples of daily variation in upper height limit for wind retrieval by the CO_2 Doppler lidar associated with the rapid decrease in aerosol density above the surface.

5. MEASUREMENT RESULTS

5.1 *Synoptic Weather Overview*

Two recent series of observations have been selected to illustrate the CO_2 Doppler lidar measurement capability. The first set was taken in March 1996 near Yuma, Arizona where the dry stable troposphere was in general dominated by broad high pressure (see Figure 4). On the 6 of March, a strong, dry cold front ahead of a high pressure system centered over northern Nevada had just passed through the observation area. On 9 March, a west-

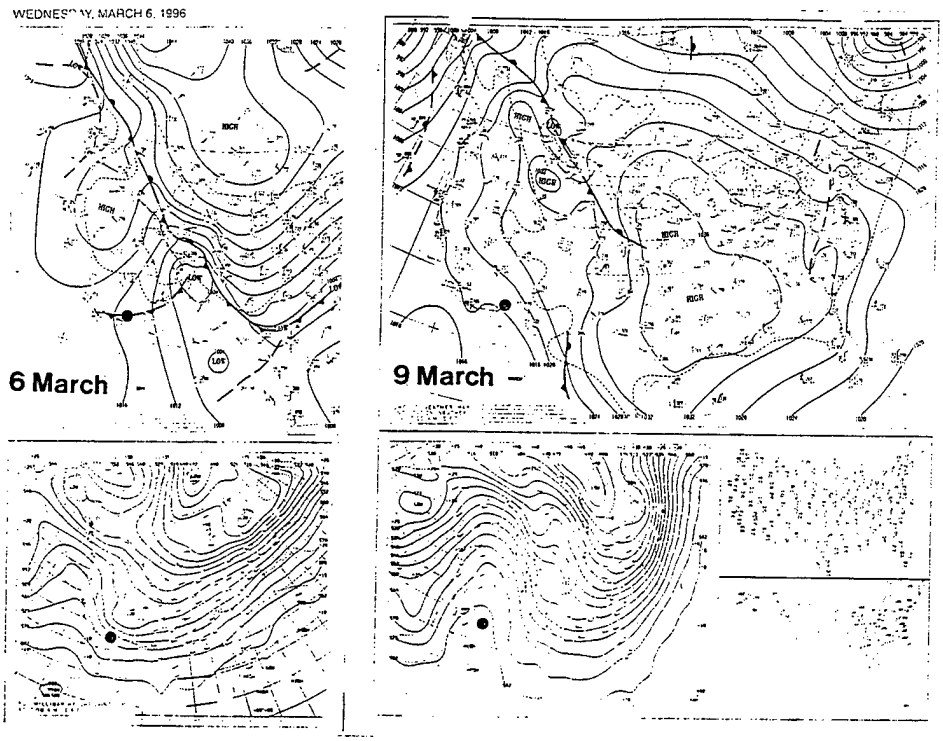


Figure 4. Surface and 500 mb. analyses for 12 GMT on 6 and 9 March 1996. "•" marks lidar observation site

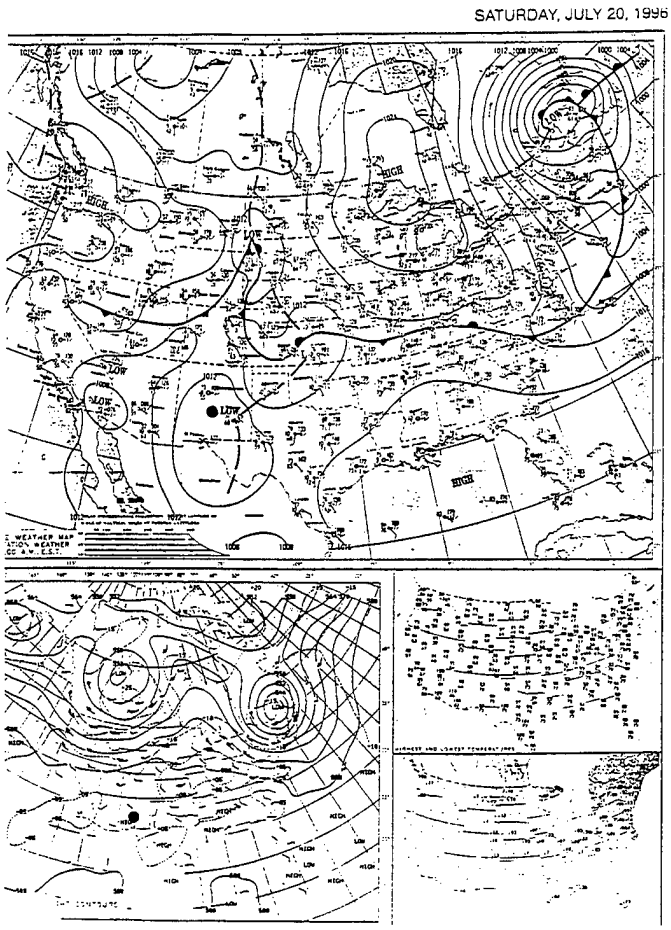


Figure 5. Surface and 500 mb. analysis for 12 GMT on 20 July 1996. "•" marks lidar observation site.

east sea level pressure gradient across southern Arizona was induced by an Arctic high centered over the Great Plains. Persistent thin cirrus associated with the subtropical jet stream was present during both days. The other set of observations was made during July 1996 in the Jornado Del Muerto region of New Mexico about 40 miles southeast of Socorro. The New Mexico observations occurred during the relatively moist summer season typically characterized by strong diurnal forcing with clear mornings and scattered afternoon thunderstorms. The sea level pressure gradient was very weak over this region (Figure 5).

5.2 *Arizona March Observations*

Two lidar measurement profiles of wind velocity and SNR from 6 and 9 March 1996 are shown in Figures 6 and 7 respectively. For 6 March, lidar observations show low level northwesterly flow between 5000 ft. and 10000 ft. AGL. A steady wind speed increase with height is also evident accompanied by strong backing above 10,000 ft. The SNR profile shows a sharp decrease with height such that the SNR threshold for useable radial velocity was being approached by 10,000 ft. Between 18,000 and 39,000 ft., the SNR values were too low (SNR <1.0) to accurately compute radial velocity. Thus, the small SNR prevents the determination of horizontal wind velocity using the VAD technique. Above 39,000 ft., sufficient backscatter from thin cirrus allowed determination of wind velocity to at least 43,000 ft. On 9 March, a low level easterly jet (which was also quite dry relative to the adjacent layers) was established below 5,000 ft. Above this level, wind speeds decreased up to 15,000 ft. where the flow became northwesterly. Most striking, however, are the much higher SNR values below 15,000 ft. when compared with the 6 March observations. Also, due to an invading thicker but lower cirrus layer, wind retrievals were possible up to 35,000 ft. except for a 5000 ft. layer of relatively low SNR just above 19000 ft. AGL.

Post Cold Front Passage -- Surface High over Nevada

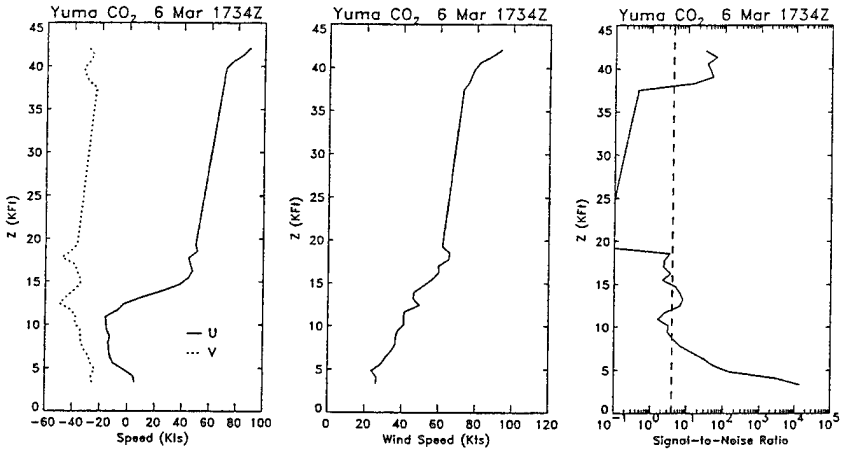


Figure 6. Wind velocity and Signal-to-Noise ratio vertical profiles for Yuma at 1734 GMT on 6 March.

Arctic High Over Plains -- Sharp Ridge Aloft

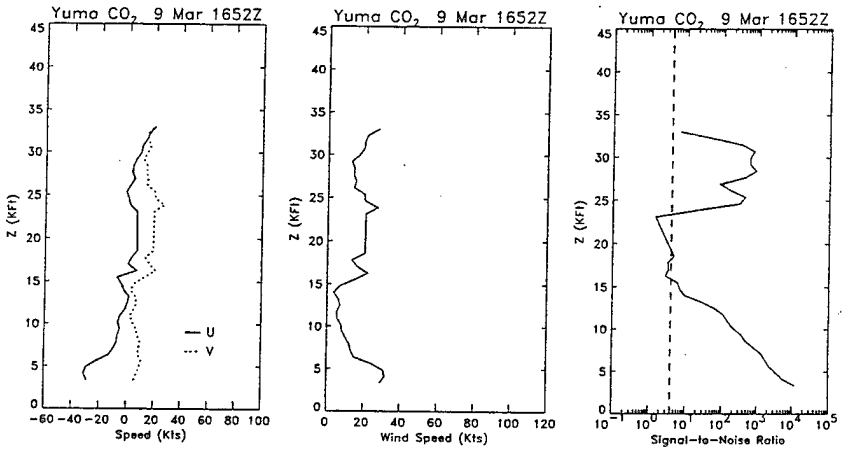


Figure 7. Wind velocity and Signal-to-Noise ratio vertical profiles for Yuma at 1652 GMT on 9 March.

5.2 *New Mexico July Observations*

A set of morning and afternoon VAD wind observations in and just above the boundary layer was made on 20 July 1996 in the Jornado Del Muerto region of south central New Mexico. These illustrate the Doppler lidar's ability to measure the rapidly changing wind profile as the boundary layer is modified both by insolation and afternoon thunderstorm activity. On the morning of 20 July, southern New Mexico was dominated by weak low pressure at the surface and weak high pressure aloft (see Figure 5). Skies remained clear overnight favoring radiational cooling of the boundary layer. The morning VAD wind profiles clearly show the evolution and decay of a low level jet (LLJ) centered near 800 m AGL (Figure 8). The LLJ is directed from SW-NE with a peak core speed of 16 knots. Above its core, the winds veer gradually to a NE direction by ~ 3.5 km AGL. By 1630 GMT, the jet core rises to about 1 km and the peak speed is reduced to about 8 knots. A secondary wind maximum (NW direction) is located just below 2 km with a peak speed half that of the low level jet.

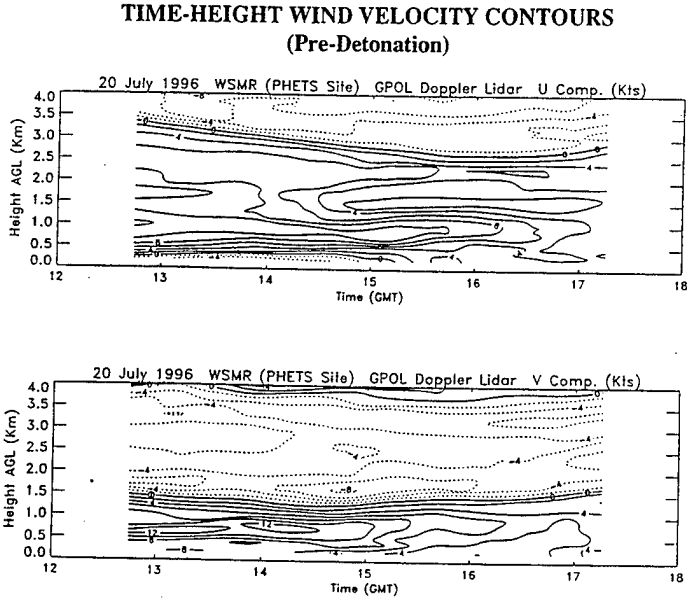


Figure 8. Time-height wind velocity structure measured by CO_2 Doppler lidar on morning of 20 July 1996.

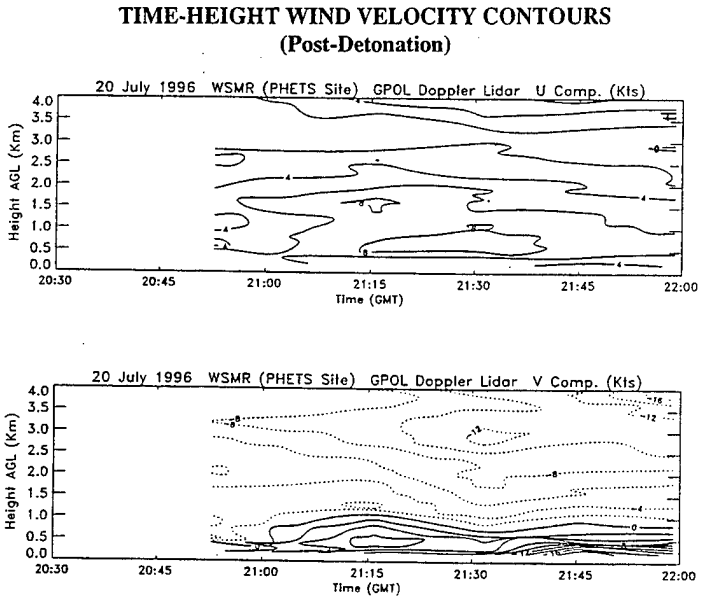


Figure 9. Time-height wind velocity structure measured by CO_2 Doppler lidar on afternoon of 20 July 1996.

The afternoon VAD wind profiles from 20 July are shown in Figure 9. They indicate a steady SW flow below 800 meters with wind speeds exceeding 18 knots near the surface by 2145 GMT. Above 800 m, winds of 8 knots from the NW were observed. The surge in the very low level surface flow just before 2145 GMT is caused by thunderstorm activity located south of the lidar site. Interestingly, a strong northerly surge of greater than 16 knots is observed near 4 km AGL prior to 2200 GMT. The sharp reversal of wind direction with height is evident also from a comparison of the 5 degree and 30 degree Plan Position Indicator (PPI) scans (not shown). Lidar observations terminated shortly after 2213 GMT.

VAD curves for 20 July (not shown) depict the transformation of the horizontal wind field from a smooth homogeneous structure prior to the decay of the low level jet to a broken inconsistent structure. This transformation including the decay of the low level jet is associated with the onset of both shallow convection within the boundary layer and deep convection. This is well illustrated in a comparison of Figure 10 and Figure 11. These figures display profiles of VAD Deviation (RMS VAD Deviation), discussed previously in Section 4, as

Morning Prior to Low Level Jet Decay

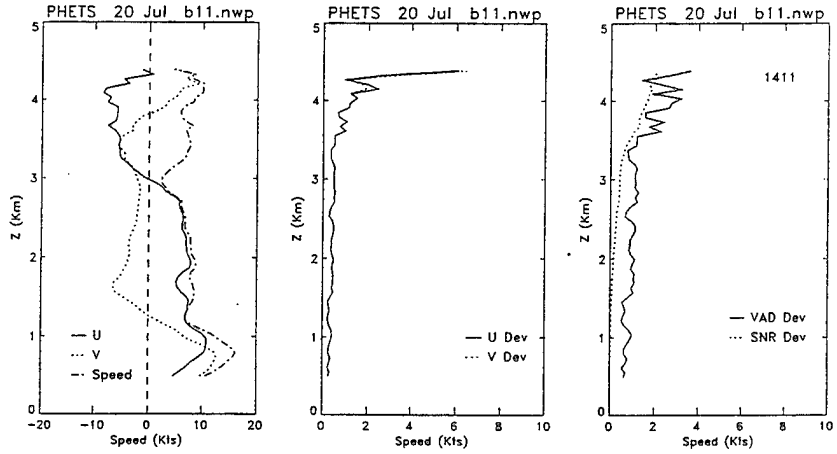


Figure 10. Vertical profiles of wind velocity and RMS VAD Deviation for 20 July at 1411 GMT measured by CO_2 Doppler lidar in south central New Mexico.

Afternoon Scattered Thunderstorms in Area

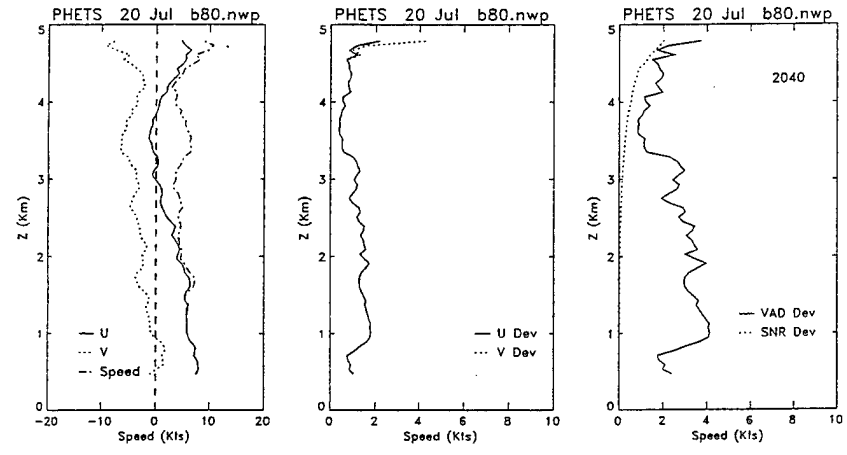


Figure 11. Vertical profiles of wind velocity and RMS VAD Deviation for 20 July at 2040 GMT measured by CO_2 Doppler lidar in south central New Mexico

well as profiles of the associated U and V wind components. In the morning prior to decay of the low level jet (~ 14 GMT), the VAD Deviation profiles are about 1 knot or less in magnitude below 3 km AGL (Figure 10). The increase above 3 km is primarily associated with an increase in the SNR Deviation associated with the rapid decrease in SNR and measurement accuracy of radial velocity. During the afternoon with scattered thunderstorms in the local area, the VAD Deviation increases by a factor of 3 or 4 below 3 km (Figure 11). This large increase is due almost solely to the SNR-independent component which is indicative of deviations in the observed wind field from the horizontally homogenous assumptions of the VAD model.

6. SUMMARY AND CONCLUSIONS

CO_2 Doppler lidar measurements of range-resolved wind velocity and aerosol backscatter were shown for two measurement campaigns in the desert southwest U.S. -- one in the stable desert troposphere of late winter and the second during the moist, convectively unstable summer. Real-time wind velocity profiles in the lower troposphere were determined at about 10 to 15 minute intervals. Signal-to-Noise (SNR) ratios were also measured which estimate the aerosol backscatter profiles. Lidar measurements clearly revealed in both campaigns the distinct nature of the low level jet (LLJ) and, for the Arizona measurements, the presence of persistent cirrus in the upper troposphere. In Arizona, an aerosol "clean zone" of variable but considerable depth imposed significant limits on lidar wind retrieval in the mid-troposphere. Cirrus layers of considerable geometric thickness were observed during the Arizona tests within an altitude range of 25000 ft. - 45000 ft. The Arizona LLJ core exhibited daily variation in speed, direction, altitude, and persistence related to changes in the large scale pressure gradient and low level stability. In the New Mexico observations, the CO_2 Doppler lidar revealed clearly the character of horizontal flow associated with diurnal changes in stability and convective activity.

The CO_2 Doppler lidar observations illustrate some of the capabilities and limitations of an eye-safe ground-based IR heterodyne lidar system. They also emphasize the importance of atmospheric factors in lidar wind sensing. The factors especially important are (1) the vertical distribution of aerosols necessary to provide sufficient backscatter and (2) horizontal flow variability, particularly in the boundary layer, and its relation to convective organization and terrain characteristics. Efforts are underway at the Geophysics Directorate to develop and employ lidar systems which measure wind velocity, absolute backscatter, and water vapor over greater vertical depths including the relatively aerosol-free regions of the middle troposphere.

7. REFERENCES

Browning, K.A. and R. Wexler, 1968: The determination of kinematic properties of a wind field using Doppler radar. *J. Appl. Met.*, **7**, 105-113.

MEASURED PERFORMANCE OF EVAPORATION DUCT MODELS

L.T. Rogers and R.A. Paulus
Propagation Division

NCCOSC RDTE DIV D883
49170 PROPAGATION PATH
SAN DIEGO CA 92152-7385
fax: (619) 553-1417

ph: (619) 553-1413
email: trogers@nosc.mil

ph: (619) 553-1424
email: paulus@nosc.mil

Abstract

Performance measures are applied to data from the NATO Research Study Group 8 propagation experiment Lorient 1989, to evaluate evaporation duct models. The data set consists of slightly-beyond-line-of-sight propagation data and mid-path meteorological data for over 6000 points in time. Evaporation duct profiles are calculated using three well-known evaporation duct models. Propagation estimates at 3.0 and 10.5 GHz are calculated using those evaporation duct profiles as inputs to a parabolic equation model and are compared to measured propagation. Composite accuracy statistics and accuracy statistics conditioned on relevant parameters are computed. Remote sensing techniques are applied to isolate those periods where the evaporative ducting is the dominant mode of propagation and the same accuracy statistics are re-computed for that subset of the data.

The analysis of the data illustrates the following important points: (1) quantitative performance measures can be applied to the evaluation of refractivity assessment systems, (2) the sampling is uniform over time, as is the operational use of refractivity information, and (3) any conditioning of the data is explicitly noted, rule based, and results are compared to statistics where the conditioning has not been applied.

INTRODUCTION

A recent resurgence of interest in bulk meteorological models of the marine atmospheric surface layer with application to the evaporation duct has prompted a re-examination of these models and the meteorological measurements required as inputs. The Integrated Refractive Effects Prediction System (IREPS) was introduced aboard US Navy ships in 1978 utilizing a surface layer model formulated in terms of potential refractivity [*Jeske*, 1971, 1973]. Jeske's algorithm has a simple determination of stability and assumes the empirical universal stability functions follow the KEYPS formula. An empirical modification to this model was subsequently applied to spuriously stable atmospheric conditions arising from thermal distortion due to the ship [*Paulus*, 1985]. This characterization of the evaporation duct has been used in radiowave propagation assessment for the past decade.

Within the meteorological community, a widely accepted bulk formulation for the marine atmospheric surface layer is that of *Liu, Katsaros, and Businger* [1979]. The LKB model is more physically rigorous than the Jeske model with an iterative approach to the determination of stability and uses empirical stability functions for temperature and moisture proportional to the square of the KEYPS formula.

These surface layer models require bulk measurements of air temperature, relative humidity, and wind speed at known heights along with a measurement of sea surface temperature. *Blanc* [1987] found that bulk methods yield a very crude estimate of the true stability influence and questioned how much is really gained by using a stability dependent scheme. Previous propagation studies have found that, for common departures from neutrality, the neutral surface layer refractivity profile is representative of the actual propagation conditions [*Anderson*, 1990]. An analysis of a radio-meteorological data set collected in the Aegean Sea found no statistically significant stability effects in comparing propagation predictions to measured signals [*Paulus*, 1994]. The results of these latter two studies could be argued to represent only open ocean conditions and not be applicable to coastal regions where onshore/offshore winds and strong horizontal gradients in meteorological and oceanographic parameters may significantly impact stability of the surface layer.

This paper provides a brief overview of three bulk meteorological formulations for refractivity in the

surface layer and analyzes the Lorient 1989 radiometeorlogical data set, taken in a coastal environment, using these three formulations as the refractive input to a propagation model.

EVAPORATION DUCT MODELS

A general expression for the gradient of a conservative scalar, S, in the atmospheric surface layer is [*Panofsky and Dutton*, 1984]

$$\frac{\partial S}{\partial z} = \frac{S_*}{\kappa z}\varphi_s\left(\frac{z}{L}\right) \qquad (1)$$

where z is altitude, S_* is the scaling parameter for the scalar, κ is von Karman's constant, L is the Monin-Obukhov length, and φ_S is an empirical stability function for the scalar. Eqn (1) can be integrated from a lower limit of $z=z_0$ to become:

$$S(z) - S_0 = \frac{S_*}{\kappa}\left[\ln\frac{z}{z_0} - \psi_s\left(\frac{z}{L}\right)\right] \qquad (2)$$

where z_0 is the roughness length for the scalar, S_0 is the value of the scalar at altitude z_0, and ψ_S is the integral of the φ_S stability function. S_0, S_*, z_0, and L are determined from bulk meteorological data at two levels in the surface layer.

Jeske/Paulus. *Jeske's* [1971, 1973] approach was to use potential refractivity, N_p, as the conservative scalar such that eqn (1) becomes

$$\frac{\partial N_p}{\partial z} = \frac{N_{p*}}{\kappa z}\varphi\left(\frac{z}{L}\right) \qquad (3)$$

Jeske further determined a characteristic height called the evaporation duct height, δ, the height at which $\partial N_p/\partial z$ = -0.13 m^{-1}, the gradient of potential refractivity at which trapping just occurs. Substituting these into eqn (3) yields:

$$-0.13 = \frac{N_{p*}}{\kappa\delta}\varphi\left(\frac{\delta}{L}\right) \qquad (4)$$

From eqn (2), in terms of potential refractivity, N_{p*} can be determined from observations of potential refractivity at heights z_1 and z_0:

$$N_{p*} = \kappa\frac{N_p(z_1) - N_p(z_0)}{\ln\left(\frac{z_1}{z_0}\right) - \psi\left(\frac{z_1}{L}\right)} \qquad (5)$$

where potential refractivity is calculated from

$$N_p = \frac{77.6P_0}{\theta} + 3.73\times10^5\frac{e_p}{\theta^2} \qquad (6)$$

Here, P_0 is a reference pressure (usually 1000 mb), θ is potential temperature in Kelvins, and e_p is potential vapor pressure in mb. Solving eqn (4) for N_{p*} and substituting into equation (3) yields

$$\frac{\partial N_p}{\partial z} = -0.13\frac{\delta}{z\varphi\left(\frac{\delta}{L}\right)}\varphi\left(\frac{z}{L}\right) \qquad (7)$$

Using the relation between potential refractivity and modified refractivity $\partial N_p/\partial z = \partial M/\partial z$ -0.13 [*Gossard and Strauch*, 1983] in eqn (7) and integrating from $z=z_0$ to z,

$$M(z) = M_0 + 0.13z - 0.13\frac{\delta}{\varphi\left(\frac{\delta}{L}\right)}\left[\ln\frac{z}{z_0} - \psi\left(\frac{z}{L}\right)\right] \qquad (8)$$

The stability-dependent functions φ and ψ are defined in *Jeske* [1971, 1973]. This model was modified by an empirical correction for spuriously stable conditions [*Paulus*, 1985]

The concept of evaporation duct height has been extremely useful in parametric propagation studies and in development of evaporation duct climatologies. Note in eqn (5) that N_{p*} is proportional to the difference between potential refractivity at the reference height and the surface. Most of the time over the ocean, this difference is negative and thus evaporation duct height calculated in eqn (4) will be positive. However, under certain meteorological conditions that cause subrefraction, the difference in potential refractivity between the reference height and the surface will be positive and a negative duct height will be calculated. The physical interpretation of this negative height is that its absolute value is the height where $\partial N_p/\partial z$ = +0.13 m^{-1} or in terms of modified refractivity $\partial M/\partial z$ = +0.26 m^{-1}. Since subrefraction is conventionally defined as M-gradients exceeding 0.157 m^{-1}, a negative evaporation duct height generates a subrefractive profile. *Jeske* [1973] referred to this situation as an "anti-duct".

LKB. The LKB approach [*Liu et al.*, 1979] uses potential temperature, θ, and specific humidity, Q, as conservative scalars yielding profiles:

$$\theta - \theta_0 = \frac{\theta_*}{\kappa}\left[\ln\frac{z}{z_T} - \psi_T\right]$$
$$Q - Q_0 = \frac{Q_*}{\kappa}\left[\ln\frac{z}{z_Q} - \psi_Q\right] \qquad (9)$$

From the profiles of eqn (9), the profile of modified refractivity is calculated:

$$M(z) = \frac{77.6P}{T} + \frac{3.73\times10^5 e}{T^2} + 0.157z \qquad (10)$$

and duct height is determined by inspection of the profile for the height at which the minimum M occurs.

Neutral. The neutral evaporation duct model derives from eqns (3)-(8) by assuming neutral stability of the surface layer for which the empirical stability-dependent functions $\varphi \rightarrow 1$ and $\psi \rightarrow 0$ yielding:

$$M(z) = M_0 + 0.13z - 0.13\delta \ln\left(\frac{z}{z_0}\right) \qquad (11)$$

Most importantly, since neutral stability is assumed, the measurement of wind speed is no longer required and the air-sea potential temperature difference is nearly zero and the sea surface temperature can be assumed equal to the air temperature to a good approximation. This is tantamount to assuming that the refractive gradient is predominantly dependent upon the gradient of vapor pressure.

RADIO-METEOROLOGICAL DATA SETS

Greek Islands Measurements. The neutral evaporation duct model was applied to a data set collected in the Aegean Sea [*Richter and Hitney*, 1988] using the Radio Physical Optics (RPO) propagation model. These data had previously been analyzed with the LKB and Paulus models [*Paulus*, 1994]. Figure 1 shows the comparison for the 9.624 GHz link (terminals at 4.8 and 4.9 m above msl). Horizontal dashed lines represent free-space (143 dB) and diffraction (191 dB) levels. The neutral duct model is qualitatively comparable to the other two models in predicting signal level. This result might not be surprising considering that stability-dependent effects were not detected in the data in previous analyses. Thus, the investigation was extended to a data set that would be a more strenuous test of the representativeness of neutral profiles.

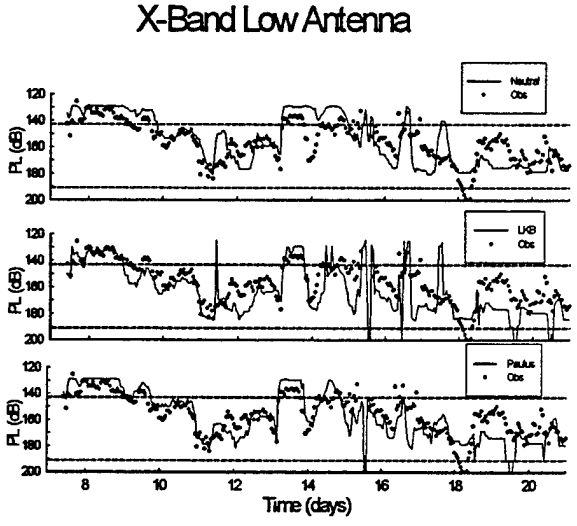


Figure 1. Predicted (solid lines) and observed (dots) propagation loss vs time for neutral, LKB, and Paulus evaporation duct models.

Lorient Radio-Meteorological Measurements. In the fall and winter of 1989, a joint experiment was conducted offshore from the city of Lorient, France on the southwest coast of Brittany [*Claverie and Hurtaud*, 1992; *Christophe, et al.*, 1995]. Figure 2 depicts the layout of the Lorient '89 experiment. The experiment was sponsored by NATO Research Study Group 8. The transmitters were located on the Quiberon peninsula and receivers were located at Gavres. The length of the transmission path was 27.7 km. The transmission frequencies, and transmitting and receiving antenna heights referenced to mean-tide level are given in Table 1. This geometry provided for a 4/3 earth horizon range of 25.3 km; however, due to tidal variations of up to 2 m, the link geometry varied from horizon to 1.2 times horizon range. The mid-path buoy shown in Figure 2 was equipped with sensors for wind direction, wind speed (U), relative humidity (RH) and air temperature (T_a). The three sensors were mounted 4.5 meters above the sea surface. The buoy was also equipped with a sea temperature (T_s) sensor which was mounted 0.6 m below the sea surface. The tide was monitored at Ile de Groix, approximately 8 km southwest of Gavres.

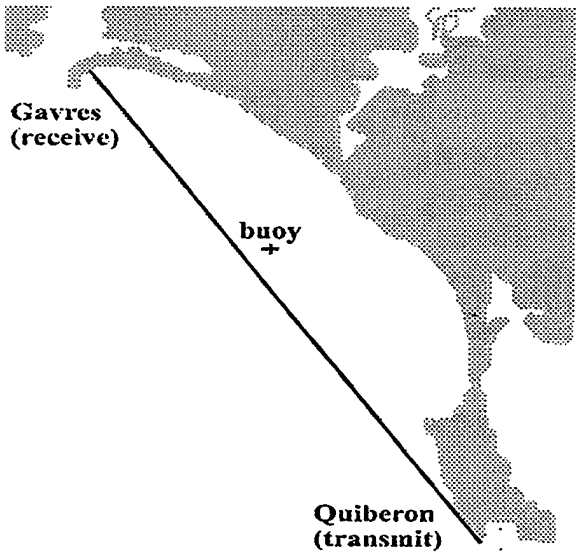


Figure 2. Layout of the NATO RSG-8/21 propagation experiment at Lorient, France, 1989, showing the transmitter and receiver sites, the 27.7 km overwater transmission path and location of the mid-path meteorological buoy.

Meteorological and propagation measurements became available on September 23, 1989; 0000Z on that date is considered to be day 0.0 of the experiment. Day 52.0 is the last day that both meteorological and propagation measurements were available. Data were recorded to disk at 10-minute intervals. In the time interval of days 0.0 to 52.0 there were 7488 data points. The data for the tide gage was missing for the interval of days 26.0 to 32.0, reducing the number of available data points to 6624.

Matched data: The following decision rules were used to determine valid data points:

1. Propagation factor measurements are available at both 3.0 and 10.5 GHz.

2. Meteorological inputs for T_a, T_s, RH, U and the tide are available.

3. All of the evaporation duct heights calculated using the duct models are below 40 meters. (note: this eliminated a large amount of data, as the LKB model frequently exceeded that threshold with stable input values)

Implementation of the three decision rules reduced the number of data points from 6624 to 6123. The important point regarding the data set of "valid" points is that it is the largest set of data containing valid inputs for both the propagation measurements and evaporation duct models.

Evaporative ducting subset: Surface-based ducts can increase signal levels to as much as 10 dB above free space levels, effectively masking the enhancement due to evaporative ducting. For the purposes of evaluating the performance of evaporation duct models, instances where the evaporation duct is not the dominant mode of propagation are "contaminants" in the data. It is desired to determine the subset of the data for which evaporation ducting is the dominant mode of propagation. This is done by using the Bayesian inference procedure described in *Rogers* [1996b]. The essence of the procedure is that the propagation effects are highly frequency dependent. Using an environmental model including both a surface-based duct and an evaporation duct as the inputs to an EM propagation model, thousands of propagation model runs are performed to determine what combination of propagation measurements are consistent with purely evaporative ducting and which are not. The subset of the valid data where evaporation ducting is believed to be the dominant mode of propagation is referred to as the "evaporation ducting subset" and consists of 5687 points which is 92% of the valid data points.

The Bayesian inference procedure used to identify the evaporation ducting subset is a relatively new development. In light of that consideration, overall statistics for both the valid data and evaporation ducting subset are provided also.

Table 1: Link frequencies and transmitter and receiver heights for the Lorient '89 experiment.

Frequency (GHz)	Receiver ht (m - Avg. Tide)	Transmitter ht. (m - Avg. Tide)
3.0	8.37	10.41
5.6	8.37	10.41
10.5	8.35	10.50
16.0	8.36	10.40
35.0	8.23	10.27
94.0	9.25	11.29

Meteorological Representativeness: Histograms of the bulk meteorological parameters obtained from the mid-path buoy for the evaporation ducting subset are shown in Figures 3 through 6. Qualitative comparison of the distributions in Figures 3-5 with climatology [*Gilhousen et al.*, 1990; *U.S. Navy*, 1995] indicates these are typical of mid-latitude ocean areas. Figure 6, however, is not typical as the mean air-sea temperature difference (ASTD) is normally negative, except in ocean areas influenced by a major ocean front or nearby land mass. Thus, we believe the ASTDs observed during Lorient '89 to be typical of many coastal environments rather than open ocean.

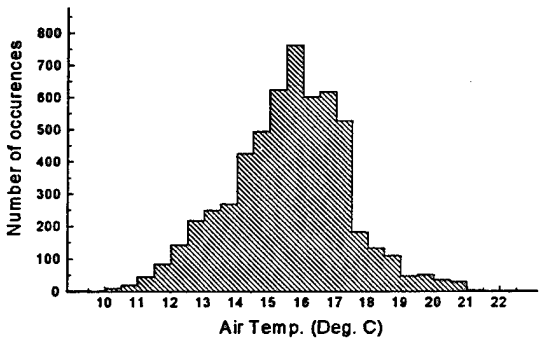


Figure 3. Air temperature histogram.

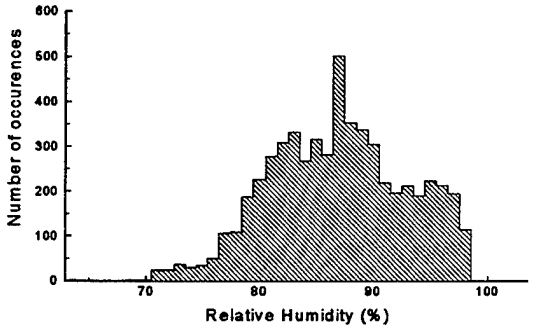


Figure 4. Relative humidity histogram.

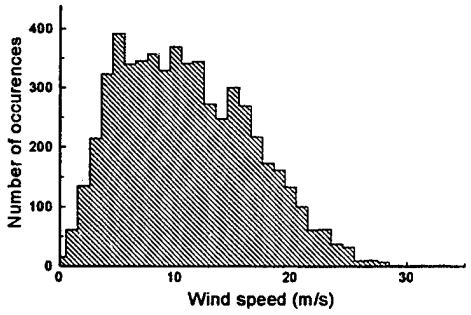


Figure 5. Wind speed histogram

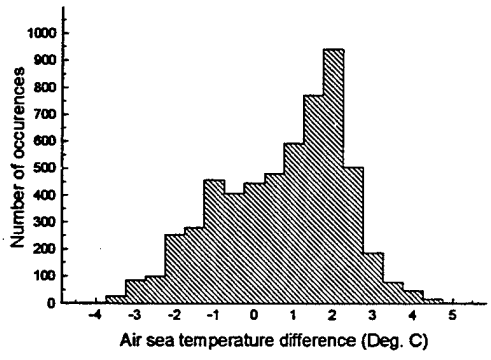


Figure 6. Air-sea temperature difference histogram.

Time series: Figure 7 illustrates the measured and estimated propagation factors for days 2 through 4 on the 3.0 GHz link. Reference lines for free space and standard propagation are provided. The variations in the standard propagation are due to the tide changing the height of the land-mounted transmitters with respect to the sea surface. The heavy solid line is the measured propagation factor. From day 2.0-2.3, 2.9-3.3 and 3.8-4.0 the propagation factor is consistent with evaporation ducting. From day 2.3-2.8 and from day 3.3-3.8, the propagation factor is well above free-space levels. During those intervals, there are deep (10 dB) fades in the measured signal levels. Both of these features are consistent with surface-based ducting. During the surface-based ducting periods, the mismatches between the measured signal levels and those estimated using the three evaporation duct models are quite large. While it appears as though the LKB model does capture the first up-transient, it is also observed that LKB model's subsequent variations are somewhat out of phase with the variations in the measured signals, hence leading to poor real-time estimation performance. For the intervals when the measured signals are consistent with evaporative ducting (days 2.0-2.3, 2.8-3.3, and 3.8-4.0), the performance of the evaporation duct models is quite good, with the LKB appearing to do the best job.

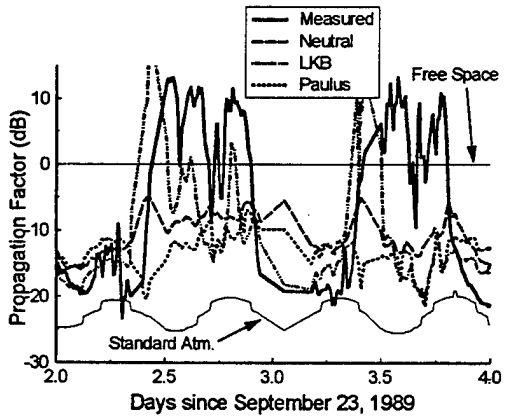


Figure 7. Time series of measured and estimated propagation factor at 3.0 GHz. Reference lines for free space and standard atmosphere are indicated by arrows. The sharp measured signal increases that are seen at days 2.5 and 3.5 are indicative of the onset of surface-based ducting.

In Figure 8, evaporation ducting appears to be the dominant mode of propagation for at least 90% of the time. Overall the performances of the three duct models appear to be comparable except for the transient in the LKB estimates that occurs about day 8.7. which leads the transient in the measured signal levels by 2 to 3 hours. Around day 8.7, the time when

the measured signal levels are at a maximum, the LKB estimates are about 20 dB below the measured values.

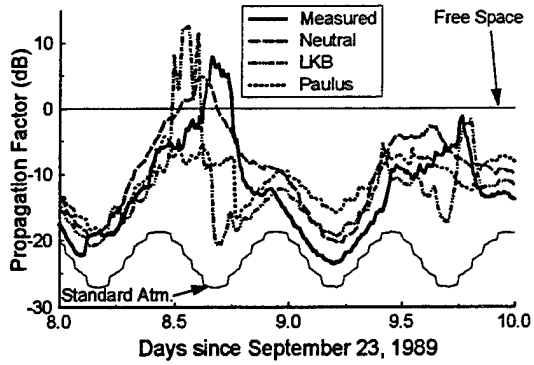


Figure 8. Time series of measured and estimated propagation factor at 3.0 GHz.

STATISTICAL ANALYSIS

Statistics for Measuring Real Time Estimation Performance. Let X and Y be propagation estimates and measurements respectively, with means μ_X and μ_Y, and standard deviations σ_X and σ_Y. Four descriptive statistics are commonly used for measuring real-time estimation performance [*Rogers*, 1996a]:

1. Root mean squared (RMS) error:
$$RMS_{X,Y} = \sqrt{E[(X-Y)^2]} \qquad (12)$$

2. Standard error:
$$STD_{X,Y} = \sqrt{E[((X-\mu_X)-(Y-\mu_Y))^2]} \qquad (13)$$

3. Correlation coefficient:
$$\rho_{X,Y} = \frac{E((X-\mu_X)(Y-\mu_Y))}{\sigma_X \sigma_Y} \qquad (14)$$

4. Bias: $b_{X,Y} = \mu_X - \mu_Y$ (15)

If the estimation errors (i.e., the X-Y's) are normally distributed and are time-independent, then any combination of three of the above statistics constitutes a complete description of the error. The primary statistic for evaluating real-time propagation estimation performance is the RMS error. Minimizing the RMS error implies minimizing both the standard error and the bias, and maximizing the correlation. The reverse, however, is not true as is seen here:

$$RMS_{X,Y}^2 = \sigma_X^2 + \sigma_Y^2 - 2\sigma_X\sigma_Y\rho_{X,Y} + b_{X,Y}^2 \qquad (16)$$

The square of the RMS error is the sum of the squares of the standard error and the bias:

$$RMS_{X,Y}^2 = STD_{X,Y}^2 + b_{X,Y}^2. \qquad (17)$$

While the RMS error should be used as the primary performance indicator, it should still be used in conjunction with the bias. For example, there might exist two models, both having an RMS error of 7.0. With model "A" the standard error is 7, so the bias is 0. With model "B" the standard error is 0 and the bias is 7.0. It is then found that applying smoothing to the model "A" estimates reduces the standard error to 3 dB; consequently, the RMS error of model "A" would be reduced to 3 dB. If the smoothing were then applied to the model "B" data though, it would have no effect. Had only the RMS error been examined, it would have been concluded that the models were essentially identical. If both the RMS error and bias are examined, it would be observed that model "A" appears to be somewhat noisy, but reasonably accurate. Model "B" on the other hand appears to have a serious problem as it consistently over-estimates or under-estimates values.

Bias Conditioned on the Air-Sea Temperature Difference. The bias at 3.0 GHz, conditioned on the air-sea temperature difference is shown in Figure 9. Observations include:

1. For ASTD values of less than 0° C, the LKB model performs the best (its bias has the smallest magnitude; it is closest to the 0 bias) although the performance of the neutral model is only marginally worse.

2. For ASTD values of 0° C and higher, the neutral model performs the best, with a bias of about 3 dB. Particularly at very high ASTD values the LKB model performs poorly, with up to a -7 dB bias.

3. It should be noted that the standard atmosphere model shows nearly as much skill at ASTD values of less than 0° C as the models driven by meteorological inputs. The reason is relatively low sensitivity of propagation at 3 GHz to evaporation ducts.

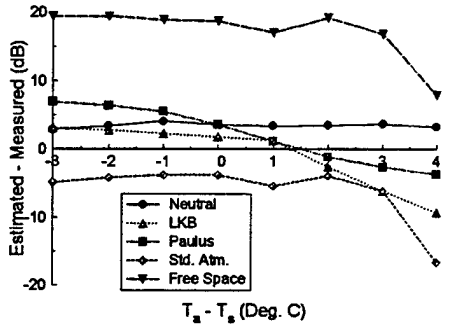


Figure 9. Bias at 3.0 GHz.

Bias at 10.5 GHz is shown in Figure 10. The results are similar except:

1. At ASTD values of greater than 0°C the performance of the Paulus and neutral models is comparable.

2. Standard propagation shows little skill as an estimator of propagation, while the assumption of free space propagation appears quite good for ASTD values less than 2° C. This is because propagation at 10.5 GHz is enhanced for the range of evaporation ducting conditions for this experiment.

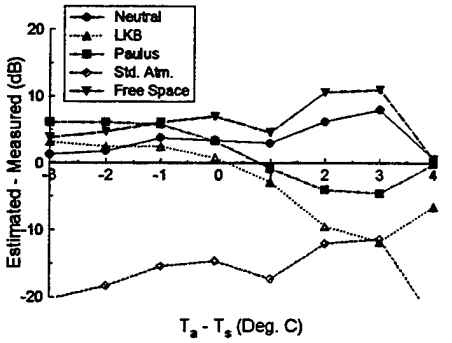


Figure 10. Bias at 10.5 GHz.

RMS Error Conditioned on the Air-Sea Temperature Difference. The RMS error of estimates at 3.0 GHz and 10.5 GHz are shown in figures 11 and 12 respectively. At both frequencies the relative performance of the three duct models are similar: For ASTD values of 0°C or less, the LKB is a dB or so better than the neutral model and 2 - 4 dB better than the Paulus model. At ASTD values of greater than 1°C, the performance of the neutral and Paulus models is similar, both are substantially better than the LKB.

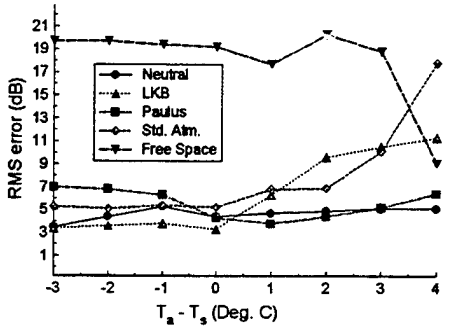


Figure 11. RMS error at 3.0 GHz.

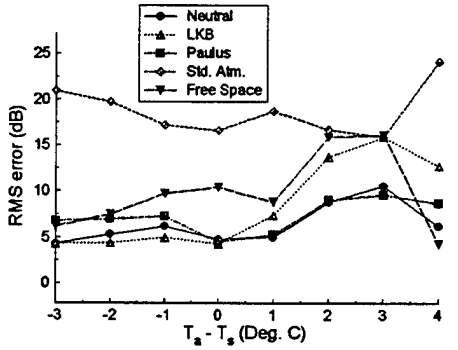


Figure 12. RMS Error at 10.5 GHz.

Overall Performance. The grain of salt that figures 9-12 must be taken with is that some ASTD values occur more often than others. Overall statistics reflect the relative likelihood that a given ASTD value occurs. Tables 2 through 5 provide the complete descriptive statistics for errors of propagation estimates calculated using the neutral (Neu.), LKB, and Paulus (Pau.) method. Errors resulting from the assumption of a standard atmosphere (Std.) or free space (FS) propagation are provided for reference. In each of the tables, σ_y is standard deviation of the measured propagation values and σ_x is the standard deviation of the propagation estimates calculated using the duct

model listed in the left hand column. Tables 2 and 3 are associated with the evaporation ducting subset. Tables 4 and 5 are associated with the set of all valid data points.

Table 2: Overall error statistics at 3.0 GHz for evaporative ducting cases. The total sample size is 5687 points for each value in the table.

	σ_y	σ_x	RMS	STD	ρ	bias
Neu	5.80	5.02	4.79	3.24	.83	3.53
LKB	5.80	8.71	7.30	7.29	.558	-0.29
Pau.	5.80	5.84	5.07	4.79	.662	1.66
Std.	5.80	2.50	7.13	5.32	.399	-4.75
FS	5.80	0.00	19.09	5.80	-	18.18

Table 3: Overall error statistics at 10.5 GHz for evaporative ducting cases. The total sample size is 5687 points for each value in the table.

	σ_y	σ_x	RMS	STD	ρ	bias
Neu	9.62	6.62	7.05	5.57	.827	4.31
LKB	9.62	14.55	10.04	9.34	.775	-3.69
Pau.	9.62	10.85	7.37	7.37	.747	0.26
Std.	9.62	3.67	17.74	9.64	.185	-14.89
FS	9.62	0.00	12.08	9.62	-	7.31

Table 4: Overall error statistics at 3.0 GHz for both non-evaporative ducting and evaporative ducting cases. The total sample size is 6123 points for each value in the table.

	σ_y	σ_x	RMS	STD	ρ	bias
Neu	7.64	5.27	5.74	5.10	.747	2.64
LKB	7.54	9.44	8.21	8.16	.561	-0.92
Pau.	7.64	5.89	6.48	6.45	.572	0.62
Std.	7.64	2.52	9.56	7.36	.272	-6.09
FS	7.64	0.00	18.49	7.64	-	16.84

Table 5: Overall error statistics at 10.5 GHz for both non-evaporative ducting and evaporative ducting cases. The total sample size is 6123 points for each value in the table.

	σ_y	σ_x	RMS	STD	ρ	bias
Neu	9.67	6.60	6.96	5.71	.819	3.99
LKB	9.67	14.68	10.35	9.68	.758	-3.66
Pau.	9.67	10.72	7.38	7.38	.742	0.09
Std.	9.67	3.67	18.30	9.70	.181	-15.52
FS	9.67	0.00	11.72	9.67	-	6.63

DISCUSSION

The most surprising result is the excellent performance of the neutral model. For unstable conditions, the neutral model performed nearly as well as the best-performing LKB model, and better than the Paulus model. For stable conditions, the neutral model outperformed all but the Paulus model at 10.5 GHz and performed better than the Paulus model at 3.0 GHz.

Another surprising result is the relative performance of the LKB model. For ASTD>1, the bias and RMS error both increase as compared to the other two evaporation duct models; for ASTD<1, LKB is only slightly better than the neutral model.

ACKNOWLEDGEMENT

The Lorient '89 radio-meteorological data set was provided courtesy of NATO AC 243 Panel 3 RSG-8. The authors performed this analysis under Office of Naval Research, ONR-322, funding.

REFERENCES

Anderson, K.D., "94-GHz Propagation in the Evaporation Duct," *IEEE Trans. Antennas Propagat., 38*(5), 746-753, 1990.

Blanc, T.V., "The Accuracy of Bulk-Method-Determined Flux, Stability, and Sea Surface Roughness," *J. Geophys. Res., 92*(C4), 3867-3876, 1987.

Christophe, F., N. Douchin, Y. Hurtaud, D. Dion, R. Makarushka, H. Heemskerk, and K. Anderson, "Overview of NATO/AC 243/Panel 3 Activities Concerning Radiowave Propagation in Coastal Environments," *NATO AGARD CP-567*, Paper 27, Feb. 1995.

Claverie, J. and Y. Hurtaud, "Propagation Transhorizon en Atmosphere Marine Modelisation et Nouveaux Resultats Experimentaux," *NATO AGARD CP-502*, Paper 4, Feb., 1992.

Gilhousen, D.B., E.A. Meindl, M.J. Changery, P.L. Franks, M.G. Burgin, and D.A. McKittrick, *Climatic Summaries for NDBC Buoys and Stations*, 454 pp., National Weather Service, National Data Buoy Center, NSTL, Miss., Feb. 1990.

Gossard, E.E. and R.G. Strauch, *Radar Observation of Clear Air and Clouds*, New York: Elsevier, 1983.

Jeske, H., "The State of Radar-Range Prediction Over Sea," in Tropospheric Radio Wave Propagation Part II, *NATO AGARD CP-70*, Paper 50, Feb 1971.

Jeske, H., "State and Limits of Prediction Methods of Radar Wave Propagation Conditions Over Sea," in *Modern Topics in Microwave Propagation and Air-Sea Interaction*, 131-148, A. Zancla, ed., Reidel Publishers, 1973.

Liu, W.T., K.B. Katsaros, and J.A. Businger, "Bulk Parameterization of Air-Sea Exchanges of Heat and Water Vapor Including the Molecular Constraints at the Interface, *J. Atmos. Sci, 36*, 1722-1735, 1979.

Panofsky, H.A. and J.A. Dutton, *Atmospheric Turbulence*, New York: Wiley, 1984.

Paulus, R.A., "Practical application of an evaporation duct model," *Radio Sci., 20*(4), 887-896, 1985.

Paulus, R.A., "Propagation in the Evaporation Duct: Model Predictions and Comparisons to Data," NRaD TR 1644, NCCOSC RDT&E Division, 1994.

Richter, J.H. and H.V. Hitney, "Antenna Heights for the Optimum Utilization of the Oceanic Evaporation Duct," vols. 1 & 2, NOSC TD1209, Naval Ocean Systems Center, Jan 1988.

Rogers, L.T., "Effects of the variability of atmospheric refractivity on propagation estimates," *IEEE Trans. Antennas and Propagat*, vol. 44, no. 4, pp. 460-465, April, 1996a.

Rogers, L.T., "Remote Sensing of Evaporation Ducts Using SHF Propagation Measurements," in Remote Sensing: A Valuable Source of Information, *NATO AGARD CP-582*, pp. 48.1-48.9, 1996b.

U.S. Navy, *U.S. Navy Marine Climatic Atlas of the World, Ver 1.1*, CD-ROM, Commander, Naval Meteorology and Oceanography Command, Aug. 1995.

Fusing data from the mesoscale model and radio remote sensing

L. T. Rogers and R. A. Paulus
NCCOSC RDTE DIV D883
49170 PROPAGATION PATH
SAN DIEGO CA 92152-7385

J. Cook
Naval Research Laboratory
Marine Meteorology Division
Monterey, CA 93943-5502

1 Introduction

The U.S. Navy has historically sponsored the development of mesoscale models and both in-situ and remote sensors. One of the driving forces behind these development efforts has been that the models and sensors can be used to estimate tropospheric refractivity gradients and therefore be used to provide input data to electromagnetic (EM) propagation models. The outputs of the EM propagation models are used as inputs to models designed to assess the performance (i.e. detection ranges) of radars and availability of communication systems.

To date, combining the outputs of the different sensors and the mesoscale model has been perceived as a computer and networking problem. While that work remains necessary, it must be realized that this is also an estimation problem. The ultimate goal of *data fusion* in refractivity estimation is the optimal estimation of propagation loss given information from the mesoscale model, radiosondes, refractivity inferred from radio measurements, *in-situ* measurements at the sea surface, and from satellites and other remote sensors. This is a fundamentally different approach than that of traditional atmospheric data assimilation.

In this initial data fusion experiment we will focus on the mesoscale model and refractivity inferred from radio measurements. In many operational scenarios, the mesoscale model may be the only practical method for obtaining range dependent refractivity estimates. A weakness of the mesoscale model though, is that its inherent spatial averaging washes out sharp refractivity gradients at the capping inversion, which in turn results in underestimation of ducting effects. Radio measurements, on the other hand, are highly sensitive to the refractivity gradients in the capping inversion but remote sensing of refractivity by radio measurements is unlikely to ever provide range dependent refractivity when used by itself. VHF and UHF emitters are plentiful in many coastal areas and monitoring them for the purpose of inferring refractivity is practical. Clearly, the two information sources are complementary and are excellent candidates for data fusion.

The data used are from the Variability of Coastal Atmospheric Refractivity (VOCAR) experiment (see *Paulus* [1994]) which took place June through September of 1993. The layout of the experiment is depicted in figure 1. Transmission links at 143, 262, and 374 MHz were operated on paths "A" and "B" that are shown in the figure. During a special two-week intensive observation period (IOP) beginning on August 23, 1993, radiosondes were launched at roughly four hour intervals from numerous locations including Point Mugu and San Clemente Island. Forecast refractivity fields were calculated from The Navy Operational Regional Atmospheric Prediction System (NORAPS) mesoscale model as described by *Hodur* [1987] and *Burk and Thompson* [1989]. Refractivity fields from the mesoscale model and the refractivity inferred from the transmission links are used to generate refractivity fields that preserve the range dependency of the mesoscale model fields, but also have a sufficiently strong trapping layer to be feasible given the measured propagation. The Research Vessel Point Sur was located at mid-path on Path A for roughly five days beginning August 27. The combination of the radiosondes from Point Mugu, San Clemente Island, and from the R.V. Point Sur are used to provide range-dependent profiles that provide validation for the data fusion method.

2 Objective of initial data fusion experiment

Figure 2 is an adaptation from *Kay* [1993] that illustrates the effect of the bias and variance of the estimator. The abscissa is estimation error and the ordinate is the probability. Ideally, we would like to have our estimation errors distributed as the minimum vari-

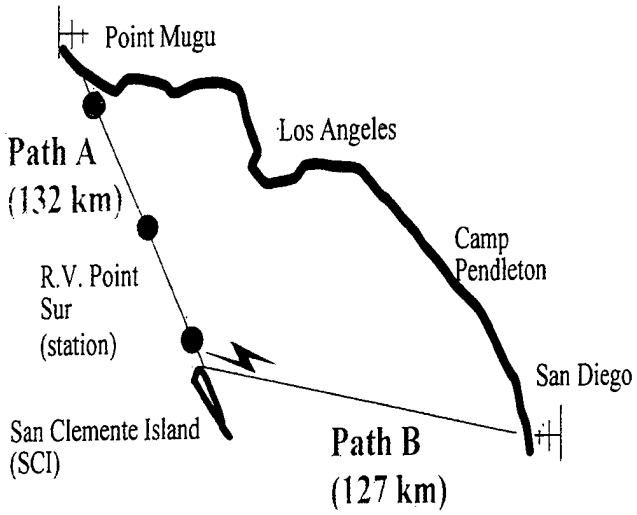


Figure 1: VOCAR layout.

ance unbiased estimator (MVUE) as shown in (a). In that case our estimation errors would be zero-mean and have the minimum variance achievable as determined by computation of the Cramer-Rao lower bound (CRLB) or other bounding criteria. If the errors have a variance greater than the lower bound but the estimates are unbiased, we might have (b). If the minimum variance is achieved but there is a non-zero bias we have (c), and if there is a non-zero bias and the minimum variance is not achieved we have (d).

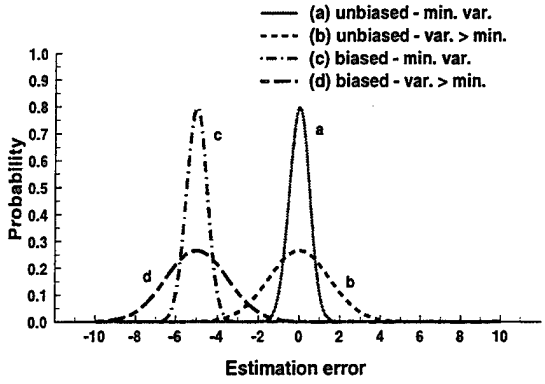


Figure 2: Illustration of variance and bias of estimation errors.

The situation using the mesoscale model by itself for propagation estimation is (d) since 1) the vertical resolution of the mesoscale model results in a non-zero bias, and 2) initialization and boundary condition errors result in greater than minimum variance. If the magnitude of the bias is nearly the same as, or greater than the square root of the variance, very little will be achieved by reducing the error variance without reducing the bias. Accordingly, our goal in this effort is to utilize the radio measurements to unbias the mesoscale model outputs while preserving the range dependent features of the mesoscale model.

3 VOCAR tri-linear model and parameterization

Figure 3 illustrates refractivity profiles corresponding to a standard atmosphere, a surface-based duct, and an elevated duct, and provides the geometry parameters used to describe the ducts. The surface-based-duct and elevated-duct profiles are associated with the marine boundary layer (MBL) capped by a stable layer. The stable MBL structure is quite common in areas such as the coastal waters of southern California and the Persian Gulf. The refractivity profiles associated with a stable MBL are often tri-linear in appearance.

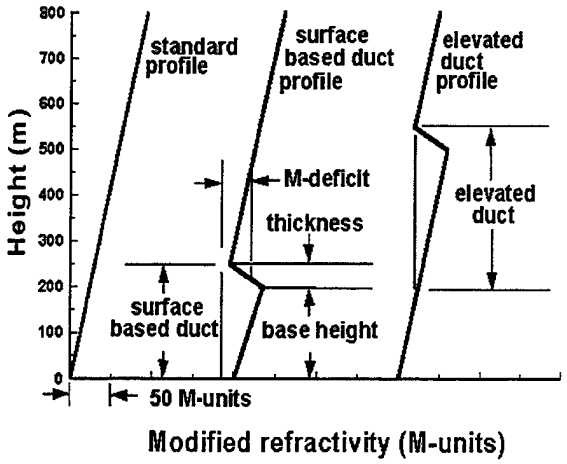


Figure 3: Idealization of refractivity profiles for duct formed by the capping inversion of the marine boundary layer.

In estimation problems it is customary to group parameters into deterministic parameters which we desire to estimate and nuisance parameters which we are not interested in, but must be accounted for, at least in the statistical sense [*Kay*, 1993]. The elements of

deterministic and random parameter vectors are of the form:

$$\Theta_D = [\theta_1, \theta_2, \ldots \theta_M]^T$$

and

$$\Theta_R = [\theta_{M+1}, \theta_{M+2}, \ldots \theta_N]^T$$

respectively. The utility of such a form is that nuisance parameters can be "integrated out". Ideally, our nuisance parameters in this problem would characterize range and height variability in the refractivity structure that occur on time and spatial scales too small to predict, infer, or measure. In general, a function $g(\Theta_D, \Theta_R)$ is a point value corresponding to a single realization of Θ_R, while $y = g(\Theta_D)$ is a random variable. If $g(\ )$ is non-linear, then,

$$\overline{G(\Theta_D)} \neq G(\Theta_D, \overline{\Theta_R})$$

but

$$\overline{G(\Theta_D)} = \int_{\Theta_R} G(\Theta_D, \Theta_R) f_{\Theta_R}(\Theta_R) d\Theta_R$$

where $f_{\Theta_R}(\Theta_R)$ is the probability density function for the nuisance parameters. This is an important point in both the forward and inverse problem in tropospheric EM propagation: that you cannot determine mean propagation values (let alone distributions of propagation values) without accounting for the random processes of the propagation medium.

The deterministic parameterization implemented in this data fusion problem is:

$$\Theta_D = [h, m]^T \quad (1)$$

where h was the height of the base of the trapping layer in meters, and m was the M-deficit as shown in figure 3. The only random parameter was the thickness of the trapping layer d, i.e.

$$\Theta_R = \theta_3 = d \quad (2)$$

and d was assumed to be uniformly distributed over the interval 10 to 90 meters, i.e. the probability density function of θ_3 is

$$f_{\theta_3}(\theta_3) = \begin{cases} \frac{1}{90} & 10 < \theta_3 < 100 \\ 0 & \text{otherwise} \end{cases} \quad (3)$$

Clearly, this parameterization is far less sophisticated than an ideal parameterization which (as described before) would characterize the range and short term temporal variations in the refractive environment. Ideally, its single random component approximates the effects introduced by the range and height variability in the true refractive environment. To some degree, this is the case; using a waveguide-mode model, it can been observed that when d is varied it tends to make large changes in the relative phase and amplitudes of the dominant propagation modes which lead to constructive and destructive interference effects that resemble those introduced by the true (dominantly range) variability. Nonetheless, as described in *Rogers* [1996], the parameterization works poorly with weak trapping layers and should be the primary area of focus in future work.

4 Input data

4.1 NORAPS mesoscale model runs for the VOCAR experiment

The mesoscale weather prediction model used to simulate the 12 day VOCAR IOP is a version of the Navy Operational Regional Atmospheric Prediction System (NORAPS) described by *Hodur* [1987] and *Burk and Thompson* [1989]. NORAPS is a hydrostatic primitive equation model with sophisticated second-order closure boundary layer physics which are important for describing near-surface atmospheric (and refractive) structures. The domain for the VOCAR experiment extends from Oregon to Baja California and from Arizona to about 1000 km off the California coast. The horizontal resolution is 20 km and the terrain following, 30 level, vertical coordinate system is distributed so that the resolution is greatest near the surface of the earth and decreases upwards. This scheme allows us to resolve the large vertical gradients in temperature and moisture typically found near the surface that are critical for evaluating refractive effects. NORAPS was run twice daily in a data assimilation mode to provide 24 h forecasts, with data archived every four hours during the forecast periods. Data assimilation is important because there is not enough data to adequately define the structure of the atmosphere across the model's domain. In the data assimilation method, the previous 12 h forecast is used as a starting point and observed data is incorporated with an optimum interpolation analysis in order to initialize the next forecast. In this way, details of atmospheric structures are maintained from one model forecast to the next and are modified using available data. This process is repeated every 12 h to maintain an updated forecast based on the most current condi-

tions. Over water, the sea surface temperature field is updated every 24 h and fixed during the intermediate forecast periods.

4.1.1 Meteorological evaluation of NORAPS VOCAR performance

The performance of NORAPS during VOCAR has been documented in *Burk et al.*,[1994] and *Burk and Thompson* [1994]. NORAPS forecast a typical California coastal summertime pattern during the beginning of the VOCAR experimental period. The predominate northerly flow aloft along the central California coast topographically forced a large-scale eddy in the bight which resulted in weak southerly flow immediately adjacent to the coast. This weak pattern allowed a significant diurnal variation in the atmospheric boundary layer and associated elevated trapping layer to develop. The trapping layer tended to be low at midday and then elevate and weaken at night. The diurnal variability decreased sharply westward, away from the coastline; at the location of the R/V POINT SUR, the diurnal behavior was discernible but not nearly as pronounced as at Pt. Mugu. As the experiment progressed, the northerlies turned more northeasterly and an eddy developed off the northern California coast, in the lee of the Siskiyou and Klamath mountain ranges. The eddy developed into a mesoscale low that drifted southward and caused the winds in the bight to shift to the west. This movement of the low caused the boundary layer in the bight to deepen and the trapping layer and associated duct to rise and weaken. The boundary layer adjacent to the coast just north of Point Conception was forecast to be somewhat shallower due to divergence associated with the acceleration of a low level jet just above the boundary layer. During this period, NORAPS forecast a weakening of upper level subsidence and the advection of moist air aloft. These two features resulted in the trapping layer rising and weakening over time. Comparison with individual soundings show that NORAPS correctly forecast the atmospheric boundary layer and trapping layer trends during the early and middle VOCAR periods, although the depth of the boundary layer (height of the trapping layer) was under forecast. The causes of these forecast errors have been attributed to the initialization procedure and to over-forecasts of near surface heating caused by the crude representation of the off shore islands [*Burk and Thompson*,1994].

4.2 Refractivity inferred from propagation measurements

The inference of refractivity parameters from the VOCAR EMpropagation data is discussed in *Rogers*, [1996]; only a brief outline will be given here. As described in section 3, $\Theta = [\Theta_D; \Theta_R]^T = [h, m; d]^T$ is a parameter vector describing a single realization of the refractive environment. $g(\Theta, f)$ is the propagation factor at frequency f associated with refractivity realization Θ. The mean propagation factor over the realizations of Θ_R is $\overline{g(\Theta_D, f)}$. In vector form, we have

$$\overline{G(\Theta_D)} = \begin{bmatrix} \overline{g(\Theta_D, f_1)} \\ \overline{g(\Theta_D, f_2)} \\ \overline{g(\Theta_D, f_3)} \end{bmatrix}$$

where $\overline{G(\Theta_D)}$ is the column vector of mean propagation factors associated with deterministic parameter vector Θ_D over the various realizations of random parameter vector Θ_R. At a single frequency f_0, $\bar{g}(h, m, f_0)$ can be pictured as contour plot in the h, m parameter space. This is illustrated in figure 4 which illustrates contours of constant propagation factor for the geometry and frequencies of the VOCAR experiment.

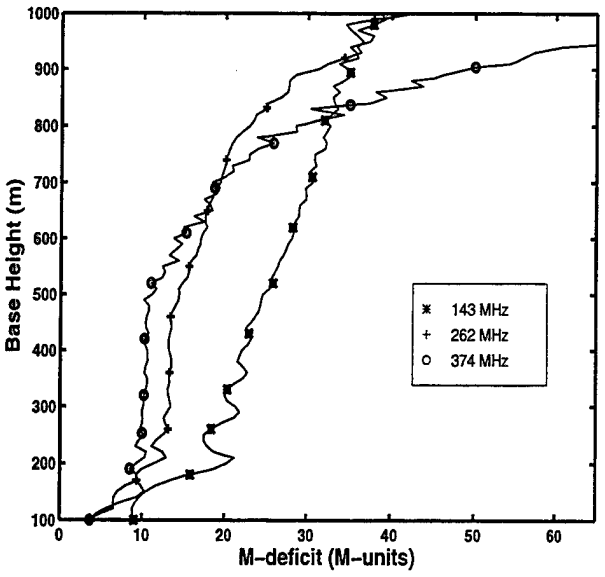


Figure 4: Three contours, each corresponding to a constant propagation factor of $F = -30$, for the three VOCAR frequencies.

$Y(t) = [y_1(t), y_2(t), y_3(t)]^T$ is the vector of measured propagation factor at the three VOCAR fre-

quencies at time t. The summed squared error of estimating the propagation factor at time t using propagation factors corresponding to Θ_D is

$$R(t, \Theta'_D) = (Y(t) - \overline{G(\Theta_D)})^T (Y(t) - \overline{G(\Theta_D)}), \quad (4)$$

where T is used to indicate the transpose.

Determining an effective error variance term σ^2_{eff} (to account for modeling and measurement errors) by *a posteriori* maximum likelihood computation, $f_{Y(t)|\Theta_D}(Y(t$ (the probability density of observing propagation factors vector $Y(t)$, given that the environment vector Θ_D is equal to Θ'_D) is

$$f_{Y(t)|\Theta_D}(Y(t)|\Theta'_D) = \frac{e^{\frac{-1}{2\sigma^2_{eff}} R(t,\Theta'_D)}}{(2\pi)^{3/2}\sigma_{eff}}.$$

The form of 5 is the result of assuming that the three individual elements of $Y(t) - \overline{G(\Theta_D)}$ have independent identically distributed Gaussian distributions.

Applying Bayes' rule we have

$$\Pr(\Theta'_D|Y) = \frac{f_{Y(t)|\Theta_D}(Y(t)|\Theta'_D) f_{\Theta_D}(\Theta'_D)}{\int_{-\infty}^{\infty} f_{Y(t)|\Theta_D}(Y(t)|\Theta_D) f_{\Theta_D}(\Theta_D) d\Theta_D},$$

where $f_{\Theta_D}(\Theta_D)$ is our prior density of Θ_D and the prime ($'$)is used to indicate that Θ'_D is a single combination of the h and m. In this problem, it was assumed that elements of Θ_D were uniformly distributed over the parameters space W defined by

$$\Theta_D \subset W \rightarrow \begin{cases} 200 < h < 1000 \\ 0 < m < 65 \end{cases} \quad (5)$$

where the limits of the parameters space were based upon examination of the VOCAR radiosondes. Consequently, the previous equation can be reduced to

$$\Pr(\Theta'_D|Y) = \frac{f_{Y(t)|\Theta_D}(Y(t)|\Theta'_D)}{\int_W f_{Y(t)|\Theta_D}(Y(t)|\Theta_D) d\Theta_D}.$$

It should be noted that while (in this case) the prior information has been used only to limit the parameter space to feasible values, the prior distribution is the way by which climatology can be incorporated into the estimation algorithm.

An example of inferring parameter values from measured propagation is shown in figure 5. We assume that at time t, a measured propagation factor vector of $Y = [-30 - 30 - 30]^T$ is recorded. The relative likelihood of any particular combination of h and m is proportional to the shading where lighter shading indicates higher likelihood.

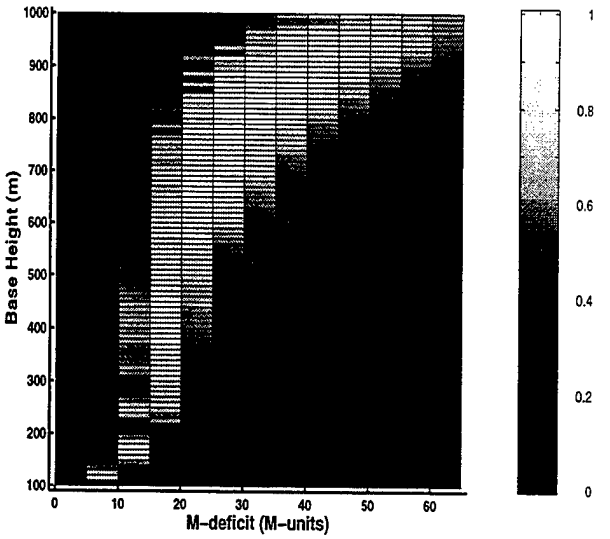


Figure 5: Relative likelihood of height h and M-deficit m corresponding to measured propagation factors vector of $Y(t) = [-30 - 30 - 30]^T$ for the VOCAR frequencies and geometries.

As with the parameterization discussed in section 3, there are weaknesses with this procedure. The greatest of these is the assumption that the mismatches (i.e. the values of $Y(t) - \overline{G(\Theta_D)}$) are Gaussian processes and are invariant over the parameter space.

5 Validation data

To prepare height-range cross sections of refractivity for the Radio Physical Optics (RPO) program, the refractivity structure matching algorithm (RSMA) was developed by *Vogel* [1991] and modified by *Cook et al.*,[1994]. Processing by RSMA guarantees that two important input data requirements for RPO are met: a) every profile contains the same number of levels, and b) the nth level in any one profile is matched to a refractivity structure at the nth level in all the other profiles. The matching of common refractive layers is accomplished in three steps. First, each level in every profile is categorized based on its refractivity structure type. The top and bottom levels are all assigned to the same category to ensure they are always matched up. Second, the primary structure types considered important for propagation are matched between adjacent profiles within physically reasonable bounds.

The matching is done iteratively, so that like structures near the same altitude are matched first. This procedure ensures the layers transition smoothly in refractive effect and altitude. Many refractive structures/pairings are considered minor and are ignored by RSMA. Third, all the remaining profile levels are matched using a secondary "best fit" algorithm that connects all the unmatched points between the primary matched levels. Any remaining unmatched points are interpolated in between the matched levels to force the structures to be consistent from profile to profile.

For this study, 14 marine cross sections were identified during VOCAR where the data were collected within about one hour of each other. Each cross section consists of three profiles starting at San Clemente Is. (NUC), runs through the NPS R/V Point Sur near the center (SUR), and ends at Pt. Mugu (NTD). Table 1 lists the profiles and the mean starting times which were used for comparison with the four hourly NORAPS data. Because RSMA was not designed to process the large number of vertical levels and fine structure associated with the profile measurements, a simple preprocessing step was required to reduce the data and make further processing feasible. The reduction was accomplished by fitting straight line segments to the profiles while preserving the important refractive structures determined by a criterion that depends on height. The criterion used was a 1/4 m-unit root-mean-square (RMS) deviation at the surface which increased three m-units per kilometer altitude. This line-fitting procedure preserved structures near the surface and considerably simplified the profiles aloft. The resulting profiles were then processed by RSMA and formatted for input into RPO. In general, the cross sections depict initially a stratified atmosphere with a strong surface-based duct, due to an elevated trapping layer whose height tends to be lowest at mid path (R/V POINT SUR). With time, the boundary layer shallows slightly then, early on 28 Aug., the boundary layer rapidly deepens, raising the elevated trapping layer and the duct. The later cross sections also describe a more homogeneous atmospheric condition, both as a function of range with a consistent trapping layer height, and as a function of height with the atmosphere exhibiting much less stratification.

6 Performance

Before examining overall results, two "events" are examined: serial days 239.167 and 241.666. The former is an instance where using the mesoscale model generated refractivity profiles results in a significant negative bias in resulting propagation estimates. Consequently, the additional information from the inverse medium problem significantly improves the accuracy of propagation estimates. In the latter case, the mesoscale model refractivity estimates have high fidelity to the true environment so that the addition of information from the inverse medium problem does not significantly improve propagation estimation.

Table I: VOCAR cross sections from San Clemente Island (NUC), through the R/V POINT SUR (SUR), and to Pt. Mugu (NTD). Times are Pacific Standard Time (PST).

#	Calendar date	Serial day
1	25 Aug. 1933	237.833
2	26 Aug. 1556	238.666
3	27 Aug. 0346	239.167
4	27 Aug. 0735	239.333
5	27 Aug. 1532	239.666
6	28 Aug. 0338	240.166
7	28 Aug. 0741	240.333
8	28 Aug. 1555	240.666
9	28 Aug. 1934	240.833
10	29 Aug. 0341	241.167
11	29 Aug. 0743	241.333
12	29 Aug. 1528	241.666
13	29 Aug. 1928	241.833
14	30 Aug. 0341	242.133

6.1 Date serial 239.167

The upper plot in figure 6 is a cross section of the refractivity fields constructed from the NORAPS temperature and humidity fields as described in section 4.1. The lower plot in figure 6 is vertical refractivity profiles for the same cross section that have been joined using the RSMA algorithm as described in section 5. Comparing the two graphs, the following is noted:

1. The average height of the base of the trapping layer is roughly the same in both the NORAPS generated profiles and the RSMA-processed measured profiles.

2. The same downward-sloping base of the trapping layer is observed in both sets of profiles.

3. The strength of the trapping layers is much, much stronger in the RSMA-processed measured profiles.

4. In the measured profiles, a weakening of the trapping layer with respect to range is observed. In the mesoscale profiles, the same, albeit weaker trend is observed.

These two plots considered thus far illustrate just how well the mesoscale model forecast can capture the horizontal evolution of the refractivity structure. They also illustrate how much weaker the trapping layer representations from the mesoscale model can be with respect to the measured values.

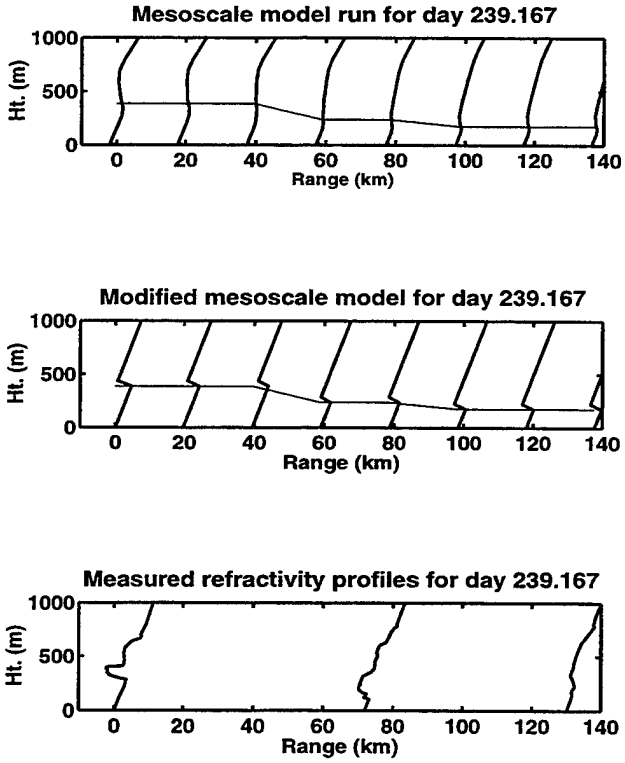


Figure 6: Refractivity cross sections for serial day 239.167 from the mesoscale model, modified (or data-fused) profiles, and from measured profiles respectively. The thin line in each the the first two plots indicates the height of the base of the trapping layer h.

6.1.1 Application of bias correction

The application of the bias-correction method is illustrated in figure 7. Obtaining the conditional probability distribution $\Pr(\Theta_D|Y) = \Pr(h, m|Y)$ is described in section 4.2. A line of feasible solutions in the $\{h, m\}$ parameters space is calculated from $\Pr(h, m|Y)$ using

$$\{h, m\}_{FEAS} = \mathrm{Max}_m(\Pr(h, m|Y)).$$

This is equivalent to saying that once we have observed Y, that for given height h, the feasible value of m is the one that maximizes $\Pr(h, m|Y)$.

Next, the averages $\bar{h}_{MES}$ and $\bar{m}_{MES}$, are computed from $h_{MES}(r)$ and $m_{MES}(r)$, the range (r) dependent values of base height and M-deficit calculated from the NORAPS generated refractivity fields (hence the subscript MES). The local gradient

$$\left\{\frac{\partial L}{\partial h}, \frac{\partial L}{\partial m}\right\}_{h_{MES}, m_{MES}},$$

is computed numerically. Moving in the direction of that local gradient we intersect the line of feasible solutions. That is our value of $(\bar{h}_{MOD}, \bar{m}_{MOD})$ where the subscript MOD is used to denote that these are the modified (or data fused) parameter values. Now a set of tri-linear profiles are determined such that:

$$h_{MOD}(r) = \bar{h}_{MOD} + h_{MES}(r) - \bar{h}_{MES} \quad (6)$$

$$m_{MOD}(r) = \bar{m}_{MOD} + m_{MES}(r) - \bar{m}_{MES}. \quad (7)$$

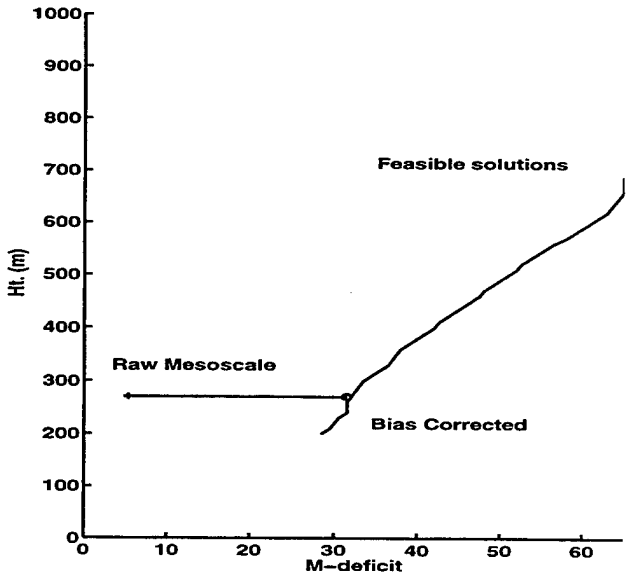


Figure 7: Parameter space for serial day 239.167.

The data-fused tri-linear profiles appear in the middle plot in figure 6. It is clear that the trapping layer strengths are substantially greater than those

observed in the raw mesoscale model outputs. Additionally, the range dependency of the base heights has been preserved and closely matches that of the measured profiles. There is a minor weakening in the trapping layer with respect to range in the modified profiles, but it is less pronounced than in the measured profiles.

6.2 Date serial 241.666

While on date serial 239.167, there exists a large difference between the mesoscale model predicted and the measured refractivity profiles, on date serial 241.666, the predicted and measured were quite close as can be seen in figure 8. As a consequence, the bias correction is small and the bias corrected profiles do not differ significantly from either the predicted or measured profiles.

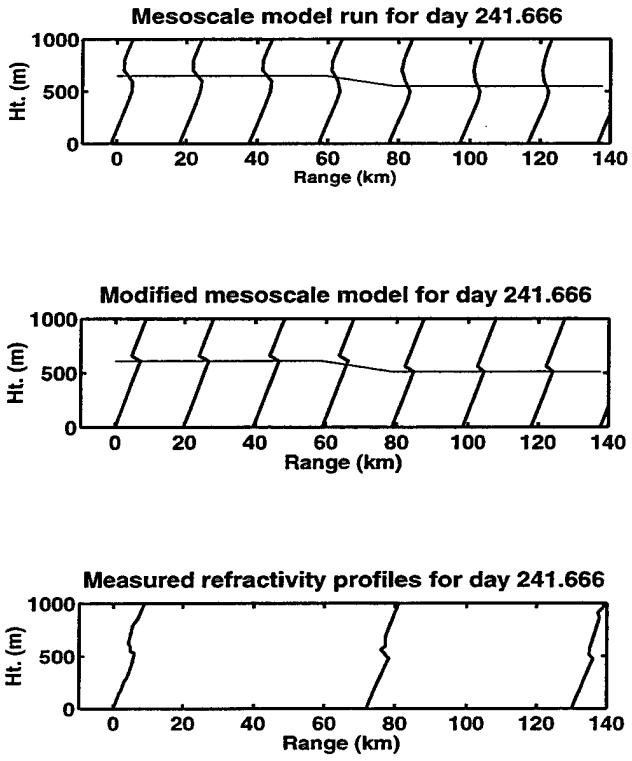


Figure 8: Refractivity cross sections for serial day 241.666.

6.3 Overall results

Figure 9 is a time series of propagation factors at 1000 GHz predicted using (a) radiosonde profiles processed using RSMA as described in section 5, (b) mesoscale model generated refractivity fields as described in section 4.1, and (c) bias corrected tri-linear profiles generated as described in section 6.1.1. It is clear that the while there are times where using the raw mesoscale model fields results in accurate refractivity estimates, there are times when their use does not. In those cases (i.e. the first three data points), the bias corrected profiles provide much better estimates.

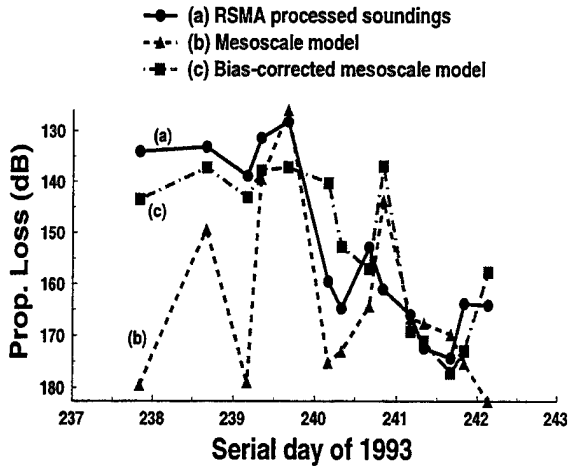


Figure 9: Time series of propagation factors at 1.0 GHz.

7 Summary

A simple algorithm has been implemented to fuse data from the mesoscale model with parameter values inferred from radio remote sensing. The major points from the work include:

1. Weaknesses:

   (a) The parameterization used is heuristic in nature and based largely upon observations of the behavior of the capping inversion layer in the Southern California bight.

(b) With results based upon only five days of test data from only a single geographical region, the representativeness of the results is open to question.

(c) There is no "physics" in the parameter space movement.

2. Strengths:

(a) As is illustrated in figure 9, the intended objective, unbiasing the mesoscale model, is achieved.

(b) The implementation is computationally simple.

7.1 Future direction

What direction the data fusion efforts should take is a function of Navy needs. In this paper we have used measured propagation data to improve mesoscale model refractivity fields. An equally pressing need is to be able to incorporate local radiosonde data into mesoscale model fields. The key element in both of these problems is parameterization.

Ultimately, a parameterization will be developed combining two very different techniques. First, large-eddy-simulation (LES) such as described in *Otte, et al.* [1996], and *Khanna, et al.* [1996] are used to develop parameterizations and other techniques that makes sense meteorologically. Equally important is to perform the sensitivity analysis to determine the modeling/parameterization that is optimal from a propagation estimation standpoint.

Acknowledgments

Radiosondes from San Clemente Island and Point Mugu courtesy of the Naval Air Warfare Center, Point Mugu, California. The mid-path radiosondes were launched from the Research Vessel Point Sur which was operated by the Naval Postgraduate School, Monterey, California. This work was funded by the Office of Naval Research.

References

[1] Burk, S.D., W.T. Thompson, J. Cook, and G.G. Love, "Mesoscale modeling of refractive conditions during the VOCAR experiment," *Proc. IGARSS,* Pasadena, CA, 1994.

[2] Burk, S.D. and W.T. Thompson, "Mesoscale modeling of refractive conditions in a complex coastal environment," *AGARD CP 567,* pp 40.1-40.7, 1994.

[3] Burk, S.D. and W.T. Thompson, "A vertically-nested regional numerical weather prediction model with second order closure physics," *Mon. Wea. Rev.,* 117, pp 2305-2324, 1989.

[4] Cook, J., G. Vogel and G. Love, "Operational support for a range-dependent radio propagation model," *AGARD CP 567,* pp 13.1-13.8, 1994.

[5] Kay, S.M. "Fundamentals of statistical signal processing: estimation theory," Prentice Hall PTR, Upper Saddle River, NJ 07458, 1993

[6] Khanna, S., J.G. Brasseur, J.C. Wyngaard, "The local structure of the atmospheric boundary layer," *Proc. Battlespace Atmosph. Conf.,* 3-5 Dec. 1996, NRaD TD 2938, 1996

[7] Hodur, R.M., "Evaluation of a regional model with an update cycle," *Mon. Wea. Rev.,* 115, pp. 2707-2718, 1987.

[8] Otte, M.J., N.L. Seaman, D.R. Stauffer and J.C. Wyngaard, "A mesoscale model for EM ducting in the marine boundary layer," *Proc. Battlespace Atmosph. Conf.,* 3-5 Dec. 1996, NRaD TD 2938, 1996

[9] Paulus, R.A., "VOCAR: An experiment in the variability of coastal atmospheric refractivity," *Proc. IGARSS,* Pasadena, CA, 1994.

[10] Rogers, L.T., "Likelihood estimation of tropospheric duct parameters from horizontal propagation measurements," accepted by *Radio Science,* Sep., 1996

[11] Vogel, G.N., "Specification for a refractivity structure matching algorithm," NOARL Tech. Note 191, Naval Research Lab., 1991.

AN EXAMINATION OF MODELLING APPROACHES FOR PREDICTING THE DISPERSION OF AEROSOLS FROM OBSCURANT GRENADES

W.S. Andrews and S.D. Roney
Department of Chemistry and Chemical Engineering
Royal Military College of Canada
Kingston, Ontario, Canada K7K 5L0

Gilles Roy
Defence Research Establishment Valcartier
Val-Belair, Quebec, Canada G3J 1X5

An artificial neural network model (ANN) has been developed to predict the aerosol concentration distribution resulting from the volley firing of screening grenades for armoured vehicles. The data were collected during trial firings using the Defence Research Establishment Valcartier (DREV) Laser Cloud Mapper (LCM), a scanning LIDAR device operating at 1.06 μm. The ANN model was able to predict volumetric extinction coefficients, and thus aerosol concentrations, to within an average error of 1.78 for a validation set of 1103 data points. A basic Gaussian plume model was also used to generate predictions over the same validation set, but the average error was 14.5, almost an order of magnitude worse than the ANN predictions. An examination of the extinction coefficients along a line-of-sight normal to the aerosol cloud revealed a bimodal distribution, which was also predicted by the ANN model. The Gaussian model predicted a monomodal distribution.

As the data set used for training, testing and validation was limited to the firing of two volleys of different composite grenades (phosphorus and metal flake), the ANN model can not be considered adequate for general application, but rather serves as a proof of principle that neural networks are capable of predicting the spacial and temporal distribution of aerosol particles better than conventional Gaussian models. A program of further data collection at DREV and subsequent analysis using ANNs is planned for the future.

Introduction

For some years, Defence Research Establishment Valcartier has used a scanning light detection and ranging (LIDAR), called a Laser Cloud Mapper (LCM)[1] to measure the attenuation of laser pulses caused by various aerosols under consideration for military use.[2,3,4] The backscatter data have been converted to volume extinction coefficient maps and give an indication of the concentration distribution of the obscurant aerosols. Although these data, collected over several years and for a wide variety of aerosols, were mainly used to assess obscuration, they also present information on the dispersion of aerosols from a point source which emits over a relatively short duration (<60 sec). It is sig-

nificant to note that obscuring grenades, which form a large portion of the data set, are neither instantaneous (puff) nor continuous (plume), but rather somewhat transient, with a short burning/emission time.

The classical prediction models are the Gaussian puff for instantaneous emissions and the Gaussian plume for continuous emissions. This paper examines the adequacy of Gaussian models to predict the aerosol dispersion measured by the LCM and to compare these to a model developed using artificial neural networks (ANNs), an aspect of artificial intelligence and a relatively new approach to modelling.

Gaussian Modelling

The two Gaussian models, the plume and the puff, are based on diffusion theory, with the concentration decreasing exponentially from the centreline or centre.[5] The more widely used, and thus the better characterized of the two is the plume model, which has a variety of applications for aerosol and vapour dispersion. The general Gaussian plume equation describing aerosol concentration, C (g/m^3), from a continuous source, is

$$C = \frac{Q}{2\pi\sigma_y\sigma_z u}\left(e^{-\left(y^2/2\sigma_y^2\right)}\right) \times \left[e^{-(z+h)^2/2\sigma_z^2} + e^{-(z-h)^2/2\sigma_z^2}\right], \quad (1)$$

where Q is the source/production rate (g/s), σ_y and σ_z are standard deviations in azimuth and elevation respectively (m), y and z are respective azimuthal and vertical distances from the centreline (m), h is the distance of the plume centreline above ground (m) and u is the wind speed (m/s) taken as being along the x axis.

A Gaussian distribution, by definition, has two fitting parameters, a mean (in this case the centreline concentration provided by the first term on the RHS of the Eq.1) and a standard deviation (here contained in the σ_y and σ_z terms). It is noteworthy that for the aerosol dispersion application, these standard deviations are determined from the appropriate Pasquill stability categories[6], which in turn are functions of distance from the source (x), cloud cover, time of day, etc. The basic assumptions inherent in the Gaussian plume model are constant emission, conservation of mass, (no ground deposition), steady wind and that the results are time averaged. Such parameters as ambient temperature, relative humidity, surface roughness as well as ground deposition, any chemical kinetics or aerosol/atmosphere reactions are not explicitly or even implicitly included in the basic model, although additional terms can be added. Two further limitations are that the Gaussian plume model predicts rather poorly less than 100 m from the source and that the quality of predictions varies inversely with distance from the centreline.[7]

Although some of the limitations mentioned above could be addressed by physically-based or semi-empirical fittings (notwithstanding that the σ_y and σ_z values are themselves semi-empirical in nature), it was decided to use the general Gaussian plume model as the basis of comparison for ANN models.

The instantaneous Gaussian puff model, which intuitively should provide a better prediction of aerosol dispersion from screening grenades than the con-

tinuous plume model, was found to perform not nearly as well. This is probably due to the fact that the wider use of the plume model has led to much better characterizations of the standard deviations (σ_y and σ_z) values used for predictions.[8]

Artificial Neural Network Models

Artificial neural networks are considered a branch of artificial intelligence and found their origins in psychologists attempts at modelling the brain's functions. The seminal work on the back propagation paradigm, the most widely used of ANN models, was only published in 1986.[9]

Basically, an artificial neural network takes raw input data, maps it into an input space, and then introduces it into the network. The network itself is an interconnection of nodes or processing elements (also sometimes called artificial neurons) which are arranged in layers (Fig. 1). The input layer contains a node for each variable, with each complete set of variables describing a specific input vector. For example, each measured value of volumetric extinction coefficient has a corresponding vector of measured experimental variables and parameters. In addition to the input variables, the input layer also contains a bias node which is permanently assigned a value of 1 and is analogous to an electrical ground. Its presence was found to aid convergence during training.

Each node in the input layer is connected to each node in the next layer, which is usually called the hidden layer. The scaled (mapped) input values each have a weight applied to them before the values are introduced into the hidden layer. At each hidden node, the weighted inputs are summed and then mapped back into the range -1 to +1 by the application of a hyperbolic tangent transfer function before being passed to the output layer. Conventionally, there are one or two hidden layers, with the interconnections between nodes in the two hidden layers being analogous to those between the input and first hidden layer.

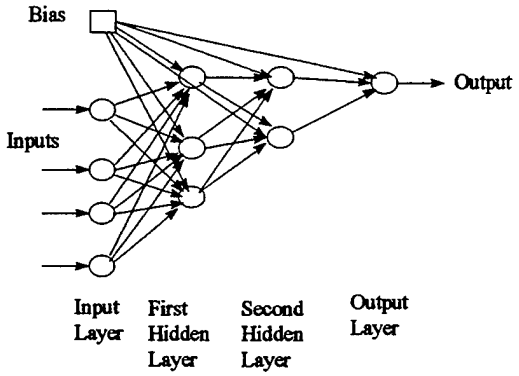


Fig. 1. Typical architecture of a back propagation neural network.

Again, each hidden node in the final hidden layer, as well as the bias node, is connected to each output node, with the process of applying weights to each connection, the weighted inputs being summed and then having a transfer function applied being repeated. The output of the output node(s) must then be mapped back into real-world value(s).

To initial scaling of input variables, is effected by:

$$x_i = 2V_i \left(\frac{M_i + m_i}{M_i - m_i} \right), \qquad (2)$$

where V_i is the unscaled i^{th} input value, M_i is the maximum value of the range of the ith input, m_i is the minimum value of the range of the ith input and x_i is the scaled i^{th} input value.

The scaled inputs (which can also be considered as the outputs of the input layer) have the appropriate connecting weights, w_{ji} applied. These weighted outputs become the inputs for the nodes of the first hidden layer, where they are summed and then transformed using a transfer function, as outlined by the following equations:

$$I_j = \sum_{i=0}^{n} w_{ji} x_i \,, \qquad (3)$$

where w_{ji} is the connection weight between the jth hidden node and the ith input node, and I_j is the sum of the weighted inputs to the jth hidden node, and

$$y_j = \tanh(I_j) = \frac{e^{I_j} - e^{-I_j}}{e^{I_j} + e^{-I_j}}, \qquad (4)$$

where y_j is the output of the jth hidden node.

This process is repeated for the second hidden layer and the output layer. The output value from the output layer must then be mapped back to provide a real value for the logarithm of the volumetric extinction coefficient. In fact, this process is essentially the reverse of the initial scaling described in Eq.2, although it is simplified by only having to consider the mapping of one variable. This is accomplished by

$$C = \frac{(M - m)z + (Rm - rM)}{R - r} \qquad (5)$$

where C is the predicted value of the logarithm of the volumetric extinction coefficient corresponding to the specific input vector defined by $x_1, x_2 \ldots x_9$, M and m are the real (measured) maximum and minimum of the output variable ($\log \sigma$), z is the network output value, whose range falls between the maximum and minimum values R and r (for the tanh function, these values are taken as 0.8 and -0.8 respectively).

At the start of the training process, the connecting weights throughout the network are given random values. When the output value is generated, it is compared to the corresponding actual measured value. The difference between these two values is considered the global error and is propagated backwards through the network. An iterative process is carried out of adjusting the connecting weights to minimize the global error. A gradient descent optimization is used to adjust each of the connecting weights locally. Once the global error has been minimized over the whole training set, the weights can be fixed and the network can be used to make blind predictions.

A trained ANN lends itself particularly well to incorporation into a spreadsheet which can be driven by a macro. It can also be incorporated into computer codes to provide real-time determination of the extinction coefficients and thus aerosol concentrations or transmittances, as required.

Data Collection

Some of the trials involving the LCM include Smoke Week IX[10], SOCMET Winter[11] and Summer[12]. The data used in this study were for two experimental screening grenades, each composed of a mix of red phosphorus (RP) and metal flake. The LIDAR was situated some 400 m from the cloud centreline so that the field of view was roughly perpendicular to the longitudinal

axis of the cloud. The grenades were 66 mm in diameter and designed for armoured fighting vehicle launchers. In each case, 12 grenades were launched together, with their impact over an arc of about 70 m. The red phosphorus was actually ignited in the air during flight through the launch arc. The metal flake was also dispersed while the grenades were in the air (at an elevation of some 10 m). As the grenades continued to burn and emit smoke after the rubberized RP particles had reached earth, the source was considered to be a ground release (h=0 in Eq.1). Even though this was not strictly true, it was not felt to contribute significantly to any modelling errors, as the data for the modelling were not collected until a coherent cloud had formed.

The scanning LIDAR is based on a 1.06 μm NdYAG laser. Although the settings are adjustable, those used for the trial from which the data were collected were such that, for one complete scan or cycle, the LCM traversed the 90° field of view six times, making 66 shots per traverse (Fig.2). The vertical field of view was 2°. The LCM measures the backscatter from the laser pulses, with a sampling frequency of 100 MHz. The resolution available was 1.5 m along the shot axis, 9.5 m at 400 m in azimuth and 2.8 m at 400 m in elevation. A typical scan would produce some 198 000 data points (backscatter values).

Electromagnetic attenuation by atmospheric or artificial aerosols can be characterized by the Beer-Lambert Law:

$$\frac{I}{I_0} = e^{-\alpha C L}, \qquad (6)$$

where I/I_0 is the transmittance through the path length L (m). The mass extinction coefficient α (m^2/g) can be considered the removal (scattering and absorption) cross section per unit mass and must be determined empirically. It is a function of aerosol particle size distribution, particle shape, and electromagnetic wavelength.[13] The product αC (m^{-1}) can be considered as the volumetric extinction coefficient, σ, and is the value that is generated by the LCM support software.

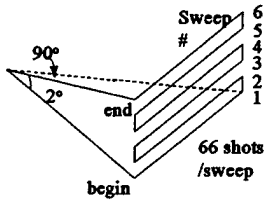


Fig. 2. Schematic of the sweep pattern of the DREV Laser Cloud Mapper.

A weakness inherent in the LCM is that aerosol clouds may be sufficiently dense to provide near-complete extinction of the laser pulses. In such cases, only the near side of the cloud (closest to the LCM) will provide reflections which can be converted to extinction coefficients or concentrations. For this reason, more confidence is placed in measurements from sparse clouds than from ones which are optically dense.

Data Handling

The backscatter signal strengths collected by the LCM are converted by support software to volume extinction coefficient values. With the vast amount of data available per six-sweep scan, locating extinction values for the aerosol cloud was not straightforward. A thresh-

old value of 2.00×10^{-4} was used as a filter, and the backscatter resulting from reflections from the natural background, such as trees and terrain features, had to be removed. The coordinate system was defined by having the x axis pass through the cloud centroid, with the origin of the cartesian coordinate system determined as the cloud centroid for the first scan.

In addition, the data had to be arranged into a format suitable for training and testing ANNs and in validating both the ANN and Gaussian models. The validation set was selected as the last scan of one of the tests and was used only for blind validation, i.e., it was not used for training or testing. This set contained 1103 data points.

The extinction coefficients available for analysis ranged over four orders of magnitude (10^{-1} to 10^{-4}). Consequently, a logarithmic transformation was performed. Another adjustment was to balance the distribution of the data points over the range of extinction coefficients. This was achieved by randomly choosing points from the residual data set (less the validation set) to fill a number of evenly wide data sub-range brackets throughout the available extinction coefficient range. The purpose of this was to preclude an inadvertent biasing of the ANN towards any particular sub-range of values.

ANN Development

The choice of ANN paradigm, back propagation, was based on the wide use and general success it has exhibited in solving prediction problems.[14,15] The version used was NeuralWare's NeuralWorks Professional II/Plus[16] with the edbd or extended delta-bar-delta option, which included dynamic adjustments to momentum and learning coefficients.

Another parameter investigated during ANN training was in choosing the input variables and parameters. The choice was limited somewhat by the nature of the data available, i.e., only two tests were used, with both conducted under relatively uniform meteorological conditions. Consequently, time of day and temperature were deemed insignificant. Further, specific details of the grenades were not available, so obvious inputs to describe the aerosols produced, such as total weight of aerosol dispersed, the burn/source emission rate and particle size distribution, were not included. Also, such values as ambient temperature, barometric pressure, relative humidity and thus chemical kinetics data were not available and so were not considered. The variables actually considered are contained in Table 1.

Table 1. Input variables for the artificial neural network, with relative significance determined by sensitivity analysis and normalized to most significant.

Input Variable or Parameter	*Relative Significance*
Downwind distance (x)	1
Crosswind distance (y)	.78
Wind velocity	.35
Cloud deviation from centreline	.28
Type of grenade	.24
Time from launch	.23
Type of grenade	.22
Vertical distance (z)	.16
Pasquill category	.05

The final area of ANN development was the architecture of the network. Here the choice was in the number of hidden processing elements or nodes and their arrangement into one or two hidden layers. The optimal architecture

arrived at, after significant investigation, was 9-9-4-1, or nine input nodes, nine nodes in the first hidden layer, four in the second hidden layer and one node in the output layer (logarithm of the volumetric extinction coefficient). In general, the fewer the number of hidden nodes the better, as this forces the model to generalize and not memorize. The larger number used in this application may well be due to synergistic effects among some of the inputs.

Model Performance

The metric chosen to assess model performance was the average relative error, E, of the validation set, which was applied to both the Gaussian and the ANN models. This is determined by

$$E = \sum_{n} \left| \frac{\sigma_m - \sigma_p}{\sigma_m} \right|, \qquad (7)$$

where $\sigma_{m,i}$ is the LCM-measured volumetric extinction coefficient (m^{-1}) and $\sigma_{p,i}$ is the model-predicted volumetric extinction coefficient (m^{-1}).

A scatter plot of the Gaussian plume model can be seen in Fig. 3. Perfect agreement between measurement and prediction would be depicted by points falling along a diagonal with a slope of 1. It can be seen that most of the data are overpredicted by the Gaussian model while a significant number (the points aligned at the bottom) were underpredicted. Here these data were arbitrarily assigned predicted values of -4.7, so that they would be shown graphically without greatly distorting the depiction of the majority of the data points. In fact, the points, in some cases, were several orders of magnitude below the measured values.

The relative error for the Gaussian model was determined to be 14.5, or almost 1.5 orders of magnitude, due largely to the underpredictions at the cloud extremities (Table 2). It is worth noting that the Gaussian plume model is the combination of 12 separate plume models, one for each grenade launched. It should also be noted that the puff model was also investigated, but the predictions were not as good as those from the plume model, probably because the standard deviations are better characterized for the more common plume model.

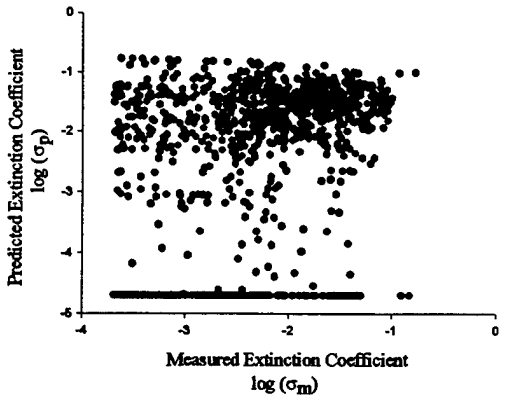


Fig. 3. Scatter plot of Gaussian plume model predictions of logarithms of volumetric extinction coefficients vs logarithm of LCM measured values for validation set of 1103 values.

Table 2. Comparison of average relative errors of ANN and Gaussian plume predictions for the validation set.

	Neural Network	*Gaussian Plume*
Error	1.78	14.5

The performance of the ANN model can be seen in Fig. 4. The data are much better distributed about the ideal line of slope 1. The relative error of 1.78 for the validation set is quite reasonable, indicating that actual predicted values are, on average, within a factor of 2 of the measured values Table 2. This difference, of course, is much smaller (0.25) when the logarithmic values are considered, as depicted in Fig. 4.

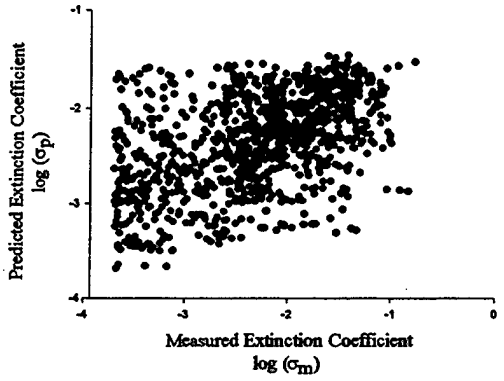


Fig. 4. Scatter plot of artificial neural network prediction of logarithm of volumetric extinction coefficient vs logarithm of LCM measured values for validation set.

Noteworthy also is the fact that the ANN model does not predict extinction coefficients above about 0.04 m^{-1}, even though some measured values were as high as 0.7 m^{-1}. This is probably due to the generalizing nature of the ANN, which was trained on a paucity of data above 0.1 m^{-1}.

It should also be borne in mind that the training, test and validation sets were limited to two tests (i.e., two separate volleys of 12 grenades each). Although more data were available, there was insufficient information on grenade compositions and meteorological conditions. Consequently only the two firings were chosen for evaluation, and data from most of the tests conducted, which could not be sufficiently characterized, were not used.

The ANN model developed, then, is not a generalized predictor of aerosol dispersion. Rather, it is a proof of principle that an artificial neural network, with the inherent flexibility of choice of input variables can provide a good prediction of a fairly complex and chaotic phenomenon, the dispersion of aerosols in the atmosphere.

Examination of the connecting weight distribution of the ANN and conducting a sensitivity analysis yields the relative significance of the input variables, as shown in Table 1. Not surprisingly, especially in light of the similarity of the atmosphere conditions, the most significant variables are spacial ones in the ground plane. At the other extreme, the Pasquill stability category, which for one test was A-B and for the other was B-C, had predictably little influence. Similarly, the vertical distance above ground had little influence, again probably due to the fact that a height of only 14m was covered by the LCM. The other variables, the type switches which indicated which grenade was used, the time after launch and the degree of cloud meander (deviation of cloud axis from wind direction at cloud centroid) all had, as could be anticipated, some influence. Also, as might be expected, the wind velocity was an important influence.

Fig. 5 depicts the extinction coefficient or concentration profile along a line of sight 1.5 m above ground at 110 m from the source and normal to the cloud longitudinal axis/wind direction. It can be seen that, in this instance, the actual cloud had a bimodal distribution,

while the Gaussian model, a composite of 12 separate Gaussian distributions, depicts a smooth monomodal distribution. (Since the source strength was unknown, the Gaussian was normalized to the highest measured extinction coefficient). The ANN model, however, did reproduce the bimodal distribution.

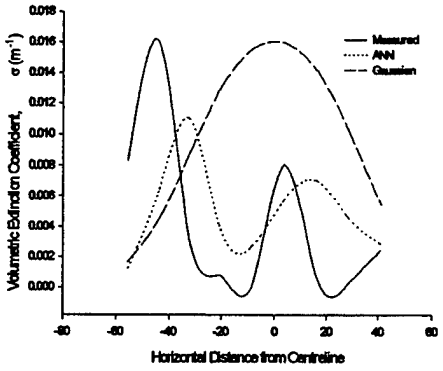


Fig. 5. Distribution of predicted and measured extinction coefficients along a line of sight 110 m from the source and normal to the cloud, 1.5 m above ground for a composite RP/metal flake cloud from a 12 grenade volley.

Conclusion

From the work reported, a number of conclusions can be drawn. The data available from the DREV trials are incomplete. The grenade compositions and values of a number of meteorological parameters were not available from the trial reports. This limited both the ability to compare different grenades and to provide a full input space to train neural networks.

On the limited data set examined, the ANN model provided better predictions than the Gaussian plume model (which, in turn, was better than the Gaussian puff model). Finally, the LCM has been found to provide time-sensitive spacial aerosol concentration distributions within clouds.

Future work being planned includes trials involving single grenades (both L8 type RP and inert simulations of M76 type metal flake) to ensure that the LCM laser signal is not extinguished by the cloud, i.e., that signals are received from throughout the cloud, and to permit comparison with COMBIC (Combined Obscuration Model for Battlefield Induced Contaminants),[17] a Gaussian-based code developed by the U.S. Army Research Laboratory.

Acknowledgement

The data reported on were collected by personnel of the Defence Research Establishment Valcartier. This work was supported, in part, by the Academic Research Program of the Department of National Defence of Canada.

References

1. Evans, A.J., "A Preliminary Assessment of the DREV Laser Cloud Mapper," CDE Porton Down, UK (1982).
2. Evans, B.T.N., Kluchert, R.E. and Levesque, R.J., "Field Evaluation of a Canadian Laser Cloud Mapper and Canadian IR Screening Aerosols," DREV 4271/82, Valcartier, Quebec (1983).
3. Evans, B.T.N., Roy, G. and Ho, J., "The Detection and Mapping of Biological Simulants: Preliminary Biological Results," DREV 4480/89, Valcartier, Quebec (1989).
4. Twardawa, P., Roy, G., Evans, B.T.N. and Vallee, G. "Cold Weather Evaluation of Visual and Infrared Screening Grenades for the Self-Protection of Armoured Fighting Vehicles," DREV R-4632/91, Quebec (1991).
5. Csanady, G.T., *Turbulent Diffusion in the Environment*, D. Reidel Publishing Co., Dordrecht Holland. (1973).
6. Pasquill, F and Smith, F.B., *Atmospheric Diffusion, 3rd Ed.*, Ellis Horwood Ltd., Chichester UK (1983).
7. Turner, D.B., *Workbook of Atmospheric Dispersion Estimates, 2nd Ed.*, Lewis, Boca Raton (1994).
8. Hanna, S.R., Briggs, G.A. and Hosker, R.P., "Handbook on Atmospheric Diffusion," DOE/TIC-11223, Springfield VA (1982).
9. Rumelhart, D.E. and McClelland, J.L., *Parallel Distributed Processing - Explorations in the Microstructure of Cognition Vol 1: Foundations*, MIT Press, Cambridge MA (1986).
10. Roy, G., Evans, B.T.N. and Gilbert, J., "An Overview of the Laser Cloud Mapper Results from JUSCAN-OASIS (Smoke Week IX) Trials," DREV R-4676/92, Quebec (1992).
11. Roy, G., Bonnier, D., De Villers, Y., Couture, G., Hutt, D. and Vallee, G., "Canadian National Report on the SOCMET Winter Test Held At DREV, Canada in March 1993," DREV-TM-9408, Quebec (1994).
12. Roy, G., Couture, G. and Vallee, G., "Canadian National Report on the SOCMET Summer Test Held at E.T.B.S., France in September 1993," DREV-TM-9434, Quebec (1995).
13. Evans, B.T.N., "An Interactive Program for Estimating Extinction and Scattering Properties of Most Particulate Clouds," MRL-R-1123, Materials Research Laboratory, Ascot Vale, Victoria, Australia (1988).
14. Patterson, D.W., *Artificial Neural Networks*, Prentice Hall, Singapore (1996).
15. Baughman D.R. and Liu, Y.A., *Neural Networks in Bioprocessing and Chemical Engineering*, Academic Press, San Diego (1996).
16. NeuralWare, Inc., *NeuralWorks Professional II/Plus*, Version 5.0. Computer Software. (1991).
17. Ayres, S.D. and DeSutter, S., *Combined Obscuration Model for Battlefield Induced Contaminants (COMBIC92) Model Documentation*, U.S. Army Research Laboratory, White Sands Missile Range NM (1995).

DETECTION OF BATTLEFIELD VISIBILITY FROM SATELLITE

Kenneth R. Knapp, Kenneth Eis, Thomas Vonder Haar and Kirk Fuller
Colorado State University / Cooperative Institute for Research in the Atmosphere
Fort Collins, CO 80523
knapp@CIRA.colostate.edu

Abstract

Today's smart weapons rely to a large extent on infrared and visible sensors seeing their targets. Atmospheric aerosols, including smoke, dust, and pollutants, contribute to the degradation of the performance of these weapons. Atmospheric scattering, due to aerosols, limits the lock-on range of most smart weapons today. CIRA is working on determining horizontal visibility and aerosol parameters remotely from the Next Generation Geostationary Observational Environmental Satellite (GOES-8) using a doubling and adding radiative transfer model developed at Colorado State University. The model has been previously used to investigate optical depth and transport of the Kuwaiti Smoke Plumes after the Persian Gulf War. Model output is validated using the National Park Services Interagency Monitoring of Protected Visual Environment (IMPROVE) data set.

1. Introduction

Aerosols degrade the performance of visible and infrared sensors, so it is important to know the extent of aerosols at and around a target. These aerosols scatter radiation emitted from or reflected by the target (signal) away from the sensor, and scatter ambient radiation (noise) into the sensor's field of view (FOV). Satellites can provide an estimation of the extinction characteristics of aerosols. Aerosols scatter solar radiation reflected by the ground (satellite noise) out of the satellite FOV and ambient solar radiation into the sensor FOV (signal). In retrieving optical depths, the noise of aerosols in satellite imagery becomes signal. For most aerosols, this has a brightening effect over dark surfaces (ocean or dense vegetation) and a darkening effect over bright surfaces. This change in the amount of solar radiation received at the satellite is dependent upon the amount of aerosol in the atmosphere, the absorptive and directional scattering characteristics of the aerosol, as well as the scattering angle from the sun to the aerosol back to the satellite (sun-earth-satellite geometry).

Previous work has concentrated on retrieving aerosol optical depth using polar orbiting satellites, such as Landsat or NOAA instruments, which have poor temporal coverage. The GOES-8 satellite provides better imagery than its predecessor GOES-7 at higher temporal resolution than the polar orbiting sensors. Work was concentrated on sensing aerosols over IMPROVE sites in the Eastern U.S. An existing Adding/Doubling Radiative transfer model (Greenwald and Stephens, 1988) was used to retrieve optical depths from GOES-8 visible imagery with assumed aerosol optical properties. Although, recent work has allowed estimation of these aerosol optical properties from *in situ* chemical composition data measured by the IMPROVE network. Comparisons of the model output were made to measurements from nephelometers and transmissometers also of the IMPROVE network. Retrievals were for 4 case periods (9 days each) during the summer of 1995 over the Eastern U.S. An error budget was

calculated and retrievals had an estimated error of $\Delta\tau = \pm(0.05 - 0.16)$ for τ ranging from 0.1 to 1.0.

Section 2 presents the retrieval method followed by a description of the datasets and the Adding/Doubling model in sections 3 and 4. Comparisons to surface data are shown in section 5, and conclusions are made in section 6

2. Optical Depth Retrieval Method

Optical depths were retrieved from GOES-8 imagery using an Adding/Doubling radiative transfer (A/D) model. Figure 1 shows a schematic of the retrieval process. The A/D model uses reflectances measured by the GOES-8 visible channel and assumed aerosol optical properties as input. Data from the GOES-8 system includes a background reflectance for a particular pixel, the reflectance of a haze over the same pixel and sun-earth-satellite geometry. The background reflectance was chosen as the lowest (darkest) pixel value during a ten day period for that specific time, excluding cloud shadows. The aerosol optical properties used in the A/D model are asymmetry parameter (g) and the single scatter albedo (ω_o). The A/D model calculates optical depth as the amount of aerosol with the assumed optical properties needed to increase the satellite detected reflectance from the background reflectance to that observed by the satellite with haze present. This method of retrieval requires excellent pixel co-registration and accurate sensor calibration. Co-registration is the controlling of the sensor such that the same pixel represents the same earth point in successive images and noise is estimated at ±7 pixels between successive days (Menzel and Purdom, 1994). However, imagery used in this study was manually navigated using visible surface features (e.g. lakes and rivers) to an estimated ±1 pixel. Calibration of the GOES-8 data is the conversion of transmitted GOES-8 counts to a reflectance value. This was accomplished using calibration coefficients from the home page of Dennis Chesters at NASA/GSFC. These were pre-flight calibration values which do not account for possible in-flight sensor degradation.

Optical depths were retrieved over the Eastern U.S. for four 9-day periods during the summer of 1995 over IMPROVE sites. These periods, which occurred in late May, mid July, mid August and late August, were determined from IMPROVE data and daily weather maps. IMPROVE data showed high extinction and scattering coefficients and surface analyses showed high pressure areas over the east during these times.

3. Data

The GOES-8 satellite has many advantages over its predecessor, GOES-7, for aerosol optical depth retrieval. GOES-7 had a non-linear 6-bit digitization, whereas GOES-8 has a linear 10-bit digitization, which allowed for more resolved changes in satellite detected radiance. The signal-to-noise ratio was improved by a factor of 4, providing higher confidence of the pixel count. This high quality sensor at geostationary orbit provides visible imagery at 15 minute intervals over the continental U.S.

A large, Eastern U.S. sector of GOES-8 imagery was archived during the summer of 1995 for morning hours, 12:15 through 15:31z for the purpose of retrieving τ. The sector area was determined by positions of IMPROVE sites. It was later expanded west in July to incorporate another IMPROVE site (the nephelometer at Mammoth Caves National Park) and extended until 20:45z, to include more daylight hours for comparison.

The IMPROVE network consists of more than 60 aerosol monitoring sites at National Parks (N.P.) around the United States. Instruments used to monitor the air quality include: transmissometers, nephelometers, aerosol collection instruments and atmospheric state variable instruments.

There are three nephelometer sites which measure the surface scattering coefficient (b_{scat}) in the area encompassed by the GOES-8 collection region at: Dolly Sods, West Virginia near the Monongehela National Forest (DOSO), Great Smoky Mountains N.P., Tennessee (GRSM), and Mammoth Cave N.P., Kentucky (MACA). The nephelometer measures atmospheric scattering at the wavelength 0.55 μm. Also, Shenandoah N.P. in Virginia (SHEN) has a transmissometer that measures the extinction coefficient (b_{ext}) at 0.55μm. Measurements by these instruments will be referred to as optical coefficients, because they refer to two separate types of measurements. They are used nearly synonymously here because the absorption coefficient is usually negligible.

Also, temporal, spatial and spectral differences in these datasets increase error in comparing their measurements of aerosols to retrieved optical depths. GOES-8 imagery is available over the Eastern U.S. at 15 minute intervals, whereas the IMPROVE data reports conditions on the hour. Retrievals of optical depth from GOES-8 were averaged to the nearest hour when compared to surface data. Also, the IMPROVE instruments have a sample volume which is about 10 orders of magnitude smaller than the GOES-8 visible channel sample volume, which is a vertical cone through the atmosphere with a 1 km^2 footprint. And spectrally, the GOES-8 visible channel has a range of 0.55-0.75μm, while the IMPROVE instruments have a narrow detection band centered at 0.55 μm.

4. Adding/Doubling Model

The adding/doubling, multiple scattering model used in this study was developed by Greenwald and Stephens (1988). It was designed to perform sky color, intensity and object contrast simulations (Tsay et. al., 1991). After some modifications by Graeme Stephens and Jan Behunek, it currently calculates optical depth from satellite detected reflectances, sun-earth-satellite geometry, and aerosol optical properties. The following is an overview of the model and its application to aerosol optical depth retrieval. For a more rigorous description of model derivation, see Greenwald and Stephens (1988). This method has previously been used to retrieve optical depths from smoke plumes during the 1991 Kuwaiti oil fires (Behunek et al., 1993).

Theory

The equation of radiative transfer for a plane-parallel, scattering atmosphere is

$$\mu\frac{dL(\tau;\mu,\phi)}{d\tau} = -L(\tau;\mu,\phi) + \frac{\omega_o}{4\pi}\int_0^{2\pi}\int_{-1}^{1} P(\tau;\mu,\phi,\mu',\phi')L(\tau;\mu',\phi')d\mu'd\phi' + J(\tau;\mu,\phi) \qquad (1)$$

where J, the "pseudo-source" term, is

$$J(\tau;\mu,\phi) = \frac{\omega_o}{4\pi}F_o P(\tau;\mu,\phi,-\mu_o,\phi_o)e^{-\tau/\mu_o} + \frac{\omega_o}{4\pi}F_o\rho_s P(\tau;\mu,\phi,\mu_o,\phi_o)e^{-(2\tau^*-\tau)/\mu_o} \qquad (2)$$

L is radiance, $\mu=\cos\theta$, θ and ϕ are geometric angles, τ is optical depth, P is the phase function, F_o is the solar irradiance at the top of the atmosphere (TOA), ρ_s is the surface specular reflectance

and τ^* is the optical depth of the atmosphere. The first term in equation 1 and the second term in equation 2 represent the extinction of the solar radiance reflected by the surface or aerosol. The second term in equation 1 and the first term in equation 2 represent the radiance scattered by the aerosol into the satellite FOV. The scattering of reflected radiance from a nearby pixel into the satellite FOV (a blurring effect) is not accounted for by this model. J is a pseudo-source term because there is no source for visible radiation in the atmosphere, but the aerosol scattering of the direct solar beam can act as a source. The phase function used is the Henyey-Greenstein phase function.

By expanding the phase function using Legendre polynomials, the intensity using Fourier series and using a Gaussian quadrature approximation, equation 1 is transformed into a series of matrix equations that can be solved using the adding/doubling technique. The end product is a 32-stream radiative transfer model which calculates the theoretical satellite observed reflectance (ρ_{sat}), at 16 satellite zenith angles (θ) due to an aerosol layer with the optical parameters g and ω_o at the sun-earth-satellite geometry (μ_o, ϕ_o, ϕ) and ρ_s determined from GOES-8 imagery.

Optical depth was then retrieved iteratively. By using the known latitude, longitude and time of the image, the scattering angles (μ, ϕ, μ_o, ϕ_o) were calculated. A background reflectance was found through an algorithm that used the darkest pixel over a time series of images. Then assuming some g and ω_o and starting with an initial guess for τ, a theoretical satellite-detected reflectance was calculated. This was then compared to the observed satellite reflectance, and a new estimate of τ was calculated from the difference in reflectances, iteratively solving for $\tau_{A/D}$.

Because the model used a background reflectance as a comparison to reflectance of haze, it only calculated the difference in τ between the background reflectance and haze satellite images due to an increase in τ from a layer of aerosols with the assumed optical properties. The reflectance used is not the actual surface reflectance, rather the darkest pixel at a location measured during the case, a background reflectance. This contained some background aerosol signal. Because the optical depth is a difference, the nearly constant Rayleigh component and background aerosol optical depth are subtracted out. So, ρ_s is a background reflectance, not a surface reflectance.

Critical Albedo

Investigation of model output has shown a scenario that renders optical depth undetectable. The same aerosol that brightens an originally dark image (e.g. a dense forest) would also darken an originally bright image (e.g. snow cover). Between these effects is a surface reflectance for which changes in aerosol amount have no effect on the reflected radiance. This condition is called the critical albedo region. It is defined as a range of surface reflectances where an increase in aerosol optical depth has no detectable effect in the amount of reflected solar radiation. This critical albedo is a function of the optical parameters of the aerosol and the solar geometry. Figure 2 shows an example of this effect. The dashed lines represent the change in satellite-detected reflectance due to an optical depth as a function of surface reflectance calculated from the A/D model. The scatter of dots are actual points from a GOES-8 visible image of the Shenandoah area. These lines cross at $\rho_s = 0.3$, showing that for the assumed aerosol optical properties the background reflectances do not approach the critical albedo region, which is 0.3 for this case.

Model Sensitivity and Error

Errors such as co-registration and calibration have already been discussed. Errors in the retrieval due to uncertainty in the A/D model parameters also exist. Table 1 shows the percent change in $\tau_{A/D}$ due to a 5% change in an input parameter. It is clear that errors in the surface reflectance or single scatter albedo can cause large errors in the retrieval of optical depth. Uncertainty in the surface reflectance was minimized in the data processing. Aerosol optical parameters used here ($\omega_o = 0.956$ and $g = 0.75$) were chosen from previous work in the Eastern U.S. and have an estimated error of ±3 and 1% for g and ω_o respectively. Therefore, $\tau_{A/D}$ retrievals have an estimated error of $\Delta\tau = \pm(0.05\text{-}0.16)$ for $\tau_{A/D}$ values of 0.05 to 1.0.

5. Comparison to Surface Data

Directly comparing surface terms (b_{ext} or b_{scat}) to a vertically integrated quantity (τ) can be ambiguous. These coefficients vary with height and are related to τ by:

$$\tau = \int_{sfc}^{TOA} b_{ext}(z)dz = \int_{sfc}^{TOA} \left[b_{scat}(z) + b_{abs}(z)\right]dz \approx \int_{sfc}^{TOA} b_{scat}(z)dz \qquad (3)$$

where $b_{abs}(z)$ is the absorption coefficient of the aerosol as a function of height in the atmosphere. The last relation in equation 3 is justified when absorption is small. Because the background reflectance is used, the change in optical depth between the pristine day and the hazy day is detected. This change in optical depth is assumed to be confined to a well mixed boundary layer. Then the optical coefficients are no longer a function of height, thus:

$$\tau = b_{ext}\,\Delta z \approx b_{scat}\,\Delta z \qquad (4)$$

where the optical coefficients are vertical averages in a boundary layer with height Δz.

b vs. $\tau_{A/D}$

Figure 3 shows scatter plots of satellite retrieved optical depth vs. optical coefficients from IMPROVE data (b_{ext} and b_{scat}) for each case and site. The correlation coefficients of the graphs are provided in Table 2. Overall, 10 of 13 show positive correlation, with better comparisons at GRSM. When first approaching these comparisons, it was expected that under low haze conditions (small b), there would be more noise because of less aerosol signal. Conversely, we expected more accuracy under hazy conditions. This can be seen in the plots for MACA cases 2 and 4 for $b < 0.3$ km^{-1}, although not all plots show this trend. Plots for case 1 have a small range of b values, which provide little insight into the retrieval accuracy. Cases 3 and 4 (late summer) seemed to have better correlations and more data points than earlier cases. Also, only three cases had any values of $b > 0.6$ km^{-1} (visibility less than 6 km). Other comparisons (e.g. DOSO case 2 and MACA case 3) show broad distribution of points without a definite relationship. This could be due to many reasons such as variations in aerosol vertical structure, aerosol optical properties or cloud contamination.

These plots are dependent upon the vertical distribution of the aerosol. An attempt to account for the variation in Δz was made using National Weather Service rawinsonde data, but variations in terrain and the large spacing between stations did not increase the correlation of the comparisons. A Lidar needs to be co-located with the surface aerosol observations, because current understanding of the vertical distribution of aerosols is limited. The broad distribution of points could also occur from a layer of aerosols advected above the boundary layer. Clouds were

visually filtered prior to optical depth retrievals. Errant τ retrieval over clouds (especially thin cirrus) would return erroneously high τ values. Changes in surface reflectance properties due to rain might also affect the retrievals. For instance, the ranges of optical coefficients in case 1 were limited due to rain occurrences twice during the time period. Other cases had no rain or rain near the end or beginning of the case. In summary, encouraging comparisons were found over GRSM and during the late summer cases.

IMPROVE Visibility vs. Satellite Visibility

Converting these values to a visibility requires use of the Koschmeider equation:

$$\mathrm{Vis} = \frac{3.912}{b_{ext}}. \tag{5}$$

The retrieved optical depth can be converted to b_{ext} using an estimate of Δz in equation 4. This has been done for GRSM case 2 (not shown in figure 3). Figure 4a shows the comparison of $\tau_{A/D}$ vs. b_{scat}. Figure 4b shows the same comparison in visibility coordinates ($\tau_{A/D}$ was converted using $\Delta z = 1.5$km). It can be seen that there is less noise for lower visibilities (Vis < 25 km), but the lowest visibility measured by the IMPROVE site is greater than 10 km. The region of visibilities less than 10 km would provide adequate aerosol signal, but no comparisons have more than one value that low.

6. Conclusions and Future Work

Aerosol optical depths were retrieved over IMPROVE sites in the Eastern U.S. with encouraging results. Correlations of most comparisons were positive and statistically significant. Although uncertainties exist that cause scatter in the comparisons. Aerosol vertical structure variations, relative humidity changes (which causes changes in g and ω_o), cloud contamination and changes in surface reflectance features (e.g. due to rain events) are speculated causes in some of the less correlated comparisons. Knapp (1996) showed that by adjusting g and ω_o using an a priori surface relative humidity increased correlation in the comparisons. Future retrievals should include estimation of boundary layer moisture content. More comparisons need to be made in heavy haze conditions, to further define what the lower limit of aerosol detectability is. Also, future work needs to have continuous optical depth retrievals, rather than case studies as presented here. This would allow insight into the temporal variability of the surface reflectance and the affect rain has on the retrievals. IMPROVE sites in this work were located in densely forested areas. Further work should also include areas with different background reflectances (deserts, plains, etc.).

Using this remote sensing method, aerosol climatologies could be developed globally that would allow DOD mission planners to get a first guess on the operational limits of their standoff weapons' performance.

Acknowledgments

The funding for this work was made possible through the Department of Defense Center for Geosciences - Phase II, grant #DAAH04-94-G-0420.

References

Behunek, J.L, J.M. Forsythe, and T.H. Vonder Haar, 1993: Satellite analysis of Kuwaiti oil smoke plumes. In Proceedings of the 1993 Battlefield Atmospherics Conference, 30 Nov. - 2 Dec. 1993, Las Cruces, NM, U.S. Army Research Lab., White Sands Missile Range, NM, 357-368.

Chesters, Dennis, 1994: http://climate-f.gsfc.nasa.gov/~chesters/text/imager.calibration.html

Greenwald, T. J. and G. L. Stephens, 1988: Application of an Adding-Doubling Model to Visibility Problems, C.S.U. Atm. Sci. Paper, 89 pp.

Kaufman, Y. J., 1987: Satellite Sensing of Aerosol Absorption, *J. Geophys. Res.*, **92**, 4307-4317.

Knapp, Kenneth R., 1996: Radiative effects of boundary layer aerosols: Detectability by GOES-8 and estimation of their direct effect, Master's of Science Thesis, C.S.U., 112 pp.

Menzel, W. P. and J. F. W. Purdom, 1994: Introducing GOES-I: The first of a new generation of Geostationary Operational Environmental Satellites, *Bull. of the Amer. Met. Soc.*, **75**, 757-781.

Tsay, S.-C., G. L. Stephens and T. J. Greenwald, 1991: An investigation of aerosol microstructure on visual air quality, *Atm. Env*, **25A**, 1039-1053.

Table 1 - The percentage change in τ due to a 5% change in the input parameter.

INPUT PARAMETER	% CHANGE IN τ
Calibration	10
Asymmetry	20
Surface Reflectance	34
Single Scatter Albedo	35

Table 2 - Table of correlation coefficients (and number of samples) for all cases and IMPROVE sites comparing b vs. $\tau_{A/D}$.

	CASE 1	CASE 2	CASE 3	CASE 4
	May 20-28	July 10-19	Aug. 8-18	Aug. 28 - Sep. 6
DOSO	0.224 (10)	-0.390 (20)	-	0.701 (21)
GRSM	0.870 (16)	0.763 (30)	0.719 (21)	0.438 (41)
MACA	-	0.265 (39)	0.562 (29)	0.536 (53)
SHEN	0.993 (9)	0.669 (9)	-	0.813 (20)

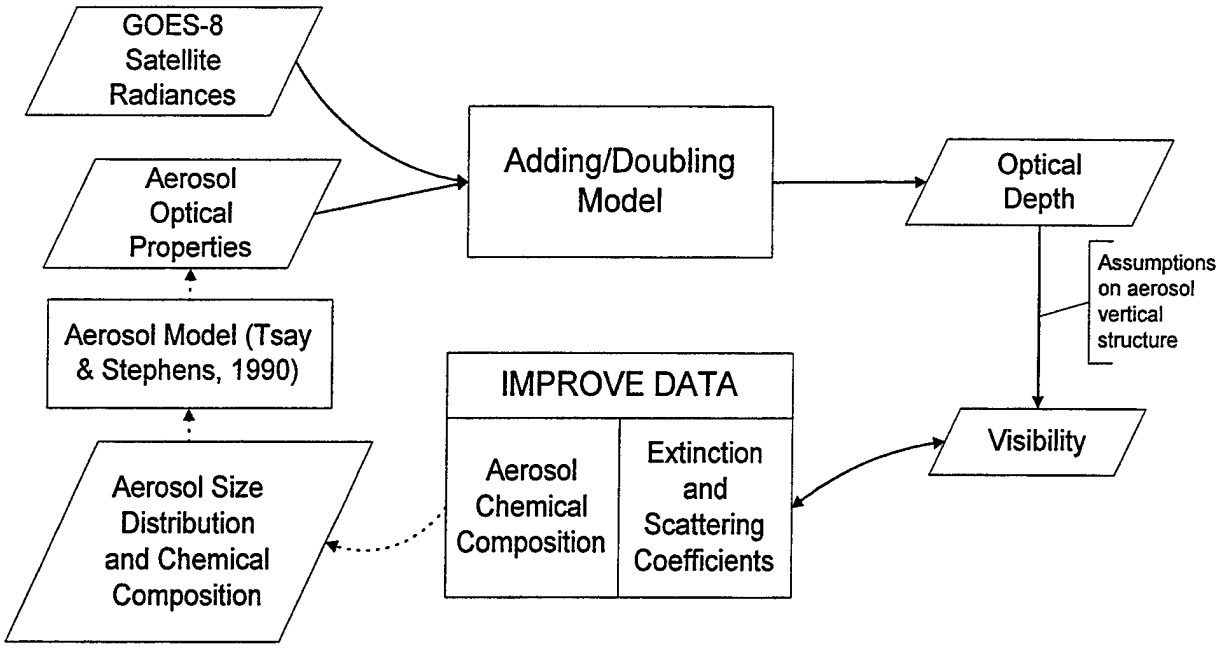


Figure 1 - Retrieval method flowchart. Solid arrows depict steps used in current results. Dashed arrows represent steps now possible through recent work.

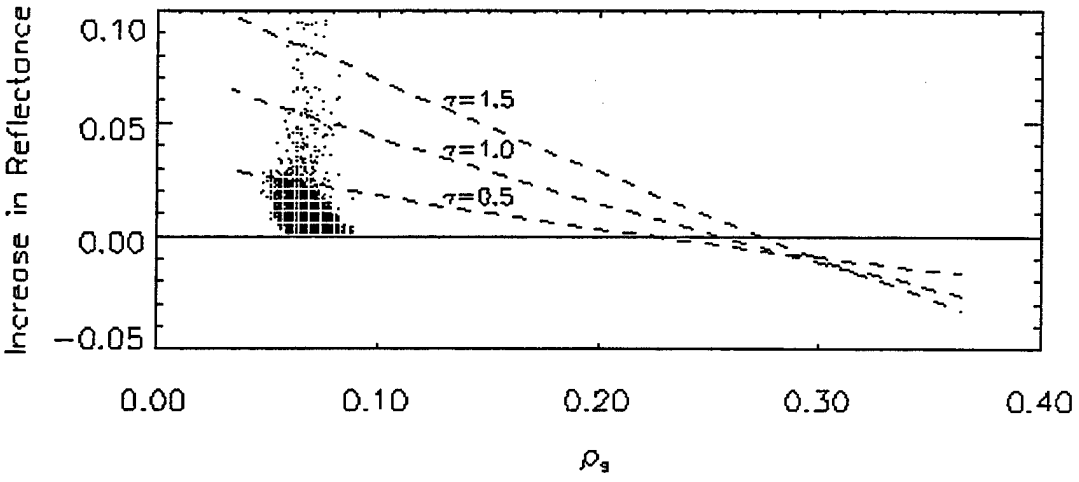


Figure 2 - An example of the critical albedo near $\rho_s = 0.3$. Dashed lines are changes in reflectance as calculated by the A/D model due to differing optical depths. Points are actual pixels from a GOES-8 image over Shenandoah N.P.

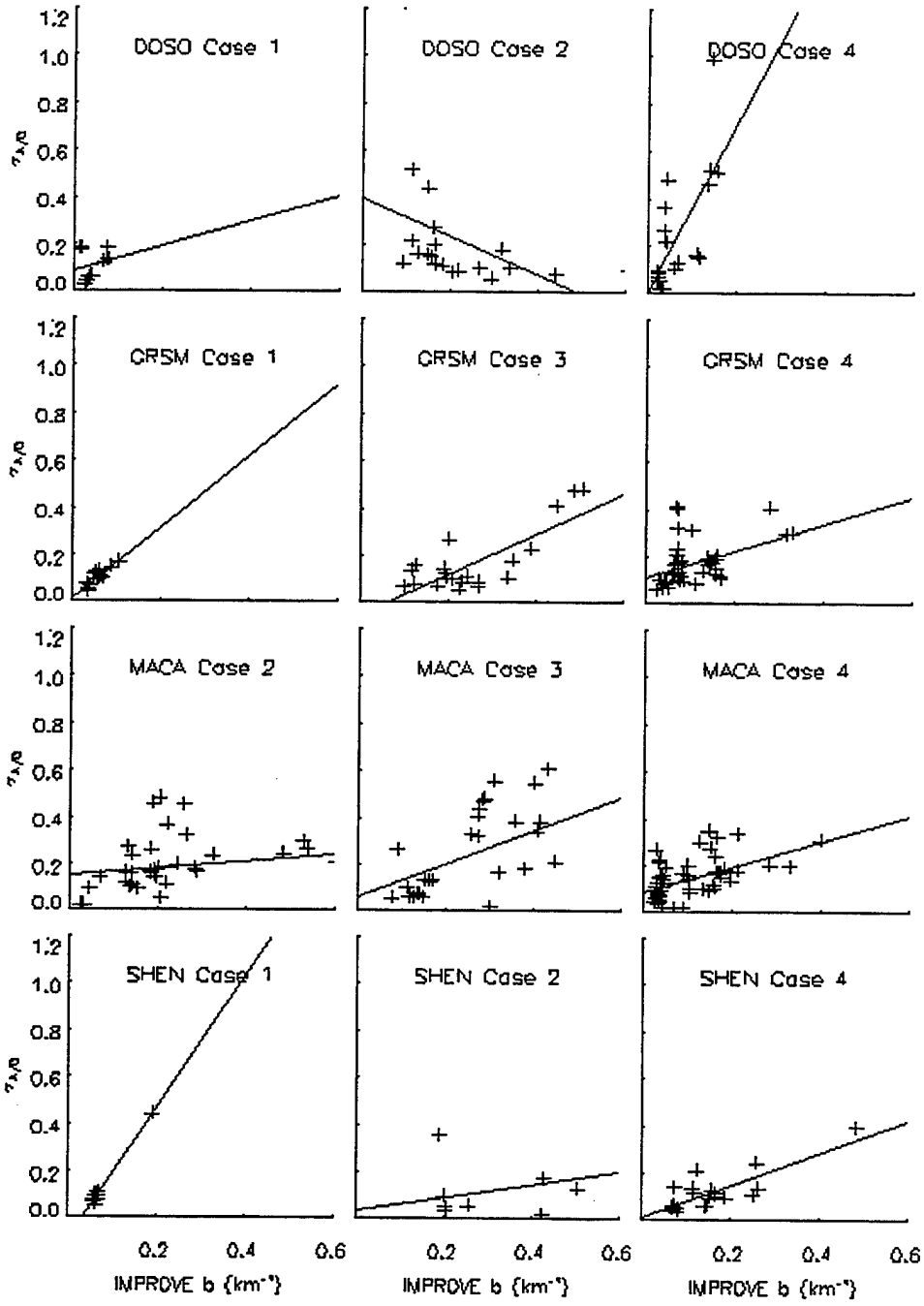


Figure 3 - Scatter plots of retrieved optical depths ($\tau_{A/D}$) vs. coefficients measured by the IMPROVE network. Lines represent linear regression best fit.

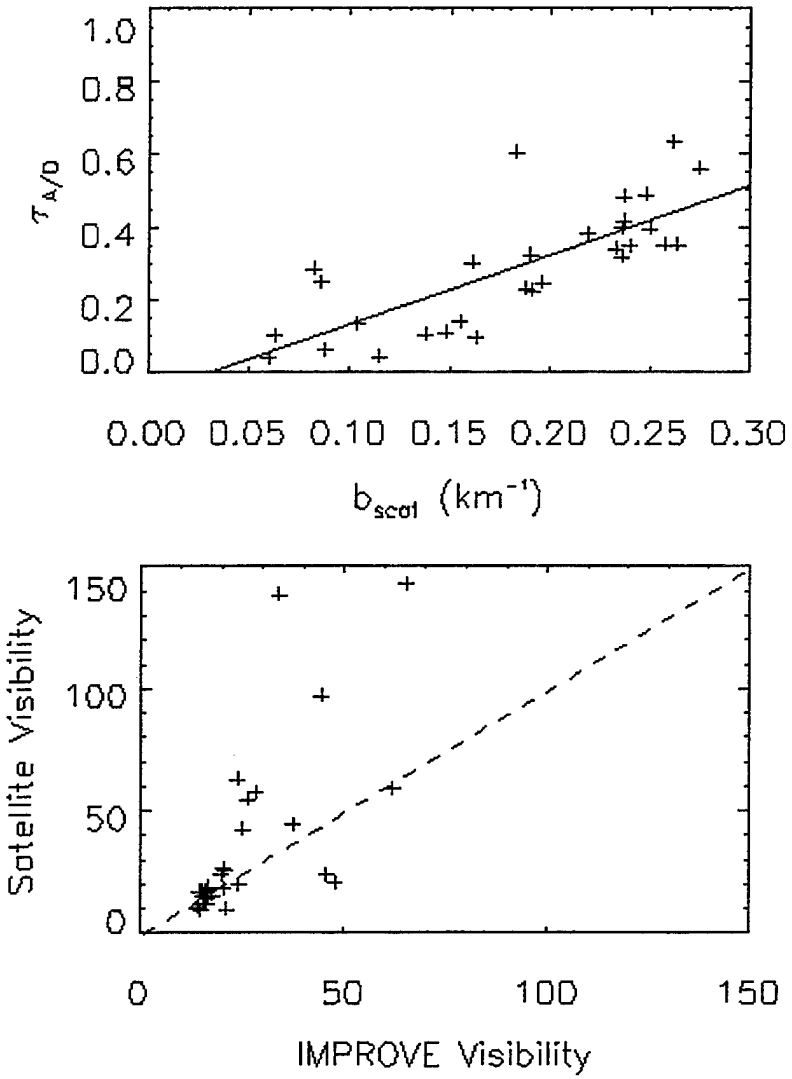


Figure 4 - a) Scatter plot of GRSM case 2 (not shown in fig. 3). Line represents linear regression best fit. b) Scatter plot of GRSM case 2 converted to visibility using $\Delta z = 1.5$ km. Dashed line is the one-to-one line.

Forecasting Applications of High Resolution Diurnal Satellite Cloud Composite Climatologies over Former Yugoslavia and the Adriatic Sea

Timothy J. Hall, Donald L. Reinke, and Thomas H. Vonder Haar

Colorado State University/CIRA
Fort Collins CO 80523
Ph: (970) 491-8398 Fax: (970) 491-8241
hall@cira.colostate.edu

1. Introduction

Clouds are a primary obstacle for military systems requiring visual or infrared target acquisition. In the past fifteen years, satellite data has greatly advanced our understanding of clouds. In this study we expand on an idea put forward by Reinke et al. (1992). They suggested that high resolution satellite cloud climatologies could be used to create a forecasting tool through a combination of cloud frequency of occurrence and cloud persistence composites.

In this paper we describe forecasting tools developed using the new Climatological and Historical ANalysis of Clouds for Environmental Simulations (CHANCES) database (Vonder Haar et al. 1995). The results show the utility of similar satellite derived climatologies for various modeling and operational forecasting applications. The analysis is limited to the summer season for a domain centered over the former Yugoslavia and Adriatic Sea. Specific target forecast applications are demonstrated for satellite data centered over the city of Sarajevo.

2. Background

Kornfield et al. (1967) created the first cloud composites for research by sequentially superimposing satellite images on photographic paper. The early composites were useful for the study of large-scale cloud systems and the general circulation. Eighteen years later Klitch et al. (1985) ushered the compositing technique into the computer age by constructing cloud composites entirely in the digital domain. They used satellite composites to study the relation of convection to terrain in Colorado. More recently, Gibson and Vonder Haar (1990) completed a similar study of convection in the southeastern United States.

On a global scale, there are two primary ongoing satellite cloud climatology projects. The International Satellite Cloud Climatology Project (ISCCP) has created a global database of many cloud properties using visible and infrared satellite data with 3hr temporal, and 250 x 250 km spatial resolution. Statistics for some regional data are also available at resolutions as low as 30km (Rossow 1993). The U.S. Air Force produces a cloud composite for operational purposes called the real-time nephanalysis (RTNEPH) (Kiess and Cox 1988). The RTNEPH is a combination of satellite and surface data and has 47 km horizontal resolution. Cloud climatologies have been created using RTNEPH (Hughes and Henderson-Sellers 1985), however, clouds vary significantly on much finer scales.

A very fine space/time domain is crucial to understanding clouds in relation to mesoscale forcings (Reinke et al. 1992), and hence is critical to the creation of cloud climatology composites that can be used as forecast tools. This is specifically true for Terminal Aerodrome Forecasts (TAFS) and remote location target forecasts for offensive operations, reconnaissance and as inputs to electro-optical tactical/meteorological decision aids. Vonder Haar et al. (1993) show that the RTNEPH cloud database as well as Probability-of-Cloud-Free-Line-of-Sight

(PCFLOS) models can be significantly improved through the development and use of a high resolution satellite cloud database.

Today's PCFLOS models are based on surface observations derived on a spatial resolution of approximately 200 km. The results presented by Vonder Haar et al. (1993) show that approximately 90 percent of all cloud-free intervals are less than 10km. So, climatological forecasts and models based on surface data will not provide a representative measure of the impact of clouds in many geographic locations (Reinke et al. 1995).

The CHANCES database used in this study was sponsored by a Small Business Innovative Research (SBIR) Phase II, U.S. Air Force grant. The purpose was to produce a 1-yr, 1-hr, 5-km resolution global cloud/no cloud (CNC) database product and to demonstrate the feasibility of producing a longer term (5-yr) climatological cloud database. CHANCES is ideal for the construction of fine scale satellite cloud composites.

3. Data

The CHANCES database is a 1-yr (Feb. 1, 1994 - Jan. 31, 1995) global satellite imagery database with 1-hr temporal and 5-km spatial resolution (Vonder Haar et al. 1995). Each chances image is a "seamless" global image created from a combination of geostationary and polar orbiting satellites. For this study we focused on a sector centered over the former Yugoslavia. The sector spans from approximately 23°E to 33°E and 42°N to 47°N. This falls entirely in the domain of the METEOSAT geostationary satellite.

To produce CHANCES, STC-METSAT in Fort Collins, Colorado did an enormous amount of pre-processing. This pre-processing included navigation and alignment, correction for various characteristic satellite errors, the creation of radiance background information, and the construction of binary CNC images. Kidder and Vonder Haar (1995) discuss other possible sources of error that can impact the analysis of meteorological satellite imagery including: attenuation, background contrast, contamination, displacement, foreshortening, sensor lag, signal interference , sun-satellite geometry, and viewing angle.

4. Method

Construction of composites begins with the geographic alignment of each image with a base image. This was done as part of CHANCES pre-processing as described in the previous section. In this study, we used only quality-controlled images without noise or data drops.

The aligned images were used to construct seasonal cloud frequency of occurrence composites for each hour of the day for the Yugoslavia/Adriatic sector. Figures 1a - 1d are cloud frequency of occurrence composites for 12, 15, 18 and 21 UTC, respectively. For this study, the summer season data spans the forty-five day period from June 22, 1994 to August 5, 1994.

In figures 1a - 1d, the frequency at each pixel was computed by simply dividing the number of cloudy days at each hour at that pixel by the number of days with cloud data available at that same pixel. The resultant cloud frequency of occurrence at each pixel was then assigned a specific brightness and displayed as a composite image. Variation of brightness from pixel to pixel in an image represents the variation in cloud frequency from location to location. The actual percentage frequency value can be estimated by comparing the brightness of the target pixel with the scale at the bottom of each image. The scale spans from 0 percent on the left (black) to 100 percent on the right (white).

Conditional probability images were prepared by comparing each image from an initial time with an image from a forecast time. If a cloud (or no cloud) exists at a pixel on the initial image and a cloud exists at the same pixel location of the target (forecast) image it is summed for that pixel. An algorithm repeated this process for every pixel of every image for each of the forty-five days of summer 1994 to compile data for one to twelve hours beyond each hour of the day.

Six hours represents the most important forecast interval for Air Force terminal aerodrome forecasts (TAFs) since active TAFs are updated every six hours. Target forecasts for offensive strikes, or reconnaissance missions may need accurate cloud forecasts with a six to twelve hour lead time or greater.

We compiled persistence data for two simple types of conditional probability forecasts: (1) Cloudy at forecast time given cloudy at initial time (type 1) ; (2) Cloudy at forecast time given clear at initial time (type 2) . Two other scenarios (clear at forecast time given clear at initial time and clear at forecast time given cloudy at initial time) can be constructed from (1) and (2), respectively, by subtracting the probability of being cloudy at forecast time from 100 percent. As with the cloud frequency data, the conditional probability (persistence) data can also be displayed as an image. Figures 2a and 2b are type 2 conditional probability images for six and nine hours after 6 UTC (8 LST). Figure 2a represents the probability of cloud at 12 UTC (14 LST) at each pixel when the pixel is clear at 6 UTC. Similarly, figure 2b depicts the probability of cloud at 15 UTC (17 LST). Following images through chronologically from the initial time (including the intermediate times not shown), one finds that the quality of a persistence forecast of clear for this sector goes down with time (e.g., the probability of cloud goes up). This is a signal of the convective diurnal cycle of cloud cover over this region in summer.

With cloud frequency and cloud persistence data, you have all the necessary tools to produce simple probability forecasts for cloud at each pixel. Reinke et al. (1990) suggest various techniques. They note that a cloud frequency composite itself can be used as a forecast tool. The frequency of occurrence of cloud over each pixel at any given time is a reasonable first guess for a cloud/no cloud forecast at that location. Individual composites can be compared to note the change in frequency of occurrence of cloud at a location. This would represent the systematic variation of cloud cover over that pixel. To account for random variation in cloud cover you need to consider information in the persistence images. Reinke et al. (1990) suggest two ways to include the persistence data. First, you could compute cloud occurrence probability by adding the cloud persistence probability to the frequency. Second, you could use both probabilities in a forecast matrix in which the final probability is based on the cloud frequency and/or conditional probability exceeding a pre-determined threshold. To get even more sophisticated, the initial image could be stratified by wind direction, air mass, or other climatologically significant variable as has been done by the Air Force Combat Climatology Center (AFCCC, formerly ETAC) for many years with conditional climatology ceiling and visibility tables.

For this study, we develop a forecast tool for Sarajevo that combines cloud frequency and persistence data (Tables 1 and 2). These tables were created by extracting cloud frequency and persistence information from many composite images for the pixel centered directed over Sarajevo. As a forecaster, this type of data would be a valuable asset for a TAF or target forecast. From personal experience, we believe that the greatest inhibitor to an accurate target forecast is not having first-hand knowledge of the weather in the target area. For remote targets, satellite-derived conditional probabilities (Tables 1 - 4) could be a viable surrogate to first-hand experience and substitute for the conditional ceiling and visibility tables familiar to forecasters in any Air Force base weather station. A forecaster could combine these statistics with knowledge of the current and forecast synoptic and mesoscale weather conditions to optimize the forecast. In the results section below, we discuss an empirical climatological forecast index developed in this study.

In Tables 3 and 4, we present a more sophisticated type of conditional probability computed for Sarajevo. For these statistics the initial condition was stratified by the percentage of cloudy or clear pixels in a 15 km x 15 km region surrounding the target location. The initial conditions were divided into three categories: (1) Less than 33 percent of pixels cloudy (clear) at initial time (Table 3); (2) 33 to 66 percent of pixels cloudy (clear) at initial time (not shown); (3) 66 to

100 percent of pixels cloudy at initial time (not shown). Table 3 depicts the conditional probability of cloud over Sarajevo at forecast times of 1-12 hours given the 33 percent or less of the pixels within 15 km of the target are overcast at the initial time. This adds a level of spatial dependence to the conditional probabilities that cannot be well duplicated with surface observation data, especially as the radius from the target increases. For instance you could expand out to 25 km from the target pixel. In the next section we compare these spatially conditional probabilities to the single pixel conditional probabilities presented in Table 1.

5. Results/Discussion

Figure 3 is a histogram of the average cloudy infrared pixel counts at each hour of the day for the Yugoslavia sector shown in figures 1 and 2. This represents the systematic change in cloud cover for the summer season. The minimum occurs just after sunrise at 7 LST (5 UTC) while the maximum occurs at 18 LST (16 UTC). This suggests that a majority of the summer season cloud cover is convective in nature. Figure 4 is a histogram of IR pixel counts at each hour of the day with a brightness temperature less than -40°C to isolate deep convection. The maximum occurs at 17 LST (15 UTC). The second column of Table 1 contains the cloud percentage frequency of occurrence at each time of day for the pixel centered over Sarajevo. Just as with the seasonal average for the entire sector (Fig. 3), there is a maximum in cloud cover at 18 LST (16 UTC). The data from Table 1 represents the systematic variation of cloud over Sarajevo, and would make a good climatological forecast in the absence of other data. However, the forecast could be greatly improved by combining the frequency statistics with cloud persistence data. Table 2 is a YES/NO climatological cloud forecast decision matrix constructed by combining the frequency and persistence data (Table 1) into a single binary index. "1" (YES) is a forecast for cloud and "0" (NO) is a forecast for clear.

Although definitive YES/NO cloud criteria are certainly a topic for further research, we use the following criteria for this study. Of the two types of data in Table 1 (frequency occurrence and conditional probability), the conditional probability is a more reliable forecast tool since it includes an initial condition. Therefore, we weight the YES/NO cloud decision more heavily to the persistence probability. If the conditional probability at any hour is greater than 70 percent, then the forecast for cloud is YES. If the persistence probability is less than 70 percent, but greater than 50 percent then we compute the average of the frequency of occurrence and the persistence probability for the forecast time. If the average is greater than 60 percent then the forecast is YES ("1"), otherwise it is NO ("0"). These particular thresholds were chosen so that the mean amount of cloud predicted in the YES/NO matrix of Table 2 was comparable to the average frequency of occurrence of cloud for all hours from column two of Table 1. The average of the frequency of occurrence for all the hours is 41 percent. Assigning 1 for YES and 0 for No, the average frequency of occurrence of cloud as predicted by the corresponding forecast matrix (Table 5) is 44 percent.

The importance of this weighting scheme is illustrated in Table 1. At 4 UTC (6 LST) the systematic frequency of occurrence of cloud is 17 percent. However, when cloud occurs at 3 UTC the probability of cloud at 4 UTC is 83 percent. Similarly, the conditional probability of cloud at 6 UTC given cloud at 3 UTC is 67 percent compared to a systematic occurrence of 14 percent. This meteorologically makes sense for Sarajevo. In the early morning any cloud is probably not convective but rather is part of a synoptic scale disturbance and hence would be more likely to persist due to larger scale dynamics. Other data in Table 1 further illustrate the importance of heavily weighting the conditional probability in the forecast index. Note that given cloud over Sarajevo at 6 UTC, the 12 hour forecast for cloud at 18 UTC is 100 percent. The systematic variation of cloud for summer 1994 was for overcast 68 percent of the time at 18

UTC. In fact, given an initial condition of cloud at any hour after 5 UTC, the conditional probability of being overcast at 18 UTC is higher than 68 percent.

As mentioned in the previous section of this paper, a more sophisticated approach is to stratify the probability in terms of a percentage of pixels in a region surrounding the target that are cloudy (clear) at the initial time. Table 4 is a forecast matrix derived from the persistence probabilities and cloud frequencies in Table 3. By considering pixels in a 15 km region surrounding the target in the conditional probability, as opposed to a single pixel, the forecast can change significantly. Table 4 is a CNC forecast matrix analogous to Table 2 with an initial condition of less than 33 percent of pixels within 15 km of the Sarajevo pixels classified as overcast. Comparing Table 4 to Table 2, one can qualitatively see that the amount of YES ("1") cloud forecasts is greatly reduced. The mean cloud forecast for all times in Table 4 is 21 percent. In contrast, the mean cloud amount from Table 2 is 44 percent. The mean amount of cloud predicted with an initial condition of 66 percent of pixels within 15 km cloudy is 44 percent. Evidently, considering only a single pixel at the initial time is equivalent to assuming overcast conditions over a larger region. This same bias would likely occur with conditional probabilities computed using cloud cover statistics from the conventional surface observations of a single station.

6. Conclusion

In this paper we have described forecasting applications of high resolution satellite cloud climatologies and developed a climatological forecasting tool that is well suited to the operational environment. The feasibility of creating a global database of IR data at full resolution was demonstrated by the CHANCES project (Vonder Haar et al. 1995). To make the tool complete, the database should be expanded to at least five years and tables created for every pixel for each month of the year for the entire globe. The climatological forecast tool described in this paper would lend itself perfectly to software that would allow a user to point and click at the desired location on a map and instantly display the climatological data through hypertext links, like those used on web pages.

In this study we demonstrated the importance of including the spatial pattern of cloud surrounding the target in creating conditional probabilities. A second level of sophistication would be to include a temporal pattern of cloud. For instance, the initial condition could be comprised of three or six hours of cloud data at the target pixel or in an area surrounding the target.

Currently, researchers at the Cooperative Institute for Research in the Atmosphere (CIRA) at Colorado State University are developing techniques to extract layered cloud information from the CHANCES database. A paper on their results was presented at the 1996 Battlespace Atmospherics Conference (Forsythe et al. 1996). The location of the bases and heights of clouds are of great importance in a target forecast. Stratifying the data in terms of meteorological variables such as wind direction and air mass would make the climatology even more reliable. The level of sophistication is virtually limitless.

The potential military and civilian forecasting applications of very high resolution satellite cloud climatologies are exciting. Combat weather forecasters could use this technique in the field to greatly improve cloud forecasts. With a single observation, the weather warrior could quickly access climatological forecast aids such as the forecast matrix developed in this study using their tactical lap top computer. With the global coverage of meteorological satellites, high resolution climatological cloud forecast tools for airfields and remote targets anywhere in the world are within our grasp.

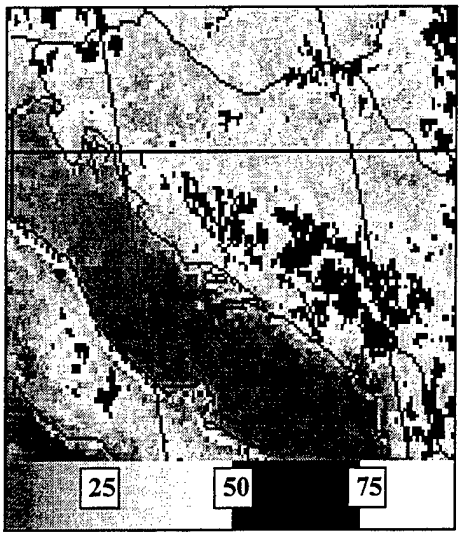


FIG. 1a. Cloud frequency composite from METEOSAT satellite for June 22, 1994 to August 5, 1994 for 12 UTC.

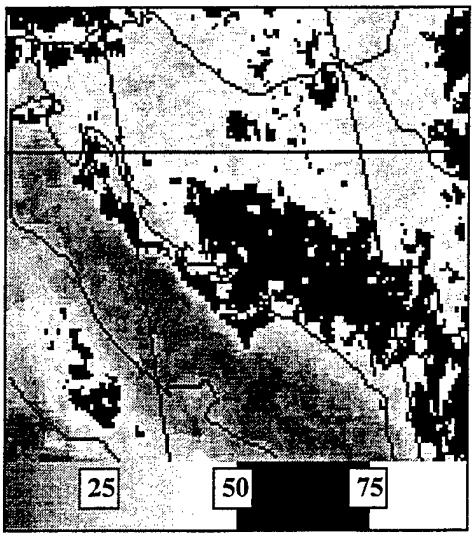


FIG. 1b. Cloud frequency composite from METEOSAT satellite for June 22, 1994 to August 5, 1994 for 15 UTC.

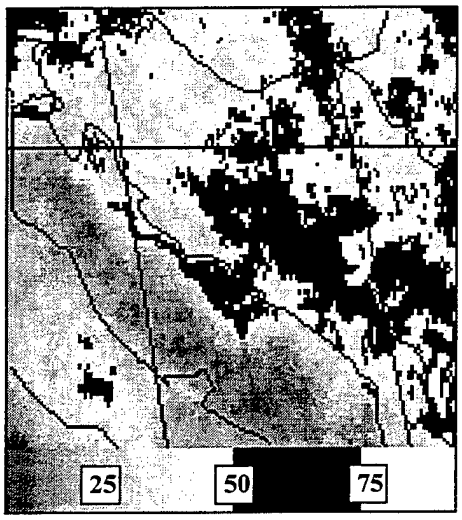


FIG. 1c. Cloud frequency composite from METEOSAT satellite for June 22, 1994 to August 5, 1994 for 18 UTC.

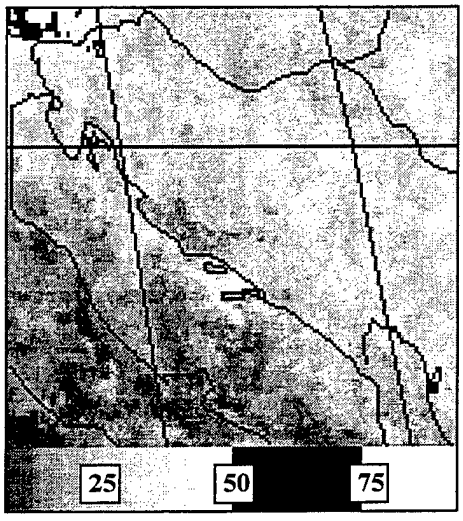


FIG. 1d. Cloud frequency composite from METEOSAT satellite for June 22, 1994 to August 5, 1994 for 18 UTC.

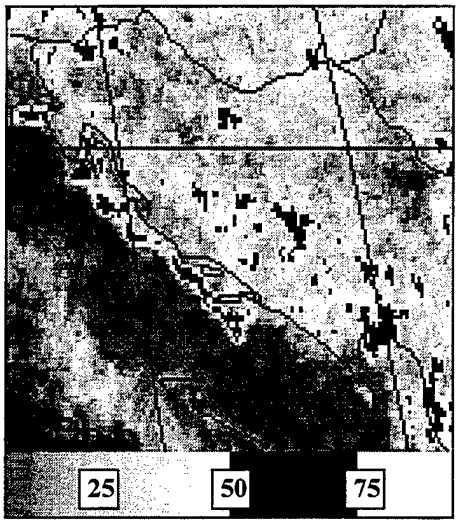


FIG. 2a. Probability of cloudy or clear persisting at 12 UTC from initial value at 6 UTC June 22, 1994 - August 5, 1994.

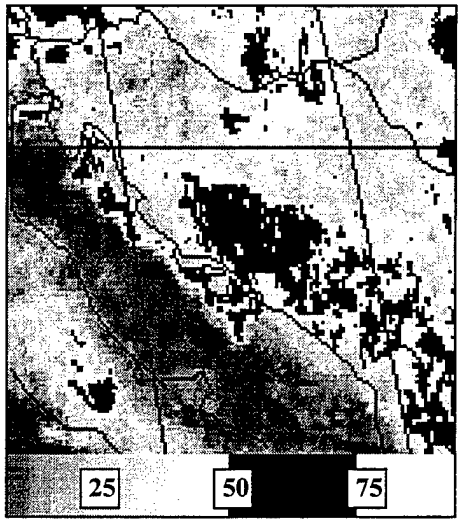


FIG. 2b. Probability of cloudy or clear persisting at 15 UTC from initial value a 6 UTC June 22, 1994 - August 5, 1994.

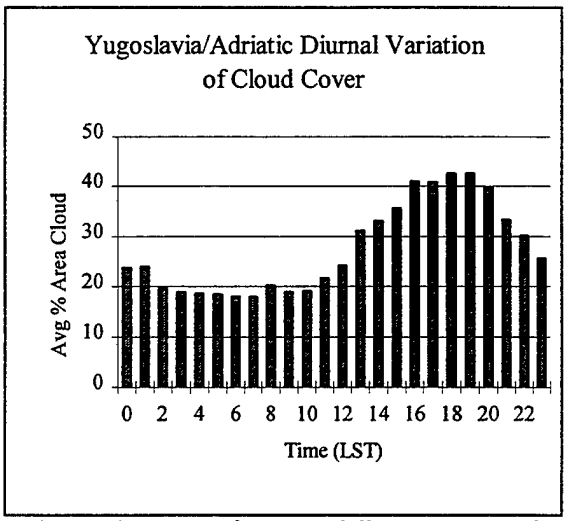


FIG. 3. Histogram of average daily percentage of area covered by cloud June 22,1994 - August 5, 1994 at each time of day.

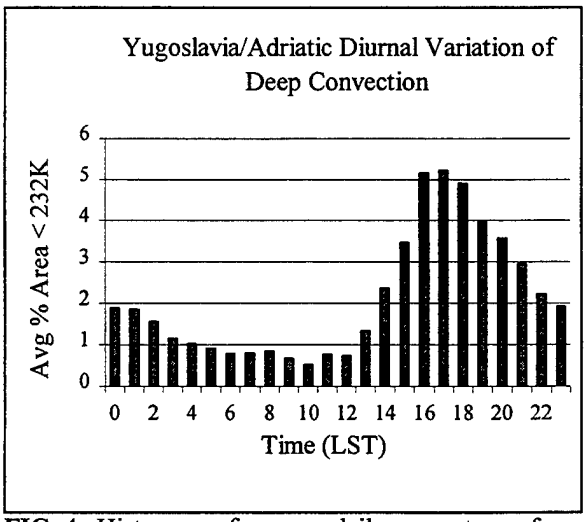


FIG. 4. Histogram of average daily percentage of area covered by cloud colder than 232 K June 22, 1994 - August 5, 1994 at each time of day.

TABLE 1. Conditional probabilities of cloud at all times given cloud at initial time for Sarajevo June 22, 1994 - August 5, 1994. Forecast hours are labeled 1 to 12 in the first row.

Time (UTC)	Cld % Freq	1	2	3	4	5	6	7	8	9	10	11	12
0	24	71	75	50	63	43	38	43	50	57	63	75	75
1	21	75	63	50	43	50	50	57	71	63	75	75	88
2	19	75	63	43	50	43	38	50	50	63	63	88	71
3	14	83	60	67	50	50	75	67	83	83	100	83	83
4	17	83	71	57	57	80	71	100	100	100	100	100	100
5	18	67	67	60	57	67	71	71	100	86	88	71	86
6	14	67	67	80	67	100	100	100	100	100	100	100	100
7	46	71	83	86	100	100	83	83	100	100	86	100	71
8	26	71	86	100	100	67	67	100	100	86	100	71	71
9	40	67	80	80	80	70	89	90	70	90	67	40	78
10	46	92	92	77	69	92	93	79	86	77	57	67	50
11	65	94	94	89	100	100	89	94	67	44	50	33	29
12	68	87	83	86	87	83	91	64	43	45	32	30	24
13	71	88	84	81	77	79	56	35	46	28	28	30	27
14	58	92	88	79	82	55	38	36	22	26	22	19	13
15	72	97	83	81	59	43	44	28	30	26	24	21	14
16	76	81	80	55	39	41	29	28	26	23	21	14	17
17	64	92	67	46	48	35	31	30	26	25	17	17	16
18	68	67	50	52	36	31	29	26	25	17	21	20	20
19	46	65	78	53	47	43	43	40	27	27	29	19	15
20	33	77	46	46	36	33	33	17	25	29	15	20	9
21	37	64	57	50	50	50	33	33	36	23	18	27	36
22	22	78	63	75	75	50	38	38	38	29	43	44	43
23	20	57	83	67	50	50	43	43	33	60	57	50	80

TABLE 2. Cloud forecast matrix based on cloud frequency and conditional probability data in Table 1. If conditional probability >70% value is "1." If conditional probability is <70% and >50%, then value is "1" if average of conditional probability and cloud frequency for forecast time is >60%. "1" is a forecast for cloud, and "0" for clear.

Time (UTC)	1	2	3	4	5	6	7	8	9	10	11	12
0	1	1	0	0	0	0	0	0	0	0	1	1
1	1	0	0	0	0	0	0	1	0	1	1	1
2	1	0	0	0	0	0	0	0	1	1	1	1
3	1	0	0	0	0	1	1	1	1	1	1	1
4	1	1	0	0	1	1	1	1	1	1	1	1
5	0	0	0	0	0	1	1	1	1	1	1	1
6	0	0	1	1	1	1	1	1	1	1	1	1
7	1	1	1	1	1	1	1	1	1	1	1	1
8	1	1	1	1	1	1	1	1	1	1	1	1
9	0	1	1	1	1	1	1	1	1	0	0	1
10	1	1	1	1	1	1	1	1	1	0	0	0
11	1	1	1	1	1	1	1	0	0	0	0	0
12	1	1	1	1	1	1	1	0	0	0	0	0
13	1	1	1	1	1	0	0	0	0	0	0	0
14	1	1	1	1	0	0	0	0	0	0	0	0
15	1	1	1	0	0	0	0	0	0	0	0	0
16	1	1	0	1	0	0	0	0	0	0	0	0
17	1	0	0	0	0	0	0	0	0	0	0	0
18	1	0	0	0	0	0	0	0	0	0	0	0
19	0	0	0	0	0	0	0	0	0	0	0	0
20	1	0	0	0	0	0	0	0	0	0	0	0
21	1	0	0	0	0	0	0	0	0	0	0	0
22	1	0	1	1	0	0	0	0	0	0	0	0
23	0	1	0	0	0	0	0	0	0	0	0	1

TABLE 3. Conditional probability of cloud given 1-33% of pixels within 15 km of Sarajevo covered with cloud at initial time June 22, 1994 - August 5, 1994.

Time (UTC)	Cld % Freq	1	2	3	4	5	6	7	8	9	10	11	12
0	24	33	0	0	0	0	0	0	33	33	33	67	67
1	21	0	0	0	0	0	0	0	0	0	0	0	0
2	19	0	0	0	0	33	33	33	100	67	100	33	33
3	14	40	40	20	60	40	60	60	80	80	60	60	80
4	17	50	50	50	0	0	0	0	0	50	50	50	50
5	18	33	33	0	0	33	33	33	67	100	100	67	100
6	14	25	25	25	25	50	50	75	75	75	75	75	75
7	46	0	0	25	25	25	75	75	75	75	50	50	25
8	26	50	75	75	75	100	100	100	75	100	100	50	50
9	40	33	67	67	83	83	83	67	83	83	50	33	17
10	46	83	83	83	83	83	83	83	83	67	33	33	17
11	65	38	50	25	38	38	25	25	13	13	13	0	0
12	68	64	55	55	45	27	27	9	0	18	9	9	18
13	71	40	80	60	60	40	20	20	20	20	20	0	0
14	58	50	50	33	50	50	33	50	33	17	17	17	17
15	72	0	0	0	0	0	0	0	0	0	0	0	0
16	76	14	43	43	14	29	14	0	14	14	14	14	14
17	64	50	33	17	17	0	0	0	0	0	0	17	17
18	68	0	0	20	0	0	20	20	20	20	20	20	0
19	46	13	13	0	0	13	13	13	13	13	0	0	0
20	33	20	0	0	0	0	0	0	0	0	0	0	0
21	37	0	0	0	0	0	0	0	0	0	0	0	0
22	22	0	33	0	0	0	33	33	0	0	0	0	67
23	20	50	25	50	25	0	0	0	0	0	25	25	25

TABLE 4. Forecast matrix as in Table 2 except with initial condition of 1-33% of pixels within 15 km of Sarajevo classified as cloudy.

Time (UTC)	1	2	3	4	5	6	7	8	9	10	11	12
0	0	0	0	0	0	0	0	0	0	0	1	1
1	0	0	0	0	0	0	0	0	0	0	0	0
2	0	0	0	0	0	0	0	1	1	1	0	0
3	0	0	0	0	0	1	0	1	1	1	1	1
4	0	0	0	0	0	0	0	0	1	0	1	1
5	0	0	0	0	0	0	0	1	1	1	1	1
6	0	0	0	0	0	0	1	1	1	1	1	1
7	0	0	0	0	0	1	1	1	1	0	0	0
8	0	1	1	1	1	1	1	1	1	1	0	0
9	0	1	1	1	1	1	1	1	1	0	0	0
10	1	1	1	1	1	1	1	1	0	0	0	0
11	0	0	0	0	0	0	0	0	0	0	0	0
12	1	0	0	0	0	0	0	0	0	0	0	0
13	0	1	1	1	0	0	0	0	0	0	0	0
14	1	1	0	0	0	0	0	0	0	0	0	0
15	0	0	0	0	0	0	0	0	0	0	0	0
16	0	0	0	0	0	0	0	0	0	0	0	0
17	0	0	0	0	0	0	0	0	0	0	0	0
18	0	0	0	0	0	0	0	0	0	0	0	0
19	0	0	0	0	0	0	0	0	0	0	0	0
20	0	0	0	0	0	0	0	0	0	0	0	0
21	0	0	0	0	0	0	0	0	0	0	0	0
22	0	0	0	0	0	0	0	0	0	0	0	0
23	0	0	0	0	0	0	0	0	0	0	0	0

REFERENCES

Combs, C.L., D.L. Reinke, E.M. Tomlinson, and T.H. Vonder Haar, 1990: Technique for Cloud Discrimination on GOES Infrared Imagery. Poster presentation at the *Cloud Impacts on DoD Systems Conf.*, Monterey, CA.

Forsythe, J.M., D.L. Randel, K.E. Eis, D.L. Reinke, C.L. Combs, 1996: CLVL - A Global High Resolution Layered Cloud Database. Presented at the *Battlespace Atmospherics Conf.*, San Diego, CA.

Gibson, H.M., and T.H. Vonder Haar, 1990: Cloud and Convection Frequency over the Southeast United States as Related to Small Scale Geographic Features. *Mon. Wea. Rev.*, **118**, 2215-2227.

Henderson-Sellers, A., and K. McGuffie, 1990: Are Cloud Amounts Estimated from Satellite Sensor and Conventional Surface-Based observations Related? Remote Sensing Letters. *Int. J. of Remote Sensing*, **11**, 543-550.

_____, and N.A. Hughes, 1985: 1979 3D-Nephanalysis Global Total Cloud Amount Climatology. *Bull. Amer. Meteor. Soc.*, **66**, 626-627.

Hughes, N.A., 1984: Global Cloud Climatologies: A Historical Review. *J. Climate Appl. Meteor.*, **23**, 724-751.

_____, and A. Henderson-Sellers, 1985: Global 3D-Nephanalysis of Total Cloud Amount: Climatology for 1979. *J. Climate Appl. Meteor.*, **24**, 669-686.

Kiess, R.B., and W.M. Cox, 1988: The AFGWC Automated Real-Time Analysis Model. AFGWC/TN-88/001, AFGWC, Air Weather Service (MAC), Offutt AFB, NE, 82 pp.

Kidder, S.Q., and T.H. Vonder Haar, 1995: Satellite Meteorology: An Introduction. Academic Press, 456 pp.

Klitch, M.A., J.F. Weaver, F.P. Kelly, and T.H. Vonder Haar, 1985: Convective Cloud Climatologies Constructed from Satellite Imagery. *Mon. Wea. Rev.*, **113**, 326-337.

Kornfield, J., A. Hasler, K. Hanson, and V. Suomi, 1967: Photographic Cloud Climatology from ESSA III and V computer produced mosaics. *Bull. Amer. Meteor. Soc.*, **48**, 878-883.

McAllister, C.R., 1969: Cloud-Cover Recurrence and Diurnal Variation. *J. Appl. Meteor.*, **8**, 769-777.

Minnis, P., and E.F. Harrison, 1984: Diurnal Variability of Regional Cloud and Surface Radiative Parameters Derived from GOES Data. Part I: Analysis Method, Part II: Cloud Results. *J. Climate Appl. Meteor.*, **23**, 993-1031.

Reinke, D.L., C.L. Combs, E.M. Tomlinson, and T.H. Vonder Haar, 1990: Persistence Forecasts From High-Resolution Cloud Composite Climatologies. Poster presentation at the *Cloud Impacts on DoD Systems Conf.*, Monterey, CA.

_____, _____, S.Q. Kidder, and T.H. Vonder Haar, 1992: Satellite Cloud Composite Climatologies: A New Tool In Atmospheric Research and Forecasting. *Bull. Amer. Meteor. Soc.*, **73**, 278-285.

_____, T.H. Vonder Haar, K.E. Eis, 1995: Climatological and Historical ANalysis of Cloud for Environmental Simulations: Applications to Battlefield Atmospherics. Presented at the *Battlefield Atmospherics Conf.*, White Sands, NM.

Rossow, W.B., A.W. Walker, and L.C. Garder, 1993: Comparison of ISCCP and Other Cloud Amounts. *J. Climate*, **6**, 2394-2418.

Vonder Haar, T.H., D.L. Reinke, K.E. Eis , C.L. Combs, and J.M. Forsythe, 1993: New High-Resolution Cloud Climatology Products from Meteorological Satellites. *METSAT Paper No. 93-102.* METSAT, Inc., Fort Collins, CO 80521.

_____, _____, _____, J.L. Behunek, C.R. Chaapel, C.L. Combs, J.M. Forsythe, M.A. Ringerud, 1995: Climatological and Historical ANalysis of Clouds for Environmental Simulations (CHANCES) Database. *Final Report.* Science and Technology Corp., Hampton, VA (USAF Phillips Lab Technical Report PL-TR-95-2101), 71pp.

MODELING THE EFFECTS OF SCREENING AEROSOLS ON PULSED DESIGNATOR SYSTEMS

Roger E. Davis and Alan C. Rishel
Science and Technology Corporation
555 Telshor Blvd., Suite 200
Las Cruces, NM 88011
Phone: (505) 521-4353
Fax: (505) 522-9062
E-mail: davis@stcnet.com

ABSTRACT

The use of high technology is now commonplace on the modern battleground. Some deployed high-technology systems use laser designators to illuminate targets. Designators are particularly effective in spectral regions unseen by the human eye because those targeted will often be unaware of impending attack. However, screening aerosols that strongly attenuate designator frequencies can defeat designator systems through concealment of targets and/or the creation of false targets.

This paper describes the Pulsed Lasers in Smoke (PULSE) model which is used to study the effects of screening aerosols on designator systems. The PULSE model provides the user with multi-layer plane parallel or Gaussian plume aerosol dispersion options. The model assumes single scattering of designator radiation in the screening aerosol. The screening aerosol is characterized by mass extinction coefficient, single-scattering albedo, and scattering phase function, all of which are functions of wavelength. The battlefield geometry is established by the designator, target, and weapon locations. Other inputs include designator pulse shape, duration, and width, target albedo, and receiver field of view.

The PULSE model output includes designator pulse shape and energy at the receiver and the location in space of the radiation returns. Results showing false target returns and stretched pulses due to their interaction with the screening aerosols are discussed.

1. INTRODUCTION

The latter part of the twentieth century has seen the development of many sophisticated weapons systems for the battlefield. Both active and passive systems are now commonly in deployed. One type of active system employs a laser designator. Designator systems are either self-designating or require a stand-off designator to lase the intended target. One particular countermeasure used against designator systems is that of smoke and obscurants. Screening aerosols that strongly attenuate designator frequencies can defeat such systems through concealment of targets and/or the creation of false target returns. To facilitate the study of the effects of smoke/obscurants on designator signals, the Pulsed Lasers in Smoke (PULSE) simulation model was developed. This paper describes the PULSE model.

2. PULSE MODEL

The basic scenario treated by the PULSE model is illustrated by Fig. 1. The PULSE code models the interaction of a designator pulse with obscurants and a target. The model uses first principles to describe the designator-obscurant interaction. Laser pulse scattering is approximated with a single scattering algorithm. The obscurant aerosol is characterized by aerosol spatial concentration (ρ), single scattering albedo (ω_o), mass

extinction coefficient (α), and scattering phase function ($P(\theta,\phi)$). The single scattering albedo is defined as the ratio of the fraction of incident radiation which is scattered to the sum of the scattered and absorbed radiation. The scattering phase function is the probability distribution of scattered radiation as a function of scattering angle. The essence of the PULSE model calculations for the designator-obscurant interaction is illustrated in Fig 2.

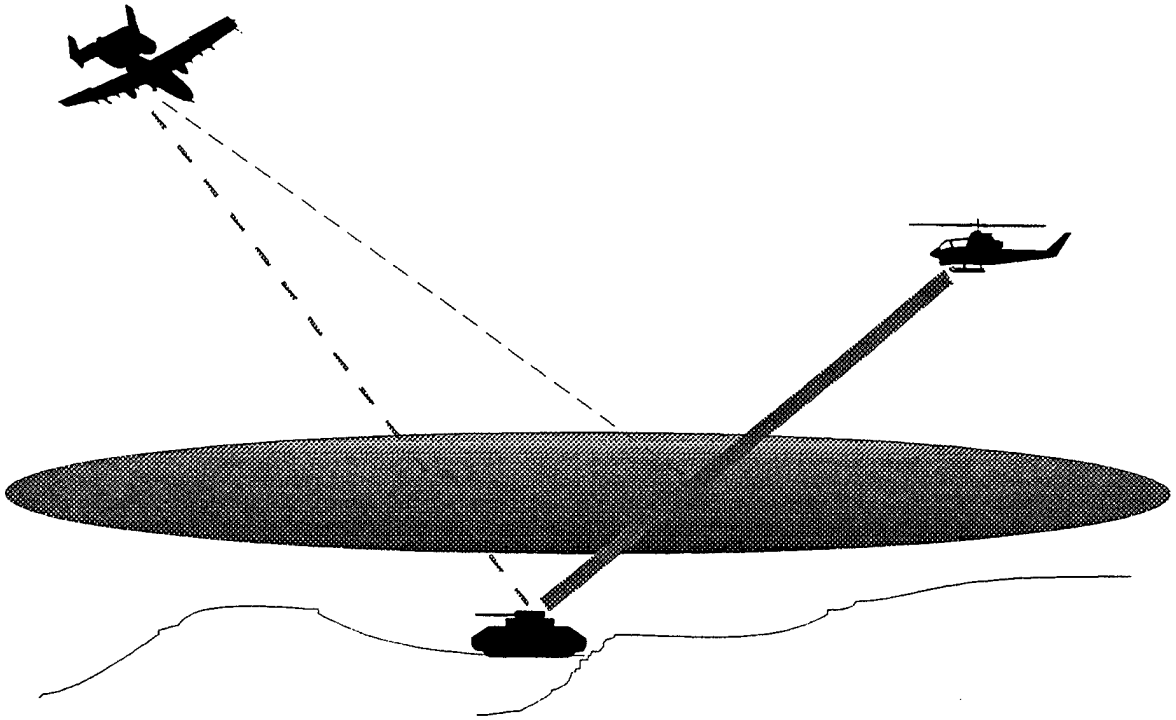


Figure 1. **PULSE model calculates the interaction of laser designators with obscurant aerosols.**

The designator-target LOS is divided into small, nominally 1 m, incremental segments. As illustrated in Fig. 2, the scattering sites are considered to be in the middle of each of these incremental segments. The pulse intensity from the designator to the scattering site is reduced by applying the Beer-Lambert law. The designator radiation "lost" from the pulse in the incremental segment is also determined from the Beer-Lambert law. The fraction of the lost radiation which is scattered is determined by the single scattering albedo for the obscurant. The single scattering albedo is, in general, wavelength dependent. The fraction of the scattered radiation which is directed toward the seeker is determined by the wavelength dependent obscurant phase function and the field geometry. Radiation scattered in all other directions or absorbed by the obscurant is ignored.

The obscurant aerosol is currently distributed by one of two methods. The first method is a stratified layer approach. Each obscurant layer is assigned its own parameters of concentration, mass extinction coefficient, single scattering albedo, and phase function. Each layer is also assigned a vertical thickness and height above the ground. This approach allows study of variable concentration and cloud "holes" along the designator-target LOS. Holes are created by assigning a layer zero concentration. The PULSE model allows 20 layers to be defined. PULSE code is written such that more layers can easily be added if required.

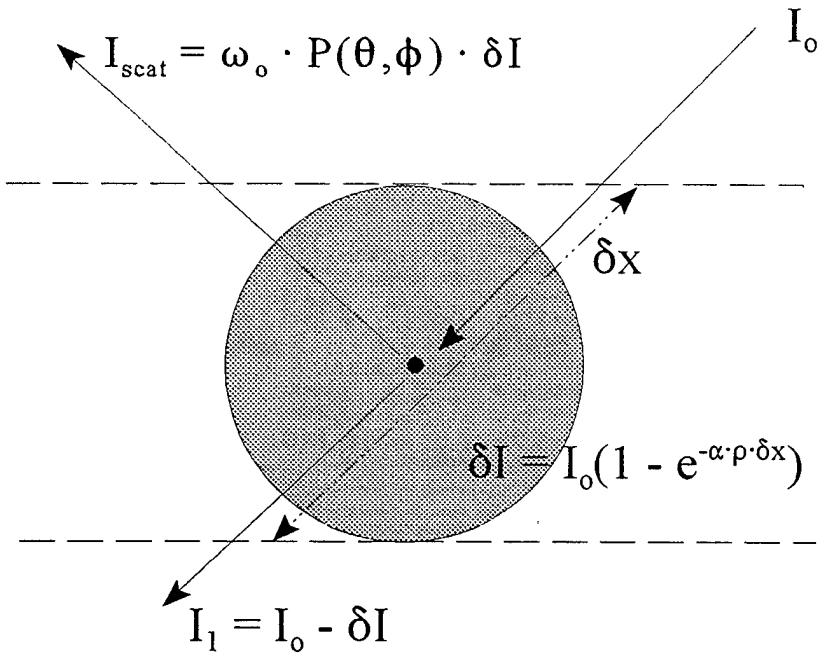


Figure 2. **Incident radiation from the top of the incremental segment is attenuated as described by the Beer-Lambert Law. The fraction of radiation scattered toward the seeker is calculated using the single scattering albedo and the phase function.**

The second option for obscurant concentration distribution a Gaussian plume model. This model allows for obscurant buoyancy, a vertical wind vector, evaporation of the fog oil as a function of downwind distance, and scavenging of obscurant material by the terrain. Both the layer model and the Gaussian model are static representations of the obscurant cloud.

The results of the PULSE model calculations are designator pulse profiles at the seeker aperture (Fig 3) as well as the spatial coordinates of scattering points in the obscurant and from the target (Fig 4). The designator-target-seeker geometry allowed by PULSE assumes that the designator and the seeker will be horizontal to or above the target.

A dynamic (time dependent) obscurant cloud algorithm is not yet verified for PULSE. However, the STATBIC (Hoock, 1994) algorithm developed by Dr. Don Hoock of the U.S. Army Research Laboratory has been included as an obscurant dissemination option in the PULSE model. This algorithm provides a time-dependent, fractal-like description of the obscurant cloud. While this algorithm has been included in the PULSE code it has not been fully verified. This option should used cautiously.

Certain "tricks" could be exercised using the aerosol static dispersions options to provide time-dependent simulations. For example, preprocessing of the weapon flight path and designator location could be accomplished to create a series of look-up tables. This preprocessing approach involves manually manipulating the obscurant cloud structure for each time step during the flight. While this technique is labor intensive, it could be employed in lieu of exercising the time-dependent algorithm.

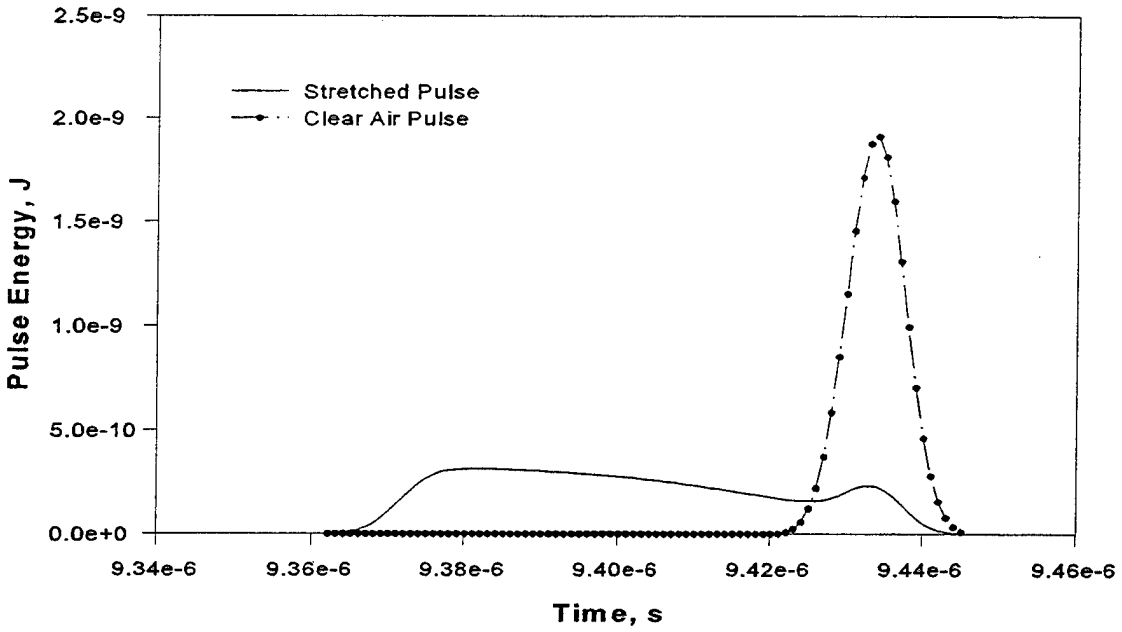


Figure 3. The dot-dash curve represents the designator pulse reflected by the target in clear air. The solid curve is the designator pulse calculated for a Gaussian plume over the target.

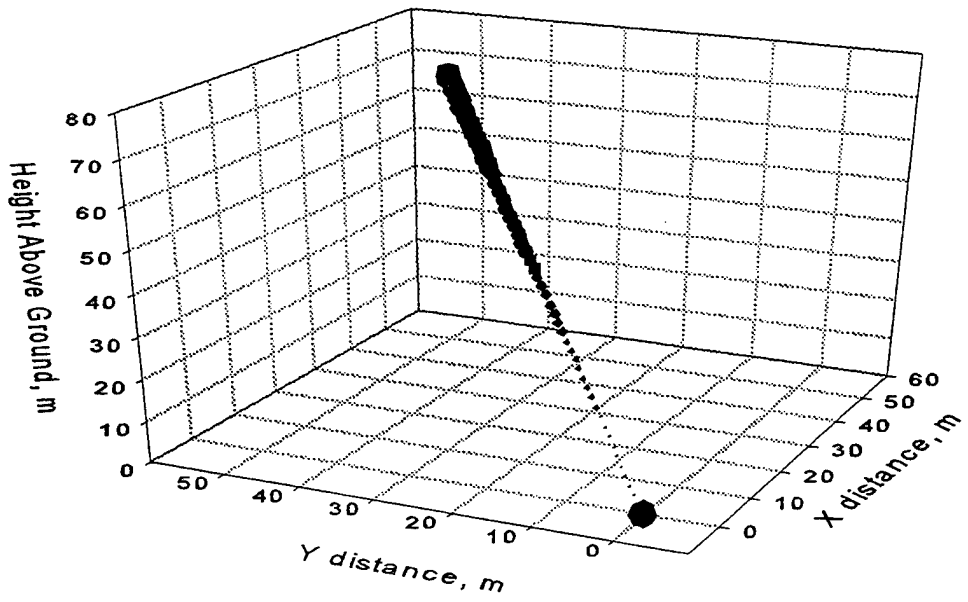


Figure 4. Locations and relative intensities of designator energy scattered by obscurant cloud.

The PULSE code is written in plain vanilla FORTRAN 77 with special attention paid to portability. The model is currently functional as described and has undergone extensive verification to identify and correct code errors or logic errors. Verification has included running both the layer and Gaussian distribution models for a wide range of geometries and optical depth conditions. Limited validation of the model has been accomplished (Davis and Rishel, 1997) using field data. A copy of the code can be obtained by contacting:

Dr. Hriar Cabayan (510) 422-8871
Lawrence Livermore National Laboratory
P.O. Box 808 (L-180)
Livermore, CA 94550

3.0 EXAMPLE PULSE RUN

The example PULSE run presented in this section is taken from a PULSE validation effort which used data acquired during the Counter Precision Guided Munitions (PGM) Smoke/CEP/Tower (SCEPTOR) trials held at Eglin AFB in June 1994. The validation compares the PULSE model pulse profile at the seeker with the pulse profile actually recorded during the trial event. This comparative validation requires the cloud concentration information to be coincident in time with the recording of the designator profile. The PGM SCEPTOR trials, the trial data sets, and the model validation effort are documented in Davis and Rishel (1997).

Instrumentation at the PGM SCEPTOR test included transmissometers, radiometers, lidar, video cameras, meteorological instruments, and seeker head. An oscilloscope connected to the seeker head recorded the designator pulses as processed by the seeker head electronics. The seeker head, lidar, one radiometer, and one transmissometer were located at the top of a 300' meteorological tower. The target, an 8' x 10' board covered with diaper cloth, was located on the ground approximately 110 m east-north-east of the tower. The board was rotated 45° south of the designator (lidar) LOS and tilted 45° from the vertical toward the sky. The slant path distance from the top of the tower to the target was approximately 194 m.

Part of the input required by the PULSE model is the specification of obscurant concentration as a function of location along the designator-target-seeker LOS. For the model validation this information was derived from the lidar optical-depth-per-meter data. The lidar, which was used to map the obscurant cloud concentration, was also used as the laser designator for the validation data sets. Because the seeker head was co-located with the lidar at the top of the tower, a backscatter geometry was established. Using the lidar as the designator allowed the mapping of the cloud concentration along the designator-target-seeker LOS.

The obscurant layer model was selected for the PULSE validation runs. This is a reasonable approach since the cloud is "frozen" for a given pulse. The backscatter geometry allows the precise placement of the cloud segment positions and of the cloud segment concentrations at the time of designation.

One of the problems encountered in performing the validation runs was the fact that the lidar information and the oscilloscope seeker head pulse profiles were not exactly time coincident. The lidar data was reported once every 3 or 4 seconds and is a 1-s average based on 16 pulses. The oscilloscope profiles were recorded on video tape, but digitized profiles for analysis were copied to files at irregular intervals with time tags only to the nearest whole second. The radiometer data shows that the concentration along a given LOS can change dramatically in a fraction of a second. Thus, the cloud structure reported by the lidar may have changed significantly from the time the seeker head pulse was recorded. Obscurant cloud lidar profile and the oscilloscope profile presented in this example are separated in time by (at least) one second.

A second problem impacting the comparative analysis was fact that the oscilloscope recorded the designator pulses after being processed by non-linear electronics in the seeker head. That is, the oscilloscope pulse profiles are non-linear in amplitude. It was learned from discussions with test engineers that no information concerning the gain switching levels was recorded and no transformation could be applied to the profiles. Therefore, the comparison between modeled pulses and observed pulses is limited in detail because the modeled pulses are linear in amplitude.

Figure 5 illustrates how concentration and path length input data was derived from the lidar cloud information. The slant path length through a cloud segment is taken to be the full width of isolated segments such as segments 1 and 4 shown in Figure 5. Specifying the width of blended segments (e.g. segments 2 and 3) is more complicated. Through some trial and error and a review of the oscilloscope profiles, it was eventually decided that some "clear air" was usually required between blends with well-defined peaks. In these cases a point half way between the lesser peak of the blend and the minimum between the peaks was chosen. From this point a line was constructed to intersection the larger peak of the blend. One-quarter of this distance was assigned as the clear air path length between the blended segments. Allowing for this amount of clear air between the segments, the path lengths through the blended segments were determined. The optical depth integrations were performed to the minimums between the peaks.

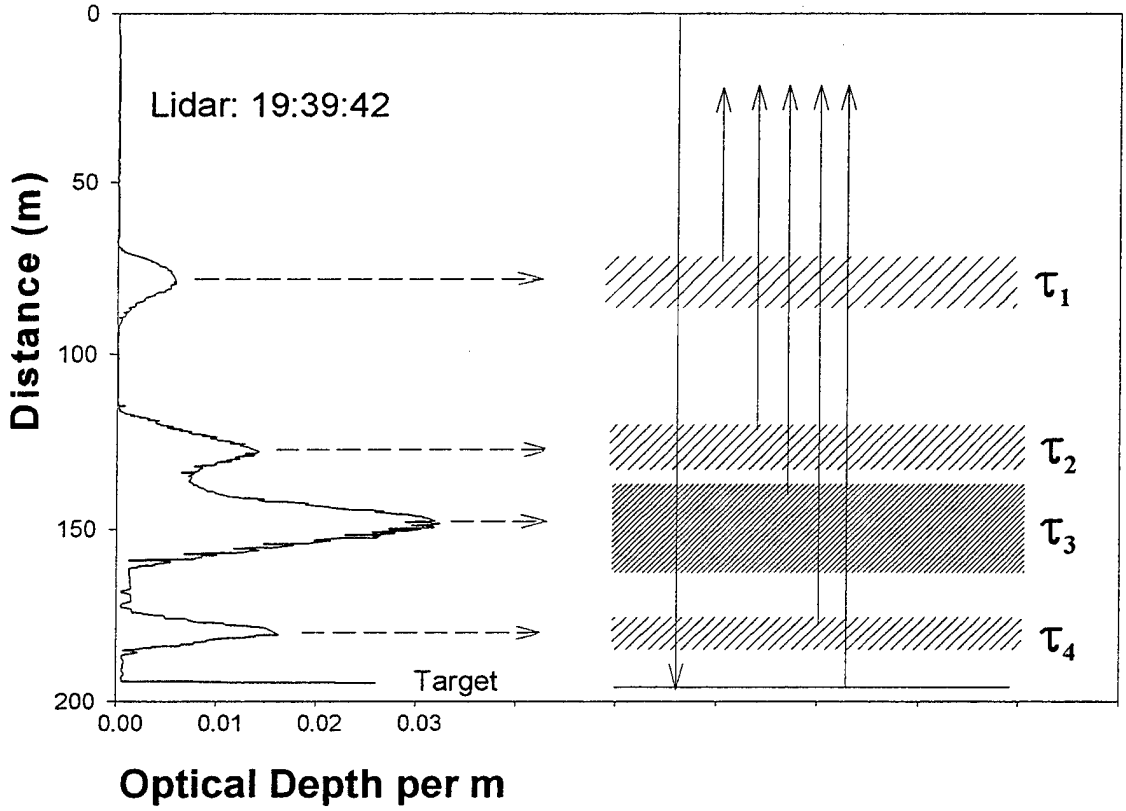


Figure 5. Optical depth, τ, and cloud segment thickness is determined from a lidar profile (left side of fig.). The optical depth for each major cloud segment is computed by integration over the segment thickness. Segment thickness is measured directly.

The locations of the cloud segments relative to the designator (and seeker in this case) were determined directly from the lidar measurements. The mean aerosol concentration in each obscurant segment, l_i, was determined by:

$$\langle \rho \rangle_i = \frac{\tau_i \, l_i}{\alpha(\lambda)} \qquad (1)$$

where:

$\alpha(\lambda)$	=	mass extinction coefficient, m^2/g
τ_i	=	segment I total (integrated) optical depth
l_i	=	slant path distance through segment I, m

A fog oil mass extinction coefficient of 1.5 m^2/g for 1.06 μm , derived from LASSEX (Bullard, et al., 1995) field transmission and nephelometer measurements, was used in eq. 1 to determine obscurant concentrations needed by the PULSE model for the example. The optical depths for the individual segments were determined by integrating the lidar optical-depth-per-m over the each segment. The slant path lengths were measured directly from the segment widths. The layer thickness for the model input was the segment slant path thickness reduced by the cosine of the lidar-target LOS as measured from the vertical.

The results of the example run are displayed in Fig. 6. Also displayed in Fig. 6 are the oscilloscope pulse profile and the lidar cloud optical-depth-per-meter data. The oscilloscope data and PULSE model profiles are presented as a function of distance rather than time. This allows a standard plot format for Fig 6. For convenience, all data sets types have been registered with the ground target position, 194 m from the lidar/seeker position at the top of the tower. The oscilloscope and PULSE model profiles may be compared directly for features as a function of distance. The cloud structure (lidar data) features can be compared with the model profiles but the distance coordinates for model designator profile features will be expanded factor of 2 due to the test geometry. In comparing the profiles, the reader is reminded that 1) the oscilloscope profiles have been processed by non-linear seeker head electronics, 2) the modeled profiles are linear and based on lidar cloud structure data, and 3) the lidar cloud structure profiles are averages of 16 profiles and are not precisely time coincidence with the seeker head (oscilloscope) profiles.

In reviewing the results presented in Fig. 6 it is obvious that the width of the modeled pulse as reflected at the target is approximately half that of the target pulse recorded at the oscilloscope. Several factors may be responsible for this difference between the observed and modeled pulse. The most important factor is probably the fact that model assumed a flat Lambertian target perpendicular to the pulse propagation. In reality, the target was rotated approximately 45° to the lidar and approximately 45° to the horizontal. This will cause the lidar spot to become elongated on the target, resulting in a broadening of the return pulse. Secondly, it is possible that the reported pulse width of the lidar could be in error. Thirdly, the non-linear amplification of the reflected pulses by the seeker head will server to magnify the base of the return pulse. This magnification of the wings of the target return is evident in the target signature which always has a small peak (the central portion of the pulse) resting on the shoulders of the target return.

The review of the results presented in the Fig. 6 also reveals that the modeled profiles tend to have somewhat concave shapes on the trailing sides of the pulses. This signature is attributed to the Beer-Lambert treatment of the designator pulse as it traverses the obscurant medium. That is, the intensity of the pulse power is reduced as $\exp(-\tau)$ as the pulse traverses the obscurant. The reasons the oscilloscope pulses do not

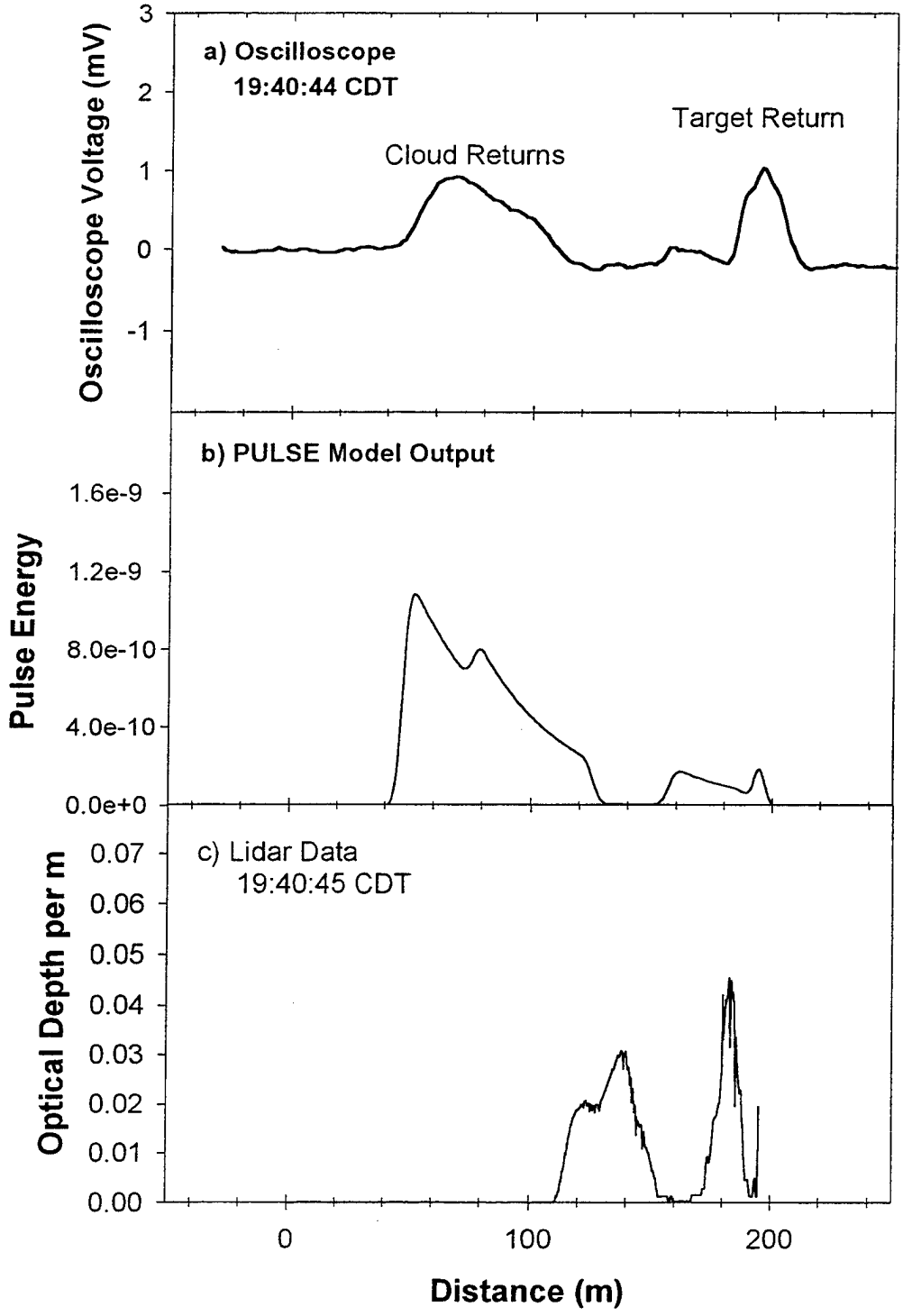


Figure 6. a) Designator profile as processed by the seeker, b) PULSE model profile at seeker aperture, and c) lidar obscurant cloud profile near time of seeker head observation.

show a distinctive concave signature include: (1) the oscilloscope profiles are processed by the non-linear seeker head electronics, and (2) the ocsilloscope profiles, unlike the PULSE model profiles, include the full effects of multiple scattering. However, the degree to which multiple scattering effects the overall profile shape is uncertain at this time.

Overall, the modeled features for the example data set compare quite favorably with the oscilloscope pulse segments. The multiple structure in the leading pulse segment is mimicked reasonably and second independent segment adjacent to the target shows the proper shape and signature. Additionally, the pulse stretching has been computed accurately.

5. SUMMARY

The PULSE model is currently operational. It is wavelength independent in the sense that the wavelength is determined by the obscurant input parameters (single scattering albedo, phase function, and mass extinction coefficient). It is also aerosol independent as long as the obscurant input parameters are available. PULSE uses either a stratified plane-parallel mode or Gaussian cloud approximation mode to distribute the obscurant cloud. Both of these modes are static in nature. A dynamic cloud distribution algorithm is available but has not been fully verified. PULSE is available (see Section 2) to interested users.

PULSE model validation is incomplete due to a lack of a comprehensive field data set. Nonetheless, as the example presented in Fig 6 shows, the PULSE model can provide a reliable and generally accurate representation of a designator pulse which has encountered an obscurant cloud.

REFERENCES

Bullard, B.R., R.E. Davis, S. Gerard, W.G. Klimek, and R.L. Laughman, 1995: *Large-Area Smoke Screen Experiment (LASSEX), Final Report.* STC Technical Report 2910, Science and Technology Corporation, Hampton, VA 23666

Davis, R.E. and Rishel, A, 1997, *Counter PGM SCEPTOR Data Analysis and PULSE Model Validation*, STC Technical Report 3125, Science and Technology Corporation, Hampton, VA 23666

Hoock, D.W., 1994, *Theory and Field Meausrements Analysis for Verification of the STATBIC Statistical Plume Visualization Algorithm, Summary Description,* MORS Handbook, U.S. Army Research Laboratory, Battlefield Environment Directorate, White Sands Missile Range, NM 88002-5501.

CLVL: A GLOBAL HIGH - RESOLUTION LAYERED-CLOUD DATABASE

John M. Forsythe, Donald L. Reinke, David L. Randel, Kenneth E. Eis and Cynthia L. Combs
Cooperative Institute for Research in the Atmosphere
Colorado State University
Fort Collins, CO 80523
http://www.cira.colostate.edu
forsythe@cira.colostate.edu

ABSTRACT

An important aspect of owning the weather is knowledge of cloud occurrence in a specific region. Clouds have a significant impact on electro-optical sensors aboard smart weapons. The task of understanding clouds in order use them to tactical advantage is a challenge with the current U.S. policy of rapid force projection to regions where U.S. forces may not have served before, with the result that military forecasters and planners may have only a rudimentary understanding of important mesoscale weather phenomena. Tactical planners need advance knowledge of cloud characteristics in a region before forces are deployed in order to choose appropriate weapons as well as plan bases of operations. Reconnaissance is also affected by clouds, as was clearly demonstrated in the "Great Scud Hunt" during the Gulf War. The impact of clouds on these matters is determined not only by the mean occurrence of cloudiness but by their vertical distribution as well. We have constructed a pilot dataset as a tool to address these issues.

The **C**limatological and **H**istorical **AN**alysis of **C**louds for **E**nvironmental **S**imulations (CHANCES) database was used, with supportive data, to produce **CLVL** (CHANCES **LeVeLs**), a multi-layer cloud database, for an initial 31 day period in July, 1994. The CLVL database is unique in that it offers a global, hourly, 5 km resolution, 8 vertical layer cloud depiction. The supportive data includes USAF High-Resolution Analysis System (HIRAS) upper-air data, surface weather observations (USAF DATSAV2 database), Special Sensor Microwave / Imager (SSM/I) precipitation retrievals from two Defense Meteorological Satellite Program (DMSP) satellites, and the U.S. Navy topographic database (ETOPO5). The CHANCES cloud detection and infrared imagery were merged with the supportive data to construct the three-dimensional cloud fields for CLVL. The HIRAS analysis and SSM/I precipitation retrievals were used to provide the vertical moisture distribution for the cloud layer assignments. The surface observations were used as input for cloud base measurements and were interpolated within the areas flagged as cloudy from the CHANCES database. Surface observations were the primary data source over land, and the HIRAS analysis and SSM/I retrievals were the primary data source over the oceans. A complementary product of precipitation, cirrus and stratus occurrence, and various data source flags was also built at the same resolution as the 8-level cloud product. The methodology used to construct the CLVL database and examples of the types of militarily relevant products which may be derived from the CLVL database are presented.

1. INTRODUCTION

Clouds play a critical role in defense-related activities. Satellite cloud climatologies (Reinke et al., 1992) are a valuable tool in recognizing preferred areas of cloud occurrence and nonoccurrence for mission planning (Reinke et al., 1993). Knowledge of the likely cloud occurrence in a specific region allows weapons and surveillance systems to be optimally placed to take advantage of the obscuration effect of clouds. Conversely, systems requiring clear conditions to operate can optimize their performance as well with high resolution cloud climatologies. Such knowledge is increasingly important with current electro-optical sensors. Simulations of cloud impacts on future military systems and training of forecasters for any part of the world can also benefit by the realistic treatment of clouds provided by high resolution cloud depictions and cloud climatologies. For contingencies where surface weather data is denied or is of poor quality, climatological properties of clouds can be a valuable tool.

The horizontal and temporal occurrence of clouds can now be studied with unprecedented global resolution by using the satellite-derived CHANCES cloud database (Vonder Haar et al., 1995). Satellite-based cloud climatologies have significant advantages over those derived from surface observations of cloud cover, such as the Real Time Nephanalysis (RTNEPH). The higher resolution of the satellite-based cloud detection allows small-scale but tactically important cloud features, such as clouds anchored to topographic features, to be exploited for a military advantage. High resolution cloud climatologies for a specific region can be a useful short-term forecasting tool, and they allow a forecaster to become familiar with cloud occurrence in an unfamiliar region (Hall et al., 1996 (in this volume)).

The Chances Levels (CLVL) pilot database described in this paper extends the power of high resolution satellite cloud climatologies into the vertical dimension. Now questions such as "What is the probability of clouds above 6 km altitude in July over Sarajevo ?" or "What is the probability of multi-layer clouds at a given location?" can be addressed. Cloud-free-line-of-sight (CFLOS) calculations with altitude dependence (e.g. Eis, 1994) are also possible with the CLVL database. In addition, the CLVL database provides researchers at CIRA a testbed with which to test and refine cloud layer retrieval algorithms on a global scale. This paper briefly describes the algorithm used to build the CLVL database and presents some examples of the types of climatological products which can be generated with such a database. More extensive documentation on the CLVL database can be found in Forsythe et al., 1996.

2. CLVL DATABASE FORMAT

The CLVL product was created as a demonstration subset from one year of the global CHANCES data. The CLVL database consists of two 8-bit images at the CHANCES 5-km global resolution for each hour of the month of July, 1994. The contents of the CLVL database are described in Table 1.

Table 1: Contents of CLVL database.

Element	Size	Contents
Cloud Layer Product	8 bits	1 bit set for each layer in which cloud is present. Layers are 1.5 km apart starting at ground level.
Quality Assessment Product (QA Image)	8 bits	High thin cloud or low cloud flag (from CHANCES visble / IR) Precipitation flag (from surface or SSM/I) Surface or SSM/I data use flag Moist atmosphere flag Persisted CHANCES data or error condition flag

3. INPUT DATA

CHANCES infrared (IR) temperatures and cloud detection (Vonder Haar et al., 1995) are the parent data used to construct the CLVL product. The cloud / no cloud field derived in CHANCES is used as a constraint for cloud layer retrieval, with no layers retrieved where CHANCES does not indicate clouds. When cloud is indicated in the CHANCES data, additional ancillary data is brought in to assist in determining the vertical extent of the clouds. The flow of data to create the CLVL product is indicated in Figure 1. The "Global Merge Processor" is the CLVL cloud layer algorithm and will be described in section 4.

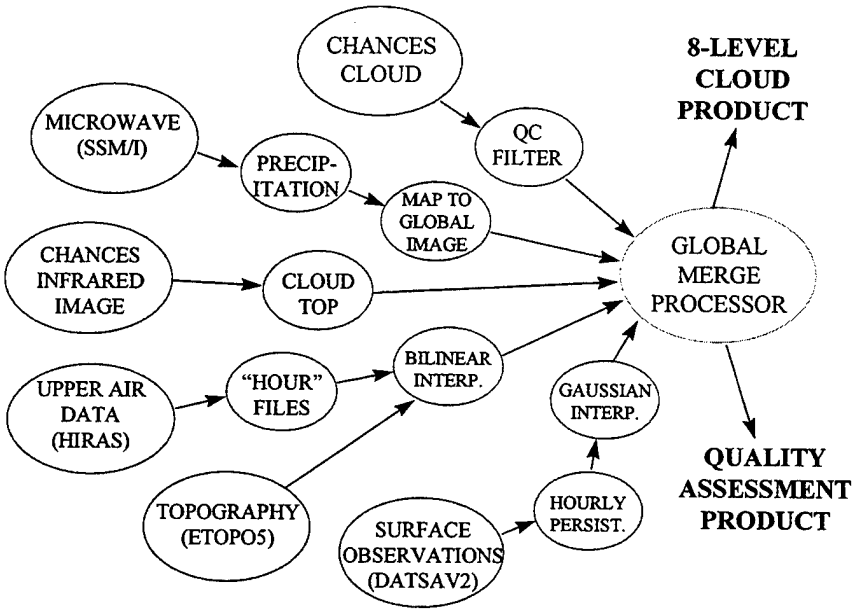


Figure 1. CLVL data flow diagram.

3.1 Satellite data

Satellite imagery that served as input to the CLVL processing was the archived CHANCES infrared image database and cloud detection database. The database consists of both geostationary and polar-orbiter data (total of eight platforms) that has been merged onto a global, 5-km, 1-hr database. Independent cloud detection from visible (during daylight) and infrared data is stored separately in the CHANCES database.

3.2 USAF HIRAS Database

The HIRAS database consists of 2.5 degree resolution gridded fields with upper level temperature, relative humidity, and heights for mandatory levels. The database is updated every 6 hours (0, 6, 12, and 18 UTC) and was interpolated to hourly files to be matched with the 1-hour resolution CHANCES database. Bilinear interpolation at each CHANCES pixel was used to construct the fields of temperature, humidity, and height at each level.

3.3 SSM/I Data

Raw SSM/I brightness temperatures from the F10 and F11 instruments were mapped into the CHANCES projection and used to detect precipitation over all surface types with the algorithm of Grody (1991). The orbit files from each instrument were broken into hourly files centered on the hour of interest.

3.4 USAF Surface Observations Database (DATSAV2)

This database is a reformatted version of standard global surface weather observations. Decoders were written to further reformat the DATSAV2 data into a more compact file structure for CLVL. Only those observational items that were of interest were saved for use in the CLVL processing. These items include station ID, location, date/time, temperature, dewpoint, cloud (sky cover) amount, cloud bases, and present weather.

Due to global patterns of weather observation reporting, there were about twice as many Surface Airways Observations (SAO) reports available at every third hour as compared to every hour (i.e., more at 0, 3, 9, 12, 15, 18, 21 UTC) in the DATSAV2 database. This was largely due to missing observations from Eastern Bloc and Southern Hemisphere countries; Western Hemisphere nations had about the same number of observations every hour. About 7000 global observations would be available every third hour, but this number decreased to about 3500 at other hours. In order to account for this in the CLVL product, observations from the closest "third" hour were persisted to the "non-third" hours when no other observations were available. For example, at 01 UTC the observation from 00 UTC would be persisted, and at 02 UTC the observation from 03 UTC was "backward persisted".

3.5 Topography Database

Topography data is taken from the U.S. Navy ETOPO5 database. This database gives surface elevation and is on a 10-km resolution grid. This database was bilinearly interpolated to the CHANCES resolution to determine the elevation of the CHANCES grid points, and to constrain the cloud base solution when necessary (i.e. cloud bases were not allowed to occur below the surface).

4. CLVL CLOUD LAYER ALGORITHM

This section briefly describes the steps occurring in the "Global Merge Processor" (in Figure 1), after all available data for a particular time and location has been gathered.

The first step in the production of the global layered cloud product is to determine if cloudiness exists in the CHANCES cloud/no cloud data. This occurs about 51 percent of the time on a global average. Clear points are not processed any further.

For cloudy points, the height corresponding to the IR temperature is set as the top of the cloud, hereafter referred to as Z (T). Additional clouds which might be added from the following steps are added only below this level.

Clouds classified as cirrus or stratus from the CHANCES product are only allowed to exist at the single layer defined by Z (T). Thus, these two cloud types are determined from the satellite data alone and not influenced by other data. Cirrus and stratus are only classified in the CHANCES data when visible data is available. Clouds not classified up to this step are sent to the general CLVL cloud layer assignment module, which merges in all available data (SSM/I, Surface Airways Observations (SAO), and upper air) to assign the 8 levels in the CLVL output.

A check is made to see if there is collocated SSMI/I data at the current location. If there is SSM/I data available, a precipitation test is done using the global algorithm of Grody (1991). If precipitation is indicated, a 9 x 9 pixel box (approximately 45 x 45 km) around the center of the SSM/I field-of-view is marked as precipitating. This corresponds to the SSM/I footprint size for the precipitation algorithm. If a CHANCES determined cloud is in a precipitating field-of-view, all layers below Z(T) are marked as cloudy.

Next, the SAO data is searched to find all observations within 150 km of the current location. If more than two stations are found, a Gaussian filter is used to objectively interpolate the SAO station fields (cloud bases, fog existence, precipitation existence). If only one or two SAO stations are found, a test is done to see if either is within 30 km of the current location. If so, the fields from the closest station are used. If no SAO stations are within 150 km, SAO data is not used in the cloud layer assignment. If precipitation is located in the SAO data, all levels below Z(T) are marked as cloudy. The lowest level is marked as cloudy for fog conditions. The DATSAV2 database reports up to three cloud heights, and levels corresponding to any clouds at these heights are marked as cloudy.

For non-precipitating clouds, regardless of whether they have SAO observations or not, the sounding from the HIRAS data at the mandatory levels is tested to determine if there are any clouds indicated from the relative humidity profile. The methodology to do this follows from Wang and Rossow (1995). In essence, this method looks for relative humidity in the layer greater than 84 percent, and also looks for sharp gradients between layers. Layers which are indicated to have cloud by the upper air method are marked as cloudy in the CLVL output layer product, and this occurrence is also noted in the QA image.

At this point in the CLVL cloud layer algorithm, all of the cloud layer assignments have been completed. The next step is to convert the cloud layer heights to an above ground level scale, using the ETOPO5 global topography data, and to handle any unrealistic situations which may arise from this (e.g. clouds below the ground, base above cloud top). In general, error conditions occurred less than 1% of the time in the CLVL processing. The error flag is set in the QA image for these conditions.

Figure 2 shows a cross section through the CLVL cloud layer retrieval and a 3-dimensional rendering of the same image. The CHANCES infrared image is also shown. This is through Tropical Storm Alberto on July 3, 1994 at 16 UTC over the southeastern U.S. Note the thick clouds through the center of the tropical storm, with low scattered clouds on the west and a higher veil of clouds over the ocean to the east.

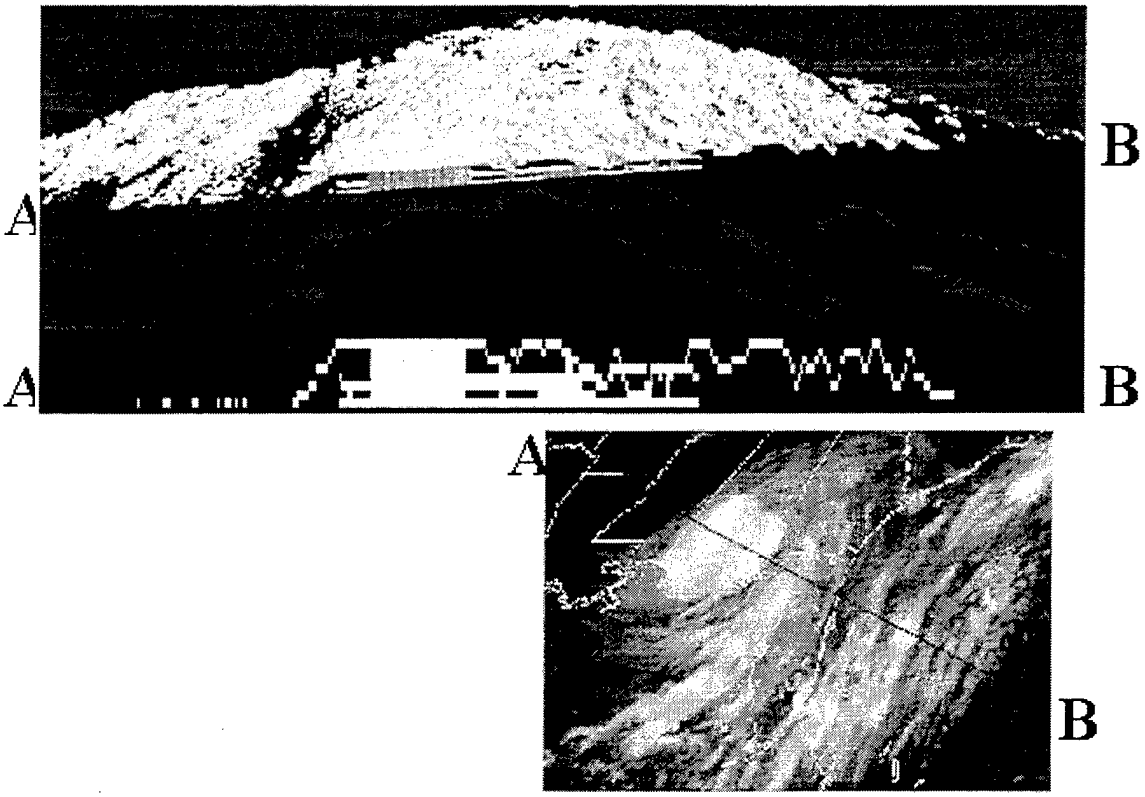


Figure 2. Sample cross-section through the 8-layer cloud product on July 3, 1994, 16 UTC. A 3-D rendering is also shown along the line A-B.

5. SAMPLE CLVL CLIMATOLOGIES

From the one month demonstration CLVL dataset from July 1994, several cloud climatologies were produced. These reveal the types of decision aids that can be generated from a layered cloud retrieval. Additional products, such as the occurrence of multiple layers of cloud in a region, can also be created with the CLVL database. There are numerous military applications of these types of products, such as reconnaissance planning and ballistic missile detection probability as a function of height.

The frequency of occurrence of cloud when cloudy in the lowest two CLVL layers is presented in Figure 3 at full CHANCES resolution for an area over Italy and the Former Yugoslavia. CLVL layered cloud retrievals from 0, 6, 12, and 18 UTC were composited for the entire month of July, 1994. Note the trend towards more clouds in the lowest layer (on right), which is typical of boundary layer convective clouds. Also note the marked gradient in cloud cover from the southwest to northeast, and over land versus water. This is a reflection of topographically forced cloudiness over the mountains in the northeast.

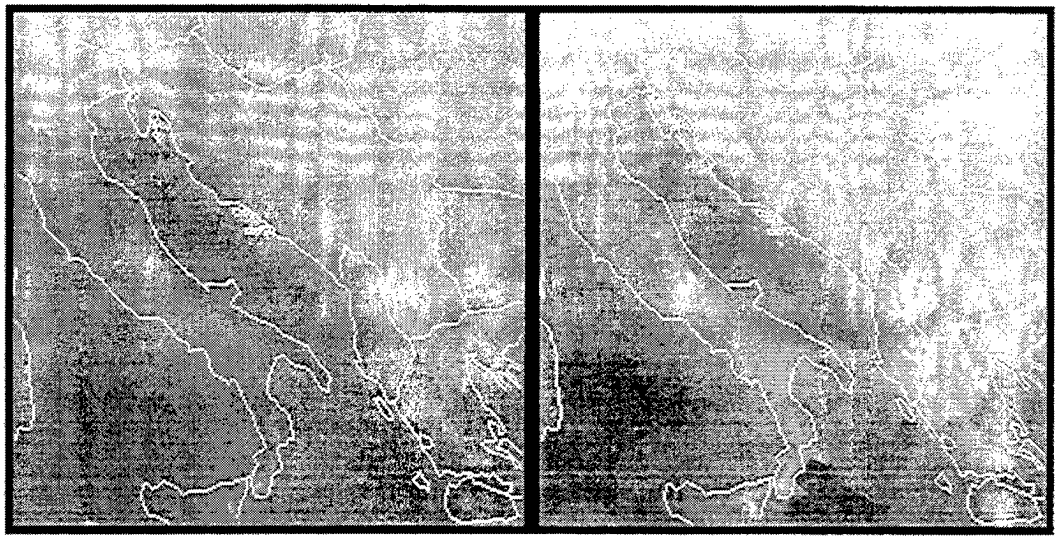


Figure 3. Examples of frequency of occurrence of cloud, when cloud is present at any CLVL layer, in the two lowest layers (1.5-3.0 km on the left and sfc-1.5 km on the right) for July, 1994 (composite of 00, 06, 12, and 18 UTC) over Italy and Former Yugoslavia. Grey shades indicate the frequency of occurrence of cloud from 0% (black) to 100% (white) in each layer.

The same type of analysis shown in Figure 3 can also be done on a global scale with the CLVL database. Figure 4 shows the frequency of occurrence of cloud at three selected layers (ground - 1.5 km, 4.5 - 6 km, > 9 km) for the globe for July, 1994 at 00, 06, 12, and 18 UTC. Figure 4 is intended to show the utility of a layered cloud climatology and is not meant to be definitive. Longer time periods would need to be analyzed for that, but essential patterns of the general circulation are apparent. The Intertropical Convergence Zone is clearly defined at all levels. There is more cloudiness close to the surface, but the decay of cloud cover with height does not occur at the same rate in all locations, for instance the central Atlantic versus the southern Atlantic ocean. Note the large regions essentially devoid of mid-level cloud over the subtropics. Knowledge of whether cloud cover is likely at a certain altitude in a region and whether it is an advantage or disadvantage could be useful for planning or avoiding air engagements in a region.

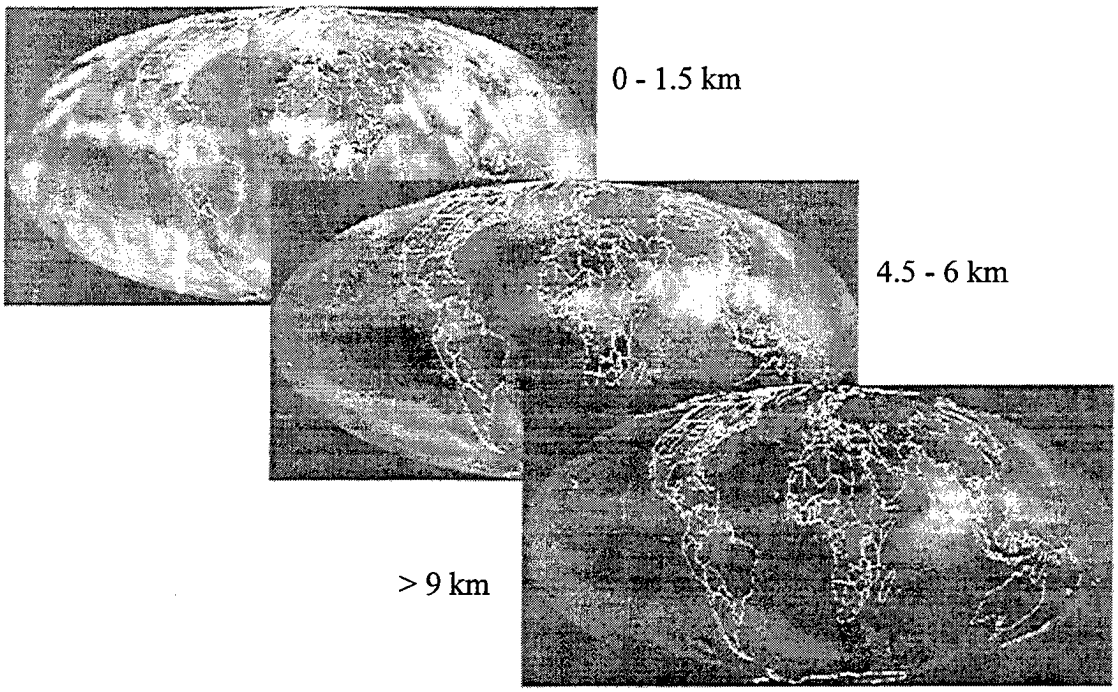


Figure 4. Global view of 3 CLVL layers shown as frequency of occurrence of cloud within a specific layer, when cloud is present in any layer, for July, 1994 (composite of 00, 06, 12, and 18 UTC). Grey shades indicate the frequency of occurrence from 0% (black) to 100% (white).

6. SUMMARY

The military has a compelling need for global cloud information. An ability to look at the global vertical occurrence of clouds together with their spatial and temporal occurrence is required. The global layered cloud CLVL demonstration database has been created at high spatial and temporal resolution to address these problems. A number of satellite and conventional weather data sources were merged together in a unique manner to create this database. All cloud detection was done from satellite data only, a distinction between CLVL and other similar products, such as the RTNEPH. The database created for this pilot study covers one month, July 1994, out of the larger CHANCES dataset.

A number of prototype high-resolution satellite cloud climatologies have been presented. By stratifying results by cloud altitude and occurrence of layers, important new militarily useful products can be created. The new views of cloud structure and occurrence hinted at in the CLVL database will provide a new understanding of how clouds impact the battlespace, and provide a tactical advantage to those who use this knowledge wisely.

7. ACKNOWLEDGMENTS

The CLVL project was sponsored by the U.S. Army Research Office under grant #DAAH-04-95-1-0661, with funding provided by USAF Phillips Laboratory at Hanscom AFB, MA. Our special thanks to Dr. Arnold Barnes at Phillips Lab for his assistance with funding, and Dr. Walter Bach for providing a mechanism to build this unique prototype database.

8. REFERENCES:

Forsythe, J.M., C. A. Chaapel, and M.A. Ringerud, 1996: CHANCES Layered Cloud (CLVL) Product - Initial 1-Month Sample - Final Report. Science and Technology Corp., Hampton, VA Technical Report 3108, 37 pp.

Grody, N.C., 1991: Classification of Snow Cover and Precipitation using the Special Sensor Microwave Imager. *J. Geophys. Res.*, **96**, 7423-7435.

Hall, T.J., D.L. Reinke and T.H. Vonder Haar, 1996: Forecasting Applications of High Resolution Diurnal Satellite Cloud Composite Climatologies Over Former Yugoslavia and the Adriatic Sea. *Proceedings of the 1996 Battlespace Atmospherics Conference*, Naval Command, Control and Ocean Surveillance Center, RTD & E Division, San Diego, California.

Reinke, D.L., C.L. Combs, S.Q. Kidder, and T.H. Vonder Haar, 1992: Satellite Cloud Composite Climatologies: A New Tool in Atmospheric Research and Forecasting. *Bull. Amer. Meteor. Soc.*, **73**, 278-285.

Reinke, D.L., T.H. Vonder Haar, K.E. Eis, J.M. Forsythe, and D.N. Allen, 1993: Climatological and Historical ANalysis of Clouds for Environmental Simulations (CHANCES). *Proceedings of the 1993 Battlefield Atmospheric Conference*, U.S. Army Research Lab, White Sands Missile Range, New Mexico, 863-870.

Vonder Haar, T. H., D.L. Reinke, K.E. Eis, J. L. Behunek, C.R. Chaapel, C. L. Combs, J.M. Forsythe, and M.A. Ringerud, 1995: Climatological and Historical ANalysis of Clouds for Environmental Simulations (CHANCES) Database - Final Report. Science and Technology Corp., Hampton, VA (USAF Phillips Lab Technical Report PL-TR-95-2101), 71 pp.

Wang, J., and W.B. Rossow, 1995: Determination of Cloud Vertical Structure from Upper-Air Observations. *J. Appl. Meteor.*, **34**, 2243-2258.

THE LATTICE BOLTZMANN METHOD: A NEW APPROACH TO RADIATIVE TRANSFER THROUGH CLOUDS

J. B. Mozer and T. R. Caudill

USAF Phillips Laboratory Geophysics Directorate
Hanscom AFB, Massachusetts 01731-3010, USA

1. INTRODUCTION

The radiative effects of clouds on operational sensors and their associated impacts on systems in use by the Department of Defense (DoD) are generally not well understood. In the case of most DoD operations, it is features of clouds at relatively small spatial scales that are of most importance. A typical infrared seeker on a guided munition, for example, must be able distinguish targets from a possible cloudy background at spatial scales that are equivalent to individual cumulus cloud elements. In this regime, the inhomogeneous three-dimensional nature of cloud fields is significant and traditional methods of treating clouds as homogeneous layers in radiometric calculations break down.

For the present work, we investigate the modeling of cloud radiative effects at very fine scales (e.g., tens of meters). At these spatial scales, the plane parallel assumptions often invoked by large-scale treatments of clouds are not valid and the full 3D inhomogeneity of cloud fields must be considered.

Radiative transport models that are applicable to finite clouds at cumulus scales are not widely available. Treatments of this problem typically involve the simulation of cloud radiative interactions using stochastic Monte Carlo methods or diffusion-limit approximations to the full radiative transfer equation. Although these methods are somewhat successful in certain applications, they each have certain undesirable attributes. Monte Carlo methods, for example, are inherently noisy and require a large number of photon simulations to produce useful results. To compensate for this, Monte Carlo simulations are typically run in reverse sense in that a given view geometry is prescribed and individual photons are tracked as they interact with the cloud media backward in time.

Recently, a new tool has emerged to model various transport phenomena based on a particle method using discrete cellular automata techniques. To date, the primary applications of this method are related to the field of computational fluid dynamics. These so-called lattice-gas methods simulate a complex dynamical system by constructing a microscale world in which space, time and velocity are discretized and fictitious particles interact with each other and their environment. In the macroscopic limit, these particles describe the time-dependent solution to a system of PDEs (e.g. Navier Stokes fluid flow) without constructing any finite-difference (or finite element) approximations to the PDEs themselves. Boon (1991) gives a review of lattice-gas methods for computational fluid dynamics applications.

From the field of lattice-gases, a separate, but closely related method has emerged in which the modeling of particles occurs at a scale that is intermediate between the microscale of the individual particles and the macroscale where the modeled physics is observed. In this intermediate, or mesoscale, one describes distributions of the particles rather than the particles themselves. This technique is known as the lattice Boltzmann method (c.f., Succi, 1991 for a review). The advantage of modeling at the mesoscale is that the scale of the problem can be increased and the noise that is due to the underlying assumptions of molecular chaos in lattice-gas methods is eliminated. One of the disadvantages of this approach, however, is that correlations between individual particles are lost due to the fact that particles are treated as ensembles.

In the present work, we have adapted the lattice Boltzmann method to the problem of three dimensional radiative transport though inhomogeneous liquid water clouds. This is a novel approach to the problem and is potentially a powerful tool for modeling cloud radiative properties at the scales necessary for sensor simulation. It has several desirable features as compared to other particle-based methods. In particular, lattice Boltzmann methods operate in a forward-in-time mode and produce results which are independent of the view geometry. Another significant feature of the method is that the algorithms are inherently efficient on parallel computer architectures due to the local computation involved.

In Section 2 we describe the lattice Boltzmann method in detail and its application to cloud radiation. Section 3 presents some results derived from the method using idealized simple clouds as well as fully 3D complex cloud geome-

tries. These results are compared with Monte Carlo simulations. In Section 4, we discuss the potential application and limitations of the lattice Boltzmann method.

2. METHOD

The Boltzmann equation for linear photonic transport can be developed by considering the change, dN, in time dt of the number of photons with velocity in d^3v about $\mathbf{v}$ which are located in a small volume V with surface S about the point $\mathbf{r}$. Then,

$$dN = d^3v dt \int_V \frac{\partial \psi(\mathbf{r}, \mathbf{v}, t)}{\partial t} d^3r, \tag{1}$$

where $\psi(\mathbf{r}, \mathbf{v}, t)$ is the expected number of photons in d^3r about $\mathbf{r}$ with velocities in d^3v about $\mathbf{v}$ at time t. In the time interval dt, the balance condition on dN is:

$$\begin{aligned} dN = & - \text{ net number flowing out of } S \\ & - \text{ number suffering collisions} \\ & + \text{ number scattered into } d^3\mathbf{v} \\ & + \text{ number produced by sources within } d^3r \\ & - \text{ number removed by sinks within } d^3r. \end{aligned} \tag{2}$$

A Boltzmann equation can be developed from Eqs. (1) and (2):

$$\mathbf{B}\psi(\mathbf{r}, \mathbf{v}, t) = q(\mathbf{r}, \mathbf{v}, t), \tag{3}$$

where the Boltzmann operator, $\mathbf{B}$, is defined as,

$$\mathbf{B} \equiv \frac{\partial}{\partial t} + \mathbf{v} \cdot \nabla + v\sigma(\mathbf{r}, \mathbf{v}) - \int v' \sigma(\mathbf{v}' \rightarrow \mathbf{v}, \mathbf{r}) dv', \tag{4}$$

where $\sigma(\mathbf{r}, \mathbf{v})$ is a scattering cross section and $q(\mathbf{r}, \mathbf{v})$ represents the net source of photons. Classical linear transport theory is aimed at finding solutions to Eq. (3) (c.f. Case and Zweifel, 1967).

In the lattice Boltzmann method, we wish to construct a form of the Boltzmann equation analogous to Eq. (3), but where space and time (hence velocity) are discrete. To accomplish this, we define a set of lattice vectors, $\mathbf{e_i}$, $(i = 1..B)$, where i is a lattice direction index and B is the total number of directions (velocities) in the lattice. Then, the lattice Boltzmann equation can take the form,

$$\Delta f_i = f_i'(\mathbf{r} + \mathbf{\Delta r}, t + \Delta t) - f_i(\mathbf{r}, t) = -\Omega_i(\mathbf{r}, t), \tag{5}$$

where, f_i represents the expected number of photons at a node in the lattice traveling with unit speed in the direction of $\mathbf{e_i}$ and Ω_i is a collision operator which acts to redistribute the photons traveling in each of the lattice directions at each lattice node. In the present context, this collision term represents the physics of the photon transport (e.g. scattering, absorption and emission).

The lattice Boltzmann method can be considered as two distinct steps–the first being the collision operation described by Eq. (5) and the second a propagation or streaming step. In streaming, the values of each of the f_i at each node are simply moved to the adjacent lattice node pointed to by the associated $\mathbf{e_i}$. This step is key to the scalability of the lattice Boltzmann method because streaming happens synchronously. In other words, the information contained in the entire set of photons is moved at once everywhere in the lattice. This is in contrast to Monte Carlo methods where each photon moves independently of the others due to the independent nature of each photon.

The collision term may take any number of forms; however, one convenient form often used in fluid transport problems is a single-time relaxation towards equilibrium–e.g.,

$$\Omega_i = \frac{1}{\tau}(f_i - f_i^*), \tag{6}$$

where τ is a relaxation parameter and f_i^* is an equilibrium distribution function for the lattice photons. This form of the collision term is analogous to the so-called BGK approximation to the Boltzmann equation and is commonly known as the lattice-BGK equation.

The equilibrium distribution function, f_i^*, is difficult to determine in the general case of linear transport. However, in the present case, we may construct f_i^* rather simply by considering the "microphysics" of the photon interactions. For simplicity, consider a case of pure isotropic scattering (i.e. no absorption or emission). In this case, the equilibrium distribution function is equal in all lattice directions (i.e., $f_i = const$). The only relevant constraint is that energy be conserved during the collision. This is equivalent to:

$$\sum_{i=1}^{B} \Omega_i = 0. \tag{7}$$

This condition implies that,

$$f_i^* = \rho/B. \tag{8}$$

It is apparent from the form of the collision operator Eq. (6) that the relaxation parameter, τ, governs the magnitude of the scattering in a collision. There are two limiting cases involving τ to note. For $\tau = 1$, Eq. (6) reduces to $f_i' = f_i^*$, where f_i' is the after-collision value of f_i. This represents a complete scattering of all of the incident photons. At the limit of $\tau = \infty$, we have $f_i' = f_i$, which can be interpreted as pure transmission (no scattering). In general, τ, is a measure of the (scattering) optical depth and is treated as a spatially varying quantity.

To determine the relationship between optical depth, δ, we consider a special case of the equilibrium distribution function–specifically,

$$f_i^* = \frac{1}{B} f_i. \tag{9}$$

In this case, we have effectively eliminated the contribution of scattered photons being re-scattered into the f_i direction. This eliminates the effects of multiple scattering and allows a direct comparison with Beer's Law,

$$I(x) = I(0)e^{-\delta x}, \tag{10}$$

where I is radiometric intensity and x is a measure of distance.

The comparison of the lattice Boltzmann radiative transport model to Beer's law proceeds by considering the ratio f_i'/f_i for a single collision (or equivalently over a single grid space) for the equilibrium distribution given by Eq. (9). We have from Eqs.(5, 6 and 9):

$$\begin{aligned} \frac{f_i'}{f_i} &= 1 - \frac{\Omega}{f_i} \\ &= 1 - \frac{1}{\tau}\left(1 - \frac{c}{B}\right). \end{aligned} \tag{11}$$

By treating the f_is as intensities, we have by comparison to Eq.(9),

$$\delta = -ln\left[1 - \frac{1}{\tau}\left(1 - \frac{c}{B}\right)\right]. \tag{12}$$

Nonconservative and anisotropic scattering are treated in the lattice Boltzmann method via a simple generalization of the equilibrium distribution function Eq. (8):

$$f_i^* = c\frac{\sum_{j=1}^{B} \xi_{ij} f_j}{\sum_{j=1}^{B} \xi_{ij}}, \tag{13}$$

where the $\xi_i j$ represent discrete values of the scattering phase function for the angle between $\hat{\mathbf{e}}_i$ and $\hat{\mathbf{e}}_j$ and c is chosen such that,

$$
\begin{aligned}
c > 1 &\rightarrow \textit{Emission} \\
c = 1 &\rightarrow \textit{Conservation} \\
0 < c < 1 &\rightarrow \textit{Absorption}
\end{aligned}
\tag{14}
$$

3. RESULTS

The scattering of photons gas from a columnar beam of light entering a homogeneous gas was shown in an earlier work (Mozer and Caudill, 1995). For this case, it was shown that the results of the LBRTE method agreed well with a traditional forward Monte Carlo approach. Here we extend this demonstration to include a inhomogeneous scattering medium–specifically a simulated cumulus cloud.

A physics and fractal-based cloud model (Cianciolo, 1996) was used to generate a field of cloud liquid water content representative of a cumulus cloud. Values of liquid water content were calculated on a cubical grid with 2-km sides and 2-m spacing. For this case, the optical depth across a volume element is considered proportional to the liquid water content in that voxel.

Figure (1) shows the results of a preliminary LBRTE calculation through the synthetic cloud field. In this case, the illumination is from the top of the cloud field (zenith angle zero) and no diffuse sources are included. The figure shows the field of photons exiting the computational cube at each visible face. Due to the geometry of the problem, all of the photons emitted along the lateral faces of the cube are a result of scattering within the volume. The bottom face represents transmission of the incident flux through the cloud volume.

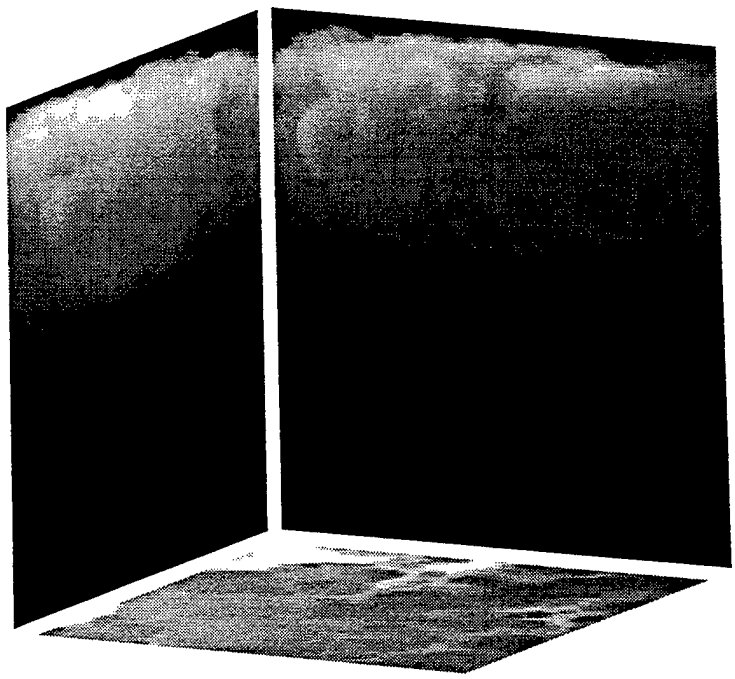


Fig. 1. Lattice Boltzmann radiative transfer calculation through a field of liquid water content representative of a cumulus cloud. The illumination is from the top. The images formed on the faces of the cube represent the photons exiting that face. No diffuse sources were included in this calculation.

3.1 Timing

One of the major benefits to the LBRTE approach is its efficiency on a parallel computer platform. We have calculated the CPU times required to perform the LBRTE calculation through the cumulus cloud shown in Fig. (1) on a parallel cluster of Pentium-based workstations. Figure (2) shows in inverse of the execution time in seconds versus the number of processors used in the calculation. Also shown in Fig. (2) are the timing results for a forward Monte Carlo (MC) code which tracked 2×10^6 individual photons.

It is apparent from the figure that the LBRTE methods are more efficient that than the MC calculation for the cases shown. However, the MC results exhibit a nearly perfect linear scalability whereas the LBRTE results depart from the straight line shown in the figure. By itself, this fact leads to the conclusion that the MC method would be more efficient when many more processors were used. However, one must consider the level of noise required in the final result. We chose to run the MC code using 2×10^6 photons because it is roughly equivalent to the number of sites in the LBRTE lattice. However, the images produced by the MC method (not shown) contain a large amount of noise. In order to suppress this noise, more photons must be run through the cloud. This leads to longer execution times. Therefore, when comparing the efficiency of the LBRTE and MC methods for a given problem, one must specify the maximum amount of noise which can be tolerated in the result.

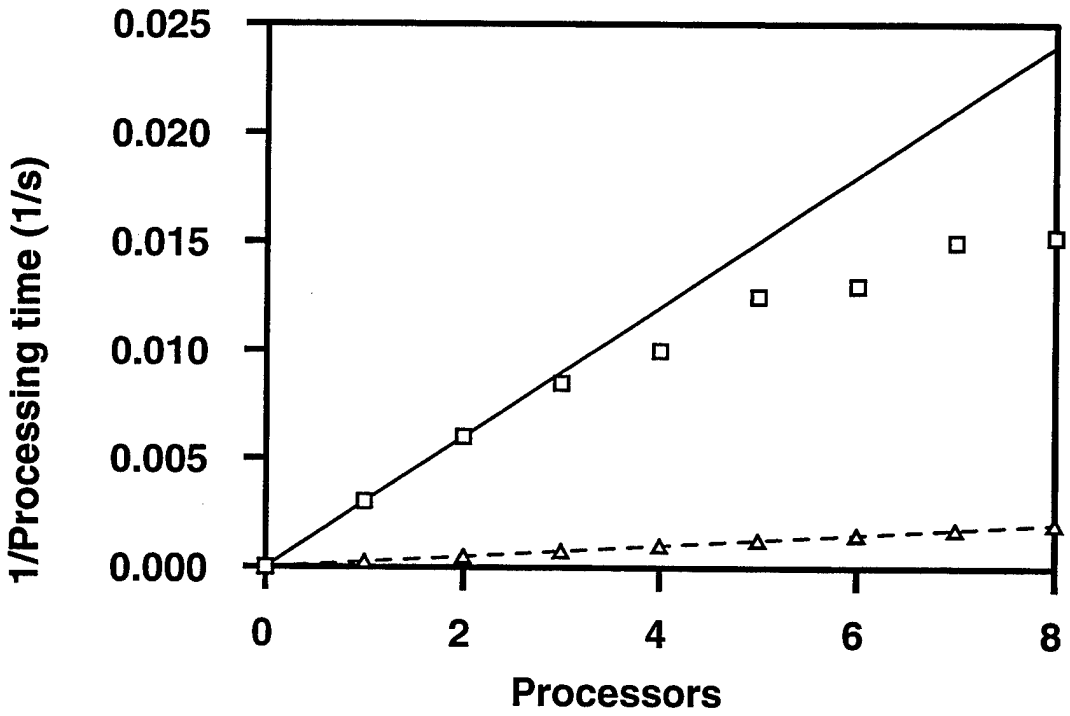


Fig. 2. Timing results for calculation shown in Fig.(1). Squares represent results for LBRTE calculation. Triangles are for a Monte Carlo calculation involving 2×10^6 photons. The solid and dashed lines represent perfect linear scaling for each method respectively

4. CONCLUSION

The Lattice Boltzmann Radiative Transfer Equation (LBRTE) method seems to be an efficient and effective method to calculate the transport of monochromatic radiation through a non-homogeneous medium. Because the LBRTE method performs an explicit streaming of photons in a discrete lattice, it is particularly adept at solving problems where multiple scattering is significant. The LBRTE method is capable of producing accurate quantitative results for cases of isotropic scattering as well as for a Rayleigh phase function. Problems involving a highly peaked scattering phase require many lattice directions to resolve the angular streaming which reduces the efficiency of the LBRTE

method. Although this is a severe limitation to the method, it is expected that the LBRTE scheme will be useful for some problems–such as the scattering of microwave radiation by atmospheric clouds.

REFERENCES

Mozer, J.B. and T.R. Caudill, 1995: The lattice Boltzmann method: a new approach to radiative transfer through clouds. *Preprint. Cloud Impacts on DoD Operations and Systems*, Hanscom AFB, MA, 135-137.

Boon, J.P. 1991: Statistical mechanics and hydrodynamics of lattice-gas automata: an overview. *Physica D*, **47**, 19-23.

Cianciolo, M.E., M.E. Raffensberger, E.O. Schmidt, J.R. Stearns, 1996: Atmospheric scene simulation modeling and visualization. PL-TR-96-2079, USAF Phillips Laboratory, Hansom AFB, MA, 110 pp.

A PRACTICAL MODEL FOR CONTRAST UNDER NIGHTTIME, ARTIFICIAL ILLUMINATION

Donald W. Hoock Jr.
U.S. Army Research Laboratory
Information Science and Technology Directorate
Battlefield Environment Division
White Sands Missile Range, NM 88002-5501

John C. Giever
Sean G. O'Brien
Physical Science Laboratory
New Mexico State University
Las Cruces, NM 88003

ABSTRACT

Under the support of TRAC-WSMR and as a long-term research project, coordinated with the U.S. Army TRADOC-lead Target-Acquisition Simulation (ACQSIM) program, we have developed a practical model for computing the effects on target contrast of artificial illumination sources (flares) in the presence of aerosols and obscurants. In this paper we describe this parametric model and its use of multi-stream radiative transfer equations and scaling laws to provide estimation of the radiance from obscurant clouds illuminated by point-source flares. The model is based on the detailed numerical calculations of direct and terrain-reflected radiance for the unobscured environment, combined with results from the 26-stream Battlefield Emission and Multiple Scattering (BEAMS) radiative transfer model for obscurant multiple scattering. We show how the resulting modeled radiances can be used to compute target/background contrasts and effective "sky-to-ground" ratio inputs required by contrast propagation models. We also show visualization examples that illustrate the interesting scenarios that can result from the relative positions of flare, aerosol cloud, illuminated target, illuminated terrain and distant dark backgrounds.

INTRODUCTION

Sensor performance calculations are based on knowing the signal available at the sensor aperture. Target acquisition models and combat simulations thus must treat various environmental effects. These include atmospheric propagation loss, available natural and man-made illumination, atmospheric effects on the spatial or angular resolution of target details, and the effects of scattered radiance on reducing target to background contrast.

The contrast equation used in models and simulations is based on the ratio of the difference in radiance L ($W/m^2/sr$) between an object and its background, relative to that of the background:

$$C(0) = \frac{L_o(0) - L_b(0)}{L_b(0)} \qquad (1)$$

where C(0) is the (dimensionless) contrast at distance zero from the object, and $L_o(0)$ is the radiance ($W/m^2/sr$) from the object at range zero. $L_b(0)$ is the radiance from the background as it appears from the position of the object, regardless of how far the background actually is beyond the object.

Over a path of distance s (m) from the object to the sensor, each radiance L(0) experiences a transmission loss (signal loss) and an accumulation of in-scattered and emitted "path radiance" L_p (usually as an unwanted noise from the sensor's point of view):

$$\begin{aligned} L(s) &= T(s) \cdot L(0) + L_p(s) \\ &= T(s) \cdot L(0) + [1 - T(s)] \cdot L_s \end{aligned} \qquad (2)$$

where transmission T(s) is usually computed internally in the simulation from:

$$T(s) = \exp\left(-k_{ext} \cdot s\right) = \exp\left(-\alpha \int c(s)\, ds\right) \quad (3)$$

where k_{ext} is an input or modeled "volume extinction coefficient" (m^{-1}), α is an input extinction per unit concentration or "mass extinction coefficient" (m^2/g), and c(s) is the modeled aerosol concentration (g/m^3) over the path. As can be seen, the relationship between path radiance $L_p(s)$ over the path and transmission is:

$$L_p(s) = \left[1 - T(s)\right] \cdot L_s \quad (4)$$

where L_s is called the average "limiting path radiance" over the path.

Substituting Eqs. 2 and 4 into Eq. 1, we can easily find the expression for contrast change over the distance s (m) that is found in most target acquisition and sensor performance models:

$$C(s) = \frac{C(0)}{1 + \left(\frac{L_s}{L_b(0)}\right)\left(\frac{1}{T(s)} - 1\right)} \quad (5)$$

The ratio of limiting path radiance Ls to zero-range background radiance $L_b(0)$ is the (usually input) "sky-to-ground ratio" Sg:

$$S_g = L_s / L_b(0) \quad (6)$$

The origins of the Sg inputs to models and simulations can be observations, models or simply "ad-hoc" values for scenarios. Observations, which are valid for near horizontal lines of sight, use the ratio of the sky radiance L_s just above the horizon to the background radiance $L_b(0)$ observed from the target location. These properly account for sun position and "sun at back" versus "sun in eyes" differences in contrast. However, they are usually meaningless at night except under moonlit conditions. Then the ratios of radiance from scattering by the atmosphere (L_s) to reflection from terrain (L_b) scale about the same regardless of whether the sun or the moon is the illumination source. Models can also be effective for daytime and moonlit conditions to treat non-horizontal lines of sight. However, it is still very common to see the use of "typical scenario" Sg as input constants. Daylight values for Sg are 3 to 5 for objects viewed against terrain, one for an object viewed against the horizon sky, and 6 to 9 when viewing near the sun and into the glare of sunlight through haze.

This situation is, of course, more complicated when the primary illumination source is a flare at night, and when obscurants such as smoke and dust produce the scattering. Then simple estimates no longer apply. However, long, detailed modeling runs are often impractical. Some combination of simplified model and interpolation in pre-computed tables is required. In the following sections we outline some of the results of a project to develop such a capability as part of an on-going process in the TRADOC Target Acquisition Simulation (ACQSIM) program and between TRAC-WSMR and the Army Research Laboratory (ARL).

AN EARLIER MODEL - COIL

The effects on contrast of an object against a background not only varies with the flare illumination dependence on range, but also on the scattering and attenuation effects of the atmosphere from flare to object (and background) and from object (and background) to the sensor. In 1975 ARPA funded a model through General Research Corporation called the Combat Illumination (COIL) model (Stathacopoulos, 1975). The COIL documentation shows that it was meant to treat the basic problem of flare geometry, terrain reflectance, and simple attenuation and scattering from a uniform atmosphere. The methods were rather crude in that radiance reaching an object was estimated by sampling along only 20 rays, including that from the flare, and most reflectance and scattering (even from terrain) was considered as isotropic into a sphere or hemisphere. The COIL computer code is apparently no longer available, however, and thus the present project was begun.

BLACK SKY BACKGROUNDS

What value of Sg should be used for night-time contrast under natural illumination and under flare illumination? Determining this value is a major goal of the present effort.

One problem is that for a black background sky or distant non-illuminated terrain, then $L_b(0)$ is zero. Thus, the required input Sg ratio L_s/L_b is infinite [as is the zero range contrast C(0)].

One solution is to allow the user to continue to choose any finite value of C(0), and then to specify an accurate illuminated object radiance $L_o(0)$. Then the physically-consistent value for Sg should be:

$$S_g = L_s \cdot \left[1 + C(0)\right] / L_o(0) \quad (7)$$

Or we can assume that the background radiance at the sensor is never less than the limiting sensor noise value. Thus if $L_b(0)$ is arbitrarily chosen as this lower limit (say a micro-watt/m^2/sr), then Eqs. 1 and 5 can consistently be used for contrast C(0) and Sg. Before considering the effects of obscurants, however, we must first treat modeling of flare-illuminated object and background radiances.

DIRECT FLARE RADIANCE

As shown in Fig. 1, we treat a single flare as a point source of radiant power (also known as the radiant flux) P_s' (watts W) at a height h_s (m) above the terrain. Define any surface directly illuminated by the flare at a height h_f' (m) above the terrain and at a ground surface range R_f' (m) from the ground point directly below the flare. (The use of "primes" on the various quantities will be made clear shortly, when we reintroduce them as scaled parameters.) The surface orientation is defined by a surface normal vector that makes an angle θ with the vector from the surface to the flare. The surface can be any terrain element or an object facet. We assume for this paper that the flare emits power equally in all directions (4π steradians sr). Thus, the radiant intensity I_s' (W/sr) of the flare is:

$$I_s' = P_s' / (4\pi) \qquad (8)$$

We will use ANSI (1986) radiometric units (W, W/sr, W/m^2, and W/m^2/sr) in favor of photometric units in this paper. Corresponding photometric units (lumens, candelas, lux, and cd/m^2) require band-integration over the photopic or scotopic spectral responses of the eye. A nice discussion of the ANSI definitions of radiometric and photometric units is given in the appendix of Ashdown (1994). The surface irradiance E_f' (W/m^2) depends on the surface's distance to the flare and on the cosine of the angle between the surface normal and the ray from the surface to the flare. In terms of the surface-normal direction cosines μ_f , i.e. (α_f, β_f, γ_f) and the direction cosines of the ray from the surface field point to the flare μ_s, i.e. (α_s , β_s, γ_s):

$$E_f' = \left(\frac{P_s'}{1000}\right) \cdot \frac{1000 \cdot (\mu_s \circ \mu_f)}{4\pi \left((h_s - h_f')^2 + R_f'^2 \right)} \qquad (9)$$

where components are defined in terms of source and field point coordinates (x_s', y_s', z_s') and (x_f', y_f', z_f'):

$$\mu_s \circ \mu_f = \alpha_s \cdot \alpha_f + \beta_s \cdot \beta_f + \gamma_s \cdot \gamma_f \qquad (10)$$

$$\alpha_s = \frac{x_s' - x_f'}{\sqrt{(h_s - h_f')^2 + R_f'^2}} = \frac{x_s - x_f}{\sqrt{(1 - h_f)^2 + R_f^2}} \qquad (11)$$

$$\beta_s = \frac{y_s' - y_f'}{\sqrt{(h_s - h_f')^2 + R_f'^2}} = \frac{y_s - y_f}{\sqrt{(1 - h_f)^2 + R_f^2}} \qquad (12)$$

$$\gamma_s = \frac{z_s' - z_f'}{\sqrt{(h_s - h_f')^2 + R_f'^2}} = \frac{z_s - z_f}{\sqrt{(1 - h_f)^2 + R_f^2}} \qquad (13)$$

In the above, x, y, z, h_f and R_f are "scaled distances" (each dimensionless) in terms of the source height. Distances are thus now expressed simply as the number of "flare heights" or "h_s units" as:

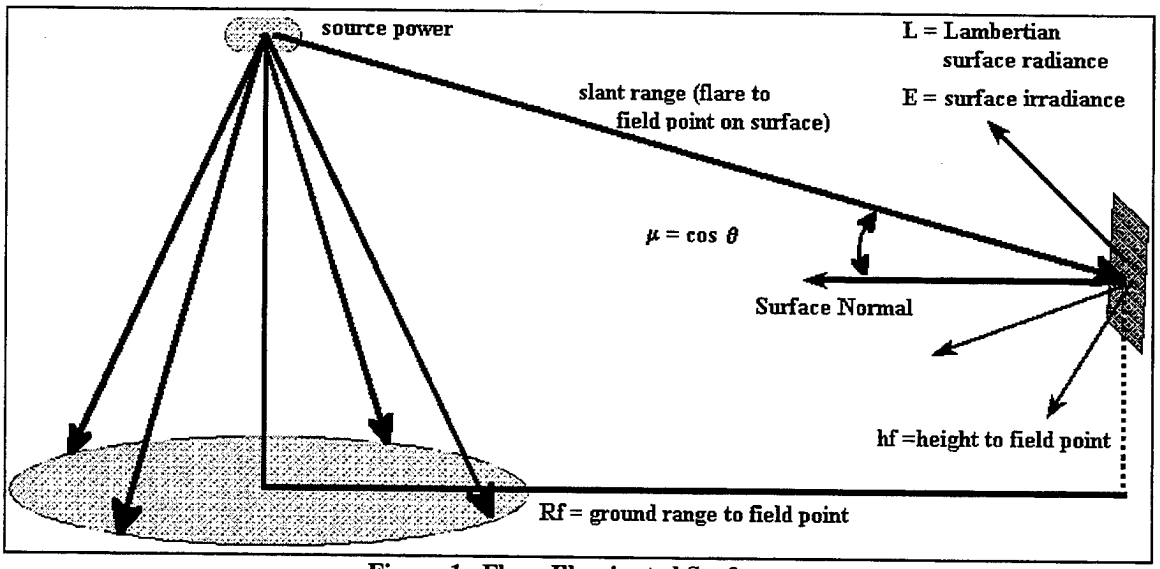


Figure 1. Flare-Illuminated Surfaces

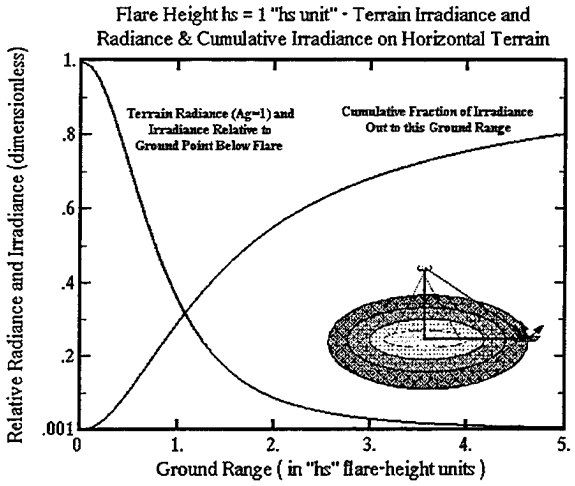


Figure 2. Relative Terrain Surface Irradiance

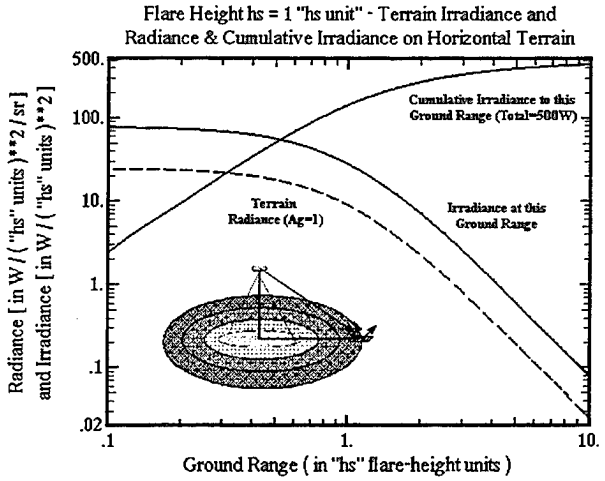


Figure 3. Diffuse Terrain Irradiance and Radiance

$$x' = x \cdot h_s, \quad y' = y \cdot h_s, \quad z' = z \cdot h_s \qquad (14)$$

$$h_f' = h_f \cdot h_s, \quad R_f' = R_f \cdot h_s \qquad (15)$$

while the "scaled irradiance" E_f (dimensionless) in terms of a 1000 W source and "h_s units" is:

$$E_f' = \frac{P_s'}{1000 \cdot h_s^2} E_f \qquad (16)$$

and where the study now concentrates on computing:

$$E_f = \frac{1000 \cdot (\mu_s \circ \mu_f)}{4\pi\,(1+R_f^2)} \qquad (17)$$

The advantage of using these scaling methods is that we then need only compute the problem for a single flare power (i.e. 1000 W) and a "unit flare height" (i.e., $h_s = 1$). Now if the irradiated surface is Lambertian with reflectance A_f, (dimensionless from 0 to 1), then it diffusely reflects the illumination, producing its own scaled radiance (sr^{-1}) in all directions:

$$L_f = A_f \cdot E_f / \pi \qquad (18)$$

and correspondingly, the actual radiance ($W/m^2/sr$):

$$L_f' = A_f \cdot E_f' / \pi \qquad (19)$$

Figure 2 plots the computed relative values of E_f (and, in fact, the direct radiance contribution to L_f) for the horizontal terrain surface and a terrain reflectance

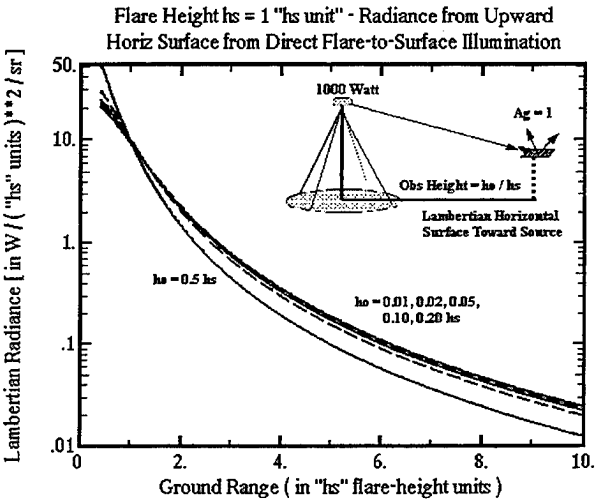


Figure 4. Horizontal Surface radiance - Direct

(albedo) of one. The horizontal axis is the scaled ground distance R_f from the flare. It can be seen that the surface irradiances and reflected radiances fall to 35%, 9% and 3% of the maximum at radii of just one, two and three flare heights respectively. However, even at a ground distance of five flare heights, where the relative irradiance and radiance are reduced to 0.1% of the maximum, only 80% of all the downward flare radiant power has illuminated the surface. The remaining 20% of the total downward radiated power is spread over the rest of the very large surrounding area.

Figure 3 shows the actual (scaled) irradiance E_b and radiance L_b for the terrain (using subscript "b" for "background") in $W/(h_s^2)/sr$ for the 1000 W reference source and a ground albedo of one. Figure 4 shows the reflected radiance due to direct radiance from the flare for any other upward-facing horizontal object surface at scaled height h_o with scaled ground range in h_s units.

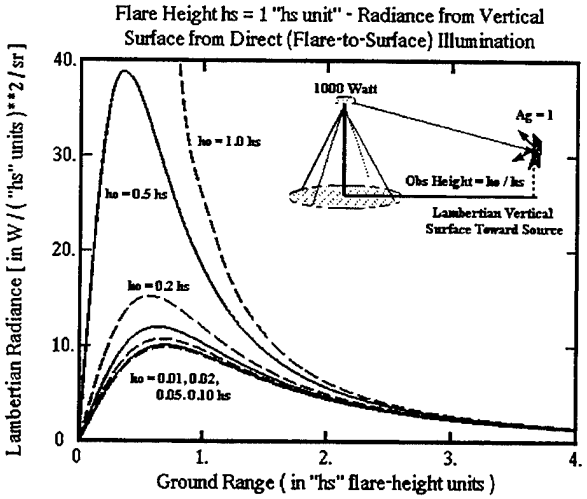


Figure 5. Vertical Surface Radiance - from Direct

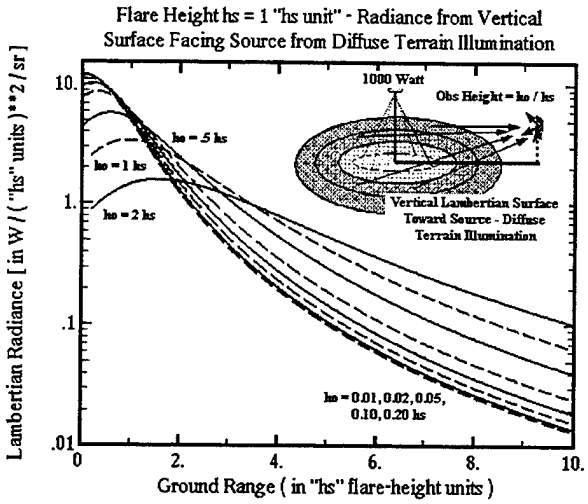


Figure 6. Vertical Surface Radiance -Diffuse

Figure 5 shows the reflected radiance due to direct flare illumination for any vertical surface that is rotated around the z-axis to face the flare. Note that as a horizontal surface (Fig. 4) is raised to about half the flare height there is little change in reflected radiance. However, vertical surface radiance (Fig. 5) shows strong dependence on height above the terrain (especially out to two or three flare-height radii) due to the dot product of the illumination ray with the surface normal.

DIFFUSE RADIANCE

Direct illumination from the flare (if any) is the dominant source of reflected radiance from surfaces such as targets above the terrain. However, the diffuse irradiance from the terrain itself can also be an important factor. To compute this contribution one must integrate the incident radiance L_b from all terrain surface elements in the relevant directions and at all ranges:

$$E_o = \int \frac{(\mu \circ \mu_o)\,\gamma_b\, L_b(x,y)}{(x-x_o)^2 + (y-y_o)^2 + h_o^2}\, dx\, dy \qquad (20)$$

where (x_o, y_o, h_o) are the coordinates of the diffusely illuminated "object surface", μ_o is the object surface normal dotted with the direction cosines of the ray from the object to the terrain element "dx dy" at position (x, y, z), and γ_b is the z-component direction cosine of the ray with respect to the normal to the terrain element. The corresponding radiance from the object surface is:

$$L_o = A_o\, E_o / \pi \qquad (21)$$

Because of the complexity of the above integral, data have been numerically computed for object

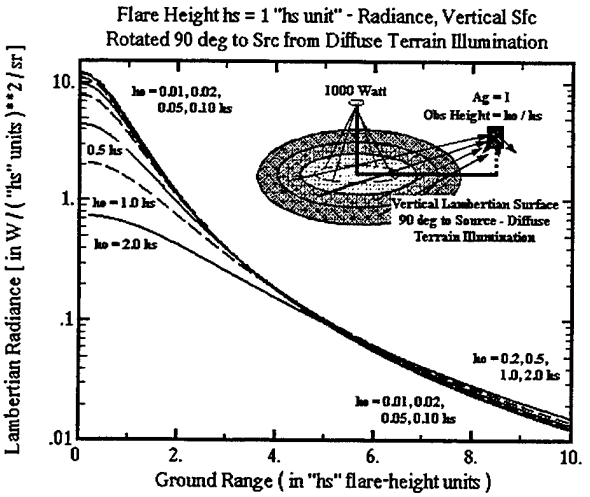


Figure 7. Vertical Surface Radiance - Diffuse

surfaces at various orientations. A few are shown in the following figures. Figure 6 shows the radiance contribution originating from diffuse terrain radiance and reflected from any vertical object surface rotated about the vertical axis to face the flare. Figure 7 is similar, but for the vertical object surface rotated at right angles to the flare (i.e., edge-on). Figure 8 is for the vertical object surface rotated to face away from the flare. Figure 9 shows the contribution of terrain diffuse radiance on the reflected radiance from any downward facing horizontal surface.

Although there are considerable differences in the diffuse terrain radiance contributions seen in these figures, these differences are mostly at the large object heights (0.5, 1.0 and 2.0 flare-heights) and at small distances from the flare. It is interesting that at large radial distances, the object surface radiances are fairly comparable, regardless of object orientation, and the

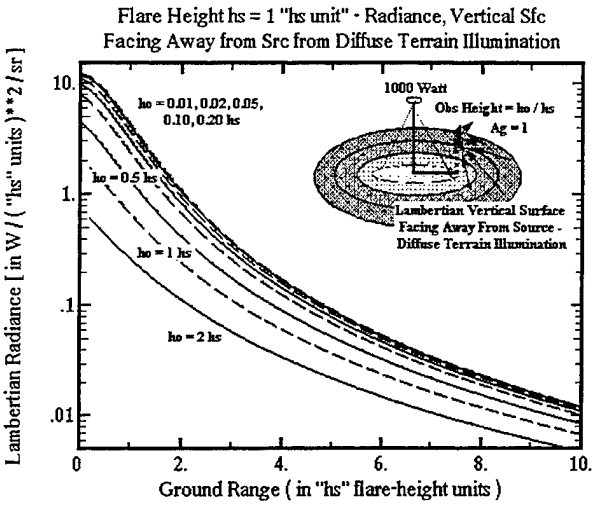


Figure 8. Vertical Surface Radiance - Diffuse

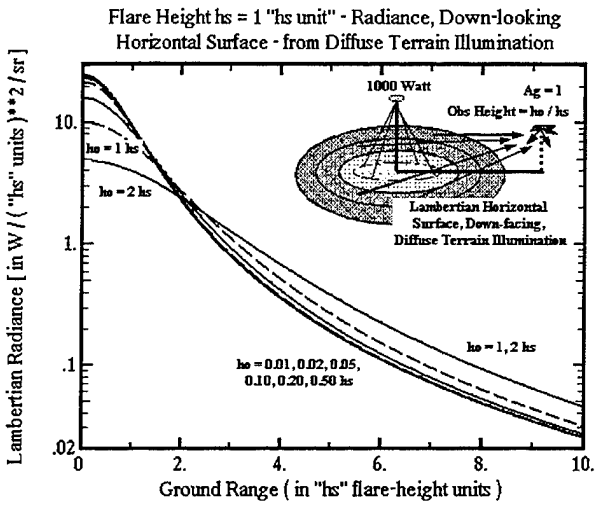


Figure 9. Horizontal Surface Radiance - Diffuse

direct radiance contributions are not appreciably larger than the diffuse contributions. At small radial distances of a few flare heights the direct illumination dominates, of course, especially as the object height is raised above the terrain. And, since the computations are for terrain and object surface albedos of one, we must also note that the direct-radiance contribution will scale as A_o (object albedo), while the diffuse contribution will scale as $A_o * A_b$ (object albedo times terrain albedo).

In the current modeling study we actually compute and store the diffuse radiance for several more surface orientations. These tables are used to interpolate to any general orientation. The contributions of direct radiance are easily computed on the fly using the direct radiance equations of the earlier section.

CLOUD TRANSMISSION AND RADIANCE

Having defined all the quantities required for flare illumination of backgrounds (L_b) and objects (L_o) in an unobscured environment, we can compute the contrast C at any point. However, we now turn to modeling the transmittance T and the limiting path radiance L_s numerator in the Sg term.

Models for smoke and dust transmittance (Ayres, 1993) are available from the Electro-Optical Systems Atmospheric Effects Library (EOSAEL, 1987). The Battlefield Emission and Multiple scattering (BEAMS) Model (Hoock, et. al. 1993, 1994, 1995; O'Brien, 1993) computes the radiance through smoke and dust clouds. In the present project we used BEAMS to compute L_s for the scattering from uniform cloud blocks 48 m long, 32 m wide and 16 m high of fog oil, phosphorus and dust. Optical depths of the clouds were varied from 0.25 to 64 across the cloud width. A 1000

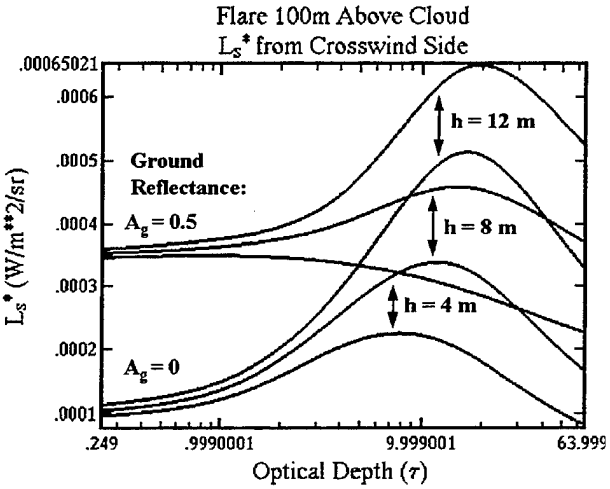


Figure 10. Cloud Ls Radiance from Sides

W flare was placed at four different locations in separate runs: directly above the cloud center at 116 m, 24m and 8 m above ground level; and for an off-axis location 62 m above the surface and 93.5 m in ground distance from the cloud center. The entire set of 60 runs were repeated for terrain albedos of zero (no terrain) and 0.5.

The analyzed radiances are being stored as tables and parametric curves. Figure 10 is an example of L_s exiting the side of a fog oil cloud with the flare 116 m above the terrain (100m above the top center of the cloud). Figures 11 and 12 show L_s values for radiance from the bottom and from the top of the cloud respectively. Note that radiance from the side of the cloud varies with height of the exit point for optically thick smoke. This quantifies the darkening near the bottom due to obscuration as radiant power is lost from the side of the cloud. The radiance exiting the bottom of the cloud shows only a small dependence on terrain albedo. The difference is due to diffusely reflected

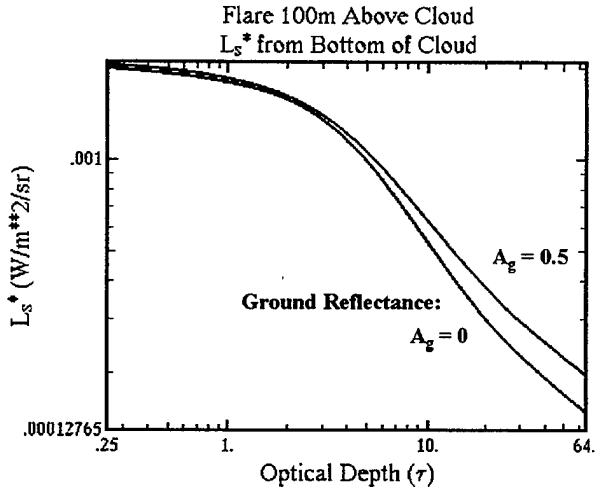


Figure 11. Cloud Ls Radiance from Bottom

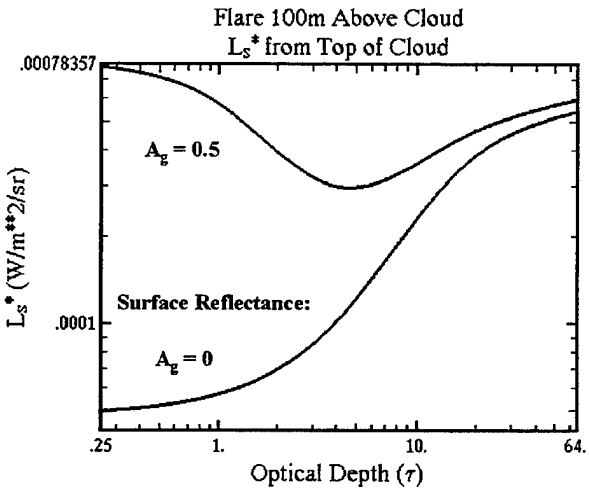


Figure 12. Cloud Ls Radiance from Top

terrain radiance back-scattered from the cloud. The large variation with albedo for radiance exiting the top of the cloud is due to the reflected terrain radiance that is only partly obscured at small optical depths.

Examples of cloud appearance are shown in Figs. 13 through 17. Figure 13 is the uniform rectangular fog oil cloud used to generate the tables and parametric curves for Ls in the study. (The ringed appearance is due to gray-level quantization in the figures in this paper.) Figure 14 shows a non-uniform fog oil cloud with optical depth of one across the 32 m width (top) and Optical Depth (OD) of four (bottom). The flare is at 116 m altitude directly above the cloud.

Figure 15 shows the flare at 30 deg elevation and 108 m range from the cloud. Cloud width OD's are one (bottom) and four (top). Figures 16 and 17 show the case of the flare just 8 m above the cloud surface for OD's of one and four respectively.

Current efforts are to better account in the parameterized data for the cloud shadow regions which alter the diffuse radiance as well as direct radiance.

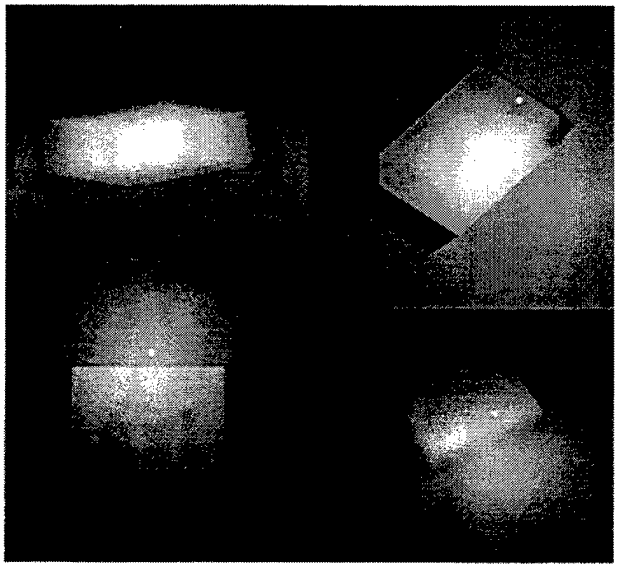


Figure 13. Illuminated Uniform Fog Oil Cloud

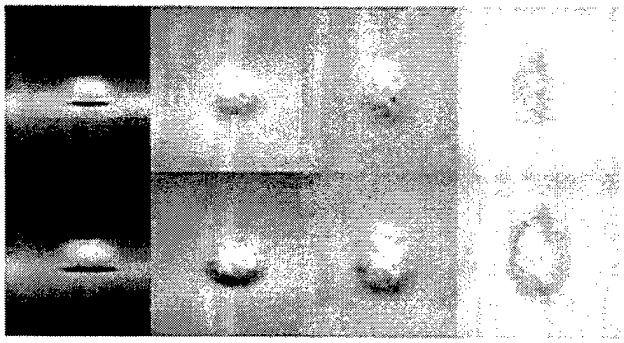


Figure 14. Flare at (0 m, 0 m, 116 m) on Fog Oil. Top Optical Depth = 1, Bottom OD = 4.

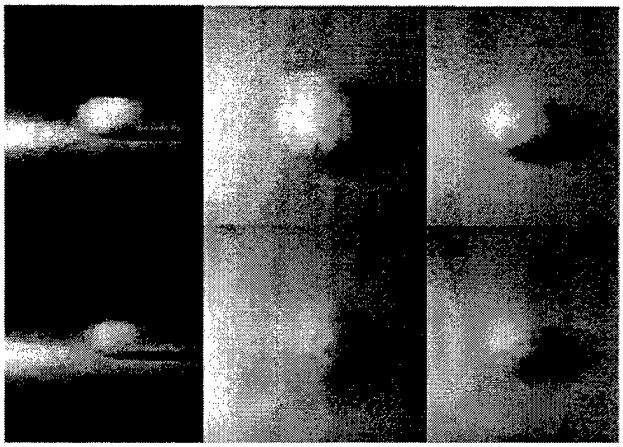


Figure 15. Flare at (0 m, 93.5m, 62m) on Fog Oil. Top Optical Depth = 4, Bottom OD = 1.

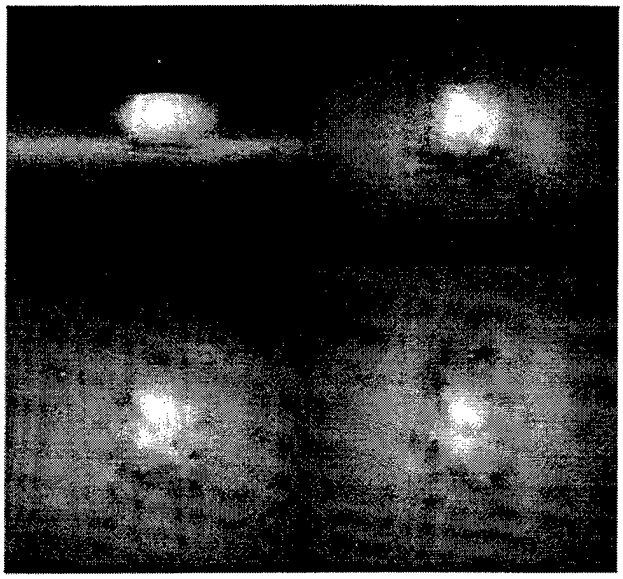


Figure 16. Illumination for Flare 8 m Above Fog Oil Cloud of Optical depth = 1

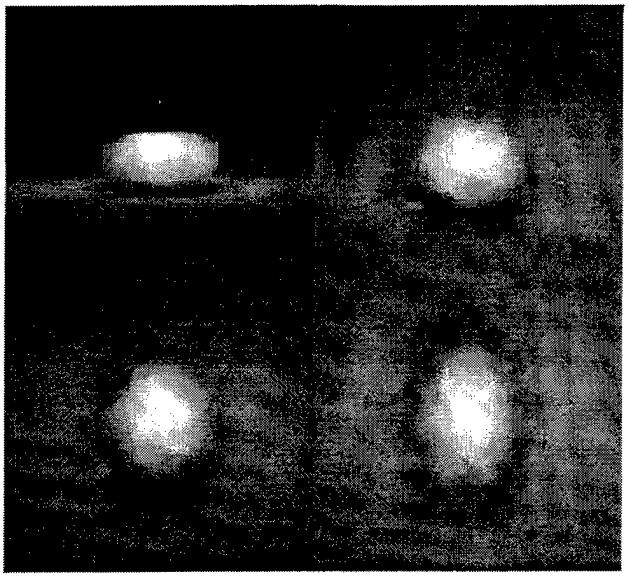


Figure 17. Illumination for Flare 8 m Above Fog Oil Cloud of Optical depth = 4

A CONTRAST EXAMPLE

Figure 18 shows an example of the changes in contrast under a flare with and without a smoke cloud. The scenario is that of a vertical-surface (object) moving toward an observer whose line of sight is a constant 1 deg elevation above the terrain. The object begins at a ground range 9 flare heights beyond the flare (point "18" on the horizontal axis), moves toward the observer and passes beneath the flare (point "9" on the axis) and finally ceases movement at a ground range of 9 "flare heights" on the observer side of the flare (point "0").

Contrast varies from minus one (a black object against a bright background) through zero (no contrast between the object and background) and to positive infinity (bright object against a black background). In order to plot this range on a log scale, we have added a constant value of one to all contrasts displayed on the vertical axis of the plot. Thus, any value of (1+C) less than one is a negative (dark object on light background) contrast. Any value of (1+C) greater than one is a positive (light object on a dark background) contrast:

$$\log_{10}\left[1+C(s)\right] = \log_{10}\left[L_o(s)\right] - \log_{10}\left[L_b(s)\right] \quad (22)$$

The example is for a 1000 W flare at 116 m above the surface. The object is 2.3 m above the terrain. Both the object and terrain have albedos of 0.5. The solid line shows that even though the reflectances are equal, the different distances of the object and the background from the observer generates a significant contrast. It is approximately 12 at the most distant point. The contrast falls slowly to about half the initial value at 2 flare-heights beyond the flare. It then falls to 0.35 contrast (or 1.35 on the vertical axis) as it passes below the flare (9 on the horizontal axis). At this point the object is illuminated only by diffuse terrain radiance from the observer side of the flare. The contrast then goes negative (less than one on the vertical axis) at about 0.15 flare heights on the observer side of the flare. As the object proceeds toward the zero point on the horizontal axis, the contrast falls to about -0.89 at 2 flare heights on the observer side (7 on the horizontal axis). Actually at this point the object attains its "best" negative contrast. As it continues to move toward the observer, the contrast again rises to a final value of -0.66 (at 0 on the horizontal axis).

Now consider the dashed line. This plot of "contrast+1" shows the immediate effect of smoke obscuration that extends from about 7 source heights beyond the cloud (16 on the horizontal axis) to about 1.5 source heights on the observer side (7.5 on the horizontal axis). The smoke cloud is 16 m high and has an optical depth of one. It intercepts the line of sight over this range. Interestingly, while the contrast falls as the object approaches the flare in the "clear air" case, it actually rises slightly in the presence of the smoke. In part this is because the cloud itself is a source of radiance that illuminates the object more than the distant background point. The fluctuating behavior as the object approaches the cloud is due in part to the shadow of the cloud, the obscuration of the diffuse terrain on the far side of the

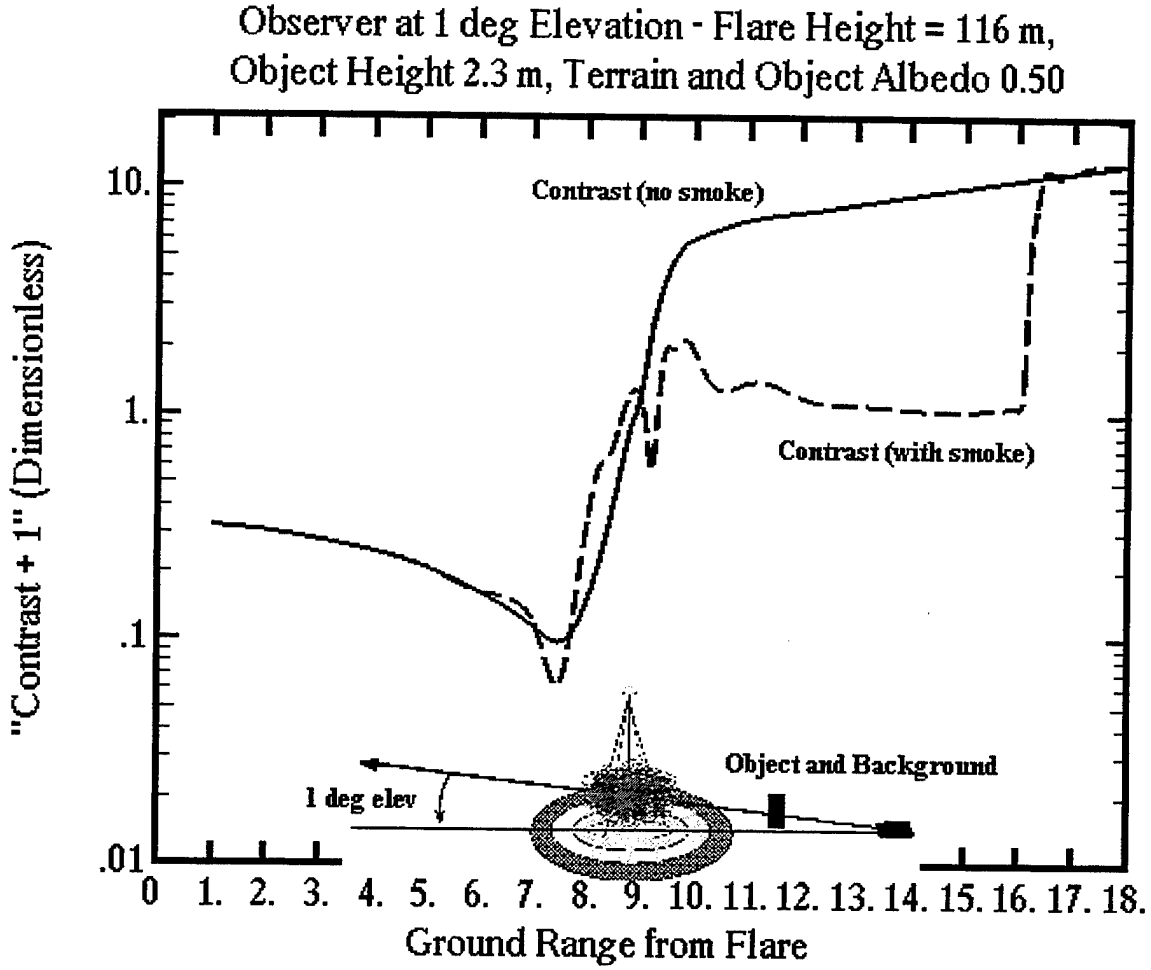


Figure 18. Example of Object Contrast Under Flare and Smoke

cloud, and the changing path length of obscurant in front of the object as it passes through and out of the cloud. The background "lags behind" the object in its passage through the cloud. Thus, for a short distance the background is obscured while the object is not obscured. By the point where both the object and background are not influenced significantly by the cloud (at about 2 source heights on the observer side of the cloud) the contrast again attains the clear air value.

Of course, the behavior under any other set of circumstances can be different. The effects are highly dependent on geometry. We should also note that the treatment of the shadow area around the flare is still being finalized. Thus, details of variations near the smoke should be considered with caution.

CONCLUSIONS

Radiometrically correct simulation of night-time conditions on visual systems is made difficult when the primary illumination is artificial. We have outlined here a project to develop a practical, parameterized model based on research model outputs. The problem of providing input contrast and sky-to-ground ratios to the standard contrast algorithms used in constructive simulations is made much more complicated by the presence of aerosols. And rendering of scenes in real-time virtual simulations with sufficient correlation to the effects used in constructive simulation is complicated primarily by the need to properly account for diffuse radiance and cloud shadowing. In fact the proper parameterization of the shadowing effect is the final aspect in the current project that was still being addressed as this paper was submitted.

ACKNOWLEDGMENTS

We wish to acknowledge the support of TRAC-WSMR in this project and the efforts of the TRAC-lead ACQSIM group for coordinating improvements in target acquisition simulation.

REFERENCES

ANSI/IES (1986). American National Standard Nomenclature and definitions for Illumination Engineering, ANSI/IES RP-16-1986, Illumination Engineering Society of North America, New York.

Ashdown, Ian (1994). Radiosity, A Programmer's Perspective, John Wiley and Sons, New York.

Ayres, Scarlett and DeSutter, S. (1993). EOSAEL 92: Vol 14. Combined Obscuration Model for Battlefield-Induced Contaminants (COMBIC), U.S. Army Research Laboratory Report, Adelphi, MD.

Hoock, D., Giever, J. & O'Brien, S (1993). Battlefield Emission and Multiple Scattering (BEAMS), a 3-D Inhomogeneous Radiance Transfer Model, Proceedings of the SPIE, 1967, 268-277. Bellingham, WA: SPIE -- The International Society for Optical Engineering.

Hoock, D. & Giever, J. (1994). Modeling Effects of Terrain and Illumination on Visibility and the Visualization of Haze and Aerosols, Proceedings of the SPIE, 2223, 450-461. Bellingham, WA: SPIE -- The International Society for Optical Engineering.

Hoock, Donald, O'Brien, S., Giever, J. and McGee, S. (1995). High Fidelity Modeling of Obscurants for Virtual and Constructive Simulations, Proceedings of the 1995 ITEA Workshop "Modeling and Simulation: Today and Tomorrow", White Sands Missile Range, NM.

O'Brien, S. (1993). Comparison of the BEAMS 2.2 Radiative Transfer Algorithm with Other Radiative Transfer Methods, Proceedings of the 1993 Battlefield Atmospherics Conference, U.S. Army Research Laboratory, Battlefield Environment Directorate, White Sands Missile Range, NM, 421-435.

Shirkey, Richard, Duncan, L. and Niles, F. (1987). Executive Summary, EOSAEL 87, Vol 1, ASL-TR-0221-1, U.S. Army Research Lab, Adelphi, MD.

Strathacopoulos, A., Gilmore H., Czipott A., Gordon, C. and Rohringer, G. (1975). Combat Illumination Model (COIL), GRC Contractor Report CR-2-548, (DTIC ADB006610), General Research Corp., Santa Barbara, CA.

DOD AIR AND SPACE NATURAL ENVIRONMENT MODELING AND SIMULATION

Gary McWilliams
Executive Agent for Air and Space Natural Environment
Air Force Combat Climatology Center (AWS)
Modeling and Simulation Division
Scott Air Force Base, IL 62225-5116
Ph: (618) 256-3902 Fax: (618) 256-3964
mcwillig@thunder.safb.af.mil

ABSTRACT

This paper discusses the role, responsibilities, organizational structure, current programs, and future plans of the Modeling and Simulation Executive Agent for Air and Space Natural Environment. This DoD level organization has been formed to foster interoperability and reuse of air and space natural environment models being developed for joint simulation programs, to ensure that there is no unnecessary duplication of effort in model development, to design and implement a process by which model and simulation developers and users can acquire data from a range of data providers, and to establish a center of excellence that facilitates the integration of the best available technology into DoD air and space models and simulations.

The Commander of Air Force Combat Climatology Center has been designated by the Secretary of the Air Force as the Modeling and Simulation Executive Agent for the Natural Environment. The Commander is provided operational support from the Modeling and Simulation Division of the Air Force Combat Climatology Center. This division is staffed by personnel from the Air Force, Army, and Navy in order to better coordinate the Tri-Service responsibilities of the Modeling and Simulation Executive Agent.

The Modeling and Simulation Executive Agent for Air and Space Natural Environment already has several projects underway for assessing customer requirements, defining data standards, improving data accessibility, identifying current technology capabilities, and addressing future technology shortfalls. Efforts of this organization are closely coordinated with efforts of the Terrain and Ocean Executive Agents to ensure a seamless environmental representation in simulation.

1. INTRODUCTION

The Modeling and Simulation Executive Agent (MSEA) for Air and Space Natural Environment (A&SNE) is one of three executive agents vested with oversight authority and responsibility for DoD modeling and simulation of the natural environment. The other two executive agents encompassing the natural environment are for Ocean and Terrain. These executive agents serve as the DoD components to whom the Under

Secretary of Defense has assigned responsibility and delegated authority for the development and maintenance of the modeling and simulation for the natural environment, including relevant standards and databases, used by or common to many models and simulations (DoD Plan 5000.59). Accordingly some of the primary responsibilities of the executive agents are: to promote interoperability and reuse capability for models and algorithms; to eliminate any unnecessary duplication of effort in model development; and to establish a process by which the best available models and data are readily accessible for DoD Modeling and Simulation (M&S) programs.

The air and space domain for which the MSEA is responsible includes the atmospheric, near-space, and interplanetary environments. It extends from the surface of the Earth, through the troposphere, stratosphere, upper atmosphere, radiation belts, and interplanetary medium, to the surface of the Sun. It includes the effects and impacts caused by human activities, but does not include those activities or objects causing the effects or impacts. The air and space environment affects, and is affected by, the oceans and terrain through the transfers of heat, momentum, and moisture. In order to ensure these effects are properly represented, the activities of all three environmental MSEAs are closely coordinated.

The Under Secretary of Defense for Acquisition and Technology (1996) designated the Department of the Air Force as the MSEA A&SNE. Subsequently the Secretary of the Air Force delegated this authority to the Commander of the Air Force Combat Climatology Center (AFCCC) located at Scott Air Force Base, Illinois. The present AFCCC Commander is Col Francis Routhier.

2. ORGANIZATIONAL STRUCTURE

Col Routhier, as the Commander of AFCCC, reports to the Commander of the Air Weather Service and as the MSEA for A&SNE, reports to the Director of the Defense Modeling and Simulation Office (DMSO). The AFCCC Commander must also closely coordinate with the Air Force Staff responsible for Modeling, Simulation and Analysis (XOC) which, starting in fiscal year 1998, will be providing all overhead funding for the MSEA functions. The AFCCC Commander, in the role as the MSEA, is supported by the Modeling and Simulation Division of AFCCC.

This division, which was created at the beginning of the 1996 fiscal year, consists of the following three branches: Requirements Analysis, Technology Integration, and Standardization. The Requirements Analysis Branch identifies and documents DoD M&S weather requirements, capabilities, and any resulting technology shortfalls. It is the responsibility of the Technology Integration Branch to identify technologies for solving shortfalls, to guide DoD short-term and long-term efforts for technology development and implementation, and to coordinate M&S weather technical support to all DoD M&S activities. The Standardization Branch develops and coordinates standards for weather products and services to ensure interoperability with DoD M&S systems, and guides the DoD verification and validation of weather models, modules, algorithms, and data used for joint M&S applications. The other two divisions of AFCCC, Systems and

Operations, also have expertise which the AFCCC Commander draws upon as required to assist with MSEA activities.

The Modeling and Simulation Division is currently staffed by five government personnel, four military and one civilian, and four on-site contractor personnel. All three branches of the Military are represented in the Division to better coordinate Tri-Service M&S activities. Navy Commander Timothy Cummings serves as the Division Chief. The Requirements Analysis and Standardization Branches are headed by Air Force Captains Anthony Moninski and Bruce Lambert, respectively. Air Force Major Spencer Chapman heads the Technology Integration Branch. An Army civilian, the author who is on loan from the Army Research Laboratory's Battlefield Environment Division, is assigned to the Technology Integration Branch.

3. CONCEPT OF OPERATIONS

The Concept of Operations (CONOPS) is described in detail in the MSEA A&SNE Execution Plan (DoD MSEA A&SNE, 1996). The CONOPS is focused on our customers and the means by which we can satisfy our customers' requirements with quality products and services. The CONOPS process is outlined in Figure 1.

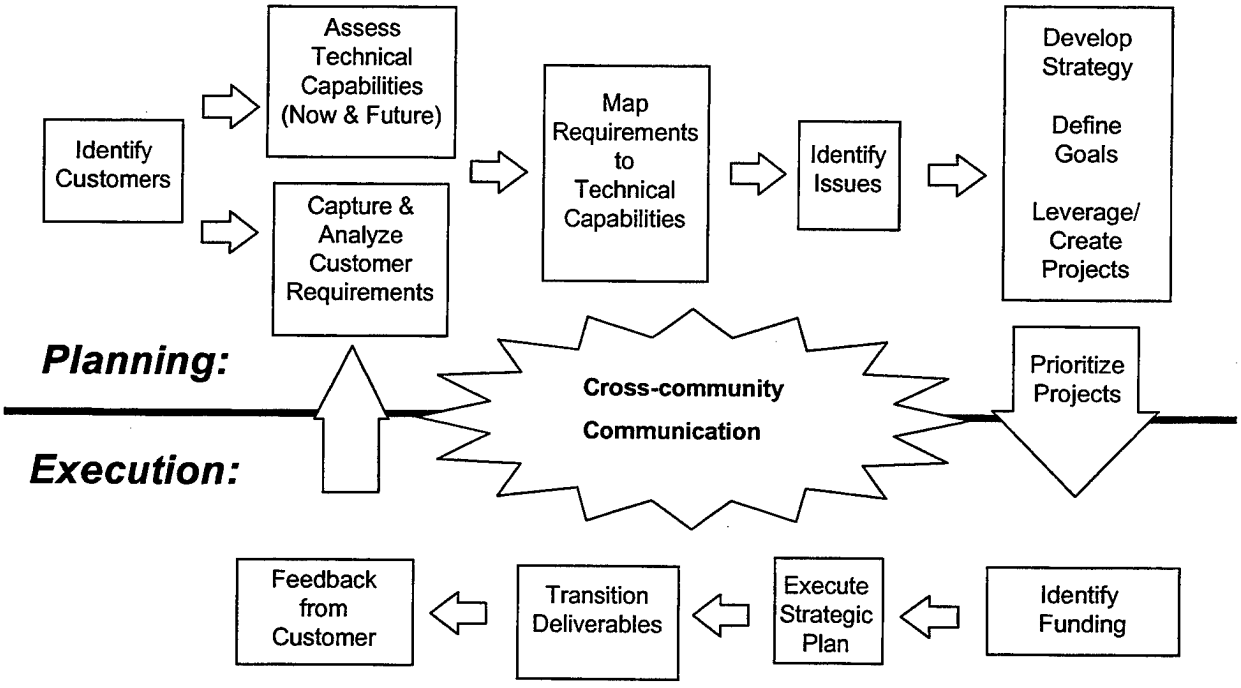


Figure 1. Diagram outlining CONOPS activities.

The two main components of the CONOPS are planning and execution. The first step for planning involves identifying customers. The customers presently identified include four major joint simulation development programs and one joint aircraft development program which has a significant simulation effort planned. The four simulation

development programs are: the Joint Warfighting System (JWARS) - to be used for analysis, the Joint Simulation System (JSIMS) - to be used for training, the Joint Modeling and Simulation System (JMASS) - to be used for engineering and acquisition, and the Synthetic Theater of War (STOW) - to be used for integrating virtual and constructive simulations from geographically distributed locations in a common synthetic battlespace. The aircraft development effort we are supporting is the Joint Strike Fighter (JSF) Program. The JSF program will make extensive use of advanced modeling and simulation techniques in all phases of the aircraft's development and acquisition. Additional customers will be added as resources permit.

Once the customer has been identified, planning progresses to defining their air and space environmental requirements and documenting them in writing as well as recording them in a relational database. This relational database is also being populated with information on technical capabilities (both existing and under development) which will allow mapping between requirements and capabilities. The requirements and capabilities analysis will be conducted on a recurring basis.

In situations where a capability already exists for a specific requirement, the MSEA will assist the customer in obtaining the technology and ensuring that the capability does in fact satisfy the customer requirement. Any requirement which is not matched to a suitable capability is identified as a shortfall. A strategy and prioritization is subsequently established for addressing the shortfall.

The execution phase begins with the creation or leveraging of a project that will address the shortfall. Next a request for proposal (RFP) will be prepared for each project and interested organizations will be invited to submit a proposal. These proposals will be reviewed by the MSEA . The proposal selected by the MSEA then will be recommended to DMSO for funding. Once a proposal is approved by DMSO, the selected organization will be funded to complete the described work. Upon completion of the project, MSEA will be responsible for transferring the technology to the customer and ensuring the customer is satisfied with the product.

The CONOPS is a continuous process and customer feedback is important throughout the process.

4. PROJECTS

The projects supported by all three environmental MSEAs are grouped into the following five program focus elements: requirements and capabilities, standards, just-in-time production, dynamic representation, and access to resources. DMSO has requested that all three MSEAs group their projects into these focus areas so that it easier to coordinate the projects to ensure that a complete and seamless representation of the environment is obtained. The MSEA A&SNE has funded projects in all five program elements for fiscal year 1997.

4.1 Requirements and Capabilities

This program element includes all projects that are primarily responsible for accumulating, interpreting, and analyzing M&S developer and user requirements and the capabilities within government, industry, and academia for satisfying those requirements. The MSEA A&SNE has funded three projects under this program element.

A requirements study is underway as a continuing effort to thoroughly define customer requirements. Initial results of this effort are summarized in the Air and Space Natural Environment Baseline Requirements Assessment report (ABACUS, 1996). All the gathered information will be stored in a relational database that will be accessible over the Internet. This work is being performed by ABACUS Corporation.

A parallel capabilities study has been initiated which will identify and describe technology that has a high potential for satisfying the customer requirements. The information gathered here will be summarized in a written report and recorded in the relational database containing the requirements information. A Technical Development and Implementation Plan (TDIP) will also be generated as part of this study. The TDIP will describe the shortfalls that result from a comparison between the requirements and capabilities information and will recommend both interim and long-term solutions for the shortfalls. The Dynamics Research Corporation (DRC) is conducting this effort.

We are funding the creation of a Tri- Service Laboratory consortium as a means to utilize the talents of the Army Research Laboratory (ARL), the Naval Research Laboratory (NRL), and Phillips Laboratory (PL). The consortium will serve as a forum for blending research from all three Services to develop and optimize M&S solutions for the Joint M&S programs.

4.2 Standards

The Standards program area includes those projects that establish rules governing models, simulations, data, and metadata. These rules allow the M&S community to build to a common understanding of the environment and thereby promote maximum interoperability and reuse. We have three projects in this focus area.

A verification, validation, accreditation and certification (VVA&C) strategy is being formulated which will allow the data producer, tool developer, M&S system developer, and M&S system user/value adder to define, build, and interchange required M&S environmental domain resources. This project is being conducted both internally and in cooperation with other environmental MSEAs and DMSO supported groups.

The Synthetic Environment Data Representation Interchange Specification (SEDRIS) project is responsible for establishing a mechanism which facilitates standard

representation of and access to existing synthetic environment data, increases the utility of legacy databases, and can be easily expanded to capture future modeling investments. The mechanism is a data model which facilitates broad reuse of synthetic environments, supports interoperability of heterogeneous simulation systems, and has application across the modeling and simulation community. The Terrain MSEA is managing the SEDRIS project. The air component of SEDRIS has been contracted to TASC, Inc. NRL is assisting with the space component of SEDRIS.

A data dictionary is being prepared as part of the data representation standards for use in air and space M&S. We are leveraging the work of the Joint Meteorology /Oceanography (METOC) Data Administration Steering Committee. As one of its goals this group will establish common METOC data definitions by developing a METOC data model as an extension to the DoD Enterprise Data Model and registering the data elements in the Defense Data Dictionary System (DDDS).

4.3 Just-in-Time Production

Just-In-Time production projects provide the capability to generate authoritative standard data or value-added data on-demand from available data sources in time to meet warfighter pre-mission, mission planning, mission rehearsal, execution, and post-mission review needs. We are funding three projects within this program element.

The High Resolution Gridded Climatology project is developing the capability to generate hourly, annual climatology of four basic atmospheric parameters (wind, temperature, precipitation, and pressure) and several derived parameters such as visibility at 10km resolution for theater-sized regions. This project is enlisting the expertise of AFCCC, PL, Meso Inc, and Saint Louis University.

We are supporting an effort which will help to model significant environmental effects on systems. This effort leverages the ongoing Wright Laboratory Extreme and Percentile Environmental Reference Tables (ExPERT) that generates climatological datasets used to determine the environmental impact occurring during the life-cycle process of a weapon system. MSEA A&SNE funds will be used to improve ExPERT by 1) developing the capability to generate correlated climatological datasets and by 2) developing tables that show the relative weighting of the impact that various atmospheric parameters have on the particular components of a weapon system.

Our third initiative within this program element provides for the additional development of PL's Cloud Scene Generation Model (CSSM). Presently, CSSM is a empirical based model that can generate 3D grids of liquid water content, and can then translate these grids into textured polygons for visual representation of clouds. We are providing funding to provide CSSM with the a validated method to generate cloud scenes that are radiometrically correct. This is a joint effort between PL and ARL.

4.4 Dynamic Representation

The Dynamic Representation program element develops technologies that focus projects providing the capability for: (1) visual and/or mathematical (physics-based) interaction or events within a simulation that change (usually in real or near-real-time) what is or can happen to affect the results of the simulation or model; (2) dynamically consistent, time dependent, authoritative, environmental runtime database implementation that changes during the execution of a model or simulation. We are currently funding three initiatives as part of this program element.

PL's Geophysics Directorate is being supported to develop the capability to model space environmental effects on satellite systems. This effort involves coupling space environmental effects models with a virtual satellite simulation system. It will leverage existing capabilities provided by PL's GEOSpace and Satellite Simulation Toolkit software packages. The final product will be a simulation system capable of diagnosing and predicting how near-space environmental effects degrade systems on-board satellite platforms.

The MSEA A&SNE is providing funding support for Project Pinpoint. This project is a joint initiative between the IMINT Program Office and the National Air Intelligence Center. Its objective is to provide target scene visualization capability that will improve mission planning confidence, increase mission flexibility, and perform mission rehearsal for a broad range of imaging infrared precision strike weapon platforms.

There have been two projects funded in the past that model atmospheric effects on systems. They are the Phillips Laboratory Unified Simulator (PLEXUS) project and the U.S. Army Space and Strategic Defense Command's FAST PROPagation (FASTPROP) project. Our PLEXUS initiative provides an improved weather input capability for the interfaces to a suite of transmissivity datasets and models. FASTPROP provides customers with weather effects on line of sight and other parameters needed for simulating the performance of air defense and other related systems. These projects are currently not funded by the MSEA due to budget constraints.

4.5 Access to Resources

Projects in the Access to Resources program element are to develop system capability needed to link metadata to the acquisition of required M&S resources. Access will be provided to all aspects of information or tools necessary to build and execute models and simulations. The data holding will be virtual (geographically distributed, available electronically, in a manner which is transparent to the customer).

Under this category of projects we have started development of a prototype Tools Catalog that will serve as the air and space environmental component of the Modeling and Simulation Repository (MSRR). MSRR is the DMSO supported master program that is envisioned as a collection of computer resources and information which will assist the M&S community in communicating and sharing information. The Tools Catalog will

provide the M&S user community with a convenient and cost effective means of locating the most suitable air and space natural environment tools (models and algorithms) available for their specific applications. It is being implemented using the Oracle relational database and will be accessible over the Internet via MSRR. The database will store sufficient metadata to properly characterize a tool to potential users. Colsa, Inc. has been contracted to develop the prototype.

5. CONCLUSION

Since the MSEA A&SNE is a new organization, our primary efforts are focused on establishing an infrastructure which will allow us to readily respond to the needs of our M&S customers. This infrastructure includes personnel, information, technology, and process. During the past 6 months four Air Force, Army, and Navy personnel have joined this organization to ensure that the interests of all the Services are represented. The efforts of the MSEA A&SNE are also being assisted by four on-site contractor personnel. We have started creating thorough knowledge bases about our customers' requirements and the capabilities available for addressing those requirements. A comparison between the requirements and capabilities will allow the identification of capability shortfalls. The latest computer and communication technology is being used to create the knowledge bases and to share the information they contain with the M&S community. Numerous procedures and standards are also being developed. Guidelines and procedures are being established for verification, validation and accreditation of models and verification, validation and certification of data used by the models. Data interface standards are also being established that will allow different simulations to exchange data.

6. REFERENCES

ABACUS, Inc., "Air & Space Natural Environment Modeling and Simulation Baseline Requirements Assessment", October 1996.

DoD Modeling and Simulation Executive Agent for Air and Space Natural Environment, "Modeling and Simulation Air and Space Natural Environment Execution Plan," March 1996.

DoD Plan 5000.59, "Modeling and Simulation (M&S) Master Plan, " October 1995.

Under Secretary of Defense (Acquisition and Technology) memorandum, " Designation of Department of the Air Force as the DoD Modeling and Simulation (M&S) Executive Agent for Aerospace Natural Environment Representations," April 1996.

ATMOSPHERIC MODELING IN THE SYNTHETIC THEATER OF WAR (STOW 97)
http://svl.tec.army.mil/SE/

Richard Shirkey[1], Jeffrey Turner[2]
and
Richard Schaffer[3]

Army Research Laboratory[1]
Information Science & Technology Directorate
Battlefield Environment Division
White Sands Missile Range, NM

US Army Topographic Engineering Center[2]
Synthetic Environments Program Office
7701 Telegraph Road
Alexandria, VA

Lockheeed Martin[3]
Advanced Distributed Simulation
50 Moulton Street
Cambridge, MA

ABSTRACT

The Synthetic Theater of War is the major application of a Defense Advanced Research Projects Agency thrust in Advanced Distributed Simulation (ADS). The STOW Program focuses on an Advanced Concept Technology Demonstration termed STOW 97 sponsored by DARPA with the United States Atlantic Command. To support ADS applications up to the Joint Task Force level, STOW seeks to develop and demonstrate technologies enabling the integration of war-fighting through virtual and constructive simulations from geographically distributed locations in a common synthetic battlespace.

The U.S. Army Topographic Engineering Center is developing, under Contract to Lockheed Martin, a synthetic environment, Dynamic Virtual Worlds, which will enhance the virtual battlefield with real world environmental effects using atmospheric models developed by the Army Research Laboratory that vary temporally and spatially. This paper summarizes the atmospheric effects that are being demonstrated in the Dynamic Virtual Worlds program within STOW 97.

1.0 Introduction

Weather has always played a decisive role in warfare. Literature, movies, and historical accounts of battles depict the struggles of the infantryman trudging through the sloppy mud of the jungle, the snowy cold of the North, or the searing heat of the desert. The eventual winner of the battle was almost always the individual or battle group who could better withstand the elements of weather and turn those elements to their benefit. A frequently heard statement is, "The weather affects the enemy just the same as it affects us, so it is not a factor to the outcome." This has been a false assumption for as long as history has recorded armed conflict. An example is Napoleon's

wintertime invasion of Russia. And it is certainly improper to assume such a posture in modern or future warfare.

The Synthetic Theater of War (STOW) is the major application of a Defense Advanced Research Projects Agency (DARPA) thrust in Advanced Distributed Simulation (ADS). The STOW Program focuses on an Advanced Concept Technology Demonstration termed STOW 97 sponsored by DARPA with the United States Atlantic Command (USACOM). The successful implementation of STOW 97 technologies in November 1997 with the United Endeavor 98-1 Exercise will mark the full operational capacity of the USACOM Joint Training, Analysis and Simulation Center. To support ADS applications up to the Joint Task Force level, STOW seeks to develop and demonstrate technologies enabling the integration of war-fighting through virtual and constructive simulations from geographically distributed locations in a common synthetic battlespace.

Serving as DARPA Agent, the U.S. Army Topographic Engineering Center has awarded research and development contracts to develop advanced technologies in four areas: 1) physics-based environmental effects under the Dynamic Virtual Worlds (DVW); 2) dynamic terrain and multi-state objects under the Dynamic Terrain and Objects; 3) atmospheric and ocean data services under the Total Atmosphere and Ocean Server (TAOS); and 4) next generation terrain data base representations under the Improved Computer Generated Forces Terrain Data Base. This paper will only discuss (1) above.

2.0 Dynamic Virtual Worlds

Lockheed Martin Advanced Distributed Simulation (LADS) of Bellevue, Washington and Cambridge, Massachusetts is performing the integration of environmental feature models into ModSAF (Modular Semi-Automated Forces), and complementary visualization capabilities known as ModStealth. ModSAF was selected as the computer generated forces system because of its open architecture, wide use, and ready availability. The visualization of environmental effects is being demonstrated in the new OpenScene "stealth" system. The DVW (Turner, 1996) program enhances the virtual battlefield with real world environmental effects that vary temporally and spatially. Examples of effects currently modeled include the variation of illumination with time-of-day; obscuration of the battlefield from artillery-generated dust, vehicle dust, smoke from burning tanks, and tactical offensive and defensive smoke sources; the effects of boundary layer aerosols (fog, haze, rain, and snow); signal and illumination flares; hydrology; and the effects of dynamic environments on mobility. All of the atmospheric models currently being used by DVW are contained in the Electro-Optical Atmospheric Effects Library (EOSAEL) (Shirkey, et al, 1987). EOSAEL has been constructed by the Army Research Laboratory's, Information Sciences and Technology's, Battlefield Environment Division; EOSAEL has been evolutionary, with its inception in 1979 and four revisions since then. A new revision is currently available through the Test and Evaluation Community Network Bulletin Board System (TECNET).

2.1 The Electro-Optical Systems Effects Library

EOSAEL provides an integrated methodology to investigate atmospheric effects on radiation passing through the fog-of-war. It is a state-of-the-art

computer library comprised of fast-running theoretical, semi-empirical, and empirical computer programs that mathematically describe various aspects of electromagnetic propagation and battlefield environments. The models are more engineering oriented than first principles. The philosophy is to include modules that give reasonably accurate results with the minimum in computer time for conditions that may be expected on the battlefield.

The modules contained in EOSAEL are organized into eight generic atmospheric effects areas: gases, natural aerosols, battlefield aerosols, radiative transfer, laser propagation, and target acquisition, system performance and support. Details of the physics embodied in these modules and their usage may be found in the various EOSAEL volumes (EOSAEL 87) and at the internet site "http://www.eosael.com".

2.2 ModSAF Weather Editor

In order to aid in the setting up and running of DVW coupled with the underlying EOSAEL, a weather editor has been constructed by LADS, appropriately named the ModSAF weather editor. The ModSAF weather editor supports uniform, homogeneous, atmospheric parameter settings. A widget controlled graphical user interface supports setting time-of-day, temperature, wind speed and direction, precipitation type and rate, extinction type and amount, cloud cover, barometric pressure and dewpoint. The weather editor establishes uniform conditions for the entire data base. Although not representative of a 3-D spatially variant natural environment, the weather editor does provide a robust tool for localized model testing and general scenario simulation. For example, an operator can modify the data base's wind speed and direction to analyze the change in a smoke plume's dispersion down wind. Likewise, an operator can set the date and time-of-day to analyze a scenario during a rising or setting sun. The atmospheric settings are also used to feed the environmental models discussed below.

2.3 Natural Illumination

Many simulation systems today operate in a static, full daylight environment. The STOW program can compute dynamic time-of-day capability to provide continuous changes to the ambient lighting contributions from solar, lunar, and sky background sources. The EOSAEL ILUMA model (Duncan, et al, 1987) describes natural illumination under realistic atmospheric conditions that include clear skies, partly cloudy and overcast conditions, precipitation and fog. The total illumination is computed as the sum of the contributions from the sun, the moon and the background sky. At night, scattered light from nearby cities (or other sources of artificial light) can significantly enhance the horizontal illumination at a given location; shadows cast by natural or man-made objects may also significantly reduce the available illumination. Neither of these problems is addressed in the current model because of the detailed, site-specific, physical modeling required for their treatments.

Computer codes based on extinction or single scattering have been widely used to predict atmospheric transmittance (Kneizys, et al, 1983). Light propagation in the atmosphere, however, is a multiple scattering process in which radiation scattered by one element can be scattered again by another

element. Numerous large computer codes have been developed for performing exacting multiple scattering radiation transfer calculations. Because of the memory requirements and execution time limitations, these codes are not practical for real-time battlefield applications. In addition, to develop a computer code that requires inputs that cannot reasonably be expected to be available is not practical. Cloud observations, especially under tactical situations, usually provide the types and amounts of high-, middle-, and low-level clouds. Since these observations are taken by a human observer, no information above an overcast layer is obtained. Also, note that this information does not include cloud thickness, types of aerosols in the cloud, and aerosol size distribution -- quantities that are desirable for detailed radiation transfer calculations.

ILUMA employs Shapiro's three-layer atmosphere model, which uses the doubling method for determining solar insolation at the surface. Details of Shapiro's methodology may be found in Shapiro (1982).

2.3.1 Calculation of Illumination

Conceptually the calculation is straightforward, given the formulas developed in (Duncan, et al, 1987). Beginning with location and time, one would calculate the zenith angles of the sun and the moon. The fractional transmittances would be computed and multiplied by known values of the illuminance at the top of the atmosphere to obtain the surface values. Because of the approximate nature of the transmission and reflection functions (and hence the fractional transmittances), an alternate procedure was adopted. The illuminance were calculated from empirical data for clear sky conditions (van Bochove, 1982). These values were then multiplied by the ratio of the fractional transmittance for the specified weather condition and the fractional transmittance for clear conditions.

When the sun and moon are well below the horizon, illumination is significantly higher than would be predicted from these two sources. Sources for this additional illumination, called the background sky illumination, include starlight and airglow (RCA, 1974). Published values for this contribution to illumination vary from 0.00007 to 0.00025 fc. A mean value of 0.00015 fc has been included in the current model.

The model has been designed to accept data that are generally available through routine weather observations. These data include the types and amounts of high-, middle-, and low-level clouds and the occurrence, or nonoccurrence, of fog or precipitation. The resultant three-layer radiative transfer model responds to inputs of the types and amounts of such clouds. Admittedly such a simplified approach results in some error in the computation of the transmission of visible light through the atmosphere. However, more detailed calculations that would probably provide more accuracy typically require input data that are not routinely available.

The comparisons (Duncan, et al, 1987) show that the model predicts reasonable values when compared to the field measurements available. The model has a general tendency to slightly under predict. Although the exact cause for this tendency has not been determined, it may be largely a result of contributions to measured illumination from artificial light sources (nearby cities).

ILUMA thus allows the STOW simulation exercises to operate around the clock by providing continuous characterizations of natural illumination from sunrise to sunset and from full daylight to total darkness.

2.3.2 Inherent Contrast

Natural illumination in STOW simulations prompted the extension of ModSAF target detection models to leverage variable lighting conditions.

Inherent contrast describes the color difference between a vehicle and its background. Developed by the U.S. Army Night Vision Laboratory (Decker, 1988), the contrast model provides a measure of a target's maximum potential visibility based on four factors: 1) target type, 2) target background, 3) illumination source for the target, and 4) spectral waveband in which the target is being sensed.

Parameters for target type include woodland and desert, Army camouflage paint, Army tan paint, fatigue uniforms, dark brown paint, light brown paint, or 3 types of foreign paint schemes. Background type is broken into the following categories: sandy soil, gravel roads, concrete, asphalt, rocky soil, map green, map light green, top soil and sky. The illumination source can consist of either sun, moon or stars, and sensor types may include daylight vision optics or night vision optics. These parameters are fed through contrast model lookup tables to determine the target's inherent contrast.

2.4 Atmospheric Transmission

The representation of haze, dust, rain and snow within ModSAF and OpenScene provide a powerful simulation mechanism to degrade once environmentally static sensor simulations. STOW currently supports simulation of these atmospheric phenomenon in the context of atmospheric transmission.

Atmospheric transmission, or transmissivity, describes the visibility effects of boundary-level aerosols (haze, dust) and precipitation. Beer's law is used to calculate the transmittance:

$$T_\lambda(R) = e^{(-K_\lambda R)}$$

where

$T_\lambda(R)$ = the transmittance at range R and wavelength λ
K_λ = the extinction coefficient at λ.

Transmissivity is determined via the use of three models: 1) the LOWTRN model, which was developed by the U.S. Air Force's Geophysics Laboratory and incorporated into EOSAEL; 2) the EOSAEL XSCALE model (for transmissivity due to snow); and 3) a model used to calculate the transmissivity of a dust storm.

In ModSAF, the output of the LOWTRN, XSCALE, and the dust storm model is stored in a series of lookup tables as extinction coefficients. These extinction coefficients are used to provide appropriate visualization cues in OpenScene and to degrade sensor and target detection in ModSAF.

The calculations of transmission within DVW for haze, fog, and rain use the formulation found in the EOSAEL version of LOWTRAN (LOWTRN) (Pierluissi and Maragoudakis, 1987). The EOSAEL version differs only in that some coding not relevant to Army usage was deleted.

There are two options for producing visible fog, haze or rain in DVW which are: using LOWTRAN and using inputs from the TAOS program. The ModSAF and OpenScene applications are run in slightly different manners: this is due to the fact that ModSAF needs data bases from LOWTRAN whereas OpenScene can use LOWTRAN on the fly (real-time).

2.4.1 LOWTRAN usage in DVW

When LOWTRAN is employed the atmosphere is considered to be horizontally homogeneous - vertical stratification that may be existent in LOWTRAN is used, but due to the nature of Army warfare (close to the ground) this vertical stratification is not frequently invoked. The following discussion is taken from the original LOWTRAN 5 and 6 reports (Kneizys, et al, 1980 and 1983). The aerosols that are currently implemented in DVW (others could be added if so desired) from LOWTRAN are rural (for haze), two types of fog (advection and radiation), and rain at six different rates.

2.4.1.1 Rural aerosol. Haze (10-, 5-, and 2-km meteorological ranges) can be represented by the rural aerosol within the boundary layer (0 - 2 km). Within the boundary layer the shape of the aerosol size distribution and the composition of the model at the surface is assumed to be invariant with altitude. The rural model is intended to represent the aerosol condition one finds in continental areas which are not directly influenced by urban and/or industrial aerosol sources. The rural aerosols are assumed to be composed of a mixture of 70 percent water-soluble substance and 30 percent dust-like aerosols. The rural size distribution is parameterized as the sum of two log-normal size distributions.

2.4.1.2 Fog models. When the air becomes nearly saturated with water vapor, fog can form. Saturation of the air can occur as the result of two different processes; the mixing of air masses with different temperatures and/or humidities (advection fogs), or by cooling of the air to the point where its temperature approaches the dew-point temperature (radiation fogs). When using a fog model it is assumed that the visibility is less than 200 m for thick fogs and the extinction will be virtually independent of wavelength. For these conditions the advection fog model should be used. For light to moderate fogs, the visibility will be 200 to 1000 m and the radiation fog model should be used. For thin fog conditions where the visibility may be 1 to 2 km, the 99 percent relative humidity aerosol models may represent the wavelength dependence of the atmospheric extinction as well as any of the fog models. A modified gamma size distribution was used to construct these fog models (Shettle and Fenn, 1979).

2.4.1.3 Rain model. The Marshall-Palmer (MP) raindrop size distribution is used because the two main components are rain rate and drop diameter, and the MP raindrop size distribution is widely accepted in the research community. Note that the extinction due to rain is independent of wavelength.

In passing it should be noted that MODTRAN (Berk, et al, 1989) is not employed

as the wavelengths used here are primarily in the visible and current sensors modeled are not narrow band. If the visualization were to be in the IR or narrow band sensors were to be used, then MODTRAN would have to be employed to represent the atmospheric transmission more accurately.

2.4.2 TAOS usage in DVW

When TAOS 4-D gridded data is available, the required information is taken from the 3-D distributed weather grid sources such as observations or weather models. In this case horizontal and vertical 3-D inhomogeneities are allowed - the extinction coefficients are more closely aligned with real weather, rather than modeled weather. When run in this mode the information passed is of three types: 1) extinction type (rural, etc.) and precipitation type (rain, etc.); 2) meteorological range; and 3) the extinction coefficient.

2.4.3 Attenuation Through Falling Snow

XSCALE (Fiegel, 1994) calculates the transmittance through the naturally occurring aerosols of haze, fog, rain, snow, and ice fog. XSCALE models the wavelength dependence of transmittance on these aerosols for line-of-sight (LOS) paths within ~2 km of the earth's surface. The aerosols are assumed to be horizontally homogeneous.

Falling snow is defined in XSCALE as precipitating snow carried by a wind of less than 5 m/s and a relative humidity of less than 95 percent. Crystals of falling snow are generally large in comparison to visible and IR wavelengths. The geometrical optics approximations are expected to be valid. Therefore, the extinction coefficient is equal to 2.0 and the resulting extinction is wavelength independent. However, field measurements of transmittance usually have exhibited a wavelength dependence in falling snow such that the extinction coefficient increases with wavelength in the absence of coexisting fog. This observed spectral dependence is explained for the most part by considering diffraction effects. Thus, as the wavelength increases, less diffracted energy is directed along the LOS to enter the transmissometer, resulting in an increasing extinction coefficient with wavelength.

2.4.4 Dust Model

The dust storm model has been constructed from extinction coefficients that were taken at the BCIS experiment at the Mounted Warfare Testbed, Ft. Knox.

2.5 Battlefield Obscurants

Obscuration of the battlefield from burning vehicle smoke, smoke signals, smoke pots, smoke generators, artillery dust and muzzle dust are provided by EOSAEL's Combined Obscuration Model for Battlefield Induced Contaminants (COMBIC) (Hoock, et al, 1987). COMBIC models the production, transport, diffusion and non-uniform structure of battlefield obscurants. The model uses semi-empirical and first-principle physics to compute the influences of wind, humidity, temperature and pressure on the aerosol yield, cloud buoyancy, transport and diffusion. The design requirement was to predict transmission for any 3-D orientation of target and observer pairs, for (in principle) any number of battlefield obscurant sources produced at different coordinates and times. Values are computed for common spectral wave bands.

The primary input to COMBIC are environmental conditions (e.g., temperature, and wind velocity) and obscurant source conditions (e.g., smoke munition type and burning vehicles). Each obscurant source is characterized by one to five subclouds, with each subcloud being either a Gaussian puff or a Gaussian plume. The model outputs a table of subcloud centerline trajectories, subcloud dimensions, the mean concentration downwind with respect to time, and the extinction. Collectively, this data is referred to as a COMBIC trajectory time history.

COMBIC calculations are performed in two phases. During Phase I, each type of obscurant source to be played is computed for one source and stored in look-up tables. These outputs are stored in a file. They include: the height of the centroid (puff) or height of the leading downwind edge of the cloud (plume); the x-y-z dimensions in Gaussian standard deviations; and the time required for the cloud to reach each downwind distance. They also include a time history of the cumulative amount of obscurant released for the total burn-time (emission time) of the obscurant. And, finally, they store certain individual values required for use in scaling the results to larger numbers or different sized fill-weights of obscurant. All meteorological conditions except horizontal wind direction are used in Phase I.

In Phase II, the user specifies LOS pairings and initiates obscurant source scenarios. COMBIC computes LOS geometries and intercepts, if any, with active clouds. For each intersection, it determines the amount of obscurant along the LOS by looking up the amount of obscurant that will have reached that LOS at that time for each source. This is multiplied by the extinction coefficients for each obscurant involved, and the total combined transmission through all relevant clouds and cloud types is computed for output at each wavelength band. Wind direction is the only meteorological condition allowed to be changed during Phase II, although vehicle directions are allowed to be changed during this phase. The final outputs are computed as the Beer-Lambert for transmittance.

Vehicular dust is a special case of battlefield obscurants. In this case, the source of the local obscuration is moving rather than stationary and the amount of obscurant is dependent upon the vehicle type (wheeled or tracked), vehicle weight, vehicle speed and the silt percentage in the soil.

2.6 Illumination and Signal Flares

Flares, launched via the ModSAF artillery editor, are modeled to burst, descend and extinguish. Upon receipt of a detonation Protocol Data Unit (PDU) for the flare munition, ModSAF looks up the configuration data for the flare and initiates simulation of the entity. The flare configuration data includes burst height, burn time, rate of fall, intensity and illumination cone angle. ModSAF calculates the movement of the flare (descent and travel with the wind) and issues environmental entity PDU's. Once the burn time has expired, the flare is marked "inactive," with a corresponding change on the ModSAF plan view display in icon color from white to black. Eight seconds after the completion of the burn time, the flare entity is terminated.

Illumination flares are used to support target detection at night, and signal flares are used to trigger ModSAF phase changes in missions.

2.7 Weather-LINC (Live InterNet Connection)

As an adjunct to the Weather Editor the capability to connect ModSAF to live internet weather feeds has been implemented. A variety of Internet sites provide periodic updates, generally on the hour, containing surface weather observations. ModSAF can access a variety of sites by parsing the textual information provided by the Internet site and implements simple rules to instantiate quantitative values from the qualitative descriptions (e.g., a reported observation of "light rain" is mapped to rain rate of 2 mm/hr).

ModSAF's ability to consume publicly available weather observations from Internet sites provides an inexpensive and powerful tool for simulations playing in dynamic environments. The STOW program has demonstrated combined live and virtual weather simulations to illustrate the power of real-time weather information. These demonstrations utilize OpenScene visualizing a region in which the environmental conditions are provided via the ModSAF Weather LINC. As a correlation test, live Network Cameras (NetCams) are accessed via the World Wide Web displaying live out-the-window views of the same region visualized by the Stealth.

3.0 Conclusions

The DVW program is enriching the virtual battlefield with a range of real-world local and ambient environmental effects garnered from physically correct atmospheric models and real-world empirical values. The local effects modeled to date include obscuration due to high explosive artillery generated dust, smoke from burning tanks and other battlefield sources, vehicular dust, and signal and illumination flares. The ambient effects modeled include the variation of illumination with time-of-day, boundary layer aerosols, clouds, precipitation, snow and dust storms, ocean waves, and hydrologic effects on terrain. The incorporation of these and other real-world environmental effects is essential for distributed simulation applications ranging from training to test and evaluation.

REFERENCES

Berk, A., L.S. Bernstein, and D.C. Robertson, 1989, MODTRAN: A Moderate Resolution Model for LOWTRAN 7, GL-TR-89-0122, AD A214337, AFGL, Hanscom AFB, MA.

Decker, W.M., 1988, Predicting the Performance of Night Vision Devices using a Simple Contrast Model, AMSEL-NV-TR-0062, ADB124064, NVEOL, Ft. Belvoir, VA.

Duncan, L.D., D.P. Sauter, 1987, Natural Illumination Under Realistic Weather Conditions, EOSAEL 87, vol 21, ILUMA, ASL-TR-0221-21, ASL, WSMR, NM.

EOSAEL 87, 1987, vols 1-30, ASL-TR-0221-1 through -30, ASL, WSMR, NM.

Fiegel, R.P., 1994, Natural Aerosol Extinction Module, XSCALE, ARL-TR-273-1, ARL, Adelphi, MD.

Hoock, D.W., R.A. Sutherland, D. Clayton, 1987, Combined Obscuration Model for Battlefield Induced Contaminants, EOSAEL 87, vol 11, COMBIC, ASL-TR-0221-11, ASL, WSMR, NM.

Kneizys, F.X., E.P. Shettle, W.O. Gallery, J.H. Chetwynd, Jr., L.W. Abreu, J.E.A. Selby, R.W. Fenn, R.A. McClatchey, 1980, Atmospheric Transmittance/ Radiance: Computer Code LOWTRAN 5, AFGL-TR-80-0067, AFGL, Hanscom Air Force Base, MA.

Kneizys, F.X., E.P. Shettle, W.O. Gallery, J.H. Chetwynd, Jr., L.W. Abreu, J.E.A. Selby, S.A. Clough, R.W. Fenn, 1983, Atmospheric Transmittance/ Radiance: Computer Code LOWTRAN 6, AFGL-TR-83-0187, AFGL, Hanscom Air Force Base, MA.

Pierluissi, J.H., C.E. Maragoudakis, 1987, Atmospheric Transmittance/Radiance Module, EOSAEL 87, vol 4, LOWTRN, ASL, WSMR, NM.

RCA Electro-Optics Handbook, 1974, RCA Corporation, Lancaster, PA.

Shapiro, R., 1982, Solar Radiation Flux Calculations from Standard Meteorological Observations, AFGL-TR-82-0039, AFGL, Hanscom AFB, MA.

Shettle, E.P., R.W. Fenn, 1979, Models for the Aerosols of the Lower Atmosphere and the Effects of Humidity Variations on Their Optical Properties, AFGL-TR-79-0214, AFGL, Hanscom Air Force Base, MA.

Shirkey, R.C., L.D. Duncan, F.E. Niles, 1987, Executive Summary, EOSAEL 87, vol 1, ASL-TR-0221-1, ASL, WSMR, NM.

Turner, J.T., 1996, Dynamic Environment and Terrain in a Virtual World, 20th Army Science Conference, Norfolk, VA.

van Bochove, A.C., 1982, The Computer Program ILLUM: Calculation of the Position of Sun and Moon and the Natural Illumination, PHL 1982-13, Physics Laboratory TNO, The Hague, The Netherlands.

TACTICAL BATTLEFIELD VISUALIZATION OF FORECAST WEATHER AND EFFECTS

Donald W. Hoock Jr.
David H. Tofsted
U.S. Army Research Laboratory
Information Science and Technology Directorate
Battlefield Environment Division
White Sands Missile Range, NM 88002-5501

John C. Giever
Physical Science Laboratory
New Mexico State University
Las Cruces, NM 88003

ABSTRACT

Someday, battlefield commanders and staff will routinely immerse themselves in virtual battlefields. There they will tap into intuitive, multi-dimensional, seamlessly-distributed digital databases. They will be aided by "smart software" to help them assess the threat, plan the mission and gain situational awareness. This will exploit knowledge of the current state of the battlespace, including forecast effects and impacts on weapons, tactics and operations of dynamic weather, terrain, illumination and battle-induced environments. The reality of the present, however, is that we are only in the first phase of these advances. An ability to collect, process and use digital information on the battlefield is fairly recent. We are just beginning to see the benefits of automating and speeding up even such traditional tasks as production of text messages, 2D data overlays and tactical maps in the field. This paper shows how existing technology might be easily adapted to further advance the visualization of meteorological information, effects and impacts. We consider Vis5D, the 3-D data visualization software from the University of Wisconsin. This publicly-licensed software has desirable properties of "open" source codes, cross-platform execution and flexibility. We demonstrate how the meteorological forecast outputs of the Battlescale Forecast Model can be interfaced to the Vis5D viewer and extended to include other data and derived effects parameters. We contrast the performance of the product on different computers to highlight the need for future tactical computer hardware standards to include graphics hardware that can run under "open" graphics languages. And we extend the data-visualization concept to 3-D visual immersion and data-focus for mission planning purposes.

INTRODUCTION

Technology demonstrations indicate that the Tactical Operations Centers (TOC's) of the future will be highly automated and interoperable, sharing many digital information products. Battlefield commanders and staff will be able to routinely immerse themselves in "virtual battlefields". There they will tap into intuitive, multidimensional, seamlessly-distributed digital information databases. They will be aided by "smart software" to help them easily extract and synthesize critical information to assess the threat, plan the mission and gain situation awareness.

Realization of this vision may be several years away, however. Currently text messages, paper maps and overlays are still evolving into digital maps and 2-D graphic screen overlays, with analysis information shared via data tables and images downloaded by direct file transfers. Data exchange interfaces may soon evolve to include distributed "push-pull" database access and "client-server" architectures, perhaps within some form of a "web-page and browser" environment.

In the spirit of this information evolution, we describe in this paper a current effort to adapt a 3-dimensional weather and effects data-visualization tool to support weather forecast analysis and display from the Battlescale Forecast Model (BFM). BFM is part of the tactical Integrated Meteorological System (IMETS). The existing 3-D weather data display software being adapted is Vis5D (Hibbard and Paul, 1996).

Vis5D is a publicly-licensed software package from the University of Wisconsin for visualizing data produced from numerical weather models. It has the desirable properties of being widely used and portable between many different computer systems. In the following sections we describe Vis5D and its application to BFM outputs. The data visualized can, however, also include derived weather effects and weather impacts.

INTEGRATED METEOROLOGICAL SYSTEM AND BATTLESCALE FORECAST MODEL

The U. S. Army's Integrated Meteorological System (IMETS) supports the warfighter in the Tactical Operations Centers on the battlefield. Fourteen units have been fielded, and an additional eighteen are scheduled. IMETS runs on Army Common Hardware/Software (ACHS). Current Block II ACHS is a SUN Sparc 20 (replacing earlier Block I HP computers). Included in IMETS is the Battlescale Forecast Model (BFM, Lee, 1994). BFM is remarkable for its ability to produce high resolution, 24 hour forecasts on this desktop battlefield system at a horizontal spacing of typically 10 km or 5 km (or even 2 km horizontal grid spacing if necessary) over regions from 500x500 km to 100x100 km, and at 16 unevenly spaced vertical levels from the ground surface up to 7 km AGL. BFM currently uses DTED terrain elevation data. BFM is initialized using coarser-grid forecast data, for example from the Air Force Global Spectral Model (GSM) and the Navy Operational Global Atmospheric Prediction System (NOGAPS), which are global-scale models, plus observations and soundings in the battle area. The U. S. Army Research Laboratory (ARL) Battlefield Environment Division is responsible for the development and integration of software models and analysis tools into IMETS.

Figure 1 shows one example of a tactical display of BFM output on IMETS. The data here are wind speed streamlines forecast for a region of Bosnia and displayed over a 2-D map provided by a map server. Using IMETS, many other types of 2-D "overlays" and 1-D vertical profile displays of meteorological forecast data can be generated in the field, including analysis outputs from Integrated Weather Effects Decision Aids (IWEDA). These latter products show the impacts of critical values of weather parameters on military subsystems, systems, platforms and mission operations. Although future emphasis will include 3-D visualization of IWEDA outputs and dynamic weather effects at finer scales, we concentrate here on improving visualization of the weather data itself for the fielded IMETS.

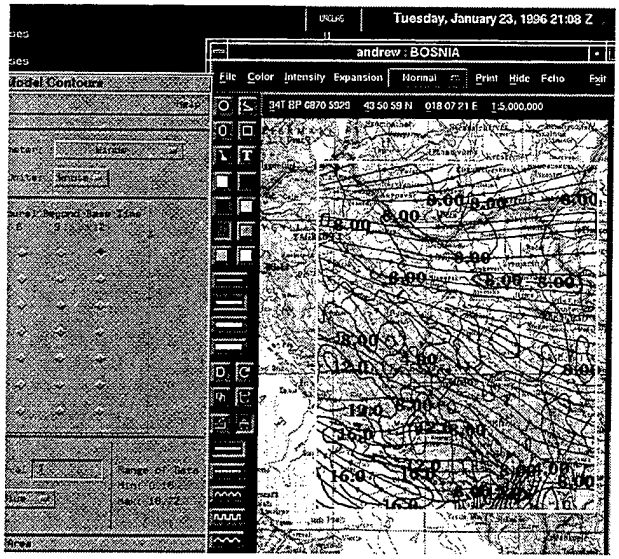


Figure 1. IMETS BFM Display

BFM is a hydrostatic forecast model that is sufficiently compact to run on the ACHS Sparc 20 desktop while delivering the high spatial resolutions needed for predicting terrain-coupled effects at tactical scales. Figure 2 shows the spatial and time scales of representative meteorological features and atmospheric effects. At scales below about 5 km, prediction of the mean meteorological conditions can be supplemented by other models or by observations. These can include: diagnostic models of near surface, terrain-coupled mean winds, such as the ARL High Resolution Wind Model (HRW, Cionco and Beyers, 1995), dynamic physical simulations (such as Large Eddy Simulation) or statistical representation of dynamic fluctuations about the mean. Future efforts will include simulation and data visualization of these finer scale data and of derived effects parameters as discussed in a later section.

ARL is currently extending IMETS basic weather data visualization capability to three dimensions and time. The requirement is for a 3D software graphics package that meets the following criteria:

(1) It must not require changes to the existing BFM and IWEDA software, but must be a true "add-on" that acts only on the forecast and analysis data outputs.

(2) It must be an easily and separately maintainable software package with at most a few, well-documented code changes required to adapt any new revisions of the graphics package library back into IMETS applications. It must allow access to the graphics source code library to permit debugging should any code problems be identified in the future. It must be easily extended to accommodate any new data types generated from future improved IMETS forecast and

Spatial Classes and Scales			Relative Time Classes and Time Scales				
			Climatological Scales	Synoptic Scales	Meso-Scales	Micro-Scales	Micro-Scales
			Months	Days	Hours	Minutes	Seconds
Macro-Scale	α	$>10^4$ km	Standing Waves	Ultra-Long Waves			
	β	$10^3 - 10^4$ km		Baroclinic Waves			
Meso-Scale	α	$10^2 - 10^3$ km		Huricanes/ Fronts	Storm Fronts		
	β	10 - 100 km			Squall Lines/ Cloud Clusters		
	γ	1 - 10 km			Thunderstorms	Cell Features	
Micro-Scale	α	0.1 - 1 km				Tornadoes	
	β	10- 100 m				Dust-Devils	
	γ	1 - 10 m					Plumes and Turbulence

Fallout
Chemicals
Smoke/Dust
Optical Turb.

Figure 2. Spatial and Time Scale Classes

analysis capabilities. And it must be both cost effective and widely used to assure that it will be able to exploit future improvements in ACHS capabilities.

(3) It must provide at least the same capabilities of portraying stream flow, labeled contours, color-coded data bands, and vector fields as current 2-D displays. This includes the ability to easily incorporate the same map underlays currently in IMETS, as well as 3-D extensions such as data isosurfaces, volumetric color-coded data and the topographic elevation data actually used in the IMETS forecast and analysis codes.

(4) It must be a tool that is easy to learn and be interactive to allow the analyst to quickly change the data displays and 3-D viewpoint. This will permit the user to concentrate on analysis of the weather data. And it must include a capability for the user to easily record "snapshots" of the displayed images for digital transmission, for incorporation into weather briefings and for publishing on a home-page environment.

A graphics package that comes very close to meeting these requirements is the University of Wisconsin Vis5D viewer. Vis5D is publicly licensed and comes with the source code. It can run on the ACHS desktop systems and on many other computers. As we discuss below, only minimal changes (actually extensions) to the Vis5D graphics library have been required that adapt contouring algorithms to the specific terrain-coupled vertical data layer spacing used by BFM. Much of the computer code developed to allow the use of Vis5D has thus focused on writing intermediate data

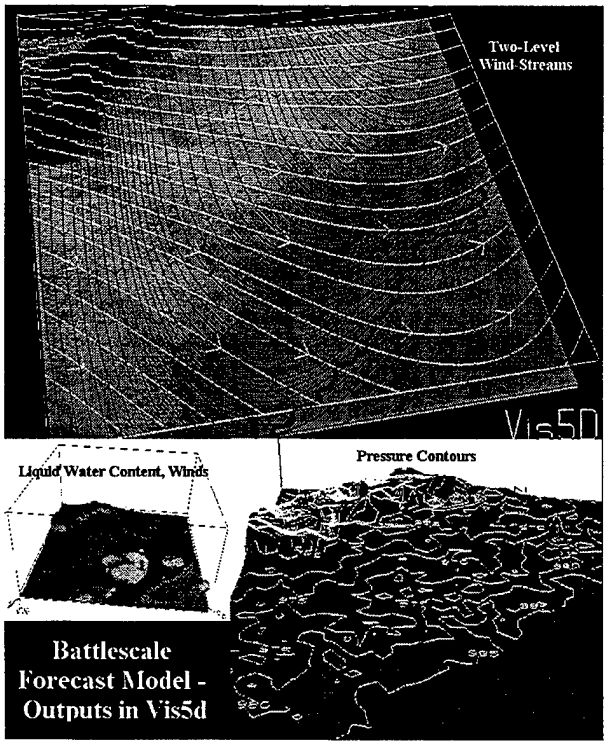


Figure 3. BFM in Vis5D Viewer

format conversion software to transform IMETS output data into standard Vis5D input data formats.

Figure 3 is a composite of examples of BFM forecast data from the Joint Warfighter Interoperability Demonstration (JWID-96) as displayed in Vis5D. It shows forecast wind streams at two levels, liquid water content contours and isosurfaces, and near-surface

pressure contours. These data are displayed over the default pseudo-colored topographic elevation data of the South and North Carolina regions, with the Appalachian mountains in the northwest corner.

Figure 4 shows another example of the more sophisticated display capabilities using Vis5D to view BFM outputs. Here a color-coded volume rendering of winds over the Appalachian region shows the strong influence of the mountains on forecast wind speeds with height. The inset figures display isosurfaces of constant liquid water content forecast over the coastline and the isosurface of pressure over the mountains.

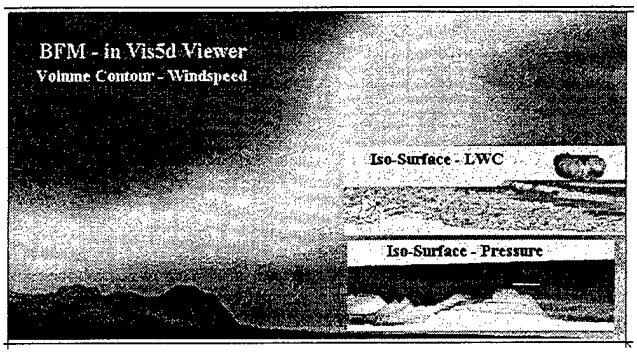


Figure 4. BFM in Vis5D Viewer

VIS5D HISTORY

Vis5D (Hibbard and Paul, 1996) is a software system for visualizing data made by numerical weather models and similar sources. Vis5D, version 4.2, 3-dimensional data-visualization software is publicly available from the University of Wisconsin under the terms of a GNU General Public License.

Vis5D version 1.0 was written in 1988 by Bill Hibbard and Dave Santek, of the University of Wisconsin Space Science and Engineering Center and by Marie-Francoise Voidrot-Martinez of the French Meteorology Office. Later version enhancements were written by Bill Hibbard, Brian Paul, and by Andre Battaiola of CPTEC, Sao Paulo, Brazil, plus porting to a number of different computer systems by a number of international contributors. Version 1.0 was written for the Stellar computer system. Version 2.1 in 1992 made Vis5D available for the SGI and IBM workstations. Version 3.3 in 1994 ported Vis5D to HP, DEC, Sun, and Kubota (DEC Alpha) workstations. Portability was enhanced by implementations in the OpenGL graphics standard. Version 4.1 in 1995 made OpenGL work-alike 3-D rendering software available for workstations that do not have dedicated graphics rendering hardware by using the Mesa graphics library. The Vis5D source code, executables and the Mesa graphics library can be downloaded from the World Wide Web at the URL: http://www.ssec.wisc.edu/~billh/vis5d.html [or by ftp from iris.ssec.wisc.edu (144.92.108.63).]

Vis5D currently works with computer systems having at least 32MB of RAM and at least an 8-bit color display, including:

Silicon Graphics workstations with IRIX versions 4.x and 5.x. (Hardware graphics is used and multiple processors are supported if present);

IBM RS/6000 workstations Model 320H or higher with AIX version 3 or later. (Hardware graphics is supported through OpenGL);

HP series 7000 or 9000 workstations with HP-UX A.09.01 or later (PEX optional);

Sun Sparc workstations with SunOS 5.x or later. (Graphics uses main CPU with the Mesa library);

DEC Alpha workstations with OSF/1 V1.3 or later. (Kubota Denali Graphics hardware is supported with KWS V1.3.3 or later and NPGL run-time license);

IBM PC compatibles with Linux 1.0 or later and 75 MHz Pentium CPU or faster. (The XFree86 X window system must be installed.)

USER INTERFACE

The Vis5D user interface consists of an options menu and a rotatable data viewing box. The screen menu is shown in Fig. 5. The data viewing area appears as a data box as shown in Fig. 6, which can be rotated to any viewpoint, shifted and zoomed. The box is labeled in latitude, longitude, height AGL (in our implementation) and identifies the north direction.

The upper part of the menu allows the user to: animate or step through the data in time; toggle on/off display of the terrain topographic elevations; toggle on/off a bitmapped texture (map) underlay over the terrain at the bottom of the box; toggle on/off a vector map underlay; initialize the view to various directions; switch between orthographic and perspective views; reverse window background to black or white; toggle time of day and legends; dump displays to image files; and includes options for additional variables and input of scripted display information.

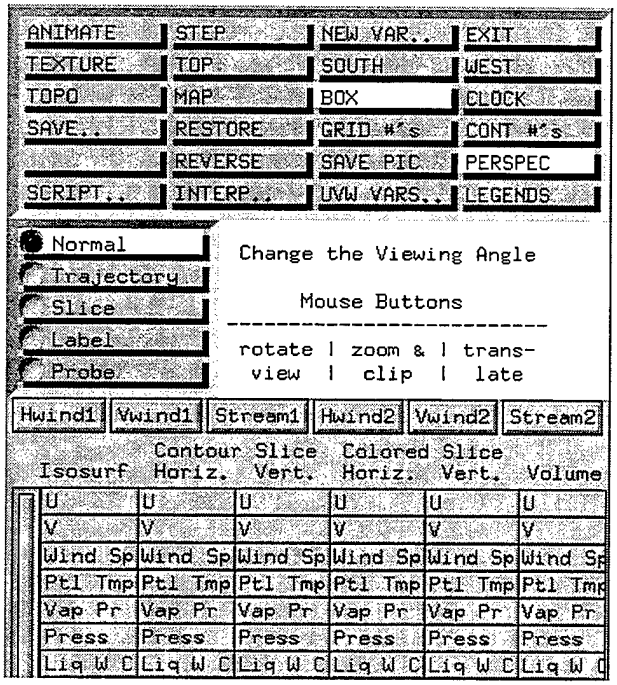


Figure 5. Vis5D Menu

The middle menu: manipulates the positions of displayed data slices in the viewing volume; adds text labels; and displays the meteorological data at any point in the 3-D volume via a pointer "probe". The bottom menu selects the data and the variables to be simultaneously displayed. Variables on menu buttons are defined in an ARL-developed input file, discussed below, while meteorological data come from a file via an ARL code that reformats them for Vis5D.

ELEVATION AND MAP DISPLAYS

Elevation data in height above mean sea level are the same values and spacing used by BFM in the forecast calculations. The Vis5D "topo" elevation data file is generated by a stand-alone pre-processor code ***CNVRTOPO.C*** provided by ARL to convert BFM topo array data conventions to Vis5D topo array data conventions. The BFM topo array convention stores data first by rows scanned south to north in each column, which are then each scanned west to east. The BFM longitude convention is negative west longitudes. The Vis5D topo array convention requires elevations stored first by columns, scanned west to east for each row, which are then each scanned north to south. The Vis5D longitude convention requires positive west longitudes. In addition, Vis5D elevation encoding requires the least significant bit to be assigned a zero or a one representing a land or water surface. Figure 7 shows displayed topographic elevations in Vis5D for the JWID-96 exercise, with the Appalachians of North Carolina in the northwest corner. When the "topo"

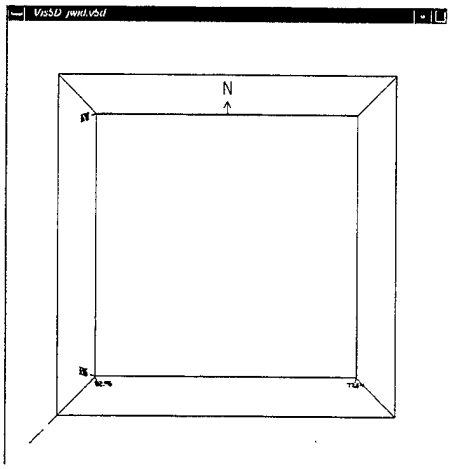


Figure 6. Vis5D Data Viewing Box

display option is turned on without "texture" turned on, then Vis5D produces a default (user-adjustable) pseudo-colored terrain with blue water, and green lowlands that shade to a yellow-red in mountain regions. Normally, we set up Vis5D to display an exaggerated vertical scale on the box (of 10 to 40 times the horizontal scale, typically). This allows the vertical detail in meteorological data levels to be more easily discerned by the user. Topographic elevations are similarly exaggerated to assure that near-surface meteorological data display properly on top of the topographic surface.

The bit-mapped underlay at the bottom of the display box is set up to accommodate any image file as a texture. The texture will drape over the elevation data when the "topo" display is turned on, or will lie flat at the bottom of the display box when the "topo" display option is turned off. One can use, for example, the map generated for the BFM output from the

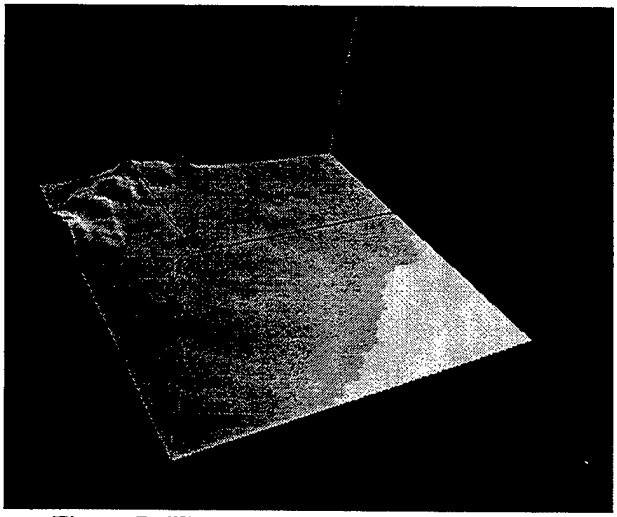


Figure 7. Vis5D Using BFM Topo Elevations

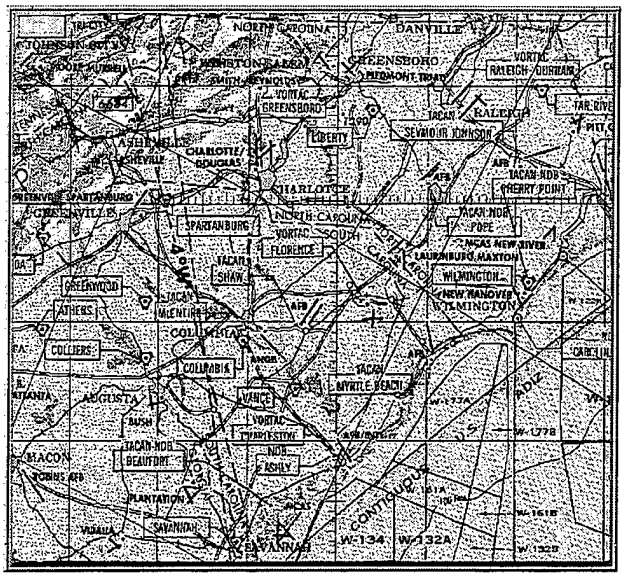


Figure 8. IMETS Generated Map Underlay

IMETS map server as shown in Fig. 8. Or the user can supply any other map, for example the U.S. Census Bureau map shown in Fig. 9, for the same region. Vis5D supports this image in SGI ".rgb" image format. We convert the image file from the more typical image formats, such as ".gif" into the SGI format in a separate pre-processing step.

Figure 10 shows an example of the combination of both "topo" elevations and the map "texture" turned on simultaneously.

CODE MODIFICATIONS REQUIRED FOR BFM

We would like to implement Vis5D without any code changes. This would facilitate very simple software maintenance by total Vis5D code replacement as new versions of Vis5D are released. Unfortunately, however, minor coding changes are necessary to accommodate the correct "terrain-following" height at which BFM forecasts are made. In BFM each of the 16 layers is specified as a "height above ground level". But at each horizontal location this means that the actual layer height relative to sea level will vary with terrain. So the data layers are not flat. The scaling convention is such that the highest (say 16th) layer is flat, while the lowest (1st) layer conforms almost exactly to the topography. The corrected vertical layer height $\mathbf{Z_{msl}}$ above sea level in terms of the BFM relative layer height above ground level $\mathbf{Z_{agl}}$ at a point where the terrain elevation above sea level is $\mathbf{Z_{ter}}$ is defined as:

$$\mathbf{Z_{msl}} = \mathbf{Z_{ter}} + \left(\mathbf{Z_{agl}} / \mathbf{Z_{max\,agl}} \right) \bullet \left(\mathbf{Z_{max\,msl}} - \mathbf{Z_{ter}} \right) \quad (1)$$

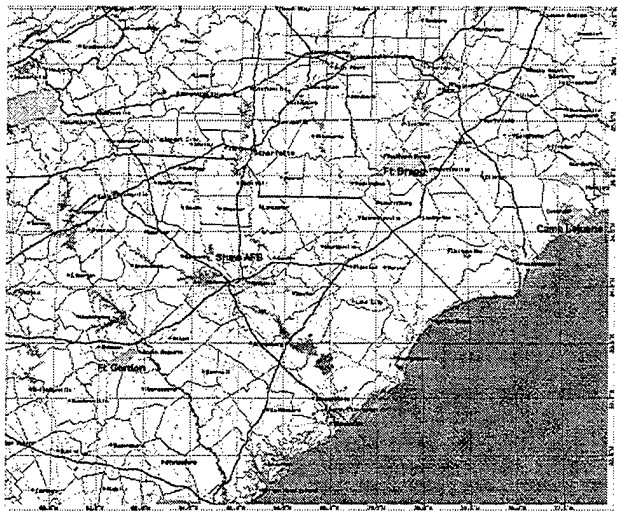


Figure 9. Arbitrary (US Census) Map Underlay

where $\mathbf{Z_{maxmsl}}$ is a fixed height of the top of the BFM computation box ($\mathbf{Z_{maxagl}}$ + max terrain height relative to sea level), and $\mathbf{Z_{maxagl}}$ is currently fixed in BFM at a value of 7000 m above ground level.

This algorithm is inserted into the vector, contouring, volumetric rendering and isosurface generation subroutines such that the meteorological data are all adjusted for the terrain elevation changes. Thus, near the surface the contours "drape" over the terrain surfaces, while at the upper height levels they become more flat. This is apparent in examples of the next sections. The coding changes are well documented and few so that maintenance for new Vis5D versions is relatively simple. Furthermore, if a user downloads Vis5D from the University of Wisconsin and uses it without the BFM layer corrections, then the BFM data are still viewable, but

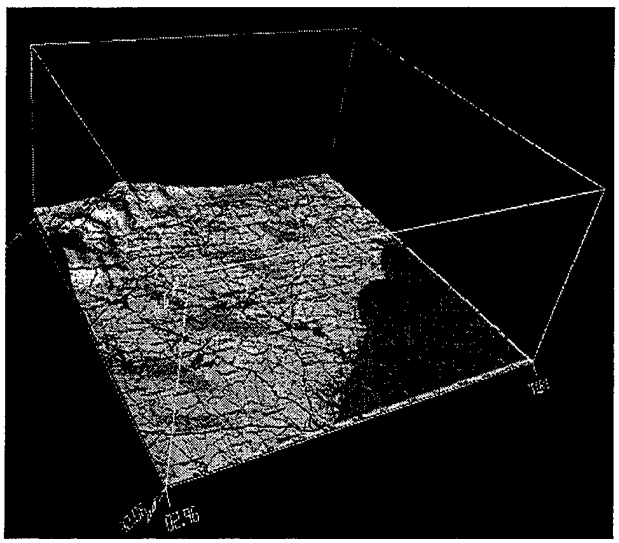


Figure 10. Both "Topo" and "Texture" On

all BFM data appear as flat layers with height relative to the bottom of the Vis5D viewing box. (Although in this case low-level data may appear "below" terrain.)

DATA INTERFACE

As BFM itself is upgraded and new meteorological variables are produced, one would like to be able to easily display these data in Vis5D. Therefore, an intermediate code to reformat BFM data into the input convention of Vis5D was produced. This separate conversion filter routine, called ***BFM_to_V5D.F,*** reads an ascii file that is easily modified using any text editor. The ascii file contains a list of all possible data labels and units (currently 37), flags the active BFM output meteorological variables (currently 13), designates units conversions, and specifies the order in which variables occur in the BFM output file. The conversion filter then reformats the data into a form that can be loaded directly into Vis5D, along with the "button labels" (up to 30) seen in the bottom portion of the Vis5D menu. This filter thus allows one to easily take into account BFM code upgrades and changes without a need to modify either BFM or Vis5D for viewing the new data.

(In spring 1997, ARL will change over from reading BFM output files directly and will instead query a database which is populated with BFM outputs. Thus, the conversion filter routine will be modified to accommodate any meteorological data in the database itself. After this change-over is complete it should not matter what the source of the data are in the database, whether from a forecast model or from a gridded set of observations. Changes in new versions of Vis5D rendering routines will still be required, however, to take the corresponding BFM vertical layer height scaling convention into account.)

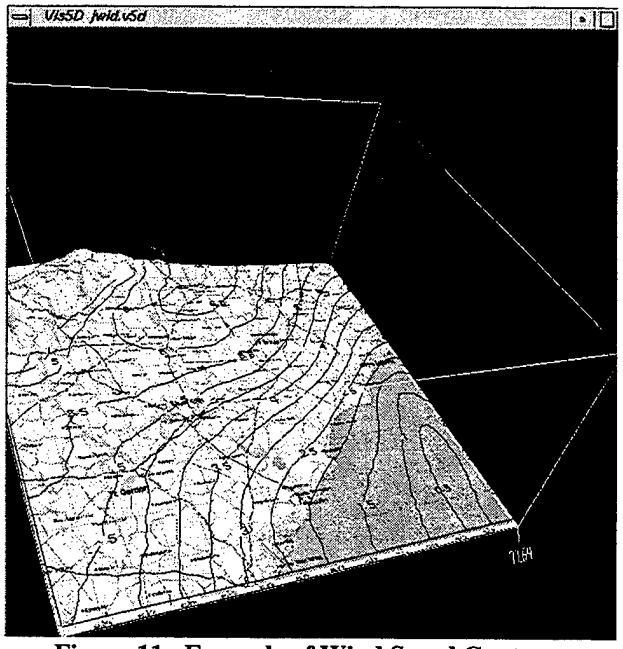


Figure 11. Example of Wind Speed Contours

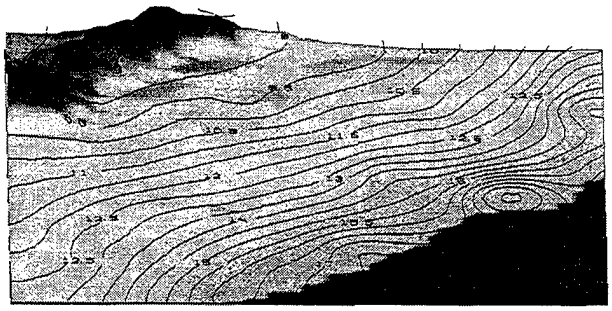


Figure 12. Water Vapor Pressure Contours

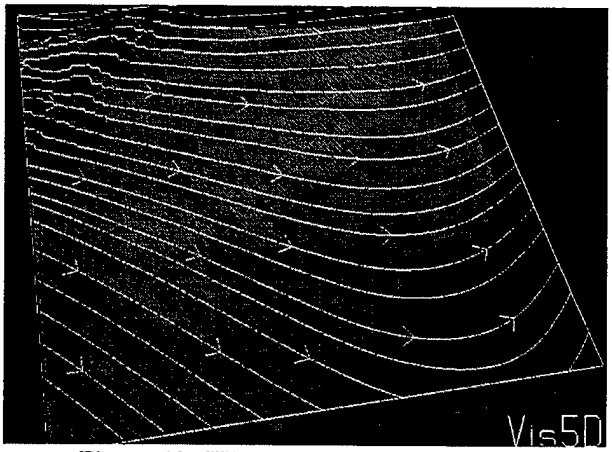


Figure 13. Wind Streams at Two Levels

EXAMPLES

Figure 11 shows a wind speed contour at a low height over the map and topo displays. In this example, Vis5D with no code modifications has been used so the data contours pass "beneath the mountain". Figure 12, however, shows near-surface water vapor pressure contours. Here the Vis5D code has been modified to include the BFM height AGL corrections. The data thus "drape" over the mountains Figure 13 displays wind streams at two heights. Note that the wind fields show significant turning between the 300 and 3000 m heights. Vis5D allows data at multiple levels to displayed (from default buttons or by "cloning" with the "new variable" button.) Thus, the analyst can identify significant features and capture an image of them for use in weather briefings and homepages. Figure 14 shows that Vis5D can also display the wind as vectors, showing both speed and direction for each layer.

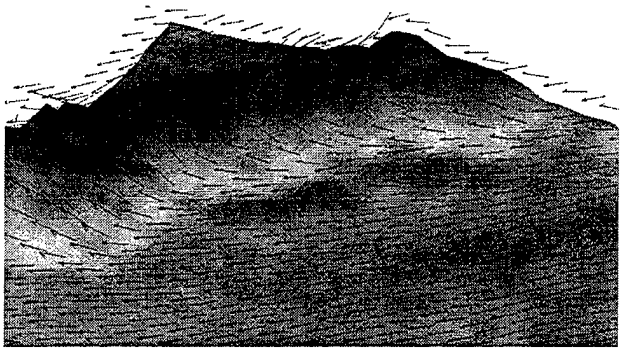


Figure 14. Near-Surface Wind Vectors

The examples thus far are from the IMETS forecasts at JWID-96. Figure 15 is an accumulated rainfall forecast for the Ft. Hood area in preparation for Task Force XXI exercises. The data are displayed in Vis5D as both labeled contours and as colorized contour areas. This combination thus displays both quantitative reference contours and also the detail in the gradual (256 color-palette) shading.

Figure 16 shows that line and area contours can also be displayed as a slice in the vertical. Colored wind speed contours above the mountain are shown along with wind streams at two horizontal levels.

FUTURE DERIVED EFFECTS DISPLAY

A new Army Science and Technology Objective (STO), Weather Effects and Battlescale Forecasts for Combat Simulation and Training, has the objective of making the IMETS capabilities an asset for use in mission planning, training and simulations.

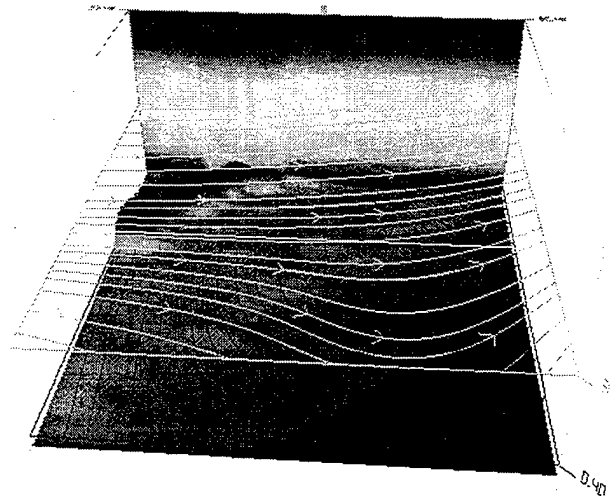


Figure 16. Wind Speed Area Contour in Vertical

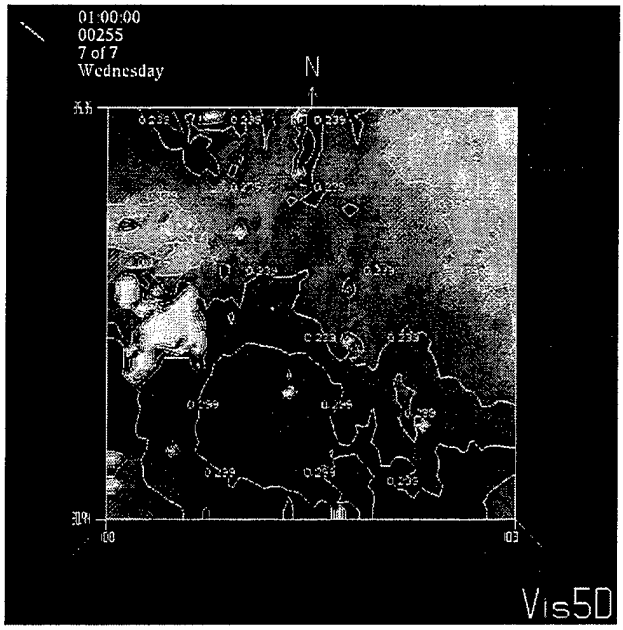


Figure 15. Accumulated Precipitation

Currently IMETS has been "isolated" to the tactical operations centers on the battlefield and to ACHS hardware and software. Under this STO we will not only make the IMETS assets available to the outside simulation communities, but will also use models and simulations to make new derived environmental effects parameters and weather impacts available to IMETS.

Examples of simple, derived parameters are shown in Vis5D displays in Figures 17 through 19. Air temperature T (°C) can be derived from the BFM potential temperature θ (°K) and pressure P (mb) from:

$$\mathbf{T = \theta \cdot \left(\frac{P}{1000} \right)^{2/7} - 273.16} \qquad (2)$$

and the optical refractivity N, required to compute refractive bending, can be derived for a wavelength λ (μm), the pressure P (mb), temperature T (°C) and water vapor pressure f (mb) from:

$$\mathbf{N = (n-1) \cdot 10^6 = A(\lambda) \cdot G(P,T) - B(\lambda) \cdot H(f,T)} \qquad (3)$$

where n is the index of refraction and:

$$\mathbf{A(\lambda) = 0.378125 + \frac{0.0021414}{\lambda^2} + \frac{0.00001793}{\lambda^4}} \qquad (4)$$

$$\mathbf{B(\lambda) = 0.0624 - \frac{0.00068}{\lambda^2}} \qquad (5)$$

$$\mathbf{G(P,T) = P \cdot \frac{\left[1 + (1.049 - 0.0157 \cdot T) \cdot P \cdot 10^{-6}\right]}{1 + 0.00366 \cdot T}} \qquad (6)$$

$$H(f,T) = \frac{f}{1 + 0.003661 \cdot T} \qquad (7)$$

Figure 17 displays forecast refractivity as contours at two levels above ground as derived from a BFM forecast. The small compact region of contours at an upper level in Fig. 17 is shown in Fig. 18 to be due to a forecast region of high liquid water content (clouds). Figure 18 shows a Vis5D isosurface of constant liquid water content, the wind stream at a high altitude, and a semi-transparent contour of refractivity at a near-surface level that allows the underlying map to show through. Vis5D allows many surfaces (area contours and isosurfaces) to be rendered with a user-adjusted semi-transparency. This is especially useful if several variables are being displayed simultaneously, with one set of features that would otherwise be hidden by another.

Another derived parameter for atmospheric effects is sound speed V (in m/s):

$$V = 331.45 \cdot \sqrt{1 + (T/273.16)} \qquad (9)$$

Figure 19 shows the derived sound speeds at two levels above ground. While sound speed itself may not be too relevant an atmospheric effects quantity, the STO will eventually make available the outputs of detailed models such as range-attenuated sound propagation. Figure 20 shows the output from the ARL Scanning Fast-Field Program (SCAFFIP, Noble 1991) acoustic model in which the wind direction and vertical changes in the wind speed also play major roles. The color contours show preferential propagation directions. (Fig. 20 shows attenuation with range over different compass headings.) One challenge is to find a way to display such range and direction-dependent area contours in a 3-D viewer.

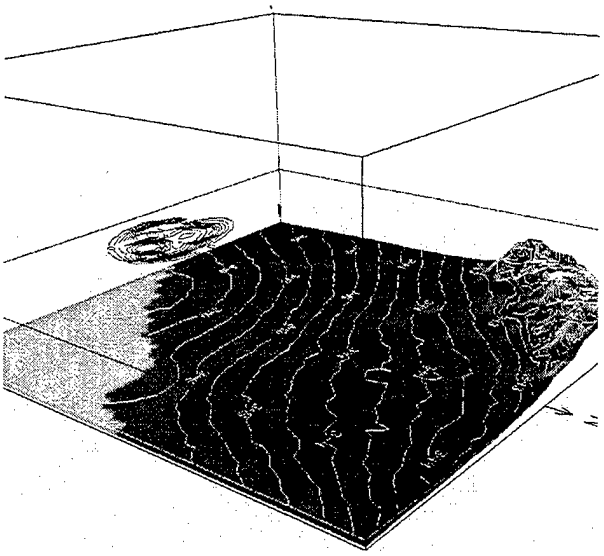


Figure 17. Refractivity at Two Levels

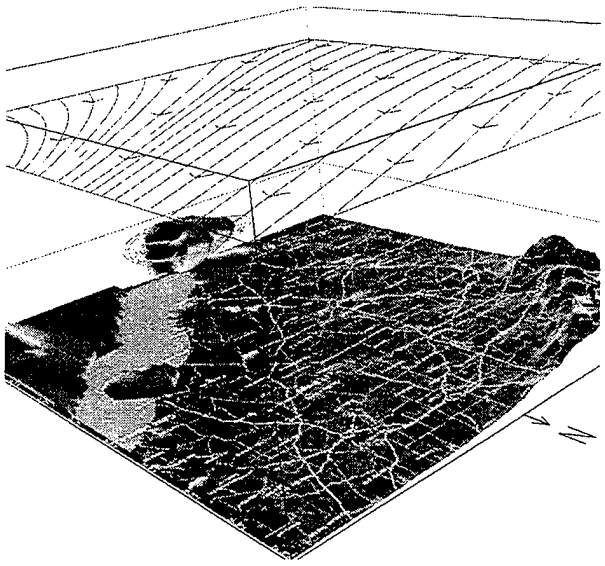


Figure 18. Refractivity and Liquid Water Content

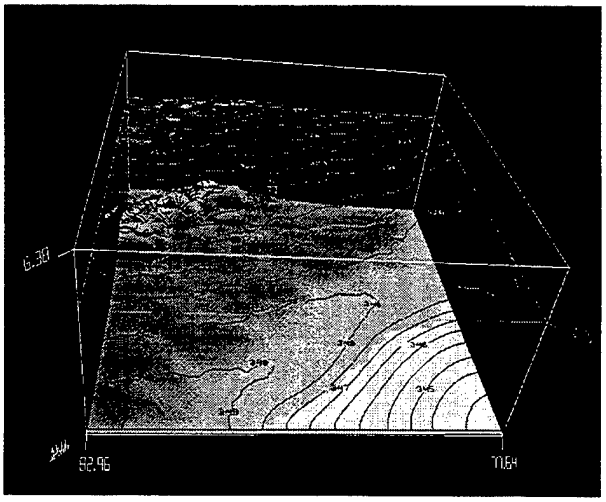


Figure 19. Sound Speed at Two Levels

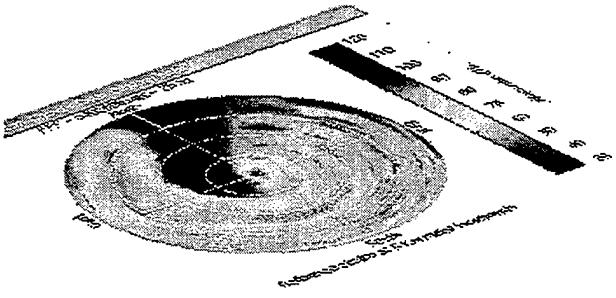


Figure 20. Acoustic Propagation from SCAFFIP

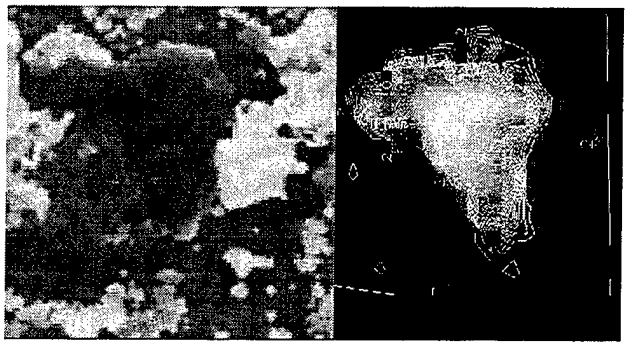


Figure 21. Modeled Clouds Seen from Below

Another example of a future capability is to display natural clouds along with various properties such as concentration, transmission and radiance. Figures 21 and 22 show modeled clouds based on their transmission and radiance (Tofsted, 1996) on the left and top, and Vis5D display of cloud liquid water content (concentration) contours on the right and below. In future such data may also be derived from satellite imagery and forecast liquid water content.

PERFORMANCE CONSIDERATIONS

Vis5D executes extremely well on computers with dedicated graphics hardware. On the SGI, the screen update is approximately 3 to 20 frames/sec depending on the amount of displayed data. On the Sun Sparc 20 ACHS the corresponding rates using the Mesa graphics library in the main cpu are about 1/10 the SGI rate. (Visualizations are virtually identical on both systems.) However, in prototype tests for IMETS at JWID-96, these are sufficient for interactive data analysis and publication on the IMETS homepage.

CONCLUSIONS

We have detailed here the use of the Vis5D graphics software for the real-time, interactive 3-D visualization of forecast data from the BFM model. Vis5D is being integrated into IMETS in the Spring of 1997 for evaluation. If evaluations go well, then Vis5D is expected to become available on the tactical battlefield for the display and analysis of weather. In future, the data and tactical weather forecast capabilities of IMETS will be made available by ARL to the mission planning, simulation and training communities through an Army Science and Technology Objective. In turn, various weather effects models and simulations will be adapted and evaluated for their use in tactical forecasting of effects and to upgrade current tactical battlefield software for the display of impacts on systems and operations.

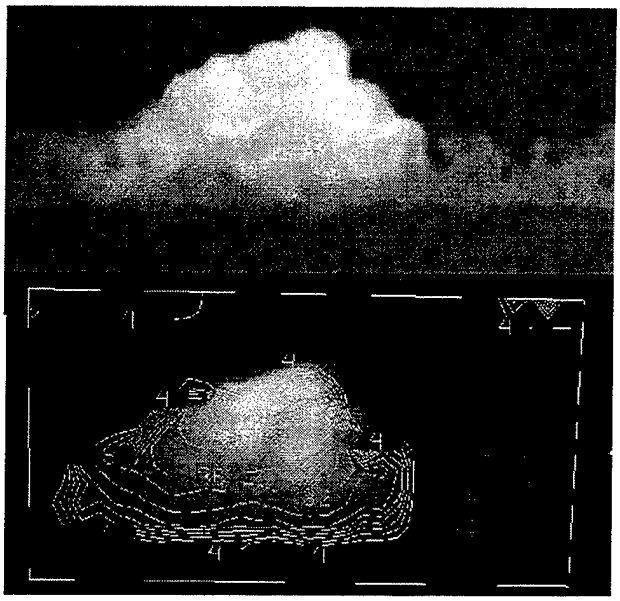


Figure 22. Modeled Clouds from the Side

REFERENCES

Cionco, Ronald and Beyers, J. (1995). High Resolution Wind Field Simulations Run Real-Time During the MADONA Field Study, in Proceedings of 11th Symposium on Boundary Layers and Turbulence, Mar 7, 1995, Charlotte, NC, pp 323-326, by the American Meteorological Society, Boston, MA.

Hibbard, Bill and Paul, Brian, (1996). Overview of Vis5D, Version 4.2, available on-line at http://www.ssec.wisc.edu/~billh/vis5d.html or ftp: iris.ssec.wisc.edu, Space Science and Engineering Center, University of Wisconsin - Madison, 1225 West Dayton Street, Madison, WI 53706

Lee, Martin, et. al. (1994). U.S. Army Battlescale Forecast Model, in Proceedings of the 1994 Battlefield Atmospherics Conference, 1 Dec 94, Army Research Laboratory, White Sands Missile Range, NM.

Noble, John (1991). Acoustic Propagation in the Atmosphere Using the Scanning Fast Field Program, in Proceedings of the 1991 Battlefield Atmospheric Conference, 3 Dec 1991, Ft. Bliss , TX. Available from ARL, IS&T Directorate, Adelphi, MD.

Tofsted, David and O'Brien, Sean (1996). Application of the WAVES Modeling Suite to the Visualization of Natural Cloud Fields, in proceedings of the 1996 Battlescale Atmospherics Conference, Dec 1996, San Diego, CA (these proceedings).

Development of an Atmospheric and Space Environmental Models and Simulations Directory

Edwin Núñez, John Medeiros, Beverly Burns
COLSA Corporation, Huntsville, Alabama 35806

and

Gary McWilliams
Executive Agent for Air and Space Natural Environment
Scott AFB, Illinois 62225

INTRODUCTION

The Defense Modeling and Simulation Office (DMSO)[1] is currently developing the Modeling and Simulation Resource Repository (MSRR). The purpose of the MSRR, as defined in their World Wide Web (WWW) site[2], is to provide a "collection of computer resources and information which will assist the Modeling & Simulation Community in communication and information sharing". They also indicate it will be "implemented as a series of WWW servers available through the Internet or the Defense Data Network (DDN)". As part of the MSRR services, there will be a repository of detailed information on the different models and simulations available at the Department of Defense (DoD). This repository of resources will be accessed via the WWW and will allow comprehensive search through the different catalogs and directories. The search will be possible by browsing, entering text, or using a text database query. As part of the MSRR, a network of at least nine servers is contemplated, each dedicated to different information, or modeling and simulation domains.

DEMS/A&S

Our current effort involves the development of a catalog/database of atmospheric and space environmental models to be located under the MSRR. It will be named the Database of Environmental Models and Simulations / Air and Space (DEMS/A&S). In the future, DEMS/A&S will include all key DoD models and simulations related to the air and space natural environments. The information available at DEMS/A&S will be detailed enough to allow users and developers to search the database and determine which models and simulations best apply to the solution of a particular technical problem.

This program was initiated and funded by DMSO, but is being managed by the Executive Agent for Air and Space Natural Environment. The program manager is Mr. Gary B. McWilliams[3], currently located at the Air Force Combat Climatology Center in Scott Air Force Base, IL. DMSO conceived DEMS/A&S as a tri-service program, covering all environmental models and simulations of importance to the three branches of the Armed Forces. As evidence of this approach, DMSO contemplates

[1] URL for DMSO is: http://www.dmso.mil
[2] URL for MSRR information is: http://mercury-www4.nosc.mil/msrr/about/whatis.htm

[3] Internet address: mcwillig@thunder.safb.af.mil

the addition, in the near future, of models and simulations related to oceans and terrains.

RELATED EFFORTS: E^{2}DIS AND MEL

DMSO has also sponsored two other major efforts related to DEMS/A&S. These are the Master Environmental Library (MEL) and the Environmental Effects for Distributed Interactive Simulation (E^{2}DIS). As described in their home page, MEL[4] is an MSRR node with a "distributed environmental data access system which allows users to search for, browse, and retrieve environmental data from distributed sources." It is a single-location access to *metadata* or information about all environmental data residing at multiple regional sites. Through the use of keywords, location and time, a user can determine what data is available and where it is located. In addition, facilities for requesting the data are provided.

The E^{2}DIS had eight tasks, one of which included a Survey Task. Burgeson, Piwowar, and Try (1996) report three objectives for the Survey Task: "to develop a baseline of the Military Services' current requirements for incorporation of the atmosphere and near-space environment and their effects in military models and simulations (the Requirements Survey), to identify atmospheric and near-space environmental models and databases that are currently available from the services (the Capabilities Survey), and to compare the results from both survey efforts and make appropriate recommendations." Thus, the emphasis of the E^{2}DIS Survey Task consisted in the identification of current *requirements* needed for the *incorporation* of data into military models and simulations. As a result, E^{2}DIS studied the gap between model and simulation data requirements and currently available data. It provided recommendations concerning the reduction of the difference between required and available data for models and simulations.

DEMS/A&S uses the excellent and comprehensive information gathered by the E^{2}DIS Survey Task as a starting point for identifying available models and simulations. Additional information is gathered and provided for the models and simulations. Contrary to E^{2}DIS , however, our concern is with providing detailed information about the models and simulations and not with the difference between required and available model data.

[4] URL for MEL is: http://www-mel.nrlmry.navy.mil/

SELECTION CRITERIA

Several selection criteria were developed to accept models and simulations in the DEMS/A&S. Agencies responsible for the development, maintenance, and use of the models and simulations had to follow these guidelines. They were:

1) *Frequency of use* - This is an indicator of the importance of a model or simulation. In general, models which are run daily are more important to an agency than those that those run monthly or yearly.

2) *Model acceptance within the air and space communities* - Model acceptance within the community can be shown by a formal Independent Validation and Verification (IV&V) process. Many of the environmental models, however, have not gone through this formal process. By their nature, they are in the research and development stage. Model acceptance is shown by the confidence placed by the community of experts who have submitted model physics and results to close scrutiny. When these results are found to be in close agreement with observations, under a wide variety of conditions, the community of experts "accepts" the model or simulation and places confidence in its results.

3) *Model maintenance* - The importance of a model to a development agency is indicated by the dedication of resources to maintain a model. Additional evidence for its importance comes from plans to continue model maintenance in the future.

4) *Activation during crisis or combat* - Some models which are not run frequently become very important during times of crisis. Their importance to a development agency derives not from the frequency of use, but from the circumstances under in which it is used.

5) *Education and training* - Many models and simulations are widely used for education and training purposes. They derive their importance from the function they accomplish and the wide familiarity of the community with them.

6) *Model information* - The more information that is available about a model, the easier it will be for the community of potential users and developers to evaluate the model's suitability to task. The information will be gathered through site visits, manuals, open literature, or interviews.

DEMS/A&S ARCHITECTURE

Database structures for DEMS/A&S will be implemented in Oracle V 7.x. It is our intent to maintain the database structure utilizing the latest commercially available versions of Oracle. The design calls for a user-friendly graphical user interface (GUI) that supports diverse functions. A complete set of functions will be available including, among others, browsing, entry, edit, search, sorting and printing.

DEMS/A&S will also seamlessly support various levels of user. Some users will have the privilege of entering or erasing data concerning the model or simulation for which they are responsible. Others will only have access to the information without the capability of changing it. In addition, the capability of storing and showing *classified* information to specific *authorized* users will be available. When exploring DEMS/A&S, unauthorized users will not even be aware that classified or sensitive information exists in fields inaccessible to them.

As part of the MSRR network of servers, DEMS/A&S will consist of a Local Area Network (LAN) and a WWW version. Within the MSRR there will be a series of LAN nodes containing databases for the different domains. Figure 1 illustrates, in the outer ring, the different LAN domains. For example, the Army, Navy, Marines, and Ballistic Missile Defense Organization (BMDO) will each have their own Relational DataBase Management System (RDBMS) node. Other organizations, as approved by DMSO, will also have their own LAN RDBMS. DEMS/A&S will be one of the LAN domains, forming part of the local environments domain. In the future, terrain and oceans data will be added as environmental extensions. These LAN nodes will be fully customizable. The organizations responsible for node maintenance will have full control over the information shown locally. In Figure 1, for example, a cost data extension for the Navy domain is presented. Although this data will be available to LAN users, it will NOT be accessible in the WWW version.

Local domains will export and import data to a centralized Oracle RDBMS. This centralized modeling and simulations database will be publicly available in the WWW to users. It is represented as the inner ring in Figure 1. A graphical interface, illustrated in the intermediate ring in Figure 1, will present the information to WWW users. It is important to emphasize that only that data which the LAN administrator specifically wants exported to the WWW will be displayed.

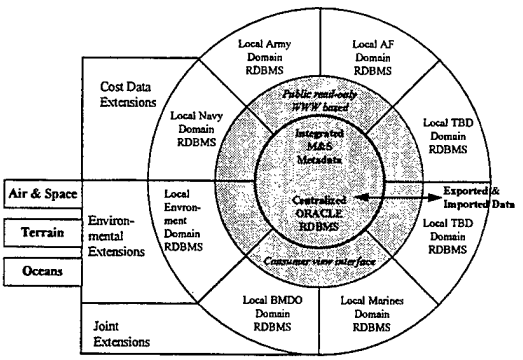


Figure 1. MSRR architecture showing the LAN and WWW versions. Local domains are illustrated in the outer ring. The WWW data shown in the inner ring will be displayed to general users through a GUI (intermediate ring).

LAN AND WWW VERSION PROPERTIES

The LAN version will have the standard Microsoft® look and feel. It will have browser tab views leading to different information categories for the model or simulation. Left-side lists will contain the results of specific queries for models with specific characteristics. These lists and their results will remain available as the

user selects and displays information for the different models. Consequently, there will be no need to conduct the search again as the user moves from one model or simulation to another.

Navigation in the LAN version will be controlled through the use of menus. Access control at the menu, window and tab levels will also be available.

The WWW version will inherit its appearance from the LAN version. As a result, it will have the same look and feel. The WWW version will also have link navigation, taking the user to specific web sites provided by the LAN domains. The general public will only have browsing capabilities in the WWW version. **Edit capabilities will only be possible through the LAN domains for authorized users.**

INFORMATION ON CANDIDATE MODELS AND SIMULATIONS

Information on the different models and simulations to be included in DEMS/A&S will be acquired through direct site visits of developer facilities. During the visits, developers will be interviewed and they will be requested to fill out questionnaires. In addition, documentation concerning the model or simulation will be collected.

In lieu of, or in addition to direct site visits, model or simulation proponents will be given the option of completing an on-line questionnaire or to submit information by fax, e-mail or regular mail.

DEMS/A&S should be considered as a vehicle to disseminate information regarding models and simulations to the community of users and developers. All information concerning the models belongs to the proponents and will be reviewed by them before it is made available on the WWW. Proponents will also be asked to review the available information periodically to check for its accuracy and to provide updates. As DEMS/A&S developers, we will not generate any information or data about the models that has not been provided by the responsible developing agencies. In addition, we will not supply any code to interested users. That would only be done by the responsible agencies.

IN-DEPTH EVALUATION

An in-depth evaluation of two models will be performed to characterize their principal algorithms. The purpose of the evaluation is to characterize the model in greater detail. In order to subsequently enhance the database structure and design to best represent all models and simulations. Another important consideration is the exploration of how to best incorporate algorithm information with a view towards facilitating algorithm re-use in the future. Under consideration for this more detailed characterization are an atmospheric mesoscale weather prediction model called the Coupled Ocean/Atmosphere Mesoscale Prediction System (COAMPS) from the Naval Research Laboratory, Monterey, and GEOspace from Phillips Laboratory, Hanscom AFB.

STATUS OF DEMS/A&S

The database structure for DEMS/A&S continues to be developed. Although it has substantial similarities to the structure of the other MSRR domains, it will also have unique information tailored to the atmospheric and space models and simulations. An on-line version of the survey questionnaire is available for WWW viewing and entry using standard web browser software. The URL for this WWW version of the survey is available through e-mail *request* to either jmedeiro@colsa.com or mcwillig@thunder.safb.af.mil. This method will enable proponents to submit the information about their model or simulation right from their computer without the need to fill out a paper form.

Another activity which is very important to the acquisition of information on models and simulations are site visits. At present several government laboratories have been visited. In the next few months several other installations will be visited where model and simulation developers will be interviewed.

The database is being populated using the information acquired during site visits. For some models and simulations data extracted from the E^2DIS study will be used until it can be

updated with more recent information submitted by model developers. In addition, efforts are under way to incorporate the DEMS/A&S data into the WWW application.

It is important that the DEMS/A&S acquire information on as many atmospheric and space environmental models and simulations as possible. We urge the community responsible for the development of atmospheric and space models and simulations to nominate all the relevant models. Nominations should be submitted to mcwillig@thunder.safb.af.mil, medeiro@colsa.com, or enunez@colsa.com.

In the future, as information on models and simulations, and the algorithms they contain, becomes disseminated through DEMS/A&S, greater use of already existing models and algorithms will be possible. As a result, appreciable monetary and time savings will be possible in the solution of environment-related problems.

REFERENCES

Burgeson, John C., Thomas M. Piwowar, and Paul D. Try, August, 1996. Natural Environmental Effects in Military Models and Simulations: Part II -- A Survey of Capabilities. Report No. PL-TR-96-2040, Phillips Laboratory, Directorate of Geophysics, Hanscom Air Force Base, MA.

Application of the WAVES Modeling Suite to the Visualization of Natural Cloud Fields

David H. Tofsted
U.S. Army Research Laboratory
White Sands Missile Range, NM 88002-5501

Sean G. O'Brien
Physical Science Laboratory, Las Cruces, NM 88003

Abstract

The Weather and Atmospheric Visualization Effects for Simulations (WAVES) suite of codes is an integrated series of computer programs designed to simulate atmospheric scattering, absorption, and turbulence effects on electro-optical imaging systems. An adaptation of this suite has been initiated to visualize the appearance of synthetic clouds for use in perspective and orthographic cloud view generators. The primary models developed for this application included a new radiative transfer (RT) module optimized for dense cloud calculations and modifications to the Air Force's CSSM (Cloud Scene Simulation Model) (Cianciolo and Rasmussen, 1992). The CSSM update included incorporation of EOSAEL CLTRAN vertical structure models of particle size distribution mode radii and imposition of horizontal periodicity to allow for tiling of cloud features. The visualization routine accesses data output formats equivalent to those in WAVES. It also uses a random cloud density field equivalent in format to the CSSM output for finer spatial resolution than the RT code output. RT code limiting path radiance results are thus coupled to higher detail transmittance results. Reflection of incident direct and diffuse radiation by the surface is also included in the visualization package, so cloud shadows may be properly depicted.

1. INTRODUCTION

For some years the effect of atmospheric illumination conditions on Army electro-optical systems has focused on target contrast. This emphasis has been of limited scope primarily due to the degree of sophistication of radiative transfer models available for determining radiance conditions in the near surface atmosphere. Typically these models have tended to be only vertical structure models. Further, the focus has traditionally been limited to transmittance or contrast transmittance alone. Several models are also focused on various extinction sources such as aerosols, molecular absorber species, and Rayleigh scattering.

However, the usage of these models was limited in that one could not develop a complete understanding of the complex interactions between observer, sensor response, and observed objects within the space through which the light travels. For instance, the textures of clouds and effects due to dynamic range of radiance changes within a scene are masked within the dimensionless contrast transmission equation approach. Clouds are also more than featureless objects or simply clutter. They have structure of their own which tends to complicate a scene, creating shadow regions resulting in dynamic range effects on systems, and producing spatially varying transmittance and path radiance effects. Thus, under many circumstances 1-D models may provide reliable results. However, for more general cases a more robust code is needed.

A second issue relates to the development of connectivity between the traditional application of electro-optical analysis methods, and weather based meteorology. Many studies have focused on sensitivity to various atmospheric effects as opposed to predictive type tactical decision aids to determine systems effectiveness under varying battlefield conditions. With the advent of models such as the Battlescale Forecast Model (BFM) and COAMPS for predicting detailed information about the weather state within 24-72 hours it is technologically feasible to ask questions about the future capabilities of systems in terms of when, where, and

with what to fight. In this type application arena, we might attempt to predict the relationships between numerical weather model estimates of vertical structures of humidity and temperature on a horizontal grid, and the vertical structures of clouds and visibility in a haze layer. Once this connectivity is established, evaluation of sensor system behavior can be predicted in mission planning.

One step in this development is the ability to generate a radiance picture of the environment, given visibility as an input along with cloud layering information. From this information one may determine the illumination present at the earth's surface, positionally varying radiance, and thereby develop line of sight information. In addition visualizations of a synthetic atmosphere are possible.

2. CURRENT PROGRAM

In particular, our task was to generate information that could be provided to a terrain perspective view generation system called PEGASUS. Originally PEGASUS was designed to replicate the performance of a UAV or a FOG-M missile. This simulation requires an operator to direct the flight of a vehicle over terrain looking for objects at or near ground level. Clouds could become significant limitations on the ability to acquire targets under these conditions. To simulate these effects in a realtime environment, we proposed the development of a cloud overlay system, whereby vertical traces would be performed through a rendered cloud volume and transmittance and limiting path radiance would be calculated along each line of sight. This information would then be templated down into a compressed form where each 16 m$\times$16 m square of the template would represent a 'pixel' position in the overlay. The templating process involved a palettized format where only 256 different transmittance/path radiance indexed pairs were retained and each pixel point was mapped into one of these indices. This process was necessary to accommodate the desire of the PEGASUS developer to represent a 64 km$\times$64 km region at 16 m resolution.

Also needed under this application was a method for ensuring that we could evaluate the radiative transfer model outputs without overloading the capabilities of the computers at hand. To generate sufficient data to actually model a 64 km squared volume would take enormous computing power and memory. As a substitute a method was developed to horizontally wrap the results of the cloud density mapping program, and the radiative transfer program, such that the results could be tiled over the terrain.

To accomplish this, the RT program was designed with an optional periodic boundary condition. The initial radiation presented to each modeled cell of the volume was computed by horizontally wrapping the density information such that when a direct ray traced toward the source of direct radiation (the Sun or Moon) left one of the sides of the modeled volume, the computation was continued on the opposite side of the volume continuing on in the same direction. Similarly, during the iterative calculation process used to evaluate the diffuse streams present within the volume elements, diffuse streams exiting one side of the volume were used to initialize the same stream directions at the outer walls in corresponding cells on the opposite side of the volume.

Periodicity was also imposed on the results being computed by the CSSM code. CSSM is designed to ingest information about cloud type, cloud layer base height, layer depth, and percentage cloud cover by layer, and output a 3-D gridded field of cloud liquid water content data. We used the 1992 version of this model (CSSM92), which has since been updated, but which apparently exhibits the same features as the version we used. The cloud field is generated using a rescale-and-add (RSA) fractal generator. This process involves a characterization of each cloud type according to a fractal dimension, a lacunarity parameter, and characteristic length and time scales. Unfortunately, this RSA approach is incompatible with a periodic conditioning of the calculated data.

A crude forcing of periodicity was nevertheless imposed on the cloud liquid water content data. Doubtless this has corrupting effects on the overall statistics of the fractal structure of the cloud fields themselves, however it is believed that this structural damage must be accepted to avoid the worse consequences of using aperiodic data in a periodic RT code, and/or subsequent tiling applications. In particular, cases were developed before the imposition of the periodic boundary conditions in which clouds were generated that abruptly ended at the boundaries of the volume. The subsequent appearance of these clouds, where a quarter

pie shaped cloud appears in the corner of the volume, with solid and flat vertical walls of cloud along the volume boundary was deemed a worse penalty, in terms of model fidelity, than the consequences of fractal structure corruptions within the CSSM model itself.

The method used to impose periodicity was to modify the sampling method used internally by CSSM. At the subroutine level a series of 2-D arrays are maintained which characterize the base height fluctuations, vertical heating function, vertical motion function, etc. for each cloud layer. In the original model the means of generating these random fields involved a single call to an RSA algorithm for each statistic at each point. Appropriate scalings of the horizontal dimensions are used to account for distance correlations that differ depending on direction. Let us call this functional dependence $Q(x/\sigma_x,\, y/\sigma_y,\, H,\, r)$, where the output of the RSA algorithm Q is modeled as a function of the horizontal (x and y) dimensions of the position within the volume, normalized by the scale lengths σ_x and σ_y, along with the Hurst parameter H and the lacunarity parameter r. In the modified approach developed, several calls were made to the generator, and used in a weighted average summation.

To accomplish the weighted averaging process, the weighting function

$$W(x) = \begin{cases} \frac{1}{2}[\sin(\pi x) + 1], & \text{if } -\frac{1}{2} \le x \le \frac{1}{2}; \\ 0, & \text{otherwise,} \end{cases}$$

is employed. Let X and Y denote the maximum horizontal dimensions of the volume to be modeled. Then the modified output from the routine calling the RSA algorithm is obtained by the sum of terms

$$Q' = \sum_{i=-1}^{i=1} W\left[\frac{(x+iX)}{X}\right] \sum_{j=-1}^{j=1} W\left[\frac{(y+jY)}{Y}\right] Q[(x+iX)/\sigma_x,\, (y+jY)/\sigma_y,\, H,\, r].$$

Due to the weighting function's form, minimal distortion is created in the RSA results near the center of the modeled region. However, near the midpoints of the sides of the volume 2 regions are being averaged together, and at the corners of the volume 4 samples are being averaged together. Because the random process being modeled has increased variance with increasing distance, when more than one sample is averaged the local correlations are reduced. In sample cases this has resulted in small patchy clouds around the volume boarder, of noticably shorter scale lengths than the overall structures of clouds near the center of the volume. As this was only a temporary solution to the problem, there should be some means of repairing the damage to the fractal structure by variable smoothing.

A second stage in the integration of the CSSM92 output as input to the RT code involved assessing the scattering properties of the aerosols predicted. In this effort a series of preëxisting models were used. These models included the EOSAEL routines CLTRAN (Low and O'Brien, 1987) and AGAUS, and the EOSAEL database PFNDAT (Shirkey et al., 1987). CLTRAN contains a series of vertical structure models of mode radius and liquid water content as functions of height above the cloud base. In CSSM92 the only structural dependence of liquid water content based on height is given as a function of temperature. Since the database of temperature information used was based on LOWTRAN7 vertical profile tables, the vertical structure of temperature available is rather coarse. Thus CSSM92 did not do well at characterizing vertical structure of most non-cumulus cloud types. Therefore, the CLTRAN vertical structure models were substituted into the relevant parts within CSSM92. In addition, CSSM92 only output liquid water content information. But since radiative transfer models require information concerning extinction and phase function, liquid water is usually not sufficient to characterize the scattering/absorbing properties of the clouds.

Characterization of cloud scattering properties was limited because the EOSAEL PFNDAT database of phase functions contains only near surface aerosol types. The other available database of cloud phase function information, contained within LOWTRAN7, is somewhat limited in that it uses parameterizations based on the Henyey-Greenstein phase function to characterize scattering properties. But this tends to restrict the ability to model clouds.

As a result of these considerations, an approach was developed to augment the PFNDAT data set by running the AGAUS Mie scattering code for a series of particle size distributions suggested by the analysis

contained in the CLTRAN model. In CLTRAN the particle size distributions of all clouds are modeled using a modified gamma phase function. Let N be the number density of aerosol particles per unit volume. Then, let $n(r) = dN/dr$ be the number of nominally spherical particles of radius r falling within a range dr about r in a unit volume. $n(r)$ is called the particle size distribution, which for a modified gamma distribution is given by:

$$n(r) = \frac{dN}{dr} = A\, r^{\alpha}\, \exp\left[-br^{\gamma}\right].$$

All the particle size distribution functions in CLTRAN use a modified gamma distribution function with $\alpha = 2$ and $\gamma = 1$, and where A and b are functions of the particle distribution mode radius $\bar{r}$. The CLTRAN model development thus gives a simple method for characterizing cloud phase functions: by running AGAUS for a standard liquid water content value at varying mode radius values.

Twenty new phase functions were developed, where mode radius varied from around 1 to 30 μm. The use of CLTRAN vertical structure models of mode radius within CSSM allows the characterization of the phase function and the optical extinction properties of clouds as functions of position with a simple extension to CSSM.

The phase functions created, along with the phase functions contained in PFNDAT were then analyzed using a processing routine to express their angular behavior as a Legendre series expansion and a forward scattering peak fraction. When evaluating the forward peak fraction the original Legendre coefficients, derived by analysis of the phase function, must be modified.

3. PHASE FUNCTION DELTA CORRECTION

The modification of phase function Legendre coefficients is a result of applying the forward scattering correction. Consider a general expression for the radiative transfer equation as given by

$$\nabla I(\hat{\Omega}) + \sigma I(\hat{\Omega}) = \varpi\sigma \int_{4\pi} I(\hat{\Omega}')\, P(\hat{\Omega},\, \hat{\Omega}')\, d\Omega' + (1 - \varpi)\, \sigma\, B.$$

Here, I is the radiance in the direction of the unit vector $\hat{\Omega}$. $d\Omega$ represents a differential solid angle. σ is the extinction coefficient, ϖ is the single scattering albedo (or probability that a scattering event occurs, given a collision with a particle), B is the blackbody function of temperature and wavelength. Therefore, the second term on the right represents emission of energy, while the first term on the right represents scattering, where $\varpi\sigma$ equals the scattering coefficient. The function $P(\hat{\Omega},\, \hat{\Omega}')$ represents the probability of energy entering from direction $\hat{\Omega}'$ and exiting in direction $\hat{\Omega}$ given that a scattering event occurs. This function is also referred to as the phase function.

For most natural aerosols P is highly peaked in the forward direction. As a result it is often difficult for a low order Legendre expansion to adequately characterize the forward scattering properties of most aerosols. Therefore, a typical technique used to improve the model of the scattering process is to assume that a fraction f of the energy actually scatters in the forward direction, and model this portion using a δ function:

$$P(\hat{\Omega},\, \hat{\Omega}') \approx f\, \delta(\hat{\Omega},\, \hat{\Omega}') + (1 - f)\, P'(\hat{\Omega},\, \hat{\Omega}'),$$

where the Legendre components of the P' phase function have been altered to reflect the removal of the forward peak.

Introducing this form for the phase function into the integral on the right hand side of the equation of transfer we find:

$$\varpi\sigma \int_{4\pi} I(\hat{\Omega}')P(\hat{\Omega},\, \hat{\Omega}')d\Omega' = \varpi\sigma f I(\hat{\Omega}) + \varpi\sigma(1 - f) \int_{4\pi} I(\hat{\Omega}')P(\hat{\Omega},\, \hat{\Omega}')d\Omega'.$$

Introducing this form back into the RT equation, we can translate the term in $I(\hat{\Omega})$ to the left-hand-side and introduce the variables:

$$\sigma' = \sigma(1 - \varpi f); \qquad \varpi' = \varpi\,(1 - f)/(1 - \varpi f).$$

These modified forms of the extinction coefficient and single scattering albedo allow us to model the RT equation using the same form as the original equation, except that the forward peak to the phase function has been removed. This approach is also referred to as a scaling transformation (McKellar and Box, 1981). Space does not allow a full detailing of the means of altering the Legendre coefficients here.

4. WAVES MODELING SUITE

The WAVES (Weather and Atmospheric Visualization Effects for Simulations) suite of codes provided the basis for generating the products used by the visualization software. WAVES was designed initially for characterization of illumination conditions and line of sight propagation effects. Products were also generated from WAVES to provide formatted information on cloud shadowing effects over terrain and 3-D radiance conditions within a scattering volume. However, the radiative transfer model contained in WAVES (the BLIRB (Boundary Layer Illumination and Radiation Balance) model) was optimized for optically thin media such as hazes. When this model was applied to optically thick media, such as clouds, the computer systems on which the models were run did not contain enough RAM to treat the clouds with adequate resolution. In addition, though visualization software had been prototyped under WAVES, this software did not render visually realistic cloud scenes. A three-fold program was therefore followed to enhance the performance obtained under WAVES: Conceptually, the first phase, previously described, augmented the CSSM92 output and available phase function databases to allow cloud characterization. In the second phase a new radiative transfer code called BLITS (Boundary Layer Illumination and Transmission Simulation) was developed. The third phase involved the adaptation of a visualization code previously developed to render the outputs of the BEAMS radiative transfer code (Hoock et al., 1992). This adapted visualization code has been named VIS42, since it is designed to operate on WAVES FastVIEW preprocessor formatted output which generates limiting path radiance information using a set of 42 directions. Interpolations are then conducted over these 42 directions in each modeled cell of the volume.

5. BLITS RADIATIVE TRANSFER MODEL

The BLITS model has been optimized for treating cloud aerosols of any density within each scattering cell of the modeled volume. The model is designed as a pure radiative transfer model with all information regarding scattering properties of the individual cells being passed off to a controller module at a higher level in the coding architecture. In our case, this means there exists a model (called the Applications Implementation Manager (AIM)) which provides a user interface, calls the CSSM92 model, generates processed input data for running BLITS, and analyzes the outputs of BLITS, in a single overall packaged environment. This means that BLITS can be used for a number of different applications, where the RT model stays constant, but the interface changes.

The main routines in BLITS ingest the input data, provide output to various files, precompute radiative transfer properties between different faces of each scattering cell type, evaluate direct radiation transmitted from the top of the modeled volume to each cell wall within the volume, and run the iteration routine that relaxes the system toward its final radiation balance state. Due to the large amount of data computed prior to starting the relaxation routine, no complicated exponentiation operations are conducted within the inner loops of the model, improving model performance. However, this means that large data arrays are maintained, and thus only a limited number of scattering classes are allowed. The current model limits the number of cell types to 80, which is a reasonable number for the 64 MB system used. For a volume 4 km deep and with a vertical resolution of 1/4 km, or 16 layers, this means that if each of the horizontally homogeneous haze layers is provided its own scattering class, only 64 classes remain with which to classify the other cells. Presumably these are all the cells containing cloud elements. The question is then how to characterize the remaining cells. The solution comes via a pattern recognition algorithm contained in the AIM interface.

6. VIS42 VISUALIZATION CODE

The VIS42 visualization program is designed to visualize the cloud radiance features being produced by the BLITS model and its post-processed output. To accomplish this the VIS42 model reads in the output data from BLITS that has been post-processed into a form identical to that used by the WAVES FastVIEW object code. This data set includes the output of a templating approach similar to that used in dividing the volume cells into different cloud types to be input to the BLITS model. To begin, each scattering cell within the volume is characterized by a set of 42 limiting path radiances in 42 directions. The templating scheme involves generating a limited set of 42-component vectors which characterize the directional dependence of these limiting path radiances across the volume. Then, when the output data for a given cell is produced all that need be output is the index of the appropriate template, the maximum limiting path radiance for this cell, and the transmission coefficient. The header to the FastVIEW file contains the information concerning these templates.

VIS42 reads this data set and develops a splining interpolation procedure for determining the limiting path radiance in any direction of user interest. VIS42 also reads an output that provides separate transmittance information concerning each scattering cell. VIS42 has the option of using data in the transmission file of the same granularity as the data contained in the FastVIEW file, or using the high resolution transmission file data. This methodology follows an approach suggested by Hoock et al. (1992): Since limiting path radiance is generally a slowly varying function of position, representing an integrated quantity, and since transmittance can vary rapidly within a medium, it should be possible to couple a higher resolution density structure calculation to a coarse resolution radiative transfer solution in performing a rendering task. In our test cases the transmittance data were available at 1/16 km resolution, while the radiance data were computed at 1/4 km resolution.

Using this approach, the transmission data file representing the modified extinction coefficient data for the cells (σ') is output to a file identical in form to the original CSSM92 output format. This data is then used in VIS42 in a first phase calculation. In this phase, for an orthographic rendering of the modeled volume, a maximum of three outer walls of the rendered volume may be visible. Points are chosen at the centers of each of the fine grid transmission data outer wall cells. For each of these points a line of sight is traced through the volume to determine the integrated transmission and path radiance. The code then proceeds to a second phase.

In the second phase the image rendering is accomplished. Each pixel is first assigned an original radiance value according to some algorithm. In the current implementation the 8 km×8 km modeled ground is rendered as a green reflecting surface. If the observation direction is downward and the line of sight is oriented toward a point on the surface, the surface brightness is modeled using the green surface reflectance coefficients, along with illumination information passed to VIS42 via the IL.OUT processed surface illumination file. This file contains surface illumination information that has been weighted to represent the normalized irradiance present at a surface element characteristic of the received signal of a sensor modeled by a weighting response function. For any point that is not part of the surface below the modeled volume a second set of results is used. This set represents the mean diffuse radiance present at the top of the modeled atmospheric volume, as weighted according to the same sensor response function. Once the initial channel based radiances are set, the code looks into its table of transmission cell centered propagation results and determines a subset of these results that represents near neighbors in terms of distance on a plane through which a series of parallel lines of sight are drawn through the modeled volume. Given this set of near neighbors, the algorithm determines weight factors of these neighboring points and determines the weighted sum of transmission and path radiance effects to apply to this pixel. Once a weighted sum is computed, the results are divided by the total weight factor, the initial radiance value is multiplied by the net transmittance, and the net path radiance is added, channel by channel. For example, a human eye perceives effects using red, green, and blue color channels. Thus the routine would determine 3 applied weighted transmittance/path radiance sets which would be applied individually to the different channels to determine the final pixel color value.

Pixel values are first computed using channel-based, floating point radiance units. Once all pixel results have been evaluated, the results are converted to an integer pixel scale by finding the maximum floating

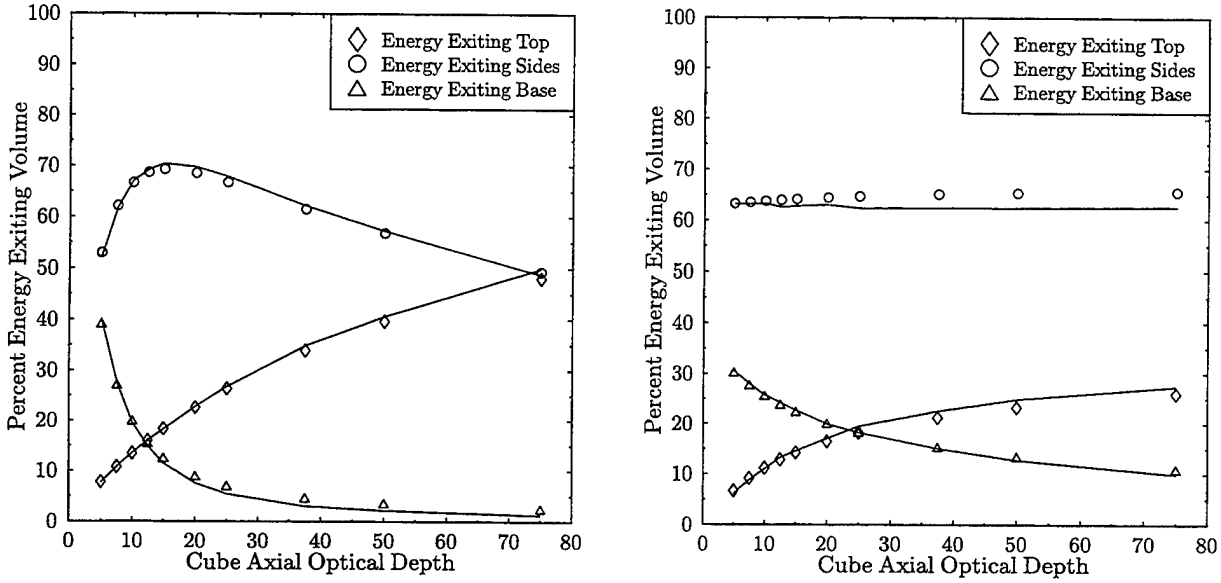


Figure 1: Comparison of BLITS radiative transfer model performance with Monte Carlo model results.

point result in any of the up to three color channels and mapping this value into a number 255.999. All other results are mapped linearly with respect to this mapping into the same range. Following this mapping all results are truncated to integer results, ensuring that the final image pixel values are limited to the range of 0 to 255, which is a 24-bit (8 bits per color channel) color image.

7. RESULTS

The radiative transfer program briefly described above was run and compared with the results of a Monte Carlo model. The scenarios tested were equivalent to the scenarios developed by McKee and Cox (1974). The shape of the scattering volume was cubical. A pure scattering medium ($\varpi = 1$) of up to 75 optical depths thickness along one axis was used. The exterior to the volume was considered a black void, except for a uniform plane parallel source of direct radiation incident at the top of the volume with a varying zenith angle of 0°, 30°, or 60° with respect to the normal of the upper surface. At angles greater than 0° the radiation also fell on the 'eastern' wall of the volume. Figure 1 shows the results for incident angles of 0° and 60°. Comparison of the results with the Monte Carlo model output shows the BLITS model performance is very good. The discrepancies which occur for energy exiting the sides of the volume are perhaps related to the limited extent of the Legendre expansion of the phase function. In the cases run, a 24-stream scattering model was used which supports up to a fourth order Legendre polynomial expansion. The comparisons were made using a fourth order expansion. For this order the forward peak fraction for most aerosols is around 50 percent. Thus after forward peak removal the total effective optical depth treated is around a maximum of 40 for the 75 optical depth case. In the examples shown, the grid used to simulate these results was a 4×4×4 representation. Each cell in the volume thus had to simulate 10 optical depths of scattering material. In previous comparisons of model results with Monte Carlo data the RT code tested was typically run using a 40×40×40 volume representation in an 8-stream model. The differences were that for an 8-stream representation approximately 75 percent of the expansion was modeled by the forward peak. Thus the maximum effective optical depth modeled per cell was only around 0.5, and the current results imply that the current model can treat significantly thicker clouds at reduced cost in memory and time than previously possible.

In figure 2 the results of the VIS42 visualization code are shown. A two cloud layer atmosphere has been modeled. The upper layer is an altostratus type. The lower layer is a cumulus layer of approximately

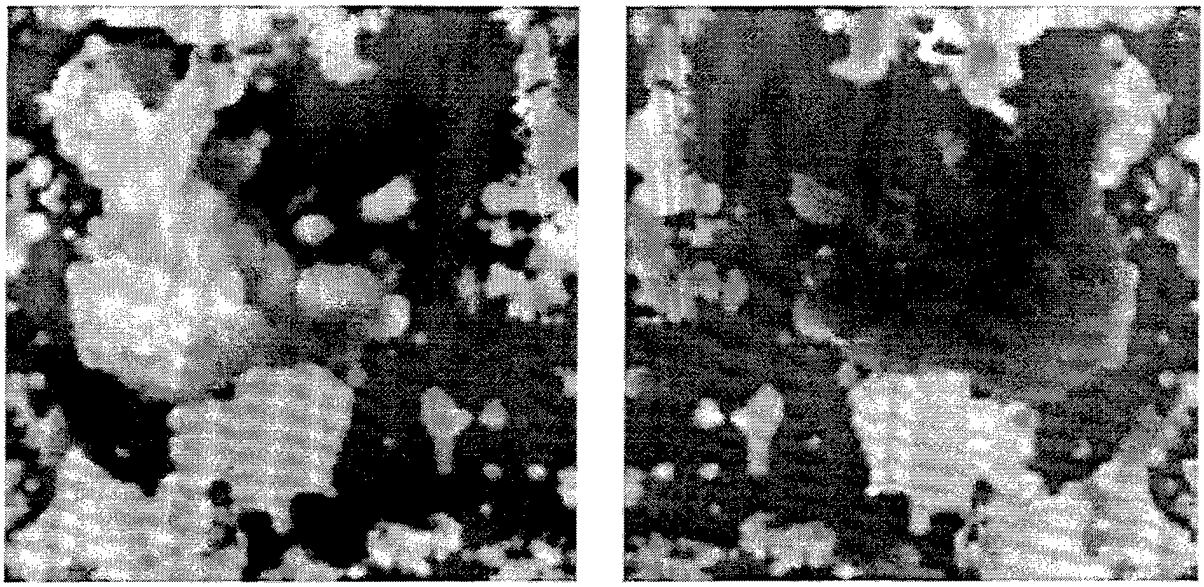


Figure 2: Downward (left-hand side) and upward (right-hand side) looking views of a cloud field.

35 percent cloud cover beginning at 1 km above the modeled surface. Two views are given of the scene: One shows the appearance of the clouds from above, looking at a rendered surface below the atmospheric volume. The other shows the clouds as they appear in orthographic rendering when looking upward.

In figure 3 we show a prototype image modification process result using a templated version of the vertically downward looking appearance of the cloud volume to modify a cloudfree initial scene. The original scene is shown on the left side. This scene is assigned a mean reflectance value $\bar{\alpha}$. Based on this value, one can analyze the image contents and deduce a mean pixel value $\bar{P}$. From this information the point-to-point reflectivities present in an image may be calculated: Let $p_{i,j}$ be a pixel RGB value at position (i,j). The point reflectance is then modeled as $\alpha_{i,j} = (\bar{\alpha}/\bar{P})p_{i,j}$. Using the positionally varying illumination information available, the brightness of that pixel can be determined as a channel-based radiance result. The limiting path radiance and transmittance effects for that point can then be applied. This process takes about 6 seconds on an SGI computer, which also entails reading the databases of transmittance/path radiance and illumination information, as well as the mean pixel calculation.

8. CONCLUSIONS

We believe that the modeling framework developed provides a reasonable approach to rendering natural clouds in currently available visualization software. Prototyped rendering techniques developed for operation with the Naval Postgraduate School's PEGASUS Perspective View Generator are capable of rendering a templated cloud image within 6 seconds. However, this prototype software contains no optimization, requires all data to be read into the model, and operates on 3 color channels for each pixel. Obviously more sophisticated software could radically reduce rendering time of this 2-D templated cloud effect, resulting in realtime visualization of 2-D clouds. On the other hand, more robust 3-D cloud rendering routines may require significant additional effort to move to a near-realtime performance. Current orthographic rendering rates of 5 minutes per frame are far from reaching realtime. However, the fidelity possible with the orthographic model developed shows significant improvements over previous capabilities, and uses may still be available for these non-realtime technologies.

We anticipate further connectivity to gridded weather data and/or satellite derived real cloud fields. These connections should improve the ability to provide high fidelity virtual simulations. Utility of these

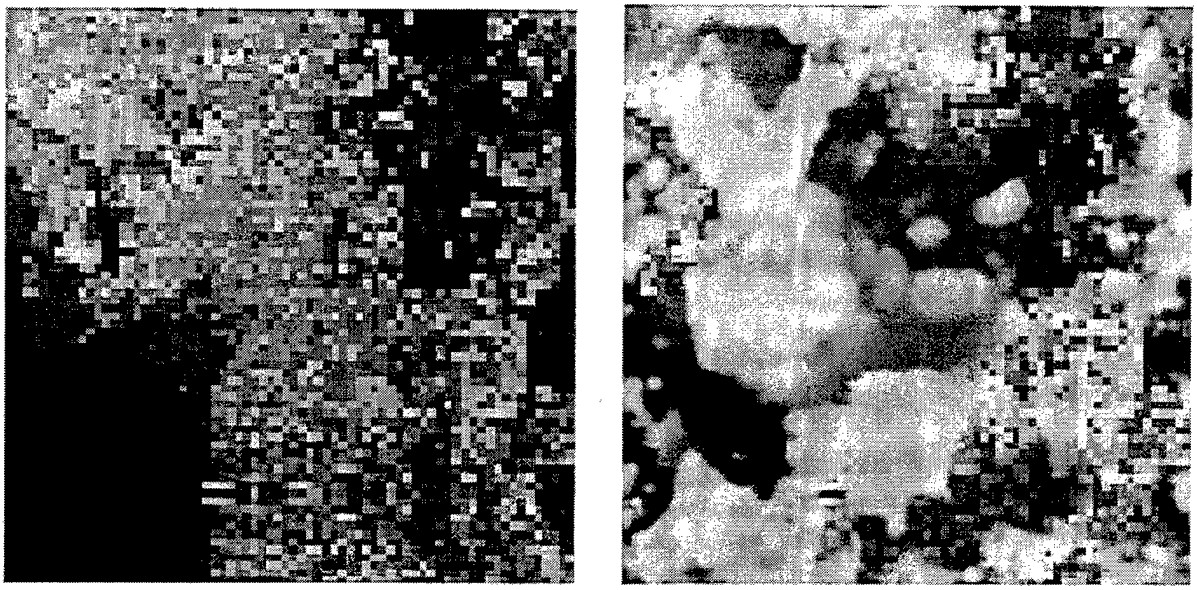


Figure 3: Original image of surface (left-hand side) and modified image following application of cloud transmission and path radiance effects (right-hand side).

simulation results should allow for better predictions of systems performance in mission planning software. Additionally, the ability to tile the simulated region across a large area is advantageous since in a DIS/HLA environment it reduces the amount of data that must be passed over a network. Lastly, the WAVES environment appears to provide useful output data formats. However, given the desire to present realistic clouds, a higher resolution extinction coefficient field appears advantageous in providing low level detail in the rendering of clouds.

REFERENCES

Cianciolo, M.E., and R.G. Rasmussen, 1992, *Cloud Scene Simulation Modeling, The Enhanced Model*, Phillips Laboratory PL-TR-92-2106, Hanscom AFB, MA 01731-5000.

Hoock, D.W., J.C. Giever, S.G. O'Brien, and E.J. Burlbaw, 1992, "A Multi-Stream Radiative Transfer Model for Inhomogeneous, Three-Dimensional Aerosol Clouds," *Proceedings of the 1992 Battlefield Atmospherics Conference*, 1-3 December, 1992, Ft. Bliss, TX, pp. 3-12.

Low, R.D.H., and S.G. O'Brien, 1987, "EOSAEL 87, Volume 9, Cloud Transmission Module, CLTRAN," U.S. Army Atmospheric Sciences Laboratory TR-0221-9, W.S.M.R., NM 88002-5501.

McKee, T.B., and S.K. Cox, 1974, "Scattering of Visible Radiation by Finite Clouds," *J. Atmos. Sci.*, 31:1885-1892.

McKellar, B.H.J., and M.A. Box, 1981, "The Scaling Group of the Radiative Transfer Equation," *J. Atmos. Sci.*, 38:1063-1068.

Shirkey, R. C., R. A. Sutherland, and M. A. Seagraves, 1987, *Aerosol Phase Function Data Base PFNDAT, EOSAEL 87, Volume 26*, U.S. Army Atmospheric Sciences Laboratory TR-0221-26, W.S.M.R., NM 88002-5501.

FASTPROP ENVIRONMENTAL EFFECTS FOR CONSTRUCTIVE SIMULATIONS

Chuck Lamar
U.S. Army Space And Strategic Defense Command

Wendell Cook
Welman Gebhart
Nichols Research Corporation

ABSTRACT

FastProp is an ultra-fast propagation simulation that models atmospheric and weather environmental effects on propagation of RF and optical signals for constructive simulations. It has been developed under the management of the US Army Space and Strategic Defense Command for the Defense Modeling and Simulation Office (DMSO). FastProp has been successfully interfaced with the EADSIM (Extended Air Defense Simulation) constructive simulation during runtime execution, and is currently being upgraded to interface with the EADTB. Since constructive simulations request propagation data for a variety of sensors and sensor/target geometries there are multi-resolution requirements on generating weather scene objects and in computing the propagation effects at different sensor wavelengths and fields of view. To minimize storage and computation times associated with generating weather scenes over a large area at very high resolutions, FastProp uses a methodology that includes a hierarchical weather object data base, stochastic indexing, and a line of sight (LOS) intersection algorithm. The stochastic indexing allows the repeatable construction of weather scenes from the hierarchical weather object database without requiring large 3-D or 4-D gridded arrays of weather scene data. The LOS intersection algorithm provides an efficient technique for determining the weather objects that affect the signal propagation at the appropriate level of resolution. The FastProp methodology and its critical components will be described in this briefing, and example interface requirements with the EASIM and EADTB constructive simulations will be discussed.

1. INTRODUCTION

U.S. Army Space and Strategic Defense Command (USASSDC) has long developed and used simulations to support the acquisition process. The Extended Air Defense Simulation (EADSIM) has provided a force-on-force modeling capability to support this process. However, the crucial element of weather has to date been modeled inadequately if at all, or has required extensive computation resources. A typical theater missile/air defense scenario may have 10s to 100s of platforms. Considering the effects of weather on each valid line-of-sight among all the platforms for scenario intervals on the order of a second or less can quickly bring an otherwise fast running

air defense simulation to a crawl. Most often this will not allow an acceptable time-frame for performing studies required to support acquisition.

FastProp works towards overcoming this problem by using a distributed simulation approach that isolates the computations required for weather effects from the calculations performed in EADSIM (flight processing, C3I, sensors,etc.). FastProp delivers to EADSIM propagation effects based on a request/response protocol data unit (PDU) scheme. These are experimental PDU's whose structure are consistent with others used for Distributed Interactive Simulation (DIS). These effects are then used by EADSIM to perform signal to noise (SNR) calculations and determine if detection has occurred. The result is an efficient methodology which allows the systems analyst to assess systems effectiveness over a wide range of weather conditions. This is a key requirement in any serious weapon/sensor acquisition exercise.

The FastProp team consists of the following:

USASSDC and NRL. The agencies have provided management to this effort which is funded by DMSO. USASSDC being the prime managing agency. NRL has managed the MIT/LL contribution to FastProp.

Hughes STX. Hughes STX developed the methodology for describing the weather using hierarchical objects (HeFeS - Hierarchical Feature Simulation). These objects can be generated quickly and stored efficiently using stochastic indexing. The inputs to this process are generated by PARGET; a software module which is driven by climatological databases.

Nichols Research Corporation. NRC has provided the FastProp preprocessor which includes a graphical user interface (GUI) for defining weather scenes and sensor types, execution of standard physics models to develop tables used by the runtime code. Integrated within the preprocessor is PARGET and FastView. NRC has also developed a software module used by the runtime code which calculates the LOS intersections with the weather objects and weather effects using the look-up tables developed in the preprocessor. In addition, a capability has been developed to generate GRIB files to be used off-line by the Extended Air Defense Testbed.

Decision Science Associates . DSA has developed the software required on both the server side (FastProp) and the client side (EADSIM) to support the network interface. This interface includes interface buffers which store and process incoming/outgoing PDU's between the two simulations. The communications itself is done using UNIX sockets configured in a user datum protocol mode (UDP). On the FastProp side, DSA has built the driver which makes the call to the NRC supplied weather effects module.

Georgia Tech Research Institute / MIT Lincoln Laboratory. These two team members have provided consultation on RF propagation and optical propagation respectively.

They have been involved in the recommendation of physics models to be used in the preprocessor, and validation of the rapid LOS techniques used to calculate weather effects.

Teledyne Brown Engineering. TBE is the primary developer/integrator of the Extended Air Defense Simulation (EADSIM). They have integrated code developed by DSA (the interface buffer) and NRC/Hughes STX (FastView) in order to support the use of the FastProp server for providing the particular weather effects used by the EADSIM sensor models. Enhancements have also been made to the EADSIM GUI to support the user in setting up sensors and scenarios for use with FastProp.

2. REQUIREMENTS

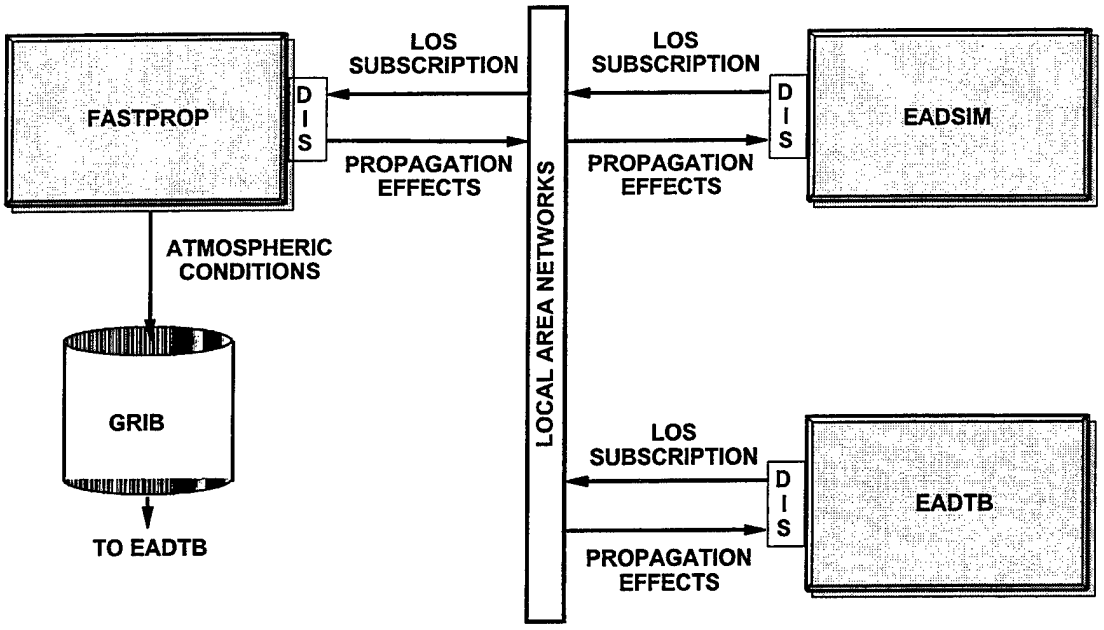
The primary requirement FastProp is to rapidly provide the user with weather effects on sensors and weapons across the visible, IR, and RF spectrums. It should also be easy to use for the analyst who does not have any meteorological training other than a familiarity with the standard terms used to describe weather by weather observers.

The outputs provided to EADSIM in real time are the transmission and background radiation for optical systems; transmission and backscatter for RF systems. Recently, a desire to supply the EADTB with a grid of physical parameters was added as an additional requirement. A file meeting the meteorological community's GRIB standard can now be generated by FastProp during preprocessing which includes ground level temperature, pressure, relative humidity, and velocity as well as the base height, top height, and liquid water content of clouds. At present there is no real-time communication scheme for interfacing with EADTB.

3. METHODOLOGY

The weather modeled in FastProp is broken out into two primary parts: 1) a layered atmosphere, which is characterized by aerosols, temperature, pressure, and humidity, and 2) clouds/rain which are characterized by their location, size and shape, liquid water content, and rain rate. The layered atmosphere can be specified by the user or it can be approximated by the preprocessor based on the location and time of year specified by the user. The cloud scenes are generated by PARGET. They are then placed in the scene in such a way to satisfy statistical data related to the location and time.

During an EADSIM scenario, a request for the weather effects along a path between an observer and target is made to FastProp. FastProp rapidly calculates the effects and returns them to EADSIM. With this distributed approach, EADSIM does not have to devote any computational resources to managing a weather scene or calculating the effects. This architecture is shown in Figure 1.



* TO BE HLA COMPATIBLE

Figure 1 Near Term Architecture

As shown in Figure 2, FastProp is made up of two primary parts; the preprocessor and the runtime code. The preprocessor includes the graphical user interface and performs all the functions of generating the cloud scene given the user inputs, and preparing look-up tables required by the runtime code. The runtime code reads these files during initiation and interacts with the interface buffer to process the requests which come across the network from EADSIM. The postprocessor allows the user to review key parameters of the run such as the number of requests that were made,and how many cloud intersections were logged.

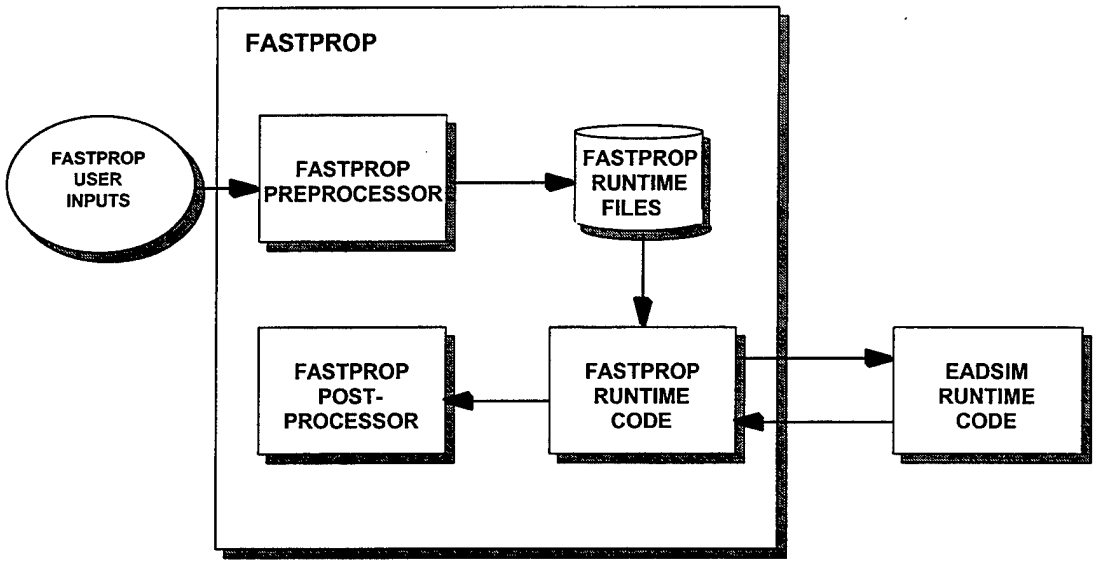


Figure 2 FastProp Elements

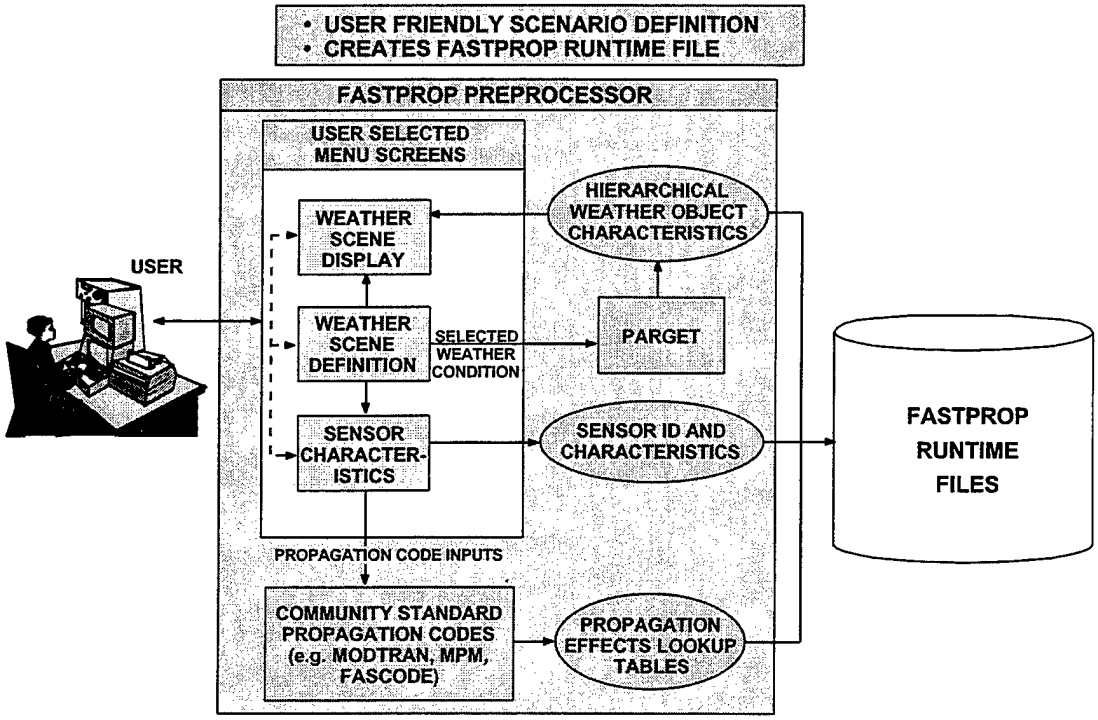


Figure 3 FastProp Preprocessor

The FastProp preprocessor is highlighted in Figure 3. The user interfaces with the preprocessor through a GUI which allows him or her to define the weather scenario and define sensors which will be used in the scenario. The weather scenario and sensor definitions are saved to ASCII files. After the weather inputs and sensors have been defined, a click of a button will cause the preprocessor to open the weather and sensor files and set up data structures in a format required for use by the physics codes. These codes are community standard codes which include MODTRAN (for visible and IR) and MPM (for RF) and FASCODE for use with laser systems. The

physics codes then generate the propagation effects lookup tables for the layered atmosphere which are used during runtime. Also, the data in the weather files are used by PARGET in order to generate the cloud objects. These objects are then stored for use by the runtime code.

The GUI which is presently being finalized will give the user the ability to define parameters consistent with the language used by weather observers (air crews, air traffic controllers,etc.) The observables will include cloud ceiling, base height, coverage conditions, humidity, temperature, and precipitation. The user will also be able to designate the location and time of year. These parameters will be used to drive the PARGET module. The top-level weather specification window is shown in

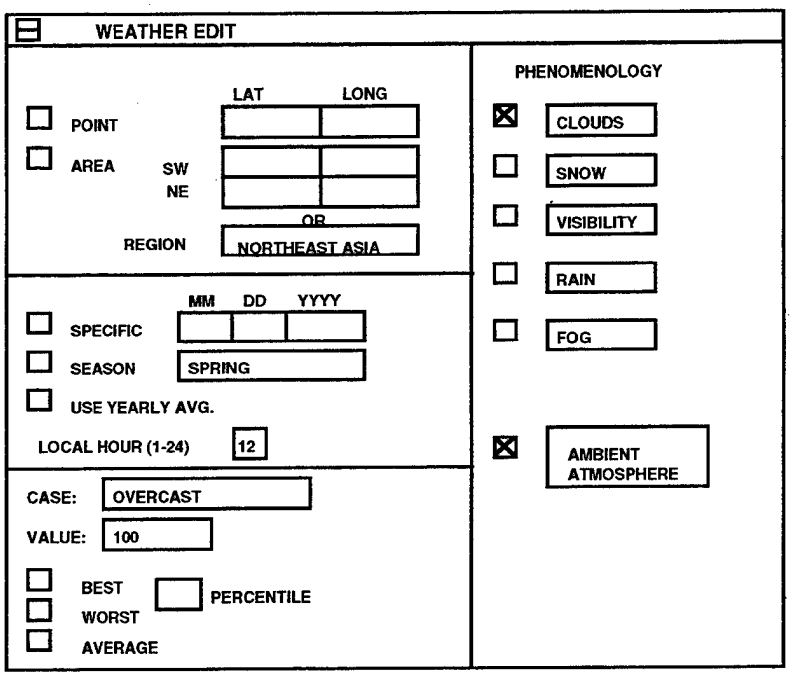


Figure 4 User Interface

Figure 4.

The runtime portion of FastProp can be run in an online and an off-line mode. The off-line mode is used to generate GRIB file inputs for EADTB and to support verification of FastProp. The online version interacts with the DSA supplied code which handles the buffering of requests and responses and the socket interface.

When running in the online mode with EADSIM, FastProp carries out calculations which derive the weather effects. The systems models which characterize the sensor and weapon performance reside in EADSIM. For the present off-line implementation with EADTB, the systems models and the effects models reside in EADTB. FastProp only provides physical attributes of the atmosphere (temperature, pressure, humidity, etc.). This demonstrates that FastProp can support clients with a wide spectrum of needs and requirements. The runtime configuration is shown in Figure 5.

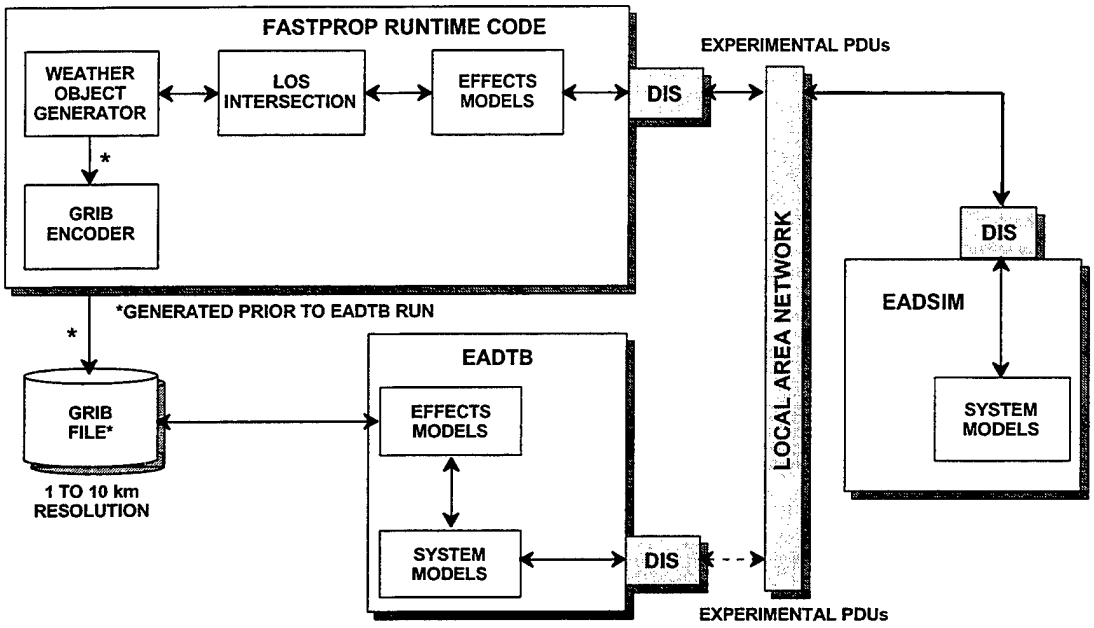


Figure 5 FastProp Runtime Elements

The approach for calculating the effects rapidly is to minimize the integration steps during runtime. The integration over the layered atmosphere is performed over the entire elevation space for different altitudes in the preprocessor and stored in a lookup table. During runtime the LOS algorithm is exercised which determines the weather objects (clouds, precipitation shafts) that are intersected. The extinction-depth product of these objects are then summed with the extinction-depth products from the layered atmosphere to get the total transmission along the path.

The key for the rapid computations is the LOS intersection algorithm and the HeFeS object generation. The object hierarchy is presently comprised of 4 levels: the slab which is typically at the mesoscale level and is made up of rows. The rows are then made up of clouds with scales on the order of 100s of meters. Each cloud can be resolved into meter scale puffs which is the lowest level. There is theoretically no limit to the resolution the process will support, but there is presently no requirement to resolve the objects beyond the puff level. In a typical scenario there may up to 50,000 puff objects or more in the region, whereas the LOS may actually intersect only 10 of these objects. The majority of these objects can be ignored by using a hierarchical filter process. As shown in Figure 6, the first check is done to determine intersection with the slabs. Because the slabs have a well defined extent in 3D space, the verification of intersection at the slab level is straight forward. The next elements that make up the slab-- the rows, clouds and puffs are generated using the HeFeS methodology that allows them to be specified by a functional relationship. When evaluating a LOS, the cloud scene is rapidly generated internally. Given the intersection with the slab, the scene is only generated for that portion of the slab that could be intersected given the geometry. The level at which this process continues (to

the cloud or puff level) depends on the FOV of the observing system and the range. Close in targets require the algorithm to evaluate intersection at the puff level in the area be evaluated. Longer range targets will cause the algorithm to stop evaluation at the cloud or even the row level. The LOS intersection process takes advantage of this functional relationship to quickly determine which objects are intersected and the thickness of the traversal through the object.

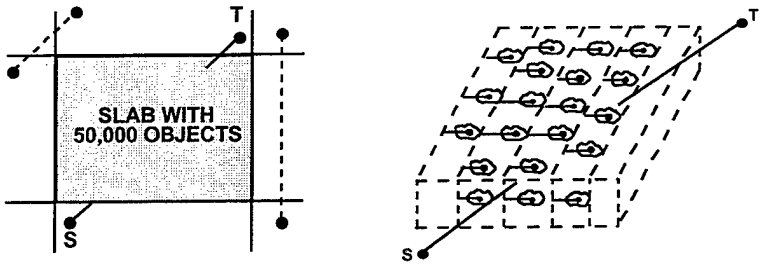


Figure 6 LOS Intersection Methodology

4. REPRESENTATIVE RESULTS

Figure 7 shows a representative weather scene over Fort Hunter Liggett. This scene consists of one slab with dimensions approximately 61 x 64 x 3 km thick. It is comprised of 31 rows, 1300 clouds with 500 meters average horizontal radius and 500 to 3000 meter vertical towers, and 85000 puffs with average radii of 100 meters. This particular view is from EADSIM.

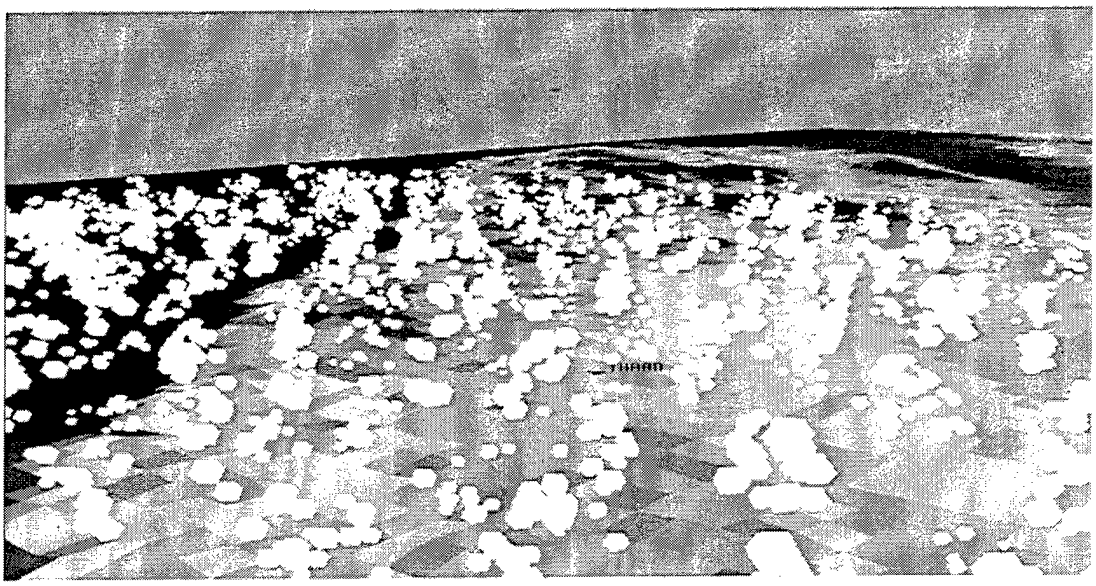


Figure 7 Single slab generated with 22 input parameters

For testing purposes a similar scene was produced and two flight paths for aircraft were defined to fly orthogonally to each other (see Figure 8). The aircraft were set at

2000 meter altitudes. One was aligned approximately along one of the slab rows (Flight Path 1) and the other flying across the rows (Flight Path 2). For this particular scene the cloud ceiling was approximately 1500 meters. A ground observer was placed at the cross-over points of these two flight paths. The aircraft were flown and the intersections and transmissions were calculated for both an LWIR sensor and a 10GHZ radar located at the ground observer point. Figure 9 shows the number of puffs intersected by the LOS paths to the targets on Flight Paths 1 and 2 for two sensors (an LWIR and radar sensors) located at the ground observer point. The radar has approximately 100 times the beamwidth of the LWIR sensor pixel, and therefore the radar intersects significantly more puffs than the LWIR sensor. However since the cloud extinction of the LWIR signal is much greater than the radar extinction, the radar transmission is through the clouds is much higher than the LWIR transmission, as illustrated in Figure 9 for the Flight Paths 1 and 2, respectively.

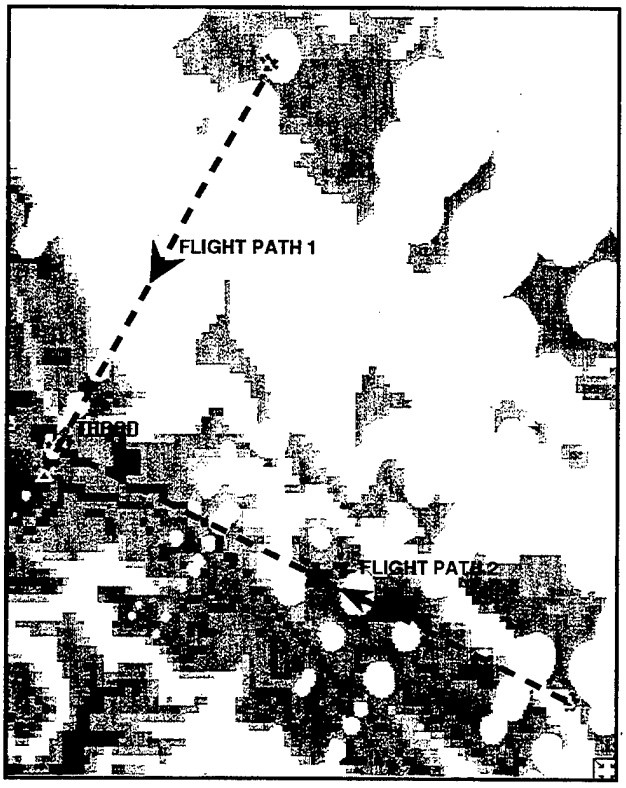


Figure 8 Target Flight Paths

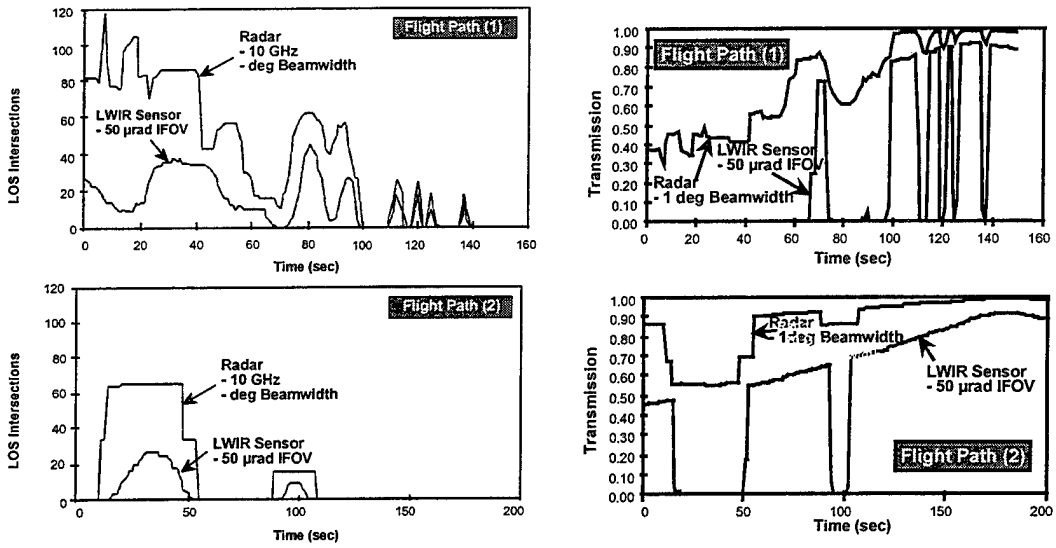


Figure 9 Runtime Results

5. SUMMARY

FastProp provides atmosphere and weather propagation effects for constructive simulations. To date it has been integrated successfully with both the EADSIM (online) and EADTB (off-line using GRIB encoded data). It is compatible with DIS technology, utilizing experimental protocol data units. It has been written in C and is organized in such a fashion as to maximize portability of the preprocessor across platforms. Future enhancements will provide a network interface with the EADTB, the ability to use encoded GRIB data as an input data source, and the incorporation of a 'subscription' protocol in working towards compatibility with the new High Level Architecture (HLA) standard.

WARGAMING ULTRA-FAST PROPAGATION ALGORITHMS FOR FASTPROP

ALBERT R. BOEHM
Hughes STX Corporation
Email address: boehm@ziplink.net

1. OVERVIEW

The purpose of this paper is to describe a set of algorithms that provide ultra-fast simulation of propagation through the atmosphere. First, the requirement is established for this type of simulation as opposed to other valid types of simulation. Next, the reason for a new set of simulation algorithms is shown by pointing out the limitations of other methods. The main part of the paper describes the algorithms.

2. THE SIMULATION REQUIREMENT

The word "simulation" can apply to a variety of activities -- numerical solution of fluid flow, message traffic, pilot training in a flight simulator, and many more. An explicit meaning for "simulation" must be assigned or else there can be considerable confusion.

The purpose of a weather simulation in wargaming is to quantify the impact of weather on system performance. Once quantified, steps can be taken to optimize, procure, or reject the system. There are at least three categories of weather impact quantification:

2.1 **System Physics and Engineering**. The goal is to determine system limits, i.e. under what conditions will the system work.

2.2 **System Effectiveness**. How efficient is the system when deployed? This question is asked for a variety of situations from the simple one-on-one case up through theater level conflict. An important tenet sometimes overlooked is that extreme weather can defeat any system. The question is **WHERE** and **HOW OFTEN?** Another tenet often overlooked is that an offensive weapon can usually wait for good weather; the effectiveness of a defensive weapon is measured in all weather.

2.3 **Training**. Two different goals differentiate the role of weather in training.

2.3.1 In a **Specified Syllabus**, specific weather is needed that develops the desired skill. The weather need not even be realistic - having five adjacent jet streams would quickly hone a pilots skill.

2.3.2 In a **Learning Exercise**, besides learning skills, lessons are learned about system usage, tactics, etc. Weather must be within the specified climate or else the wrong lessons will be learned.

The methods detailed in this paper are designed to meet goals 2.2 (system effectiveness) and 2.3.2 (learning exercises). However, these methods can be employed effectively for specified weather.

Of all weather impacts, seeability (both passive and active – visual, IR, radar) is needed at the most frequent intervals, requires the most calculations, and varies most rapidly. Although there is more to seeability than just transmission, rapid calculation of propagation through the atmosphere is the vital first step. Propagation also affects radio and optical communications. Thus, the rest of this paper focuses on propagation.

Numerous calculations of propagation are generally required. The large number is due to the number of sensors and targets, and the fact that they can rapidly change location. For many applications, a complete scene must be rendered and displayed. In addition, many simulations require multiple views – as seen by a land observer, a pilot, a radar, an infrared sensor, etc. FASTPROP generates a virtual atmosphere scenario and then allows ultra-fast calculations within it.

3. THE DILEMMA

Facts and premises are only stated here. Justification is found in Boehm (1994c), Boehm (1995), Boehm (1996), and LaMar et al. (1994).

The atmosphere has layers that are effectively uniform with respect to transmission, but there are other layers, particularly those with clouds, that have intricate detail. It is the intricate detail that is hardest to specify and often has the strongest effect on propagation.

Current physical fluid dynamic methods cannot specify intricate details in the atmosphere. The basic problem is not the lack of computer power nor observations of initial or boundary conditions. It is due to lack of complete physical principles with respect to the stress tensor, water droplet/crystal/vapor transformation, and radiation flux in clouds. For example, the size of cloud puffs within a cloud can not be found using only first principle physics. That is not to say that such relationships will never be discovered, and work in such area should be encouraged. But the fact remains that there are unknown areas in the basic equations for turbulent motion and in water transformations in the atmosphere.

Clouds and associated rain contribute the most to the variability of propagation, yet are poorly measured. Standard surface observations give only fractional cover and type – no information is recorded on orientation, shape of gaps, or physical properties. Cloud types are based on visual appearance. The liquid water per cubic meter can vary over an order of magnitude within the same cloud type. Weather satellite data must use inferential methods of limited accuracy to determine cloud properties. Current archived observations fall far short of

specifying intricate detail in the atmosphere. Only a small fraction of atmospheric motion and constituents are actually measured.

Furthermore, raw observations contain a host of biases, idiosyncrasies, and instrument and archiving errors to fool the unwary simulator.

Current methods of calculating propagation are much too slow for operational simulation. MODTRAN running on a high end work station would take several days to calculate the radiances in a single picture.

A propagation beam is affected by structure of many scales -- from a single droplet on a sensor lens to a complete cloud field when viewed from hundreds of kilometers away as shown in Figure 1.

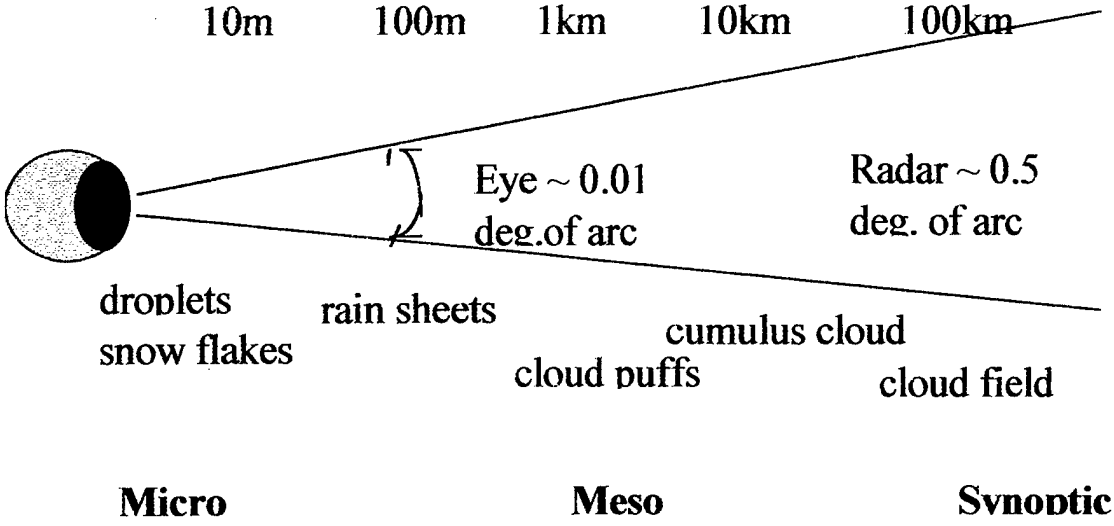


FIGURE 1. The scale of objects seen in a beam is a function of distance.

Meteorologists have for many years divided atmospheric motion into various scales depending on what forces are important at that scale. Various scales, from a single droplet (e.g. on a lens) to large domains as seen by a distant millimeter system, are required for effective propagation simulations.

Propagation is along a beam which is not infinitesimally thin, but can often be described by a cone specified by some solid angle. The width of this cone at the target or at some atmospheric obstruction can be measured as the distance across the beam. There are beams which are very narrow (a centimeter or less in width), very short (less than 50 meters), very wide (10 km or more), or very long (500 km or more). What a sensor sees when looking through the atmosphere depends very much on its beam width and path length.

A meteorological satellite infrared sensor may have a beam width of 3 km or more at the height of the clouds. A high resolution surface based infrared sensor may have a beam width of

less than 5 meters when looking at the same cloud. What they see will not have the same emissivity nor structure. A realistic simulation must have the ability to provide propagation at various scales.

There are numerous statistical and stochastic models of the atmosphere that have been validated for specific purposes. These range from simple rain/no rain Markov chains to complex four-dimensional non-homogeneous anisotropic global models such as CFARC which produce minute be minute results for decades. However, a new kind of stochastic algorithm was needed to meet the ultra fast computation requirements.

4. Algorithm Design

In order to overcome the limitations of other methods, three methodologies were developed: 1. The Morficon, 2. Stochastic Indexing, and 3. HEFeS (Hierarchical Environmental Feature Structure). Together the three methods can form a weather expander. This weather expander takes a small set of input values and using stochastic generators produces a complete weather scenario.

4.1. The Morficon

Consider the calculation of monochromatic transmission along a beam,

$$I_S = I_T e^{\int_S^T K dx} \tag{1}$$

Where I_S is Illumination at sensor S
I_T is Illumination at target T
K is the absorption coefficient
x is along a line-of-sight

If the line-of-sight is through a homogeneous layer, then the calculation is straight forward. Many transmission codes do just that; they assume a series of homogeneous layers.

In a region of intricate detail, a more general method is needed. A series of grid points along the line-of-sight can be defined and absorption interpolated to these points. However, a regularly spaced grid is inefficient. There are too many grid points where there is little change and too few where there is intricate detail.

The Morficon algorithm overcomes this shortcoming and has other desirable attributes as well. Instead of using ray tracing methods to render a scene, radiometric properties are precalculated for each object under various lighting conditions and stored as prototype objects called morficons. These morficons are stretched (morphed is the computer term) to adjust for viewing perspective, exact lighting, and individual shapes. By selecting a set of morficons based on physical and climatological principals, the resulting scene is consistent with the climatology

of the place and time and the physics of the atmosphere. For homogeneous or linear gradient objects, the transmission can rapidly be calculated using sumations over objects,

$$I_S = I_T e^{\sum_{i=1}^{n} K_i \Delta x_i} \quad or \quad \ln(I_S) = \ln(I_T) + \sum_{i=1}^{n} K_i \, \Delta x_i \tag{2}$$

where K_i is the absorption coefficient for the ith object or K_i is $(K_{enter} + K_{exit})/2$ for a linear gradient object. Subscripts enter and exit indicate where the line-of-sight enters and exits the object. Δx is the distance along the line-of-sight through the object.

The morficon is not merely a computer trick to produce fast images, although it does appear to be one of the fastest ways to generate an image. Propagation calculations generally require various parameters to be integrated along a line of sight. Typically, a grid of these parameters is used to interpolate the parameters to spacing along the line of sight. These values are then summed to approximate the integration.

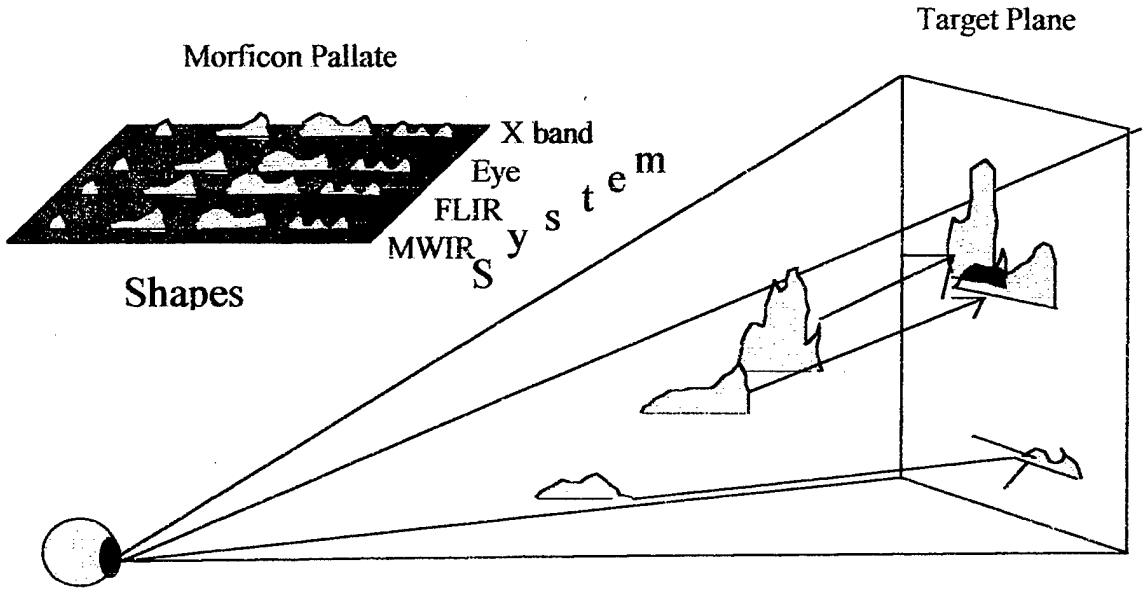


FIGURE 2 The transmission of various object is rapidly projected onto a plane at the distance of the target. Values on this plane can be added to objects beyond the target plane to produce a background plane.

With a morficon, the exact value of the distance through an object (e.g. a cloud) is known. Also the exact value of transmission or other parameter is know. These values are summed up by adding morficons to a target plane. The results are exact line-of-sight integrations – to within computer precision. See Figure 2.

A pallet of morficons is used to provide calculations for various sensors and atmospheric structures. Usually there is a tradeoff between speed and accuracy. With the morficon, both ultra-speed and accuracy result. Part of this advantageous situation is due to the prior calculation in making the morficon palette.

4.2 STOCHASTIC INDEXING

Rather than store all the information for viewing from different angles, the reproducibility property of pseudo-random number generators is used to index location and properties of each object. This "Stochastic Indexing" allows for millions of objects to be specified and retrieved with nearly zero storage. A backward running random number generator allows desired properties (e.g. 95% coldest temperature) to be generated. Algorithms are described and computer routines are presented in Boehm and Willand (1996). An illustrative demonstration of stochastic indexing is found in Boehm (1994b).

The typical computer random number generator starts with a seed number and rapidly returns one or more numbers -- a sequence -- that appears to be random. However, if the same starting seed is used, the exact same sequence will result.

Many types of scene-generating algorithms use this feature to produce the same scene by using the same seed. But if only a part of the scene is needed, the whole scene must be redone in order to obtain that section of the sequence pertinent to the desired part. If an inverse Fourier transform method is used, the whole random sequence must be calculated to get the random phases (the amplitudes are usually set to produce a desired spatial spectrum).

Stochastic Indexing goes one step further. It uses multiple starting seeds to generate what is needed at a point. The advantage of stochastic indexing is that the very large number of objects required for intricate detail can be indexed rapidly without a huge data base.

4.3 HEFeS (Hierarchical Environmental Feature Structure)

A hierarchy of feature objects, see Table 1, has been devised to specify structure over the scales of interest. We know from work reported in Boehm et al. (1993) and Eis (1997) that structure is not scale invariant. That is, structures at one scale do not occure at the same frequency (or sometimes at all) at other scales. To say the same thing another way, some of the terms in the equations of motion that are dominant at one scale are negligible at other scales.

The location and orientation of sub-objects are relative to the parent object. This technique allows rapid sorting of objects as to whether they are in a view or not, since the sub-objects do not need to be checked if the parent object is out of view.

TABLE 1 Typical HEFeS Objects

OBJECT CLASS	TYPICAL SIZE	TYPICAL TIME	EXAMPLE
Climate regime	global	1 month	wet spring
planetary wave	5000km	1 week	zonal jet
synoptic feature	1000km	3 days	cold front
meso feature	100km	12 hours	squall line
cluster	1km	1 hour	cloud cluster
cell	30m	10 min.	cloud cell
sheet	5m	5 min	rain streamer
voxel	1m	10 sec.	droplet dist.
particle	1mm	1 sec	snow flake

4.4 Climatology to Simulation Parameters -- PARGET

The purpose of PARGET, "PARameter GETer", is to specify the parameters of the simulated atmosphere so that it is representative of a given location, season, time of day and/or desired weather. PARGET transforms general user specifications into parameters required to establish a specific HEFeS Specification. PARGET consists of five sections: 1. Input Interface , 2. Output Interface, 3. Logic Section, 4. Stochastic selection, and 5. HEFeS Climate Data. Only a portion of PARGET will be discussed here, namely the types of input and an illustrative example of stochastic selection from a climatic distribution.

4.4.1 The input to PARGET is location, time of day, time of year, and kind of selection. The kind of selection is one of three:

4.4.1.1 A random draw from the appropriate climate.

4.4.1.2 A selection of a percentage and a condition for the percent worst observed condition. The condition may be a single variable, rain rate, or it may be a joint condition such as the lowest ceiling and/or visibility.

4.4.1.3 A specified feature. The feature may be a desired condition such as a large thunderstorm right there. The feature may also be a point observation or forecast, e.g. a METAR surface observation or TAF. The specified feature may be at any scale. For example, the feature may also be a synoptic field. (See Boehm, 1995) or it could be a droplet on a sensor's lens. In either case, the other scales of objects are selected to be consistent with the specified feature.

4.4.2 An illustrative example of stochastic selection is the rain rate for Northern Israel. Based on the algorithms developed by Tattleman et al. (1995), it was found that the climatic probability of rain rate for the month of February is,

$$P = \Phi [\, 3.5 + 0.955 \, \mathrm{Ln}\,(R)] \tag{3}$$

where P is the probability, R is the rain rate in mm/min, and Φ is the cumulative normal function.

Equation 3 is easily inverted to find the rain rate that corresponds to a specified probability,

$$R = \exp[\, \Phi^{-1}(P) - 3.5 / 0.955] \tag{4}$$

where Φ^{-1} is the inverse cumulative normal distribution.

Thus, if the percent heaviest, P, is specified, the corresponding rain rate, R, for northern Israel in February can be calculated for use in simulating the 100 P percent heaviest precipitation . Following Tattleman (1994) the Liquid Water Content, LWC, can also be calculated,

$$LWC = 0.052 \, R^{0.864} \tag{5}$$

5. Recapitulation

The HEFeS/Stochastic Indexing/Morficon combination is an accurate, very fast method for simulation of weather impacts in a relatively small inexpensive program. Some desirable capabilities such as the 95% worst simulation are hard to do any other way.

Many people have trouble grasping the stochastic generator concepts. They appear too simple. However, the underlying laws are quite complex indeed. To some they appear as Voodoo. However, stochastic laws rest on theorems and proofs much tighter than most meteorological derivations.

6. ACKNOWLEDGMENTS

This work was supported by the Geophysics directorate of the Phillips Laboratory with Mr. Donald D. Grantham as contract monitor for contract number F19628-93-C-0051 and by the US Army Space and Strategic Defense Command with Chuck LaMar as project leader.

7. REFERENCES

Boehm, A. R., Willand, J., and Gray, G., 1993: Reconciling Satellite and Surface Cloud Observation, Eighth Conference On Applied Climatology, American Meterological Society, pJ89-J94.

Boehm, A.R., 1994a: Visual Translucent Algorithm (VISTA), *Simulation, 62*, No. 2, 91-97.

Boehm, A. R., 1994b: Stochastic Indexing, Phillips Lab. , Hanscom AFB MA 01731, PL-TR 94-2012, ADA283143.

Boehm, A. R., 1994c: Methods of Supplying Atmospheric Effects in Simulation, 11DIS Workshop on Standards for the Interoperability of Distributed Simulations, Vol 1, Position Papers, Institute for Simulation and Training, University of Central Florida, Orlando, FL, p161-164.

Boehm, A.R, 1995: Objective Analysis Using A Hierarchy Of Climate Features, Proceedings of the Sixth International Meeting on Statistical Climatology, University College, Galway, Ireland.

Boehm, A. R. and Willand, J. H., 1996: Cloud Simulation Using HEFeS - Hierarchical Environmental Feature Structure, Phillips Laboratory, Hanscom AFB, MA 01731, PL-TR 96-2092, AD number not assigned yet.

Eis, K.E., Reinke, D., Foresyth, J., 1997: The Fractal Nature of Clouds, Battlespace Atmospheric Conference, NCCOSC RDTE DIV 88, San Diego, CA 92152-5230, URL: http://sunspot.nosc.mil/bac96.

Lamar, C., Boehm, A., Gebhart,W., Cook, W., Lazarus, E., 1994: Environmental Effects For Constructive Simulations, 11DIS Workshop on Standards for the Interoperability of Distributed Simulations, Vol 1, Position Papers, Institute for Simulation and Training, University of Central Florida, Orlando, FL, p297-304.

Harms, D. 1986: Cloud-free Line-of-Sight Simulation Models (Users Manual), USAFETAC, Scott AFB, 30pp, AD-B102926

Tattleman, P., Larson, K. P., Mazzella Jr., A. J., 1995: A Cimatology Model for 1-min Precipitation rates, J. Applied Meterology, V34, No 5, 1020-1027.

Proposal for Validation of a Multispectral Synthetic Scene Generator Model

by:

Marcos C. Sola, Mark W. Orletsky, Quochien B. Vuong, and Charles R. Kohler

Synthetic Imagery Branch, Sensors and Electron Devices Directorate,
U. S. Army Research Laboratory, 2800 Powder Mill Road, Adelphi, Maryland 20783.

ABSTRACT

The establishment of a sufficient, field-measured database to support the analysis of ATR algorithms, sensor fusion effectiveness, and sensor system performance for multiple combinations of targets, environments, sensors, and locations will severely challenge the limited, available resources within the Army. However, the use of a high-resolution, synthetic scene generator model (SSGM) for time-independent applications can alleviate the database requirement. A methodology for a robust validation of SSGM is proposed, which will consist of defining sets of images (real and corresponding SSGM imageries) and using human observers to define a baseline. First-order comparisons of a real scene to a synthetic scene will be performed with the use of the filters in the TARDEC [20] model or a comparable computational vision model (CVM). The similarity of target to background histograms as a function of various CVM filters will need to be analyzed to define first order-effects. Second-order metrics are defined in terms of probability of detection, detection timeline, and false alarm rate. A metric for the target signature will be mathematically defined to test these second-order effects. For a given application, the necessary and sufficient metrics are discussed.

1. INTRODUCTION

A great number of Army programs require a significant number of signature databases in order to satisfy program development. A partial listing of these programs include Intelligence Signature Assessment, Battlefield Visualization Test Bed (BVTB), ATR Algorithm Development, Sensor Performance Analyses, Multi-Sensor Fusion, Countermeasure/Counter-Countermeasure (CM/CCM), Target Acquisition (TA) Modeling Improvement, Required Operational Capability Requirements, Tri-Service Smart Missile/Munitions Testing, and Computer War Gaming Input.

Any of the programs listed above would require signatures related to target acquisition. Target acquisition is a function of many variables; among them are the target, background, environment, geographical location, time, and sensor. Each of these sets is composed of subsets. To physically measure signatures in the field to satisfy a wide dynamic range of signature conditions would be a substantial budgetary challenge for any project manager [14]. The physically measured data must not only answer the requirements of the project, but also must be general and of sufficient resolution to take into account other near term signature requirements [21]. Hence, there is the need to make use of synthetic databases to augment, supplement, and/or complement field databases. However, this requires a robust validation of the particular synthetic scene generator model (SSGM) that is used so that it gains credibility and acceptance in the modeling and simulation community.

2 APPROACH

An integral step in the validation of an SSGM is to compare a set of image pairs under the criteria that are relevant to the given application. An image pair is defined here to be the physically measured scene (target in background/clutter) and the corresponding synthetically generated scene based on model input requirements. For example, if we had a real-synthetic pair of images of a simple block world, with well-defined lighting, angles, etc., we would almost definitely do well by comparing the images on a pixel-to-pixel basis. While not every pixel of the synthetic image would have the same value as the corresponding pixel of the real image, a sufficient number would be close enough to indicate the quality of the synthesis. In this case, the simplicity of the "world" under consideration would almost definitely permit synthesis of images that are pixel-wise very similar to real images.

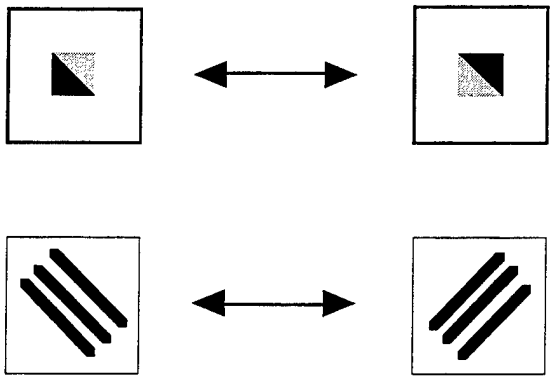


Figure 1. Examples of different images that have the same grey-level histograms.

For most applications of synthetic images, however, a bit-wise comparison to a corresponding real image is impractical as a validation criterion. Take, for example, the task of comparing images of a natural scene containing trees, grass, sky, water, etc. Here the variations that could be expected between the images would be large. For example, the wind may sway the objects in different directions, the clouds may cast shadows in different places, and so forth. Thus, the use of a pixel-to-pixel comparison would almost definitely be too exacting to effectively evaluate the quality of the synthesis.

An alternative method of comparison that has seen substantial use involves the comparison of statistics [2, 3, 4, 5, 8, 9, 20] that have been derived over the entire image. Such statistics include grey-level histograms, local-energy histograms, and many others. These statistics frequently give information about the quality of a synthetic image, but rely on obtaining the statistics from the image as a whole, and thus can be misleading, as the following examples show.

Intensity histogram (also called grey-level histogram) is a necessary but not sufficient tool for comparative assessment of an image pair. Figure 1 shows two different image pairs that would produce the same intensity histogram for both images in each of the given pairs, while Figure 2 shows two different weapon platforms with exactly the same intensity histogram. Figure 2 was produced by a C-program that repositions the pixels of one image to approximate the other. Thus virtually any image can be slightly modified to have a grey-level histogram of another image while still retaining its original "look". Thus, given this example, sole reliance on histogram distribution as a similarity-metric for image comparison can lead to a wrong conclusion.

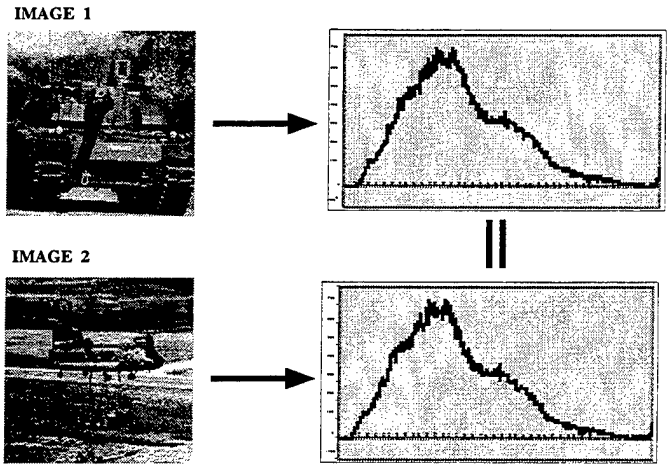


Figure 2. A tank and a helicopter with their identical grey-level histogram.

The validation approach taken by the Army Research Laboratory (ARL) is to develop a robust SSGM validation methodology for any synthetic rendering model. In particular, we would like to test this methodology against our own model for generating synthetic images, CREATION [6, 7, 10, 11, 17, 18]. Figure 3 is a generic approach to the problem of image validation. An "image pair" is passed through a comparator, and its output is statistically analyzed to identify a validation metric.

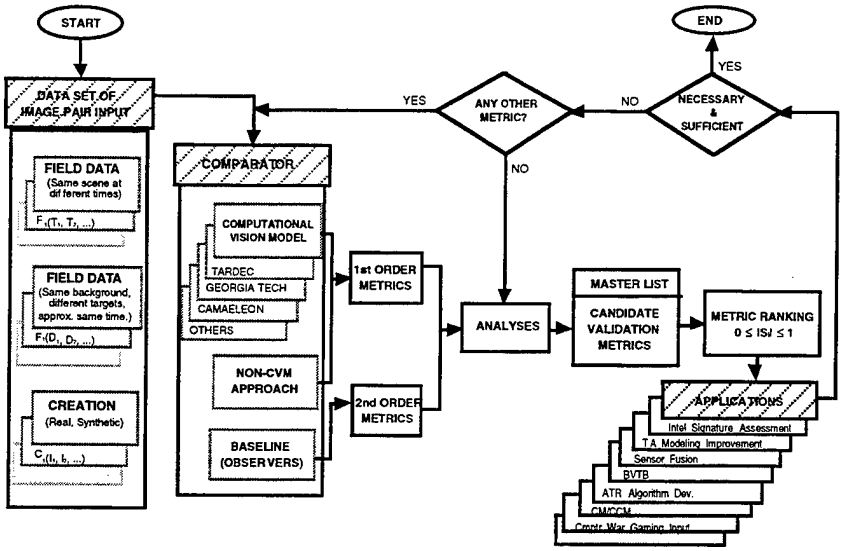


Figure 3. Diagram of an approach to image validation.

The comparator is composed of three components: a computation vision model, a non-computational vision model approach, and always a group of human observers used as a baseline. First-order validation metrics are obtained from a computational vision model such as the Georgia Tech Vision Model [2, 3], TARDEC [20] Vision Model, German CAMAELEON [4, 5, 9] Model, or other suitable candidates. Second-order metrics are obtained by using trained, human observers to provide probability of detection, highest level of acquisition (classification, recognition, identification) given detection, detection timeline, and false alarm rate. The noncomputational vision model approach can provide either first-order or second-order metrics. Note that if an image has the same second-order metrics as another, this does not necessarily mean that their validation metrics will be the same. Consider as an example two images that provide all the same second-order metrics as previously mentioned. Such a condition can be satisfied, for example, by a low observable tank at close range vs. a high contrast tank at long range (all other variables being equal). A robust set of validation metrics should provide an indication of two different scene conditions.

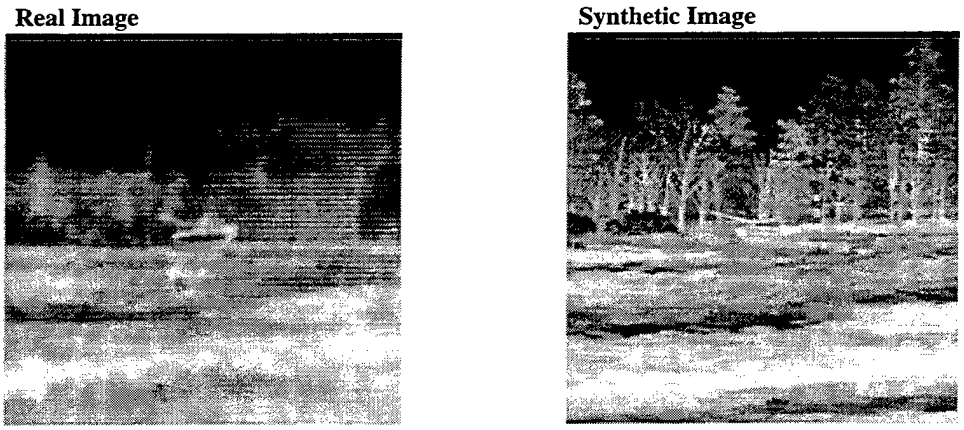
From the comparator, a master list of candidate validation metrics is compiled. A sufficient set of image pairs is parsed through the particular component of the comparator that is being tested for statistical analysis. These metrics are then "rank-ordered" from zero to one in terms of how similar the synthetic scene is compared to the real scene. A similarity of one is a perfect fit, while a similarity of zero signifies no correlation between the two images being compared. The number of validation metrics required is a function of the SSGM application. For high-resolution applications, such as target acquisition modeling improvement, most if not all the validation metrics with high similarity values may be required. For low-resolution applications, such as real time computer war gaming, only a certain portion of the validation metrics may be needed and their similarity metric requirement will be less stringent. It is therefore necessary to rank-order the validation metrics from the master list for a given synthetic scene-rendering application. In the CREATION model, we have a problem of field measured data from which we can generate a synthetic scene. Part of the problem is that this particular model requires a 24-hour diurnal cycle target signature history in order for us to be able to create a synthetic scene. Note that although ARL needs to validate the CREATION model, it must first be able to develop a robust validation methodology. To alleviate the image pair database problem, some pairs could be created from real field data, as, for example, scenes at different times or for the same time and background, but different targets.

3.0 PRESENT METHODOLOGY

Our current validation approach is to postulate a similarity metric that is defined as:

$$0 \le |S_i| \le 1, \qquad \text{where: } S_i = \begin{cases} 0, \text{ no match} \\ 1, \text{ perfect match} \end{cases}$$

and i = statistical validation metric (0, 1, 2, ...n) in the master validation metric list.



(a) (b)

Figure 4. M60-A1 tank.

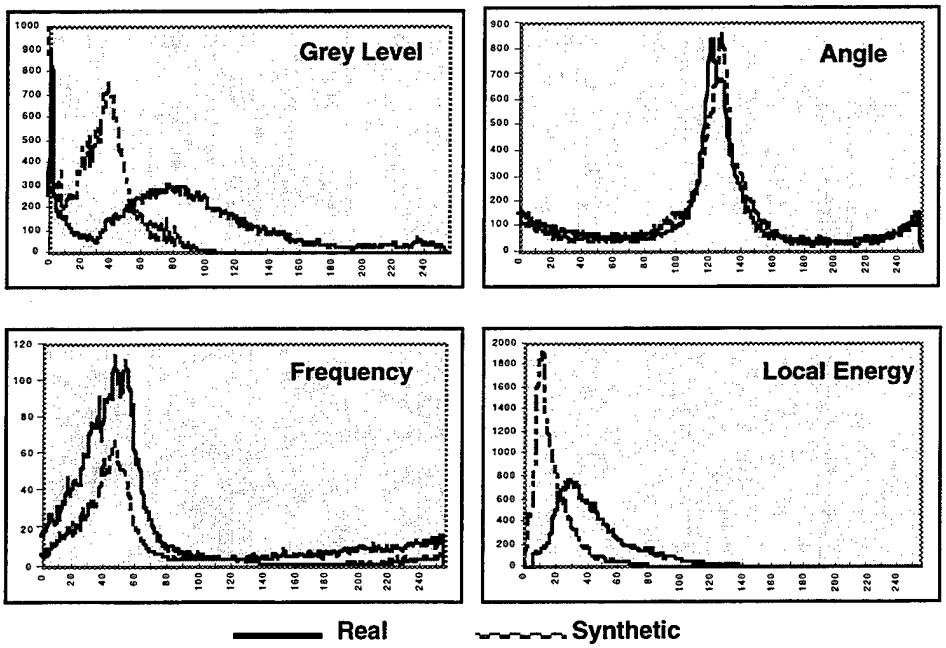


Figure 5. CAMAELEON histograms.

A wide dynamic range of signature image pairs is created from field measured data and its corresponding synthetic scene or from field data with differences in either time, background, target, environment, or other measurable variables. Each image set is parsed through a comparator using, in this case, the German computational

vision model CAMAELEON [4, 5, 9]. This model provides, as an output, the first-order metrics such as grey level, frequency, orientation, and local energy distributions. For each of these metrics, a statistical analysis is applied in terms of mean, median, mode, variance, standard deviation, absolute deviation, skew, kurtosis, and entropy. Figure 4a shows the field-measured data of an M60-A1 tank scene taken with a calibrated infrared sensor at Fort AP Hill, VA. A data artifact was introduced unintentionally because every other field was missed during the digitization process, resulting in a lower quality image than what a high-resolution, calibrated DL FLIR [16] is capable of showing. Figure 4b is the synthetic infrared rendering by the CREATION model. It contains some statistical sampling rather than first principle rendering of background data. Figure 5 shows the comparison between the real and the synthetic scene based on the output of the CAMAELEON model. Figure 6 shows our use of the similarity metric with our present validation approach. Two noncomputational vision approaches developed by ARL for comparing images, the "Region-Based" and the "Symmetric Difference" methods, are discussed next.

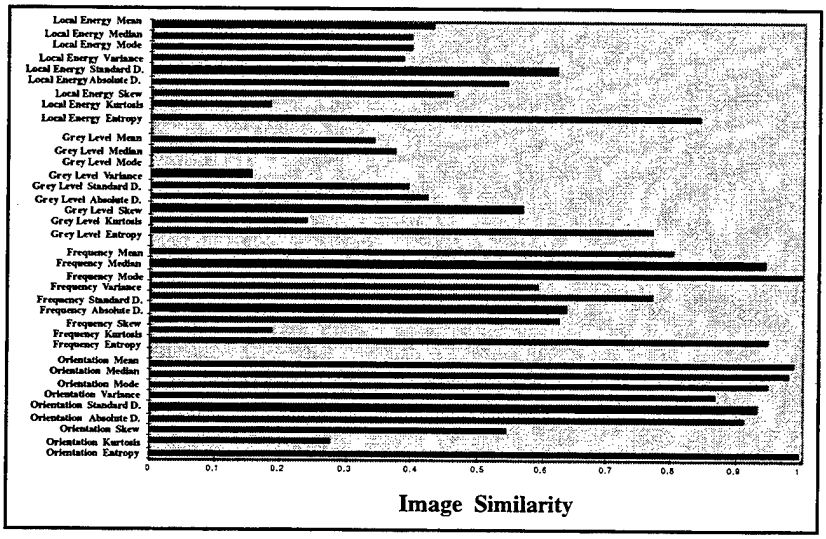


Figure 6. Image similarity.

3.1 A Region-Based Method of Comparing Images

Historically, there have been two different approaches for comparing a real scene to the synthetically rendered scene. One relies on very local information such as pixels, and the other relies on global information such as statistics generated over the entire image. Our approach is to use the middle ground between these approaches. We call it a *region-based* method of comparing images.

In region-based image comparison, we produce a mask that defines nominally 40 to 100 regions in the real or the synthetic image under comparison. This mask is then applied to both the real image and the synthetic image, and image-statistics (grey-level histograms, local-energy, etc.) are computed over each region. Comparisons are then made from the statistics obtained from each region to the statistics obtained from the same region in the other image. A real-synthetic image comparison is then obtained by computing the area-weighted average of the similarity metrics that resulted from each of these local comparisons.

For example, note that the images in Figure 2 have identical global grey-level histograms. Thus any comparisons based on global grey-level histograms will indicate that the two images compare identically. Suppose, alternatively, that we generated any arbitrary tessellation and applied that tessellation to both images. We could then generate the grey-level histograms over each of the regions produced, and then compare the histogram of a particular region to the histogram in the corresponding region in the other image. While the grey-level statistics over the images as a whole were identical, the same statistics over a small portion of each of the images would most likely not be.

Thus, regionalization has the potential to reduce the negative effects of false matches that can occur when comparisons based on global image statistics are used. Additionally, the use of regionalization cannot produce

results that make images appear to be statistically more similar than that which would be obtained from a global comparison. Specifically, if the images compare favorably on a region-to-region basis, they will also compare favorably globally. In short, regionalization can be used to allow a more rigorous application of common global statistics, and achieves a balanced medium between the very demanding bit-wise image comparisons and the somewhat ineffectual global comparisons.

As to the question of *which* regionalization to use, it is the opinion of the authors that any regionalization or tessellation would be acceptable since an arbitrary regionalization has the potential for producing more accurate image comparisons than the corresponding global comparison, and no regionalization has the potential for producing comparisons that are less appropriate than global comparisons. We, however, also see an advantage in producing regionalizations that are consistent with the low-frequency variations that are naturally present in the image.

3.1.1 A Method of Comparing Images Under a Low-Frequency Mask

In this section we describe step-by-step a region-based approach of comparing two images. Step 1 aligns the two images with each other, Step 2 matches the average brightness of one image to that of the other image, Step 3 creates a low-frequency mask, and Step 4 uses the mask to apply a global image comparison metric.

Step 1: Register and crop the images.
The first step in comparing images is to make sure they are (1) registered (or aligned) with each other and (2) of identical size. We accomplish this as follows. A human operator locates a well-defined point in each image and determines the pixel coordinates of that point. At present, a tool such as *xv* (x-windows view) is used to determine the coordinates of that point. Note that the real and synthetic images have not been previously registered, so the coordinates of the "well-defined point" will in general be different for the two images. Our program *crop* is then used to produce a new image for each of the two original images. The new images will be of a specific size and centered at the chosen point. We used a size of 256 pixels by 256 pixels for the initial trials. At this point we have a real-synthetic pair of images that are the same size and registered with each other.

This registration process involves translation only. A more sophisticated method of registration would also include rotation and scaling. However, this would necessitate a method of mapping the rectilinear grid of pixels of the original image to another grid of a different angular orientation and having a different scale. Methods for performing such a mapping exist, though they generally introduce artifacts, and the artifacts would have a great potential to pose problems for the comparison. Thus, we insist that the real and synthetic images be made to the same scale and oriented at the same angle, and then the registration is done by performing only a translation.

Step 2: Gamma-match the images.
A process that we call *gamma-matching* is used to change the brightness levels of the synthetic image so that the total brightness of the synthetic image is within a small factor of the total brightness of the real image. This is done with gamma-correction as follows. If the synthetic image is dimmer than the real image, gamma values are successively chosen starting at 1 and increasing in steps of 1 until the brightness of the corrected synthetic image exceeds the brightness of the real image. If the synthetic image is brighter than the real image, gamma values are successively chosen starting at 1 and decreasing in steps of 0.1 until the brightness of the corrected synthetic image is less than the brightness of the real image. When such cross-over points are found, the process is repeated with smaller step sizes, specifically step sizes of one tenth the size currently being used. This entire process is repeated until the ratio of the total brightness of the synthetic image to the total brightness of the real image is within a small constant of 1. We have been using the constant 0.001.

Step 3: Construct a template for one of the two images.
The process of constructing a low-frequency template for an image involves three steps: low-pass filtering the image, multilevel thresholding the image, and uniquely labeling the regions that result. These three steps are explained next.

Step 3a: Low-pass filter the image.
The image is low-pass filtered by convolving it with a square template containing a normalized Gaussian function.

Here, the user specifies the size of the "radius" of the template to be used and then the template is automatically generated. For example, if the template radius is chosen to be 5, then an 11 by 11 template will be generated. This template is then filled with a two-dimensional Gaussian function centered at the center pixel in the template and having a sigma chosen so that the area under the Gaussian curve over the template is 99% of the total area under the Gaussian curve over the entire real plane. The entries in the template are then normalized over the template (i.e., scaled so that they sum to 1). When the image has been convolved with such a template, the brightness values of the image will be "smooth" in the sense that there will be no rapid changes in brightness. The image will actually appear blurred. This is done so that the next step of thresholding will not produce many small regions, which would be possible if the image contained high-frequency components.

Step 3b: Apply multilevel thresholds to the image.
After Step 3a, the image will have brightness values that do not change rapidly throughout the image. In fact, the image can be thought of as a landscape in which the brightness values represent altitudes. After the low-pass filtering, all the hills and valleys will be smooth and gently rounded. There will be no sharp peaks, no spikes, no cliffs, no abrupt changes of any sort.

We now apply a multilevel thresholding process to the low-pass filtered image. Here, we (arbitrarily) choose 4 levels of brightness uniformly spaced between the dimmest pixel value and the brightest pixel value. Thus, every single pixel in the image falls into exactly one range. Each pixel is then assigned a number from 1 to 5 corresponding to the range into which it falls. After this thresholding process, the image appears somewhat like a topographic map in that the regions shown correspond to the brightness range of the pixels in the region. This looks very similar to topographic maps that show the altitude ranges between the curves on the map.

Step 3c: Label the regions produced.
The next step is to give the region that result from the above step a unique label and to give all pixels the label of the region into which they fall. To accomplish this, we initially set all pixels to be unlabeled and then start in the upper left corner of the image and proceed in a raster-like scan. During the scan, we do the following. When an unlabeled pixel is encountered, we use a recursive process that we call "flooding" to label each pixel in the same region as the newly encountered pixel with the "next available label". When the single raster scan completes, all pixels in the image will be labeled, either from the scan itself or from the recursive flooding process.

Here we scan the image from left to right and from top to bottom in a raster pattern. If a pixel is encountered that is unlabeled, it is given the "next available label" and the recursive "flooding" procedure is invoked. This procedure will attempt to recurse one pixel left, one pixel right, one pixel up, and one pixel down from the recently labeled pixel. Specifically it will recurse in those directions if and only if the pixel in that direction has not been previously labeled, the pixel in that direction exists (i.e., it is not at the edge of the image), and the pixel in that direction has the same brightness value (after the thresholding) as the recently labeled pixel. Thus the recursion will proceed to label all pixels in the given region and it will not proceed across region boundaries. At the completion of recursively labeling a region, the raster scan will continue until another unlabeled pixel is encountered at which point the region containing it will be flooded in a similar manner. This continues until the entire image has been scanned and labeled.

Step 4: Apply a global-metric according to the mask produced.
Upon completion of the mask, or tessellation, that was produced by Step 3, we can now use that mask to apply a similarity metric in a region-based fashion. As an example, let us consider using the "common area overlap" of the gray-level histogram as our metric. Recall that if we were using this metric in the global sense, we would generate the gray-level histogram for the real image and also for the synthetic image, normalize each of those histograms, and then determine the area under the histograms that is common to both histograms. Note that this area will be zero if the histograms are completely disjoint and it will be one if the histograms are identical. In the region-based method, we will apply this metric not to the images as a whole, but to each of the individual regions of the tessellation. Thus we will obtain a number between zero and one for each of the regions that indicates the extent to which the gray-level histograms of the two images resemble each other in that region. To obtain the final image metric, we simply take an area-weighted average of the similarity metrics that we obtained for the regions.

3.1.2 The Symmetric Difference Method

The segmentation of images into regions as described above can also be used to produce a figure of metric of comparison between two images. Consider generating one mask based on the real image and another mask based on the synthetic image. Comparing the masks, then, could be used as a method of comparing the images.

The manner in which we compare the masks is as follows. For one of the two masks, say that derived from the real image, consider a particular region in the mask. Calculate the symmetric difference between this region and every region in the mask of the other (synthetic) image and choose the minimum. Notice that if this region closely coincides with a region in the other image, this minimum will be small. In fact, if there is a region in the other mask that is identical to the region under comparison, this minimum will be zero. Now choose a second region in the real image and repeat this process to obtain another "minimum symmetric difference". If we continue this for all regions in the image, we will develop a string of minimum symmetric differences. We use the sum of this sequence as the image metric.

Notice that this sum will be small when each region in the real image closely coincides with a related region in the synthetic image, and it will be large otherwise. Thus, we have a metric that will be zero upon comparing two identical images, it will be small when comparing two images with similar low-frequency structures, and it will increase for images that have few such commonalties.

4. GOALS

The near-term goals are to be able to generate a sufficient number of image pairs over a wide dynamic signature range based on high-quality field measurement data. Investigation of other candidate validation metrics [19] will need to be analyzed.

The long-term goal is to compare various target acquisition models in terms of their capability to predict second-order effects, again over a wide dynamic signature range. The prediction results from these various models can be compared to the baseline (human observers), and the differences can be analyzed using validation metrics identified to date from this work.

A vision to allow optimization of resources in this particular research area is to apply this methodology for dual technology application (military and nonmilitary). The methodology being developed for validation will lend itself well for the analysis to allow improvement of target acquisition modeling. One pristine area for target acquisition enhancements for the military, as well as for law enforcement, is in the littoral environment [12, 13, 15]. A coalition force is being attempted between DoD agencies that could be extended to NATO working groups that are interested in this particular area of R&D.

5. ACKNOWLEDGMENT

This effort was made possible by the members of the ARL Synthetic Imagery Branch [Khang Bui, Janice Colby, Glenn Dockery, Giap Huynh, Teresa Kipp (Branch Chief), Hung Nguyen, Joseph Penn, and Paul Zirkle], who provided the real-synthetic image pairs presented in this paper, and who provided many hours of consultation and technical support. Further technical support was provided by Matthew Thielke of the ARL Automatic Target Recognition Branch. Jim McManamey and Eddie Jacobs, members of the Night Vision Electro-Optics Laboratory Camouflage Modeling Branch, Fort Belvoir, Virginia, ran our images through the CAMAELEON software package. This includes the images presented in this paper and many, many others.

[20] Gary Witus, and Thomas Meitzler, *TARDEC Visual Perception Model, Calibration and Validation*, Seventh Annual Ground Target Modeling and Validation Conference, August 20-22, 1996, Warren, Michigan

[21] Andrew Zembower and Marcos C. Sola, *Signature Quality Metrics*, Eleventh Annual Ground Vehicle Symposium, KRC, 22 August 1989.

7.0 Biographical Sketches of the Authors

Mr. Marcos C. Sola is the technical leader of the Modeling Validation Group in the Synthetic Image Branch of the U.S. Army Research Laboratory in Adelphi, Maryland. His research interests include synthetic signal validation, mathematical modeling of target signatures, modeling of atmospheric effects on multispectral electromagnetic wave propagation, and systems performance analysis. In addition to his current position, Mr. Sola's career has included work as Technology Associate for Signatures for the Sensors, Signatures, and Signal Processing Office, Project Leader for the Survivability and Management Office, the CM/CCM Office, and the Night Vision and Electro-optics Laboratory in Fort Belvoir Virginia. Mr. Sola holds B.S. and M.A. degrees in Physics from American University, has received numerous U.S. Army Achievement Awards, and publishes extensively.

Dr. Mark Walter Orletsky was born in Johnstown, Pennsylvania on September 25, 1960. He received a Bachelor of Science degree in Electrical Engineering from the Pennsylvania State University in 1982, a Master of Science degree in Electrical Engineering and Computer Science from the Johns Hopkins University in 1984, and the degree of Doctor of Philosophy in Computer Science from the Johns Hopkins University in 1996. Dr. Orletsky's research interests include Computational Geometry, Computer Graphics, Fault-tolerant Computing, and Computer Vision. He currently holds a position with the U.S. Army Research Laboratory in Adelphi, Maryland where his efforts are focused toward multispectral synthetic scene production and validation.

Mr. Quochien B. Vuong received B.S. and M.S. degrees in electrical engineering from George Masson University in 1988 and 1993, respectively. He was a research engineer at the U.S. Army, CECOM, Center for Night Vision and Electro-optics, Fort Belvoir, Virginia from 1990 through 1992. During this period Mr. Vuong worked primarily in the area of optical signal processing and had received two U.S. Army Achievement Awards. In 1992, Mr. Vuong joined the U.S. Army Research Laboratory in Fort Belvoir, Virginia. He is currently a research engineer at the U.S. Army Research Laboratory in Adelphi, Maryland, where his present research interests include digital image processing, and the production and validation of synthetic imagery.

Mr. Charles R. Kohler was born in New York City and received a Master of Science degree from Cornell University, Ithaca, New York in Engineering Physics and Mathematics. He was commissioned a 2ND Lieutenant, ROTC, Infantry, in the US Army and spent about 3 years on active duty in Germany. He is "Airborne" and "Special Forces" Qualified, a Vietnam Era Veteran, and currently a member of the US Army Ready Reserves. He has over 38 years of federal service and was recently selected by the Department of the Army to be a Judge at the International Science and Engineering Fair. He has a keen interest in simulating science and engineering, education, among American youth. He has been an outstanding volunteer judge at many science fairs in the past. His current interest is modeling, simulation, and synthetic imagery.

6. REFERENCES

[1] E. L. Ayers, J. F. Nicoll, *Comparison Between IRTOOL-Simulated Ocean-Sky Scenes and IRAMMP Data for Target Detection*, IDA Task # A-180, ARPA/STO.

[2] T. J. Doll, S. W. McWhorter, D. E. Schmieder, *Computational Model of Human Visual Search and detection.* Proceedings of the March 1994, IRIS Passive Sensors Symposium, Albuquerque, New Mexico.

[3] T. J. Doll, S. W. McWhorter, D. E. Schmieder, A. A. Wasilewski, and G. Welch, *Georgia Tech Vision (GTV) Model*, Version GTV94a, Analyst's Manual, Georgia Tech Research Institute., Atlanta, Georgia.

[4] R. Hecker, *CAMAELEON - Camouflage Assessment by Evaluation of Local Energy, Spatial Frequency, and Orientation*, Proceedings of the Third Annual Ground Target Modeling and Validation Conference, Anne Marie L. LaHaie, Ed, U.S. Army TACOM, Warren MI (1993).

[5] R. Hecker, "CAMAELEON - Camouflage Assessment by Evaluation of Local Energy, Spatial Frequency, and Orientation", *Characterization, Propigation, and Simulation of Sources and Backgrounds II*, Dieter Clement and Wendell R. Watkins, Editors, Proceedings of SPIE-1687, Pages 342-349.

[6] Charles Kohler, and Marcos Sola, *CREATION - Multispectral Synthetic Scene Generation*, Seventh Annual Ground Target Modeling and Validation Conference, August 20-22, 1996, Warren, Michigan.

[7] G. H. Kornfeld, *Various FLIR Sensor Effects Applied to Synthetic Thermal Imagery*, Proceedings of SPIE, April 1993.

[8] G. H. Lindquist, G. Witus, T. H. Cook, J. R. Freeling, and Grant Gerhart, *Target Discrimination Using Computational Vision Human Perception Models*, Proceedings of the SPIE Meeting, Arpil 7, 1994.

[9] James R. McManamey, *An Initial Investigation of the CAMAELEON Model*, Proceedings of the Sixth Annual Ground Target Modeling and Validation Conference, August 1995, Houghton, Michigan, Pages 239-248.

[10] Joseph A. Penn, Hung Nguyen, Teresa Kipp, Charles Kohler, Giap Hyunh, and Marcos Sola, *The CREATION Scene Modeling Package Applied to Multispectral Missile Seekers and Sensors,* Proceedings of the 1995 Conference on Multispectral Missile Seekers and Sensors, November 1-2, 1995, Redstone Arsenal, Alabama.

[11] Joseph A. Penn, H. Nguyen, M. Sola, C. Kohler, J. Weber, and S. Hawley, *The CREATION Scene Modeling Package Applied to Theater Air Defense Fire Control Situations*, Proceedings of the 1995 National Fire Control Symposium, Montery, California, July 31 - August 3, 1995.

[12] Marcos C. Sola, *Active/Passive Signature Enhancer*, Patent Application, ARL Docket # 96-34, 26 October 1996.

[13] Marcos C. Sola, *Application of Optical Augmentation Technique for Maritime Search and Rescue Operations*, National Target/Threat Signature Data Systems Conference, Naval Air Warfare Center, Point Mugu, California, 23-25 July 1996.

[14] Marcos C. Sola, and Tadeusz M. Drzewiecki, *A Proposed Technical Methodology to Reduce the Number of Physical Infrared Signature Measurements*, Eleventh Annual Ground Vehicle Symposium, KRC, 22 August 1989.

[15] Marcos C. Sola, Joseph A. Penn, E. Glenn Dockery, Paul Zirkle, Charles R. Kohler, Teresa Kipp, and Janice F. Colby, *A Proposal for an Active/Passive Signature Enhancer (APSE) for IFF*, Accepted for publication in 1997 Joint Service Combat Identification Systems Conference (CISC-97), 15-17 April 1997, Navy Amphibious Base Coronado, San Diego, California.

[16] William Stump, Notes from *M60A1 Tank Diurnal IR Signatures*, 1995 Night Vision and Electro-optics Division (NVESD) Report.

[17] J. Weber and J. A. Penn, *CREATION User's Manual* (draft) Version 1.27, U.S. Army Research Laboratory, Signature Modeling Branch, Fort Belvoir, Virginia, S3ID/SMB, November 1994.

[18] J. Weber and J. Penn, *Creation and Rendering of Realistic Trees*, SIGGRAPH 95 Computer Graphics Conference Proceedings, Annual Conference Series 1995, pp.119-128, ACM SIGGRAPH, August 1995.

[19] James P. Welsh, *Smart Weapons Operability Enhancement (SWOE), Joint Test and Evaluation (JT&E) Program Final Report*, SWOE Report 94-10, August 1994.

Local Refractive Index Structure-function Parameter and its Application to Wave Propagation

Samir Khanna and John C. Wyngaard

Department of Meteorology
The Pennsylvania State University
University Park, PA 16802

Abstract

Large-eddy simulation (LES) can provide the energy-containing, three-dimensional, time-dependent turbulent fields of the atmospheric boundary layer (ABL) that are useful in studying the diffusion of contaminants and effects of atmospheric turbulence on propagation of electro-magnetic, electro-optical, and acoustic waves. We focus on the local structure of the refractive index field and its local structure-function parameter in a convective atmospheric boundary layer. We use the local structure-function parameter in enhancing the instantaneous vertical LES profiles of refractive index fluctuations to account for turbulence fine structure. These enhanced refractive-index fields should be useful in PE calculations of wave propagation through the ABL.

1. Introduction

Large-eddy simulation is a powerful technique that provides three-dimensional, time-dependent, energy-containing fields of the atmospheric-boundary-layer turbulence. Such information has been very useful in analyzing turbulence closures (Moeng and Wyngaard, 1989) and in understanding the instantaneous local structure of the atmospheric boundary layer (Schmidt and Schumann, 1989; Khanna and Brasseur, 1997). However, LES has not been fully explored for studying the effects of atmospheric turbulence on wave propagation, in part because of the insufficient spatial resolution of LES data.

The propagation of electro-magnetic waves, for example, is influenced by local fluctuations in the refractive index n. A statistical measure of these local fluctuations in the inertial subrange of spatial scales is the local refractive index structure-function parameter $\tilde{C}_{N^2}$ introduced by Peltier and Wyngaard (1995). It is defined as

$$\tilde{C}_{N^2} = 1.6\tilde{\epsilon}^{-1/3}\tilde{\chi}_n, \tag{1}$$

where $\tilde{\epsilon}$ is the local volume-averaged dissipation rate of turbulent kinetic energy, and $\tilde{\chi}_n$ is the local volume-averaged destruction rate of refractive-index variance. $\tilde{C}_{N^2}$ is a three-dimensional, time-dependent, fluctuating quantity as opposed to the ensemble-mean structure-function parameter C_{N^2} defined through the ensemeble-mean quantities ϵ and χ_n and traditionally used in wave-propagation studies (Tatarskii, 1971). Further discussion on local volume-averaging and the relevance of $\tilde{C}_{N^2}$ to wave propagation is provided in section 2.

For propagation applications, for example PE calculations (Gilbert et al., 1996), one often needs refractive index fields that are vertically well resolved (on roughly one-meter scales), since the refractive-index gradients are largest at these small length scales. LES typically provides fields that are spatially resolved to $20 - 50$ m. Typical LES profiles, therefore, can lack the fine structure significant for propagation applications. We will use the local refractive index structure-function parameter in adding fine structure to the instantaneous LES profiles.

We present the local structure of $\tilde{C}_{N^2}$ in a convective boundary layer ($-z_i/L \approx 450$) simulated over a 5 km $\times$ 5 km $\times$ 2 km domain using Moeng (1984) LES code. We also show the LES profiles of refractive index fluctuations at arbitrary X-Y locations in the horizontally homogeneous boundary layer and present the enhanced versions of these profiles.

2. Local Structure-function Parameters

In large-eddy simulation as well as remote sensing one simulates or measures locally averaged quantities. For example, in LES the resolvable-scale velocity is defined as

$$u_i^r(\vec{X}) = \int_{-\infty}^{+\infty} u_i(\vec{X} - \vec{Y}) G(\vec{Y})\, d\vec{Y}, \tag{2}$$

where u_i is the velocity, a random variable, and G is a spatial filter function. The simplest filter function is that of local grid-volume averaging:

$$\begin{array}{rcll} G(\vec{X}) & = & 1; & |X| \leq r \\ G(\vec{X}) & = & 0; & |X| > r. \end{array} \tag{3}$$

In typical LES applications, r is of the order of 20-50 m.

In remote sensing the scattered intensity from a small volume in the boundary layer (Tatarskii, 1971) is given by

$$E_s(\vec{k}, \vec{r}, t) \propto \int_V e^{i\vec{k}\cdot\vec{x}} n(\vec{x})\, d\vec{x} \int_V e^{i\vec{k}\cdot\vec{y}} n(\vec{y})\, d\vec{y}, \tag{4}$$

where $\vec{k}$ depends on the frequency of propagating wave and the orientation of the source and the receiver with respect to the scattering volume as shown in figure 1. If the characteristic length scale of the scattering volume is large compared to the propagating wave length, (4) can be approximated as

$$E_s(\vec{k}, \vec{r}, t) \propto \hat{n}_v(\vec{k}, \vec{r}, t)\, \hat{n}_v^*(\vec{k}, \vec{r}, t), \tag{5}$$

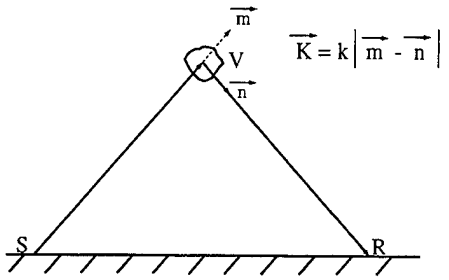


Figure 1 A schematic of scattering geometry. S is the source; R the receiver; V the scattering volume; $\vec{m}$ and $\vec{n}$ the unit vectors; and k the wavenumber.

where $\hat{n}_v$ is the Fourier coefficient of n (Batchelor, 1953). Locally averaged E_s, averaged over different directions of $\vec{k}$ or time smaller than the subgrid-eddy characteristic time scale (Wilson et al., 1996), is then given by

$$E_s(\vec{k},\vec{r},t) \propto \overline{\Phi}_n(\vec{k})|_{\tilde{C}_{N^2}} = \tilde{C}_{N^2}(\vec{r})k^{-11/3}, \tag{6}$$

where $\overline{\Phi}_n(\vec{k})|_{\tilde{C}_{N^2}}$ is the conditionally averaged spectral density function defined by Kolmogorov (1962) and $\tilde{C}_{N^2}$ is the local structure-function parameter as defined by Peltier and Wyngaard (1996). The scattered intensity, is therefore proportional to the local structure-function parameter.

3. Preliminary Results

To study the local structure of $\tilde{C}_{N^2}$ in a convective boundary layer over ocean, we carried out a 128^3 simulation over a 5 km $\times$ 5 km $\times$ 2 km domain with mild geostrophic wind speed (1 m/s) and strong surface temperature and moisture fluxes (0.24 m/s K and 0.08 m/s (g of vapor/kg of air), respectively). The boundary layer depth was roughly 700 m and the Monin-Obukhov length scale L was 1.5 m. Due to the entrainment of dry air aloft, the moisture flux at the capping inversion was nearly same as its surface flux; the temperature flux at the capping inversion was roughly 10 % of its surface value.

Figure 2 shows the isosurfaces of $\tilde{C}_{N^2}$ along a vertical plane covering the entire boundary layer and along a horizontal plane near the ground. The values are particularly large in the interfacial layer, thereby highlighting its instantaneous local structure. The near-ground structure forms a cellular pattern characteristic of Raleigh-Bénard convection.

Figure 3 shows the isosurfaces of the upward vertical velocity fluctuations within the mixed layer and the isocontours of $\tilde{C}_{N^2}$ along a horizontal plane (semi-opaque) within the interfacial layer. The figure indicates that the $\tilde{C}_{N^2}$ values within the interfacial layer are

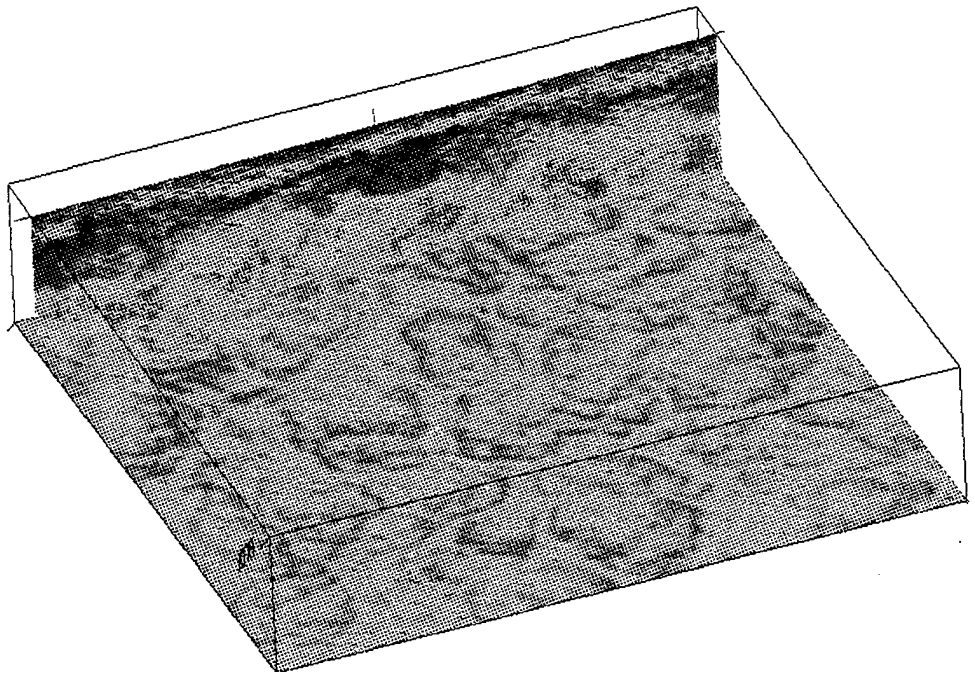


Figure 2 Isocontours of the local refractive index structure-function parameter along a horizontal and a vertical plane in a convective boundary layer. Red represents the most intense region and blue the least intense.

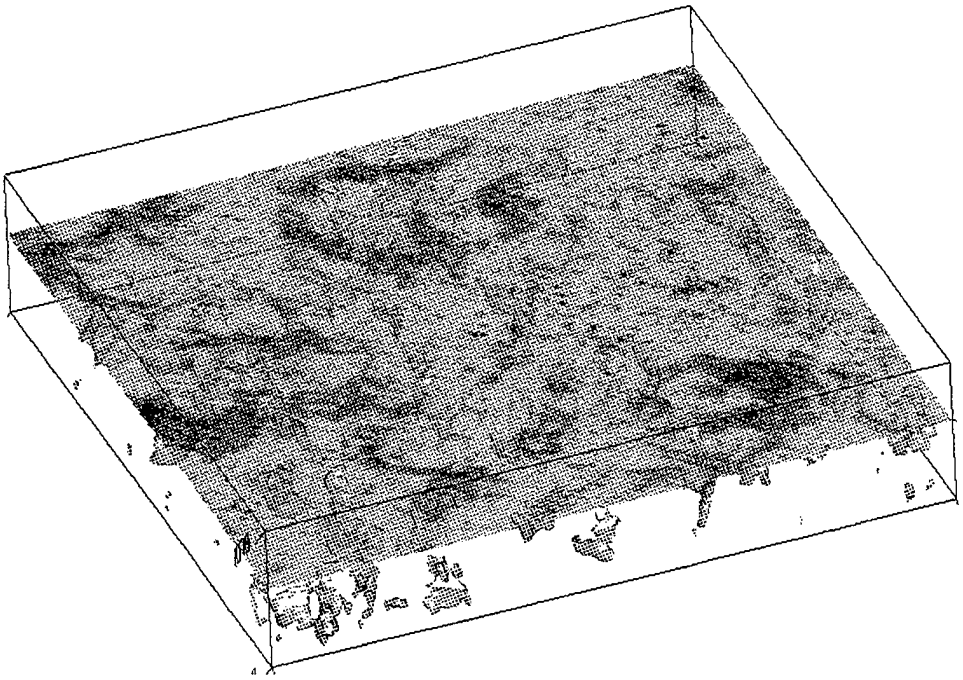


Figure 3 Isosurfaces of the positive vertical velocity (yellow) within the mixed layer and isocontours of the local refractive index structure-function parameter along a horizontal plane (semi-opaque) within the capping inversion. For the isocontours, red represents the most intense region and blue the least intense.

particularly large around the thermals as they penetrate the capping inversion.

We use these local structure-function parameters in adding fine structure to the instantaneous refractive-index profiles from LES in order to make them useful in applications to signal propagation. In our technique, we assume that the turbulence scales smaller than the LES grid size are locally isotropic and hence exhibit the classical inertial subrange $\kappa^{-5/3}$ scaling. To account for intermittency effects, as suggested by Kolmogorov (1962), we use the local structure-function parameters to set the inertial-range amplitude. We add Gaussian variability within these ensemble-mean arguments to account for local fluctuations. A manuscript discussing our technique for enhancing fine structure is under preparation.

Figure 4 shows the instantaneous vertical profiles of refractive index as obtained directly from LES and after we enhanced the fine structure. The figure shows the fine-scale enhancement depends on the large-scale features predicted by LES; this is a consequence of using the local structure-function parameter to determine the amplitude of the added fine structure. We believe the enhanced refractive-index profiles from LES can form a powerful data base for studying the effects of turbulence on EM and acoustic wave propagation.

4. Summary

We focus on the potential of large-eddy simulation for providing instntaneous three-dimensional data sets for analyzing the affects of atmospheric turbulence on EM, EO, or acoustic wave propagation. We discuss the relevance of local structure function parameters to propagation applications, and analyze their instantaneous local behavior in some detail. We show an application of the local structure-function parameters in enhancing the instantaneous LES profiles to account for turbulence fine structure. Further studies using the enhanced profiles are currently underway.

Acknowledgments

We are grateful to D. K. Wilson, K. E. Gilbert, T. Rogers, and C. Tong for helpful discussions. This work is supported by ARO (# DAAL03-92-G-0117) and ONR (# N00014-92-J-1688), we are grateful to them. We thank W. D. Bach, Jr., our program monitor, for his support and constant encouragement.

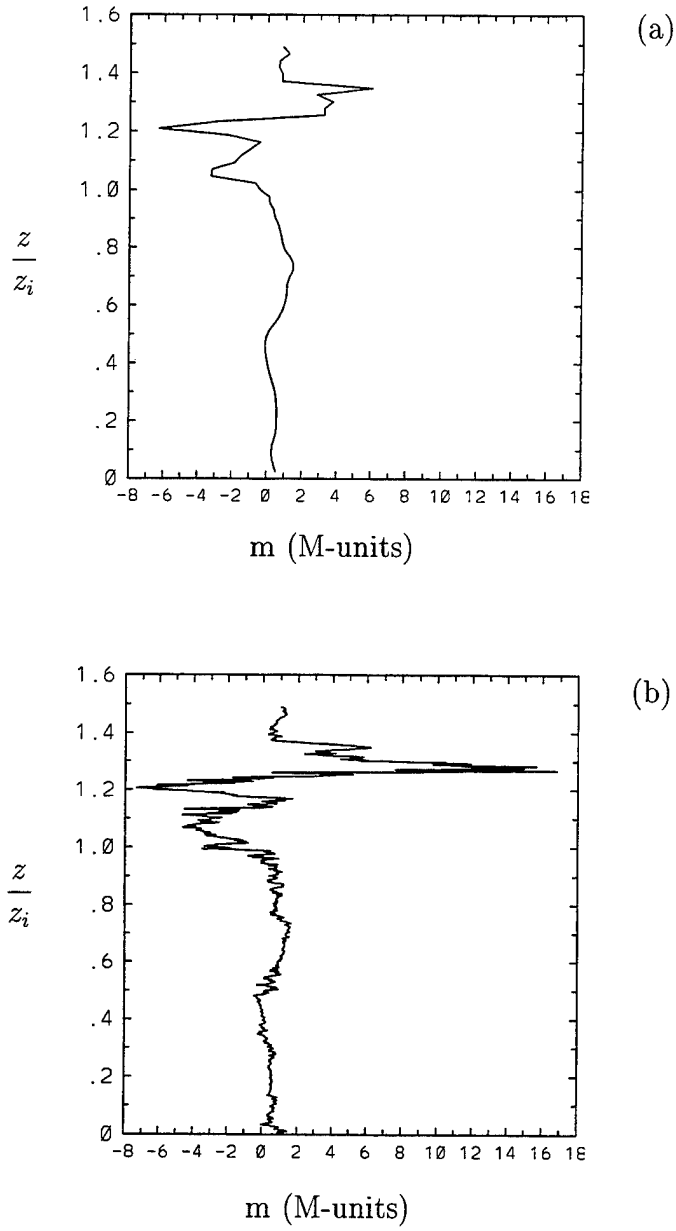


Figure 4 Instantaneous profiles of the modified refractivity fluctuations, $(n-1) \times 10^6$, in a convective boundary layer: (a) resolvable profile from LES, and (b) enhanced profile including subgrid-scale contribution.

References

Batchelor G. K., 1953: The theory of homogeneous turbulence. Cambridge University Press, Cambridge, U.K.

Gilbert K. E., Di X., and Korte R. R., 1996: Distorted-wave born approximation analysis of sound levels in a refractive shadow zone. In the *Proceedings of the 7th Long Range Sound Propagation Symposium*, Ecole Centrale de Lyon, France.

Khanna S. and Brasseur J. G., 1997: Three-dimensional buoyancy- and shear-induced local structure of the atmospheric boundary layer. Submitted to *J. Atmos. Sci.*

Kolmogorov A. N., 1962: A refinement of previous hypotheses concerning the local structure of turbulence in a viscous incompressible fluid at high Reynolds number. *J. Fluid Mech.*, **13**, 82–85.

Moeng C.-H., 1984: A large-eddy simulation model for the study of planetary boundary-layer turbulence. *J. Atmos. Sci.*, **41**, 2052–2062.

Moeng C.-H. and Wyngaard J. C., 1989: Evaluation of turbulent transport and dissipation closures in second-order modeling. *J. Atmos. Sci.*, **46**, 2311–2330.

Peltier L. J. and Wyngaard J. C., 1995: Structure-function parameters in the convective boundary layer from large-eddy simulation. *J. Atmos. Sci.*, **52**, 3641–3659.

Schmidt H. and Schumann U., 1989: Coherent structure of the convective boundary layer derived from large-eddy simulations. *J. Fluid Mech.*, **200**, 511–562.

Wilson D. K., Wyngaard J. C. and Havelock D. I., 1996: The effect of turbulent intermittency on scattering into an acoustic shadow zone. *J. Accoust. Soc. Am.*, **99**, 3393–3400.

Tatarskii V. I., 1971: The effects of the turbulent atmosphere on wave propagation. Keter, Jerusalem.

A Mesoscale Model for EM Ducting in the Marine Boundary Layer

Martin J. Otte*, Nelson L. Seaman, David R. Stauffer, and John C. Wyngaard

The Pennsylvania State University
University Park, Pennsylvania

1. INTRODUCTION

Meteorological processes within the marine boundary layer (MBL) play an important role in determining EM propagation conditions. The profiles of temperature and humidity in the atmosphere determine the refractivity conditions. Often, these profiles can lead to anomalous propagation mechanisms within the MBL. Examples of these nonstandard propagation mechanisms include evaporation ducts where the specific humidity of water vapor decreases rapidly just above the sea surface, and elevated trapping layers caused by the simultaneous rapid increase in temperature and decrease in water vapor within the inversion which typically caps the MBL.

Advances in numerical weather prediction methods, coupled with increased computing power, are now allowing for improved forecasts of refractivity conditions on the mesoscale. Mesoscale weather prediction models can provide three-dimensional, time-dependent forecasts of refractivity on horizontal scales of about 10 km over a total area of over 50,000 km^2. Burk and Thompson (1995) demonstrate the validity of mesoscale model forecasts of refractivity using the Navy Operational Regional Atmospheric Prediction System (NORAPS). They found that the mesoscale forecasts performed well in describing the general refractivity conditions observed during the Variability of Coastal Atmospheric Refractivity (VOCAR) experiment which was conducted off the coast of California between Pt. Conception and San Diego.

However, Burk and Thompson note that the model did not behave as well in predicting trapping layers and ducting events. There are three basic shortcomings of mesoscale models which we have identified that need to be addressed for them to be useful for propagation assessment:

1) Proper model initialization. Mesoscale models typically use a combination of global forecast model fields and observed conditions for initialization. Unfortunately, the MBL is often not represented well in coarse global models, and there is a tremendous lack of meteorological observations over the ocean. The proper temperature and moisture fields, which determine the propagation environment, generally will be absent in mesoscale initial conditions over the ocean. Leidner and Stauffer (1996) correct for this deficiency by using climatological data within the assimilation cycle of a mesoscale model with sufficient resolution to represent the MBL.

2) Improved model physics. Mesoscale models contain "submodels" which represent meteorological processes that the host mesoscale model cannot explicitly resolve. Examples of these processes include solar and longwave radiative fluxes, the influence of subgrid clouds, and marine boundary layer turbulence. For modelling the propagation environment, it is important that the MBL parameterizations within the mesoscale model provide realistic MBL structure. We are augmenting the MBL scheme within the mesoscale model to provide realistic profiles of temperature and humidity, including

* *Corresponding author address*: Martin J. Otte, 503 Walker Bldg., Department of Meteorology, University Park, PA 16801-5013. *Email*: otte@essc.psu.edu

the trapping layer height and structure.

3) Inclusion of turbulent structure. There are many meteorological processes that occur on scales smaller than the grid spacing of the mesoscale model. Khanna *et al.* (1997) show with a fine-scale numerical model the turbulent motions which exist in the atmosphere and are not represented by the mesoscale fields. It is known that these turbulent motions can have important influences on the refractivity field, and produce scattering of the EM waves. Gilbert *et al.* (1990) demonstrate the importance of the scattering contribution to propagating sound waves in the atmosphere. These subgrid effects must be considered for mesoscale refractivity forecasts to be complete.

The Penn State University/National Center for Atmospheric Research (PSU/NCAR) mesoscale model MM5 (Grell *et al.*) is being used to determine the validity of using mesoscale models to forecast the propagation environment. The model is being augmented to correct for the deficiencies noted above. A description of the necessary improvements to the mesoscale model follows.

2. Marine Boundary Layer Initialization

The MM5 mesoscale model is initialized using Four-Dimensional Data Assimilation (FDDA). With FDDA, analysis or individual observations are assimilated into the model fields during a preforecast assimilation period (Stauffer and Seaman, 1994). Observation nudging is typically used in data-sparse regions to assimilate data into the model. With these techniques, the model fields are nudged toward the observed values during the initialization period using a Newtonian nudging term in the governing equations.

With few data available to define the MBL in the initial conditions, this technique does not produce a realistic initial MBL. Leidner and Stauffer hypothesized that including climatological information in the assimilation cycle would produce improved MBL structure over ocean locations. Even though the climatological conditions would not be expected to describe the meteorology at a particular day, they provide statistically significant input which, when combined with the model equations, produces a better initial state. The climatology of Neiburger *et al.* (1961) is used to characterize the northeast Pacific Ocean during summer.

Fig. 1 shows a cross section of potential temperature and cloud water fields near Pt. Conception at the end of the initialization cycle. In Fig. 1a, no climatological information was assimilated, while Fig. 1b includes the climatological assimilation. The climatological information allows for a much stronger inversion, which slopes upward towards the west. Leidner and Stauffer also note that the cloud field produced in Fig. 1b agrees better with observations than Fig. 1a. The stronger, sloping inversion in Fig. 1b also agrees better with observations, and would conceivably yield an improved refractivity environment. Fig. 2 shows the results after a 24 hr forecast using the results of the assimilation cycle shown in Fig. 1. The important point to note is that the model is able to retain the strong, sloping inversion through the forecast period, while this structure has not yet formed in the experiment without the climatological nudging.

3. Model Parameterizations

With improved model initialization, the next step is to improve the model physical parameterizations to ensure realistic profiles within the marine boundary layer. The three distinct regions of the MBL to be parameterized are the surface layer, the mixed layer, and the inversion layer. Each of these regions is shown in Fig. 3, along with a schematic of the mean profiles of potential temperature Θ, specific humidity q, and modified refractivity M typically found within the marine boundary layer. These regions typically produce an elevated trapping layer and surface-based duct within the MBL.

The surface layer occupies approximately the lowest 10% of the MBL adjacent to the sea surface. It is the region of the MBL which is the most studied. An evaporation duct often exists within the marine surface layer due to the rapid decrease of humidity with height just above the sea surface. The mean temperature and humid-

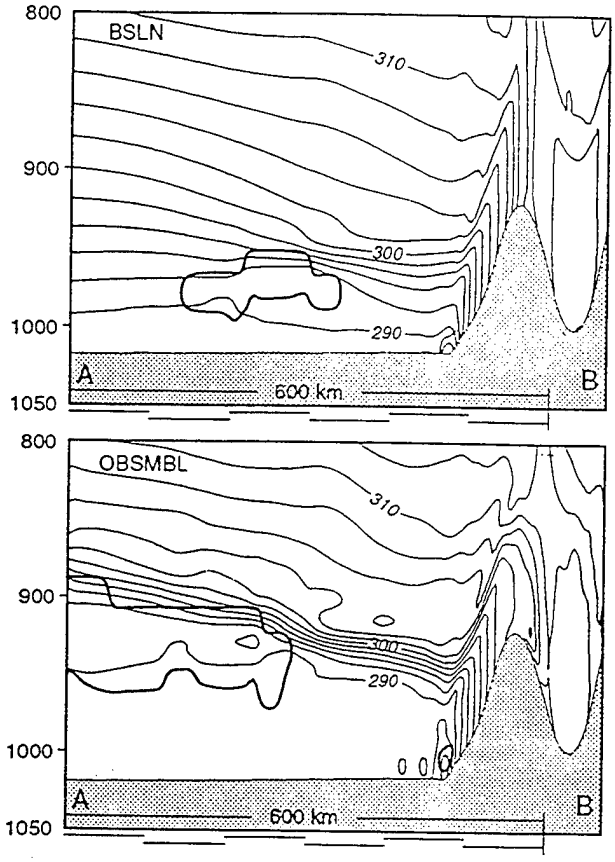


FIG. 1. Simulated cross sections of potential temperature (thin, every 2K) and cloud boundary at t=0 (0000 UTC 4 August 1990) for (a) no climatological assimilation and (b) with climatological assimilation. After Leidner and Stauffer (1996).

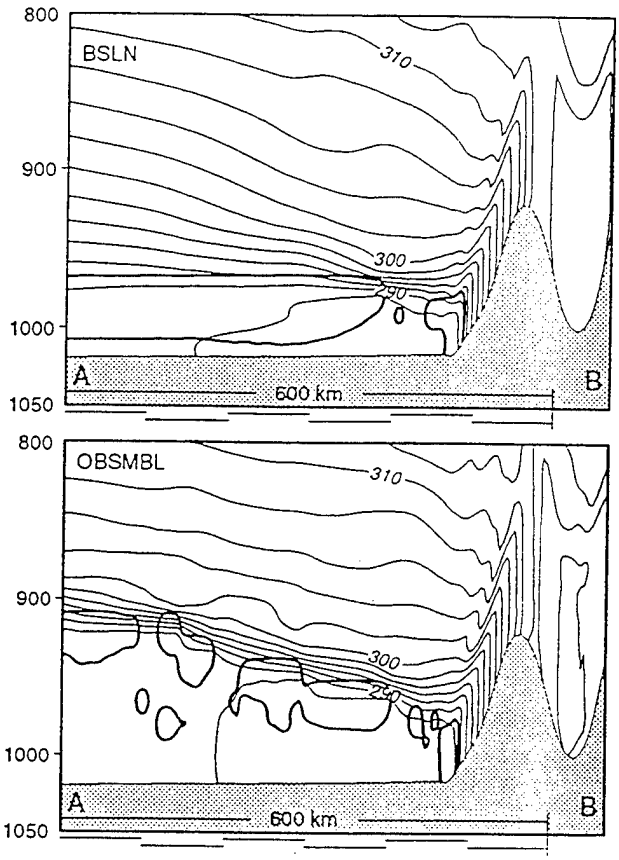


FIG. 2. Same as Fig.1, but at t=24 h.

ity profiles within the surface layer can be modelled using Monin-Obukhov similarity as:

$$\Theta(z) = \Theta_s - \frac{\Theta_*}{k}\left(\ln\frac{z}{z_0} - \Psi_h\right) \qquad (1)$$

$$q(z) = q_s - \frac{q*}{k}\left(\ln\frac{z}{z_0} - \Psi_h\right) \qquad (2)$$

where Θ is the potential temperature and q the specific humidity of water vapor at height z, k is Von Karman's constant, z_0 is the surface roughness length, Θ_* and q_* are scales for temperature and humidity, respectively, and Ψ_h is a stability-dependent correction to the neutral profile. Rogers and Paulus (1997a) give a good summary on how models based on Monin-Obukhov similarity are used to provide the re-

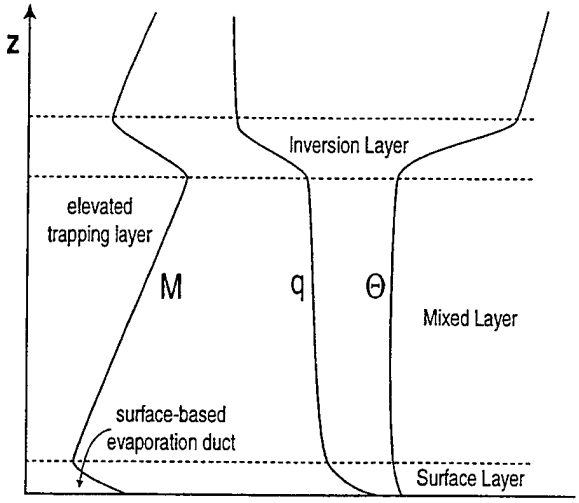


FIG. 3. An idealized schematic showing the three regions of the MBL along with typical mean profiles of potential temperature Θ, humidity q, and resulting modified refractivity M.

fractive conditions within the surface layer and predict evaporation ducts.

The mixed layer extends from just above the surface layer up to the inversion which caps the MBL. The mean profiles of potential temperature and humidity are often nearly well-mixed in this region due to the large turbulent eddies which exist within the mixed layer. The turbulent eddies get their energy from the mean shear, surface buoyancy forcing, and radiative cooling produced at the top of the stratocumulus clouds which often cap the MBL. We are currently looking at observations and fine-scale numerical modeling datasets to formulate a model of the marine mixed layer which will provide realistic mean temperature and humidity profiles.

Within the inversion region which caps the MBL, the potential temperature increases and the specific humidity decreases rapidly with height, often leading to elevated trapping layers and surface-based ducts. The important considerations for modeling this region include the height of this trapping layer, and the vertical gradients which exist there. Ignoring advection, the trapping layer depth h is determined from:

$$\frac{\partial h}{\partial t} = w - w_e \tag{3}$$

where w is the large-scale vertical velocity produced by the mesoscale model, and w_e is the rate that the MBL turbulence is entraining air from above; w_e must be parameterized. Often, a fine balance exists between these two values, resulting in discrepancies in trapping layer depth between models. Again, we are looking at datasets from large-eddy simulation (LES) to parameterize the entrainment rate which determines the trapping layer depth and the mean gradients which exist there.

4. Subgrid Information

Even if the mesoscale model could produce perfect forecasts of the mean refractive conditions, there would still be problems in using the mesoscale profiles due to the subgrid meteorological effects which are not represented by the mesoscale model. Turbulence which is subgrid to the mesoscale model induces random perturbations on the large-scale refractive profiles produced by the mesoscale model. Fig. 4 shows the local refractive index structure function parameter $\tilde{C}_{N^2}$ obtained through LES by Khanna *et al.* (1997). Peltier and Wyngaard (1995) discuss the importance of this parameter to the scattering of transmitted waves by turbulence. This field represents a snap-shot of the squared intensity of refractivity n at inertial-range scales of motion.

It is clear from Fig. 4 that there is a large turbulent influence on the refractivity field near the inversion region at the top of the MBL. This is due to the undulations in the inversion caused by the MBL turbulence. These undulations in the inversion result in additional anamolous propagation and scattering of EM waves. Data from vertically pointing acoustic sounders also clearly show the strong turbulent scattering of waves due to the large perturbations in the refractivity field at the inversion.

Khanna *et al.* discuss large-eddy simulation and how it can help describe the propagation characteristics within the MBL. However, LES is not an operational tool to predict the propagation environment. With the large computing time needed to run LES, it is only used as a research tool to help us understand the structure of the MBL. LES is being used to develop datasets that will allow us to augment the fields produced by the mesoscale model to include the effects of turbulence on the refractivity environment.

5. Conclusions

Advances in mesoscale meteorological modeling and increased computing power are allowing for forecasts of refractive conditions within the MBL. However, there still are some improvements needed in mesoscale models for them to be applicable for propagation assessment. We identified problems with mesoscale model initialization, MBL physical parameterizations, and the influence of subgrid turbulence. We have begun to look at these problems, but they will only be solved by interaction between the mesoscale modeling, atmospheric turbulence, and EM propagation communities.

The data assimilation results show how using alternate forms of data over observation-sparse areas can result in improved initial conditions and model forecasts. Other forms of data which may be useful over ocean locations include propagation measurements (Rogers and Paulus, 1997b). Even with the inherent ambiguities in inverting propagation measurements to determine the atmospheric state, this data may still give statistically significant information which, when combined with the mesoscale model equations, produces better initial conditions and forecasts.

Acknowledgements. This work is supported by Navy contract No. N00039-92-C-0100, Task No. 07A-2015.

6. References

Burk, S. D., and W. T. Thompson, 1995: Mesoscale modeling of refractive conditions in a complex coastal environment. *Propagation Assessment in Coastal Environments*, AGARD Conf. Proc. 567, 40-1–40-6.

Gilbert, K. E., R. Raspert, and X. Di, 1990: Calculation of turbulence effects in an upward-refracting atmosphere. *J. Acoust. Soc. Am.*, **87**, 2428–2437.

Grell, G. A., J. Dudhia, and D. R. Stauffer, 1994: *A Description of the Fifth-Generation Penn State/NCAR Mesoscale Model (MM5).* NCAR Technical Note 398+STR, National Center for Atmospheric Research, Boulder, CO, 138 pp.

Khanna, S. and J. C. Wyngaard, 1997: Local refractive index structure-function parameter and its application to wave propagation. This volume.

Leidner, S. M., and D. R. Stauffer, 1996: Improving California coastal-zone forecasting by initialization of the marine boundary layer. *Preprints, 11th Conference on Numerical Weather Prediction*, 177–179.

Neiburger, M. D., D. Johnson, and C. Chien, 1961: *Studies of the Structure of the Atmosphere Over the Eastern Pacific Ocean in Summer: I Inversion Over the Eastern North Pacific Ocean*, Univ. Calif. Publ. Meteor., **1**, No. 1, 94 pp.

Peltier, L. J. and J. C. Wyngaard, 1995: Structure-function parameters in the convective boundary layer from large-eddy simulation. *J. Atmos. Sci.*, **52**, 3641–3660.

Rogers, L. T., and R. A. Paulus, 1997a: Measured performance of evaporation duct models. This volume.

Rogers, L. T., and R. A. Paulus, 1997b: Fusing data from the mesoscale model and radio remote sensing. This volume.

Stauffer, D. R. and N. L. Seaman, 1994: Multiscale four-dimensional data assimilation. *J. Appl. Meteo.*, **33**, *416–434.*

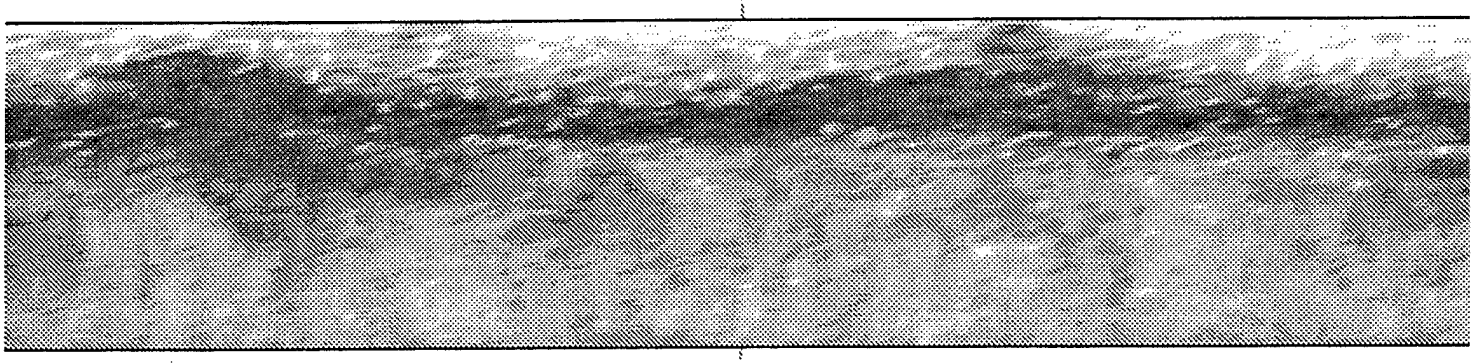


FIG. 4. A cross section of a large-eddy simulation of the MBL showing the local refractive index structure function parameter $\tilde{C}_{N^2}$. Dark regions denote high $\tilde{C}_{N^2}$ indicating large turbulent perturbations in the refractivity field at inertial-range scales. The model shows the largest $\tilde{C}_{N^2}$ near the top of the MBL at the inversion, which is caused by turbulent undulations in the inversion. The model domain is about 1 km in the vertical and 2 km in the horizontal

The Fractal Behavior of Cloud Systems

Kenneth E. Eis, John Forsythe, Donald Reinke
Cooperative Institute for Research in the Atmosphere
Foothills Campus, Colorado State University
Fort Collins, CO 80523
Phone: (970) 491-8397, fax (-8241)
E-MAIL: eis@cira.colostate.edu

Abstract

The DOD and other agencies interested in cloud simulations have used fractal-based synthetic cloud generators since Lovejoy (1982) showed the fractal behavior of clouds. Fractal generators are attractive because they allow simulations managers to control the synthetic cloud's statistical moments. One of the most appealing features of fractal methods is that simulated scenes can be produced at a variety of scales with just one number, the fractal dimension. This paper analyzes the temporal and spatial behavior of the fractal dimension of cloud fields of scale sizes from 1280 km to 10 km. The variations in the fractal dimension over time and space will be shown to be significant and must be considered by the simulations community.

Introduction

Fractal scene generators create realistic looking clouds as the environmental backdrop for DOD weapons and exercise simulators. Realism, as an esthetic parameter judged by the human eye, may not be sufficient to produce simulated results whose output must reproduce results that mimic real-world scenarios. If the simulations scenarios are based on specific locations and times in the real-world, then the synthetic clouds should exhibit the same mean cloud coverage, structure, and gradients as the cloud climatologies. This paper represents the first fractal analysis using the CHANCES database (Vonder Haar, 1995). This 5-km, hourly, global database is ideal for generating the fractal dimension for large cloud fields. This study produced fractal dimensions for a massive data set which includes over 80 percent of the Northern Hemisphere for June and July of 1994. Approximately 1600 hourly 5-km cloud scenes of the Northern Hemisphere were used in this analysis.

Methodology and Data

The CHANCES database is described in a companion paper in the Conference Preceedings, Forsythe et al. (1997). Fractal analysis of clouds using this dataset is straightforward because the database is in a constant area molwede projection. The nature of the database, i.e. a 5-km, hourly, global coverage, makes it ideal to probe the fractal nature of large-scale cloud systems. Three specific scenes were analyzed for fractal dimension. These three scenes were created by using the IR images in the CHANCES dataset and thresholding the radiances for temperatures greater than 273, 263 and 253 Kelvin, respectively. Because of the nature of the satellite geometry and retrieval, the 273 degree threshold cloud analysis contains all of the 263 scene and the 263 degree scene contains all of the 253 degree thresholded scene. These three closely spaced temperature threshold analyses were selected to investigate the multifractal or textural nature of the scenes.

We used the Box Counting method of fractal analysis as describe by Walsh and Watterson (1993). Each of the cloud/no cloud scenes generated by the three temperature thresholds were run against the box counting method. We selected an outside domain of 256 x 256 pixels or 1280 x 1280 kilometers. Larger domain sizes were "saturated" in that they provided no useful information since they invariably had at least one pixel filled with cloud.

Via box counting, the filled vs. Total domain size counts of the image were collected as the domain size was halved in both dimensions. A log-log plot was generated and a linear regression fit was applied to the points. The six data points that the linear fit was generated from were limited, like all box counting techniques, by the smallest (5 km) and largest (1080 km) scale sizes allowed by the data. The slope of the linear regression line defined the fractal dimension of the scene in question.

Data Domain

The CHANCES data, including all consecutive hours from June and July of 1994 was analyzed.



Figure 1 - CHANCES domain used in box-counting analysis

We selected most of the Northern Hemisphere from the equator to about 30 degrees north latitude for the region. Adjacent 256 by 256 pixel analysis domain boxes were created across this data domain.

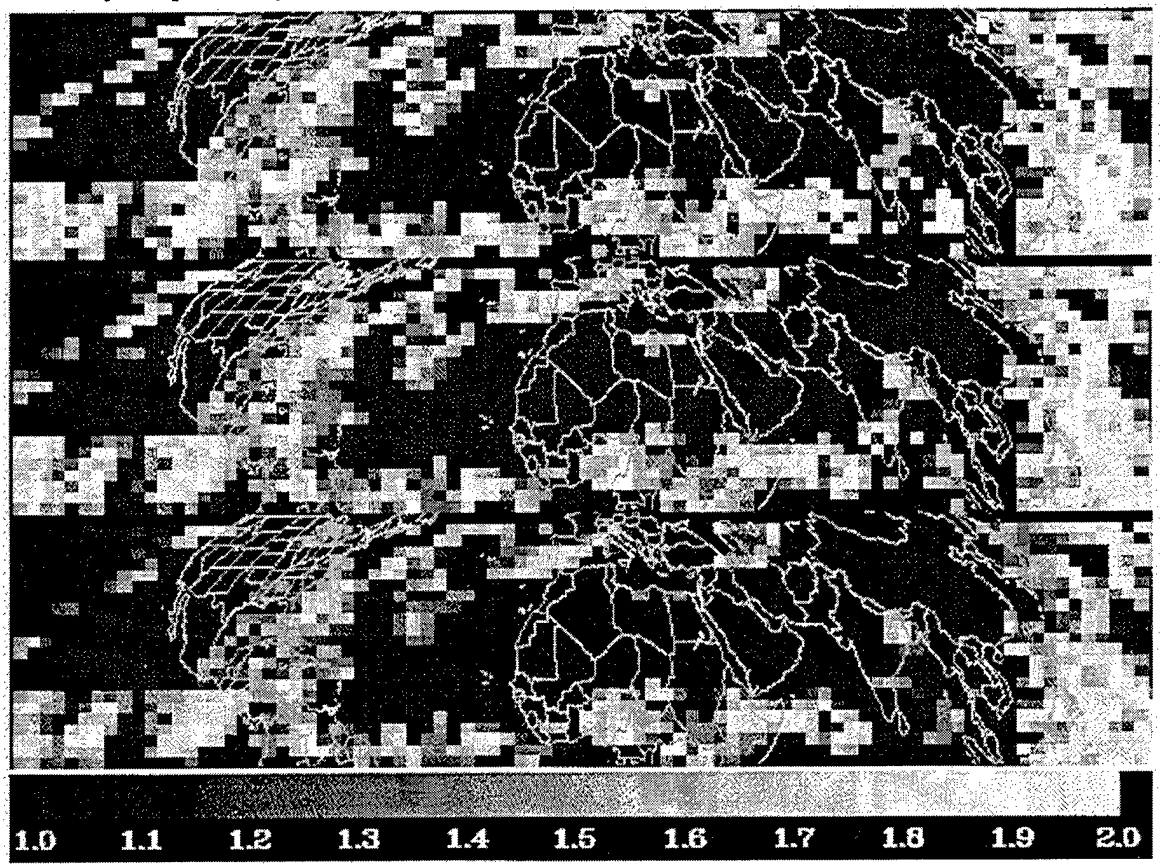


Figure 2 - Grayscale depiction of Fractal Dimension at 273, 263, and 253 Degree Thresholds

Figure 2 shows the fractal dimension of the three temperature thresholds. Note that the blocks in the images are the 256 x 256 pixel domains of the box counting analysis. The gray scale indicates the fractal dimension. These three plates are simultaneous in time and the same time as the IR image in Figure 1. The difference at any pixel location between the three analyses is the multi-fractal texture. Black density depicts a fractal dimension of 1.0 or represents clear areas in the cloud analysis. One of the more interesting findings of this analysis was the strong dependence of the fractal dimension on the cloud cover percentage.

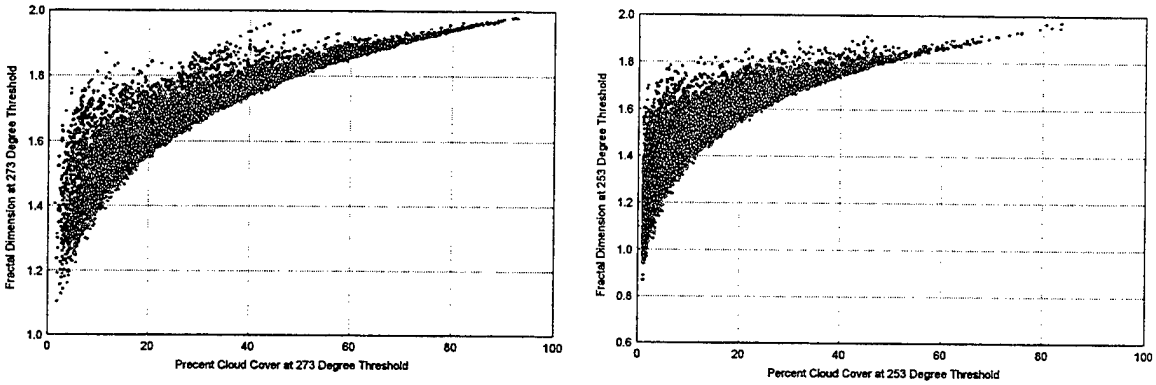


Figure 3 - Fractal Dimension vs Cloud Cover Percentage all Data for 273 and 253 Degree Threshold Analysis

Figure 3 shows the fractal dimension vs. cloud cover for the 273 and the 253 degree threshold analyses. After inspection of the scatter diagrams, the scatter is predicable. At low cloud cover fractions, the satellite is more likely to detect multiple layers of clouds in different turbulence regimes in one scene. Also the degrees of freedom or the possible ways clouds can be structured are more numerous. Both of these possibilities are reflected in the high scatter of the fractal dimension on the low end of the cloud cover axis. On the other hand, as the scene approaches total cloud cover, the likelihood of a cloud shield obscuring lower level clouds increases and the satellite view is more likely to only see one turbulence regime associated with the top and obscuring layer of cloud. Additionally, the fractal dimension of a totally covered scene is always 2.0. Lower numbers are not possible so it stands to reason that high cloud cover fractions must approach 2.0 in fractal dimension and that the scatter must approach zero as the coverage approaches 100 percent.

Temporal Variations in Fractal Dimension and Multi-Fractal Values

Figure 4 shows a 500 hour consecutive time series of fractal dimension variation in a single domain along the central Florida coast starting on 22 June, 1994. Several features are worth comment:

1. As expected, the fractal dimension of the 273 degree threshold is always larger than the 263 degree threshold analysis which in turn is larger than the 253 degree threshold analysis. This is the result of the strong dependence on cloud cover which shares the same relative ranking.
2. There is a strong diurnal signal in the cloud cover and even a stronger signal in the fractal dimension.
3. The textural or multi-fractal signal, which is represented by the divergence in the fractal dimension between the three threshold values is strongly dependent upon cloud cover percentage with the most "texture" associated with the less cloudy periods.
4. The variation in fractal dimension and texture have similar temporal behaviors.

These conclusions are representative of all locations and times in the study domain.

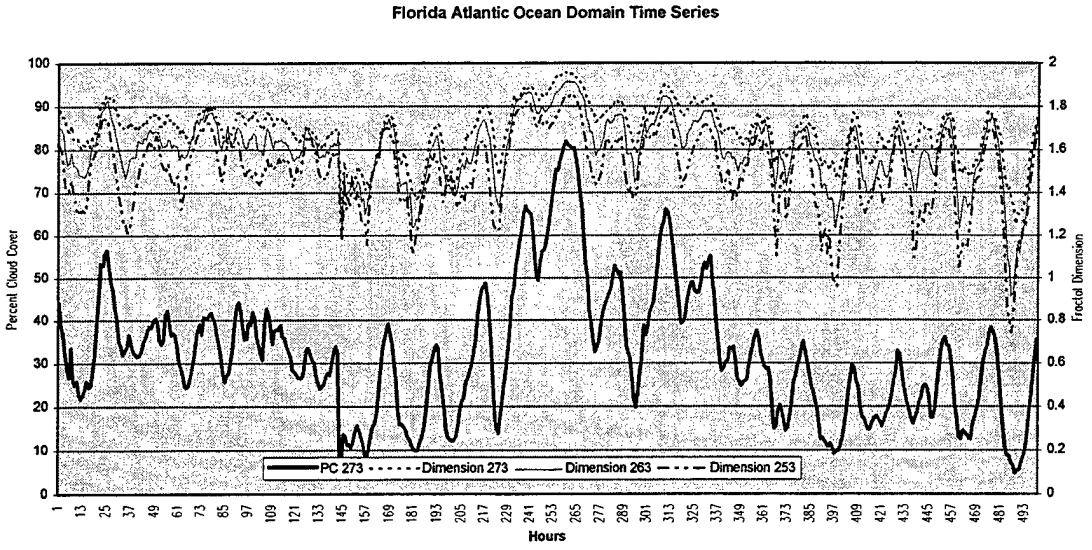


Figure 4 Time series of fractal dimension for central eastern Florida coast

Scale Break Considerations

The six data points generated by the Box Counting, and used to calculate the fractal dimension were also used to determine whether there was a scale break feature in the fractal domain. This was accomplished by filtering the data points for regression fit and assuming the data fit two different lines when the lower R^2 regression fits were observed. The subsequent R^2 for the two line regressions were again filtered to include only regressions of greater than 0.9999. This very high correlation thus assured that the two lines represented real fractal dimension values. The two lines were then solved for their intersection. This intersection represents the scale break in kilometers in the analyzed domain.

Figure 5 shows the histograms of scale break frequencies for the entire data set. The histograms are categorized in two different ways. First in standard 50 km cases and second, in 97 km cases. The 97 km bin was selected because it represents twice the RTNEPH's 47 km resolution. Many DOD researchers use the RTNEPH cloud analysis to generate fractal dimensional values. Often, fractal dimensions are extrapolated to smaller scales so cloud scenes at resolutions well below the resolution of the supporting data, can be generated in tactical and one-on-one simulators. This is acceptable if there is no scale break. As an example, if the Army is interested in a fractally generated cloud scene at the 5-km scale, and used a fractal dimension seed from the RTNEPH database, the artificial cloud would only be representative of real-world clouds if there was no scale break between 5 km and 97 km. If there were a break at these scale lengths, the fractal dimension of the correct cloud scene would be unresolvable by the RTNEPH database. The histograms indicate that there are scale breaks unresolvable by the RTNEPH approximately 50 percent of the time over most of the Northern Hemisphere. Our analysis misses another class of scale breaks entirely, i.e. scale breaks below 10 km where the CHANCES database is unable to resolve the fractal dimension change.

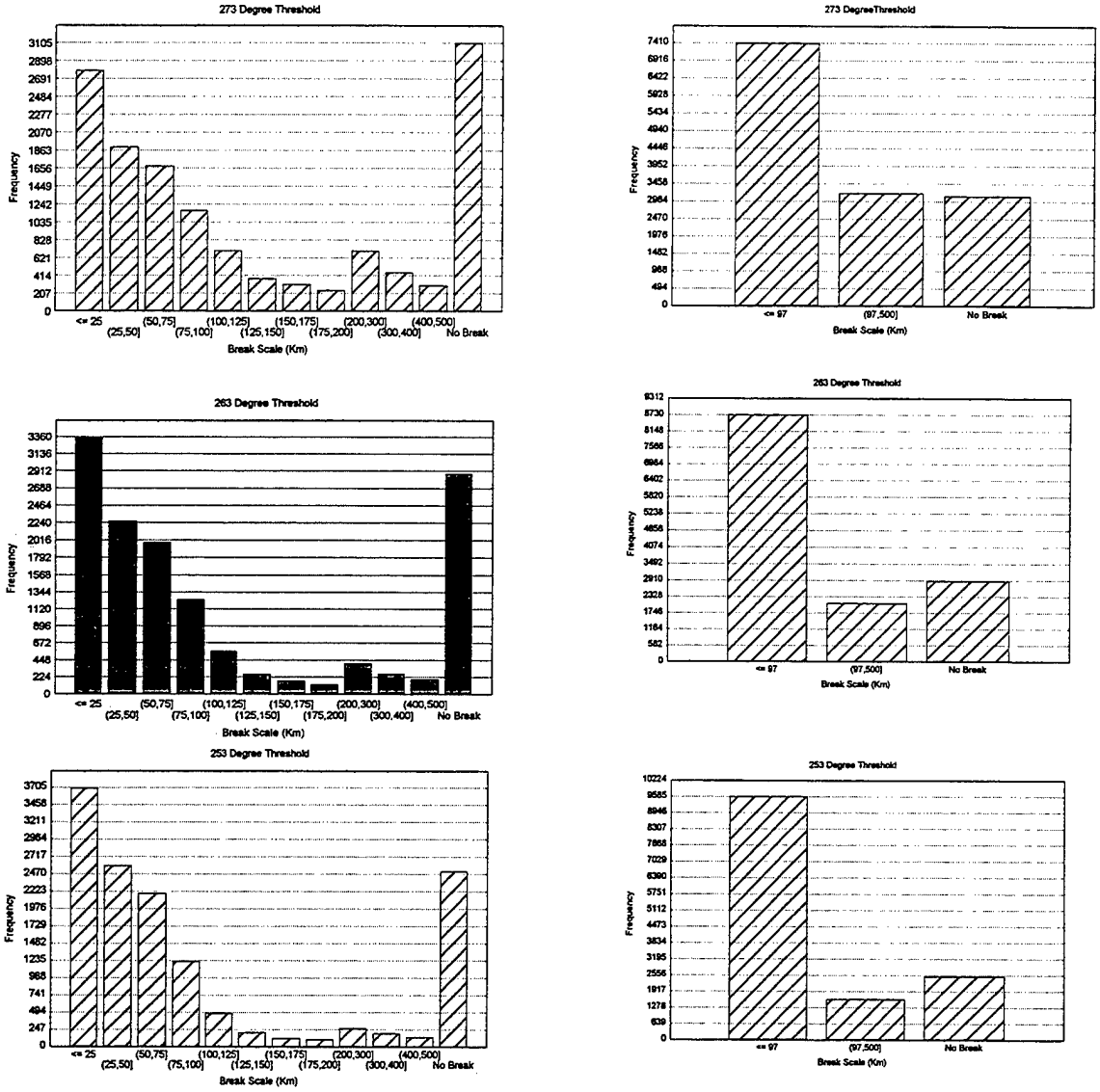


Figure 5 - Scale Break Histograms for July 1994 Northern Hemisphere

The Linear Regression Issue - Are All Cloud Fields Fractal?

The assumption in this paper and the opinion of many researchers is that clouds are fractal. Lovejoy's first paper showed an analysis with the data collected for a large cloud scene with the data falling amazingly close to a linear regression line. The question is how good a fit is required to be fractal. In preliminary studies we used the Box Counting method on simple geometrical objects. Objects such as a square are clearly not fractal because they do not conform to the basic requirement of self similarity at various scale sizes. Box Counting yields an R^2 regression fit of 0.9933 and a fractal dimension of 1.1346 for a square of 3 by 3 in a analysis domain of 8 x 8 pixels. Most researchers in the physical sciences would be quite happy with correlations of better than 0.9. Apparently, very high correlations do not necessarily imply fractal behavior. Figure 6 shows the breakdown of correlation coefficients for all of the Northern Hemisphere summer data. The data in the case bins less than 0.99 and between 0.99 and .995 are suspect in terms of their fractal behavior. Cloud features anchored to terrain or coastal features may not be treatable with fractal methods.

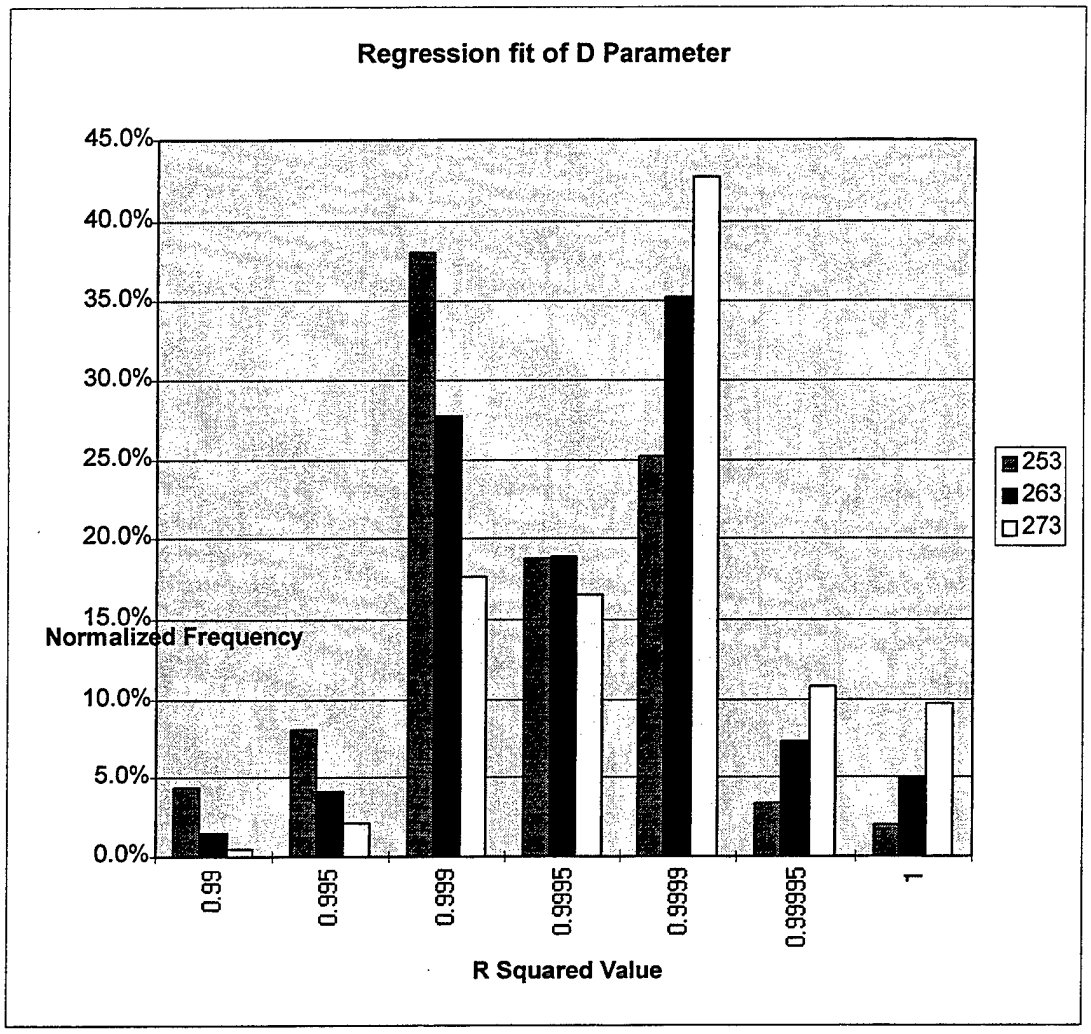


Figure 6 Histograms of Linear Regression Fit for all Analyzed Data

Conclusions

1. Large scale cloud features can in general be treated with fractal techniques.
2. The application of a given fractal dimension, generated at a given place and time must not be used at other locations or times. The temporal and spatial variation in the fractal dimension is too great to assume much representative spread in its use.
3. If fractal cloud scene generators are being used to yield extrapolated scenes with resolutions well below twice the resolution of the original data set, the fractal dimension used to seed the generator has at least a 50-50 chance of being in error. If the intent of the artificial scene is just to show a realistic looking cloud, there is no problem. If on the other hand, the intent is to create a cloud scene that represents the proper statistical moments of the real cloud climatology for a specific location and time, the result is likely to be wrong.

Variables for Northern Hemisphere	Number of Samples	Mean	Std. Deviation
Cloud % 273	13680	30.53	17.99
Cloud % 263	13680	21.68	15.07
Cloud % 253	13680	14.46	12.067
Fractal Dim 273	13680	1.687	.145
Fractal Dim 263	13680	1.61	0.162
Fractal Dim 253	13680	1.506	0.186
Variables for Florida Domain only	**Number of Samples**	**Mean**	**Std. Deviation**
Cloud % 273	961	29.26	14.67
Cloud % 263	961	21.48	12.68
Cloud % 253	961	15.22	10.42
Fractal Dim 273	961	1.654	0.143
Fractal Dim 263	961	1.567	0.174
Fractal Dim 253	961	1.472	0.211

Acknowledgments

The research described in this paper was funded by the Department of Defense under Task 10 of the Center for Geosciences Grant # DAAH04-94-G-0420

The authors would like to thank Dr. Phillip Gabriel for his advice and counsel on fractal issues.

Bibliography

Forsythe, J.M., D.L. Reinke, D.L. Randel, K.E. Eis, and C.L. Combs, 1997: CLVL: A global high-resolution layered-cloud database. Proceedings, 1996 Battlespace Atmospherics Conference, San Diego, CA.

Liebovitch, L.S., Toth, T., 1989: A fast algorithm to determine fractal dimensions by box counting. *Physics Letters A,* 141 (8,9), 386-390.

Lovejoy, S., 1982: Area-perimeter relation for rain and cloud areas. *Science,* 216 (9), 185-187.

Lovejoy, S., D. Schertzer, A.A. Tsonis, 1987: Functional box-counting and multiple elliptical dimensions in rain. *Science,* 235, 1036-1038.

Reinke, D.L., T.H. Vonder Haar, K.E. Eis, J.M. Forsythe, and D.N. Allen, 1993: Climatological and Historical Analysis of Clouds for Environmental Simulations (CHANCES). Proceedings, 1993 Battlefield Atmospherics Conference, U.S. Army Research Lab, White Sands Missle Range, New Mexico, 863-870.

Vonder Haar, T.H., D.L. Reinke, K.E. Eis, J.L. Behunek, C.R. Chaapel, C.L. Combs, J.M. Forsythe, and M.A. Ringerud, 1995: Climatological and Historical Analysis of Clouds for Environmental Simulations (CHANCES) Database. Final Report (USAF Phillips Lab Tech. Rept. PL-TR-95-2101). Science and Technology Corp., Hampton, VA.

Walsh, J.J., and J. Watterson, 1993: Fractal analysis of fracture patterns using the standard box-counting technique: valid and invalid methodologies. *J. Structural Geology,* 15, 1509-1512.

Wang, J., and W.B. Rossow, 1995: Determination of cloud vertical structure from upper-air observations. *J. Appl. Meteor.,* 34, 2243-2258.

Forecasting of fog/cloud and precipitation by the Battlescale Forecast Model (BFM)

Teizi Henmi
US Army Research Laboratory
Information Sciences and Technology Directorate
Battlefield Environment Division
White Sands Missile Range, New Mexico 88002-5501

The Battlescale Forecast Model (BFM), which was developed at the US Army Research Laboratory (ARL), is a major part of the US Army Integrated Meteorological System (IMETS) Block II software. The BFM can be used operationally over any part of the world by using meteorological data obtained through the Automated Weather Distribution System (AWDS).

The BFM is capable of making 24 hour weather forecast which includes wind, temperature, and relative humidity, as well as fog/cloud coverage and precipitation rate/amount. In the model, the cloud liquid water content is calculated by using the probability density function (Sommeria and Deardoff, 1977, Mellor, 1977, and Yamada and Mellor, 1979), and the precipitation rate/amount are calculated by the scheme of Sundqvist et al(1989).

The model has been applied to several precipitation cases over different areas, and produced reasonable forecast results.

I. Introduction

The U.S. Army Research Laboratory, Battlefield Environment Directorate (ARL, BED) has developed the Battlescale Forecast Model (BFM) for operational short-range (up to 24 hours) forecasting over areas of 500 km by 500 km or smaller. The BFM can be used operationally over any part of the world by using meteorological data obtained through the U.S. Air Force Automated Weather Distribution System (AWDS), and is a major part of the U.S. Army Integrated Meteorological System (IMETS) Block II software. Meteorological data includes the U.S. Air Force Global Spectral Model (GSM) gridded forecast data, in addition to conventional upper air sounding and surface data.

The BFM is composed of several elements such as (1) terrain elevation data deduction program, (2) three dimensional data analysis programs for initialization and assimilation, (3) prognostic mesoscale model, HOTMAC (Yamada and Bunker, 1989), (4) horizontal and vertical displays of forecasting results, (5) graphical user interfaces for execution of the BFM and for display of different output, (6) input/output archiving system, and (7) map background module to help execution and display.

The objectives of the present paper are to describe how cloud/fog and precipitation are calculated in the BFM, and to show some examples of fog/cloud and precipitation forecast results.

II. Cloud/Fog formation

In most of the mesoscale models (i.e, Golding, 1990, Pielke et al, 1992, Anthes and Warner, 1978), the critical humidity for cloud formation is saturation over water or ice, which depends on temperature, and all water vapor in excess of water/ice saturation is converted to cloud water/ice.
Furthermore, it is assumed that a computational grid volume is either entirely saturated or entirely unsaturated. Even for a relatively small grid volume such as $(50\ m)^3$, this assumption is sometimes in error because substantial portions of cloud volume may contain unsaturated air near the cloud edge or in the cloud due to mixing and entrainment (Sommeria and Deardorff, 1977).

The present scheme takes into consideration the dependencies of mean cloud fraction and mean liquid (cloud) water content upon humidity statistics, assuming Gaussian quasi-conservative properties. It is assumed that the quasi-conservative variables, liquid water potential temperature (Θ_l) and liquid water mixing ratio (Q_l) have the Gaussian joint normal probability distributions within any given volume. This assumption implies that those air parcels existing within any given volume have had complicated past trajectories and have not selectively been subjected to rapid changes in Θ_l and Q_l.

The Gaussian joint normal distribution function is given by:

$$G=\frac{1}{2\pi\sigma_{\theta l}\sigma_{qw}(1-r^2)^{1/2}}\exp\left[-\frac{1}{(1-r^2)}\left(\frac{\theta_l^2}{2\sigma_{\theta l}^2}-r\frac{\theta_l q_w}{\sigma_{\theta l}\sigma_{qw}}+\frac{q_w^2}{2\sigma_{qw}^2}\right)\right] \tag{1}$$

where θ_l and q_w are the fluctuations of , respectively, liquid water potential temperature and total water mixing ratio, and

$$\sigma_{\theta l}=\overline{\theta_l^2} \tag{2}$$

$$\sigma_{qw}^2=\overline{q_w^2} \tag{3}$$

$$r=\frac{\overline{\theta_l q_w}}{\sigma_{\theta l}\sigma_{qw}} \tag{4}$$

Overbars represent the mean properties of variables. The local condensation is assumed to be

given by

$$Q_l = (Q_w - Q_s)H(Q_w - Q_s) \tag{5}$$

where Q_w is total cloud water content, Q_s is saturation mixing ratio, and H(x) is a Heaviside function, defined as

$$H(x)= 0, \quad x<0 \tag{6}$$

$$1, \quad x>0$$

Let us define the following parameters:

$$a=(1+Q_{sl,T}\frac{L_v}{c_p})^{-1} \tag{7}$$

$$b=a\frac{<T>}{<\theta>}Q_{sl,T} \tag{8}$$

$$\Delta Q = Q_w - Q_{sl} \tag{9}$$

$$Q_{sl,T}=(\frac{\partial Q_s}{\partial T})_{T=T_l}=0.622\frac{L_v}{R_d}\frac{Q_{sl}}{T_l^2} \tag{10}$$

$$Q_{sl} = 0.622e_s(T_l)/(P - e_s(T_l)) \tag{11}$$

$$e_s(T_l)=6.11\exp[\frac{L_v}{R_w}(\frac{1}{273}-\frac{1}{T_l})] \tag{12}$$

and

$$T_l = (P/P_0)^k\Theta_l \tag{13}$$

Here Q_{sl} is the mean saturation mixing ratio of water vapor at T_l: T_l is the liquid water temperature, $e_s(T_l)$ is the saturation water vapor pressure at T_l; R_w is the gas constant for water vapor, and L_v is the latent heat of condensation.

A function R which indicates a fraction of cloud coverage for a given volume of air is given by (Mellor, 1977):

$$R=\int_{-\infty}^{\infty}\int_{-\infty}^{\infty}H(Q_w-Q_s)G\,dQ_w\,d\theta_l=\frac{1}{2}[1+erf(Q_1/\sqrt{2})] \tag{14}$$

$$erf(x)=\frac{2}{\sqrt{\pi}}\int_0^x \exp(-y^2)dy \tag{15}$$

Cloud water mixing ratio Q_l *is given by:*

$$Q_l=2\sigma_s[RQ_1+\frac{1}{\sqrt{2\pi}}\exp(-\frac{Q_1^2}{2})] \tag{16}$$

where

$$Q_1=a\frac{\Delta Q}{2\sigma_s} \tag{17}$$

$$\sigma_s^2=\frac{1}{4}(a^2\overline{q_w^2}-2ab\overline{q_w\theta_l}+b^2\overline{\theta_l^2}) \tag{18}$$

Finally, q_c^2, the variance of the cloud water mixing ratio, is expressed as

$$\frac{\overline{q_c^2}}{4\sigma_s^2}=R[1+(Q_1-2\frac{Q_l}{2\sigma_s})]+(Q_1-\frac{Q_l}{2\sigma_s})\frac{1}{\sqrt{2\pi}}\exp[-\frac{Q_1^2}{2}] \tag{19}$$

Figure 1 shows R, $Q_c/2\sigma_s$, and $q_c^2/4\sigma_s^2$ as a function of Q_1 obtained according to eqns. (14), (16), and (19), respectively.

As seen from Figure 1, a fraction of cloud coverage R varies gradually with Q_1 and takes non-zero values even if Q_1 is negative. In other words, clouds can exist even if the mixing ratio of water vapor averaged over a grid volume is not saturated. This is realistic because the grid spacing normally used in mesoscale models is larger than the size of small clouds. Therefore, the present cloud model can use a relatively large grid spacing that could save computational time substantially. A statistical cloud model such as the present one avoids the ambiguous condensation criteria often used by coarse grid models; saturation values are lowered arbitrarily to compensate for the amount of cloud that is not resolved by grid.

In the BFM, the total cloud water content, W_{total}, from the ground surface to the top of model atmosphere is calculated and the horizontal distribution of W_{total} is displayed. W_{total} is calculated as:

$$W_{total}=\int_{z_g}^{H}\rho Q_c dz=\frac{\overline{H}+z_{gmax}-z_g}{\overline{H}}\int_0^{\overline{H}}\rho Q_c dz. \qquad (20)$$

where ρ is the air density.

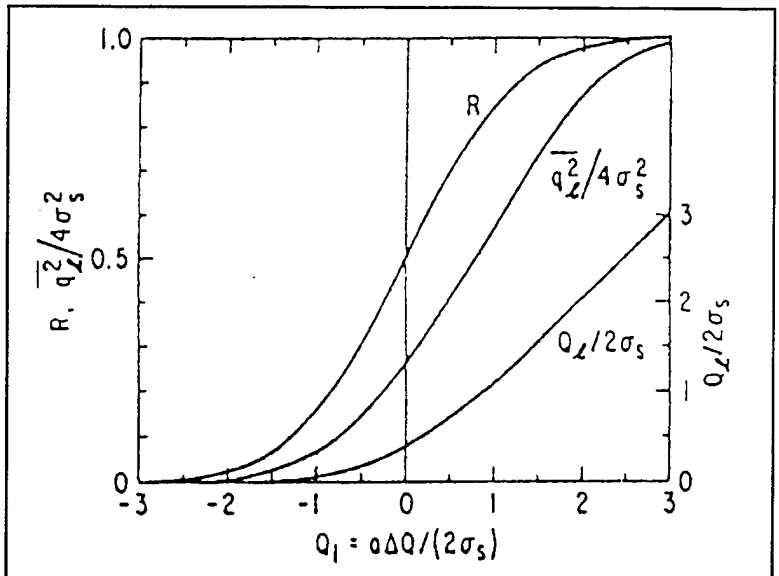


Figure 1 R, $Q_c/2\sigma_s$ and $q_c^2/4\sigma_s^2$ as a function of Q_1 (=$a(Q_w - Q_{sl})/2\sigma_s$)

III Precipitation rate

Since micro-physical processes of precipitation formation are not included in the model, the precipitation rate is parameterized as a function of cloud liquid water. The scheme developed by Sundqvist et al (1989) is incorporated in the BFM. The basic assumption is that the denser the cloud the higher the precipitation rate.

The rate of release of precipitation is described by

$$P=C_0 Q_c[1-\exp(-(\frac{Q_c}{RQ_{c,cr}})^2] \qquad (21)$$

Here, $1/C_0$ is regarded as a characteristic time for the conversion of cloud droplets into precipitation particles (raindrops, or snow particles), R is a fraction of cloud coverage described in the previous section, and $Q_{c,cr}$ is a kind of threshold value for cloud water, which Q_c/R must exceed before the release of precipitation can become efficient. The parameter $Q_{c,cr}$ should have

a value typical of individual cloud type, which is invariant to grid resolution.

The rate of precipitation, $P_r(z^*)$, at a z*-level is given by

$$P_r(z*)=\int_0^H \rho P dz=(\frac{\overline{H}+z_{g,max}-z_g}{\overline{H}})\int_{z*}^{\overline{H}}\rho(z*)Pdz* \quad (22)$$

Here, H is the depth of model atmosphere, $z_{g,max}$ is the highest terrain elevation in model domain, z_g is terrain elevation, and ρ_a is the air density.

In order to simulate the coalescence process, Sundqvist et al (1989) introduced an additional parameter F_∞. This parameter increases with the rate of precipitation and multiplies C_0 and divides $Q_{c,cr}$. The relation is:

$$F_\infty (z^*) = 1 + C_1 Pr(z^*)^{1/2} \quad (23)$$

Similarly, C_0 increases and $Q_{c,cr}$ decreases by a temperature function, F_{BF}, when the temperature is lower than -5 °C in clouds containing a mixture of droplets and ice crystals (Bergeron-Findeisen mechanism). This formulation is:

$$F_{BF}= 1 + C_2(268.0 - T(z^*))^{1/2} \quad (24)$$

The two modified parameters C_{0F} and $Q_{(c,cr)F}$ become, respectively:

$$C_{0F} = C_0 \cdot F_\infty \cdot F_{BF} \quad (25)$$

$$Q_{(c,cr)F}=Q_{c,cr}/(F_\infty \cdot F_{BF}) \quad (26)$$

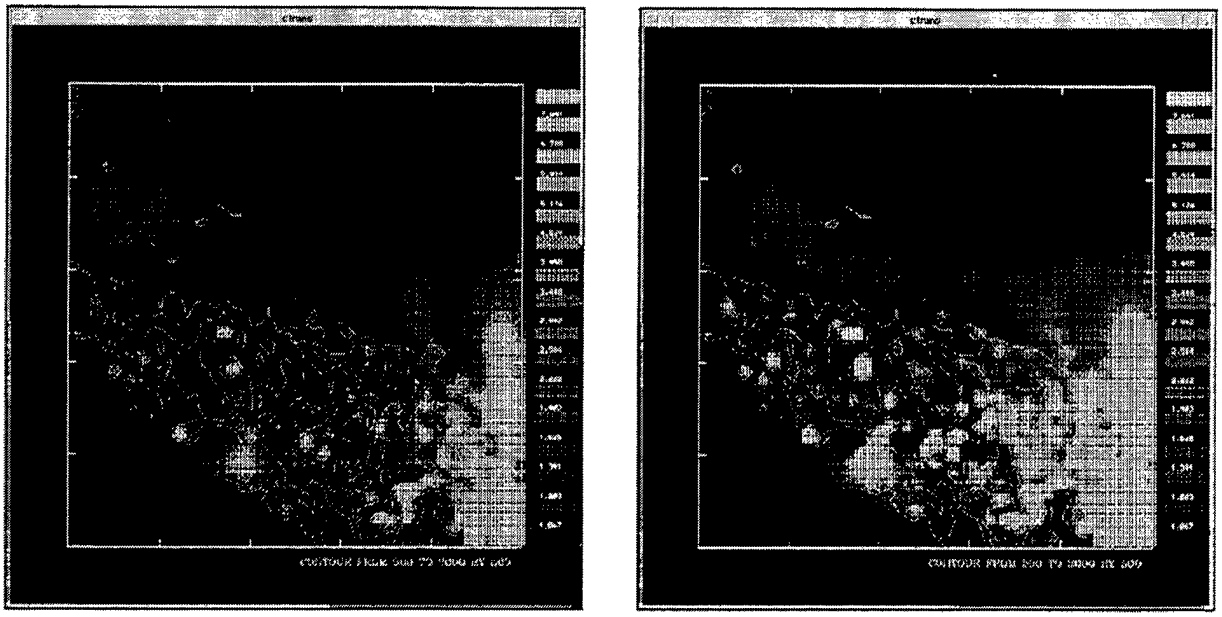
Thus, the precipitation rate at the surface is calculated as:

$$Pr(0)=(\frac{\overline{H}+z_{g,max}-z_g}{\overline{H}})\frac{1}{\rho_w}\int_0^{\overline{H}}\rho_a(z*)C_{0F}Q_c(z*)[1-\exp(-(\frac{Q_c(z*)}{RQ_{(c,cr)F}})^2)]dz* \quad (27)$$

where ρ_w is the density of water. Pr(0) is calculated in the unit of (mm/hr) or (inches/hr).

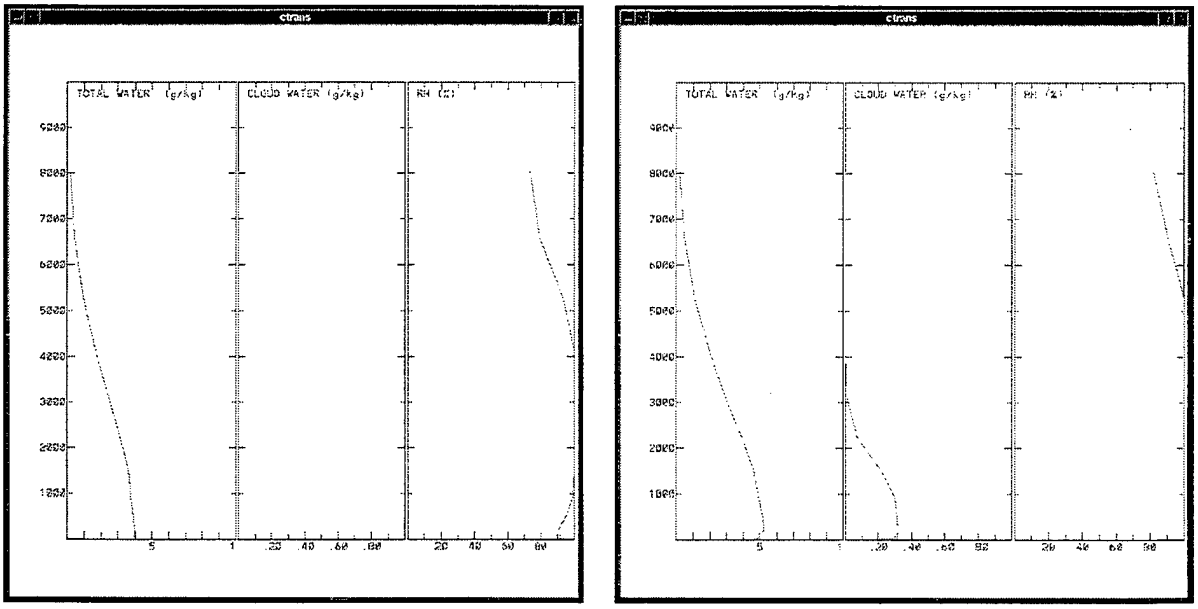
IV. Examples of fog/low level cloud and precipitation

The BFM was applied to the Bosnia area for the 24 hour period of 12 GMT, December 19 through 12 GMT, December 20, 1995. On December 20, the air traffic over the area was hampered by bad visibility and falling snow. The model simulated cloud formation over the area



(1) (2)

Figure 2. Cloud cover over Bosnia, (1) at 23 GMT on December 19, 1995, and (2) at 00 GMT on December 20, 1995.



(1) (2)

Figure 3. Vertical profiles of total water content (g/kg), cloud water content (g/kg), and relative humidity (%), (1) at 00 GMT, and (2) at 01 GMT, December 20, 1995.

at the late evening of December 19, and total cloud coverage over the entire model domain from 01 GMT to 12 GMT of December 20.

Figure 2 (1) and (2) show the cloud coverages at 23 GMT on December 19, and 00 GMT on December 20. The figures show the distribution of the weight of liquid water over a unit area (g /m^2), and the denser the white color, the denser the cloud. The figures may represent the cloud picture taken from far above. As can be seen, the area covered by cloud increased in the one hour, and at 01 GMT on December 20, the entire area was covered by cloud.

Figure 3 (1) and (2) show the vertical profiles of total water content (g/kg), cloud water content (g/kg), and relative humidity (%), at the center point of the model domain. (1) is for 00 GMT, December 20, and (2) is for 01 GMT, December 20. At 01 GMT, the entire area was covered by cloud. In one hour, total water water content increased significantly, and cloud water content profiles show significant increase in the lower atmosphere after one hour. The relative humidity has also increased in one hou, and deep layer of atmosphere has become satureted by 01 GMT. From the figures, it can be seen that a very small portion of total water is converted into cloud water.

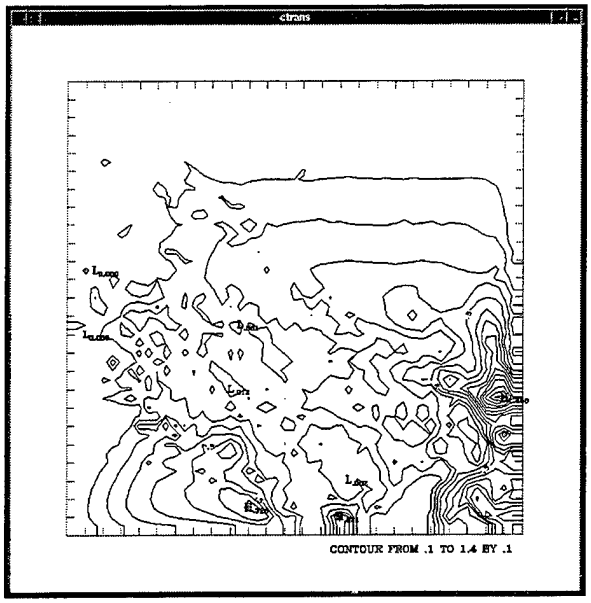


Figure 4 . Precipitation rate (mm/hr) distribution over Boznia, at 01 GMT, December 20, 1995. Maximum rate is 1.4 mm/hr, and mimimum rate is .1 mm/hr.

Figure 4 shows the distribution of precipitation rate (mm/hour) at 01 GMT on December 20. The precipitation rate was calculated by the equation 27. The figure shows the precipitation rate varied from 0.1 to 1.4 mm/hour over the area. There was no precipitation over the model domain at 00 GMT.

It should be emphasized that fog/cloud and precipitation schemes in the model have yet to be throughly evaluated, and the results shown shold be regarded as preliminary. Further study will be required.

V. Concluding Remarks

The forecasting period of the BFM has been extended to 24 hours, and recently the forecast schemes for fog/cloud as well as non convective precipitation has been added. Other IMETS Block II software such as the Atmospheric Sounding Program (ASP) and the Integrated Weather Effects Decision Aids (IWEDA) utilize the BFM output file to calculate the values of their parameters. ASP generates products such as probability of thunderstorm occurrence, icing, visibility, turbulence,etc.

The BFM is numerically stable, and, as long as reasonable input data are used, the BFM produces numerically reasonable output. Currently, on the IMETS BLOCK II computer (SUN SPARC 20, 75 Mega Hertz, 256 Mega Bytes RAM single processor), the BFM requires about two hours of computing time for the 24 hour forecast duration, using the model configuration of 51 x 51 x 16 grid points and 10 km grid spacing.

The evaluation of the BFM forecasting capability is currently ongoing, and the results will be published in the near future. Forecasting capabilities of wind, temperature and relative humidity, as well as cloud coverage and precipitation amount distribution will be evaluated by comparing the model output and observed data.

The presently-known limitation of the BFM are the following:

i) Hydrostatic and Boussinesq approximations. Extremely large changes in the large-scale temperature field advected into the BFM grid (via time-dependent boundary values resulting from the GSM) over 24 hours could possibly reduce the validity of the Boussinesq approximation, based on the BFM definition of basic state for θ_v.
ii) No cloud microphysics.
iii) No convective cloud parameterization, thus no ability to handle features generated by convective systems, such as meso-fronts (i.e., gust fronts),meso high/low, unless they are resolved by the initial fields.
iv) Rather crude specification of surface parameters, such as albedo, emissivity, soil moisture, snow, etc.
v) Somewhat time-consuming to run at resolutions less than 5 km.

vi) The present BFM uses only 16 computational layers and extends up to 7,000 m above the highest grid point of model domain, in order to save computational time.

The BFM forecasting capability will be improved when the output of the regional scale forecasting models such as the US Air Force's Relocatable Window Model (RWM) or the US Navy Operational Regional Atmospheric Prediction System (NORAPS) are used instead of the GSM. The GSM output is at present available every 381 km. We will start studying the

utilization of finer grid model output to initialize the BFM.

VI. References

Golding, B. W., 1990: The meteorological office mesoscale model, Meteorological Magazine, 119, 81-96.

Mellor, G. L., "The Gaussian Cloud Model Relation", Journal of Atmospheric Sciences, 34, 356 - 358, 1977.

Pielke, R. A., " Mesoscale Meteorological Modeling", Academic Press, New York, 1984.

Sommeria, G. and J. W. Deardorff, " Subgrid Scale Condensation in Cloud Models", Journal of Atmospheric Sciences, 34, 344 - 355, 1977.

Sundqvist, H., E. Berge and J. E. Kristja'nsson, " Condensation and Cloud Parameterization Studies with a Messoscale Numerical Weather Prediction Model", 117, 1641 - 1657, 1989.

Yamada, T. and S. Bunker, " A Numerical Model Study of Nocturnal Drainage Flows with Strong Wind and temperature gradients", Journal of Applied meteorology, 28, 545 - 554, 1989.

Yamada, T., and G. L. Mellor, 1979: A simulation of BOMEX data using a turbulence closure model coupled with ensemble cloud relations, Quarterly Journal of the Royal Meteorological Society, 105, 915-944.

ASSIMILATION OF REMOTELY SENSED DATA IN A PORTABLE ANALYSIS AND FORECAST SYSTEM

Frank H. Ruggiero
Phillips Laboratory
Hanscom AFB, MA 01731, U.S.A.

Keith D. Sashegyi and Rangarao V. Madala
Naval Research Laboratory
Washington, DC 20375, U.S.A.

ABSTRACT

Previously a portable mesoscale analysis and forecast system was introduced. The system was designed to run on a workstation and provide high resolution short-range 3-12 hour forecasts. In order to meet DoD wartime tactical needs it is important that this system make optimal use of remotely sensed data. Enhancements have been made to the original system to use satellite data in the assimilation of thermodynamic profiles and in an aid in the diabatic initialization of the model. Assimilation of satellite retrieved thermodynamic profiles is accomplished using the coupled approach in which the forecast model provides the first guess for the retrievals. The retrieved profiles are then analyzed using the portable analysis and forecast system's successive corrections objective analysis scheme. This objective analysis is modified to take into account the spatial correlation of the satellite observation error. Results from a case study show the assimilation of the retrievals improves the analyses but has mixed results with the forecasts. The diabatic initialization adds diabatic forcing from stratiform precipitation to a vertical normal-mode initialization. The technique uses satellite estimated precipitation amounts and cloud-top heights with analyzed thermodynamic and kinematic fields to vertically distribute diabatic heating that arises from stratiform precipitation. Simulation experiments reveal the importance of incorporating this heating into the initialization. An adiabatic initialization recovered about 65-75% of the maximum upward vertical motion whereas a diabatic initialization with respect to stratiform precipitation recovered nearly all the original vertical motions. In real data cases, short-term forecasts from a diabatically initialized model, with respect to stratiform precipitation, demonstrate improvement over forecasts from an adiabatically initialized model.

1. INTRODUCTION

Sashegyi et al. (1994) presented a portable analysis and forecast system capable of running on a workstation that provides high resolution short-range 3-12 hour forecasts. Its components include the Bratseth (1986) objective analysis scheme as implemented by Sashegyi et al. (1993) for radiosonde data and Ruggiero et al. (1996a) for surface observations. The Bratseth scheme is iterative, computationally efficient, and will converge to an optimal interpolation solution. The model initialization uses the vertical normal-mode initialization approach as described by Sashegyi and Madala (1993). The initialization also contains the capability to include the diabatic effects of convective precipitation (Harms et al. 1993). The forecast model is the same as used in the Navy Operational Regional Analysis and Prediction System (NORAPS) and has been described by Madala et al. (1987), Hodur (1987), Liou et al. (1990) and Liou et al. (1994). The NORAPS forecast model is a hydrostatic model capable of nesting. Using a simplified version of the model with two nests and running on a RISC- type workstation with a floating point performance of 30

Mflops, Sashegyi et al. (1994) was able to produce a 12-h forecast in approximately 30 mins. The portable analysis and forecast system was designed to use an intermittent assimilation strategy since it is computationally less expensive than a 3 or 4-dimensional variational approach. In addition, since it forces all the assimilated data to go through the initialization phase, intermittent assimilation limits the creation of physical imbalances that are possible in nudging (Walko et al. 1989).

In order to be of use to DoD in wartime, the portable analysis and forecast system must be able to work with the data denial that occurs in tactical situations. Given tactical and communication constraints the use of radiosonde and in-situ surface observations will be limited. Reliance will be on data from passive remote sensors that can be down linked to the forward sites. The focus here is to describe the enhancements to the portable analysis and forecast system that make use of certain satellite borne sensors that meet this requirement. In particular, this includes the assimilation of satellite sounder thermodynamic retrievals and the inclusion of a diabatic initialization with respect to stratiform precipitation.

2. ASSIMILATION OF SATELLITE SOUNDER RETRIEVALS

Traditionally, the standard way of retrieving thermodynamic profiles from satellite sounders are iterative methods that rely on an intelligent choice of a first guess profile. The selection of the first guess is important since the inverse solution of determining atmospheric thermodynamic profiles from satellite measured radiances is non-unique. Recently, much work has been put into using three-dimensional variational analyses to directly assimilate the satellite radiances. Indeed this method has shown great promise (Andersson et al. 1994), however it is computationally expensive to employ and thus not considered here. Here the assimilation of the satellite sounder retrievals is carried out using the coupled approach as described by Lipton and Vonder Haar (1990). A schematic outlining how the coupled approach works is given in Figure 1. The process starts with the output of a short-term forecast interpolated to the retrieval locations (unless radiosonde data is available in which case one could use the output from the radiosonde analysis). The retrievals are then calculated and the deviations of the retrievals from the first guess

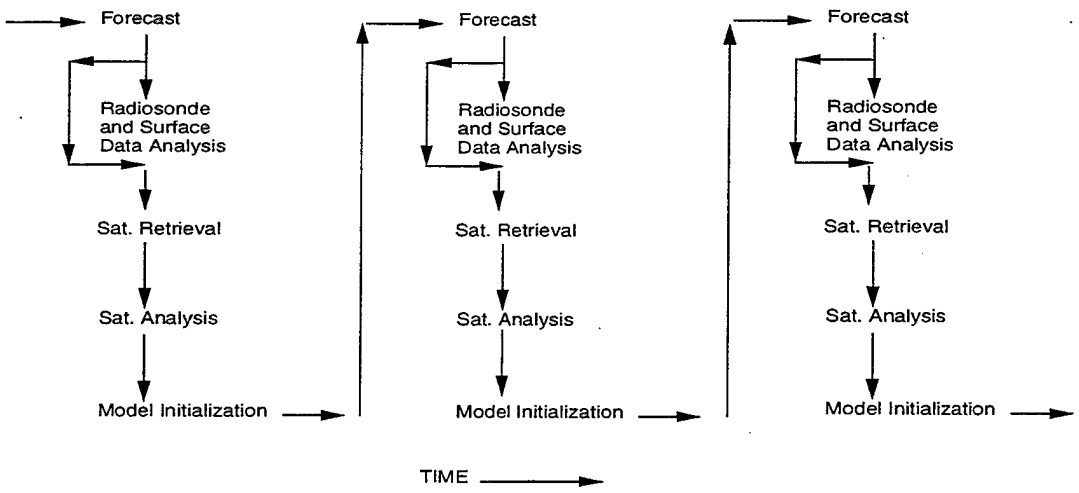


Figure 1. Schematic showing the flow of the model-satellite sounder coupled approach.

profiles are interpolated back to the model grid using the Bratseth objective analysis. The same forecast that provides the first guess for the retrievals is used as the background field for the objective analysis. One important change to the analysis scheme is the inclusion of a spatially correlated portion of the observation error. Previously the observation error was assumed to be to be totally random. When the fields on the model grids are updated an initialization can then be run and the model integrated forward. This cycle can be repeated as often as necessary and data is available.

To examine the utility of the coupled analyses method for assimilating atmospheric temperature and moisture in the portable analysis and forecast system, two experiments were conducted using data from the second 1986 Genesis of Atlantic Lows Experiment (GALE) Intensive Observation Period (IOP). Both experiments started off with a radiosonde and surface data analysis at 1200 UTC 24 January 1986. A control experiment was run by integrating the model forward 24 hours from this point. An assimilation experiment run was done by assimilating retrievals at 1200, 1500, 1800, 2100 UTC 24 January 1986, and 0000 UTC 25 January 1986 using the coupled procedure as described above. Comparison of the temperature results from the two runs at 1800 UTC 24 January 1986 can be seen in Figure 2 which depicts the root-mean-square (rms) errors of temperatures from an analysis constructed with radiosonde data. The computations of the rms errors are limited to those locations where the retrievals and radiosonde observations are nearly collocated. It can be seen that the analysis resulting from the retrievals improved upon the background field even though the actual retrieval errors were high. The amount of improvement of the analysis over the background field was small. This was due to the high observation error that was ascribed to the retrievals (3.6 K of which 1 K was assumed to be horizontally spatially correlated and the rest random). In addition, one should note that the coupled analysis was improved over the control run. A similar pattern can be seen with relative humidity at the same time in Figure 3. In this case the amount of improvement over the first guess was more significant than it was for temperature. Again the observation error for the humidity retrievals was substantial (15% horizontally spatially correlated and 25% random).

Given the relatively modest improvement of the coupled run analyses over the control run, it is not surprising that the forecasts generated from the coupled run do not show a great improvement over the control run forecast. Rms errors of temperature and relative humidity were computed for each forecast run relative to a radiosonde analysis at the radiosonde observation locations at 0600 UTC 24 January 1986. The control run forecast was an 18-h forecast initialized from radiosonde and surface data analyses at 1200 UTC 24 January 1986. The coupled run was also 18-h forecast that used the same initial data as did the control run and that assimilated geostationary sounder data at 3 h intervals from 1200 to 2100 UTC 24 January 1986. The rms errors were similar for the control and coupled runs. For temperature, the values were 1.996 and 2.150 K for the coupled and control runs respectively. For relative humidity, the respective values were 9.346 and 8.618%.

3. DIABATIC INITIALIZATION WITH RESPECT TO STRATIFORM PRECIPITATION

When using frequent intermittent assimilation one has to take care not to continually lose the model generated convergence fields during each analysis and initialization step. One way to mitigate this problem is through inclusion of latent heating in the balance to be achieved at initialization. The latent heating is offset by adiabatic cooling from upward vertical motion. As mentioned in Sashegyi et al. (1994) the portable analysis and forecast system already includes a diabatic initialization with respect to convective precipitation. A companion scheme developed by Ruggiero at al. (1996b) performs diabatic initialization with respect to stratiform precipitation. The two schemes work together in that for every grid point at which precipitation has been observed

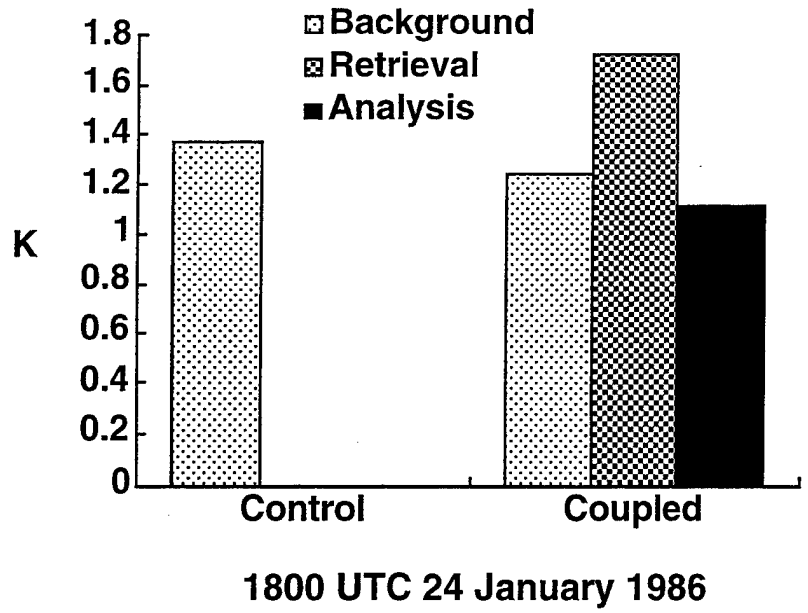


Figure 2. Rms errors of temperature of the control and coupled runs from a radiosonde analysis at locations that have nearly coincident radiosonde soundings and retrievals at 1800 UTC 24 January 1986.

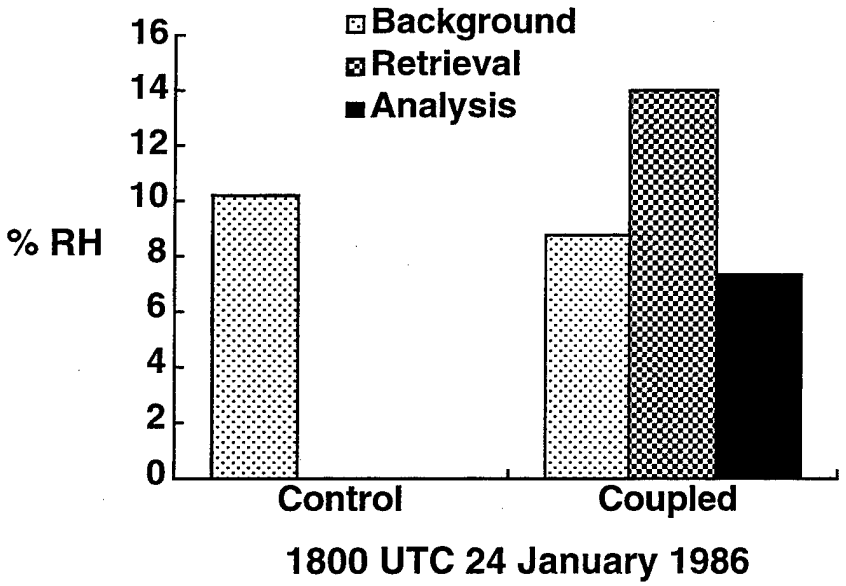


Figure 3. Rms errors of relative humidity of the control and coupled runs from a radiosonde analysis at locations that have nearly coincident radiosonde soundings and retrievals at 1800 UTC 24 January 1986.

during the past three hours, a check of conditional stability is carried out. If the column is conditionally unstable than the convective diabatic initialization of Harms et al. (1993) is used, otherwise the stratiform scheme is used. A detailed description of the diabatic initialization procedure for stratiform precipitation is given in Ruggiero et al. (1996b) and is briefly summarized here. The technique starts off by using the output of three iterations of the adiabatic vertical normal mode initialization. This is done to generate an initial vertical velocity field. The underlying assumption in the Ruggiero et al. (1996b) approach is that the adiabatic initialization will produce the right orientation of the vertical motion fields although the magnitudes are insufficient. The cloud top height for each column is estimated by matching the infrared (11.24 μm) brightness temperature with that from the initial field. The two model layers below the estimated cloud top height are saturated if not already so. A one-dimensional water vapor convergence calculation is carried out using the kinematic fields from the adiabatic initialization. Water vapor in excess of saturation is condensed out and precipitated down. The total amount of precipitation generated in this manner is added up and compared to the observed precipitation rate. When the generated precipitation matches up with the observed, the latent heat generated at each level is calculated and is added to the physical forcings in the vertical normal-mode initialization. In addition, the moisture fields are adjusted by boosting to 90% the RH at those model levels that are deemed to be producing precipitation. If the RH at those levels already exceed 90% they are left alone.

In order to reveal the importance of including the stratiform precipitation diabatic effects in the initialization, a simulation experiment was run. Using radiosonde and surface data from GALE IOP 2 at 1200 UTC 25 January 1986, the model was integrated forward 12 hours to 0000 UTC 26 January 1986. The output from the model at 0000 UTC 26 January 1986 was considered "truth". At that point two initializations were run using the model output. The first was an adiabatic initialization. The second was diabatic with respect to stratiform precipitation. The input precipitation used for the diabatic initialization was the three hour accumulated stratiform precipitation valid at 0000 UTC 26 January 1986 from the model integration. The cloud top heights were determined by using the highest model level at which supersaturation occurs. Thus the simulations were essentially using perfect input data. Figure 4 shows the 700 mb vertical velocity fields valid at 0000 26 January 1986 for the model forecast, adiabatic initialization, and diabatic initialization. Comparing the vertical motion between the model forecast and the adiabatic initialization one can see that the process of going through the adiabatic initialization results in the loss of approximately 25-35% of the original maximum vertical motion in the areas of upper Chesapeake Bay and Southern Alabama. However when including the diabatic effects of stratiform precipitation nearly all the original maximum vertical motion is retained in the two areas.

To judge the ability of the diabatic initialization with respect to stratiform precipitation using real data, a second set of experiments was run. In these experiments analyses of radiosonde and surface data were done and the resulting fields were used as input for an adiabatic and diabatic initialization. For the diabatic initialization a 3 hour accumulated precipitation analyses derived from a combination of geostationary satellites and rain gauges was used as the input precipitation field. In evaluating the diabatic initialization it is important to look at precipitation forecasts since the main reason to retain the divergence fields via diabatic initialization is to improve precipitation forecasts. Figure 5 contains the threat scores for the 0.25 cm 3 hour accumulated precipitation contour levels for the forecasts generated from the adiabatic and diabatic initializations at 0000 UTC 26 January 1986. In general, the threat scores are low but that just points up the current difficulty that exists in forecasting precipitation with a numerical prediction model. At each of the three hour intervals the diabatic initialized forecast produces better results. It should be noted that the diabatic run shows the most improvement over the adiabatic run at earlier times. In the second 6-h period the adiabatic run becomes closer to the diabatic run as the model circulation's spin up.

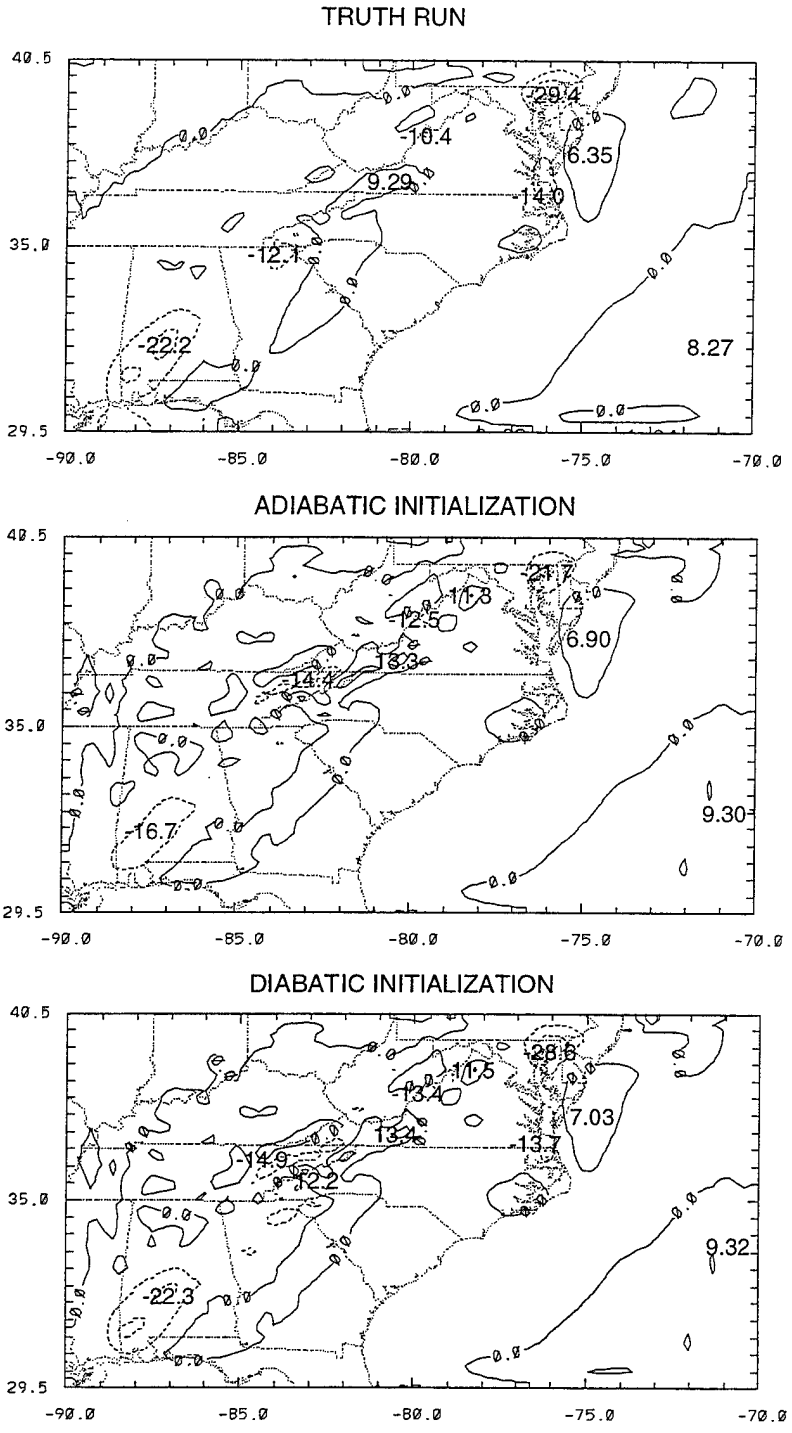


Figure 4. Vertical velocity (μb s^{-1}; contoured every 10 μb s^{-1}; negative contours are dashed) at 700 mb valid at 0000 UTC 26 January 1986 for (a) model output from "truth". (b) adiabatic initialization and (c) diabatic initialization.

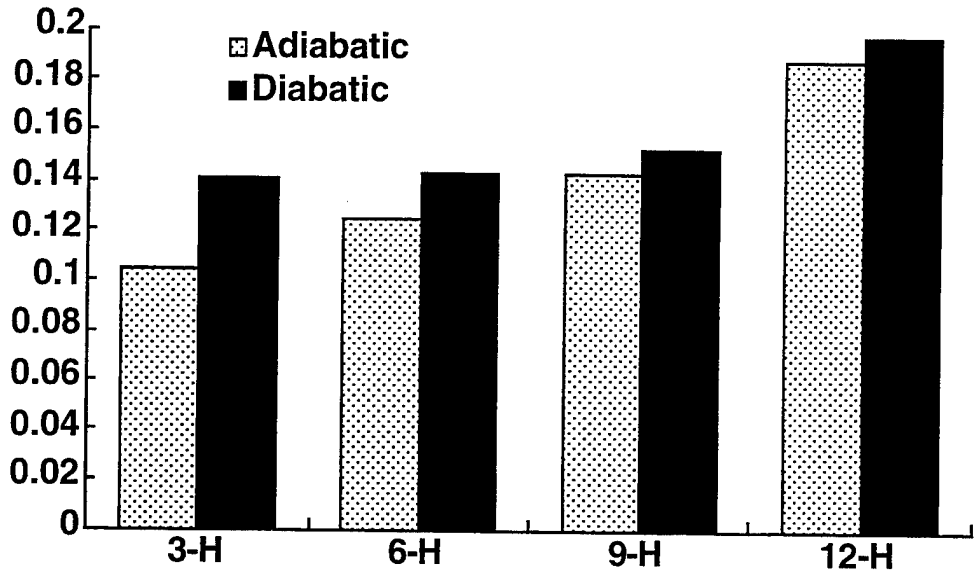


Figure 5. Threat scores at the 0.25-cm contour level for the real data forecasts initialized at 0000 UTC 26 January 1986.

4. CONCLUDING REMARKS

Two major changes have been made to the portable analysis and forecast system described by Sashegyi et al. (1994). One is the modification of the analysis to assimilate satellite retrieved thermodynamic profiles using the coupled approach. The results of tests showed that the assimilation of the geostationary satellite sounder data will improve the temperature and moisture fields during the assimilation period. However these improvements were relatively modest and did not significantly improve the model forecasts. The main reason for the limited success of the assimilation of the retrievals was that the ratio of the observation errors to background field errors did not allow the retrievals to strongly impact the analysis. Both sets of errors were derived from other sources and perhaps are not well suited to be used with either the VAS sounder or the NORAPS model. In hindsight it appears that the observation errors used for the retrievals were generally too high. This can be corrected by gathering error statistics for the coupled procedure retrievals over a large number of cases. In addition, with the new sounder onboard the new generation of GOES (Menzel and Purdom, 1994), the retrievals may be even more accurate than seen here.

The second change to the portable analysis and forecast system is the inclusion of the diabatic effects of stratiform precipitation in the model initialization. Simulation and real data experiments reveal the importance of including this in the initialization. The results are improved short-term precipitation forecasts. Improvements to this approach can be to use radar reflectivity data (if available) to produce an enhanced precipitation analysis. If three-dimensional radar reflectivity data is available than a more direct method of determining the vertical latent heat distribution is possible. In addition if the time evolution of the precipitation rates are available then perhaps this derivative information can be used to include a time dependent diabatic forcing to the model.

In addition to the above mentioned improvements to the portable analysis and forecast system, work is underway in other areas. Since the next generation of mesoscale models will have the ability to explicitly produce clouds via prognostic variables of cloud liquid and ice water, work is ongoing to come up with initial fields for these variables in order to have accurate short-term forecasts of clouds and precipitation fields. Again the emphasis in this work will focus on determining the required fields using satellite data.

REFERENCES

Andersson, E., J. Pailleux, J.-N. Thépaut, J. R. Eyre, A. P. NcNally, G. A. Kelly, and P. Courtier, 1994: Use of cloud-cleared radiances in three/four dimensional variational data assimilation. *Quart. J. Roy. Meteor. Soc.*, **120**, 627-653.

Bratseth, A. M., 1986: Statistical interpolation by means of successive corrections. *Tellus*, **38A**, 439-447.

Harms, D. E., R. V. Madala, S. Raman, K. D. Sashegyi, 1993: Diabatic initialization tests using the Naval Research Laboratory limited-area numerical weather prediction model, *Mon. Wea. Rev.*, **121,** 3184-3190.

Hodur, R. M., 1987: Evaluation of a regional model with an update cycle. *Mon. Wea. Rev.*, **115**, 2707-2718.

Liou, C.-S., R. M. Hodur, and R. H. Langland, 1994: Navy Operational Atmospheric Prediction System (NORAPS): A triple nested mesoscale model. Preprints, *Tenth Conf. on Numerical Weather Prediction,* Portland Oregon, Amer. Meteor. Soc., 423-425.

Liou, C.-S., C. H. Wash, S. M. Heikkinen, and R. L. Elsberry, 1990: Numerical studies of cyclogenesis events during the Second Intensive Observation Period (IOP-2) of GALE. *Mon. Wea. Rev.*, **118,** 218-233.

Madala, R. V., S. W. Chang, U. C. Mohanty, S. C. Madan, R. K. Paliwal, V. B. Sarin, T. Holt, and S. Raman, 1987: Description of the Naval Research Laboratory limited area dynamical weather prediction model. NRL Memo. Rep., 5992. Naval Research Laboratory, Washington, D. C., 132 pp. [NTIS A182780.]

Menzel, W. P., and J. F. W. Purdom, 1994: Introducing GOES-I: The first of a new generation of Geostationary Operational Environmental Satellites. *Bull. Amer. Meteor. Soc.*, **75**, 757-781.

Ruggiero, F. H., K. D. Sashegyi, R. V. Madala, and S. Raman, 1996a: The use of surface observations in four-dimensional data assimilation with a mesoscale model. *Mon. Wea. Rev.*, **124**, 1018-1033.

Ruggiero, F. H., K. D. Sashegyi, R. V. Madala, and S. Raman, 1996b: Diabatic initialization of stratiform precipitation for a mesoscale model. *J. Appl. Meteor.*, **35**, 1111-1128.

Sashegyi, K. D., and R. V. Madala, 1993: Application of vertical-mode initialization to a limited-area model in flux form. *Mon. Wea. Rev.*, **121**, 207-220.

Sashegyi, K. D., R. V. Madala, D. E. Harms, and S. Raman, 1994: A numerical weather prediction system for regional and mesoscale forecasting on a high performance workstation. Preprints, *Tenth Conf. on Numerical Weather Prediction,* Portland, OR, Amer. Meteor. Soc., 363-365.

Sashegyi, K. D., D. E. Harms, R. V. Madala, and S. Raman, 1993: Application of the Bratseth scheme for the analysis of GALE data using a mesoscale model. *Mon. Wea. Rev.*, **121**, 2331-2350.

Sashegyi, K. D., R. V. Madala, F. H. Ruggiero, and S. Raman, 1994: A portable system for data assimilation in a limited area model. Preprints, *Battle Atmospherics Conference,* White Sands, NM.

Walko, R. L., C. J. Tremback, and W. R. Cotton, 1989: Assimilation of Doppler radar wind data into a numerical prediction model: A demonstration of certain hazards. Preprints, *24th Conf. on Radar Meteor.*, Tallahassee, FL, Amer. Meteor. Soc., 248-250.

RESULTS AND IMPLICATIONS OF NEURAL NETWORK RETRIEVALS OF SATELLITE TEMPERATURE SOUNDINGS

Donald Bustamante[1], James Cogan[2],
William Gutman[1], Edward Measure[2], and Gail Vaucher[2]

ABSTRACT

Back propagation neural networks were used to retrieve atmospheric temperature profiles from meteorological satellite sounder radiances. The networks were trained in TIROS Operational Vertical Sounder (TOVS) data collected during 1992 and 1993 over the United States and Canada. The truth sets for training and testing the neural networks consisted of data from the University of Wisconsin's TOVS Export Package and near-to-coincident rawinsonde data. The retrievals had a root-mean-square (RMS) error over mandatory levels (1000 to 10 hPa) of < 3.5 K for the complete set of data. For a subset consisting of data from the Southeastern United States, the error dropped to < 2.5 K over most levels (i.e. not near the surface and tropopause).

These studies demonstrate that neural networks can provide reasonable results using only the TOVS infrared (HIRS/2) sounding channels. Inclusion of the MSU radiances led to a small improvement. A sensitivity analysis identified ten HIRS/2 channels as the most significant input. A "reduced" net using only those ten channels produced results that suggest a "degradation" of only 0.2 or 0.3 K relative to the full net. The potential significance of these results is discussed.

Recently, the neural network methodology has been applied to infrared sounder data obtained with GOES I-M sounders carried aboard current generation Geostationary Operational Environmental Satellites (GOES). Comparable or better levels of accuracy have been obtained with GOES retrievals. These results are also discussed.

1. RETRIEVAL APPROACHES

Following Houghton (1985), for a cloudless atmosphere, the radiance of the earth's atmosphere as measured by a satellite-borne radiometer may be expressed as

$$I(\upsilon) = B(\upsilon, T_s)\tau(\upsilon, p_s) - \int_{x(0)}^{x(p_s)} B(\upsilon, p)\frac{d\tau(\upsilon, p)}{dx(p)}dx(p)$$

where $I(\upsilon)$ is the radiance at wavenumber υ; $B(\upsilon, T)$ is the Planck radiance at wavenumber υ and surface temperature T_s; τ is the atmospheric fractional transmittance from a given pressure level to the top of the atmosphere; $x(p)$ is a function of pressure, usually $\ln p$. The first term represents the

[1] Author is with the Physical Science Laboratory, New Mexico State University, Las Cruces, New Mexico 88003.

[2] Author is with the Information Sciences and Technology Directorate, Army Research Laboratory, White Sands Missile Range, New Mexico 88002.

spectral radiance emitted by the surface and attenuated by the atmosphere; the second term represents the radiance emitted by the atmosphere.

Correcting for surface contributions, the equation becomes

$$I_\upsilon(\upsilon) = \varepsilon_\upsilon B_\upsilon(T_s)\tau(0,p_s) + \int_0^{p_s} B(T)W_\upsilon(p)\frac{dp}{p}$$

$$W_\upsilon(p) = -\left\{1-(1-\varepsilon_\upsilon)\left[\frac{\tau_\upsilon(0,p_s)}{\tau_\upsilon(0,p)}\right]^2\right\}\frac{\partial\tau_\upsilon(0,p)}{\partial\ln p}$$

where ε is the emissivity, and W is the Planck weighting function. The term

$$\frac{\partial\tau_\upsilon(0,p)}{\partial\ln p}$$

is referred to as the sensor weighting function. These weighting functions are specific for each channel of a sounding instrument such as the TOVS or GOES Sounder, and vary with p. In the infrared region covered by most sounder channels instrumentation, ε is approximately unity. Although the forward equation is easily solved, the inverse is ill-posed; small changes in I result in large errors in T. There is no unique solution, since the contribution to the radiances observed by the satellite arise from deep within the atmosphere and the sensor channels are not spatially independent (Houghton, 1985).

1.1 Conventional Retrieval Approaches

Conventional approaches utilize additional data to regularize the problem and obtain a solution. These additional data include *in-situ* rawinsonde observations and statistics of atmospheric structure, pattern recognition (to match a rawinsonde profile with an initial guess profile), and the use of Numerical Weather Prediction (NWP) model output to condition the retrieval. Mathematically, these approaches involve the use of linear and non-linear techniques. Linear techniques such as linearization, basis functions, least squares regression, statistical regularization, and minimal information approaches have been used. Non-linear approaches typically involve an iterative form of solution. Detailed reviews can be found in Rodgers (1976) and Deepak, *et al.* (1988). The conventional algorithm used in this study was the TOVS Export Package (TEP) developed by the University of Wisconsin (Smith, *et al.*, 1983).

1.2 Neural Network Retrieval Approaches

The application of neural networks to the retrieval of atmospheric temperature profiles has been studied by several researchers, who have used a variety of data and data sources in their studies. Bustamante *et al.* (1996a) provide a brief description of some of this work. The effort reported here is based on work that has been reported previously by Bustamante *et al.* (1992, 1993, 1994a, 1996a, 1996b).

2. TIROS AND TOVS

The TIROS satellites are near-polar orbiting satellites operated by the National Environmental Satellite Service of the National Oceanic and Atmospheric Administration (NOAA). These satellites provide data used for meteorological prediction and warning, oceanographic and hydrologic data and space environment sensing (Schwalb, 1982). The satellites are equipped with environmental sensors that include the TIROS Operational Vertical Sounder (TOVS).

The TOVS instrumentation consists of the High Resolution Infrared Radiation Sensor (HIRS/2), the Stratospheric Sounding Unit (SSU), and the Microwave Sounding Unit (MSU). The HIRS/2 is a 20 channel sensor, primarily infrared, which is used for obtaining vertical temperature profiles, atmospheric water content, and ozone measurements. The SSU is a 3 channel sensor which measures the radiation emitted by carbon dioxide in the stratosphere. The MSU is a 4 channel Dicke radiometer which measures the 5.5 mm oxygen band. Detailed specifications on scan spot size, swath width, and other sounding parameters may be found in Schwalb (1982) and Barnes and Smallwood (1982).

2.1.1 Data

Data were collected by the U. S. Army Research Laboratory's Information Science & Technology Directorate (ARL/IS&TD) using SeaSpace TerraScan hardware and software. Data from the satellite passfiles were processed to yield radiance values for the TOVS sensor channels. Additional information such as site elevation, latitude, longitude, satellite zenith angle, solar zenith angle, and solar phase angle were computed and appended to the datasets.

At the ARL/IS&TD site only the HIRS/2 radiances were collected. The present study had access to 19 of 20 HIRS/2 data channels. Data were available for time periods in 1992 and 1993. TOVS HIRS/2 data for the United States and Canada were collected by the ARL/IS&TD TerraScan system. Additional TOVS radiance data, which included MSU and SSU, were obtained from Louisiana State University's Coastal Studies Institute (Southeastern United States). The SeaSpace system uses the TEP to retrieve atmospheric profiles of temperature and moisture.

National Weather Service (NWS) rawinsonde observational (RAOB) data for North America were provided by the ARL/IS&TD Upper Air Database and NOAA's National Climatic Data Center (NCDC). The data were selected to cover the time period July 1992–August 1993. These data were also used as truth in the training of the networks. For ease in handling, these data were partitioned into geographical sectors covering half month periods.

RAOBS are typically taken at 0000 UTC and 1200 UTC. By convention, the geographic coordinates of the release point are used, and a vertical rise is assumed. Satellite coverage of the geographic region of interest occurs when the satellite passes over that region, The TIROS orbital period is approximately 102 minutes, resulting in 14.1 orbits per day. Since the TIROS satellites are near-polar orbiters, the geographic coverage on subsequent passes is not identical; a two satellite configuration can pass over the same location approximately every 5 hours (average value; more often near the poles).

TOVS radiance data were spatio-temporally matched with RAOBS. The matching program permitted user specification of latitude, longitude, and time windows. Spatio-temporal criteria used are based on the satellite observation. A spatial separation of ±0.5 degree was used for latitude and longitude, and observations taken within 1.5 hours before and 2.0 hours following the satellite observation were considered to be matched.

Feed-forward backpropagation networks were created using Neural Ware's Neural Works Professional II neural network development environment running on an HP 9000/735 workstation. The initial network utilized HIRS/2 Channels 1 through 19, latitude, longitude, satellite zenith angle, solar zenith angle, scatter phase angle, sun reflection angle, and elevation as inputs. Other networks were tested that used combinations of HIRS/2 and MSU channels and differences and ratios between various channels. The output nodes for all networks consisted of the temperatures at the meteorological mandatory levels (1000, 850, 700, 500, 400, 300, 250, 200, 150, 100, 70, 50, 30, 20, and 10 mb) and at the surface.

The networks were instrumented to record the root-mean-square (RMS) error of the network during training using the following equation:

$$RMS = \sqrt{\left(\frac{1}{n}\sum_{i=1}^{n}(O_i - T_i)^2\right)}$$

where n is the number of thermal profiles derived, O_i is the i-th output of the neural network, and T_i is the i-th "truth" value. The networks were trained until the RMS error was minimized. This typically occurred at 15,000 training iterations. The final RMS error at the completion of training was 0.02. This RMS value is the overall value for all output nodes.

Various neural network retrievals were performed with the data. Both rawinsondes and conventionally retrieved profiles (using the TEP) were used as truth. The training and testing were performed using data collected between September 1 and October 15, 1992. The RMS error as a function of mandatory level is shown if Figure 1 for a case using rawinsonde data as truth. Typical RMS error values are 3–4 K. The sensitivity of the RMS error to the number of nodes in the single hidden layer was investigated by training and testing networks with various numbers of nodes. As seen in Figure 2, this analysis demonstrates that ten nodes is the optimum number.

An important aspect of the investigation was a sensitivity analysis to determine whether any of the HIRS/2 channels could be omitted from the network. In fact, a network utilizing only HIRS/2 channels 1, 3, 4, 7, 12, 13, 14, 16, 17, and 19 was found to yield results comparable to those from the full network. The RMS error of the reduced network is somewhat greater at the surface. It is within 0.5 K at 500 mb, and it is actually smaller than that of the full network at the tropopause. This suggests that a simpler, less expensive sensor suite could be used on future satellites without significant loss of temperature retrieval accuracy.

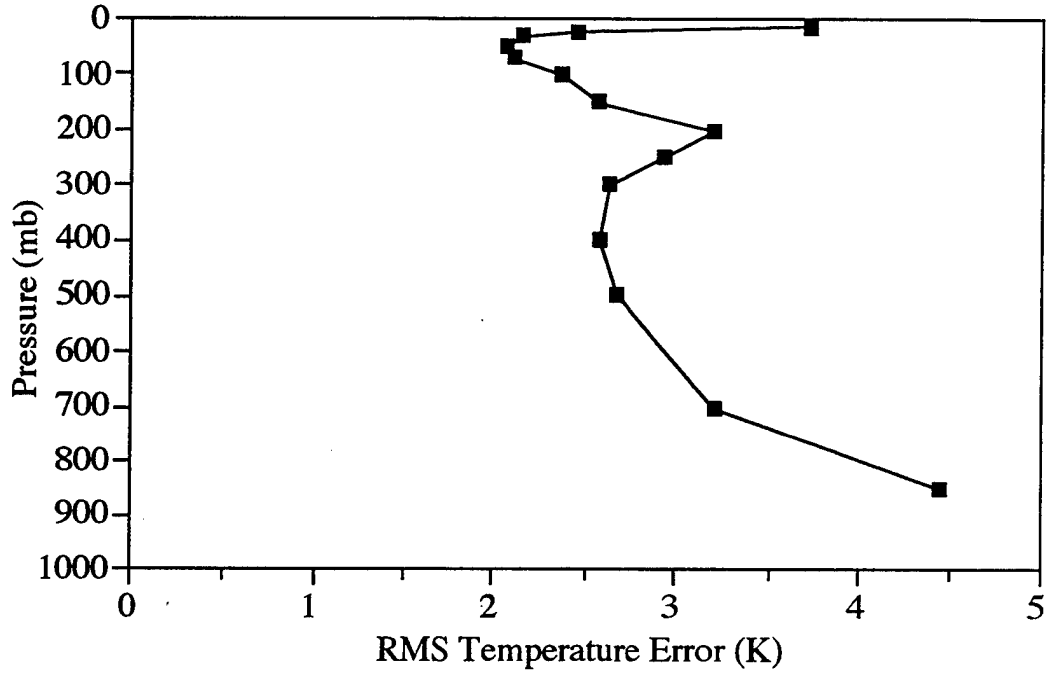


Figure 1. RMS temperature retrieval error as a function of atmospheric level for a neural network trained and tested with TOVS data using rawinsonde data as truth.

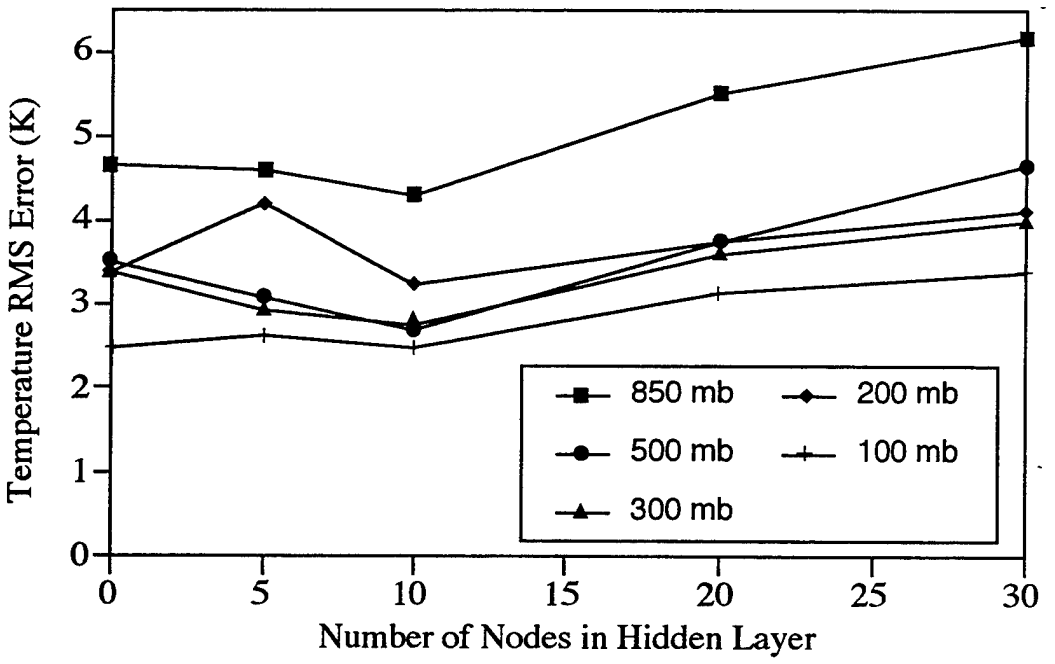


Figure 2. TOVS RMS temperature retrieval error as a function of number of nodes in the hidden layer of the neural network. Ten nodes is the optimum number.

3. GOES AND GOES I-M SOUNDERS

The most recent work extends the neural network retrieval methodology to atmospheric sounder data sets obtained from geosynchronous satellites. Geosynchronous satellites provide the obvious benefit that most of the earth facing the satellite is continuously within view of the sensors. The Geostationary Operational Environmental Satellites (GOES) provide high resolution visible and infrared imagery and multiband infrared soundings. Currently, there are 2 operational GOES platforms, GOES 8, and GOES 9. These satellites are also called GOES East and Goes West because they are stationed at longitudes 75° W and 135° W respectively. Both are from the GOES I-M series that incorporates significant improvements over earlier designs. One of the instruments carried aboard is the GOES I-M sounder. This is a multiband, high spatial resolution radiometer. The GOES I-M sounder is similar to the HIRS/2 instrument of the TOVS package. The eighteen infrared channels have similar center frequencies and bandwidths, and similar applicability to retrieval of atmospheric parameters.

Ten GOES data sets were obtained through the National Climatic Data Center. These data corresponded in time to the 0000 and 1200 UTC rawinsonde launches over a five day period from November 8–12, 1994. Corresponding rawinsonde data were taken from *Rawinsonde Data of North America, Volume IV, 1990–1994 (Updated)* published by the National Climatic Data Center. The actual GOES infrared data acquisition times were 1146 and 2346 UTC each day. All rawinsonde launch times were within 0.8 hour of the GOES data acquisition, and most were within 0.6 hour. GOES infrared sounder data were extracted from the distribution data files using the University of Wisconsin's MCIDAS software product. Spatial reference information for the GOES infrared pixels was used to assemble neural network training and testing files. Raw infrared radiance values were used rather than derived brightness temperatures. Any pixel for which all eighteen sounder channels were valid and which was within 0.5 degree in both latitude and longitude of the corresponding rawinsonde launch point was used. Because of the curvature of the earth, the latitude and longitude spacing of the pixels is a function of position, so the number of pixels that could be used with each rawinsonde varied.

The temperatures at the 850, 700, 500, 400, 300, 250, 200, 150, and 100 mb mandatory levels as well as the surface temperatures were used to train and test the neural networks. These levels were consistently available in the rawinsonde database. Nevertheless, a large fraction of the data could not be used because of missing levels. In total, over 14,000 training/testing vectors were assembled from the rawinsonde and infrared sounder data. These vectors were randomly partitioned into two approximately equal size files. One file was used for training, and the other was used for testing.

RMS errors associated with the extraction were computed by comparing rawinsonde temperatures with temperatures retrieved from the testing set. The RMS errors are plotted as a function of level in Figure 3. Numerous variations of neural network architecture were tested. In all cases, a single hidden node was used, but the number of nodes in the hidden layer was varied from 5 to 25. Consistent with the findings from the TOVS retrieval (Bustamante, *et al.*, 1996b), the RMS errors were minimized with 10 hidden nodes, although as seen in Figure 4, the GOES Sounder retrievals exhibited much less sensitivity to this parameter than did the TOVS retrieval.

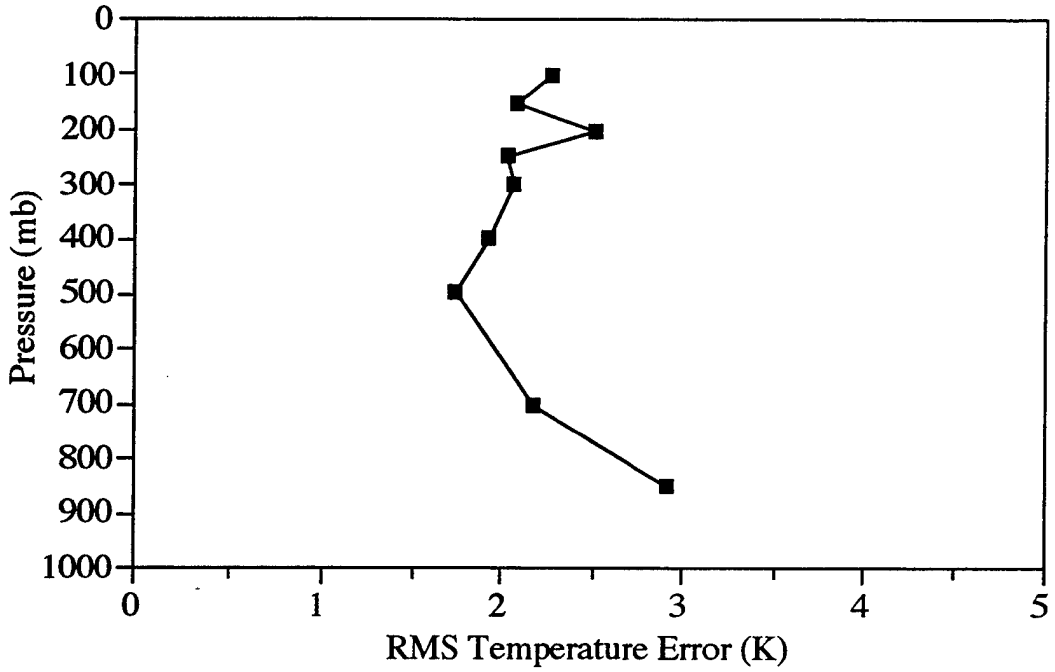


Figure 3. RMS temperature retrieval error as a function of atmospheric level for a neural network trained and tested with GOES Sounder data using rawinsonde data as truth.

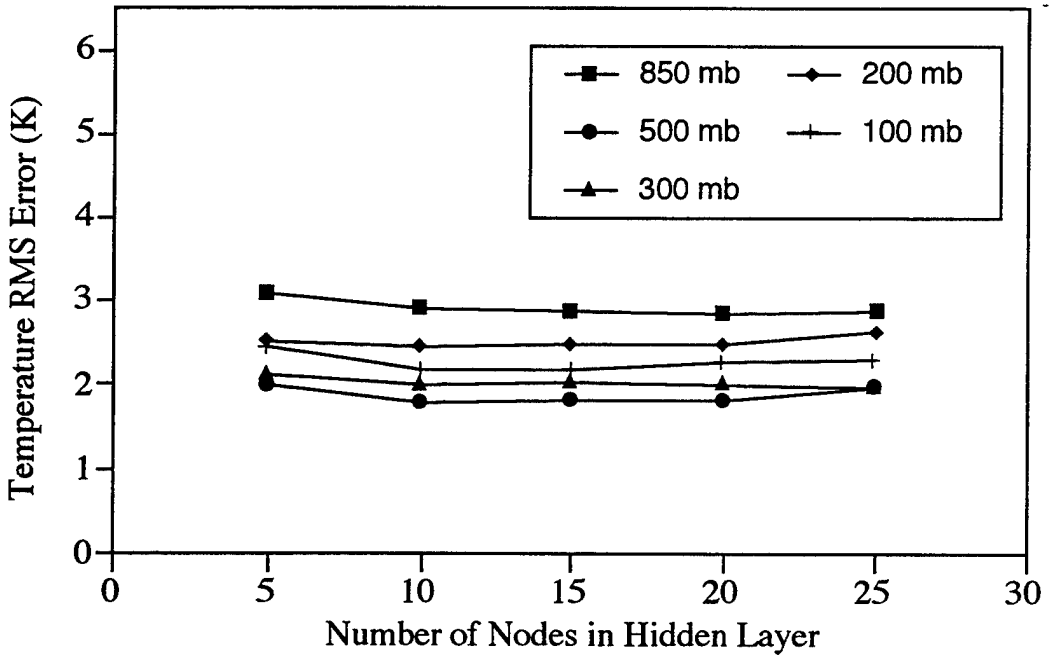


Figure 4. GOES Sounder RMS temperature retrieval error as a function of number of nodes in the hidden layer of the neural network. Ten nodes is the optimum number.

Other network details were also varied. The RMS errors were relatively insensitive to details such as the learning rule and transfer function. The RMS error was < 4 K at the surface and < 3 K at 850 mb. Between 700 and 100 mb, the errors ranged from < 2 K to approximately 2.5 K near the tropopause. These results are somewhat better than those obtained from the TOVS data. In part, this may be because the temporal matching with the rawinsonde data was significantly better. It is noteworthy that the results from both TOVS and GOES data were obtained without the use of a technique for removal of cloud "contamination." In fact, the addition of input to the net in the form of the radiance ratios and differences used in standard "cloud removal" techniques did not noticeably improve the results (Bustamante, *et al.*, 1996a, 1996b). Nevertheless, inclusion of an effective means to significantly reduce the effect of clouds in the field of view, either by pre-processing or within the net input, should lead to better accuracies.

4. FUTURE DIRECTIONS

Our efforts to date have shown the potential utility of neural net methods for retrieval of temperature soundings from meteorological satellite radiances. Further work on refining the method for GOES data should lead to further improvement to the already promising results, and to a more generalized neural network or set of networks where a net is derived for each climate region (Bustamante, *et al.*, 1996a). Extension of the work using polar orbiter data to the microwave sounder (Special Sensor Microwave/Temperature, SSM/T) on the Defense Meteorological Satellite Program (DMSP) satellite has the potential to improve accuracy through the ability to more easily remove cloud "contaminated" radiance profiles. Work by Butler *et al.* (1996) indicated the high accuracy possible with SSM/T data. Also, we plan to develop neural networks for retrieval of dewpoint profiles.

In spite of the progress made herein and elsewhere on retrieval of temperature and humidity profiles from satellite data, extraction of reasonably accurate wind velocity soundings remains out of reach. For most applications average wind speed accuracies of around 8 to 10 ms^{-1} from current techniques (Cogan, *et al.*, 1997) are not adequate. Wind direction errors may reach 90 ° (Jedlovec, 1985) as a result of errors in gradient of geopotential height. Current methods derive winds from geopotential height gradients using, for example, the geostrophic or gradient wind assumption, which in turn are estimated from temperature soundings and surface information (e.g., surface pressure). Cloud tracking is too uncertain and large scale for many applications. However, a neural network approach may allow one to go directly from radiance gradients to wind velocity or wind velocity components. We plan to test the feasibility of such an approach using the data on hand. If the method shows sufficient potential, we will concentrate our efforts on devising an appropriate neural network or set of networks for extracting wind "directly" from satellite sounder radiances.

5. CONCLUSION

We have developed neural networks for retrieval of temperature soundings from radiances gathered by atmospheric sounders on meteorological satellites. Work to date suggests the potential for accuracies equal or somewhat better than that of current methods. The ability to obtain profiles of nearly the same accuracy relative to rawinsondes from a reduced set of sounder

radiances opens the possibility for simpler, less expensive, instruments. Since the method does not use *a priori* information once the net is trained, retrieval of temperature profiles requires fewer computer resources and should produce soundings more rapidly than present techniques. The need for smaller, less expensive, processors and the ability to generate numerous soundings in a relatively short time should make satellite temperature soundings more amenable for a variety of applications. Future work in this area may lead to an operationally capable retrieval package that produces temperature profiles with noticeably upgraded accuracy. Further work may determine the feasibility of deriving wind velocities "directly" from satellite sounder radiances. Potentially, neural network methods may lead to the ability to extract wind profiles that are sufficiently accurate for quantitative uses, such as input to mesoscale models.

REFERENCES

Barnes, James C. and Michael D. Smallwood, 1982. TIROS-N Series Direct Readout Services Users Guide, National Oceanic and Atmospheric Administration, Washington, D.C.

Bustamante, Donald D., Arthur W. Dudenhoeffer, and James L. Cogan, 1992. "Neural Network Retrieval of Atmospheric Profiles from TOVS Radiances," *AIRIES '92: Artificial Intelligence Research in Environmental Sciences*, Monterey, CA, October 27–29.

Bustamante, Donald D., Arthur W. Dudenhoeffer, and James L. Cogan, 1993. "Neural Network Retrieval of Atmospheric Parameters from Meteorological Satellites Using TOVS Data," *Proc. 1993 Battlefield Atmospherics Conference*, Las Cruces, NM November 30–December 2, pp. 743–756.

Bustamante, Donald D., Arthur W. Dudenhoeffer, and James L. Cogan, 1994a. "Retrieval of Atmospheric Thermal Profiles from Meteorological Satellite Soundings Using Neural Networks," *Proc. SPIE Applications of Artificial Neural Networks V*, pp. 562–570.

Bustamante, Donald D., Arthur W. Dudenhoeffer, and James L. Cogan, 1994b. "Comparison of Neural Network Derived Atmospheric Thermal Profiles with Rawinsonde Data," *Proc. 7th Conference on Satellite Meteorology and Oceanography*, pp. 509–511.

Bustamante, Donald D., Arthur W. Dudenhoeffer, and James L. Cogan, 1996a. "Analysis of Neural Network Derived Atmospheric Thermal Profiles," *Proc. IASTED Modeling, Simulation, and Optimization Conference '96*, Gold Coast, Australia, May 6–9.

Bustamante, Donald, James Cogan, and Arthur Dudenhoeffer, 1996a. "Neural Network Retrieval of Atmospheric Temperature Profiles from TOVS Data," submitted to *Met. Applications.*

Butler, Charles T., R. v Z. Meredith, and A. P. Stogryn, 1996. "Retrieving Atmospheric Temperature Parameters from DMSP SSM/T-1 Data with a Neural Network," *J. Geophys. Res.*, 101(D3), pp. 7075–7083.

Cogan, J., E. Measure, and D. Wolfe, 1997. "Atmospheric Soundings in Near Real-Time Using Combined Satellite and Remotely Sensed Ground-Based Data," *Army Research Laboratory Technical Report*, White Sands Missile Range, NM (in press).

Deepak, A., E. Fleming, and I. S. Theon, eds., 1988. *RSRM '87: Advances in Remote Sensing Retrieval Methods*, Deepak Publishing Co., Hampton, VA.

Houghton, David D., ed. 1985. *Handbook of Applied Meteorology*, John Wiley & Sons, New York.

Jedlovec, G. J. , 1985. "An Evaluation and Comparison of Vertical Profile Data from the VISSR Atmospheric Sounder (VAS)," *J. Atmos. Oceanic Tech.*, 2, pp. 559-581.

Rodgers, C. D., 1976. "Retrieval of Atmospheric Temperature and Composition from Remote Measurements of Thermal Radiation," *Rev. Geophys. Space Phys.*, 14(4), 609-628.

Schwalb, Arthur, 1982. *The TIROS-N/NOAA A-G Satellite Series*, NOAA Technical Memorandum NESS 95, National Oceanic and Atmospheric Administration.

Smith, W. L., H. M. Woolf, C. M. Hayden, A. J. Schreiner, and J. M. Le Marshall, 1983. "The Physical Retrieval TOVS Export Package," *Proc. First International TOVS Study Conference*, Igls, Austria, August 29–September 2.

THE ENVIRONMENTAL ELECTROMAGNETIC MODELLING SYSTEM (EEMS) PROJECT OVERVIEW.

David Lewis and Paul Beattie

Maritime Warfare Centre, HMS Dolphin, Gosport, UK

INTRODUCTION.

The EEMS project was set up by the MWC (Maritime Warfare Centre) as a result of a priority one tasking from the UK Royal Navy's Meteorological Staff to develop an operational replacement for the Integrated Refractive Effects Prediction System (IREPS).

Despite having been used operationally by the RN since the early 1980s, IREPS was only ever intended as a technology demonstrator. Although IREPS has been successful, it has several limitations associated with it. These include a lack of terrain handling, an inability to deal with elevated antennae, a limited in its ability to assess effect of rapidly changing refractivity. Perhaps the biggest constraint is that IREPS only provides an indication of presence of anomalous propagation (ANAPROP), this is not of sufficient detail to quantitatively assess the impact of ANAPROP.

Since IREPS there have been many advances in the computational methods available to calculate the effect of the environment on electromagnetic wave propagation, and EEMS is to take advantage of these emerging techniques.*[Lewis and Moore, 1995].*

Since EEMS was always intended to be an operational package it was necessary that it should operate in "real time". For the purposes that EEMS is intended, "real time" means that all calculations and data processing must be completed within an operationally useful time frame *[Moore and Lewis, 1994].* For example if the aircrew of an airborne early warning platform is to be briefed on the likely effects of the environment upon their radar coverage then the output of the tactical decision aids within EEMS must be available in minutes not hours.

The overall aim of EEMS is to provide improved tactical advice by allowing a greater understanding of the effects of the current operational environment on the sensors and communications of the relevant platforms (e.g. air defence units).

THE COMPONENTS OF EEMS

Although EEMS is to be the RN successor to IREPS it is not just a radar propagation model. The radar propagation model (TERPEM TERrain Parabolic Equation Model) is one module within the whole of EEMS. The components that comprise EEMS are an EM propagation model, Tactical Displays, a High Frequency Communications Model, Links to a terrain database/GIS system and an Electro Optic Tactical Decision Aid (EOTDA).

For example, if an operation was taking place in a littoral region the tactical display/GIS system would be used to plot the positions of a task group's platforms. EEMS can then take, directly from the Geographical Information System(GIS) terrain database, all the relevant geographical information to allow the other components to determine the effect of the terrain on sensor/communications coverage. This component of EEMS is still currently under development at MWC.

DEVELOPMENT PHASES

EEMS is to be developed in three phases, the two earlier phases having been completed. An outline of the development phases is given below:

Phase 1 (completed July 95): Includes the prototype radar propagation model and the development of tactical displays.

Phase 2 (completed July 96): Includes enhancements to the radar model and a prototype human-computer interface.

Phase 3 (expected 1997): Includes the HF communications model integration, the interim EO TDA integration and platform stationing and tracking algorithms.

EM-WAVE PROPAGATION MODEL

The principal module within EEMS is the EM-wave propagation model, and as such the choice of the particular model used was of high importance.

In determining the choice several factors had to be considered. Firstly, the output had to be of greater fidelity than IREPS and be able to produce a high degree of user confidence The analysts at MWC were already familiar with tools such as PC-PEM. This model had been extensively used in analysis of naval operations and the fidelity of its' output considered sufficient. The main draw back of this package was the length of time needed to calculate the coverage of radars especially for the case of elevated antennas (typically many hours). For an operational tool then the radar model would have to operate in a time frame that is operationally useful, typically around a minute to calculate the coverage of an airborne radar.

The objective in developing the EM_wave propagation model was to investigate the relationship between accuracy and time- *could a high fidelity solution (e.g. PE models) be made timely and could a fast analytical solution (e.g. ray tracing) be sufficiently precise?*

Approaches using both techniques were considered using the criteria of varying fidelity, range dependency and timeliness. However it was found that neither approach fully met the EEMS performance requirements. Despite this both approaches offered considerable improvement on IREPS.

Consequently it was apparent that a phase of development would be needed to meet the requirements for EEMS .Taking into account the level of fidelity, user confidence and the technical (and financial) risks associated with development it was concluded that the PE-Hybrid approach (TERPEM) would be the most suitable way ahead. The development of TERPEM is described by *Levy and Craig [1996].*

TACTICAL POST PROCESSING AND MEASURES OF EFFECTIVENESS

Typically the output from a propagation model has been presented in the form of a vertical coverage diagram of either path loss or conventional probability of detection. This type of approach allows a subjective assessment of when a target is likely to be detected. For the purposes of platform stationing further processing needs to be carried out in order to provide an objective assessment and degree of confidence in the level of coverage provided by a sensor.

Within EEMS a suite of software has been created to allow a further degree of tactical post processing beyond the traditional probability of detection. This incorporates the dynamic and operator factors that are all part of an operational radar system. Figure 1 below displays all the major components that are part of a radar system.

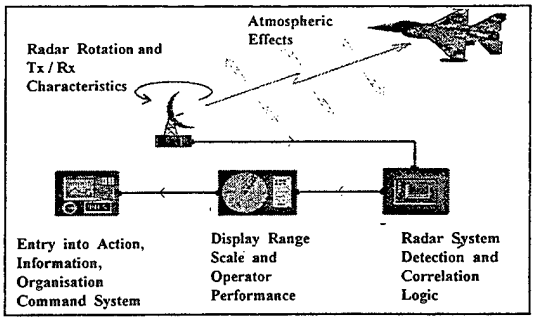


Figure 1: Components of a radar system

For operational assessment a radar system consists not only of the antenna/receiver, signal generator and detection logic but also factors such as the operator performance, and how the information from the operator is delivered to the command team. Until the target details are injected into the action information organisation (AIO) system a response cannot be made. The dynamic nature of an AAW scenario can have a large impact on the detection range as will be shown later.

The software developed to carry out the processing of the radar model output is known as the Target Detection Range Software Suite (TDRSS). The two components of TDRSS are the MWC developed models PRAM (Predator Radar Model) and PREDATOR (Predicted Detection Ranges of Airborne Targets in Operational Regimes). Although detailed in detail *by Williams and Ayoola [1996]* PRAM is essentially a conventional application of the radar range equation using the physical parameters of the system of interest to produce a continuous curve of probability of detection (PoD) against range. PREDATOR is used to consider the dynamic situation by means of a Monte Carlo approach. This includes the effects such as aerial rotation rate, target speed, detection logic and operator factors. The full list of factors included are the radar aerial rotation rate, a valid contact criteria (n returns above threshold OUT OF m sweeps of aerial), the operator efficiency, the operator delays, the radar range scales and the target speed.

By considering the cumulative frequency of detections (number of simulated detections as a percentage of total number of simulations) as a function of range a Tactical Radar Range (TRR)

can be defined. The MWC definitions of PoD and TRR are given below:

Probability of Detection: *the range for a given probability that a static but fluctuating target will be illuminated and provide a paint on an operator's display.*

Tactical Radar Range: *the range, for a given probability, that a valid contact is recognised by the operator and injected into the tactical system.*

In order to appreciate the differences between PoD and TRR (and the advantage TRR provides in terms of platform stationing) it is necessary to examine an example of the type of analysis EEMS can provide.

EXAMPLE OF MEASURES OF EFFECTIVENESS.

For this example the refracting environment is assumed to be a strong low level duct extending up to approximately 300 metres. A surface based antenna is placed within the duct. The path loss was calculated using TERPEM and is displayed below in figure 2.

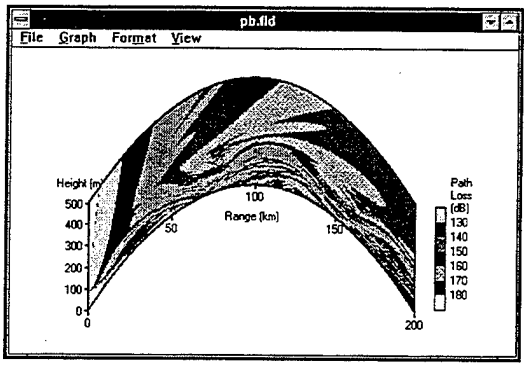


Figure 2: Path loss diagram calculated using TERPEM.

A target is assumed to be flying directly toward the antenna at an altitude of approximately 100 metres. As can be seen from figure 2 extended detection ranges would be expected against low flying targets. However some quantitative estimate of the range at which this target would be detected is required in order to aid a command team to deploy their assets effectively. Traditionally this has been done by application of the radar range equation to calculate the probability of detection as a function of range.

Figure 3 below displays the PoD as a function of range for a target flying toward the antenna at a height of 100 metres. The presence of the duct makes itself felt with the PoD being very discontinuous. This provides a problem in defining a detection range for planning purposes. If a 50% PoD is to be used as the basis of the range then there is an ambiguity as to whether the range is 45 miles or 18 miles. Making a decision as to which range to use means making a subjective assessment, which is to a degree defeating the point of applying a quantitative analysis.

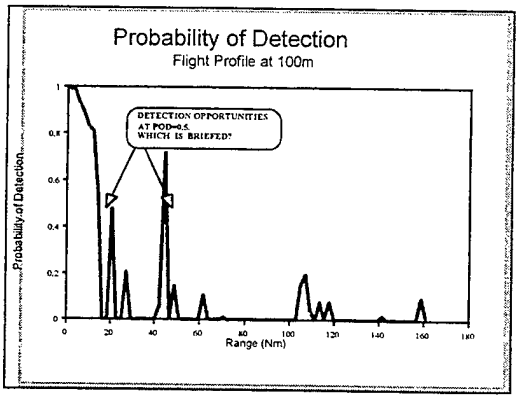


Figure 3 Probability of detection as a function of range.

It is at this stage that PREDATOR would be used to further process the conventional PoD curve to generate a cumulative frequency graph of the number of detections made against range. The effect of including the dynamics of the scenario plus the valid contact criterion is to allow a non-ambiguous single value for the detection range based upon the percentage of targets that would have been detected at that range. If this approach is applied to a smooth and continuous PoD curve as might be expected in standard refracting conditions, the effect is to produce a curve with a profile that tends toward a step function. An example is displayed below in figure 4. This is effectively a "cookie cutter" for the detection range and as such is heavily used in search and screening doctrine to determine optimum asset placement *[United States Naval Institute, 1977].*

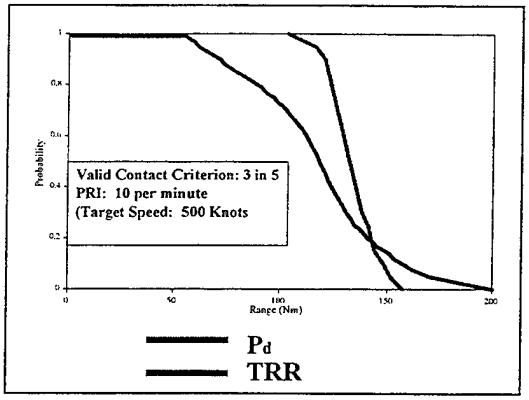


Figure 4 Effect of application of PREDATOR on a smooth PoD curve.

For the problem of a discontinuous PoD curve as in figure 3, the application of PREDATOR is particularly useful. Since the dynamics of the situation are now being considered it enables the command team to appreciate the impact of these dynamics upon the tactical situation. In figure 5 below the TRR curves for a target travelling at 100 knots and at 600 knots are overlaid on the PoD curve. As can be seen the slow moving target presents enough opportunities for illumination around 110 NM that by this range 50% of the targets would have been detected and the radar operator alerted. The fast moving target however has usually passed through the small detection possibility at 110 NM and usually isn't recognised until approximately 45 NM. Being able to consider such factors can have a major impact on the stationing of assets. In a simplistic approach it could be said that if the threat is expected to be relatively slow then assets could be spread further since the TRR for this threat larger. For the 600 knot target units would have to be placed closer together to provide seamless coverage.

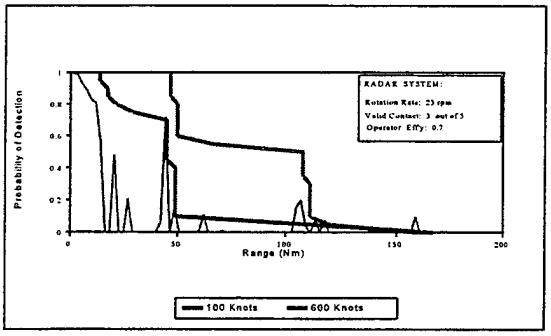


Figure 5 Effect of target speed on Tactical Radar Range

This approach makes the assumption that the target is flying directly toward the antenna. This may be a reasonable assumption if the antenna happens to be attached to the mission essential unit in a task group. A more likely scenario is that the TRR for an air defence ship is going to be needed against a crossing target. Modifications have already been made to the components of EEMS to take into account changing aspect of target and the other factors needed to assess the coverage against crossing targets.

HF COMMUNICATIONS MODULE

The HF communications model is derived from JIVE (Jamming Interception Vulnerability Estimator) which was originally developed at DRA Malvern. The details of this module are detailed by *Moore and Shukla [1996]* and *Shukla et al [1996].*

LINKS TO TERRAIN DATABASE

When conducting littoral operations the ability to predict inshore/overland radar/radio coverage is essential, hence terrain features are an important data requirement. Phase three of EEMS will incorporate a GIS system which will provide all necessary geographical information. The tactical displays and terrain database will provide both a visual display of sensor/communication coverage and act as a method of defining the scenario, in effect acting as both the input and output of EEMS.

ELECTRO-OPTIC TDA

The Electro-Optic Tactical Decision Aid (EO TDA) is being sourced via an international exchange program with the US Navy.

FUTURE DEVELOPMENTS

The prime reason for presenting the coverage as the Tactical Radar Range is to enable the command team to deploy their assets to their best advantage. As mentioned above, the single valued nature of the TRR allows the coverage range for an acceptable confidence level (for example 95% of targets will have been recognised and the unit alerted) to be considered as a "cookie cutter". This can be used to simply display this coverage visually and overlay on some form of map display (see figure 6).

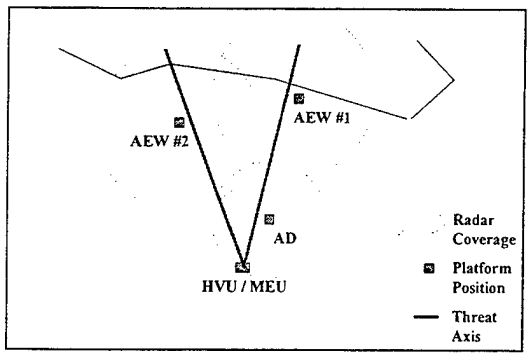


Figure 6: Platform stationing using TRR to define a simple "cookie cutter".

The underwater warfare community has for many years used the Tactical Sonar Range (TSR), and using this range developed many useful search and screening type doctrine. The tools are now available in the above water warfare world to be able to take account of the environment and determine its' impact on sensors and consequently tactics. By making use of concepts such as TRR it is now possible to make use of the lessons learnt in the underwater world, and their ability to exploit the environment to their advantage, and use them for a fresh approach to above water warfare doctrine and analysis.

SUMMARY

The EEMS project is aimed at providing the above water community with a tool that enables the command team to exploit the environment to their advantage. The final product will allow the user to determine the coverage of both radar and electro-optic sensors and the coverage of radio communications. By incorporating concepts such as TRR with modern GIS systems, classical search and screening doctrine can be applied and optimised to the above water environment. This can be used for optimal asset deployment.

REFERENCES

Williams M. and Ayoola A., "Blue Water EEMS - TDRSS", *Battlespace Atmospherics Conference, San Diego, US,* 1996

Levy M. F. and Craig K. H.,"TERPEM propagation package for operational forecasting with EEMS", *Battlespace Atmospherics Conference, San Diego, US,* 1996.

United States Naval Institute,"Naval Operations Analysis", *ISBN 0-87021-440-3,* 1977.

Lewis D. and Moore M., "EEMS Phase 1 EM-Model Evaluation", *MoD Report (Unpublished),* 1995

Moore M. and Lewis D., "Operational Sensor Performance Prediction and Analysis". *AGARD Conf. Proc. 567, "Propagation Assessment in Coastal Environments.",* 1994.

Moore M. R. and Shukla A. K., "High Frequency Coverage Predicion for EEMS", *Battlespace Atmospherics Conference, San Diego, US,* 1996.

Shukla A., Cannon P. and Moore M., "A HF Tactical Decision Aid for Conventional and Automated Radio Control Systems", *Battlespace Atmospherics Conference, San Diego, US,* 1996.

METEOROLOGICAL SUPPORT FOR UK NAVY OPERATIONS

S J Moss and A C Steele

Meteorological Office, London Road, Bracknell, Berks, RG12 2SZ, U.K.

1. INTRODUCTION

Atmospheric refraction effects are well known to the Royal Navy (RN) as a factor that can dramatically affect the performance of radars, giving extended ranges in ducting conditions and reduced ranges in sub-refracting conditions. The RN currently use IREPS (Integrated Refractive Effects Prediction System) operationally to predict radar performance. This system uses a single radiosonde ascent to represent the propagating environment. This is then used to calculate the predicted radar coverage.

Since 1990 the RN have also been using a PC-PEM (Parabolic Equation Method), which was developed by Rutherford Appleton Laboratory, in addition to IREPS to support radar propagation and modelling and range prediction. This model is described by Craig and Levy (1989) and was found to give reliable propagation predictions.

The accuracy of both the PC-PEM and IREPS models is limited by the quality of the available meteorological data. Radiosonde ascents are routinely made at 6 hourly intervals (4 per day) from 8 locations around the UK (in addition to several sited in Europe). No data are routinely available over the sea, and the spatial resolution is relatively poor. This means that the most appropriate ascent available for a specific forecast of radar propagation may be hundreds of kilometres from the operating area, and several hours old. To overcome these problems a study was carried out to investigate the possibility of using UK Met Office Mesoscale Model output, in conjunction with a PE model for forecasting radar performance.

2. THE MET OFFICE MESOSCALE MODEL

The Met Office Mesoscale Model (MM) forms an integral part of the operational Unified Model (UM) suite which is run routinely by the Met Office at Bracknell. The UM suite, which has been described by Cullen (1993), consists of global, limited area and Mesoscale versions of the Unified Model. The Mesoscale version of the model has a grid length of 0.15° (about 17 km) on a 92×92 grid covering an area of about 1500 km×1500 km and has 31 levels up to 4.6 mb. In the lower atmosphere, which is the region of interest for radar propagation predictions, there are 11 levels below 1500 m. These are shown in Table 1, where the heights are approximate since the levels are defined using a hybrid sigma/pressure co-ordinate system.

The MM can be run for a number of relocateable windows, a standard version is run for the UK, and two 'crisis-area' models can also be run at the same time. Currently the model is run for the Gulf and the region around the former Yugoslavia.

Level	Height (m)	Level	Height (m)
0	0	6	435
1	10	7	595
2	40	8	770
3	100	9	955
4	190	10	1155
5	300	11	1365

Table 1. Approximate heights of levels below 1500 m in the Met Office MM.

A joint trial between the Met Office and the Royal Navy Fleet Weather and Oceanographic Centre (FWOC) was carried out in the summer of 1994, in the Adriatic, to assess the usefulness of the MM forecasts for predicting radar ducting. Full details of this trial are given in Tunnicliffe *et al.* (1994).

3. PREDICTION OF PROPAGATION CONDITIONS

During the period of the trial radiosonde ascents were made from a ship at sea at 00Z and 12Z. These data were then compared with MM data for the nearest grid point to the ship. Initially the propagation conditions at low levels were diagnosed from both the model and actual profiles, and the results were compared. Comparisons were made for (i) surface evaporation ducts and (ii) other ducts.

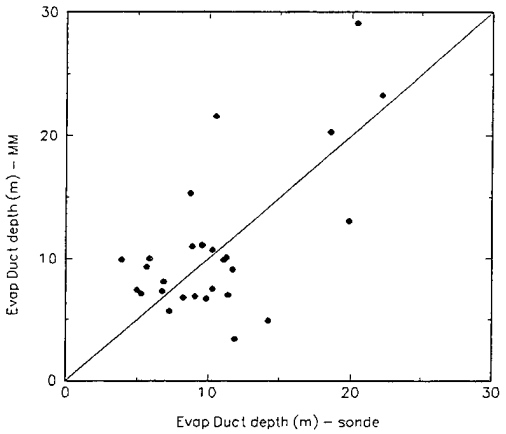


Figure 1. Comparison of derived evaporation duct depths from radiosonde and MM data.

Evaporation ducts were diagnosed from the radiosonde profiles using the evaporation duct model in the IREPS PC-2.0 software. This gave duct depths ranging from 4 m to 22 m. Evaporation duct depths were similarly diagnosed from the MM data by inputting the predicted surface parameters. The results gave a mean depth error of +0.3 m, with an rms error of 4.7 m. These results, shown in Figure 1, suggest that reasonable predictions of evaporation duct depth can be determined from the MM.

The other ducts considered were those ducts which were all, or part, found below 1000 ft; this being the region of the atmosphere which is most important to RN radar operations. The results are summarised in the matrix in Table 2. This shows that ducting conditions occurred on 82% of all occasions. Clearly the MM is capable of predicting low level ducts, although it often misrepresented the duct structure since it tended to predict simple surface ducts rather than the S-shaped structure which generally occurred.

The MM forecasts were also compared to predictions based on persistence (i.e. assuming conditions are unchanged from the previous radiosonde ascent when it was no more than 24 hours old). The predictions based on persistence have a very good 'hit rate', however they exhibit a much larger 'false alarm rate' than the MM forecasts. The forecast methods were compared by means of a 'skill' parameter, where the skill score lies in the -100% to +100%, where 0 would result from a random forecast. The skill score from the above cases for persistence predictions is -4%, whereas the skill score for the MM predictions is 45%.

MM	Radiosonde				
	Nil	Simple	S-Shaped	Elevated	All
Nil	4	0	7	1	12
Simple	1	0	8	0	9
S-Shaped	0	0	5	0	5
Elevated	0	0	1	1	2
All	5	0	21	2	28

Table 2. Ducting conditions matrix for MM forecasts.

3.1 RADAR RANGE PREDICTIONS

Whilst the above results have examined the capability of the MM for refractivity forecasting and determining the propagation conditions, it can be argued that it is operationally more relevant to judge the MM on its usefulness for making radar range predictions. Therefore range predictions were made with the RN's version of the PC-PEM using both the predicted (mm) and actual conditions.

Figure 2 shows examples of the predictions from PC-PEM for midday on 3 June 1994. The three grey shades correspond to detection ranges for small, medium and large targets. The example on the left shows a prediction using an actual ascent. In this case a strong duct some 580 ft deep was

evident, giving extended ranges. The MM forecast suggested a duct of a similar depth, although the predicted duct was much weaker than that observed.

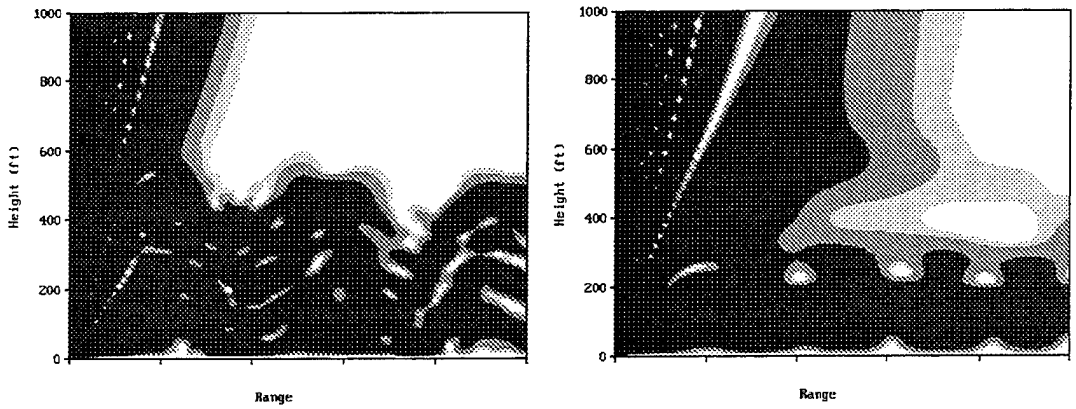


Figure 2. PC PEM coverage displays based on (left) measured radiosonde data and (right) MM forecast.

3.2 RANGE DEPENDENCY

So far the refractivity predictions from the MM have only been compared to single point measurements made from a ship. However, in such a coastal environment the structure of the boundary layer will be modified across the land/water transition. This may lead to significant range-dependent behaviour such that the radar coverage predictions based on a single profile can sometimes be misleading. The coverage of a ship-borne radar looking towards land (and also a coastal radar looking out to sea) will often be affected by a range dependent environment. This includes both the effect of the changing surface (sea/land), terrain effects (Levy, 1993) and a range dependent atmospheric structure.

An example illustrating the type of range dependent behaviour that can be predicted by the MM is given here. In this case, from midday on 3 June 1994, the MM prediction showed good agreement with the measured profile from the ship. The MM suggested a surface based duct 190 m deep and the observations showed a surface S-shaped duct of 177 m depth. There was also a shallow near surface evaporation duct embedded within the ducting layer. Figure 3 shows the modified refractivity profiles along a line crossing the Dalmatian coast. The profiles have been offset by 100 M-units for clarity. This line, defined by 3 grid points, was about 96 km long and virtually perpendicular to the coastline, which coincides with the right-most profile in Figure 3. Here the model coast line is quite simple, whereas the actual coastal region in this area is a complex network of islands and peninsulas.

In this example the structure of the ducting layer in the MM changes significantly as the land is approached. The simple surface duct becomes S-shaped as the base of the trapping layer rises and the duct detaches from the ground (i.e. it becomes an elevated duct) before the coastline is reached. The duct also weakens as the coast is approached. On this occasion the whole area was

under a large anticyclone extending across the Mediterranean and the Black Sea, with a moderate SSW'ly breeze (i.e. blowing along the coastline).

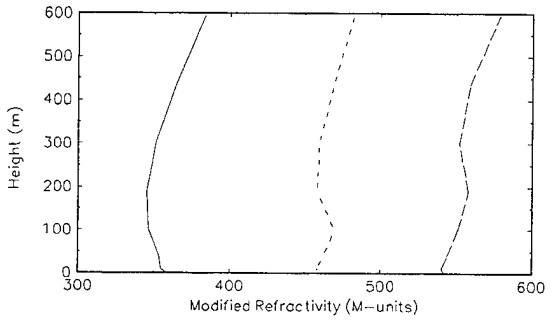


Figure 3. MM predicted modified refractivity profiles along a line perpendicular to the coast line (for midday on 3 June 1994)

Although the above shows that the MM is capable of resolving range dependencies in a coastal environment, the accuracy of the predictions is unknown at present, since there are no measurements with which to compare the MM. To overcome this problem the Meteorological Support Group (MSG) of the MOD have sponsored aircraft flights by the Met. Office Meteorological Research Flight (MRF) C-130 Hercules in coastal areas. The MRF C-130 is a fully instrumented Hercules, which is capable of measuring a full range of meteorological parameters including; temperature, dew point, pressure, wind speed and direction, cloud physics, radiation, and atmospheric chemistry. It has a long (12 hour) endurance; a 5000 km range and a ceiling of 10000 m.

Two flights will be carried out over the south east coast of England (East Anglia), as shown in Figure 4. This area has been chosen because of the proximity of the coastal radiosonde station at Hemsby. The data from the radiosondes will give information on the structure of the atmosphere over the land. The C-130 will measure the structure of the atmosphere over the sea and coastal regions. The flight will include profiles over the sea from above the boundary layer to 50 ft above sea level. 50 km straight and levels runs will also be carried out perpendicular to the coast. These will be carried out at various heights, ranging from 100 ft above sea level to the top of the boundary layer. Runs above 250 ft will be continued for 30 km inland (250 ft is the lowest permitted altitude for flights over land).

In addition to the two flights off the south east coast of England, the MSG are also sponsoring 20 flying hours for a European experiment called Variability of Coastal Atmospheric Processes (VCAP). This experiment is part of the Scientific Training and Access to Aircraft for Atmospheric Research Throughout Europe (STAAARTE) programme. The flights will follow a similar pattern to the UK flights, but they will be located off the coast of Sweden. This experiment will take place in April/May 1997. The operating area for the VCAP flights are also shown in Figure 4.

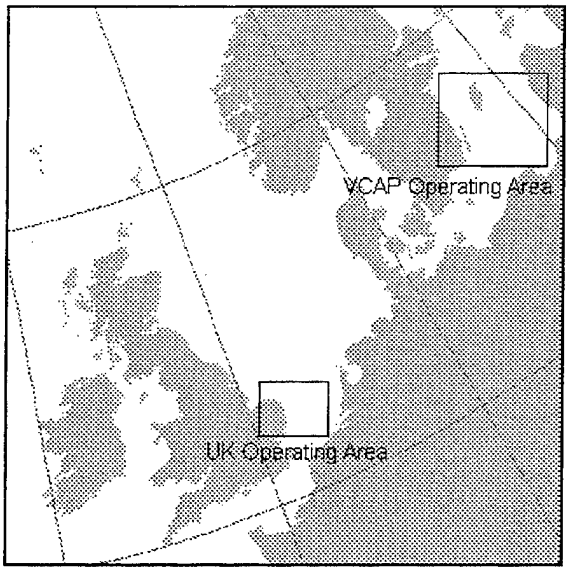


Figure 4. C-130 operating areas for UK and VCAP flights.

These flights will enable the detailed measurement of the structure of the coastal environment to be made. The results can be compared with the MM output to determine if the MM performs sufficiently well in coastal regions. The results will also be used to determine how to interpolate between MM grid points in littoral environments (see section 4).

4. ENVIRONMENTAL ELECTROMAGNETIC MODELLING SYSTEM

The above results have illustrated that the MM can be used in conjunction with a PE model to give reliable predictions of the propagation environment. Additionally the MM is able to model changing refractivity conditions in littoral regions. However, the RN have an operational requirement for a fast, accurate RF/microwave prediction system able to model propagation in the littoral environment over mixed (land/sea) paths. Neither the IREPS nor the PC-PEM models meet this requirement. The IREPS model cannot take account of a range dependent environment, and PE models are generally too slow to be used operationally in real-time.

To overcome this problem, the RN have embarked on a project to develop a timely, high fidelity, fully range dependant electromagnetic/electro-optic modelling system. The new model, called EEMS (Environmental Electromagnetic Modelling System), is being developed in collaboration with the Maritime Warfare Centre (Gosport), Signal Sciences Ltd (UK) and the Meteorological Office. EEMS will include an advanced RF propagation model which can take account of a range dependent environment, and it will have links to a terrain database. To overcome the problem of the amount of processing time required for full PE models, a combined PE/ray optics model has been developed (by Signal Sciences Ltd.). Only regions where the full detail is required are processed with PE models, with the other regions being treated with simpler and faster ray optics techniques. This hybrid model is described in more detail by Levy and Craig (1996).

The Met. Office are developing a meteorological pre-processor for EEMS. MM data for the Adriatic is being used for development purposes. The ideal position would be to have all model grid points at all levels for the whole model area at 6 hour intervals to T+24. However, this would involve vast amounts of data which could not be transmitted in a timely manner. As a compromise, a subset of the MM area will be extracted; either a small area, or a larger area with a coarser resolution (i.e. every other grid point) would be available. Data retrieval will be carried out via a PC program. A prototype of the user interface is illustrated in Figure 5. The user will be able to use the mouse to locate the ship's position and the bearing of interest (the 'threat axis').

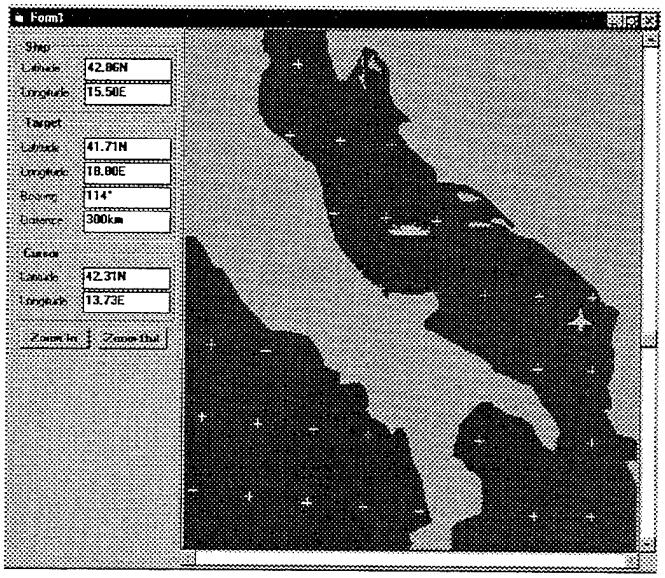


Figure 5. Prototype of the user interface for the EEMS met. pre-processor.

Environmental profiles will be calculated for points at specified intervals along the threat axis. Initially the nearest MM grid point to each point on the threat axis will used. This method should give a good indication of the range dependency along the threat axis. In littoral regions, this approach may not give the best representation. For example, a point on the threat axis may be over the sea while the nearest grid point may be over the land. In this case, the environment may differ greatly from the specified point on the threat axis to the nearest grid point.

To overcome this problem, it is planned to include an interpolation scheme between the surrounding grid points to give a series of derived profiles which lie along the line of the threat axis. Some of the possible interpolation techniques which are being considered are;

(i) a simple linear or quadratic interpolation, and
(ii) the Refractivity Structure Matching Algorithm (RSMA), developed by the Naval Research Laboratory (NRL) and Analysis & Technology, Inc, Monterey.

It is possible that the best method may differ for different environmental conditions. For example, in a truly maritime environment, the boundary layer will not vary greatly from one grid point to another, so a simple linear interpolation between the points may prove to be sufficient. However

in the coastal regions, the boundary layer is likely to change significantly from one grid point to another, especially if the grid spacing spans the sea/land interface. In these cases a more complex interpolation, perhaps linked with the RSMA technique may be necessary. The results from the C-130 flights will be used to determine the most appropriate interpolation technique for the MM in the various environments.

5. REFERENCES

Craig, K.H. and M.F. Levy, 1989: A forecasting system using the parabolic equation—application to surface-to-air propagation in the presence of elevated layers. *In the NATO AGARD conference proceedings No. 435, 'Operational decision aids for exploiting or mitigating electromagnetic propagation effects.'*

Cullen, M.J.P., 1993: The unified forecast/climate model. *Meteorol. Mag.*, **122,** 81–94.

Levy, M.F., 1993: Combined effects of atmosphere and terrain on UHF/microwave paths. *In the NATO AGARD conference proceedings, No 543, 'Multiple mechanism propagation paths, their characterisation and influence on system design'.*

Levy, M.F. and K.H. Craig, 1996: Hybrid models for operational EM forecasting with EEMS. *In the proceedings of the IEE colloquium on common modelling techniques for operational EM forecasting techniques for E-M wave and acoustic wave propagation. 8 March 1996.* **96/055,** 2/1–2/6.

Tunnicliffe, Lt Cdr P., Lt Cdr B. Robinson, Cdr S. Bevan and J.D. Turton, 1994: An assessment of the operational potential of the Meteorological Office Mesoscale Model for predicting Royal Navy radar performance. *In the NATO AGARD conference proceedings,' Propagation assessment in coastal environments.* NATO RESTRICTED.

TERPEM PROPAGATION PACKAGE FOR OPERATIONAL FORECASTING WITH EEMS

M.F. Levy and K.H. Craig
Signal Science Ltd and Rutherford Appleton Laboratory
Chilton, Didcot, Oxon OX11 0QX, U.K.
Tel: +44 1235 446522, Fax +44 1235 446140
e-mail: m.levy@rl.ac.uk

INTRODUCTION

Electromagnetic sensors in the 30 MHz to millimetre wave frequency range are affected by refractive effects in the troposphere and by diffraction and reflection due to terrain. Defence applications require fast and accurate propagation models for operational EM forecasting. The TERPEM propagation package has been commissioned by the Royal Navy for inclusion in its electromagnetic forecasting tool EEMS (Environmental Electromagnetic Modelling System) [1]. The TERPEM propagation models are based on the hybrid model approach, which provides fast computation while retaining high fidelity of the results.

TERPEM includes a Windows or Windows 95 interface allowing easy parameter input and flexible display options. The general structure of the package is shown in Figure 1. The first release of EEMS does not include a terrain interface, and terrain profiles must be provided by the user. A full geographical information system interfacing with DTED will be provided at a later stage.

The main output of TERPEM is a two-dimensional path loss array, which can either be displayed as a coverage diagram or used for extraction of path loss values along a user-defined trajectory. Path loss values along a trajectory can be displayed or passed to the TDRSS radar performance analysis suite [2] for postprocessing. Figure 2 shows a general view of the TERPEM interface products.

METEOROLOGICAL MODELS

TERPEM includes several options for entering upper-air and evaporation duct data at a given range. Upper-air data can be entered manually or read from a file, and are accepted in several forms (WMO code, refractivity or modified refractivity versus height, pressure-temperature-relative humidity versus height). Alternatively a standard well-mixed atmosphere model with a user-defined k-factor can be used. Evaporation duct data can be entered as duct height, or via the bulk parameters (sea temperature and air temperature, humidity and wind speed). In the latter case the full Battaglia model is used to calculate the low-level refractivity profile, taking boundary layer stability into account. It is also possible to suppress the evaporation duct if desired. A merging algorithm is used to combine smoothly the evaporation duct and upper-air data. An overview of the meteorological module is given in Figure 3.

Range-dependent options include the possibility of feature interpolation between vertical profiles, allowing for example the modelling of sloping ducts, or of step changes when a new profile is encountered. At a later stage in EEMS development, range-dependence capabilities will be extended using the mesoscale model interface developed by the Meteorological Office [3].

TERPEM HYBRID PROPAGATION MODELS

The parabolic equation (PE) method has for some years been the preferred technique for solving the wave equation in complex tropospheric environments. When backscatter can be neglected, the one-way PE provides a rigorous full-wave solution incorporating both atmospheric and terrain effects [4,5]. However integration times can become too long for operational use when the solution is required at high altitudes and for large propagation angles. It turns out that in most tropospheric environments, the full power of the PE is unnecessary for large angles and heights. The idea of using faster techniques in these regions was pioneered by Herb Hitney with RPO (Radio Physical Optics) [6]. RPO is an excellent model for oversea propagation, currently restricted to source heights below 100 m.

Since EEMS must have the capability to model coastal or land environments, and must not be limited to low sources, the TERPEM models had to add new building blocks to the basic RPO concept. One major change is the use of the horizontal parabolic equation (HPE) method instead of extended optics to extend the coverage diagram upwards [7]. HPE is a rigorous full-wave solution to the wave equation, which calculates the field above a certain height from known values at that height. Terrain and range-dependent refractivity features below the threshold height can be handled without difficulty. The numerical HPE solution is based on Fast Fourier Transforms in the range variable. Another important novel feature is the use of incoming energy PE techniques to model high antennas while keeping integration times small.

Figure 4 shows the regions of the coverage diagram where the different models are used. The flat Earth (FE) and ray-optics (RO) models are adapted from RPO. Once the limiting height **zlim** for the PE domain is chosen, angle **psilim** is calculated as a function of frequency and the environment in order to ensure that rays launched from the source and hitting the ground at angles greater than **psilim** will neither be affected by terrain diffraction nor trapped by ducting layers. The vertical parabolic equation (VPE) region includes trapping layers and terrain.

Any vertical PE algorithm may be used in the VPE region. Since speed is the prime consideration here, we have opted for the Fourier/split-step algorithm, based on a sine transform for smooth perfectly conducting terrain and on the mixed transform [8] for more general cases. Terrain is modelled as a sequence of horizontal steps rather than with the more time-consuming conformal mapping approach [9]. An absorbing layer is added at the top of the VPE domain to avoid parasitic reflections.

The mixed transform option allows the modelling of finite-impedance boundaries, giving accurate results for vertical polarisation. TERPEM also allows the modelling of sea-surface roughness, using a model based on wind speed to compute a range-dependent effective

impedance which is then used to calibrate the mixed transform [8]. Local angles of incidence are computed with geometrical optics. Roughness effects can be severe, as shown in Figure 5.

TERPEM includes an atmospheric absorption calculation based on the line-by-line MPM model. In the current release, the pressure, temperature and humidity for the MPM calculation are assumed independent of range and height, in order not to complicate the input interface. Full height and range specification, which could be important for some millimetre-wave applications, will be available at a later stage.

HIGH ANTENNAS

If no extra ingredient is used, the VPE region must include the source, and hence integration times and memory requirements can become prohibitive for airborne systems. Recent work on non-local boundary conditions [10,11] demonstrated that with finite-difference implementations of the PE, the VPE domain can in fact be truncated cleanly at any height above which the propagation medium becomes fully upwards transmitting (no energy coming from below is bent back downwards).

Recent developments have produced a split-step/Fourier version of the rigorous non-local boundary condition approach. The basic idea is to look at the solution that would be obtained by putting a perfect mirror at the upper boundary, and to compare it to the wanted solution (i.e. without the mirror). Incoming energy is fed in through the discontinuity caused by the mirror. It is added at each step via multiplication with a suitable kernel. This technique requires knowledge of the mirror solution. For some cases (linear medium above the boundary and Gaussian source), this can be obtained in closed form. The more general solution adopted for TERPEM is to use ray-optics, with a suitable filter the avoid a brutal cut-off at the optical horizon. Figure 6 shows a schematic of the incoming energy PE approach for high antennas. The angular domain for the VPE region is kept to the minimum required for accurate treatment of ducting layers and terrain, and ray-optics are used for larger angles.

With this technique, the VPE domain does not depend on source height, but only on environmental constraints. A matching generalized HPE technique is available to extend the solution upwards if required. The resulting algorithm is very efficient since the VPE region is usually limited to a few hundred metres above the surface, and propagation angles generally remain small at these low heights. If only low altitude coverage is required, the HPE stage can be skipped, thus giving further speed-up since the range-step constraints are then relaxed. Integration times can be reduced even further if near-horizon coverage is the main application, since integration can then start at near-horizon ranges. In all cases, comparison with a pure VPE method gives near-perfect agreement.

Figure 7 shows the coverage diagram of a 10 GHz source at altitude 3000 ft with an elevated duct. This was obtained in less than a minute on a 100 MHz Pentium machine, compared to about 10 minutes with the standard VPE method where the domain must include the source. The VPE/HPE threshold height for this case was 1320 ft. A comparison with the standard VPE method at a range of 150 nmi shows excellent agreement.

Figure 8 shows the coverage diagram of a 3 GHz airborne source at altitude 30000 ft with multiple ducts and hilly terrain. This was obtained in less than 2 minutes, compared to about 30 minutes with the standard VPE method. The VPE/HPE threshold height for this case was 4350 ft.

INTEGRATION TIMES

Integration times depend mainly on frequency, maximum range and environmental parameters. The dependence of integration times on domain size is roughly linear on maximum range, and logarithmic on maximum height, while the dependence on frequency is approximately linear. The main environmental constraints are the height of trapping layers and the maximum terrain height. The influence of antenna pattern is negligible, and with the new incoming energy models, antenna height is not a major concern. The use of the mixed transform for roughness or vertical polarisation modelling adds an overhead of roughly 50% to the VPE computation time. Table 1 gives typical integration times on a 100 MHz Pentium desktop computer.

Table 1: Typical TERPEM integration times

Freq	Tx height	Max range	Max height	Environment	Time
3 GHz	80ft	100nmi	5000ft	evaporation duct oversea	4s
10 GHz	80 t	100nmi	5000ft	evaporation duct oversea	10s
3 GHz	80ft	150nmi	5000ft	surface duct coastal terrain	30s
10 GHz	80ft	150nmi	5000ft	surface duct coastal terrain	1min
3 GHz	30000ft	250nmi	30000ft	multiple ducts mountains	5min
10 GHz	3000ft	150nmi	5000ft	elevated duct oversea	2min

CONCLUSIONS

The hybrid models described above provide a robust and fast solution for EEMS requirements, giving accurate propagation assessment including terrain and refractive effects for both surface and airborne antennas. Current work focuses on the rigorous treatment of finite impedance and rough surfaces with generalised impedance techniques, and on the modelling of clutter.

ACKNOWLEDGEMENTS

This work was carried out with the the support of the Royal Navy and of the Radiocommunications Agency of the DTI.

REFERENCES

[1] D.J.W. Lewis and P. Beattie, "The Environmental Electromagnetic Modelling System (EEMS) project overview", BAC 96.

[2] M. Williams and A. Ayoola, "IT implementation of blue water EEMS - TDRSS", BAC 96.

[3] S.J. Moss and A.C. Steele, "Meteorological support for UK Navy operations", BAC 96.

[4] K.H. Craig and M.F. Levy: "Parabolic equation modelling of the effects of multipath and ducting on radar systems", IEE Proc-F, Vol 138, pp 153-163, 1991.

[5] A.E. Barrios: "A terrain parabolic equation model for propagation in the troposphere", IEEE Trans. Ant. Prop., Vol 42, pp 90-98, 1994.

[6] H.V. Hitney: "Hybrid ray-optics and parabolic equation methods for radar propagation modeling", Proceedings of Radar 92, IEE Conf. Pub No 365, pp 58-61, 1992.

[7] M.F. Levy: "Horizontal parabolic equation solution of radiowave propagation problems on large domains", IEEE Trans. Ant. Prop., Vol 43, pp 137-144, 1995.

[8] G.D. Dockery and J.R. Kuttler, "An improved impedance boundary algorithm for Fourier split-step solutions of the parabolic wave equation", IEEE Trans. Ant. Prop., Vol 44, No 12, 1996.

[9] A.E. Barrios: "Terrain and refractivity effects on non-optical paths", AGARD CP No 543, Paper 10, 1994.

[10] M.F. Levy: "Fast PE models for mixed environments", AGARD CP No 567, Paper 18, 1995.

[11] M.F. Levy: "Transparent boundary conditions for parabolic equation solutions of radiowave propagation problems", IEEE Trans. Ant. Prop., Vol 45, pp 1-7, 1997.

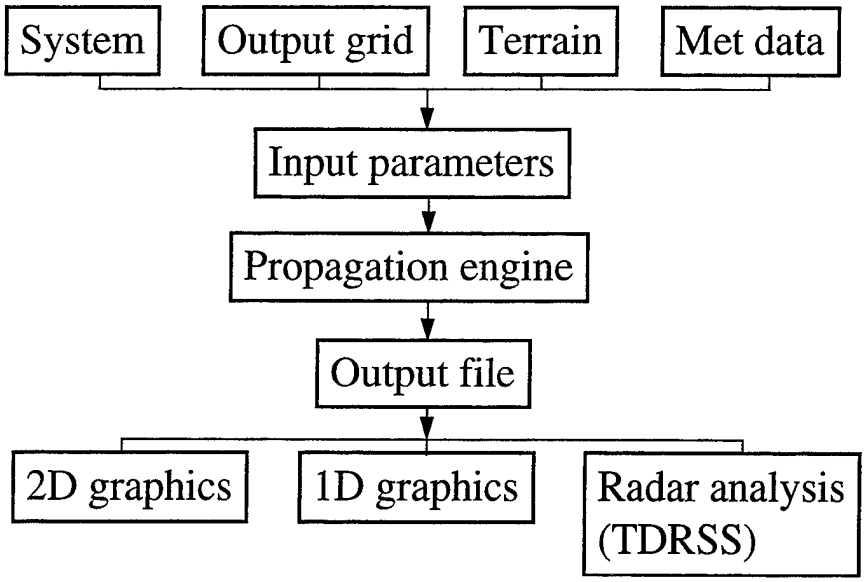


Figure 1. TERPEM structure

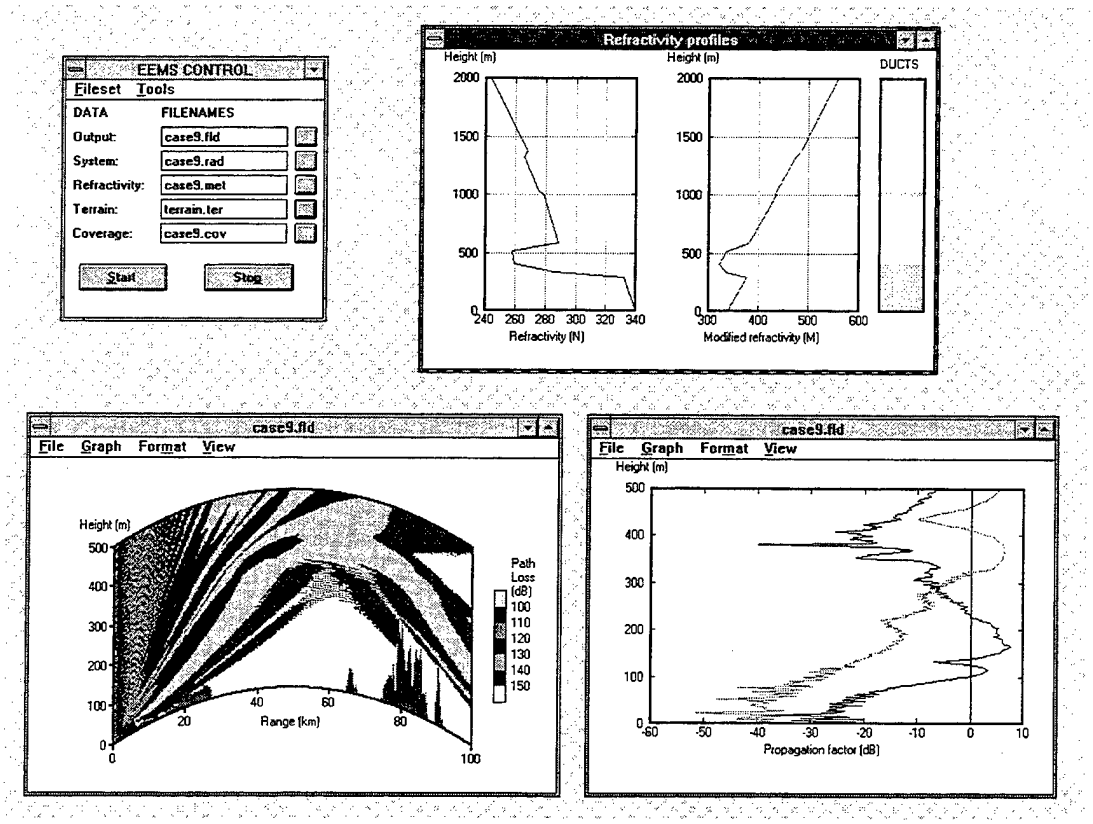


Figure 2. Overview of TERPEM interface

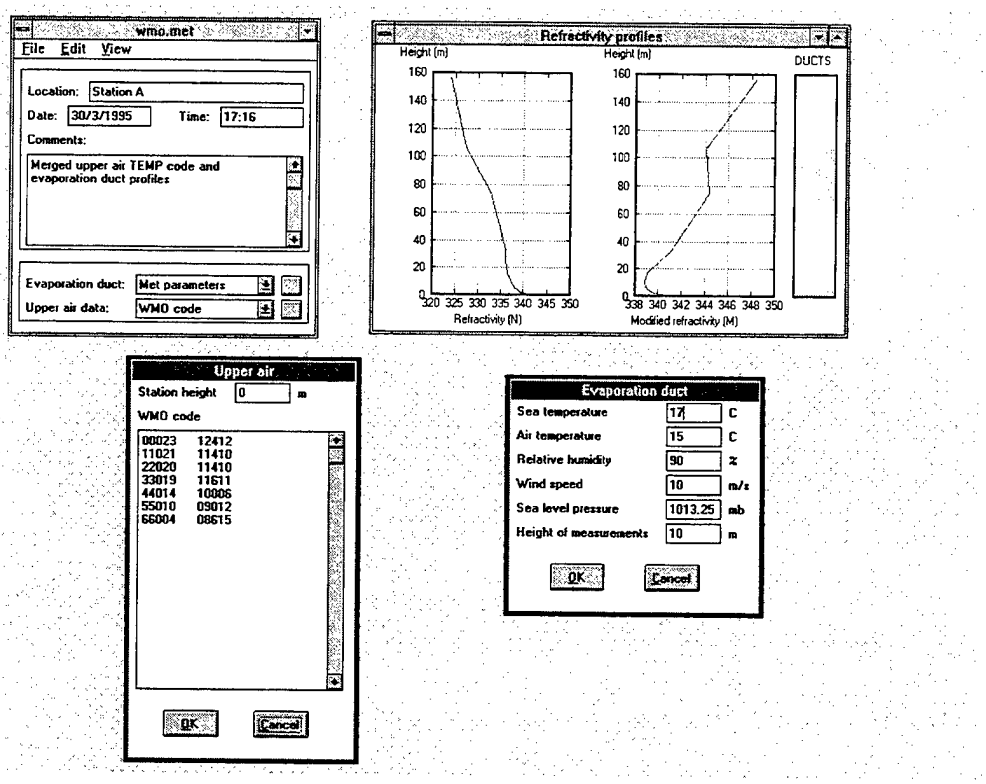


Figure 3. TERPEM meteorological module

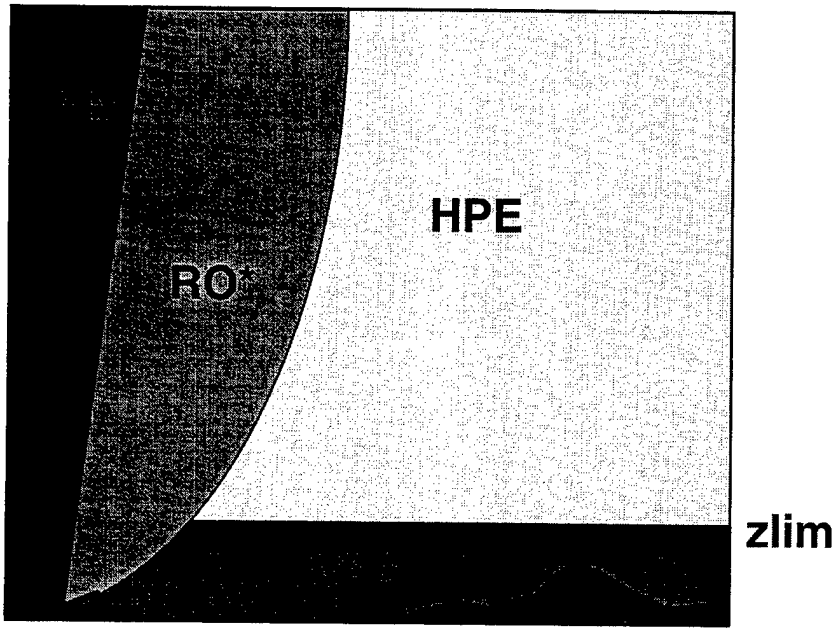
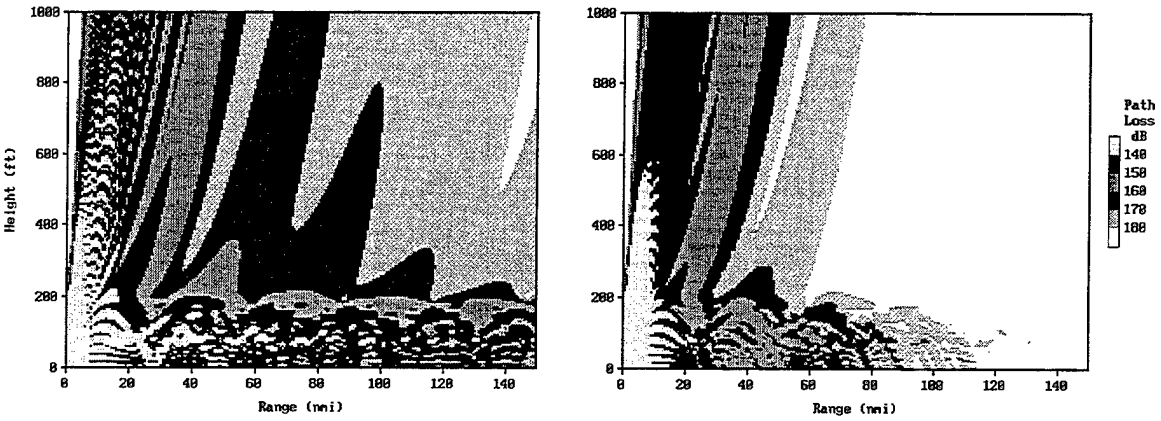


Figure 4. TERPEM regions for hybrid models.



Smooth sea

Rough sea (wind = 14m/s)

Figure 5. Rough sea effects for X-band antenna in strong surface duct.

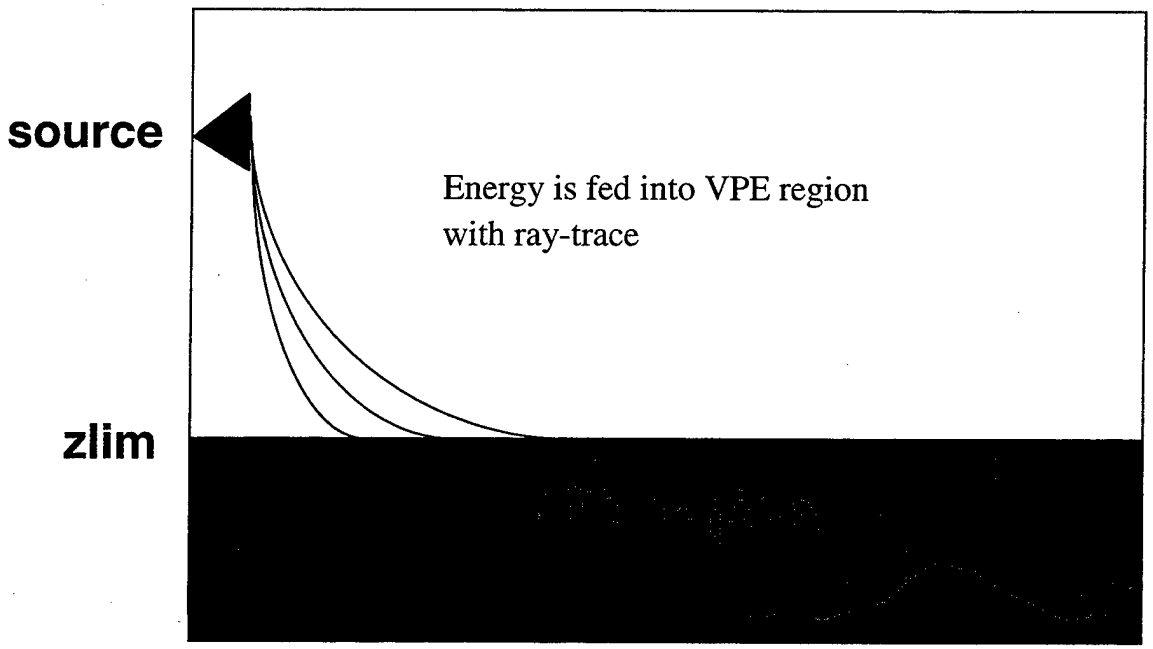


Figure 6. Framework for incoming energy PE.

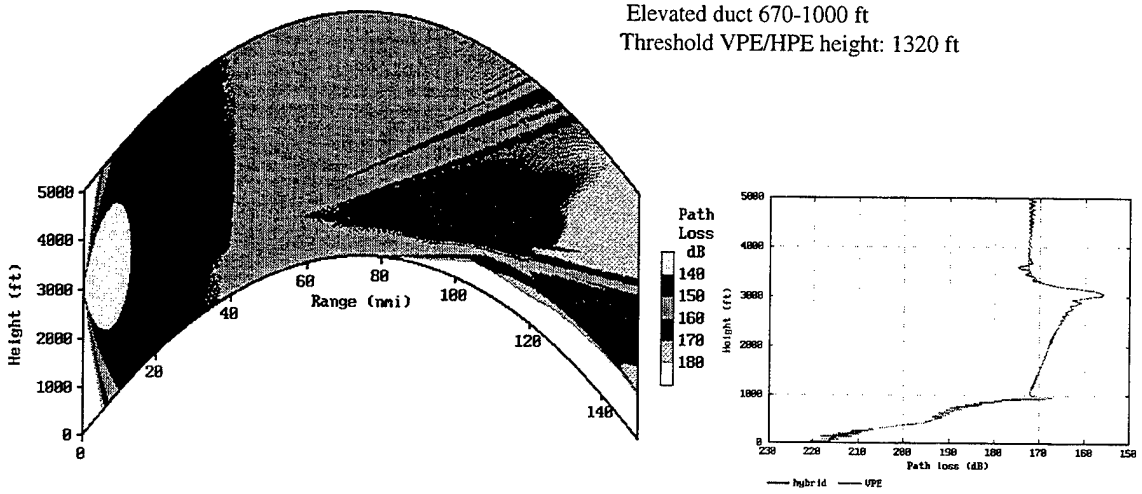
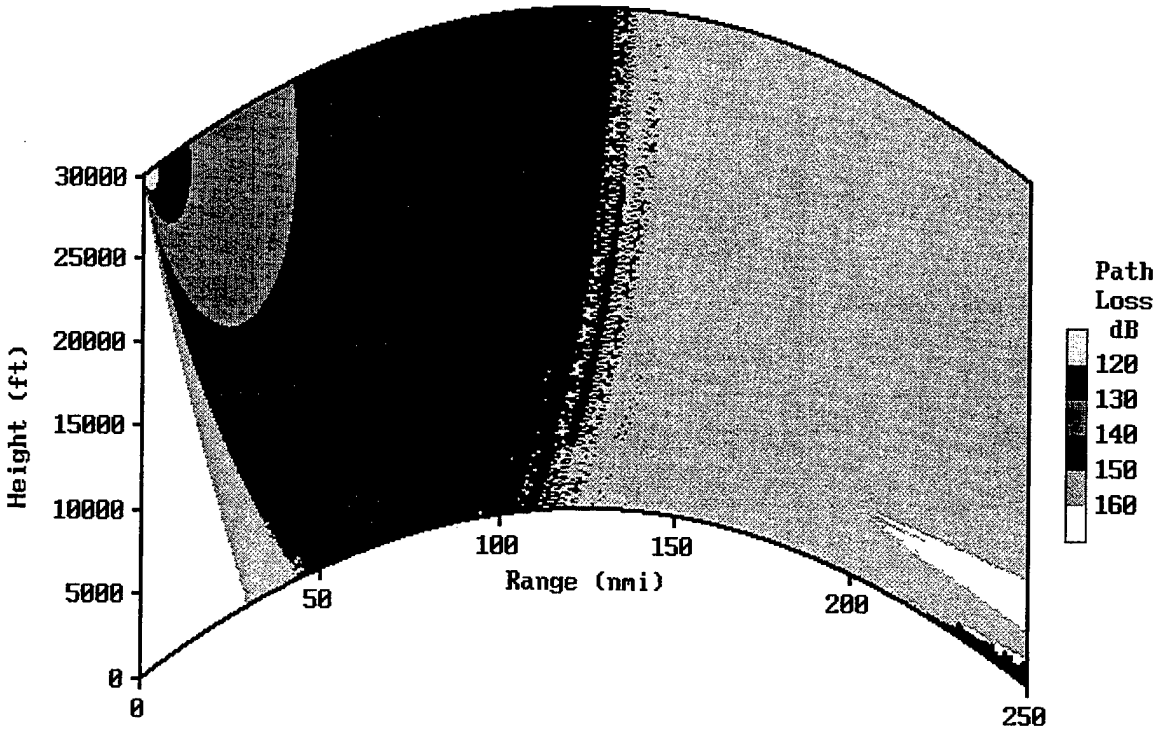


Figure 7. Airborne X-band antenna calculation with incoming energy PE.



Surface and elevated ducts (0-300 and 3300-4000ft)
Threshold VPE/HPE height: 4350 ft

Figure 8. Airborne S-band antenna calculation with incoming energy PE.

Blue-Water EEMS - TDRSS

Michelle Williams and Adesola Ayoola

Maritime Warfare Centre, HMS Dolphin, GOSPORT, UK

SUMMARY

The Environmental Electromagnetic Modelling System (EEMS) package is being developed in two stages. EEMS v1.0, colloquially called Blue-Water EEMS, is intended to provide the Royal Navy with an interim capability prior to the introduction of the new Command Support System (CSS). Blue-Water EEMS is a direct replacement for the existing Integrated Refractive Effects Prediction System (IREPS) package and does not incorporate terrain handling in its calculations.

Blue-Water EEMS consists of the radar propagation model TERrain Parabolic Equation Model (TERPEM) and the Target Detection Range Software Suite (TDRSS). The TERPEM module will support the production of the path-loss coverage diagrams and will be the primary input into TDRSS. The TDRSS module will then calculate the radar performance and susceptibility to detection of a specific threat using the radar receiver and operator characteristics.

INTRODUCTION

TDRSS investigates the performance of radar systems in detecting incoming targets and generates tactically useful information. The targets are assumed to be approaching the radar directly in a straight path, flying towards or away from the radar antenna. The model predicts the detection ranges of airborne targets by airborne and shipborne surveillance radars in the prevailing refractivity regime.

The primary objectives when designing TDRSS were to construct representations of, and determine the effects of, the following aspects of the target detection and identification process:

- radar antenna rotation rate;
- target closing speed;
- radar system detection logic;
- radar operator performance;
- radar screen range settings.

INPUTS

Two prototype packages: PREdicted Detection Ranges of Airborne Targets in Operational Regimes (PREDATOR) and the Predator Radar Model (PRAM), both developed in-house by MWC (OAD), form the TDRSS module of EEMS. The following are inputs into TDRSS:

Radar type - A high level description of the radar system detailing the radar system transmission characteristics.

Environment - details electromagnetic propagation in specific environments. This information comes from the TERPEM model as a file containing a set of path-loss against range values for a target height profile in the prevailing refractivity environment.

Target height - is used to select the appropriate path-loss vs range table from the TERPEM output file. It will be expanded to provide a full height vs range profile of the target during its flight.

Target RCS - based on the RCS value given in m^2.

Target Closing Speed - is the actual closing speed between the radar platform and target.

System Performance (S_p) - defines the 'Blip-scan' relationship that characterises the valid contact criteria. Typically there will need to be a number of returns above a nominal detection threshold before the system will respond to a valid contact. In a number of warfare areas this is defined by the 5 out of 8 rule i.e. there must be 5 successful detections in a gate of 8 before the system will respond to the contact.

Operator Efficiency (O_e) - defines how successful the operator is at responding to a valid contact i.e. what percentage of contacts that meet S_p the operator responds to and injects as a contact in the tactical command system. In the Hunt Class MCMV O_e is approximately 0.7 during Weapon Practice Assessment (WPA) trials.

Operator Delay (O_d) - defines how long it takes for the operator to inject the contact (success on both S_p and O_e) into the tactical command system. In search scenarios where closing speeds between ship and target are small O_d has little significance on calculating the target to ship range (TSR). However, in faster moving scenarios where closing rates are high O_d can become significant.

Radar Range Scale - is the radar scale setting that is used in a realistic scenario and is user defined. If this value is not of particular importance, setting it to a very large figure (e.g. 1000 nm) will in effect remove its influence on the modelled scenario.

AIO inject time delay - The Action Information Organisation time delay can be calculated from empirical sources e.g. time measurements during trials or standard reaction times as stated in tactical manuals.

MODES OF OPERATION

TDRSS operates in two modes: In-Depth and Snapshot to support analytical and operational requirements respectively. In Snapshot mode the user will have reduced capability for modifying datafiles and displaying results.

TDRSS uses the radar system transmission characteristics and the target RCS to produce path-loss figures covering all valid Probability of Detection (PoD) values. The following sections outline the algorithms used in calculating the path-loss values given the selected mode of operation.

SNAPSHOT

To derive the path-loss values, TDRSS in the Snapshot mode utilises the radar equation 1 *[King 1989]* to calculate the radar free space detection range (R_{fs}) and path-loss over the distance of R_{fs}:

$$R^4 = \frac{P_t G^2 \sigma \lambda^2}{(4\pi)^3 (S/N)_0 N \; kT_0 L \; B_N}$$

Equation 1: Radar Equation

where:

- R = radar free-space detection range in km
- P_t = peak power in kW
- G = antenna gain in dB m^2
- σ = target RCS in m^2
- λ = radar's transmitting wavelength in MHz
- $(S/N)_0$ = single pulse signal to noise ratio required for detection
- N = receiver noise figure in MHz
- k = Boltzmann's constant ($1.3807 * 10^{-23}$ JK^{-1})
- T_0 = ambient temperature (290K)
- L = assumed system losses
- $B_N = 1/\iota$ = noise bandwidth of the i.f filter, taken to be the inverse of pulse length ι.

The single pulse signal-to-noise ratio $(S/N)_0$ is dependent on the required probability of detection PoD, the probability of false alarm (PFA) and the target fluctuation model (i.e. Swerling case). For the snapshot mode of TDRSS, all targets are fluctuating i.e. Swerling case 1. The probability of false alarms is assumed to be constant at 10^{-8}.

In the Snapshot mode of operation, TDRSS adopts the IREPS algorithm for calculating path-loss.

The equivalent one-way path-loss *[Hattan 1989]* at free space range is calculated using equation 2.

$$\text{Loss} = 32.45 + 20\log(R_{fs} f_{MHz})$$

Equation 2: Path-loss equation

where:

- R_{fs} = radar free-space detection range in km
- f_{MHz} = radar system frequency in megahertz

IN-DEPTH

The In-Depth mode uses the Engineering Refractive Prediction System (EREPS) algorithms *[Hattan 1989]*. The EREPS algorithm allows the representation of non-fluctuating and slowly fluctuating targets (Swerling case 0 and 1 respectively).

The EREPS algorithm determines the radar free-space ranges for arbitrary radar cross sections for

any probability of detection between 0.1 and 0.9, and for any probability of false alarm between 10^{-12} and 10^{-4}. The corresponding one-way free-space path-loss at the free-space range is also calculated.

The equation used in the calculation of radar free-space detection range is given below:

$$R_{fs} = 58.0\left(\frac{G_t^2\, P_t\, \sigma\, \tau}{f_{MHz}^2\, N_f\, (S/N)_{min}\, L}\right)^{1/4}$$

Equation 3: Radar free space equation

where:

R_{fs} = maximum radar free-space detection range in kilometres
P_t = transmitted power in kilowatts
G_t = radar antenna power gain ratio
σ = target RCS in m^2
τ = pulse width (or length) in microseconds
f_{MHz} = radar system frequency in megahertz
$(S/N)_{min}$ = minimum signal to noise ratio for a specified probability of detection, probability of false alarms, and Swerling case 0 or 1
N_f = receiving system noise figure
L = assumed system losses expressed as a ratio

This process results in a R_{fs} path-loss value against PoD table for given RCS values.

METHOD

With the reference R_{fs} path-loss vs PoD table devised; it is a matter of pattern-matching the path-loss values calculated from the propagation module with those in the reference table to produce a corresponding probability of detection.

This process is repeated for each path-loss value. The final output is a composite PoD vs range table which may be displayed as the graph in Figure 1. This table is a vital data requirement used in the overall identification procedure. In the generation of the PoD against range table, TDRSS assumes that all targets have a constant RCS, are at a constant height and travel on a radial path. It is planned to update this facility to take into account crossing targets (hence varying RCS) and changing heights.

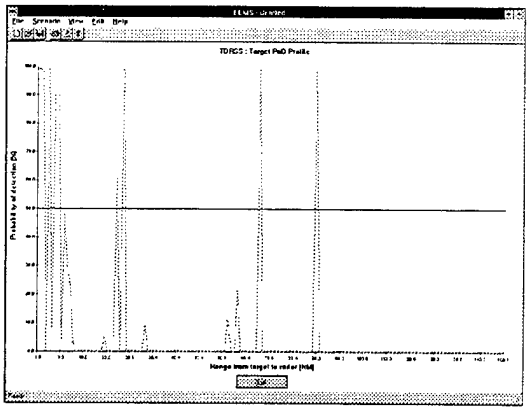


Figure 1: Probability vs Range Graph

TDRSS uses the PoD against range to investigate the performance of radar systems in detecting incoming targets and generate tactically useful information on the performance of a chosen radar system in particular scenarios.

The TDRSS model is based upon a simple model of radar performance: blip-scan theory. This assumes that the outcomes of successive radar scans are independent. It also defines a detection criteria which must be satisfied before a target can be defined as a valid contact *[United States Naval Institute, 1977]*. TDRSS expands on the blip-scan theory by including factors relating to operator efficiency and target inject delays.

An initial expression for indicating whether or not radar target correlation has occurred based on the blip-scan theory can be characterised by equation 4.

$$\left[\left(\sum_{i=1}^{s} f(i)\right) \geq d\right]$$

Equation 4: Radar Target Correlation Expression

where:

s = number of stored consecutive scans of the radar antenna
d = number of detections required to correlate a target

f(i) = function returns 1 if target detection occurred on scan i, 0 otherwise.

In order to determine if detection has occurred at a given time, the following information is required:

- the range from the target to the radar;
- the target probability of detection at that range;
- whether or not the radar beam is sweeping over the target i.e. if there is a detection opportunity.

Determining the result of a detection opportunity is formulated in equation 5.

$$\left[(f(rand) \leq PoD(rt) \wedge f(illum)\right]$$

Equation 5: Detection opportunity expression

where:

f(rand) = a function that returns a randomly generated value in a range 0-1
rt = range from the radar to the target
PoD = probability of detection of the target at a given range
f(illum) = a function indicating whether a target is being illuminated or not.

Combining Equation 4 and 5 gives the following simple radar target identification expression:

$$\text{Id} = \left[\left(\Sigma_{i=1}^{s}\left[f(rand) \leq PoD(rt)) \wedge f(illum)\right]\right) \geq d\right]$$

Equation 6: Identification Expression

The function f(rand) is required to provide the model with a means of performing Monte Carlo simulation of the detection scenario. This expression is not adequate to represent the entire identification process. It must also take into account the following:

- operator efficiency;
- radar range scale;
- information processing delay;
- tactical identification range.

$$\left[(scale \geq rd) \wedge (f(r) \wedge o_e)\right]$$

Equation 7: Recognition of Target

Target (inject range) = $(r_i - (s_t * delay))$

Equation 8: Target range at inject into AIO

where:

scale = the maximum radius of the radar display scale range
r_d = the range at which the target detection has been fulfilled
f(r) = function returning a random variable in steps of 0.001
o_e = a value representing operator efficiency (between 0 and 1)
r_i = the range at which the target has been identified by the operator
s_t = the speed of the target
delay = time delay between target identification and inject into AIO

The process of calculating the range at which a valid inject occurs (inject range), and the target becomes tactically significant is repeated a number of times in accordance with Monte Carlo modelling methods. TDRSS defaults to 1000 repetitions for scenario modelling, although any user-defined number may be performed

OUTPUT

TDRSS outputs the target range at which it has determined a target inject would taken place. The results may be displayed either graphically (in the form of statistical graphs) or in pre-defined tables of values.

The cumulative frequency graph produced by TDRSS will aid tactical decision makers in their analysis. For instance, there might be a requirement to determine the range at which a particular radar system will detect an incoming missile to a 75% confidence level, this can easily be read off the cumulative frequency graph. Figure 2 shows the cumulative frequency graph produced by TDRSS.

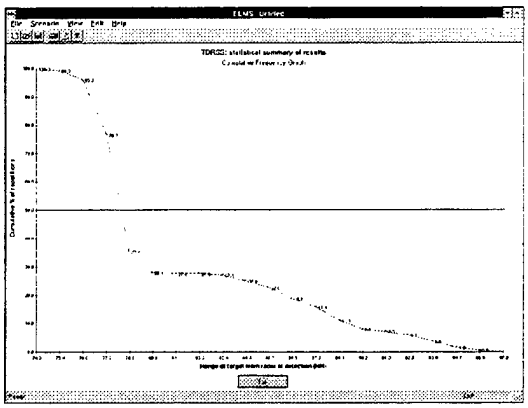


Figure 2: Cumulative Frequency Graph

TDRSS also provides a small statistics module for analysis of the results, values such as the mean detection range, standard deviation, maxima and minima can be determined (Figure 3). The results generated by TDRSS provide the capability for mission planning and/or front-line battle management that requires rapid responses to a constantly changing scenario.

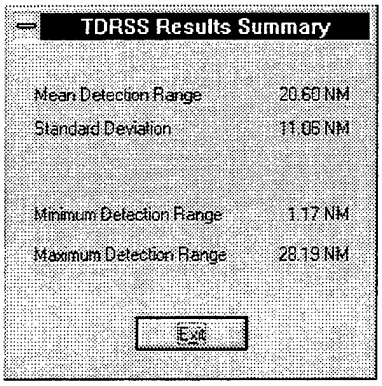


Figure 3: TDRSS Results Summary

The TDRSS concept performs best when considering radar system performance against very fast moving targets of small radar cross section. In these scenarios target speed, radar antenna rotation rate and operator performance become the dominant factors in determining the scenario outcome.

Traditional predictive models have not considered such scenarios in sufficient depth to provide such comprehensive results. From the implementation of TDRSS, the RN can evaluate whether the 50% PoD is the most tactically useful reference to use and consider whether a different PoD may provide a greater confidence limit.

FUTURE DEVELOPMENTS

Future developments include modifying the TDRSS module to handle crossing targets.

Although Blue-Water EEMS is capable of calculating EM wave propagation over terrain, this functionality will not become effective until the integration of the Terrain Handling utility in the next stage of EEMS development.

The IT Implementation of EEMS (v2.0) will consist of: TERPEM; TDRSS; Terrain handling (THEEMS); High Frequency (HF EEMS) and an Electro-Optical (EO) tactical decision aid.

CONCLUSION

The IT implementation for Blue-Water EEMS (v1.0) is near completion and following further evaluation will be used operationally in Jan 97.

EEMS (v2.0) is currently in the planning stage. Delivery for operational use is expected end of 1997.

REFERENCES

King D. J., "An Evaluation of the IREPS program and its use with the Fleet", *MOD Report (Unpublished)* 1989.

Hattan C. P., "Specification for Radar Free-Space Detection Range and Free Space Intercept Range Calculations", *Naval Ocean Systems Center, San Diego Technical Document,* 1989.

United States Naval Institute, "Naval Operations Analysis", *ISBN 0-87021-440-3,* 1977

Levy, M. F. and Craig K. H., 'TERPEM propagation forecasting with EEMS', *Battlespace Atmospheric conference, San Diego, US,* 1996

High Frequency Coverage Prediction For EEMS.

Mark R Moôre[1] and Anil K Shukla[2]

[1] Maritime Warfare Centre, HMS Dolphin, Gosport, UK
[2] Defence Research Agency, Malvern, UK

INTRODUCTION

The present day UK Royal Navy has an operational shortfall in the ability to determine the extent of its HF coverage from a single transmitter. It currently relies on HF prediction packages, primarily developed for Army antennae, that prescribe the optimum working frequency for a signal propagating between two points.

Work is being undertaken at the Maritime Warfare Centre (Gosport), supported by the UK Defence Research Agency Tactical Communications Department at Malvern, to develop a package that will enable the operator to assess the optimum working frequencies. The functionality will include an overlay routine outlining the extent of coverage within the geographical battlespace. Other benefits can be obtained from the package by assessing the risk of hostile interception in addition to supporting Electronic Support Methodologies.

This paper outlines the development work being undertaken to provide the Environmental Electromagnetic Modelling System (EEMS) HF module. The potential concepts of operational use are discussed along with future developments of the system.

THE REQUIREMENT

The primary aim for a HF propagation prediction system is for timely and accurate predictions to support tactical exploitation of RN communications equipment. It should also be hosted on a system for eventual incorporation into the RN EEMS Project *[Moore and Lewis, 1994].*

BACKGROUND AND EXISTING HF PLANNING AIDS

"There is currently no HF prediction tool covering both Skywave and Groundwave available to the tactical commander to assist with either HF/DF or countersurveillance"*[Moore and Lynch 1996].* However, there are software packages, paper documents and equipment available to the RN to assist in the planning of HF frequencies, such as the GEC Marconi Orange Book, MICROPS II, NAVMUF Program and the oblique CHIRPSOUNDER Equipment.

To assist the user in initialising the different software programs, a daily Short Term Ionospheric Forecast (STIF) is produced as an input to the program to determine the nature of the ionosphere (e.g. SSN, 10.7 flux). The following is a description of the models available.

MICROPS II

MICROPS II, based on the CCIR recommendation model REC533, only considers the Skywave element. The software operator and paper documents require detailed knowledge of the antennae and the power levels that are to be used for the transmissions. The outputs given by the program are a series of charts that detail the Maximum Useable Frequency (MUF), Lowest Useable Frequency (LUF) and the Frequency of Optimum Transmission (FOT) for a particular transmission. Within these charts, the program highlights which of the specified frequencies are likely to support the propagation over a given path. The groundwave component of the signal is not calculated. Following the release of the GEC-MARCONI Orange Book software, MICROPS II is no longer used.

GEC Marconi Orange Book

Originally issued to the FLEET in a hardcopy format, this package is now issued on an annual basis on a 3.5" floppy diskette. The orange book software, based on the CCIR REC894 Skywave prediction package, calculates the predictions for both Skywave and Groundwave propagation and is originally designed for applications using Army

antennae. The program is executed in the DOS environment of a PC.

The use of navy antennae has not been fully implemented. Assumptions, therefore, have to be made for RN transmitter and receiver antenna parameters. The results are based on two outputs; Signal-to-Noise Ratio Graphs and Frequency Tables.

Signal-to-Noise Ratio Graphs

These graphs show the frequencies which will support propagation on the circuit at each time of the day. Each graph depends on the particular sunspot activity, season and equipment parameters that are chosen from the list of input parameters. In general, the highest frequency envelope is governed by the state of the ionosphere whereas the lowest frequency envelope is more sensitive to the type of equipment that is used eg. radiated power, antenna choice, modulation type, etc.

Frequency Tables

This table shows the lowest, recommended and highest frequencies that will achieve the required grade of service for the particular equipment and modulation type chosen for each 2 hourly segment of the day. These minimum and maximum frequencies correspond to LUF and MUF envelopes shown in the signal-to-noise ratio graphs.

It is not possible to configure the software according to the communications plan inputs and equipment onboard the surface vessel. As a consequence, the results may be of little use to the operator.

There is a groundwave option built into the software for the Orange Book program. It is not possible to display the results for the groundwave simultaneously with the skywave results.

NAVMUF Program

The Naval Maximum Useable Frequency (NAVMUF) program enables the HF path length, the MUF and FOT between two stations to be calculated. There are the usual parameter inputs comprising the Latitude and Longitude positions of the transmitter and receiver sites and the date and time of day for the transmission as is common with all HF prediction programs. The results are a hard copy printout detailing the MUF and the FOT at hourly intervals for the required period and are based on the Skywave component. No indication as to the extent of the Groundwave is given.

CHIRPSOUNDER

A Chirpsounder system can simultaneously provide path sounding and frequency occupancy monitoring as an aid to 'real-time' HF frequency management. The Chirpsounder measures the propagation conditions in the HF band between a low power transmitter and a receiving station. Displays at a receiving station enable the operator to select the most suitable channel. Additional equipment details the current channel occupancy and those available for use.

The shore transmitters radiate continuously and may be used by ships to predict the best frequency range for use on HF Ship/Shore, Broadcast and Maritime Rear Link (MRL) services. The system provides the user with frequency information that will reach the receiver site (e.g. the Barry RCS5 gives the integrated power for all transmission delays). This is not always the most tactically useful frequency as no consideration is given to where the transmission propagates.

Idealised HF Decision Aid

An assessment of the current HF prediction tools available has been carried out with a view to selecting the most appropriate software that achieves the majority of the requirements outlined earlier. A HF decision aid system *[Shukla and Cannon, 1994]* should ideally comprise of three elements; an information gathering and distribution system; a jamming and interception model and a communications system interface.

The displays afforded by the decision aid are the key to the success of such a system. For operational use, the user does not wish to be presented with endless pages of text. It is considered that the most tactically useful display is that of a map detailing the area of interest with the coverage of the transmission superimposed.

HF Decision Aid

A HF decision aid (The Jamming and Intercept Vulnerability Estimator (JIVE)) was originally devised by the Defence Research Agency at Malvern under the 19g programme in support of RAF requirements. This decision aid calculates both the skywave and the groundwave coverage *[Shukla and Cannon, 1994].*

In general, the function of the decision aid may best be defined as ***"an automated decision aid to predict, using near real-time environmental and systems information, those communications parameters (e.g. frequency, power, receiver station location) which minimise communications vulnerability".*** *[Shukla and Cannon, 1995]*

The difference between the DRA decision aid and other HF propagation models is that the decision aid incorporates a Jamming and Interception Model (JIM). The JIM allows the user to input information relating to hostile and friendly forces (e.g. hostile locations from intelligence gathering units), Electronic Support Measures (ESM) and Electronic Protective Measures (EPM) in addition to environmental data. The ionospheric model currently used comes from the conventional HF systems prediction program REC533A. *[CCIR, 1994]* The Groundwave component of the JIVE system is based on the commercial GR-WAVE prediction package *[CCIR, 1994].* The system is described in more detail by *Shukla et al [1996].*

REC533A employs a median model ionosphere during its calculations and, as such, has been acknowledged by the CCIR and ITU as being of sufficient accuracy to be used for propagation prediction software. This acknowledgement, together with the knowledge that the precursor to REC533A, REC894 (also using a median model ionosphere), has been used operationally by the RN (MICROPS II), will alleviate the need for the RN to conduct evaluation trials on the propagation software.

HF EEMS

HF EEMS has been designed using the empirical version of the JIVE system. This was originally developed in the DOS environment, relying on the memory allocation utilities within this setup. As a consequence, the JIVE system was not fully compatible with MS WINDOWS. With the primary aim of the HF EEMS system being for incorporation into a WINDOWS-based package, it became apparent that major user-interface alterations had to be made to the JIVE software.

The HF module of the EEMS software is designed to operate using a two-tier operating procedure; the operator mode and the expert mode. All the functionality that is present in the operator mode will be present in the expert mode with the additional editors that are required to update the databases held within the system.

Input Parameters

The ergonomics of an operational package to be used at sea by the RN is paramount to the success of the software. With this in mind, the HF EEMS development has concentrated on the Graphical User Interface (GUI) to minimise the operations required and reduce the specialist information required to operate the system successfully.

The main control screen that the user encounters is a scenario editor based on the antennae at the transmitter, the friendly receivers and the hostile receivers. The power output is initialised and the communications plan that the ship is operating to is initialised. This initialisation screen is shown at figure 1.

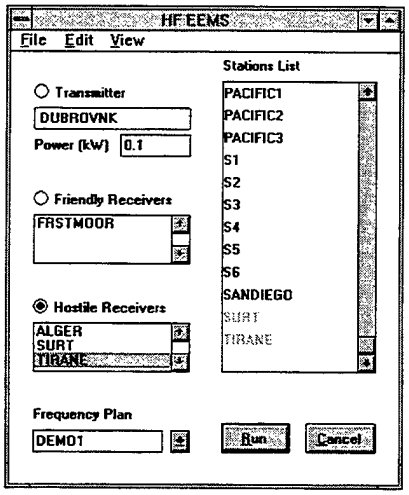


Figure 1: HF EEMS Parameter Input

On initialisation of the package, the sunspot number for predictions is read from a file, with

SSN predictions obtained from NCCOSC or other world data centres. The current time of the PC is also used to produce HF coverage predictions for the current time of day. The user is able to alter these inputs in order to produce coverage prediction for any time of year, thereby enabling the package to be used for future planning of exercises.

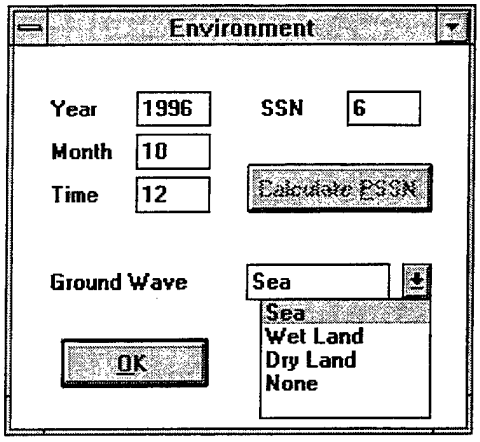


Figure 2: Prediction Time/Groundwave Editor

The groundwave editor is located in the environment editor screen. This allows the user to select the most appropriate ground type that is at the transmitter location. Currently, the package defaults to the Sea option owing to the main user being the at-sea communicator. It must be stressed that the results produced from the groundwave calculations are a crude representation. The package does not take into account the differences in the ground type as the signal propagates from its transmit site to the receive site. As a result of the EEMS system having a resident geographical information system (GIS), future improvements to the package will enable HF EEMS to access the groundtype cover for assessment of any groundwave attenuation.

The user is able to select the transmitter and receiver sites from a database within the program. If any of the transceivers are mobile the location of the antenna can be inserted manually, either from its Latitude and Longitude co-ordinates or from a location on a map of the area. The eventual host for EEMS will be the RN's Command Support System (CSS), which will enable the locations of all mobile sites to be inserted automatically from the GPS systems and General Operations Plot (GOP) located in the Ship's operations room. Any new receive sites can be inserted into the package from the site editor as described. The edit function for the transmitter and receiver sites can be accessed from the operator mode by clicking on the station in the selection box. This same method can be used in the expert mode, with an additional editor for updating the database of stations.

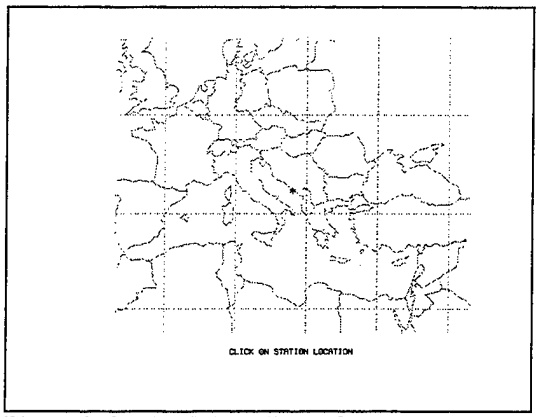


Figure 3: Station Editor Input Screen

The other parameter inputs that are required from the package are the development of the frequency communications plans. These will be created before a ship deploys on an exercise or an operation. The capabilities are only available in the expert mode of the software. The communications plan comprises a list of frequencies that are available to the ship at any given period of time. These are normally promulgated to the ships before an exercise or an operation takes place. An example of the communications plan editor is given at figure 4:

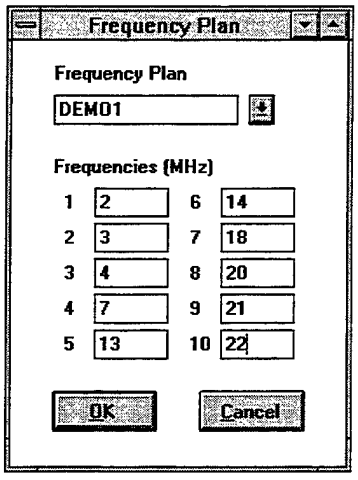


Figure 4: Communications Plan Editor

Also available in the expert mode is the ability to create new transceiver sites. The current version of the propagation tool bases all its predictions on an isotropic commercial aerial. This is a simple representation of the RN transmitters, however further development is anticipated to include aerials specific to ship and shore bases. The information that is required from the station editor is shown at figure 5.

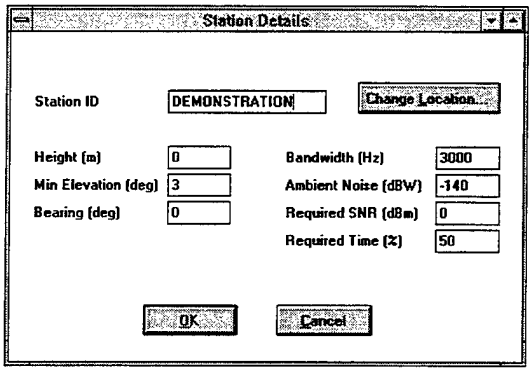


Figure 5: Station Editor

Database Population

Prior to deployment on an exercise or operation, it is necessary to populate the station and communications plan databases. This will be carried out in the operator mode. However, the aim of the EEMS system is to work in conjunction with the Royal Navy's FLEET Data Management Unit (FDMU) which provides all relevant data for each of the ships' systems. It is anticipated that the FDMU will hold station information for populating the HF EEMS module.

Display Modules

The powerful functionality of the HF module for EEMS is concentrated in its display utilities. The majority of current day HF propagation prediction systems are either based on the skywave component or the groundwave component of the signal. HF EEMS allows for both components of the wave to be displayed simultaneously.

Coverage map displays can also be varied according to the requirements of the user. This can range from the simple dB pathloss of the signal to the signal to noise strength ratio for any part of the Area of Interest (AOI).

This aspect of coverage mapping is of great advantage to the tactical communicator. The coverage displays that are calculated detail a single frequency from a selection of those frequencies of interest to the user; eg the communications plan. The coverage displays allow the user to analyse multiple skips occurring with the skywave element of the transmission.

The output screens are controlled from a single controller. This control unit remains the same for both the expert and the operator modes with additional functionality available to the expert user. Essentially, there are two parts to the control panel for the display section; the coverage plots and the frequency plots.

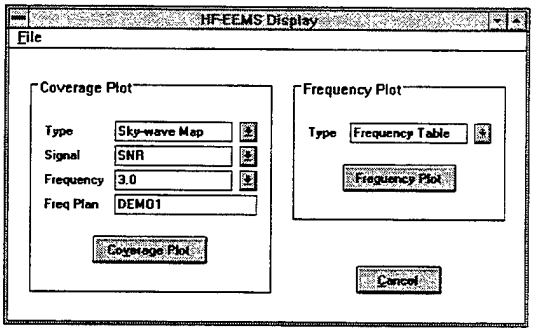


Figure 6: HF-EEMS Display Controller

It is the former of the two types that demonstrates the improved capability of the idealised HF propagation system. There are two types of displays that can be obtained from this section. These detail the Signal Power level, in relation to the distance that the signal has propagated, and the Signal-to-noise ratio signal coverage.

The Signal Power display diagram has been modified for the operator; the power level of the signal is represented by a scale of 1 to 10, with 10 being the strongest signal strength. It is intended that the expert user will have the option to display the power displays as a function of dBs.

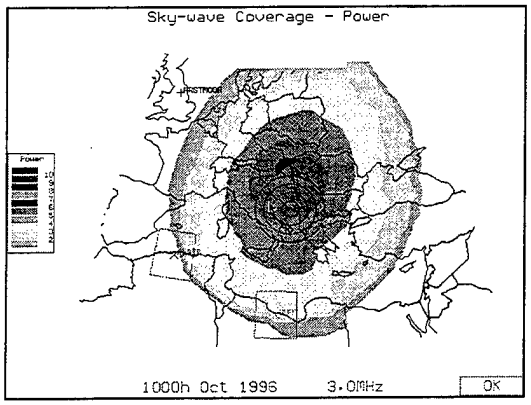


Figure 7: HF EEMS Power Level Display

The second graphical output for the mapping system details the signal to noise ratio of the signal at a particular site. This, tactically, is more useful than the former display. The ambient background noise levels are taken into account, thereby requiring a greater sensitivity in the receive equipment to potentially intercept a stray signal.

It can be noted that the coverage differences are apparent between figures 7 and 8. The additional benefit of the SNR plot highlights the significant effects of the background noise levels around the area of interest.

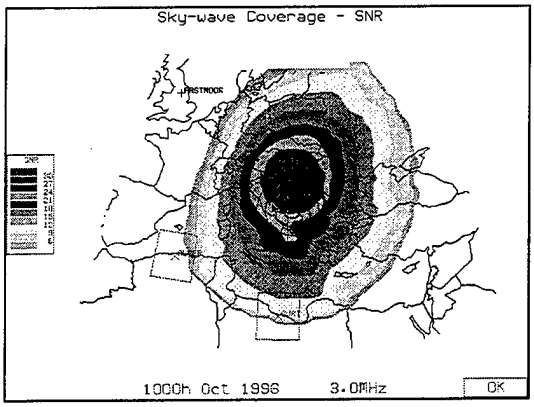


Figure 8: SNR Display Screen

The groundwave component of the signal is shown in both the Power and SNR displays as concentric circles based around the transmitter site.

There are a variety of outputs that can be obtained from the JIVE system. These range from the typical FOT/MUF diurnal plots that are given in the standard HF prediction programs to the displays of maps with the transmission coverage overlaid. This coverage can be a combination of both the skywave and the groundwave elements of a HF transmission, or the user can display a single component.

The groundwave component of the transmission can also be calculated and the coverage plotted onto the map of the AOI. This facility will enable the user to determine those frequencies that are more conducive for tactical communications within a task group.

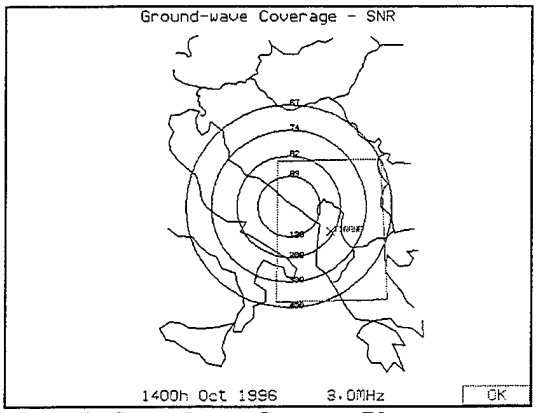


Figure 9: Groundwave Coverage Plot

The second component of the Display Controller concentrates on the traditional HF prediction plots. There is, however, additional functionality to this section in the guise of information relating to the hostile intercept sites (HIS). The traditional MUF and LUF plots are detailed in the chart shown at figure 10. There are additional curves detailing the MUF for the hostile receivers. At the top of the graph denotes which of the friendly receivers is the most secure station between the UT hours. If there were more than one friendly station, this graph would denote the composite operational MUF.

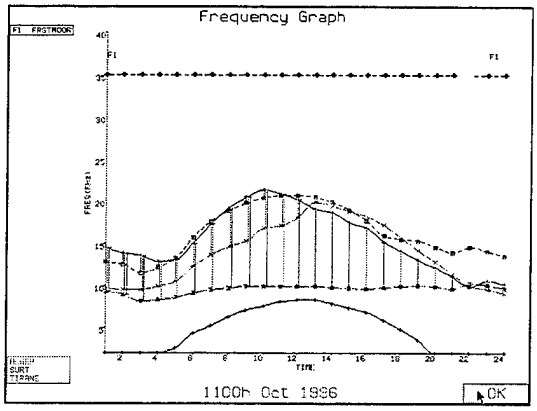


Figure 10: A 24 hour MUF prediction graph

Other displays that can be obtained from the display controller denotes a 24 hour minimum interception frequency schedule. This is a colour coded schedule which recommends frequency ranges and the optimum friendly receiver stations that should be used to minimise interception. The hostiles are listed with the highest friend-to-hostile operational MUF first. Hostiles predicted to receive the signal are indicated by an asterisk. If all hostiles intercept the signal, then no frequency range is approved and a blank line is displayed. It should be noted that signal interception by at least three hostiles is required for accurate position fixing

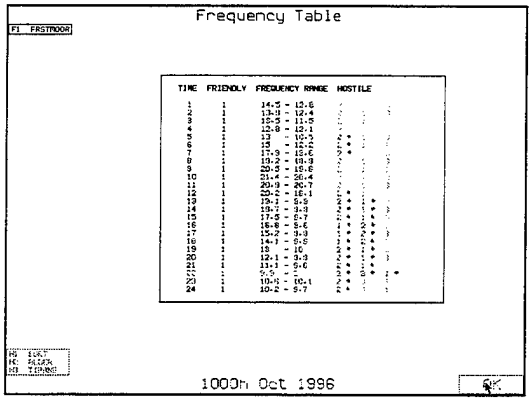


Figure 11: A 24 hour minimum interception frequency schedule

FUTURE DEVELOPMENTS

Although the future development of the HF EEMS module has been described by *Shukla et al [1996]*, the main points affecting the future use of EEMS are outlined as follows:

There are plans to incorporate a pseudo sun spot number, calculated from updated results using the onboard Chirpsounder equipment. This will provide an improvement in the MUF that are calculated. Plans are also underway to make more use of the LUF in the decision making routines of the package. Other plans include an improved antenna model developer. This will allow the package to be ported across to other users in the military field, where different antennae are used for HF communications.

CONCLUSIONS

The current HF propagation packages that are available to FLEET do not meet the specified requirements. None of the packages assists the user in selecting the LRI/LPI frequencies from the communications plan. Chirpsounder equipment enables the user to establish a propagation path for effective transmission. It does not calculate LRI/LPI frequencies.

The benefits to the RN in using the HF EEMS system encompass more than simple HF frequency management. With the ability to plot hostile and friendly locations, the coverage obtained from a transmission can be controlled. The facility to input receiver sensitivities into the model may provide the Electronic Warfare (EW) and Intelligence Community with possible counter detection and CESM benefits.

It can be seen that different interpretations of results obtained from HF prediction programs can alter the use of the tools altogether. Before the implementation of the HF EEMS package, the RN were in no position to determine the extent of coverage that their HF signals were achieving. It is now possible to have greater control on the management of HF circuits and a revised methodology for achieving a secure HF propagation path.

REFERENCES

Moore M. R., Lynch D. J. M., "HF Skywave and Groundwave Prediction Tool for Tactical Usage", *MoD Report (Unpublished)* 1996.

Moore M. R., Lewis D. J. W., "The Development of an Operational Radio/Radar Propagation Package", *MoD Report (Unpublished)* 1994.

CCIR International Telecommunications Union Radio Communications Bureau, *Recommendation 533*, Computer program for satellite communications, Geneva 1994.

Shukla A.K., Cannon P.S., "A BLOS HF Decision Aid", *AGARD SPP Symposium, Rome,* 1994.

Shukla A. K., Cannon P. S., Interim Milestone Report on the HF Forecasting Study. *DRA Technical Report (Unpublished),* 1995.

Shukla A., Cannon P., Moore M., "A HF Tactical decision Aid for EEMS and Automated Radio Control Systems", *Battlespace Atmospherics Conference, San Diego, US,* 1996

CCIR International Telecommunication Union Radio Communications Bureau, *Recommendation 368*, GRWAVE - Computer program for satellite communications, Geneva 1994.

(c) British Crown Copyright 1996 /DERA

Published with the permission of the Controller of Her Britannic Majesty's Stationery Office

A HF Tactical Decision Aid for Conventional and Automated Radio Control Systems.

Anil Shukla[1], Paul Cannon[1], Mark Moore[2]

[1] Defence Research Agency, Malvern U.K.
[2] Maritime Warfare Centre, HMS Dolphin, Gosport, U.K.

Introduction

Beyond line of sight (BLOS) communications systems, operating within the high frequency (HF) range (2-30 MHz), propagate electromagnetic waves via the ionisation present in the upper atmosphere (i.e. the ionosphere). The ionosphere, usually considered to lie between heights of ~60 and 1000 km, varies in structure over the earth's surface. The vertical ionisation concentration (which historically has been divided into three regions, D, E and F) varies over orders of magnitude and depends on time of day, season, and sunspot number. From a HF communications aspect, the E and F regions essentially act as reflectors whilst the D region acts as an attenuator.

To exploit the time and spatially varying ionosphere for high 'quality' and high 'reliability' HF communications links, the HF system signal power, operating frequency, antenna, modulation, and data-rate etc., should be matched to the prevailing ionospheric conditions. Some manual matching is currently performed by HF operators using daily frequency schedules based on the maximum usable frequencies (MUF). These frequencies can be anticipated using HF prediction programs such as REC533A [*CCIR*, 1994] and IONCAP [*Teters et al.*, 1983]. Alternatively the frequencies may be measured in near real-time using oblique chirp ionosondes [*Barry et al.*, 1969, *Arthur et al.*, 1994], or simply estimated based on HF operators experience and expertise.

The communications matching process currently performed is limited, time intensive and often requires an experienced HF operator. Frequently it results in the selection of sub-optimal system configurations (e.g. incorrect frequency, insufficient transmitter power). To overcome these drawbacks automatic link establishment (ALE) systems have been developed. The next generation of HF communications system may incorporate an improved version of ALE known as Automated Radio Control Systems (ARCS *Arthur and Maundrell*, 1994). ARCS will match a number of system parameters (e.g. data rate, modulation, optimum receiver station as well as frequency and power) and requirements to the prevailing measured ionospheric conditions. Both manual and automated matching techniques, however, are primarily concerned with maximising link 'reliability' and 'quality'. Little attention is given to the Electronic Protective Measures (EPM) required to minimise the jamming, interception and direction finding vulnerability of the communications link about to be established.

EPM procedures employed by HF systems are currently based on techniques, such as spread spectrum, cryptography, and antenna nulling. Unfortunately, these techniques, may still propagate electromagnetic energy to unwanted or unauthorised receivers causing interference or resulting in the transmission of intelligence. There is, however, an alternative technique. This technique is based on the tactical use of signal propagation [*Argo and Rothmuller*, 1979, *Goodman et al.*, 1982, *Shukla and Cannon*, 1992] and exploits detailed knowledge of the ionosphere and ray-tracing techniques to minimise the signal coverage and thereby deny unauthorised access to the radiated electromagnetic energy. The technique could be used either in isolation or in conjunction with other EPM approaches such as antenna nulling and spread spectrum techniques.

This paper describes the tactical propagation technique via the development of an HF decision aid. This decision aid uses an ionospheric environmental model in conjunction with a communications model to predict both the interception and jamming vulnerability of required HF links. Based on the model outputs, the decision aid recommends system configurations (e.g. best frequency, best ground station, best transmission time) which minimise system vulnerability. The tactical decision aid can be used by HF operators in near real-time, as an additional component in other electromagnetic modelling systems (e.g.

EEMS [*Moore and Lewis,* 1994]) or, off-line during mission planning to predict and configure the least vulnerable HF communications links. The decision aid could also be used to automatically configure current HF equipment. This latter approach is particularly powerful when used in conjunction with ARCS [*Arthur and Maundrell* 1994] based systems with the decision aid contributing to the automatic channel selection (ACS) process.

This paper first outlines the general concepts of an HF decision-aid. A decision-aid currently being developed at the Defence Research Agency, the utility of which is also described by *Moore and Shukla* [1996] will then be described. The paper shows how the decision aid uses simple frequency management techniques to minimise signal interception and will outline the future development of the decision-aid.

Principle elements of a HF communications decision aid systems

A decision aid system designed to optimise EPM communications characteristics should ideally comprise three principle elements (Figure 1): an information gathering and distribution system, a jamming and interception model (JIM), and a communications equipment interface. The first element should provide the second element (JIM) with as much near real-time data as possible. This data may consist of wanted (i.e. friendly) and unauthorised or unwanted (i.e. hostile) receiver locations, hostile capabilities, ionospheric data from sounders, sunspot number, time, date, etc.

The final element, the communications equipment interface, should ensure that the recommended system configurations are presented to the operator and used by the communications system in the most effective manner. The information gathering and distribution system and, the communications interface are not detailed any further at this stage suffice to say that some of the main elements can be found within ARCS [*Arthur and Maundrell,* 1994].

The jamming and interception element should ideally comprise of six primary models (Figure 1): an input/update interface, a propagation prediction model, an ionospheric model, a communications model, a vulnerability assessment model and, a systems recommendations model. The following details an idealised design of a JIM and some implementations of a JIM will not have all the elements outlined below.

The JIM input/update interface is the primary communications interface between the operator and the information gathering and distribution system and, the models used within JIM. The interface should ideally handle operational data (e.g. message type, vulnerability requirements, station locations), and specialist environmental data (e.g. from sounders, or other modelling systems such as EEMS [*Moore and Lewis,* 1994]). The information flow should be bi-directional since data passed to the models may be ephemeral. Ideally, the interface should be designed for the inexperienced operator but it should be flexible enough to enable an 'expert' operator to interrogate the system in depth and, if necessary, update the model parameters manually.

The ionospheric model characterises the environment through which HF signals propagate. Typical specialist parameters required by the models may be electron density profiles at control-points, sunspot number etc. The ionospheric model is used by the propagation prediction model to determine the ray-paths and signal propagation modes (e.g. 1E, 1F). The typical outputs of the propagation model are signal coverage dimensions, received signal power, MUFs, etc. These predicted propagation parameters can then be used by the communications model to predict the communications characteristics of the received signals. Typical input parameters to this communications model may be signal-to-noise ratio and antenna polar diagrams. The predicted communications system parameters can then be passed to the vulnerability assessment model for evaluation.

The assessment model compares the predicted vulnerability of the operator defined system configuration with the vulnerability requirements defined earlier. The operator defined configuration may not provide the communications resilience requested and, consequently alternative system

configurations (e.g. additional frequencies) and options (different receive stations and different transmission times) should also be assessed.

The assessment model may predict more than one HF system configuration that satisfies the users' requirements. The system recommendations model uses the results of the vulnerability assessment model, and other relevant data from other systems (e.g. EEMS [*Moore and Lewis*, 1994]) and, ideally, recommendations from other communications decision-aid systems (e.g. satellite, meteor burst) to first rank the configurations and then recommend the optimum EPM and ECM configuration. The recommended configurations are then output via the communications equipment interface.

Decision-aid prediction accuracy

The accuracy of the recommendations produced by any decision-aid are directly related to the data and models used. The models associated with greatest error at HF are the ionospheric model, and the propagation prediction model. The ionospheric model used in conventional HF prediction programs, e.g. REC533A [*CCIR*, 1994], IONCAP [*Teters et al.*, 1983], all use the CCIR or URSI map coefficients such as foF2, foE, hmF2, at anchor points to synthesise a median-model ionospheric profile. These simplified models, unfortunately, result in qualitatively low prediction accuracies and signal range errors of, typically, ~200km. Limited improvements to these median models, however, may be obtained using sunspot updating techniques [*Uffleman et. al.*, 1982, *Shukla and Cannon*, 1994,]. Updating is performed by comparing measured path parameters, e.g. MUF using a sounder, with a predicted path parameters using a model such as REC533A [*CCIR*, 1994]. The difference between a measured and predicted parameter such as MUF is then minimised using the ionospheric model's driving parameter (e.g. sunspot number). The new sunspot number derived is then used to make a prediction until a new measured parameter becomes available. The advantage of this 'pseudo-sunspot number' technique is its simplicity. The technique, however, has limited applicability; for example the measured path must be close to the wanted communications path. Significant ionospheric model improvements may be obtained using near real-time data to synthesise a real-time ionosphere e.g. PRISM (Parameterised Real-time Ionospheric Specification Model, [*Daniell et al*, 1994]).

HF propagation prediction models use one of three propagation techniques: mirror reflection, analytic ray-tracing, or numerical ray-tracing. Conventional HF prediction programs (e.g. REC533A [*CCIR*, 1994]) use the mirror reflection technique for computational speed. The range and signal power accuracies, however, are low using this simple method. Superior accuracy can be achieved by analytic [*Platt and Cannon*, 1994] or numerical ray-tracing [*Jones and Stephenson*, 1975] with the former being less computationally intensive but typically less accurate. A novel analytical technique, however, is described by *Norman and Cannon*, [1996] which runs an order of magnitude faster than numerical approaches but with errors less than 2% of the numerical technique.

The DRA developed decision aid

In Version 1.0 of the decision-aid developed at DRA, the jamming and interception model (Figure 1) and the input/update interface are the major aspects. The information gathering and distribution system, and the communications interface are represented by the host 486-PC. In this early version of the decision-aid a modified version of the REC533A [CCIR, 1994] prediction program performs the functions of the ionospheric model, propagation prediction model, and the communications prediction model.

The input/update interface in Version 1.0 is a windows environment screen and has two modes of operation, one for the inexperienced HF 'operator', and the second for the experienced 'expert'. The interface developed ensures that the number of inputs required by the inexperienced 'operator' are kept to an absolute minimum. The 'operator' is denied access to required signal-to-noise ratio, required availability, operating frequencies, receiver bandwidth etc., since these only give rise to confusion and complicated input screens. These detailed parameters are input independently by the 'expert', or loaded

from data files (e.g. sunspot number file, frequency plan file) prior to the decision aid being deployed with the operator.

The vulnerability assessment model in Version 1.0 is limited. Assessments are currently performed based on signal coverage within user specified areas, using the system configurations (e.g. frequencies, power) input by the expert operator. In Version 1.0 it is assumed that all receivers have equivalent systems and technologies (e.g. identical modems). This assumption, along with the use of an isotropic antenna, results in the modelling of worst case interception scenarios.

For completeness, Version 1.0 also contains a simple ground-wave propagation model for Line of Sight (LOS < 200 km) systems. This element is currently only used to display contours of signal strength and is not used in the decision making process within the vulnerability assessment model, and the systems recommendations model. The ground-wave propagation characteristics are calculated by a modified version of GRWAVE [*CCIR*, 1994] which computes the field strength of the ground wave signal on a smooth curved homogeneous earth. In this model the refractive index of the troposphere is assumed to decrease exponentially with height and the conductivity and dielectric constants, defined at the transmitter location (based on CCIR parameters), are assumed to be constant up to a range of 400 km and constant in azimuth.

The recommendations model (Figure 1) proposes system configurations based on: signal coverage predictions, and frequency range predictions. The utility of the decision-aid is described in detail by *Moore and Shukla* [1995], however, the typical outputs are summarised below.

Decision aid outputs

The decision aid displays data in two output formats. The first format is a colour sky and ground wave signal-coverage map (e.g. Figure 2) indicating station locations. The signal coverage maps, for a monthly median day, enable operators to visually inspect signal coverage consequences of potential communications link configurations and evaluate the potential effectiveness of broadcast transmission. The decision-aid currently displays the sky and ground wave signal coverage from one of ten frequencies for one time, in terms of signal-to-noise ratio (SNR) and received signal power (dBμV/m). Basic statistics of the skywave signal coverage within a 5° box centred on each hostile receiver can also be requested by the operator. Figure 2 illustrates the utility of the tactical propagation technique. At 26 MHz the signal coverage map shows that two of the friendly stations are predicted to receive signals and two hostiles and one friendly are predicted to be in the 1F and 2F propagation skip zone.

The second output format are colour frequency prediction graphs similar to those produced by PROPHET [*Argo and Rothmuller*, 1979] and facilitate point-to-point vulnerability predictions. The first graphical output shows the operational Maximum Usable Frequency (i.e. the basic MUF considering ionospheric parameters, and a correction factor to allow for propagation mechanisms above the basic MUF [*CCIR*, 1994]) over a 24 hour period. Figure 3 shows the operational MUF between one transmitter and a friendly receiver (Tx-Atlantc1), and between the transmitter and three hostile receivers (Atlantc4, 5, 6). Version 1.0 allows the maximum of 10 friendly and 10 hostile receiver locations to be analysed. The vertical lines indicate frequency ranges that are predicted ***not*** to propagate to the hostile receivers with the number of lines reflecting the number of hostiles not receiving signals. For example, in Figure 3 at 17 UT, the frequency range 17-19.5 MHz is not received by one hostile. The frequency range 19.5-22.5 MHz is not received by two hostiles and the frequency range 22.5-24.5 MHz is not received by three hostiles. For completeness, the Lowest Usable Frequency (LUF) from the friendly transmitter to the friendly receiver is also plotted.

If more than one friendly receiver station is available for communications, a composite operational MUF, i.e. the greatest hourly operational MUF, between the transmitter and any friendly is plotted and an algorithm determines the optimum friendly receiver that should be used to minimise interception. Figure 4 is a (colour) composite operational MUF output assuming three friendly and three hostile

stations. Again the vertical lines indicate frequency ranges that ***cannot*** be intercepted, and the number of vertical lines reflect the number of hostiles ***not*** intercepting the signal. The colour of the horizontal bar at 35 MHz denotes the most secure friendly station. In the illustrative example, Figure 4, Friend F2 should be used between 00-04 UT, Friend F1 between 04-08 UT, F3 between 10-12 UT and F1 between 13-24 UT. No recommendation is made at 09 and 12 UT since all three hostiles are predicted to intercept the signal.

The two MUF graphs described above are only displayed to the HF 'expert'. The 'operator' receives the MUF data as a 24 hour, colour coded, frequency management table (Figure 5). The table recommends frequency ranges and the optimum friendly receiver stations that should be used to minimise interception. Hostiles predicted to intercept signals are indicated by an asterisk, and the hostile ordering, from left to right, indicates decreasing probability of interception. If all hostiles intercept the signal, then the frequencies recommended are coloured red (e.g. 09 and 12 UT) indicating that all propagating frequencies are intercepted. Under these conditions signal transmission should be avoided whenever possible. If this is not possible the red frequency range displayed is the best available to minimise signal coverage. The yellow coloured frequencies (e.g. 3-8 UT) are those that should be used with caution because at least one hostile can intercept the signal. The green frequencies (e.g. 16-23 UT) are those predicted to be safe from signal interception.

Future development of the HF decision-aid

The signal coverage predictions calculated by the jamming and interception element of the decision aid are currently based on REC533 [*CCIR*, 1994] predictions which uses a median ionospheric model and basic mirror reflection ray-tracing technique. Although improvements to the median ionospheric model will be achieved using updating techniques, is anticipated that in future versions of the decision aid (Figure 6) an improved ionospheric specification model such as PRISM [*Daniell et al*, 1994] may be used. The potential improvements to skywave jamming and interception model are outlined in Figure 6.

A more accurate propagation prediction model using ray-tracing techniques such as the analytic ray-tracing model [*Norman and Cannon*, 1996] or the computationally intensive numerical ray-tracing technique [*Jones and Stephenson*, 1975] must also be incorporated. Within the propagation model the decision aid currently assumes isotropic antennas for worst case interception scenarios. More realistic antenna models may also be incorporated to enable more realistic system scenarios to be examined.

The vulnerability assessment model currently examines signal coverage and the path MUFs. In a future version of the model the lowest usable frequency (LUF) will also be considered to minimise signal coverage [*CCIR*, 1993]. At low frequencies, close to the LUF, skywave signals are attenuated but near vertical incidence coverage can be maintained as can ground wave coverage. Consequently, secure communications can be established within a small area. This is illustrated in Figure 7. The signal coverage at 3 MHz is restricted to the Northern Atlantic region and is intercepted by the three nearby friendlies and denied to the three distant hostiles.

In Version 1.0 the GRWAVE [*CCIR*,1994] ground wave prediction program has been incorporated for completeness but is currently not used within the assessment model. The ground conductivities used within the current decision aid are assumed to be constant in azimuth for all ranges, and land-sea boundaries are not considered. It is anticipated that in future version of the decision-aid these deficiencies will be corrected to enable a more complete HF vulnerability assessment to be made. The vulnerability model may also include hostile equipment characteristics such as signal processing time, antenna tuning time etc. These parameters will enable the effectiveness of hostiles to be evaluated more accurately within the assessment model.

The enhancements outlined above will be incorporated within the decision-aid with commensurate improvements to the users input/update interface ensuring easy use for the inexperienced 'operator'. For example, if only crude predictions are required then the operator may select the mirror reflection

technique and the median ionospheric model for computational ease and speed. If, however, very accurate predictions are required in a specific area then the improved ionospheric model (e.g. PRISM *Daniell et al.*, [1994]) may be selected in conjunction with analytic or numerical ray-tracing .

Conclusion

This paper has outlined a somewhat idealised design of a HF decision-aid to minimise communications vulnerability. The aid is based on the tactical use of signal propagation and exploits knowledge of the ionosphere and ray tracing techniques to minimise signal coverage and deny, or minimise, the enemies access to the radiated electromagnetic energy. The EPM improvements obtained may be used in isolation or to complement other sophisticated systems techniques such as antenna nulling and spread spectrum system.

A decision-aid system currently being developed at the DRA, for the inexperienced and expert HF communicator, has been described. This system currently uses simple frequency management techniques to minimise communications vulnerability. The decision-aid, however, suffers from an inaccurate ionospheric and propagation prediction model, but new more accurate analytic ray-tracing, and ionospheric specification models are currently being developed.

The tactical decision-aid described may be used by conventional HF operators in near real-time, as a component of other electromagnetic modelling systems (e.g. EEMS [*Moore and Lewis*, 1994]) or off-line during the mission planning stage, to predict and configure the least vulnerable HF communications links. The system could also be used to automatically configure current HF equipment. This latter approach will be particularly powerful when used in conjunction with ARCS [*Arthur and Maundrell* 1994] based systems. Although this paper has concentrated on the application of the decision-aid to maximising EPM characteristics, the system may also be used to optimise communications link quality and reliability and contribute to the effective deployment of ECM systems, or even just as a HF communications training aid.

References

Argo and Rothmuller, "PROPHET"; an application of propagation forecasting principles", *Solar-Terrestrial Predictions Proc.* Vol. I, 312-321, 1979.

Arthur P.A, and M.J. Maundrell, "Automated HF systems- a framework for a way ahead". *HF Radio Systems and Techniques, IEE*, CP392, York, U.K. 1994.

CCIR International Telecommunication Union Radio Communications Bureau, *Rec. 533*, Computer program for satellite communications, Geneva 1994.

CCIR "Propagation factors affecting frequency sharing in HF terrestrial systems". Draft recommendation to question 38/6, WP 6A, Sept. 1993.

Daniell, R. E., W.G. Whartenby, L. D. Brown, D. N. Anderson, M. W. Fox, P. H. Doherty, D. T. Decker, J. J. Sojka, and R. W. Schunk, PRISM: A Parameterised Real Time Ionospheric Specification Model, submitted to *Radio Science* 1994.

Goodman, J. M., D. R. Uffleman, and F. Fahlsing, "The role of the propagation environment in HF electronic warfare". Propagation effects on ECM-resistant systems in communications and navigation. *AGARD*, CP331, London, U.K., 1982.

Jones, R. M. and J.J. Stephenson, A three dimensional ray-tracing computer program for radio-waves in the ionosphere, *OT Report 75-76*, US Dept of Commerce, Office of Telecommunications, 1975.

Platt I., and P. S. Cannon, "A propagation model for the mid and high latitude ionosphere over Europe", *HF Radio Sys. and Tech IEE,* CP392, York, U.K. 1994.

Shukla A. K, and P. S. Cannon . "Interim report on ECCM interception for HF BLOS communications". *DRA Technical Report 1992 (Unpublished).*

Teters, L. R., J. L. Lloyd, G. W. Haydon, and D. L. Lucas, "Estimating the performance of telecommunications systems using the ionospheric transmission channel: Ionospheric Communications Analysis Prediction Program (IONCAP) user's manual", *NTIA Report 83-127, NTIS order no N70-24144,* NTIA Springfield, VA, USA, 1983.

Uffleman D. R., O. H. Harnish, J. M. Goodman. "The application of real-time model update by oblique Ionospheric sounders to frequency sharing" *AGARD EPP, CP332,* 1982

Shukla A. K, Cannon P. S. "Prediction model updating using the ROSE-200 oblique sounder at mid and higher-latitudes", *IEE 6th Int. Conf. on HF radio systems and techniques, York, U.K.* 1994

Arthur P. C. , N. C. Davies, P.S. Cannon and M. J. Angling "Rose-300: A flexible architecture for a high performance oblique ionosonde". *IEE 6th Int. Conf on HF Rad.. Syst. & Tech. York, U.K.* 1994

Barry G. H., R.B. Fenwick "Oblique chirp sounding" in Jones T.B. (Ed). "Oblique ionospheric radio wave propagation" *AGARD Conf Proc. No 13, p487* 1969.

Norman R., P. S. Cannon "A new two-dimensional analytic ray-tracing technique accommodating horizontal gradients" *Accepted Radio Science* 1996.

Moore M R., D.J W. Lewis, "The development of an operational radio /radar propagation package " *MoD Report (Unpublished)* 1994.

Moore M. R., A.K. Shukla "High frequency coverage predictions for EEMS", *Battlespace Atmospherics Conference, NRAD, San-Diego,* 1996

CCIR International Telecommunication Union Radio Communications Bureau, *Recommendation 368,* GRWAVE - Computer program for satellite communications, Geneva 1994

© British Crown Copyright 1997/DERA

Published with the permission of the Controller
of Her Britannic Majesty's Stationary Office

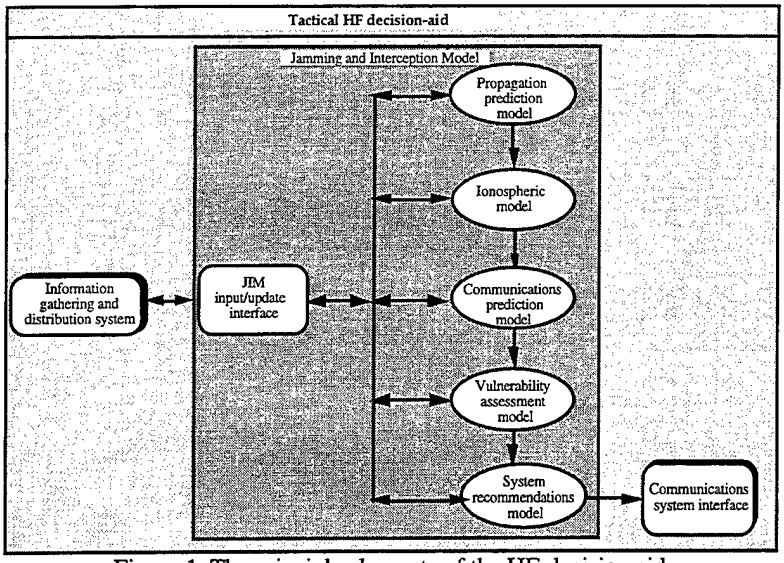


Figure 1. The principle elements of the HF-decision aid

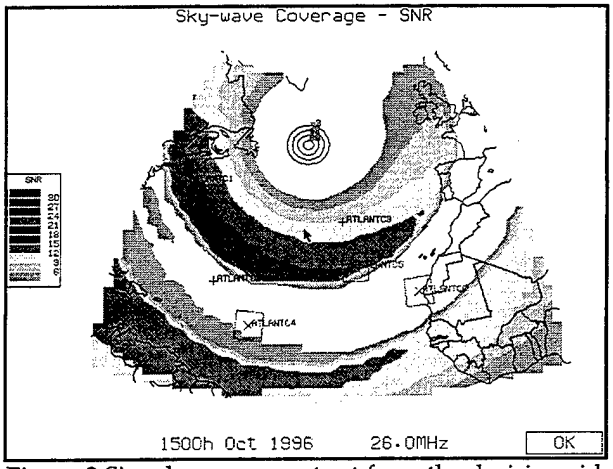


Figure 2 Signal coverage output from the decision aid showing ground and skywave propagation.

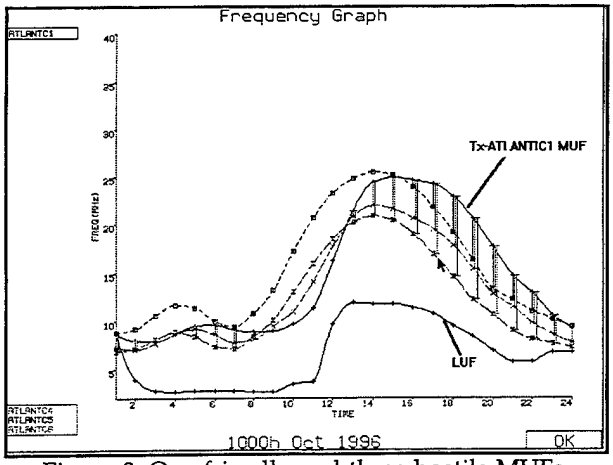


Figure 3. One friendly and three hostile MUFs.

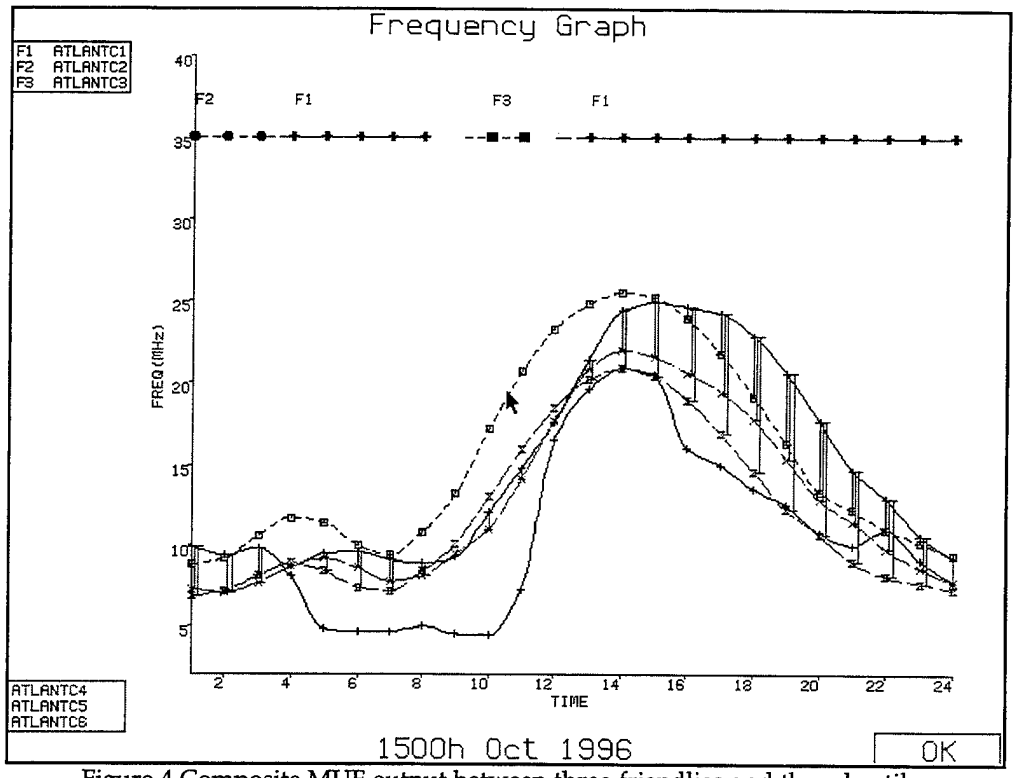


Figure 4 Composite MUF output between three friendlies and three hostiles

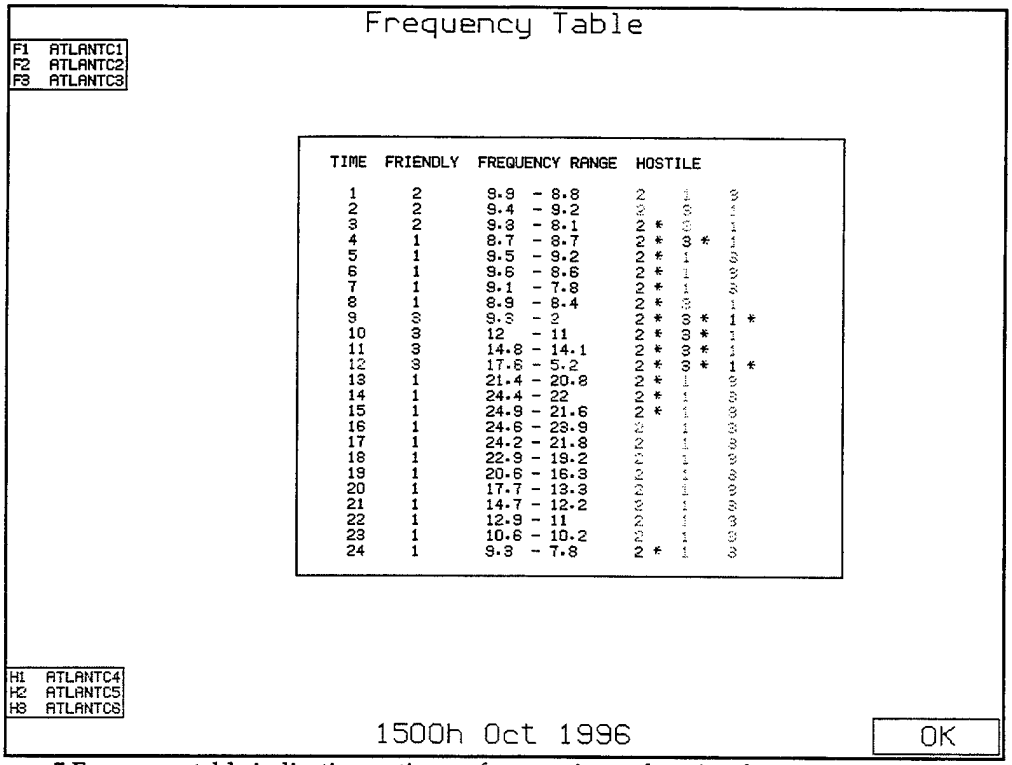


Figure 5 Frequency table indicating optimum frequencies and station for minimum interception.

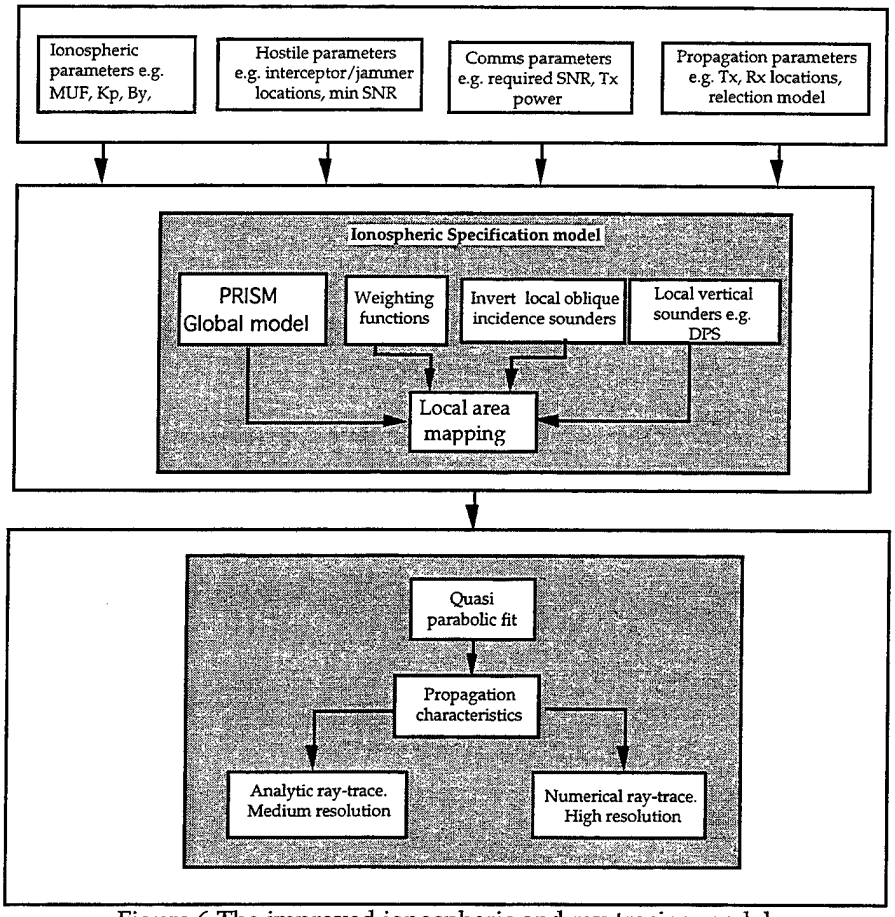


Figure 6 The improved ionospheric and ray-tracing model

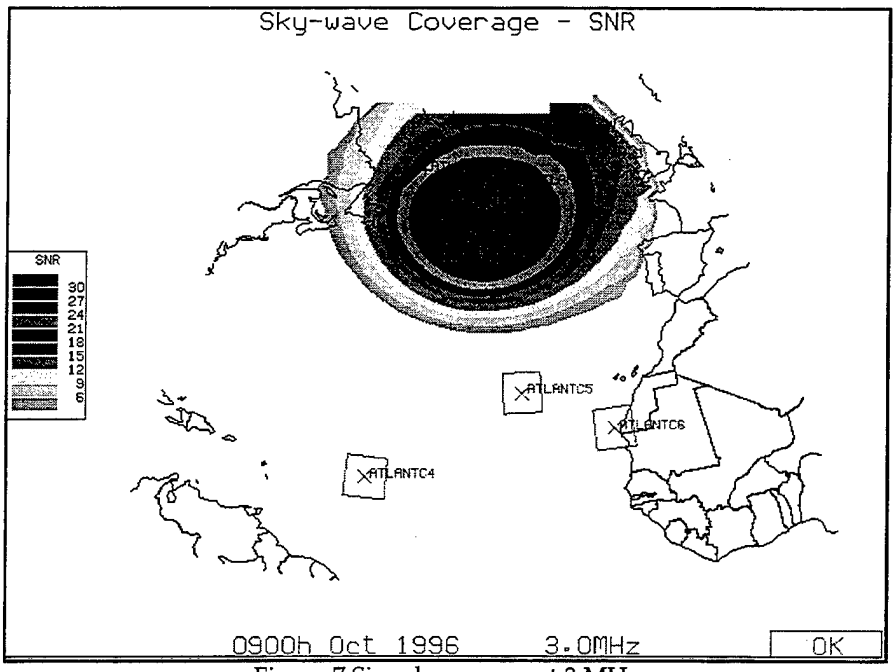


Figure 7 Signal coverage at 3 MHz

TACTICAL WEATHER RADARS FOR THEATER METEOROLOGICAL DATA COLLECTION AND ASSIMILATION

Nicholas J. Bucci, Henry S. Owen, Dr. James V. Melody, John F. Heimmer
Lockheed Martin Government Electronic Systems, 199 Borton Landing Road, Moorestown, NJ, 08057

ABSTRACT

The efficiency and safety of all operations conducted within the battlespace can be improved with knowledge of environmental conditions. The warfighter, whether at sea, on land, or in the air, can 1) optimize the performance of electro-magnetic and optical sensors by adjusting operational parameters, 2) select proper weapons or sensors, or 3) change the engagement scenario to take greatest advantage of the environmental conditions by knowing the propagation conditions and clutter environment which are being encountered. In addition, knowledge of wind fields can aid in a number of aspects of theater operations, including ballistic trajectory corrections and determination of path and dispersion of radioactive, chemical and biological agent weapon clouds.

Lockheed Martin Corporation has developed a signal processing technique that enables meteorological information to be collected by tactical radars. The technique allows the radar to operate using its normal tactical doctrine, and processes the return data separately to extract meteorological information. The concept has been tested through simulation and laboratory experiment, and is being used to examine the capability of the AEGIS SPY 1 B/D radar to measure meteorological information. This paper will examine the use of this signal processing technique in a number of sensors deployed throughout theater operations to extend this capability. By implementing this signal and data processing capability on a number of sensors, weather information can be collected from the edges of the theater at sea and as far as 300 miles inland.

1.0 Introduction

The efficiency and safety of all operations conducted within the battlespace can be improved with knowledge of environmental conditions. Knowing propagation conditions and the clutter environment enable the warfighter, whether at sea, on land, or in the air to aid the warfighter in decisions to: 1) optimize the performance of electro-magnetic and optical sensors by adjusting their operational parameters, 2) select proper weapons or sensors for a particular engagement, or 3) change the engagement scenario to take greatest advantage of the environmental conditions.

Knowledge of three dimensional wind fields can aid in a number of aspects of theater operations as well. Measured winds improves ballistic trajectory corrections for Naval Surface Fire Support, land based counter-battery fire and tactical ballistic missile defense. In addition, three dimensional winds information will help in the determination of path and dispersion rate of radioactive, chemical and biological agent weapon clouds.

Lockheed Martin Corporation Government Electronic Systems has developed a novel signal processing technique [1] that enables the collection of meteorological information by tactical radars. All current operational meteorological radars use uncoded waveforms for determining weather phenomena parameters, such as the three primary spectral moments. Most tactical radars use coded waveforms and pulse compression for tactical operations such as search and tracking to gain additional sensitivity and improved range resolution. Combining the two functions of tactical operations (search and track) and weather surveillance has not been appropriate until recently because of this major difference in the transmitted waveform and the signal processing and the technological barrier of the use of pulse compression in weather radars.

Meteorological sensors have not used pulse compression because of the range sidelobes generated by the pulse compression process. The technique introduced by LM GES is a doppler tolerant range sidelobe suppression (DTRSLS) technique. This technique is designed to maintain low range sidelobes over a range of doppler frequency shifts on the return pulse data. In tactical sensors, coded waveforms do not present range sidelobe problems because the requirements are not as stringent since the targets of interest are not extended over large ranges. For detection of point phenomena, peak range sidelobe (or perhaps average or RMS sidelobe) levels are of the most interest and these levels are not as sensitive to doppler shift on the return signal.

The DTRSLS technique allows the radar to operate using its normal tactical doctrine, that is, using the coded waveforms that it uses for target search and track. The DTRSLS concept has been tested through extensive simulation [2,3] and laboratory experiment [4,5]. It is currently being used to examine the capability of the AEGIS SPY 1 B/D radar to measure meteorological information at the Navy's

Combat System Engineering Development (CSED) Site in Moorestown, NJ [6].

By implementing this signal and data processing capability on sensors deployed throughout the theater, weather information can be collected from the edges of the theater at sea and as far as 300 miles inland. This assumes that the deployed forces are arriving to a theater operation from the sea, and penetrating inland. Using shipboard sensors (AN/SPY-1 B/D, AN/SPN-43 AN/SPS-48, and AN/SPS-49 radars) weather information can be collected at sea, at the land-sea interface, as well as inland for approximately 50 nautical miles or more. This data can support all naval operations in the area, but in particular amphibious and landing operations, Naval Surface Fire Support, and strike operations. Once land based sensors have been deployed ashore, ground based radars such as the TPQ-37 and the Patriot radar, can be used to collect weather information approximately 150 miles inland, depending on sensor emplacement. This information can support land based operations further inland, such as forward troop movements and counter battery fire support. Finally, airborne support sensors aboard E3A AWACS aircraft can be used to collect meteorological information 300 miles or more inland. Combining this weather information enables theater command to better conduct all operations in a safer more efficient manner.

The weather information from all of the tactical sensors can be used by each sensor's operator to better optimize operating parameters and better understand the clutter and propagation environment. The data from each sensor can be fed to Fleet Numerical and Meteorology and Oceanography Center (Fleet Numeric) or other forecasting organizations for use in global and local forecasting models. To reduce time latency of the data transmission networks and the time required to assimilate the data into models and run the forecasting models at the forecasting organizations, the weather data can be used onboard a sensor's platform (those with the processing power available) to provide in situ short term local forecasts for the theater. The data collected by tactical sensors combined with the ever increasing computing power available in vector and scalar processors enables in situ forecasting within the theater. The individual sensors can use the data to:

- visualize clutter environment with a high temporal and spatial resolution, accurate clutter map to aid in waveform selection and to suppress clutter detections and tracks for improved sensor performance monitoring, optimization, and prediction;
- produce advanced weather products such as detection of hazardous weather phenomena (wind shears/shifts, storm tracking and storm structure),
- provide a three dimensional wind field maps to aid in fire control and fire support and to better understand the dispersion of chemical, biological and radioactive clouds, and
- (if sensor has sufficient sensitivity) provide detection of clear air phenomena - cloud layers and clear air wind fields.

The remainder of this paper will introduce the signal processing technique, and examine its use in a number of sensors deployed throughout the theater to extend this weather capability. In addition, preliminary hypotheses for uses in tactical operations of the data to be collected by the tactical sensors will be presented.

2.0 Tactical Weather Radar Concept

The primary functions of most tactical radars deployed in a battle environment are for the surveillance and tracking of targets, either planes, missiles/shells, and surface targets (ground vehicles or surface ships). The environment in which most tactical sensors operate includes a tremendous amount of clutter and environmental returns as well as returns from these desired targets. A passing storm can significantly change the picture observed by the radar operator by presenting numerous unwanted "clutter" detections that are moving at about the velocity of the local winds or the storm movement. A chaff cloud can present a similar picture. Ducting can produce surface tracks to the operator in beam positions that would indicate these targets have altitudes of thousands of feet. Knowledge of the clutter environment and ducting conditions can change the picture displayed to a radar operator. In addition, the knowledge of the ducting and clutter can improve the performance of the sensor by allowing the operator to optimize the sensor parameters to best deal with the clutter environment at the moment, and to change the parameters as the clutter environment changes.

The challenge for the Tactical Weather Radar (TWR) Concept is to obtain as much information as possible about the weather, clutter, and propagation conditions so that the performance of the sensor and hence the warfighter can be improved. The desire is to extract this meteorological information with as

little impact on the operational sensor as possible. The impact to the sensor is measured in many ways, two of the most important are: 1) additional hardware required to perform weather processing, and 2) changes in the sensor's operational doctrine, that is, altering its resource allocation budget. The goal of the TWR is minimize both of these impacts while maximizing the amount of information collected on the weather phenomena, clutter, and ducting conditions.

Ideally, the TWR will collect weather information from the same tactical dwells the radar uses to detect point targets by using an alternate processing channel. In general, the weather data collection begins with the generation of the three primary spectral moments of the phenomena. These three moments are: Reflectivity, mean doppler velocity, and doppler spectrum spread. The reflectivity is a measure of the reflected power from the scatterers within a particular resolvable range, azimuth, elevation cell; it is essentially a volumetric form of radar cross section since it is normalized by the radar parameters and the range from the radar. It is normally expressed as reflectivity factor with some adjustments made for transmit wavelength and particle scatterer type. The mean doppler velocity measure is the mean radial movement of the scatterers within the resolvable cell. The doppler spectrum spread is a measure of the variability of the doppler components that exist within the resolvable cell; it is an indication of the turbulence, bimodality or variation of the doppler.

The measurement for reflectivity does not require a multiple pulse coherent dwell, since it is a measure of the reflected power from a particular cell. To measure reflectivity, it is only required that sufficient independent samples of the weather phenomena are collected by the system to form accurate estimates of the reflectivity, if the number of independent looks can be obtained by averaging a number of range intervals and/or a number of multiple simultaneous transmissions (such as multiple transmit and receive beams or frequency channels) then a single pulse dwell can be used to determine the reflectivity. To measure the mean velocity and spectrum spread parameters a coherent multiple pulse dwell is needed. To measure these doppler characteristics, the pulse to pulse characteristics of the phenomena must be determined, such as pulse to pulse phase change which indicates doppler shift. The mean pulse to pulse phase shift is proportional to mean velocity, and the variance of this phase change is proportional to spectrum spread.

From these moments, advanced weather products can be generated describing the weather environment, its movement and evolution. These moments are used for detection of weather phenomena as well as forecasting of weather conditions. Using intelligent pattern recognition algorithms, certain patterns within the spectral moments will describe the presence of a particular type of weather phenomena, such convective storms, microbursts, and many others. In addition, the spectral moments and their change with time can be used along with other meteorological information available from other sensors aboard or satellites such as winds, temperature, barometric pressure and others to produce near and long term forecasts. Wind fields are generated using the data collected from multiple sensors (wind triangularization from radial winds) or from one sensor (existing single doppler wind retrieval algorithms).

The doctrine and mission of a sensor must be considered in the way that the TWR concept is applied. In some applications, impact on hardware (requirement to remain compact and mobile) is as important or even more important than impacting that operational doctrine. In these cases, the TWR aims to introduce little (if any at all) new hardware to perform the weather processing. Weather information can be extracted by time sharing available hardware or altering the processing in the tactical chain, without impacting the tactical performance, such that some of the signal processing for the weather information extraction can be performed in the tactical processing channel. In other cases, the impact to doctrine is important because the critical nature of the mission such as: the SPY-1 radar and providing self and area defense and for the safety of the sensor and crew, or the TPQ-37 radar where radar resources are limited for the firefinder and counter battery functions to avoid detection.

In some cases, additional meteorological information can be obtained with little additional impact to the sensor, such as small requirements on radar resources to collect additional weather information while the radar is not in a battle condition. A radar control program which is adaptable in this way can enable the system to use the amount of radar resources which are available, that is, in battle situations, minimal weather information may be collected (that available from tactical dwells),

but in other conditions, an abundance of weather information can be collected because resource requirements can be reduced for some of the tactical portions of the radar's doctrine.

In some radars, multiple pulse dwells are used only in areas where clutter rejection is needed (for surface scans and where clutter exists), and this could limit the scan volume in which mean doppler and doppler spread are collected. It would be useful to extend the use of multiple pulse dwells to provide estimates of all three spectral moments throughout volume. The detailed clutter map could be used to define where multiple pulse dwells should be used, such that when a threshold is crossed a flag is set to transmit multiple pulses in a beam position. The rejection of surface clutter is important in mapping weather phenomena, the presence of surface clutter spectra in a return will produce biased estimates of the reflectivity, mean velocity and spectral spread. If radar resources are available, extra pulses could be used in the low elevation tiers to provide improved surface clutter characterization and in some cases improved surface clutter rejection. To be able to perform wind profiling and clear air observations long coherent dwells are generally used. The long coherent dwells provide signal integration (many pulses are coherently integrated) such that weak signals (like clear air) are detectable. The benefits of providing 3D wind fields and cloud layers can far outweigh the resource requirements.

The overriding goal of the TWR is provide as much weather information at as little cost as possible, where the cost is measured by dollars to place equipment for processing, and by radar resource requirements to collect weather information. Figure 1 shows a typical tactical weather radar adjunct processor. The additional processing required provides control for the weather processor side which is tied to the overall radar controller. The weather processor includes signal and data processing to calculate the three spectral moments and to provide the advanced weather products.

The TWR adjunct processor will tie into the tactical radar in a number of ways. First, the received radar data will be extracted from the tactical system's receiver / signal processor by the weather signal processor (WSP). In addition, the radar control parameters will be passed to the weather system controller (WSC) by the tactical system's radar controller so that information concerning the radar operating parameters for each transmit sequence can be extracted. The WSC determines if the mode type indicates that the dwell is used for weather data collection. If so, the WSC extracts necessary information such as beam position, dwell type, operating parameters (pulsewidth, transmit frequency, pulse repetition interval (PRI), and so on) so that the WSP can perform the proper signal processing. The WSP performs the computationally intensive signal processing such as pulse compression and doppler processing. The weather data extractor (WDE) takes the periodogram estimates or the estimates of the first lag of the autocorrelation function and calculates the spectral moments. Detailed discussion of this processing is given in [7]. The spectral moments are then passed to the weather data processor (WDP) so that weather phenomena features can be extracted by automated detection algorithms, such as gust fronts, microbursts, wind field, etc. The WDP is also used to generate short and long term in situ forecasts using both the data generated by the ownsensor and data from other tactical sensors received via the weather communication processor (WCP). The output

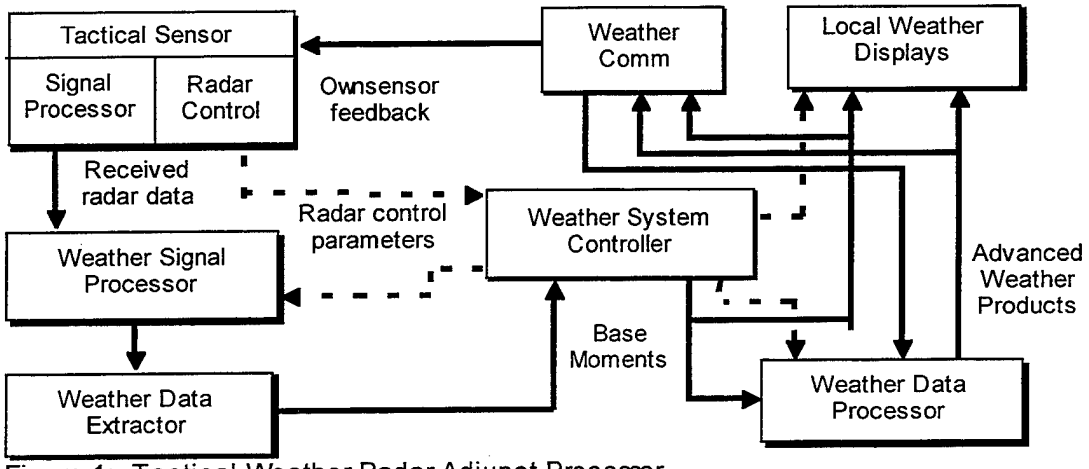


Figure 1: Tactical Weather Radar Adjunct Processor

of the WDP is formatted for presentation on the local displays as a synopsis of the weather picture, In some cases, it is desirable to view the raw spectral moments, and these will be made available for the displays as well. Finally, spectral moments and advanced weather products are sent to the WCP for formatting and message formation for transmission to other tactical radars, to theater command and/or forecasting organizations for long and short term forecasting

Minimizing the hardware impact could also minimize weather processor's achievable functionality. The trade of weather information obtained versus hardware and radar resource impact much be made on a sensor by sensor basis. The tactical mission and hardware configuration of each sensor will change the trades sufficiently such that a solution for one sensor may not easily extend to others.

3.0 Weather Surv. and Pulse Compression

Weather phenomena are random processes, the spectral moments of weather phenomena are also random. In measuring the primary spectral moments, a sensor must obtain multiple independent looks of a resolvable cell so that the variability in the measurement can be reduced and accurate measures of reflectivity, mean velocity and spectrum width can be obtained. The number of looks required is dependent on the parameters of the radar (pulse repetition frequency, transmit frequency, sensitivity parameters which determine signal to noise ratio - gain, transmit power, losses) and the assumed properties of the weather phenomena (spectral spread, coherence time), as well as the required accuracy of the spectral moments. A typical value for the number of independent samples for an S-Band radar is 100. The multiple independent looks at a resolvable cell can be obtained in any number of ways, including: multiple transmit pulses, multiple simultaneous transmit/receive channels, range sample to range sample, and multiple scans.

All current operational meteorological radars use uncoded waveforms for determining weather phenomena parameters. Tactical radars, on the other hand, use coded waveforms and pulse compression for tactical operations such as search and tracking to gain additional sensitivity and improved range resolution. Combining tactical operations and weather surveillance has not been appropriate until recently because of this major difference in the transmitted waveform and the signal processing and the technological barrier of the use of pulse compression in weather radars.

Meteorological sensors have not used pulse compression because of range sidelobes which are a result of pulse compression. Range sidelobes arise from the distributed nature of the pulse compressed signal. Range sidelobes are energy received at the desired sampling time but from other ranges than that of the desired range interval . When a coded waveform is pulse compressed, what results is a function of time whose range extent covers more than the compressed pulsewidth (the inverse of the transmit signal's bandwidth). Figure 2 shows a typical pulse compression function, its time extent is twice the transmit pulsewidth, its range resolution is equal to the width of the mainlobe portion which is approximately the inverse of the transmit signal's bandwidth. The distributed nature of weather requires extremely low range sidelobes to avoid corruption, since the weather extent is greater than the compressed pulse length.

In tactical sensors, coded waveforms do not present range sidelobe corruption problems since the targets of interest are not extended over large ranges. In addition, for detection of point phenomena, peak range sidelobe level (PSL) (or perhaps average or RMS sidelobe levels - RSL) levels are of the most interest and these levels are not as sensitive to doppler shift on the return signal. For extended phenomena such as weather, the figure of merit for the range sidelobes is integrated sidelobe level (ISL). ISL is the measure of the total sidelobe energy divided by the total mainlobe energy. ISL is an acceptable measure of sidelobe performance for distributed phenomena since it measures the amount of energy received from all range sidelobes compared to the mainlobe return just as would be expected from an extended weather return. The smaller the ISL, PSL, or RSL (greater negative values in dB), the better the sidelobe performance.

Many methods exist for reducing range sidelobes but these techniques are very sensitive to doppler. Without a priori knowledge of the doppler environment, the range sidelobes that are achieved through these suppression techniques may not be sufficient to avoid corruption from range sidelobes. The DTRSLS technique is designed to maintain significant range sidelobe suppression over a range of doppler frequency shifts on the return pulse data. Figure 3 shows the improved integrated sidelobe levels that are achieved with the DTRSLS versus those with non doppler

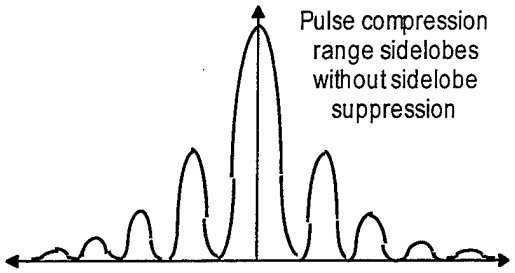


Figure 2: Pulse compression function

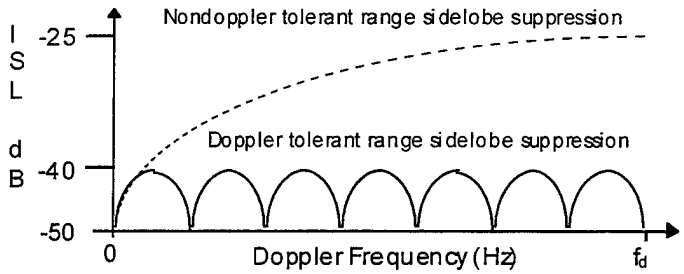


Figure 3: Integrated sidelobe levels versus doppler shift

tolerant range sidelobe suppression. The DTRSLS technique allows a radar performing tactical and weather surveillance to operate using its normal tactical doctrine, that is, using the coded waveforms that it uses for target search and track. The meteorological information is extracted by processing the return data separately from the normal tactical signal and data processing using an optimized range sidelobe suppression processing channel.

The DTRSLS concept has been tested through simulation and laboratory experiment. An extensive simulation effort analyzed its performance in accurately mapping weather phenomena, including range sidelobe level performance in the presence of certain weather phenomena and system characteristics, which includes the fluctuating nature of the weather phenomena and the transmitter and receiver characteristics of the radar. Laboratory tests were conducted using research weather radars to collect time series data transmitted virtually simultaneously using "normal" weather radar waveforms (uncoded) and processing, and using coded waveforms and pulse compression with DTRSLS. The data were then processed off-line to determine the weather parameters of the volume scanned. The Tactical Weather Radar concept is being used to examine the capability of the SPY 1 B/D radar to measure meteorological information at the Navy's Combat System Engineering Development (CSED) Site in Moorestown, NJ.

Pulse compression for weather surveillance provides significant benefits. The two major improvements are: 1) increased sensitivity to detect weaker weather phenomena, and 2) data collection time reductions [8]. The sensitivity increase is achieved by transmitting more average power on the weather phenomena (increasing the average power by increasing the pulsewidth). The increase in sensitivity through pulse compression is then equivalent to the time bandwidth product of the coded waveform (when compared to a system that has the same range resolution without using pulse compression and the same peak transmit power). The data collection time reductions are achieved through a higher transmit signal bandwidth which provides improved range resolution (smaller resolvable range cells), which are averaged as independent samples of the return signal to achieve accurate spectral moment estimates. Pulse compression can be used to change the way that radars perform weather surveillance. Figure 4 depicts current weather radar surveillance technology, and weather surveillance technology employing pulse compression. Present weather surveillance technology uses a mechanically scanned reflector antenna with long multiple pulse coherent dwells using uncoded transmit pulse over a single transmit / receive channel.

Many tactical radars have properties that provide significant capability for weather surveillance. As explained above, pulse compression provides significant performance enhancements in the way of increased sensitivity and reduced data collection times. Since most tactical sensors employ transmit waveforms that are of much higher bandwidth than a typical weather radar these advantages are easily employed in a TWR.

Also, many tactical sensors are electronically scanned phased arrays (scanning either 1D or 2D), and this property of tactical sensors also provides significant benefits to weather surveillance. In general, an electronically scanned phased array can scan a volume faster than a mechanically scanned array because of mechanical scan speed limitations that are applicable to electronic scanning. In addition, a phased array can employ time division multiplexing of beams to collect data faster. Time division multiplexing collects data from multiple beam positions at a singe time on one transmit channel, by transmitting and receiving at each beam position for only a limited amount of time during each pulse [9]. Another advantage of electronic scanning is the inertia-less beam pointing. Scan modulation introduces a bias error into the spectral width by amplitude modulating the return signals because the point on the beam at which the

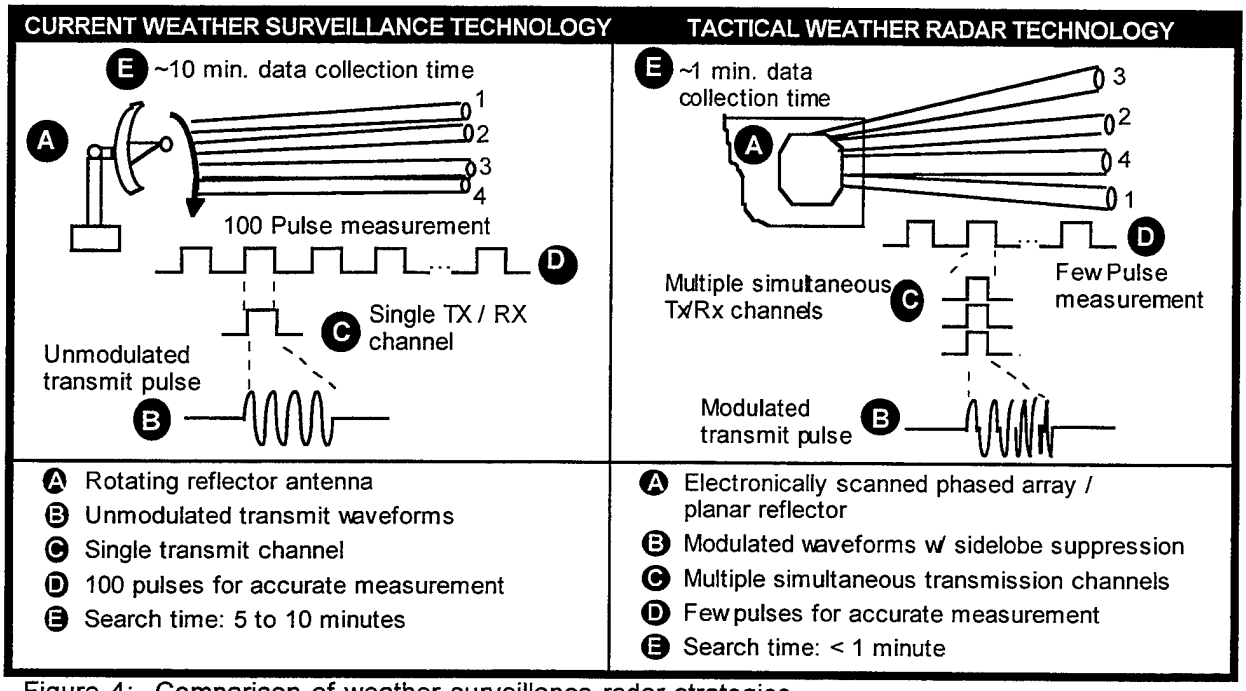


Figure 4: Comparison of weather surveillance radar strategies

return is measured changes during the dwell as a result of the mechanical scanning. Using a two dimensional electronically scanned phased array eliminates the scan modulation that is inherent in a mechanically scanned system, a one dimensional electronic scan will reduce but not eliminate scan modulation since it still mechanically scans in one dimension.

Mechanically scanned systems use fixed radar resource scheduling, and do not normally stray from this fixed scan sequence. Phased arrays, however, can dynamically allocate resources to various functions to enable multiple prioritized functions to be built into the same sensor. In addition, resource allocation can be optimized to provide full functionality for each function based on it's radar resource requirements. The radar can allocate resources to the function with the highest priority requiring resources at that time, and can accommodate new functions like dedicated weather dwells which provide significantly improved functionality.

Many tactical radars utilize multiple simultaneous transmit / receive channels which enables the radar to collect data from multiple operating frequencies, beam positions, polarizations, etc, at one time. For weather surveillance, these channels can be used to collect the independent samples that are required to reduce the variance of the spectral moment estimates as discussed previously.

In most tactical sensors operating doctrine, there are multiple radar scans that comprise the radar's full scan capabilities. These scans can be single pulse horizon search and volume search scans, multiple pulse horizon and volume search scans, single pulse and multiple pulse track scans, and many others. These individual scans may have properties which can be exploited in the collection of weather data. In addition, the multifunction scans allow new scans to be added that may allow improved weather data collection but also have some benefits for tactical operation, such as a pulsed doppler dwell on the horizon for a sensor that does not currently employ such a scan. This dwell provides capability for both weather and tactical operations by improving the surface clutter spectrum characterization.

4.0 Theater Met. Data Collection Concept

The TWR concept enables Theaterwide weather data collection and assimilation. This concept calls for a multitude of tactical sensors deployed throughout the theater to collect weather information in the TWR fashion, and to share this information and also to provide the information to Fleet Numeric or other forecasting organizations. The weather data, basic spectral moments, advanced weather products and forecasts - including short term in situ forecasts, can be used at each sensor for performance optimization and at theater command and throughout the theater for planning, execution and evaluation of all operations. Figure 5 shows a concept for a

theaterwide, TWR based, weather data collection and assimilation concept.

The theaterwide data collection concept allows weather information to be collected at sea, at the land-sea interface, and inland as much as 300 miles or more to the target area using multiple deployed tactical sensors aboard ship, deployed inland, and airborne. The amount and type of weather information collected will depend on the deployment of each of the sensors in the theater, and the tactical weather radar capability built into each of the sensors used to collect the data.

The inherent line of sight for each type of sensor (shipborne, land based, or airborne) limits the weather data collection capability. For shipborne sensor weather capabilities using the TWR concept, an inherent line of sight range capability is on the order of 50 - 100 Miles inland depending on the deployment of the ship in relation to the shore. A shipborne weather capability will have a range extent of approximately 150 miles. The shipborne weather capability will be useful in collecting data for the detection of storms, the mapping three dimensional winds, and the detection of cloud layers. For land based sensor weather capabilities using the TWR concept, an inherent line of sight range capability is on the order of 100 to 150 miles inland depending on the deployment of the land based sensor in relation to the shore and the sensitivity of the sensor. A land based weather capability will have a range extent of approximately 50 to 150 miles. The land based weather capability will be useful in collecting data for the detection of storms, and the mapping of three dimensional winds. For airborne sensor weather capabilities using the TWR concept, an inherent line of sight range capability is on the order of 150 to 300 miles inland depending on the flight path of the airborne sensor in relation to the shore and the sensitivity of the sensor. An airborne weather capability will have a range extent of approximately 100 to 200 miles. The airborne weather capability will be useful in collecting data for the detection of storms. The detection range extent for each type of system will be dependent on the sensitivity of the system (transmit power, antenna gains, losses, etc.). The sensitivity of the systems varies greatly from sensor to sensor, such the weather sensing capabilities will also vary greatly. Each of the three types of sensor will be able to provide the three primary spectral moments along with any of the advanced weather products that are generated for each application.

A variety of sensors can be used in the TWR concept. Table 1 shows properties and functionality for a number of radars. The three current generation radars used by the National Weather Service (NWS) and the Federal Aviation Administration (FAA) for weather surveillance are included: Next Generation Doppler Weather Radar (NEXRAD) - NWS, Terminal Doppler Weather Radar (TDWR) - FAA, Airport Surveillance Radar - 9 (ASR-9) - FAA. Also included in the table are list of tactical sensors that could be used with a TWR adjunct processor to provide weather data collection capabilities. Included are shipborne sensors (AN/SPY-1, AN/SPN-43, AN/SPS-48, AN/SPS-49), ground based sensors (TPQ-37 and Patriot Radar), and an airborne sensor (AWACS radar). In each case, the tactical radars selected share some of the aspects of the three operational weather sensors. In general, all of the tactical sensors use pulse compression (some also use uncoded waveforms) and achieve fine range resolution and increased sensitivity as a result. The range resolution is in general smaller than that of the three operational weather sensors. The tactical sensors have sensitivities that vary widely as a

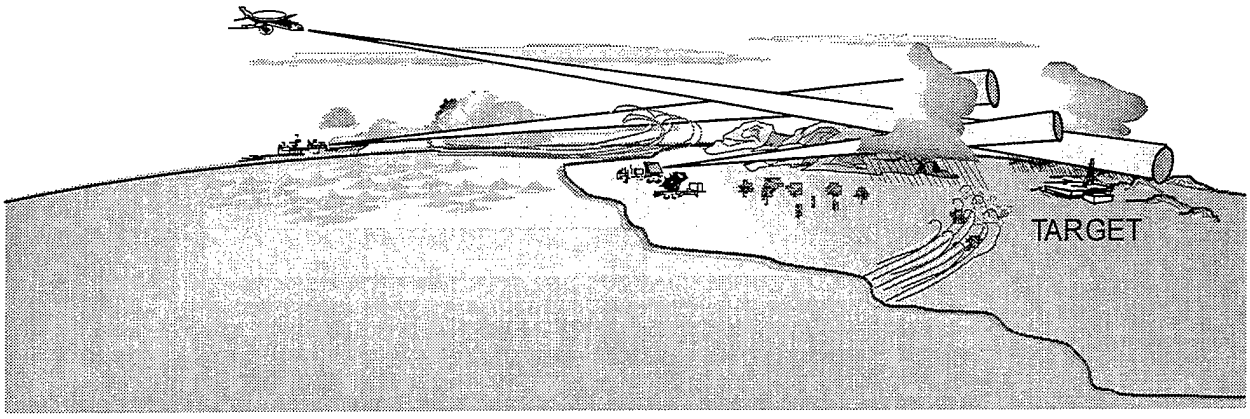


Figure 5: Theaterwide meteorological data collection through data fusion from multiple sensors

Table 1: Tactical weather radar candidate sensor comparison with weather radars

Radar / Property	NEXRAD	TDWR	ASR-9	SPY-1	TPQ-37
Frequency	2.7 - 3.0	C-band	2.7-2.9	S-band	S-band
Power	750 kW	250kW	1 MW	High	Low
PRF	1 kHz nom.	1 kHz nom.	1 kHz nom.	can achieve	can achieve
Pulse Type	Uncoded	uncoded	uncoded	coded	uncoded / coded
Dwell type	Multiple pulse	Multiple pulse	Multiple pulse	single / Multiple pulse	Multiple pulse
Range resolution	0.25 and 1.0 km	0.25 and 1.0 km	150 m	can achieve	can achieve
Beam type	1° pencil	1° pencil	Fan	Pencil	Pencil
Antenna type	Rotating reflector	Rotating reflector	Rotating reflector	Stationary Phased array	Trainable phased array
Function	Weather surveillance	Hazardous Weather surveillance / Aviation weather	Air Traffic Control / Weather Surveillance	Volume & horizon search / track, Missile commun. & fire control	Firefinder / Counter battery
Radar / Property	**AWACS**	**AN/SPN -43**	**AN/SPS- 48**	**AN/SPS- 49**	**Patriot**
Frequency	S Band	S Band	S band	L band	C-Band
Power	Low / medium	~850 kW	High	High	High
PRF	can achieve	can achieve	can achieve	can achieve	can achieve
Pulse Type	uncoded / coded	uncoded / coded	coded	coded	coded
Dwell type	Multiple pulse	single / Multiple pulse	single / Multiple pulse	single / Multiple pulse	single / Multiple pulse
Range resolution	can achieve in "Maritime Mode"	can achieve	can achieve	can achieve	can achieve
Beam type	Fan	Pencil	Pencil	Fan	Pencil
Antenna type	Rotating phased array	Rotating reflector	Rotating planar array	Rotating reflector	Trainable phased array
Function	Airborne surveillance	Aircraft approach	Surveillance & tracking - long range & horizon	Long Range Air Surveillance and Track	AAW / Firecontrol

result of their different operating frequencies, beamwidths, peak transmit powers, pulsewidths, etc. but in most cases, they provide sufficient sensitivity to match or exceed at least one of the three sensors and can provide weather surveillance over a limited range extent.

5.0 Benefits to the Warfighter

The TWR provides many benefits to the warfighter deployed throughout the theater.

For forecasting and modeling of weather phenomena and its movement, the TWR weather data provides improved accuracy, resolution, and timeliness of weather forecasting to warfighters. The TWR weather data collection is an enabling technology for in-situ forecasting models, allowing the warfighter to have direct access to forecasting and modeling data within the theater. The TWR allows rapid and accurate local nowcasts (short term forecasts). It provides high resolution local measurements to warfighters throughout the theater. Improved forecasting capabilities supports safer, more efficient littoral, amphibious and expeditionary operations, improved force mobility, and improved long term and global forecasts from Fleet Numeric and other forecasting operations.

For aircraft operations, the nowcasts provided by the TWR generate weather information up to and over the target area which support safer, more efficient air strikes, helo operations and aircraft carrier operations. The nowcasts and detection of weather phenomena by the TWR provide the warfighter with winds, wind shear, gust fronts, as well as cloud tops and bottoms, and storm extent and structure.

The TWR weather data can improve force self defense and area anti-air warfare (AAW) for each sensor. The sensitivity of the sensors can be improved in two ways. First, the radar system can lower its detection thresholds (added sensitivity by detecting smaller targets) in the presence of clutter, which would inherently generate more clutter detections that can be screened by the detailed clutter map. Second, the waveform selection process uses the detailed clutter map to choose the proper waveform parameters (number of pulses, pulse repetition frequency, etc.) based in the reflectivity, mean velocity and spectrum spread of the clutter in the region of the transmission.

The radar system will have better radar resource management and improved awareness through the clutter map. Clutter tracks can be reduced, eliminating resources required to "track clutter". In addition, waveform selection can be made more efficiently eliminating the need to revisit beam positions with multiple dwells with varied parameters to achieve the necessary clutter visibility. The clutter map can also be used in conjunction with detection reports to infer propagation conditions. The detection results

can confirm if surface tracks appear at higher elevations meaning that a surface duct exists. This can substantiate or refute the predicted propagation conditions and their homogeneity, particularly between propagation condition measurements. The improved situational awareness provided by the weather data can be useful in capability assessment for tactical decision aids (TDAs) for a sensor. The SPY -1 system has a TDA called the AEGIS Tactical Assessment Capability (ATAC) that provides insight into the AEGIS Weapons System's performance against a threat given the current environmental conditions and system status.

For Tactical Ballistic Missile (TBM) missions, TWR provides improved battlespace awareness through: assessment of cloud cover (by cloud layer detection), detection of three dimensional wind fields and spectral characterization of the environment. The cloud cover assessment and storm structure supports the seeker selection for the defensive missile, to assure that IR seekers are not blind during an engagement in clouds or storms. The wind field maps aid in the prediction of the dispersion of the cloud produced by the warhead within the TBM. The winds fields and spectral characterization aid in the analysis of the environment within a TBM complex for kill assessment and perhaps debris discrimination. Wind fields and spectral characterization can aid in the engagement process if enough time is available and resources are limited, the engagement decision can be influenced by the predicted impact point and the anticipated dispersion cloud movement in relation to forces and civilians.

In Chemical, Biological and Radioactive scenarios (CBR), wind fields can be used in much the same way it is used for TBM. Dispersion models can be driven with measured 3D winds rather than point measurements and modeled winds. Impact zones can be determined using the winds information. Also, the TWR wind data can improve: the engagement decisions, force mobility in the impact area, and evacuation of forces and civilians from impact areas and areas of anticipated dispersion cloud contamination.

The winds information aids all types of fire support with improved accuracy of weapon delivery from measured accurate and timely 3D winds not point measurements or modeled winds, both at the gun and over the target area. Naval Surface Fire Support and Army ground based counterbattery fire will both be supported with accurate ballistic corrections. Also, the clutter maps will aid the fire support in identification of chaff for improved tracking.

6.0 Summary

A concept for the collection of weather information from tactical sensors has been presented. This concept has wide applicability for sensors deployed throughout the battlespace. The data collected from the various sensors can be fused to yield a picture of the propagation and clutter conditions within the theater. In addition, 3D wind fields and other advanced weather products such as storm tracks and storm structure can be generated and made available

The weather data has wide reaching benefits for the warfighter. Beginning with improved performance of each sensor, as well as aiding in the capability assessment of each sensor. In addition, the data aids in more efficient, safer operations throughout the battlespace, from amphibious and landing operations, to expeditionary operations and force mobility to air operations.

7.0 References

1. H. Urkowitz and N. J. Bucci, "Doppler Tolerant Range Sidelobe Suppression in Pulse Compression Meteorological Radar", Proceedings Int'l Geoscience & Remote Sensing Symposium, Houston, TX, May 26-29, 1992, Volume Number pages 206-208.
2. N. J. Bucci and H. Urkowitz, "Testing of Doppler Tolerant Range Sidelobe Suppression in Pulse Compression Meteorological Radar", Proceedings 1993 IEEE National Radar Conference, Boston, MA, April 20-22, 1993, pages 206-211.
3. R. L. Nevin, J. M. Ashe, N. J. Bucci, H. Urkowitz and J. D. Nespor, "Range Sidelobe Suppression of Expanded / Compressed Pulses with Droop", Proceedings IEEE National Radar Conference, Atlanta, GA, March 29-31, 1994.
4. N. Bucci, J. Nespor, H. Urkowitz, D. Mokry, R. Brown, and W. Baldygo, "An Experiment with an S-Band Radar Using Pulse Compression and Range Sidelobe Suppression for Meteorological Measurements", Proceedings of 1994 IEEE National Radar Conference, Atlanta, GA, March 29-31, 1994, pgs 35-40.
5. N. J. Bucci, H. S. Owen, C. M Hawes, K. Woodward, "Validation of Pulse Compression Techniques for Meteorological Functions", Contract Final Report for DTFA01-95-C-00021, June 1, 1996.
6. H. S. Owen, H. Urkowitz, N. J. Bucci, J. V. Melody, R. McLean, "Tactical Weather Radar Experiment For a Shipborne Radar", Proceedings of Battlespace Atmospherics Conference; Naval Command, Control and Ocean Surveillance Center, RDT&E Division; San Diego, CA; December 3-5, 1996
7. R. Doviak and D. Zrnic, Doppler Radar and Weather Observations, New York: Academic Press, Inc., 1993.
8. R. J. Keeler and C. L. Frush, "Rapid Scan Doppler Radar Development Considerations, Part II: Technology Assessment", 21st Conference on Radar Meteorology, AMS, Edmonton, Canada, 1983, pp 3.1-3.5.
9. S. L. Katz, J. D. Nespor, "Advantages of Agile Beam Radar for Meteorological Surveillance", Proceedings of the 26th Int'l Conference on Radar Meteorology, May 24-28, 1993, Norman, OK, pp 396 - 398.

Tactical Weather Radar Experiment for a Shipborne Radar

H. Owen, H. Urkowitz, N. Bucci, J. Melody, and R. McLean
Lockheed Martin Corporation, Government Electronic Systems,
Moorestown, NJ

Abstract:

Meteorological conditions affect almost every aspect of naval warfighting operations. Precipitation and winds affect the operational tempo of combat forces at sea, during amphibious operations, and during aviation operations. Precipitation generates a clutter environment that degrades electromagnetic and electro-optical sensor performance. Specific propagation paths, such as surface ducts, can develop which greatly affect an electromagnetic sensor's performance. Wind fields affect ballistic weapon trajectories and the dispersion of chemical and biological agents which are becoming more common as warheads. If measurements can be accurately made of environmental conditions, the warfighter can be better prepared to adjust operational schedules, sensor employment, and weapon deployment to complete a specific mission.

Using innovative signal processing techniques, Lockheed Martin Corporation, Government Electronic Systems, is currently exploring the use of a tactical multifunction shipborne radar, the AN/SPY-1 B/D, for the measurement of meteorlogical conditions. The SPY-1 radar's normal tactical waveforms, if processed correctly, can provide maps of reflectivity, scatterer mean radial velocity, and spectrum width (indicative of turbulence and wind shear) throughout a search volume. This can be done without interruption to the radar's tactical scan. These measurements are often referred to as the three spectral moments in radar meteorology. Application of advanced signal processing techniques allow for the SPY-1 to make these measurements using coded tactical waveforms and a very small number of pulses (where traditionally uncoded waveforms and long pulse doppler dwells have been required for weather observations).

Overview of Conventional Radar Meteorology Techniques:

The National Weather Service's newest doppler weather radar, NEXRAD, measures precipitation intensity and charactristics of wind fields of a storm. These radars have been deployed throughout the U.S., and they provide the up-to-the-minute mosaics of weather conditions now available throughout the country.

Measurements are generally made of three basic spectral moments: reflectivity (a measure of scatterer density), mean radial velocity, and spectrum width (an indicator of turbulence and shear). NEXRAD takes measurements of these characteristics using the pulse pair processing technique on data taken from long sequences of uncoded pulses. In this technique, measurements of received signal power and characteristics of the first lag of the weather signal's autocorrelation function are used to generate estimates of the three spectral moments. It should be noted that estimates of these three moments can be made through pulse pair processing without actually generating a spectrum of the weather signal. The relationship between pairs of pulses is enough to provide information on signal intensity, mean radial velocity, and the width of the weather signal spectrum. Use of long, uncoded, multiple pulse dwells allows for the radar to take a large number of samples of a phenomenon to make accurate measurements , and it allows for clutter filtering techniques to be applied at the lowest elevation to remove the effects of ground clutter from the signal spectrum.

At this point, it is appropriate to provide a brief overview of the definitions for the three spectral moments. This discussion is largely taken from reference [1].

Estimation of the level of reflectivity in a storm is relatively straight forward. A number of samples, on the order of 100, are typically taken of the received signal power over a region of interest. These samples are averaged, and a conversion is made from received signal intensity to reflectivity, based on radar beam width, sample range, transmission power, and system losses. The reflectivity factor (a meterological measurement) is calculated from the general radar value of reflectivity. The term "reflectivity factor" is defined as

$$Z = \left(\frac{\eta \, \lambda^4}{\Pi^5 \, |K|^2} \right)$$

where
η = backscattering cross section per unit volume,
λ = transmitted wavelength, and
$|K|^2$ = a constant based on the backscatterers' index of refraction (approximately 0.93 for water phase precipitation).

The reflectivity factor is is generally described on a logarithmic scale (units of dBZ), calculated as 10 log Z, where Z is in units of mm^6/m^3. Typical values range from 10 dBZ (drizzle) through 40 dBZ (rain)

to 70 dBZ (rain and hail). Nonprecipitating clouds have values ranging from -15 dBZ to -30 dBZ.

Estimation of mean radial velocity is made using an estimate of the first lag of the weather signal's autocorrelation function. Again, a number of samples (on the order of 100) are typically used to make this measurement. The estimate of the autocorrelation function is given as

$$R(T_S) = \frac{1}{M} \sum_{m=0}^{M-1} V^*(m)\ V(m+1).$$

where V(m) represents the complex basedband voltage samples taken at a single range position at a sample rate equal to the radar's pulse repetition interval (PRI). In the most straightforward approach, one sample is taken each pulse, so that the number of pulses becomes M. The estimate of mean radial velocity becomes

$$V_r = -\left(\frac{\lambda}{4\ \Pi\ T_S}\right) arg\ R(T_S)$$

where
T_S = the pulse repetition interval (PRI).

This estimator of mean radial velocity is not biased by white noise. Even when the spectrum is not symmetric, the mean radial velocity is accurate as long as the weather signal is contained in a small band relative to the Nyquist interval which results from the sample rate. More detail of the pulse pair mean velocity estimator is provided in reference [1].

The spectrum width estimator is a function of the magnitude of the first lag of the autocorrelation function. If this value is relatively large, the signal can be considered to be more coherent (and have less spread). If it is relatively small, the signal is less coherent (and has more spread). One spectrum width estimator is given as

$$\sigma_v = \left(\frac{\lambda}{2\sqrt{2}\ \Pi\ T_S}\right)\left[\left|\ln\frac{S}{|R_1|}\right|\right]^{1/2} sgn\left[\ln\left(\frac{S}{|R_1|}\right)\right]$$

where
R_1 = the autocorellation estimate evaluated for T_S equal to the waveform PRI
S = the estimate of signal power (total received power minus noise power).

The accuracy of the estimates made using the pulse pair technique depends on several factors, including signal to noise ratio (SNR), spectrum width of the signal being measured, and numbers of independent samples used in the estimation of signal power and the first lag of the autocorrelation function. Many tradeoffs can be made to optimize the spectral moment estimation accuracy.

If SNR and signal spectrum width are held constant, however, the number of independent samples becomes the main issue for spectral moment accuracy. In general, a larger number of independent samples of a signal results in improved spectral moment accuracy.

There are a number of ways to increase the number of independent samples taken of a weather event. Larger numbers of pulses can be transmitted (the most straightforward approach). Multiple transmission and receive channels can be employed to take more than one sample simultaneously. If a radar scans a region fast enough, scan to scan averaging of the spectral moments themselves can be used to reduce the estimate variance. And finally, range averaging of the samples taken can help reduce the variance of the spectral moments.

This last technique has been investigated previously, as outlined in reference [2]. Range averaging is an attractive option for collecting an increased number of samples, however it requires that smaller range resolutions be achieved for individual measurements so that range reporting intervals are not increased when these individual samples are averaged over range. Coded waveforms have traditionally been used in tactical radars to improve range resolution, but coded waveforms have not been used in operational weather radars due to the degradation of the weather measurements from range sidelobes. The range sidelobes which result from coded waveforms have the effect of "smearing" the weather picture, masking weak features or sharp reflectivity and velocity changes in the face of stronger signals which are flooded through range sidelobes.

Short, uncoded pulses could be used to achieve the better range resolution required for range averaging, but the reduction in pulse width in this approach would reduce signal to noise ratio. This would result in larger errors in the spectral moment measurements.

Tactical Weather Radar Operation:

Many tactical radar systems share a set of common characteristics: operation at or near S-band, use of coded waveforms, use of small numbers of pulses (such as MTI waveforms) in search modes,

and good system sensitivity. These basic radar characteristics, with the proper signal processing, can produce accurate spectral moments estimates without the use of dedicated waveforms.

With pulse pair processing, it is not necessary to have 100 pulses in a dwell to make weather measurements. In the Tactical Weather Radar (TWR) concept, small numbers of pulses (typical of MTI dwells) can be used to make these measurements. Consider the case of a tactical system with the following parameters. (Note: these parameters are not necessarily reflective of the SPY-1 radar but are used here as an example and include characteristics of a number of tactical systems.)

Pulse Type:	MTI
Number of Pulses:	3
# Simult. Trans/Rec Channels:	3
Range Resolution:	50 m
Reporting Range Required:	500 m
Waveform Coding:	Yes

Using traditional radar processing with only pulse to pulse averaging, there would be 3 pulses and 2 pulse pair groups to make spectral moment estimates. However, this fictional tactical radar has three channels from which to collect data and 500 meters over which to average results prior to reporting the spectral moment data. Therefore, the total number of samples becomes 90 (3 x 3 x 10), and the total number of pulse pairs becomes 60 (2 x 3 x 10). Although 3 pulse samples and 2 lag samples are not adequate for estimation of the three spectral moments, 90 pulse samples and 60 lag samples are generally adequate.

The use of a coded waveform, however, poses another problem. Coded waveforms result in range sidelobes that smear weather measurements in range. Range sidelobe suppression techniques can be used to reduce the effect of range sidelobes. However, these techniques (such as sidelobe suppression filters and inverse filters) degrade quickly in the presence of doppler shifts in the received signal. Therefore, doppler tolerant techniques must be applied.

Lockheed Martin developed a doppler tolerant range sidelobe suppression technique that has been successfully demonstrated in research radars for Federal Aviation Administration (FAA) applications (see references [3], [4], [5], and [6]). A signal processor testbed has been developed as part of these investigations, and this testbed is being used to process SPY-1 data in this experiment. In the FAA case, a coded pulse doppler waveform was used to make spectral moment measurements. In this experiment, the technique is adapted for MTI waveform processing, and single pulse coded waveform processing. Consider figure 1 which illustrates the TWR signal processor testbed.

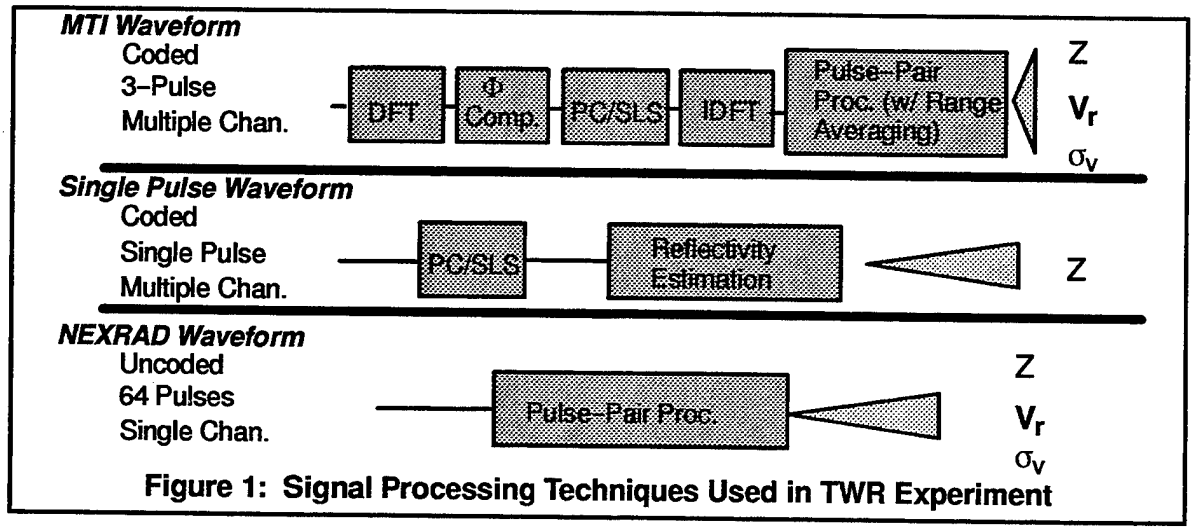


Figure 1: Signal Processing Techniques Used in TWR Experiment

This figure outlines three of the processing approaches used in the experiment. First, a processing approach for a 3 pulse MTI system is presented. In this case, each of the simultaneous channels of the radar system is processed separately, and the results are averaged once the autocorrelation function estimate is made. A Discrete Fourier Transform (DFT) is performed across the three samples taken at each range interval. Phase compensation is applied so that the combined pulse compression (PC) / sidelobe suppression (SLS) filter is matched to each of the three outputs

of the DFT. After PC/SLS filtering, an Inverse DFT is taken to produce the 3 pulse sequence that is used in pulse-pair processing. The results of the pulse pair processing (estimates of total signal power and the first lag of the signal's autocorrelation function) are then averaged over multiple pulses, multiple channels, and over range to produce a result which accurately reflects the weather spectrum characteristics.

The second approach is appropriate for a single pulse waveform. In a single pulse waveform, no doppler phase compensation is possible since only one pulse is transmitted. However, measurements can still be made of reflectivity. Since most tactical systems use something like MTI in regions where clutter (such as precipitation) is expected, it is probable that a multiple pulse waveform will be transmitted in regions of precipitation.

The last signal processing path represents that of the NEXRAD waveform. No pulse compression is used since the waveforms are uncoded. Almost all averaging is done over pulses. Therefore, the processing approach is simpler but requries a large number of pulses to be transmitted in each beam position to make the desired measurements (on the order of 60 or 100).

Outline of Experiment:

The primary goal of this experiment is to determine what weather information can be gained through processing of normal, tactical search waveform data through a separate signal processor. A second goal of the experiment is to determine what dedicated dwells would be required to provide for measurements of additional phenomena not covered by typical search dwells. It is expected that dedicated weather dwells are appropriate when very low reflectivity phenomena are being observed, and when surface clutter filtering is desired to remove the effects of surface clutter from the weather spectral moment estimates.

The experiment consists of an equipment preparation period followed by three data collection phases. The equipment installation period is required to install a data tap so that raw radar data can be extracted from the signal processor and stored for post-mission processing and analysis. The first data collection phase is the Baseline data set and is required to test out the data tap, general data quality, and the software patches required to control the radar in a manner that will allow for the collection of appropriate experimental weather data. Lessons learned in this portion of the experiment were applied to subsequent data collection sets to improve data collection and data processing techniques. The second data collection phase is the Proof of Concept data set, and it primarily involves the collection of precipitation data to compare the results of the SPY-1 radar with those of a nearby NEXRAD doppler weather radar taken simultaneously. It is during this phase of the experiment that SPY-1's ability to collect precipitation weather data is assessed. The last data collection phase is the Clear Air Observations data set in which specialized, dedicated waveforms will be used to investigated SPY-1's ability to detect low observable weather phenomena such as clear air turbulence and cloud layers. This paper primarily deals with data collected during the Proof of Concept data set.

Two basic types of comparisons are used in the Proof of Concept data set to determine the accuracy of SPY-1 weather measurements using tactical waveforms. First, reflectivity maps taken from a SPY-1 radar, located at the Navy's Combat System Engineering Development (CSED) Site in Moorestown, NJ, are compared with those taken from a nearby NEXRAD. The NEXRAD is located approximately 44 kilometers to the East of the SPY-1 radar. Coverage of the two radars overlaps over much of New Jersey. Data collection events were focused on central and northern New Jersey, extending past New York City to the North in some cases. Reflectivity measurements do not depend upon radar aspect relative to the phenomenon measured (assuming neither radar is attempting to make measurements beyond the radar horizon). Therefore, comparison of results from two radars is appropriate for this investigation.

When comparing radial velocity, however, radar aspect angle is important. Two radars viewing a single storm cell will make two different radial velocity measurements if they are not colocated. In this case, it is desirable to transmit both waveform types (SPY-1 and NEXRAD) from a single radar without any delay between the two and compare the results. In this experiment, software patches to the computer program which controls the radar allows SPY-1 to transmit an uncoded waveform which is very similar to NEXRAD's. In each beam position, SPY-1 is configured to transmit the NEXRAD waveform followed immediately (within milliseconds) by a SPY-1 waveform. The results from the two waveforms can then be compared for the entire search region.

Spectrum width measurements can be evaluated by using both ray trace comparisons with data tak-

en from SPY-1 alone, and from spectrum width maps taken from SPY-1 and NEXRAD.

Results from two Precipitation Events:

Two sets of results are presented in this paper. One is from a precipitation event that passed through southern New Jersey on June 19, 1996. The other is from one which passed through on August 21, 1996. The June data is presented first. These data are typical of those collected throughout the summer collection events.

Two basic comparisons are presented in the June 19 data. First, a comparison is made between the spectral moment estimates made from an MTI waveform transmitted from the SPY-1 radar at CSEDS and the spectral moment estimates made from an uncoded NEXRAD dwell sequence from the same radar.

Figure 2 shows a comparison of reflectivity measurements from the MTI and NEXRAD waveforms. The estimates from the MTI waveform (solid line) match well with the reflectivity estimates made a few milliseconds later with the NEXRAD waveform (dashed line). The estimates were averaged to a 1 kilometer range interval, typical of the reporting intervals required for most of the reflectivity based weather products used by the National Weather Service. It should be noted that the reflectivity traces match well even over steep gradients, such as the one located at the range interval between 10 and 13 kilometers. This is a reflectivity shift of approximately 35 dBZ. It is in steep gradient regions where range sidelobe corruption is expected to have the greatest impact on spectral moment measurements. The traces continue to match well over a low reflectivity region at a range of 39 kilometers, and over a variety of peaks and valleys. The variations between the between the SPY-1 waveform and NEXRAD waveform reflectivity estimates are reflective of the random nature of the weather phenomenon, and match the level of variance expected of these estimates.

Figure 2:

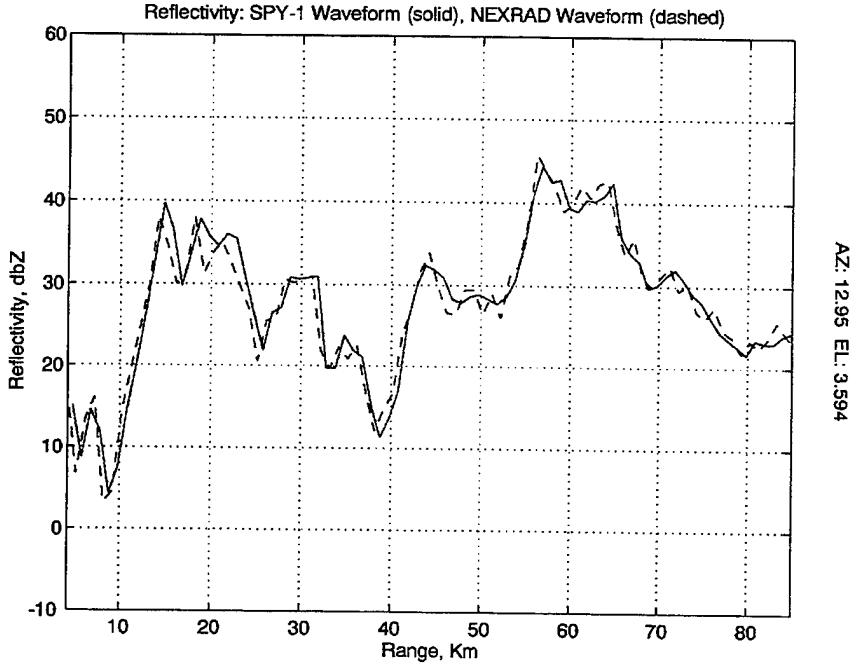
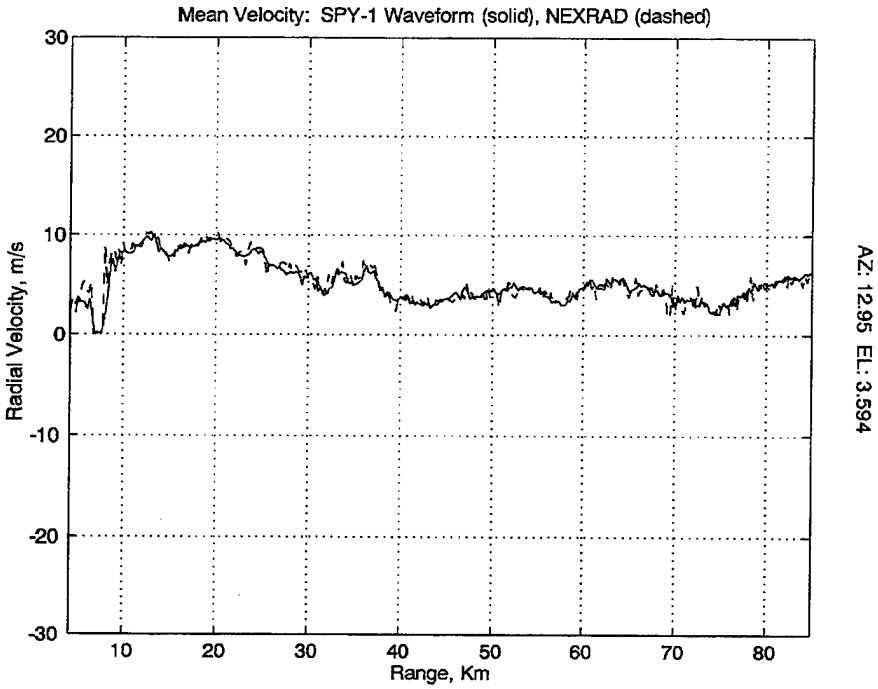


Figure 3 illustrates the performance of the mean velocity estimator for both the MTI waveform and a NEXRAD waveform transmitted from SPY-1. These radial velocity estimates were taken from the same pulses as the previously presented reflectivity estimates. Once again, the measurements made from the SPY-1 waveform match well with those from the NEXRAD uncoded waveform. A number of detailed features can be seen along both radial velocity traces. The radial velocity values presented here are in meters per second (double these values to approximate speed in knots).

Figure 4 shows a comparison between spectrum width values generated by an MTI waveform and those generated from an uncoded NEXRAD waveform also transmitted from the CSEDS SPY-1 ra-

Figure 3:



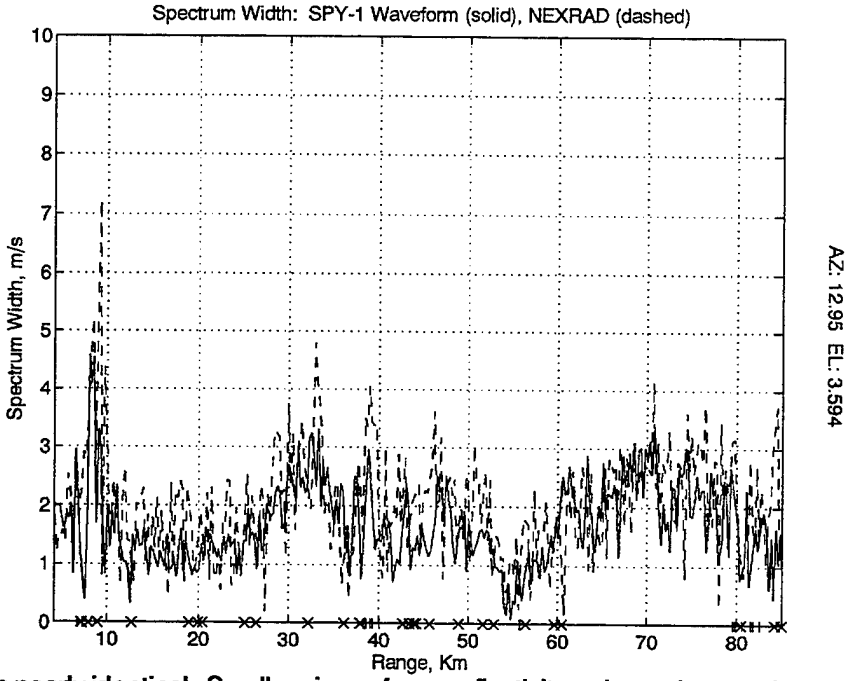
dar. The MTI waveform values are represented by a solid line, and the NEXRAD waveform values are represented by a dashed line. The spectrum width estimation usually appears to have a relatively high variance (appears to be more noisy) than the other moments. However, both waveform types are reporting very similar values and the same trends over the full range interval. Large spectrum width values (indicating phenomena such as shear and turblulence) appear at approximately 8 kilometers. Small spectrum width values are reported by both waveforms at a range of approximately 55 kilomters.

In the spectrum width calculation described previously, it is necessary to take the ratio of total signal power (total received power minus the receiver noise power) to the magnitude of the first lag of the autocorrelation function. Since the estimated receiver noise is subtracted from total noise power, and since the total received power is an estimate with a nonzero variance, sometimes the result is that the total signal power value is actually smaller than the absolute value of the first lag. In theory this is impossible, but it occurs as a result of the errors inherent in any measurement where noise is present. Therefore, sometimes the spectrum width value may not be a valid one. In these cases, the value is flagged and not used.

In the spectrum width comparison shown here, these invalid estimates are marked with an "x" for the NEXRAD waveform and with a small vertical line for the SPY-1 waveform, along the x-axis of the plot. Over a 10 kilometer region forty estimates are displayed. On average approximately three or four estimates (for the NEXRAD waveform -- one or two for the SPY-1 waveform) are invalid and thrown away. This means that over 90 % of the estimates are valid in this plot.

The next results presented involve entire maps of spectral moment estimates. They are displayed using the National Weather Service's WVS display package. In the first two color figures included at the end of this paper (Figures 5 and 6), maps of radial velocity are displayed for the same scan from which the previously discussed ray traces were taken. The first figure is a map of SPY-1 waveform radial velocity estimates taken at an elevation of 3.6 degrees. The range rings are provided 30 kilometers apart (measurements are shown out to approximately 90 kilometers). On the second plot the radial velocity estimates from the NEXRAD waveform are displayed. The green regions indicate a radial velocity inbound to the radar at approximately two meters per second. The white region indicates zero radial velocity (all motion is tangential to the radar). The dark brown region indicates an outflow of approximately four meters per second. The lighter brown region shows outflows of seven meters per second, and occasional orange pixels indicate an outflow of eleven meters per second.

Figure 4:



The two plots are nearly identical. Small regions of inflow occur directly north of the radar, with tangential flow just to the right of these regions. The wind fields show an outflow which increases as the radar scans to the East. Detailed features visible in the white regions, and between the brown shaded regions, are clearly visible in both plots. Overall, the wind field illustrated by the SPY-1 MTI waveform matches very well with that of the NEXRAD uncoded pulse doppler waveform. The MTI waveform reduces the data collection time for the volume by more than an order of magnitude. Both radial velocity plots generally agree with storm motion indicated by storm cell movement and by radial velocity plots provided by the nearby NEXRAD.

The last three color pictures, figures 7-9, illustrate a series of reflectivity maps from an August storm. Since the SPY-1 radar has an agile beam with a flexible scan, and since the MTI waveform can make radial velocity measurements with an order of magnitude reduction in time, the SPY-1 radar is capable of generating accurate, rapid snapshots of storm events not possible by rotating parabolic antenna radars such as NEXRAD.

Figure 7 is a composite reflectivity plot generated from SPY-1 MTI data. In composite reflectivity maps, the largest reflectivity value from any altitude at a given geographic position is reported as the composite reflectivity for that position. The reports are made on a cartesian grid with a 1 kilometer grid spacing. The brown region indicates high reflectivity values of approximately 43 dBZ. The white regions show reflectivity values of 38 dBZ. The green regions vary from 33 to 23 dBZ. And the blue regions go down to 8 dBZ (light rain). Below this point, the SPY-1 reflectivity maps are thresholded (although these values are still well above the receiver noise floor). This is done to keep the results unclassified and still provide valid, useful measurement data.

This data was collected over a time interval less than 10 seconds. The extent of the reflecitivy map is limited only by the experimental data collection device used in the mission (in real operation, such a radar would be able to provide 360 degrees of coverage). The range rings are provided 30 kilometers apart, with the first ring visible corresponding to a range of 60 kilometers, relative to SPY-1. The azimuth mark in the figures correspond to 30 degrees from North.

Two distinct cells are visible in the first figure. They are relatively small (1 to five pixels in size for the brown region). Velocity plots from the day indicate general storm motion was going from West to East.

The second SPY-1 plot (figure 8), was taken 2.5 minutes later. The same two cells, as well as other distinct matching features, appear. They are still small in size, and the centroids have moved just under 2 kilometers eastward (indicating a speed of approximately 12 m/s, or about 24 knots).

The last color plot, figure 9, shows the composite reflectivity map taken from the nearby NEXRAD

radar located approximately 43 kilometers to the SSW of the two dominant cells near the center of the screen. The NEXRAD radar is closer to the storm cells than the SPY-1 radar is. The map is generated with the same composite reflectivity calculation, and with the same grid spacing. The azimuth and range rings in this plot are centered on the SPY-1 radar located at the CSED Site. The scan used to collect the NEXRAD data took approximately 5 minutes, a significantly slower scan than that of the SPY-1 radar. The region scanned by SPY-1 is shown with a dark border. The two cells in this plot clearly correlate to the two cells in figures 7 and 8. The other general features of the green and blue regions also correlate well to figures 7 and 8. However, the main cell is significantly larger in size and almost appears as one cell. This cell appears smeared because of the effect that the slower NEXRAD scan has on the composite reflectivity calculation used to generate the images in Figures 7-9. Combination of Figures 7 and 8 results in a cell which more closely resembles that of Figure 9. The temporal resolution gained with an agile beam radar using range averaging also improves the spatial resolution which results from calculations such as composite reflectivity.

Conclusions:

Detailed analysis of the data continues. Efforts are focused on identifying and analyzing especially stressing cases, such as when measurements are being made near fast point targets or when steep reflectivity gradients occur. With a preliminary analysis complete, however, several main conclusions can be drawn from this work.

MTI waveforms, using small numbers of pulses (such as 3 and 4 pulse MTI systems), can provide accurate measurements of the three spectral moments typically observed by radar meteorologists. The results from this experiment show that measurements taken from a SPY-1 radar compare favorably with those taken from a NEXRAD or those taken using the NEXRAD uncoded pulse sequence transmitted by a SPY-1. This means that tactical radar systems can provide valuable weather data without interrupting their normal tactical search scans.

Another advantage of this processing approach is that the shorter dwells, typical of tactical systems, can provide these measurements very quickly. When this is combined with the fact that many tactical systems use flexible electronic scan techniques, very rapid updates can be provided of developing weather conditions.

Dedicated weather dwells will be required for certain types of information. When surface clutter interferes with weather signal returns, a longer dwell sequence is required to filter the surface clutter from the weather signal. Also, when clear air observations are desired, longer pulse sequences are required to allow the typical tactical system to achieve the required sensitivity. Implementation of infrequent dedicated dwells, however, have less of an impact on agile beam tactical systems such as SPY-1. In such systems, they can be transmitted, on a low priority basis, when the tactical system can afford to schedule them. In tactically critical situations where no radar resources are available for any dedicated weather scan, they can be eliminated entirely.

Future work on this experiment will include investigations into making clear air observations with the SPY-1 radar.

Acknowledgements:

The authors thank Dr. Scott Sandgathe of ONR for sponsoring this work. Also, we would like to thank the AEGIS Program Office for providing the SPY-1 resources which made this experiment possible, and to the CSED Site personnel who assisted in the data collection events. We are grateful to Dr. Frank Herr from ONR and CDR Markham from NRL for their support of the program, and to Dr. Juergen Richter of NRaD for his contributions as technical advisor to the experiment. And we would like to thank the personnel from the National Weather Service's Mount Holly, NJ office for their outstanding support, and the National Center for Atmospheric Research for their support and use of their RDSS display software package.

References:

[1] R. Doviak and D. Zrnic, *Doppler Radar and Weather Observations*, New York: Academic Press, Inc., 1993.

[2] R. J. Keeler and C. L. Frush, "Rapid Scan Doppler Radar Development Considerations, Part II: Technology Assessment", *Proceedings 21st Conference on Radar Meteorology*, AMS, Edmonton, Canada, 1983, pp 3.1-3.5.

[3] H. Urkowitz and N. Bucci, "Doppler Tolerant Range Sidelobe Suppression in Pulse Compression Meteorological Radar", *Proceedings Internation Geoscience and Remote Sensing Symposium 92*, Houston, TX, May 26-29, 1992, Vol. I, pp. 206-208.

[4] R. Nevin, J. Ashe, N. Bucci, H. Urkowitz, and J. Nespor, "Range Sidelobe Suppression of Expanded/Compressed Pulses with Droop", *Proceedings 1994 IEEE National Radar Conference*, Atlanta, GA, March 29–31, 1994, pp. 116–122.

[5] N. Bucci, J. Nespor, H. Urkowitz, D. Mokry, R. Brown, W. Baldygo, "An Experiment with an S–Band Radar Using Pulse Compression and Range Sidelobe Suppression for Meteorological Measurements", *Proceedings 1994 IEEE National Radar Conference*, Atlanta, GA, March 29–31, 1994, pp. 35–40.

[6] N. Bucci, J. Nespor, and H. Urkowitz, "Use of Pulse Compression and Range Sidelobe Suppression for Meteorological Radar Measurements at S– and X–Band", *Proceedings International Conference on Advanced Radar Meteorology*, COST 75, Brussels, Belgium, September, 1994.

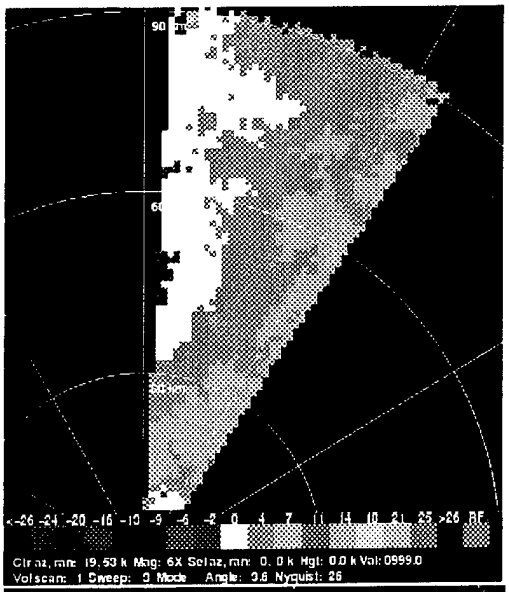


Fig 5

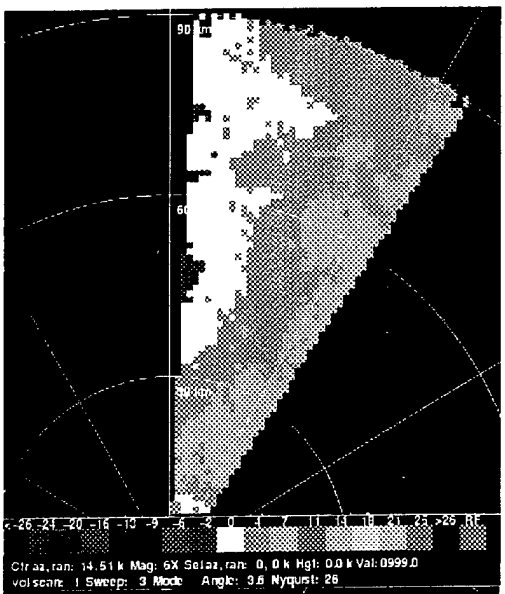


Fig 6

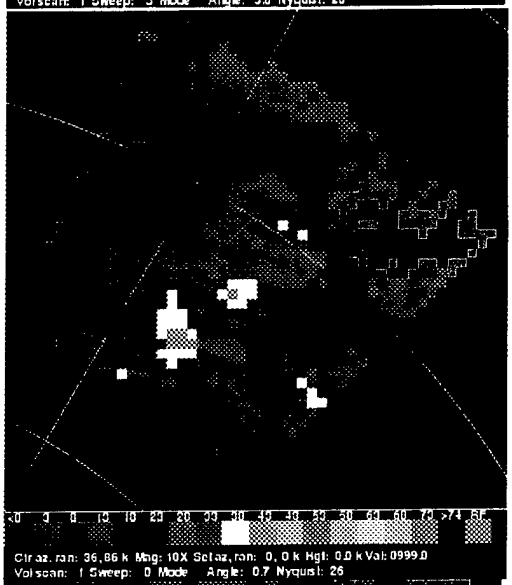


Fig 7

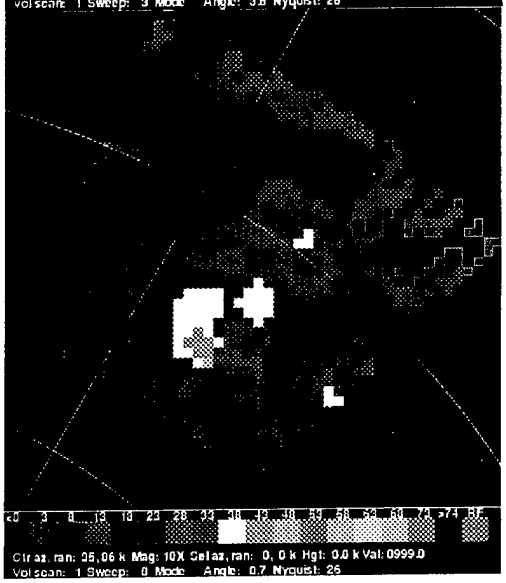


Fig 8



Fig 9

Figure 5: Radial Velocity Map, 3.6 deg. el., taken from SPY-1 using MTI Waveform

Figure 6: Radial Velocity Map, 3.6 deg. el., from SPY-1 using NEXRAD Waveform

Figure 7: Rapid Composite Reflectivity Snapshot Taken by SPY-1 Using MTI Waveform

Figure 8: Second Rapid Composite Reflectivity Snapshot Taken by SPY-1 Using MTI Waveform

Figure 9: Composite Reflectivity Picture From NEXRAD, Located Approx. 44 Km to East of SPY-1

Atmospheric Soundings in Near Real Time from Combined Satellite and Ground-Based Remotely Sensed Data

James Cogan, Edward Measure
Information Sciences and Technology Directorate
Army Research Laboratory
White Sands Missile Range, NM 88002-5501

Daniel Wolfe
Environmental Technology Laboratory
National Oceanic and Atmospheric Administration Boulder, CO 80303-3328

INTRODUCTION

The mobile profiling system (Profiler) has been upgraded from that described by Wolfe et al (1995). It combines ground based instruments, including a five beam 924 MHZ radar wind profiler, a Radio Acoustic Sounding System (RASS), a passive microwave sounder, with a receiver and processor for meteorological (met) satellite data. With appropriate met satellite input it can probe the atmosphere from the surface to over 30 km. The upgrades include a new antenna that combines the wind radar and RASS, and a newer, better designed shelter housing the processors and other electronics. These and other improvements have led to a more robust system that is easier to transport and set up.

The method for combining these data is not site specific and requires no *a priori* information. The merging method provides soundings with an accuracy in temperature (or virtual temperature) relative to rawinsonde soundings at least equal to other currently published methods. Data at the lower satellite sounding altitudes are modified based on measured values from the ground based sensors. However, the wind velocity accuracy above the maximum radar data level is limited by inaccuracies in current methods of deriving wind velocity from satellite data. New ways to derive satellite wind velocities are being investigated. In the interim, we have the option of merging data from rawinsondes, where the latter system provides data for higher levels, adjusted to take into account changes in profiles of wind and other variables detected by the ground based remote sensors since the rawinsonde launch. The Profiler may be used for detailed analysis of meteorological variables for research and operations over mesoscale areas (e.g., pollution studies and severe storm forecasting), plus a number of military applications. It has operated successfully in several different climates: the Los Angeles Free Radical Experiment at Claremont, CA; tests at White Sands Missile Range, NM; Erie, CO; Wallops Island, VA; and other sites.

SYSTEM DESCRIPTION

Wolfe, et al (1995) and Cogan (1995) describe the earlier configuration of the Profiler in some detail. Here we emphasize improvements to the system implemented during the past year

and planned for the first few months of 1997.

A new antenna system combines the wind profiling radar with the RASS, thereby eliminating the need for separate RASS units. The acoustic portion of the phased array RASS consisting of 120 sound transmitter elements points into the wind at an elevation and azimuth angle as determined by the wind speed and direction measured by the radar profiler. By slightly tilting into the wind the sound waves will be over the radar (except at very high wind speeds). Current sytems use four separate RASS arrayed around the radar to insure that at least one will be upwind. The acoustic phase front may have a slight tilt, but turbulence will tend to wash out any noticeable effect. The radar operating at 924 MHZ can provide wind profiles as often as once every 3 or 4 minutes with a vertical resolution of 100 m up to a height of 3 - 5 km on average, depending on atmospheric conditions. Under certain atmospheric conditions (i.e., moist and turbulent) heights over 6 km are possible. The RASS can produce soundings of virtual temperature (T_v) up to around 0.8 - 1.6 km, again depending on atmospheric conditions, at a vertical resolution of about 100 m. A microwave radiometer operating in the oxygen band from 50 - 60 GHz is able to produce useful temperature (T) profiles to an altitude of around 3 - 5 km. A second radiometer produces estimates of total water content (vapor and liquid). These older radiometers are being phased out and replaced by a single radiometer in a package smaller than either of the older ones. Preliminary evaluations show a significant improvement in T accuracy. The Profiler has certain elements in common with fixed-site systems described by Parsons et al. (1994) and Stokes and Schwartz (1994), but has a number of additional features. These additions include software for processing and quality control of data from the ground-based sensors (e.g., Merritt, 1995), and for combining satellite soundings with ground-based profiles in near real time.

The merging algorithm applies no matter where the Profiler is located; i.e., it is not site specific and requires no a priori information. The microwave radiometer, however, uses a statistical retrieval method that is site specific. Previous methods for merging satellite and other data (Westwater et al., 1984a, 1984b; Schroeder et al. 1991) to retrieve profiles of T (or Tv) required site specific statistical data.

A new algorithm calculates a satellite sounding for the location of the Profiler instead of simply using the nearest one (Spalding, 1996). The algorithm fits a plane to the nearest three soundings at each pressure level for each variable. Interpolation of a value of a given variable is performed when the Profiler lies within the boundary of the triangle defined by the three satellite sounding locations. The routine extrapolates values for Profiler locations within a short distance outside of the triangle (e.g., 50 km). Beyond that "extrapolation distance" the program reverts to the older method of using the nearest sounding, if the distance does not exceed a user determined maximum (e.g., 300 km). This type of situation could occur, for example, when atmospheric conditions or some instrument error severely limited the number of "good" satellite soundings, or the Profiler is positioned outside the swath of the particular satellite pass. These distances are used for determination of the weight to be given to the satellite values when the lower sounding heights "overlap" the upper part of the ground-based profiles. The procedure for merging the ground based and satellite profiles sets the distance to the Profiler to 0 km when the Profiler lies within the larger triangle defined by the three closest soundings plus the extrapolation distance. The actual distance is used when the nearest sounding method is required. To determine the best

pass for merging we add a "time distance" to the spacial distance to account for data "staleness." Presently we calculate the time distance at 30 km/hr. The best pass is considered to be the one with the least time-space distance.

Neural net methods under development will provide the Profiler with more rapid retrievals of satellite soundings of temperature and possibly other meteorological variables. Bustamante, et al (1997), also in these Proceedings, provide a description of the neural network for retrieval of temperature profiles. Some benefits of a neural net approach include the elimination of the need for first guess profiles for each inversion and a faster retrieval process. Faster running inversion software should mean the ability to apply the soundings closer to real-time than currently possible. Also, these methods can easily run on current and planned Profiler processors.

TEST RESULTS

The Profiler has generated soundings for several field experiments and system tests in different climatic regions. Examples include Claremont, CA; White Sands Missile Range, NM; Erie, CO; Wallops Island, VA; and other sites. Some of the results are described in Wolfe, et al (1995) and Cogan (1995). Here we summarize a few of these earlier results and present new data that also show potential application to mesoscale analysis and forecasting. Wolfe, et al (1995) and Cogan (1995) also present color charts showing time vs. height wind barb plots of wind velocity from some of the aforementioned test sites.

Personnel from ARL and ETL participated in the LAFRE, using the Profiler to obtain detailed sounding data for the California Air Resources Board. These data also served to check out the system and algorithms. The system operated almost continuously from 28 August 1993 through 23 September 1993. From 28 August through 11 September 1993 the Los Angeles basin was under a strong upper ridge, at times a closed high pressure area from the surface through 300 hPa. The marine boundary layer was consistently capped by one or more inversions. Wolfe et al. (1995) and Cogan (1995) present charts that show wind velocities from the radar profiler for typical days during this early part of the LAFRE, depicting light and often variable winds. Combining these profiles with the nearest useful satellite sounding, sometimes as much as 300 km distant, led to a "worst case" situation on several days, in that atmospheric conditions, especially wind velocity, are often quite different 200 or 300 km to either side of a strong ridge.

Table 1, derived from data in Cogan and Wolfe (1995), shows mean and standard deviation of wind speed differences in ms^{-1} for the radar profiler and the satellite (adjusted at lowest three satellite data levels) relative to rawinsonde during part of the LAFRE. The maximum number of data comparisons was 36 over the first period (five days) compared with a maximum of 12 over the seven days of the second period. Cogan and Wolfe (1995) also presented data from the LAFRE that suggested that for combined soundings the mean and standard deviation of T_v differences were about $\pm$ 0.4 and 1 to 1.5 K, respectively.

TABLE 1. Means and averages of 0.1 km standard deviations of wind speed differences (ms^{-1}) for 0.3 km layers (indicated sensor vs. rawinsonde). Radar = radar wind profiler, Sat = Satellite.

Mean		Standard Deviation		Layers		Dates
Radar	Sat	Radar	Sat	Radar	Sat	(Sept, 1993)
0.75	10.84	1.88	8.60	14	6	7-11
1.53	8.61	2.75	2.88	11	6	17-23

At times rawinsonde data may contain serious errors. Fisher et al. (1987) present information on the average errors found in several types of rawinsonde systems. To gain an idea of the quality of the rawinsonde data at the LAFRE, soundings were compared from two similar systems (MARWIN and CLASS) receiving data from one sonde. Differences in T_v from comparisons using a single sonde averaged around $\pm$ 0.2 to 0.4 K, with maximum differences of about $\pm$ 1 K. Cogan and Wolfe (1995) compared wind speed differences between the two systems. Their figure 2 showed a periodic pattern that is consistent with other data examined to date. The large differences of up to 3 ms^{-1} near and above 3 km were on the high side, but values around $\pm$ 1 ms^{-1} were not uncommon. Cogan (1995) presented data showing a few wind direction variations of $> 90°$ in one case during the LAFRE, although wind direction differences for most of the 100 m layers in data examined to date were $< 10°$. This type of comparison suggests that differences in Profiler wind speed and direction of around $\pm$ 1 ms^{-1} and 10 °, respectively, relative to rawinsonde may be close to the "best" one could expect. A possible partial explanation for the wind speed differences is that the MARWIN software has more extensive built-in checks and somewhat smoothes the data.

A test of the Profiler at the NASA Wallops Flight Facility (WFF) on Wallops Island, VA, provided the opportunity to compare wind profiles for the lowest 1.9 km with those obtained from radar-tracked pibal balloons. An unusual aspect of this experiment as compared with other similar studies (e.g., Weber and Wuertz 1990) was the ability to examine the background wind variability at the same time as the comparisons. During the week of 17-21 July 1995, for morning and afternoon periods lasting about 1 to 1-1/2 h, two pibals were launched about 3 min apart every 15 min (four to five "pairs" each period). The Profiler operated continuously during these periods with the capability of producing wind profiles every 3 min. A 3 min sounding was generated starting prior to the second pibal of each pair. The Profiler sounding was compared with the profile from the second pibal of each pair, and comparisons were made between the two pibals. Surface values shown were taken from the WFF and Profiler surface sensors. The site of the experiment was about 0.2 km west of the ocean, with the Profiler located < 50 m east from the pibal launch site. Tables 2 and 3 present the means and standard deviations of the wind speed and direction differences between Profiler and pibal, and similar values from concurrent pibal "pairs" during 18 July (eight "pairs"), 20 July (nine "pairs"), and 21 July 1995 (five "pairs"). These tables show values for 100 m layers averaged from the surface to 1.9 km.

TABLE 2. Means and standard deviations of differences of wind speed between Profiler (3 min. averages) and pibal, and between pibals 3 min apart. Averages of 100 m layer values shown, for the surface through 1.9 km.

Day (July 1995)	Number of comparisons	Mean (ms^{-1}) Profiler vs. Pibal	Mean (ms^{-1}) Pibal vs. Pibal	Standard Deviation (ms^{-1}) Profiler vs. Pibal	Standard Deviation (ms^{-1}) Pibal vs. Pibal
18	8	-0.70	0.00	0.91	0.63
20	9	-0.31	-0.01	0.69	0.84
21	5	-0.36	-0.09	0.92	0.65

TABLE 3. Means and standard deviations of differences of wind direction between Profiler (3 min. averages) and pibal, and between pibals 3 min apart. Values in parentheses are for $z \geq 300$ m. Averages of 100 m layer values shown, for the surface (or 300 m) through 1.9 km.

Day (July 1995)	Number of comparisons	Mean (deg) Profiler vs. Pibal	Mean (deg) Pibal vs. Pibal	Standard Deviation (deg) Profiler vs. Pibal	Standard Deviation (deg) Pibal vs. Pibal
18	8	19.14 (18.92)	-0.31 (1.25)	13.00 (9.72)	9.53 (5.67)
20	9	7.13 (4.46)	-0.66 (-1.08)	8.56 (8.55)	8.13 (8.30)
21	5	11.71 (9.00)	0.64 (0.65)	3.96 (3.86)	4.21 (3.01)

The Profiler vs. pibal comparison for 18 July showed significantly greater differences in wind direction than for the other two comparison days (20 and 21 July). The pibal vs. pibal comparison for that day also showed somewhat larger differences in the standard deviation of wind direction relative to those for the other days. The standard deviation of wind direction differences (100 m layers) exceeded 10 ° for pibal vs pibal for heights (z) $\leq$ 0.3 km and z = 1.1 km, and for the Profiler vs. pibal at $z \leq 0.8$ km and z = 1.2 km. The magnitude of mean differences in wind direction between Profiler and pibal was ≥ 20 ° at z = 0.6 km, $0.8 \leq z \leq 1.2$ km, and $1.5 \leq z \leq 1.8$ km (maximum of about 25 ° at 1.6 km). On this day the pibals traveled eastward, passing over the ocean within a minute after launch. These larger differences were not unexpected since the pibals drifted over the ocean after reaching 200 or 300 m in altitude, leaving the highly convective conditions that existed over the land. Later in the afternoon small, but intense, thunderstorms passed through from the west, forcing the test to be canceled before 1500 EDT (1900 UTC) due to the danger of lightning strikes.

The largest direction difference between the Profiler and pibal was at the "surface" (about 5 m AGL) for the latter two days and at 0.1 km on 18 July. Both systems relied on surface stations separated by about 10 m horizontally and 1 - 2 m vertically (the WFF anemometer was higher). The location only about 200 m from the ocean and the mix of land and water surfaces near the launch site may account for much of the observed direction differences in the lowest 0.1 to 0.2 km. The balloons drifted off roughly to the northwest except on 18 July, soon after turning

toward the east to northeast, passing over the northern half of the island, and out over the water. Since the ascent rate of the pibals was about 5 ms^{-1} and the average wind speed for most of the test periods was about 5 to 7 ms^{-1} during much of each ascent, the balloon ended up about 2 to 3 km from the Profiler and pibal launch site by the time it reached an altitude of 2 km. On 21 July the wind speed at most heights exceeded 10 ms^{-1}, causing the pibal to drift about 4 km by the time it rose to 2 km.

The variations between profiles from pibals launched 3 min apart were not insignificant, and on occasion exceeded those between Profiler and pibal. These results support the idea that differences between radar profiler and rawinsonde wind soundings in earlier data (e.g., Weber et al, 1990) may be partly a result of real atmospheric temporal and spatial variation.

FUTURE WORK

Several initiatives are planned for the near future. One involves a better extraction of satellite temperature wind velocity profilers using neural network methods as noted above. Bustamante, et al (1997) present work performed in 1996 and earlier on retrieval of temperature soundings, and note planned work on improved temperature profiles and wind velocity estimation. Initial results on wind velocity should begin to appear within a year. Also, the software for fitting a satellite sounding for the location of the Profiler should help improve accuracy. The new antenna that combines the radar and RASS functions shows promise in improving the ground based profiles of both wind and virtual temperature. An early test at Erie, CO provided profiles to 4.1 km (maximum height for radar parameters used) during conditions of light snow. Additional tests are planned at WSMR, NM that will give a more complete indication of performance of the system with the new antenna. After installation of new, higher power, amplifiers in February-March 1997 the tests will continue. The additional power should increase performance further.

The new, passive, microwave radiometer has run in a test mode, but has not been integrated into the Profiler. However, comparisons between radiometer output and rawinsonde data at Wallops Island, VA and WSMR, NM suggest a marked improvement over the older, larger radiometer for heights > 0.5 km. Root Mean Square (RMS) differences between radiometer temperatures and those from rawinsonde were about 1 K for $z \leq 1.2$ km (< 0.5 K near 0.2 km) over 9 comparisons at Wallops Island. These values compare favorably with those reported by Moran and Strauch (1994) for comparisons between RASS and rawinsonde. For $1.2 < z \leq 3$ km the RMS differences were ≤ 1.6 K, greater than values reported by Moran and Strauch (1994), but within stated requirements. If confirmed in ongoing tests, the radiometer may supplant the RASS, thereby allowing for a smaller, more portable Profiler.

ETL plans to introduce new software for improved control and data processing for the radar and RASS during the spring of 1997. This software will consist of "standard" architecture and coding, and eliminate the necessity of special signal processing boards. It will allow easier control by the user, and potentially "hands off" operation by non-specialists. This software package will be integrated into the Profiler during the ongoing re-configuration into a smaller, more mobile system.

The next version of the Profiler will have the processors in a shelter suitable for a High Mobility Multi-Wheeled Vehicle (HMMWV) instead of a towed, enclosed trailer. A newer, more compact receiver and processor for meteorological satellites (both NOAA and DMSP) currently being integrated into the present system also will reside in the shelter. Two small enclosed tracking antennas (0.46 m flat plates) will soon replace the present much larger enclosed tracking antenna (1.2 m dish). The combined size and weight of the newer antennas are less than the one older one. The lower size and weight of the microwave radiometer now undergoing evaluation will allow it to fit easily on the new system. The upgraded software is being reworked to fit as close as possible to Army common hardware and software standards. Lightweight Computer Unit (LCU) computers, or equivalent civilian PC's (e.g., 200 MHZ Pentium computers), will replace the current mix of workstations and PC's. The resulting Profiler "platform" will consist of a standard shelter on a HMMWV or equivalent vehicle that will tow a smaller trailer containing the radar antenna.

CONCLUSION

An upgraded Profiler prototype is being developed to answer Army requirements as stated in the approved Profiler ORD and MNS. This system will provide a means of collecting data from a variety of profiling instruments and merging those data into combined meteorological soundings for near real time operational uses. The data provided by the MPS will have a variety of military and civilian applications. The MPS can provide timely support for airfield operations, giving, for example, near real time indications of potentially hazardous wind conditions. Mesoscale models will have access to detailed, very rapid refresh, atmospheric soundings within and somewhat above the boundary layer. Through access to data from environmental satellites, and potentially from UAV sensors and dropsondes, the Profiler will obtain meteorological data throughout the domain of a mesoscale model. The ability to generate a picture of very short-term flow and virtual temperature patterns in the lower troposphere can lead to a better understanding of the atmosphere and to better modeling at smaller scales. As the Los Angeles Free Radical Experiment showed, this type of system can be invaluable for pollution studies.

REFERENCES

Bustamante, D., J. Cogan, and A. Dudenhoeffer, 1997. Results and implications of neural network retrievals of satellite temperature soundings, Proceedings of the Battlespace Atmospherics Conference, San Diego, CA, in press.

Cogan, J., 1995. Test results from a Mobile Profiler System, Meteor. Appl., 2, 97-107.

----------, and D. Wolfe, 1995: The mobile profiler: data analysis and display. *27th Conference on Radar Meteorology*, Vail CO, 376-379.

Fisher, E. E., F. Brousaides, E. Keppel, F. J. Schmidlin, H. C. Herring, and D. Tolzene, 1987: Meteorological Data Error Estimates. Document 353-87, Meteorology Group, Range Commanders Council, White Sands Missile Range, NM, 23 pp.

Merritt, D., 1995, "A statistical averaging method for wind profile Doppler spectra," *J. Atmos. Ocean. Technol.*, 12, 985-995.

Moran, K. P., and R. G. Strauch, 1994: The accuracy of RASS temperature measurements corrected for vertical air motion. *J. Atmos. Ocean. Technol.*, 11, 995-1001.

Parsons, D., W. Dabberdt, H. Cole, T. Hock, C. Martin, A. Barrett, E. Miller, M. Spowart, M. Howard, W. Ecklund, D. Carter, K. Gage and J. Wilson, 1994. The integrated sounding system: description and preliminary observations from TOGA COARE. Bull. Amer. Meteor. Soc., 75, 553-567.

Schroeder, J. A., E. R. Westwater, P. T. May and L. M. McMillin, 1991. Prospects for temperature sounding with satellite and ground-based RASS measurements. J. Atmos. and Ocean. Technol., 8, 506-513.

Spalding, J. B., 1996. Mobile Profiler System Software Description: Interpolation of Satellite Soundings, Final Report, Physical Sciences Laboratory, New Mexico State University, NM, 55 pp.

Stokes, G. M., and S. E. Schwartz, 1994. The atmospheric radiation measurement (ARM) program: programmatic background and design of the cloud and radiation testbed. Bull. Amer. Meteor. Soc., 75, 1201-1221.

Strauch, R. G., D. A. Merritt, K. P. Moran, K. B. Earnshaw, and D. C. Welsh, 1984: The Colorado wind profiling network. *J. Atmos. Ocean. Technol.*, 1, 37-49.

Weber, B. L. and D. B. Wuertz, 1990: Comparison of rawinsonde and wind profiler radar measurements," *J. Atmos. Ocean. Technol.*, 7, 157-174.

----------, ----------, R. G. Strauch, D. A. Merritt, K. P. Moran, D. C. Law, D. Van de Kamp, R. B. Chadwick, M. H. Ackley, M. F. Barth, N. L. Abshire, P. A. Miller and T. W. Schlatter, 1990: Preliminary evaluation of the first NOAA demonstration network wind profiler., *J. Atmos. Ocean. Technol.*, 7, 909-918.

Westwater, E. R., W. B. Sweezy, L. M. McMillin and C. Dean, 1984a. Determination of atmospheric temperature from a statistical combination of ground-based profiler and operational NOAA 6/7 satellite retrievals. J. Climate Appl. Meteor., 23, 689-703.

----------, W. Zhendui, N. C. Grody and L. M. McMillin, 1984b. Remote sensing of temperature profiles by a combination of ground-based profiler and satellite-based MSU radiometric observations, Proceedings, Conf. on Satellite/Remote Sensing and Applications, Clearwater, FL, Amer. Meteor. Soc., 191-196.

Wolfe, D., B. Weber, D. Weurtz, D. Welsh, D. Merritt, S. King, R. Fritz, K. Moran, M. Simon, A. Simon, J. Cogan, D. Littell and E. Measure, 1995. An overview of the mobile profiler system

(MPS): preliminary results from field tests during the Los Angeles free radical study, Bull. Amer. Meteor. Soc., 76, 523-534.

New Cloud Profiling Radar for Air Operations

Madison J. Post
Kenneth P. Moran
NOAA Environmental Technology Laboratory
325 Broadway
Boulder, Colorado 80303

Introduction

In the late 1960s and early 1970s the U. S. Air Force used several AN/TPQ-11 [Paulsen and Petrocchi, 1970] 35-GHz radars to aid airfield controllers. Unfortunately, the reliability of the high peak power magnetron transmitters used in those radars was low, and they were quickly decommissioned. An alternate technology, Traveling Wave Tube Amplifiers (TWTAs), can now be used to produce an equivalent level of average transmitted power at 35 GHz frequency. The Department of Energy (DOE), in collaboration with NOAA's Environmental Technology Laboratory (ETL), is now producing 35-GHz Doppler cloud-profiling radars based on TWTA technology for five global Cloud And Radiation Testbed (CART) sites, as part of the Atmospheric Radiation Measurement (ARM) program [Stokes and Schwartz, 1994]. The first of these highly-sensitive, vertically-pointing, unattended radars has been producing continuous data from the Southern Great Plains (SGP) CART site since November 12, 1996. The system monitors its own health, environmental conditions, and status of external power. It shuts down and reboots gracefully and automatically. It is also capable of automatic, routine calibration, and it manages data through both local archiving (backup) and transmission to an external data management and display system. The new radar is intended to gather data for 10-15 years in many different climatological regimes, to better understand the climatology and layering of clouds, and the role they play in radiative balance and climate change.

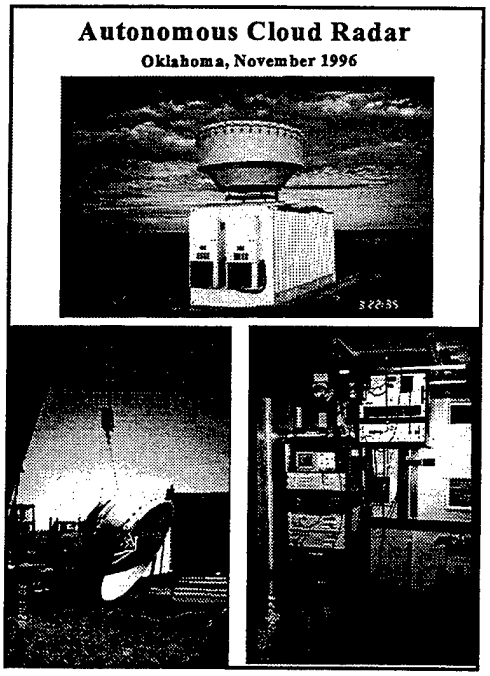


Fig., 1. Unattended 35-GHz cloud-profiling radar as installed in a seatainer at DOE's CART site near Lamont, Oklahoma. Antenna is 3 m in diameter. Radar is mounted in a single rack and weighs about 140 kg.

It occurred to the authors that this system might be of interest to participants of the Battlespace Atmospherics Conference, for applications previously served by the AN/TPQ-11 radar, namely air traffic control, both on land and at sea.

Description

Fig. 1 shows the seacontainer-housed radar at the SGP site near Lamont, Oklahoma. DOE/ARM plans to house many other instruments in the same container, so the size of this facility is not necessarily representative of what is needed solely for the cloud radar. The radar itself, *sans* 3-m-diameter radomed antenna, weighs about 140 kg and is mounted in a single 2-m tall rack. For remote sites and overseas installations we plan to use 2-m diameter antennas that can

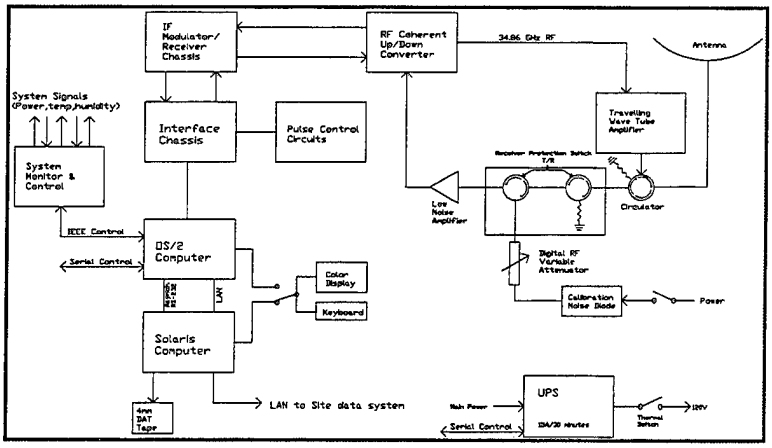


Fig. 2. Block diagram or radar. Note provisions for receiver protection and automatic calibration via noise diode and attenuators. Computer controls, health monitoring, and data system are not indicated.

Table 1
Operating Characteristics DOE/ETL Cloud Radar at SGP

Frequency	34.86 GHz (λ=8.66 mm, Ka-band)
Peak Transmitted Power	100 W
Max. Duty Cycle	25%
Antenna Diameter / On-Axis Gain	10 ft. / 57.3 dB
Beam Width	0.2 deg.

OPERATING MODE →	1	2	3	4
Inter-pulse Period (μs)	90	120	86	72
Pulse Width (ns)	300	600	300	300
Delay (ns)	1800	1800	2000	1800
Gate Spacing (ns)	300	600	300	300
Number of Coherent Avgs.	6	6	6	4
Number of Spectral Avgs.	16	21	24	37
FFT Length	64	64	64	64
Number of Coded Bits	32	32	8	not coded
Number of Gates	218	150	240	218
Duty Cycle (%)	10.7	16.0	2.8	0.4
Dwell Time (s)	0.6	1.0	0.8	0.7
Observation Time (s)	9	9	8	9
Min. Detectable Signal (dBm)	-129	-133	-130	-132
Range Resolution (m)	45	90	45	45
Height Coverage (km)	0.3-10.1	0.3-13.8	0.3-11.1	0.3-10.1
Unambiguous Velocity (m/s)	±4.0	±3.0	±4.2	±7.5
Velocity Resolution (m/s)	0.13	0.09	0.13	0.23
Unambiguous Range (km)	13.5	18.0	12.9	10.8
Estm. Sensitivity (dBZ at 5) km)	-44	-50	-39	-32

be transported more easily, either separately or as part of a smaller container. A block diagram of the radar design is shown in Fig. 2, and we list in Table 1 typical operating characteristics of the radar.

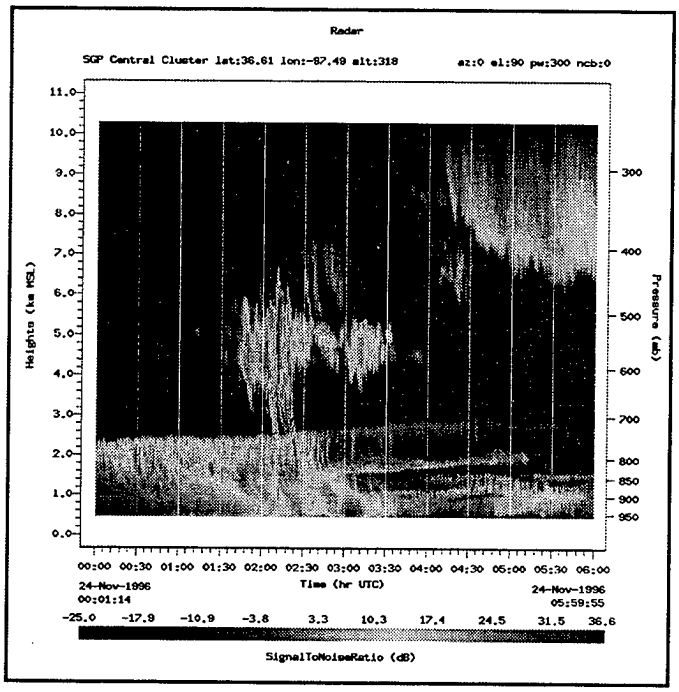


Fig. 3. A time-height display of signal-to-noise ratio for mode 3 in Table 1 (uncoded) at the Southern Great Plains (SGP) CART site near Lamont, Oklahoma, for a 6-hour period on November 24, 1996. Range resolution is 45 m, dwell time is 9 s.

Up to four different modes of operation can be locally or remotely established, through which the radar routinely cycles. Maximum sensitivity for the modes postulated here is -38 dBZ at 20 km altitude, which compares favorably with NOAA's much more sophisticated and expensive scanning research radar, NOAA/K [Kropfli et al., 1990, Kropfli and Kelly, 1996]. Cycling automatically and rapidly through modes of varying sensitivity permits one to better accommodate the huge dynamic range in atmospheric reflectivities experienced in practice, from low-level precipitation to cirrus at high-altitude. Time and height resolutions are on the order of 10 s and 50 m, although within reason these can be adjusted for the needed application. Fig. 3 is a typical time-height display of the radar signal-to-noise ratio (zeroth spectral moment) in a situation where several layers and types of clouds are present. The radar is a full Doppler system, hence it calculates and can store complete spectra for each range gate, but typically it only retains the first three spectral moments calculated from the spectra, in an effort to reduce the quantity of data. The Doppler capability permits one to easily discern the melting layer in cold, precipitating clouds, because at that height the precipitation fall speed increases abruptly as the snow/graupel condenses to liquid droplets and accelerates. Doppler capability is especially important when combining the radar measurements with other instruments, such as radiometers and lidars [Matrosov et al., 1994, Intrieri et al., 1995], to measure important microphysical parameters of the clouds, such as vertical profiles of effective particle radius, ice mass content, etc. These combined techniques potentially permit one to automatically detect those portions of clouds where icing conditions exist, an important piece of knowledge for aircraft controllers.

Range Sidelobes

The radar achieves its relatively high average power output (25 w) from the low peak power (100 w) TWTA by employing pulse compression techniques, i.e. by transmitting long pulses (up to 20 μs) that are internally phase-coded, typically in 0.6 μs segments. Standard techniques [Schmidt et al., 1979] used to receive and decode such pulses permit us to retain the range resolution associated with the phase-coded segments (90 m), but at the expense of generating weak, artificial returns at ranges other than the true range. Since these artificial signals are typically 25-35 dB below the true returns, and

occur at ranges bounded by the length of the code used, they are easy to identify in most situations. However, they can be a problem when strong gradients in reflectivity and/or large Doppler velocities are present. By automatically cycling through several modes of radar sensitivity, from no pulse compression to maximum compression, we find it is possible for an experienced analyst to unambiguously understand the true layering of clouds. However, we are working to incorporate improved coding and processing techniques to further reduce the level of range sidelobe artifacts, since they are clearly an unwanted distraction.

Plans

We are planning to deploy one additional radar every six months in the next two years to ARM's other CART sites, e.g. to the north slope of Alaska and Manus Island, Papua New Guinea. At such locations, the radars will need to run in a truly unattended mode, since only relatively inexperienced local personnel will be available to monitor the radar's operation. In addition, ETL expects to deploy a similar cloud radar for 12-16 months on the ice pack north of Alaska as part of the Office of Naval Research (ONR) and National Science Foundation (NSF) joint Surface HEat Budget of the Arctic Ocean (SHEBA) campaign, beginning in late 1997.

While ETL develops and deploys the radars for DOE, it is also working to establish a Cooperative Research and Development Agreement (CRADA) with industry to transfer the technology to the private sector, because it is not in a research laboratory's mission to market technology to users, or to support it over many years. A CRADA will make the technology more robust and keep it abreast of the latest improvements, make it commercially available, and help ensure long-term, professional support. We expect the CRADA to be signed in early 1997 and for a commercial version of the 35-GHz cloud-profiling Doppler radar to be available within one year. At that time, or sooner, we hope supervisors of both military and civilian air traffic control facilities will seriously consider the benefits of having available to controllers, both on land and at sea, detailed knowledge of local cloud layering, turbulence, and icing conditions provided by these inexpensive ($500K), compact radars.

References

Intrieri, J.M., W.L. Eberhard, T. Uttal, J.A. Shaw, J.B. Snider, Y. Han, B.W. Orr, and S.Y. Matrosov, 1995: "Multiwavelength observations of a developing cloud system: the FIRE-II 26 November case study," *J. Atmos. Sci.*,**52**, 4079-4093.

Kropfli, R.A. and R.D. Kelly, 1996: "Meteorological research applications of mm-wave radar," *Meteor. and Atmos. Phys.*, **59**, 105-121.

Kropfli, R.A., B.W. Bartram, and S.Y. Matrosov, 1990: "The up-graded WPL dual-polarization 8-mm wavelength Doppler radar for microphysical and climate research," *Proc. Conf. on Cloud Physics*, San Francisco, Amer. Meteor. Soc., 341-345.

Matrosov, S.Y., B.W. Orr, R.A. Kropfli, and J.B. Snider, 1994: "Retrieval of vertical profiles of cirrus cloud microphysical parameters from Doppler radar and infrared radiometer measurements," *J. Appl. Meteor.*, **33**, 617-626.

Paulson, W.H. and P.J. Petrocchi, 1970: "Operational utilization of the AN/TPQ-11 cloud detection radar," *Air Force Cambridge Instrumentation Papers*, No. 166, 37 pp.

Schmidt, G., R. Rüster, and P. Czechowsky, 1979: "Complementary code and digital filtering for detection of weak VHF radar signals from the mesosphere," *Geosci. Electronics,* **GE-11**, 154-161.

Stokes, G. M., and S. E. Schwartz, 1994: "The Atmospheric Radiation Measurement (ARM) program: programmatic background and design of the Cloud and Radiation Test Bed," *Bull. Amer. Meteor. Soc.*, **75**, 1201-1221.

Shipboard Wind Profiling by Radar: Problems and Possible Solutions

Madison J. Post
Christopher W. Fairall
Allen B. White
James R. Jordan
NOAA Environmental Technology Laboratory

and

Kenneth S. Gage
John Wilson
Leslie M. Hartten
NOAA Aeronomy Laboratory

325 Broadway
Boulder, Colorado 80303

Introduction

Using modern UHF radars to profile boundary-layer winds from ships offers many advantages. These systems are relatively small and inexpensive (20 m^3, $200K) and they can run unattended for many months in all weather conditions. Temporal and vertical resolution of the wind measurements can be as fine as 5 minutes and 60 m, respectively. Such measurements offer unparalleled, cost-effective performance for tactical operations, resource protection, forecasting, and research.

Table 1

Shipboard Radar Wind Profiling
NOAA/ERL Experience

Year	Ship	Location	Months	Days
1991	Baldridge	Miami-Puerto Rico	May	15
1991	Mauna Wave	Tiwi (0°, 140W)	Nov. - Dec.	30
1992	Baldridge	East Atlantic	May - July	90
1992	"Science 1"	Trop. West. Pac.	Nov. - Feb.	120
1992	"Exp. 3"	Trop. West. Pac.	Nov. - Feb.	120
1992	Mauna Wave	Trop. West. Pac.	Nov. - Feb.	120
1993	Titan	Channel Islands	Sept.	30
1994	Wecoma	California - Oregon	Mar. - Apr.	60
1995	Discoverer	Tasmania	Oct. - Nov.	60
1996	Discoverer	Trop. West. Pac.	Mar. - Apr.	60
1997	Knorr	N. Atlantic	Jan.	30
1997	Ka'Imimoana	Cent. Eq. Pac.	- - -	---

Two of the National Oceanic and Atmospheric Administration's (NOAA) Environmental Research Laboratories, the Environmental Technology Laboratory (ETL) and the Aeronomy Laboratory(AL)

have acquired over 600 days of experience operating such profilers at sea. Table 1 lists the research campaigns by ship, location, and duration. Results from the first deployment in 1991 on the NOAA R/V *Malcolm Baldridge* are presented in Carter, et al. [1992]. Subsequent AL developments in profiler technology are summarized in Carter et al., [1995].

Our systems operate at 915 MHz and are mechanically stabilized to eliminate the effects of ship motion. They typically use phased-array antennas to transmit and receive energy along at least one pair of beams oriented about 20° off the vertical and along orthogonal azimuthal directions. Normally the cycling of beams along different directions also includes a vertically-oriented beam as well. The Doppler-shift of the energy scattered back from the atmosphere along all beams is determined and used with information on the ship's orientation and motion to produce estimates of earth-relative wind speed and direction at many range gates, typically encompassing the height interval 0.15 to 3.0 km. Typically we save the complete Doppler spectra of the signal in each gate, and archive the first three moments computed from the spectra as well. The first three moments of the Doppler spectra are related to backscattered energy, radial velocity, and velocity spread in the sensing volume, respectively. Time-height displays of the vertical beam spectral moments reveal interesting and useful atmospheric features, such as precipitation fall speed, melting layer, cloud bottoms and tops, and turbulence [White, et al., 1996].

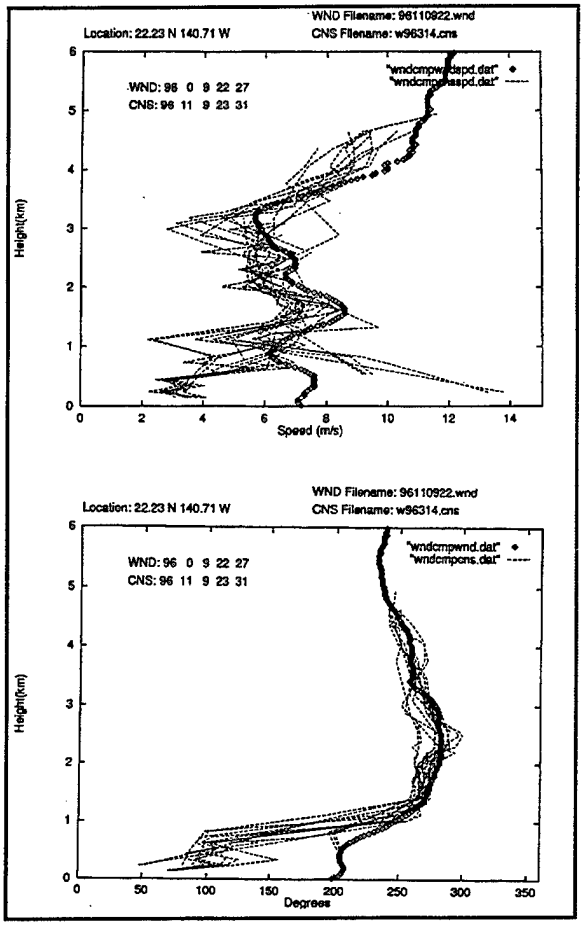


Fig. 1. Comparison of profiler-derived winds for multiple soundings (dashed lines) with a contemporaneous balloon sounding (diamond markers) from NOAA R/V *Ka'imimoana* in 1996. Low-level profiler winds are likely in error due to contamination of radar signals by sea clutter.

Problems

Despite the potential of this technology and its remarkably good performance during the first shipboard deployment [Carter, et al., 1992], we have subsequently learned that one must take precautions in locating the hardware onboard ships to minimize the effects of sea clutter, and in using the data products generated by the system's software, the Profiler On-line Program (POP). POP uses consensus averaging [Weber et al., 1993] of Doppler spectral moments to compute wind products, and assumes the spectra contain only atmospheric signals. When spectra are contaminated, the spectral moments, and hence the wind products, can be in error.

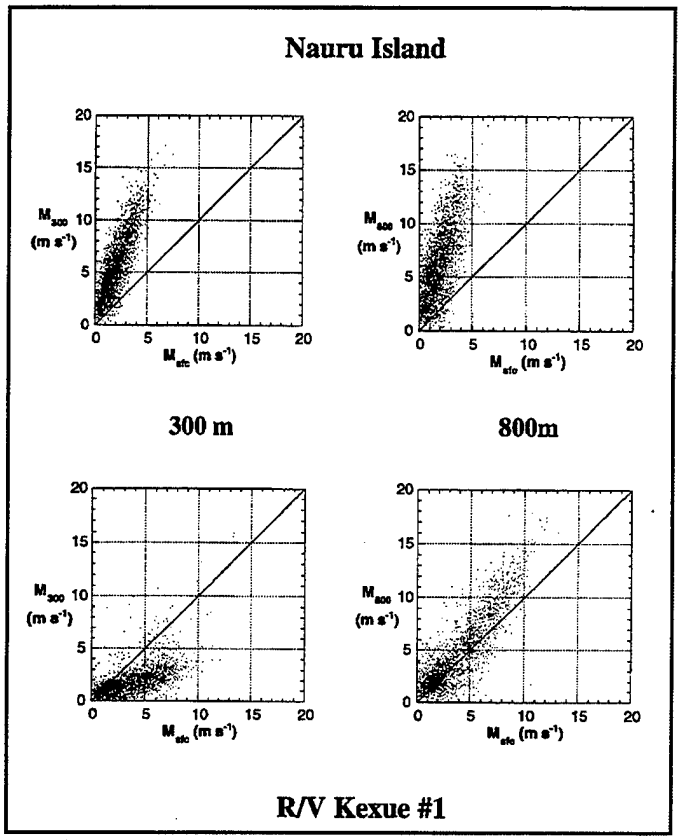


Fig. 2. Scatter diagrams of surface winds (x-axis) vs. profiler winds at altitude (y-axis) for 300 m altitude (left plots) and 800 m altitude (right plots). Island winds (above) with little sea clutter show expected trends in the diagrams while ship--based winds (below) show effects of sea clutter contamination.

Fig. 1 displays the effects that sea clutter often has on the radar-estimated wind products. Here we compare winds measured by ship-launched radiosondes with the radar-derived winds, for a research cruise of the NOAA R/V *Ka'imimoana* in 1996 in the central Pacific. Since sea clutter often appears near zero frequency in the Doppler spectrum, it biases the wind estimates low. This creates underestimates of wind speed, and some error in wind direction, primarily at short ranges (low altitudes) where clutter can dominate the desired atmospheric signals from the main beams. In a separate study of island-based and ship-borne profilers deployed November, 1992, to February, 1993, in the western Pacific, Hartten [1996] compared radar-derived winds in the lower gates with surface winds. One expects the surface winds to be lower than winds from the lowest radar gates, and to see a consistent pattern of differences vs. altitude for both platforms. Instead we see more spread in the scatter diagrams, and surface winds up to 5 m s^{-1} stronger than low-level profiler winds, for the ship-borne systems, as depicted in Fig. 2. Riddle et al. [1996] describe other similar intercomparisons made during the Coupled Ocean-Atmosphere Response Experiment (COARE) of the Tropical Ocean and Global Atmosphere (TOGA) program. From March to April, 1996, we deployed another stabilized 915 MHz wind profiling system at sea. We took care to position it nearly optimally low on the rear fantail of NOAA R/V *Discoverer*, and we installed diffraction-softening baffles on top of the standard clutter fences. This was our most successful deployment since the initial one on the *Malcolm Baldridge*. Table 2 compares radar-derived winds with both surface and balloon winds. Note that although the lower radar gates display possible negative biases in wind velocity estimates, the biases are not as large, or as high-reaching, as in Fig. 1.

Other problems that are encountered by all radar wind profilers, including those at sea, are radio frequency interference and contamination by fliers (birds and planes). Both types of non-atmospheric signals can enter through sidelobes or the main beam. We do not have statistical analyzes of the effects of these contaminants, but in general the effects are more intermittent and cause larger errors than sea clutter.

Table 2

Correlation between CSP 915-MHz radar-derived winds and

1) Surface Winds

	Gate 1 (120 m)	Gate 2 (219 m)	Gate 3 (318 m)	Gate 4 (417 m)	Gate 5 (516 m)
N	237	257	459	517	535
R^2	0.61	0.63	0.64	0.68	0.65
U_s	4.8	4.9	5.3	5.4	5.5
Bias	-1.5 m/s	-0.9	+0.2	+0.7	+1.2

2) Rawinsondes

	Gate 1-5 (100-500 m)	Gate 6-10 (600-1000 m)	Gate 11-15 (1100-1500 m)	Gate 16-20 (1600-2000 m)
N	460	601	604	578
R^2	0.51	0.74	0.78	0.71
U_s	6.2	7.2	7.5	7.2
Bias	-0.9 m/s	+0.3	0.0	0.0

N = # Cases R^2 = Correlation Coefficient U_s = 1) Surface Mean Wind; 2) Balloon Mean Wind; Both 1) and 2) only for cases involved in N.

Solutions

To minimize contamination of the radar's Doppler spectra by sea clutter, one must take care in siting the profiler to avoid reflection of the antenna's sidelobes by ship structures, because the radar then "sees" the surface of the ocean. This typically involves placing the profiler as far away as possible from tall structures, orienting its orthogonal beams 45° from the centerline of the ship, and keeping it as low as possible on the ship (as close to water level as feasible). It might also prove helpful to install diffraction-softening baffles along the upper edges of the radar's clutter screens, as we did on the *Discoverer* deployment. We have found mechanical (gyro) stabilization of a horizontally-oriented phased array antenna panel to be quite satisfactory, but such stabilization adds to the bulk and price of the system. We are investigating the feasibility of using unstabilized antennae (e.g., on buoys) and computer-correcting for instantaneous platform motion and orientation, for both ship and buoy applications.

However, even for optimal antenna designs there always will remain antenna sidelobes, due to the antenna's finite size and the radar wavelength (.33 m). Contamination of atmospheric signals, which are quite weak, can occur through the sidelobes or even the main beam (in the case of fliers and RFI). Therefore, advanced signal processing is needed to decontaminate the data stream before Doppler spectra and spectral moments are computed. To this end, the labs are producing and testing several new algorithms, together with new operating systems to more efficiently implement them. Jordan et al. [1996] are applying wavelet transforms to the radar time series to remove sea clutter and flier contamination, with notable success. Merritt [1995] has created an algorithm using statistical techniques to automatically edit the resultant spectra and remove more of the erroneous data.

Finally, Weber et al. [1993] use time-height continuity editing to cleanup data at the moment level, before consensus winds are computed. The POP program is being upgraded and modularized to permit integration of some of the new algorithms, and an entirely new operating system named CASPER (Control, Acquisition, and Signal Processing Engine for Radar) is also being developed and tested. For a description of CASPER visit web site http://ics.etl.noaa.gov/.

Summary

We have operated 915 MHz radar wind profiling systems onboard moderate- to large- sized research vessels (100-300 ft long) over a span of 5 years, accumulating more than 600 days of operating experience at sea in a wide range of weather conditions. Our conclusion is that these systems are robust and that they can provide reliable, continuous, unattended wind observations from about 150 m to more than 3 km altitude. However, because of sea clutter and other possible contamination of radar signals, one must be cautious and not blindly use wind products from the lower gates. Higher gates are typically unaffected by contamination. We have found that proper siting of the profilers away from tall structure and as low as possible on the ship is critical in minimizing the introduction of sea clutter through reflected antenna sidelobes. And we are working to develop, test, and implement new signal processing techniques and operating systems to minimize the deleterious effects of sea clutter and other interferences on profiler wind products.

References

Carter, D.A., W.L. Ecklund, K.S. Gage, M. Spowart, H.L. Cole, E.F. Chamberlain, W.F. Dabberdt, and J. Wilson, 1992: "First test of a shipboard wind profiler," *Bull. Am. Met. Soc.*, **73**, 1587-1592.

Carter, D.A., K.S. Gage, W.L. Ecklund, W.M. Angevine, P.E. Johnston, A.C. Riddle, J. Wilson, and C.R. Williams, 1995: "Developments in UHF lower tropospheric wind profiling at NOAA's Aeronomy Laboratory," *Radio Science*, **30**, 977-1001.

Hartten, L.M., 1996: "Reconciliation of surface and profiler winds at ISS sites," submitted to *J. Atmos. and Ocean. Tech.*, July 1996.

Jordan, J.R., R.J. Lataitis, and D.A. Carter, 1996: "Removing ground and intermittent clutter contamination from wind profiler signals using wavelet transforms," submitted to *J. Atmos. Oceanic Tech.*

Merritt, D.A., 1995: "A statistical averaging method for wind profiler Doppler spectra," *J. Atmos. Oceanic Tech.*, **12**, 985-995.

Riddle, A.C., W.M. Angevine, W.L. Ecklund, E.R. Miller, D.B. Parsons, D.A. Carter, and K.S. Gage, 1996: "In situ and remotely sensed horizontal wind and temperature intercomparisons obtained using Integrated Sounding Systems during TOGA COARE," *Beitr. Phys. Atmosph.*, **69**, 49-61.

Strauch, R.L., D.A. Merritt, K.P. Moran, K.B. Earnshaw, and D. VanDe Kamp, 1984: "The Colorado wind profiling network," *J. Atmos. and Oceanic Tech.*, **1**, 37-49.

Weber, B.L., D.B. Wuertz, D.C. Welsh, and R. McPeek, 1993: "Quality controls for profiler measurements of winds and RASS temperatures," *J. Atmos. and Oceanic Tech.*, **10**, 452-464.

White, A.B., C.W. Fairall, A.S. Frisch, B.W. Orr, and J.B. Snider, 1996: "Recent radar measurements of turbulence and microphysical parameters in marine boundary layer clouds," *Atmos. Res.*, **40**, 177-221.

Evaluation of the Continuous Profiling of Refractive Index Gradients and Humidity Using Wind Profiling Radars

Madison J. Post, Earl E. Gossard, B. Boba Stankov,
Daniel E. Wolfe, and Kenneth P. Moran
NOAA Environmental Technology Laboratory
325 Broadway
Boulder, Colorado 80303

Introduction

Radar wind profilers are designed to measure the Doppler spectrum of the radial wind along several different beam directions as a function of range [Strauch et al., 1984]. The first moment of the spectrum corresponds to the mean radial velocity of air in the sensing volume, permitting one to calculate horizontal wind speed v and direction, and vertical shear of horizontal wind dv/dz, from range-gated measurements of the off-vertical beams. When the radar beam is directed vertically, the Doppler spectrum can be used to determine not only mean vertical motion w (first moment), but also turbulent vertical velocity fluctuations, through the width (second moment) of the spectrum. These permit C_w^2, the structure parameter of the turbulent vertical velocity field, and ϵ, the turbulent dissipation rate, to be calculated.

Gossard et al. [1982] have shown that wind profiler Doppler spectra contain enough information to compute the vertical gradient of refractivity $d\Phi/dz$, namely,

$$\left(\frac{d\Phi}{dz}\right)^2 = \left(\frac{L_\Phi}{L_w}\right)^{4/3} \left(\frac{dv}{dz}\right)^2 \frac{C_\Phi^2}{C_w^2}$$

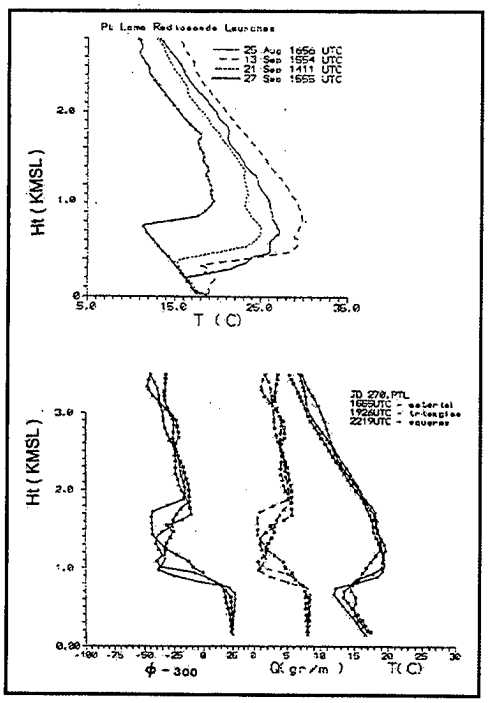


Fig. 1. Typical balloon temperature soundings (above) at Pt. Loma during the experiment, showing strong gradients at various heights. Below are profiles of refractivity, humidity, and temperature computed from successive balloon ascents on Sept. 27, 1995 (Julian Day 270).

Here Φ is the mean refractivity at level z. The vertical shear of horizontal wind dv/dz is obtained from the radar's first spectral moment while C_Φ^2, the structure parameter of turbulent refractive index fluctuations, is obtained from the zeroth moment (power) of the atmospheric contribution to the Doppler spectra. L_ϕ and L_w are the turbulent length scales of refractivity and velocity, respectively.

Previous attempts to calculate these parameters from profilers operating in a high-time-resolution mode were discouraging, primarily because the radar spectra, and hence the spectral moments, are routinely contaminated by aircraft, birds, radio frequency interference, clutter, etc.

In 1994 we tried using manually edited Doppler spectra recorded with ETL's new transportable 449 MHz profiler with much greater success. Editing involves manually deleting false targets prior to calculating spectral moments. Encouraged by these results, in 1995 we collected 449 MHz radar, Radio Acoustic Sounding System (RASS) temperature, and integrated precipitable water vapor (IPW) at Pt. Loma in southern California, near San Diego, during a time when large contrasts in air mass occur, creating large atmospheric gradients to better evaluate the technique.

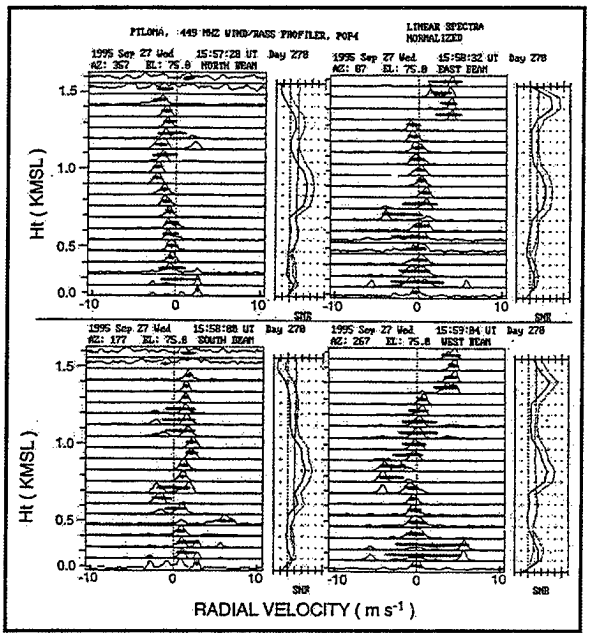


Fig. 2. Range-gated wind profiler spectra for the north, east, south and west beams. Dwell time for each beam was about 33 s. The center of the horizontal line on each spectrum represents the computer-estimated first moment (radial velocity) while the length of the horizontal line is the computer estimate of second moment (velocity spread) in the sensing volume. Unedited, these type of data can lead to errors in wind estimates, particularly at low altitudes.

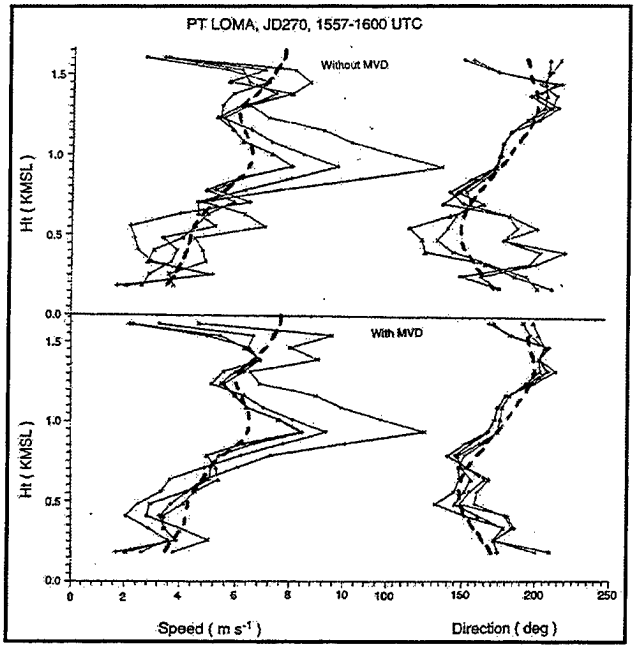


Fig. 3. Wind speed (right) and direction (left) estimates from 5-beam wind profiler data using conventional processing algorithms (above) and using Minimization of the Variances of Differences (MVD)(below), for four successive cycles of the radar beams. The balloon sounding made during radar data acquisition is shown by the heavy dashed line.

Pt. Loma Results

Fig. 1 shows typical soundings of temperature obtained from rawinsonde data during the Pt. Loma experiment. To avoid the severe clutter found in the lower range gates we performed our analyses during times when temperature inversions were above 500 m (e.g. Sept. 27, 1995, Julian day 270). Fig. 2 shows range-gated spectra generated by NOAA Aeronomy Laboratory's Profiler On-line Program (POP) for one cycle of four beams. The dwell time for each beam was approximately 33 s. Superimposed on the spectra are horizontal lines indicating the spectral width (second moment) calculated by POP. It is obvious that spectral features not associated with atmospheric winds severely contaminate POP moment products. For this study we manually edited individual spectra to select single spectral peaks that we judged to originate from atmospheric returns.

In addition to manual editing, we applied a new technique called Minimization of the Variance of Differences (MVD) to the off-vertical beams before calculating the horizontal winds, and used the same technique to calculate and correct for vertical air motion in the analysis of RASS temperature profiles. Figures 3 and 4 show improvements to standard POP-derived wind and temperature profiles that result from application of MVD.

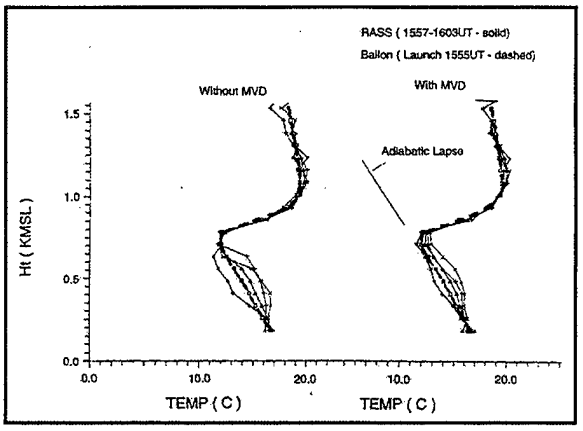


Fig. 4. Applying MVD to better estimate vertical atmospheric motion leads to improved RASS-measured temperature profilers (right) with respect to profiles computed with vertical motion measured in a standard fashion (left), for four successive radar soundings. The balloon sounding made during radar data acquisition is indicated by the heavy dashed line.

Profiles of various quantities derived solely from radar signatures (after editing out false targets in the spectra and application of MVD) for three successive cycles of the radar beams that occurred during a single balloon ascent are presented in Fig. 5. The right-most profiles of $d\Phi/dz$ include values calculated independently from balloon data (dashed line) for comparison. The consistency of the derived radar profiles and the good agreement with the balloon profiles are encouraging and suggest that the information content of radar wind profiler signals is sufficient to calculate useful profiles of refractive index gradients. Much work remains to make such calculations routine and operational, however, because human judgement is still required to edit out false targets in contaminated spectra. Please note that we did not discuss other important concerns, such as how compensation was made for radar beam broadening, the determination of important atmospheric constants such as temperature or velocity length scales, gradient sign ambiguity, or the extension of the technique to non-stable atmospheres as described by Gossard et al. [in publication, 1997].

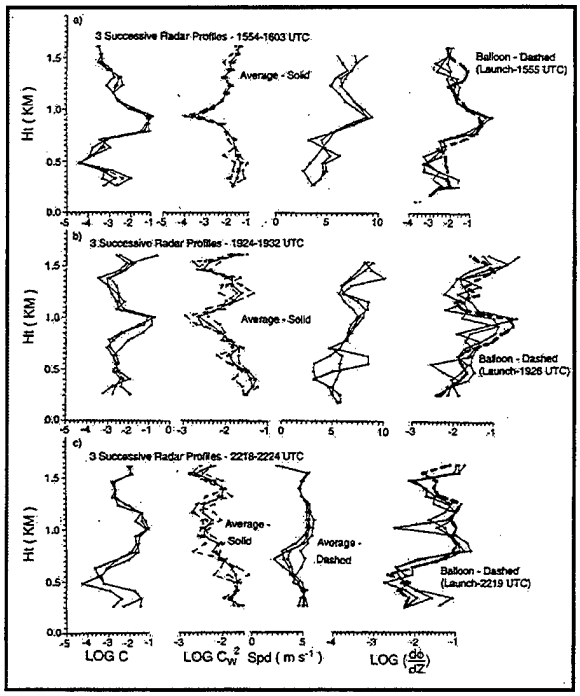


Fig. 5. Profiles (from left to right) of refractive index structure parameter, vertical velocity structure parameter, horizontal wind speed, and gradient of refractivity, for three sets of three successive radar measurements. The right-most profiles of refractivity gradients also include profiles computed from a balloon sounding whose ascent time was comparable to the period of time it took to make the radar measurements.

Humidity Gradients

For subjective analyses, humidity profiles are of more use to meteorologists than refractive index gradients. However, we know that the gradient of humidity is closely related to refractivity through the equation

$$\frac{dQ}{dz} = \frac{1}{b}\frac{d\Phi}{dz} + \frac{a}{b}\frac{d\theta}{dz}$$

Here $d\theta/dz$ is the gradient of potential temperature θ with height, which can be measured well by the same radar using RASS, and a and b are physical constants. Fig. 6 shows profiles of the graident of humidity derived solely by radar, and derived by balloon. Again, the degree of correlation between these independent profiles gives us hope that the radar alone might someday be able to operationally measure humidity gradients. Then, if the radar's measurements are combined with a measurement of surface humidity and a measurement of IPW, e.g., by inexpensive Global Positioning System (GPS) techniques [Rocken et al., 1993, Gutman et al., 1995], one could potentially integrate the radar-derived humidity gradients with sufficient constraint to obtain profiles of humidity in the boundary layer (and above), where most atmospheric water vapor resides.

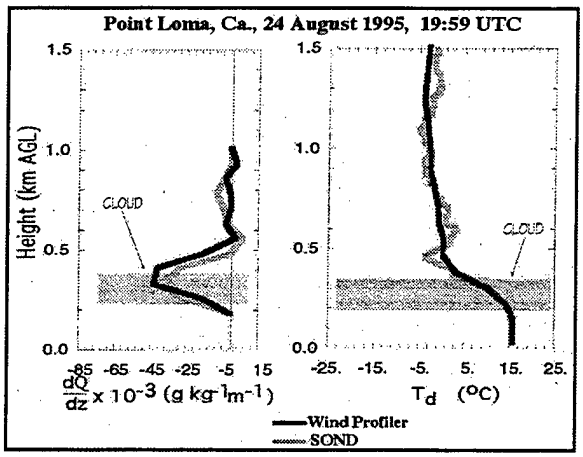


Fig. 6. Gradients of humidity calculated solely by radar and by balloon, in the presence of clouds. Clouds would prevent similar measurements by lidar above cloud base. Combined with a surface measurement of humidity and a GPS measurement of integrated humidity, both inexpensive additions to the radar, continuous all-weather profiling of boundary layer humidity would be possible, with temporal resolution of a few minutes.

Summary

We have conducted an experiment to assess the ability of a 449 MHz radar wind profiler to measure gradients of refractivity, and are encouraged by the results obtained when strong gradients were present. However, advances in automatic signal processing are required to make the technique operationally feasible, because current standard wind profiler spectral moment products are too inaccurate to use without considerable editing and averaging, because spectral contamination is often encountered. Once gradients of refractivity are calculated accurately, it is possible to combine them with other measurements to obtain profiles of humidity throughout the boundary layer (and above). For input to numerical weather forecast models, however, direct assimilation of radar-observed refractive index or humidity gradients may prove most useful.

References

Gossard, E.E., R.B. Chadwick, W.D. Neff, and K.P. Moran, 1984: "The use of ground-based Doppler radars to measure gradients, fluxes, and structure parameters in elevated layers," *J. Appl. Meteor.*, **21**, 211-226.

Gossard, E.E., D.E. Wolfe, K.P. Moran, R.A. Paulus, K.D. Anderson, and L.T. Rogers, 1997: "Measurement of clear-air gradients and turbulence properties with ground-based Doppler radars," submitted for publication.

Gutman, S.I., D.E. Wolfe, and A.M. Simon, 1995: "Development of an operational water vapor remote sensing system using GPS: a progress report," *FSL Forum*, Dec. 1995, 21-32.

Rocken, C., R.H. Ware, T. Van Hove, F. Solheim, C. Alber, J. Johnson, and M.G. Bevis, 1993: "Sensing atmospheric water vapor with the Global Positioning System," *Geophys., Res. Lett.*, **20**, 2631-2634.

Strauch, R.G., D.A. Merritt, K.P. Moran, K.B. Earnshaw, and D. Van de Kamp, 1984: "The Colorado wind-profiling network," *J. Atmos. and Oceanic Tech.*, **1**, 37-49.

AUTOMATED THERMAL INJURY RISK ASSESSMENT IN THE DISMOUNTED INFANTRY BATTLESPACE

William T. Matthew, William R. Santee, Reed W. Hoyt
U.S. Army Research Institute of Environmental Medicine, Natick Massachusetts

Peter Tikuisis
Defence and Civil Institute of Environmental Medicine, North York, Ontario, Canada

Eugene S. Barnes, Gary B. McWilliams
U.S. Army Research Laboratory, White Sands Missile Range, New Mexico

Heather D. Pfeiffer and Jim Furlong
Science Applications International Corporation, Joppa, Maryland and McLean, Virginia

ABSTRACT

Weather and environmental effects on dismounted soldiers can substantially impair mission performance and, in the extreme, may result in severe or life threatening thermal injuries. An automated real-time capability to assess these soldier system risks in the temporal and spatial domain of dismounted infantry battlespace scenarios is synergistic with larger efforts to improve the overall effectiveness of dismounted warfighters. We have completed initial integration of a suite of human thermal strain prediction models with automated real-time weather and terrain information resources. Current models predict scenario-dependent exposure limits in hot or cold environments and during cold water immersion. In June 1996 a test bed system was installed at the U.S. Army Ranger training facilities at Camp Rudder, Eglin Air Force Base, Florida. The MERCURY-Ranger Test Bed system uses the existing network resources and automated weather data acquisition infrastructure at Eglin to obtain required predictive model inputs such as air temperature, humidity, wind speed, solar radiation and, for the cold immersion model, water temperature and depth. Using standard Internet connections between MERCURY and Eglin's Range Automated Weather Stations (RAWS) base station computer, weather data from seven to ten RAWS stations are automatically ingested at hourly intervals. These geo-located weather data sets are then interpolated in the context of Digital Topographic Elevation Data (DTED) to provide gridded weather information at 1 km spatial resolution across a 100 by 100 kilometer Eglin area window. Individual weather parameters or predictive model outputs are then displayed over a DTED greyscale image as simple color-coded overlay products. The test bed is used to validate methods needed to extend this capability to operational settings.

1. INTRODUCTION

1.1 Dismounted Infantry Battlespace. One of the most austere and demanding military environments is that experienced by the dismounted infantry soldier during sustained or continuous combat operations. The soldier, and the equipment he carries to establish a tactical advantage in survivability and lethality, must function in a temporally and spatially dynamic natural environment. Local weather conditions and the physiological demands of movement over terrain, load carriage, and chemical protective clothing can interact to produce a significant impact on both the health and performance of the soldier system (Matthew and Santee, 1991). Although considerable meteorological resources are focused on aviation operations and atmospheric conditions above tree top level, it is the very lowest part of the atmosphere that affects humans on the ground. The vertical dimension for the volume space in which the dismounted soldier operates is the lowest two meters of the atmosphere, down to and including the surface terrain. In field training or operational settings, the horizontal dimensions are typically on the order of tens of kilometers across the terrain. The potential for physiologically significant spatial and temporal differences in environmental parameters within this "human-scale" battlespace is substantial (Santee et al., 1994). In spite of the inherent complexity of lower boundary layer meteorology, a growing recognition of the tremendous influence of surface level atmospheric effects on battlefield systems has driven requirements for improved tactical weather information resources. Current efforts to exploit, validate, and integrate those technologies needed to develop near real-time soldier system oriented decision aids are necessary and synergistic with the wider Army thrust to manage battlefield weather effects on the total warfighting system.

1.2 Assessing Thermal Injury Risks. The ability to identify and quantify thermal injury risk to warfighters in real-time training or operational settings, without direct physiological measurements, is an important baseline capability for command and control . Thermal strain prediction models, mathematical representations of what we know about human responses to the environment, provide a way to integrate human and mission-related factors with weather data to estimate soldier-system effects. The practical application of these models is critically dependent upon the availability of weather data across the domain. Evolving battlefield computer and communications resources provide the essential infrastructure needed to automatically ingest weather information and could run appropriate soldier system-oriented predictive models.

1.3 The MERCURY System. Originally developed by the Army Research Laboratory's Battlefield Environment Directorate as an integrated software system for acquiring, analyzing, and extrapolating meteorological data in real time, MERCURY provides an automated capability to spread data from a limited number of weather stations across a region roughly 100 by 100 km at up to 1 km spatial resolution (Fields et al., 1992). The resulting gridded weather data, as well as informational products derived from that data, can be visualized in MERCURY as digital terrain overlay images. A logical extension of these capabilities is real time overlay products focused on thermal injury risk assessments for dismounted infantry scenarios. The fusion of MERCURY's intermediate process weather products with physiological models provides the spatial and temporal context relevant to warfighters in the dismounted infantry battlespace. In

1993 we began an effort to develop software interfaces that would enable thermal strain prediction models to exploit MERCURY's gridded weather data as input fields in a highly automated, real time computing and display environment. The USARIEM Heat Strain Model (Pandolf et al., 1986; Gonzalez and Stroschein, 1991) was the first thermal strain prediction model to be integrated with MERCURY. Science Applications International Corporation (SAIC) completed the initial Prototype MERCURY/Heat Strain software in February 1994 (McNally et al., 1994; Matthew et al., 1994). In October 1994 we obtained approval to incorporate a Cold Survival Time model developed by the Defence and Civil Institute of Environmental Medicine (DCIEM), Ontario, Canada (Tikuisis and Frim, 1994; Tikuisis, 1995).

1.4 The MERCURY-Ranger Test Bed. In February 1995, four hypothermia deaths occurred among U.S. Army Ranger students during swamp training exercises along the Yellow River, Eglin Air Force Base, Florida. This incident sparked a critical reevaluation of current procedures and resources for thermal injury risk assessment in general and hypothermia in particular. Following a briefing of MERCURY's current and planned capabilities to the Ranger leadership in May 1995, it was determined that the installation of a test bed MERCURY system at Camp Rudder would benefit the Ranger training operations there (McWilliams, 1996). Initial installation was completed in June 1996 and DCIEM's prototype cold immersion model was added in October 1996.

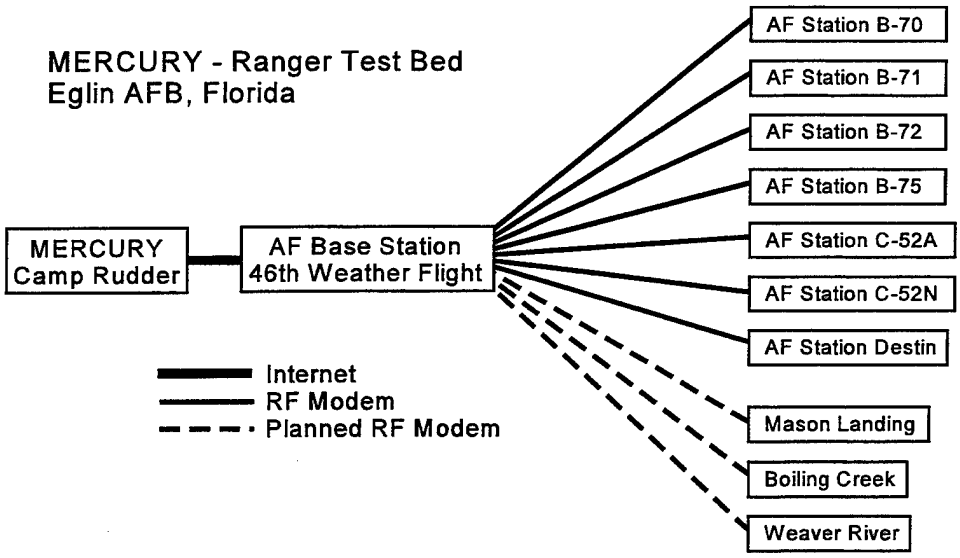
2. OBJECTIVES AND SCOPE

Our primary objective is to briefly describe the MERCURY- Ranger Test Bed system currently located at Camp James E. Rudder, Eglin AFB, Florida. Scope is limited to functional descriptions of the local infrastructure support that enables the continuous weather data input stream to MERCURY, the suite of physiologically based thermal strain prediction models that have now been linked within it, and the user level input and output display facilities. The origin and development of MERCURY's weather spreading algorithms/heuristics as well as estimates of their performance accuracy have been described previously (Fields et al., 1992) and will not be addressed in this paper.

3. SYSTEM DESCRIPTION

3.1 Overview. The Ranger Test Bed consists of three essential components: The fixed site weather stations deployed across Eglin, the communications systems that connect the stations with MERCURY , and finally, the Unix computer running MERCURY that controls the data flow, accepts the user input, processes the data and displays the output product. An overall schematic of the current system is shown at Figure 1.

Figure 1. Schematic overview.



It should be noted that the link between the Air Force central weather station computer at Eglin and MERCURY at Camp Rudder is an Internet link using standard Transmission Control Protocol/Internet Protocol (TCP/IP). This means that MERCURY running remotely (from any physical location) and in real time, could evaluate data for any region in the world that has Internet accessible hourly local weather station data.

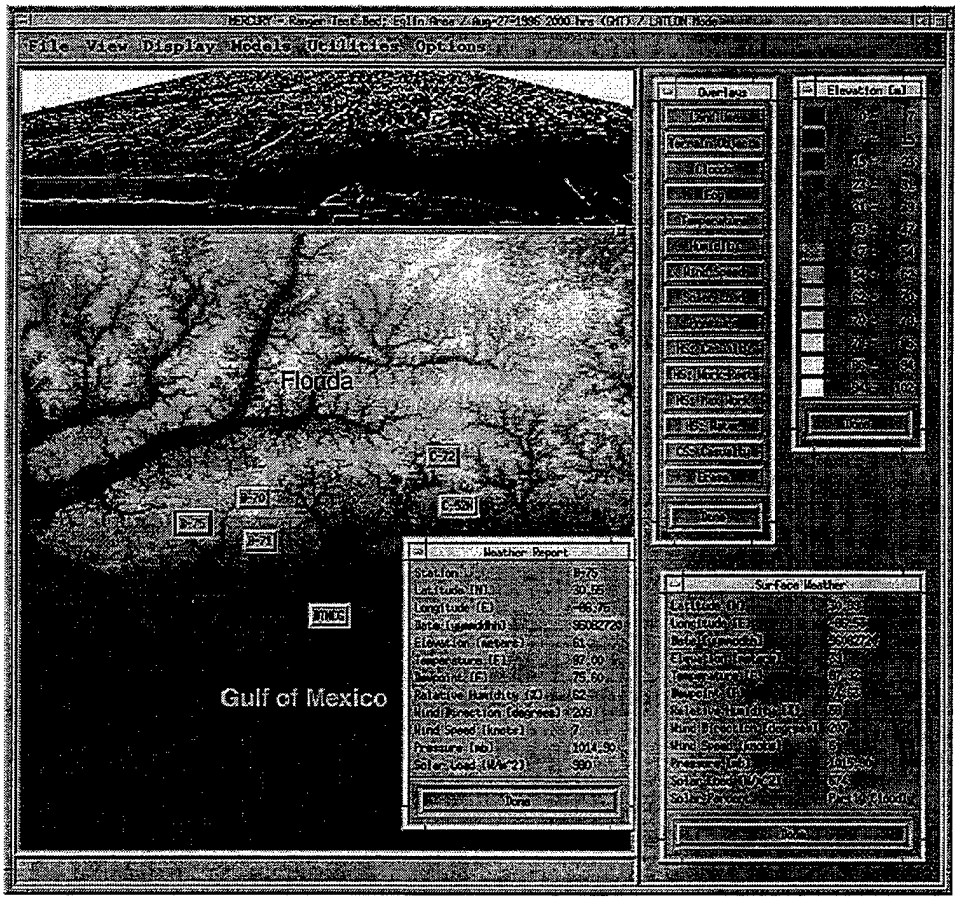
3.2 Weather Stations. Seven automated weather stations located across the Eglin area are controlled and maintained by the U. S. Air Force. This system, known as the Range Automated Weather Stations (RAWS) is critical supporting infrastructure for the MERCURY implementation at Camp Rudder. The weather stations automatically measure and record air temperature, humidity, wind speed, wind direction, solar radiation, barometric pressure, rainfall and other parameters that relate to forest fire hazards. Three additional weather stations, purchased by the Rangers and located along the Weaver and Yellow Rivers, measure water temperature and depth as well as the standard RAWS parameters.

3.3 Weather Data Communications Links to MERCURY. At hourly intervals, date and time stamped weather data, along with each station's identification code, are transmitted by radio frequency modem to a central computer, the RAWS base station, located at the U.S. Air Force 46th Weather Flight offices at Eglin. In early 1997 the three stations along the Yellow and Weaver rivers, currently accessible by cell phone modem only, will be connected to the RAWS base station by radio frequency modem. Because the weather data files on this computer are accessible using TCP/IP and the network File Transfer Protocol (FTP), national infrastructure communications resources can be exploited to complete the link between the weather station sensor readings and MERCURY.

3.4 The MERCURY Computer System. The MERCURY computer at Camp Rudder runs under a Unix operating system. A Sun SPARCstation 5, running Sun Solaris 2.4, provides all needed Internet facilities and the Openwindows windowing environment. MERCURY currently needs a minimum of 48 MBytes RAM and 150 MBytes of free disk space to run. The test bed computer has 96 MBytes of RAM, 4 GBytes of total disk space, a 20 inch color monitor and is linked to the Eglin computer network via ethernet. Every hour the computer automatically connects to the RAWS base station, downloads the latest weather data files via FTP, and, using a specialized parsing procedure, converts the weather data files to the MERCURY format. A Hewlett Packard Color LaserJet printer provides hard copy prints of user selected output images.

3.5 Terrain Data and Field of View. The test bed field of view at Eglin is 1 arc degree of latitude and longitude: from 30° to 31° North Latitude and from 86° to 87° West Longitude. Using those coordinates, Defense Mapping Agency's Level 1 Digital Topographic Elevation Data (DTED) data were extracted from our CDROM library and referenced to the Clark 1866 spheroid to allow geolocation in either latitude/longitude or Universal Transverse Mercator (UTM) coordinate space. The DTED file, in greyscale representation, provides the background image for the overlay products on the MERCURY screen. This region encompasses key sections of the Yellow and Weaver Rivers, where Ranger training is conducted, as well as most of Choctawhatchee Bay and a section of the Gulf coast, East and West of Fort Walton Beach, Florida. A black and white image of a MERCURY display screen is shown at Figure 2.

Figure 2. Black and white image of MERCURY display screen.



3.6 Thermal Strain Models. The thermal strain prediction models currently integrated with MERCURY consist of a heat strain model, a cold survival time model, and a prototype partial immersion hypothermia model. It should be noted that the cold survival time model software module, though not relevant to risk management at Camp Rudder, resides as a potential application for search and rescue operations in other locations.

3.7 Weather Data for the Models. Each of the reporting weather stations is represented by an icon on the MERCURY display window. Data from individual stations may be reviewed by point and click using the computer mouse. The hourly MERCURY-processed weather data used for input to the test bed heat strain and cold survival time model implementations have a spatial resolution of approximately 2.5 kilometers. The Eglin field of view thus represents a 40 by 40 array of 1600 cells, each cell in effect containing an air temperature, humidity, wind speed, and solar radiation value for input to the selected model. The data sets for the partial immersion model consist exclusively of water and ambient atmosphere parameters actually measured by the three stations along the river. The immersion model input and output thus reflects conditions at the three station locations along the river, a "discrete point" rather than "area" representation.

3.8 User Input Requirements. The test bed thermal models share certain common requirements, the most important of which, from a user perspective, is the need for information about the average warfighter being modeled. Although the weather data input stream is automated, the thermal strain models that run within MERCURY require user input of soldier characteristics, clothing type, and the level of physical effort required by the military mission. These inputs, crucial to any realistic determination of risk level by the models, are selected by an intuitive "point and click" graphical interface using the system mouse. Until field validation and sensitivity studies are completed it is not possible to make rational decisions on appropriate default values to streamline the user input process. It is expected that the test bed itself will be a prime resource in those studies.

3.8.1 Heat Strain Inputs. The heat strain model currently requires user input/selection of body height and weight, hydration status (5 categories), acclimatization (days of prior heat exposure), estimated work load (4 categories), and clothing type (5 categories).

3.8.2 Cold Survival Time Inputs. The cold survival time model requires user input/selection of body height and weight, percent body fat, and clothing insulation. This model assumes minimal physical activity.

3.8.3 Cold Water Partial Immersion Inputs. The partial immersion model currently requires user input/selection of body height and weight, percent body fat, age, clothing insulation, non-immersed clothing wetness, walking speed, load carried, and terrain type (4 categories).

3.9 Output from the Models. The common thermal strain model output format in the MERCURY environment is based on a classification of predicted results into three color coded categories: green for low risk, amber for moderate risk, and red for high risk. For the heat strain and cold survival time models, the spatial resolution of the color coded terrain overlay image is currently about 2.5 kilometers, and each output parameter image represents model results from

1600 individual weather data cells within the MERCURY field of view. The output from the cold water partial immersion model is a point estimate for each river station location.

3.9.1 Heat Strain Output. The heat strain model outputs consist of user selectable color coded overlays for casualty risk, optimal work/rest cycle limits, maximum safe work time, and hourly drinking water needs.

3.9.2 Cold Survival Time Output. The cold survival time model output consists of a color coded overlay of time in hours until a body temperature of 30 °C would be reached.

3.9.3 Cold Water Partial Immersion Output. The partial immersion model output is based on the time required to reach a body core temperature of 35.5 °C and the user specified estimate of mission duration. If the time to 35.5 °C is substantially longer than the mission time, the station icon is shown in green. If the time to 35.5 °C is less than the expected mission duration, the station icon is shown in red. Marginal times are shown in amber. By clicking the mouse on the station icon, a text panel showing the predicted values may be viewed.

4. FUTURE EFFORTS

4.1 Validation Studies. Field research studies using soldier volunteers in tactically realistic settings are a critical part of the forward evolution of the MERCURY's thermal stress modeling capabilities. USARIEM will conduct human use approved protocols with Ranger volunteers in 1997 to build the physiological database needed to improve and validate test bed model implementations, and ultimately transition their functionality to operational users.

4.2 Additional Site Implementations. The establishment of additional real-time test beds in other locations will provide an important opportunity to test and evaluate the predicted physiological responses of dismounted soldiers in a variety of terrain types and mission scenarios. USARIEM and ARL will assist the Dismounted Infantry Battlespace Battle Lab with a MERCURY installation at Fort Benning, Georgia in 1997.

4.3 Real Time Physiological Monitoring. The test bed's network and computing resources could also be exploited in real time to process physiological sensor data and display individual warfighter status. In future command and control instantiations, fusion of real time physiological data with predictive models would allow automated input and initialization of individual soldier modeling runs to identify soldiers at risk, well in advance of actual injury.

4.4 Weather Forecast. MERCURY currently relies on hourly weather data to provide products which are essentially a "nowcast." The integration of a high resolution mesoscale weather forecast model with MERCURY's thermal strain models would allow site-specific thermal injury risk predictions out to 24 hours. The Battlescale Forecast Model (BFM), currently under development by ARL's Battlefield Environment Directorate, is an ideal mesoscale model to provide the required gridded weather data.

5. CONCLUSION

The MERCURY-Ranger Test Bed represents an essential first step in defining the technical requirements for operational systems that could provide highly automated, spatially and temporally accurate representations of thermal injury risks in the dismounted infantry battlespace.

REFERENCES

Pandolf, K.B., L.A. Stroschein, L.L. Drolet, R.R. Gonzalez, and M.N. Sawka, 1986: Prediction modeling of physiological responses and human performance in the heat. *Computers in Biology and Medicine*, **16**, 319-329.

Gonzalez, R.R. and L.A. Stroschein, 1991: Predicting the soldier's heat transfer and work capabilities in MOPP. In Proceedings of the 23rd Annual Military Testing Conference, San Antonio, Texas.

Fields, C.A., J.E. Newberry, H.D. Pfeiffer, C.A. Soderlund, S.F. Kirby, and G.B. McWilliams, 1992: MERCURY: A heterogeneous system for spatial extrapolation of mesoscale meteorological data. *International Journal of Man-Machine Studies*, **36**, 309-326.

Matthew, W.T., R.E. McNally, G.B. McWilliams, S.F. Kirby, and H.D. Pfeiffer, 1994: Integration of a heat strain prediction model with Army weather data resources. In Proceedings of the 1993 Battlefield Atmospherics Conference, White Sands Missile Range, New Mexico, 479-485.

Matthew, W.T. and W.R. Santee, 1991: Potential heat casualty risk assessment in Southwest Asia: Weather data requirements in the spatial domain. In Proceedings of the Eleventh Annual EOSAEL/TWI Conference, Las Cruces, New Mexico, 315-324.

McWilliams, G. B., 1992: Integrating Battlefield weather and terrain data for IPB through automated techniques. In Proceedings of the 1991 Battlefield Atmospherics Conference, Fort Bliss, Texas, 405-410.

McWilliams, G., 1996: Real-time thermal risk assessment for the dismounted soldier. U.S. Army Research Laboratory, Report No. ARL-TR-1022, White Sands Missile Range, New Mexico.

Santee, W.R., W.T. Matthew, and L.A. Blanchard, 1994: Effects of meteorological parameters on adequate evaluation of the thermal environment. *Journal of Thermal Biology* **19**, 187-198.

Tikuisis, P. and J. Frim, 1994: Prediction of survival time in cold air. Defence and Civil Institute of Environmental Medicine, Report No. DCIEM 94-29, North York, Ontario, Canada.

Tikuisis, P., 1995: Predicting survival time for cold exposure. *International Journal of Biometeorology* **39**, 94-102.

The CREATION Scene-Generation Program Applied to Battlespace Flight Scenarios

Joseph A. Penn, Hung M. Nguyen, Charles R. Kohler, and Marcos C. Sola
U. S. Army Research Laboratory, Synthetic Imagery Branch
Adelphi, MD 20783-1197
Phone: (301) 394-0803, FAX: (703) 394-1245
e-mail: ckohler@arl.mil

Abstract

The CREATION (Computer generation of Realistic Environments with Atmosphere for Thermal Imagery with Optics and Noise) scene-simulation program produces high-quality, realistic, 3-dimensional battlefield environments suitable for simulating battlefield flight scenarios. CREATION simulates detailed scene geometries based on actual geographical locations using Defense Mapping Agency (DMA) Digital Terrain Elevation Data (DTED) with dynamic targets and sensor platforms controlled in all six degrees of freedom. Target signatures and background component temperature are predicted by existing thermal prediction models using actual meteorological and environmental input data. The weather data may also be used to simulate LOWTRAN-equivalent atmospheric transmission and accurate battlefield obscurant effects. The CREATION program suite includes a feature editor to digitally map scene components. The CREATION scene simulator also includes a state-of-the-art vegetation-rendering program with a library of tree files applicable to a variety of geographical areas. Other CREATION scene-rendering methodologies discussed include efficient ground-texturing techniques and the vegetation model.

Introduction

The objective of the CREATION scene-generation program is to simulate realistic, multispectral, three-dimensional scenes (e.g., IR, visible) of a wide variety of geographical locations and environmental conditions. This capability will reduce the US Army's dependence on actual field data-collection activities by providing a verified/validated synthetic scene-generation methodology that can be used to supplement real data for many applications. Some of these applications include the development, testing, and evaluation of automatic target recognizer (ATR) algorithms, image-clutter metrics research, signature phenomenology research, mission planning, training, human perception study, and multispectral-sensor modeling.

General Design of CREATION

The CREATION simulation model consists of several programs developed in-house that integrate/ interface various target geometry, terrain data, and thermal-prediction model outputs into an extremely powerful research tool. The internally developed software includes the Feature Editor, the CREATION scene generator program (graphics user interface, vegetation model, surface-texturing process, and atmospheric and sensor-simulation models). The relationship of CREATION to other models is shown in figure 1.

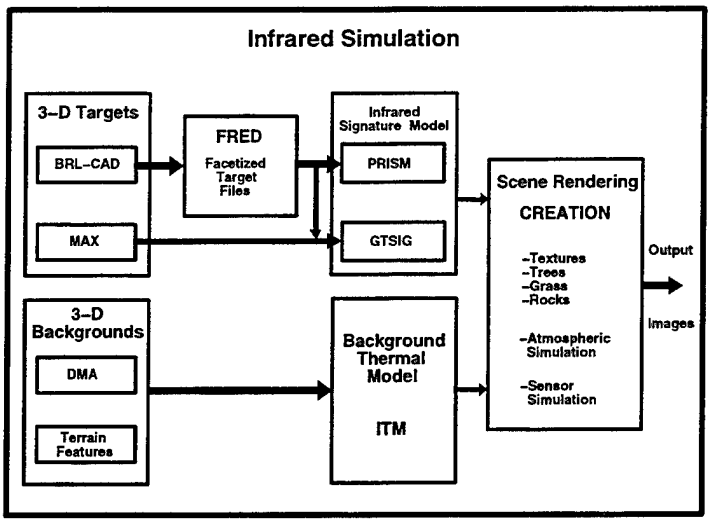


Figure 1. Overview of CREATION scene generation process.

External Models/Input Databases

Generally, CREATION requires existing, externally generated data files to create simulations of specific locations and scenarios. The following data are produced by other programs and processes.

(1) Digital terrain elevation data (DTED) is the standard, digitally formatted DMA-surveyed data that consists of an array of elevation samples at either 100-meter or 30-meter intervals.

(2) Target geometry files are either (a) Ballistic Research Laboratory computer assisted design (BRL-CAD) combinatorial solid geometry (CSG) files that are converted to faceted geometry via the Faceted Region EDitor (FRED) from the Tank Automotive Command Research, Development, and Engineering Center (TARDEC), or (b) MAXCAD-faceted geometry from the Georgia Technological Research Institute (GTRI).

(3) Target-thermal prediction output files are generated using either (a) the Physically Reasonable Infrared Signature Model (PRISM) via FRED, or (b) GTSIG with MAXCAD target geometric input data files. The thermal-prediction files must be generated consistent with the desired scenario (i.e., the physical location, target operating state (e.g., velocity, orientation), and meteorological conditions) to realistically simulate the temperature profile.

(4) Background thermal-prediction output files are created using the Interim Thermal Model (ITM) from the Smart Weapons Operability Enhancement (SWOE) program/Waterways Experiment Station (WES). This model uses meteorological data to predict the temperature profiles of vegetation, roads, and soil surfaces

Internally Generated Data

The location and type of the sensor, types of vegetation present, locations of roads, bodies of water,and the like must be specified to simulate realistic scenarios. The following files are alternatively generated or edited in the CREATION program, or in CREATION's Feature EDitor (FED):

(1) Feature maps are rasterized representations of the data necessary to define the scene content with respect to vegetation, soil, rocks, roads, and bodies of water in the final DMA DTED-mapped area.

(2) Color-spectral files are required for image synthesis. The inputs describe color and lighting model parameters (e.g. ambient light, diffuse light, specular light, and highlighting) for the principal background and target components, exclusive of the trees. The emissivities and reflectivities in the 3-5 and 8-12 μ bands are also defined.

(3) Object-attribute files describe munitions, targets, and nonsolar light sources. These files specify the following: (a) target geometry, (b) target thermal prediction, (c) target camouflage pattern, and (d) target position(s). The target-position file specifies the target's orientation with respect to each of its six degrees of freedom in time. The positions/orientations of munitions and up to seven independent, nonsolar light sources are similarly specified. The munitions are defined according to the COMBIC obscurant model types. The RGB specifications of each munition's smoke and the independent-light- source colors are defined in the object-attribute files, along with general lighting characteristics for movable point sources and spotlights.

(4) Target-camouflage patterns may either be selected predefined visible camouflage patterns or user-created patterns.

(5) The camera sensor-position file is analogous to the position file for the target. The sensor's position, orientation, and its field of view determine what will be seen at any instant.

(6) Input into the atmospheric-transmission parameter file controls atmospheric transmission effects through specification of properties such as humidity, rate of precipitation, reference altitude, and wavelength limits. These internal, atmospheric-transmission model inputs can be either empirical or modeled, using a variety of other atmospheric-transmission models (e.g., LOWTRAN, MODTRAN, or HITRAN).

(7) Sensor-simulation data files consist of several pre-existing sensor files; if they don't contain the pre-existing files, the user may create new sensor-simulation data files by following the recommendations and specifications described in the user's manual. [1]

CREATION Models and Processes

Tree Geometry Model

For realistic high-resolution rendering of natural backgrounds, an accurate representation of vegetation geometry is needed, especially for trees. An algorithmic method of generating tree geometries using a compact parametric description set is preferable to simulate many separate species, and variations of each species. The model should render realistic trees efficiently, so that a large number of individual trees can be included in the background scene. The CREATION tree model [2] meets these criteria by adopting a rule-based methodology that divides the branching levels into structural hierarchies from the main trunk to the smallest branches and leaves. Each level has its own set of specifications and subsequent variational limits to permit the variability of structures found in nature, and to allow the same software code to generate a wide variety of

different tree species geometries (see Figure 2). The parameter set is based on basic geometric observables, such as, trunk and branch lengths, cross-sectional ratios, and branching angles. The schematic diagram, Figure 3, shows the basic design concept.

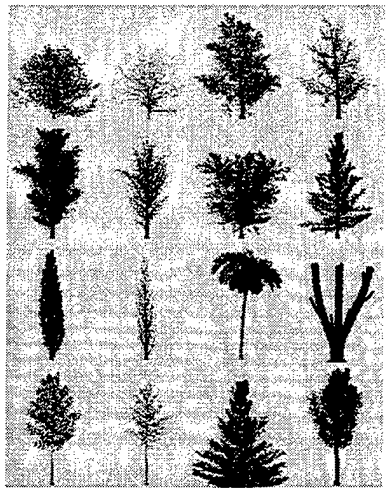


Figure 2. Sample of synthetic trees.

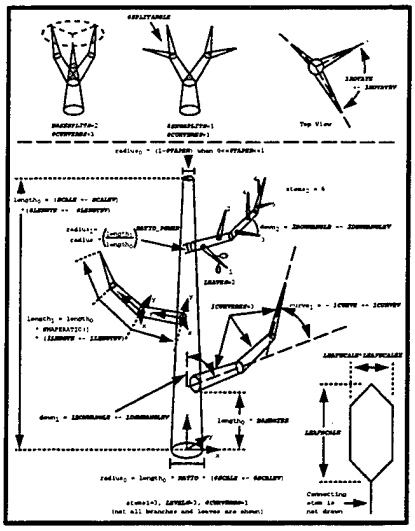


Figure 3. Schematic tree diagram.

Feature Editor

The tree model uses a range-degradation methodology that reinterprets the geometrical description of the tree to substitute fewer lines and points for polygons as range increases and the need for high-resolution rendering is relaxed. This process is performed gradually, so that it is seamless and virtually undetectable, while greatly decreasing the drawing time per tree at longer ranges. This feature is, of course, extremely important for rendering massed trees in a forest for an animation consisting of thousands of frames.

An important part of the CREATION scene-generation package is the feature editor, FED. It enables modelers to create and edit rasterized maps used as input by the rendering software. FED is essentially a specialized multilayer drawing program, with a user-friendly interface to aid the bit-wise manipulation of the resolution-cell data. For instance, the bit-pattern toggle buttons for the vegetation feature map activate 1 of 3 possible kinds of grass and as many as 14 tree types, simultaneously. The road, water, and soil feature maps are similarly specified. This feature-mapping capability permits high-resolution, controlled rendering of realistically cluttered generic or actual natural backgrounds.

The feature editor can overlay multiple digital maps as semitransparencies with perfect coregistration of the rasterized data. It also permits the use of top-down aerial photographs or satellite imagery as templates to create accurate cultural-feature maps (e.g., roads, bodies of water, vegetation) that can closely approximate actual locations, when the necessary supporting data (e.g., road maps, vegetation present, soil properties) are available.

Ground-Surface Texturing

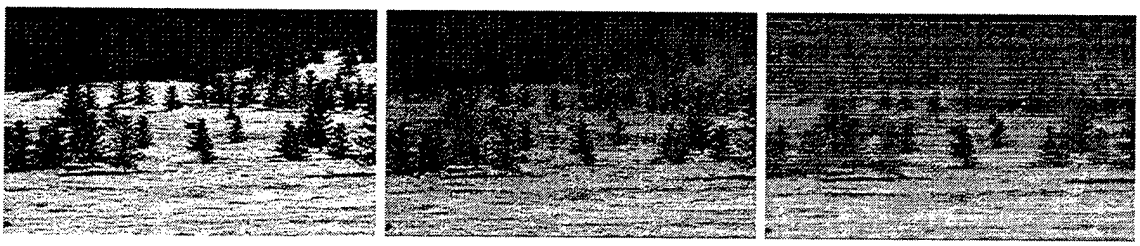
The CREATION texture-mapping process produces surface-conforming coarse, fine, and very fine textural effects. These effects include vegetation shadows, road surfaces, soil maps, simplified water waves, and topographically specific gullying. Vegetative ground cover variations are applied to the surface texture map, according to vegetation feature-map location and defined or modeled characteristics (e.g., the general color or temperature of each grass type). Individual grass blades are drawn when image resolution and fidelity require that application.

Texture mapping proceeds in four basic stages: (1) ground-surface texture differences, (2) erosive effects (gullying) that are dependent on the local-terrain-surface gradient, (3) tree shadows drawn according to solar inclination and azimuth angles, and (4) vegetative ground texturing to modulate assigned grass colors or temperatures, and to characterize the grass surfaces at ranges where resolution is so good that it diminishes the necessity to render individual grass blades.

Ground-surface texturing is, itself, a multistage investigative technique, consisting of: (1) finding gross surface texture over the entire area, (2) applying fine texture with 16 times the resolution of the gross surface texture map, and (3) applying very fine texture covering the same area as the fine texture, but adding bounded Gaussian random noise to diminish the pattern repetition that would otherwise be obvious over larger areas. The patterns of gross and fine texture are generated using a growth-rule algorithm that is conceptually similar to the propagation of bacterial colonies in a culture medium.

Atmospheric Transmission and Battlespace Obscurants

The CREATION simulation package has a computationally efficient, simplified LOWTRAN-equivalent atmospheric transmission model for the visible and infrared spectral bands that applies attenuation and scattering effects, with input parameters that correspond to empirical meteorological data [3]. The atmospheric model also predicts altitude-dependent background sky-radiance effects. Other models (e.g., LOWTRAN, MODTRAN, HITRAN) can use the image and range-buffer output for post-processing atmospheric effects. Figure 4 shows (a) an input image, with (b) a foggy atmosphere applied, followed by (c) the application of sensor effects to the image.



(a) (b) (c)

Figure 4. Input image (a), with atmosphere applied (b), and with sensor applied (c).

The CREATION model also has a menu interface to define, locate, and set detonation or ignition times of munitions or fires; set wind velocities; and then process visible battlespace obscurants using the COMBICV model.

Sensor, Optics, and Noise Modeling

CREATION scene-generation software is a powerful sensor simulation model that uses a super-set of the FLIR92 sensor parameters and specifications to emulate the performance of a large variety of existing and proto-typical thermal and visible sensor systems [1] [4]. The model simulates optical blurring effects, including depth-of-field or focus, that vary according to aperture size, range-to-pixel, and position on the image plane, in addition to other optical aberrations. Sensor-sampling effects are modeled when processing high-resolution images (i.e., more than one pixel-per-detector instantaneous-field-of-view (IFOV)). Noise, particularly Gaussian-shot noise, various detector nonuniformities and nonlinearities, and sensor- scanning and -sampling artifacts, are added in thermal sensor simulations. This model can easily emulate the effects seen (especially) in older first-generation forward-looking infrared (FLIR) systems, as well as those seen in more advanced systems. Of course, other sensor models can be used to post-process stored output imagery.

Conclusion

The integrated and coordinated scenarios that are simulated with CREATION can be useful for a wide range of applications relevant to battlespace flight scenarios (either as attacker or defender), as well as surface warfare. Applying our simulation methodology, a defense modeler can model aerial attacks from fixed- or rotary-wing aircraft in various realistic weather conditions, using modeled visual- and thermal-sensor systems, and also produce geometric facet data for input into advanced radar models. The study of the effects of factors such as weather, sensors, and obscurants, on mission effectiveness can be made by relatively simple changes to the appropriate model inputs, without altering the majority of the files in the scenario database. Very accurate mission-specific simulations can be modeled when the supporting modeling tools or outputs are made available. If self-consistent input data are entered into the external-prediction models, accurate, high-fidelity, high-resolution output imagery and output geometrical representations will be generated by CREATION. These simulations have many applications, including training and mission planning, as well as scientific research, engineering development, and testing of ATR algorithms, human perception, multispectral sensor modeling, and others.

References

1. J. Weber, and J.A. Penn, *CREATION User's Manual (draft),* Version 1.27., U. S. Army Research Laboratory (ARL), S3ID/SMB, November, 1994.

2. J. Weber, and J.A. Penn, *Creation and Rendering of Realistic Trees,* SIGGRAPH 95 Computer Graphics Conference Proceedings, Annual Conference Series, 1995, pp.119-28. ACM SIGGRAPH August, 1995.

3. G.H. Kornfeld, *Theoretical and Experimental Justification for a Simplified LOWTRAN 6 Equivalent Model,* Proceedings of the Seventh EO-SAEL Meeting, December, 1986.

4. G.H. Kornfeld, *Various FLIR Sensor Effects Applied to Synthetic Thermal Imagery,* 1993

Proceedings of SPIE (Society of Photo-Optical Instrumentation Engineers), April, 1993.

Acknowledgments

The authors would like to thank Ms. Teresa Kipp for clarifying many of the technical concepts that are presented in this paper. It is also acknowledged that Dr. Mark Orletsky, Mr. Quochien B. Vuong, and Mr. Matthew Thielke contributed to the preparation and technical review of this paper.

Biographies of the Authors

Mr. Charles R. "Chuck" Kohler was born in New York City and received a Master of Science degree from Cornell University, Ithaca, New York in Engineering Physics and Mathematics. He was commissioned a 2ND Lieutenant, Infantry, in the US Army and spent about 3 years on active duty in Germany. He is "Airborne" and "Special Forces" Qualified, a Vietnam Era Veteran, and currently a member of the US Army Ready Reserves. He has over 38 years of federal service and was recently selected by the Department of the Army to be a Judge at the International Science and Engineering Fair. He has a keen interest in simulating science and engineering education among American youth. He has been an oustanding volunteer judge at many science fairs in the past. His current interest is in modeling, simulation, and synthetic imagery.

Mr. Hung M. Nguyen was born in Vientiane, Laos. He received his BSEE from the University of Bordeaux, France and his M.S. in Electronics and Computer Engineering from the George Mason University. He has been with the Night Vision and Electro-Optics Laboratory since 1989 and joined the U.S. Army Research Laboratory in 1992 where he works on thermal and radar signature modeling, FLIR sensor simulation, and computer scene simulation. He is currently the project leader of the Multispectral scene generation program. Mr. Nguyen has numerous publications in the area of Radar signature modeling and Infrared computer scene simulation.

Mr. Joseph A. Penn was born in Easton, Maryland on November 11, 1949. He graduated in May, 1984 with a Bachelors Degree in Physics and Chemistry from *Millersville University of Pennsylvania*, Millersville, PA. Prior to entering college, Mr. Penn worked for eight years as a landscape artist. He has been employed by the U.S. Army Research Laboratory (ARL) for three years and for the last twelve years has worked for the Army on various aspects of physical and geometric modeling in the thermal and visible spectral domains. Mr. Penn developed algorithms for vegetation geometry and surface texturing that are included in ARL's CREATION scene modeling software.

Mr. Marcos C. Sola is the technical leader of the Modeling Validation Group in the Synthetic Image Branch of the U.S. Army Research Laboratory in Adelphi, Maryland. His research interests include synthetic signal validation, modeling of target signatures and of atmospheric effects on multispectral electromagnetic wave propagation, and systems performance analysis. In addition to his current position, Mr. Sola's career has included work as Technology Associate for Signatures for the Sensors, Signatures, and Signal Processing Office, Project Leader for the Survivability and Management Office, the CM/CCM Office, and the Night Vision and Electro-optics Laboratory in Fort Belvoir Virginia. Mr. Sola holds B.S. and M.A. degrees in Physics from American University, has received numerous U.S. Army Achievement Awards, and publishes extensively.

LIDAR MEASUREMENTS OF METEOROLOGICAL PROPERTIES AND PROFILES OF RF REFRACTIVITY

C. Russell Philbrick and Daniel B. Lysak, Jr.
ARL Remote Sensing Department
Penn State University
State College PA 16804
(814) 863-7682

ABSTRACT

The refractivity of the lower atmosphere effects the propagation paths of radars, radio communications and navigational systems. Variations in RF propagation conditions are of concern in many civilian and military operational systems. The refractivity, thus local propagation conditions, can be fully described if the profiles of the molecular scatters, i.e. molecular density and particularly water vapor profiles, are known. The traditional techniques used to measure these atmospheric properties are based upon balloon sonde point sensor measurement of temperature and water vapor. Laser remote sensing techniques can now provide these measurements with high spatial and temporal resolution, under most conditions. Thus, lidar measurements can directly provide RF refractivity profiles. A semi-automated operational prototype instrument has been prepared, Lidar Atmospheric Profile Sensor (LAPS), which provides the meteorological properties and refractivity as real time data products. Examples of the measurement capability for atmospheric properties obtained with the new operational prototype (LAPS) instrument are presented which indicate the capability of Raman lidar techniques to provide the real time profiles of atmospheric properties and RF refraction. The LAPS lidar was tested onboard the USNS Sumner during September and October 1996 and successfully demonstrated that high quality meteorological profiles can be obtained from Raman lidar. Results from the real time measurements of the atmospheric profiles will be presented.

INTRODUCTION

The Lidar Atmospheric Profile Sensor (LAPS) was developed as a prototype for an operational instrument which can be deployed on aircraft carriers or other large ship and at shore facilities to meet atmospheric and meteorological data requirements. The LAPS instrument can provide profiles of the water vapor and temperature through the lower troposphere. These measurements provide the profiles of RF refractivity. The LAPS instrument uses vibrational Raman scatter to measure the water vapor profiles and rotational Raman scatter to measure the temperature. The daytime measurements of water vapor are obtained by using the "solar blind" portion of the ultraviolet spectrum. The ultraviolet measurements also provide the capability for measuring the tropospheric ozone profiles from a DIAL (DIfferential Absorption Lidar) measurement of the Raman shifted N_2 and O_2 signals. The fabrication of the LAPS instrument was completed in April 1996 and performance tests were conducted during the rest of the year. During September and October 1996, the LAPS instrument was deployed onboard the USNS Sumner for performance testing. The

instrument has successfully demonstrated capability to provide the meteorological profiles as real time data products. This report summarizes the significant results obtained during the shipboard tests and describes the instrument performance. Though not covered in this report, several significant scientific findings will be addressed in future scientific publications.

The objective of the LAPS Program was to develop a lidar profiler capable of providing real time measurements of atmospheric and meteorological properties, particularly those profiles which directly determine the RF refractivity in an operational environment.

BACKGROUND

The LAPS Program was begun in 1991 with the goal of using laser remote sensing techniques to provide an operational lidar sensor prototype instrument for at sea demonstration within 5 years. The instrument should be rugged, provide automated operation, and be field serviceable such that it can be operated by Navy personnel on Navy ships with a reasonable amount of training. Measurements of water vapor and temperature profiles provide RF refractivity profiles covering altitudes from the surface to 5 km with emphasis on the region up to 3 km. The instrument has been prepared to become a SMOOS sensor and provide data through an interface with the TESS(3) system. Future developments will include upgrades which add a capability to measure the wind velocity and describe the electro-optical environment. A most successful demonstration with sea tests of performance was completed in October 1996 on the USNS Sumner. The LAPS instrument was prepared as an operational prototype for use on aircraft carriers and at shore based sites. Many factors, such as measurement costs, personnel requirements, volume (for storing expendable instruments helium and preparation of the instrumented balloons), pollution from battery acid, radio signal give-away of ship location, and others, make it important to implement this new technology. The LAPS instrument can replace most of the requirements for rawinsonde balloons, particularly with the addition of the wind sensing capability which has been temporally delayed. Since the formulation of the original requirements for use on aircraft carriers and shore sites, the need to employ such an instrument on small surface combatants has arisen. The lessons learned in the development of the LAPS instrument also provide a basis for the preparation of an advanced compact diode pumped lidar which will be able to provide the data required for smaller surface ships and on aircraft, where instrument size and weight are more critical factors.

RAMAN MEASUREMENT TECHNIQUES

The vibrational Raman back scatter signals from the molecules of the water vapor and molecular nitrogen are at wavelengths widely separated from the exciting laser radiation and can be easily measured using modern filter technology and sensitive detectors [Ref 1-4]. The atmospheric temperature measurements have been made using the rotational Raman scattering of the molecular nitrogen and molecular oxygen, which together with the water vapor measurements permits determination of the RF-refractivity [Ref 5-9]. In order to push the lidar measurement capability into the daylight conditions, we have used the "solar blind" region of the spectrum between 270 and 300 nm [Ref 8,10]. Night time measurements are made using the 660nm/607nm (H_2O/N_2) signal

ratio from the doubled Nd:YAG laser radiation at 532 nm. Daylight measurements are obtained using the 294.6nm/283.6nm (H_2O/N_2) ratio from the quadruple Nd:YAG laser radiation at 266 nm. A small correction for the tropospheric ozone must be applied. That correction can be obtained from the ratio of the O_2/N_2 signals from 277.5nm/283.6nm, and the lower troposphere ozone profile is obtained.

RF-REFRACTIVITY

The molecular density effect on the refraction can be determined from the temperature profile and a surface pressure measurement. We have been able to demonstrate that the rotational Raman signal provides a useful temperature profile. The design and construction of the narrow band filters to eliminate the large back scatter signal from the nearby fundamental laser line presents the primary challenge. The ratios of the measured signals at 530nm/528nm from the doubled Nd:YAG at 532 nm have been used to provide a robust technique to obtain the temperature profile.

The RF-refractivity, N, represents the significant figures of the refractive index, n, and is based upon the following empirically derived relationship,

$$N = (n - 1) \times 10^6 \qquad (1)$$

$$= 77.6\, P/T + 3.73 \times 10^5\, e/T^2\,, \qquad (2)$$

where the water vapor partial pressure, e (mbar), is related to the specific humidity, r (gm/kg), by the relation,

$$e\ (mb) = (r\, P)/(r + 621.97). \qquad (3)$$

The errors associated with the measurement may be considered based upon analysis of the propagation of errors. The errors have the approximate values given by,

$$\Delta N = (\delta N/\delta r)\, \Delta r + (\delta N/\delta T)\, \Delta T + (\delta N/\delta P)\, \Delta P\,, \qquad (4)$$

$$\delta N/\delta r \sim 6.7 \qquad \delta N/\delta T \sim -1.35 \qquad \delta N/\delta P \sim 0.35$$

$$dN/dz = 6.7\, dr/dz - 1.35\, dT/dz + 0.35\, dP/dz\,. \qquad (5)$$

The values used in these relationships, which are typical of the lower atmosphere, show that the gradients in water vapor are most important in determining RF ducting conditions.

The Raman techniques, which use of ratios of the signals for measuring water vapor and temperature, remove essentially all of uncertainties, such as the need for knowledge of the absolute sensitivity and non-linear factors caused by aerosol and cloud scattering.

MEASUREMENT CAPABILITY

The LAPS lidar instrument has been developed from lessons learned in preparing and using prior research instruments. The LAPS unit was designed to include many automated features which make the instrument "user friendly" for operators who are not specialists in lasers or electro-optics.

The instrument was fabricated during FY95/96 and has been deployed onboard the USNS Sumner, a Navy survey ship, in the Gulf of Mexico and along the Atlantic coast of Florida during September-October 1996, to perform tests and validate its performance. It has performed well and provided excellent data products. The LAPS instrument was designed to provide the real-time data product of RF-refractive conditions with automated control of most operating features. More than twenty features have been designed into the instrument to control and simplify the instrument operation. It is intended that a weather officer could obtain the data on demand or acquire data according to some planned schedule. Advanced versions of the instrument are planned to include capability to measure the wind field, the electro-optical environment and other parameters [Ref 10-13]. The long term plan for the instrument is to replace most of the current balloon sonde profiling and thus enable data collection at more frequent intervals to support radar operations or weather affected missions.

The shipboard testing periods for the Lidar Atmospheric Profile Sensor (LAPS) instrument were intended to demonstrate its ability to measure the RF refractivity and demonstrate the capability for automated operation under a wide range of meteorological conditions. The instrument measures the water vapor profile based on the vibrational Raman scattering and the temperature profile based on the rotational Raman scattering, and these measurements provide real-time profiles of RF refractivity. The characteristics of the primary sub-systems of the LAPS instrument are listed in Table 1. Profiles are currently obtained at each minute, with a vertical resolution of 75 meters from the surface to 7 km. The vertical resolution will be improved to 15 meters, in the near future, using a new fast electronics package, which has recently been tested in our laboratory. The prototype instrument includes several sub-systems to automate the operation and provide the real-time profiles. Also, the instrument includes an X-band radar which detects aircraft as they approach the beam and automatically protects a 6 degree cone angle around the beam. The instrument also includes self calibration, performance testing and built-in-tests to check many functions.

Table 1. LAPS Lidar Characteristics

Transmitter	Continuum 9030 -- 30 Hz 5X Beam Expander	600 mj @ 532 nm 130 mj @ 266 nm
Receiver	61 cm Diameter Telescope	Fiber optic transfer
Detector	Seven PMT channels Photon Counting	528 and 530 nm -- Temperature 660 and 607 nm -- Water Vapor 294 and 285 nm -- Daytime Water Vapor 276 and 285 nm -- Raman/DIAL Ozone
Data System	DSP 100 MHZ	75 meter range bins (upgrade to 15 m)
Safety Radar	Marine R-70 X-Band	protects 6° cone angle around beam

In addition to the water vapor and temperature profiles, the true extinction and ozone profiles are also measured. By comparing the molecular profiles of the N_2 Raman and rotational Raman with the neutral atmosphere density gradient, the extinction profile can be obtained. The day time measurements of water vapor are determined using the solar blind ultraviolet wavelengths. The ratio

of the N_2 and O_2 vibrational Raman measurements on the slope of the Hartley band of ozone provide a DIAL measurement of the ozone profile in the lower atmosphere, surface up to 3 km.

The LAPS development has been directed toward the measurement of the refractivity of the atmosphere for determination of electromagnetic ducting conditions. The equations which are usually adopted for calculations of the refractive index are based upon temperature, pressure and water vapor partial pressure. Figure 1 shows an example of the comparison of the LAPS lidar water vapor profile (data points with $\pm 1\sigma$ statistical error of the photon count) with a rawinsonde balloon released at the same time period (solid line). The lidar measurement points represent individual measurements at 75 meter range bins integrated over 15 minutes, no smoothing of the lidar vertical profile has been applied. The gradual departure between the mean value of the two profiles at high altitude is attributed to the spatial homogeneity of the atmosphere as the balloon drifts away from the release site, often by several 10's of kilometers during the time while it rises to 5 km altitude. The profile in Figure 1 was obtained from the integration of 15 minutes of data collected at 23:20 EDT on 23 June 1996. The time sequence of the data is very useful in observing the changes in meteorological conditions. Figure 2 shows two examples of the temperature profiles determined from the LAPS lidar compared to the rawinsonde balloon corresponding results, the measurements were made at 21:34 EDT on 30 May 1996 and 23:27 on 20 July 1996. These measurements also show the $\pm 1\sigma$ error but there has been a three point smoothing filter applied at middle altitudes and a five point smooth applied at upper altitudes. Below 2 km, the statistical error is small, a fraction of a degree, but the errors grow rapidly at higher altitude. The temperature measurements are not optimized and approximately ten times improvement in signal is expected from two changes. The detector currently uses neutral density filters to maintain the signal in a liner operating region, which will be extended by a factor of five using the newer high speed electronics. The current limit is set by the saturation of the photon count rate due to the electronics limitations.

The LAPS program has been focused on preparation of an operational prototype for measurements of atmospheric RF refraction. The development has been very successful and provided an operational prototype instrument which can provide the real time profiles of the atmospheric and meteorological properties required for mission support on Navy ships. The prototype testing has included a successful demonstration on a Navy ship.

SHIPBOARD TESTING

The installation of the LAPS instrument on the USNS Sumner was accomplished on 30 August at Pascagoula MS. During the weekend, 31 August - 2 September, the instrument was tested and prepared for shipboard operation. Testing of the LAPS instrument was carried out during the period while the USNS Sumner carried out survey operations in the areas near the Florida Keys and near the Bahama Islands during the periods 3 - 21 September and 27 September - 15 October. Between 21 and 27 September, the USNS Sumner was in Port Everglades at Fort Lauderdale, FL, where tours were given for scientists attending the OCEANS 96 Conference.

During the period while the USNS Sumner was at sea, the LAPS lidar was used to gather data in 352 hourly subdirectories. Thus measurements were obtained during an average of 10 hours each day during the sea trials. Measurements were obtained during both day and night time conditions. On several occasions, the LAPS lidar instrument was run continuously for extended periods, including one period of 24 hours and one of 36 hours. Measurements were made in all

weather conditions and the instrument was available 99 % of the time. It was only down during one period of 10 hours for scheduled routine maintenance and alignment. The operations during cloudy periods where generally successful in providing sufficient data between clouds and through light clouds to provide useful profiles. Approximately 5 to 10 % of the time period (the detail survey has not been completed at this time), we experienced clouds with optical thickness such that limited operations provided profiles only below their base.

The LAPS lidar can be used to characterize the marine boundary layer. The results show unprecedented ability to characterize the variations that occur in the marine boundary layer which causes important effects upon Navy missions. The measured properties provide the capability to generate the real time profiles of RF refractivity, visibility and the meteorological profiles which are needed to forecast the weather conditions. Examples of the shipboard real time data display of the water vapor profiles and the temperature profiles measured are shown in Figures 3 - 6.

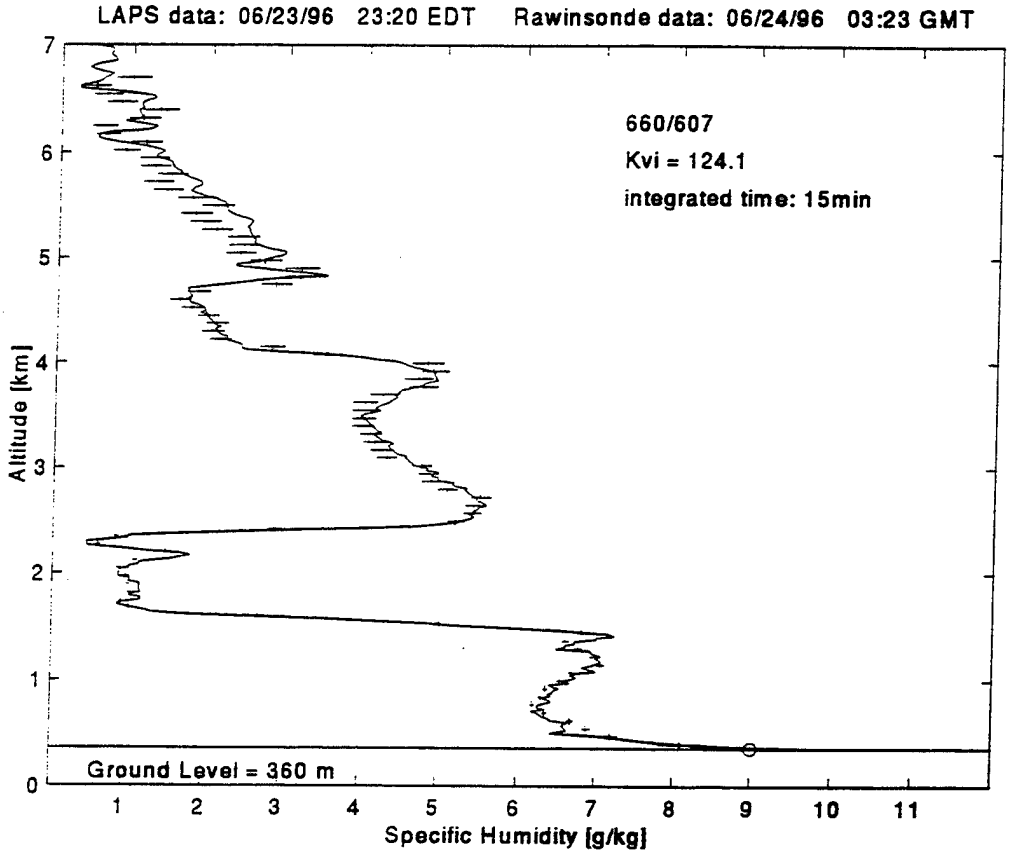


Figure 1. The profile of specific humidity measured by the LAPS instrument on 23 June 1996. The lidar measurement points at 75 meter spacing are shown with their $\pm 1\sigma$ statistical error (no smoothing between individual measurements). A rawinsonde profile from a balloon package released at the same time is shown as a line for comparison. The symbol $\oplus$ indicates the surface measurement made by a point sensor in the LAPS instrument.

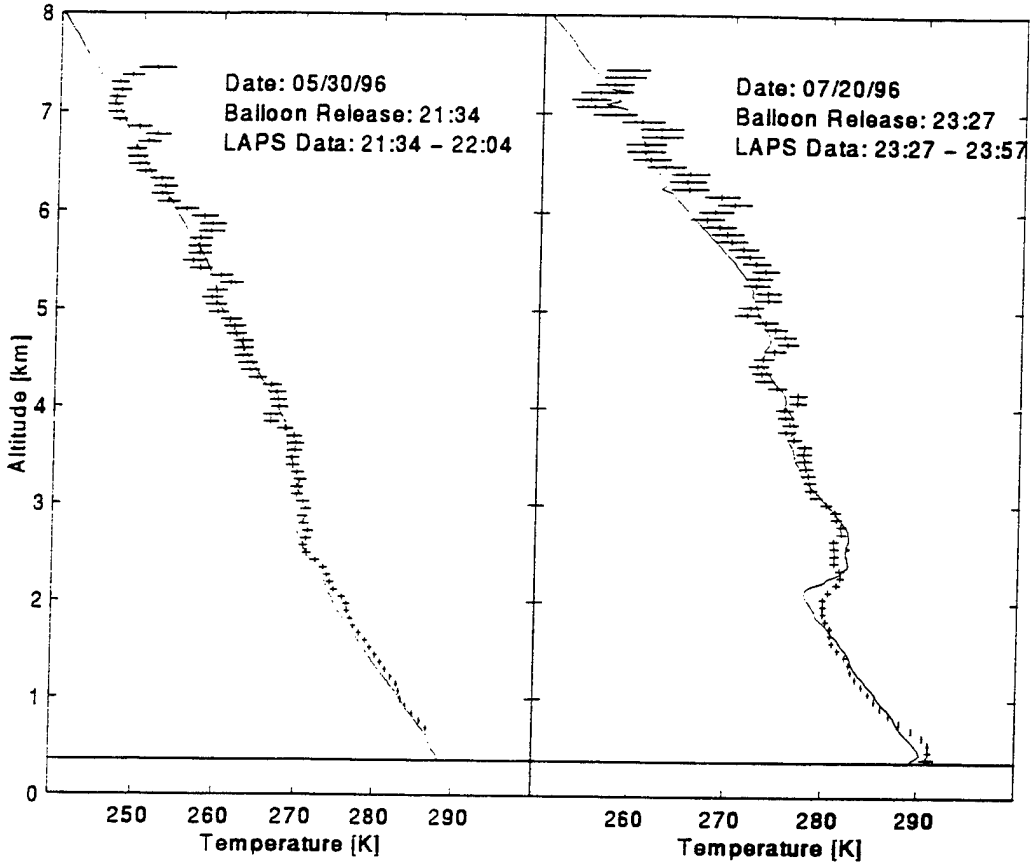


Figure 2. Temperature profiles are measured from the rotational Raman scatter signal from the LAPS lidar instrument. Examples of measurements obtained on 30 May 1996 at 21:34 EDT and 20 July 1996 at 23:27 are shown.

Figure 3 and 4 show the real time display for water vapor and temperature profiles at 0200 GMT on 17 September 1996 from the shipboard data records. These figures show the same graphical display that is available to the operator in Figures 3a and 4a. The $\pm 1\sigma$ statistical count error is shown for every second data point on the real time plots, so the significance of the variations can be observed. Figures 3b, 3c, 3d and 4b also show the post mission analysis which compares the lidar and balloon profiles. Figure 3e shows the grey scale representation of the operator's real time display of the water vapor time sequence. The time sequence display is convenient for detecting changes in the local meteorology that indicates the approach of a weather front or a change in the weather conditions. Figure 5 shows the one minute time sequence of the water vapor profiles as a false color display (the scale represents the specific humidity in gm/kg), this display is a grey scale

representation of the false color display in the real time display package. Figure 6 shows a display of the refractive conditions. In the lower panels of Figure 6, the temperature and water vapor components are shown that were used to calculate the RF refractivity, N (light line), and modified refractivity, M (dark line), in the upper panel of Figure 6. The modified refractivity shows the adjustment which accounts for the earth curvature and permits an easy interpretation of the location of RF refracting ducts.

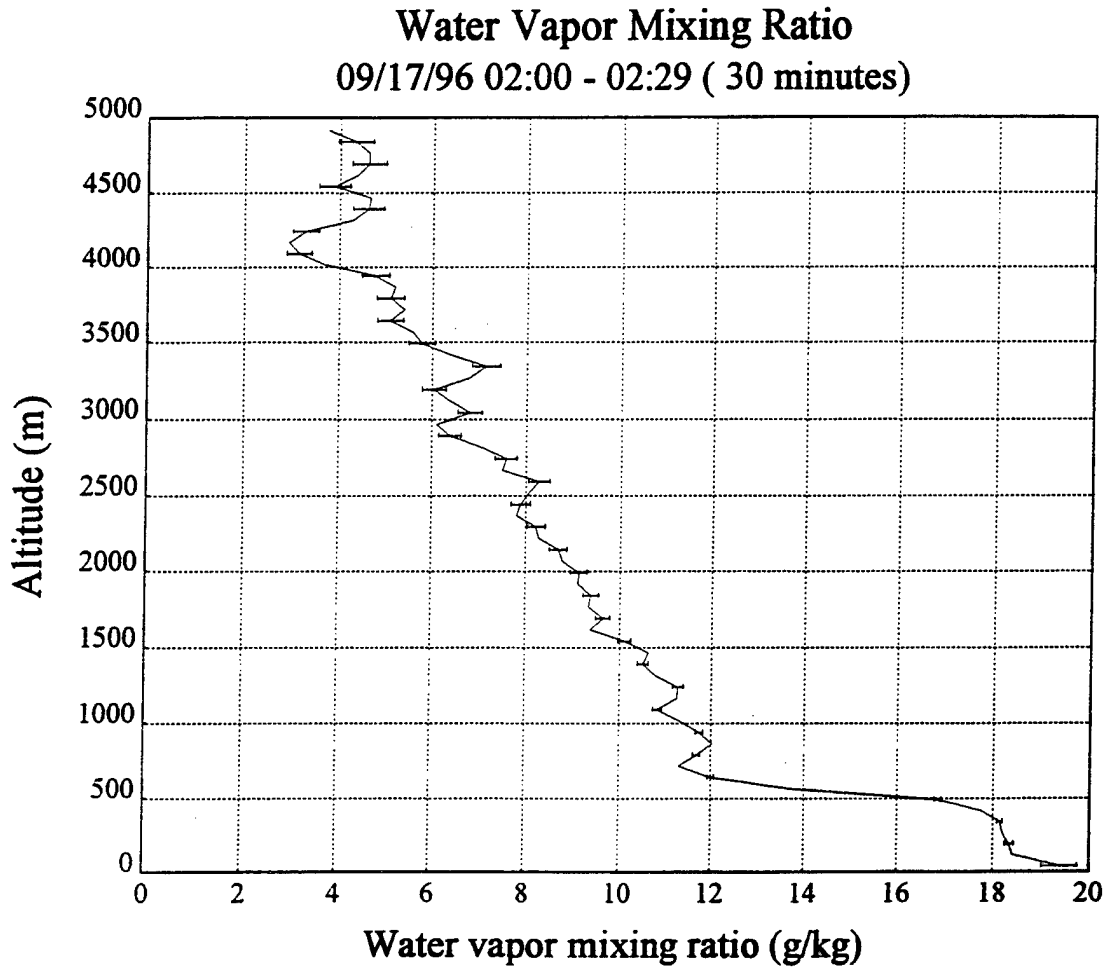


Figure 3 (a). The water vapor measurements as displayed by the real time display program of the LAPS instrument obtained on the USNS Sumner on 17 September 1996 at 0200-0230 Z. The profile includes the statistical error bars ($\pm 1\sigma$) on every other data point.

The LAPS instrument was operated and data obtained on every operation attempted or planned during the period of the sea trial. All of the indications and investigations of the data show that the instrument was fully successful in demonstrating the capability to obtain the meteorological data and RF refractivity conditions during day and night conditions and in all weather conditions. The LIDAR system offers the capability to obtain high quality RF ducting prediction data with real time data products and routine update without the use of radiosonde expendables.

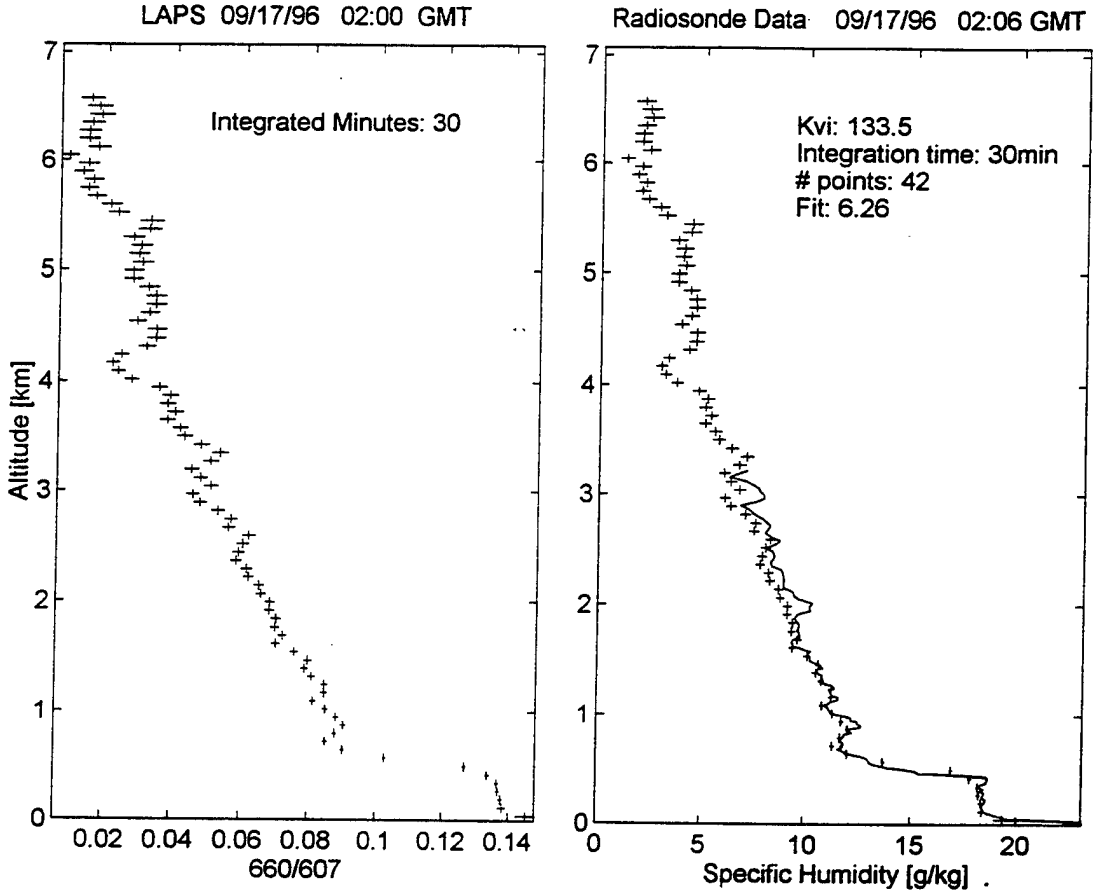


Figure 3 (b). The water vapor measurements of the LAPS instrument obtained on the USNS Sumner on 17 September 1996 at 0200-0230 Z (same data as Figure 3a). The profiles show the raw 660/607 wavelength ratio and the fit to the balloon sonde (solid line) at the same time period, both profiles show the statistical error bars ($\pm 1\sigma$) on each data point.

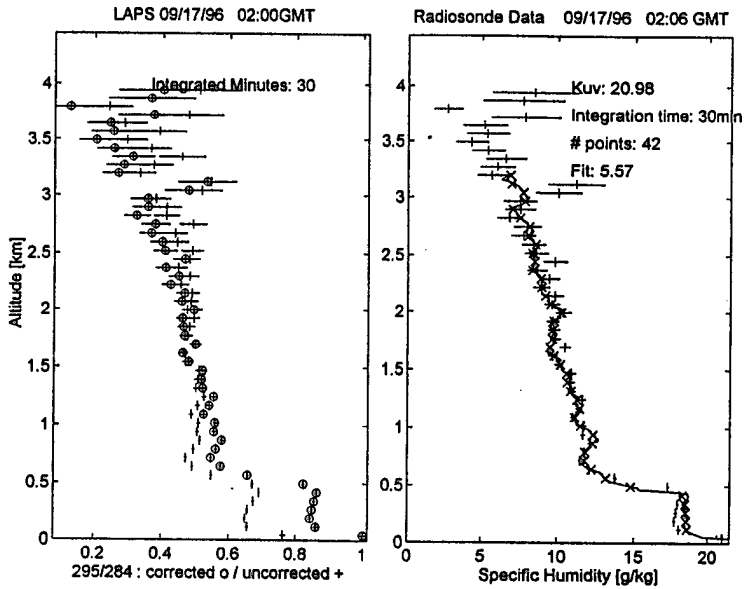


Figure 3(c). The ultraviolet water vapor measurements of the LAPS instrument obtained on the USNS Sumner on 17 September 1996 at 0200-0230 Z (same data as Figure 3a). The profiles show the raw 295/284 wavelength ratio and the fit to the balloon sonde (solid line) at the same time period, both profiles show the statistical error bars (±1σ) on each data point. The difference between the corrected (⊕) and uncorrected (+) signals is due to the ozone absorption.

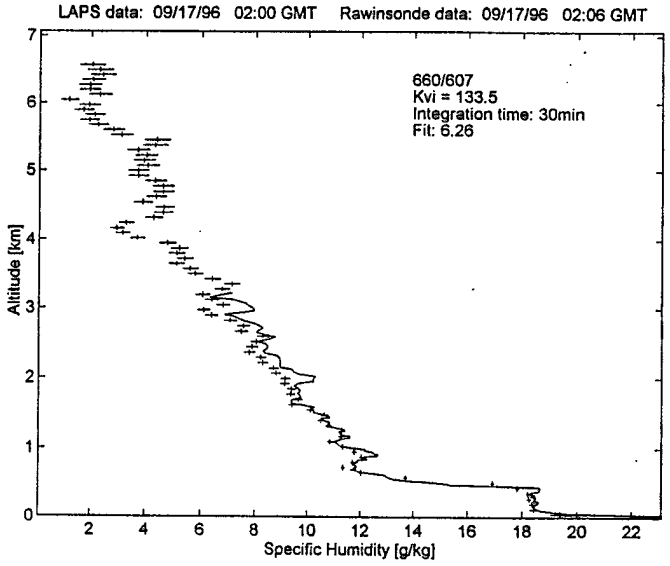


Figure 3(d). The water vapor measurements of the LAPS instrument and rawinsonde balloon obtained on the USNS Sumner on 17 September 1996 at 0200-0230 Z (same data as Figure 3a). The profiles show the water vapor measurements from the lidar and from the balloon sonde (solid line) at the same time period, the lidar profile shows the statistical error bars (±1σ) on each data point.

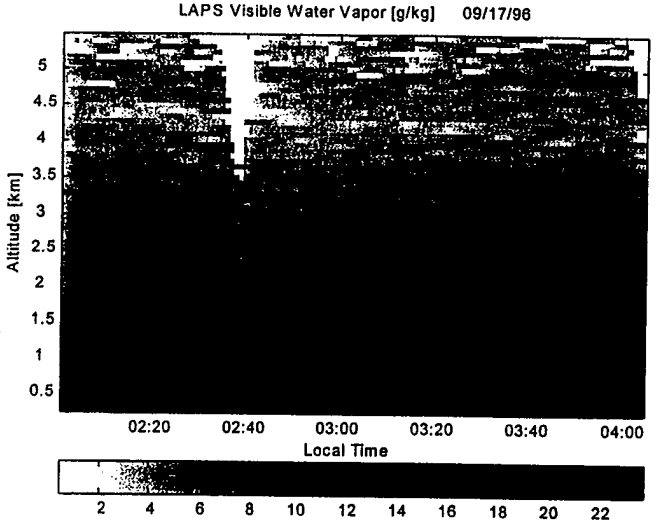


Figure 3(e). The trend of the 1 minute water vapor data is displayed for the period between 0200 and 0400 on 17 September 1996. The black and white display shown here does not give a good indication of the data quality observed by the operator in real time from the false color display. The scale gives the specific humidity in gm/kg. These measurements were obtained during a cloudy period and at 0238 a small cloud is observed to drift through the lidar beam.

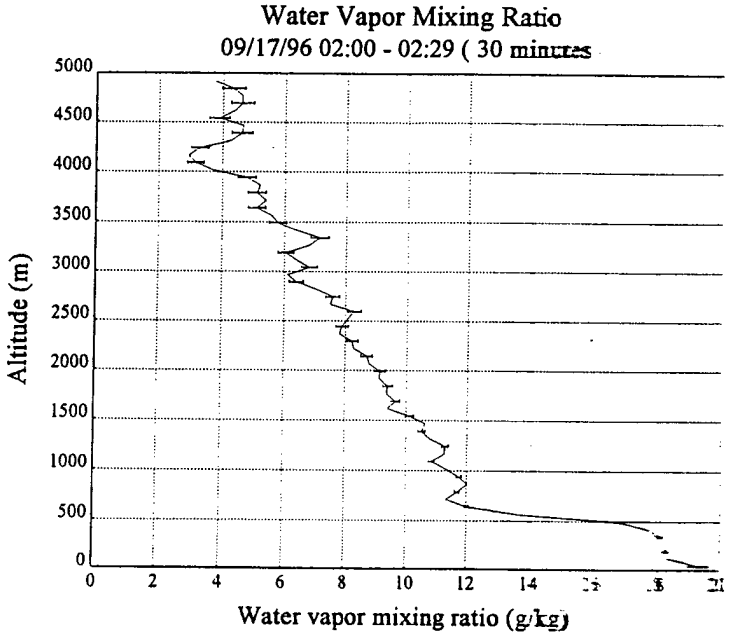


Figure 4(a). The temperature measurements as displayed by the real time display program of the LAPS instrument obtained on the USNS Sumner on 17 September 1996 at [illegible] Z. The profile includes the statistical error bars (±1σ) on every other data point. At upper altitudes the temperature data has been smoothed using a Hanning filter.

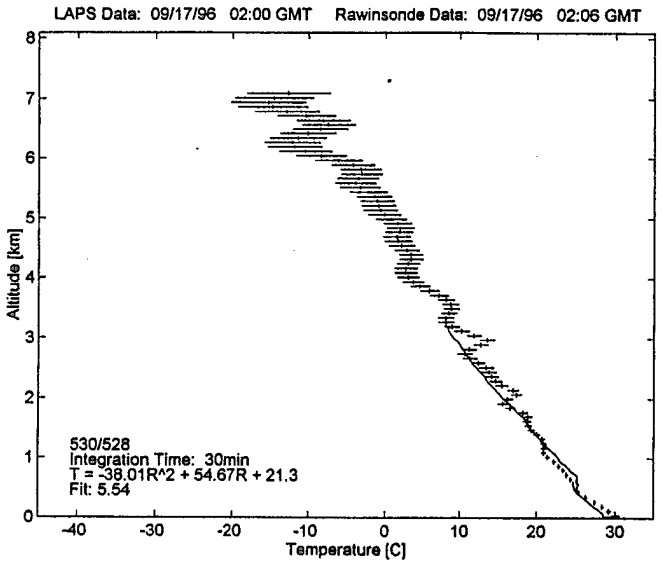


Figure 4(b). The temperature measurements from the LAPS instrument compared with a rawinsonde balloon release on the USNS Sumner on 17 September 1996 at 0200-0230 Z. The lidar profile includes the statistical error bars (±1σ) on every other data point. At upper altitudes the temperature data has been smoothed using a Hanning filter. These are the same results as the lidar data as those displayed in the real time display shown in Figure 4a.

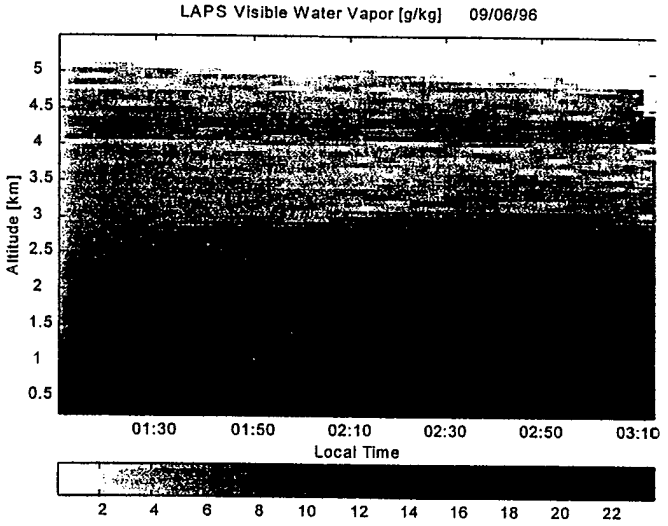


Figure 5. A time sequence of the 1 minute water vapor profiles show the variations that occur in the water vapor. The period of 0100 to 0300 on 6 September shows one of the typical unsettled periods where large variations occur in the boundary layer and elevated moist layers. This display is an attempt to show the variations observed by the operator in the false color display as a black and white figure.

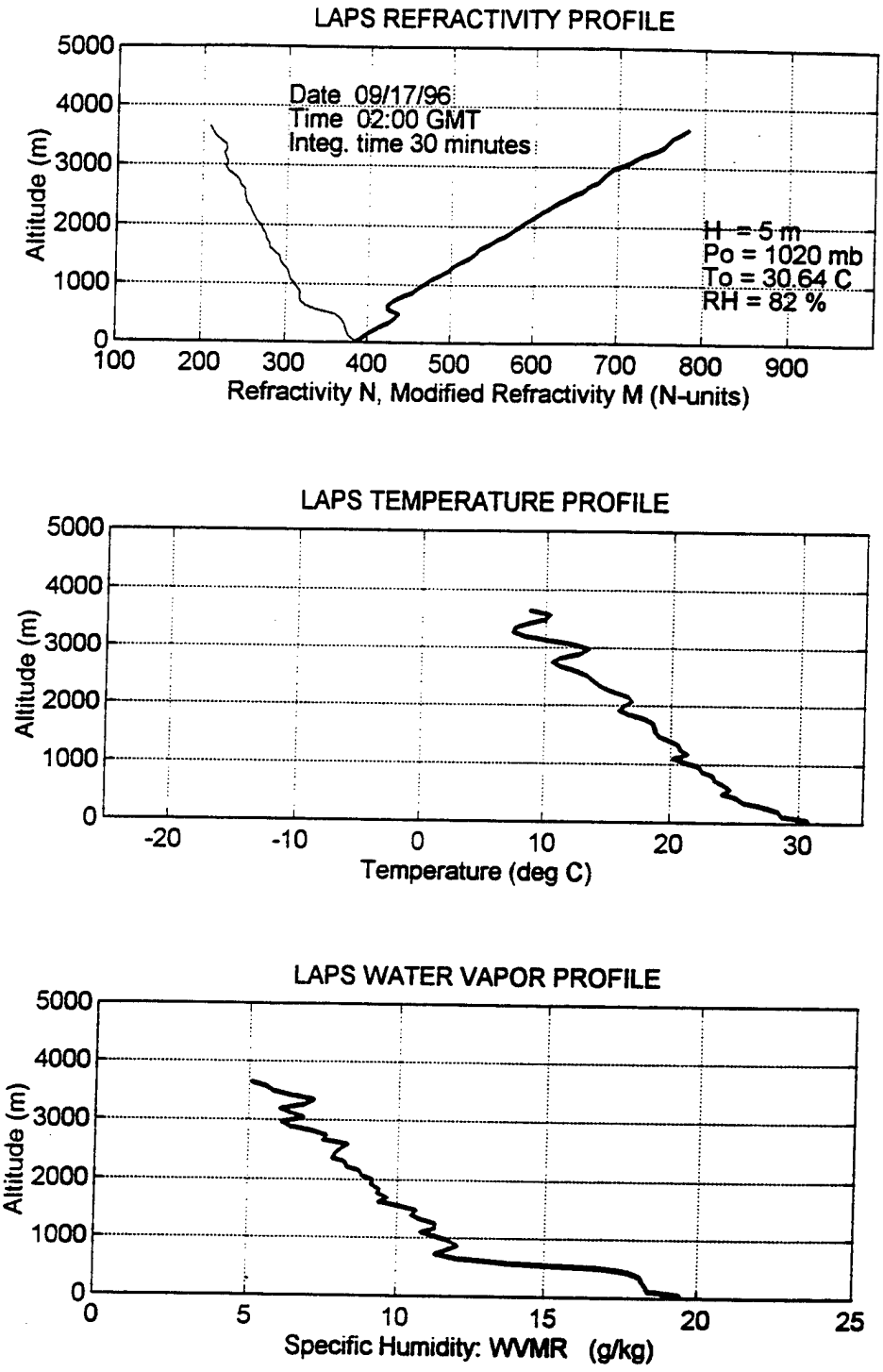


Figure 6. The lower panels show the water vapor (Figure 3a) and temperature (Figure 4a) measurements from the data gathered onboard the USNS Sumner on 17 September 1996. The upper panel shows the RF-refractivity (thin line) and modified refractivity (thick line) profiles calculated from the lidar measurements of water vapor and temperature.

SUMMARY

The completion of the fabrication and demonstration testing of the LAPS instrument during 1996 has shown that lidar can be developed to a level which permits routine measurements of atmospheric properties. The automated controls of many functions, which have typically isolated lidar within research laboratories, are not a problem and should not continue to limit the useful applications of lidar techniques. The LAPS has demonstrated that a rugged, weather sealed, instrument can be operated routinely and provide real time data products. The measurements can be made 24 hours per day and though limited in height, the daytime measurements of the lower atmosphere can certainly be performed.

The LAPS instrument tests have demonstrated the measurements of the real time profiles of the properties which determine the RF-refractivity. The temperature and water vapor measurements are part of the critical parameters which weather balloons provide today and the lidar techniques will provide in the future. Basically, the tests and evaluation of the LAPS lidar has demonstrated the following points:

(1) Real-time profiles of RF refractivity
(2) Nighttime measurements of water vapor, 0 - 10 km
(3) Daytime measurements of water vapor, 0 - 4 km
(4) Rotational Raman temperature profiles, 0 - 10 km
(5) Aerosol extinction profiles, 0 - 10 km
(6) Ozone measurements, 0 - 3 km

The measurements of the LAPS instrument have been limited to 75 meter range resolution, however, the bench testing on newly developed high speed electronics will allow us to measure the future profiles with 7 meter resolution. The LAPS instrument is ready to be commercialize for use as land-based and shipboard instrument.

REFERENCES

1. "LAMP Lidar Tests at Point Mugu" Report for METOC Systems Program Office PMW-175, **ARL Report No. 94-2084-LP029**, July 1994.

2. "Multiple-wavelength Raman Lidar Measurements of Atmospheric Water Vapor," S. Rajan, T. J. Kane and C. R. Philbrick, **Geophys. Res. Let.** 21, 2499-2502, 1994.

3. "Lidar Measured Refractive Effects in a Coastal Environment," D. W. Blood, S. McKinley, C. R. Philbrick, R. Paulus and T. Rodgers, **Proceedings of IGARSS'94** (International Geophysics and Remote Sensing Symposium) at UCLA in Pasadena CA, August 1994, Vol I, pg 394-396, 1994.

4. "Lidar Measurements of Water Vapor Concentrations in the Troposphere," C. R. Philbrick, **Proceedings of IGARSS'94** (International Geophysics and Remote Sensing Symposium) at UCLA in Pasadena CA, August 1994, Vol IV, pg 2043-2045, 1994 .

5. "Pure Rotational Raman Lidar for Temperature Measurements in the Lower Troposphere," Paul A. T. Haris, PhD Thesis for Penn State University, Department of Electrical Engineering, August 1995.

6. "Lidar Measurements of Refractive Propagation Effects," C. R. Philbrick and D. W. Blood, in **Propagation Assessment in Coastal Environments**, NATO-AGARD CP 567, Paper 3, 13 pg, 1995.

7. "Remote Sensing by Active and Passive Optical Techniques," C. R. Philbrick, M. D. O'Brien, D, B. Lysak, T. D. Stevens and F. Balsiger, **NATO/AGARD Proceedings on Remote Sensing**, AGARD-CP-582, 8.1-8.9, 1996.

8. "Comparison of Lidar Water Vapor Measurements Using Raman Scatter at 266 nm and 532 nm," R. Harris, F. Balsiger and C. R. Philbrick, **Proceeding of IGARSS96 Conference on Remote Sensing for a Sustainable Future**, (International Geophysics and Remote Sensing Symposium) at Lincoln NB, May 1996, Vol III pg 1826-1829, 1996.

9. "Lower-tropospheric Temperature Measurements Using a Rotational Raman Lidar," F. Balsiger, P. A. T. Haris and C. R. Philbrick, in **Optical Instruments for Weather Forecasting**, SPIE Proceedings Vol. 2832, 53-60, 1996.

10. "Comparison of Lidar Water Vapor Measurements Using Raman Scatter at 266nm and 532 nm," F. Balsiger and C. R. Philbrick, in **Applications of Lidar to Current Atmospheric Topics**, SPIE Proceedings Vol. 2833, 231-240 1996.

11. "Particle Size Distributions and Extinction Determined by a Unique Bistatic Lidar Technique," T. D. Stevens and C. R. Philbrick, **Proceeding of IGARSS96 Conference on Remote Sensing for a Sustainable Future** (International Geophysics and Remote Sensing Symposium) at Lincoln NB, May 1996, Vol II pg 1253-1256, 1996.

12. "Optical Extinction from Raman Lidar Measurements," M. D. O'Brien, T. D. Stevens and C. R. Philbrick, in **Optical Instruments for Weather Forecasting**, SPIE Proceedings Vol. 2832, 45-52, 1996.

13. "Bistatic Lidar Measurements of Lower Tropospheric Aerosols," Timothy D. Stevens, PhD Thesis for Penn State University, Department of Electrical Engineering, May 1996.

Battle Space Weather Conditions for Joint Strike Support

by
Jay Rosenthal, Matt McGovern, and Roger Helvey
Geophysics Branch
Naval Air Warfare Center Weapons Division
Point Mugu, California 93042

Abstract:

Battlespace meteorological and oceanographic (METOC) conditions can be defined and displayed using the Navy's C4I architecture for use in strike planning, optimizing weapons performance, and post-operation assessment. Using the Tactical Environmental Support System (TESS), METOC satellite imagery has been exploited to derive estimates of temperature and cloud conditions along Tomahawk flight paths, and integrated with operational geometry to support missile launches conducted during Joint Warrior Interoperability Demonstration (JWID)-95. The integrated displays were sent from the Battle Management Interoperability Center (BMIC) at the Naval Air Warfare Center Weapons Division at Point Mugu, and transmitted via JMCIS/SIPRNET to CINCPACFLT at Pearl Harbor, where they were inserted as strike warfare support products on a home page for transmission to other JWID participants.

TESS architecture is also being used to define cloud and other METOC conditions during support of Joint Stand-Off Weapon (JSOW) testing, during SHAREM exercises in the Arabian Gulf, and for transfer of METOC data to the Tactical Aircraft Mission Planning System (TAMPS).

Additional capability is being developed using processed visual and infrared satellite data to estimate duct height topography over low-cloud covered regions of the ocean covering thousands of square miles. In combination with overlays of large scale pressure and temperature fields, the products are also useful in relating weather map features to anticipated EM/EO propagation conditions.

1. Background:

As one of the most crucial factors in determining the outcome of warfare, weather and other METOC data describing conditions

throughout the battlespace need to be quickly transmitted and understood by the warrior and mission planner. Although current efforts are underway to exploit METOC data in a PC environment, considerable capability exists now within the present C4I architecture to provide automated data directly to the warfighter. As an integral part of the Joint Maritime Command Information System (JMCIS), the Navy's Tactical Environmental Support System (TESS) can transmit digital grid and satellite data via SIPRNET from its TESS Remote Workstation (TRWS) to another TRWS-equipped platform anywhere afloat. By combining satellite imagery and extracted digital data on one display, some simple but highly informational products can be provided to describe METOC conditions throughout the battlespace in time for use as real-time or planning products. Some of this capability is both being developed and demonstrated in the Battle Management Interoperability Center (BMIC) located at the Naval Air Warfare Center Weapons Division (NAWCWPNS), Point Mugu, California. Under the sponsorship of the Space and Naval Warfare Systems Command METOC Systems Program Office (PMW-185), these capabilities are being developed, demonstrated, validated and transitioned to operational products.

2. Joint Strike Weapons Support:

During the test and evaluation of the Joint Stand-Off Weapon (JSOW) at both the China Lake Land Range and Point Mugu Sea Range, Geophysics Branch personnel exploited the TESS capabilities to ready the JSOW planning process for eventual operational use of METOC data. Since wind is a critical parameter for this glide weapon, gridded winds from the Navy's Operational Regional Atmospheric Prediction System (NORAPS) were received from the Fleet Numerical METOC Center (FNMOC) in Monterey at several levels and displayed over a grid of the Southern California operation area (figure 1). This enabled consideration of the inherent resolution and representativeness of the model output.

Since cloud occurrence, height and temperature will also be important for subsequent variants of JSOW, METOC satellite imagery has been used to demonstrate the ability to diagnose these conditions at launch, enroute, and target areas. A valuable and easy to interpret display was developed on the TRWS by combining a visual TIROS satellite image showing cloud conditions and specific geographical features over the operational area of interest, as shown in figure 2. Superimposed were isotherms of surface temperature derived from the TESS data base for as close to operation time as possible. Last, but

not least, an overlay of the planned/actual missile flight path was developed so that the environmental weather conditions displayed on the screen could be specifically related to the actual coordinates and location of the missile path. By implementing this relatively easy to produce product on the TRWS, the display can then be relayed via the JMCIS system to any other participant in the operation for use in planning or performance assessment.

3. Mission and Strike Planning:

To effectively exploit METOC data for use in mission or strike planning, it is necessary to define weather conditions throughout the battlespace in real-time or for short periods in advance, and be able to provide the product to the warfighter in a quick and easy-to-understand form. Although the architecture is still evolving, several aspects of this requirement can be demonstrated and utilized today using the current configurations of TESS.

As was shown above for JSOW support, similar satellite-based capabilities were demonstrated for strike planning by NAWCWPNS in support of JWID-95. In this scenario, a Tomahawk missile was launched from the Sea Range to a target at Fallon, Nevada. As was done for real missions during Desert Storm, METOC satellite data was used to estimate temperatures along the flight path, only this time, the process was largely automated through TESS and displayed on the TRWS along the planned missile flight path. In addition, visual cloud conditions, geographic features and operational information were also displayed on the single product, so that the integrated effects of the METOC environment could be quickly assessed over each segment of the planned operation. This is shown in figure 3.

To demonstrate the ability to put these capabilities in the hands of the user, strike warfare products were transmitted via SIPRNET in BMIC to CINCPACFLT at Pearl Harbor where they were installed on the JWID METOC Home Page. The menus and product listings were then posted as shown in figures 4 and 5 where they could be accessed by other JWID participants. In addition, Geophysics personnel were able to successfully demonstrate sending strike planning products directly to the Tomahawk shooter.

In order to provide short-term forecasts of cloud cover in a form readily useable by the warrior, NAWCWPNS, under SPAWAR sponsorship, collaborated with the Naval Research Laboratory (NRL) in Monterey and NRaD in San Diego to implement the Nagle Cloud Advection Model (NCAM) which essentially provides forecast 'satellite' images based on sound physical and meteorological

processes. NCAM has been implemented on the TESS Maxion computer as well as on a TAC-3 computer. An early form of the capability was successfully demonstrated during a recent SHAREM exercise at the Naval European METOC Center at Rota, Spain.

Successful tactical exploitation of METOC satellite data will also necessarily require the use of geostationary imagery so that changes in cloud/storm conditions can be quickly detected and animated. NAWCWPNS has been performing test and evaluation of a geostationary satellite display system and has successfully demonstrated the ability to animate several images in a time-sequence (similar to satellite 'loops' available on television) and transmit the images from the TRWS to Rota and to San Diego. Although a great deal of development remains to combine these functionalities into other existing satellite display systems, the crucial capability of providing high-resolution geostationary satellite imagery to a TRWS-equipped platform anywhere afloat has been demonstrated for the first time without the need for special satellite-receiving antennaes onboard.

Another mission planning application of METOC data is also being tested and evaluated in BMIC at NAWCWPNS. The Tactical Aircraft Mission Planning System (TAMPS) will be the provider of METOC data and products to a variety of mission planning and weapons support activities. With the assistance of personnel from NRaD and SPAWAR, the ability to transfer METOC data from TESS and TRWS to TAMPS, long a goal of NAVAIR and SPAWAR, has been recently demonstrated at Point Mugu. Gridded data and horizontal weather depictions were successfully sent from BMIC to the Central Data Base Server (CDBS) from where TAMPS was able to access the data. After some planned updates in hardware and configuration, the ability to send a variety of products from TESS to TAMPS should be feasible.

4. EM/EO Propagation Environment

To characterize the EM/EO propagation environment over broad sub-tropical ocean regions, capabilities are being developed to automatically translate satellite-derived estimates of cloud-top temperatures into estimates of elevated duct height. Termed the "Satellite IR-duct" technique, the capability provides a description of how the propagation environment varies in the horizontal. As shown in figure 6, duct height estimates can then be displayed atop satellite imagery (either visual or IR), and overlayed with synoptic scale analyses of pressure, height and temperature fields to improve the understanding and predictability of how weather systems influence

propagation conditions. The satellite-IR duct technique requires clouds in inversion-dominated weather regimes. A complementary technique under development by the Naval Postgraduate School allows duct height estimates from satellite data in cloud-free regions. An independent method of estimating duct height over either cloudy or clear conditions has been developed from gridded data by Roger Helvey. Termed the "Equivalent Altitude", results from this method are displayed in figure 7 for approximately the same time as shown in figure 6.

5. Summary:

The process of exploiting satellite and other METOC data for real-time weapons support and mission/strike planning has been demonstrated at Point Mugu in a much more automated fashion than has been previously used operationally. Even as the architecture migrates to a more PC environment, the critical elements of combining satellite-derived depictions of cloud cover, temperature, duct height geographical and operational data and other important environmental information, and sending simple and useful displays via JMCIS and standard communication links to the warrior has been demonstrated.

6. References:

(1) McGovern, M., J. Rosenthal and R. Nagy, "Summary of TESS(3) METOC Support for JWID-95 from the BMIC", Geophysics Technical Note No. 193, NAWCWPNS, Point Mugu, 1995

(2) McGovern, M., "Tactical Environmental Support System (TESS(3) Semi-Automated Procedures for Displaying and Exploiting Satellite-Derived Land Temperatures Along Missile Flight Paths", Geophysics Technical Note No. 198, NAWCWPNS, Point Mugu, Nov 1996

(3) Greiman, P., J. Rosenthal and R. A. Helvey, "Synoptic Variability Revealed by Satellite and Equivalent Altitude", paper No. 40, NATO AGARD Conference on Remote Sensing, AGARD-CP-582, Oct 1996

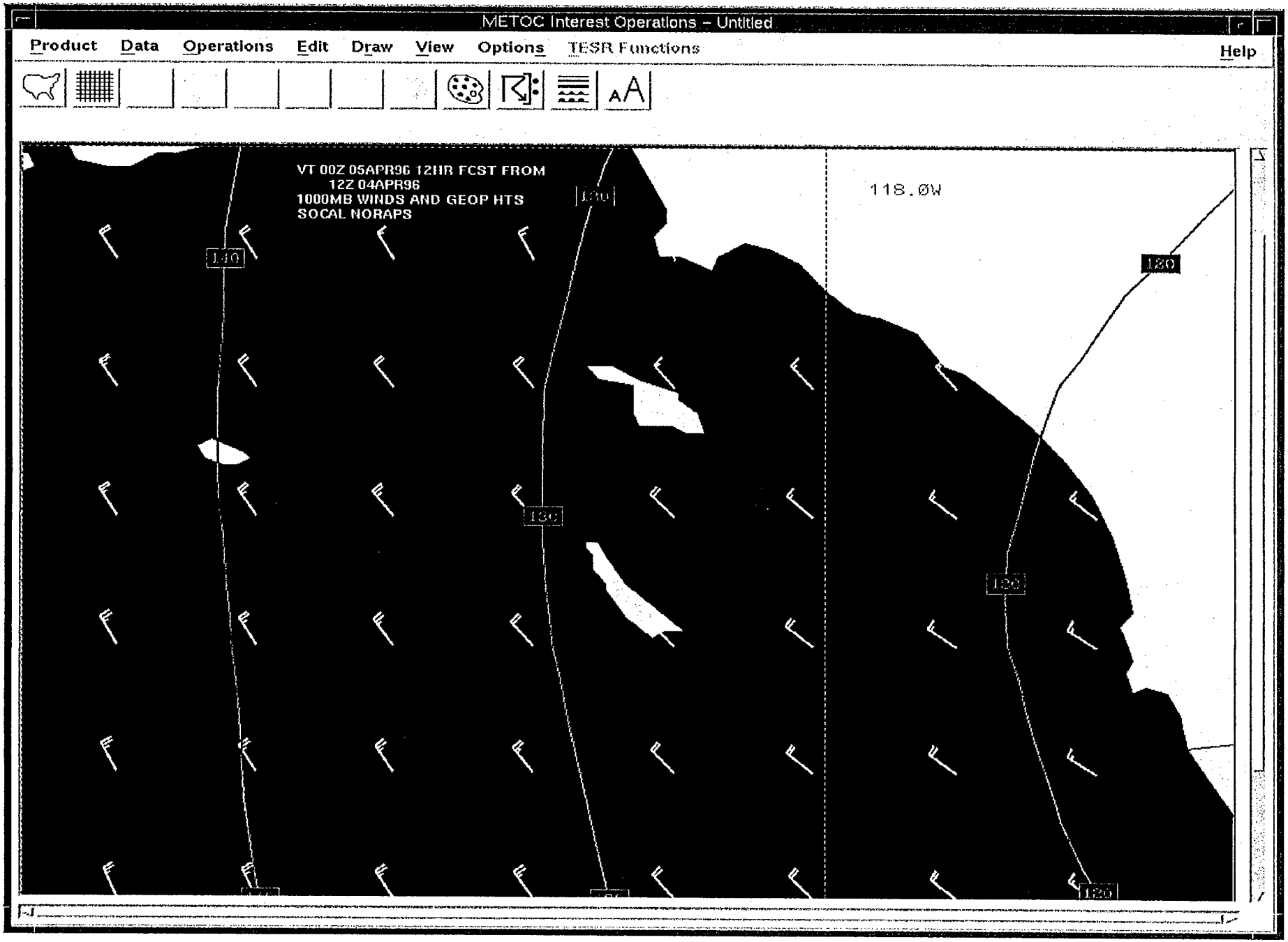


Figure 1. TESS-provided high resolution wind field for JSOW T&E

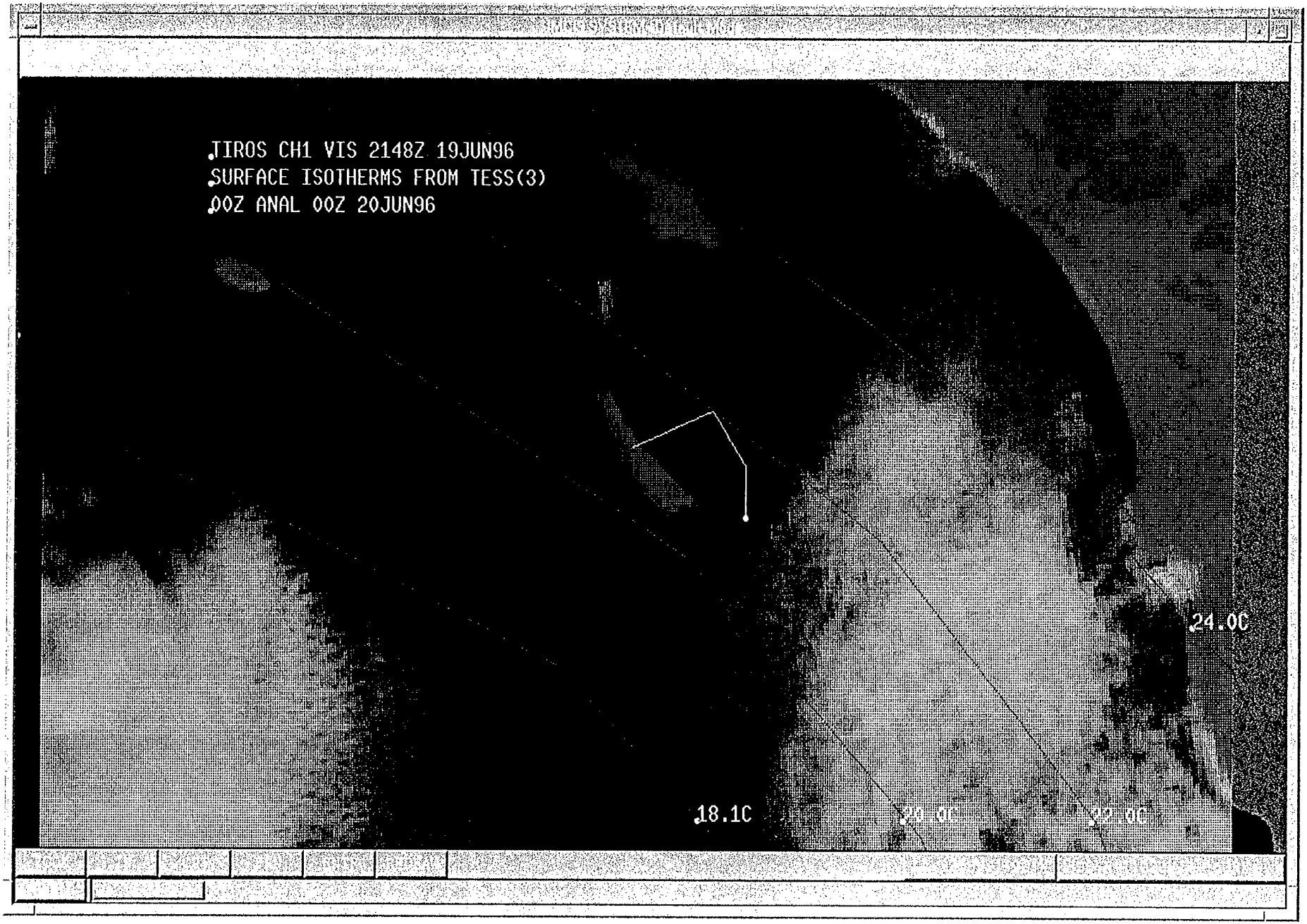


Figure 2. TRWS satellite product for JSOW combining cloud cover, temperature and operational geometry

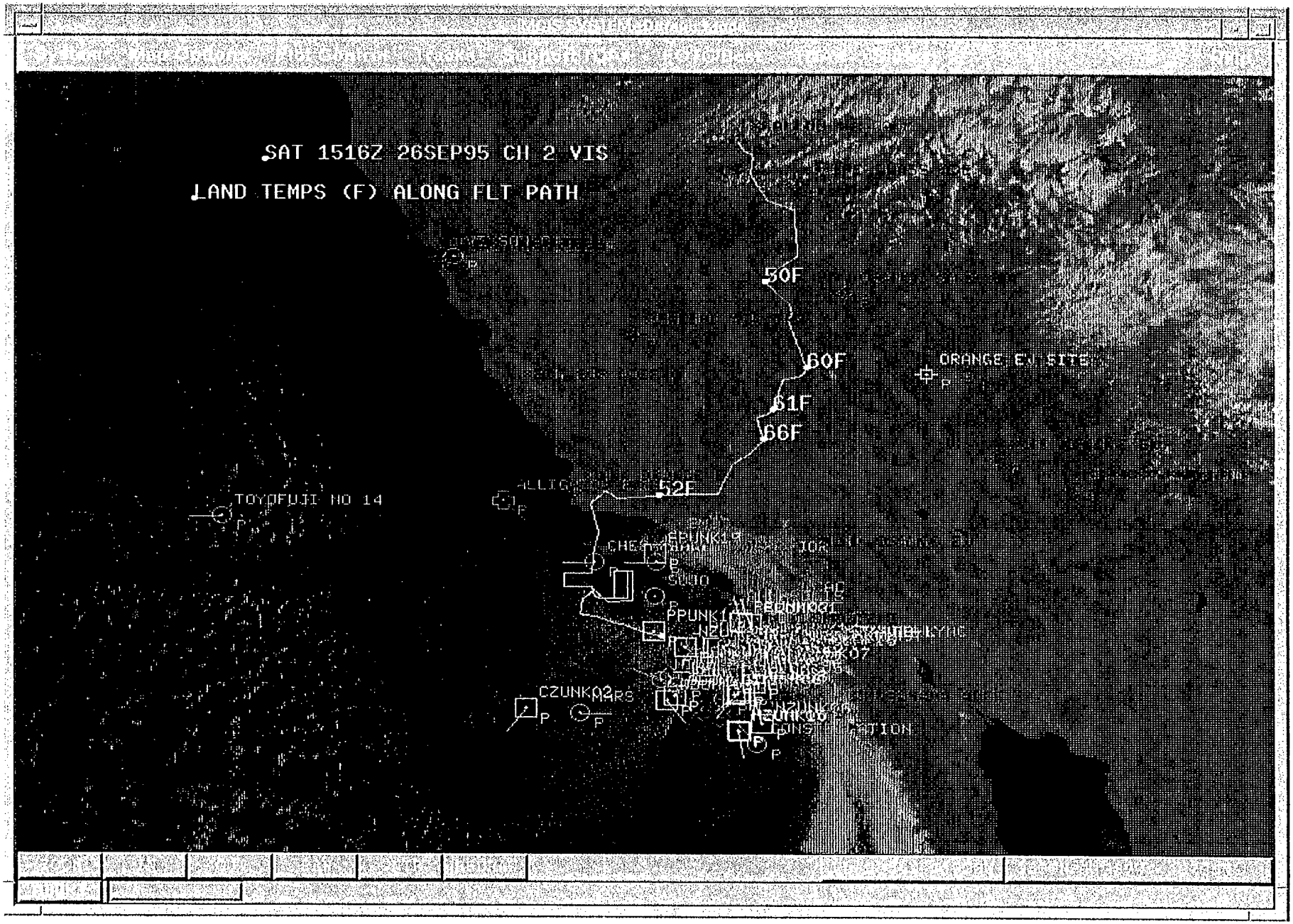


Figure 3. JWID-95 strike warfare support product combining cloud cover, Tomahawk flight path geometry and temperature along path

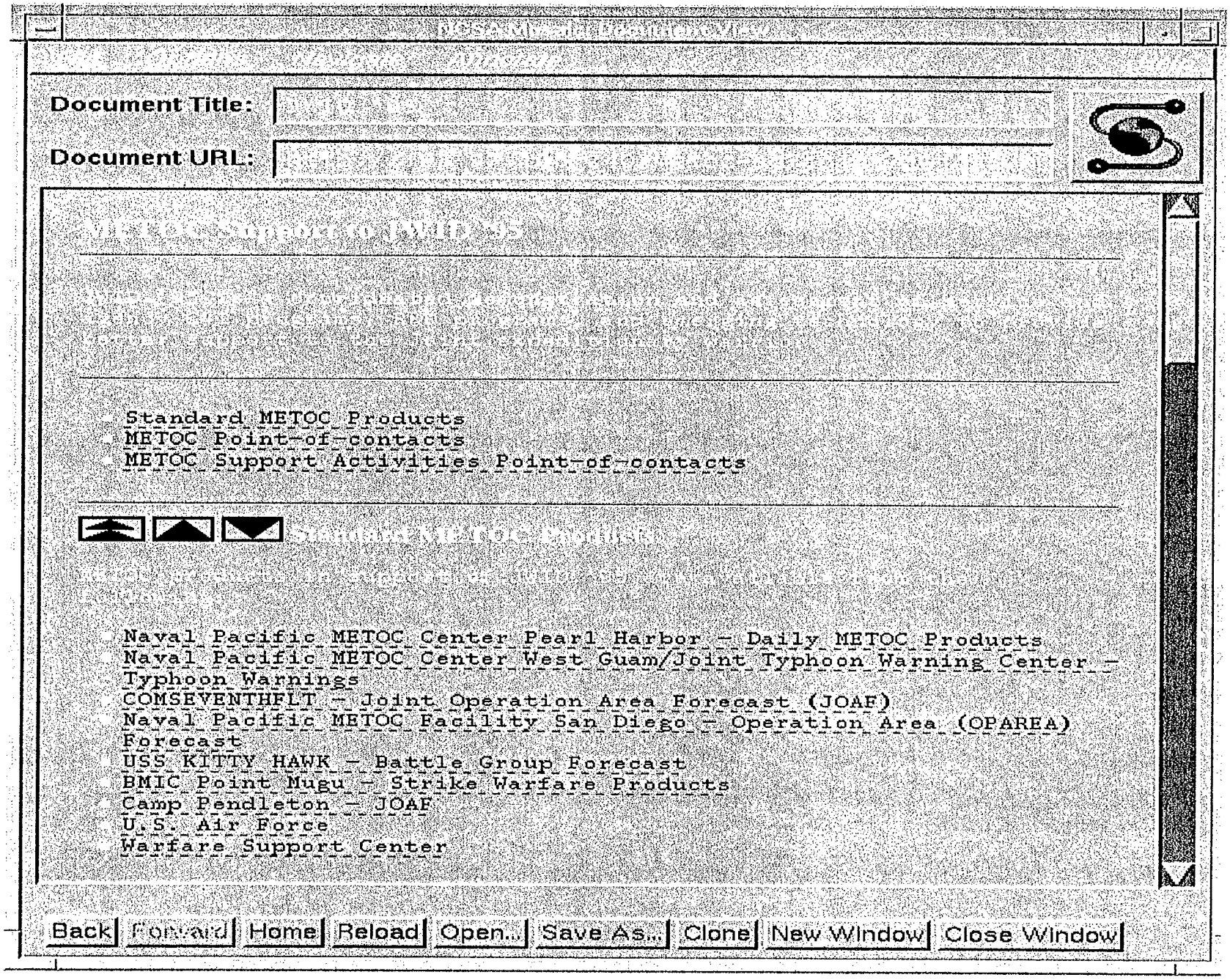


Figure 4. JWID-95 CINCPACFLT METOC Home Page product sources

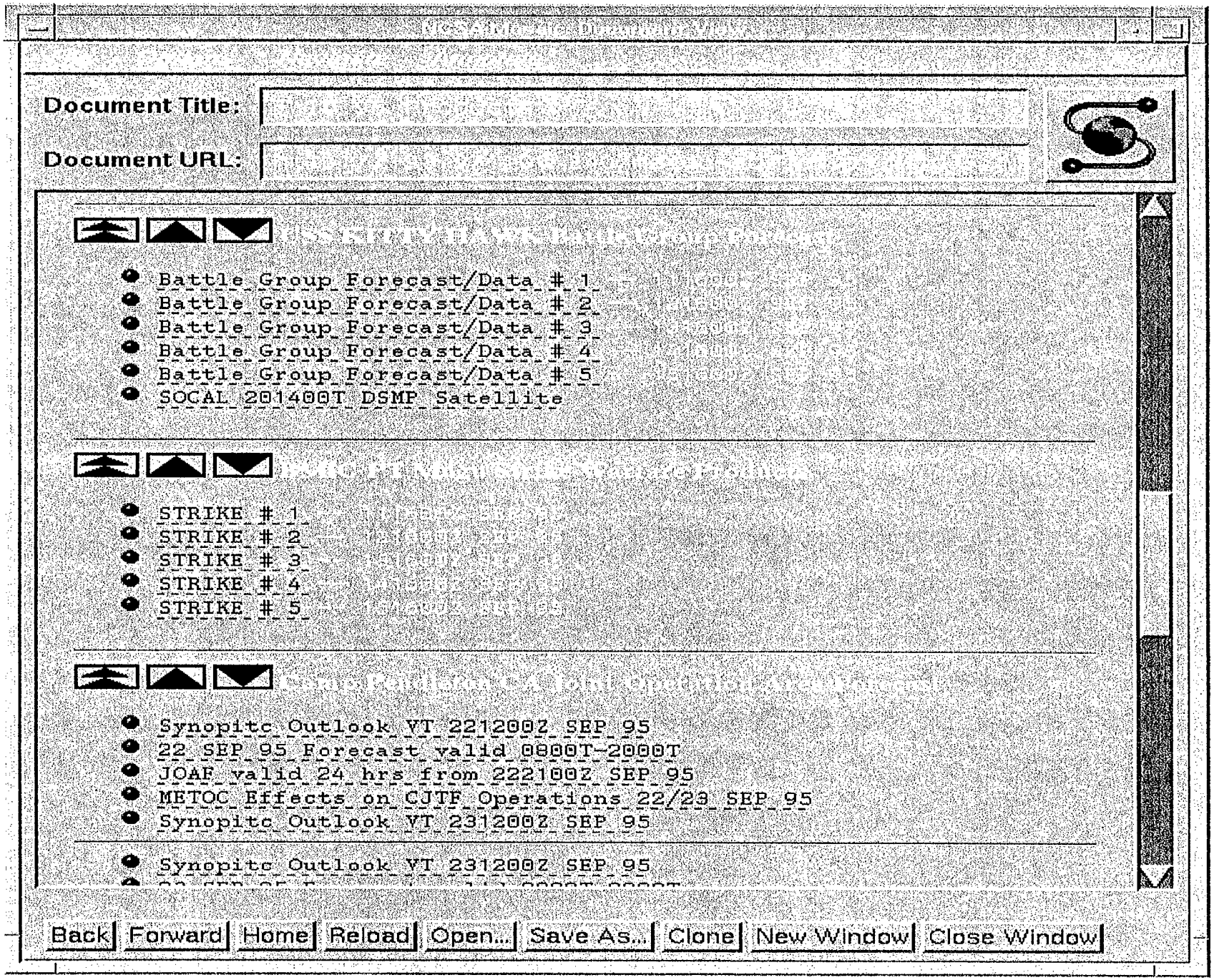


Figure 5. JWID-95 CINCPACFLT METOC Home Page product listings

Figure 6. Duct height estimates from Satellite-IR duct technique superimposed on visual cloud image and upper air flow pattern.

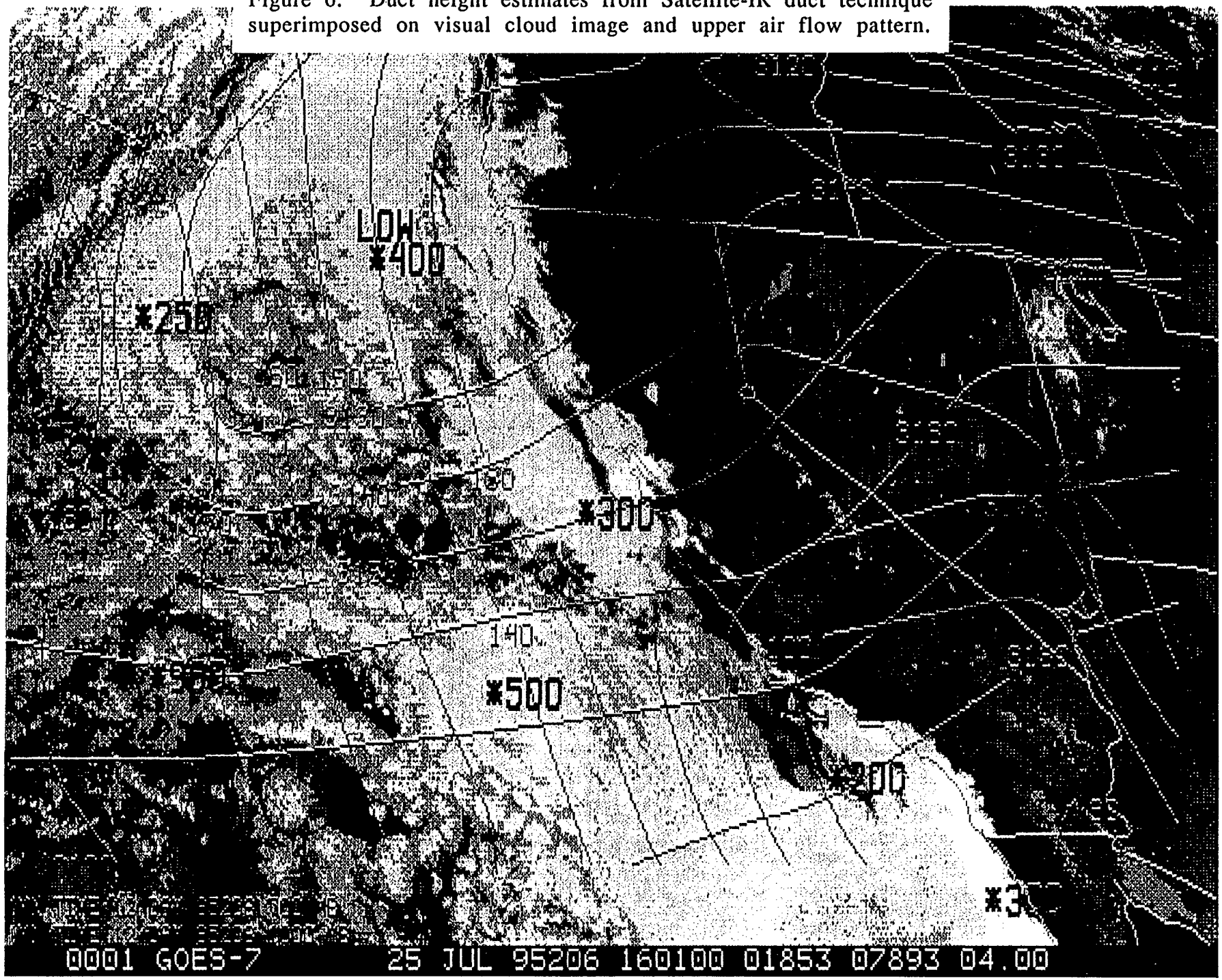
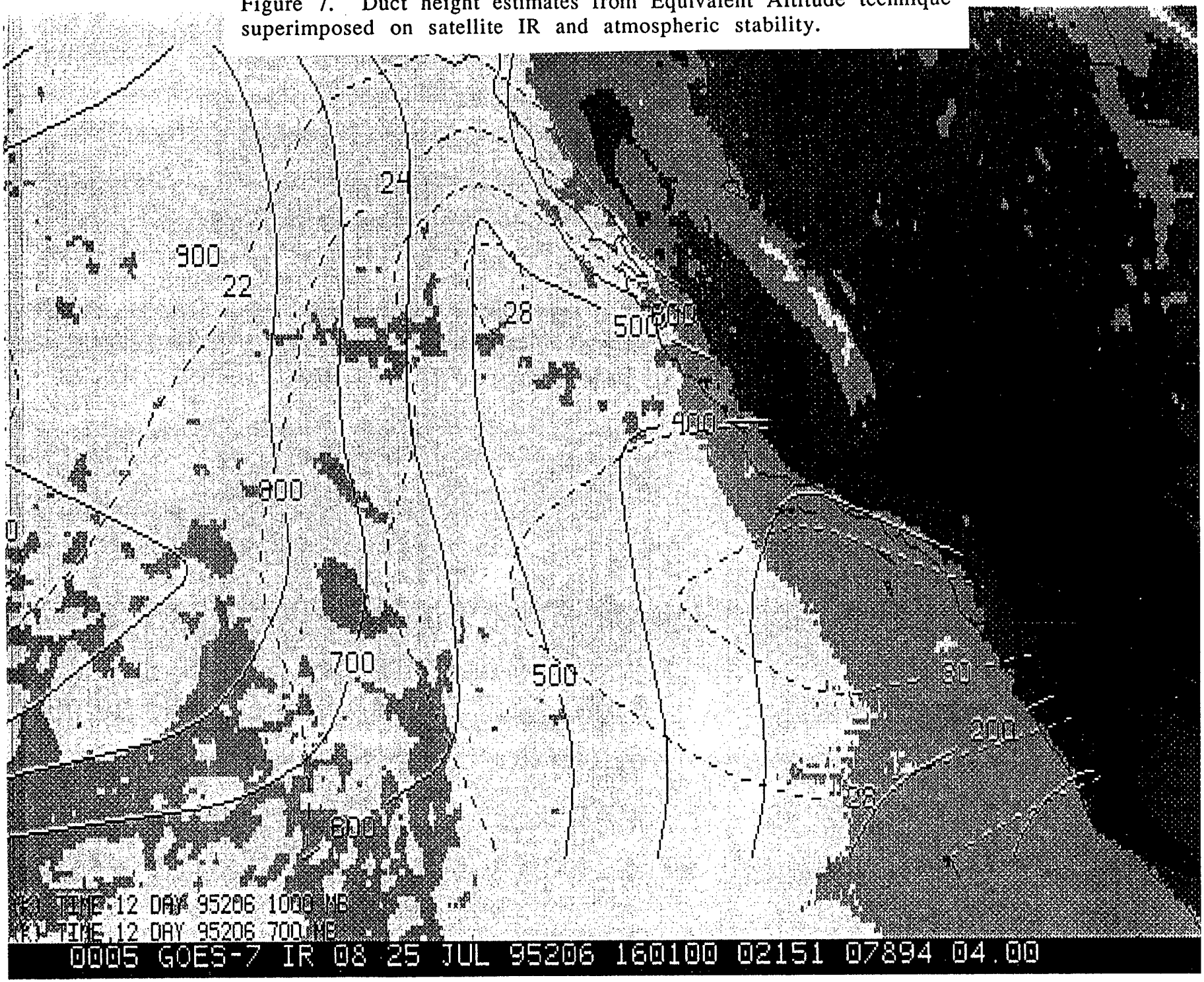


Figure 7. Duct height estimates from Equivalent Altitude technique superimposed on satellite IR and atmospheric stability.



REPORT DOCUMENTATION PAGE

Form Approved
OMB No. 0704-0188

Public reporting burden for this collection of information is estimated to average 1 hour per response, including the time for reviewing instructions, searching existing data sources, gathering and maintaining the data needed, and completing and reviewing the collection of information. Send comments regarding this burden estimate or any other aspect of this collection of information, including suggestions for reducing this burden, to Washington Headquarters Services, Directorate for Information Operations and Reports, 1215 Jefferson Davis Highway, Suite 1204, Arlington, VA 22202-4302, and to the Office of Management and Budget, Paperwork Reduction Project (0704-0188), Washington, DC 20503.

1. AGENCY USE ONLY *(Leave blank)*	2. REPORT DATE	3. REPORT TYPE AND DATES COVERED
	December 1996	Final 3–5 December 1996

4. TITLE AND SUBTITLE
PROCEEDINGS OF THE BATTLESPACE ATMOSPHERICS CONFERENCE 3–5 DECEMBER 1996

5. FUNDING NUMBERS
PE: 06022435N
AN: DN302216
WU: D88-MPB3

6. AUTHOR(S)
J. H. Richter, K. D. Anderson, eds.

7. PERFORMING ORGANIZATION NAME(S) AND ADDRESS(ES)
Naval Command, Control and Ocean Surveillance Center (NCCOSC)
RDT&E Division
San Diego, California 92152–5000

8. PERFORMING ORGANIZATION REPORT NUMBER
TD 2938

9. SPONSORING/MONITORING AGENCY NAME(S) AND ADDRESS(ES)
Office of Naval Research
800 North Quincy Street
Arlington, VA 22217–5660

10. SPONSORING/MONITORING AGENCY REPORT NUMBER

11. SUPPLEMENTARY NOTES

12a. DISTRIBUTION/AVAILABILITY STATEMENT
Approved for public release; distribution is unlimited.

12b. DISTRIBUTION CODE

13. ABSTRACT *(Maximum 200 words)*

The 1996 Battlespace Atmospherics Conference was held in San Diego, California from 3–5 December 1996. The conference covered modeling, measurement, and prediction of atmospheric effects on electromagnetic, electrooptical, and acoustic systems. A total of 67 papers and 5 poster sessions were presented. This document contains the written versions for most of the presentations and posters.

14. SUBJECT TERMS
Mission area: Surveillance

electromagnetics, electrooptics, acoustics, atmospheric effects

15. NUMBER OF PAGES
640

16. PRICE CODE

17. SECURITY CLASSIFICATION OF REPORT	18. SECURITY CLASSIFICATION OF THIS PAGE	19. SECURITY CLASSIFICATION OF ABSTRACT	20. LIMITATION OF ABSTRACT
UNCLASSIFIED	UNCLASSIFIED	UNCLASSIFIED	SAME AS REPORT

21a. NAME OF RESPONSIBLE INDIVIDUAL	21b. TELEPHONE *(include Area Code)*	21c. OFFICE SYMBOL
K. D. Anderson	(619) 553-1420	Code D883